

# **System and safety studies of accelerator driven transmutation**

## **Annual Report 2005**

Waclaw Gudowski, Jan Wallenius, Vasily Arzhanov,  
Mikael Jolkkonen, Marcus Eriksson, Per Seltborg,  
Daniel Westlén, Christina Lagerstedt, Patrick Isaksson,  
Carl-Magnus Persson, Alexandra Ålander

Department of Nuclear and Reactor Physics  
Royal Institute of Technology  
Stockholm, Sweden

November 2006

**Svensk Kärnbränslehantering AB**

Swedish Nuclear Fuel  
and Waste Management Co  
Box 5864  
SE-102 40 Stockholm Sweden  
Tel 08-459 84 00  
+46 8 459 84 00  
Fax 08-661 57 19  
+46 8 661 57 19



ISSN 1402-3091

SKB Rapport R-06-122

# **System and safety studies of accelerator driven transmutation**

## **Annual Report 2005**

Waclaw Gudowski, Jan Wallenius, Vasily Arzhanov,  
Mikael Jolkkonen, Marcus Eriksson, Per Seltborg,  
Daniel Westlén, Christina Lagerstedt, Patrick Isaksson,  
Carl-Magnus Persson, Alexandra Ålander

Department of Nuclear and Reactor Physics  
Royal Institute of Technology  
Stockholm, Sweden

November 2006

The full report including all Appendices is available as a .pdf-file on the enclosed CD-ROM-disc. The printed version contains only the main text and a list of the Appendices.

This report concerns a study which was conducted for SKB. The conclusions and viewpoints presented in the report are those of the authors and do not necessarily coincide with those of the client.

## Preface

The research on safety of Accelerator-Driven Transmutation Systems (ADS) at the Department of Nuclear and Reactor Physics reported here has been focused on different aspects of safety of the Accelerator-Driven Transmutation Systems and on Transmutation research in more general terms. An overview of the topics of our research is given in the Summary which is followed by detailed reports as separate chapters and subchapters.

Some of the research topics reported in this report are referred to appendices, which have been published in the open literature. Topics, which are not yet published, are described with more details in the main part of this report. The main report is also included in a PDF-format on a CD-ROM attached to this report. The Appendices are only included on the CD-ROM disc.

Blue text color in a PDF version of this report implies links which can take a reader by a mouse click to the referred part of the report or to a referred Appendix.

A summary in Swedish is given in the chapter called “SAMMANFATTNING”.

# SUMMARY

The results of the research activities on System and Safety of Accelerator-Driven Transmutation (ADS) at the Department of Nuclear and Reactor Physics are described in this report followed by the Appendices of the relevant scientific papers published in 2005. PhD and Licentiate dissertations of Marcus Ericsson, Per Seltborg, Christina Lagerstedt and Daniel Westlén (see Appendices) reflect the research mainstream of 2005. Year 2005 was also very rich in international activities with ADS in focus. Summary of conferences, seminars and lecturing activities is given in Chapter 9

Research activities of 2005 have been focused on several areas:

- system and safety studies of ADS
- subcritical experiments
- ADS source efficiency studies
- nuclear fuel cycle analysis
- potential of reactor based transmutation
- ADS fuel development
- simulation of radiation damage
- development of codes and methods

Large part of the research activities has been well integrated with the European projects of the 5<sup>th</sup> and 6<sup>th</sup> Framework Programmes of the European Commission in which KTH is actively participating. In particular European projects: RED-IMPACT, CONFIRM, FUTURE, EUROTRANS and NURESIM.

Most important results and conclusions from our studies are summarised below.

## SYSTEM AND SAFETY STUDIES OF ADS:

Design and safety studies have been performed of ADS with americium based fuels and lead-bismuth coolant. Three different types of fuels were investigated:

- Solid solution nitride fuel with zirconium nitride matrix:  $(\text{Pu,Am,Cm,Zr})^{15}\text{N}$
- Composite oxide fuel with magnesium oxide matrix (cercer):  $(\text{Pu,Am,Cm})\text{O}_{2-x} - \text{MgO}$
- Composite oxide fuel with molybdenum matrix (cermet):  $(\text{Pu,Am,Cm}) \text{O}_{2-x} - {}^{92}\text{Mo}$

The inert matrix improve a thermal stability (nitride fuels) and/or to raise the effective thermal conductivity (oxide fuels).

The coolant void worth was identified as the major safety issue of these cores.

A gas-cooled accelerator-driven system dedicated to transmutation of minor actinides has been designed. Thanks to the excellent neutron economy of the uranium-free fuel employed, the pin pitch to diameter ratio (P/D) could be increased to 1.8. The increased

coolant fraction allows for decay heat removal at ambient pressure. The large coolant fraction further results in a low pressure loss—26 kPa over the core, 35 kPa in total. Thanks to the large P/D, the elevation of the heat exchanger necessary to remove decay heat by natural circulation is just more than 1 m. The absence of uranium in conjunction with the presence of 35% (heavy atom) americium in the fuel results in a low effective delayed neutron fraction and a vanishing Doppler feedback, making subcritical operation mandatory ([Appendix 7](#)).

## **SUBCRITICAL EXPERIMENTS**

Two major subcritical experiments have been in focus in 2005:

- Yalina-Booster subcritical experiment in Minsk
- SAD experiment in Dubna

The new experimental program at Yalina-Booster was launched during the fall 2005 with a sophisticated 2 zone core: a fast neutron zone and the thermal neutron zone. A series of experiments have been performed:

- Reaction rates for different detectors at different positions in the core.
- Pulsed neutron source measurements (PNS).
- Source jerk measurements (SJ)
- Noise measurements
- Measurement of the neutron flux at the periphery of the active core.

Experiments were successful in spite of some technical deficiencies which have been noticed and improvement program has been prepared. KTH prepared an IAEA coordinated research program for 2006-2009 focused on Yalina experiment. Integration program of the Yalina experiment with the European Project Eurotrans has been proposed and is under implementation.

SAD experiment experienced a major difficulty in 2005 because of the fire accident at the accelerator site. Parallel to reconstruction work at the accelerator an experimental program of integration of SAD experiment into the Domain 2: Experimental Coupling of Accelerator, Spallation Target and Subcritical Core (ECATS) of the Eurotrans Project has been outlined and proposed to be implemented (see [Appendix 15](#)).

## **DYNAMICS AND KINETICS OF ADS**

Studies on Dynamics and Kinetics of ADS together with Source Efficiency studies have been concluded in two PhD dissertations of Marcus Ericsson ([Appendix 8](#)) and Per Seltborg ([Appendix 9](#)). Major conclusions are:

By itself, subcritical operation provides a distinct safety advantage over critical reactor operation, distinguished by high operational stability and additional margins for positive reactivity insertion. For a uranium-free minor actinide based fuel important safety parameters deteriorate. Specific analyses suggest that operation of such cores in a critical state would be very difficult. The studies of unprotected transients indicate that lead-bismuth cooled accelerator-driven reactors can be effective in addressing the low effective delayed neutron fraction and the high coolant void reactivity that comes with the minor actinide fuel, but some supportive prompt negative feedback mechanism might be considered necessary to compensate for a weak Doppler effect in case of a prompt critical transient. Although lead-bismuth features a high boiling point, the work underlines the

importance of maintaining a low coolant void reactivity value. The transient design studies identified a molybdenum-based Ceramic-Metal (CerMet) fuel with favourable inherent safety features. A higher lattice pitch is suggested to avoid mechanical failure during unprotected loss-of-flow. Detailed coupled neutron kinetics and thermal hydraulic analyses demonstrated that the point kinetics approximation is capable of providing highly accurate transient calculations of subcritical systems. The results suggest better precision at lower  $k_{\text{eff}}$  levels, which is an effect of the reduced sensitivity to system reactivity perturbations in a subcritical state resulting in small spatial distortions. In the course of a beam reliability study, the accelerator was identified as responsible for frequent beam interruptions. It is clear that extensive improvement in the mean-time between beam failures is required.

### ADS SOURCE EFFICIENCY STUDIES

An original concept of the proton source efficiency,  $\psi^*$ , has been developed at KTH during last years in order to study the energy gain of an ADS.  $\psi^*$ , has been studied for various ADS models.  $\psi^*$  is defined in analogy with the neutron source efficiency,  $\varphi^*$ , but relates the core power directly to the source protons instead of to the source neutrons. The main advantages of using  $\psi^*$  instead of commonly used neutron efficiency  $\varphi^*$  are that the way of defining the external source is unique and that  $\psi^*$  is proportional to the energy gain.  $\psi^*$  as a function of different system parameters provides basis for an ADS design with optimal properties for obtaining a high core power over beam power ratio. For instance,  $\psi^*$  was found to decrease considerably with increasing spallation target radius (see Appendix 9). For a gas-cooled systems one can conclude:

- Americium introduction in the fuel of a subcritical core decreases  $\psi^*$ . In a core loaded with americium-based fuels,  $\psi^*$  is around 10% lower than in a MOX fuelled core.  $\psi^*$  is reduced by another 10% when helium is replaced by LBE.
- Both of these effects are due to the strong dependence of fission and capture cross-sections on the incident neutron energy in the 1 MeV region in even-N nuclides, and to slight energy shift in this behaviour of the cross-sections in between the nuclides.

### NUCLEAR FUEL CYCLE ANALYSIS

Studies of the Fuel Cycle at KTH are strongly related to the European Project RED-IMPACT, coordinated by KTH, and has been focused on a hypothetical Swedish scenario. In order to perform these studies new, advanced simulation tools have been developed and are under continuous improvement.

**Equilibrium studies** have been performed showing that four ADS, of 800 MWt each, are sufficient to burn an amount of plutonium and americium corresponding to the build-up of those isotopes in the Swedish reactor fleet with an installed capacity of approximately 10 GWe. It was showed that the plutonium inventory could be more reduced by MOX-recycling in LWR prior to the ADS operations, but on account of slightly higher americium production.

**In a detail Swedish scenario** few options have been defined and considered:

- To dispose the spent fuel as it is in a waste repository for permanent storage and monitoring (Phase-out Scenario);
- To restart several BWR or PWR units to burn/transmute existing plutonium and/or minor actinides in a form of Mixed Oxide or MOX fuel;
- To build one or several Accelerator Driven Systems (ADS) for use as stand alone reactors or more probably for use with a combination with BWR or PWR burners;

BWR MOX reactors are more efficient in burning plutonium in the form of MOX fuel. In this respect BWR reactors supersede PWR ones by approximately 10%. In addition, BWR reactors produce about 10% less americium inventory. However, neither BWRs alone nor PWRs alone are capable of incinerating 99% of TRU.

It was found that ADS reactor park can theoretically in the ideal case burn 99% of transuranium isotopes. The duration of this scenario heavily depends on the time needed for cooling the spent fuel. If we assume 10 years of cooling the nuclear waste from ADS, the scenario duration becomes at least 200 years under most optimistic technical assumptions. The use of advanced pyro-processing with a cooling time of only 2 years dramatically decreases the incineration time down to 50 years only. Moreover, ADS reactors have turned out to be a necessary component to decrease the americium inventory because neither BWR nor PWR alone can provide prevalence of americium destruction over its production during the operation time. Economical advisability of these scenarios calls for further investigation.

Economic analysis of various scenarios has been performed under a number of simplifying assumptions. It has been found that the MOX scenario is more than twice as expensive as ordinary UOX fuel cycle. ADS burners reduce this factor down to about 1.5, in other words electricity produced after year 2025 at a hypothetical combination of BWR MOX reactors together with ADS MOX reactors appears to be approximately 50% more expensive in comparison with the nowadays situation.

**Criticality studies** of the different geological disposal scenarios and different containers show no concerns.

### **POTENTIAL OF REACTOR BASED TRANSMUTATION: The Deep Burn - Modular Helium Reactor (DB-MHR)**

Studies show that DB-MHR can effectively burn LWRs Pu. The benefits of the helium-cooled graphite-moderated reactors are several: many features of passive safety mechanism, low cost, flexibility in the choice of fuel, high conversion energy efficiency, high burnup, resistant TRISO fuel cladding and low power density. Neutronic parameters of this reactor are also very favorable.

Major focus has been on:

- Impact of burnable poison on DB-MHR safety performance have been studies showing of important role of burnable poison for the safety characteristics.
- Axial shuffling simulations
- Possibilities to incinerate the LWRs waste in fertile thorium matrix

More details can be found in [Appendices 3, 4, 5 and 6](#).

## **NUCLEAR FUEL DEVELOPMENT FOR TRANSMUTATION**

In the Confirm project collaboration (Am,Zr)N pellets were fabricated at ITU using dust free methods. The pellets feature good mechanical stability, but their density is low, due to limitations in sintering temperature of AmN.

Modelling of the thermochemical properties of advanced fuels has been continued.

The main areas of fuel modelling have been:

- Calculation and evaluation of mathematical expressions for the inclusion of metallic uranium, uranium nitrides and uranium oxides in the thermochemical database module "ALCHYMY"
- Computer-assisted modelling aiming to examine the possibility of internal redox reactions in (U,Pu)N
- Evaluation of the thermochemical stability of four experimental Russian composite fuels.
- Evaluation of selected properties of candidate fuels discussed in EUROTRANS DM3 in order to select the best fuel for the European Transmuter Project.

## **MATERIAL STUDIES FOR ADS - SIMULATION OF RADIATION DAMAGE**

The present version of the two-band model enables for the first time to simulate the formation of the alpha-prime phase in Fe-Cr, but it needs to be extended to take into account the effects of magnetism. This work is in progress.

The primary damage production in neutron induced collision cascades, extensive simulations were performed by molecular dynamics using different sets of potentials. These potentials (created by us and other authors) predict different displacement threshold energies (for the creation of a single Frenkle pair).

## **DEVELOPMENT OF CODES AND METHOD**

### **Monte-Carlo source convergence acceleration:**

In a frame of the European Project NURESIM a methodology for computing the steady-state core conditions by stochastic approximation was developed by KTH for the Monte Carlo transport TRIPOLI-4 code, together with necessary data flows and implementation details.

Various methods for accelerating the source convergence of the Monte Carlo criticality calculations were studied and compared. The fission matrix method has been selected for a detailed investigation. The performed tests showed the fission matrix method is very suitable to accelerate the source convergence in large reactors with a high dominance ratio. Therefore the fission matrix method is a candidate for implementation into the TRIPOLI-4 code.

### **Fuel Cycle Analyzer (FCA)**

A computer code named Fuel Cycle Analyzer (FCA) has been developed. The code effectively solves point reactor equations of isotopic kinetics by using evaluated production-depletion rates. The code simulates user-defined reactor scenarios to evaluate the impact on the transuranium elements inventory. FCA is meant to be a forerunner for a future more advanced tool for reactor cycle simulations being developed at the department of Nuclear and Reactor Physics, Kungliga Tekniska Högskolan.



## SAMMANFATTNING

Resultaten från forskningsaktiviteten kring System och Säkerhet för Accelerator driven Transmutation (ADS) vid avdelningen för Kärn- och Reaktor fysik beskrivs i denna rapport. Rapporten åtföljs av en CD-ROM med Appendici innehållande de relevanta vetenskapliga artiklar som publicerats av avdelningen under 2005. År 2005 var också rikt på internationella aktiviteter, med ADS i fokus. En sammanfattning av konferenser, seminarier, och undervisningsaktivitet ges i Kapitel 9.

Forskningsaktiviteten under 2005 har fokuserat på flera områden:

- system- och säkerhetsstudier av ADS
- subkriticitetsexperiment
- kalleffektivitetsstudier för ADS
- kärnbränslecykelanalys
- potentialen för reaktor baserad transmutation
- utveckling av ADS-bränsle
- simulering av strålskador
- utveckling av källkod och metoder

En stor del av forskningsaktiviteten har varit väl integrerad med europeiska projekt (inom EU: s 5: e och 6: e ram-program), där KTH deltar aktivt, speciellt inom projekten RED-IMPACT, CONFIRM, FUTURE, EUROTRANS, and NURESIM.

Några viktiga resultat och slutsatser från våra studier sammanfattas nedan.

### SYSTEM- OCH SÄKERHETSSTUDIER AV ADS:

Design- och säkerhetsstudier har utförts av ADS med americium-baserat bränsle och bly-vismuth-kylmedel. Tre olika typer av bränsle studerades:

- fast lösning av nitridbränsle med zirkoniumnitridmatris:  $(\text{Pu,Am,Cm,Zr})^{15\text{N}}$
- kompositoxidbränsle med magnesiumoxidmatris (cermet):  $(\text{Pu,Am,Cm})\text{O}_{2-x} - \text{MgO}$
- kompositoxidbränsle med molybdenmatris (cermet):  $(\text{Pu,Am,Cm})\text{O}_{2-x} - {}^{92}\text{Mo}$

Den inerta matrisen förbättrar den termiska stabiliteten (nitridbränslen) och/eller ökar den effektiva termiska konduktiviteten (oxidbränslen).

Void-fraktionen hos kylmediet identifierades som den huvudsakliga säkerhetsaspekten hos dessa reaktorhärddar.

*Ett gaskylt accelerator drivet system dedicerat för transmutation har designats.* Tack vare den utomordentligt goda neutronekonomin hos det använda uran-fria bränslet så har förhållandet mellan pinnavstånd och pindiameter (P/D) kunnat ökas till 1.8. Den ökade andelen kylmedium möjliggör tillräcklig god värmetransport vid omgivningstrycket. Dessutom resulterar den stora andelen kylmedium i ett tryckfall på endast 26 kPa över härden, och 35 kPa totalt.

Tack vare det stora värdet på P/D så är den nödvändiga höjningen av värmeväxlaren, för att säkerställa transport av värmets från radioaktivt sönderfall, endast drygt en meter. Avsaknaden av uran, tillsammans med närvaro av 35 % americium i bränslet, resulterar i en låg effektiv andel fördröjda neutroner och en avsaknad av Doppler-återkoppling. En förutsättning för denna design är således underkriticitet. ([Appendix 7](#))

## UNDERKRITICITETSEXPERIMENT

Två stora subkriticitetsexperiment har varit i fokus under 2005:

- "Yalina-Booster subcritical experiment" i Minsk
- "SAD experiment" i Dubna

Det nya experimentella programmet vid Yalina-Booster startades under hösten 2005 med en sofistikerad 2-zons-härd: en snabb-neutron-zon och en termisk-neutron-zon. Ett antal experiment har utförts vid anläggningen:

- "Reaction rates" för olika detektorer vid olika positioner i härdens.
- Mätningar med en pulsad neutronkälla (PNS).
- "Source jerk"-mätningar (SJ)
- Brusmätningar
- Mätningar av neutronflödet vid utkanten av den aktiva härdens.

Experimenten var framgångsrika trots vissa tekniska brister. Förbättringar av systemet är planerade och förberedda. KTH förberedde ett forskningsprogram för 2005-2006 koordinerat av IAEA, med fokus på Yalina-experiment. Ett integrationsprogram för Yalina-experimenten och det europeiska projektet EUROTRANS har förberetts och implementeras.

SAD-experimentet fick stora svårigheter 2005 pga en brand i acceleratorbyggnaden. Samtidigt med återuppbyggnaden av acceleratoren så har ett experimentellt program planerats där SAD-experimentet integreras i EUROTRANS-projektet, under "Domain 2: Experimental Coupling of Accelerator, Spallation Target and Subcritical Core (ECATS)", se [Appendix 15](#).

## DYNAMIK OCH KINETIK I ADS

Studier av dynamik och kinetik för ADS tillsammans med kalleffektivitetsstudier har sammanfattats i två doktorsavhandlingar av Marcus Ericsson ([Appendix 8](#)) respektive Per Seltborg ([Appendix 9](#)).

Några huvudsakliga slutsatser är:

Underkritisk drift av reaktorer innebär, i sig själv, en distinkt ökad säkerhet i jämförelse med kritiska reaktorer. Anledningen är en hög stabilitet under drift och ökade marginaler vid insättning av positiv reaktivitet. För ett uranfritt bränsle baserat på aktinider så försämrar några viktiga säkerhetsparametrar. En analys av detta visar att användning av sådant bränsle i en kritisk reaktor vore mycket svår genomförbart. Studier av transienter indikerar att bly-vismuth-kylda reaktorer kan klara sig trots den låga andelen fördröjda neutroner och den höga voidreaktiviteten som aktinidbränslet medför, men eventuellt är en negativ prompt feedback nödvändig för att kompensera den svaga Dopplereffekten vid en prompt kriticitetstransient.

Trots att bly-vismuth har en hög kokpunkt så visar dessa studier på vikten av att ha ett lågt värde på voidreaktiviteten. Transientstudierna identifierar ett molybdenbaserat metall-keram-bränsle (CerMet) med goda inbyggda säkerhetsegenskaper. Ett större pinnavstånd föreslås som ett sätt att undvika mekaniska skador vid kylmedelsförlust.

Detaljerade analyser av neutronkinetik och termohydralik visar att punktkinetik-approximationen är tillräcklig även för mycket noggranna transientberäkningar för underkritiska system. Resultaten visar på bättre noggrannhet vid låga k-effektiv-värden en effekt av den reducerade känsligheten för störningar i systemets reaktivitet i ett underkritiskt tillstånd. Detta ger en mycket liten spatial störning. En studie av protonbestrålningens tillförlitlighet visade att många avbrott inträffar som en följd av problem med acceleratorm. Det är uppenbart att en stor förbättring i denna tillförlitlighet är nödvändig.

## KÄLLEFFEKTIVITETSSTUDIER FÖR ADS

Ett nytt sätt att beskriva proton-käll-effektiviteten,  $\Psi^*$ , har utvecklats vid KTH under de senaste åren för att kunna studera energiutbytet för en ADS.  $\Psi^*$  har studerats för ett antal ADS-modeller.  $\Psi^*$  definieras i analogi med neutron-käll-effektiviteten,  $\varphi^*$ , men relaterar härdeffekten direkt till protonkällan, istället för till källneutronerna. Huvudfördelen med  $\Psi^*$ , istället för den vanligare neutroneffektiviteten,  $\varphi^*$ , är att sättet som man definierar den externa källan är entydigt, och att  $\Psi^*$  är proportionell mot energiutbytet.  $\Psi^*$  beskrivet som en funktion av olika systemparametrar ger en grund för ADS-design med optimala egenskaper för att få en hög härdeffekt i förhållande till stråleffekten. Som ett exempel ser man att  $\Psi^*$  minskar avsevärt med ökande spallationstargetradie (se [Appendix 9](#)). För ett gaskylt system så kan vi sammanfatta:

- Americium som introduceras i bränslet, i en subkritisk härd, minskar  $\Psi^*$ . I en härd med americiumbaserat bränsle, så är  $\Psi^*$  ca 10% lägre än i en MOX-baserad härd.  $\Psi^*$  minskar med ytterligare 10% när helium byts ut mot LBE.
- Båda dessa effekter beror på det starka beroendet mellan fission och infångningstvårsnitt på den neutronenergin i 1 Mev-området i jämna N-nuklider, och på ett litet energiskift i detta beroende på tvärsnitten mellan nukliderna.

## KÄRNBRÄNSLECYKELSTUDIER

Studier av bränslecykler vid KTH är starkt kopplade till det europeiska projektet RED-IMPACT, koordinerat av KTH, och har fokuserat på ett hypotetiskt svenskt scenario. För att göra dessa studier har nya, avancerade simuleringsverktyg utvecklats, och fortsätter att förbättras kontinuerligt. Jämviktsstudier har utförts, och visar att fyra ADS-reaktorer, med 800 MWt var, är tillräckligt för att bränna en mängd plutonium och americium som motsvarar den uppbyggda mängden av dessa isotoper i den svenska reaktorparken med en installerad kapacitet på ca 10 GWe.

Studierna visar att plutoniuminventariet kunde reduceras mer genom MOX-återcykling i lättvattenreaktorer före användningen av ADS, men med nackdelen av en något försämrade americiumutbränning. I ett detaljerat svenskt scenario så har ett antal möjligheter behandlats:

- Att skicka det använda bränslet som det är till ett bränsleförvar för permanent förvar och övervakning (Utfasningsscenario)
- Att starta om ett antal BWR- och PWR-enheter för att bränna/transmutera existerande plutonium och/eller aktinider i form av bland-oxid- bränsle (MOX).

- Att bygga en eller flera acceleratordrivna system (ADS) att användas som en "stand-alone" reaktor eller, troligare, för att användas i kombination med BWR- och PWR.

BWR är mer effektiva i att bränna plutonium i MOX-form. I detta avseende så överträffar BWR PWR med ca 10 %. Dessutom producerar BWR ca 10 % mindre americium. Trots detta är varken BWR eller PWR sig själva tillräckliga för att transmutera 99 % av transuranerna (TRU) i det använda UOX-bränslet. Man har å andra sidan kommit fram till att en reaktorpark med ADS kan teoretiskt bränna ca 99 % av TRU som bildats i UOS från ett LWR-system av svensk storlek. Tiden för ett dylikt scenario beror mycket på den tid som krävs för att kyla det använda bränslet före upparbetning mellan varje successiv återföring. Om vi antar att det behövs 10 år för att kyla bränslet från en ADS, så blir scenariets längd åtminstone 200 år, med de mest optimistiska tekniska antagandena. Användningen av avancerad pyro-processing med en avsvälningstid på bara 2 år skulle dock minska tiden för scenariet till ca 50 år.

Dessutom har ADS-reaktorer visat sig vara nödvändiga för att minska inventariet av americium, eftersom varken BWR eller PWR kan bränna mer americium än de producerar. Fler studier krävs för att ge tillförlitliga svar angående dessa scenariers ekonomi.

Ekonomiska analyser av olika scenarier har utförts, med ett antal förenklade antaganden. Man har funnit att MOX-scenariet är mer än dubbelt så dyrt som en ordinär UOX-bränslecykel. Införandet av ADS-reaktorer reducerar denna faktor till ca 1.5. Med andra ord; elektricitet som produceras efter år 2025 med en hypotetisk kombination av BWR/MOX-reaktorer och ADS/MOX-reaktorer skulle kunna vara ca 50 procent dyrare än från dagens LWR.

Kriticitetsstudier av de olika geologiska slutförvaren av använt bränsle, och de olika behållarna, visar inga risker som behöver uppmärksammas.

## **POTENTIALEN HOS REAKTORBASERAD TRANSMUTATION: DEN S.K. "DEEP BURN" - MODULÄRA HELIUMREAKTORN (DB-MHR)**

Studier har visat att DB-MHR kan bränna plutonium mycket effektivt. Fördelarna med heliumkylda, grafitmoderade reaktorer är många: många egenskaper för passiv säkerhet, låg kostnad, flexibilitet i bränsleval, hög energieffektivitetskonversionsfaktor, hög utbränning, resistent TRISO bränslehölje, samt låg effektdensitet.

Neutronikparametrarna för denna reaktortyp är också mycket gynnsamma. Huvudfokus har legat på:

- Betydelsen av brännbara gifter för säkerheten i en DB-MHR.
- Simulering av axiell omflyttning av bränsle.
- Möjligheter att bränna LWR-bränsle i en torium-matris

Mer detaljer ges i [Appendix 3,4,5 och 6](#).

## **UTVECKLING AV KÄRNBRÄNSLE FÖR TRANSMUTATION**

Inom samarbetet i Confirm-projektet tillverkades pellets av (Am,Zr)N vid ITU med dammfria metoder. Dessa pellets har god mekanisk stabilitet, men de har låg densitet pga begränsningar i sintringstemperaturen för AmN.

Modellering av de termo-kemiska egenskaperna av avancerade bränslen har varit ett pågående arbete. Huvudområdena för bränslemodellering har varit:

- Beräkningar och utvärdering av matematiska uttryck för att inkludera metalliskt uran, urannitrider och uranoxider i den termo-kemiska databasmodulen ALCHMY.
- Datorstödd modellering med målsättning att undersöka möjligheten för interna redox-reaktioner i (U,Pu)N
- Utvärdering av den termo-kemiska stabiliteten för fyra experimentella, ryska kompositbränslen.
- Utvärdering av utvalda egenskaper hos de bränslekandidater som diskuteras inom EUROTRANS DM3, för att välja ut det bästa bränslet för "the European Transmuter Project".

## **MATERIALSTUDIER FÖR ADS - SIMULERING AV STRÅLSKADOR**

Den nuvarande versionen av tvåbandsmodellen har för första gången möjliggjort simulering av formationen av alfa-prim-fasen i Fe-Cr, men modellen behöver byggas ut för att ta hänsyn till effekterna av magnetism. Detta arbete pågår.

Omfattande simuleringar har utförts för att studera molekyldynamiken, med flera olika potentialer, för skador från neutroninducerade kaskader. Dessa potentialer (utvecklade av oss och andra forskargrupper) förutspår bl a nya energier för förskjutningströsklar (för bildandet av ett enstaka Frenkle-par).

## **UTVECKLING AV MJUKVARA OCH METODER**

### ***Acceleration av källkonvergens för Monte-Carlo.***

Inom ramen för det europeiska projektet NURESIM har en metod utvecklats för att beräkna steady-state-tillståndet i en reaktorhård med stokastisk approximation. Detta gjordes av KTH för Monte-Carlo-koden TRIPOLI-4, tillsammans med den nödvändiga databehandlingen.

Olika metoder för att accelerera källkonvergens av kriticitetsberäkningar med Monte-Carlo studerades och jämfördes. Fissionsmatrismetoden har valts ut för en detaljerad undersökning. De utförda testerna visade att denna metod är mycket lämpad för acceleration av källkonvergens i en stor hård med en hög "dominance ratio". Därför är metoden en kandidat för att implementeras i TRIPOLI-4.

### ***Fuel Cycle Analyzer (FCA)***

En mjukvara med "Fuel Cycle Analyser" (FCA) har utvecklats. Datorprogrammet löser effektivt punktreaktorekvationer av isotopkinetik genom att använda utvärderade produktions- och utbränningsrater. Programmet simulerar användardefinierade reaktorscenarier för att utvärdera inverkan på inventariet av transuraner. FCA är menad att vara ett steg på vägen mot ett mer avancerat verktyg för reaktorcykelsimulering som utvecklas på avdelningen för Reaktor fysik vid KTH.

# TABLE OF CONTENT

|  |           |
|--|-----------|
| <b>SUMMARY</b>   | <b>4</b>  |
| <b>SAMMANFATTNING</b>                                      | <b>9</b>  |
| <b>TABLE OF CONTENT</b>                                    | <b>14</b> |
| <b>LIST OF APPENDICES</b>                                  | <b>15</b> |
| <b>ABBREVIATIONS AND ACRONYMS</b>                          | <b>17</b> |
| <b>OTHER ABBREVIATIONS AND ACRONYMS</b>                    | <b>18</b> |
| <b>1 SYSTEM AND SAFETY STUDIES OF ADS</b>                  | <b>21</b> |
| <b>2 SUBCRITICAL EXPERIMENTS</b>                           | <b>24</b> |
| <b>3 ADS SOURCE EFFICIENCY STUDIES</b>                     | <b>32</b> |
| <b>4 NUCLEAR FUEL CYCLE ANALYSIS</b>                       | <b>35</b> |
| <b>5 POTENTIAL OF REACTOR BASED TRANSMUTATION</b>          | <b>47</b> |
| <b>6 ADS FUEL DEVELOPMENT</b>                              | <b>54</b> |
| <b>7 SIMULATION OF RADIATION DAMAGE</b>                    | <b>56</b> |
| <b>8 DEVELOPMENT OF CODES AND METHODS</b>                  | <b>59</b> |
| <b>9 INTERNATIONAL INTERACTIONS, SEMINARS, CONFERENCES</b> | <b>65</b> |
| <b>10 REFERENCES</b>                                       | <b>68</b> |
| <b>11 APPENDICES</b>                                       | <b>70</b> |

## LIST OF APPENDICES

1. Carl-Magnus Persson, Per Seltborg, Alexandra Ahlander, Waclaw Gudowski, Thomas Stummer, Hanna Kiyavitskaya, Victor Bournos, Yuriy Fokov, Ivan Serafimovich, Sergey Chigrinov  
*“Analysis of reactivity determination methods in the subcritical experiment Yalina”, Nuclear Instruments and Methods in Physics Research A 554 (2005) 374–383*
2. Carl-Magnus Persson, Per Seltborg, Alexandra Ahlander and Waclaw Gudowski, Sergey Chigrinov, Ivan Serafimovich, Victor Bournos, Yuriy Fokov, Christina Routkovskaia, Hanna Kiyavitskaya  
*“Comparison of neutron kinetic parameters of the subcritical ADS experiments Yalina and Yalina Booster” 12th International Conference on Emerging Nuclear Energy Systems (ICENES’2005) Brussels, Belgium, August 21–26, 2005, on CD-ROM, SCK•CEN, Mol, Belgium (2005)*
3. Alberto Talamo, Waclaw Gudowski  
*“Performance of the gas turbine-modular helium reactor fuelled with different types of fertile TRISO particles” Annals of Nuclear Energy 32 (2005) 1719–1749*
4. Alberto Talamo, Waclaw Gudowski  
*“Comparative Studies of JENDL-3.3, JENDL-3.2, JEFF-3, JEF-2.2 and ENDF/B-6.8 Data Libraries on the Monte Carlo Continuous Energy Modeling of the Gas Turbine-Modular Helium Reactor Operating with Thorium Fuels” Journal of NUCLEAR Science and Technology, Vol. 42, No. 12, p. 1040–1053 (December 2005)*
5. Alberto Talamo, Waclaw Gudowski  
*“Adapting the deep burn in-core fuel management strategy for the gas turbine – modular helium reactor to a uranium–thorium fuel” Annals of Nuclear Energy 32 (2005) 1750–1781*
6. Alberto Talamo, Waclaw Gudowski  
*“Managing the reactivity excess of the gas turbine-modular helium reactor by burnable poison and control rods” Annals of Nuclear Energy 33 (2006) 84–98*
7. Daniel Westlén and Janne Wallenius  
*“Neutronic and safety aspects of a gas-cooled subcritical core for minor actinide transmutation” Nuclear Technology Vol. 154 Apr 2006*
8. Marcus Eriksson  
*“Accelerator-driven Systems: Safety and Kinetics”, Doctoral Thesis, Department of Nuclear and Reactor Physics, Royal Institute of Technology, Stockholm 2005, ISBN 91-7283-988-0*
- 8.1 Marcus Eriksson, Janne Wallenius, Mikael Jolkkonen, James Cahalan  
*“Inherent safety of fuels for accelerator-driven systems” Nuclear Technology 151 (2005) 314.*
- 8.2 Janne Wallenius, Marcus Eriksson  
*“Neutronics of minor actinide burning accelerator-driven systems with ceramic fuel” Nuclear Technology 152 (2005) 367*

9. Per Seltborg *“Source efficiency and high-energy neutronics in accelerator-driven systems”*, Doctoral Thesis, Department of Nuclear and Reactor Physics, Royal Institute of Technology, Stockholm 2005, ISBN 91-7178-147-1
10. Daniel Westlén *“Transmutation of nuclear waste in gas-cooled sub-critical reactors”* Licentiate Thesis, ISBN 91-7178-196-X, KTH 2005
11. Pär Olsson, Janne Wallenius, Christophe Domain, Kai Nordlund, Lorenzo Malerba *“Two-band modeling of alpha-prime phase formation in Fe-Cr alloys”* *Physical Review B* 72 214119 (2005)
12. Christina Lagerstedt *“Simulation of Radiation Damage in Fe and FeCr”*, Doctoral Thesis, Department of Nuclear and Reactor Physics, Royal Institute of Technology, Stockholm 2005, ISBN 91-7178-198-6
- 12.1 Janne Wallenius, Pär Olsson, Christina Lagerstedt *“Relation between thermal expansion and interstitial formation energy in pure Fe and Cr”*, *Nuclear Instruments and Methods in Physics Research B* 228 (2005) 122
- 12.2 D. Terentyev, C. Lagerstedt, P. Olsson, K. Nordlund, J. Wallenius, C.S. Becquart, L. Malerba *“Effect of the interatomic potential on the features of displacement cascades in  $\alpha$ -Fe: a molecular dynamics study”*, *Proceedings of the Symposium on Microstructural Processes in Irradiated Materials San Francisco, CA, 13–17 February 2005 (Annual TMS meeting)*
13. Alexandra Åhlander *“Analysis of Fuel Cycle Scenarios for Transmutation of Nuclear Waste”*, Master of Science Thesis, KTH 2005
14. Alexandra Åhlander, Jan Dufek, Waclaw Gudowski *“From Once-through Nuclear Fuel Cycle to Accelerator-Driven Transmutation”*, *Proceedings of the International Conference on Accelerator Applications 2005, Venice, Italy 29 August–1 September 2005, Elsevier Science 2006*
15. V.N.Shvetsov, C. Broeders, I.S. Golovnin, E.Gonzalez, W. Gudowski et al *“The Subcritical Assembly in DUBNA (SAD) – Part I and Part II”*, *Proceedings of the International Conference on Accelerator Applications 2005, Venice, Italy 29 August–1 September 2005, Elsevier Science 2006*
16. W. Gudowski *“Optimizing the Nuclear Fuel Cycle by means of Partitioning / Conditioning and/ or Transmutation”*, *Assemblée Nationale République Française, AUDITIONS PUBLIQUES, January 20, 2005, Paris*



## ABBREVIATIONS AND ACRONYMS

### *EUROPEAN PROJECTS:*

|            |  |
|------------|--|
| ADOPT      | “Thematic Network on Advanced Options for Partitioning and Transmutation.”   |
| CONFIRM    | "Collaboration On Nitride Fuel Irradiation and Modeling"– shared cost project  |
| ECATS      | Domain 2 of the Eurotrans Project:” Experimental Coupling of Accelerator, Spallation Target and Subcritical Core “                             |
| EUROTRANS  | “ A EUROpean Research Programme for the TRANSmutation of High Level Nuclear Waste in an Accelerator Driven System”                             |
| FUETRA     | “Fuel for Transmutation” – cluster of nuclear fuel related EU-projects   |
| FUTURE     | “Fuels for transmutation of long lived radiotoxic elements"– shared cost project   |
| ITEM       | “Network - Development of multiscale modeling for simulation of radiation effects for Virtual Test Reactors (VTR).                             |
| MOST       | “Network - Review and reevaluation of Molten Salt Reactor technology and previous realizations or projects.”                                   |
| MUSE       | "Multiplication avec Source Externe"- Experiment for Subcritical Neutronics Shared cost project  |
| NURESIM    | The European Platform for NUclear REactor SIMulations  |
| PDS-XADS   | “Preliminary Design Studies of an eXperimental Accelerator Driven System” – shared cost project  |
| RED-IMPACT | Impact of Partitioning, Transmutation and Waste Reduction Technologies on the Final Nuclear Waste Disposal                                     |
| SPIRE      | SPallation and IRradiation Effects - "Irradiation Effects in Martensitic Steels under Neutron and Proton Mixed Spectrum" – shared cost project |
| TECLA      | “Technologies, Materials and Thermal-hydraulics and Safety for Lead  |
| TETRA      | Technology for Transmutation – cluster of EU-projects  |

## OTHER ABBREVIATIONS AND ACRONYMS

|         |  |
|---------|--|
| ADS     | Accelerator Driven (Transmutation) System  |
| ALMR    | Advanced Liquid Metal Reactor  |
| ANSALDO | Italian electromechanical company, Ansaldo Nucleare is a part of this company                        |
| BA      | Burnable Absorber  |
| BCC     | Body Centered Cubic - type of a crystallographic lattice   |
| BISO    | Double isotropic coated fuel particles, fuel particles for gas cooled high temperature reactor       |
| BOC     | Beginning of Cycle   |
| BOL     | Beginning of Life  |
| BR      | Breeder Reactor  |
| CAPRA   | Consummation Accrue de Plutonium dans les Rapides – Enhanced Burning of Plutonium in Fast Reactors   |
| CERCER  | CERamic-CERamic – type of nuclear fuel   |
| CERMET  | CERamic-METallic – type of nuclear fuel  |
| CFD     | Computational Fluid Dynamics   |
| CR      | Control Rods   |
| DB-MHR  | Deep Burn Modular Helium Reactor   |
| DF      | Driver Fuel (for the high temperature gas cooled reactors)   |
| DIF3D   | The multigroup steady state neutron diffusion and transport code                                     |
| DLC200  | Nuclear Data Library release following the standard version of the MCNP-code                         |
| DPA     | Displacement Per Atom  |
| EAF99   | European Activation File, version 99. Nuclear data file containing neutron activation cross-sections |
| EAM     | Embedded Atom Method   |
| EBR     | Experimental Breeder Reactor   |
| EFPD    | Effective Full Power Days  |
| EM10    | type of ferritic steel   |
| ENDFB   | Evaluated Nuclear Data File, suffix indicates a version of the file e.g.ENDFB6.8                     |
| EOC     | End of Cycle   |
| EOL     | End of Life  |
| ERMT    | European Research on Materials for Transmutation Workshops   |
| FAE     | Fuel Adjacency Effect  |
| FBR     | Fast Breeder Reactor   |

|         |   |
|---------|---|
| FCC     | Face Centered Cubic - type of a crystallographic lattice  |
| FCTT    | Fuel Cladding Transient Test  |
| FFTF    | Fast Flux Test Facility   |
| fpo     | Full power operation  |
| FTF     | Flat-to-Flat, a core design strategy  |
| FZK     | Forschungszentrum Karlsruhe   |
| GENEPI  | Generateur de Neutrons Pulsés Intenses (High intensity neutron generator)<br>-external neutron source for MUSE experiments          |
| GeV     | Giga-electron-Volt, energy unit   |
| GWd     | GigaWatt day, energy unit   |
| HfN     | Hafnium Nitride   |
| HTGR    | High Temperature Gas Cooled Reactors  |
| HM      | Heavy Metal   |
| HT-9    | High quality stainless steel  |
| H451    | Symbol of the nuclear-grade graphite  |
| ISOTX   | A format of string/representing of multigroup data neutron cross-sections   |
| ITU     | Institute of Transuranium Elements, Karlsruhe   |
| JEF     | Joint Evaluated (Nuclear Data) File, suffix indicates a version of the file<br>e.g. JEF2.2  |
| JENDL   | Japanese Evaluated nuclear Data Library, suffix indicates a version of the<br>file e.g. JENDL3.2                                    |
| JNC     | Japan nuclear cycle development institute   |
| keV     | kilo-electron-Volt – energy unit  |
| KCODE   | A MCNP module for keff (eigenvalue) calculations  |
| KMC     | Kinetic Monte Carlo   |
| LA150   | Nuclear data cross section library up to 150 MeV for the MCNPX-code,<br>standard release of the Los Alamos (LA) National Laboratory |
| LBE     | Lead Bismuth Eutectic   |
| LOCA    | Loss of Coolant Accident  |
| LOF     | Loss of Flow  |
| LOHS    | Loss of Heat Sink   |
| LWR     | Light Water Reactor   |
| MA      | Minor Actinides   |
| MASURCA | Maquette SURgénératrice de Cadarache -Fast reactor at Cadarache,<br>hosting MUSE-experiments  |
| MCB     | Monte Carlo based computer program for burnup calculations  |
| MCNP    | Monte Carlo Neutron Photon transport code   |
| MCNPX   | Monte Carlo Neutron Photon and Light Ion transport code   |
| MeV     | Mega-electron-Volt, energy unit   |

|            |   |
|------------|---|
| MHTGR      | Modular High Temperature Gas Cooled Reactor   |
| MOX        | Mixed Oxide (fuel)  |
| NEA        | Nuclear Energy Agency   |
| NJOY       | A computer program for processing evaluated nuclear data files  |
| NNC        | NNC Holdings Limited, an international engineering support company, participant of the PDS-XADS Project                         |
| ORIGEN2    | A computer code system for calculating the buildup, decay, and processing of radioactive materials                              |
| P/D        | Pitch to Diameter ratio   |
| pcm        | pro cent mille, a reactivity unit equal to $10^{-5}$  |
| PDF        | Post Driver Fuel (for the high temperature gas cooled reactors)   |
| Pf         | (Power) Peaking factor  |
| PPS        | Plant Protection System   |
| PRISM      | Advanced fast reactor concept   |
| P0, P1     | Approximation symbols of the nodal transport theory   |
| RSC        | Reserve Shutdown Control Rods   |
| SA, S/A    | SubAssembly (of the nuclear fuel)   |
| SAS4       | Reactor kinetic calculation code  |
| SAS/DIFF-K | Reactor kinetic calculation code system   |
| SNR300     | SNR, Schneller Natriumgekühlter Reaktor - fast sodium-cooled reactor, the German fast breeder reactor prototype of 300 MW power |
| SS         | Stainless Steel   |
| SSC        | Sing-Sing Core, an accelerator driven system concept of KTH   |
| STAR-CD    | Computer program for fluid dynamics problems  |
| TF         | Transmutation Fuel (for the high temperature gas cooled reactors)   |
| TiN        | Titanium nitride  |
| TOP        | Transient Overpower   |
| TRADE      | Triga Accelerator Driven Experiment, ADS-related experiment in Italy  |
| TRISO      | Triple isotropic coated fuel particles, fuel particles for gas cooled high temperature reactor                                  |
| TRU        | TRansUranium elements   |
| TWODANT    | A deterministic neutron transport code  |
| UREX       | URanium and fission products Extraction, nuclear fuel reprocessing technology   |
| UTOP       | Unprotected Transient Overpower   |
| VARIANT-K  | A Nodal transport and diffusion module for the DIF3D  |
| WP         | Workpackage   |

# 1 SYSTEM AND SAFETY STUDIES OF ADS

Design and safety studies have been performed of accelerator driven systems with americium based fuels and lead-bismuth coolant. Three different types of fuels were investigated:

- Solid solution nitride fuel with zirconium nitride matrix:  $(\text{Pu,Am,Cm,Zr})_{15}\text{N}$
- Composite oxide fuel with magnesium oxide matrix (cercer):  $(\text{Pu,Am,Cm})\text{O}_{2-x} - \text{MgO}$
- Composite oxide fuel with molybdenum matrix (cermet):  $(\text{Pu,Am,Cm})\text{O}_{2-x} - {}_{92}\text{Mo}$

The inert matrix is present to improve thermal stability (nitride fuels) and/or to raise the effective thermal conductivity (oxide fuels).

800 MWth cores were used as a basis for the studies. An example of a core map shown in *Figure 1.1*. In the centre, the spallation target is located. The core is divided into three fuel zones. Each fuel zone has a different volume fraction of inert matrix, in order to reduce power peaking. Initially, the fraction of plutonium was set to 40%, in order to minimise reactivity swing over a large number of burnup cycles. Difficulties were found in designing molybdenum core with at least 50 volume percent of inert matrix, due to the larger absorption cross section of Mo, as compared to Zr and Mg. Thus the plutonium fraction in the cermet core had to be raised to 50%.

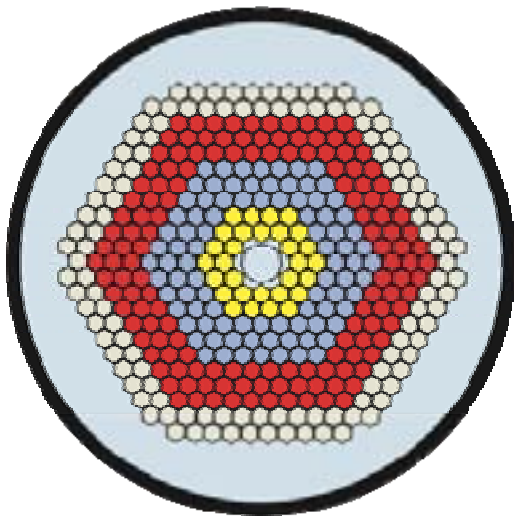


*Figure 1.1 Core map of an 800 MWth ADS with cermet fuel.*

Core parameters and matrix fractions resulting in a radial power peaking less than 1.3 are exemplified in Table 1.1. The corresponding calculations were made using the continuous energy Monte Carlo Burnup code MCB, developed at the department.

Table 1.1: Core parameters of the ADSs studied.

| Core                      | MgO        | <sup>92</sup> Mo | ZrN        |
|---------------------------|------------|------------------|------------|
| Average rating            | 20 kW/m    | 29 kW/m          | 35 kW/m    |
| Clad inner/outer diameter | 6.0/6.8 mm | 6.0/6.8 mm       | 5.0/5.7 mm |
| P/D                       | 1.60       | 1.70             | 1.75       |
| Fuel assemblies per zone  | 42/156/252 | 42/108/156       | 42/108/96  |
| Pu/Am/Cm                  | 40/50/10   | 50/42/8          | 40/50/10   |
| Matrix fractions          | 83/64/49   | 67/59/50         | 66/61/50   |
| Peaking factor            | 1.33       | 1.28             | 1.29       |

The proton beam power at BOL was calculated with MCNPX to be 15.8 MW for the nitride, 17.6 MW for the cermet and 23.0 MW for the cercer core, based on a proton energy of 1 GeV. The more compact design of the cores with high linear rating thus results in significantly higher source efficiency. This is however offset by a larger reactivity loss for the nitride and cermet core. In the case of the nitride, the harder neutron spectrum leads to smaller build-up of curium (smaller curium fraction at equilibrium), while in the cermet core, the larger Pu/Am ratio increases reactivity losses. The reactivity losses in the first cycle of the cercer core were calculated to be 130 pcm per percent burnup, which may be compared to 310 pcm for the cermet and 250 pcm for the nitride core. In order to keep the proton beam power variation small (preferably less than 50%), the cermet and nitride cores would probably have to be shuffled before reaching their burnup target.

It has been observed in the studies that the harder neutron spectrum of the nitride and cermet cores results in a slightly lower core averaged burnup of 15% at 180 DPA in the highest fluence node, compared to 18% and 17% for the zirconia and magnesia cores. As this dose is obtained in the inner fuel zone, where the burnup reaches 24-28 percent, shuffling could increase the total burnup of the fuel. In that case another strategy for power peaking management would have to be developed. The residence time of the fuel in the LBE coolant, being limited by corrosion damage rates, could impose stricter limitations than neutron damage to the clad. The residence time of the oxide fuels are in the order of three full power years, which is significantly longer than the proven lifetime of T91 clad in LBE at the suggested operating temperature ( $T_{max} = 820K$ ). The smaller actinide inventory of the nitride fuels yields a residence time of 2 full power years.

The coolant void worth was identified as the major safety issue of these cores. Since the prompt thermal feedback of ADS fuels is very small, one has to ensure that the core never becomes prompt super-critical. One potential source of positive reactivity is the introduction of gas bubbles into the core. Such bubbles could emanate from a broken heat exchanger, or as releases of fission and helium gas from a ruptured fuel

pin. The full core void worth was calculated to be about 3000, 5000 and 6000 pcm for the cermet, nitride and cermet cores, respectively. In the two latter cases, it would be advisable to operate the cores at  $k$ -values below 0.97.

A series of transients were simulated using the SAS4A code system. It was found that the cladding is most sensitive to loss of flow events. Thus the primary system should be designed in order for natural convection to provide sufficient cooling for decay heat removal, as well as loss of one pump due to mechanical failure. This can be achieved mainly in three different ways: by reduction of coolant velocity under normal operation, by increase of coolant fraction in the core, or by raising the elevation of the heat exchanger above the thermal centre of the core. A seismic analysis showed that the primary vessel of a lead-bismuth cooled reactor would be limited in height to about 10 m, which limits the elevation of the heat exchanger to less than 6 meters above the core. For the cores investigated, this is more than enough for removal of decay heat, but since natural convection provides about 20% of the flow, the loss of pumping power may lead to clad temperatures exceeding the rapid creep limit of the ferritic steels considered for application in lead-cooled reactors. Therefore, it would be relevant to assess the performance of austenitic steels in the ADS. These steels have better mechanical properties at high temperatures, but feature poorer swelling and corrosion resistance. Optimised austenitic steels like 15-15Ti have reached doses of 150 dpa in test irradiations, which is not much less than the proven dose for the T91 ferritic-martensitic steel that is presently the reference steel of the European ADS program. Special coating materials would however be mandatory for the austenitic steel in a heavy-liquid metal environment, in order to avoid corrosion damage at temperatures above 800 Kelvin. Such coatings (Fe-Al alloys) are under development at FZK in Germany.

Detailed results of these studies have been described in papers [1] – [Appendix 8.1](#), [2] – [Appendix 8.2](#), [3] – [Appendix 8](#) and [20].

## 2 SUBCRITICAL EXPERIMENTS

During 2005 the research connected with the subcritical experiment *Yalina* in Belarus has continued. The results from 2004 were published in the journal *Nuclear Instruments and Methods in Physics Research, Section A* – see [Appendix 1](#). The experiment has continued with a new facility – *Yalina Booster*. Some preliminary Monte Carlo analysis of this new core was presented at the ICENES 2005 conference in Brussels in August 2005 – see [Appendix 2](#). The experimental program at *Yalina Booster* was launched during the fall and the main part of work has been connected to that. The results of the first measurements are summarized below. These results are not published.

### 2.1 FIRST MEASUREMENT CAMPAIGN AT YALINA BOOSTER NOVEMBER 2005

#### 2.1.1 Introduction

The core was 2005-11-21 loaded to 1180 thermal fuel pins according to Figure 2.1. The sources and detectors in Table 2.1 were available during the measurements.

*Table 2.1. Sources and detectors available during the measurements.*

| Sources                         |   | Detectors                |   |
|---------------------------------|---|--------------------------|---|
| $^{252}\text{Cf}$ (INK7)        | $3.16 \cdot 10^6$ n/s (2005-09-01)  | $^3\text{He}$ , 10 mm    | Cannot be used in EC1-b   |
| $^{252}\text{Cf}$ (INK5)        | $2.26 \cdot 10^5$ n/s (2005-09-01)  | $^3\text{He}$ , 250 mm   | Cannot be used in EC1-b   |
| $^{252}\text{Cf}$ (INK3)        | $1.03 \cdot 10^3$ n/s (2005-09-01)  | Fission chambers, 1 mg   | $^{232}\text{Th}$ , $^{235}\text{U}$ , $^{\text{Nat}}\text{U}$ , Fits in all channels |
| (D,D)-continuous (small target) | 0-1.1 mA  | $^{235}\text{U}$ , 0.5 g | Fits only in corner channels  |
| (D,D)-pulsed (small target)     | 0-1.1 mA, pulse width<br>$2 \mu\text{s} - 130 \mu\text{s}$ , frequency<br>< 7.6 kHz | $^{235}\text{U}$ , 1 g   | Fits only in corner channels  |

The following measurements were performed:

- Reaction rates for different detectors at different positions in the core.
- Pulsed neutron source measurements (PNS).
- Source jerk measurements (SJ)
- Noise measurement
- Measurement of the neutron flux at the periphery of the active core.



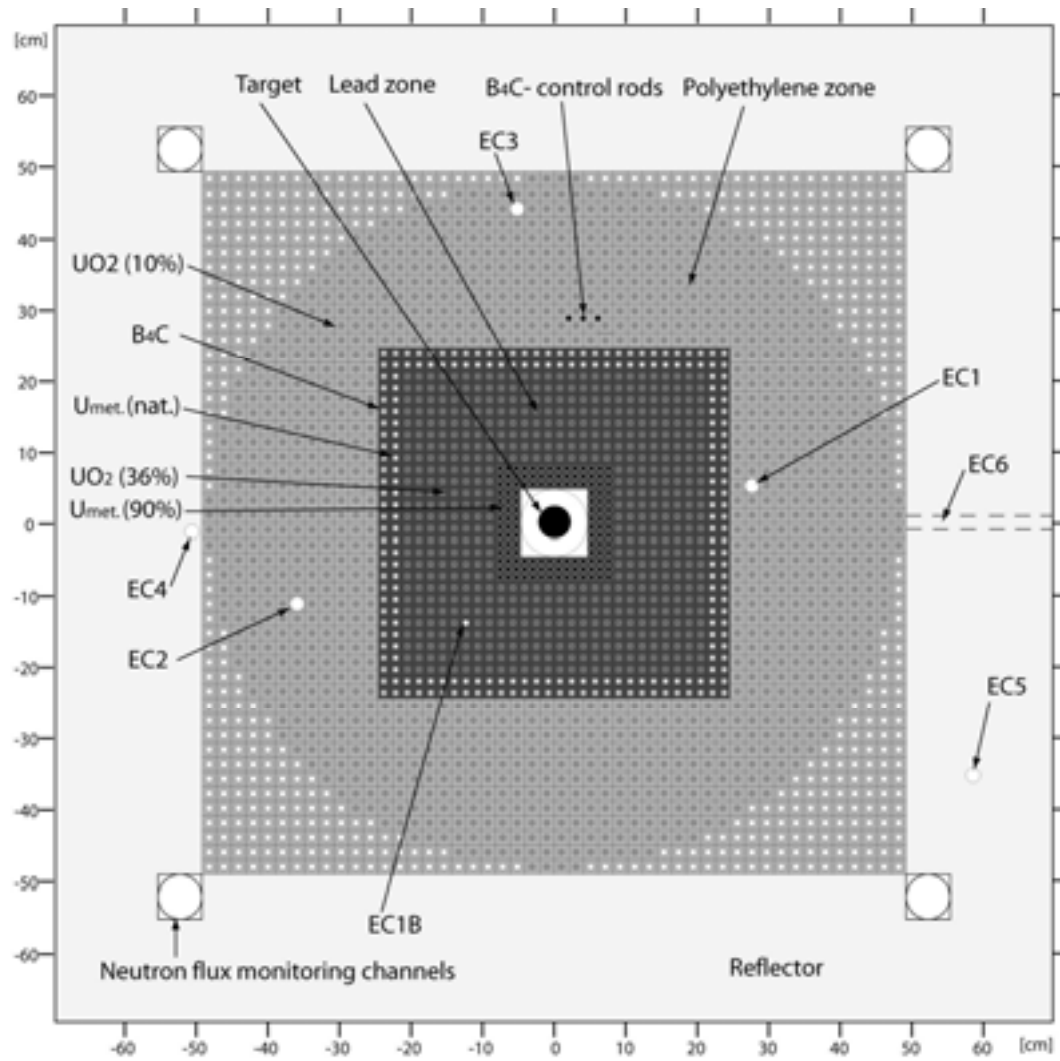


Figure 2.1 The 1180-loading of Yalina Booster.

### 2.1.2 Reaction rates

Table 2.2. Count rates in counts per second for different detectors at different positions. Black is measured values and blue is estimated.

| Source   | Detector                   | EC1b | EC1    | EC2    | EC3    | EC4    | EC5   | EC6 | Corner channel |
|--|----------------------------|------|--------|--------|--------|--------|-------|-----|----------------|
| $^{252}\text{Cf}$<br>$3 \cdot 10^6$ n/s                              | $^3\text{He}$ ,<br>10mm    |      | 4600   | 5250   | 3950   | 1830   | 570   |     |                |
| $^{252}\text{Cf}$<br>$3 \cdot 10^6$ n/s                              | $^3\text{He}$ ,<br>250mm   |      | 460000 | 525000 | 395000 | 183000 | 57000 |     |                |
| (D,D) in<br>DC<br>mode,<br>1.1 mA                                    | $^3\text{He}$ ,<br>10mm    |      |        |        |        |        | 39800 |     |                |
| (D,D) in<br>DC<br>mode,<br>0.5 mA                                    | $^3\text{He}$ ,<br>10mm    |      |        |        |        |        | 24500 |     |                |
| (D,D) in<br>pulsed<br>mode,<br>1.1 mA,<br>66 Hz,<br>10 $\mu\text{s}$ | $^3\text{He}$ ,<br>10mm    |      | 545    |        |        |        |       |     |                |
| (D,D) in<br>DC<br>mode,<br>1.1 mA                                    | $^{235}\text{U}$ , 1 g     |      |        |        |        |        |       |     | 20000          |
| (D,D) in<br>DC<br>mode,<br>1.1 mA                                    | $^{235}\text{U}$ ,<br>1 mg | 19   |        |        |        |        | 15    |     |                |

The results from the measurement are presented in Table 2.2. From the table it can be concluded that the source strength of the (D,D)-source is approximately  $2 \cdot 10^8$  n/s for 1.1 mA. Moreover, the detection rate in the booster zone (EC1-b) is not sufficient for measurements in pulsed mode operation.

### 2.1.3 Pulsed source measurements

Conditions: pulsed (D,D)-source, 1 mA peak current, frequency 73 Hz,  $^3\text{He}$ -detector of 10 mm active length in EC1-4, pulse width 10  $\mu\text{s}$ , measurement time 2-3 h. One measurement was done in EC1 with  $f = 115$  Hz.

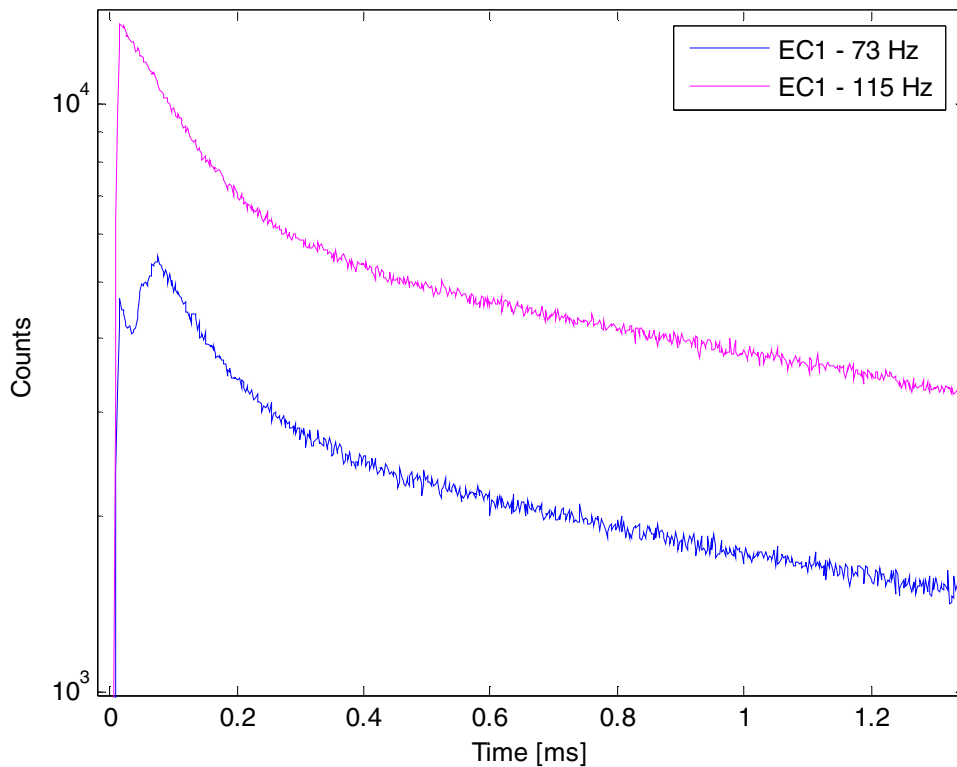
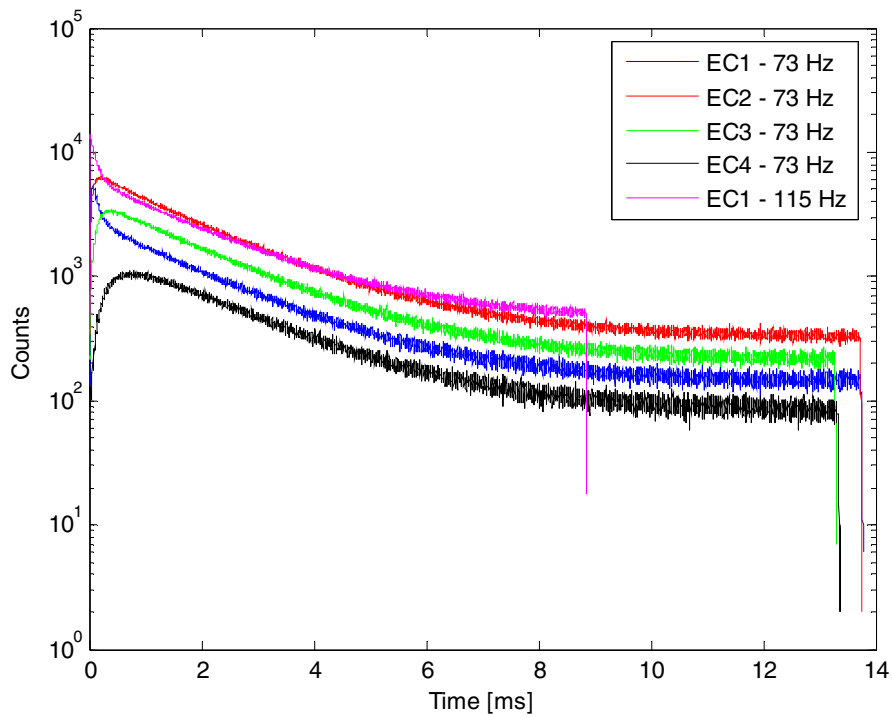


Figure 2.2 Neutron flux after pulse insertions.

During the measurements, some problems with the neutron generator were encountered. For frequencies below 100 Hz, almost every second pulse is followed by another pulse after 20 to 30  $\mu\text{s}$ . This “double pulse” can be seen in the lower picture

on the previous side as a second top in the blue curve. Above 100 Hz the neutron generator uses another dipole which doesn't have this problem.

Preliminary calculations show that  $k_{eff} = 0.985 \pm 0.003$  (slope fit) and  $0.980 \pm 0.002$  (Sjöstrand). The value obtained by the Sjöstrand method, is to some extent disturbed by the double pulses of the neutron generator. The alpha-values (Sjöstrand) should not be affected of this.

#### 2.1.4 Source Jerk / Beam trip

It has been proposed proposed to make a repeated source jerk experiment with the neutron generator producing a beam trip of 1 ms with a frequency of 1 Hz followed by a complete source jerk (beam shut down). But the neutron generator is not designed for this kind of experiment at the moment. Instead the generator was operated in pulsed mode at 7.6 kHz with a pulse width of 130  $\mu$ s (practically continuous). The beam was then manually shut down by letting a titanium foil fall into the beam line. It was noted that in pulsed mode there is no fast way to shut down the deuteron beam. With the titanium foil, it takes a few ms to close the beam. However, in continuous mode the source can be shut down by discharging the dipole magnet within less than 1 ms. Therefore this kind of measurement should be done in continuous mode operation. If this is going to be done, there must be a trigger for the source shut-down.

It was also noted that the intensity of the continuous wave is oscillating 30% with a frequency of 50 Hz. This is caused by the dipole magnet, which is powered by street electricity.

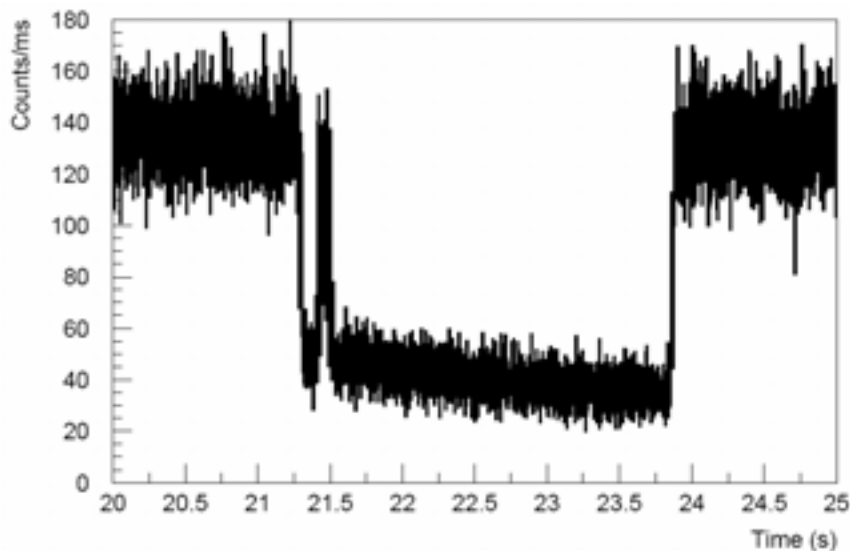


Figure 2.3. Beam interruption by titanium foil. The second peak is due to a recoil of the titanium foil when it reaches its bottom position.

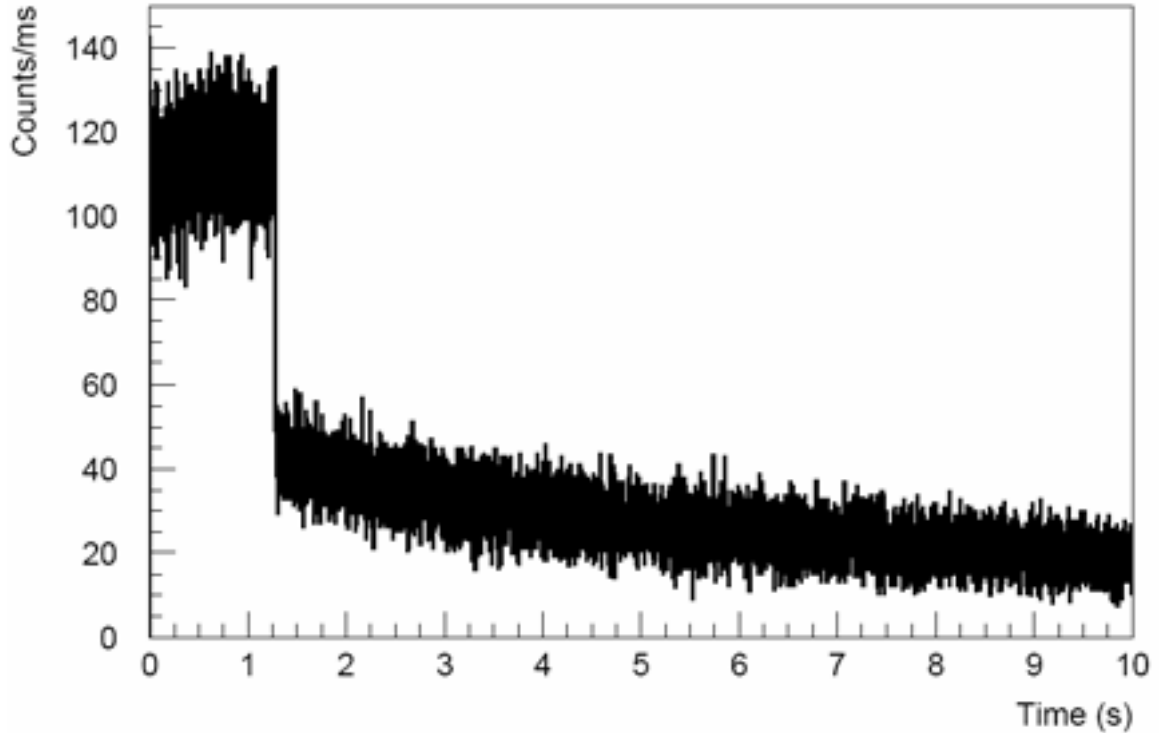


Figure 2.4 Ion source interruption in continuous mode operation.

### 2.1.5 Measurement of the neutron flux at the periphery

The neutron flux at the periphery of the active core was measured by the large  $^3\text{He}$ -detector at 120 different places (Figure 2.4). The result is currently not reproduced by the new detailed MCNP-input, but quit well reproduced by the old input-file.

### 2.1.6 Noise measurement

The  $^{252}\text{Cf}$ (INK5) was situated in the core centre and the 250mm  $^3\text{He}$ -detector was situated in EC2. The arrival time of each neutron detection during almost 4 h was recorded. The precision of the arrival time is 12.5 ns. This data can be used for Feynman- $\alpha$  and Rossi- $\alpha$  analysis.

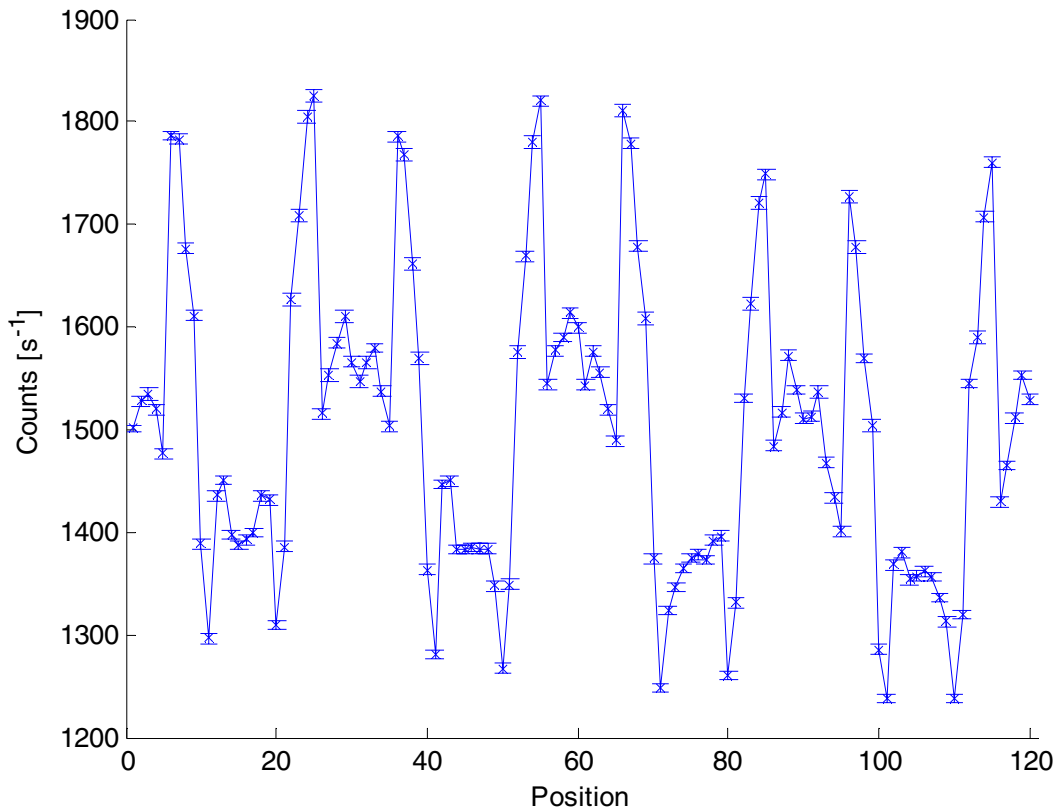


Figure 2.5 Neutron flux at the periphery of the active core. Position 1 is at core bottom.

### 2.1.7 Things that must be improved

- At the moment, only one electronic chain and two cables from the core to the control room are present. In order to make measurements in several channels at the same time, there must be more electronic chains available. At least five has been suggested.
- The beam intensity in pulsed mode and the small target must be increased to 10 mA.
- The twin pulses from the neutron generator at frequencies below 100 Hz must be removed.
- The intensity must be stabilized.
- Better pilot system for the pulsing system, to make it possible to perform repeated beam trips.
- Trigger signal for beam shut down.
- Better signals for deuteron current monitoring.
- Absolute calibration of the neutron source and an available signal of the neutron production.
- New experimental channel in the 36%-booster zone and in the lead target, large enough to allow the use of the 0.5 g <sup>235</sup>U detector.

- New 1 g  $^{232}\text{Th}$ ,  $^{238}\text{U}$  (ultra pure) and  $^{237}\text{Np}$  fission chambers that can fit the new experimental channels.
- Enlargement of the experimental channels to allow the use of these new big fission chambers.
- The acquisition system in Sosny has some drawbacks. For instance they cannot perform good noise measurements.
- The people in Sosny are aware of the problems concerning the neutron generator and they say that they can fix everything within a few months or so. For problems concerning electronic chains and acquisition systems it depends on money. Concerning the new experimental channels they would like to have a clear decision from EUROTRANS people.

Concerning the MCNP-input, there are two input-files available. The original file, on which all calculations before the construction is based on, seems to give quite ok results in comparison with experimental data. However, some major details in the geometry are not described accurately. It is now high priority to find all errors in this input file.

## 3 ADS SOURCE EFFICIENCY STUDIES

### 3.1 INTRODUCTION

Efficient incineration of americium, curium and even higher actinides require fast spectrum cores to yield a reduction of the overall radiotoxicity, avoiding production of even heavier nuclides. However loading a fast reactor with large fractions of minor actinide fuels is lead to cumbersome safety issues. As an example, the Doppler effect vanishes with the removal of  $^{238}\text{U}$ , and the situation is further worsened by introduction of americium. Further the effective delayed neutron fraction is significantly reduced.

Subcritical core are commonly discussed as a means of overcoming the safety issues. Such a core would be operated with a large enough margin to criticality to allow for sudden accidental reactivity insertions. External spallation neutron sources are envisioned to supply the extra neutrons needed to sustain a chain reaction. Typically, 1 GeV neutrons impinging on a liquid metal target are foreseen. At impact, the protons produce neutrons via spallation reactions. These multiply in the target through further spallation reactions and through (n, xn)-reactions.

The efficiency of the spallation source is an important parameter for the transmutation system as a whole. The multiplication production of neutrons in the target and the subsequent multiplication of these neutrons in target and fuel region depends on a set of parameters such as target size and geometry, target material, proton beam energy et cetera. In our work designing subcritical system, the impact of the core coolant and fuel on source efficiency have been recurrent questions.

To study the impact on source efficiency of changes in fuel and coolant, we have modeled the two core designs suggested by the PDS-XADS project. Helium and lead-bismuth eutectic (LBE) have been tested as coolants. MOX and a transuranium fuel have been tested as fuels.

#### 3.1.1 Source efficiency

Seltborg suggested proton source efficiency to be defined as [13]:

$$\psi^* = \left( \frac{1}{k_{eff}} - 1 \right) \cdot \frac{\langle F\phi_s \rangle}{\langle S_p \rangle} . \quad (1)$$

For a given  $k_{eff}$ ,  $\langle F\phi_s \rangle$  is approximately proportional to the total power produced in the core, and thus to the beam power amplification.

The neutron source efficiency on the other hand relates the multiplication of “source neutrons” to fission multiplication. However, the definition of what is considered as source neutrons may vary inbetween different systems. This is why we choose to discuss effects on the proton source efficiency, which is uniquely defined.



### 3.1.2 System descriptions

The PDS-XADS-project, funded by the European fifth framework programme, presented two concepts of sub-critical cores [14][15]. They were both 80 MW<sub>th</sub> experimental core designs. One of them was cooled by lead-bismuth eutectic and the other by helium. A 600 MeV proton beam impinging on an LBE-target was assumed.

Our modelling was made with MCNPX 2.5e [16]. Two different fuel options have been tested. MOX fuel has been assumed as the reference case. In a more innovative setup, a transuranium (TRU) nitride fuel, with a Pu/Am/Cm composition of 40/50/10% respectively is assumed. This fuel has been chosen as an eligible candidate for fuel in a full-scale transmutation reactor, as the Pu/Am ratio correspond to the equilibrium nuclide vector that would eventually be reached in a transmutation fuel cycle with multi-recycling [17].

Together with two options for coolant, this gave us four cases, for which the proton source efficiency have been studied.

### 3.1.3 Results

The proton source efficiency for the four different coolant-fuel combinations is displayed in Table 3.1 There are significant differences in the proton source efficiency in the four cases, both with respect to the choice of fuel and to the choice of coolant. Changing coolant from helium to LBE lowers  $\psi^*$  by 10%. Replacing MOX fuel for TRU fuel further degrades the proton source efficiency by 10%.

Table 3.1:  $\psi^*$ , for the four cores studied and the relative difference to the He-MOX case

|          | He-MOX | LBE-MOX      | He-TRU       | LBE-TRU      |
|----------|--------|--------------|--------------|--------------|
| $\psi^*$ | 19.4   | 16.8<br>-13% | 16.8<br>-13% | 15.2<br>-22% |

In a previous study by Pelloni [18], the neutron source efficiency  $\phi^*$  was calculated for the He- and LBE-cooled XADS core designs respectively by deterministic methods, assuming a spallation neutron source modelled with Monte Carlo methods [19]. The absolute values for  $\psi^*$  found in the present study may be recalculated to neutron source efficiency by dividing the numbers by  $Z$ , representing the number of source neutrons per source proton. Of course  $Z$  is dependent of the source neutron definition. In this case as well as in the reference [18], the cut off neutron source definition is applied. A neutron is defined as a source neutron as its energy falls below 20 MeV, regardless of its geometrical position. It shows our values are higher than those of reference [18]. The qualitative effects of changing the coolant, observed in the two studies, are similar though.

An analysis of this discrepancy showed that the difference in geometries of the spallation targets in the two studies is important for the results. Increasing the radius, from the 20 cm of the present study to the 31.5 cm used by Pelloni, reproduces the previous results with good agreement. The comparative study is summarised in *Table 3.2*.

Table 3.2: Comparison of  $\phi^*$  to the values calculated by Pelloni

| $\phi^*$             | He-MOX | LBE-MOX |
|----------------------|--------|---------|
| Main result          | 1.545  | 1.304   |
| Pelloni              | 1.212  | 0.986   |
| Pelloni reproduction | 1.142  | 0.969   |

### 3.1.4 Conclusions

Americium introduction in the fuel of a subcritical core decreases  $\psi^*$ . In a core loaded with americium-based fuels,  $\psi^*$  is around 10% lower than in a MOX fuelled core.  $\psi^*$  is reduced by another 10% when helium is replaced by LBE.

Both of these effects are due to the strong dependence of fission and capture cross-sections on the incident neutron energy in the 1 MeV region in even-N nuclides, and to slight energy shift in this behaviour of the cross-sections in between the nuclides.

More details are given in [Appendix 7](#).

## 4 NUCLEAR FUEL CYCLE ANALYSIS

### 4.1 EUROPEAN PROJECT RED-IMPACT

Partitioning, transmutation and conditioning (P&T/C) and waste reduction technologies, if implemented properly and in full consultation with the geological disposal community, are expected to significantly reduce the burden associated with radioactive waste management and disposal. P&T is likely to ease the final repository requirements and it will also contribute to the sustainability of nuclear energy in those countries that pursue this source of energy.

RED-IMPACT is a 3-year, European project under the sixth framework programme with the title *Impact of Partitioning, Transmutation and Waste Reduction Technologies on the Final Nuclear Waste Disposal*. The project is coordinated by the department of Nuclear- and Reactor Physics at KTH.

#### 4.1.1 Objectives of the red-impact

The objectives of the 3-year RED-IMPACT project (Total budget 4 M€ including EC contribution of 2 M€) are:

- Assess the impact of P&T on geological disposal and waste management.
- Assess economic, environmental and societal costs/benefits of P&T.
- Disseminate results of the study to stakeholders (scientific, general public and decision makers) and get feedback during the course of the study.
- Iterate and refine the work based on stake-holders' feedback to achieve full impact of this study on the implementation of the waste management policy of the European Community.

The work of the project is subdivided into six work packages:

- **WP1:** Waste management and transmutation strategies will be reviewed and a number of representative scenarios will be selected for in-depth impact studies.
- **WP2:** Feasibility of the industrial deployment of selected scenarios will be made and their impact on waste management will be studied.
- **WP3:** Assessment of waste streams, waste features, leach resistance, heat generation, reprocessing capability etc will be studied for selected fuel cycles.
- **WP4:** Assessment will be made of the benefits and costs of P&T/C in advanced fuel cycles for waste management and geological disposal.
- **WP5:** Economic, environmental and societal assessment of fuel cycle strategies will be performed.
- **WP6:** Synthesis and dissemination of results of the above studies will be made to stakeholders.

The Consortium of RED-IMPACT project is unique in that it has assembled the most relevant actors in this field and it has a very broad multi-disciplinary scientific and industrial background of partners from 11 countries across Europe:

- Waste Management Agencies/Companies: ENRESA (ES), NIREX (UK), RAWRA (CZ) and SKB (S).
- Nuclear Industries and Utilities: BN (B), BNFL (UK), COGEMA (F), EA (ES), FRAMATOME (F and D) and EnBW (D).
- Research Institutes and Universities: CEA (F), CIEMAT (ES), CITON (Romania), FZJ (D), GRS (D), KTH (S), ITU (EC), NRG (NL), USTUTT (D), SCK.CEN (B), VUJE (Slovakia) and NRI (CZ).

At its completion, the present project is expected to provide a major advance to the P&T research by producing and disseminating a comprehensive and coherent assessment of environmental and societal costs, benefits and difficulties of the deployment of P&T, conditioning and waste reduction technologies for nuclear waste management.

#### **4.1.2 WP4 Activities –Criticality calculation**

##### **4.1.2.1 Introduction**

In WP4 KTH among other tasks has to calculate the criticality for different fuel cycle scenarios defined in other work packages. These scenarios are referred to as A1, A2, A3, B1 and finally B2. The scenarios are:

- A1- open UO<sub>2</sub> fuel cycle, which also is the reference scenario
- A2- monorecycling of plutonium in PWR:s
- A3- multirecycling of MOX in PWR:s
- B1- fast neutron Gen IV reactors
- B2- PWR plus ADS reactors

The waste produced in the selected scenarios differs. The A1 scenario produces waste in the form of spent fuel in sub assemblies, while A3, B1 and B2 produce waste in the form of extracted fission products and losses during reprocessing of the spent fuel. A2 scenario produce both sub assemblies with spent fuel and extracted fission products together with losses. The spent fuel sub assemblies are assumed to be put in copper KBS3 canisters, and the reprocessing waste losses together with the fission products will be mixed up with borosilicate glass and poured in so called universal canisters, thus forming a vitrified waste form.

##### **4.1.2.2 Method**

The criticality calculations are carried out using Monte Carlo code MCNP4c. The result is given as an estimated multiplication factor together with an associated

standard deviation of the mean:  $\bar{k} \pm \sigma_k$ . In order to perform the calculations, two input data are needed; detailed data about the geometry model of the waste package and the isotopic composition and density of the waste. Input for the geometry and isotopic content will be taken from RED-IMPACT deliverable D3.3, which represents the situation after a cooling time of 50 years. The time evolution of the isotopic inventory

will be calculated using MCB, the Monte Carlo continuous Burnup code. The calculations will be carried out at time 0, 50, 100 500, 1000, 5000, 10 000, 50 000, 100 000 and 1000 000 years, after which the waste is put in the waste package.

#### 4.1.2.3 Assumptions

The calculations will be based on a few assumptions. First it will be assumed that the canisters are surrounded by a 75 cm thick layer of montmorillonite (high quality bentonite). Data is taken from [webmineral.com/data/Montmorillonite.shtml](http://webmineral.com/data/Montmorillonite.shtml) and composes of (weight percent): Na 0.84%, Ca 0.73%, Al 9.83%, Si 20.46%, H 4.04% and finally O 64.11%. It is also assumed that the bentonite has a water saturation of 25% and a wet density of 2 g/cm<sup>3</sup> (SKB report TR-00-12 s 67). It is further assumed that the vitrified waste is homogenously distributed through the universal canister.

#### 4.1.2.4 Technical description of waste packages

##### 4.1.2.4.1 PWR UO<sub>2</sub> spent fuel waste package

For scenario A1 a once through fuel cycle is adopted., which requires canisters housing PWR fuel assemblies. Further a total cooling (or decay) time of 50 years has been assumed before the emplacement of the sub assemblies inside the waste packages and the deep disposal repository. The characteristic of a PWR fuel assembly is presented in *Table 4.1*.

Table 4.1 Technical specification for the scenario A1 UO<sub>2</sub> fuel assembly and A2 MOx fuel assembly

| Lattice/reactor type                      | 17 * 17   | PWR             |
|---|-----------|-----------------|
| Physical dimensions:                      |           |                 |
| - Total length                            | 4100      | mm              |
| - Section                                 | 217 * 217 | mm <sup>2</sup> |
| Mass of structure                         | 145       | kg              |
| Mass of initial heavy metal               | 459.5     | kg              |
| 264 fuel rods                             |           |                 |
| 24 thimble guides                         |           |                 |
| Semi diameter of pellet                   | 0,41266   | cm              |
| intern semi diameter of the clad          | 0,41266   | cm              |
| extern semi diameter of the clad          | 0,474364  | cm              |
| intern semi diameter of the thimble guide | 0,572945  | cm              |
| extern semi diameter of the thimble guide | 0,6132012 | cm              |

The cladding and thimble guide material consists of Zircaloy 4. Data is taken from FRAGEMA 900 MWe standard PWR fuel assembly.

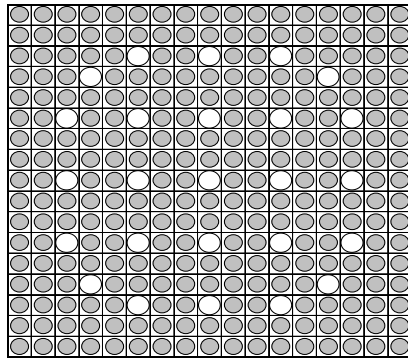


Figure 4.1 PWR sub assembly model

The properties of the canister are taken from the Swedish SKB model called KBS3. The residual thermal power of one fuel assembly after this time will be in the order of 400 W, and, in case of disposal in granite, it is reasonable that four spent fuel assemblies is loaded in each waste package.

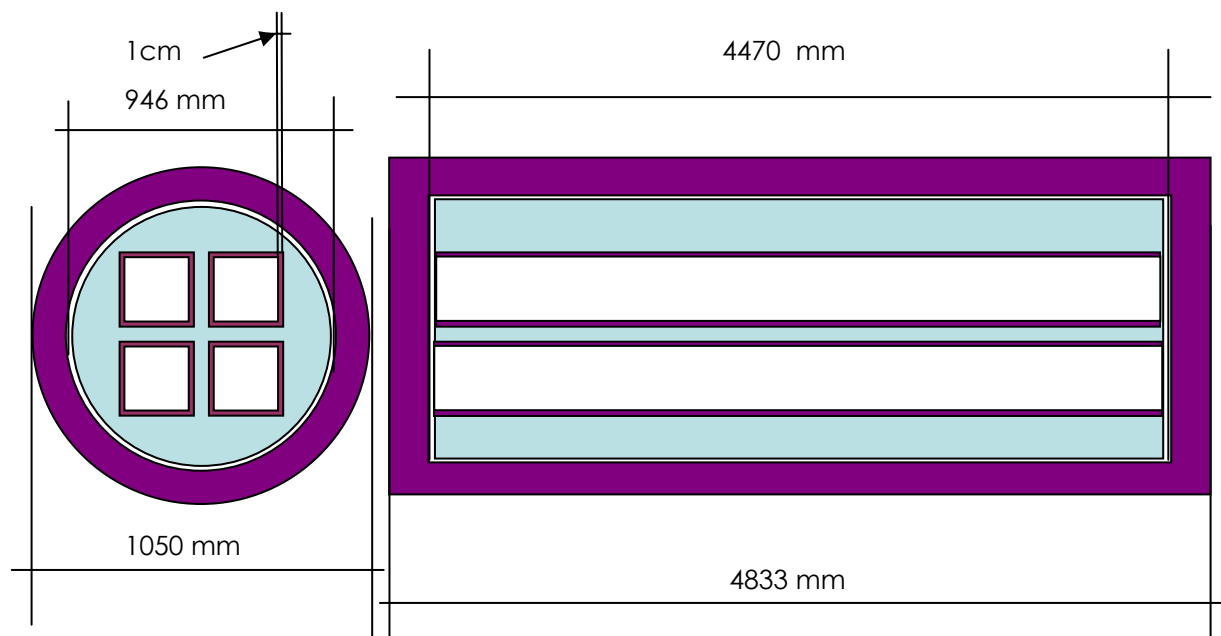


Figure 4.2. A1 scenario: Waste package for 4  $UO_2$  spent fuel assemblies

#### 4.1.2.4.2 Spent MOX fuel assembly

Scenario A2 consists of a strategy in which Pu is recycled once in Light Water Reactors as MOx type fuel. The waste being produced in the A2 strategy is composed of both the spent MOx assemblies and the waste losses being produced during reprocessing of initial LWR  $UO_2$  assemblies together with the non-volatile fission products. The latter waste type will be dealt with as vitrified HLW. The subassembly for MOx fuel is the same as for the  $UO_2$  fuel, see characteristics in Table 4.1. After

irradiation, the spent fuel assemblies are assumed first to be housed in the reactor pool for 5 years and thereafter in the interim storage for 45 years, all in all a total cooling time of 50 years. The residual thermal power of one MOX fuel assembly after this time will be in the order of 1550 W, and therefore only one spent fuel assembly will be placed in each waste canister. The proposed waste package consists of an adopted KBS3 copper cylinder. Inside the package there is a cast iron insert provided with one 1 cm thick steel channel where the MOX assembly is placed. Figure 4.3 shows a schematic out of scale drawing of the waste package for scenario A2:

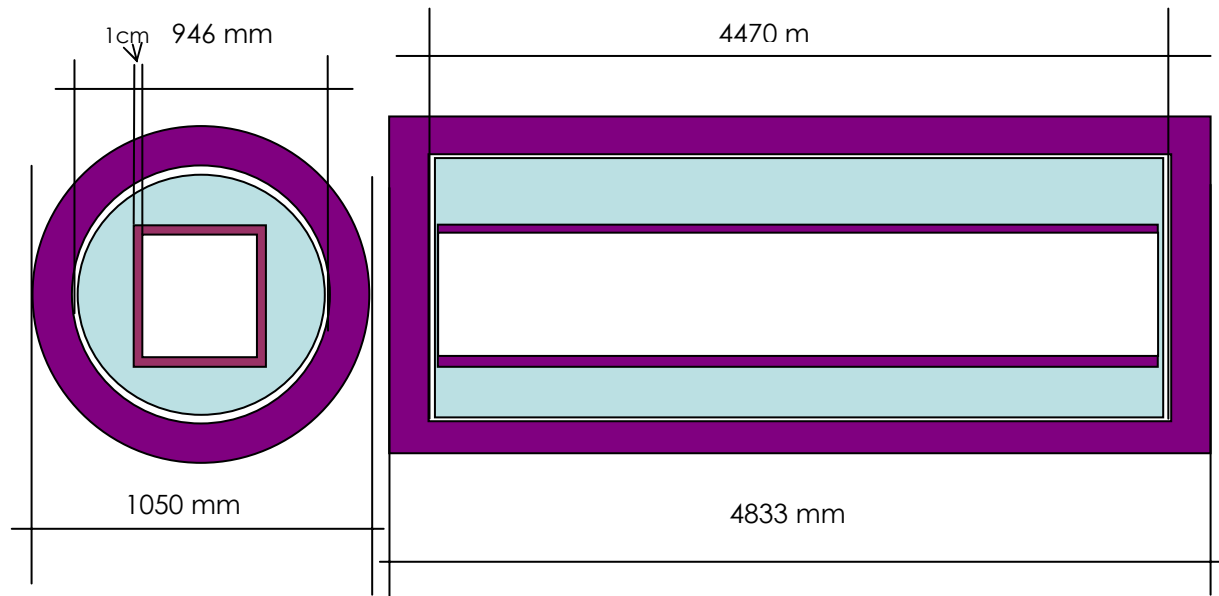


Figure 4.3 Waste package for 1 MOx spent fuel assembly: Scenario A2: Waste package for 1 MOX spent fuel assembly

#### 4.1.2.4.3 Universal canister waste package

The liquid HLW from the PUREX reprocessing contains all non-volatile fission products and minor actinides, also some small amounts of uranium and plutonium, i.e. reprocessing losses. It has been supposed that all the fuel impurities in the spent fuel go to the liquid waste. This liquid waste is calcinated, mixed up with molten borosilicate glass, and poured into Universal Canisters. The main companies offering spent fuel reprocessing services in the world (BNFL and Cogéma) make use of a standard canister, named Universal Canister, where the vitrified waste is confined. The main characteristics of the Universal Canisters are summarized in *Table 4.2*.

Table 4.2 : Characteristics of Universal Canister (scenarios A2, A3, B1, B2)

| Material             | Stainless Steel<br>(C: 0.15%; Cr: 24%; Ni: 13%) |
|----------------------|---|
| Physical dimensions: |   |
| - Length             | 1 338 mm  |
| - External Diameter  | 430 mm  |
| - Wall thickness     | 5 mm  |
| Mass:                |   |
| - Total              | 492 Kg  |
| - Empty              | 80 Kg   |
| Volume:              |   |
| - External           | 175 l   |
| - Internal           | 170 l   |
| - Vitrified Waste    | 150 l   |

It has been assumed that the waste content of each Universal Canister is 40 kg of fission products and actinides while 372 kg out of the total 412 kg of waste will be the glass matrix. The waste is assumed to be stored for a decay and cooling time of totally 50 years. The proposed waste package consists of an overpack containing one single Universal Canister. The overpack is made of a carbon steel cylinder 1.60 m long and 0.65 m external diameter. The wall thickness is 0.10 m and the two lids are 0.12 m thick. Figure 4.4 shows a model of the waste package:

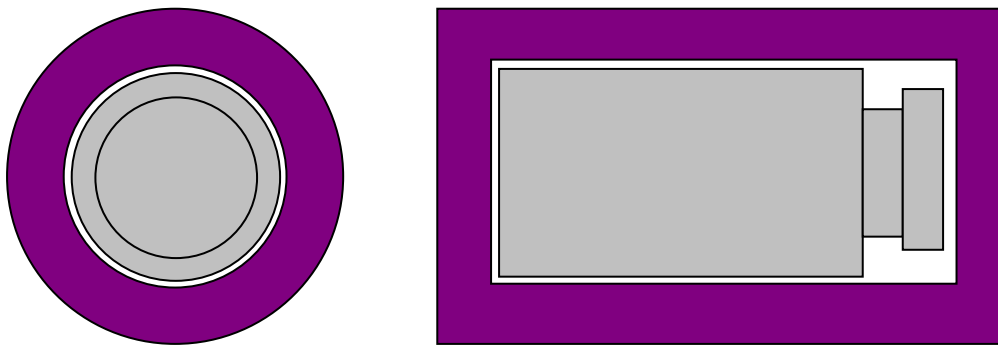


Figure 4.4 Universal waste package for VHLW

The mass of the waste package will be 2 950 kg from which 2 460 kg correspond to the external container and 490 kg to the Universal Canister.



### 4.1.3 Results

The calculations has in the case of spent fuel A1 and A2 scenario been performed for both a basic condition and a condition with waterfilled canisters, which significantly raisens the criticality.

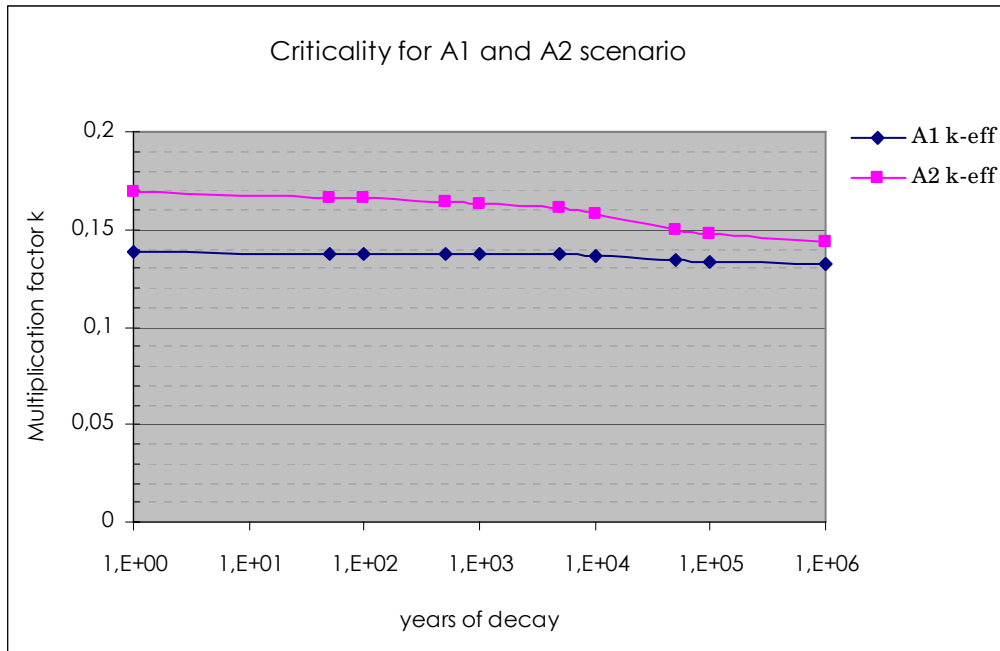


Figure 4.5 Criticality for basic condition

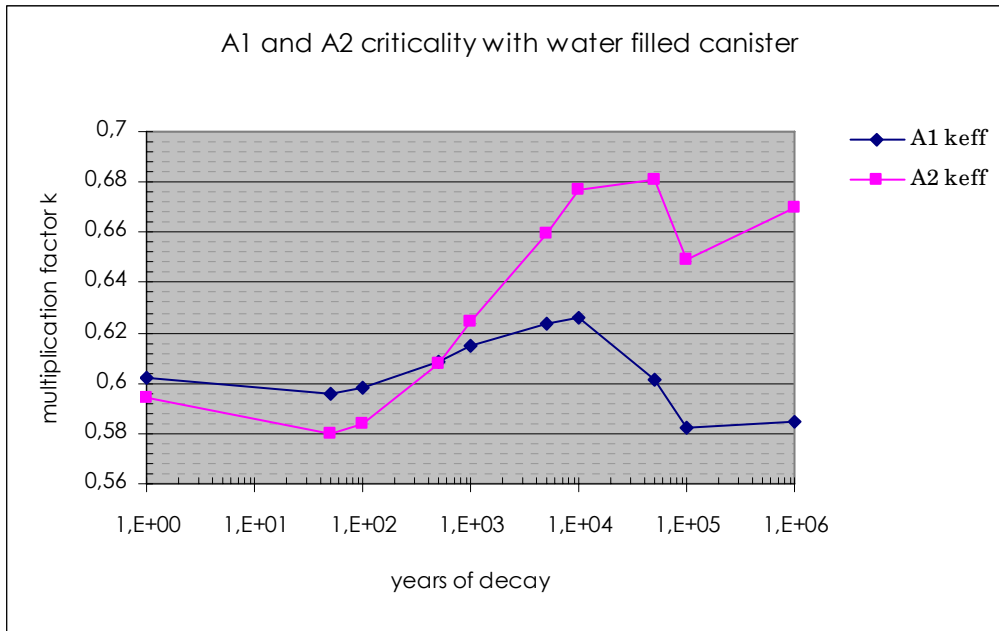


Figure 4.6 Criticality for condition with water filled canisters

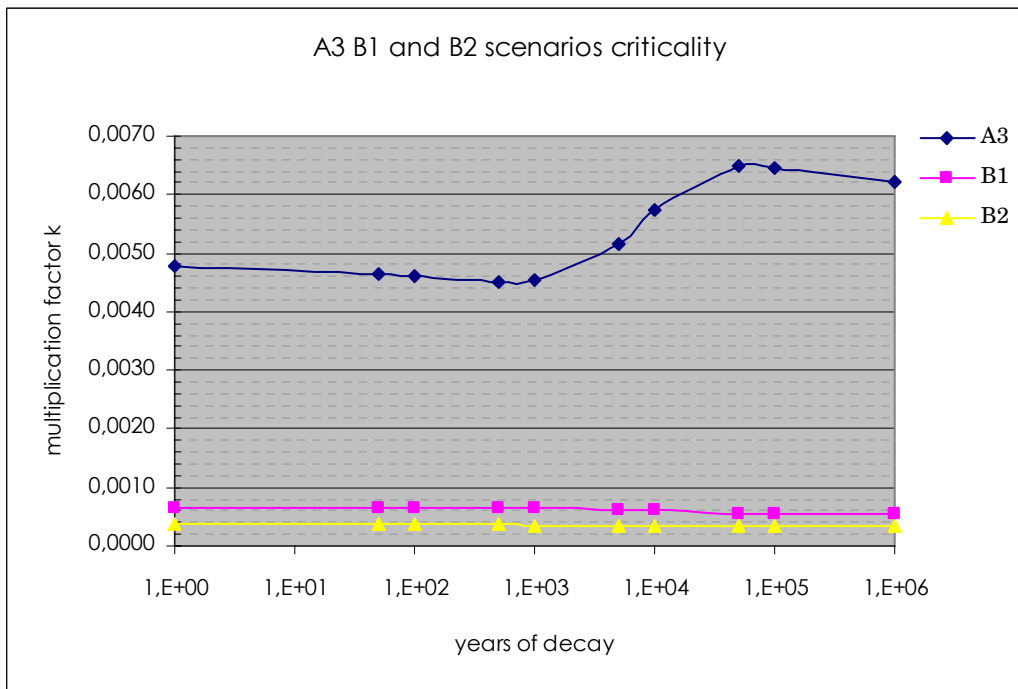


Figure 4.7 Criticality for A3, B1 and B2 vitrified high level waste universal canister

The results show that the only situation in which any significant criticality is reached is for the spent fuel and when the canisters are ruptured and water filled. However there is still a large margin of approximately 30 000 pcm to  $k_{eff} = 1$  and a self sustaining chain reaction. The MOX fuel cycle has the highest criticality properties in both the spent fuel case and in the vitrified high level waste.

## **4.2 ANALYSIS OF THE SWEDISH NUCLEAR FUEL CYCLE FOR RED-IMPACT PROJECT**

A study of advanced nuclear fuel cycles has been performed aimed to optimize the nuclear waste management for the Swedish nuclear reactor fleet, i.e. a medium size nuclear power system based currently on a simple once-through strategy. The reference scenario is the Swedish LWR-park which aims at characterizing the final spent nuclear fuel inventory of the Swedish LWR fleet when it is retired. The accumulated spent LWR-fuel is then used to feed a park of accelerator-driven systems, with the goal to reduce the radiotoxic inventory through incineration of plutonium and americium. Subsequently the benefits of deploying the ADS are examined.

Two types of scenarios are analyzed; one long-term equilibrium scenario and one phase-out scenario. The objective of the equilibrium scenario is to assess the ratio of LWR over number of ADS needed to consume the LWR-generated TRU. In the equilibrium scenario the Swedish reactor park operates at a constant nuclear electricity production, with an optimal number of ADS integrated into the park, in order to stabilize the plutonium and americium production/destruction. The simulation covers the time period from the start-up of the first reactor Oskarshamn-1 in 1972 until 2100. A modification of the equilibrium scenario is also performed, with the introduction of LWR MOX-recycling prior to actinide burning in ADS.

The short-term phase-out scenario addresses a country adopting a phase-out of existing reactors. The approach is to find an optimal number of ADS to reduce the radiotoxic burden of the final waste, through the recycling of the spent LWR generated americium and plutonium. The future need for electricity supply is of no concern but instead focus is put on reducing the burden of radiotoxic spent fuel for the Swedish spent fuel repository. As to the referendum in 1980 the nuclear power in Sweden is to be phased out and the phase-out simulations were carried out under these assumptions and thus decommissioning the reactors after 40 years of operation.

### **4.2.1 Simulation tool**

The fuel cycle simulations in this thesis were done using the Nuclear Fuel Cycle Simulation code - NFCSim, developed at Los Alamos National Laboratory. NFCSim tracks the size and composition of the nuclear material which evolves with time. It contains a detailed description with time-dependent accounting of location and accessibility of nuclear reactors, enrichment plants, reprocessing facilities, fuel fabrication plants and storage facilities. The code models life-cycle material balances for an arbitrary number of reactors and includes a cost database. The modelling capabilities include LWR oriented fuel cycles with the option of actinide recycling in fast reactors and ADS. NFCSim groups fuel batches by fuel type and burnup calculations are carried out for each batch. The burnup and reactivity calculations are performed through invoke of the burnup code ORIGEN2.2. All the necessary one-group cross-section libraries were prepared using the 3D continuous energy Monte Carlo burnup code Monteburns.

## 4.2.2 Results

The simulation of the equilibrium scenarios showed that four ADS, of 800 MWt each, were sufficient to burn an amount of plutonium (Figure 4.8) and americium corresponding to the build-up of those isotopes in a system of 10 LWR, with an installed capacity of approximately 10 GWe. The fraction of plutonium and americium in the spent fuel was significantly reduced when ADS were integrated into the LWR-park. Furthermore it was showed that the plutonium inventory could be more reduced by MOX-recycling in LWR prior to the ADS operations, but on account of slightly higher americium production. The simulation of the long-term scenarios indicates the enormous difference made by operating ADS for incineration of spent LWR fuel. Even though this study only dealt with mass differences, the impact on the final disposal from a radiotoxic point of view is obvious.

The simulation of phasing-out the Swedish LWR-park, after 40 years of operating the reactors, accumulated an amount of 9900 tons spent UOX fuel. The scenario deploying three ADS, with a simulated life-time of 50 years, resulted in the decrease of the plutonium and americium inventory by 70% and 60% respectively. While in the scenario deploying four ADS, the simulation was terminated after only 35 years. The early shutdown by NFCSim in this scenario is due to the fact that NFCSim only accounts for the amount of spent fuel stored in the spent fuel inventory and not the amount that is loaded into the reactor cores. In this case the plutonium inventory was not sufficient to continue feeding the four ADS cores, although more plutonium remained in the system which was thereby left un-recycled. In a virtual scenario the operation would of course continue and the optimal solution, in a Swedish phase-out scenario, could be to have three or four ADS running at a first round and to have one final ADS which would operate after shutdown of the first ones and fed with the plutonium and americium contained in their cores. This could optimise the transmutation strategy and finish as much as possible of the remaining plutonium and americium still available in the system.

From an economically point of view it is open to discussion if it would be worth the price to construct a park of ADS, with the purpose of closing a fuel cycle of a LWR-park which is doomed to be phased-out. Although the amount of long-lived radiotoxic elements will be significantly less in a scenario pursuing transmutation, a certain amount of long-lived elements will always remain due to losses in reprocessing and fuel fabrication. If instead, Sweden or a country with similar energy policy, wishes to sustain/develop the use of nuclear power, the construction of ADS for transmutation of nuclear waste in a long-term perspective (compared to a phase-out scenario), is more justified economically. And even more important considering the continued use of nuclear power, the most valuable argument pro-transmutation in the perspective of long-lived radioactive elements, would not be purely of economically character but rather that of the morally and ethically aspects. Pursuing transmutation would eliminate most of the long-term radiotoxicity and should be considered a possibility to clear the back-end of the fuel cycle, and not preserve some the most radiotoxic of the longlived radionuclides for 100 000 years.

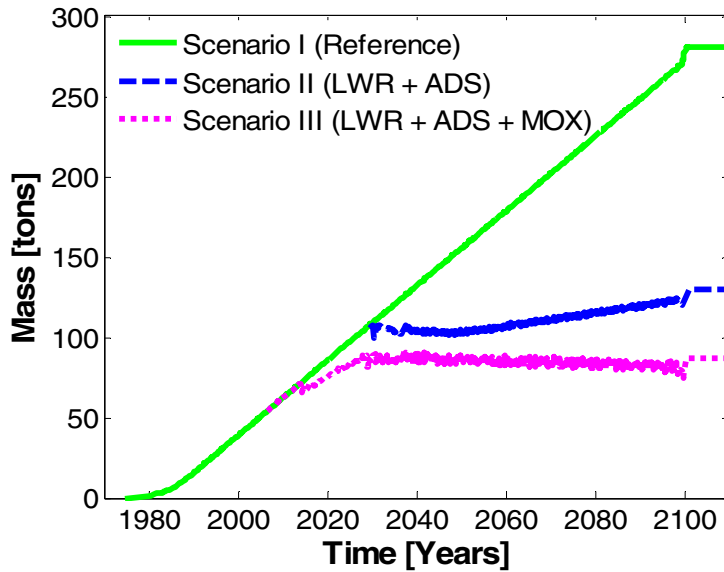


Figure 4.8 Plutonium out of core inventory in the equilibrium scenarios.

Even though transmutation is adopted as a strategy to decrease the burden of nuclear waste the need to manage high level waste will always exist, as losses occur during reprocessing and fuel fabrication. And even though the waste management of irradiated ADS fuel will not need as long supervision as spent UOX fuel, it will demand other disposal techniques. Investigation of transmutation strategies applied to the Swedish nuclear waste management would need to investigate not only this, but should also include a cost analysis and a much more detailed analysis of the radiotoxic inventory, isotopic composition and doses to public and workers. These investigations were, however, beyond the scope of this study.

Details of this work have been described in [Appendix 13](#) and [Appendix 14](#).

### 4.3 DETAILED ANALYSIS OF THE SWEDISH NUCLEAR FUEL CYCLE: ANALYSIS OF SPENT FUEL MANAGEMENT SCENARIOS

The purpose of this study was to analyze the potential of transmutation up to 99% of transuranium isotopes found in the Swedish spent nuclear fuel by year 2025. To this end, a computer code named Fuel Cycle Analyzer (FCA) has been developed by J. Dufek. The code implements a novel method to effectively solve point reactor equations of isotopic kinetics by using evaluated production-depletion rates.

Only few options have been defined and considered:

- To dispose the spent fuel as it is in a waste repository for permanent storage and monitoring (Phase-out Scenario);
- To restart several BWR or PWR units to burn/transmute existing plutonium and/or minor actinides in a form of Mixed Oxide or MOX fuel;
- To build one or several Accelerator Driven Systems (ADS) for use as stand alone reactors or more probably for use with a combination with BWR or PWR burners;

- Finally, to build one or several Fast Reactors (FR) which are reportedly very effective as transuranium burners.

The last option, Fast Reactors as transuranium burners, has been deliberately left unexplored in this report.

Several scenarios have been modeled with a help of the FCA code:

- Phase-out scenario;
- BWR MOX burners;
- PWR MOX burners;
- ADS MOX burners;
- BWR + ADS MOX burners.

A very general conclusion has been made about BWR MOX reactors being more efficient in burning plutonium in the form of MOX fuel. In this respect BWR reactors supersede PWR ones by approximately 10%. In addition, BWR reactors produce about 10% less americium inventory. However, neither BWRs alone nor PWRs alone are capable of incinerating 99% of TRU.

It was found that ADS reactor park can theoretically in the ideal case burn 99% of transuranium isotopes. The duration of this scenario heavily depends on the time needed for cooling the spent fuel. If we assume 10 years of cooling the nuclear waste from ADS, the scenario duration becomes at least 200 years under most optimistic technical assumptions. On the other hand, the use of advanced pyro-processing with a cooling time of only 2 years dramatically decreases the incineration time down to 50 years only. Moreover, ADS reactors have turned out to be a necessary component to decrease the americium inventory because neither BWR nor PWR alone can provide prevalence of americium destruction over its production during the operation time. Nevertheless, the economic advisability of these scenarios calls for further investigation.

In addition, a combination of MOX1->MOX2->ADS has been found more efficient (approximately by 10%) in reducing the transuranium inventory.

Economic analysis of various scenarios has been performed under a number of simplifying assumptions. It has been found that the MOX scenario is more than twice as expensive as ordinary UOX fuel cycle. On the other hand, ADS burners reduce this factor down to about 1.5, in other words electricity produced after year 2025 at a hypothetical combination of BWR MOX reactors together with ADS MOX reactors appears to be approximately 50% more expensive in comparison with the nowadays situation. However, the cost for permanent disposal and monitoring of the spent fuel in the phase-out scenario has not been taken into account.

This study has been separately published by SKB in 2006 [21]

## 5 POTENTIAL OF REACTOR BASED TRANSMUTATION

### 5.1 MILITARY PLUTONIUM INCINERATION

In the future development of nuclear energy, the graphite moderated, helium cooled reactors may play an important role because of their technical advantages: many features of passive safety, low cost, flexibility in the choice of fuel, high conversion energy efficiency, high burnup, more resistant fuel cladding and low power density. General Atomic possesses a long time experience with this type of reactors and it has recently developed a design in which the nuclear power plant is structured into 4 reactors modules of 600 MW<sub>th</sub>: the Gas Turbine – Modular Helium Reactor (GT-MHR). The GT-MHR offers a rather large flexibility in the choice of fuel type; Th, U, and Pu may be used in the manufacture of fuel with some degrees of freedom. As a consequence, the GT-MHR fuel cycle maybe flexibly designed for different objective aside if energy production, e.g. the reduction of actinides waste production trough fuel cycles based on thorium.

In our previous studies [5]-[8] we analyzed the behavior of the GT-MHR with a fuel based on LWRs waste. In the present study we focused on the incineration of military Pu. This choice of fuel requires a detailed numerical modeling of the reactor, since a high value of  $k_{\text{eff}}$  at the beginning of the fuel cycle requires modeling of control rods and burnable poison. By contrast, in the reactor fueled with LWRs waste, breeding of fissile isotopes (mainly Pu isotopes) at the equilibrium ensures almost constant value of  $k_{\text{eff}}$ .

After an irradiation of three years, the GT-MHR transmutes about 66% of the <sup>239</sup>Pu mass of the DF (Figure 5.1); at the same time, the fraction of <sup>240</sup>Pu accumulates and a small quantity of <sup>241</sup>Pu builds up; whereas, the production of <sup>242</sup>Pu and <sup>241</sup>Am remains limited to a few kilograms.

Since 50% of the mass of the irradiated DF becomes PDF the right columns of Figure 5.2 are equal to the left ones of Figure 5.1 divided by 2. During the irradiation of the PDF, the concentration of <sup>239</sup>Pu and <sup>240</sup>Pu respectively diminishes of 75% and 53% (Figure 5.2).

If GT-MHR is fueled by military plutonium at the equilibrium of the fuel composition 66% of <sup>239</sup>Pu is burned in three years and 92% in six years.

#### 5.1.1 Light Water Reactors Waste Incineration

The Gas Turbine – Modular Helium Reactor coupled to the Deep Burn in-core fuel management strategy offers the extraordinary capability to incinerate over 50% of the initial inventory of fissile material. This extraordinary feature, coming from an advanced and well tested fuel element design, which takes advantage of the TRISO particles technology, is maintained while the reactor is loaded with the most different types of fuels. In the present work, we assumed the reactor operating at the equilibrium of the fuel composition, obtained after six years irradiation of transuranium isotopes from spent the LWR-fuel (LWR-TRU). We investigated the effects of introducing burnable poison and control rods. We equipped the core with all the three types of control rods: operational, startup and shutdown ones. We employed

as burnable poison natural erbium, due to the  $^{167}\text{Er}$  increasing neutron capture microscopic cross section in the energy range where the neutron spectrum exhibits the thermal peak; in addition, we utilized boron carbide, with 90% enrichment in  $^{10}\text{B}$ , as the absorption material of the control rods.

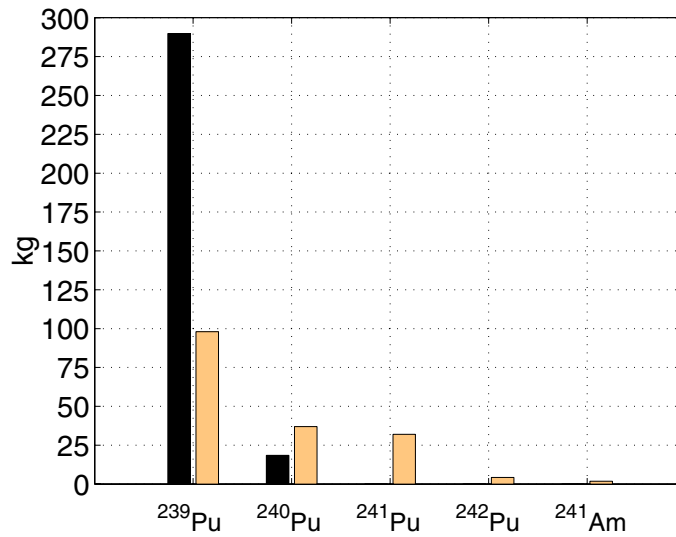


Figure 5.1 Mass of the most abundant actinides of the fresh DF (central ring at beginning of the 12<sup>th</sup> year) and after three years irradiation (inner ring at the end of the 12<sup>th</sup> year).

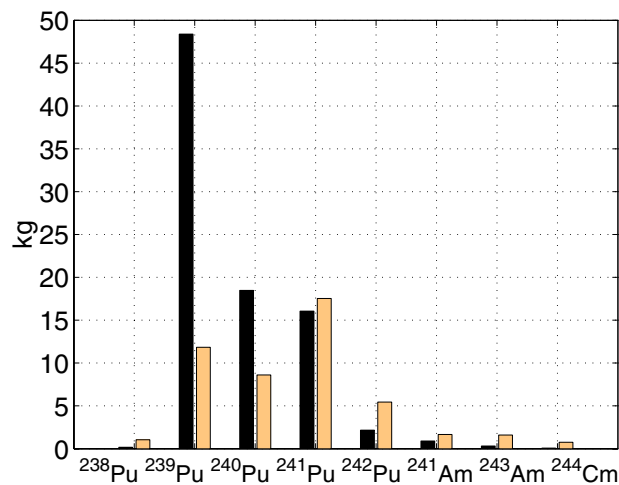


Figure 5.2 Mass of the most abundant actinides of the fresh PDF (outer ring at beginning of the 12<sup>th</sup> year) and after three years irradiation (central ring at the end of the 12<sup>th</sup> year).

Concerning the burnable poison studies, we focused on the  $k_{\text{eff}}$  value, the  $^{167}\text{Er}$  mass during burnup, the influence of modifying the radius of the BISO particles kernel and the fuel and moderator coefficients of temperature. Concerning the control rods studies, we investigated the reactivity worth, the changes in the neutron flux profile



due to a partial insertion, the influence of modifying the radius of the BISO particles kernel and  $k_{eff}$ , at the beginning of the operation.

Figure 5.3 depicts the evolution of  $k_{eff}$  for three different cases: empty burnable poison holes and burnable poison holes filled with two years irradiated TF or erbium pins. We can note that the employment of erbium flattens the curve of the  $k_{eff}$  time evolution since the initial excess of reactivity is limited to only 3940 pcm and at the same time, the life of the fuel is shorted only by 70 days, compared to the case of empty burnable poison holes. The curve referring to the TF pins collocates inbetween the other two ones and it exhibits an initial excess of reactivity of 5180 pcm with a penalty in the fuel life of 40 days, compared to the case of empty burnable holes. In all the curves it is clearly visible the poisoning of the short life fission products that diminishes the initial excess of reactivity of 1000 pcm already after 10 days.

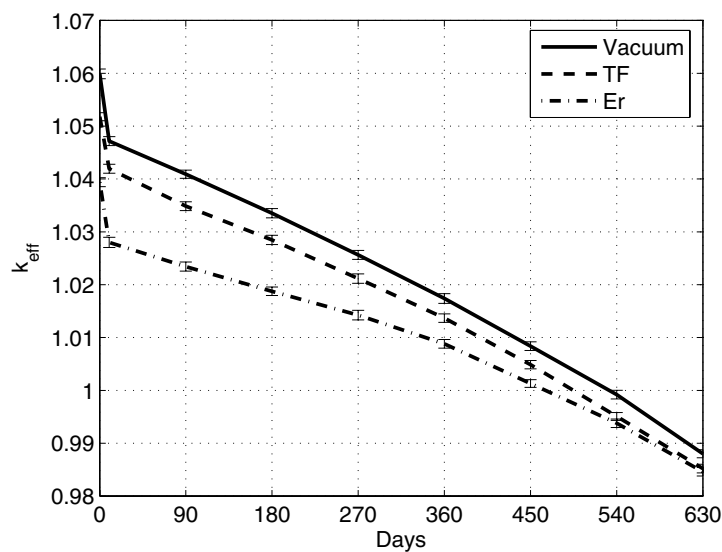


Figure 5.3 Evolution of  $k_{eff}$  for the burnable poison holes filled by: vacuum, erbium and TF. The standard deviation is indicated by the small horizontal ticks and it is given with 95% confidence.

## 5.2 THE BLACK BURNABLE PARTICLES THEORY

According to the different geometry shape, the theory of black burnable particles predicts that the evolution of the poison macroscopic absorption cross section is exponentially, quadratic or linear when the burnable poison is displaced in homogeneous distribution, microspheres or needle-cylinders heterogeneous distributions, respectively. In the present studies, we took advantage of the Monte Carlo Continuous Energy Burnup Code MCB to verify the black burnable particles theory on the Gas Turbine – Modular Helium Reactor fuelled by military plutonium at the year the fuel reaches the equilibrium composition; we investigated 8 different burnable poisons, B, Cd, Er, Eu, Gd, Dy, Hf and Sm, in three different geometry configurations and we have found that the numerical results well match the theory predictions when BPs are disposed in small particles.

Figure 5.4, which plots the  $k_{\text{eff}}$  evolution for different radii of the Gd kernels, emblematically illustrates that the kernel radius is the key parameter that regulates the distinction of the microspheres and needle-cylinders curves as well as the sharpest and smoothest decrease of the  $k_{\text{eff}}$  curves for the microspheres and the homogeneous distributions, respectively. The gadolinium example permits to assert that for a large radius, the three curves are parallel and those one of the heterogeneous distributions are almost united; whereas, for a small radius, the curves of the heterogeneous distributions are plainly discernible and the position of the homogeneous distribution tend to invert with that one of the microspheres at the end of the irradiation period.

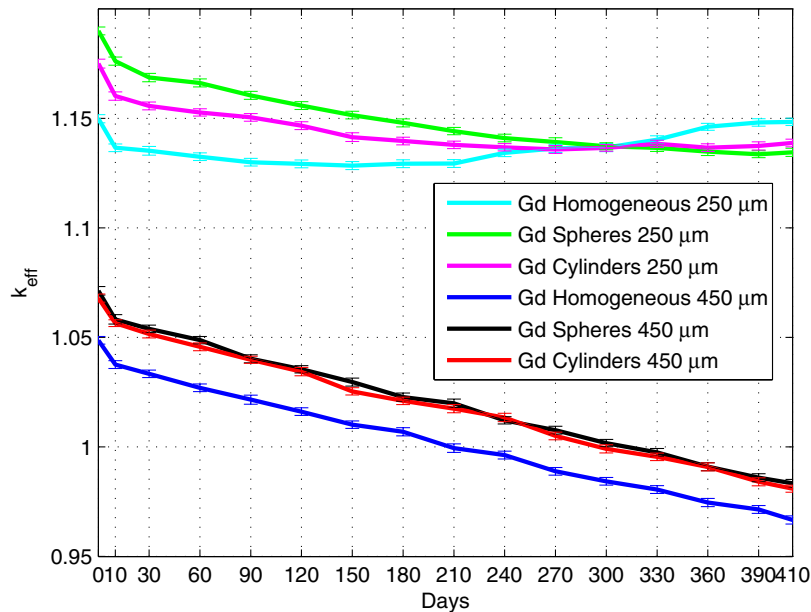


Figure 5.4  $k_{\text{eff}}$  evolution for gadolinium BP with microspheres kernel radii of 250 and 450  $\mu\text{m}$ . The horizontal ticks indicate the standard deviation with 95% confidence.

### 5.3 AXIAL SHUFFLING IN THE LIGHT WATER REACTORS WASTE IN-CORE FUEL CYCLE

In this study we investigated the influence of the axial shuffling and the operational control rods maneuvering on the incineration of LWR-TRU by a generation IV High Temperature Gas Reactor: the Gas Turbine - Modular Helium Reactor. Axial shuffling at Gas Cooled Reactors is possible because the reactor core is built in blocks stapled on each other vertically. Replacement/shuffling of these blocks is called axial shuffling.

During the reactor operation, while simulating the axial shuffling, it is quite important to take into account also the adjustment of control rods position, for the rods insertion alters the neutron flux shape and therefore changes the fuel depletion axial profile. We aimed at implementing a numerical simulation as much as possible close to a real scenario and therefore we took advantage of the powerful geometrical modeling capability of the MCB code to describe the reactor in a detailed 3D geometry model in which we simulated over 120 different burnable materials exposed to different neutron flux intensities. We adjusted the position of the control rods each 90 days of

irradiation to maintain the core as close as possible close to the criticality condition; thereafter, we recalculated the neutron flux and cross sections by a new MCNP run. At the present time, this sophisticated approach can be realized only by a computer cluster of at least 10 64bits processors working in parallel mode.

## 5.4 TRANSMUTATION OF AMERICIUM AND CURIUM

Finally, we investigated the benefit of transmuted americium and curium by considering two different types of fuels, one consisting of neptunium and plutonium and the other doing of americium and curium. This clear distinction in the fuel type allowed the comparison between the toxicity of the fresh americium and curium fuel versus that one of the irradiated fuel and it demonstrated that it is not worth to transmute americium and curium by the current design of the Gas Turbine – Modular Helium Reactor.

We focus on  $^{239}\text{Pu}$  (Figure 5.5 ), for this nuclide drives the fission chain; at the end of the first irradiation period, the leftover mass is increasing in the axial direction because the control rods adjustments induce a larger depletion of the nuclides in the lower regions of the core where the flux results higher due to the absence of the control rods (the leftover  $^{239}\text{Pu}$  mass, in the first axial region, over all rings, is 35.1 kg and, in the tenth axial region, is 73.2 kg); at the beginning of the second irradiation period, the axial upside-down shuffling turns the axial profile decreasing; at the end of the third irradiation period, the effect of the control rods withdrawal reverts, once again, the profile set by the axial shuffling (the  $^{239}\text{Pu}$  mass in the first axial region, summed over all rings, is 56.42 kg and in the tenth axial region, summed over all rings, is 116.41 kg); during the fourth irradiation period, the profile remains unchanged. Moreover, between the beginning of the second period (third groups of columns) and the end of the third one (fourth groups of columns), the transmuted mass of  $^{239}\text{Pu}$  is greater at the bottom of the reactor and it constantly decreases towards the higher axial regions; whereas, during the fourth period, the transmuted mass is larger at the center of the core. The above phenomenon is the consequence of the different lengths of the axial burnup wave: during the second and third periods the wave does not reach the top of the reactor, but it does during the fourth period. In fact, at the beginning of the fourth year, the upper regions of the core are richer in fissile plutonium and that balances the depressing effect on the neutron flux due to the presence of the control rods; this configuration sets a flatter axial neutron flux profile and it enhances the worth of the operational control rods, allowing the wave to reach the top of the reactor. Let us observe also that during the first and third irradiation periods, which have a short axial wave, the third region has the highest burnup of  $^{239}\text{Pu}$ ; this phenomenon is visible also in the other nuclides.

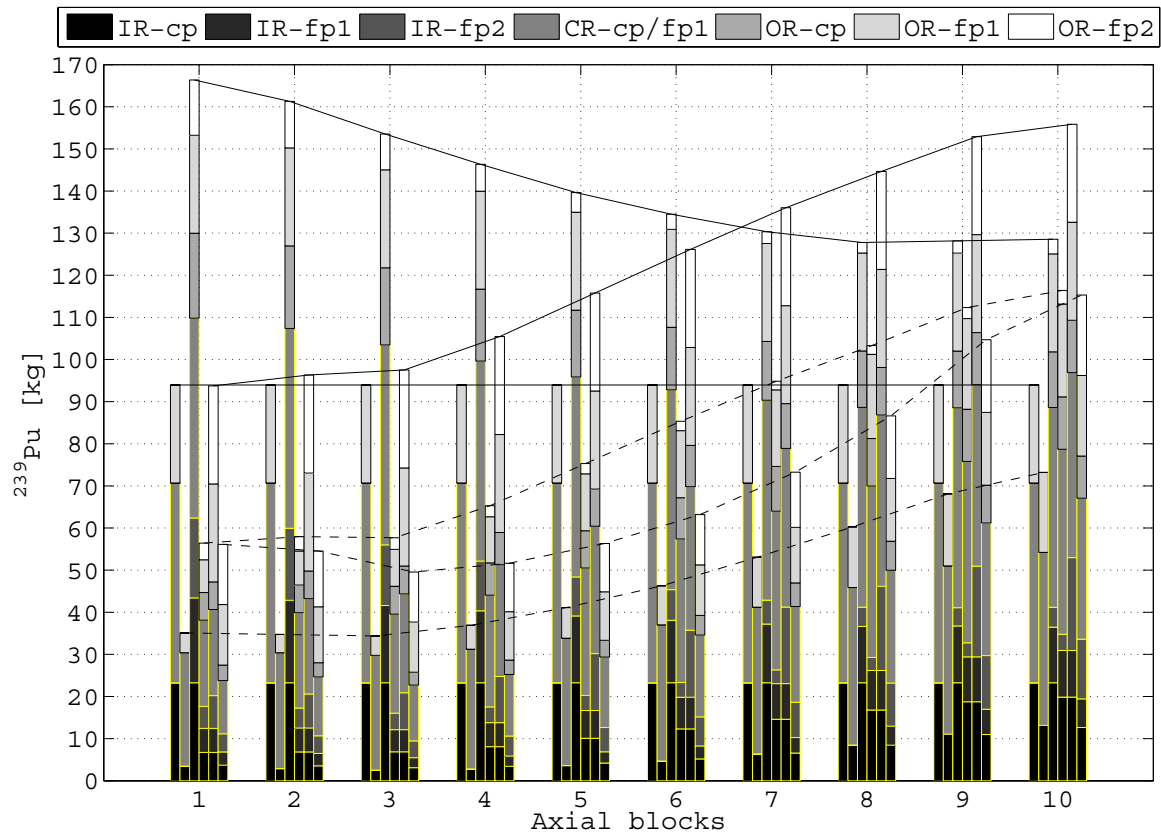


Figure 5.5  $^{239}\text{Pu}$  evolution during the four irradiation periods. For each axial block, the group of six columns represents, from the left to the right, the beginning of the first irradiation period, the end of the first one, the begin of the second one, the end of the third one, the begin and end of the fourth one. Solid and dashed lines mark the axial profiles at the beginning and end, respectively, of the irradiation periods.

## 5.5 THORIUM – LIGHT WATER REACTORS WASTE IN-CORE FUEL CYCLE FEASIBILITY

The capability to operate on LWRs waste constitutes one of the major benefits of the Gas Turbine – Modular Helium Reactor; in this paper, we evaluated the possibility to incinerate the LWR-TRU and at the same time breeding fissile  $^{233}\text{U}$  by fertile thorium. Since a mixture of pure  $^{239}\text{Pu}$ -thorium has shown a quite poor neutron economy, we tested the LWR-TRU-thorium fuel performance when plutonium and thorium are allocated in different TRISO particles. In fact, when fissile and fertile actinides share the same TRISO kernel, the resonance at 0.29 eV of the fission and capture microscopic cross sections of  $^{239}\text{Pu}$  can diminish also the absorption rate of fertile  $^{232}\text{Th}$  and thus degrade the breeding process. Consequently, in the present studies, we utilized two different types of fuel: the Driver Fuel, made of the LWR-TRU, and the Breed Fuel (called also by analogy to previous concepts – Transmutation Fuel), made of fertile thorium. Since, in the thermal neutron energy range, the microscopic capture cross section of  $^{232}\text{Th}$  is about 100 times smaller than the fission one of  $^{239}\text{Pu}$ , we propose to set thorium in particles with a large TRISO kernel and LWR-TRU in particles with a small one, so that the reaction rates are better equilibrated. At the light of the above consideration, which drives to load as much thorium as possible, we selected the JAERI TRISO particles, packed 40%, for the Breed Fuel and we tested different packing fractions and kernel radii of the Driver Fuel particles. Since no

configuration allowed the reactor to work, we repeated the above procedure when fertile particles are packed 20%; the latter choice permits over one year of operation, but the build up of  $^{233}\text{U}$  represents only a small fraction of the depleted  $^{239}\text{Pu}$ . Finally, we tested the previous configuration when the fertile and fissile fuels share the same kernel or when the fertile fuel axially alternates with the fissile one.

Figure 5.6 illustrates the initial and after 10 full power operation (fpo) days  $k_{\text{eff}}$  for different packing fractions of the DF, we can plain see that no configuration allows the reactor to operate since the excess of reactivity is small or negative already after 10 fpo days. Nevertheless, these calculations inspire some remark: we can note that the peak of the initial  $k_{\text{eff}}$  lies for a peaking factor of 15% and the final one for 20%, that suggests the range 15-20% as the best one where the GT-MHR can operate on LWR-TRU, as indicated also by recent independent GA studies. The decrease of the initial excess of criticality after a peaking factor of 20% is due to a spectral effect on the plutonium isotopes, as we will see later while discussing the actinides one-group averaged microscopic cross sections. A pf of 5%, corresponding to an initial  $^{239}\text{Pu}$  mass of 120 kg, sets the sub-criticality condition of the core already at the beginning of life.

More details can be found in Appendices 3, 4, 5 and 6.

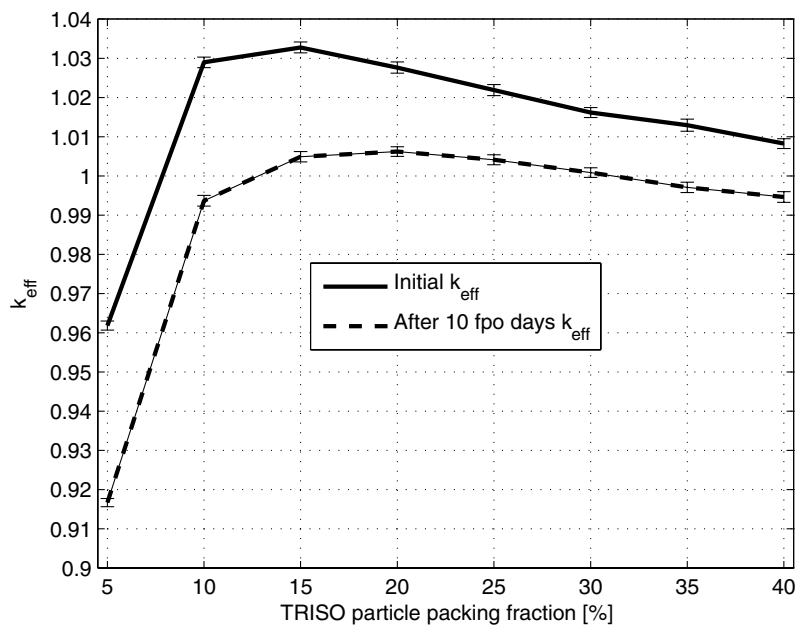


Figure 5.6  $k_{\text{eff}}$  at BoL and after 10 fpo days for different packing fractions. The standard deviation is given with 95% confidence.

## 6 ADS FUEL DEVELOPMENT

### 6.1 NITRIDE FUEL DEVELOPMENT

CONFIRM is a 5th FP project coordinated by Jan Wallenius, devoted to the development of nitride fuels for ADS. In 2005, the main effort was done on moving the irradiation of four (Pu,Zr)N fuel pins from Studsvik to the HFR reactor at Petten, Holland. After negotiations, it was agreed that Studsvik pays back part of the money spent, which enabled to fund a reduced scope irradiation in HFR. NRG has designed an irradiation rig, and delivery of the fuel pins to Petten is expected to take place in 2006.

In ITU, (Am,Zr)N pellets were fabricated using dust free methods, which is essential for industrial applicability. The method is based on infiltration of an americium solution into porous beads of zirconium oxide, which then are converted into nitride by carbothermic reduction. In Figure 6.1, the fabricated pellets are shown.



*Figure 6.1: (Am,Zr)N pellets fabricated by ITU.*

The golden color indicates low oxygen impurity in the material. The pellets feature good mechanical stability, but their density is low, due to limitations in sintering temperature of AmN. At the moment, it appears difficult to fabricate americium bearing nitride fuels with sufficiently low fraction of porosity using the methods developed at ITU and PSI within the CONFIRM project [11]. It is therefore very interesting to test methods developed in Russia, based on direct nitridation of metals followed by electrovortex blending. In the ISTC funded MATINE project, that was initiated by KTH, (Pu,Zr)N pellets with high density (85-90%) have been fabricated using this method [12].

## 6.2 THERMOCHEMISTRY OF ADVANCED FUELS

### 6.2.1 Modeling of fuel properties

Modeling of the thermo-chemical properties of advanced fuels has been continued.

The main areas of fuel modeling have been:

- Calculation and evaluation of mathematical expressions for the inclusion of metallic uranium, uranium nitrides and uranium oxides in the thermo-chemical database module "ALCHYMY" version 2.2.
- Computer-assisted modeling aiming to examine the possibility of internal redox reactions in (U,Pu)N, i.e., the tendency towards asymmetric nitrogen distribution between U and Pu, over a range of temperatures. Such a reaction, leading to the formation of uranium sesquinitride and metallic plutonium, could explain the appearance of liquid plutonium in high-temperature tests under hermetically sealed conditions. While the results appeared to contradict this hypothesis, it should be noted that the thermodynamic parameters for uranium sesquinitride are extrapolated above 1200 K and thus empirically unverified for the temperatures at which the phenomenon has been observed.
- Evaluation of the thermo-chemical stability of four experimental Russian composite fuels suggested as candidates in an ISTC project suggested by KTH and the community of the Confirm project .
- Calculations and modeling tasks, and comparison with results and estimates found in literature, in order to evaluate selected properties of candidate fuels discussed in EUROTRANS DM3 in order to select the best fuel for the European Transmuter Project,

## 7 SIMULATION OF RADIATION DAMAGE

Simulation of radiation damage in Fe-Cr alloys is a joint undertaking in the frame of SKB and Swedish Nuclear Technology Centre (SKC) funded project. Previously we had shown that the mixing enthalpy of the alloy is negative for small concentrations of chromium ( $< 10\%$ ). This transition can be identified with the formation of the alpha-prime phase that is observed under ageing at high temperature. Fe-Cr forms a perfect ferro-magnetic alloy for Cr concentrations up to ten percent at  $T = 750$  K, but decomposes into two isomorphous phases, iron rich alpha and chromium rich alpha-prime, for Cr concentrations ranging from 10 - 90 atomic %. The size of the chromium rich precipitates is on the nanometer scale. The kinetics of the phase separation is faster under irradiation than under thermal ageing, which leads to embrittlement of the ferritic steels that are considered for application in ADS, Generation IV and fusion reactors, due to their excellent swelling resistance.

Our earlier Embedded Atom Method model for the alloy were successful in describing the kinetics of Cr precipitate formation, but did not result in the correct composition of the alpha-prime phase. The reason was that the set of potentials could only describe parabolic behavior of the mixing enthalpy. In 2005, we were however able to develop a “two-band” model of the alloy, where we by assigning the change in sign of the mixing enthalpy to interactions between s-electrons of Fe and Cr, could reproduce the formation energy calculated with ab initio methods over the relevant range of Cr concentration. Thus the many-body contribution to the total energy was written as a sum of functionals of d, and s-electron densities, in line with theoretical understanding of transition metals, which state that while s-electrons contribute with minor parts to the cohesive energy, they provide significant parts of pressure and dominate bulk moduli.

This model was applied in molecular dynamics simulation of defect formation energies, and it was shown that the “two-band” set of potentials were capable of reproducing the formation and binding energies of a wide range of interstitial configurations including one or two Cr atoms in bulk Fe. Using the potential in Kinetic Monte Carlo simulations of phase segregation, formation of the alpha-prime phase was observed with cluster characteristics typical for those observed in experiment. Figure 7.1 shows the positions of Cr atoms in originally random alloys after simulated ageing at 750 Kelvin.

For lower Cr concentrations than 9%, no segregation is observed, In Fe-10Cr, the spherical shape of the precipitates are those typical for the nucleation and growth mechanism, expected to occur for positive curvatures of Gibbs' energy, while in Fe-32Cr, the precipitates have the diffuse shape typical for spinodal decomposition. The composition of the precipitates is similar to those found experimentally, with Cr concentrations ranging from 50-90%, as seen in Figure 7.2.



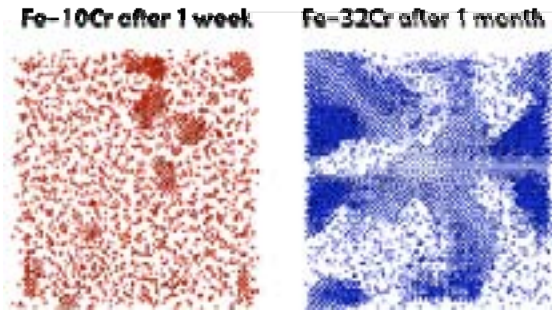


Figure 7.1 Positions of Cr atoms in initially random FeCr alloys after simulated thermal ageing.

While the present version of the two-band model enables for the first time to simulate the formation of the alpha-prime phase in Fe-Cr, it needs to be extended to take into account the effects of magnetism. This work is in progress.

Concerning the primary damage production in neutron induced collision cascades, extensive simulations were performed by molecular dynamics using different sets of potentials. These potentials (created by us and other authors) predict different displacement threshold energies (for the creation of a single Frenkle pair).

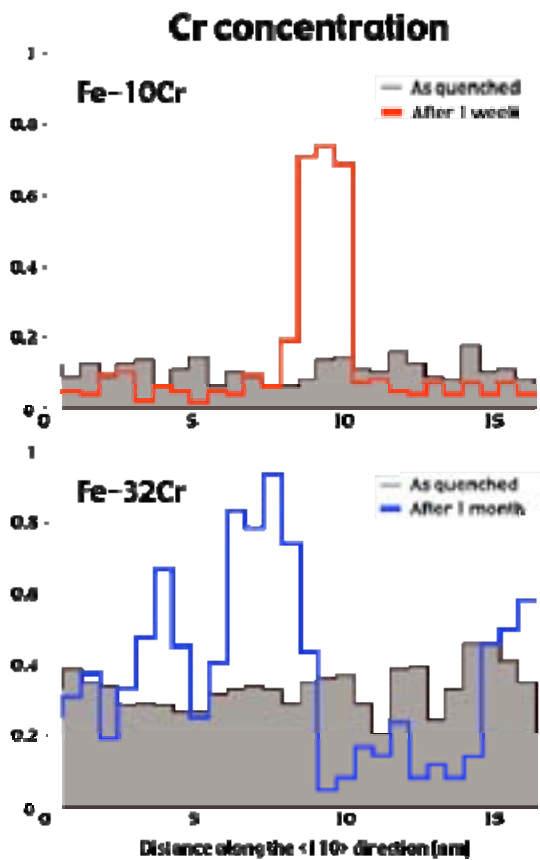


Figure 7.2 Cr concentration along principal crystal directions by end of KMC simulation.

Contrary to expectation, it was found that the total number of Frenkel pairs produced in high energy cascades did not correlate with the displacement threshold energy. Instead a correlation with the stiffness of the potentials was found. Potentials with high interstitial formation energy, as the one fitted for iron by us were observed to result in less dense cascades and small defect cluster sizes. The number of final defects produced by the different potentials was however largely independent on how the cascade behaved at peak time.

More details can be found in Appendices [11](#), [12](#), [12.1](#), [12.2](#)

## **8 DEVELOPMENT OF CODES AND METHODS**

### **8.1 THE MONTE CARLO METHODOLOGY FOR ADVANCED REACTOR/FUEL CYCLE SIMULATIONS - EUROPEAN PROJECT NURESIM**

NURESIM is an acronym for the European Project – The European Platform for NUclear REactor SIMulations.

The NURESIM project is envisaged to provide the initial step towards a Common European Standard Software Platform for modeling, recording and recovering computer data for nuclear reactor simulations. Such a common platform would also facilitate the exchange of data across sites, application codes and computing platforms.

Key objectives of NURESIM include: (i) integration of advanced physical models in a shared and open software platform; (ii) promoting and incorporating the latest advances in reactor and core physics, thermal-hydraulics, and coupled (multi-) physics modeling; (iii) progress assessment by using deterministic and statistical sensitivity and uncertainty analyses, verification and benchmarking; and (iv) training, dissemination, best practice and quality assurance.

The specific objectives of NURESIM are to initiate the development of the next-generation of experimentally validated, “best-estimate” tools for modeling (thermal-hydraulics, core physics, and multi-physics) present and future reactors. The improved prediction capabilities, standardization and robustness of the envisaged NURESIM European Platform would address current and future needs of industry, waste management agencies, reactor safety organizations, academic, government, and private institutions.

KTH is very actively participating in the Multiphysics workpackage of NURESIM working on the Monte Carlo methodology for advanced reactor/fuel cycle simulations.

A methodology for computing the steady-state core conditions by stochastic approximation was proposed for the Monte Carlo transport TRIPOLI-4 code, together with necessary data flows and implementation details. An efficient computing of the steady-state conditions is necessary for a Monte Carlo analysis of a running reactor and further on for advanced fuel cycle analyses.

Issues of a Monte Carlo analysis of a reactor cycle have been studied. The existing coupling methods of Monte Carlo codes with isotopic production/depletion codes were compared from the stability and efficiency point of view. This study showed that most of the existing Monte Carlo burnup codes can not handle the analysis of a reactor cycle; the simulations diverge.

Various methods for accelerating the source convergence of the Monte Carlo criticality calculations were studied and compared. We have selected the fission matrix method for a detailed investigation. Therefore we have written a simple Monte

Carlo transport code, and implemented the fission matrix method to study its performance. The performed tests showed the fission matrix method is very suitable to accelerate the source convergence in large reactors with a high dominance ratio. Therefore the fission matrix method is a candidate for implementation into the TRIPOLI-4 code. Convergence of the source in Monte Carlo simulations on large reactors might take more CPU time than the actual simulation; therefore the source convergence acceleration is needed.

## 8.2 DEVELOPMENT OF SIMULATION TOOLS FOR FUEL CYCLE STUDIES

### 8.2.1 Fuel Cycle Analyzer (FCA)

A computer code named Fuel Cycle Analyzer (FCA) has been developed at the department of Nuclear and Reactor Physics, Kungliga Tekniska Högskolan. The code effectively solves point reactor equations of isotopic kinetics by using evaluated production-depletion rates. The code simulates user-defined reactor scenarios to evaluate the impact on the transuranium elements inventory. FCA is meant to be a forerunner for a future more advanced tool for reactor cycle simulations being developed at the department of Nuclear and Reactor Physics, Kungliga Tekniska Högskolan.

#### 8.2.1.1 Methodology

The calculation of the isotopic inventory in the whole system is a complex problem. The TRU isotopes may arise by neutron capture or by radioactive decay of another isotope. The isotopes may be changed into other isotopes by fission, neutron capture or radioactive decay. One can form the following Bateman equations for each isotope  ${}^Z_A X$  as

$$\begin{aligned} \frac{dN({}^Z_A X)}{dt} = & -\sigma_a({}^Z_A X)N({}^Z_A X)\Phi - \lambda({}^Z_A X)N({}^Z_A X) + \sigma_c({}^{Z-1}_A X)N({}^{Z-1}_A X)\Phi + \\ & + \lambda_\alpha({}^{Z+4}_{A+2} X)N({}^{Z+4}_{A+2} X) + \lambda_{\beta^-}({}^Z_{A-1} X)N({}^Z_{A-1} X) + \lambda_{\beta^+}({}^Z_{A+1} X)N({}^Z_{A+1} X) \end{aligned} \quad (1)$$

where

- $\Phi$  is one-group neutron flux.
- $N({}^Z_A X)$  is a concentration of  ${}^Z_A X$
- $\sigma_a$  is a one-group microscopic cross-section for neutron absorption (fission and capture)
- $\sigma_c$  is a one-group microscopic cross-section for neutron capture
- $\lambda$  is a decay constant

The FCA code solves Bateman equation for the actinides in the whole inventory, which means the in-core inventory plus the waste cooling storage plus the waste repository storage. All isotopes are present in one vector during the calculation.

Let us assume the neutron flux is proportional to the thermal power of a reactor ( $\Phi = c \cdot P$ ), then one can write

$$\frac{dN({}_A^Z X)}{dt} = p({}_A^Z X)P + \sum_{A_2, Z_2} \lambda_{A_2 Z_2 \rightarrow AZ} N({}_{A_2}^{Z_2} X) - \lambda({}_A^Z X)N({}_A^Z X) \quad (2)$$

where

$$p({}_A^Z X) = -\sigma_a({}_A^Z X)N({}_A^Z X)c + \sigma_c({}_A^{Z-1} X)N({}_A^{Z-1} X)c \quad (3)$$

we denote represents a production/depletion rate of  ${}_A^Z X$  caused by the neutron flux irradiation of the fuel.

In the vector form one can write the Bateman equation simply as

$$\frac{d\mathbf{N}(t)}{dt} = \mathbf{R}(t) + \mathbf{A}\mathbf{N}(t) \quad (4)$$

where  $\mathbf{N}(t) = [N_1(t), N_2(t), \dots, N_m(t)]^T$  is the actinide vector ( $N_i(t)$  represents a total number of atoms of the  $i$ -th isotope in the system);  $\mathbf{R}(t)$  is a vector of total production/depletion rates (total change of the isotope number per time unit) for the actinide isotopes from the neutron absorption (by irradiation in the reactor);  $\mathbf{A}$  is a matrix of decay constants (created from ENDF/B-VI.8).

Assuming time independent  $\mathbf{R}$  and  $\mathbf{A}$  within the time interval  $[t_0, t_1]$ , one can write the solution to equation (4) as

$$\mathbf{N}(t) = e^{\mathbf{A}t} \mathbf{N}_0 + \mathbf{A}^{-1}(e^{\mathbf{A}t} - \mathbf{I})\mathbf{R} \quad (5)$$

Here,  $\mathbf{N}_0 \equiv \mathbf{N}(0)$  and the matrix exponential function is defined as

$$e^{\mathbf{A}t} = \mathbf{I} + \mathbf{A} \frac{t}{1!} + \mathbf{A}^2 \frac{t^2}{2!} + \mathbf{A}^3 \frac{t^3}{3!} + \dots \quad (6)$$

In general, the production/depletion rate,  $\mathbf{R}$ , varies in time. Our basic assumption is that this time dependency is piecewise constant, i.e. equation (5) refers only to a corresponding time period within which  $\mathbf{R}$  may be considered time independent. On a large scale, the vector function  $\mathbf{R}(t)$  represents the corresponding scenario. The next section deals with the way of computing of this function.

### 8.2.1.2 Production/Depletion Rates

The total production/depletion rate (**PD** rate)  $\mathbf{R}(t)$  represents the sum of particular production/depletion rates of all reactors

$$\mathbf{R}(t) = \sum_j P_j(t) \mathbf{p}_j \quad (7)$$

where  $P_j(t)$  is the thermal power of the  $j$ -th reactor (if the reactor is shut down then has no contribution to the PD rate);  $\mathbf{p}_j$  is a vector of average production/depletion

rate for the actinide isotopes from the neutron absorption in the  $j$ -th reactor per unit thermal power per unit time.

The vector  $\mathbf{p}_j$  must be averaged over the whole fuel cycle. Vectors  $\mathbf{p}_j$  can be evaluated from the ORIGEN [4] calculation in the following way. First, one writes the equation for  $\mathbf{p}_j$  as

$$\frac{d\mathbf{N}_j(t)}{dt} = P_j \mathbf{p}_j + \mathbf{A} \mathbf{N}_j(t) \quad (8)$$

with the initial and final conditions

$$\begin{aligned} \mathbf{N}_j(0) &= \mathbf{N}_{j0} \\ \mathbf{N}_j(T) &= \mathbf{N}_{jT} \end{aligned} \quad (9)$$

Second, the vector  $\mathbf{N}_{jT}$  is computed directly by ORIGEN2. Finally, the solution is found by demanding that  $\mathbf{p}_j$  in equation (8) provide the same final condition,  $\mathbf{N}_{jT}$ , as ORIGEN2 does. It has been found, by using equation (5), that the solution is given by

$$\mathbf{p}_j = \frac{1}{P_j} \mathbf{A} (\mathbf{I} - e^{-\mathbf{A}T})^{-1} [e^{-\mathbf{A}T} \mathbf{N}_{jT} - \mathbf{N}_{j0}] \quad (10)$$

Numerical calculations have shown that the solution as presented by equation (10) is not sufficiently accurate probably due to large times,  $T \sim 1$  year or even greater. One can dramatically increase the numerical precision, first, by putting the calculated rate,  $\mathbf{p}_j^{(0)}$ , as given by (10), back into equation (5) to evaluate the expected final value

$$\mathbf{N}_{j,T}^{(0)} \equiv \mathbf{N}(T) = e^{\mathbf{A}T} \mathbf{N}_0 + \mathbf{A}^{-1} (e^{\mathbf{A}T} - \mathbf{I}) P_j \mathbf{p}_j^{(0)} \quad (11)$$

Second, we calculate the discrepancy in the final value

$$\Delta \mathbf{N}_{j,T} = \mathbf{N}_{j,T} - \mathbf{N}_{j,T}^{(0)} \quad (12)$$

Third, we use this discrepancy to evaluate a small correction to the rate  $\mathbf{p}_j$

$$\Delta \mathbf{p}_j = \frac{1}{P_j} \mathbf{A} (\mathbf{I} - e^{-\mathbf{A}T})^{-1} \Delta \mathbf{N}_{j,T} \quad (13)$$

Finally, we calculate a numerical solution that is sufficiently accurate

$$\mathbf{p}_j = \mathbf{p}_j^{(0)} + \Delta \mathbf{p}_j \quad (14)$$

Vector  $\mathbf{p}_j$  must be computed for each reactor type, and each reprocessing strategy.

### 8.2.1.3 Calculation Data Flow

A reactor can be loaded with various fuels (UOX, MOX), and each fuel can have generally a different PD ratio. The PD ratio of the reactor must therefore be weighted over the PD ratios which correspond to the particular fuels. In order to be able to decide which fuel (MOX1, MOX2 ... ADS1, ADS2 ...) is to be loaded at a certain time into a certain core, the code creates several databases. Each reactor core has an in-core database of fuels and corresponding dates of loading. Each fuel type has also its own repository database. If the fuel is unloaded from the core, the corresponding

waste repository notes which year the fuel was unloaded from the core and what the fuel energy equivalent was (released energy).

The input file assigns a preferable order in which a certain core should be loaded with different fuel, e.g. a core BWR-MOXa will have the following preferable order of fuel MOX1 MOX2 MOX3. That means the core will be loaded with MOX1 fuel preferably. The MOX1 fuel is a MOX fuel which is reprocessed from the UOX waste. If the UOX waste repositories contain no sufficiently long cooled waste then the core can be loaded with MOX2 fuel which is reprocessed from the MOX1 waste, and so on. If the waste repository contains sufficiently long cooled waste to reprocess it into a new fuel then a certain amount of fuel is removed and new fuel is loaded into a core. The energy equivalent of the waste removed from the repository is not equal to the energy equivalent of the new fuel. The ratio of those equivalents must be stated in the input file for each fuel which is reprocessed from waste.

At each time step, the code has to find out which cores are to be loaded. When a core is to be loaded then a new PD ratio is weighted over the PD ratios of the fuels from the in-core inventory database. After that the fuel is burned, and the time is increased by the time step. If a certain reactor can not be loaded because of lack of fuel, then the reactor is automatically shut down.

#### 8.2.1.4 Code Implementation

The code was written in MATLAB which is suitable for vector and matrix operations. MATLAB also allows subsequent printing the figures.

#### 8.2.1.5 Considered Isotopes

We consider the following 40 isotopes:  $^{234}\text{U}$ ,  $^{235}\text{U}$ ,  $^{236}\text{U}$ ,  $^{237}\text{U}$ ,  $^{238}\text{U}$ ,  $^{239}\text{U}$ ,  $^{236}\text{Np}$ ,  $^{236\text{m}}\text{Np}$ ,  $^{237}\text{Np}$ ,  $^{238}\text{Np}$ ,  $^{239}\text{Np}$ ,  $^{240}\text{Np}$ ,  $^{240\text{m}}\text{Np}$ ,  $^{236}\text{Pu}$ ,  $^{237}\text{Pu}$ ,  $^{238}\text{Pu}$ ,  $^{239}\text{Pu}$ ,  $^{240}\text{Pu}$ ,  $^{241}\text{Pu}$ ,  $^{242}\text{Pu}$ ,  $^{243}\text{Pu}$ ,  $^{244}\text{Pu}$ ,  $^{245}\text{Pu}$ ,  $^{240}\text{Am}$ ,  $^{241}\text{Am}$ ,  $^{242}\text{Am}$ ,  $^{242\text{m}}\text{Am}$ ,  $^{243}\text{Am}$ ,  $^{244}\text{Am}$ ,  $^{244\text{m}}\text{Am}$ ,  $^{245}\text{Am}$ ,  $^{241}\text{Cm}$ ,  $^{242}\text{Cm}$ ,  $^{243}\text{Cm}$ ,  $^{244}\text{Cm}$ ,  $^{245}\text{Cm}$ ,  $^{246}\text{Cm}$ ,  $^{247}\text{Cm}$ ,  $^{248}\text{Cm}$ ,  $^{249}\text{Cm}$ .

The considered actinides and decay constants are stated in Table 8.1.

We note here that the bulk of the results have been obtained by the FCA code that uses the nuclides listed in *Table 8.1* only.

#### 8.2.1.6 Input Files

The FCA code uses two main plain text input files. The “Reactor\_database” file contains all details to create the required reactor scenario, and the “PD\_database” file contains all details to compute PD ratios for each fuel. Apart from these input files, the FSA code uses a number of data files from ORIGEN2 calculations, which are also necessary to compute the PD ratios.

Table 8.1. Actinides and decay constants considered in the calculation

| Isotope            | $\lambda$  | Fraction |           |           |       |       |
|--------------------|------------|----------|-----------|-----------|-------|-------|
|                    |            | $\alpha$ | $\beta^-$ | $\beta^+$ | SF    | IS    |
| <sup>234</sup> U   | 8.9398E-14 | 1.000    |           |           |       |       |
| <sup>235</sup> U   | 3.1214E-17 | 1.000    |           |           |       |       |
| <sup>236</sup> U   | 9.3787E-16 | 1.000    |           |           |       |       |
| <sup>237</sup> U   | 1.1885E-06 |          | 1.000     |           |       |       |
| <sup>238</sup> U   | 4.9161E-18 | 1.000    |           |           |       |       |
| <sup>239</sup> U   | 4.9222E-04 |          | 1.000     |           |       |       |
| <sup>236</sup> Np  | 1.9100E-13 |          | 0.089     | 0.910     |       |       |
| <sup>236m</sup> Np | 8.5574E-06 |          | 0.480     | 0.520     |       |       |
| <sup>237</sup> Np  | 1.0264E-14 | 1.000    |           |           |       |       |
| <sup>238</sup> Np  | 3.7896E-06 |          | 1.000     |           |       |       |
| <sup>239</sup> Np  | 3.4066E-06 |          | 1.000     |           |       |       |
| <sup>240</sup> Np  | 1.8663E-04 |          | 1.000     |           |       |       |
| <sup>240m</sup> Np | 1.6001E-03 |          | 1.000     |           |       |       |
| <sup>236</sup> Pu  | 7.5741E-09 | 1.000    |           |           |       |       |
| <sup>237</sup> Pu  | 1.7761E-07 |          |           | 1.000     |       |       |
| <sup>238</sup> Pu  | 2.5046E-10 | 1.000    |           |           |       |       |
| <sup>239</sup> Pu  | 9.1103E-13 | 1.000    |           |           |       |       |
| <sup>240</sup> Pu  | 3.3468E-12 | 1.000    |           |           |       |       |
| <sup>241</sup> Pu  | 1.5307E-09 |          | 1.000     |           |       |       |
| <sup>242</sup> Pu  | 5.8809E-14 | 1.000    |           |           |       |       |
| <sup>243</sup> Pu  | 3.8850E-05 |          | 1.000     |           |       |       |
| <sup>244</sup> Pu  | 2.7456E-16 | 1.000    |           |           |       |       |
| <sup>245</sup> Pu  | 1.8337E-05 |          | 1.000     |           |       |       |
| <sup>240</sup> Am  | 3.7827E-06 |          |           | 1.000     |       |       |
| <sup>241</sup> Am  | 5.0763E-11 | 1.000    |           |           |       |       |
| <sup>242</sup> Am  | 1.2019E-05 |          | 0.827     | 0.173     |       |       |
| <sup>242m</sup> Am | 1.5578E-10 |          |           |           |       | 1.000 |
| <sup>243</sup> Am  | 2.9803E-12 | 1.000    |           |           |       |       |
| <sup>244</sup> Am  | 1.9063E-05 |          | 1.000     |           |       |       |
| <sup>244m</sup> Am | 4.4433E-04 |          | 1.000     |           |       |       |
| <sup>245</sup> Am  | 9.3922E-05 |          | 1.000     |           |       |       |
| <sup>241</sup> Cm  | 2.4459E-07 | 0.010    |           | 0.990     |       |       |
| <sup>242</sup> Cm  | 4.9236E-08 | 1.000    |           |           |       |       |
| <sup>243</sup> Cm  | 7.7070E-10 | 0.998    |           | 0.002     |       |       |
| <sup>244</sup> Cm  | 1.2135E-09 | 1.000    |           |           |       |       |
| <sup>245</sup> Cm  | 2.5841E-12 | 1.000    |           |           |       |       |
| <sup>246</sup> Cm  | 4.6438E-12 | 1.000    |           |           |       |       |
| <sup>247</sup> Cm  | 1.3728E-15 | 1.000    |           |           |       |       |
| <sup>248</sup> Cm  | 6.4603E-14 | 0.917    |           |           | 0.083 |       |
| <sup>249</sup> Cm  | 1.8009E-04 |          | 1.000     |           |       |       |



## 9 INTERNATIONAL INTERACTIONS, SEMINARS AND CONFERENCES

### 9.1 SEMINARS

| <i>Seminar Leader</i> | <i>Date</i>   | <i>Topic</i>  | <i>Place</i>         |
|-----------------------|---------------|---|----------------------|
| Waclaw Gudowski       | July-August   | Guest lecturer and mentor at World Nuclear University   | Idaho Falls          |
| Waclaw Gudowski       | October 2005  | Lectures at IVA meeting in Kiev   | Kiev, Ukraine        |
| Waclaw Gudowski       | October 2005  | Lectures at IAEA Adbus Salam International Centre, Trieste  | Trieste              |
| Janne Wallenius       | Jan 2005      | Lecture on Mikael Björnbergs memorial seminar   | Helsinki             |
| Janne Wallenius       | March 2005    | Acting for SVT program about transmutation in Oskarshamn  | Oskarshamn<br>Sweden |
| Janne Wallenius       | March 2005    | Lecture on Fe-Cr workshop in Brussels   | Brussels             |
| Janne Wallenius       | April 2005    | Lecture on Vetenskapsfestivalen   | Gothenburg           |
| Janne Wallenius       | May 2005      | Acting for STv program at ITU   | Karlsruhe            |
| Janne Wallenius       | May 2005      | Lecture at IVA meeting in S:t Petersburg  | Russia               |
| Janne Wallenius       | May 2005      | Acting for SVT program in Obninsk   | Russia               |
| Janne Wallenius       | May 2005      | Acting for SVT program in Dubna   | Russia               |
| Janne Wallenius       | June 2005     | Lecture at ANS summer meeting in San Diego  | USA                  |
| Janne Wallenius       | Aug 2005      | Opponent at dissertation  | Helsinki             |
| Janne Wallenius       | Aug 2005      | Lecture at AccApp 2005 conference   | Venice               |
| Janne Wallenius       | Dec 2005      | Dissertation committee chairman at Chalmers   | Gothenburg           |
| Daniel Westlén        | January 2005  | YG Start up seminar   | Västerås             |
| Daniel Westlén        | February 2005 | RedImpact meeting on indicators   | London               |
| Daniel Westlén        | April 2005    | Lecture for Forsmarks Gymnasium, "Transmutation och avancerade kärnbränslecykler"                       | Stockholm            |
| Daniel Westlén        | April 2005    | Department seminar, "Gas-cooled fast reactors"  | Stockholm            |
| Daniel Westlén        | May 2005      | Study visit Chernobyl   | Chernobyl            |
| Daniel Westlén        | June 2005     | ENS-YGN seminar, invited speaker, "Closing the nuclear fuel cycle"                                      | Zagreb               |
| Daniel Westlén        | July 2005     | Pu management workshop, invited speaker, "Reducing radiotoxicity in the long run"                       | Cambridge            |
| Daniel Westlén        | October 2005  | Seminar in Eurotrans training course, "Gas and liquid metal coolants in accelerator driven systems"     | Stockholm            |
| Daniel Westlén        | October 2005  | Lecture for KTH class F45, "Transmutation – En långsiktig strategi för långlivade radioaktiva nuklider" | Stockholm            |
| Daniel Westlén        | October 2005  | Sino-Swedish science week, invited speaker, "Closing the nuclear fuel cycle"                            | Beijing              |

## 9.2 INTERNATIONAL MEETINGS AND CONFERENCES

| <i>Participant</i>  | <i>Date</i>                      | <i>Meeting or Conference</i>   | <i>Place</i>                       |
|---------------------|----------------------------------|--|------------------------------------|
| Waclaw Gudowski     | January 2005                     | Invited guest for the Public Hearing of the French Parliament on the French Waste Management Programme ( <a href="#">Appendix 16</a> ) | Paris                              |
| Waclaw Gudowski     | January 2005                     | SAD/Yalina Steering Committee meeting  | Minsk                              |
| Waclaw Gudowski     | February 2005                    | Invited speaker for the International Seminar Program of the Heidelberg University   | Heidelberg                         |
| Waclaw Gudowski     | March, June, September, December | Eurotrans project, Domain 2: ECATS programmatic meetings   | Brussels, Paris, Karlsruhe, Madrid |
| Waclaw Gudowski     | May 2005                         | Invited guest for the Fast Reactor – ADS Working Group of IAEA meeting   | San Paolo, Brasil                  |
| Waclaw Gudowski     | May, November 2005               | Red-Impact semiannual meetings   | Prague, Brussels-Mol               |
| Waclaw Gudowski     | June 2005                        | Invited speaker on International Symposium on Utilisation of Accelerators  | Dubrovnik, Croatia                 |
| Waclaw Gudowski     | June, September, October 2005    | Presentation of Eurotrans and SAD projects. SAD/Yalina Steering Committee  | Dubna, Russia                      |
| Waclaw Gudowski     | August 2005                      | Invited speaker at AccApp 2005 ( <a href="#">Appendix 15</a> )   | Venice                             |
| Waclaw Gudowski     | August 2005                      | Invited speaker, ICENES 2005   | Brussels                           |
| Waclaw Gudowski     | October 2005                     | Sino-Swedish science week, invited speaker, “Nuclear Technology in Sweden + Red-Impact Project”  | Beijing                            |
| Waclaw Gudowski     | October 2005                     | Le   | TRieste                            |
| Waclaw Gudowski     | December 2005                    | IAEA Yalina CRP meeting  | Minsk, Belarus                     |
| Vasily Arzhanov     | May 2005                         | the XII Meeting on Reactor Physics Calculations in the Nordic Countries  | Halden Norway                      |
| Jan Dufek           | May 2005                         | The XII Meeting on Reactor Physics Calculations in the Nordic Countries  | Halden Norway                      |
| Patrick Isaksson    | November 2005                    | RedImpact semi annual meeting incl visit to Mol  | Brussels                           |
| Mikael Jolkkonen    | April 2004                       | EUROTRANS kick-off meeting   | Karlsruhe                          |
| Mikael Jolkkonen    | May 2005                         | Research institutes in Kiev and the nuclear power plant in Chernobyl   | Ukraine                            |
| Mikael Jolkkonen    | June 2005                        | FUTURE progress meeting/EUROTRANS Joint DM1-DM3 meeting  | Winfrith, England                  |
| Carl Magnus Persson | August 2005                      | Speaker, ICENES 2005   | Brussels                           |
| Carl Magnus Persson | December 2005                    | IAEA Yalina CRP meeting  | Minsk, Belarus                     |
| Alberto Talamo      | June 2005                        | American Nuclear Society, Summer Meeting   | San Diego, USA                     |
| Janne Wallenius     | April 2005                       | Participation in Eurotrans kick-off meeting  | Karlsruhe                          |
| Janne Wallenius     | May 2005                         | Visit to Chernobyl   | Ukraine                            |
| Janne Wallenius     | June 2005                        | Participation in FUTURE meeting  | Winfrith,                          |

|                 |                |   |                                   |
|-----------------|----------------|---|-----------------------------------|
|                 |                |   | England                           |
| Janne Wallenius | Oct 2005       | Participation in FUTURE meeting   | Brussels                          |
| Janne Wallenius | Oct 2005       | Lecture and session chair at GLOBAL conference  | Tsukuba, Japan                    |
| Janne Wallenius | Nov 2005       | Participation in AFTRA meeting  | Paris                             |
| Daniel Westlén  | May 2005       | RedImpact semi annual meeting   | Prague                            |
| Daniel Westlén  | August 2005    | AccApp'05, oral presentation, "Source efficiency in gas- and lead-bismuth-cooled subcritical cores"   | Venice                            |
| Daniel Westlén  | September 2005 | Study visits; Nuclear Regulatory Commission, Nuclear Energy Institute, Department of Energy, North Anna nuclear power plant, IAEA and UNMOVIC | Washington, Richmond and New York |
| Daniel Westlén  | September 2005 | Study visit to Finland 5  | Olkiluoto                         |
| Daniel Westlén  | November 2005  | Executive committee meeting for the IYNC2006 conference   | Washington                        |
| Daniel Westlén  | November 2005  | RedImpact semi annual meeting   | Brussels                          |

---

## 10 REFERENCES

- [1] Marcus Eriksson, Janne Wallenius, Mikael Jolkkonen and James Cahalan “Inherent safety of fuels for accelerator-driven systems” *Nuclear Technology* 151 (2005) 314.
- [2] Janne Wallenius and Marcus Eriksson,” Neutronics of minor actinide burning accelerator-driven systems with ceramic fuel” *Nuclear Technology* 152 (2005) 367
- [3] Marcus Eriksson, Kinetics and safety studies of accelerator-driven systems PhD thesis, KTH (2005).P. SELTBORG et al., “Definition and Application of Proton Source Efficiency in Accelerator Driven Systems,” *Nucl. Sci. Eng.*, 145, p390 (2003).
- [4] A.G. GROFF, “A User’s Manual for the ORIGEN2 Computer Code,” Oak Ridge National Laboratory Report ORNL/TM-7175, (1980).
- [5] A. Talamo, W. Gudowski and F. Venneri. The burnup capabilities of the Deep Burn Modular Helium Reactor analyzed by the Monte Carlo Continuous Energy Code MCB. *Annals of Nuclear Energy* 31/2, pp. 173-196, (2004).
- [6] Alberto Talamo, Waclaw Gudowski, Jerzy Cetnar and Francesco Venneri, Key physical parameters and temperature reactivity coefficients of the deep burn modular helium reactor fueled with LWRs waste, *Annals of Nuclear Energy* 31 (2004) 1913–1937
- [7] Alberto Talamo, Waclaw Gudowski and Jerzy Cetnar Comparative Studies of ENDF/B-6.8, JEF-2.2 and JENDL-3.2 Data Libraries by Monte Carlo Modeling of High Temperature Reactors on Plutonium Based Fuel Cycles. *Journal of Nuclear Science and Technology* 41/12, pp. 1228-1236, 2004.
- [8] [Alberto Talamo and Waclaw Gudowski, Performance of the Gas Turbine – Modular Helium Reactor fuelled with different types of fertile TRISO particles. *Annals of Nuclear Energy* 32/16, pp. 1719-1749, 2005.
- [9] Alberto Talamo and Waclaw Gudowski, Adapting the Deep Burn In-Core Fuel Management Strategy for the Gas Turbine - Modular Helium Reactor to a Uranium-Thorium Fuel. *Annals of Nuclear Energy* 32/16, pp. 1750-1781, (2005).
- [10] Alberto Talamo and Waclaw Gudowski, Comparative Studies of JENDL-3.3, JENDL-3.2, JEFF-3, JEF-2.2 and ENDF/B-6.8 Data Libraries on the Monte Carlo Continuous Energy Modeling of the Gas Turbine - Modular Helium Reactor Operating with Thorium Fuels. *Journal of Nuclear Science and Technology* 42/12, pp. 1040-1053 (2005).

- [11] Sylvie Pillon and Janne Wallenius Oxide and Nitride TRU-Fuels: Lessons Drawn from the CONFIRM and FUTURE Projects of the 5th European Framework Programme Nuclear Science and Engineering, in press.
- [12] Janne Wallenius, Sylvie Pillon and Ludmila Zaboudko Fuels for accelerator driven systems Nuclear Instruments and Methods in Physics Research A, in press.
- [13] P. Seltborg, J. Wallenius, K. Tucek and W. Gudowski, "Definition and application of proton source efficiency in accelerator driven systems", Nuclear Science and Engineering, 145, 390-399 (2003).
- [14] NNC LTD, "PDS-XADS Work Package 4.2 Deliverable 65: Core Design Summary", C6862/TR/0028 (2004)
- [15] ANSALDO NUCLEARE, "Core Design Summary Report for the LBE-Cooled XADS", XADS 41 TNIX 064 Rev. 0 (2004)
- [16] D. B. PELOWITZ, ed., "MCNPX Version 2.5.0 User's Manual", LA-CP-05-0369 (2005)
- [17] K. TSUJIMOTO et al., "Neutronics Design for Lead-Bismuth Cooled Accelerator-Driven System for Transmutation of Minor Actinides", J. Nucl. Sci. Tech., 41, p21 (2004)
- [18] S. PELLONI, "Static analysis of the PDS-XADS LBE and gas-cooled concepts", Ann. Nucl. Energy 32, p13 (2004)
- [19] A. HOGENBIRK et al., 2003 "Uncertainty evaluation of the nuclear design of PDS-XADS", International Workshop on P&T and ADS Development, Mol, Belgium, 6-9 October (2003)
- [20] K. Tucek, M. Jolkkonen, J. Wallenius and W. Gudowski: Neutronic and burnup studies of an accelerator-driven transuranium burner in a start-up mode. (Submitted to Nuclear Technology, presently under revision)
- [21] Dufek J, Arzhanov V, Gudowski W, „Nuclear spent fuel management scenarios. Status and assessment report”, SKB Rapport R-06-61, June 2006

## **11 APPENDICES**



## Analysis of reactivity determination methods in the subcritical experiment Yalina

Carl-Magnus Persson<sup>a,\*</sup>, Per Seltborg<sup>a</sup>, Alexandra Åhlander<sup>a</sup>,  
Waclaw Gudowski<sup>a</sup>, Thomas Stummer<sup>b</sup>, Hanna Kiyavitskaya<sup>c</sup>, Victor Bournos<sup>c</sup>,  
Yurij Fokov<sup>c</sup>, Ivan Serafimovich<sup>c</sup>, Sergey Chigrinov<sup>c</sup>

<sup>a</sup>Department of Nuclear and Reactor Physics, Albanova University Centre, Royal Institute of Technology, S-106 91 Stockholm, Sweden

<sup>b</sup>Vienna University of Technology, Austria

<sup>c</sup>Joint Institute of Power and Nuclear Research, National Academy of Sciences of Belarus, Minsk, Sosny

Received 18 May 2005; received in revised form 18 July 2005; accepted 20 July 2005

Available online 18 August 2005

### Abstract

Different reactivity determination methods have been investigated, based on experiments performed at the subcritical assembly Yalina in Minsk, Belarus. The development of techniques for on-line monitoring of the reactivity level in a future accelerator-driven system (ADS) is of major importance for safe operation. Since an ADS is operating in a subcritical mode, the safety margin to criticality must be sufficiently large. The investigated methods are the Slope Fit Method, the Sjöstrand Method and the Source Jerk Method. The results are compared with Monte Carlo simulations performed with different nuclear data libraries. The results of the Slope Fit Method are in good agreement with the Monte Carlo simulation results, whereas the Sjöstrand Method appears to underestimate the criticality somewhat. The Source Jerk Method is subject to inadequate statistical accuracy.

© 2005 Elsevier B.V. All rights reserved.

PACS: 28.50.Dr

Keywords: Yalina; Reactivity determination; Subcritical; MCNP; ADS

### 1. Introduction

In order to reduce the radiotoxic inventory of the nuclear waste, accelerator-driven systems

(ADS) have been suggested to transmute the accumulated transuranic elements [1]. In a subcritical core it is possible to use large fractions of “exotic” fuels, apart from plutonium also consisting of the minor actinides americium and curium. Intensive research programs investigating the physics and technology of proton accelerators, spallation targets and subcritical cores are required

\*Corresponding author. Tel.: +46 8 55 37 82 04;

fax: +46 8 55 37 84 65.

E-mail address: [calleg@neutron.kth.se](mailto:calleg@neutron.kth.se) (C.-M. Persson).

for the development of full-scale ADS in the future. This present work is dedicated to the study of reactivity determination methods of a subcritical zero-power core. The development of reliable methods for reactivity determination is essential for the safe operation and for the licensing of a future ADS.

Recently, the comprehensive MUSE program (multiplication with an external source), performed at the MASURCA facility in Cadarache, France, was completed [2]. In the MUSE experiments, a neutron generator, mainly consisting of a deuteron accelerator and a tritium target, was coupled to a subcritical core operating with a fast neutron energy spectrum. A major part of the experiments in MUSE was devoted to the investigation of methods for reactivity determination of different subcriticality levels [2].

Parallel with the MUSE program, another European program devoted to ADS studies has been running at the Yalina facility outside Minsk, Belarus [3,4]. This facility has the same basic construction with a neutron generator coupled to a subcritical core, but the neutron spectrum of Yalina is thermal. The fact that the fission chain process relies mainly on reactions induced by thermal neutrons, implies that the neutronic time scales are in the order of a factor  $10^3$  larger than in a fast system. The methods used in this study, earlier evaluated in a fast spectrum in the MUSE experiments, will now be investigated in a thermal spectrum. A pulsed neutron source (PNS) experiment has been analyzed by the Slope Fit Method [5] and the Sjöstrand Method [6], and a source jerk experiment [5] has been performed and analyzed. The results have been compared with the results from the MUSE experiments and Monte Carlo simulations.

## 2. The Yalina facility

Yalina is a subcritical assembly operating with a thermal neutron energy spectrum. The external source coupled to the core is provided by a neutron generator consisting of a deuterium accelerator and a Ti–D or Ti–T target (Table 1). In the experiments, the Ti–T target was used, situated in the center of the core. As fuel, EK-10

type fuel rods with 10% enriched uranium oxide are used in polyethylene blocks for moderation. Under normal conditions, the core is loaded with 280 fuel rods, but this number can easily be modified. The very low power of the core makes the natural convection of the surrounding air sufficient for cooling.

The core (Fig. 1) consists of subassemblies surrounding the target and the ion channel up to the side dimensions of  $400 \times 400 \times 576$  mm. Each subassembly is made of nine blocks ( $80 \times 80 \times 63$  mm) of polyethylene (density  $0.927 \text{ g/cm}^3$ ) with 16 channels for the fuel rods, with a diameter of 11 mm. At the sides and behind the target, the polyethylene blocks are replaced by lead blocks of the same geometry. The purpose of these lead blocks is to diffuse the energy spectrum of the (D,T)-neutrons into a more spallation-like spectrum, by ( $n, xn$ )- and scattering reactions. The core is surrounded by a graphite reflector with a thickness of approximately 400 mm. Only at the side facing the accelerator, and its opposite side, no shielding or borated polyethylene is used, for ease of handling. Five axial experimental channels (EC) with 25 mm diameter are located inside the core and reflector [7].

## 3. Initial Monte Carlo simulation

The experimental setup has been analyzed using MCNP version 4c3 [8]. The effective multiplication factor,  $k_{\text{eff}}$ , and the effective delayed neutron

Table 1  
Main parameters of the neutron generator (NG-12-1)

|                            |                       |   |
|----------------------------|-----------------------|---|
| Deuteron energy            |                       | 100–250 keV                               |
| Beam current               |                       | 1–12 mA                                   |
| Pulse duration             |                       | 0.5–100 $\mu\text{s}$                     |
| Pulse repetition frequency |                       | 1–10 000 Hz                               |
| Spot size                  |                       | 20–30 mm                                  |
| Ti–T target                | Maximum neutron yield | $\sim 2.0 \times 10^{12} \text{ ns}^{-1}$ |
|                            | Reaction $Q$ -value   | 17.6 MeV                                  |
| Ti–D target                | Maximum neutron yield | $\sim 3.0 \times 10^{10} \text{ ns}^{-1}$ |
|                            | Reaction $Q$ -value   | 3.3 MeV                                   |



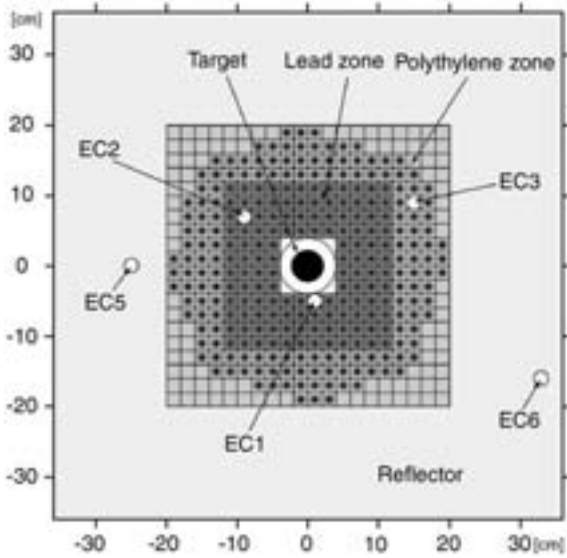


Fig. 1. Vertical cross-sectional view of the Yalina core.

fraction,  $\beta_{\text{eff}}$ , have been calculated for three different data libraries; ENDF/B-VI, JEFF3.0 and JENDL3.3 [9]. The effective delayed neutron fraction was calculated from the following relation:

$$\beta_{\text{eff}} = \frac{N_d}{N_{\text{Tot}}} \quad (1)$$

where  $N_d$  is the number of fissions induced by delayed neutrons and  $N_{\text{Tot}}$  is the total number of fissions [10]. The results for the different libraries are displayed in Table 2. For the following analysis, the mean generation time,  $\Lambda$ , is needed. Since MCNP calculates non-adjoint-weighted time parameters, not suitable for kinetic calculations, another approach must be adopted. This is described in the next section.

## 4. Reactivity determination

### 4.1. Pulsed neutron source experiment

When a neutron pulse enters a subcritical core, a number of fission chains start to propagate in the fuel. Because of the subcriticality, every fission chain will die out rapidly, which is characterized by a global exponential decay of the neutron flux.

Table 2

Effective multiplication factor,  $k_{\text{eff}}$ , and effective delayed neutron fraction,  $\beta_{\text{eff}}$ , calculated with MCNP

|           | $k_{\text{eff}}$      | $\beta_{\text{eff}}$ (pcm) |
|-----------|-----------------------|----------------------------|
| ENDF/B-VI | $0.91803 \pm 0.00005$ | $788 \pm 9$                |
| JEFF3.0   | $0.92010 \pm 0.00007$ | $793 \pm 9$                |
| JENDL3.3  | $0.92114 \pm 0.00006$ | $742 \pm 9$                |

By studying the prompt neutron decay after a neutron pulse, it is possible to determine the reactivity of the core in two different ways, either by applying the Slope Fit Method or the Sjöstrand Method, frequently also called the Area Method. These two methods have been used to analyze the data collected from the pulsed neutron source experiment. During the experiment, the neutron generator was operating at 43 Hz emitting deuterium pulses of duration  $2 \mu\text{s}$ . The  $^3\text{He}$ -detector was situated in different experimental channels at the core mid-plane. Fig. 2 shows the accumulated detector counts after 40,000 source pulses. The inherent source can in all experiments be neglected.

#### 4.1.1. Slope fit method

This method was first introduced already in Ref. [11], but the method has achieved increased interest during the last years, due to its possible applicability to ADS [2,12–14].

Neglecting the delayed neutrons, the point-kinetic equations take the following form for a reactor without sources [5,15]:

$$\frac{dn(t)}{dt} = \alpha n(t). \quad (2)$$

This equation has an exponential solution given by

$$n(t) = n_0 e^{\alpha t} \quad (3)$$

where  $\alpha$  is the prompt neutron decay constant:

$$\alpha = \frac{\rho - \beta_{\text{eff}}}{\Lambda}. \quad (4)$$

In a subcritical reactor,  $\alpha$  is negative, which gives rise to an exponential decrease of the neutron flux. In the short time-scale after a neutron pulse

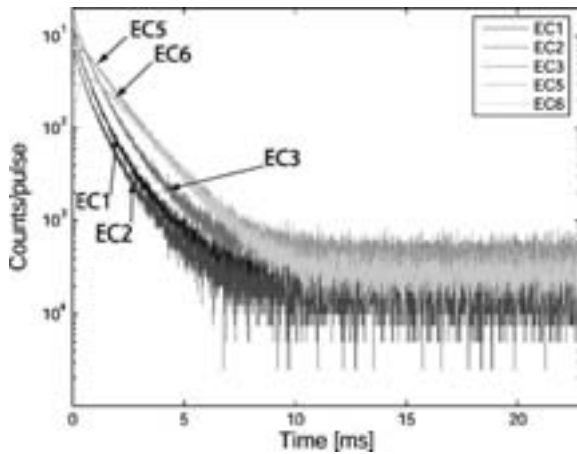


Fig. 2. Accumulated  $^3\text{He}$ -detector counts in different experimental channels after 40,000 pulse insertions.

injection, the neglecting of the delayed neutrons is legitimate and thus, the decay is mainly described by the prompt neutron decay constant. By measuring  $\alpha$  experimentally, the reactivity,  $\rho$ , can be found if  $\beta_{\text{eff}}$  and  $\Lambda$  are known.

From Fig. 2 it is evident that one single exponential is not enough to describe the complete behavior of the neutron flux decay after a neutron pulse insertion. During the first milliseconds, there is an injection and an adjustment period. During the injection period, the flux decreases rapidly in the three innermost experimental channels, located inside the core, and at the same time in the reflector channels, the neutron population is subject to a fast increase. After the injection period follows the adjustment period, when the neutron flux approaches a common decay rate in all channels. After approximately 4 ms, the neutron flux reaches a fundamental decay mode, characteristic of the inherent reactor properties and described by the point-kinetic equations. During this process, the neutron flux decreases with approximately the same rate in all channels. Finally, the neutron flux reaches a constant level, due to the delayed neutron background.

Due to the exponential behavior of neutron flux changes in the reactor according to Eq. (3), it is appropriate to describe the neutron pulse response mathematically by a series of exponentials. By

Table 3  
Results from the slope fit method

|     | $\alpha$ ( $\text{s}^{-1}$ ) | $\rho$ (pcm)    |
|-----|------------------------------|-----------------|
| EC1 | $-675 \pm 13$                | $-8240 \pm 260$ |
| EC2 | $-722 \pm 19$                | $-9050 \pm 260$ |
| EC3 | $-711 \pm 11$                | $-8870 \pm 160$ |
| EC5 | $-634 \pm 21$                | $-8130 \pm 310$ |
| EC6 | $-653 \pm 2$                 | $-8560 \pm 30$  |

$\beta_{\text{eff}}$  and  $\Lambda$  were calculated using ENDF/B-VI.

fitting a function of the form

$$f(t) = \sum_{i=1}^{\infty} A_i e^{\alpha_i t} \quad (5)$$

to all data points, using the function fitting code MINUIT [16], it is possible to determine the exponential component which represents the fundamental decay mode. During the fitting procedure, all data points describing each pulse are used. It turns out that four terms are necessary to describe the response function with satisfactory statistical agreement. Two fast exponentials are required for the injection and adjustment periods, one exponential for the fundamental decay mode and finally, one constant for the delayed neutron background. The  $\alpha$ -values, describing the fundamental decay mode, are summarized in Table 3 and displayed visually for EC3 and EC5 in Fig. 3. The values are followed by a one standard deviation statistical error. Throughout this study, only statistical errors are considered.

The neutron pulse and the subsequent neutron flux have also been simulated with MCNP, relying on the nuclear data library ENDF/B-VI. The reaction rate with  $^3\text{He}$  has been tracked in each experimental channel during a period of 10 ms after the neutron pulse. The results for EC 2, 3 and 5 are displayed in Fig. 4. These data can be analyzed in the same way as the experimental data, to find the  $\alpha$ -values. In this case, the reactivity is already known, through earlier simulations, which means that the mean generation time can be found from Eq. (4).

In the simulated case, three exponentials are sufficient to describe the response function with

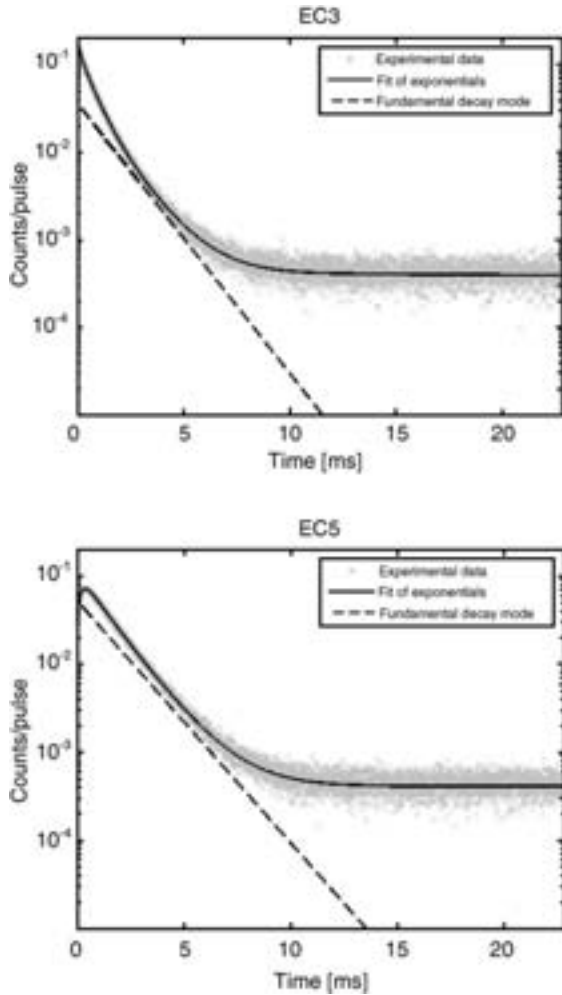


Fig. 3. Fit of exponentials to the experimental data in the experimental channels in the core (EC3) and in the reflector (EC5). The dashed lines represent the fundamental decay mode.

satisfactory statistical agreement, since the delayed neutrons are not included in the simulation. Two fast exponentials are required for the injection and adjustment periods and one exponential for the fundamental decay mode. The  $\alpha$ -values and their corresponding mean generation time, for each experimental channel, are summarized in Table 4.

By using the simulated values of the mean generation time in Table 4, it is possible to calculate the reactivity from the experimental values of  $\alpha$  (Table 3). The maximum difference between the experimental  $\alpha$ -values for different

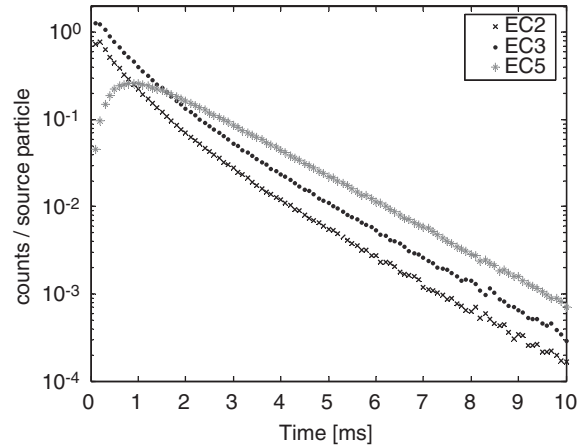


Fig. 4. MCNP-simulation of the pulsed neutron source experiment. The curves describe the reaction rate with  $^3\text{He}$  in EC2, EC3 and EC5.

Table 4

$\alpha$ -values and corresponding mean generation times,  $\Lambda$ , determined from the MCNP simulation of the PNS-experiment (ENDF/B-VI)

|     | $\alpha$ ( $\text{s}^{-1}$ ) | $\Lambda$ ( $\mu\text{s}$ ) |
|-----|------------------------------|-----------------------------|
| EC1 | $-726 \pm 16$                | $134 \pm 3$                 |
| EC2 | $-713 \pm 3$                 | $136.3 \pm 0.6$             |
| EC3 | $-716 \pm 2$                 | $135.7 \pm 0.5$             |
| EC5 | $-690 \pm 7$                 | $140.8 \pm 1.5$             |
| EC6 | $-679 \pm 1$                 | $142.2 \pm 0.3$             |

channels is approximately 10%. The differences are caused by statistical errors from the fitting procedure and different physical properties around the different experimental channels. The slope is found to be a little lower in the reflector channels. In Table 4, it can be seen that the simulated values deviate somewhat from the experimental values in Table 3, but they follow more or less the same pattern.

#### 4.1.2. Sjöstrand method

Considering the much shorter time scale of the decay of the prompt neutron flux compared to the delayed neutron precursor lifetimes, the delayed neutron flux contribution can be regarded as constant during the studied time interval. If the area under the response function is divided into a

prompt neutron area,  $A_p$ , and a delayed neutron area,  $A_d$ , as illustrated in Fig. 5, the reactivity in dollars can be expressed as [6]

$$\frac{\rho}{\beta_{\text{eff}}} = -\frac{A_p}{A_d}. \quad (6)$$

The prompt area is obtained by trapezoidal numeric integration and the delayed neutron area is obtained by averaging the values from the last milliseconds where the curve has flattened out. The results are listed in Table 5 and the maximal difference between the values is approximately 7%.

#### 4.2. Source jerk experiment

The idea behind the Source Jerk Method is to operate the subcritical reactor at steady state, at

flux level  $n_0$ , and then suddenly remove the neutron source. At this point, the system will make a prompt jump to a lower level,  $n_1$ , determined by the delayed neutron background. This level is only quasistatic and will decay according to the decay rate of the delayed neutron precursor groups [5]. The reactivity in dollars is given by

$$\frac{\rho}{\beta_{\text{eff}}} = \frac{n_1 - n_0}{n_1}. \quad (7)$$

During the source jerk experiment, the neutron flux is measured with a  $^3\text{He}$ -detector in EC2 (Fig. 6). The neutron flux levels are estimated by the flux values before and immediately after the prompt jump, which gives the reactivity  $\rho = -8.9 \pm 1.7\text{\$}$ . The statistical error is large due to the low count rate after the source jerk.

#### 4.3. Experimental estimation of the mean generation time

It is of interest to verify the Monte Carlo-based values of the mean generation time (Table 4) experimentally. An estimation of the ratio  $\lambda/\beta_{\text{eff}}$  can be found by rewriting Eq. (4) as

$$\frac{\lambda}{\beta_{\text{eff}}} = \frac{1}{\alpha} \left( \frac{\rho}{\beta_{\text{eff}}} - 1 \right) \quad (8)$$

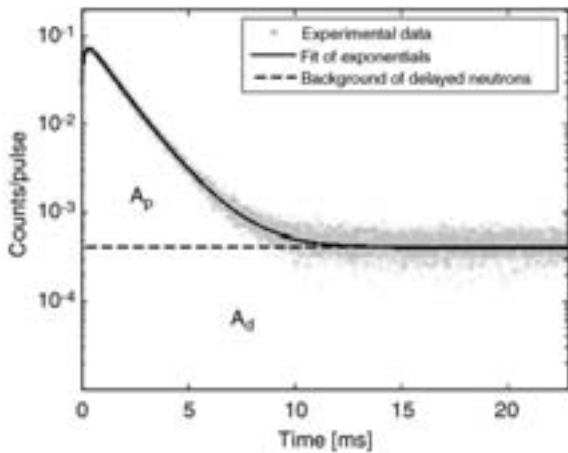


Fig. 5. Illustration of the prompt and the delayed neutron areas utilized in the Sjöstrand Method.

Table 5  
Results from the Sjöstrand Method

|     | $\rho$ (\$)     |
|-----|-----------------|
| EC1 | $-13.9 \pm 0.1$ |
| EC2 | $-13.7 \pm 0.1$ |
| EC3 | $-12.9 \pm 0.1$ |
| EC5 | $-13.0 \pm 0.1$ |
| EC6 | $-13.5 \pm 0.1$ |

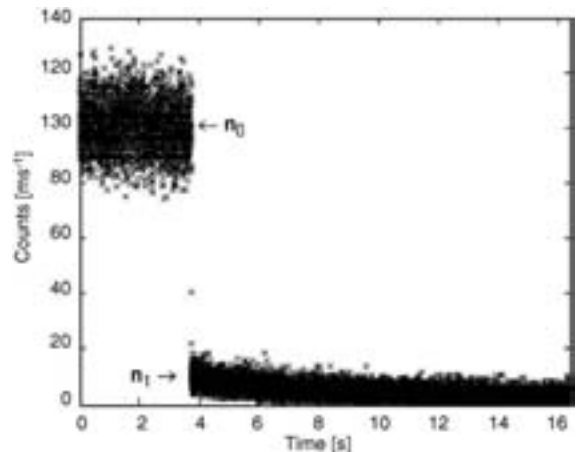


Fig. 6. Application of the Source Jerk Method in Yalina.

Table 6  
Experimental estimation of the mean generation time,  $\Lambda$

|                              | $\Lambda/\beta_{\text{eff}} (10^{-3} \text{ s})$ | $\Lambda (\mu\text{s})$ |             |             |
|------------------------------|--|-------------------------|-------------|-------------|
|                              |  | ENDF/B-VI               | JEFF3.0     | JENDL3.3    |
| <i>Slope Fit+Sjöstrand</i>   |  |                         |             |             |
| EC1                          | $22.1 \pm 0.4$                                   | $174 \pm 4$             | $175 \pm 4$ | $164 \pm 4$ |
| EC2                          | $20.3 \pm 0.6$                                   | $160 \pm 5$             | $161 \pm 5$ | $151 \pm 5$ |
| EC3                          | $19.5 \pm 0.3$                                   | $154 \pm 3$             | $155 \pm 3$ | $145 \pm 3$ |
| EC5                          | $22.1 \pm 0.7$                                   | $175 \pm 6$             | $175 \pm 6$ | $164 \pm 6$ |
| EC6                          | $22.2 \pm 0.2$                                   | $175 \pm 3$             | $176 \pm 3$ | $164 \pm 2$ |
| <i>Slope Fit+Source Jerk</i> |  |                         |             |             |
| EC2                          | $14.5 \pm 1.1$                                   | $114 \pm 9$             | $115 \pm 9$ | $108 \pm 8$ |

and combining the values of  $\alpha$  obtained from the Slope Fit Method with the values of  $\rho/\beta_{\text{eff}}$  obtained from the Sjöstrand Method or the Source Jerk Method. By using the calculated values of  $\beta_{\text{eff}}$  (Table 2), it is possible to find an estimate for  $\Lambda$ . From the results listed in Table 6, obtained by combining the Slope Fit Method and the Sjöstrand Method, it can be expected that the true value of  $\Lambda$  is in the range 140–180  $\mu\text{s}$ . The combination of the Slope Fit Method and the Source Jerk Method gives a lower value. The results diverge since the different methods give different values of the reactivity. However, this simple method shows that the values obtained by simulation (Table 4) should be good estimations of the real value. As a comparison, it can be mentioned that the non-adjoint-weighted mean generation time<sup>1</sup> calculated by MCNP, which is a very poor estimation of the true value, is approximately 370  $\mu\text{s}$ .

#### 4.4. Validity of the point-kinetic model

Since all three methods used in this study are based on the point-kinetic model, the validity of the model when applied to this system has been investigated.

<sup>1</sup>The (non-adjoint-weighted) neutron mean generation time is not given explicitly by MCNP. It must be calculated as the ratio between the prompt removal lifetime,  $l$ , and  $k_{\text{eff}}$ , or as the ratio between the prompt fission lifetime,  $\tau$ , and the number of prompt neutrons per fission,  $\nu_p$  [15,17,18].

The point-kinetic equations were developed for critical reactor calculations, and do not describe a subcritical system driven by an external neutron source strictly mathematically correct [19]. In a critical reactor, reactivity changes can be described by perturbation of an equilibrium state around criticality, where spatial flux shapes change slowly [20]. A subcritical facility, such as Yalina, with its driving point-like source, cannot be described in the same manner [21]. Thereby, the use of the point-kinetic approximation becomes questionable and its applicability to ADS is subject to investigation [20–22]. However, in the experiments of this study, the source is shut down and the decay of a well-established neutron population is studied. During this process, the reactor is not driven by an external source and the only driving source is the decaying fission source. Moreover, all points in the reactor are subject to the same time dependence. These circumstances make the use of the point-kinetic approximation acceptable, at least for a compact subcritical core, such as Yalina. In a large core, the spatial effects are worse, which make the point-kinetic approximation difficult or inappropriate to apply.

One basic assumption when deriving the point-kinetic equations is that the time-part of the solution can be separated from the energy and spatial part [15]. In other words, if the spatial one-energy group flux profile is constant in time, the assumption is valid. By using MCNP, the radial flux profile as a function of time after a neutron pulse has been simulated. Since the core relies mainly on thermal fissions, a one-energy group assumption should be well founded. Similar studies have been performed in Ref. [23]. The simulation has shown that after approximately 4 ms after the pulse, the relative values of the radial flux profile do not change in time. At this point, the injection and adjustment periods have past and all points in the system are subject to the same time-dependence (the fundamental decay mode). These results indicate that the point-kinetic model is applicable as an appropriate approximation of the time behavior of the neutron flux decay.

## 5. Discussion of results

### 5.1. Comparison between the methods

The Slope Fit Method, the Sjöstrand Method and the Source Jerk Method have been applied to the same configuration of the Yalina experiments. In comparison with the MCNP calculations, the Slope Fit Method shows similar results, whereas the Sjöstrand Method and the Source Jerk Method underestimates and overestimates  $k_{\text{eff}}$ , respectively. Both the Sjöstrand Method and the Slope Fit Method produce results with low statistical errors. The Source Jerk Method, on the other hand, is connected with larger errors due to the large uncertainty in the lower neutron flux level, which makes it difficult to make comparisons with the other methods. All results are summarized in Table 7 and Fig. 7.

When applying the Slope Fit Method on deep subcritical configurations, as in the present case, it can sometimes be difficult to find the correct slope through a fitting procedure. The effects from the injection and adjustment periods have disappeared after about 4ms, as mentioned in the previous

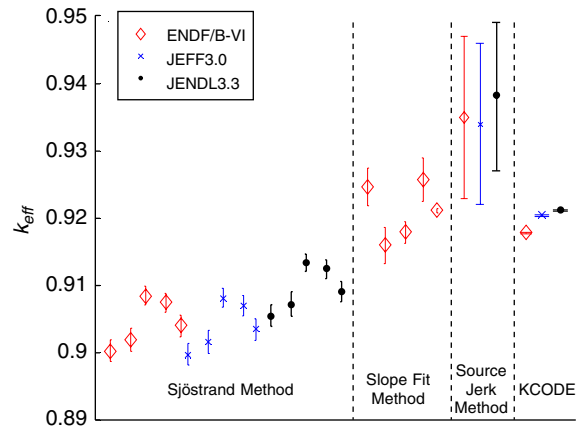


Fig. 7. Summary of all  $k_{\text{eff}}$  obtained through different methods applied on data from five experimental channels (Sjöstrand Method and Slope Fit Method). The error bars correspond to one standard deviation in each direction. The different libraries refer to the chosen value of  $\beta_{\text{eff}}$ .

Table 7

Summary of all  $k_{\text{eff}}$  obtained through the utilized methods and for different values of  $\beta_{\text{eff}}$  from different libraries

|                           | $k_{\text{eff}}$  |                   |                   |
|---------------------------|-------------------|-------------------|-------------------|
|                           | ENDF/B-VI         | JEFF3.0           | JENDL3.3          |
| <i>Sjöstrand Method</i>   |                   |                   |                   |
| EC1                       | 0.9012 ± 0.0013   | 0.9008 ± 0.0013   | 0.9065 ± 0.0013   |
| EC2                       | 0.9027 ± 0.0013   | 0.9022 ± 0.0013   | 0.9079 ± 0.0013   |
| EC3                       | 0.9076 ± 0.0011   | 0.9072 ± 0.0011   | 0.9126 ± 0.0011   |
| EC5                       | 0.9069 ± 0.0011   | 0.9064 ± 0.0011   | 0.9119 ± 0.0011   |
| EC6                       | 0.9040 ± 0.0013   | 0.9036 ± 0.0013   | 0.9091 ± 0.0012   |
| <i>Slope Fit Method</i>   |                   |                   |                   |
| EC1                       | 0.9239 ± 0.0022   | —                 | —                 |
| EC2                       | 0.9170 ± 0.0022   | —                 | —                 |
| EC3                       | 0.9185 ± 0.0013   | —                 | —                 |
| EC5                       | 0.9248 ± 0.0026   | —                 | —                 |
| EC6                       | 0.9211 ± 0.0002   | —                 | —                 |
| <i>Source Jerk Method</i> |                   |                   |                   |
| EC2                       | 0.935 ± 0.012     | 0.934 ± 0.012     | 0.938 ± 0.011     |
| MCNP                      |                   |                   |                   |
|                           | 0.91803 ± 0.00005 | 0.92010 ± 0.00007 | 0.92114 ± 0.00006 |

section, and the delayed neutron background starts to influence the shape after approximately 7ms (Fig. 3). Consequently, the fundamental decay mode is the dominating mode during a relatively short time period. The situation is most problematic in the experimental channels in the core, where it is very difficult to visually distinguish a single slope. In the reflector, on the other hand, the fast exponentials have opposite sign, due to the fast increase in neutron flux during the injection period, which makes the fundamental decay mode evident.

According to the results, the Sjöstrand Method has a tendency to give lower values of  $k_{\text{eff}}$  than other methods. Especially the difference between the Sjöstrand Method and the Slope Fit Method is worth to notice, since they are based on the same measurement. The same tendency was also observed in the MUSE-4 experiments [2,12]. The main probable reason for the discrepancies is the use of the point-kinetic approximation. When analyzing the experimental data with the Sjöstrand Method, all data from the pulse insertion to the end of the pulse response are used. However, only the data representative for the fundamental decay mode, used in the Slope Fit Method analysis, is valid according to the point-kinetics. Since the fundamental decay mode will be more and more

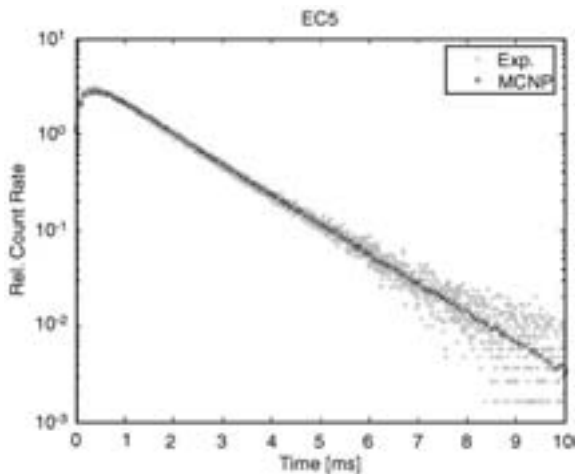


Fig. 8. Comparison between PNS experiment and Monte Carlo simulation for EC5.

dominating closer to criticality, the gap between the two methods is expected to decrease when approaching criticality. This effect was also observed in the MUSE-4 experiments [12].

The differences between the calculations based on the different nuclear data libraries are small; approximately 4% for the reactivity and 6% for  $\beta_{\text{eff}}$ . In comparison, the data library ENDF/B-VI gives a somewhat lower value of  $k_{\text{eff}}$  and JENDL3.3 gives a lower value of  $\beta_{\text{eff}}$ . However, the choice of nuclear data library does not induce prominent effects on the result.

### 5.2. Comparison between the PNS experiment and MCNP

As mentioned before, there is no delayed neutron background when simulating the pulsed neutron source experiment in MCNP. In order to compare the simulation with the experiment, this background must be subtracted from the experimental data. The result for EC5 is depicted in Fig. 8 and indicates good agreement.

## 6. Conclusions

Three reactivity determination methods, the Slope Fit Method, the Sjöstrand Method and the

Source Jerk Method, have been investigated by applying them to the Yalina experiments. Two types of experiments were performed at the facility; a pulsed neutron source experiment (PNS) and a source jerk experiment. The PNS experiment has also been simulated with MCNP. The simulations provided parameters, such as effective delayed neutron fraction and mean generation time, which were necessary for the evaluation of the reactivity and the effective multiplication constant from the experiments.

From the measurements it can be concluded that:

- The Sjöstrand Method underestimates the criticality slightly in comparison with MCNP and the other methods, but gives low statistical error.
- The Slope Fit Method is inconvenient to apply to deep subcritical configurations, but gives reliable results in comparison with MCNP. The cleanest response functions are achieved in the reflector channels.
- The Source Jerk Method is connected with large uncertainties.
- Although the neutron spectrum of Yalina is thermal and has different kinetic parameters than in MUSE, the results show many similarities.

Moreover, from the simulations it can be concluded that:

- MCNP gives reliable results, which was shown by the simulations in comparison with the experiments. However, care must be taken when calculating time parameters.
- The point-kinetic approximation describes the system well under the studied circumstances.

In this work, differences between different reactivity levels were not studied. Even if the methods do not predict the absolute value of the reactivity absolutely correct, they may be able to predict reactivity changes with good precision.

None of the methods investigated in this study have the capability of measuring the reactivity without disturbing a running system. However, the

methods can be used to estimate the subcriticality during loading and for calibration of other possible measurement techniques, for example the current-to-flux reactivity indicator. In the profound study of different measurement techniques for reactivity monitoring in an ADS performed within the MUSE-4 program, the method based on the current-to-flux reactivity indicator has appeared to be the major candidate for on-line monitoring [24].

### Acknowledgements

This work was financially supported by SKB AB (Swedish Nuclear Fuel and Waste Management Co) and SKI (Swedish Nuclear Power Inspectorate). The authors would like to thank R. Klein Meulekamp for calculations of effective delayed neutron fractions and for useful discussions.

### References

- [1] M. Salvatores, et al., Nucl. Instr. and Meth. A 414 (1998) 5.
- [2] R. Soule, et al., Nucl. Sci. Eng. 148 (2004) 124.
- [3] A.I. Kievitskaia, et al., Experimental and theoretical research on transmutation of long-lived fission products and minor actinides in a subcritical assembly driven by a neutron generator, in: The Third International Conference on Accelerator Driven Transmutation Technologies and Applications, ADTTA'99, Praha, Czech Republic, June, 1999.
- [4] I.G. Serafimovitch, et al., A small-scale set-up for research of some aspects of accelerator driven transmutation technologies, in: The Third International Conference on Accelerator Driven Transmutation Technologies and Applications, ADTTA'99, Praha, Czech Republic, June 1999.
- [5] G.R. Keepin, Physics of Nuclear Kinetics, Addison-Wesley, Reading, MA, 1965.
- [6] N.G. Sjöstrand, Ark. Fys. 11 (1956) 13.
- [7] S.E. Chigrinov, I. G. Serafimovich, Experimental and theoretical research of the peculiarities of transmutation of long-lived fission products and minor actinides in subcritical assembly driven by a neutron generator, Technical report, Joint Institute of Power and Nuclear Research, National Academy of Sciences of Belarus, Minsk, Sosny, ISTC Project B-070-98.
- [8] J.F. Briesmeister (Ed.), MCNP—A general Monte Carlo N-Particle Transport Code, Version 4c, LA-13709-M, Los Alamos National Laboratory, USA, 2000.
- [9] OECD/NEA [www.nea.fr](http://www.nea.fr).
- [10] S.C. Van Der Marck, R. Klein Meulekamp, Calculating the Effective Delayed Neutron Fraction Using Monte Carlo Techniques, PHYSOR, Chicago, IL, USA, 2004 (April).
- [11] B.E. Simmons, J.S. King, Nucl. Sci. Eng. 3 (1958) 595.
- [12] D. Villamarin, Análisis dinámico del reactor experimental de fisión nuclear MUSE-4, Doctoral Thesis, Universidad Complutense de Madrid, Departamento de Física Atómica, Molecular y Nuclear, 2004.
- [13] M. Rosselet, et al., Nucl. Sci. Eng. 135 (2000) 33.
- [14] S. Dulla, et al., Kerntechnik 67 (2002).
- [15] K.O. Ott, R.J. Neuhold, Introductory Nuclear Reactor Dynamics, American Nuclear Society, 1985.
- [16] F. James, M. Winkler, MINUIT User's Guide, CERN, Geneva, 2004.
- [17] G.D. Spriggs, et al., On the definition of neutron lifetimes in multiplying and non-multiplying systems, LA-UR-97-1073, Brazilian Meeting on Reactor Physics and Thermo hydraulics, Pocos de Caldas Springs, MG, Brazil, 1997.
- [18] R.D. Busch, et al., Definition of neutron lifespan and neutron lifetime in MCNP4B, LA-UR-97-222, American Nuclear Society Meeting, Orlando, FL, June 1997.
- [19] D.G. Cacuci, Nucl. Sci. Eng. 148 (2004) 55.
- [20] D.G. Cacuci, On Perturbation Theory and Reactor Kinetics: From Wigner's Pile Period to Accelerator Driven Systems, PHYSOR, Seoul, Korea, 2002.
- [21] A. Rineiski, W. Maschek, Ann. Nucl. Energy 32 (2005) 1348.
- [22] A. Rineiski, W. Maschek, On application of quasistatic and point-kinetics schemes for subcritical systems with external neutron source, Nuclear Mathematical and Computational Sciences: A Century in Review—A Century Anew, M&C 2003, Gatlinburg, TN, USA, 6–11 April 2003.
- [23] M. Eriksson, et al., Nucl. Sci. Eng. 149 (2005) 298.
- [24] EU Project FIKW-CT-2000-00063, Final report—The MUSE experiments for subcritical neutronics validation, unpublished.



## COMPARISON OF NEUTRON KINETIC PARAMETERS OF THE SUBCRITICAL ADS EXPERIMENTS YALINA AND YALINA BOOSTER

**Carl-Magnus Persson, Per Seltborg, Alexandra Åhlander and Waclaw Gudowski**  
Department of Nuclear and Reactor Physics, Royal Institute of Technology  
Roslagstullsbacken 21, S-106 91, Stockholm, Sweden  
calle@neutron.kth.se; per@neutron.kth.se; alex@neutron.kth.se; wacek@neutron.kth.se

**Sergey Chigrinov, Ivan Serafimovich, Victor Bournos, Yurii Fokov,  
Christina Routkovskaia and Hanna Kiyavitskaya**  
Joint Institute for Power and Nuclear Research – Sosny of the National Academy of Sciences  
Krasina str. 99, 220109 Minsk, Belarus  
burvik@tut.by; fokov@sosny.bas-net.by; chris@sosny.bas-net.by; anna@sosny.bas-net.by

### ABSTRACT

Subcritical experiments, devoted to investigation of characteristics of accelerator-driven systems, have been constructed at the Joint Institute for Power and Nuclear Research – Sosny in Minsk, Belarus. Different methods for reactivity determination have previously been investigated in the thermal ADS experiment “Yalina”, and recently, a coupled fast-thermal facility “Yalina Booster” was launched. This study presents the neutron kinetic characteristics of the Yalina and the new Yalina Booster setups, and points out some important differences. For the Yalina setup, neutron kinetic parameters, such as  $k_{eff}$ ,  $\alpha$ ,  $\beta_{eff}$  and  $\Lambda$  have been determined by Monte Carlo simulations and they have previously been verified experimentally. For Yalina Booster, these parameters have been estimated by Monte Carlo simulations in a preliminary study, and they will be verified in upcoming experiments.

*Key Words:* Yalina, Yalina Booster, ADS, subcriticality monitoring, MCNP

### 1 INTRODUCTION

As a step towards a full-scale accelerator-driven system (ADS) for transmutation of nuclear waste, a small-scale research facility “Yalina” has been constructed at the Joint Institute for Power & Nuclear Research in Sosny, Belarus [1,2]. The kinetic behavior of neutrons in subcritical systems is very important to understand in order to determine the reactivity, which is essential for the safety of the reactor and for the licensing. Such studies have also been performed within the MUSE-4 program [3] and future similar experiments will take place in both Russia [4] and USA [5]. In this context, different reactivity determination methods have been investigated in a thermal neutron spectrum in the Yalina facility.

In the Yalina Booster, the investigation is extended to a reactor setup employing a coupled fast-thermal neutron spectrum [6]. This kind of facility, which has a central fast zone and a surrounding thermal zone, gives access to a fast neutron spectrum, but with a neutron generation time characteristic of a thermal core [7]. Historically, electron accelerators coupled to fast spectrum subcritical cores have been used to generate neutron bursts with pulse duration of only a few microseconds [8]. The purpose of the subcritical core, in these

facilities, has been to intensify, or “boost”, the charged particle-induced neutron source. In a similar manner, the central fast zone in Yalina Booster boosts the source in order to get a high thermal neutron flux in the surrounding thermal zone.

## 2 EXPERIMENTAL SETUPS: YALINA AND YALINA BOOSTER

Both Yalina and Yalina Booster are subcritical cores coupled to a neutron generator. The neutrons are created through the fusion reaction between deuterium and tritium (D,T) or between deuterium and deuterium (D,D), which generates neutrons with energy around 14 MeV or 2.5 MeV respectively. The neutron generator, consisting mainly of a deuteron accelerator and a Ti-T or Ti-D target located in the center of the core, provides the possibility to generate high intensity neutron beams with a frequency from 1 Hz to 10 kHz and with a pulse duration of 0.5 – 100  $\mu$ s. The deuteron energy is between 100 and 250 keV and a beam current of 12 mA can be achieved. These parameters give a maximum neutron yield of approximately  $1.5 \cdot 10^{12}$  neutrons per second. The high maximum frequency and the long pulse duration of the neutron generator make it possible to regard the neutron source as continuous in time, which can represent typical conditions of a real ADS. The experimental setups of Yalina and Yalina Booster are described in detail below.

### 2.1 Yalina

In the Yalina core, the target is surrounded by fuel consisting of uranium dioxide with 10% enrichment in  $^{235}\text{U}$ . The fuel pins are situated in subassemblies constituting a lattice of quadratic geometry, depicted in Figure 1. In the region closest to the target, the subassemblies are made of lead in order to diffuse the energy spectrum of the source neutrons into a more spallation-like spectrum, by (n,xn)- and scattering reactions. Outside the lead zone, there is a moderating region, with subassemblies made of polyethylene ( $\text{C}_2\text{H}_4$ ). This is a rather efficient moderator with a moderating ratio ( $\zeta\Sigma_s\Sigma_a^{-1}$ ) of 122, compared to 71 for light-water moderator. The reflector is made of graphite with a thickness of about 40 cm. Five experimental channels (EC) are placed at different positions at different distances from the core centre. The relative positions of the experimental channels are chosen in order to minimize their influence on each other.

As can be seen in Figure 1, EC1 is close to the source, EC2 is in the lead zone, EC3 is in the moderating thermal zone and EC5 and EC6 are situated in the reflector. There are totally 280 fuel pins, each of them with a diameter of 11 mm. The spacing between two adjacent fuel pins is 20 mm and the length of the active part of the fuel pins is 500 mm.

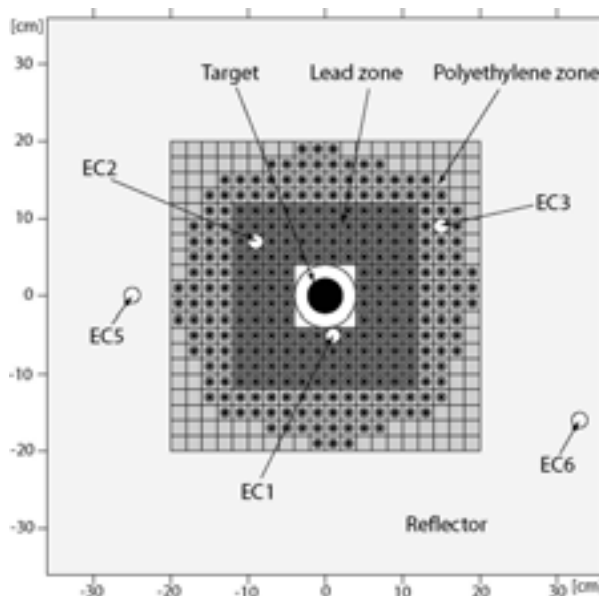


Figure 1. Vertical cross-sectional view of the Yalina core.

## 2.2 Yalina Booster

The fast zone, in the center of the core, is fuelled with  $\text{UO}_2$  with an enrichment of 36% in  $^{235}\text{U}$ , except the innermost layers which are fuelled with metallic uranium with an enrichment of 90% (Figure 2). The fuel pins are placed in a quadratic lattice geometry of lead. In the surrounding thermal zone, the fuel pins are located in polyethylene for moderation. The fuel in the thermal zone is  $\text{UO}_2$  of 10% enrichment. In order to prevent thermal neutrons from leaking into the fast zone, there is an interface between the zones consisting of one layer of  $\text{B}_4\text{C}$  and another layer of metallic natural uranium. Thermal neutrons diffusing from the thermal zone to the fast zone will either be absorbed by the boron or by the natural uranium, or they will be transformed into fast neutrons through fission in the natural uranium. In this way, the boron and natural uranium layers act like a thermal neutron filter. The core is surrounded by a graphite reflector and a biological shielding of borated polyethylene. There is one experimental channel in the fast zone (EC1) and three in the thermal zone (EC2-4). Moreover, there is one neutron flux monitoring channel in each corner of the core. Three  $\text{B}_4\text{C}$ -control rods, with a total reactivity worth of approximately 300 pcm, are located in the thermal zone. In the investigated configuration, all three control rods were fully inserted.

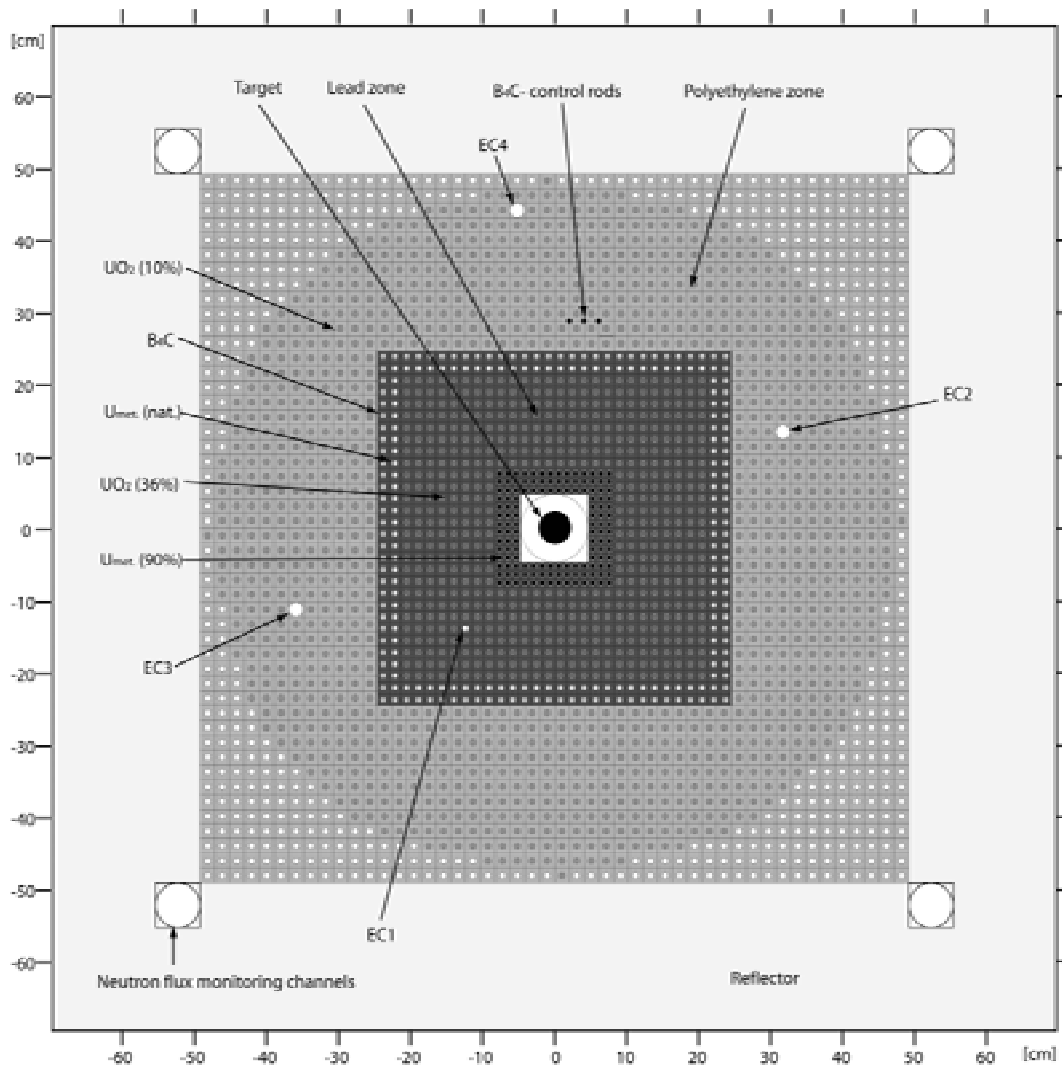


Figure 2. Vertical cross-sectional view of Yalina Booster.

### 3 REACTIVITY DETERMINATION BY PULSED NEUTRON SOURCE TECHNIQUE

After a neutron pulse injection into a subcritical core, a number of fission chains start to propagate in the fuel. Due to the subcriticality, every fission chain will die out rapidly, which is characterized by a global exponential decay of the neutron flux. By studying the prompt neutron decay after a neutron pulse injection, it is possible to determine the reactivity of the core by applying the Slope Fit Method.

Neglecting the delayed neutrons, the point-kinetic equations take the following form for a reactor without sources [9,10]:

$$\frac{dn(t)}{dt} = \alpha n(t). \quad (1)$$

This equation has an exponential solution given by

$$n(t) = n_0 e^{\alpha t}, \quad (2)$$

where  $\alpha$  is the prompt neutron decay constant defined as

$$\alpha = \frac{\rho - \beta_{eff}}{\Lambda}. \quad (3)$$

In this equation,  $\rho$  is the reactivity,  $\beta_{eff}$  is the effective delayed neutron fraction and  $\Lambda$  is the neutron mean generation time. In a subcritical reactor,  $\alpha$  is negative, which gives rise to an exponential decrease of the neutron flux. In the short time-scale after a neutron pulse injection, the neglecting of the delayed neutrons is legitimate and thus, the decay is mainly described by the prompt neutron decay constant. This is often referred to as the decay of the fundamental mode [11]. By measuring  $\alpha$  experimentally, the reactivity,  $\rho$ , can be found if  $\beta_{eff}$  and  $\Lambda$  are known.

### 4 MONTE CARLO SIMULATIONS

For the analysis of subcritical systems, the kinetic parameters  $\alpha$ ,  $\beta_{eff}$  and  $\Lambda$  must be known in order to determine the reactivity, as was shown in section 3. Therefore, it is of interest to evaluate these parameters, including  $\rho$ , by Monte Carlo simulations using MCNP-4C3 [12]. It turns out that the neutron mean generation time is difficult to estimate by Monte Carlo methods, since MCNP calculates non-adjoint-weighted time parameters. However,  $\Lambda$  can be obtained from the other parameters, under the condition that the point-kinetic approximation is valid, using Eq. (3).

From the pulsed neutron source (PNS) experiment,  $\alpha$  is obtained from the Slope Fit Method and the reactivity in dollars,  $\rho/\beta_{eff}$ , can be obtained e.g. from the Sjöstrand Method [13]. By rewriting Eq. (3) as

$$\frac{\Lambda}{\beta_{eff}} = \frac{1}{\alpha} \left( \frac{\rho}{\beta_{eff}} - 1 \right), \quad (4)$$

it is possible to obtain an experimental value of the fraction  $\Lambda/\beta_{eff}$ , once again under the condition that the point-kinetic approximation is valid. In this way it is possible to verify the simulated value of  $\Lambda$  experimentally if  $\beta_{eff}$  is assumed to be correct.

Since all methodology described in this study is derived from the point-kinetic approximation, a study of its validity in the Yalina experiments has been performed [14].

#### 4.1 Monte Carlo Simulation of the Yalina Setup

A detailed description of the Yalina setup geometry has been implemented in MCNP. The criticality option KCODE in MCNP has been used to estimate the effective multiplication constant,  $k_{eff}$ . Moreover, a modified version of MCNP has been used to calculate the effective delayed neutron fraction,  $\beta_{eff}$ , according to the definition

$$\beta_{eff} = \frac{N_d}{N_{Tot}}, \quad (5)$$

where  $N_d$  is the number of fissions induced by the delayed neutrons and  $N_{Tot}$  is the total number of fissions in the system [15]. Three libraries; ENDF/B-VI, JEFF3.0 and JENDL3.3, were used for the simulations [16], and the results, with a one standard deviation statistical error, are displayed in Table I. JENDL3.3 gives a somewhat lower estimation of  $\beta_{eff}$  than the other libraries, as for the rest, the different libraries show good agreement with each other.

In order to determine  $\alpha$ , the reaction rate with  $^3\text{He}$  after a neutron pulse insertion of duration 2  $\mu\text{s}$  has been tracked in the different experimental channels during 20 ms. From Figure 3 it can be seen that during the first milliseconds, there is an injection period when the neutron flux decreases rapidly in the core (EC2 and EC3) and increases in the reflector (EC5). After the injection period follows an adjustment period when the neutron flux approaches the fundamental decay mode. During the fundamental decay mode, the decay rate is common for all channels, characteristic for the inherent reactor properties, as described by the point-kinetics. In the simulation, no delayed neutrons were included, which makes the fundamental decay mode more visible. The slope of the fundamental decay mode,  $\alpha$ , for different experimental channels, together with the corresponding value of  $\Lambda$ , calculated from Eq. (3), are displayed in Table II. For the calculations, the library ENDF/B-VI was used and the function fitting code MINUIT [17] was used to find  $\alpha$ . The experimental results from determining these parameters are presented in ref. [14].

**Table I. Effective multiplication constant,  $k_{eff}$ , and effective delayed neutron fraction,  $\beta_{eff}$ , for Yalina, calculated with MCNP using different libraries.**

| Library   | $k_{eff}$             | $\beta_{eff}$ [pcm] |
|-----------|-----------------------|---------------------|
| ENDF/B-VI | $0.91803 \pm 0.00005$ | $788 \pm 9$         |
| JEFF3.0   | $0.92010 \pm 0.00007$ | $793 \pm 9$         |
| JENDL3.3  | $0.92114 \pm 0.00006$ | $742 \pm 9$         |

**Table II.  $\alpha$ -values and corresponding neutron mean generation times,  $\Lambda$ , for Yalina, determined from the MCNP simulation of the PNS experiment (ENDF/B-VI).**

| Experimental channel | $\alpha$ [ $s^{-1}$ ] | $\Lambda$ [ $\mu s$ ] |
|----------------------|-----------------------|-----------------------|
| EC1                  | $-726 \pm 16$         | $134 \pm 3$           |
| EC2                  | $-713 \pm 3$          | $136.3 \pm 0.6$       |
| EC3                  | $-716 \pm 2$          | $135.7 \pm 0.5$       |
| EC5                  | $-690 \pm 7$          | $140.8 \pm 1.5$       |
| EC6                  | $-679 \pm 1$          | $142.2 \pm 0.3$       |

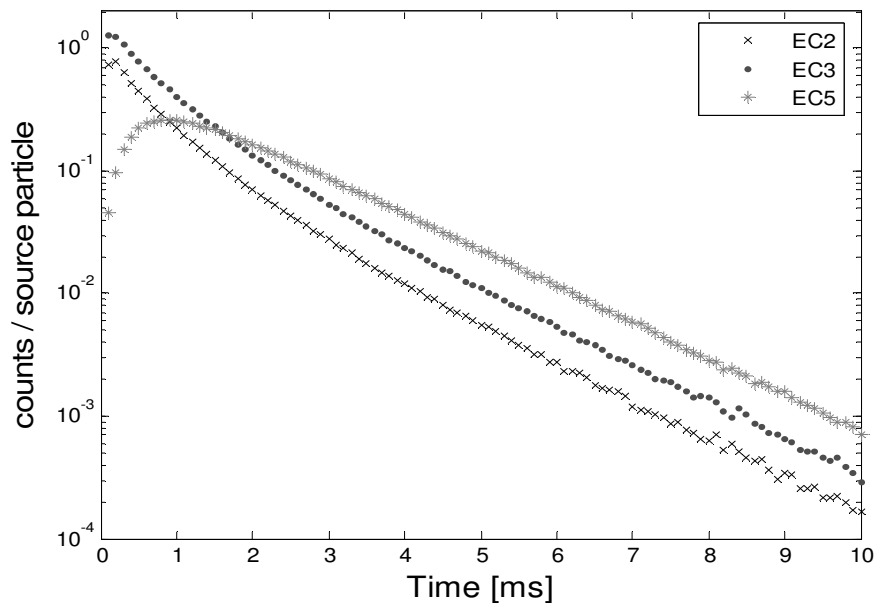


**Figure 3. MCNP-simulation of a pulsed neutron source experiment in Yalina. The curves describe the reaction rate with  $^3\text{He}$  in EC2, EC3 and EC5.**

#### 4.2 Preliminary Monte Carlo Simulation of the Yalina Booster Setup

A preliminary MCNP-input has been created for preparatory studies of the upcoming experimental program at the Yalina Booster facility. A similar analysis as for Yalina has been performed and is presented here.

First of all,  $k_{eff}$  and  $\beta_{eff}$  have been estimated using different nuclear libraries (Table III). In this preliminary study, the “prompt method” for effective delayed neutron fraction evaluation has been used:

$$\beta_{eff} \approx 1 - \frac{k_p}{k_{eff}}, \quad (6)$$

where  $k_p$  represents the effective multiplication of prompt neutrons only [18]. The accuracy of this method in comparison with the more accurate method used for Yalina has been investigated [15] and it has turned out that both methods perform well.

**Table III. Effective multiplication constant for Yalina Booster, calculated with MCNP.**

| Library   | $k_{eff}$             | $\beta_{eff}$ [pcm] |
|-----------|-----------------------|---------------------|
| ENDF/B-VI | $0.98190 \pm 0.00004$ | $761 \pm 6$         |
| JEFF3.0   | $0.98208 \pm 0.00006$ | $761 \pm 9$         |
| JENDL3.3  | $0.98273 \pm 0.00006$ | $744 \pm 9$         |

A PNS experiment has been simulated in the same way as for the Yalina setup, but with the delayed neutrons included. Figure 4 shows the reaction rate with  $^{232}\text{Th}$  in EC1 and the reaction rate with  $^3\text{He}$  in EC2 and EC4 (EC3 has been excluded since it is more or less identical to EC2). After only 1 ms, the same time-dependence is found in both the fast and the thermal zone. The fundamental decay mode is dominating until the delayed neutrons start to influence the behavior after approximately 16 ms. The slope of the fundamental decay mode for different channels and the corresponding neutron mean generation time, calculated from Eq. (3), are displayed in Table IV.

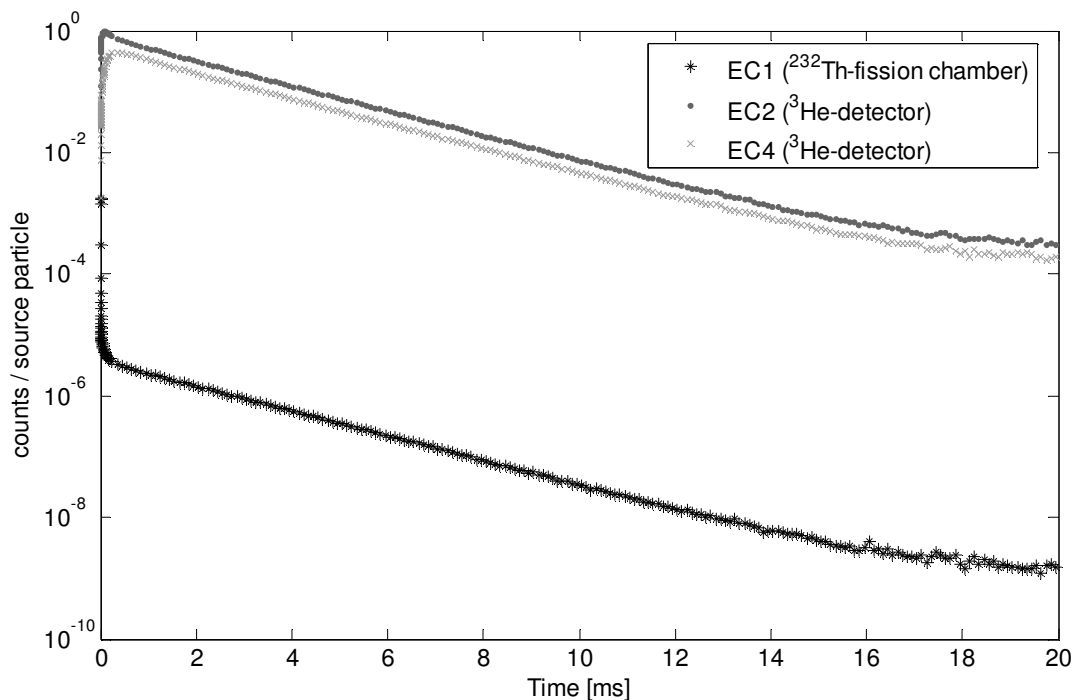


**Figure 4.** MCNP-simulation of a pulsed neutron source experiment in Yalina Booster. The curves describe the reaction rate with  $^{232}\text{Th}$  in EC1 and  $^3\text{He}$  in EC2 and EC4.

**Table IV.**  $\alpha$ -values and corresponding neutron mean generation times,  $\Lambda$ , for Yalina Booster, determined from the MCNP simulation of the PNS experiment (ENDF/B-VI).

| Experimental channel | $\alpha$ [ $\text{s}^{-1}$ ] | $\Lambda$ [ $\mu\text{s}$ ] |
|----------------------|------------------------------|-----------------------------|
| EC1                  | $-468.5 \pm 1.5$             | $55.6 \pm 0.2$              |
| EC2                  | $-468.2 \pm 0.4$             | $55.6 \pm 0.2$              |
| EC3                  | $-469.4 \pm 0.1$             | $55.5 \pm 0.2$              |
| EC4                  | $-469.6 \pm 0.7$             | $55.5 \pm 0.2$              |

## 5 CONCLUSIONS

Approximate values of the kinetic parameters for Yalina and Yalina Booster, calculated from ENDF/B-VI, are summarized in Table V. Since the studied configuration of Yalina Booster is closer to criticality than Yalina, the uncertainty of the values are lower. At deep subcriticalities, the fundamental decay mode is dominating during a very short time period. In Yalina, the injection and adjustment periods take approximately 5 ms and the delayed neutrons start to influence the pulse after approximately 7 ms. However, in the Monte Carlo simulation of the PNS experiment in Yalina, the delayed neutrons were excluded, but the count rate after such long time is low.

Concerning the neutron mean generation time, the value is considerably lower for Yalina Booster than for Yalina, but still higher than for a fast system. A typical value for a fast system is on the microsecond-scale; for MASURCA, used in the MUSE-program, the mean generation time is 0.58  $\mu\text{s}$  [3]. This shows that the fission chain generation process in Yalina Booster is mainly driven by fissions induced in the thermal zone. Monte Carlo simulations have shown that the effective multiplication constant for the fast zone by itself is approximately 0.60 and for the thermal zone 0.95.

The effective delayed neutron fraction is somewhat lower for Yalina Booster than for Yalina. This is expected since the softer spectrum of the delayed neutrons, in comparison with the fission neutron spectrum, results in a higher fission probability in a thermal reactor and the opposite in a fast reactor.

In a near future, PNS experiments will be performed at the Yalina Booster facility and the values of the kinetic parameters will be verified.

**Table V. Summary of the quantitative values of the kinetic parameters for Yalina and Yalina Booster as evaluated from ENDF/B-VI.**

| Parameter     | Yalina               | Yalina Booster       |
|---------------|----------------------|----------------------|
| $k_{eff}$     | 0.92                 | 0.982                |
| $\alpha$      | -700 $\text{s}^{-1}$ | -469 $\text{s}^{-1}$ |
| $\Lambda$     | 140 $\mu\text{s}$    | 56 $\mu\text{s}$     |
| $\beta_{eff}$ | 790 pcm              | 760 pcm              |

## 6 ACKNOWLEDGEMENTS

The program of experimental investigations at the Yalina facility has been realized within the framework of the ISTC Project #B-070, and the construction of the Yalina Booster facility has been done within the framework of the Belarus State Scientific Program "Instruments for Scientific Research". The realization of the experiments and simulations has also been financially supported by SKB AB (Swedish Nuclear Fuel and Waste Management Co) and SKI (Swedish Nuclear Power Inspectorate). The authors would like to thank R. Klein Meulekamp for calculations of effective delayed neutron fractions and for useful discussions.



## 7 REFERENCES

1. A. I. Kievitskaia et al., “Experimental and theoretical research on transmutation of long-lived fission products and minor actinides in a subcritical assembly driven by a neutron generator,” *The 3<sup>rd</sup> International Conference on Accelerator Driven Transmutation Technologies and Applications, ADTTA '99*, Czech Republic, Praha, June (1999).
2. I. G. Serafimovitch et al., “A small-scale set-up for research of some aspects of accelerator driven transmutation technologies,” *The 3<sup>rd</sup> International Conference on Accelerator Driven Transmutation Technologies and Applications, ADTTA '99*, Czech Republic, Praha, June (1999).
3. R. Soule et al., “Neutronic Studies in Support of Accelerator-Driven Systems: The MUSE Experiments in the MASURCA Facility,” *Nucl. Sci. Eng.*, **148**, 124 (2004).
4. “Subcritical Assembly at Dubna (SAD),” <http://www.sad.dubna.ru> (2005).
5. D. Beller, “Overview of the AFCI Reactor-Accelerator Coupling Experiments (RACE) Project,” *OECD/NEA 8th Information Exchange Meeting on Partitioning and Transmutation*, Las Vegas, November 9-11 (2004).
6. S. E. Chigrinov et al., “Booster Subcritical Assembly, Driven by a Neutron Generator” (in Russian), JIPNR 14, Preprint of National Academy of Sciences of Belarus, Joint Institute for Power and Nuclear Research – Sosny, Minsk (2004).
7. R. Avery, “Coupled Fast-Thermal Power Breeder,” *Nucl. Sci. Eng.*, **3**, pp.129-144 (1958).
8. E. P. Shabalin, *Fast Pulsed and Burst Reactors - A comprehensive account of the physics of both single burst and repetitively pulsed reactors*, Pergamon Press (1979).
9. G. R. Keepin, *Physics of Nuclear Kinetics*, Addison-Wesley (1965).
10. K. O. Ott and R. J. Neuhold, *Introductory Nuclear Reactor Dynamics*, American Nuclear Society (1985).
11. G. I. Bell & S. Glasstone, *Nuclear Reactor Theory*, Van Nostrand Reinhold Company (1970).
12. J. F. Briesmeister, editor, “MCNP – A general Monte Carlo N-particle transport code, version 4c,” LA-13709-M, Los Alamos National Laboratory, USA (2000).
13. N. G. Sjöstrand, “Measurements on a subcritical reactor using a pulsed neutron source,” *Arkiv för Fysik*, **11:13**, pp.233-246 (1956).
14. C.-M. Persson et al., “Analysis of reactivity determination methods in the subcritical experiment Yalina,” Accepted for publication in *Nuclear Instruments and Methods in Physics Research, Section A* (2005).
15. S. C. Van Der Marck & R. Klein Meulekamp, “Calculating the Effective Delayed Neutron Fraction Using Monte Carlo Techniques,” *PHYSOR 2004*, Chicago, Illinois, USA, April (2004).
16. “OECD/NEA,” <http://www.nea.fr>.
17. F. James & M. Winkler, “MINUIT User’s Guide,” CERN, Geneva (2004).
18. M. M. Bretscher, “Evaluation of Reactor Kinetic Parameters without the need for Perturbation Codes,” *Proc. Int. Meeting on Reduced Enrichment for Research and Test Reactors*, Wyoming, USA, Oct. (1997).



ELSEVIER

Available online at [www.sciencedirect.com](http://www.sciencedirect.com)

SCIENCE @ DIRECT®

Annals of Nuclear Energy 32 (2005) 1719–1749

annals of  
NUCLEAR ENERGY

[www.elsevier.com/locate/anucene](http://www.elsevier.com/locate/anucene)

# Performance of the gas turbine-modular helium reactor fuelled with different types of fertile TRISO particles

Alberto Talamo \*, Waclaw Gudowski

*Department of Nuclear and Reactor Physics, Royal Institute of Technology,  
Roslagstullsbacken 21, S-106 91 Stockholm, Sweden*

Received 23 February 2005; accepted 18 June 2005

Available online 26 August 2005

---

## Abstract

Preliminary studies have been performed on operation of the gas turbine-modular helium reactor (GT-MHR) with a thorium based fuel. The major options for a thorium fuel are a mixture with light water reactors spent fuel, mixture with military plutonium or with fissile isotopes of uranium. Consequently, we assumed three models of the fuel containing a mixture of thorium with  $^{239}\text{Pu}$ ,  $^{233}\text{U}$  or  $^{235}\text{U}$  in TRISO particles with a different kernel radius keeping constant the packing fraction at the level of 37.5%, which corresponds to the current compacting process limit. In order to allow thorium to act as a breeder of fissile uranium and ensure conditions for a self-sustaining fission chain, the fresh fuel must contain a certain quantity of fissile isotope at beginning of life; we refer to the initial fissile nuclide as triggering isotope. The small capture cross-section of  $^{232}\text{Th}$  in the thermal neutron energy range, compared to the fission one of the common fissile isotopes ( $^{239}\text{Pu}$ ,  $^{233}\text{U}$  and  $^{235}\text{U}$ ), requires a quantity of thorium 25–30 times greater than that one of the triggering isotope in order to equilibrate the reaction rates. At the same time, the amount of the triggering isotope must be enough to set the criticality condition of the reactor. These two conditions must be simultaneously satisfied. The necessity of a large mass of fuel forces to utilize TRISO particles with a large radius of the kernel, 300  $\mu\text{m}$ . Moreover, in order to improve the neutron economics, a fuel cycle based on thorium requires a low capture to fission ratio of the triggering isotope. Amid the common

---

\* Corresponding author. Fax: +46 8 5537 8465.  
E-mail address: [alby@neutron.kth.se](mailto:alby@neutron.kth.se) (A. Talamo).

fissile isotopes,  $^{233}\text{U}$ ,  $^{235}\text{U}$  and  $^{239}\text{Pu}$ , we have found that only the uranium nuclides have shown to have the suitable neutronic features to enable the GT-MHR to work on a fuel based on thorium.

© 2005 Elsevier Ltd. All rights reserved.

---

## 1. Introduction

In the recent studies (Talamo et al., 2004a,b,c, 2005), we analyzed the gas turbine-modular helium reactor (GT-MHR) (Baxter and Fikani, 2002; Baxter and Rodriguez, 2001; General Atomics, 2002; Kiryushin et al., 1997; Kodochigov et al., 2003; Labar, 2002; Labar and Simon, 1994; Ohashi et al., 2000; Plukiene and Ridikas, 2003; Rodriguez and Baxter, 2003; Shenoy, 1995; Tsuchie, 2000) burnup capability to transmute light water reactors (LWRs) waste and military plutonium. In both cases, we applied the so-called *deep burn* in-core fuel management strategy, which divides the fuel cycle into two irradiation periods of three years each.

In the fuel cycle based on LWRs waste, two types of fuel have been used: the driver fuel (DF), loaded during the first irradiation period, and the transmutation fuel (TF), which is employed in the next irradiation periods. The DF contains neptunium and plutonium from the reprocessing of LWRs waste and it maintains the criticality of the reactor by depleting the fissile isotopes. The TF consists of irradiated DF plus some set-aside americium and curium from the reprocessing of the LWRs waste; TF depletes non-fissile isotopes by capture, followed by natural decay or fission, and it also offers a negative reactivity feedback. The summary results of the LWRs waste fuel cycle show the possibility to incinerate, during a total irradiation time of six years, 94% of  $^{239}\text{Pu}$ , 61% of plutonium and 53% of all actinides (Talamo et al., 2004a).

In the fuel cycle based on military plutonium, the fresh DF contains 94% of  $^{239}\text{Pu}$  and 6% of  $^{240}\text{Pu}$ ; therefore, the spent DF is still so rich in fissile plutonium that it does not provide a negative reactivity feedback; therefore, we referred to the TF, in the military plutonium context, as post driver fuel (PDF). The high reactivity of military plutonium, forces both to model the control rods and to add erbium as burnable poison. The summary results of the military plutonium waste fuel cycle show the possibility to incinerate, during a total irradiation time of six years, 92% of  $^{239}\text{Pu}$  (Talamo and Gudowski, 2005).

In the present work, we performed some preliminary studies on the possibility to operate the gas turbine-modular helium reactor (GT-MHR) on a fuel based on thorium; at the moment, we do not propose any Deep Burn fuel management strategy for the case of thorium fuel. We have been just studying in details the performance of a nuclear fuel based on a mixture of LWRs waste or military plutonium with thorium and a mixture of uranium with thorium. Natural thorium is composed only by the fertile isotope  $^{232}\text{Th}$ , which, by neutron capture, becomes  $^{233}\text{Th}$ ;  $^{233}\text{Th}$  transmutes into  $^{233}\text{Pa}$  and then into fissile  $^{233}\text{U}$ , with a corresponding half life of 22 minutes and 27 days, respectively (Fig. 1). At beginning of life, the fuel must

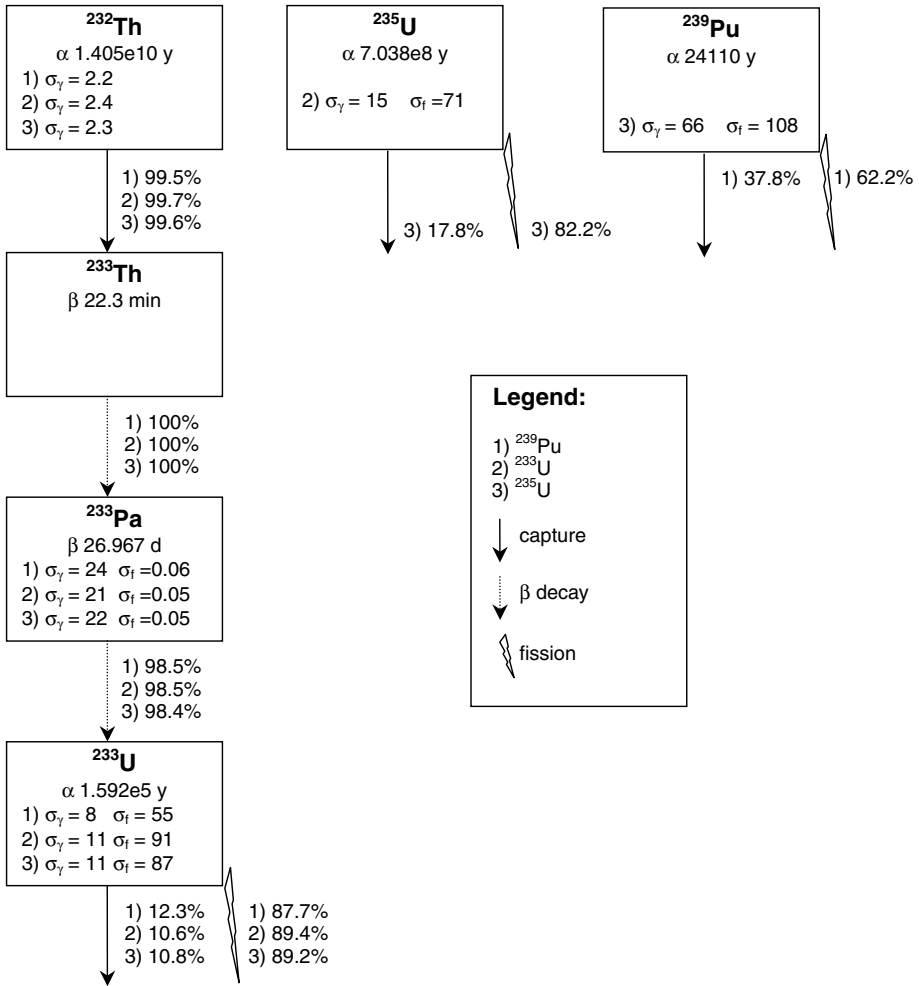


Fig. 1. Transmutation chain of a thorium based fuel. In the second rows of the boxes are reported the half lives. The values of cross-sections are expressed in barns and calculated by MCB, they are sampled in the inner ring after 20 days of full power operation.

also contain some fissile nuclide ( $^{239}\text{Pu}$ ,  $^{233}\text{U}$  or  $^{235}\text{U}$ ) to guarantee the criticality of the reactor and we refer to it as the triggering isotope. If thorium is abundantly present in the fuel, then it starts to act as breeder of  $^{233}\text{U}$ , which is a fissile isotope, and, in the optimal condition, the buildup of the  $^{233}\text{U}$  compensates the corresponding depletion of the triggering isotope. We did not add any burnable poison since the captures of the fertile isotope  $^{232}\text{Th}$  already keeps close to criticality the reactor. By contrast, we modeled the control rods according to the technical report General Atomics (GA) has submitted to the US Nuclear Regulatory Commission (General Atomics, 2002).

The thorium fuel exhibits several valuable benefits (Gruppelaar and Schapira, 2000; Kimura, 1995; Herring et al., 2001; Lung and Gremm, 1998; Rütten and Haas, 2000):

- large resources of thorium are available all over the world;
- thorium needs for reactors are much less than presents uranium needs for LWRs;
- the total radioactive waste mass production is about two orders of magnitude lower than in the case of present LWRs.

## 2. The gas turbine-modular helium reactor

The reactor consists of a  $12 \times 12$  matrix of reactor grade graphite (H451) hexagonal blocks confined into a cylinder of 3.5 m radius and 10 m height; the interstitial gap amid the hexagonal blocks is 0.1 cm. The fuel is loaded into three concentric rings of hexagonal blocks and it axially covers only 7.93 m of the height of the reactor, since at top and at the bottom of the reactor two cylinders of graphite, equally long, act as neutron reflectors. The horizontal section of the reactor core is shown at top of Fig. 2 and enlarged in Fig. 3; the GT-MHR is equipped with 12 startup control rods located in the inner fuel ring, 6 shutdown ones in the central ring, 12 shutdown ones in the outer ring and 36 operational ones in the graphite reflector blocks surrounding the outer fuel ring. We modeled in the numerical simulations all the types of control rods, but we have kept them full extracted during the operation of the reactor because we retain the presence of the control rods of secondary importance for the transmutation analysis. Each control rod consists of a cylinder of graphite filled by a lattice of TRISO particles containing boron carbide with an enrichment of 90% in  $^{10}\text{B}$ . The operational rods are cave cylinders, whereas the shutdown and startup ones are plenum cylinders. All the geometry parameters of the reactor are shown in Table 1, whereas Table 2 contains all information about the materials employed in the reactor.

Fig. 4 shows the details of a hexagonal fuel block containing a control rod, it allocates 95 coolant channels and 192 fuel pins; whereas, in the case the block does not contain a control rod, as shown in Fig. 2, these numbers, respectively, increase to 108 and 216. The bottom of Fig. 2 shows the structure of a TRISO particle (Chapelot et al., 2001; Fukuda et al., 1995; Miller et al., 2001, 2002; Minato et al., 1993, 2000a; Nabielek et al., 1989; Nickel et al., 2002; Porta et al., 2001; Sawa et al., 2001a,b; Sawa and Tobita, 2003) of fuel and it highlights its components: the actinide oxide central sphere (kernel), the porous carbon layer, the inner pyrocarbon layer, the ZrC layer, the outer pyrocarbon layer. We can note in Fig. 2 that a fuel pin, in the current General Atomics design, contains 45 TRISO particles in its horizontal section; whereas, along the  $z$ -axis there are about 6000 particles. Since the coolant enters the reactor at  $485^\circ\text{C}$  and it exits at  $850^\circ\text{C}$ , we have set the temperature of the fuel in the TRISO particles to 1500 K and the temperature of all other materials to 1200 K, with the exception of that one in the carbon in the pure graphite hexagonal blocks (all the blocks without fuel pins or operational control rods), which has been set to 900 K (with the scattering function  $s(\alpha, \beta)$  evaluated at 800 K).

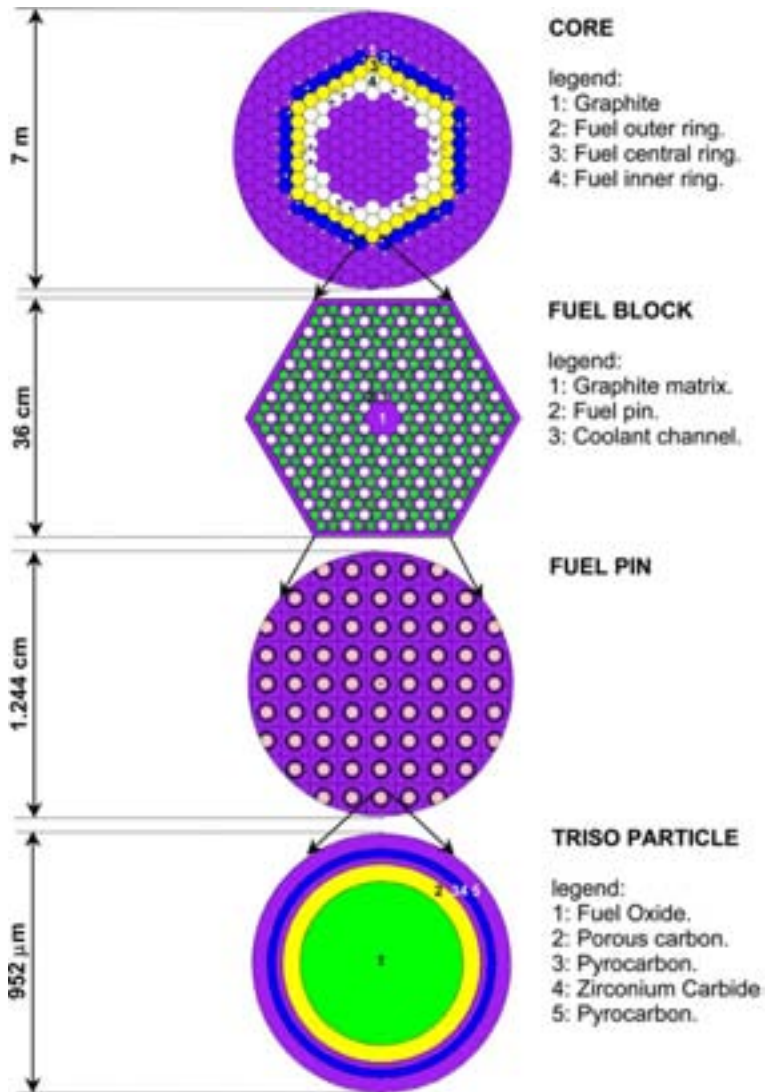


Fig. 2. The gas turbine-modular helium reactor plotted by MCNP.

### 3. The Monte Carlo numerical simulations

We used the extraordinary capability of the Monte Carlo codes MCNP-4c3/ MCB-1c2 (Briesmeister, 2002; Cetnar et al., 1999, 2001), coupled to a nuclear data library based on JEF2.2 and enlarged with JENDL-3.2, ENDF/B-6.8, DCL-200 and EAF-99, both to handle the triple heterogeneity of the GT-MHR in a detailed

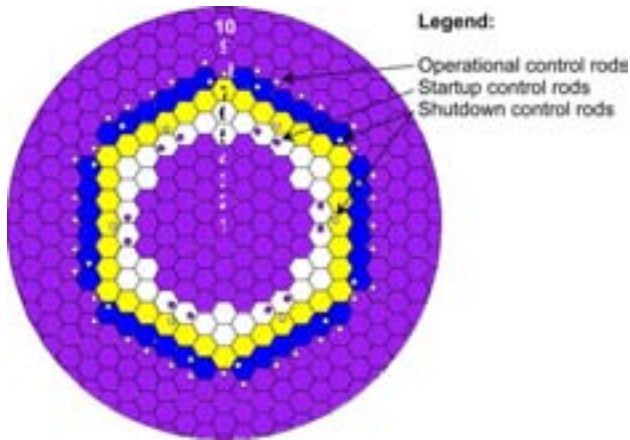


Fig. 3. Core of the gas turbine-modular helium reactor plotted by MCNP.

Table 1

Geometry data of the GT-MHR

|  |                    |
|--|--------------------|
| Core – radius (cm)   | 350                |
| Core – height (cm)   | 1000               |
| Control rods – startup (inner ring)  | 12                 |
| Control rods – operational (outer moderator reflector ring)                      | 36                 |
| Control rods – shutdown (central ring/outer ring)                                | 6/12               |
| Control rods – internal radius (startup/operational/shutdown) (cm)               | 0/2.64/0           |
| Control rods – external radius (cm)  | 4.13               |
| Control rods – hole radius (cm)  | 5.05               |
| Control rods – distance from the center of the hexagon (cm)                      | 9.75614            |
| Control rods – height at bol (startup/operational/shutdown) (cm)                 | 0/0/0              |
| Hexagonal fuel blocks – number   | 36 × 3             |
| Hexagonal fuel blocks – width (cm)   | 35.99688           |
| Hexagonal fuel blocks – height (cm)  | 793                |
| Hexagonal blocks – interstitial gap (cm)   | 0.1                |
| Fuel blocks – DF pins (with control rod/without control rod)                     | 216/192            |
| Fuel blocks – coolant channels (with control rod/without control rod)            | 108/95             |
| Pins – radius (cm)   | 0.6223             |
| Pins – height (cm)   | 793                |
| Pins – distance between pins (cm)  | 3.25628            |
| Pins – hole radius (fuel/coolant channel) (cm)                                   | 0.635/0.795        |
| TRISO particles – kernel radius (GA/JAERI/control rods) (μm)                     | 150/300/300        |
| TRISO particles – width porous carbon layer (GA/JAERI/control rods) (μm)         | 150/64/50          |
| TRISO particles – width inner pyrocarbon layer (GA/JAERI/control rods) (μm)      | 35/26/15           |
| TRISO particles – width ZrC layer (GA/JAERI) (μm)                                | 35/31              |
| TRISO particles – width outer pyrocarbon layer (GA/JAERI) (μm)                   | 40/55              |
| TRISO particles – body centered square lattice side (GA/JAERI/control rods) (cm) | 0.11542/0.134/0.12 |
| TRISO particles – packing fraction (GA/JAERI/control rods) (%)                   | 37.55/37.55/23.58  |

three-dimensional model (as shown in the previous paragraph) and to describe the evolution of the fuel composition with a continuous energy approach. We remand to our previous papers for the code description.

Table 2  
Material data of the GT-MHR

| Material                | Atomic percentage   | Density at bol (g/cm <sup>3</sup> ) |
|-------------------------|---|-------------------------------------|
| TRISO kernel            | <sup>239</sup> Pu/ <sup>233</sup> U/ <sup>235</sup> U– <sup>232</sup> Th (37.04%); <sup>16</sup> O (62.96%) | 10.2                                |
| TRISO porous graphite   | C (100%)  | 1                                   |
| TRISO pyrocarbon        | C (100%)  | 1.85                                |
| TRISO zirconium carbide | Zr (50%); C (50%)   | 6.56                                |
| Graphite                | C (100%)  | 1.74                                |
| Control rods            | <sup>10</sup> B (72%); <sup>11</sup> B (8%); <sup>12</sup> C (20%)  | 2.47                                |

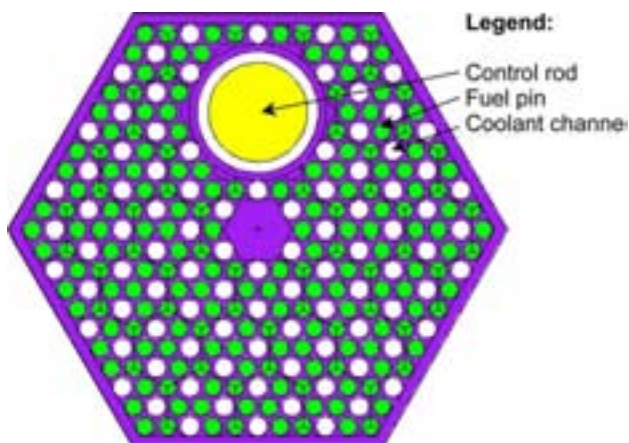


Fig. 4. Fuel block, equipped with control rod, plotted by MCNP.

#### 4. The tight balance of the reaction rates

Fig. 5 compares the capture cross-section of <sup>232</sup>Th with the fission one of the common fissile isotopes both in the thermal neutron energy range and in the fast one. At first glance, Fig. 5 suggests some very important remark on the possibility to operate the GT-MHR with a thorium fuel: the capture cross-section of <sup>232</sup>Th in the thermal range is about 10 times smaller than the fission cross-section of uranium fissile isotopes and 100 times than that one of plutonium nuclides. This difference means that, in order to set the reaction rate of the <sup>232</sup>Th capture equal to that one of the triggering isotope fission, one must set a much larger mass of thorium when the triggering isotope consists of plutonium rather than uranium.

Fig. 6 plots the capture to fission ratio, well known in the literature also as the  $\alpha$  factor, of the fissile isotopes available as candidates for the triggering isotope; we can note that the neutron economy in the thermal range is much more efficient for uranium than plutonium. The above consideration signifies that it is more difficult to set a dynamic self-sustaining fission chain, in a thorium fuel and in the thermal neutron energy range, with plutonium than uranium. In fact, even if one would succeed in



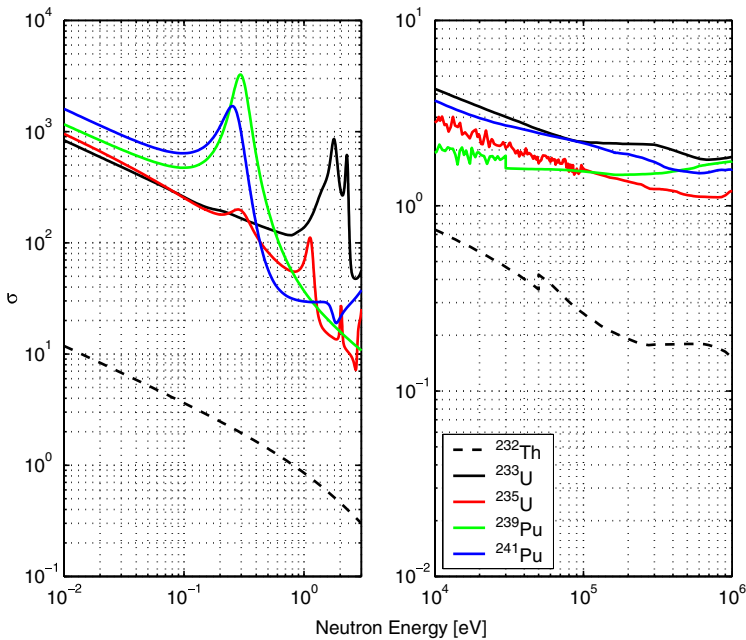


Fig. 5. Capture cross-section of <sup>232</sup>Th compared to the fission cross-sections of the common fissile isotopes in the thermal energy (left) and in the fast one (right) plotted by IANIS-2.0.

setting the capturing rate of <sup>232</sup>Th equal to the fission rate of plutonium (therefore in compensating, partially, the burnup of plutonium with the buildup of <sup>233</sup>U), the capture rate of plutonium would deplete the fissile material anyhow. By contrast, this behavior is much mitigated when the triggering isotope is uranium due to its smaller capture to fission ratio.

All the considerations we stated so far do not apply when the reactor operates in a fast energy spectrum; in fact, by a particles accelerator; in fact, the capture cross-section of <sup>232</sup>Th becomes closer to the fission cross-section of the fissile isotopes (Fig. 5). In addition, in the fast energy range the difference between the neutronic efficiency of <sup>239</sup>Pu and that one of <sup>235</sup>U might attenuate since the first nuclide, compared to the second one, has a higher fission cross-section (above 100 keV, Fig. 5) and also a lower capture to fission ratio (above 30 keV, Fig. 6).

As we already discussed previously, the low capture cross-section of <sup>232</sup>Th in the thermal range, compared to the fission cross-section of the triggering isotope, forces to manufacture a fuel with a mass of thorium 25–30 times higher than that one of the triggering isotope. In fact, it is necessary to compensate the absorption of the triggering isotope with the capture of fertile thorium in order to set a dynamic self-sustaining reaction chain. However, at the same time, the total mass of the triggering isotope must be great enough to set the criticality condition of the reactor; that arises the need of a huge mass of thorium to operate the reactor. This necessity has driven us to evaluate not only the current design of the General Atomics TRISO particles,

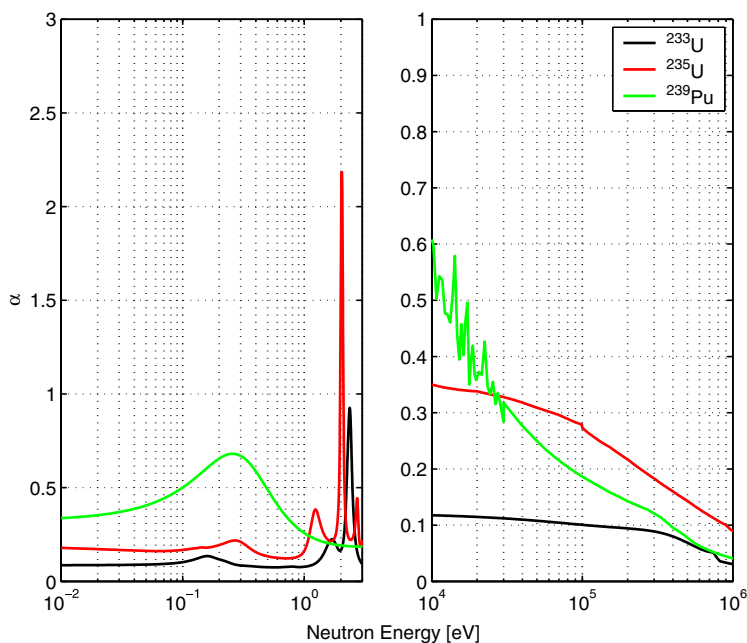


Fig. 6. Capture to fission ratio of the common fissile isotopes in the thermal energy (left) and in the fast one (right) plotted by IANIS-2.0.

that we employed for our previous studies and that have a kernel radius of 150  $\mu\text{m}$ , but also particles with a much larger radius; amid all the designs of TRISO particles (Table 2 of Sumita et al., 2003), that of the Japan Atomic Energy Research Institute (JAERI) offers the largest radius of the kernel, 300  $\mu\text{m}$ , and therefore it allows to allocate more fuel. Of course, the modification of the structure of a TRISO particle alters its resistance under irradiation; Golubev et al. (2002) have shown that the failure probability of TRISO particles exponentially increases with a larger radius of the kernel and it diminishes with a smaller porous graphite buffer layer width. Nevertheless, geometry is not the only factor affecting the resistance of TRISO particles; for instance, the fission product palladium, has revealed to be a strong chemical attacker of the silicon carbide layer. In order to diminish the damage induced by the palladium, we replaced the silicon carbide with zirconium carbide, since the latter has shown a better performance (Minato et al., 1997, 1998, 2000b,c).

We maintained the packing fraction of the TRISO particles – defined as the total volume of the TRISO particles divided by the corresponding volume of the fuel pin – to the upper limit of 37.55%, imposed by the compacting process (Fig. 7). A lower value would imply higher enrichments of fuel, keeping constant the initial excess of reactivity and the kernel radius, and therefore higher fuel costs and more proliferation concerns. Last but not least, a higher enrichment would also result in degrading the breeding process, as already discussed.

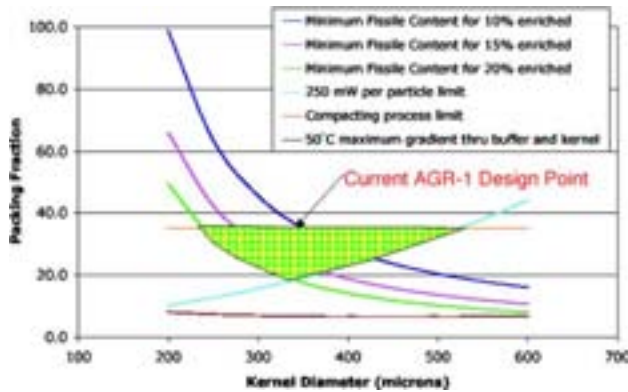


Fig. 7. Constrains of the current American TRISO particles design (Feltus, 2004).

In the Fort St. Vrain reactor (Habush and Harris, 1968), the forerunner of the GT-MHR, the radius of the kernel, 250  $\mu\text{m}$ , was smaller than our large particles and the packing fraction equal to 50%. This high packing fraction may however cause some performance problems since Nabilek et al. (2004) have shown that many particles failures are due to the isostatic pressure of particles contacting each other during fuel manufacture.

We enriched the fertile thorium with about 3–4% of the fissile isotopes in order to set the initial excess of reactivity in the range 5000–15000 pcm to allow over one year burnup.

## 5. Analysis of small TRISO particles, 150- $\mu\text{m}$ kernel radius

### 5.1. $k_{\text{eff}}$ and mass

The first trial to operate the GT-MHR on a thorium fuel utilized the General Atomics TRISO particles which we already used for the LWRs waste and military plutonium (Talamo et al., 2004a). The details of geometry and the material composition of the TRISO particles are reported in Tables 1 and 2, respectively; whereas, Table 3 summarizes the concentration of the triggering isotope in the fuel. We used three different enrichments of the triggering isotope ranging from 3% to 4.4%, according to the fuel rings. A heterogeneous enrichment is important to flatten the neutron flux between the three rings and, therefore, to obtain similar transmutation rates. Otherwise, with a homogeneous enrichment, the inner ring would tend to have a very high value of flux, due both to the moderation of the adjacent graphite and the circular shape, and it would too rapidly deplete the triggering isotope. Table 3 shows that the relative peak of the average flux in the three rings (defined as the highest value of the flux between the three rings divided the lowest one), in case of heterogeneous enrichment, is only 1.2; whereas, with a homogeneous enrichment, it is 1.3.

Table 3

Fuel enrichment and neutron flux at the beginning of life in the 150- $\mu\text{m}$  radius kernels

| Triggering nuclide | Inner ring |                 | Central ring |                 | Outer ring |                 |
|--------------------|------------|-----------------|--------------|-----------------|------------|-----------------|
|                    | (%)        | Flux/ $10^{14}$ | (%)          | Flux/ $10^{14}$ | (%)        | Flux/ $10^{14}$ |
| $^{239}\text{Pu}$  | 3.0        | 1.70            | 3.5          | 1.61            | 3.3        | 1.40            |
| $^{233}\text{U}$   | 3.0        | 3.50            | 3.5          | 3.44            | 3.3        | 2.94            |
| $^{235}\text{U}$   | 3.6        | 3.20            | 4.4          | 3.15            | 3.9        | 2.71            |

Fig. 8 shows that the burnup of  $^{239}\text{Pu}$  is so fast that the reactor cannot operate longer than 3 months even with a very high initial value of  $k_{\text{eff}}$  (over 1.3); whereas, the operation with uranium isotopes is restricted to only one month. Fig. 9 shows that a relatively small quantity of the triggering isotope, about 140 kg, is enough to set the criticality condition of the reactor, but the depletion of just 20 kg of fissile isotope, during 1 month, produces a reactivity feedback of 5000–10000 pcm. Fig. 10, showing the buildup of  $^{233}\text{Pa}$ , indicates that after 6 months of reactor operation the mass of this isotope still does not reach the equilibrium and it arrives just at 11–17 kg. Finally, we can see in Fig. 11 that the buildup of  $^{233}\text{U}$  during one month is only 2–5 kg, over 4 times smaller than the 20-kg depletion of the triggering isotope. We may conclude here that it would be quite difficult to operate the GT-MHR with the small TRISO particles.

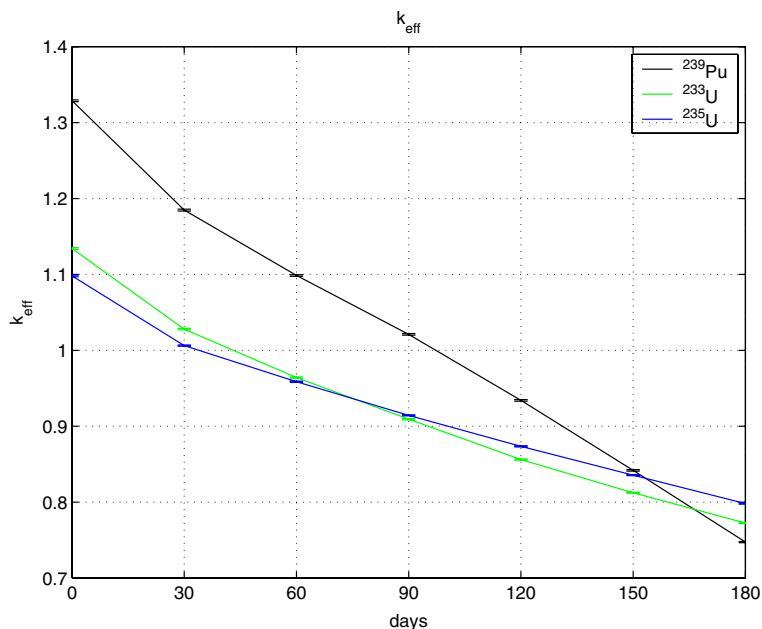


Fig. 8. Evolution of  $k_{\text{eff}}$  in the GT-MHR fuelled with small particles. The horizontal ticks represent the standard deviation with 68% confidence.

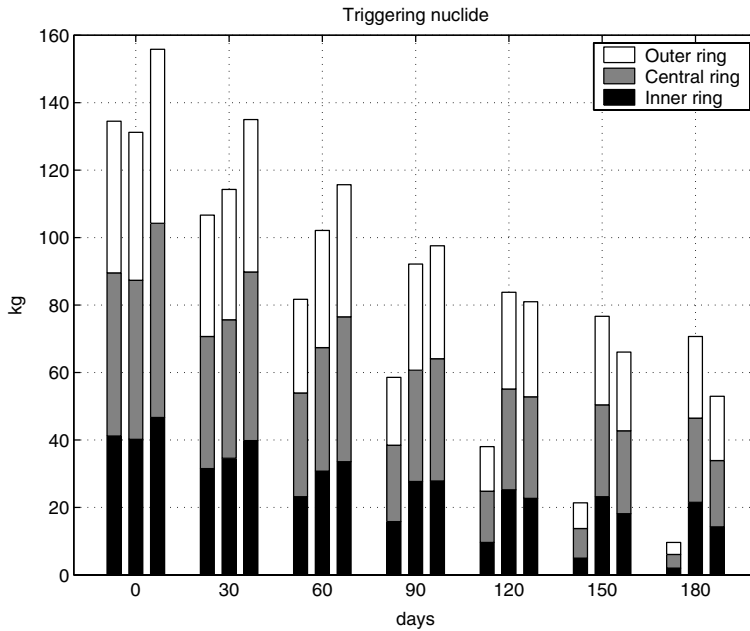


Fig. 9. Evolution of the triggering nuclides,  $^{239}\text{Pu}$  (left columns),  $^{233}\text{U}$  (central columns) and  $^{235}\text{U}$  (right columns), in the GT-MHR fuelled with small particles.

## 6. Analysis of large TRISO particles, 300 $\mu\text{m}$ kernel radius

### 6.1. $k_{\text{eff}}$ and mass

The modest results obtained with small particles encouraged us in evaluating the possibility to fuel the GT-MHR with 300- $\mu\text{m}$  kernel radius particles (see Tables 1 and 2 for the geometry and material data) and the same packing fraction (37.55%), corresponding to the upper limit determined by the compacting process (Fig. 7); this choice comes from the possibility to allocate a much larger fuel mass. A larger mass of fuel may allow both a larger quantity of the triggering nuclide, which is important to set the criticality condition, and, at the same time, it keeps the mass of thorium 25–30 times that one of the triggering isotope, which is important to properly balance the reaction rates. The simultaneous fulfillment of these two conditions is important to establish a dynamic self-sustained fission chain during the operation of the reactor. Also in this case we used three different enrichments, corresponding to the three fuel rings (see Table 4), and they are about 10% higher than those ones used for the small particles. Fig. 12 demonstrates that the uranium isotopes allow the reactor to work at least for 330 full power operation days, which is a good starting point for implementing a Deep Burn in-core fuel management strategy. Let us remark that the average flux in

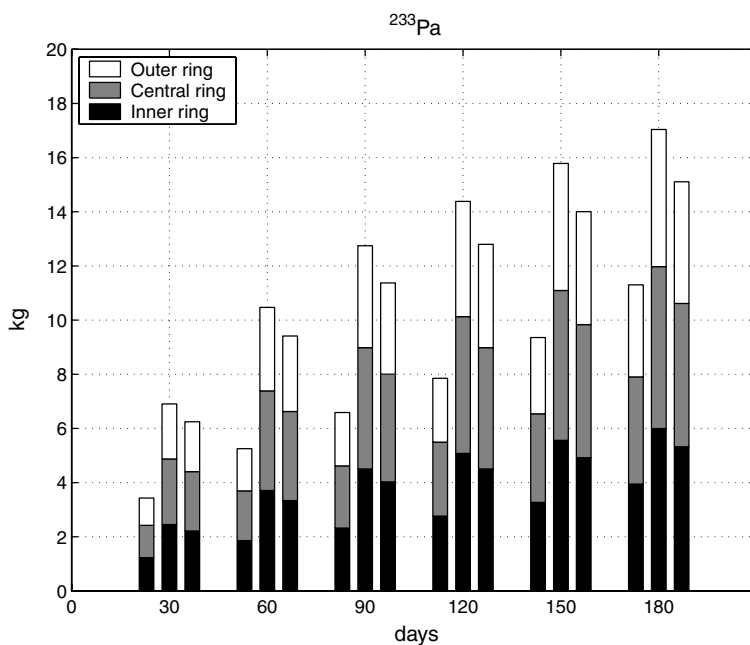


Fig. 10. Evolution of  $^{233}\text{Pa}$  with different triggering nuclides,  $^{239}\text{Pu}$  (left columns),  $^{235}\text{U}$  (central columns) and  $^{238}\text{U}$  (right columns), in the GT-MHR fuelled with small particles.

the fuel for large particles (Table 3) is 1.3–2.5 times lower than for small particles (Table 4), since in both cases the neutron flux is normalized to produce 600 MW<sub>th</sub> and the total quantity of fissile isotopes allocated by the large particles is 5 times greater.

Fig. 12 shows that the large particles do solve the problem of the very fast depletion of  $^{239}\text{Pu}$  since the operation of the reactor remains limited to only 2 months. In fact,  $^{239}\text{Pu}$  has a one-group averaged absorption microscopic cross-sections 2–2.8 times greater than that one of the uranium isotopes (Fig. 1) and, therefore, its depletion results faster (Fig. 13). The flat neutron flux profile amid the different rings (Table 4) leaves the relative mass of the triggering isotope between the rings almost unchanged during the 330 days of operation, as it is confirmed in Fig. 13. Figs. 14 and 15, which illustrate the evolution of  $^{233}\text{Pa}$  and  $^{233}\text{U}$ , respectively, show no significant differences between the uranium nuclides and the plutonium one. After 6 months of the operation protoactinium reaches its asymptotic level of 20 kg (Fig. 14); the decay of protoactinium generates a buildup of 12 kg per month of  $^{233}\text{U}$  (Fig. 15) that partially compensates the 24-kg depletion of the triggering isotope (Fig. 13).

The faster decrease of  $k_{\text{eff}}$  in the case of  $^{239}\text{Pu}$ –Th, compared to that one of uranium–thorium, is due to a worse neutron economy. In fact, in the case the GT-MHR operates with  $^{239}\text{Pu}$ –Th, 38% of absorbed neutrons are captured; by contrast

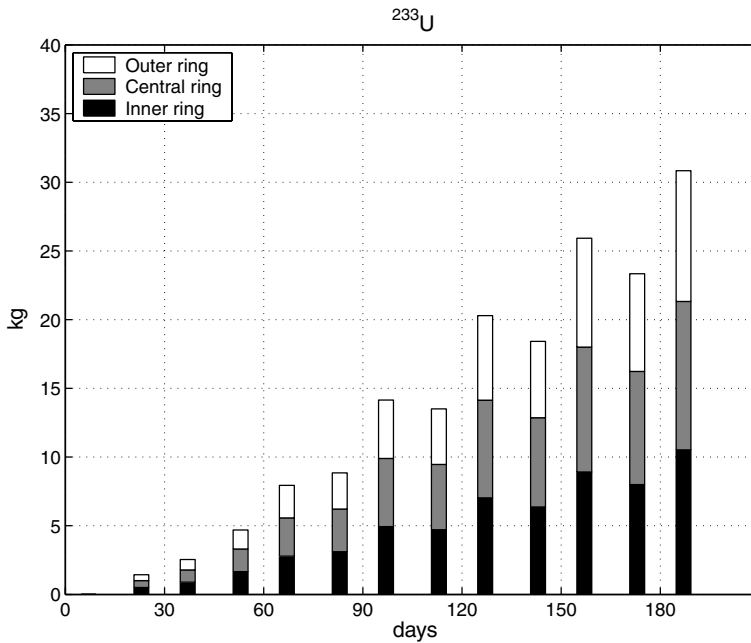


Fig. 11. Evolution of  $^{233}\text{U}$  with different triggering nuclides,  $^{239}\text{Pu}$  (left columns) and  $^{235}\text{U}$  (right columns), in the GT-MHR fuelled with small particles.

Table 4

Fuel enrichment and neutron flux at the beginning of life in the 300- $\mu\text{m}$  radius kernels

| Triggering nuclide | Inner ring |                 | Central ring |                 | Outer ring |                 |
|--------------------|------------|-----------------|--------------|-----------------|------------|-----------------|
|                    | (%)        | Flux/ $10^{14}$ | (%)          | Flux/ $10^{14}$ | (%)        | Flux/ $10^{14}$ |
| $^{239}\text{Pu}$  | 3.3        | 1.25            | 3.8          | 1.12            | 3.6        | 1.04            |
| $^{233}\text{U}$   | 3.3        | 1.44            | 3.8          | 1.38            | 3.6        | 1.25            |
| $^{235}\text{U}$   | 3.9        | 1.44            | 4.6          | 1.35            | 4.2        | 1.23            |

this percentage drops to 18% and 11% in the case of  $^{235}\text{U}$ -Th and  $^{233}\text{U}$ -Th, respectively, (Fig. 1). Even if  $^{239}\text{Pu}$ -Th operates at a double concentration of  $^{135}\text{Xe}$ , comparing to the uranium-thorium (Fig. 16), the faster diminishing of  $k_{\text{eff}}$  in the plutonium case is not related to it; in fact, Table 5 reports that the reactivity feedback due to all short-life fission products is larger in the cases uranium-thorium, compared to  $^{239}\text{Pu}$ -Th, and equal to 3000 pcm. Finally, the production of palladium is 6–12 times higher if the fuel contains plutonium rather than uranium (Fig. 17); that may arise some complication for the integrity of TRISO particles during irradiation since this fission product is very mobile and might attack the zirconium carbide layer.

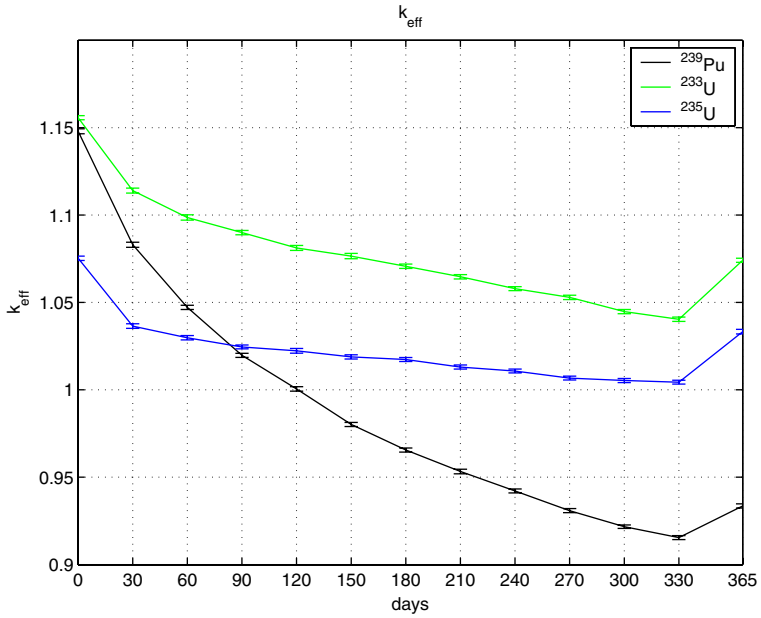


Fig. 12. Evolution of  $k_{\text{eff}}$  in the GT-MHR fuelled with large particles. The horizontal ticks represent the standard deviation with 68% confidence.

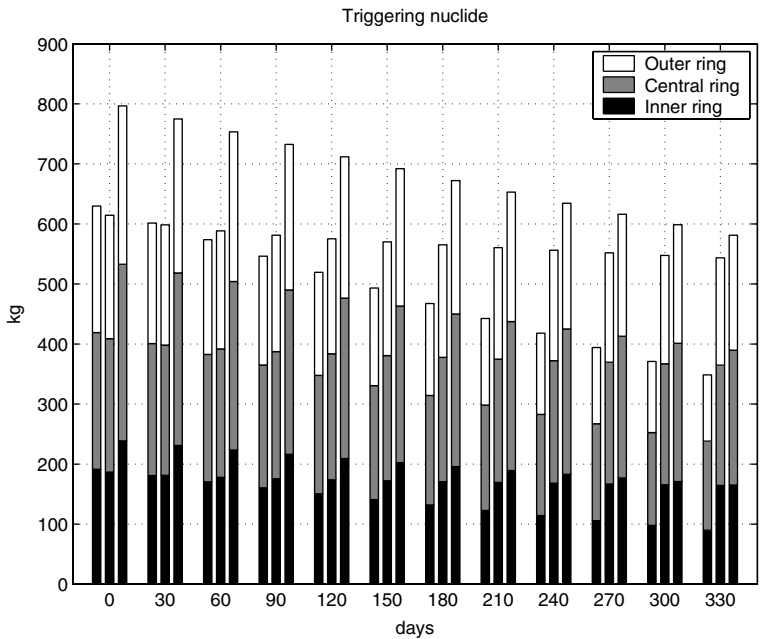


Fig. 13. Evolution of the triggering nuclides,  $^{239}\text{Pu}$  (left columns),  $^{233}\text{U}$  (central columns) and  $^{235}\text{U}$  (right columns), in the GT-MHR fuelled with large particles.



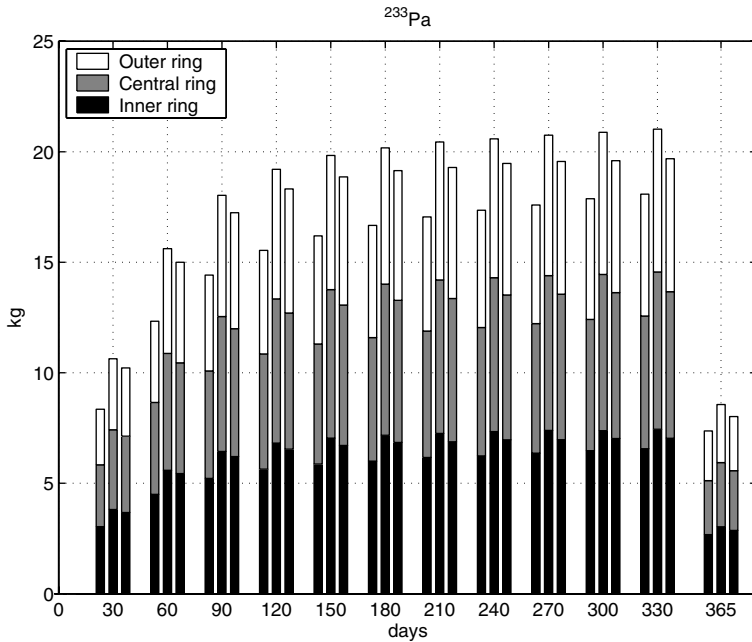


Fig. 14. Evolution of  $^{233}\text{Pa}$  with different triggering nuclides,  $^{239}\text{Pu}$  (left columns),  $^{233}\text{U}$  (central columns) and  $^{235}\text{U}$  (right columns), in the GT-MHR fuelled with large particles.

## 6.2. Control rods worth

Tables 6–8 reports the reactivity worth of the operational, shutdown and startup control rods for  $^{239}\text{Pu}$ –Th,  $^{233}\text{U}$ –Th and  $^{235}\text{U}$ –Th, respectively. In the case of plutonium, the negative reactivity negative feedback is 25% less than in the uranium cases, which gave similar results. Moreover, the reactivity worth of the operational control rods is 20% less than the shutdown ones and 20% more than the startup control rods.

We can note that only  $^{235}\text{U}$ –Th allows the operation of the reactor with the present design of the control rods. Nevertheless, the present study is only preliminary and we believe that the control rods parameters, e.g., the packing fraction or the radius of the kernel, may require a modification according to the period the reactor is intended to operate: for irradiation periods longer than 330 days the present design of control rods is not suitable.

## 6.3. Comparison of the exponential matrix method versus the MCB

The transmutation chain of the fuel, drawn in Fig. 1, can be formulated in a mathematical form through the following simple system of differential equations:

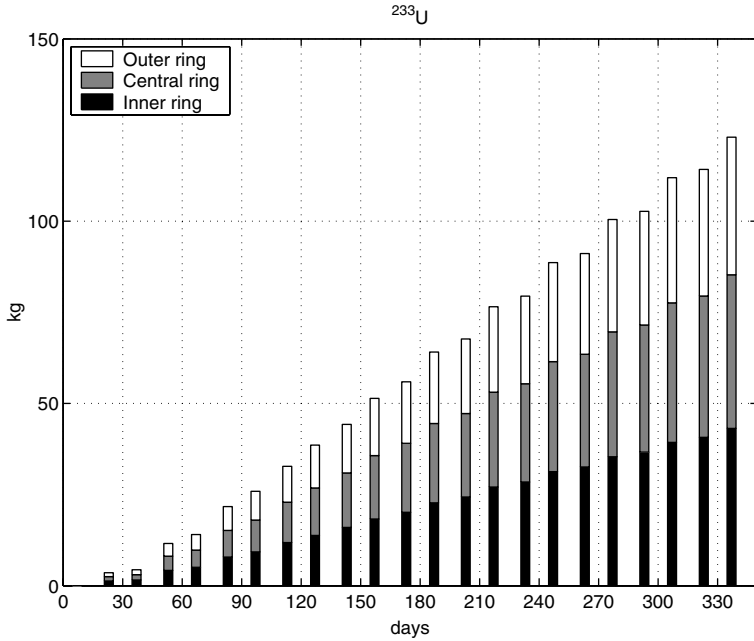


Fig. 15. Evolution of  $^{233}\text{U}$  with different triggering nuclides,  $^{239}\text{Pu}$  (left columns) and  $^{235}\text{U}$  (right columns), in the GT-MHR fuelled with large particles.

$$\left\{ \begin{aligned}
 \frac{d^{232}\text{Th}}{dt} &= -(\lambda^{232}\text{Th} + \sigma_a^{232}\text{Th} \Phi) ^{232}\text{Th}, \\
 \frac{d^{233}\text{Th}}{dt} &= -(\lambda^{233}\text{Th} + \sigma_a^{233}\text{Th} \Phi) ^{233}\text{Th} + \sigma_c^{232}\text{Th} \Phi ^{232}\text{Th}, \\
 \frac{d^{233}\text{Pa}}{dt} &= -(\lambda^{233}\text{Pa} + \sigma_a^{233}\text{Pa} \Phi) ^{233}\text{Pa} + \lambda^{233}\text{Th} ^{233}\text{Th}, \\
 \frac{d^{233}\text{U}}{dt} &= -(\lambda^{233}\text{U} + \sigma_a^{233}\text{U} \Phi) ^{233}\text{U} + \lambda^{233}\text{Pa} ^{233}\text{Pa}, \\
 \frac{d^{235}\text{U}}{dt} &= -(\lambda^{235}\text{U} + \sigma_a^{235}\text{U} \Phi) ^{235}\text{U}, \\
 \frac{d^{239}\text{Pu}}{dt} &= -(\lambda^{239}\text{Pu} + \sigma_a^{239}\text{Pu} \Phi) ^{239}\text{Pu}.
 \end{aligned} \right. \quad (1)$$

where the symbols have the traditional meaning from the reactor physics literature. The system of equations (1) can be simplified by the following assumptions (based on the data of Fig. 1):

- the decay of  $^{232}\text{Th}$ ,  $^{239}\text{Pu}$ ,  $^{233}\text{U}$ ,  $^{235}\text{U}$  can be neglected because of the long half life;
- the fissions of  $^{232}\text{Th}$  and  $^{233}\text{Pa}$  can be neglected because of the small value of the microscopic fission cross-section;
- $^{233}\text{Pa}$  immediately decays to  $^{233}\text{U}$ .

At the light of the above assumptions, the system of differential equations (1) simplifies to

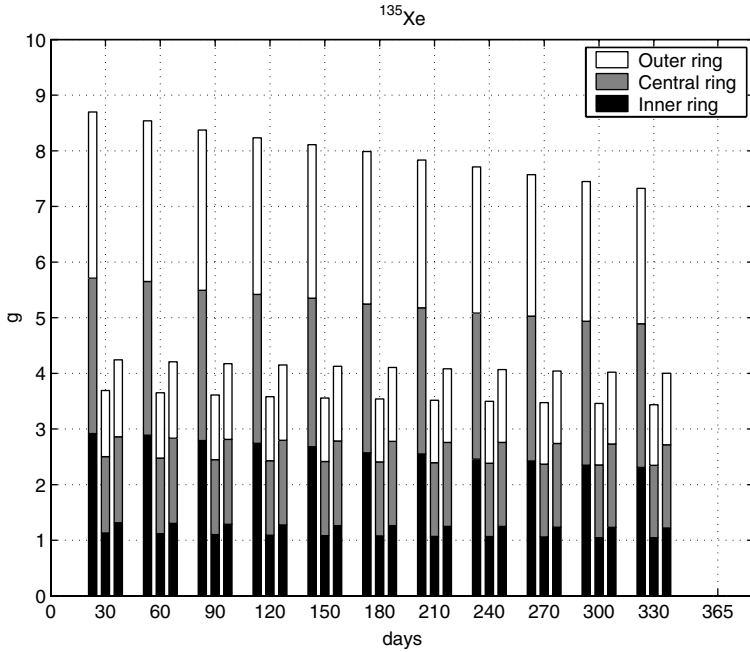


Fig. 16. Evolution of  $^{135}\text{Xe}$  with different triggering nuclides,  $^{239}\text{Pu}$  (left columns),  $^{233}\text{U}$  (central columns) and  $^{235}\text{U}$  (right columns), in the GT-MHR fuelled with large particles.

Table 5  
Reactivity associated to short life fission products

| Reactivity media  | $k_{\text{eff}}$ after 330 fpo days | $k_{\text{eff}}$ after 30 days decay | $\rho$ (pcm) |
|-------------------|-------------------------------------|--------------------------------------|--------------|
| $^{239}\text{Pu}$ | 0.91545                             | 0.93355                              | -1977        |
| $^{233}\text{U}$  | 1.04036                             | 1.07410                              | -3243        |
| $^{235}\text{U}$  | 1.00436                             | 1.03327                              | -2878        |

Values of  $k_{\text{eff}}$  correspond to the final value after 330 full power operation (fpo) days and thereafter 30 days of natural decay. All  $k_{\text{eff}}$  values have a relative standard deviation less than 129 pcm.

$$\left\{ \begin{aligned}
 \frac{d^{232}\text{Th}}{dt} &= -\sigma_c^{232}\text{Th} \Phi^{232}\text{Th}, \\
 \frac{d^{233}\text{Pa}}{dt} &= -(\lambda^{233}\text{Pa} + \sigma_c^{233}\text{Pa} \Phi)^{233}\text{Pa} + \sigma_c^{232}\text{Th} \Phi^{232}\text{Th}, \\
 \frac{d^{233}\text{U}}{dt} &= -\sigma_a^{233}\text{U} \Phi^{233}\text{U} + \lambda^{233}\text{Pa}^{233}\text{Pa}, \\
 \frac{d^{235}\text{U}}{dt} &= -\sigma_a^{235}\text{U} \Phi^{235}\text{U}, \\
 \frac{d^{239}\text{Pu}}{dt} &= -\sigma_a^{239}\text{Pu} \Phi^{239}\text{Pu}.
 \end{aligned} \right. \tag{2}$$

We calculated the values of the cross-sections of the differential equations system 2 after 20 days of full power operation in the inner ring by MCB for the case of

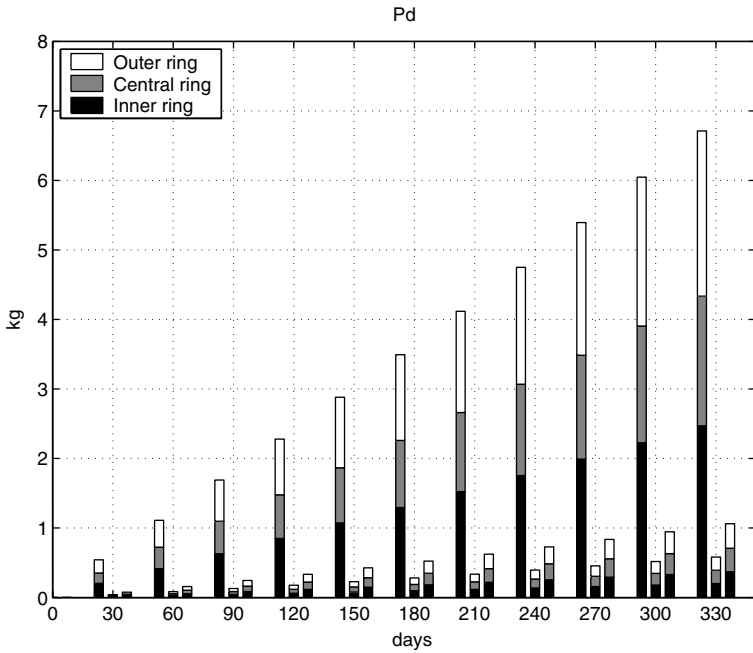


Fig. 17. Evolution of palladium with different triggering nuclides,  $^{239}\text{Pu}$  (left columns),  $^{233}\text{U}$  (central columns) and  $^{235}\text{U}$  (right columns), in the GT-MHR fuelled with large particles.

Table 6  
Reactivity worth and corresponding  $k_{\text{eff}}$  at the beginning of life for  $^{239}\text{Pu}$ -Th fuel

| Reactivity control       | $\rho$ (pcm) | $k_{\text{eff}}$ |
|--------------------------|--------------|------------------|
| None                     | 0            | 1.14793          |
| Operational control rods | -5947        | 1.07966          |
| Shutdown control rods    | -7178        | 1.06553          |
| Startup control rods     | -5090        | 1.08950          |

All  $k_{\text{eff}}$  values have a relative standard deviation less than 127 pcm.

Table 7  
Reactivity worth and corresponding  $k_{\text{eff}}$  at the beginning of life for  $^{233}\text{U}$ -Th fuel

| Reactivity control       | $\rho$ (pcm) | $k_{\text{eff}}$ |
|--------------------------|--------------|------------------|
| None                     | 0            | 1.15569          |
| Operational control rods | -8015        | 1.06306          |
| Shutdown control rods    | -10234       | 1.03742          |
| Startup control rods     | -6838        | 1.07666          |

All  $k_{\text{eff}}$  values have a relative standard deviation less than 145 pcm.

$^{235}\text{U}$ -Th (Fig. 1). Therefore, the simplified system of Eq. (2) may be solved analytically through the exponential matrix method, which is exposed by the matrices 3 and 4.

Table 8

Reactivity worth and corresponding  $k_{\text{eff}}$  at the beginning of life for  $^{235}\text{U}$ –Th fuel

| Reactivity control       | $\rho$ (pcm) | $k_{\text{eff}}$ |
|--------------------------|--------------|------------------|
| None                     | 0            | 1.07527          |
| Operational control rods | –7941        | 0.98988          |
| Shutdown control rods    | –9672        | 0.97127          |
| Startup control rods     | –6521        | 1.00515          |

All  $k_{\text{eff}}$  values have a relative standard deviation less than 132 pcm.

$$\frac{d\vec{N}}{dt} = \vec{N}_0 e^{\hat{A}t}, \quad \vec{N} = \begin{bmatrix} {}^{232}\text{Th} \\ {}^{233}\text{Pa} \\ {}^{233}\text{U} \\ {}^{235}\text{U} \end{bmatrix}, \quad (3)$$

$$\hat{A} = \begin{bmatrix} \sigma_c^{232}\text{Th}\Phi & 0 & 0 & 0 \\ \sigma_c^{232}\text{Th}\Phi & -(\lambda^{233}\text{Pa} + \sigma_c^{233}\text{Pa}\Phi) & 0 & 0 \\ 0 & \lambda^{233}\text{Pa} & -\sigma_a^{233}\text{U}\Phi & 0 \\ 0 & 0 & 0 & -\sigma_a^{235}\text{U}\Phi \end{bmatrix}. \quad (4)$$

Figs. 18 and 19 compare the results obtained by solving Eq. (3) with those ones given by the MCB code for the concentrations of  $^{233}\text{Pa}$ ,  $^{233}\text{U}$  and  $^{235}\text{U}$ , respectively. There is no significant difference between the exponential matrix method and the numerical results of MCB: therefore, the exponential matrix approach may be used for a fast estimation of the key isotopes transmutation in the fuel. In fact, the exponential matrix method produces the results in a couple of seconds compared to 1 day of MCB computing time necessary to simulate 1 month of full power operation. The analytical solution slightly outperforms the MCB results because it assumes a constant flux; whereas, the MCB simulations have been performed by keeping constant the power level, which, of course, produces a decrease of flux. By the term outperform we intend a little over-buildup of  $^{233}\text{Pa}$  and  $^{233}\text{U}$  and an over-burnup of  $^{235}\text{U}$ , as it appears from the curves in Figs. 18 and 19, which little diverge with the operation time.

Finally, let us observe that in the case the reactor operates with  $^{233}\text{U}$ –Th, in a hypothetical equilibrium state where the reaction chain would be dynamically self-sustaining, the concentration of both  $^{233}\text{Pa}$  and  $^{233}\text{U}$  would be constant. In this scenario, the perfect ratio between the mass of  $^{233}\text{U}$  and thorium could be calculated according to the following formula:

$$\frac{d^{233}\text{Pa}}{dt} = \frac{d^{233}\text{U}}{dt} = 0 \Rightarrow \frac{\text{Th}^{232}}{\text{U}^{233}} = \frac{\sigma_a^{233}\text{U}(\lambda^{233}\text{Pa} + \sigma_c^{233}\text{Pa}\Phi)}{\lambda^{233}\text{Pa}\sigma_c^{232}\text{Th}}. \quad (5)$$

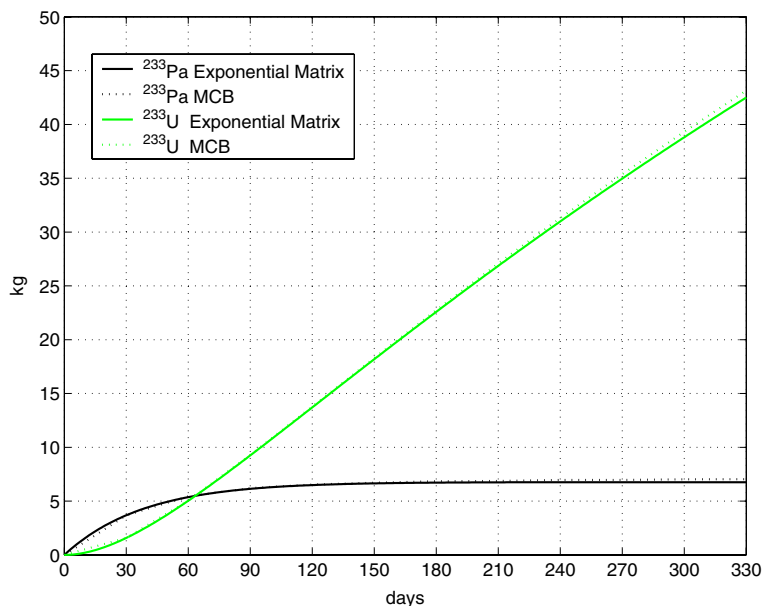


Fig. 18. Comparison of the evolution of  $^{233}\text{Pa}$  and  $^{233}\text{U}$  between the exponential matrix method and MCB. The data for the exponential matrix method have been taken from Fig. 1 for  $^{235}\text{U}$ –Th.

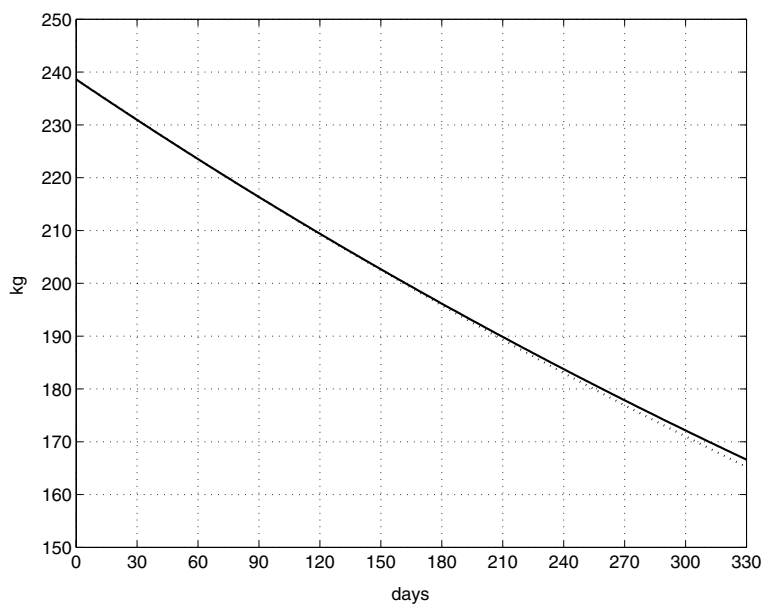


Fig. 19. Comparison of the evolution of  $^{235}\text{U}$  between the exponential matrix method and MCB. The data for the exponential matrix method have been taken from Fig. 1 for  $^{235}\text{U}$ –Th.

By substituting the data of Fig. 1 into Eq. (5), we obtain that a perfect ideal ratio between  $^{232}\text{Th}$  and  $^{233}\text{U}$  would be about 42.5, which corresponds to an enrichment of  $^{233}\text{U}$  in the thorium equal to 2.35%. Unfortunately, the initial excess of reactivity, corresponding to a homogeneous enrichment of 2.35%, is only 3700 pcm, which considerably reduces already after 10 days due to the poisoning of the short-life fission products.

#### 6.4. Flux and spectrum

We calculated the average flux in the radial hexagonal blocks from the first one, in the center of the reactor, to the 10th one, which is the last one uncut by the reactor edge (see the labels in Fig. 3). In addition, we split each hexagonal block into 10 equivolume regions along the  $z$ -axis to evaluate also the axial profile. Due to the axial symmetry we plotted in Figs. 20–22 the average flux in upper 5 axial equivolume regions of the radial hexagonal blocks for  $^{239}\text{Pu}$ –Th,  $^{233}\text{U}$ –Th and  $^{235}\text{U}$ –Th, respectively. Let us observe that in Figs. 20–22 the fuel is located in the 5th, 6th and 7th rings that, respectively, correspond to the inner, inner and central rings. All three pictures exhibit a quite flat flux in the different rings, as the values of Table 4, which refers to TRISO kernels, confirm. Fig. 20 shows that, in the case of  $^{239}\text{Pu}$ –Th, the peak of flux lies in the inner graphite reflector, the 4th one, because of the moderation of the inner graphite hexagonal block. The moderation of neutrons in the graphite is stronger for plutonium than for uranium isotopes, because in the first case the

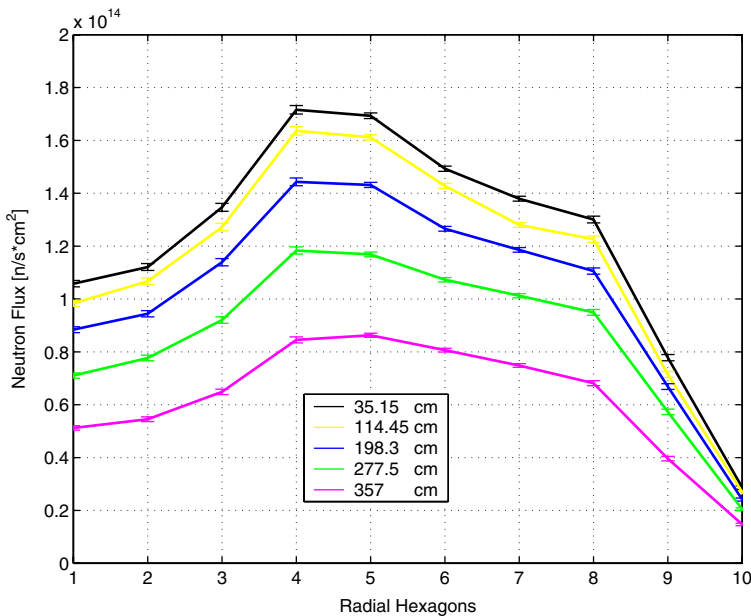


Fig. 20. Flux of the GT-MHR fueled with large particles and  $^{239}\text{Pu}$ –Th. The radial hexagons are numbered according to the labels of Fig. 3.

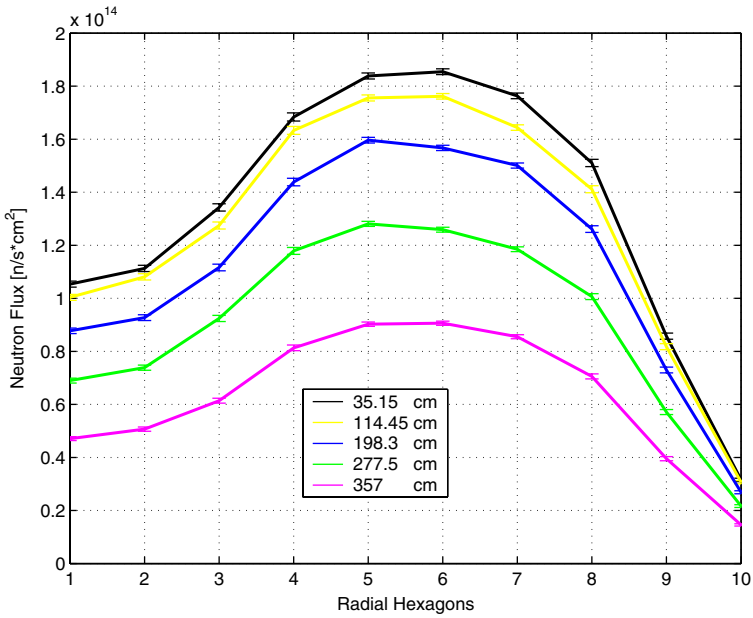


Fig. 21. Flux of the GT-MHR fueled with large particles and <sup>233</sup>U–Th. The radial hexagons are numbered according to the labels of Fig. 3.

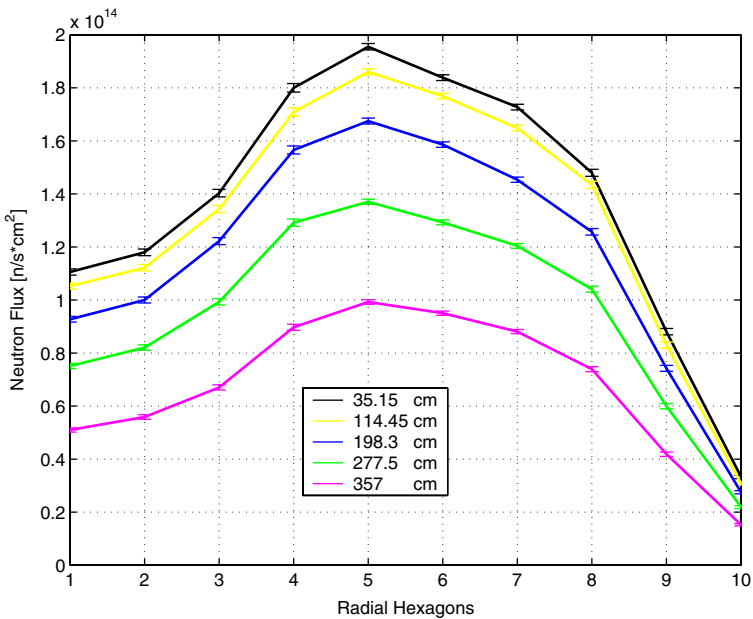


Fig. 22. Flux of the GT-MHR fueled with large particles and <sup>235</sup>U–Th. The radial hexagons are numbered according to the labels of Fig. 3.



spectrum averaged in the TRISO kernel is faster (as we are going to see while discussing the neutron spectra). The average flux in the fuel blocks is lower in the case of plutonium than in the case of uranium (Fig. 20 versus 21 and 22) since the system is normalized to the thermal power and the fission microscopic cross-section of plutonium is higher than that of uranium (Fig. 1). Moreover, the average flux in the fuel hexagonal blocks (5th, 6th and 7th) is more flattened in the  $^{233}\text{U}$ –Th case than in  $^{235}\text{U}$ –Th one (Fig. 21 versus 22) because the enrichment of fuel in the central and outer ring are closer for  $^{233}\text{U}$ –Th (3.8% and 3.6%, Table 3) than for  $^{235}\text{U}$ –Th (4.6% and 4.2%, Table 3).

In order to plot the neutron spectra, we used the energy binning corresponding to the 69 energetic groups of the WIMS cross-section library (Kim et al., 1989; Taubman, 1975) for thermal reactors; these groups are composed of 14 fast groups, 13 resonance groups, and 42 thermal groups. Fig. 23 plots the average spectra in the reactor and shows no significant differences between the three different types of the triggering isotopes. Whereas, the average spectra in the TRISO kernels of the inner ring, reported in Fig. 24, demonstrates that the peak of the capture to fission ratio of  $^{239}\text{Pu}$  at 0.3 eV, well distinct both in Figs. 6 and 24, generates a faster spectrum in the fuel for the case of  $^{239}\text{Pu}$ –Th than for the case of uranium nuclides. The spectra of uranium isotopes, Fig. 24, is well thermalized both in the whole reactor, with a peak at 0.15 eV (Fig. 23), and in the fuel, with a peak at 0.2 eV (Fig. 24).

We conclude this paragraph by observing that the capture to fission resonance of  $^{235}\text{U}$  at 0.15 eV (Fig. 6) may set a positive reactivity feedback since the peak of the

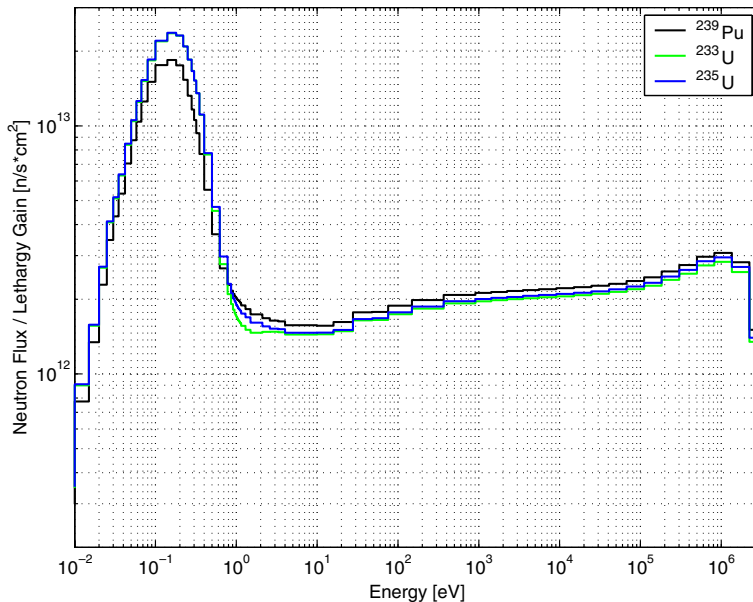


Fig. 23. Spectrum of the GT-MHR fuelled with large particles.

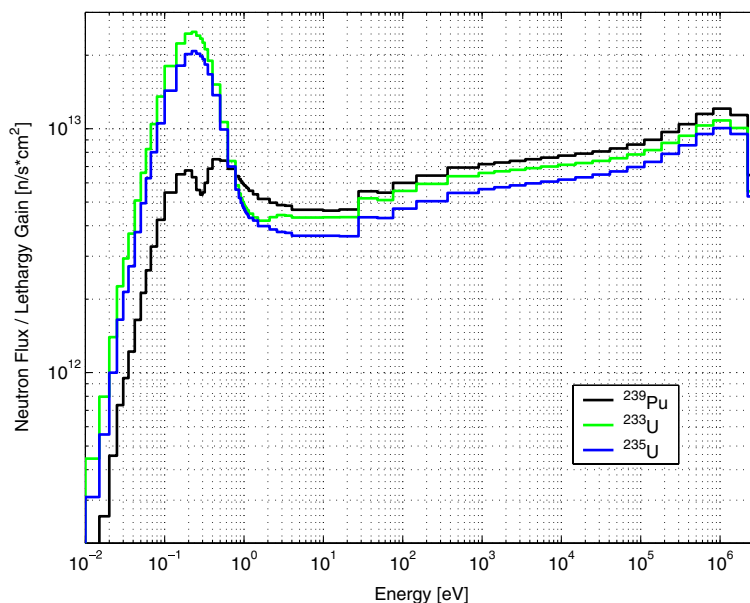


Fig. 24. Spectrum of the fuel kernels, located in the inner ring, of the GT-MHR fuelled with large particles.

spectrum, averaged in the TRISO kernels, shifts from 0.2 to 0.3 eV for a fuel temperature raise of 300–400 K.

### 6.5. Radiotoxicity of the irradiated fuel

As final study, we compared the radiotoxicity, intended as the dose potentially taken by human population in case of ingestion on the base of the EURATOM directive, of the three irradiated fuels. We simulated  $10^5$  years of natural decay of the fuel in the inner ring after an irradiation of 240 days and we normalized the radiotoxicity of the fuel with that one of natural uranium, intended as a mixture, containing 0.0055% of  $^{234}\text{U}$ , 0.72% of  $^{235}\text{U}$  and 99.2745% of  $^{238}\text{U}$ , with the same mass density of the fuel. Fig. 25 shows that for the first 10 years all the three curves are very close; afterwards, the radiotoxicity in the case of uranium isotopes diminishes much faster than in the case of plutonium. Nevertheless, after 300 years, the radiotoxicity in the case of uranium nuclides starts to increase and the curve of  $^{233}\text{U}\text{--Th}$  crosses that one of  $^{239}\text{Pu}\text{--Th}$  at 30,000 years. After 100,000 years, the radiotoxicity of  $^{233}\text{U}\text{--Th}$  fuel is still 240 times larger than that one of natural uranium; whereas, the radiotoxicity of  $^{235}\text{U}\text{--Th}$  remains limited to 300 times the value of natural uranium already after 250 years. Figs. 26–28, showing the dose of the isotopes with a large contribution to the total radiotoxicity of the irradiated fuel, explain the different behavior of the three types of fuel. In fact, we can note in Fig. 26 that the total dose of irradiated  $^{239}\text{Pu}\text{--Th}$ , after the decay of the fission products  $^{90}\text{Sr}$  and  $^{137}\text{Cs}$ , comes mainly from

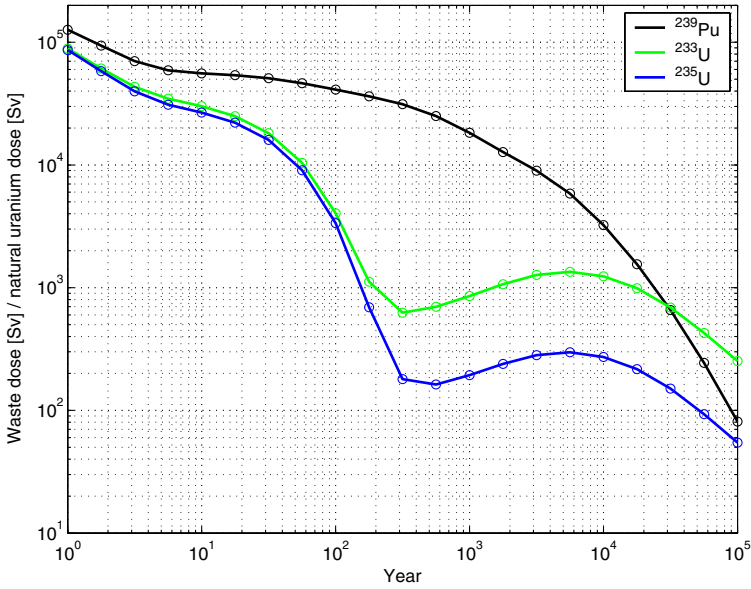


Fig. 25. Radiotoxicity of the spent fuel of the GT-MHR normalized to that of natural uranium.

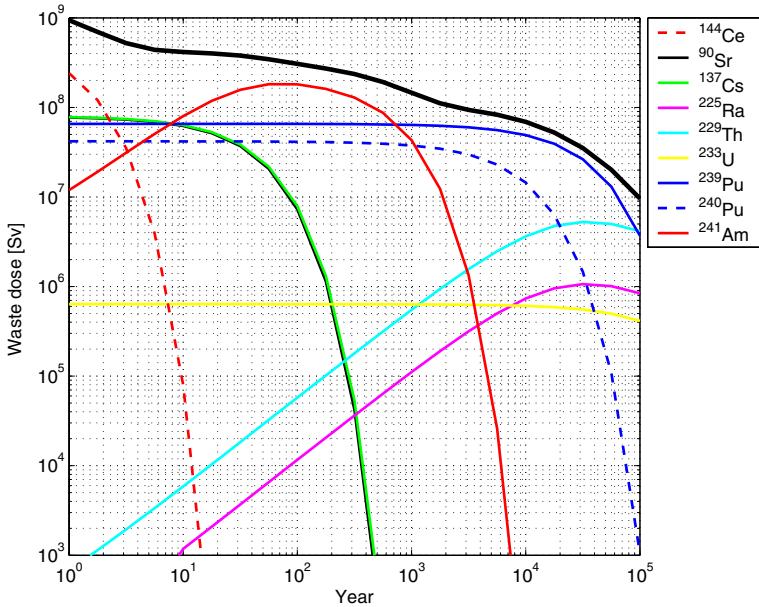


Fig. 26. Radiotoxicity of  $^{239}\text{Pu}$ -Th irradiated fuel. The bold line represents the total value.

$^{241}\text{Am}$  up to 1000 years and then from  $^{239}\text{Pu}$  and  $^{240}\text{Pu}$ , which have a long half life (24110 and 6563 years, respectively). By contrast, the absence of plutonium and americium in the uranium–thorium fuels allows the dose of the irradiated fuel to

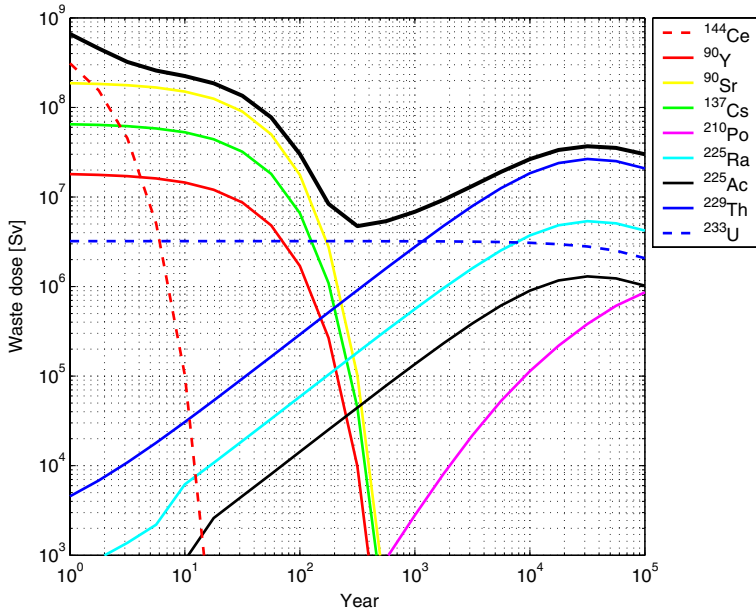


Fig. 27. Radiotoxicity of  $^{233}\text{U}$ -Th irradiated fuel. The bold line represents the total value.

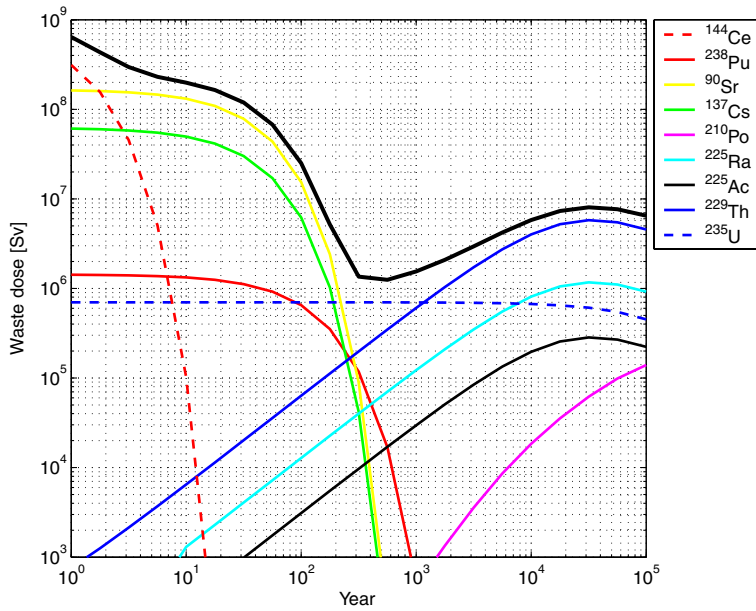


Fig. 28. Radiotoxicity of  $^{235}\text{U}$ -Th irradiated fuel. The bold line represents the total value.

diminish much faster. After 200 years, the dose of the uranium–thorium comes from  $^{233}\text{U}$  and after 1000 years from  $^{229}\text{Th}$ . The latter isotope is produced, by a  $\alpha$  decay with half life of 159,200 years, from  $^{233}\text{U}$  and it transmutes, by  $\alpha$  and  $\beta$  decays with half life of 7340 years and 14.9 days, respectively, into  $^{225}\text{Ra}$  and then into  $^{225}\text{Ac}$ .

## 7. Conclusion

In the present studies, we experienced a serious difficulty to operate the GT-MHR with small particles (150  $\mu\text{m}$  kernel radius) containing fertile fuel; whereas, large particles (300  $\mu\text{m}$  kernel radius) gave much better results because they can allocate a larger mass of fuel. The necessity to set a large mass of fuel arises from two constraints. First, the very little capture cross-section of thorium, compared to the fission one of the common fissile isotopes (e.g.  $^{239}\text{Pu}$ ,  $^{233}\text{U}$  and  $^{235}\text{U}$ ) in the neutron energy range where the reactor operates (about 0.15 eV), induces to set a mass of thorium 25–30 times larger than that one of the triggering isotope. Second, the mass of the triggering isotope must be enough to maintain the criticality of the reactor during burnup.

A heterogeneous enrichment between the fuel rings helps in setting a flatter radial profile of the neutron flux, so that the life of the fuel is prolonged; we adopted a percentage of the triggering isotope in the fuel of 3.3–4.6%. In the case of large particles, the reactor can operate for longer than 1 year only with the fissile uranium isotopes ( $^{233}\text{U}$  and  $^{235}\text{U}$ ), since the  $^{239}\text{Pu}$ –Th fuel reaches the subcritical condition already after 2 months. This behavior derives from the higher capture to fission ratio of  $^{239}\text{Pu}$  compared to the fissile uranium isotopes in the thermal range of neutron energy. Moreover, the plutonium–thorium fuel generates a much larger concentration of  $^{135}\text{Xe}$  and palladium, a very aggressive fission product that may compromise the integrity of TRISO particles.

The exponential matrix approach has revealed to be in a very good agreement with the MCB predictions on the burnup results. The analytical approach would suggest a mass of thorium 42.5 times larger than  $^{233}\text{U}$  in the case the fuel consists of  $^{233}\text{U}$ –Th; nevertheless, this configuration generates a too low initial excess of reactivity.

The effect of the graphite moderation is stronger for plutonium–thorium fuel than for uranium–thorium since the first produces a faster spectrum. The spectra of uranium isotopes are well thermalized both in the whole reactor, with a peak at 0.15 eV and in the fuel, with a peak at 0.2 eV.

Amid  $^{239}\text{Pu}$ –Th,  $^{233}\text{U}$ –Th and  $^{235}\text{U}$ –Th, the last fuel grants the lowest radiotoxicity of the irradiated fuel and after 250 years it remains always less than 300 times that one of natural uranium.

Finally, the neutron economy of  $^{239}\text{Pu}$  is too poor to allow the reactor to work on a mixture of thorium and LWRs waste or military plutonium; moreover, the  $k_{\text{eff}}$  curve of  $^{235}\text{U}$  is more flatten than that one of  $^{233}\text{U}$  and, therefore, it allows a smaller initial excess of reactivity, which can be managed by the present design of the control rods only for 330 full power operation days.

## References

- Baxter, A., Fikani, M., 2002. Reactor-based Transmutation – Physics Studies of the Gas-cooled Graphite-moderated Deep Burn Reactor. General Atomics, GA-501-0-TRT-000140.
- Baxter, A., Rodriguez, C., 2001. The application of gas-cooled reactor technologies to the transmutation of nuclear waste. *Progress in Nuclear Energy* 38, 81–105.
- Briesmeister, J.F., 2002. A General Monte Carlo N-Particle Transport Code – version 4c. LANL, LA-13709-M.
- Cetnar, J., Gudowski, W., Wallenius, J., 1999. MCB: a continuous energy Monte Carlo burnup simulation code, in actinide and fission product partitioning and transmutation. EUR 18898 EN, OECD/NEA 523.
- Cetnar, J., Gudowski, W., Wallenius, J., Tucek, K., 2001. Simulation of nuclide transmutation with Monte-Carlo Continuous Energy Burnup Code (MCBIC). In: *Proceedings of the Accelerator Application 2001 and ADTTA 2001 Nuclear Application in the New Millennium*, Reno, USA.
- Chapelot, P. et al., 2001. Requirements for high temperature reactor fuel particle design assessment. *Progress in Nuclear Energy* 38.
- Feltus, M.A., 2004. Overview of the DOE advanced gas reactor fuel development and qualification program and gas reactor R&D. In: *IAEA Technical Meeting on Current Status and Future Prospects of Gas Cooled Reactor Fuels*, Vienna, Austria.
- Fukuda, K., Kashimura, S., Tobita, T., Kikuchi, T., 1995. Irradiation behavior of HTGR coated particle fuel at abnormally high temperature. *Nuclear Engineering and Design* 157, 221–230.
- General Atomics, 2002. GT-MHR Conceptual Design Description Report. GA/NRC-337-02.
- Golubev, I., Kadarmetov, I., Makarov, V., 2002. Mathematical model and computer code for coated particles performance at normal operating conditions. In: *IAEA Proceedings of the Conference on High Temperature Reactors*, Petten, Holland.
- Gruppelaar, H., Schapira, J.P., 2000. Thorium as a Waste Management Option. European Commission, EUR-19142.
- Habush, A.L., Harris, A.M., 1968. 330 MW<sub>e</sub> Fort St.Vrain High-Temperature Gas-Cooled Reactor. *Nuclear Engineering and Design* 7, 312–321.
- Herring, J.S., Mc Donald, P.E., et al., 2001. Low Cost, proliferation resistant, uranium–thorium dioxide fuels for light water reactors. *Nuclear Engineering and design* 203, 65–85.
- Kim, J.J., Lee, J.T., Kim, H.R., 1989. Generation and benchmarking of a 69 group cross-section library for thermal reactor applications. *Journal of the Korean Nuclear Society* 21, 245.
- Kimura, I., 1995. Review of cooperative research on thorium fuel cycle as a promising energy source in the next century. *Progress in Nuclear Energy* 29, 445–452.
- Kiryushin, A.I., Kodochigov, N.G., Kouzavkov, N.G., et al., 1997. Project of the GT-MHR high temperature helium reactor with gas turbine. *Nuclear Engineering and Design* 173, 119–129.
- Kodochigov, N., Sukharev, Y., et al., 2003. Neutronic features of the GT-MHR. *Nuclear Engineering and Design* 222, 161–171.
- Labar, M., 2002. The Gas Turbine-Modular Helium Reactor: A Promising Option for Near Term Deployment. General Atomics, GA-A23952.
- Labar, M.P., Simon, W.A., 1994. Comparative Economics of the GT-MHR and Power Generation Alternatives. General Atomics, GA-A 21722.
- Lung, M., Gremm, O., 1998. Perspectives of the thorium fuel cycle. *Nuclear Engineering and Design* 180, 133–146.
- Miller, G.K., Petti, D.A., Maki, J.T., 2002. Development of an integrated performance model for TRISO-coated gas reactor particle fuel. In: *IAEA Proceedings of the Conference on High Temperature Reactors*, Petten, Holland.
- Miller, G.K., Petti, D.A., Varacalle, D.J., Maki, J.T., 2001. Consideration of the effects on fuel particle behavior from shrinkage cracks in the inner pyrocarbon layer. *Journal of Nuclear Materials* 295, 205–212.
- Minato, K., Ogawa, T., et al., 1993. Release behavior of metallic fission products from HTGR fuel particles at 1600 and 1900 °C. *Journal of Nuclear Materials* 202, 47–53.

- Minato, K., Sawa, K., et al., 2000a. Fission products release behavior of individual coated fuel particles for HTGR. *Journal of Nuclear Science and Technology* 131.
- Minato, K., Ogawa, T., Koya, T., et al., 2000b. Retention of fission product cesium in ZrC-coated fuel particles for high-temperature gas-cooled reactors. *Journal of Nuclear Materials* 279, 181–188.
- Minato, K., Ogawa, T., Sawa, K., et al., 2000c. Irradiation experiment on ZrC-coated particles for high temperature gas cooled reactors. *Journal of Nuclear Science and Technology* 130.
- Minato, K., Fukuda, K., Sekino, H., et al., 1998. Deterioration of ZrC-coated fuel particle caused by failure of pyrolytic carbon layer. *Journal of Nuclear Materials* 252, 13–21.
- Minato, K., Ogawa, T., Fukuda, K., Sekino, H., Kitagawa, I., Mita, N., 1997. Fission product release from Zr-coated fuel particles during post-irradiation heating at 1800 and 2000 °C. *Journal of Nuclear Materials* 249, 142–149.
- Nabielek, H., et al., 2004. Can we predict a coated particle failure? A conversation on CONVOL, PANAMA and other codes. In: IAEA Technical Meeting on Current Status and Future Prospects of Gas Cooled Reactor Fuels, Vienna, Austria.
- Nabielek, H., Schenk, W., Heit, W., Mehner, A.W., Goodin, D.T., 1989. The performance of HTR fuel particles at extreme temperatures. *Journal of Nuclear Science and Technology* 84, 62–81.
- Nickel, H., Nabielek, H., et al., 2002. Long time experience with the development of HTR fuel elements in Germany. *Nuclear Engineering and Design* 217, 141–151.
- Ohashi, K., Okamoto, F., Hayakawa, H., 2000. Modular High temperature reactor contributing the global environmental protection. *Progress in Nuclear Energy* 37, 307–312.
- Porta, J., Lo Pinto, P., Bonnet, M., Kugeler, K., et al., 2001. Coated particle fuel to improve safety, design, and economics in water-cooled and gas-cooled reactors. *Progress in Nuclear Energy* 38, 407–410.
- Plukiene, R., Ridikas, D., 2003. Modeling of HTRs with Monte Carlo: from a homogeneous to an exact heterogeneous core with microparticles. *Annals of Nuclear Energy* 30, 1573–1585.
- Rodriguez, C., Baxter, A., et al., 2003. Deep-Burn: making nuclear waste transmutation practical. *Nuclear Engineering and Design* 222, 299–317.
- Rütten, H.J., Haas, K.A., 2000. Research on the incineration of plutonium in a modular HTR using thorium-based fuel. *Nuclear Engineering and Design* 195, 353–360.
- Sawa, K., Suzuki, S., Shiozawa, S., 2001a. Safety criteria and quality control of HTTR fuel. *Nuclear Engineering and Design* 208, 305–313.
- Sawa, K., Ueta, S., et al., 2001b. Prediction of fuel performance and fission gas release behavior during normal operation of the high temperature engineering test reactor by JAERI and FZJ modeling approach. *Journal of Nuclear Science and Technology*, 411–419.
- Sawa, K., Tobita, T., 2003. Investigation of irradiation behavior of SiC-coated fuel particle at extended burnup. *Journal of Nuclear Science and Technology* 142.
- Shenoy, A.S., 1995. Modular Helium Reactor for Non-electric Applications of Nuclear Energy. General Atomics, GA-A22701.
- Sumita, J., Ueta, S., Kunitomi, K., Yoshimuta, S., Sawa, K., 2003. Reprocessing technologies of the high temperature gas-cooled reactor (HTGR) fuel. *Transactions of the Atomic Energy Society of Japan* 2 (4), 546–554.
- Talamo, A., Gudowski, W., Venneri, F., 2004a. The burnup capabilities of the deep burn modular helium reactor analyzed by the Monte Carlo continuous energy code MCB. *Annals of Nuclear Energy* 31/2, 173–196.
- Talamo, A., Gudowski, W., Cetnar, J., Venneri, F., 2004b. Key physical parameters and temperature reactivity coefficients of the deep burn modular helium reactor fueled with LWRs waste. *Annals of Nuclear Energy* 31/16, 1913–1937.
- Talamo, A., Gudowski, W., Cetnar, J., 2004c. Comparative studies of ENDF/B-6.8, JEF-2.2 and JENDL-3.2 data libraries by Monte Carlo modeling of high temperature reactors on plutonium based fuel cycles. *Journal of Nuclear Science and Technology* 41/12.
- Talamo, A., Gudowski, W., 2005. A deep burn fuel cycle strategy for the incineration of military plutonium in the gas turbine-modular helium reactor modeled in a detailed 3D geometry by the Monte Carlo continuous energy burnup code. Internal report.

- Taubman, C.J., 1975. The WIMS 69-Group Library Tape 166259. Report AEEW-M1324, U.K. Atomic Energy Authority, Winfrith, Great Britain.
- Tsuchie, Y., 2000. Desirability of small reactors, HTGR in particular. *Progress in Nuclear Energy* 37, 253–258.



## TECHNICAL REPORT

# Comparative Studies of JENDL-3.3, JENDL-3.2, JEFF-3, JEF-2.2 and ENDF/B-6.8 Data Libraries on the Monte Carlo Continuous Energy Modeling of the Gas Turbine-Modular Helium Reactor Operating with Thorium Fuels

Alberto TALAMO\* and Waclaw GUDOWSKI

Royal Institute of Technology (KTH), Roslagstullsbacken 21, Stockholm S-10691, Sweden

(Received July 11, 2005 and accepted in revised form October 20, 2005)

One of the major benefits of the Gas Turbine-Modular Helium Reactor is the capability to operate with several different types of fuel; either Light Water Reactors waste, military plutonium or thorium represent valid candidates as possible types of fuel. In the present studies, we performed a comparison of various nuclear data libraries by the Monte Carlo Continuous Energy Burnup Code MCB applied to the Gas Turbine-Modular Helium Reactor operating on a thorium fuel. A thorium fuel offers valuable attractive advantages: low fuel cost, high reduction of actinides production and the possibility to enable the reactor to act as a breeder of fuel by the neutron capture of fertile  $^{232}\text{Th}$ . We evaluated the possibility to mix thorium with small quantities, about 3% in atomic composition, of  $^{239}\text{Pu}$ ,  $^{233}\text{U}$  and  $^{235}\text{U}$ . The mass of thorium must be much larger than that one of plutonium or uranium because of the low capture cross section of thorium compared to the fission one of the fissile nuclides; at the same time, the quantity of the fissile isotopes must grant the criticality condition. These two simultaneous constraints force to load a huge mass of fuel in the reactor; consequently, we propose to allocate the fuel in TRISO particles with a large radius of the kernel. For each of the three different fuels we calculated the evolution of the fuel composition by the MCB code equipped with five different nuclear data libraries: JENDL-3.3, JENDL-3.2, JEFF-3, JEF-2.2 and ENDF/B.

**KEYWORDS:** *GT-MHR, JENDL, JEF, JEFF, ENDF/B, TRISO, gas-cooled, graphite-moderated, thorium*

## I. Introduction

During the 1990s, General Atomics (GA) has developed the Gas Turbine-Modular Helium Reactor (GT-MHR), a graphite-moderated helium-cooled High Temperature Gas Reactor (HTGR).<sup>1-18)</sup> The GT-MHR belongs to the generation IV of nuclear reactors, which introduces many advances in the current standards of the nuclear power plant: the reactor operates at higher temperatures, it supports the production of hydrogen and it improves sustainability, economics, safety, reliability and proliferation-resistance. We utilized the report GA has submitted in 2002 to the US Nuclear Regulatory Commission<sup>6)</sup> to describe the GT-MHR in a detailed three-dimensional geometry and in a continuous energy burnup by the extraordinary capability of the MCB code. We modeled the reactor as a  $12 \times 12$  matrix of H451 nuclear-grade graphite hexagonal blocks, with an interstitial gap of 0.1 cm, confined into a cylinder of 3.5 m radius and 10 m height. The fuel is disposed into three concentric rings of hexagonal blocks and it axially covers only 7.93 m of the height of the reactor since, at top and at the bottom of the reactor, two equally long cylinders of graphite act as neutron reflectors. The fuel block containing a control rod allocates 95 coolant channels and 192 fuel pins; whereas, in the case the block does not contain a control rod, the above numbers respectively increase to 108 and 216. The reactor is equipped with 12 startup control rods located in the inner fuel ring, 6

shutdown ones in the central ring, 12 shutdown ones in the outer ring and 36 operational ones in the graphite reflector blocks surrounding the outer fuel ring. Each control rod consists of a cylinder of graphite filled by a square lattice of BISO particles containing boron carbide enriched 90% in  $^{10}\text{B}$ ; the fuel pin has a structure similar to that one of a control rod with the only difference that TRISO particles contain fuel instead of boron carbide. TRISO particles are microscopic spheres, with a radius of few hundreds micrometers, of fuel oxide covered by a cladding structured into four different layers: porous carbon layer, inner pyrocarbon, zirconium carbide and outer pyrocarbon; BISO particles are like TRISO particles without the last two outer layers. **Figure 1** shows the horizontal cross sections of the core, a hexagonal block, a fuel pin and a TRISO particle; **Table 1** reports the geometry data of the reactor and **Tables 2** and **3** do the materials ones.

We have set the temperature of the fuel in the TRISO particles to 1,500 K and the temperature of all other materials to 1,200 K, but the temperature of the carbon in the pure graphite hexagonal blocks, all the hexagonal blocks without fuel pins or operational control rods, which has been set to 900 K, with the scattering function  $S(\alpha, \beta)$  evaluated at 800 K.

The present paper extends our previous work on the thorium fuel,<sup>5)</sup> which discussed the performances of different types of fertile TRISO particles, and it focuses on the comparison of the previous results by diverse nuclear data libraries.

\*Corresponding author, Tel. +46-8-55-37-8204,  
Fax. +46855378465, E-mail: alby@neutron.kth.se

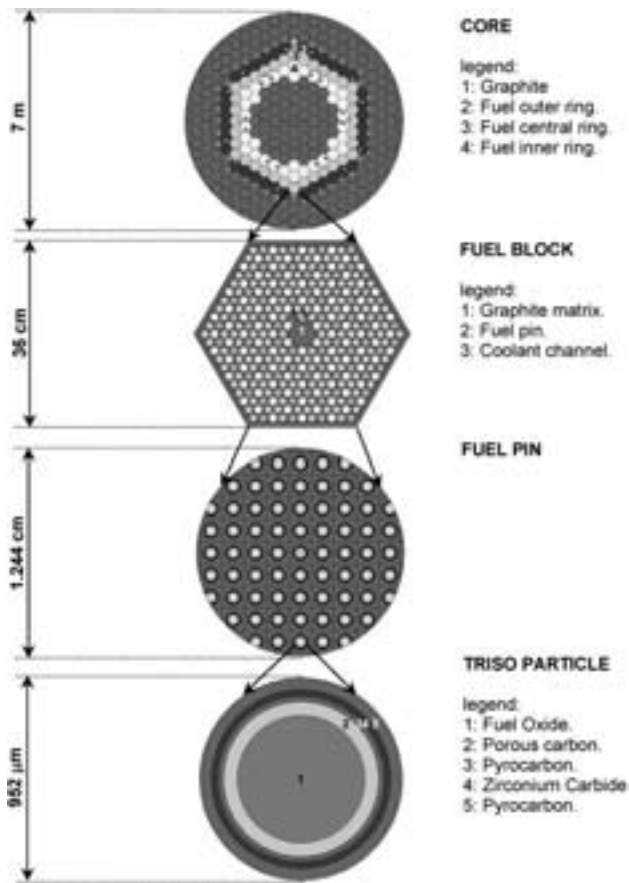


Fig. 1 The Gas Turbine-Modular Helium Reactor plotted by MCNP

## II. The Thorium Fuel—A Tight Balance of Reaction Rates

A thorium fuel offers several attractive benefits:<sup>19)</sup>

- Large resources of thorium are available all over the world.
- Thorium needs for reactors are much less than presents uranium needs for LWRs.
- During fuel fabrication, the total radioactive waste coming from mill tailings is about two orders of magnitude lower than in the case of present LWRs.
- The contribution of the actinides to the total dose of the irradiated fuel is rather small.

Natural thorium is composed only by the fertile isotope <sup>232</sup>Th, which, while irradiated, undergoes a neutron capture and it becomes <sup>233</sup>Th; <sup>233</sup>Th transmutes into <sup>233</sup>Pa and then into <sup>233</sup>U, with a corresponding half life of 22 min and 27 d respectively. At the beginning of life, the fuel must also contain some fissile nuclide, <sup>239</sup>Pu, <sup>233</sup>U or <sup>235</sup>U, in order to set the criticality of the reactor; we refer to the initial fissile nuclide as the *trigger isotope*. If thorium is abundantly present in the fuel, then the reactor starts to breed fissile <sup>233</sup>U and, in a hypothetical optimal condition, the buildup of <sup>233</sup>U compensates the corresponding depletion of the trigger isotope. Nevertheless, setting this hypothetical optimal condition is arduous because thorium has a quite small capture cross section (2 b) comparing to the absorption one of the trigger isotopes (87–185 b). Therefore, it is necessary a mass of thorium at least 30–40 times higher than that one of the fissile isotope to balance the reaction rates so that the cap-

Table 1 Geometry data of the GT-MHR

|   |                |
|---|----------------|
| Core – radius   | 350 cm         |
| Core – height   | 1000 cm        |
| Control rods – startup (inner ring)                                   | 12             |
| Control rods – operational (outer moderator reflector ring)           | 36             |
| Control rods – shutdown (central ring/outer ring)                     | 6/12           |
| Control rods – internal radius (startup/operational/shutdown)         | 0/2.64/0 cm    |
| Control rods – external radius  | 4.13 cm        |
| Control rods – hole radius  | 5.05 cm        |
| Control rods – distance from the center of the hexagon                | 9.75614 cm     |
| Control rods – height at bol (startup/operational/shutdown)           | 0/0/0 cm       |
| Hexagonal fuel blocks – number  | 36 × 3         |
| Hexagonal fuel blocks – width   | 35.99688 cm    |
| Hexagonal fuel blocks – height  | 793 cm         |
| Hexagonal blocks – interstitial gap                                   | 0.1 cm         |
| Fuel blocks – DF pins (with control rod/without control rod)          | 216/192        |
| Fuel blocks – coolant channels (with control rod/without control rod) | 108/95         |
| Pins – radius   | 0.6223 cm      |
| Pins – height   | 793 cm         |
| Pins – distance between pins  | 3.25628 cm     |
| Pins – hole radius (fuel/coolant channel)                             | 0.635/0.795 cm |
| TRISO particles – kernel radius (fuel/control rods)                   | 300/300 μm     |
| TRISO particles – width porous carbon layer (fuel/control rods)       | 64/50 μm       |
| TRISO particles – width inner pyrocarbon layer (fuel/control rods)    | 26/15 μm       |
| TRISO particles – width ZrC layer                                     | 31 μm          |
| TRISO particles – width outer pyrocarbon layer                        | 55 μm          |
| TRISO particles – distance between particles (fuel/control rods)      | 0.134/0.12 cm  |
| TRISO particles – packing fraction (fuel/control rods)                | 37.55/23.58%   |

**Table 2** Material data of the GT-MHR

The temperature of graphite in the hexagonal blocks not containing fuel pins or control rods has been set to 900 K (with the scattering function  $S(\alpha, \beta)$  evaluated at 800 K) otherwise to 1,200 K (with the scattering function  $S(\alpha, \beta)$  evaluated at 1,200 K).

| Material                | Atomic percentage  | Density (g/cm <sup>3</sup> ) and Temperature (K) at bol |
|-------------------------|--|---|
| TRISO kernel            | <sup>239</sup> Pu/ <sup>233</sup> U/ <sup>235</sup> U- <sup>232</sup> Th (37.04%);<br><sup>16</sup> O (62.96%) | 10.2–1,500  |
| TRISO porous graphite   | C (100%)   | 1–1,200   |
| TRISO pyrocarbon        | C (100%)   | 1.85–1,200  |
| TRISO zirconium carbide | Zr (50%); C (50%)  | 6.56–1,200  |
| Graphite                | C (100%)   | 1.74–900/1,200  |
| Control rods            | <sup>10</sup> B (72%); <sup>11</sup> B (8%); <sup>12</sup> C (20%)   | 2.52–1,200  |

**Table 3** Atomic percentage of the trigger nuclide in the fuel actinides

| Trigger nuclide   | Inner ring (%) | Central ring (%) | Outer ring (%) |
|-------------------|----------------|------------------|----------------|
| <sup>239</sup> Pu | 3.3            | 3.8              | 3.6            |
| <sup>233</sup> U  | 3.3            | 3.8              | 3.6            |
| <sup>235</sup> U  | 3.9            | 4.6              | 4.2            |

tures of thorium equal the absorptions of the trigger nuclide. At the same time, the mass of the trigger isotope must be large enough to grant the criticality condition of the reactor. The simultaneous satisfaction of the two above conditions induces to load a huge quantity of fuel in the reactor. The necessity to allocate a huge initial mass of fuel forces to dispose the fuel in the TRISO particles designed at Japan Atomic Energy Research Institute (JAERI) because of their large value of the kernel radius, 300  $\mu\text{m}$ , compared to the current GA design, 150  $\mu\text{m}$ .

### III. The MCB Code

The Monte Carlo Continuous Energy Burnup Code (MCB)<sup>20–22</sup> approaches the apotheosis of the numerical simulation of a burnup process since it offers not only the possibility to model the triple heterogeneity of the GT-MHR in a very detailed three-dimensional geometry but it performs also the transmutation of nuclides with a continuous energy approach, *e.g.* it takes into account the energy dependent isomer formation of <sup>242m</sup>Am and <sup>244m</sup>Am. The strategy of MCB is to divide the burnup time into several steps: at beginning of each step the MCNP<sup>23</sup> track length estimator of neutron flux scores, for each neutron collision, the contribution to the reaction rates of the burnable materials; then, it calculates the decay probability of all nuclides, until a default threshold value of  $10^{-10}$ , and thereafter it updates densities and cross sections. Version 1C of MCB can provide: the burnup and buildup reaction rates, the decay probabilities, the neutron flux, the fission products distributions, the radiation heating, the decay heating, the transmutation transitions, the density evolution and the radiotoxicity (dose in case of ingestion according to the EURATOM Directive).

We remand to our previous papers for a detailed description of the MCB code.

MCB esteemed the neutron flux, by a MCNP run, each month of the simulated operation time, until a period of 11 months, with a simulation of 375,000 neutrons distributed over 25 non-active cycles and 100 active cycles (3,000 neutrons per cycle); afterwards, it simulated the composition evolution of three burnable materials, corresponding to the fuel in the TRISO kernels of the three fuel rings of the core, which undergo a different intensity of the neutron flux.

### IV. The Nuclear Data Files

Nuclear structure and decay data have been compiled and evaluated for nearly seventy years; the first collection of data has been published in Italy by Giorgio Fea in 1935: *Summary Tables of Artificial Transmutations*.<sup>24</sup> Later compilations involved the efforts of several academic institutions all over the world; nowadays, the International Network of Nuclear Structure and Decay Data Evaluators (NSDD), under the direction of the International Atomic Energy Agency Nuclear Data Section (IAEA/NDS), coordinates the work to collect and maintain the evaluated nuclear data. The most common current libraries are: JENDL in Japan, JEFF in Europe, ENDF/B in the United States, BROND in Russia and CENDL in China. In the present studies, we focused our attention on JENDL-3.3, JENDL-3.2, JEFF-3, JEF-2.2 and ENDF/B-6.8; all of them cover the energy range from  $10^{-5}$  eV up to 20 MeV.

The first version of the Japanese Evaluated Nuclear Data Library JENDL-1 was released in 1977; it was mainly addressed to satisfy the requirements to simulate Fast Breeder Reactors (FBRs). JENDL-1 contained transport cross sections for only 72 isotopes, including 28 fission products.<sup>25</sup> In 1985, JENDL-2 added to JENDL-1 the data for 72 additional fission products and the total number of isotopes increased up to 181.<sup>26</sup> No new nuclides were introduced in 1989 by JENDL-3.0. In 1990, it was released JENDL-3.1, which contained a total number of 324 nuclides, including 172 fission products from <sup>75</sup>As to <sup>159</sup>Tb; the number of fission products remained unchanged in the following releases.<sup>27,28</sup> JENDL-3.2 was released in 1994 and contained neutron transport data for 340 (338 in the data library processed

for the present paper) nuclides.<sup>29,30</sup> The latest version of the Japanese library is JENDL-3.3, which has been released in 2002 and it contains transport data for 337 (335 in the data library processed for the present paper) isotopes.<sup>31)</sup>

The first version of the Joint Evaluated File (JEF) has been completed in 1985 mostly by merging the United Kingdom nuclear libraries and the CEA ones; at that time, the radioactive decay data contained about 700 fission products. The second version of the European nuclear data library came in 1990. JEF-2.2 has been released in 1993: it contains radioactive decay data for 2,345 nuclides, including 860 fission products and transport data for 313 (304 in the data library processed for the present paper) nuclides.<sup>32,33)</sup> In 2002, the Nuclear Energy Agency (NEA) released the Joint Evaluated Fission and Fusion nuclear data library (JEFF) version 3.0, which contains 340 (335 in the data library processed for the present paper) isotopes with neutron transport data.<sup>34)</sup>

In America, the first tabulation of neutron cross section data, containing both experimental measurements and theoretical calculations, has published in 1955 with the BNL-325, the so called “barn book,” which rapidly grew up to six volumes in the 1960s. In 1967 it has been released ENDF/B-1; during the 1970s, new versions came, until version 5, released in 1979, which contained data for 200 fission products from  $^{72}\text{Ge}$  to  $^{163}\text{Dy}$ ; the next and latest version, with transport cross sections for 329 (317 in the data library processed for the present paper) nuclides, has been distributed in 1990.<sup>35,36)</sup>

In addition to the evaluated nuclear data files described above, the MCB code has been equipped with a burnup library (BPLIB), which is included in the MCB code package and composed by four files: TOI.LIB, XS.LIB, ISB.LIB and FY.LIB. The TOI.LIB file is based on the Table of Isotopes, edition 8E,<sup>37)</sup> and it describes decay schemes for over 2,400 isotopes; the XS.LIB file is a decay data file used by the ORIGEN code<sup>38)</sup> and it includes the energy integrated ratios of nuclide formation in excited state; the ISB.LIB file contains the the energy dependent ratios of nuclide formation in excited state for  $^{242\text{m}}\text{Am}$  and  $^{244\text{m}}\text{Am}$  according to the Mann & Schenter model;<sup>39)</sup> the FY.LIB file contains the energy dependent fission products yields for 36 heavy nuclides and it is based on the Wahl model.<sup>40)</sup> Let us observe that all calculations using different evaluated nuclear data libraries have been performed with the same burnup library (BPLIB).

## V. The Criticality Condition

### 1. Physical Considerations

We simulated 330 d of full power operation (fpo), with an output of 600 MW<sub>th</sub>, followed by 35 d of natural decay to allow the shuffling of the fuel and the refueling of the reactor. In the numerical simulations, we have kept all the control rods full extracted because the presence of the control rods does not strongly affect the transmutation analysis. **Figures 2, 3** and **4** show the evolution of  $k_{\text{eff}}$  for  $^{239}\text{Pu}$ -Th,  $^{233}\text{U}$ -Th and  $^{235}\text{U}$ -Th, respectively. The sharp decrease of  $k_{\text{eff}}$  (about 2,500 pcm/month, Fig. 2), in the case of  $^{239}\text{Pu}$ -Th fuel, renders quite difficult to operate the GT-MHR with a plutonium-thorium fuel; by contrast, the uranium-thorium

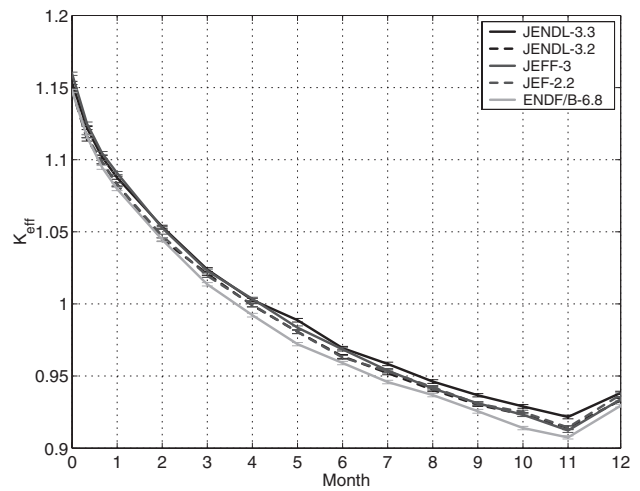


**Fig. 2**  $k_{\text{eff}}$  evolution for  $^{239}\text{Pu}$ -Th; the standard deviation is lower than 143 pcm

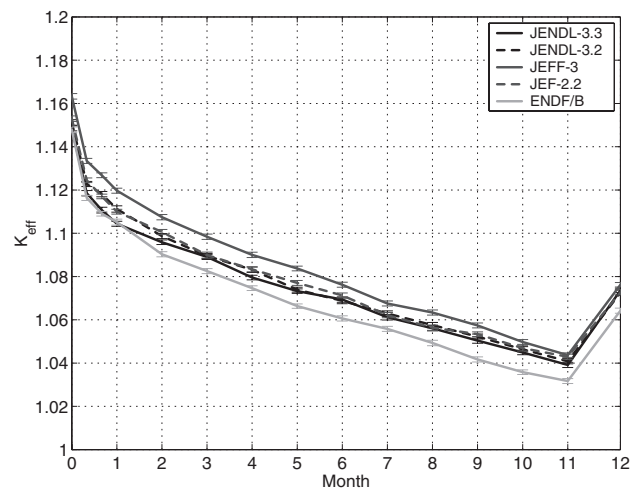


**Fig. 3**  $k_{\text{eff}}$  evolution for  $^{233}\text{U}$ -Th; the standard deviation is lower than 147 pcm

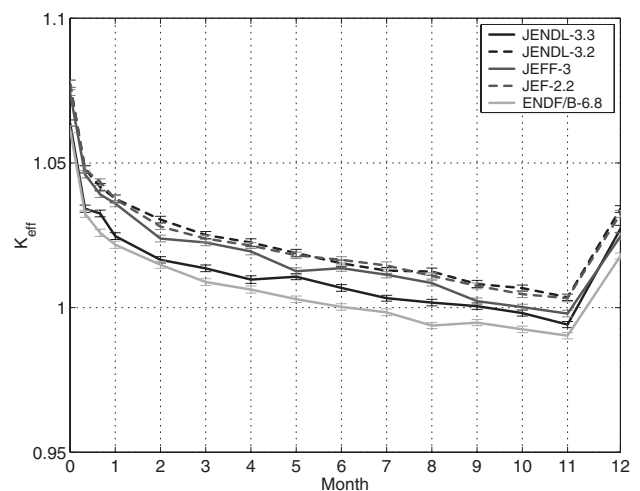


**Fig. 4**  $k_{\text{eff}}$  evolution for  $^{235}\text{U}$ -Th; the standard deviation is lower than 138 pcm

**Table 4** Neutron flux, divided by  $10^{14}$ , between 120 and 150 fpo days

The first three rows, 1), refer to  $^{239}\text{Pu}$ –Th; the next three ones, 2), do to  $^{233}\text{U}$ –Th; the last three ones, 3), do to  $^{235}\text{U}$ –Th. The values of JEFF-3 with asterisk refer to a MCB run simulating 6 millions neutrons each MCNP call (48,000 neutrons per cycle and 125 cycles).

| Isotope         | JENDL-3.3 | JENDL-3.2 | JEFF-3     | JEF-2.2 | ENDF/B-6.8 | Max. diff. (%) |
|-----------------|-----------|-----------|------------|---------|------------|----------------|
| 1) Inner ring   | 1.34      | 1.35      | 1.46–1.44* | 1.40    | 1.44       | 8.9            |
| 1) Central ring | 1.21      | 1.23      | 1.30–1.30* | 1.23    | 1.30       | 7.3            |
| 1) Outer ring   | 1.15      | 1.20      | 1.23–1.25* | 1.16    | 1.24       | 7.9            |
| 2) Inner ring   | 1.46      | 1.50      | 1.53       | 1.50    | 1.57       | 7.0            |
| 2) Central ring | 1.41      | 1.46      | 1.49       | 1.46    | 1.53       | 8.4            |
| 2) Outer ring   | 1.28      | 1.32      | 1.34       | 1.32    | 1.41       | 9.4            |
| 3) Inner ring   | 1.47      | 1.49      | 1.58       | 1.49    | 1.59       | 7.8            |
| 3) Central ring | 1.42      | 1.41      | 1.50       | 1.41    | 1.51       | 6.7            |
| 3) Outer ring   | 1.32      | 1.29      | 1.38       | 1.29    | 1.39       | 7.2            |

fuel may work for longer than one year. Amid fissile nuclides,  $^{235}\text{U}$  exhibits the smoothest  $k_{eff}$  curve (about 300 pcm/month, Fig. 4). The poisoning of short life fission products is stronger for  $^{233}\text{U}$ –Th (about 3,700 pcm, Fig. 3) than for  $^{239}\text{Pu}$ –Th and  $^{235}\text{U}$ –Th (about 2,500 pcm, Figs. 2 and 4).

## 2. Comparative Studies

We can note in almost all the  $k_{eff}$  pictures (Figs. 2–4) some common features:

- The curves referring to JENDL-3.2 superimpose with those ones referring to JEF-2.2;
  - ENDF/B-6.8 always produces the lowest curve of  $k_{eff}$ .
- For  $^{239}\text{Pu}$ –Th,  $^{233}\text{U}$ –Th and  $^{235}\text{U}$ –Th, the highest  $k_{eff}$  is produced by JENDL-3.3 (Fig. 2), JEFF-3 (Fig. 3) and JENDL-3.2/JEF-2.2 (Fig. 4), respectively; in addition, JEFF-3 generates a value of  $k_{eff}$  higher than that one of JENDL-3.3 both for  $^{233}\text{U}$ –Th (Fig. 3) and  $^{235}\text{U}$ –Th (Fig. 4).

## VI. The Neutron Flux in the Three Fuel Rings

### 1. Physical Considerations

We evaluated, by the MCB code, the average neutron flux in the TRISO kernels of the three rings of fuel between 120 and 150 fpo days (when the  $^{233}\text{Pa}$  mass reaches the asymptotic level) for  $^{239}\text{Pu}$ –Th,  $^{233}\text{U}$ –Th and  $^{235}\text{U}$ –Th by the libraries: JENDL-3.3, JENDL-3.2, JEFF-3, JEF-2.2 and ENDF/B-6.8 (**Table 4**). The inner ring experiences the highest value of neutron flux, due to the circular disposition of the fuel and the moderation of adjacent graphite hexagonal blocks; whereas, the outer ring undergoes the lowest flux. Moreover, amid the three different types of fuel,  $^{235}\text{U}$ –Th generates the highest flux and  $^{239}\text{Pu}$ –Th the lowest one. The heterogeneous enrichment of the trigger isotope in the fuel lowers the relative peak of the flux in the three rings (defined as the highest flux between the three rings divided the lowest one) from 1.3, corresponding to a homogeneous enrichment, to 1.2.

### 2. Comparative Studies

In agreement with our previous studies,<sup>3)</sup> the neutron flux maximal difference, defined as the difference between the

maximum value of the neutron flux and the minimum one divided by the average of the five values, keeps always lower than 9.4%; without the data of ENDF/B, the maximal difference would be lower than 8%. Moreover, we can note that the values of JENDL-3.2 are very close to those ones of JEF-2.2; whereas, JEFF-3 and JENDL-3.3 generally exhibit a flux respectively higher and lower than the two previous libraries; finally, ENDF/B-6.8 shows the highest estimation of the neutron flux. In the case of  $^{239}\text{Pu}$ –Th and JEFF-3, the values of the neutron flux averagely changed only 0.7% in a MCB run simulating a total of 6 million neutrons each MCNP call.

## VII. Fuel Transmutation

### 1. Physical Considerations

**Figure 5** illustrate the actinides transmutation chain of the three different types of fuel (up to neptunium) and **Fig. 6** focuses only on  $^{239}\text{Pu}$ –Th (up to curium). A rapid glance at **Fig. 5** suggests few considerations:

- The absorption cross section of  $^{239}\text{Pu}$ , 185 b, is much higher than those ones of  $^{233}\text{U}$ , 103 b, and  $^{235}\text{U}$ , 87 b; that explains the behavior of the  $k_{eff}$  curves (Figs. 2–4) by a faster depletion of  $^{239}\text{Pu}$  and a slower one of  $^{235}\text{U}$ ;
- The ratio between the trigger nuclide absorption cross section and the thorium one is 86 for  $^{239}\text{Pu}$ , 103 for  $^{233}\text{U}$  and 87 for  $^{235}\text{U}$ ;
- The neutron economy of  $^{239}\text{Pu}$ –Th is very poor since 38% of  $^{239}\text{Pu}$  transmutes by neutron capture; whereas for the uranium isotopes the capture branch reduces to 20% for  $^{235}\text{U}$  and 11% for  $^{233}\text{U}$ . That confirms the difficulty to balance properly the reaction rates for  $^{239}\text{Pu}$ –Th;
- $^{239}\text{Pu}$ –Th generates a lower quantity of  $^{233}\text{Pa}$  and therefore of  $^{233}\text{U}$ ;
- $^{240}\text{Pu}$ , with an average capture cross section of 300 b, confirms to be a very strong capturing nuclide;
- Over 98% of  $^{233}\text{Pa}$  decays into  $^{233}\text{U}$ ;
- The uranium–thorium fuels cut the buildup of all actinides higher than neptunium.

**Figure 6** highlights that the production of americium and curium for  $^{239}\text{Pu}$ –Th is low, since all the three fuel rings contain, after 150 fpo days, only 130 g of  $^{242}\text{Pu}$  and 40 g of

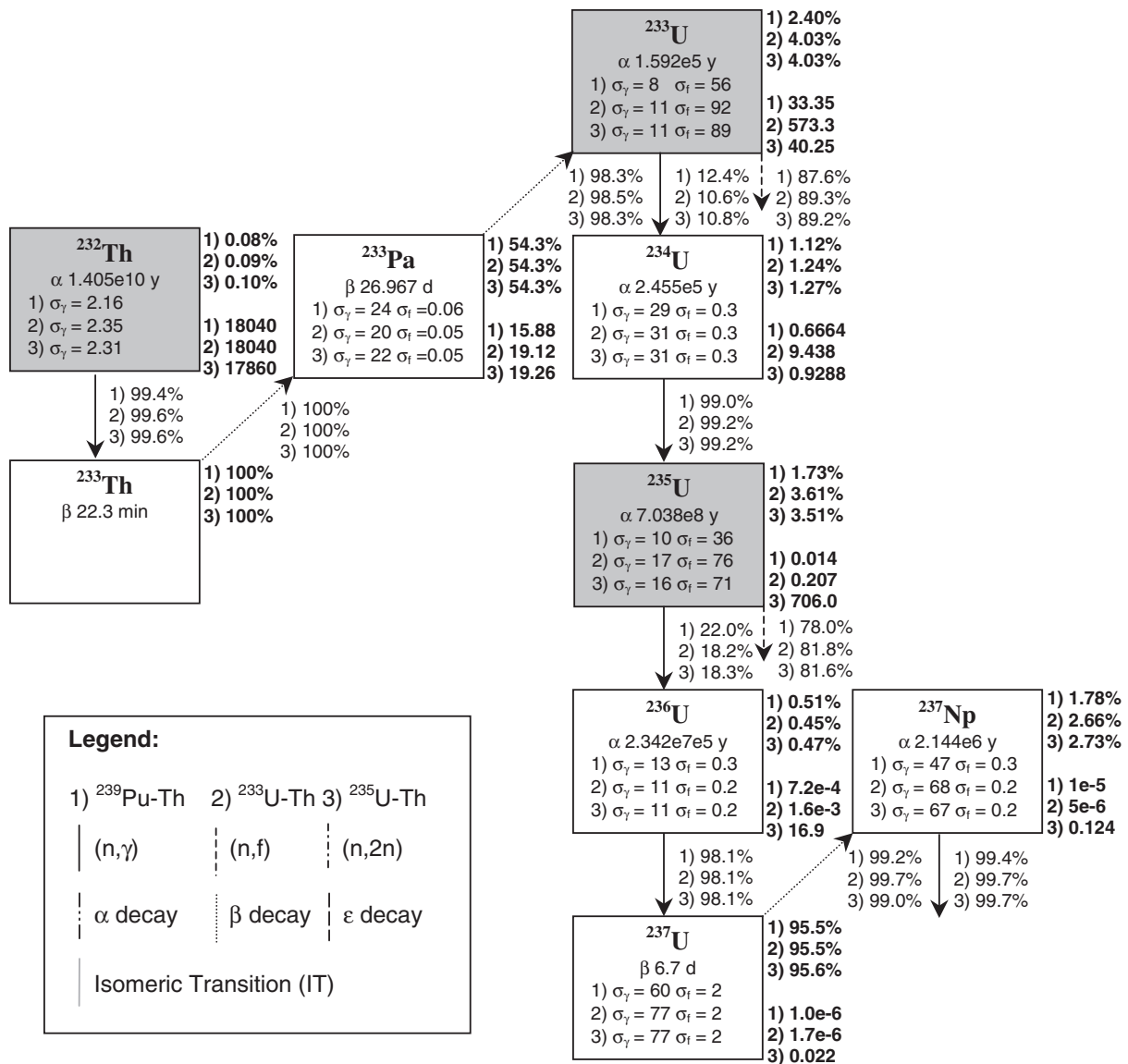


**Fig. 5** Transmutation chain of a thorium based fuel

The second row of the boxes reports the half live; other lines do the cross sections in the inner ring between 120 and 150 fpo days; the percentages in bold and the below values report respectively the transmuted fraction (taking into account only one parent nuclide), in the inner ring, between 120 and 150 fpo days, and the mass, in kilograms in all the three rings after 150 fpo days; the percentages that are not in bold represent the relative transmutation branches. Data have been calculated by JEFF-3.

$^{241}\text{Am}$ ; nevertheless, after the shutdown of the reactor, about 8 kg of  $^{241}\text{Pu}$  decay into  $^{241}\text{Am}$  with a half life of 14.35 years.

**Figures 7 and 8** illustrate the mechanism of production of  $^{135}\text{Xe}$  and  $^{149}\text{Sm}$ , respectively, for the three different types of fuels. In the  $^{135}\text{Xe}$  production scheme, we neglected the representation of the meta-stable state  $^{135m}\text{Xe}$ , since it decays into the ground state with a half-life of 15.3 m, as well as the inclusion of  $^{135}\text{Sm}$  and  $^{135}\text{Te}$ , since they shortly decay into  $^{135}\text{I}$  (the MCB code applies the same approximations). In spite the half-life of  $^{135}\text{Xe}$  is very short, only 9.14 h, a large fraction of xenon (44% and 67–68% for  $^{239}\text{Pu-Th}$  and uranium–thorium, respectively) transmutes into  $^{136}\text{Xe}$  due to its very high microscopic capture cross section. In fact, the microscopic capture cross section of  $^{135}\text{Xe}$ , at the thermal en-

ergy (0.025 eV), is 2.7 Mb and the one-group averaged is about 100,000–300,000 b; moreover, for uranium–thorium it is three times larger than for  $^{239}\text{Pu-Th}$ , due to the resonance at 0.3 eV of  $^{239}\text{Pu}$ . In our previous studies (Fig. 22 of Ref. 5) we observed that the peak of the neutron spectrum averaged in the core of the GT-MHR, operating on a fertile fuel, lies at 0.15 eV, where the  $^{135}\text{Xe}$  capture cross section is 850,000 b (JEF-2.2 data).

The capture reaction of  $^{134}\text{Xe}$  contributes less than 0.7–2% to the production of  $^{135}\text{Xe}$ , in spite  $^{134}\text{Xe}$  is a stable isotope, because of its very low capture cross section (about 50 mb). Figure 8 highlights that all Nd and Pm isotopes contribute to the generation of  $^{149}\text{Sm}$ .  $^{146}\text{Nd}$  and  $^{148}\text{Nd}$  accumulate because they are stable nuclides and their capture cross sections are 0.2–1.1 b. The transmutation of  $^{147}\text{Pm}$  generates

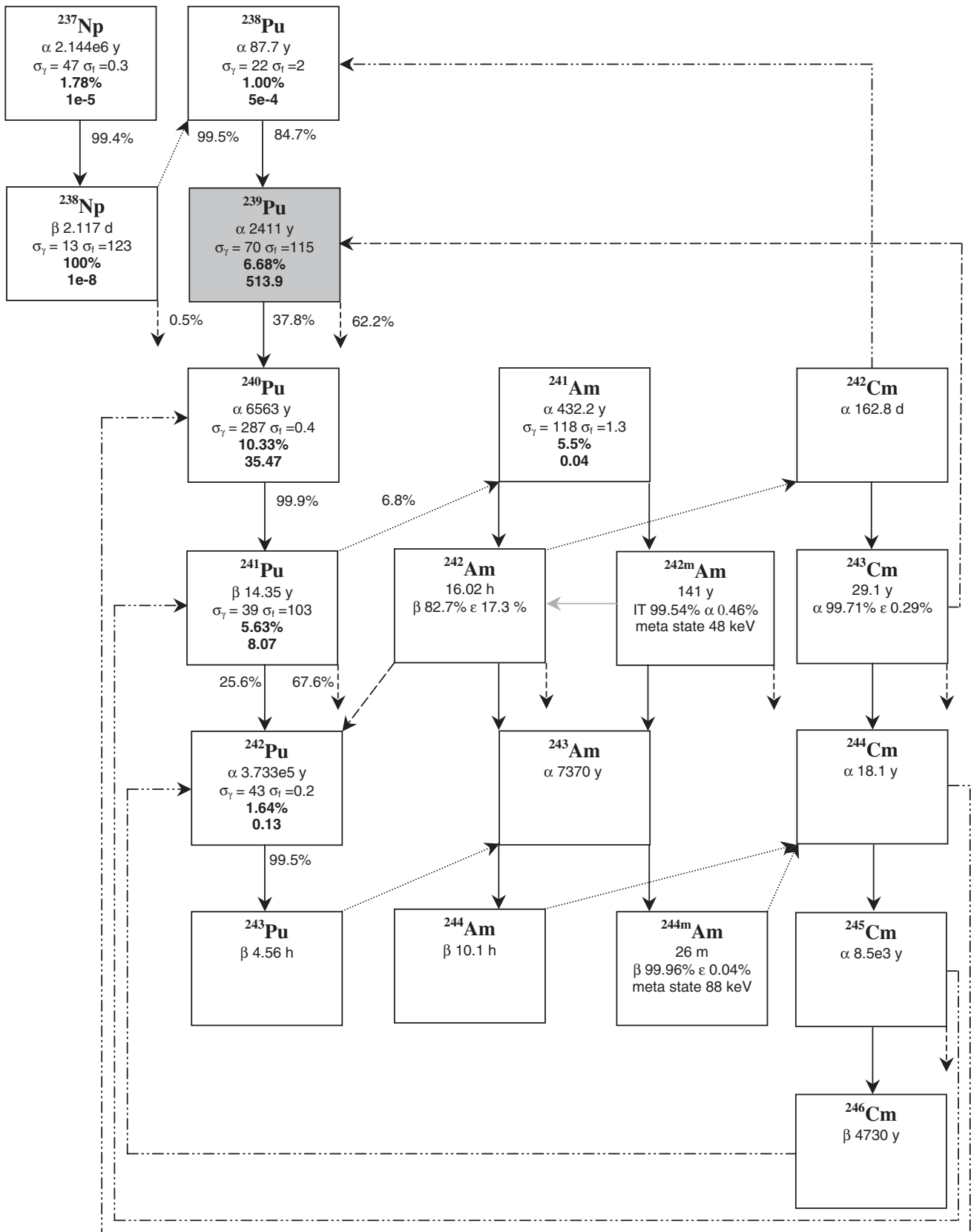


**Fig. 6** Transmutation chain of the  $^{239}\text{Pu}$ -Th fuel

The second row of the boxes reports the half live; the third row does the cross sections in the inner ring between 120 and 150 fpo days; the fourth and fifth rows do respectively the transmuted fraction (taking into account only one parent nuclide), in the inner ring, between 120 and 150 fpo days, and the mass, in kilograms in all the three rings after 150 fpo days; the percentages that are not in bold represent the relative transmutation branches. Data have been calculated by JEFF-3.

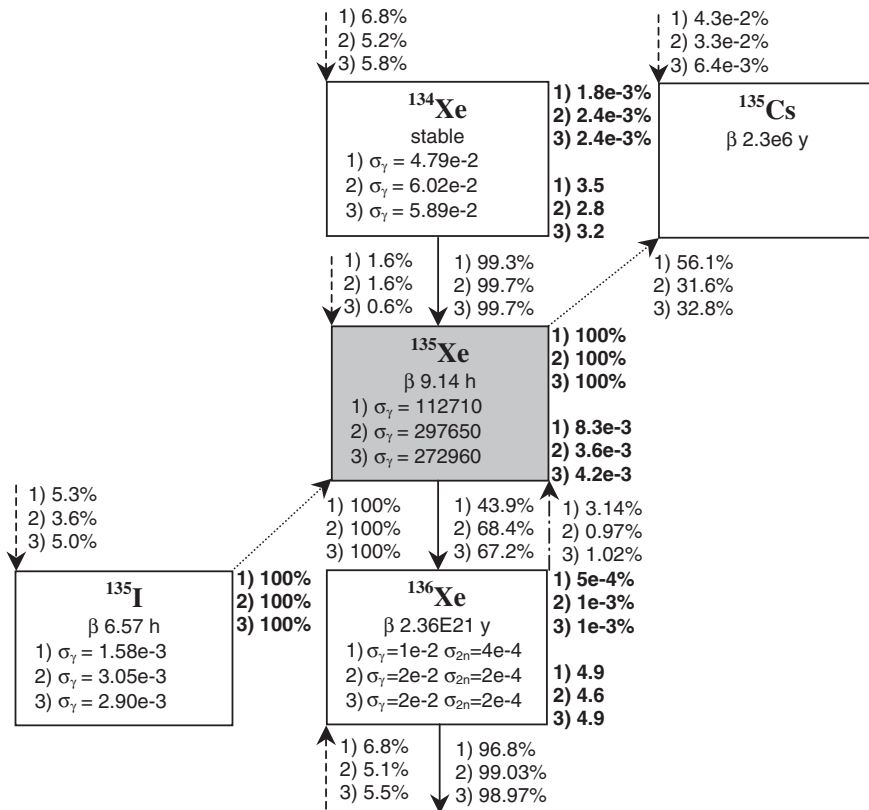


Fig. 7  $^{135}\text{Xe}$  production

The second row of the boxes reports the half live; the other lines do the cross sections in the inner ring between 120 and 150 fpo days; the percentages in bold and the below values report respectively the transmuted fraction (taking into account only one parent nuclide), in the inner ring, between 120 and 150 fpo days, and the mass, in kilograms in all the three rings after 150 fpo days; the percentages that are not in bold represent the relative transmutation branches. The percentages beside the fission reactions represent the fission yields between 120 and 150 fpo days. Data have been calculated by JEFF-3.

$^{148\text{m}}\text{Pm}$ ,  $^{148}\text{Pm}$  and  $^{147}\text{Sm}$ , with respective branches: 34, 27 and 39%. The decay branch of  $^{148\text{m}}\text{Pm}$  into the ground state depends on the fuel type, since it is 38% for  $^{239}\text{Pu}$ -Th and 18% for uranium-thorium. The capture cross section of  $^{149}\text{Sm}$  is about 30 times lower than that one of  $^{135}\text{Xe}$ ; moreover, the value for  $^{239}\text{Pu}$ -Th is half of that one for the uranium-thorium because of the spectral effect due to the 0.3 eV low energy wide resolved resonance of  $^{239}\text{Pu}$ . Finally, let us observe that the  $^{149}\text{Sm}$  production scheme presented by Suyama *et al.*<sup>41)</sup> neglected the contribution of  $^{146}\text{Nd}$ .

Figures 9, 12 and 14 plot the mass of  $^{233}\text{Pa}$  respectively for  $^{239}\text{Pu}$ -Th,  $^{233}\text{U}$ -Th and  $^{235}\text{U}$ -Th; Figures 10, 13 and 15 do the mass of  $^{233}\text{U}$  respectively for  $^{239}\text{Pu}$ -Th,  $^{233}\text{U}$ -Th and  $^{235}\text{U}$ -Th; Figures 11 and 16 do the mass of  $^{239}\text{Pu}$  and  $^{235}\text{U}$  respectively for  $^{239}\text{Pu}$ -Th and  $^{235}\text{U}$ -Th. The figures relative to the transmutation of  $^{233}\text{Pa}$  show that this isotope reaches the asymptotic mass (about 20 kg) after five months; moreover, after 35 days since the shut down of the reactor, half of  $^{233}\text{Pa}$  mass decays. The high absorption cross section of  $^{239}\text{Pu}$  generates a depletion of about 20 kg/month (Fig. 11), which is not compensated by the build up of about 10 kg/month of  $^{233}\text{U}$  (Fig. 10); the buildup of  $^{233}\text{U}$  is about 10 kg/month also for the  $^{235}\text{U}$ -Th fuel (Fig. 15). The total consumption of 60 kg of  $^{233}\text{U}$ , 220 kg for  $^{235}\text{U}$ , allows the

GT-MHR to work for over 330 days on a uranium-thorium based fuel.

2. Comparative Studies

We can note in almost all the transmutation pictures (Figs. 9–16) some common features:

- The curves referring to JENDL-3.2 superimpose with those ones referring to JEF-2.2;
- ENDF/B-6.8 shows a higher build up and burnup than JEFF-3, the latter shows a higher one than JEF-2.2/JENDL-3.2, the latter shows a higher one than JENDL-3.3;
- The transmutation curves diverge with time, the  $k_{\text{eff}}$  ones do not.

The depletion of  $^{239}\text{Pu}$  in the  $^{239}\text{Pu}$ -Th fuel (Fig. 11) is almost identical for ENDF/B-6.8 and JEFF-3. The buildup of  $^{233}\text{Pa}$  in the  $^{233}\text{U}$ -Th fuel (Fig. 12) for JENDL-3.2/JEF-2.2 coincides with that one for JEFF-3 and in the  $^{235}\text{U}$ -Th fuel (Fig. 14) it does with that one for JENDL-3.3. In the transmutation of  $^{233}\text{U}$  in the  $^{233}\text{U}$ -Th fuel (Fig. 13), the curve of JEFF-3 exhibits the highest burnup and the curve of JENDL-3.3 superimposes with those ones of JENDL-3.2/JEF-2.2, the latter effect occurs also in the  $^{235}\text{U}$ -Th fuel (Fig. 15). In the depletion of  $^{235}\text{U}$  in the  $^{235}\text{U}$ -Th fuel



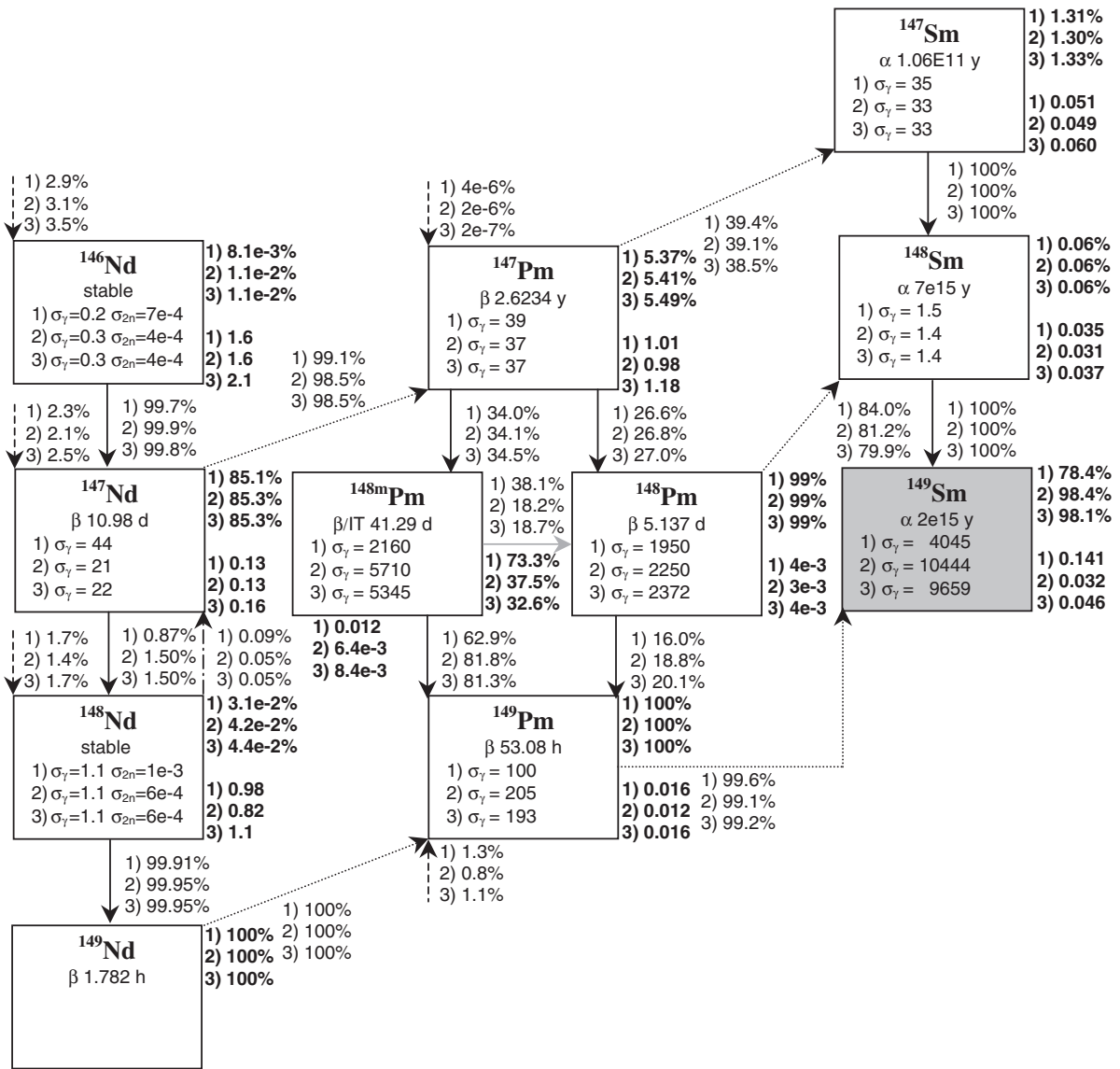


Fig. 8 <sup>149</sup>Sm production

The second row of the boxes reports the half live; the other lines do the cross sections in the inner ring between 120 and 150 fpo days; the percentages in bold and the below values report respectively the transmuted fraction (taking into account only one parent nuclide), in the inner ring, between 120 and 150 fpo days, and the mass, in kilograms, in all the three rings after 150 fpo days; the percentages that are not in bold represent the relative transmutation branches. The percentages beside the fission reactions represent the fission yields between 120 and 150 fpo days (the omitted data on some isotopes indicate that the values are below 2e-7%). Data have been calculated by JEFF-3.

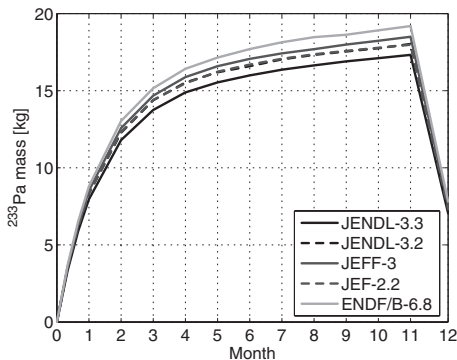


Fig. 9 <sup>233</sup>Pa evolution for <sup>239</sup>Pu-Th

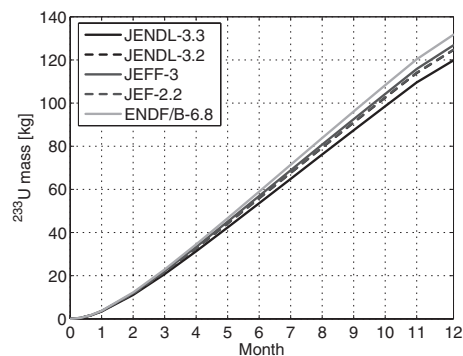


Fig. 10 <sup>233</sup>U evolution for <sup>239</sup>Pu-Th

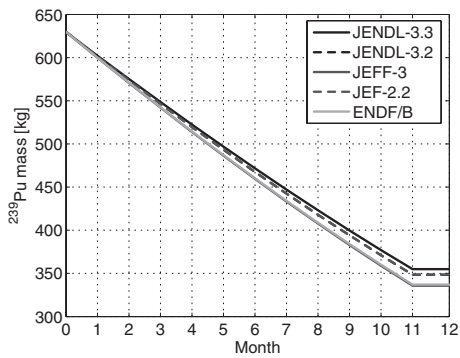


Fig. 11  $^{239}\text{Pu}$  evolution for  $^{239}\text{Pu}\text{-Th}$

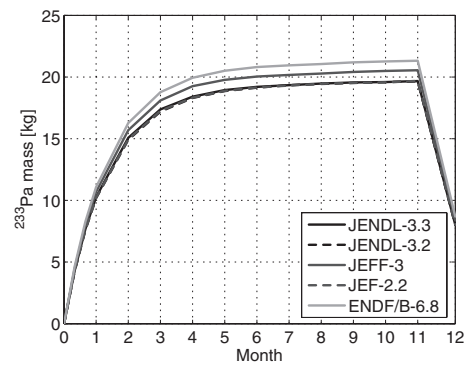


Fig. 14  $^{233}\text{Pa}$  evolution for  $^{235}\text{U}\text{-Th}$

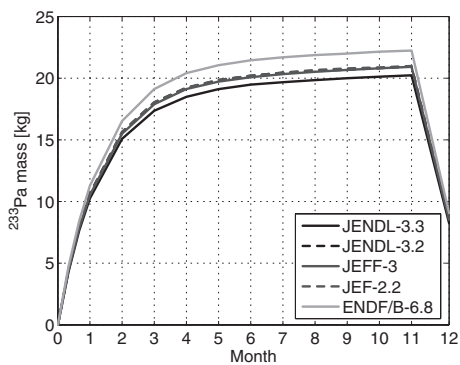


Fig. 12  $^{233}\text{Pa}$  evolution for  $^{233}\text{U}\text{-Th}$

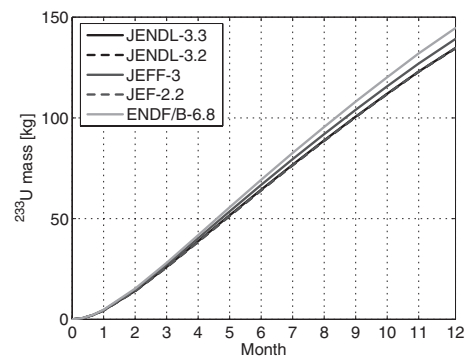


Fig. 15  $^{233}\text{U}$  evolution for  $^{235}\text{U}\text{-Th}$

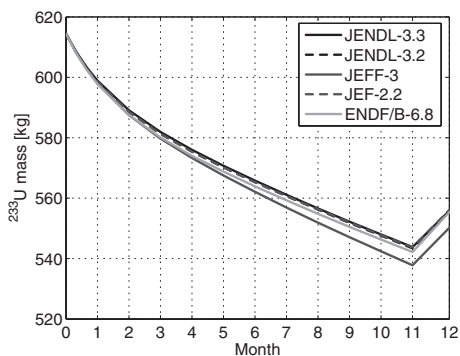


Fig. 13  $^{233}\text{U}$  evolution for  $^{233}\text{U}\text{-Th}$

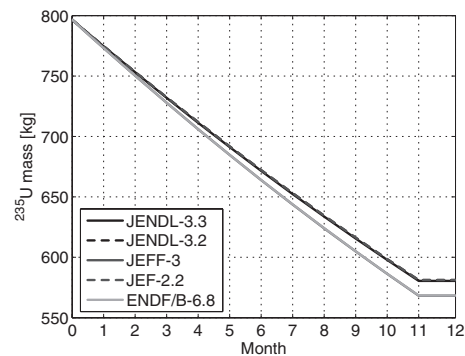


Fig. 16  $^{235}\text{U}$  evolution for  $^{235}\text{U}\text{-Th}$

(Fig. 16), the curves of ENDF/B-6.8 and JENDL-3.3 respectively coincide with those ones of JEFF-3 and JENDL-3.2/JEF-2.2.

### VIII. The One Group Averaged Cross Sections of the Most Abundant Actinides and the Most Absorbing Fission Products

#### 1. Physical Considerations

We reported in Tables 5–10 the fission and capture microscopic cross sections of the most abundant isotopes involved in the transmutation chain of the fuel, according to Figs. 5 and 6:

- $^{232}\text{Th}$ ,  $^{233}\text{Pa}$ ,  $^{233}\text{U}$ ,  $^{234}\text{U}$ ,  $^{239}\text{Pu}$ ,  $^{240}\text{Pu}$ ,  $^{241}\text{Pu}$ , for  $^{239}\text{Pu}\text{-Th}$ ;
- $^{232}\text{Th}$ ,  $^{233}\text{Pa}$ ,  $^{233}\text{U}$ ,  $^{234}\text{U}$ ,  $^{235}\text{U}$  for  $^{233}\text{U}\text{-Th}$ ;

- $^{232}\text{Th}$ ,  $^{233}\text{Pa}$ ,  $^{233}\text{U}$ ,  $^{234}\text{U}$ ,  $^{235}\text{U}$ ,  $^{236}\text{U}$  for  $^{235}\text{U}\text{-Th}$ .

We reported in Tables 8–10 the capture microscopic cross sections of all the nuclides involved in the transmutation chains leading to  $^{135}\text{Xe}$  and  $^{149}\text{Sm}$ , the two fission products with the highest capture microscopic cross section, according to Figs. 7 and 8:

- $^{134}\text{Xe}$ ,  $^{135}\text{Xe}$ ,  $^{146}\text{Nd}$ ,  $^{147}\text{Nd}$ ,  $^{148}\text{Nd}$ ,  $^{147}\text{Pm}$ ,  $^{148}\text{Pm}$ ,  $^{148\text{m}}\text{Pm}$ ,  $^{149}\text{Pm}$ ,  $^{147}\text{Sm}$ ,  $^{148}\text{Sm}$ ,  $^{149}\text{Sm}$ .

#### 2. Comparative Studies

The fission cross section results (Tables 5–7) demonstrate that the maximal difference between the five libraries, for the fissile nuclides, keeps below 6% and that one of the trigger isotope is always lower than 2%. For some non-fissile isotopes, which exhibit a very low fission cross section (lower

**Table 5** Comparison of  $\sigma_f$  for  $^{239}\text{Pu}$ –Th between 120 and 150 fpo days in the inner ring

The values of JEFF-3 with asterisk refer to a MCB run simulating 6 millions neutrons each MCNP call (48,000 neutrons per cycle and 125 cycles).

| Isotope           | JENDL-3.3 | JENDL-3.2 | JEFF-3 | JEF-2.2 | ENDF/B-6.8 | Max. diff. (%) |
|-------------------|-----------|-----------|--------|---------|------------|----------------|
| $^{232}\text{Th}$ | 0.0107    | 0.0096    | 0.0107 | 0.0107* | 0.0103     | 10.8           |
| $^{233}\text{Pa}$ | 0.0554    | 0.0649    | 0.0655 | 0.0652* | 0.0662     | 17.0           |
| $^{233}\text{U}$  | 55.74     | 55.20     | 56.06  | 56.11*  | 55.28      | 1.8            |
| $^{234}\text{U}$  | 0.290     | 0.288     | 0.291  | 0.290*  | 0.289      | 1.2            |
| $^{239}\text{Pu}$ | 113.53    | 114.35    | 115.17 | 115.12* | 114.55     | 1.4            |
| $^{240}\text{Pu}$ | 0.396     | 0.423     | 0.393  | 0.392*  | 0.423      | 11.9           |
| $^{241}\text{Pu}$ | 102.09    | 105.40    | 103.35 | 103.19* | 105.59     | 3.4            |

**Table 6** Comparison of  $\sigma_f$  for  $^{233}\text{U}$ –Th between 120 and 150 fpo days in the inner ring

| Isotope           | JENDL-3.3 | JENDL-3.2 | JEFF-3 | JEF-2.2 | ENDF/B-6.8 | Max. diff. (%) |
|-------------------|-----------|-----------|--------|---------|------------|----------------|
| $^{232}\text{Th}$ | 0.0079    | 0.0070    | 0.0079 | 0.0070  | 0.0077     | 12.0           |
| $^{233}\text{Pa}$ | 0.0416    | 0.0476    | 0.0483 | 0.0478  | 0.0493     | 16.4           |
| $^{233}\text{U}$  | 92.19     | 92.14     | 92.50  | 91.87   | 91.51      | 1.1            |
| $^{234}\text{U}$  | 0.245     | 0.256     | 0.258  | 0.256   | 0.259      | 5.4            |
| $^{235}\text{U}$  | 75.62     | 77.02     | 75.67  | 76.88   | 75.48      | 2.0            |

**Table 7** Comparison of  $\sigma_f$  for  $^{235}\text{U}$ –Th between 120 and 150 fpo days in the inner ring

| Isotope           | JENDL-3.3 | JENDL-3.2 | JEFF-3 | JEF-2.2 | ENDF/B-6.8 | Max. diff. (%) |
|-------------------|-----------|-----------|--------|---------|------------|----------------|
| $^{232}\text{Th}$ | 0.0079    | 0.0072    | 0.0079 | 0.0073  | 0.0077     | 9.2            |
| $^{233}\text{Pa}$ | 0.0420    | 0.0497    | 0.0486 | 0.0498  | 0.0494     | 16.3           |
| $^{233}\text{U}$  | 88.72     | 87.75     | 89.32  | 87.41   | 88.04      | 2.2            |
| $^{234}\text{U}$  | 0.246     | 0.261     | 0.257  | 0.260   | 0.258      | 5.8            |
| $^{235}\text{U}$  | 70.70     | 71.40     | 71.19  | 70.98   | 70.67      | 1.0            |
| $^{236}\text{U}$  | 0.211     | 0.209     | 0.213  | 0.212   | 0.213      | 1.7            |

**Table 8** Comparison of  $\sigma_\gamma$  for  $^{239}\text{Pu}$ –Th between 120 and 150 fpo days in the inner ring

The values of JEFF-3 with asterisk refer to a MCB run simulating 6 millions neutrons each MCNP call (48,000 neutrons per cycle and 125 cycles).

| Isotope                   | JENDL-3.3 | JENDL-3.2 | JEFF-3  | JEF-2.2  | ENDF/B-6.8 | Max. diff. (%) |
|---------------------------|-----------|-----------|---------|----------|------------|----------------|
| $^{232}\text{Th}$         | 2.18      | 2.22      | 2.16    | 2.16*    | 2.22       | 3.1            |
| $^{233}\text{Pa}$         | 24.48     | 24.25     | 24.08   | 24.20*   | 24.14      | 2.1            |
| $^{233}\text{U}$          | 7.94      | 7.74      | 7.95    | 7.95*    | 7.78       | 2.6            |
| $^{234}\text{U}$          | 28.10     | 28.91     | 29.43   | 29.22*   | 28.86      | 4.6            |
| $^{239}\text{Pu}$         | 69.01     | 69.74     | 70.06   | 69.97*   | 69.85      | 1.5            |
| $^{240}\text{Pu}$         | 293.0     | 291.5     | 287.1   | 288.9*   | 286.9      | 2.4            |
| $^{241}\text{Pu}$         | 36.88     | 36.61     | 39.07   | 39.03*   | 36.67      | 6.6            |
| $^{134}\text{Xe}$         | 0.0470    | 0.0485    | 0.0479  | 0.0479*  | 0.0483     | 16.0           |
| $^{135}\text{Xe}$         | 111,660   | 110,950   | 112,710 | 112,205* | 111,610    | 1.6            |
| $^{146}\text{Nd}$         | 0.222     | 0.215     | 0.217   | 0.217*   | 0.217      | 8.6            |
| $^{147}\text{Nd}$         | 44.95     | 43.79     | 44.12   | 44.13*   | 43.72      | 5.7            |
| $^{148}\text{Nd}$         | 0.84      | 1.11      | 1.10    | 1.10*    | 1.11       | 25.4           |
| $^{147}\text{Pm}$         | 39.45     | 38.34     | 38.73   | 38.54*   | 38.47      | 3.9            |
| $^{148}\text{Pm}$         | 209.5     | 1,967     | 1,950   | 1,956*   | 1,953      | 1.8            |
| $^{148\text{m}}\text{Pm}$ |           | 2,135     | 2,160   | 2,148*   | 2,135      | 1.2            |
| $^{149}\text{Pm}$         | 129.7     | 98.97     | 99.66   | 99.58*   | 99.21      | 29.1           |
| $^{147}\text{Sm}$         | 33.92     | 35.19     | 34.87   | 34.95*   | 35.02      | 4.3            |
| $^{148}\text{Sm}$         | 2.30      | 1.48      | 1.49    | 1.49*    | 1.49       | 49.4           |
| $^{149}\text{Sm}$         | 3,754     | 3,871     | 4,045   | 4,018*   | 3,882      | 7.5            |

**Table 9** Comparison of  $\sigma_{\gamma}$  for  $^{233}\text{U}$ -Th between 120 and 150 fpo days in the inner ring

| Isotope                   | JENDL-3.3 | JENDL-3.2 | JEFF-3  | JEF-2.2 | ENDF/B-6.8 | Max. diff. (%) |
|---------------------------|-----------|-----------|---------|---------|------------|----------------|
| $^{232}\text{Th}$         | 2.40      | 2.41      | 2.35    | 2.41    | 2.43       | 3.3            |
| $^{233}\text{Pa}$         | 20.54     | 20.44     | 20.54   | 20.42   | 20.38      | 0.8            |
| $^{233}\text{U}$          | 11.01     | 10.90     | 11.02   | 10.89   | 10.84      | 1.7            |
| $^{234}\text{U}$          | 30.06     | 31.27     | 31.27   | 31.31   | 31.28      | 4.1            |
| $^{235}\text{U}$          | 16.81     | 16.37     | 16.80   | 16.34   | 16.77      | 2.8            |
| $^{134}\text{Xe}$         | 0.0603    | 0.0602    | 0.0602  | 0.0601  | 0.0653     | 8.4            |
| $^{135}\text{Xe}$         | 300,550   | 300,270   | 297,650 | 299,400 | 296,104    | 1.5            |
| $^{146}\text{Nd}$         | 0.301     | 0.298     | 0.296   | 0.296   | 0.309      | 4.6            |
| $^{147}\text{Nd}$         | 72.67     | 72.89     | 72.54   | 72.75   | 70.95      | 2.7            |
| $^{148}\text{Nd}$         | 0.91      | 1.10      | 1.10    | 1.10    | 1.08       | 18.5           |
| $^{147}\text{Pm}$         | 37.51     | 37.14     | 37.46   | 37.28   | 36.76      | 2.0            |
| $^{148}\text{Pm}$         | 344.6     | 2,256     | 2,250   | 2,253   | 2,236      | 0.3            |
| $^{148\text{m}}\text{Pm}$ |           | 5,751     | 5,710   | 5,748   | 5,702      | 3.4            |
| $^{149}\text{Pm}$         | 229.1     | 206.1     | 204.7   | 205.7   | 204.0      | 12.0           |
| $^{147}\text{Sm}$         | 31.81     | 32.73     | 32.94   | 32.58   | 31.04      | 5.9            |
| $^{148}\text{Sm}$         | 2.04      | 1.42      | 1.42    | 1.42    | 1.42       | 40.1           |
| $^{149}\text{Sm}$         | 9,904     | 10,220    | 10,444  | 10,193  | 10,095     | 5.3            |

**Table 10** Comparison of  $\sigma_{\gamma}$  for  $^{235}\text{U}$ -Th between 120 and 150 fpo days in the inner ring

| Isotope                   | JENDL-3.3 | JENDL-3.2 | JEFF-3  | JEF-2.2 | ENDF/B-6.8 | Max. diff. (%) |
|---------------------------|-----------|-----------|---------|---------|------------|----------------|
| $^{232}\text{Th}$         | 2.37      | 2.35      | 2.31    | 2.36    | 2.39       | 3.3            |
| $^{233}\text{Pa}$         | 21.63     | 21.50     | 21.67   | 21.51   | 21.60      | 0.8            |
| $^{233}\text{U}$          | 10.78     | 10.58     | 10.85   | 10.55   | 10.64      | 2.9            |
| $^{234}\text{U}$          | 29.57     | 30.88     | 30.80   | 30.84   | 30.96      | 4.5            |
| $^{235}\text{U}$          | 15.94     | 15.38     | 16.00   | 15.31   | 15.92      | 4.4            |
| $^{236}\text{U}$          | 11.03     | 10.89     | 11.21   | 11.06   | 10.84      | 3.4            |
| $^{134}\text{Xe}$         | 0.0596    | 0.0584    | 0.0589  | 0.0583  | 0.0641     | 9.6            |
| $^{135}\text{Xe}$         | 272,130   | 270,520   | 272,960 | 268,010 | 270,107    | 1.8            |
| $^{146}\text{Nd}$         | 0.291     | 0.285     | 0.288   | 0.286   | 0.299      | 4.7            |
| $^{147}\text{Nd}$         | 69.14     | 68.71     | 69.36   | 68.49   | 67.46      | 2.8            |
| $^{148}\text{Nd}$         | 0.89      | 1.09      | 1.09    | 1.09    | 1.07       | 19.4           |
| $^{147}\text{Pm}$         | 36.99     | 36.72     | 37.16   | 36.65   | 36.70      | 1.4            |
| $^{148}\text{Pm}$         | 330.2     | 2,348     | 2,372   | 2,358   | 2,358      | 1.3            |
| $^{148\text{m}}\text{Pm}$ |           | 5,282     | 5,345   | 5,260   | 5,292      | 5.6            |
| $^{149}\text{Pm}$         | 217.3     | 191.9     | 193.4   | 191.0   | 192.1      | 13.3           |
| $^{147}\text{Sm}$         | 31.92     | 32.50     | 32.71   | 32.58   | 30.91      | 5.6            |
| $^{148}\text{Sm}$         | 2.09      | 1.41      | 1.42    | 1.42    | 1.42       | 43.6           |
| $^{149}\text{Sm}$         | 9,021     | 9,266     | 9,659   | 9,178   | 9,270      | 6.9            |

than 0.5 b), the maximal difference is larger than 6%; nevertheless, for most of the non-fissile nuclides it keeps lower than 12%. However, JENDL-3.3 and JEFF-3 are respectively responsible for the 17% difference in the fission cross section of  $^{233}\text{Pa}$  (Tables 5–8). The results of JENDL-3.2 are very close to those ones of JEF-2.2 also for the fission cross sections, as already seen for the neutron flux; whereas, the results of JENDL-3.3 are very similar to those ones of JEFF-3.

The discrepancy amid the different libraries for the capture cross sections of the actinides keeps below 4.6% (Tables 8–10), with the only exception of  $^{241}\text{Pu}$ , which exhibits a value of 6.6% (Table 8). The data for the capture cross section of  $^{148\text{m}}\text{Pm}$  is missing on the column referring to JENDL-3.3 and that one of  $^{148}\text{Pm}$  is far away from those ones of the other libraries; these discrepancies might have been generated by a misprocessing of the  $^{148}\text{Pm}$  and

$^{148\text{m}}\text{Pm}$  JENDL-3.3 data by the NJOY99 code; therefore, the maximal difference, in Tables 8–10, excludes the JENDL-3.3 data of  $^{148}\text{Pm}$  and  $^{148\text{m}}\text{Pm}$ . The difference between the five libraries for the capture cross section of the nuclides involved in the production of  $^{135}\text{Xe}$  and  $^{149}\text{Sm}$  generally maintains below 7.5% with the exceptions of  $^{134}\text{Xe}$ ,  $^{146}\text{Nd}$ ,  $^{148}\text{Nd}$  and  $^{148}\text{Sm}$ , which have a small absorption cross section (below 1.5 b), and  $^{149}\text{Pm}$ , which has a short half life (53 h). JENDL-3.3 produces larger values for  $^{149}\text{Pm}$  and  $^{148}\text{Sm}$  and a lower one for  $^{148}\text{Nd}$ ; whereas, ENDF/B generates higher values for  $^{134}\text{Xe}$  and  $^{146}\text{Nd}$ . Finally, let us conclude that the capture cross section maximal difference for  $^{135}\text{Xe}$  is below 1.8%.

In the case of  $^{239}\text{Pu}$ -Th and JEFF-3, the values of the fission and capture cross sections averagely changed only 0.16 and 0.08%, respectively, in a MCB run simulating a total of 6 million neutrons each MCNP call.

**Table 11** Comparison of  $^{135}\text{Xe}$  and  $^{149}\text{Sm}$  mass [g] after 150 fpo days in the inner ring  
1) refers to  $^{239}\text{Pu}$ –Th; 2) does to  $^{233}\text{U}$ –Th; 3) does to  $^{235}\text{U}$ –Th.

| Isotope              | JENDL-3.3 | JENDL-3.2 | JEFF-3 | JEF-2.2 | ENDF/B-6.8 | Max. diff. (%) |
|----------------------|-----------|-----------|--------|---------|------------|----------------|
| 1) $^{135}\text{Xe}$ | 2.68      | 2.74      | 2.78   | 2.71    | 2.80       | 4.4            |
| 2) $^{135}\text{Xe}$ | 1.08      | 1.09      | 1.10   | 1.09    | 1.11       | 2.7            |
| 3) $^{135}\text{Xe}$ | 1.26      | 1.27      | 1.29   | 1.28    | 1.29       | 2.3            |
| 1) $^{149}\text{Sm}$ | 39.36     | 39.71     | 38.80  | 39.73   | 39.59      | 2.4            |
| 2) $^{149}\text{Sm}$ | 8.58      | 9.19      | 9.02   | 9.18    | 9.26       | 7.5            |
| 3) $^{149}\text{Sm}$ | 12.59     | 13.57     | 13.12  | 13.57   | 13.53      | 7.4            |

## IX. $^{135}\text{Xe}$ and $^{149}\text{Sm}$ Mass

### 1. Physical Considerations

**Table 11** reports the mass of  $^{135}\text{Xe}$  and  $^{149}\text{Sm}$  after 150 fpo days; we can note that  $^{239}\text{Pu}$ –Th has an higher accumulation of these two fission products than the uranium thorium due to higher fission yields (Figs. 7 and 8); whereas, the higher quantity of xenon and samarium in  $^{235}\text{U}$ –Th, compared to  $^{233}\text{U}$ –Th, is explained by the higher initial mass of  $^{235}\text{U}$ , compared to  $^{233}\text{U}$  (797 and 614 kg, respectively).

Let us remark that  $^{149}\text{Pm}$  and  $^{146}\text{Nd}$  give, respectively, an higher and lower contribution to the accumulation of  $^{149}\text{Sm}$  in  $^{239}\text{Pu}$ –Th than in uranium–thorium (see fission yields in Fig. 8 as well as Figs. 1.2–1.4 of Soodak);<sup>42)</sup> the above remark suggests that  $^{148}\text{Pm}$  and  $^{148\text{m}}\text{Pm}$  transmutation paths to  $^{149}\text{Sm}$  contribute more for uranium–thorium than for  $^{239}\text{Pu}$ –Th.

### 2. Comparative Studies

The maximal difference between the different nuclear data libraries of the  $^{135}\text{Xe}$  mass maintains below 4.5% (Table 11), this value is higher than that one referring to the capture cross section, 1.8%, because of the influence of other isotopes in the  $^{135}\text{Xe}$  transmutation chain.

The incorrect cross sections data of  $^{148}\text{Pm}$  and  $^{148\text{m}}\text{Pm}$  make the mass of  $^{149}\text{Sm}$  obtained by JENDL-3.3 a little different from that one obtained by the other libraries; this effect is more visible for uranium–thorium fuels, where the maximal difference reaches the value of 7.5%; the discrepancy is mitigated for the  $^{239}\text{Pu}$ –Th fuel due to the different weight of the transmutation paths (as seen in Sec. IX-1).

## X. Conclusions

The higher microscopic cross section of  $^{239}\text{Pu}$  at the thermal energies coupled to a high capture branch make difficult to operate the reactor with a thorium fuel based on plutonium. The uranium isotopes, with an enrichment of 3.3–4.2% in the fuel, offer a much better neutron economy and they allow an operation of 330 fpo days by the depletion of 60 kg of  $^{233}\text{U}$  or 220 kg of  $^{235}\text{U}$ . The build up of  $^{233}\text{Pa}$  reaches the asymptotic value after 5 months.

Concerning the comparative studies, the  $k_{\text{eff}}$  curves referring to JENDL-3.2 superimpose with those ones referring to JEF-2.2; ENDF/B-6.8 always produces the lowest  $k_{\text{eff}}$  value. The maximal difference of the neutron flux keeps always lower than 9.4%; without the data of ENDF/B the result

would reduce to 8%. Moreover, the values of JENDL-3.2 are very close to those ones of JEF-2.2; whereas, JEFF-3 and JENDL-3.3 generally produce a flux respectively higher and lower than those ones of the two previous libraries; ENDF/B-6.8 generates the highest estimation of the neutron flux. The transmutation curves referring to JENDL-3.2 superimpose with those ones referring to JEF-2.2. ENDF/B-6.8 shows a higher build up and burnup compared to JEFF-3, the latter one does compared to JEF-2.2/JENDL-3.2 and the latter one does compared to JENDL-3.3.

The maximal difference of the fission cross section of the trigger isotope is always lower than 2% and that one of the most abundant actinides keeps below 6%; the few isotopes that exceed this threshold have a very low fission cross section. The maximal difference of the capture cross section of the actinides generally maintains below 5% and that one of the fission products involved in the production of samarium and xenon remains below 7.5%, with the exceptions of the isotopes that have a small absorption cross section (below 1.5 b) and  $^{149}\text{Pm}$ , which has a short half life.

## References

- 1) A. Talamo, W. Gudowski, F. Venneri, "The burnup capabilities of the Deep Burn Modular Helium Reactor analyzed by the Monte Carlo Continuous Energy Code MCB," *Ann. Nucl. Energy*, **31**[2], 173–196 (2004).
- 2) A. Talamo, W. Gudowski, J. Cetnar, F. Venneri, "Key physical parameters and temperature reactivity coefficients of the deep burn modular helium reactor fueled with LWRs waste," *Ann. Nucl. Energy*, **31**[16], 1913–1937 (2004).
- 3) A. Talamo, W. Gudowski, J. Cetnar, "Comparative studies of ENDF/B-6.8, JEF-2.2 and JENDL-3.2 Data Libraries by Monte Carlo Modeling of High Temperature Reactors on plutonium based fuel cycles," *J. Nucl. Sci. Technol.*, **41**[12], 1228–1236 (2004).
- 4) A. Talamo, W. Gudowski, "A deep burn fuel management strategy for the incineration of military plutonium in the Gas Turbine-Modular Helium Reactor Modeled in a detailed 3D geometry by the Monte Carlo Continuous Energy Burnup Code," *Nuc. Sci. Eng.*, Submitted for publication, (2005).
- 5) A. Talamo, W. Gudowski, "Performance of the Gas Turbine-Modular Helium Reactor fuelled with different types of fertile TRISO particles," *Ann. Nucl. Energy*, **32**[16], 1719–1749 (2005).
- 6) General Atomics, *GT-MHR Conceptual Design Description Report*, GA/NRC-337-02, (2002).
- 7) C. Rodriguez, A. Baxter, *et al.*, "Deep-Burn: making nuclear waste transmutation practical," *Nucl. Eng. Des.*, **222**, 299–

- 317 (2003).
- 8) N. Kodochigov, Y. Sukharev, *et al.*, "Neutronic features of the GT-MHR," *Nucl. Eng. Des.*, **222**, 161–171 (2003).
  - 9) R. Plukiene, D. Ridikas, "Modeling of HTRs with Monte Carlo: from a homogeneous to an exact heterogeneous core with microparticles," *Ann. Nucl. Energy*, **30**, 1573–1585 (2003).
  - 10) A. Baxter, M. Fikani, *Reactor-based Transmutation—Physics Studies of the Gas-cooled Graphite-moderated Deep Burn Reactor*, GA-501-0-TRT-000140, General Atomics, (2002).
  - 11) M. Labar, *The Gas Turbine-Modular Helium Reactor: A Promising Option for Near Term Deployment*, GA-A23952, General Atomics, (2002).
  - 12) A. Baxter, C. Rodriguez, "The application of gas-cooled reactor technologies to the transmutation of nuclear waste," *Prog. Nucl. Energy*, **38**, 81–105 (2001).
  - 13) K. Ohashi, F. Okamoto, H. Hayakawa, "Modular high temperature reactor contributing the global environmental protection," *Prog. Nucl. Energy*, **37**, 307–312 (2000).
  - 14) Y. Tsuchie, "Desirability of small reactors, HTGR in particular," *Prog. Nucl. Energy*, **37**, 253–258 (2000).
  - 15) A. I. Kiryushin, N. G. Kodochigov, N. G. Kouzavkov, *et al.*, "Project of the GT-MHR high temperature helium reactor with gas turbine," *Nucl. Eng. Des.*, **173**, 119–129 (1997).
  - 16) J. D. Wistrom, W. A. Simon, "Where does the GT-MHR go from here?," *Nucl. Eng. Int.*, **41**, 10 (1996).
  - 17) A. S. Shenoy, *Modular Helium Reactor for Non-electric Applications of Nuclear Energy*, GA-A22701, General Atomics, (1995).
  - 18) M. P. Labar, W. A. Simon, *Comparative Economics of the GT-MHR and Power Generation Alternatives*, GA-A 21722, General Atomics, (1994).
  - 19) H. Gruppelaar, J. P. Schapira, *Thorium as a Waste Management Option*, EUR-19142, European Commission, (2000).
  - 20) J. Cetnar, W. Gudowski, J. Wallenius, "Monte Carlo continuous energy burnup MCB1C—The description, methods and benchmarks," In preparation for *Nucl. Sci. Eng.*
  - 21) J. Cetnar, W. Gudowski, J. Wallenius, K. Tucek, "Simulation of nuclide transmutation with Monte-Carlo Continuous Energy Burnup Code (MCB1C)," *Proc. Accelerator Application 2001 and ADTTA 2001 Nuclear Application in the New Millennium*, Reno, (2001).
  - 22) J. Cetnar, W. Gudowski, J. Wallenius, *MCB: A Continuous Energy Monte Carlo Burnup Simulation Code, in Actinide and Fission Product Partitioning and Transmutation*, EUR 18898 EN, OECD/NEA 523, (1999).
  - 23) J. F. Briesmeister, *A general Monte Carlo N-Particle Transport Code—Version 4c*, LANL, LA-13709-M, (2002).
  - 24) G. Fea, "Tabelle Riassuntive e Bibliografia delle Trasmutazioni Artificiali," *Nuovo Cimento*, **6**, 1 (1935).
  - 25) S. Igarasi, T. Nakagawa, Y. Kikuchi, T. Asami, T. Narita, *Japanese Evaluated Nuclear Data Library, Version-1, JENDL-1*, JAERI 1261, (1979).
  - 26) T. Nakagawa, *Summary of JENDL-2 General Purpose File*, JAERI-M 84–103, (1984).
  - 27) K. Shibata, T. Nakagawa, T. Asami, T. Fukahori, T. Narita, S. Chiba, M. Mizumoto, A. Hasegawa, Y. Kikuchi, Y. Nakajima, S. Igarasi, *Japanese Evaluated Nuclear Data Library, Version-3, JENDL-3*, JAERI 1319, (1990).
  - 28) M. Kawai, S. Iijima, T. Nakagawa, Y. Nakajima, T. Sugi, T. Watanabe, H. Matsunobu, M. Sasaki, A. Zukeran, "JENDL-3 Fission Product Nuclear Data Library," *J. Nucl. Sci. Technol.*, **29**, 195 (1992).
  - 29) T. Nakagawa, K. Shibata, S. Chiba, T. Fukahori, Y. Nakajima, Y. Kikuchi, T. Kawano, Y. Kanda, T. Ohsawa, H. Matsunobu, M. Kawai, A. Zukeran, T. Watanabe, S. Igarasi, K. Kosako, T. Asami, "Japanese Evaluated Nucl. Data Library Version 3 Revision-2: JENDL-3.2," *J. Nucl. Sci. Technol.*, **32**, 1259 (1995).
  - 30) *JENDL-3.2, The Japanese Evaluated Nucl. Data Library*, IAEA-NDS-110, Rev. 5, (1994).
  - 31) K. Shibata, T. Kawano, T. Nakagawa, O. Iwamoto, J. Katakura, T. Fukahori, S. Chiba, A. Hasegawa, T. Murata, H. Matsunobu, T. Ohsawa, Y. Nakajima, T. Yoshida, A. Zukeran, M. Kawai, M. Baba, M. Ishikawa, T. Asami, T. Watanabe, Y. Watanabe, M. Igashira, N. Yamamuro, H. Kitazawa, N. Yamano, H. Takano, "Japanese Evaluated Nuclear Data Library Version 3 Revision-3: JENDL-3.3," *J. Nucl. Sci. Technol.*, **39**, 1125 (2002).
  - 32) C. Nordborg, M. Salvatores, "Status of the JEF Evaluated Data Library," *Proc. Int. Conf. on Nuclear Data for Science and Technology*, Gatlinburg, Tennessee, USA, May 9–13, 1994, Vol. 2, p. 680 (1994).
  - 33) J. Blachot, C. Nordborg, "JEF-2.2 Radioactive Decay Data," *Int. Symp. on Nuclear Data Evaluation Methodology*, BNL, (1992).
  - 34) R. Jacqmin, R. Forrest, J. Rowlands, A. Nouri, M. Kellett, "Status of the JEFF-3 Project," *Proc. Int. Conf. on Nuclear Data for Science and Technology*, Oct. 7–12, 2001, Vol. 1, p. 54 (2002).
  - 35) P. F. Rose, *ENDF-201, ENDF/B-VI Summary Documentation*, BNL-NCS-17541, 4th Ed., (1991).
  - 36) *ENDF/B-VI, The US Evaluated Nuclear Data Library*, IAEA-NDS-110, Rev. 6, (1995).
  - 37) R. B. Firestone, V. S. Shirley, C. M. Baglin, S. Y. F. Chu, J. Zipkin, *The 8<sup>th</sup> Edition of the Table of Isotopes, book and cdrom*, John Wiley & Sons, (1996).
  - 38) M. J. Bell, *ORIGEN—The ORNL Isotope Generation and Depletion Code*, ORNL-4628 UC-32, (1973).
  - 39) F. M. Mann, R. E. Schenter, *Nucl. Sci. Eng.*, **63**, 242–249 (1977).
  - 40) A. Wahl, *Phys. Rev. C*, **32**, 184 (1985).
  - 41) K. Suyama, J. Katakura, T. Kiyosumi, T. Kaneko, Y. Nomura, "Comparison of burnup results using several evaluated nuclear data file," *J. Nucl. Sci. Technol.*, **39**[1], 82–89 (2002).
  - 42) H. Soodak, *Reactor Handbook*, John Wiley & Sons, Vol. III, Part A, (1962).



Technical note

# Adapting the deep burn in-core fuel management strategy for the gas turbine – modular helium reactor to a uranium–thorium fuel

Alberto Talamo <sup>\*</sup>, Waclaw Gudowski

*Department of Nuclear and Reactor Physics, Royal Institute of Technology,  
Roslagstullsbacken 21, S-10691, Stockholm, Sweden*

Received 7 July 2005; accepted 29 July 2005

Available online 12 September 2005

---

## Abstract

In 1966, Philadelphia Electric has put into operation the Peach Bottom I nuclear reactor, it was the first high temperature gas reactor (HTGR); the pioneering of the helium-cooled and graphite-moderated power reactors continued with the Fort St. Vrain and THTR reactors, which operated until 1989. The experience on HTGRs lead General Atomics to design the gas turbine – modular helium reactor (GT-MHR), which adapts the previous HTGRs to the generation IV of nuclear reactors. One of the major benefits of the GT-MHR is the ability to work on the most different types of fuels: light water reactors waste, military plutonium, MOX and thorium. In this work, we focused on the last type of fuel and we propose a mixture of 40% thorium and 60% uranium. In a uranium–thorium fuel, three fissile isotopes mainly sustain the criticality of the reactor:  $^{235}\text{U}$ , which represents the 20% of the fresh uranium,  $^{233}\text{U}$ , which is produced by the transmutation of fertile  $^{232}\text{Th}$ , and  $^{239}\text{Pu}$ , which is produced by the transmutation of fertile  $^{238}\text{U}$ . In order to compensate the depletion of  $^{235}\text{U}$  with the breeding of  $^{233}\text{U}$  and  $^{239}\text{Pu}$ , the quantity of fertile nuclides must be much larger than that one of  $^{235}\text{U}$  because of the small capture cross-section of the fertile nuclides, in the thermal neutron energy range, compared to that one of  $^{235}\text{U}$ . At the same time, the amount of  $^{235}\text{U}$

---

<sup>\*</sup> Corresponding author. Fax: +46 8 5537 8465.

E-mail address: [alby@neutron.kth.se](mailto:alby@neutron.kth.se) (A. Talamo).

must be large enough to set the criticality condition of the reactor. The simultaneous satisfaction of the two above constrains induces the necessity to load the reactor with a huge mass of fuel; that is accomplished by equipping the fuel pins with the JAERI TRISO particles. We start the operation of the reactor with loading fresh fuel into all the three rings of the GT-MHR and after 810 days we initiate a refueling and shuffling schedule that, in 9 irradiation periods, approaches the equilibrium of the fuel composition. The analysis of the  $k_{\text{eff}}$  and mass evolution, reaction rates, neutron flux and spectrum at the equilibrium of the fuel composition, highlights the features of a deep burn in-core fuel management strategy for a uranium–thorium fuel.

© 2005 Elsevier Ltd. All rights reserved.

---

## 1. Introduction

The development of high temperature gas reactors (HTGRs) evolved parallelly into two branches: power and research reactors. The first power HTGR, the Peach Bottom I (in Pennsylvania), has been finished to construct in 1966 by Philadelphia Electric; it had a power of 115 MW<sub>th</sub> and an outlet temperature of 1000 °C. A decade after, General Atomics (GA) put into operation the Fort St. Vrain reactor (in Colorado) which had a much larger power, 842 MW<sub>th</sub>; in 1986, Hochttemperatur Kernkraftwerk GmbH (HKG) launched the Thorium High Temperature Reactor (THTR) (in Germany), which utilized for the first time graphite pebbles. At the same time, two research HTGRs have been built in Europe: the British Dragon, in 1966, and the German Arbeitsgemeinschaft Versuchsreaktor (AVR), in 1967, with a thermal power of 20 and 46 MW<sub>th</sub>, respectively. At the beginning of the new millennium, the investigation on the HTGRs started in Asia by the Japanese HTR-2000 and the Chinese HTR-10, which became operative in the year 2000 and 2003, respectively, with a power of 30 and 10 MW<sub>th</sub>. [Table 1](#) briefly summarizes the history and technical data of the major HTGRs. In year 2002, GA submitted to the US Nuclear Regulatory Commission its latest design of HTGR ([General Atomics, 2002](#)): the Gas Turbine – Modular Helium Reactor (GT-MHR), which has a power of 2400 MW<sub>th</sub> and it is structured into 4 HTGRs modules of 600 MW<sub>th</sub> ([Baxter and Fikani, 2002](#); [Baxter and Rodriguez, 2001](#); [Kiryushin et al., 1997](#); [Kodochigov et al., 2003](#); [Labar, 2002](#); [Labar and Simon, 1994](#); [Ohashi et al., 2000](#); [Plukiene and Ridikas, 2003](#); [Rodriguez et al., 2003](#); [Shenoy, 1995](#); [Tsuchie, 2000](#); [Wistrom and Simon, 1996](#)).

One of the key benefits of the HTGRs, and therefore of the GT-MHR, is the utilization of the fuel in the form of actinide oxide confined into TRISO particles; in fact, the ratio between the width of the cladding and the radius of the fuel is above 1.5 for TRISO particles and only 0.14 for ordinary light water reactors (LWRs) fuel pins. Ordinary TRISO particles are composed of an actinide oxide central sphere (kernel) covered by: a porous carbon layer, an inner pyrocarbon layer, a ZrC layer and an outer pyrocarbon layer. The inner pyrocarbon layer usually is the first layer of a TRISO particle that fails, since it is subjected to counteracting mechanical



Table 1  
 Technical data of the power (normal text) and research (italics text) high temperature gas reactors

|                                  | Peach<br>Bottom I                               | Fort St.<br>Vrain                              | THTR                      | <i>Dragon</i>                                   | <i>AVR</i>           | <i>HTTR</i>                                    | <i>HTR-10</i>         |
|----------------------------------|---|--|---------------------------|---|----------------------|--|-----------------------|
| Operation                        | 1966–1974                                       | 1966–1989                                      | 1986–1989                 | 1966–1975                                       | 1967–1988            | 2000   | 2003                  |
| Power (MW <sub>th</sub> )        | 115   | 842  | 750                       | 20  | 46                   | 30   | 10                    |
| Coolant                          |   |  |                           |   |                      |  |                       |
| Pressure (MPa)                   | 2.5   | 4.8  | 4                         | 2   | 1.1                  | 4  | 3                     |
| Inlet/outlet<br>temperature (°C) | 344/750   | 406/785  | 250/750                   | 350/750   | 270/950              | 395/950  | 300/900               |
| Fuel                             |   |  |                           |   |                      |  |                       |
| Type                             | (U-Th)C <sub>2</sub><br>PyC coated<br>particles | (U-Th)C <sub>2</sub><br>TRISO                  | (U-Th)O <sub>2</sub> BISO | (U-Th)C <sub>2</sub><br>PyC coated<br>particles | UO <sub>2</sub> BISO | UO <sub>2</sub> TRISO                          | UO <sub>2</sub> TRISO |
| Peak temperature (°C)            | 1000  | 1260   | 1350                      | 1000  | 1350                 | 1250   |                       |
| Form                             | Graphite<br>compacts in<br>hollow rods          | Graphite<br>compacts<br>in hexagonal<br>blocks | Graphite pebbles          | Graphite<br>hexagonal<br>blocks                 | Graphite pebbles     | Graphite<br>compacts in<br>hexagonal<br>blocks | Graphite<br>pebbles   |

stresses: swelling, due to the pressure of fission products gases, and shrinkage, due to the neutron irradiation. This phenomenon may be mitigated by a new type of TRISO particles which introduces two more layers: a porous pyrocarbon layer, after the porous graphite layer, and a pyrocarbon-ZrC layer, before the ZrC layer. In the new type of TRISO particles the density change between the different layers is more gradual so that mechanical stresses attenuate; moreover, in order to allocate more volume for the gaseous fission products, the density of the porous carbon layer is lower. The new type of TRISO particles reduce the gaseous fission products release (release/build) by a factor 10–15 comparing to the ordinary TRISO particles at parity of irradiation conditions (Odeychuk et al., 2004). Irradiation conditions are very important for the measure of the release of fission products, e.g. just a change of 50 °C in the temperature affects the value by a factor 10 (Nabielek et al., 2004). Let us remind also that the manufacture process, in which the Germans have a long time experience (Nickel et al., 2002), is extremely important for the functioning of TRISO particles. In fact, during the manufacture, in the case of large mechanical tolerances, the failure may be generated, by the isostatic sphere pressure of particles touching each other, when the radius of the kernel is larger than designed and the thicknesses of the layers smaller (Nabielek et al., 2004).

## 2. The GT-MHR operating on LWRs waste, military plutonium and uranium–thorium

In our previous studies (Talamo et al., 2004a,b,c; Talamo and Gudowski, 2005), we focused on the burnup capacities of the GT-MHR operating on LWRs waste and military plutonium by a refueling and shuffling schedule called deep burn. In the deep burn strategy, the irradiation time is divided into two periods of three years each.

For the fuel based on LWRs waste, we utilize the driver fuel (DF), during the first irradiation period, and the transmutation fuel (TF), during the second one; after the first period, the spent fuel is reprocessed by extraction of the fission products. The DF contains neptunium and plutonium from the reprocessing of LWRs waste and it maintains the criticality of the reactor by the depletion of the fissile isotopes. The TF consists of irradiated DF plus some set-aside americium and curium from the reprocessing of the LWRs waste; TF depletes non-fissile isotopes by capture, followed by natural decay or fission, and it also offers a negative reactivity feedback. The deep burn strategy, for the fuel based on LWRs waste, produces the incineration of 94% of  $^{239}\text{Pu}$ , 61% of plutonium and 53% of all actinides.

In the fuel cycle based on military plutonium, the DF is composed of 94% of  $^{239}\text{Pu}$  and 6% of  $^{240}\text{Pu}$ ; therefore, the irradiated DF is so rich in fissile plutonium that it is not suitable to provide a negative reactivity feedback. At the light of the above consideration, we referred to the TF, for the fuel based on military plutonium, as post driver fuel (PDF). The high reactivity of military plutonium, forces both to model the control rods and to add erbium as burnable poison. The deep burn strategy, for the fuel based on military plutonium, produces the incineration of 92% of  $^{239}\text{Pu}$ .

In the present work, we tried to implement a deep burn refueling and shuffling schedule for a fuel based on a mixture of 40% thorium and 60% uranium, enriched 20% in  $^{235}\text{U}$ . Since we do not propose any reprocessing of the irradiated fuel, we refer to the fuel during the first three years of irradiation as DF and during the following three years as PDF; of course, DF is richer in  $^{235}\text{U}$  than PDF. For the case of uranium–thorium fuel, we did not add any burnable poison since the captures of the fertile isotopes already keep close to criticality the reactor; whereas, we modeled the control rods. A fuel based on thorium exhibits several valuable benefits (Herring et al., 2001; Gruppelaar and Schapira, 2000; Rütten and Haas, 2000; Lung and Gremm, 1998):

- Large resources of thorium are available all over the world.
- Fuel consumption in thorium fueled reactors is 5–10 times less than presents uranium consumption in LWRs.
- Consequently, the total radioactive waste mass production is about two orders of magnitude lower than in the case of present LWRs (Gruppelaar and Schapira, 2000).

### 3. Equilibrating the burnup of $^{235}\text{U}$ with the breeding of $^{233}\text{U}$ and $^{239}\text{Pu}$

Fresh fuel contains two fertile isotopes,  $^{232}\text{Th}$  (natural thorium contains only this isotope) and  $^{238}\text{U}$ , and one fissile isotope,  $^{235}\text{U}$ . When  $^{232}\text{Th}$  undergoes a neutron capture it becomes  $^{233}\text{Th}$  and it transmutes first into  $^{233}\text{Pa}$  and then into fissile  $^{233}\text{U}$ , with a corresponding half life of 22 min and 27 days, respectively. When  $^{238}\text{U}$  undergoes a neutron capture it becomes  $^{239}\text{U}$  and it transmutes first into  $^{239}\text{Np}$  and then into fissile  $^{239}\text{Pu}$ , with a corresponding half life of 23 min and 2.4 days, respectively. If the fertile isotopes are abundantly present in the fuel, then the breed of  $^{233}\text{U}$  and  $^{239}\text{Pu}$  compensates the depletion of  $^{235}\text{U}$  (fresh uranium fuel is enriched 20% in  $^{235}\text{U}$ ).

Fig. 1 compares the capture cross-section of  $^{232}\text{Th}$  and  $^{238}\text{U}$  with the fission one of the fissile isotopes both in the thermal neutron energy range and in the fast one; we can note that the capture cross-section of the fertile nuclides in the thermal range (the spectrum averaged over the core of the GT-MHR has a peak at 0.2 eV) is about 100 times smaller than the fission cross-section of uranium fissile isotopes and about 800 times than that one of  $^{239}\text{Pu}$ ; therefore, in order to equilibrate the breeding of  $^{233}\text{U}$  and  $^{239}\text{Pu}$  with the depletion of  $^{235}\text{U}$ , the mass of  $^{232}\text{Th}$  and  $^{238}\text{U}$  must be much larger than that one of  $^{235}\text{U}$ . However, at the same time, the total mass of  $^{235}\text{U}$  must be great enough to set the criticality condition of the reactor. The simultaneous satisfactions of the two above constrains arises the need of a huge mass of fuel to operate the reactor; therefore, we utilized the Japan Atomic Energy Research Institute (JAERI) TRISO particles (Minato et al., 2000) for they have a radius of the kernel twice as long as that one of the current GA TRISO particles.

Fig. 2 plots the capture to fission ratio, in literature known also as the alpha factor, of the fissile isotopes; we can note that the neutron economy in the thermal range is much more efficient for uranium than for plutonium. The latter remark underlines the difficulty to operate the GT-MHR on a plutonium–thorium fuel. In fact, not only

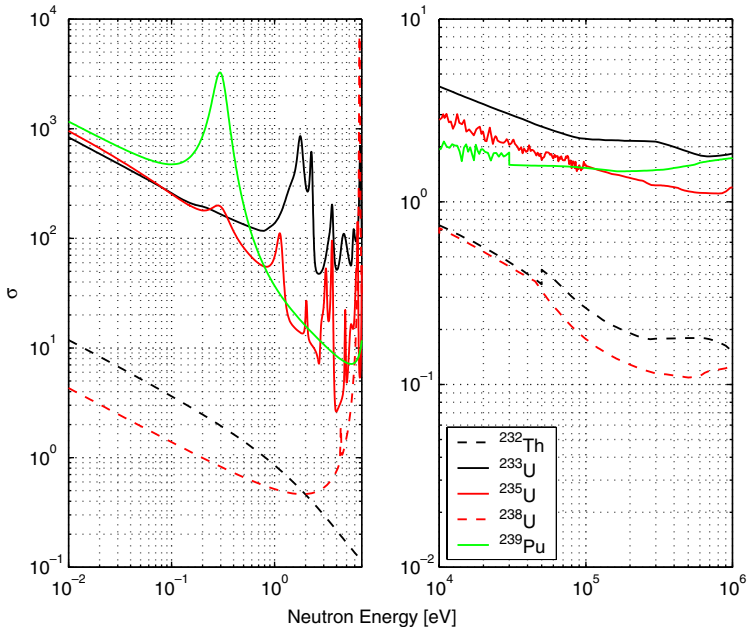


Fig. 1. Capture cross-section of  $^{232}\text{Th}$  and  $^{238}\text{U}$  compared to the fission cross-sections of  $^{233}\text{U}$ ,  $^{235}\text{U}$  and  $^{239}\text{Pu}$  in the thermal energy range (left) and in the fast one (right). The data of JEF-2.2 have been supplied by JANIS-2.0.

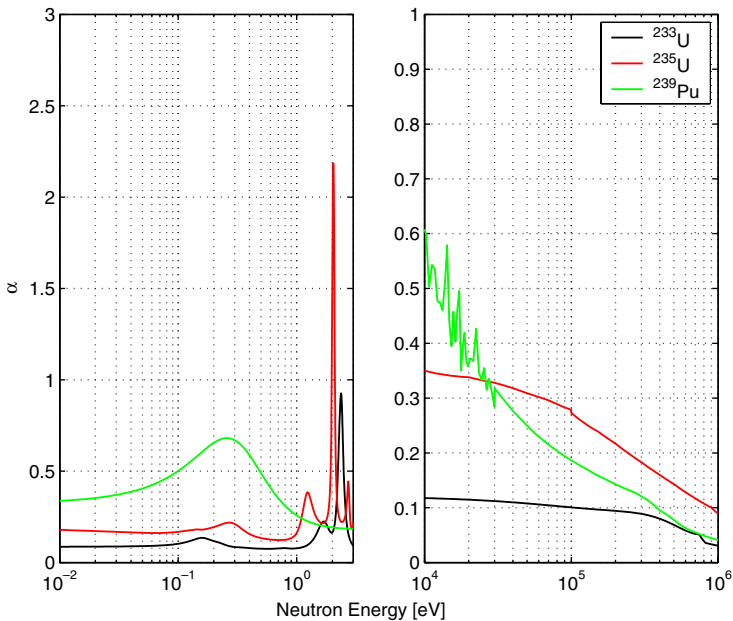


Fig. 2. Capture to fission ratio of  $^{233}\text{U}$ ,  $^{235}\text{U}$  and  $^{239}\text{Pu}$  in the thermal energy range (left) and in the fast one (right). The data of JEF-2.2 have been supplied by JANIS-2.0.

the plutonium neutron economy is worse than uranium, at thermal energies, but also the mass of thorium for a plutonium–thorium fuel should be 8 times larger than that one for a uranium–thorium fuel to properly balance the reaction rates (as discussed previously).

If one be would design a reactor with the same type of fuel but operating in a fast energy spectrum, the capture cross-section of  $^{232}\text{Th}$  and  $^{238}\text{U}$  become only 10 times smaller than those ones of the fissile isotopes (Fig. 1). In addition, in the fast energy range the difference between the capture to fission ratio of  $^{239}\text{Pu}$  and that one of  $^{233}\text{U}$  and  $^{235}\text{U}$  attenuate (Fig. 2). This indicates a fast reactor may have better performances with a Th–U–Pu fuel.

#### 4. The modeling of the gas turbine – modular helium reactor

We modeled the GT-MHR as a  $12 \times 12$  matrix of H451 reactor grade graphite hexagonal blocks, with an interstitial gap of 0.1 cm, confined into a cylinder of 3.5 m radius and 10 m height. Three concentric rings of hexagonal blocks are equipped with fuel pins; each pin axially covers only 7.93 m of the height of the reactor, since at top and at the bottom of the reactor two equally long cylinders of graphite act as neutron reflectors. The horizontal section of the reactor core is shown at top of Fig. 3 and enlarged in Fig. 4; the GT-MHR is equipped with 12 startup control rods located in the inner fuel ring, 18 shutdown ones, 6 in the central ring and 12 in the outer ring, and 36 operational ones in the outer graphite reflector blocks. We have kept all control rods full extracted during the operation of the reactor because we focused only at the transmutation analysis and because the excess of reactivity at the beginning of each irradiation period is relatively small. A control rod consists of a cylinder of graphite filled by a lattice of TRISO particles containing boron carbide with an enrichment of 90% in  $^{10}\text{B}$ ; the operational rods are cave cylinders, whereas the shutdown and startup ones are plenum cylinders. A fuel hexagonal block, equipped with a control rod, allocates 95 coolant channels, 128 DF and 64 PDF pins (Fig. 5); the previous numbers, respectively, increase to 108, 144 and 72 (Table 2) for a block not equipped with control rods. Since the number of DF pins is twice as much as that one of PDF pins, the volume of DF is double than the volume of PDF. All the geometry data of the reactor are shown in Table 2, whereas Table 3 contains the material data.

Since the coolant enters the reactor at 485 °C and it exits at 850 °C, we have set the temperature of the fuel in the TRISO particles to 1500 °C and the temperature of all other materials to 1200 °C, with the exception of that one in the carbon in the pure graphite hexagonal blocks (all the blocks without fuel pins or operational control rods), which has been set to 800 °C.

#### 5. The Monte Carlo numerical simulations

The burnup numerical calculations have been performed by Monte Carlo Continuous Energy (MCB) code (Cetnar et al., 2001, 1999), version 1c2, which is an exten-

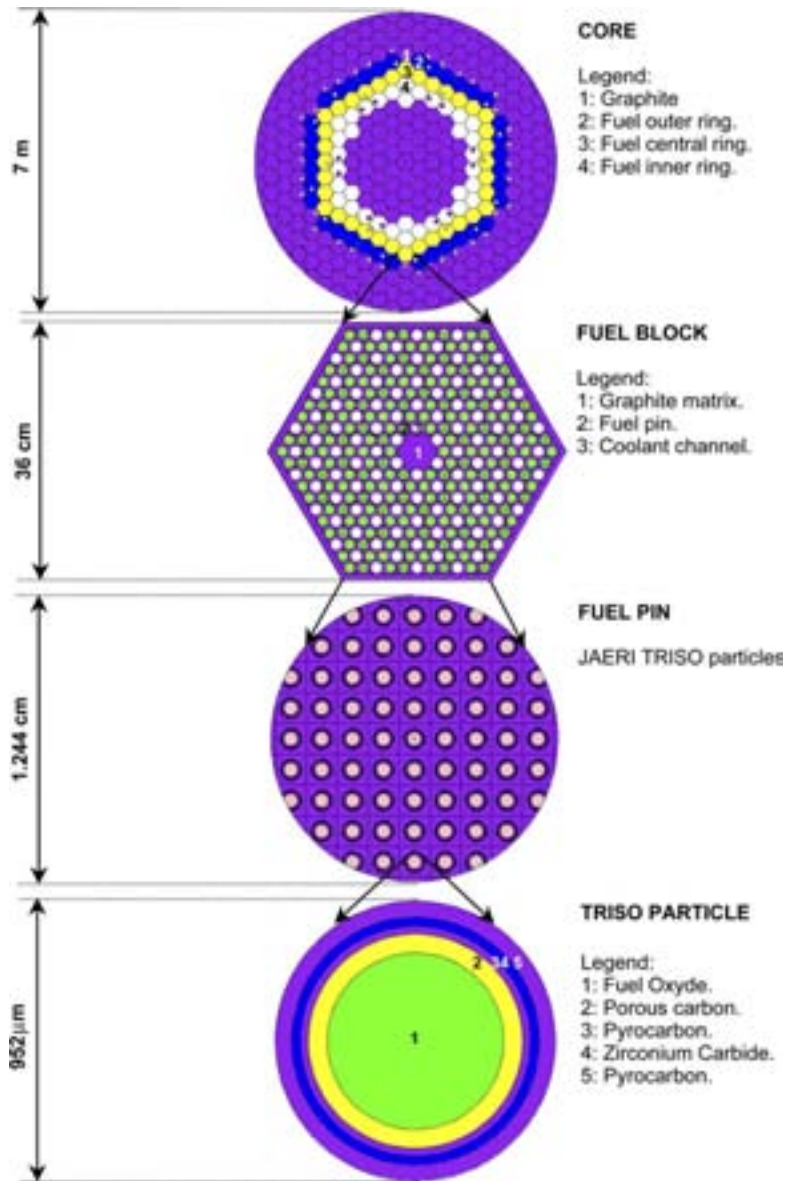


Fig. 3. The gas turbine – modular helium reactor plotted by MCNP.

sion of the well known MCNP code, version 4c3 (Briesmeister, 2002). We equipped the MCB code with a nuclear data library based on JEF-2.2 (Blachot and Nordborg, 1992; Nordborg and Salvatores, 1994) and enlarged with JENDL-3.2, ENDF/B-6.8, DCL-200 and EAF-99. We handled the triple heterogeneity of the GT-MHR in a

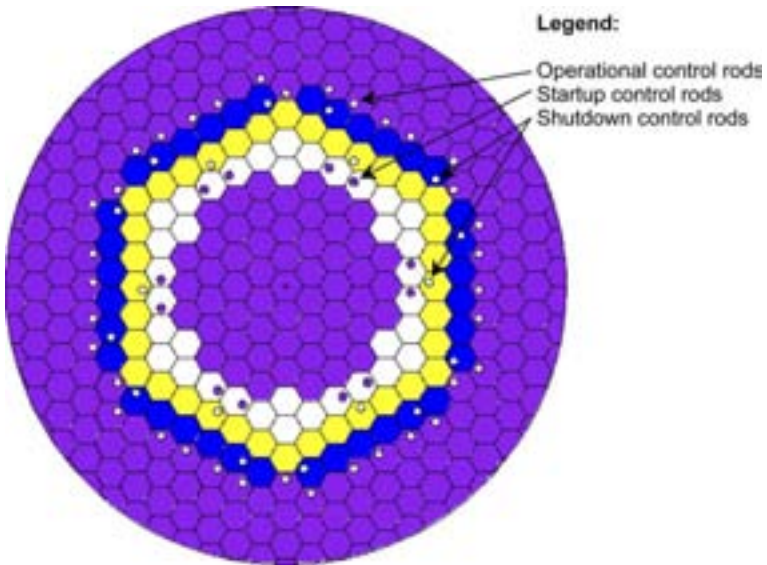


Fig. 4. Core of the gas turbine – modular helium reactor plotted by MCNP.

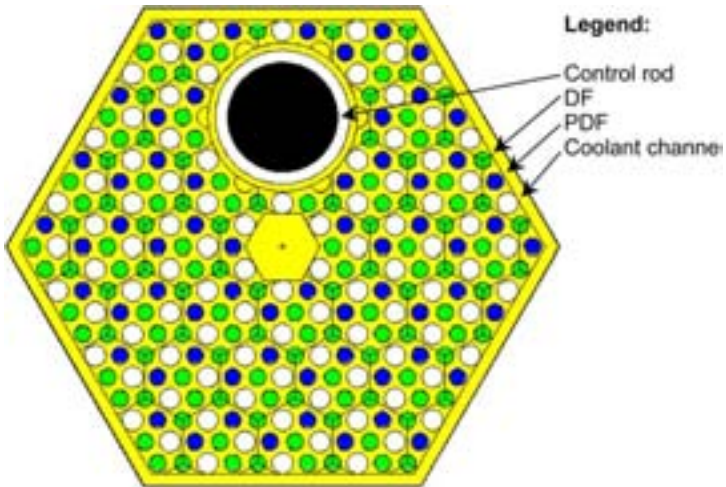


Fig. 5. Fuel block, equipped with a control rod, of the gas turbine – modular helium reactor plotted by MCNP.

detailed three-dimensional model, as shown in the previous paragraph. Moreover, we simulated the evolution of the fuel composition with a continuous energy approach. We remand to our previous papers for further details on the MCB code (Talamo et al., 2004a).

Table 2

## Geometry data of the GT-MHR

|  |                 |
|--|-----------------|
| <i>Core</i>  |                 |
| Radius (cm)  | 350             |
| Height (cm)  | 1000            |
| <i>Control rods</i>  |                 |
| Startup (inner ring)   | 12              |
| Operational (outer moderator reflector ring)                               | 36              |
| Shutdown (central ring/outer ring)   | 6/12            |
| Internal radius (startup/operational/shutdown) (cm)                        | 0/2.64/0        |
| External radius (cm)   | 4.13            |
| Hole radius (cm)   | 5.05            |
| Distance from the center of the hexagon (cm)                               | 9.75614         |
| Height at bol (startup/operational/shutdown) (cm)                          | 0/0/0           |
| <i>Hexagonal fuel blocks</i>   |                 |
| Number   | 36 × 3          |
| Width (cm)   | 35.99688        |
| Height (cm)  | 793             |
| Interstitial gap (cm)  | 0.1             |
| <i>Fuel blocks</i>   |                 |
| DF pins (with control rod/without control rod)                             | 144/128         |
| PDF pins (with control rod/without control rod)                            | 72/64           |
| Coolant channels (with control rod/without control rod)                    | 108/95          |
| <i>Pins</i>  |                 |
| Radius (cm)  | 0.6223          |
| Height (cm)  | 793             |
| Distance between pins (cm)   | 3.25628         |
| Hole radius (fuel/coolant channel) (cm)                                    | 0.635/0.795     |
| <i>TRISO particles</i>   |                 |
| Kernel radius (GA/JAERI/control rods) (μm)                                 | 150/300/300     |
| Width porous carbon layer (GA/JAERI/control rods) (μm)                     | 150/64/50       |
| Width inner pyrocarbon layer (GA/JAERI/control rods) (μm)                  | 35/26/15        |
| Width ZrC layer (GA/JAERI) (μm)  | 35/31           |
| Width outer pyrocarbon layer (GA/JAERI) (μm)                               | 40/55           |
| Distance between particles (JAERI/control rods) (cm)                       | 0.134/0.12      |
| Packing fraction (JAERI/control rods) (%)                                  | 37.55/23.57     |
| <i>Fuel total volume</i>   |                 |
| PF (inner ring/central ring) (outer ring = inner ring) (cm <sup>3</sup> )  | 452,758/461,464 |
| PDF (inner ring/central ring) (outer ring = inner ring) (cm <sup>3</sup> ) | 226,378/230,732 |

We performed all the numerical simulations on a cluster of ten 1800 MHz 64 bits AMD Opteron processors mounted of five Tyan Tiger-K8W dual processor motherboards. The computer cluster operated on Linux Mandrake9.2-Erbium and Parallel Virtual Machine (PVM) version 3.4.4.16, which is the first release supporting the compilation on the 64-bits architecture.



Table 3  
Material data of the GT-MHR

| Material                | Atomic percentage (%)   | Initial density (g/cm <sup>3</sup> ) |
|-------------------------|---|--------------------------------------|
| TRISO kernel            | <sup>235</sup> U (4.2857); <sup>238</sup> U (17.143);<br><sup>232</sup> Th (14.286); <sup>16</sup> O (64.286) | 10.2                                 |
| TRISO porous graphite   | C (100)   | 1                                    |
| TRISO pyrocarbon        | C (100)   | 1.85                                 |
| TRISO zirconium carbide | Zr (50) ; C (50)  | 6.56                                 |
| Graphite                | C (100)   | 1.74                                 |
| Control rods            | <sup>10</sup> B (72); <sup>11</sup> B (8) ; <sup>12</sup> C (20)  | 2.47                                 |

Fresh fuel consists of 40% thorium and 60% uranium.

In the case of the burnup calculations the MCNP subroutine of the MCB code had been invoked after 10 days of simulated operation and then after each month. Each MCNP subroutine simulated a total of 1250000 neutrons distributed over 125 k-code cycles, including 25 non-active ones, it lasted 4 hours and 15 minutes and it employed 214 Mb of RAM memory per processor. For the calculation of neutron flux and spectrum the number of simulated neutrons has been increased by a factor of 10. The computing time gain factor of the 64-bits architecture over the 32-bits one is 1.8; this factor might be further increased by a 64-bits compilation of the MCB code.

## 6. Approach to the equilibrium of the fuel composition

### 6.1. Description of the refueling and shuffling schedule

At the beginning of life, we loaded all three rings with fresh fuel in order to quickly reach the equilibrium of the fuel composition; therefore, all the fuel holes of all the hexagonal blocks have been filled with fresh DF pins. Moreover, we increased the thorium percentage in the fuel of the inner ring from 40% to 50% to flat the radial neutron flux profile in the core since the inner ring tends to have the highest value of flux amid the three rings. After the first operation period, which consisted of 810 days of irradiation and 35 days of natural decay, we shuffled the DF from the central ring into the inner one and we filled the central ring with fresh DF; we have repeated these two operations after all the following irradiation periods. After the second operation period, which consisted of 450 days of irradiation and 35 days of natural decay, we shuffled the DF from the inner ring into the outer one; we have repeated this operation after all the following irradiation periods. After the third operation period, which consisted of 480 days of irradiation and 35 days of natural decay, we moved half of the DF pins into the central ring as PDF pins; we have repeated this operation after all the following irradiation periods. In the next operation periods, we followed for the PDF the same shuffling policy than for DF. The fourth irradiation period lasted 390 days and all the next ones 300 days.

After a total of 9 operation periods the fuel reaches the isotopic composition equilibrium. Fig. 6 illustrates the refueling and shuffling schedule during the first six operation periods and Fig. 7 does in the further three irradiation periods.

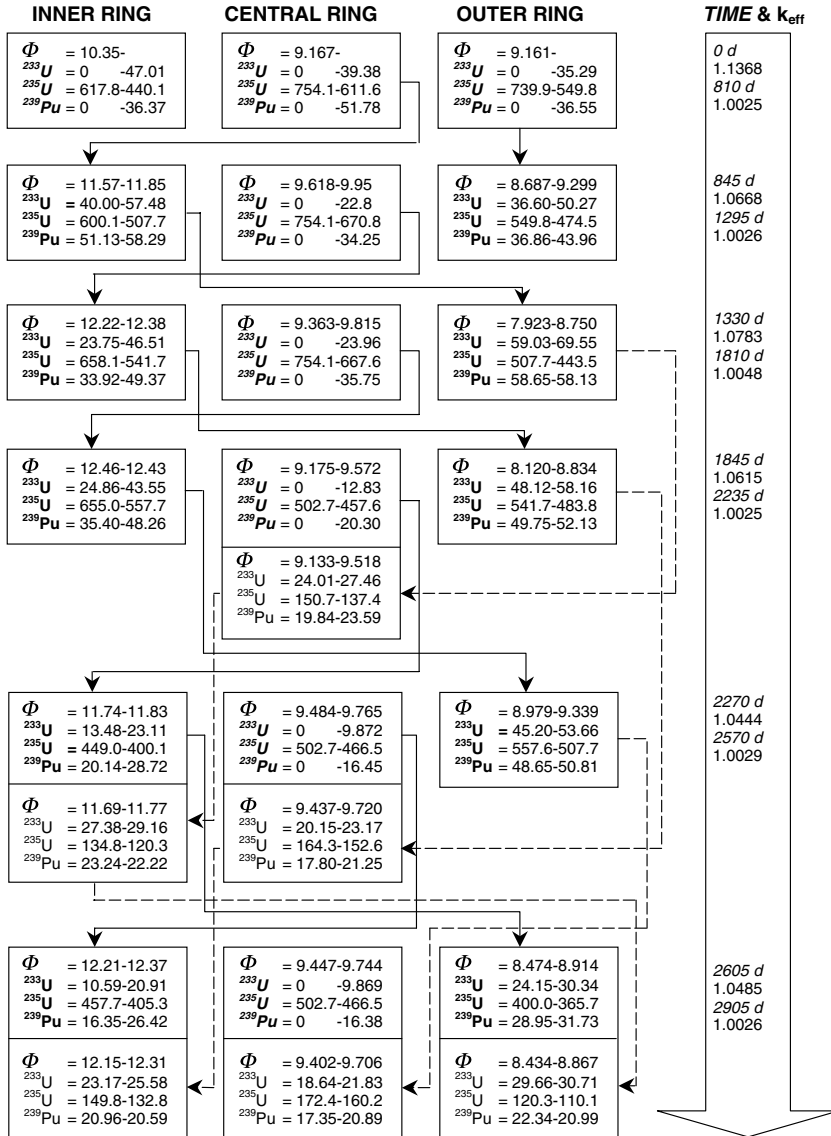


Fig. 6. Approach to the equilibrium, first six operation periods. Fresh DF is reported in italics and bold text, irradiated DF in bold text and PDF in normal text. The shuffling of DF and PDF are, respectively, indicated by normal and dashed lines. The left columns report the neutron flux, divided by  $10^{13}$ , and the mass, in kilograms, at the beginning of the irradiation periods and the right columns do at the end of the irradiation periods. All  $k_{eff}$  values have a standard deviation lower than 85 pcm.

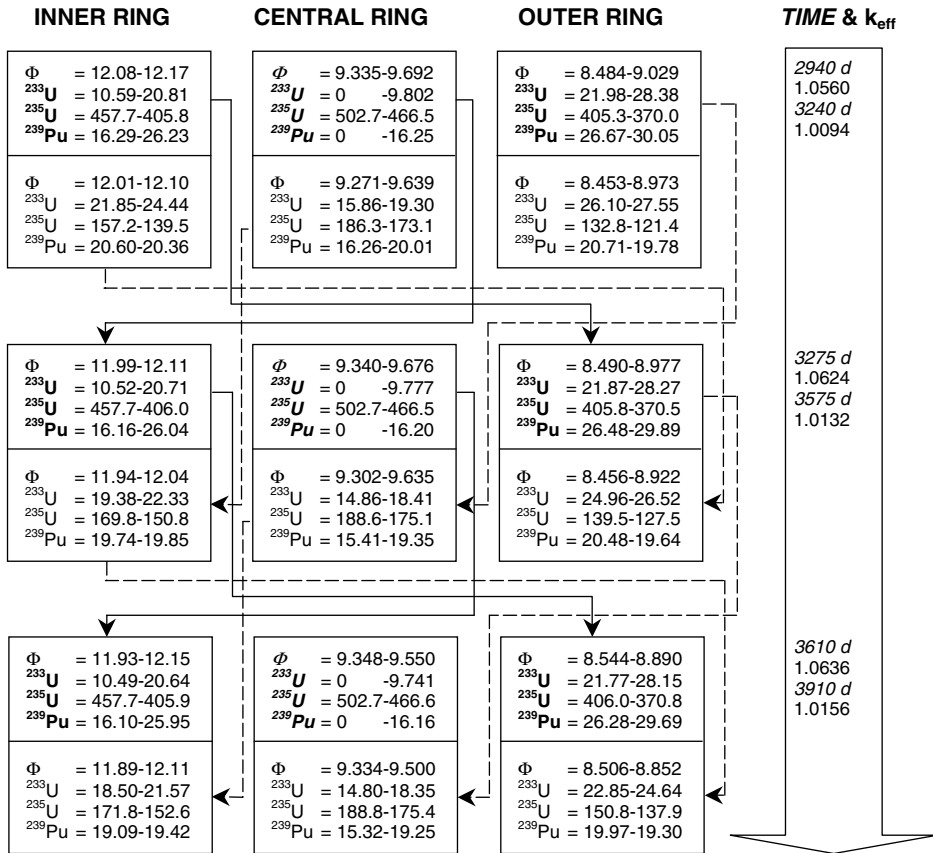


Fig. 7. Approach to the equilibrium, further three operation periods. Fresh DF is reported in italics and bold text, irradiated DF in bold text and PDF in normal text. The shuffling of DF and PDF are, respectively, indicated by normal and dashed lines. The left columns report the neutron flux, divided by  $10^{13}$ , and the mass, in kilograms, at the beginning of the irradiation periods and the right columns do at the end of the irradiation periods. All  $k_{eff}$  values have a standard deviation lower than 90 pcm.

### 6.2. Neutron flux

We can note in Figs. 6 and 7 that the inner ring exhibits the highest value of neutron flux, about 40% higher than the value in the outer ring, which has the lowest intensity; nevertheless, all the values are lower than  $1.25 \times 10^{14}$  n/cm<sup>2</sup> s. The difference between the rings attenuates during irradiation; in fact, at the end of each irradiation period the central and outer rings have 2.5–6% higher values of flux, whereas the value of the inner ring is almost constant. As expected, the level of flux depends only on the ring since both DF and PDF experience the same flux intensity.

### 6.3. Transmutation of the fissile isotopes

We can observe in Figs. 6 and 7 that the DF in the inner and outer rings favors the  $^{233}\text{U}$  production, while in the central one it does the  $^{239}\text{Pu}$ . We address this behavior to the neutron spectra in the kernel of TRISO particles of different rings (the inner and outer rings are more moderated than the central one). In the case of the PDF in the inner and outer rings, we can note that there is no accumulation of  $^{239}\text{Pu}$  (with the outer ring even depleting  $^{239}\text{Pu}$ ) and the production of  $^{233}\text{U}$  is reduced; we address this behavior to the isotopic composition of the fuel (PDF is richer in  $^{239}\text{Pu}$  and  $^{233}\text{U}$  than DF and that enhances their absorption rate). We remand to paragraphs 7.5 and 7.6 for a detailed discussion of the neutron spectrum and atomic density effects in different rings and fuel types. As a consequence of these quite complicated effects, the irradiation of DF in the central ring produces a mass of  $^{239}\text{Pu}$  1.67 times greater than that one of  $^{233}\text{U}$ ; by contrast, the irradiated PDF in the outer ring depletes  $^{239}\text{Pu}$  and generates a small quantity of  $^{233}\text{U}$ .

Of course, the mass of  $^{233}\text{U}$  and  $^{239}\text{Pu}$  increase during the 35 days of natural decay because of the  $\beta$  decay of  $^{233}\text{Pa}$  and  $^{239}\text{Np}$ ; nevertheless, the increase is quite small since the mass of the latter nuclides is two orders of magnitude lower than that one of their daughter isotopes. Moreover, in the shuffling involving the central ring, the mass of fuel changes because of the different total number of control rods in the central ring comparing to the other rings; this difference traduces into a larger volume of fuel in the central ring (Table 2).

During the 810 days of full power operation of the first period, the fresh fuel depletes 510 kg of  $^{235}\text{U}$ , which is very close to the mass of fresh DF loaded in the central ring at the equilibrium.

### 6.4. Time evolution of $k_{\text{eff}}$

Figs. 8 and 9 show the  $k_{\text{eff}}$  curves during the 9 irradiation periods. As a consequence of loading fresh fuel into all the three rings, the excess of reactivity is pretty high at the beginning of life, 13700 pcm, and it needs to be managed by the startup and operational control rods; of course, this initial excess of reactivity allows a quite long uninterrupted period of irradiation (810 days).

After 10 days of operation, the poisoning of the short life fission products generates a 1000–1500 pcm decrease of the initial  $k_{\text{eff}}$ ; thereafter, the inclination of the curves (about 200–400 pcm/month) is quite constant so that the curves resemble right lines.

The quite long irradiation of the first period, 810 days, has the effect of lowering the initial  $k_{\text{eff}}$  at the second and fifth periods. In fact, at the beginning of the second period, the  $k_{\text{eff}}$  is lower than that one at the beginning of the third period because the inner ring, which exhibits the highest neutron flux, loads a rather depleted fuel (600.1 kg of  $^{235}\text{U}$ ), coming from a previous irradiation of 810 days, compared to the fuel loaded at the beginning of the third period (658.1 kg), coming from a previous irradiation of 450 days. Similarly, at the beginning of the fifth period, the 810 days irradiated, and depleted, fuel reaches the inner ring in the form of PDF

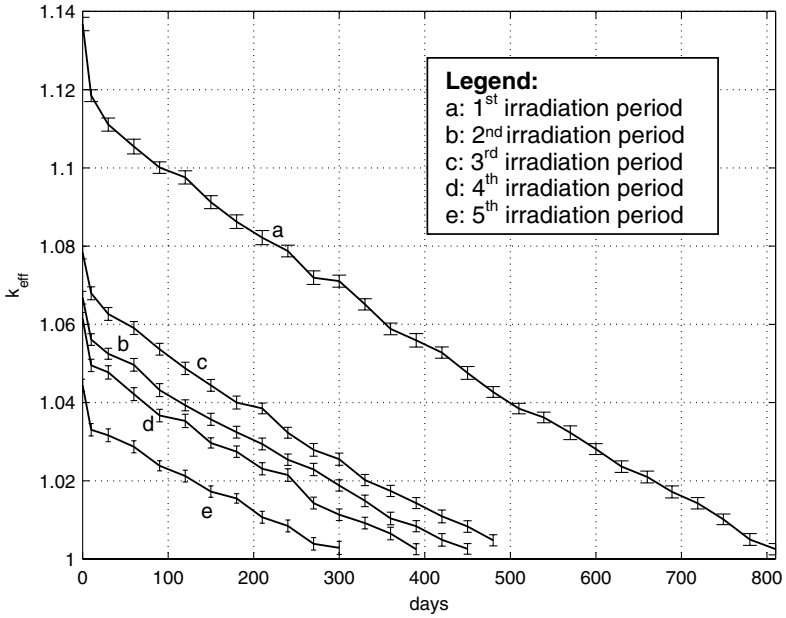


Fig. 8.  $k_{\text{eff}}$  evolution during the first five irradiation periods. The standard deviation, indicated by the small horizontal ticks, is given with a 95% confidence.

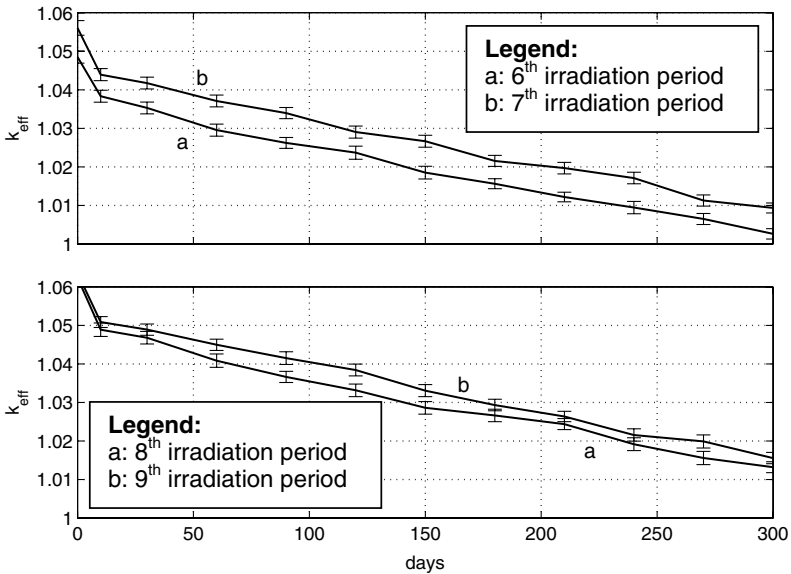


Fig. 9.  $k_{\text{eff}}$  evolution during the last four irradiation periods. The standard deviation, indicated by the small horizontal ticks, is given with a 95% confidence.

producing the lowest value of  $k_{\text{eff}}$  in all the periods (1.0444). After the fifth period, the initial value of  $k_{\text{eff}}$  starts increasing because the fuel comes from previous periods with a shorter irradiation time; in fact, after the sixth period the 810 days irradiated fuel is out of the reactor.

## 7. The operation at the equilibrium

### 7.1. Transmutation rates

Fig. 10 sketches the transmutation chain of the actinides in the DF of the inner ring during the first 10 days of irradiation at the equilibrium of the fuel composition. The values of the one-group averaged cross-sections, reported in the third row of the boxes, may be different in the other rings since the other two rings are subjected to different neutron spectra. At first glance, it appears that the production of americium and curium is quite limited; in fact, the total quantity of  $^{241}\text{Am}$  in the three years irradiated PDF is 0.33 kg, one order of magnitude lower than the yearly production in a LWR of 3  $\text{GW}_{\text{th}}$  (16.6 kg). In addition, in spite of the high absorption cross-section (111 b), 99.65% of  $^{238}\text{Np}$  transmuted mass generates  $^{238}\text{Pu}$  because of its very short decay half life (2.1 days). Moreover, about 18% of  $^{238}\text{Pu}$  transmuted mass undergoes a fission or a  $(n, \alpha)$  reaction.

A deeper look into Fig. 10 highlights that the capture cross-section of  $^{238}\text{U}$  is 1.26 times larger than that one of  $^{232}\text{Th}$  and the decay half life of  $^{239}\text{Np}$  is 0.09 times shorter than that one of  $^{233}\text{Pa}$ ; therefore, the breeding of  $^{239}\text{Pu}$  is larger and faster than that one of  $^{233}\text{U}$ . Nevertheless, the neutronic efficiency of  $^{239}\text{Pu}$  is the worst amid all the fissile nuclides; in fact, only 62% of the  $^{239}\text{Pu}$  transmuted mass undergoes fission; whereas, this percentage increases to 79% and 88% for  $^{235}\text{U}$  and  $^{233}\text{U}$ , respectively.

The conversion ratio (CR) of the fuel, defined as the production rate of fissile isotopes from the fertile nuclides divided by the depletion rate of the fissile isotopes, can be approximated by the following formula (where the neutron flux has been omitted since it contributes both to the numerator and to the denominator):

$$\text{CR} = \frac{{}^{232}\text{Th}\sigma_{\gamma}{}^{232}\text{Th} + {}^{238}\text{U}\sigma_{\gamma}{}^{238}\text{U}}{{}^{235}\text{U}\sigma_{\text{a}}{}^{235}\text{U}}$$

where, for instance,  ${}^{232}\text{Th}\sigma_{\gamma}$  represents the one-group averaged capture cross-section of  $^{232}\text{Th}$  and  ${}^{232}\text{Th}$  does its atomic density; whereas,  $\sigma_{\text{a}}$  does the absorption cross-section. Since the relative abundance of  $^{232}\text{Th}$ ,  $^{238}\text{U}$  and  $^{235}\text{U}$  in the fuel is 13.96%, 16.68% and 3.50%, respectively, the CR in the DF of the inner ring is 0.7, a value higher than that one of ordinary LWRs but below the value of 0.8 that a HTGR may reach (Duderstadt and Hamilton, 1976). Of course, the CR depends on the fuel type and ring.

The capture and  $(n, \alpha)$  cross-sections of graphite are  $1.98 \times 10^{-4}$  and  $1.07 \times 10^{-4}$  b, two order of magnitudes lower than the fission cross-section of  $^{235}\text{U}$ , and several

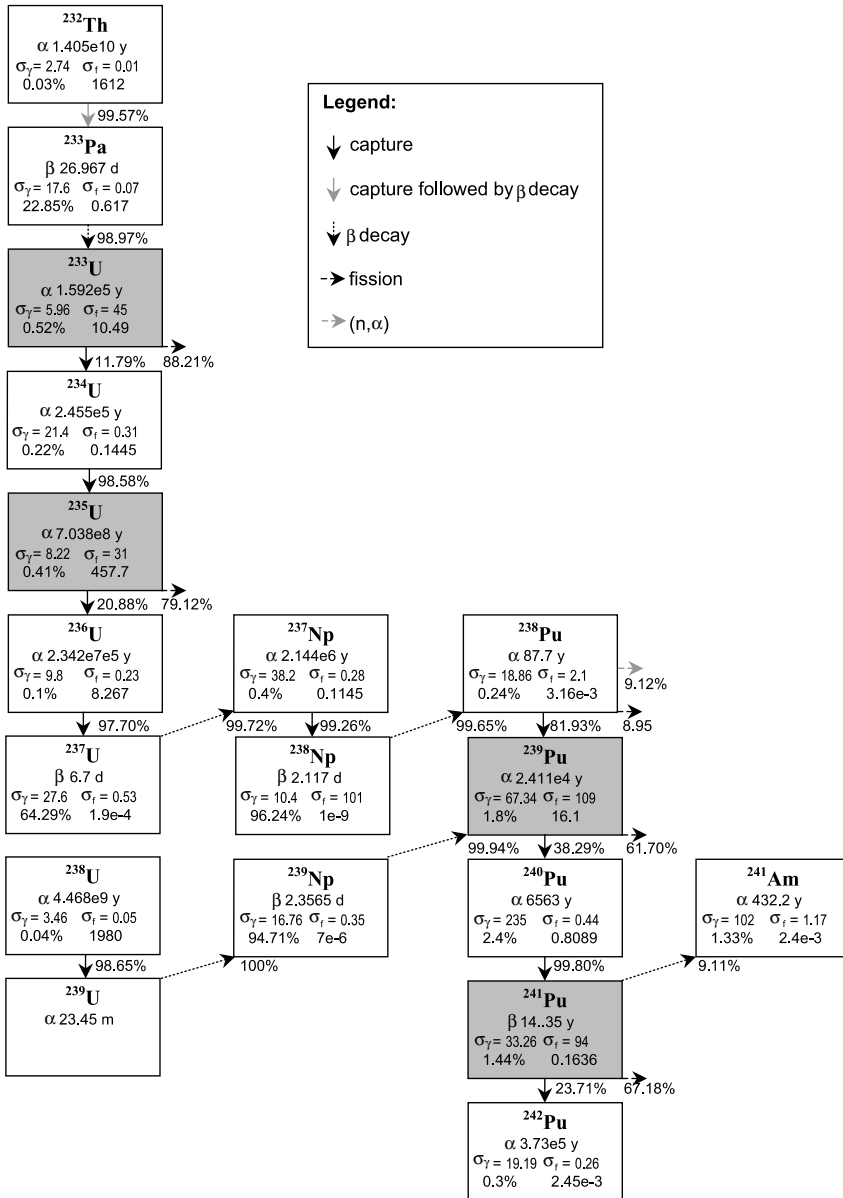


Fig. 10. Transmutation chain of the uranium–thorium fuel at the equilibrium of the fuel composition (inner ring at the beginning of the irradiation period). The half life is reported in the second rows of the boxes. In the third row, the cross-sections are expressed in barns and calculated by MCB. The mass (kg) in the DF of the inner ring, at the beginning of irradiation, and the transmutation percentage (which considers each isotope as a single parent nuclide and differs from the transmuted percentage, which considers the effects of all parent nuclides), during 10 days, are reported in the fourth row. Fissile nuclides are indicated by a dark box.

thousands lower than the graphite scattering cross-section at the thermal energy, which is constant and equal to 5 b.

7.2. Evolution of the fissile isotopes

Figs. 11 and 12 illustrate the transmutation of the fissile isotopes of DF and PDF. We can note that the accumulation of  $^{239}\text{Pu}$  in the fresh DF (central ring) is faster and larger than that one of  $^{233}\text{U}$ , as already discussed in the previous section. After 300 days of irradiation, the total quantity of  $^{239}\text{Pu}$  in the central ring is 1.66 times that one of  $^{233}\text{U}$ ; at the same time the mass of  $^{233}\text{U}$ ,  $^{235}\text{U}$  and  $^{239}\text{Pu}$  of DF change of +96.76%, -11.32%, and +61.18% in the inner ring (the minus sign stands for burn up and the plus one for build up); whereas, in the outer ring the previous percentages reduce to +29.31%, -8.67% and +12.98%. Let us remind that the “fresh” PDF consists of three years irradiated DF coming from the outer ring; therefore, only the white segments of the most right group of columns of Fig. 11 contribute in the most left group of columns of Fig. 12; that explains why the mass of  $^{235}\text{U}$ , divided by 10, is comparable with the mass of other fissile isotopes in Fig. 12 whereas it is double in Fig. 11. In the PDF the breeding of  $^{233}\text{U}$  is mitigated, comparing to DF, and the concentration of  $^{239}\text{Pu}$  is almost constant, as we already noted and discussed in paragraph 6.C. During the irradiation of 300 days, the mass of  $^{233}\text{U}$ ,  $^{235}\text{U}$  and  $^{239}\text{Pu}$ , in the PDF of the inner/central/outer rings, transmutes of +16.59/+23.99/+7.83%, -11.18/-7.1/-8.55% and +1.73/+25.65/-3.36%, respectively.

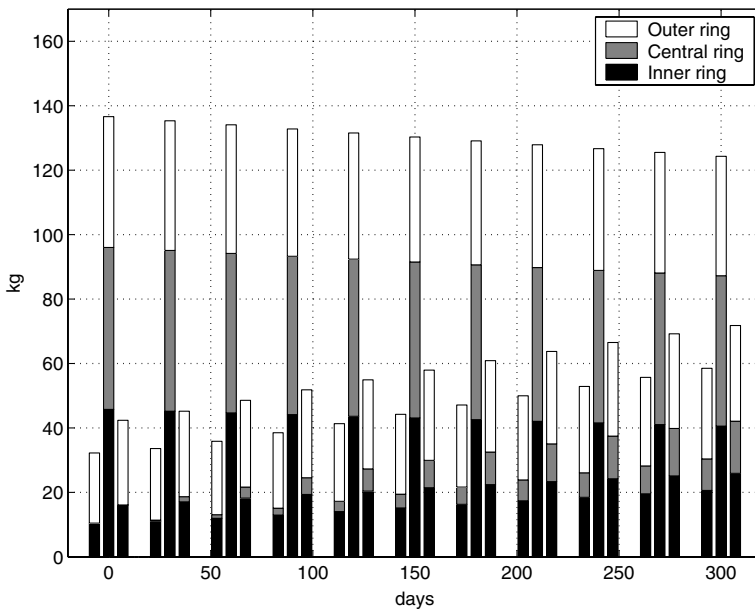


Fig. 11. Transmutation of  $^{233}\text{U}$  (left columns),  $^{235}\text{U}$  (central columns) and  $^{239}\text{Pu}$  (right columns) in the DF during the ninth period of irradiation. The mass of  $^{235}\text{U}$  has been divided by 10.



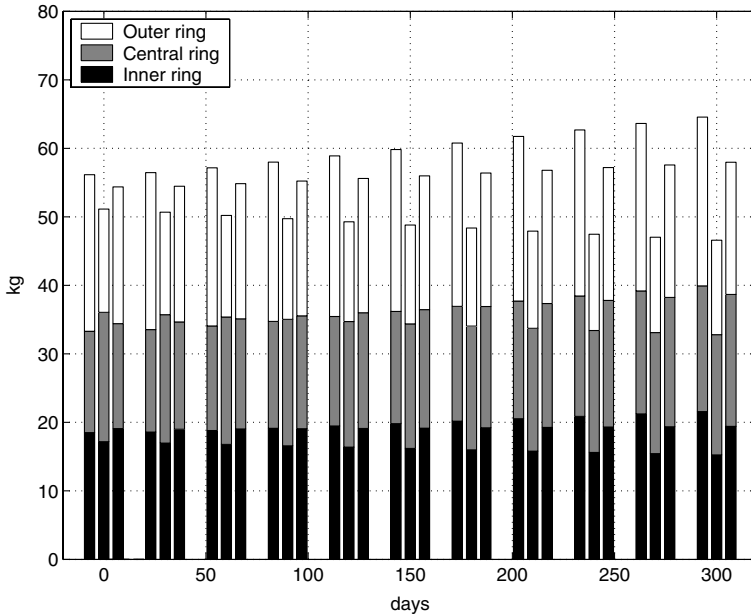


Fig. 12. Transmutation of  $^{233}\text{U}$  (left columns),  $^{235}\text{U}$  (central columns) and  $^{239}\text{Pu}$  (right columns) in the PDF during the ninth period of irradiation. The mass of  $^{235}\text{U}$  has been divided by 10.

### 7.3. Mass flow

Fig. 13 illustrates the mass flow at the equilibrium; the consumption of only 36.1 kg of  $^{235}\text{U}$  DF allows an irradiation longer than 300 days because of the simultaneous breeding of fissile nuclides. During the irradiation of the DF, the transmutation of the most abundant isotopes,  $^{232}\text{Th}$ ,  $^{235}\text{U}$ ,  $^{238}\text{U}$ , is 3.99%, 26.24% and 4.66%, respectively; during the following irradiation of the PDF, the previous percentages increase to 4.2%, 26.96% and 4.89%.

After a total irradiation period of five years, distributed over DF and PDF, only 46.16% of  $^{235}\text{U}$  transmutes; therefore, we acknowledge that a Deep Burn in-core fuel management strategy is not possible for this type of fuel in terms of the depletion of the initial fissile material (in our previous studies the transmutation of  $^{239}\text{Pu}$ , which represented the most abundant fissile nuclide of the fuel, was over 90%), because of the presence of the fertile nuclides. Nevertheless, we continue addressing to the present refueling and shuffling schedule as a Deep Burn strategy in terms of analogy with our previous studies (Talamo et al., 2004a and 2004d) and also in terms of the total irradiation time (5 years).

Since the spent PDF is still rich in fissile nuclides, 24.6 kg of  $^{233}\text{U}$ , 137.9 kg of  $^{235}\text{U}$  and 19.3 kg of  $^{239}\text{Pu}$ , we would suggest the reprocessing of the waste; anyhow, with or without reprocessing, each year the geological repository receives 236.7 kg of fission products.

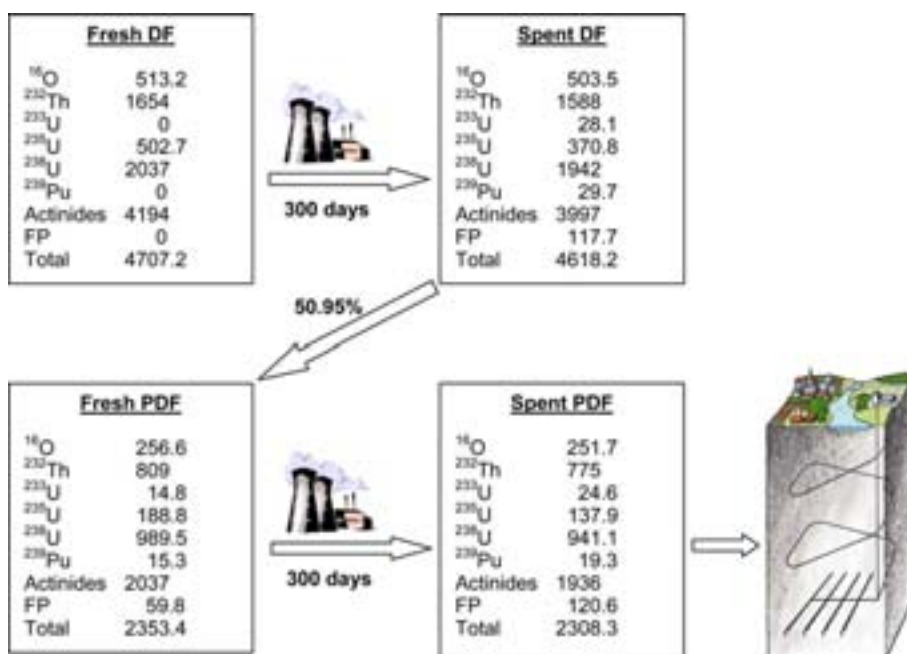


Fig. 13. Mass flow of the GT-MHR fueled with uranium–thorium at the equilibrium of fuel composition (ninth operation period). The left boxes report the mass values (kg) at the beginning of the irradiation period, in the central ring, and the right ones do after 300 days of irradiation, in the outer ring.

#### 7.4. Neutron flux profile

We evaluated the radial flux profile in the reactor core by calculating the average flux in 10 consecutive hexagonal blocks, for the eleventh block is cut by the edge of the reactor, disposed along the radial direction from the center of the core (which corresponds to the vertical direction of Fig. 4). Moreover, we divided each hexagonal block into 10 axial sub-blocks equally spaced along the  $z$ -axis in order to estimate the axial flux at different heights. We limited our studies only to the upper 5 axial sub-blocks for we always kept the control rods withdrawn and therefore the flux is symmetric along the  $z$ -axis. We neglected the flux in the two axial reflectors. Fig. 14 plots the flux radial profile in the consecutive hexagonal blocks at different heights; each curve represents one of the five upper axial sub-blocks at the beginning of the ninth irradiation period. The neutron flux drops after the eighth block due to the increase of leakage in the outer blocks; the same effect is visible in the last two axial sub-blocks, where, in addition, the flux becomes more flattened because neutrons with a higher energy tend to escape the more. The peak of the neutron flux emerges in the fourth block, which corresponds to the pure graphite blocks adjacent to the inner ring; this behavior is explained by the moderation of neutrons and by the circular shape of fuel, which reduces the leakage since half of the fission neutrons propagate towards the center of the reactor.

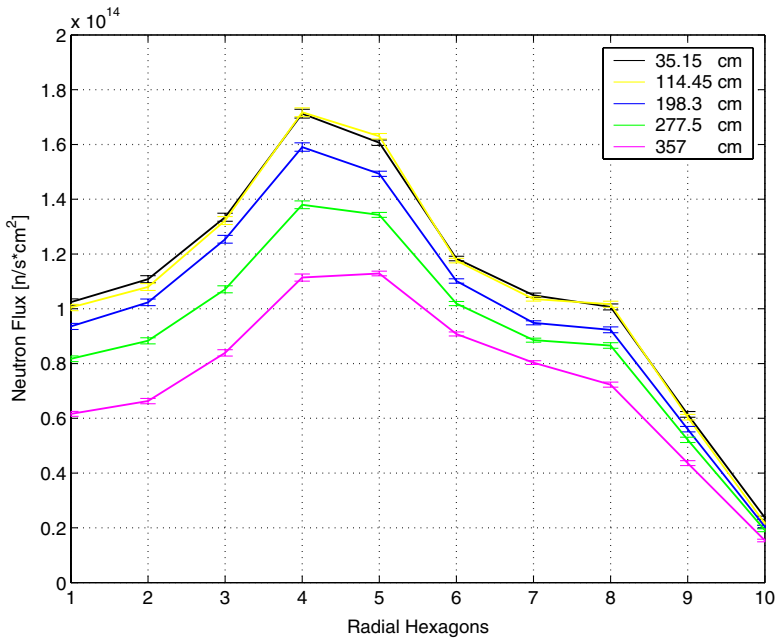


Fig. 14. Neutron flux profile at the beginning of the ninth irradiation period. The flux has been averaged in 10 axial sub-blocks and 10 radial hexagonal blocks from the center of the reactor. The curves refer to the upper 5 axial sub-blocks. The fifth and sixth hexagonal blocks correspond to the inner ring, and the seventh one does to the central ring. The small horizontal ticks on the curves represent the standard deviation with a 68% confidence.

The flux radial-peaking factor, defined as the maximum flux divided the average among the rings, is greater in the axial central region of the core, in the axial sub-block at 35.15 cm, and equal to 1.32 (since the outer ring in the axial sub-block at 35.15 cm has a flux of  $1 \times 10^{14}$  n/s  $\text{cm}^2$ ); whereas, the flux axial-peaking factor is greater in the inner ring and equal to 1.13.

### 7.5. Neutron spectrum

Fig. 15 shows the neutron spectrum averaged over the whole reactor, but the two axial reflectors, at the beginning of the ninth irradiation period; the spectrum has been calculated on continuous energy and plotted by using the energy binning corresponding to the 69 energetic groups of the WIMS cross-section library for thermal reactors. The WIMS groups are composed of 14 fast groups, 13 resonance groups and 42 thermal groups (Kim et al., 1989; Taubman, 1975). The reactor clearly operates in a thermal spectrum with a spectral peak located at the energy of 0.15 eV, which a little less than the value we calculated in our previous studies for a fuel based on LWRs waste, 0.2 eV (Talamo et al., 2004b). The more thermalized flux explains the larger one-group averaged cross-sections of Fig. 10 compared to Fig. 15 of

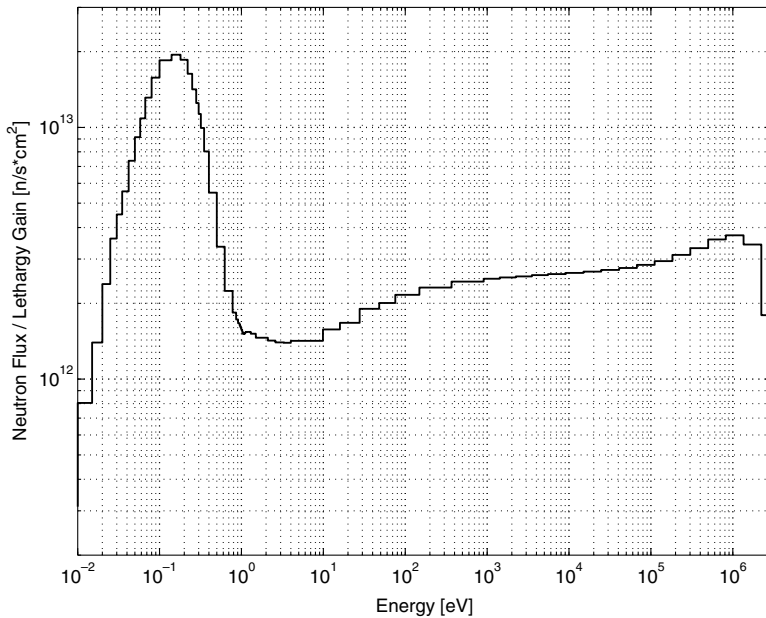


Fig. 15. Neutron spectrum at the beginning of the ninth irradiation period averaged in the whole reactor but the two axial reflectors.

Talamo et al. (2004a): e.g. the fission cross-section of  $^{239}\text{Pu}$  is 109 b against 65.2 b. The more thermalized spectrum of the uranium–thorium fuel, comparing to the plutonium fuel (LWRs waste or military plutonium), may be related to the average energy loss  $\Delta E$  of neutrons in the scattering collisions with heavy nuclei, which, with the assumption of stationary nuclei, is:

$$\Delta E = \frac{1 - \alpha}{2} E_i,$$

$$\alpha = \left( \frac{A - 1}{A + 1} \right)^2,$$

where  $E_i$  is the initial energy of the neutron and  $A$  the mass of the nucleus. In a collision with  $^{232}\text{Th}$  the neutron loses, in average, 0.85% of its initial energy, whereas with  $^{239}\text{Pu}$  only 0.42%. The elastic scattering cross-sections of  $^{232}\text{Th}$  and of  $^{239}\text{Pu}$  are almost constant, and equal to 10 b, in the thermal energy range; whereas in the fast energy range their values halves. The inelastic cross-sections give a smaller contribution than the elastic ones to the total scattering because they raise only above 1 MeV and keeps below 2.6 and 1.6 b, for  $^{232}\text{Th}$  and  $^{239}\text{Pu}$ , respectively.

Figs. 16 and 17 report the spectra averaged in the TRISO kernels containing DF and PDF for the three rings; we can immediately observe that they resemble a fast profile since the maximum peak is located at 1 MeV. Nevertheless, the thermal energy range of the spectrum gives a large contribution to the one-group cross-sections averaged in the TRISO particles kernels, even if the spectrum is fast. In fact, the

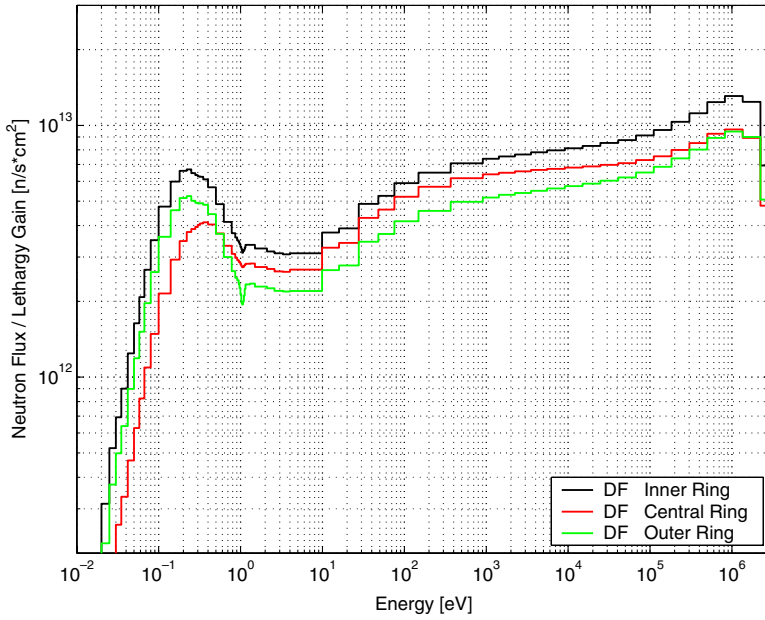


Fig. 16. Neutron spectrum at the beginning of the ninth irradiation period averaged in the TRISO particles kernels of DF.

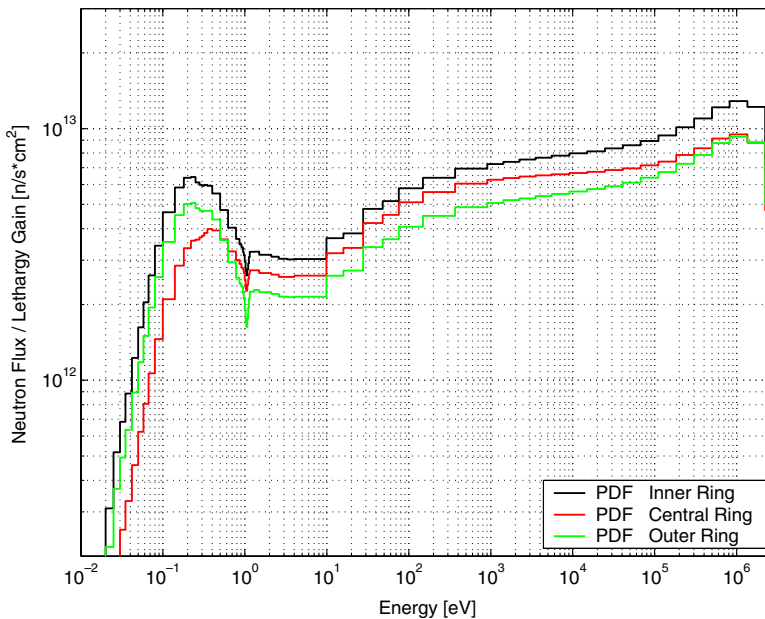


Fig. 17. Neutron spectrum at the beginning of the ninth irradiation period averaged in the TRISO particles kernels of PDF.

capture cross-sections of  $^{232}\text{Th}$  and  $^{238}\text{U}$  in the thermal range are over one order of magnitude larger than in the fast one (Fig. 1) while the flux just doubles from the thermal energy to the fast one (Figs. 16 and 17).

The spectrum in the inner and outer rings has higher peaks at 0.2–0.3 eV than the peak at 0.4 eV in the central ring, because of the moderation of the adjacent pure graphite blocks. In addition, the flux in inner ring is higher than that one of the outer ring because of the latter ring experiences more leakage and it contains more depleted fuel. Moreover, the thermal peaks of the inner and outer rings equal the fast tail at 200–300 eV, whereas the thermal peak of the central ring does already at 30 eV (Fig. 16).

Concerning the PDF (Fig. 17), the production of  $^{239}\text{Pu}$  does not visibly depress the spectrum at 0.3 eV, as it does instead for a LWRs based fuel (Talamo et al., 2004b, Figs. 11–16). By contrast, the accumulation of  $^{240}\text{Pu}$  accentuates the dip of the spectrum at 1.056 eV, where its microscopic capture cross-section is 11,764 b, according to JEF-2.2. The spectra of DF are slightly more moderated than the corresponding spectra of PDF: e.g. one can compare the area under the curves of the spectra of the inner ring above the threshold of  $10^{12.6}$  n/s cm<sup>2</sup> on the y-axis and at 0.2 eV on the x-axis for both Figs. 16 and 17.

#### 7.6. 4-groups neutron flux and cross-sections

In order to understand better the transmutation rates in different fuel types and rings, we calculated the neutron flux, absorption rate per nucleus and absorption rate for four energetic groups:  $10^{-5}$ –2, 2–30, 30–300 and  $300$ – $2 \times 10^7$  eV. The first group includes the thermal peak of the neutron spectrum in the TRISO kernels; the second group does the capture resonance of  $^{238}\text{U}$  at 6.674 eV and it marks the point where the capture cross-section of  $^{238}\text{U}$  becomes larger than that one of  $^{232}\text{Th}$  (Fig. 1); the boundaries of the third group have been selected by the matching between the thermal peak of the neutron spectrum and its fast tail (the thermal peaks of the inner and outer rings equal the fast tail at 200–300 eV, whereas the thermal peak of the central ring does already at 30 eV, Fig. 16); finally, the fourth group takes into account the fast tail of the spectrum. Table 4 reports the 4-groups flux tallied by MCNP; Tables 5 and 6 do the capture rates per nucleus of  $^{232}\text{Th}$ ,  $^{238}\text{U}$ ; Tables 7–9 do the absorption rates per nucleus of  $^{233}\text{U}$ ,  $^{235}\text{U}$  and  $^{239}\text{Pu}$ ; Tables 10–14 sample the same values of

Table 4  
4-groups flux averaged on TRISO kernels at the beginning of the ninth irradiation period

|                                | Inner ring  |             | Central ring |             | Outer ring  |             |
|--------------------------------|-------------|-------------|--------------|-------------|-------------|-------------|
|                                | DF          | PDF         | DF           | PDF         | DF          | PDF         |
| $10^{-5}$ –2 eV                | 13.616      | 13.443      | 10.747       | 10.565      | 14.275      | 14.156      |
| 2–30 eV                        | 7.354       | 7.333       | 8.083        | 8.065       | 7.267       | 7.262       |
| 30–300 eV                      | 10.429      | 10.440      | 11.678       | 11.692      | 10.249      | 10.277      |
| $300$ – $2 \times 10^7$ eV     | 68.602      | 68.784      | 69.492       | 69.679      | 68.210      | 68.305      |
| $10^{-5}$ – $2 \times 10^7$ eV | 1.267E + 14 | 1.242E + 14 | 9.967E + 13  | 9.772E + 13 | 9.088E + 13 | 8.903E + 13 |

The 4-groups values are expressed in percentages and the one-group values in n/s cm<sup>2</sup>. The relative standard deviation of flux per source particle and energy deposition per source particle are lower than 110 and 40 pcm, respectively.

Tables 5–9 but multiplied by the atomic density. Tables 5–9, 11–14 have been calculated according to the following formulas, respectively:

$$\int_{E_i}^{E_{i+1}} \sigma(E)\varphi(E) dE, \quad i = 0, 1, 2, 3,$$

$$\int_{E_i}^{E_{i+1}} N\sigma(E)\varphi(E) dE, \quad i = 0, 1, 2, 3,$$

Table 5

4-groups capture rate per nucleus of  $^{232}\text{Th}$  averaged on TRISO kernels at the beginning of the ninth irradiation period

|                                | Inner ring           |                      | Central ring         |                      | Outer ring           |                      |
|--------------------------------|----------------------|----------------------|----------------------|----------------------|----------------------|----------------------|
|                                | DF                   | PDF                  | DF                   | PDF                  | DF                   | PDF                  |
| $10^{-5}$ –2 eV                | 11.522               | 11.389               | 7.340                | 7.224                | 12.169               | 12.025               |
| 2–30 eV                        | 30.680               | 30.741               | 32.255               | 32.412               | 30.610               | 30.824               |
| 30–300 eV                      | 35.930               | 36.034               | 37.982               | 38.008               | 35.577               | 35.651               |
| $300$ – $2 \times 10^7$ eV     | 21.868               | 21.836               | 22.423               | 22.357               | 21.644               | 21.500               |
| $10^{-5}$ – $2 \times 10^7$ eV | $3.470\text{E} + 14$ | $3.414\text{E} + 14$ | $2.883\text{E} + 14$ | $2.834\text{E} + 14$ | $2.476\text{E} + 14$ | $2.445\text{E} + 14$ |

The 4-groups values are expressed in percentages and the one-group values in n b/s  $\text{cm}^2$ . The relative standard deviation (assuming exact the values of the energy deposition per source particle) is lower than 450 pcm.

Table 6

4-groups capture rate per nucleus of  $^{238}\text{U}$  averaged on TRISO kernels at the beginning of the ninth irradiation period

|                                | Inner ring           |                      | Central ring         |                      | Outer ring           |                      |
|--------------------------------|----------------------|----------------------|----------------------|----------------------|----------------------|----------------------|
|                                | DF                   | PDF                  | DF                   | PDF                  | DF                   | PDF                  |
| $10^{-5}$ –2 eV                | 3.806                | 3.757                | 2.471                | 2.412                | 4.022                | 3.944                |
| 2–30 eV                        | 47.088               | 47.018               | 47.287               | 47.377               | 47.216               | 47.389               |
| 30–300 eV                      | 35.761               | 35.897               | 36.852               | 36.912               | 35.543               | 35.590               |
| $300$ – $2 \times 10^7$ eV     | 13.345               | 13.328               | 13.391               | 13.299               | 13.219               | 13.077               |
| $10^{-5}$ – $2 \times 10^7$ eV | $4.396\text{E} + 14$ | $4.327\text{E} + 14$ | $3.731\text{E} + 14$ | $3.695\text{E} + 14$ | $3.129\text{E} + 14$ | $3.110\text{E} + 14$ |

The 4-groups values are expressed in percentages and the one-group values in n b/s  $\text{cm}^2$ . The relative standard deviation (assuming exact the values of the energy deposition per source particle) is lower than 410 pcm.

Table 7

4-groups absorption rate per nucleus of  $^{233}\text{U}$  averaged on TRISO kernels at the beginning of the ninth irradiation period

|                                | Inner ring          |                     | Central ring        |                     | Outer ring          |                     |
|--------------------------------|---------------------|---------------------|---------------------|---------------------|---------------------|---------------------|
|                                | DF                  | PDF                 | DF                  | PDF                 | DF                  | PDF                 |
| $10^{-5}$ –2 eV                | 67.180              | 67.002              | 58.946              | 58.651              | 68.274              | 68.137              |
| 2–30 eV                        | 19.006              | 19.070              | 23.795              | 23.920              | 18.393              | 18.454              |
| 30–300 eV                      | 7.249               | 7.307               | 9.288               | 9.379               | 6.986               | 7.032               |
| $300$ – $2 \times 10^7$ eV     | 6.565               | 6.622               | 7.971               | 8.050               | 6.346               | 6.377               |
| $10^{-5}$ – $2 \times 10^7$ eV | $6.40\text{E} + 15$ | $6.23\text{E} + 15$ | $4.40\text{E} + 15$ | $4.28\text{E} + 15$ | $4.68\text{E} + 15$ | $4.57\text{E} + 15$ |

The 4-groups values are expressed in percentages and the one-group values in n b/s  $\text{cm}^2$ . The relative standard deviation (assuming exact the values of the energy deposition per source particle) is lower than 180 pcm.

Table 8

4-groups absorption rate per nucleus of  $^{235}\text{U}$  averaged on TRISO kernels at the beginning of the ninth irradiation period

|                                | Inner ring          |                     | Central ring        |                     | Outer ring          |                     |
|--------------------------------|---------------------|---------------------|---------------------|---------------------|---------------------|---------------------|
|                                | DF                  | PDF                 | DF                  | PDF                 | DF                  | PDF                 |
| $10^{-5}$ –2 eV                | 69.216              | 68.933              | 57.707              | 57.242              | 70.535              | 70.315              |
| 2–30 eV                        | 11.657              | 11.780              | 16.004              | 16.213              | 11.216              | 11.333              |
| 30–300 eV                      | 11.478              | 11.582              | 16.061              | 16.226              | 10.949              | 11.029              |
| $300$ – $2 \times 10^7$ eV     | 7.649               | 7.705               | 10.228              | 10.319              | 7.300               | 7.323               |
| $10^{-5}$ – $2 \times 10^7$ eV | $4.98\text{E} + 15$ | $4.86\text{E} + 15$ | $3.14\text{E} + 15$ | $3.05\text{E} + 15$ | $3.69\text{E} + 15$ | $3.61\text{E} + 15$ |

The 4-groups values are expressed in percentages and the one-group values in n b/s  $\text{cm}^2$ . The relative standard deviation (assuming exact the values of the energy deposition per source particle) is lower than 160 pcm.

Table 9

4-groups absorption rate per nucleus of  $^{239}\text{Pu}$  averaged on TRISO kernels at the beginning of the ninth irradiation period

|                                | Inner ring          |                     | Central ring        |                     | Outer ring          |                     |
|--------------------------------|---------------------|---------------------|---------------------|---------------------|---------------------|---------------------|
|                                | DF                  | PDF                 | DF                  | PDF                 | DF                  | PDF                 |
| $10^{-5}$ –2 eV                | 91.759              | 91.623              | 88.092              | 87.822              | 92.440              | 92.357              |
| 2–30 eV                        | 3.531               | 3.568               | 5.128               | 5.215               | 3.241               | 3.266               |
| 30–300 eV                      | 3.122               | 3.187               | 4.576               | 4.699               | 2.860               | 2.898               |
| $300$ – $2 \times 10^7$ eV     | 1.588               | 1.622               | 2.204               | 2.264               | 1.459               | 1.479               |
| $10^{-5}$ – $2 \times 10^7$ eV | $2.22\text{E} + 16$ | $2.14\text{E} + 16$ | $1.34\text{E} + 16$ | $1.28\text{E} + 16$ | $1.71\text{E} + 16$ | $1.66\text{E} + 16$ |

The 4-groups values are expressed in percentages and the one-group values in n b/s  $\text{cm}^2$ . The relative standard deviation (assuming exact the values of the energy deposition per source particle) is lower than 210 pcm.

Table 10

4-groups capture rate of  $^{232}\text{Th}$  averaged on TRISO kernels after 10 days since the beginning of the ninth irradiation period

|                                | Inner ring          |                     | Central ring        |                     | Outer ring          |                     |
|--------------------------------|---------------------|---------------------|---------------------|---------------------|---------------------|---------------------|
|                                | DF                  | PDF                 | DF                  | PDF                 | DF                  | PDF                 |
| $10^{-5}$ –2 eV                | $3.69\text{E} + 11$ | $3.51\text{E} + 11$ | $1.97\text{E} + 11$ | $1.86\text{E} + 11$ | $2.76\text{E} + 11$ | $2.63\text{E} + 11$ |
| 2–30 eV                        | $9.83\text{E} + 11$ | $9.48\text{E} + 11$ | $8.65\text{E} + 11$ | $8.36\text{E} + 11$ | $6.94\text{E} + 11$ | $6.74\text{E} + 11$ |
| 30–300 eV                      | $1.15\text{E} + 12$ | $1.11\text{E} + 12$ | $1.02\text{E} + 12$ | $9.80\text{E} + 11$ | $8.07\text{E} + 11$ | $7.79\text{E} + 11$ |
| $300$ – $2 \times 10^7$ eV     | $7.01\text{E} + 11$ | $6.73\text{E} + 11$ | $6.01\text{E} + 11$ | $5.77\text{E} + 11$ | $4.91\text{E} + 11$ | $4.70\text{E} + 11$ |
| $10^{-5}$ – $2 \times 10^7$ eV | $3.20\text{E} + 12$ | $3.08\text{E} + 12$ | $2.68\text{E} + 12$ | $2.58\text{E} + 12$ | $2.27\text{E} + 12$ | $2.19\text{E} + 12$ |

All the values are expressed in n/s  $\text{cm}^3$ . The relative standard deviation (assuming exact the values of the energy deposition per source particle) is lower than 120 pcm.

where the symbols assume the meaning of the reactor physics literature (e.g. [Duderstadt and Hamilton, 1976](#)). The neutron flux has been calculated by the following formula:

$$\bar{\varphi} = 600 \times 10^6 \frac{\int \int \int_v \varphi(\vec{r}) \, d\vec{r}}{v\epsilon_{\text{RV}}},$$

where  $\bar{\varphi}$  is the average neutron flux in the TRISO kernels (n/s  $\text{cm}^2$ );  $\varphi(\vec{r})$  the neutron flux per MCNP source particle (its integral over the total TRISO kernels volume,  $v$ ,



Table 11

4-groups capture rate of  $^{238}\text{U}$  averaged on TRISO kernels after 10 days since the beginning of the ninth irradiation period

|                                | Inner ring |            | Central ring |            | Outer ring |            |
|--------------------------------|------------|------------|--------------|------------|------------|------------|
|                                | DF         | PDF        | DF           | PDF        | DF         | PDF        |
| $10^{-5}$ –2 eV                | 1.85E + 11 | 1.75E + 11 | 1.03E + 11   | 9.66E + 10 | 1.38E + 11 | 1.30E + 11 |
| 2–30 eV                        | 2.29E + 12 | 2.19E + 12 | 1.97E + 12   | 1.90E + 12 | 1.62E + 12 | 1.56E + 12 |
| 30–300 eV                      | 1.74E + 12 | 1.67E + 12 | 1.53E + 12   | 1.48E + 12 | 1.22E + 12 | 1.17E + 12 |
| $300$ – $2 \times 10^7$ eV     | 6.49E + 11 | 6.19E + 11 | 5.58E + 11   | 5.33E + 11 | 4.52E + 11 | 4.31E + 11 |
| $10^{-5}$ – $2 \times 10^7$ eV | 4.86E + 12 | 4.65E + 12 | 4.16E + 12   | 4.01E + 12 | 3.42E + 12 | 3.30E + 12 |

All the values are expressed in  $\text{n/s cm}^3$ . The relative standard deviation (assuming exact the values of the energy deposition per source particle) is lower than 150 pcm.

Table 12

4-groups absorption rate of  $^{233}\text{U}$  averaged on TRISO kernels after 10 days since the beginning of the ninth irradiation period

|                                | Inner ring |            | Central ring |            | Outer ring |            |
|--------------------------------|------------|------------|--------------|------------|------------|------------|
|                                | DF         | PDF        | DF           | PDF        | DF         | PDF        |
| $10^{-5}$ –2 eV                | 2.61E + 11 | 8.81E + 11 | 6.64E + 08   | 4.17E + 11 | 3.99E + 11 | 8.12E + 11 |
| 2–30 eV                        | 7.38E + 10 | 2.51E + 11 | 2.68E + 08   | 1.70E + 11 | 1.08E + 11 | 2.20E + 11 |
| 30–300 eV                      | 2.81E + 10 | 9.61E + 10 | 1.05E + 08   | 6.66E + 10 | 4.09E + 10 | 8.39E + 10 |
| $300$ – $2 \times 10^7$ eV     | 2.55E + 10 | 8.71E + 10 | 8.98E + 07   | 5.72E + 10 | 3.71E + 10 | 7.60E + 10 |
| $10^{-5}$ – $2 \times 10^7$ eV | 3.88E + 11 | 1.32E + 12 | 1.13E + 09   | 7.10E + 11 | 5.85E + 11 | 1.19E + 12 |

All the values are expressed in  $\text{n/N s cm}^3$ . The relative standard deviation (assuming exact the values of the energy deposition per source particle) is lower than 190 pcm.

Table 13

4-groups absorption rate of  $^{235}\text{U}$  averaged on TRISO kernels after 10 days since the beginning of the ninth irradiation period

|                                | Inner ring |            | Central ring |            | Outer ring |            |
|--------------------------------|------------|------------|--------------|------------|------------|------------|
|                                | DF         | PDF        | DF           | PDF        | DF         | PDF        |
| $10^{-5}$ –2 eV                | 8.90E + 12 | 6.49E + 12 | 5.04E + 12   | 3.65E + 12 | 5.96E + 12 | 4.32E + 12 |
| 2–30 eV                        | 1.50E + 12 | 1.11E + 12 | 1.40E + 12   | 1.04E + 12 | 9.48E + 11 | 6.96E + 11 |
| 30–300 eV                      | 1.48E + 12 | 1.09E + 12 | 1.40E + 12   | 1.04E + 12 | 9.26E + 11 | 6.77E + 11 |
| $300$ – $2 \times 10^7$ eV     | 9.83E + 11 | 7.25E + 11 | 8.93E + 11   | 6.59E + 11 | 6.17E + 11 | 4.50E + 11 |
| $10^{-5}$ – $2 \times 10^7$ eV | 1.29E + 13 | 9.41E + 12 | 8.73E + 12   | 6.38E + 12 | 8.45E + 12 | 6.14E + 12 |

All the values are expressed in  $\text{n/s cm}^3$ . The relative standard deviation (assuming exact the values of the energy deposition per source particle) is lower than 410 pcm.

is given by the tally type 4 of MCNP and it corresponds to the numerator of the fraction);  $e_{\text{RV}}$  is the energy deposition per MCNP source particle in the reactor volume (given by the tally type 6 of MCNP and calculated on the whole reactor); finally, the factor  $600 \times 10^6$  normalizes the flux according to the thermal power generated by the reactor ( $600 \text{ MW}_{\text{th}}$ ). Since the MCB code takes into account also the energy

Table 14

4-groups absorption rate of  $^{239}\text{Pu}$  averaged on TRISO kernels after 10 days since the beginning of the ninth irradiation period

|                                | Inner Ring |            | Central Ring |            | Outer Ring |            |
|--------------------------------|------------|------------|--------------|------------|------------|------------|
|                                | DF         | PDF        | DF           | PDF        | DF         | PDF        |
| $10^{-5}$ –2 eV                | 1.85E + 12 | 4.14E + 12 | 2.70E + 10   | 1.88E + 12 | 2.31E + 12 | 3.38E + 12 |
| 2–30 eV                        | 7.12E + 10 | 1.61E + 11 | 1.57E + 09   | 1.12E + 11 | 8.11E + 10 | 1.20E + 11 |
| 30–300 eV                      | 6.29E + 10 | 1.44E + 11 | 1.40E + 09   | 1.01E + 11 | 7.16E + 10 | 1.06E + 11 |
| 300– $2 \times 10^7$ eV        | 3.20E + 10 | 7.33E + 10 | 6.76E + 08   | 4.86E + 10 | 3.65E + 10 | 5.42E + 10 |
| $10^{-5}$ – $2 \times 10^7$ eV | 2.02E + 12 | 4.52E + 12 | 3.07E + 10   | 2.15E + 12 | 2.50E + 12 | 3.66E + 12 |

All the values are expressed in n/s cm<sup>3</sup>. The relative standard deviation (assuming exact the values of the energy deposition per source particle) is lower than 410 pcm.

deposition of  $\gamma$  rays, whereas tally type 6 of MCNP does not, the values of flux of Table 4, calculated by MCNP, are 6% larger than the values of Fig. 7, calculated by MCB. In fact, the MCB inclusion of the energy deposition associated to the  $\gamma$  rays, in the calculation of neutron flux, increases  $\varepsilon$  and therefore decreases  $\bar{\varphi}$ . The discrepancy between MCNP and MCB disappears while considering the cross-sections since the flux modifies at the same time both numerator and denominator:

$$\bar{\sigma} = \frac{\int_{10^{-5}}^{20 \times 10^6} \sigma(E) \varphi(E) dE}{\int_{10^{-5}}^{20 \times 10^6} \varphi(E) dE}.$$

Consequently, the cross-section values of Fig. 10 are coherent between the two codes.

Table 4 confirms that the flux in the inner ring is 24% and 33% higher than the central and outer rings; in addition, over 68% of the neutron flux comes from the contribution of the fast tail of the spectrum (fourth group, above 300 eV), whereas the first group contributes for less than 14.5%; moreover, as expected, the central ring has the hardest spectrum since the first group contributes only 10.5% to the one-group flux.

The contribution of the groups changes while analyzing the capture and absorption rates per nucleus of the most abundant isotopes in the fuel (Tables 5–9); in fact, even if the flux of the fourth group is higher the corresponding values of the microscopic cross-sections drop. As a consequence, over 65% of the capture rate of  $^{232}\text{Th}$  occurs between 2 and 300 eV (second and third groups) and about 47% of the capture rate of  $^{238}\text{U}$  comes from the second group due to the resonance of 7126 b at 6.674 eV (according to JEF-2.2). In the case of  $^{233}\text{U}$  and  $^{235}\text{U}$ , the first group gives a share of 60–70% to the total absorption rate (60% in the central ring and 70% in the other two rings); whereas, in the case of  $^{239}\text{Pu}$  about 90% of the total absorption rate comes from the first group.

As general rule, the values of the reaction rates per nucleus (Tables 5–9) are lower in the PDF since the  $^{235}\text{U}$  depletion lowers the local flux (Table 4) and therefore the rate. That is confirmed also by the data of Table 4 concerning the thermal flux up to 2 eV (first group), for the PDF values are smaller than those ones of the DF because

the PDF is richer in plutonium ( $^{239}\text{Pu}$  and  $^{240}\text{Pu}$  have capture resonances of 2186 and 117649 b at 0.293 and 1.056 eV, respectively, according to JEF-2.2).

The harder spectrum of the central ring does not have a strong impact on the values of the capture rates per nucleus of  $^{232}\text{Th}$  and  $^{238}\text{U}$ , but it does in the case of the fissile isotopes: in fact, the values of the absorption rate per nucleus reported (Tables 7–9) in the central ring are lower than those one in the outer ring, a phenomenon which does not occur for the fertile nuclides (Tables 5 and 6). Moreover, the drop of the absorption rate per nucleus of  $^{239}\text{Pu}$  in the central ring (Table 9) is larger than that one of  $^{233}\text{U}$  (Table 7). In fact, in a harder spectrum the  $^{239}\text{Pu}$  capture and fission resonances of 2186 and 3255 b at 0.293 and 0.296 eV (according to JEF-2.2), respectively, are under-weighted. At the light of the above considerations, we can now explain why, in Figs. 6 and 7, the DF in the inner and outer rings favors the production of  $^{233}\text{U}$  whereas in the central one does the production of  $^{239}\text{Pu}$ . Finally, two counteracting characters play a visible role in the absorption rate per nucleus of the fissile isotopes: the neutron flux, which is higher in the inner ring, with the values of the central ring staying between those of the inner and outer rings, and the neutron spectrum, which is harder in the central ring, lowering the relative contribution of the first group (up to 2 eV) and therefore the one-group absorption rate. Nevertheless, both DF and PDF have very close values of the capture and absorption rate per nucleus of their most abundant isotopes (Tables 5–9).

In the case of the capture and absorption rate, another character enters the scene: the change of the atomic densities during irradiation, for the  $^{233}\text{U}$  and  $^{239}\text{Pu}$  relative abundances increase, but those ones of  $^{235}\text{U}$  and  $^{239}\text{Pu}$ , in the PDF of the outer ring, decrease. Consequently, the absorption rate of the fissile nuclides in the PDF, compared to the DF, changes (Tables 12–14). As a result of neutron flux and atomic composition in different type of fuels, the breeding of the fissile isotopes changes while considering the same fuel ring but a different fuel type. In fact, the breeding ratio (BR, defined as the one-group capture rate of the fertile nuclide divided the absorption rate of its corresponding daughter fissile isotope) of  $^{232}\text{Th}/^{233}\text{U}$  is always greater than unity and very large for DF comparing to PDF (Table 15); whereas the breeding ratio of  $^{238}\text{U}/^{239}\text{Pu}$  is less than unity in the PDF of the outer ring (Table 15). At the light of the above considerations, we can now explain why, in Figs. 6 and 7, the  $^{239}\text{Pu}$  of the PDF in the inner and outer rings keeps constant or depletes and the  $^{233}\text{U}$  little builds up. Of course, the very large values of the BR of the DF in the central ring are due to the fact that the fresh DF does not contain  $^{233}\text{U}$  and  $^{239}\text{Pu}$ .

Table 15

Breeding ratio (BR) of  $^{232}\text{Th}/^{233}\text{U}$  and  $^{238}\text{U}/^{239}\text{Pu}$  averaged on TRISO kernels at the beginning of the ninth irradiation period

| BR                               | Inner ring |       | Central ring |       | Outer ring |       |
|----------------------------------|------------|-------|--------------|-------|------------|-------|
|                                  | DF         | PDF   | DF           | PDF   | DF         | PDF   |
| $^{232}\text{Th}/^{233}\text{U}$ | 8.258      | 2.344 | 2379.500     | 3.630 | 3.876      | 1.833 |
| $^{238}\text{U}/^{239}\text{Pu}$ | 2.411      | 1.029 | 135.810      | 1.867 | 1.368      | 0.900 |

Table 16

Reactivity worth and corresponding  $k_{\text{eff}}$  at beginning of the irradiation period at the equilibrium the fuel composition

| Reactivity control       | $\rho$ (pcm) | $k_{\text{eff}}$ |
|--------------------------|--------------|------------------|
| None                     | 0            | 1.06359          |
| Operational control rods | -4777        | 1.01278          |
| Shutdown control rods    | -5573        | 1.00432          |
| Startup control rods     | -5574        | 1.00430          |

All  $k_{\text{eff}}$  values have a relative standard deviation lower than 73 pcm.

### 7.7. Control rods worth

We calculated the reactivity of the control rods neglecting the stuck-rod criterion since the annular shape both of the fuel and of the control rods makes the worth of a rod belonging to the same type, operational, shutdown or startup, quite constant. Since the flux is lower in the outer ring, the total worth of the 36 operational control rods is 4777 pcm; whereas, the worth of the shutdown and startup control rods is 5570 pcm (Table 16). We can note that the startup and operational control rods can manage the initial excess of reactivity of all periods with exception of the first one which has an excess of 13,680 pcm. Nevertheless, this may be overcome by loading a minor quantity of fresh fuel at the beginning of life of the reactor; in fact, the equilibrium of the fuel composition depends little on the initial configuration of the fuel.

## 8. Conclusions

The gas turbine – modular helium reactor has the capability to operate with a uranium–thorium fuel, provided that the pins are fueled with the JAERI TRISO particles, and the application of a deep burn strategy sets the equilibrium of the fuel composition after 3575 days and 9 operation periods. Nevertheless, after a total irradiation period of five years, distributed over DF and PDF, only 46.16% of  $^{235}\text{U}$  transmutes, for the fertile isotopes contribute to the generation of fissile nuclides with a conversion ratio of 0.7. We suggest the reprocessing of the irradiated PDF, for it contains many fissile and fertile nuclides: 24.6 kg of  $^{233}\text{U}$ , 137.9 kg of  $^{235}\text{U}$ , 19.3 kg of  $^{239}\text{Pu}$ , 941 kg of  $^{238}\text{U}$  and 775 kg of  $^{232}\text{Th}$ .

The flux radial-peaking factor is greater in the axial central region of the core, in the axial sub-block at 35.15 cm, and equal to 1.32; whereas, the flux axial-peaking factor is greater in the inner ring and equal to 1.13.

The neutron spectrum is thermalized and exhibits a peak at 0.15 eV; whereas, the spectrum averaged inside the TRISO particles kernels is fast with a peak at 1 MeV.

Due to neutron spectrum effects in different rings and fuel compositions, the DF in the inner and outer rings favorites the  $^{233}\text{U}$  production, while in the central one it does the  $^{239}\text{Pu}$  one; at the same time, the PDF inhibits  $^{239}\text{Pu}$  accumulation and reduces the build up of  $^{233}\text{U}$ .

The startup and operational control rods can manage the initial excess of reactivity of all periods with exception of the first one.

## References

- Baxter, A., Fikani, M., 2002. Reactor-based transmutation – physics studies of the gas-cooled graphite-moderated deep burn reactor. General Atomic, GA-501-0-TRT-000140.
- Baxter, A., Rodriguez, C., 2001. The application of gas-cooled reactor technologies to the transmutation of nuclear waste. *Progress in Nuclear Energy* 38, 81–105.
- Blachot, J., Nordborg, C. 1992. JEF-2.2 radioactive decay data. In: International Symposium on Nuclear Data Evaluation Methodology, BNL.
- Briesmeister, J.F. 2002. A General Monte Carlo N-Particle Transport Code – Version 4c. LANL, LA-13709-M.
- Cetnar, J., Gudowski, W., Wallenius, J. 1999. MCB: a continuous energy Monte Carlo burnup simulation code, in actinide and fission product partitioning and transmutation. EUR 18898 EN, OECD/NEA 523.
- Cetnar, J., Gudowski, W., Wallenius, J., Tucek, K. 2001. Simulation of nuclide transmutation with Monte-Carlo Continuous Energy Burnup Code (MCB1C). In: Proceedings of the Accelerator Application 2001 and ADTTA 2001 Nuclear Application in the New Millennium, Reno, USA.
- Duderstadt, J.J., Hamilton, L.J., 1976. Nuclear Reactor Analysis. Wiley, New York, ISBN 0-471-22363-8.
- General Atomics, 2002. GT-MHR Conceptual Design Description Report. GA/NRC-337-02.
- Gruppelaar, H., Schapira, J.P. 2000. Thorium as a waste management option. European Commission, EUR-19142.
- Herring, J.S., Mc Donald, P.E., et al., 2001. Low cost, proliferation resistant, uranium–thorium dioxide fuels for light water reactors. *Nuclear Engineering and Design* 203, 65–85.
- Kim, J.J., Lee, J.T., Kim, H.R., 1989. Generation and benchmarking of a 69 group cross section library for thermal reactor applications. *Journal of Korean Nuclear Society* 21, 245.
- Kiryushin, A.I., Kodochigov, N.G., Kouzavkov, N.G., et al., 1997. Project of the GT-MHR high temperature helium reactor with gas turbine. *Nuclear Engineering and Design* 173, 119–129.
- Kodochigov, N., Sukharev, Y., et al., 2003. Neutronic features of the GT-MHR. *Nuclear Engineering and Design* 222, 161–171.
- Labar, M., 2002. The Gas Turbine – Modular Helium Reactor: a promising option for near term deployment. General Atomics, GA-A23952.
- Labar, M.P., Simon, W.A., 1994. Comparative economics of the GT-MHR and power generation alternatives. General Atomics, GA-A21722.
- Lung, M., Gremm, O., 1998. Perspectives of the thorium fuel cycle. *Nuclear Engineering and Design* 180, 133–146.
- Minato, K., Ogawa, T., Koya, T., Sekino, H., Tomita, T., 2000. Retention of fission product caesium in ZrC-coated fuel particles for high-temperature gas-cooled reactors. *Journal of Nuclear Materials* 279, 181–188.
- Nabielek, H., Verfondern, K., Werner, H., 2004. Can we predict coated particle failure? A conversation on Convol, Panama and other codes. In: IAEA, Current Status and Future Prospects of Gas Cooled Reactor Fuels, Vienna, Austria.
- Nickel, H., Nabielek, H., et al., 2002. Long time experience with the development of HTR fuel elements in Germany. *Nuclear Engineering and Design* 217, 141–151.
- Nordborg, C., Salvatores, M. 1994. Status of the JEF evaluated data library. In: Proceedings of International Conference on Nuclear Data for Science and Technology, Gatlinburg, TN, USA, May 9–13, 1994, vol. 2, 1994, p. 680.
- Odeychuk, M.P., Zelenskiy, V.F., Gurin, V.A., Yakovlev, V.K., 2004. The current state of HTGR core components fabrication technologies in Ukraine and some properties of the materials and products. IAEA, Current Status and Future Prospects of Gas Cooled Reactor Fuels Vienna, Austria.

- Ohashi, K., Okamoto, F., Hayakawa, H., 2000. Modular High temperature reactor contributing the global environmental protection. *Progress in Nuclear Energy* 37, 307–312.
- Plukiene, R., Ridikas, D., 2003. Modeling of HTRs with Monte Carlo: from a homogeneous to an exact heterogeneous core with microparticles. *Annals of Nuclear Energy* 30, 1573–1585.
- Rodriguez, C., Baxter, A., et al., 2003. Deep-Burn: making nuclear waste transmutation practical. *Nuclear Engineering and Design* 222, 299–317.
- Rütten, H.J., Haas, K.A., 2000. Research on the incineration of plutonium in a modular HTR using thorium-based fuel. *Nuclear Engineering and Design* 195, 353–360.
- Shenoy, A.S., 1995. Modular Helium Reactor for non-electric applications of nuclear energy. General Atomics, GA-A22701.
- Talamo, A., Gudowski, W., Venneri, F., 2004a. The burnup capabilities of the Deep Burn Modular Helium Reactor analyzed by the Monte Carlo Continuous Energy Code MCB. *Annals of Nuclear Energy* 31/2, 173–196.
- Talamo, A., Gudowski, W., Cetnar, J., Venneri, F., 2004b. Key physical parameters and temperature reactivity coefficients of the Deep Burn Modular Helium Reactor fueled with LWRs waste. *Annals of Nuclear Energy* 31 (16), 1913–1937.
- Talamo, A., Gudowski, W., Cetnar, J., 2004c. Comparative studies of ENDF/B-6.8, JEF-2.2 and JENDL-3.2 data libraries by Monte Carlo modeling of high temperature reactors on plutonium based fuel cycles. *Journal of Nuclear Science and Technology* 41 (12).
- Talamo, A., Gudowski, W. 2005. A Deep Burn Fuel Management Strategy for the Incineration of Military Plutonium in the Gas Turbine – Modular Helium Reactor Modeled in a Detailed 3D Geometry by the Monte Carlo Continuous Energy Burnup Code. Internal report.
- Taubman, C.J. 1975. The WIMS 69-Group Library Tape 166259. Report AEEW-M1324, UK Atomic Energy Authority, Winfrith, Great Britain.
- Tsuchie, Y., 2000. Desirability of small reactors, HTGR in particular. *Progress in Nuclear Energy* 37, 253–258.
- Wistrom, J.D., Simon, W.A., 1996. Where does the GT-MHR go from here? *Nuclear Engineering and Design* 41.

Technical note

# Managing the reactivity excess of the gas turbine-modular helium reactor by burnable poison and control rods

Alberto Talamo \*

*Department of Nuclear and Reactor Physics, Royal Institute of Technology, Roslagstullsbacken 21, S-10691, Stockholm, Sweden*

Received 7 July 2005; accepted 24 August 2005

Available online 19 October 2005

## Abstract

The gas turbine-modular helium reactor coupled to the deep burn in-core fuel management strategy offers the extraordinary capability to incinerate over 50% of the initial inventory of fissile material. This extraordinary feature, coming from an advanced and well tested fuel element design, which takes advantage of the TRISO particles technology, is maintained while the reactor is loaded with the most different types of fuels. In the present work, we assumed the reactor operating at the equilibrium of the fuel composition, obtained by a 6 years irradiation of light water reactor waste, and we investigated the effects of the introduction of the burnable poison and the control rods; we equipped the core with all the three types of control rods: operational, startup and shutdown ones. We employed as burnable poison natural erbium, due to the  $^{167}\text{Er}$  increasing neutron capture microscopic cross-section in the energy range where the neutron spectrum exhibits the thermal peak; in addition, we utilized boron carbide, with 90% enrichment in  $^{10}\text{B}$ , as the absorption material of the control rods. Concerning the burnable poison studies, we focused on the  $k_{\text{eff}}$  value, the  $^{167}\text{Er}$  mass during burnup, the influence of modifying the radius of the BISO particles kernel and the fuel and moderator coefficients of temperature. Concerning the control rods studies, we investigated the reactivity worth, the changes in the neutron flux profile due to a partial insertion, the influence of modifying the radius of the BISO particles kernel and the  $\beta_{\text{eff}}$ , at the beginning of the operation.

© 2005 Elsevier Ltd. All rights reserved.

## 1. Introduction

The high temperature gas reactors (HTGRs) have 2 main designs: pebble bed and prismatic core types; in the first type, the fuel element consists of a 6 cm diameter sphere, whereas in the latter one it does of a cylindrical pin with a radius of 0.6 cm and a height of 8 m. The HTGRs constitute one of the major hopes for the future of nuclear energy and they may be launched as the next generation of nuclear power plants. Some countries in Asia already started practically HTGR-projects: Japan has planned by 2018 to commercialize the GTHR300 (Kunitomi et al., 2004) and it already set the criticality of a 30 MW prismatic research reactor in 1998 (Shiozawa et al., 2004); in year 2000 China started operation of the

HTR10, a pebble bed research reactor with a 10 MW thermal output (Xu and Zuo, 2002). In the present work, we consider a 600 MW<sub>th</sub> prismatic HTGR, the gas turbine-modular helium reactor (GT-MHR) (Baxter and Fikani, 2002; Baxter and Rodriguez, 2001; General Atomics, 2002; Kiryushin et al., 1997; Kodochigov et al., 2003; Ohashi et al., 2000; Rodriguez et al., 2003) that has been developed by General Atomics (GA) in the USA during the 1990s. In our previous studies, we have analyzed the key neutronic parameters and the burnup performance of the GT-MHR with: light water reactors (LWRs) waste (Talamo et al., 2004a,b,c), military plutonium (Talamo and Gudowski, 2005a) and thorium (Talamo and Gudowski, 2005b,c). We referred to our refueling and shuffling schedule as a deep burn (DB) in-core fuel management strategy, since in all the types of fuels we obtained a depletion of the initial inventory of all fissile isotopes superior to 50%, with the exception of the thorium fuel. The DB in-core fuel management strategy is structured into the utilization of

\* Fax: +46 8 5537 8465.

E-mail address: [alby@neutron.kth.se](mailto:alby@neutron.kth.se).

two different types of fuel: the driver fuel (DF) and the post driver fuel (PDF), which we denominated transmutation fuel (TF) in the case of LWRs waste. The first type of fuel maintains the criticality of the reactor and the latter, consisting of 3 years irradiated DF, enhances the transmutation rates of the DF by a further irradiation of 3 years. The major conclusions of our previous studies of the GT-MHR fueled with LWRs waste have been that: the equilibrium destruction rates for  $^{239}\text{Pu}$ , overall Pu and all actinides are, respectively: 94%, 61% and 53%; the spectral peak of neutron flux averaged in the core is at 0.2 eV; the neutron spectrum averaged in the fuel exhibits two dips in the thermal region due to resonance captures of  $^{239}\text{Pu}$  and  $^{240}\text{Pu}$ ; the temperature reactivity coefficients for fuel and moderator are both negative and the moderator one is quite large, 12 pcm/K. The thermalized spectrum of the reactor is a clear benefit for the integrity of TRISO particles; in fact, the displacements per atom (DPA) cross-section of silicon carbide is greater of 10 b only for neutrons with an energy above 3.4 keV (Table I of Heinisch et al., 2004); moreover, in the neutron spectrum of a ordinary LWR the DPA cross-section is 2.5 times higher than in the case of a HTGR (Table II of Heinisch et al., 2004).

## 2. The GT-MHR operating on LWRs waste

In order to approach the equilibrium of the fuel composition, we started the beginning of life of the reactor just

with the inner ring (white ring in Fig. 1). After the first year, the DF is shuffled into the central ring (gray/green ring in Fig. 1) and fresh DF is loaded again into the inner one. During the second year the reactor operates with only the inner and central rings loaded with DF. After the second year, the DF from central ring is moved into the outer ring (dark-gray/blue ring in Fig. 1) and the fuel from inner ring takes its place; fresh DF is loaded into the inner ring. Finally, during the third year, the DF fills all the three rings. At the end of the third year, the spent DF from the outer ring is reprocessed (Pu and minor actinides extraction) and mixed with some set-aside, from LWRs waste,  $\text{AmCmO}_{1.7}$  to build the fresh TF. At the beginning of the fourth year, both fresh Driver and Transmutation Fuel fill the inner ring and in the following years we adopted both for the DF and for the TF the same outward radial shuffling and refueling schedule of the first three years. At the beginning of the 6th year DF and TF fill all the three rings of the core, but the equilibrium of the fuel composition is approached only at the beginning 12th year. We remand to our previous studies (Talamo et al., 2004a) and for a more detailed description of the deep burn strategy applied to the LWRs waste; whereas, we report in Tables 1 and 2 the geometry and material data of the core.

In the present studies, we improved our previous MCB model of the GT-MHR, which we have used for the approach of the fuel equilibrium composition, with the introduction of some small changes:

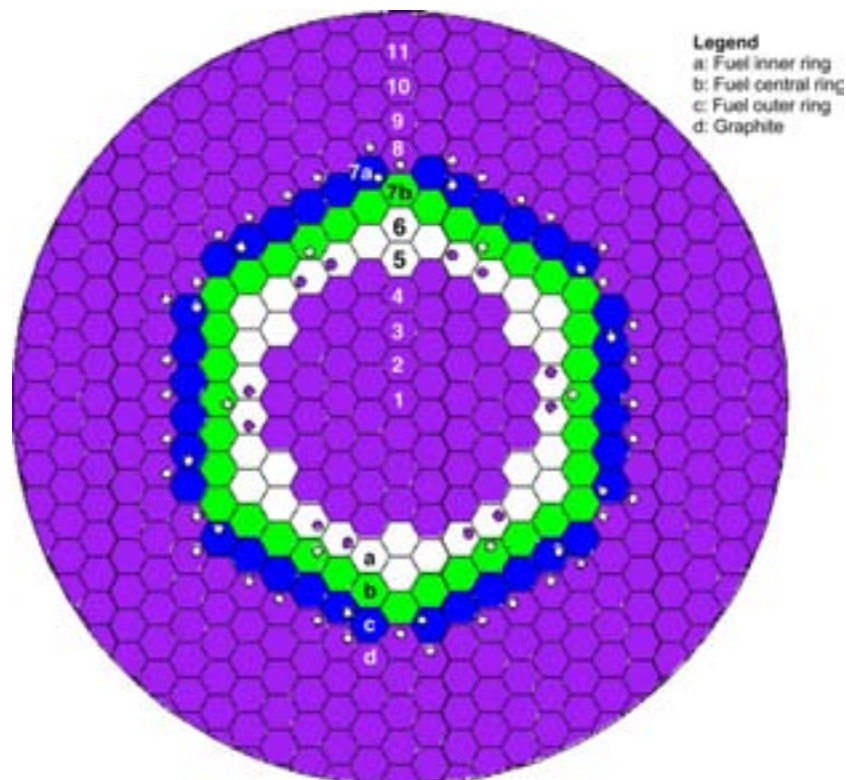


Fig. 1. Disposition of the fuel blocks and of the control rods. The inner ring of fuel (white) contains 12 startup control rods, the central (gray/green) and outer ring (dark-gray/blue) respectively do 6 and 12 shutdown control rods, the outer graphite reflector ring does 36 operational control rods. MCNP plot.



Table 1  
MCB geometry data of the GT-MHR

|  |                 |
|--|-----------------|
| Core – radius (cm)   | 400             |
| Core – height (cm)   | 1000            |
| Control rods – startup (inner ring)  | 12              |
| Control rods – operational (outer moderator reflector ring)                                    | 36              |
| Control rods – shutdown (central ring/outer ring)  | 6/12            |
| Control rods – internal radius (startup/operational/shutdown) (cm)                             | 0/2.64/0        |
| Control rods – external radius (cm)  | 4.13            |
| Control rods – hole radius (cm)  | 5.05            |
| Control rods – distance from the center of the hexagon (cm)                                    | 9.75614         |
| Control rods – height at bol (startup/operational/shutdown) (cm)                               | 0/0/0           |
| Hexagonal fuel blocks – number   | 36 × 3          |
| Hexagonal fuel blocks – width (cm)   | 35.99688        |
| Hexagonal fuel blocks – height (cm)  | 793             |
| Hexagonal blocks – interstitial gap (cm)   | 0.1             |
| Fuel blocks – DF pins (with control rod/without control rod)                                   | 140/124         |
| Fuel blocks – TF pins (with control rod/without control rod)                                   | 70/62           |
| Fuel blocks – coolant channels (with control rod/without control rod)                          | 108/95          |
| Fuel blocks – BP pins (with control rod/without control rod)                                   | 6               |
| Pins – radius (DF and TF/BP) (cm)  | 0.6223/0.5715   |
| Pins – height (cm)   | 793             |
| Pins – distance between pins (cm)  | 3.25628         |
| Pins – hole radius (fuel/coolant) (cm)   | 0.635/0.795     |
| TRISO particles – kernel radius (DF/TF/BP/CR) (μm)   | 150/100/150/300 |
| TRISO particles – width porous carbon layer (DF/TF/BP/CR) (μm)                                 | 150/150/25/25   |
| TRISO particles – width inner pyrocarbon layer (DF/TF/BP/CR) (μm)                              | 35              |
| TRISO particles – width ZrC layer (DF/TF) (μm)   | 35              |
| TRISO particles – width outer pyrocarbon layer (DF/TF) (μm)                                    | 40              |
| TRISO particles – body centered square box latus (DF/BP/CR) (cm)                               | 0.1588276       |
| TRISO particles – body centered square box latus (TF) (cm)                                     | 0.105885        |
| TRISO particles – packing fraction (DF/TF) (%)   | 14.41/32.92     |
| TRISO particles – packing fraction (BP/CR) (%)   | 1.94/9.76       |
| TRISO kernels DF – volume (inner ring/central ring/outer ring = inner ring) (cm <sup>3</sup> ) | 33006.6/33660.2 |
| TRISO kernels TF – volume (inner ring/central ring/outer ring = inner ring) (cm <sup>3</sup> ) | 16503.3/16830.1 |
| TRISO kernels BP – volume (three rings) (cm <sup>3</sup> )                                     | 3720.88         |
| TRISO kernels CR – volume (36 operational control rods) (cm <sup>3</sup> )                     | 51,075          |

- The modeling of the operational, startup and shutdown control rods.
- The application of the burnable poison.
- The introduction of the interstitial gap between the hexagonal blocks.
- The replacement of silicon carbide with zirconium carbide in the TRISO particles.
- The setting of the graphite temperature at 900 K, with a scattering function  $S(\alpha, \beta)$  evaluated at 800 K, for all hexagonal blocks not containing fuel pins or control rods, instead of 1200 K.

Let us remark that the change in the  $k_{\text{eff}}$  value due to the last improvement is small; in fact, when all graphite is at 1200 K, the  $k_{\text{eff}}$  value increases of 190 pcm. Fig. 1 shows the horizontal section of the core and it illustrates the disposition of the control rods: the GT-MHR is equipped with 12 startup control rods located in the inner fuel ring, 6 shutdown ones in the central ring, 12 shutdown ones in the outer ring and 36 operational ones in the graphite reflector blocks surrounding the outer fuel ring. Fig. 2 provides a zoom of the hexagonal blocks in different rings and it allows distinguishing the 6 burnable poison pins located at the corners of each hexagonal block. We have chosen natural erbium as burnable poison because  $^{167}\text{Er}$  has an increasing neutron capture cross-section at 0.1–0.3 eV (Fig. 3), the energy range where the neutron spectrum averaged in the core has a peak, and that allows a large decrease of the reactivity for a fuel temperature raise in case of accident. We utilized boron carbide, with a 90% enrichment in  $^{10}\text{B}$ , as absorption material of the control rods; let us remark that the  $^{10}\text{B}$  ( $n, \alpha$ ) cross-section, on the contrary of  $^{167}\text{Er}$ , exhibits no resonances (Fig. 3).

As we already wrote in Section 1, the equilibrium destruction rates for  $^{239}\text{Pu}$ , overall Pu and all Actinides are, respectively: 94%, 61% and 53%. In other similar studies (Fig. 16 of Rodriguez et al., 2003), the corresponding numbers appear to be 99.9%, 82% and 75%. It is most probably an overestimation due to one-group averaged cross-sections, e.g., the fission cross-section of  $^{239}\text{Pu}$  seems to be ten times higher than our value (Fig. 5 of Rodriguez et al., 2003 versus Fig. 15 of Talamo et al., 2004a).

Let us observe that the real GT-MHR differs from our numerical model because of four major approximations:

- The approach of the equilibrium of the fuel composition neglected the modeling of the burnable poison and the control rods.
- The approach of the equilibrium of the fuel composition neglected the axial shuffling.
- TRISO particles have been disposed by a body centered square infinite lattice whereas in reality they are randomly located.
- TRISO particles, in the numerical model, might be cut at the edge of the fuel pin.

Concerning the first two approximations, we believe that the equilibrium of the fuel composition is independent on the way it is being reached, at least as the first approximation; of course, the presence of low energy absorbers may depress the thermal region of the spectra and affect somewhat the transmutation rates. The introduction of the control rods changes the axial neutron flux profile; therefore, in the case the reactor is equipped with the control rods the transitory of the fuel composition must consider also the axial shuffling to optimize the burnup of the fuel. The above topic is a good starting point for further studies. Concerning the third approximation, Brown and Martin (2004) evaluated that, for a graphite box filled by a

Table 2  
MCB material data of the GT-MHR at the equilibrium of the fuel composition

| Material  | Atomic composition (%)   | Initial density (g/cm <sup>3</sup> )–temperature (K) |
|---|--|--|
| TRISO kernel – fresh DF   | <sup>237</sup> Np(1.91); <sup>238</sup> Pu(0.56); <sup>239</sup> Pu(21.11); <sup>240</sup> Pu(8.5); <sup>241</sup> Pu(3.09);<br><sup>242</sup> Pu(1.87); <sup>16</sup> O(62.96)  | 10.2–1500  |
| TRISO kernel – fresh TF   | <sup>237</sup> Np(1.23); <sup>238</sup> Pu(1.23); <sup>239</sup> Pu(5.39); <sup>240</sup> Pu(6.62); <sup>241</sup> Pu(5.23);<br><sup>242</sup> Pu(2.50); <sup>241</sup> Am(3.88); <sup>242m</sup> Am(0.03); <sup>243</sup> Am(1.25); <sup>244</sup> Cm(0.06);<br><sup>244</sup> Cm(0.36); <sup>245</sup> Cm(0.03); <sup>16</sup> O (72.19) | 15.676–1500  |
| TRISO kernel – BP   | <sup>162</sup> Er(0.10); <sup>164</sup> Er(1.14); <sup>166</sup> Er(23.78); <sup>167</sup> Er(16.22); <sup>168</sup> Er(18.95);<br><sup>170</sup> Er(10.56); <sup>16</sup> O(60.00)  | 4.8633–1200  |
| TRISO kernel – CR   | <sup>10</sup> B(72); <sup>11</sup> B(8); <sup>12</sup> C(20)   | 2.52–1200  |
| TRISO porous graphite   | C(100)   | 1–1200   |
| TRISO pyrocarbon  | C(100)   | 1.85–1200  |
| TRISO zirconium carbide   | Zr(50); C(50)  | 6.56–1200  |
| Graphite matrix (fuel blocks<br>and control rods blocks/<br>pure graphite blocks) | C(100)   | 1.74–1200/900  |

The burnup isotopes of the burnable poison are indicated in *Italics* text and they do not contribute to the value of the initial density, which includes only the transport isotopes.

$5 \times 5 \times 5$  matrix of TRISO particles, the difference between a regular body centered lattice and a random distribution may have an impact of 200 pcm in the value of the  $k_{\text{eff}}$ ; nevertheless, only MCNP5 (Briesmeister, 2002) with somewhat

limited distribution, supports the definition of a random geometry. However, while considering a whole hexagonal fuel block, the difference in the  $k_{\text{eff}}$  may grow up to 500 pcm (Kim et al., 2004). Concerning the 4th approxima-

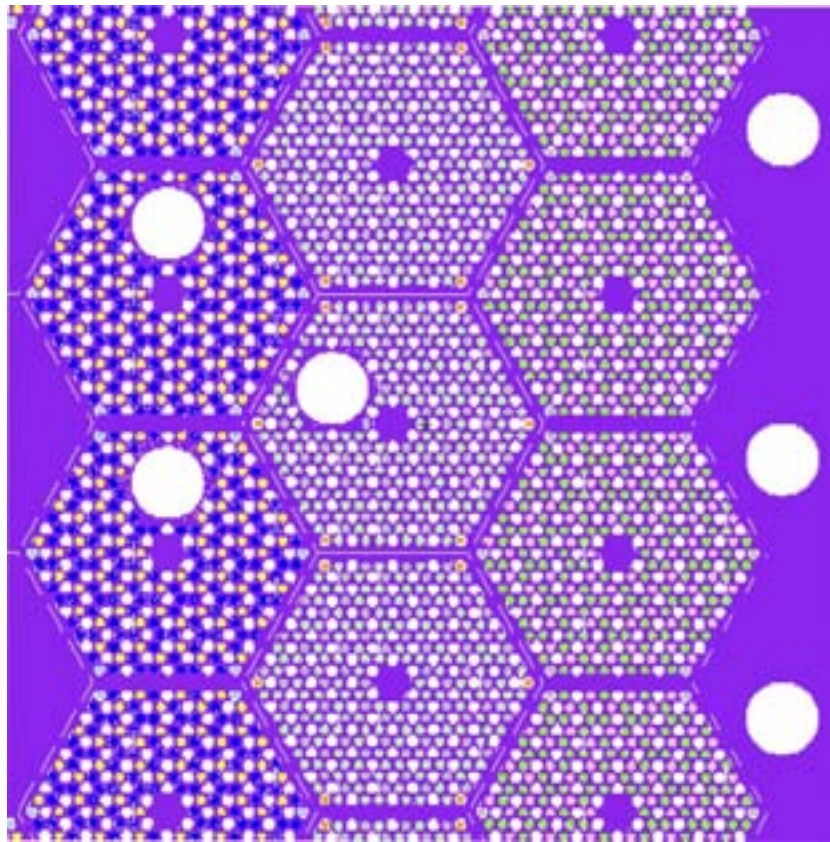


Fig. 2. Detail of the fuel blocks in the inner, central and outer rings. The DF pins are in blue, light-green and green in the inner, central and outer rings; the TF pins are in yellow, gray and pink in the inner, central and outer rings; the burnable poison pins, located at the corners of the hexagons, are in light-blue, orange and gray in the inner, central and outer rings; the control rods holes correspond to the big white circles and the coolant channels do to the small ones. MCNP plot.

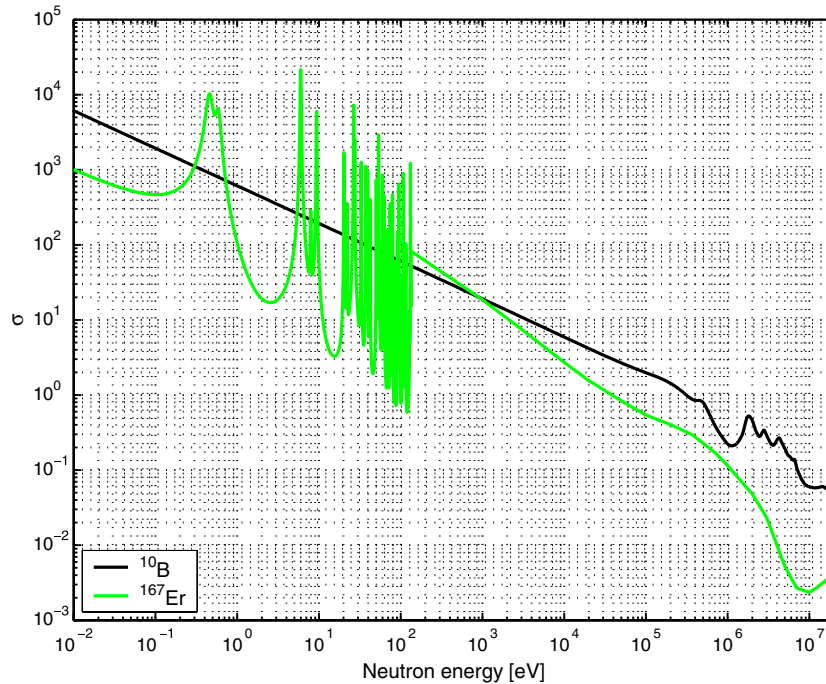


Fig. 3. Capture and  $(n,\alpha)$  cross-sections of  $^{167}\text{Er}$  and  $^{10}\text{B}$ , respectively.

tion, the impact is difficult to evaluate because the removal of a cutting edge corresponds to the removal of a piece of TRISO particle and therefore of the associated mass; we have found a difference of 2100 pcm, for a fuel composed of military plutonium, between a burnable poison BISO particles lattice cutting the edge of fuel pins and an uncut lattice, but in the latter case the mass of erbium was 27 kg less and that contributed to this large reactivity difference. Moreover, our main simulation tool MCNP4c3 has a significant limitation: the TRCL cards, used for geometry description are limited to only 999; that makes difficult an implementation of a numerical model with an uncut lattice (see Section 3.2).

### 3. The GT-MHR modeled by the MCB code

#### 3.1. The MCB code

All numerical simulations have been performed by the Monte-Carlo Burnup Code MCB1c2, which has been developed at the Stockholm Royal Institute of Technology and at the Cracow University of Science and Technology (Cetnar et al., 1999, 2001). We remand to our previous papers for the details of the code features and we limit to state that the MCB code is an extension of the well-known MCNP4c3 code with the implementation of the burnup capability; in addition, the nuclides transmutation takes full advantage of the continuous energy cross-sections data libraries, e.g., by the evaluation of the energy dependent yield of the isomers nuclides.

The MCB code predictions have been recently compared with the experimental data from MOX fuel in the Beznau-4

boiling water reactor (BWR) in Switzerland and the Ringhals-4 pressurized water reactor (PWR) in Sweden. The relative error  $\varepsilon$  between the MCB results  $C$  and the experimental data  $E$  has been defined by the following formulas:

$$\varepsilon = \frac{C - E}{E}. \quad (1)$$

With the above definition, the MCB code, equipped with JEF-2.2, produced a relative error of  $-0.8$ ,  $0.5$ ,  $18.7$ ,  $-4.2$ ,  $0.5$ ,  $-0.3$  and  $10.7\%$  for  $^{235}\text{U}$ ,  $^{238}\text{U}$ ,  $^{238}\text{Pu}$ ,  $^{239}\text{Pu}$ ,  $^{240}\text{Pu}$ ,  $^{241}\text{Pu}$  and  $^{242}\text{Pu}$  (Table VI of Grisell, 2004); for americium and curium the absolute value of  $\varepsilon$  ranged from 12% to 40% (Table VII of Grisell, 2004); for the average for 32 fission products,  $\varepsilon$  is about 28% (Table VIII of Grisell, 2004). The validation of other burnup codes did not reproduce better results than MCB; for instance the ORIGEN-2 code, equipped with JENDL-3.2 and validated on the Dodewaard BWR experimental data, produced a value of  $\varepsilon$  close to 10% for the mass of  $^{235}\text{U}$  (Fig. 7 of Ando et al., 2003). A better result,  $\varepsilon$  between 3% and 5% for  $^{235}\text{U}$ , has been obtained instead by ORIGEN-ARP, equipped with ENDF/B-6.8 and validated on the Dodewaard BWR and the Beznau PWR in Netherlands, before its permanent shutdown in 1997 (Figs. 15–17 of Gauld, 2003).

#### 3.2. The GT-MHR numerical model

In the burnup simulations, we adopted 7 burnable materials, one material for each type of fuel (DF and TF) per ring and one material for the burnable poison; therefore,

the burnable poison has been irradiated by the average flux amid the three rings of fuel; the boron carbide of the control rods has not been set as burnable material. The modeling of the burnable poison material required two different types of erbium isotopes: the transport and the burnup isotopes. The erbium transport isotopes  $^{166}\text{Er}$  and  $^{167}\text{Er}$ , available from the JEF-2.2 data library (with extension 12c), contributed in the simulation of neutron transport; whereas, the burnup isotopes  $^{162}\text{Er}$ ,  $^{164}\text{Er}$ ,  $^{168}\text{Er}$  and  $^{170}\text{Er}$ , available from the EAF99 data library (with extension 12y), did not contribute in the neutron transport simulation (MCB automatically upgrades a burnable isotope to a transport one only if its total cross-section represent a fraction larger than  $10^{-10}$  in the total cross-sections of its material); nevertheless, the densities of the burnup isotopes of erbium changed according to the level of the neutron flux and their cross-sections. For each material, not only erbium but also the other 6 materials for DF and TF, the MCB code defines transport and burnup isotopes.

The Monte-Carlo code has been equipped with a nuclear data library based on JEF-2.2 and extended with: JENDL-3.2, ENDF/B-6.8, DLC200, which has been used just for the scattering function  $S(\alpha, \beta)$  of graphite, and EAF99, which has been used just to enlarge the data of fission products.

The number of lines of the present MCB input is about 2700, including 120 TRCL MCNP cards, and it requires over 420 MB of computer RAM memory per processor. We performed all the numerical simulations on a cluster of ten 1800 MHz 64 bits AMD Opteron processors mounted of five Tyan Tiger-K8W dual processor motherboards. The computers cluster operated on Linux Mandrake9.2-Erbium and Parallel Virtual Machine (PVM)

version 3.4.4.16, which is the first release supporting the compilation on the AMD dual processor 64-bits architecture. Let us observe that nowadays the Linux AMD Opteron processor represents the fastest solution for high performance computing (<http://jsekhon.fas.harvard.edu/macosx/>).

In the case of the burnup calculations the MCNP subroutine of the MCB code had been invoked after 10 days of simulated operation and then after each month. Each MCNP subroutine, simulating a total of 3.75 millions of neutrons distributed over 125 k-code cycles, including 25 non-active ones, lasted 6.5 h. For the calculation of neutron flux and spectrum, the total number of simulated neutrons has been increased to 37.5 millions.

#### 4. The application of burnable poison

Fig. 4 plots the evolution of  $k_{\text{eff}}$  for three different cases: empty burnable poison holes and burnable poison holes filled with two years irradiated TF or erbium pins. We can note that the employment of erbium flattens the curve of the  $k_{\text{eff}}$  time evolution since the initial excess of reactivity is limited to only 3940 pcm and at the same time, the life of the fuel is shorted only by 70 days, compared to the case of empty burnable poison holes. The curve referring to the TF pins collocates in between the other two ones and it exhibits an initial excess of reactivity of 5180 pcm with a penalty in the fuel life of 40 days, compared to the case of empty burnable holes. In all the curves, it is clearly visible the poisoning of the short life fission products that diminishes the initial excess of reactivity of 1000 pcm already after 10 days. The results we obtained with the introduction of the control rods and the burnable poison well match our

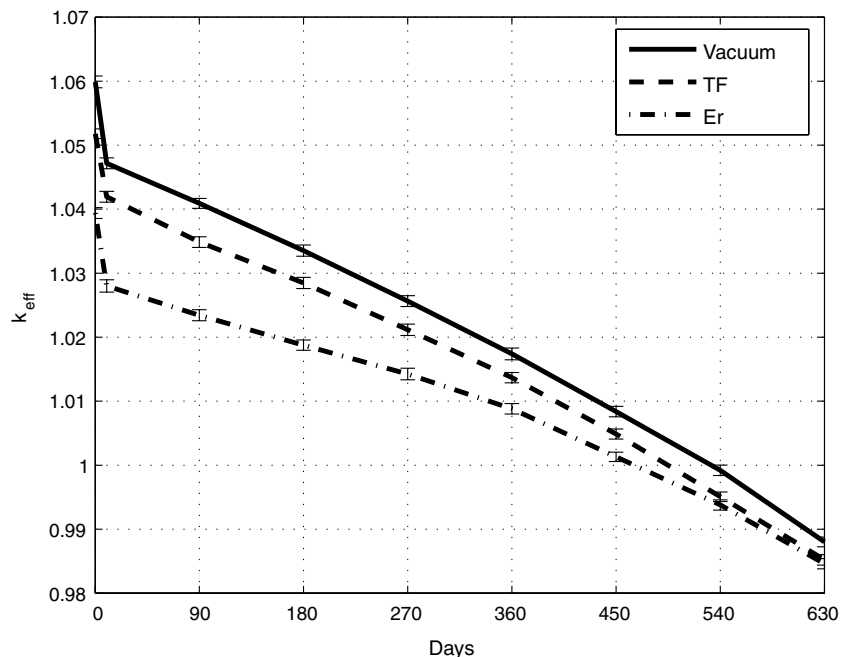


Fig. 4. Evolution of  $k_{\text{eff}}$  for the burnable poison holes filled by: vacuum, TF and erbium. Standard Deviation (SD) is indicated by the small horizontal ticks and it is given with 95% confidence.

previous results, where the burnable poison holes had been filled both with DF and TF pins. In fact, either the burnable poison holes are filled with DF and TF pins or they are left empty, the initial excess of reactivity remains about 6000 pcm, since, in the neutron balance, the fissile nuclides of DF are compensated by the absorbing ones of the TF (Fig. 8 of Talamo et al., 2004a versus Fig. 4). In studies where the GT-MHR has been fueled with military plutonium, the flattening of the  $k_{\text{inf}}$  time evolution curve by the utilization of erbium (Fig. 3 of Kodochigov et al., 2003) was more accentuated, almost resembling an horizontal line, than our  $k_{\text{eff}}$  results for LWRs waste (Fig. 4). Nevertheless, the shape of the curve of our results is confirmed also by other independent researches; in fact, Plukiene and Ridikas (2003a, Fig. 2) pointed out that, when the excess of reactivity is managed by erbium, the  $k_{\text{eff}}$  curve, associated to a homogeneous core description, increases; whereas, the  $k_{\text{eff}}$  curve, associated to a double heterogeneous core description, decreases, due to the spatial self shielding. Moreover, with the homogenization of the triple heterogeneity of the core, the initial  $k_{\text{eff}}$  value may be underestimated of 14,000 pcm (p. 1579 of Plukiene and Ridikas, 2003a) and the erbium mass transmutes faster (p. 1580 of Plukiene and Ridikas, 2003a).

The transmutation of the erbium isotopes, shown in Fig. 5, confirms that the only nuclide relevant, from a neutronic point of view, is  $^{167}\text{Er}$ , which produces the accumulation of  $^{168}\text{Er}$  by neutron capture. The initial mass of  $^{167}\text{Er}$

passes, during 450 days of operation, from 6.44 to 1.74 kg; therefore, the reactor burns most of the burnable poison, about 73%. Other studies suggest that an initial mass of  $^{167}\text{Er}$  equal to 11.4 kg, of course with a corresponding increase of the fuel inventory, would allow an operation of 800 days without refueling (Fig. 2 of Plukiene and Ridikas, 2003b).

The optimization of the erbium BISO particles kernel radius must take into account at least two key parameters: the reactivity excess and the leftover mass. Fig. 6 indicates that the feedback due to a variation of 25  $\mu\text{m}$  in the radius of the burnable poison kernel is 700–1000 pcm, a change that is larger than that one obtained in the case of operational control rods or fuel. In fact, in our previous studies (Talamo et al., 2004b) we have found that an increase of 25  $\mu\text{m}$  in the DF kernel radius produces an increase of 500 pcm in the  $k_{\text{eff}}$  value.

As the last test, we compared the fuel and moderator coefficients of temperature (CT) for a cross-section temperature raise of 300 K in three scenarios: when the burnable poison holes are left empty or filled with erbium or TF. In the case of the fuel CT, we increased the temperature of the fuel and eventually also that one of erbium or TF. In the case of the moderator CT, we increased the graphite temperature in all regions of the reactor with the exception of the pure graphite hexagonal blocks; therefore, we used graphite cross-section at 1500 K with the scattering function  $S(\alpha, \beta)$  evaluated at 1600 K. Tables 3 and 4 report

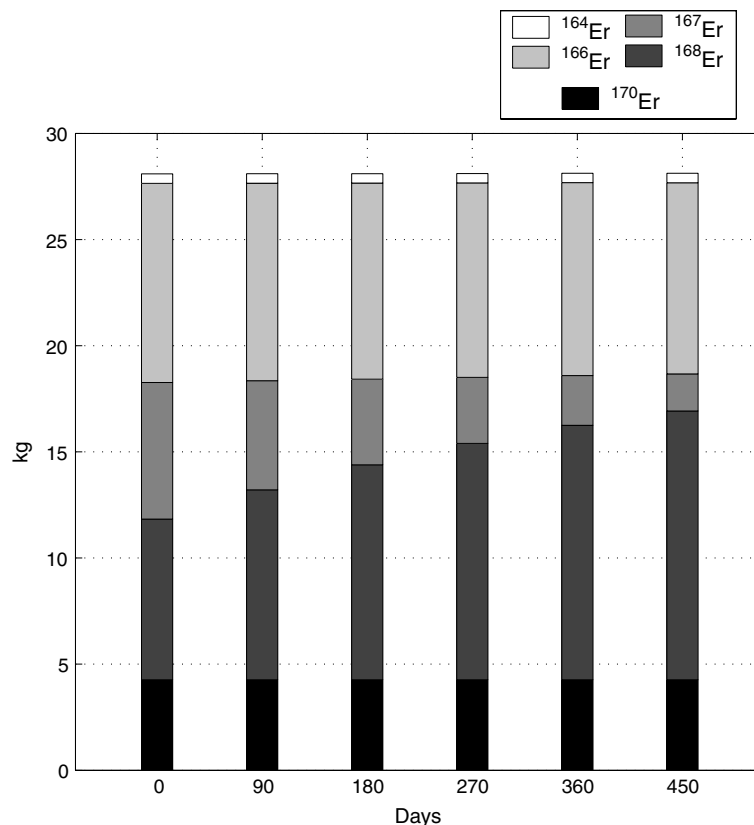


Fig. 5. Evolution of erbium mass.

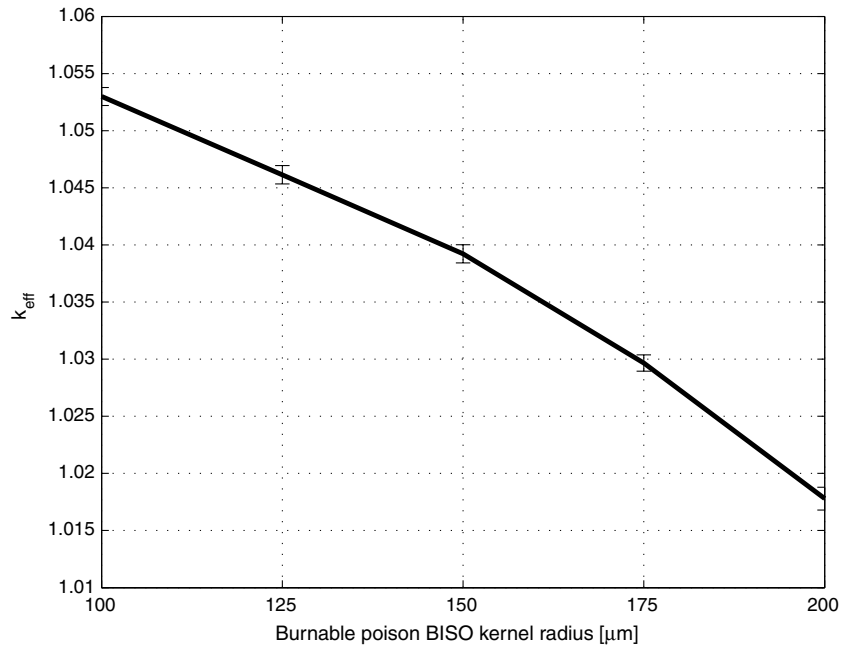


Fig. 6. Variation of the initial  $k_{\text{eff}}$  with different radii of the burnable poison BISO kernels. SD is indicated by the small horizontal ticks and it is given with 95% confidence.

Table 3

$k_{\text{eff}}$  and temperature coefficient ( $C_T$ ) for a raise of 300 K in the temperatures of the cross-sections of the fuel and the burnable poison at the equilibrium of the fuel composition when the burnable poison holes are filled with: vacuum, erbium and TF

|                                  | Vacuum  | Erbium  | TF      |
|----------------------------------|---------|---------|---------|
| $k_{\text{eff}}$ (operational T) | 1.05989 | 1.03941 | 1.05178 |
| $k_{\text{eff}}$ (increased T)   | 1.05449 | 1.03404 | 1.04847 |
| $C_T$ (pcm/K)                    | -1.6105 | -1.6661 | -1.0020 |

The maximal SD, with 68% confidence, of  $k_{\text{eff}}$  is lower than 42 pcm.

Table 4

$k_{\text{eff}}$  and temperature coefficient ( $C_T$ ) for a raise of 400 K in the temperatures of the cross-sections of the graphite at the equilibrium of the fuel composition when the burnable poison holes are filled with: vacuum, erbium and TF

|                                  | Vacuum  | Erbium  | TF      |
|----------------------------------|---------|---------|---------|
| $k_{\text{eff}}$ (operational T) | 1.05989 | 1.03941 | 1.05178 |
| $k_{\text{eff}}$ (increased T)   | 1.02058 | 0.99905 | 1.01416 |
| $C_T$ (pcm/K)                    | -9.0852 | -9.7171 | -8.8183 |

The maximal SD, with 68% confidence, of  $k_{\text{eff}}$  is lower than 45 pcm.

the results for the fuel and the moderator CT, respectively; the moderator CT is six times larger than the fuel one. In the present studies, we obtained a moderator CT of about 9 pcm, we consider this value a better estimation than the value obtained in our previous studies, 12–15 pcm (Table II of Talamo et al., 2004b), because the evaluation of the scattering function  $S(\alpha, \beta)$  of graphite is by far more important than the graphite cross-section temperature (Table III Talamo et al., 2004b) and therefore the real increase of the temperature of the moderator is 400 K instead of 300 K.

Other studies have confirmed the large difference between the fuel and moderator CT since they have found values equal to 2.1 and 8.5 pcm/K, respectively (Table II of Plukiene and Ridikas, 2003b); nevertheless, those values have been calculated by the formulas  $\Delta k/\Delta t$  whereas in the present studies we used  $\Delta\rho/\Delta t$ . Let us also highlight that the CT calculated in our similar studies (Table III of Talamo and Gudowski, 2004d) was not fully correct because it adopted  $k_{\text{eff}}$  at the reference temperature that one of vacuum case also for burnable poison holes filled with erbium or TF.

Since the utilization of  $^{167}\text{Er}$  reduces the initial reactivity excess and it also grants an operation longer than one year, we assumed for all the remaining calculations that the burnable poison holes are filled with erbium pins.

## 5. The modeling of control rods

We analyzed the variation of  $k_{\text{eff}}$  due to the progressive insertion of the control rods and we plotted the results in Fig. 7. We can note that the operational, startup and shutdown control rods generate a very similar variation in the criticality of the reactor; each group of rods has a worth of about 5100–5500 pcm while they are fully inserted. The similarity of the reactivity worth, amid the different type of control rods, is explained by their disposition in the core; in fact, in spite the number of the operational control rods is twice as much as that one of the shutdown control rods (the GT-MHR is equipped with 36 operational control rods and 18 shutdown ones), the first ones are located in a region with a much lower neutron flux. The same criterion applies between the startup and the shutdown control rods (the GT-MHR is equipped with 12 startup control rods and 18 shutdown ones) since the first ones

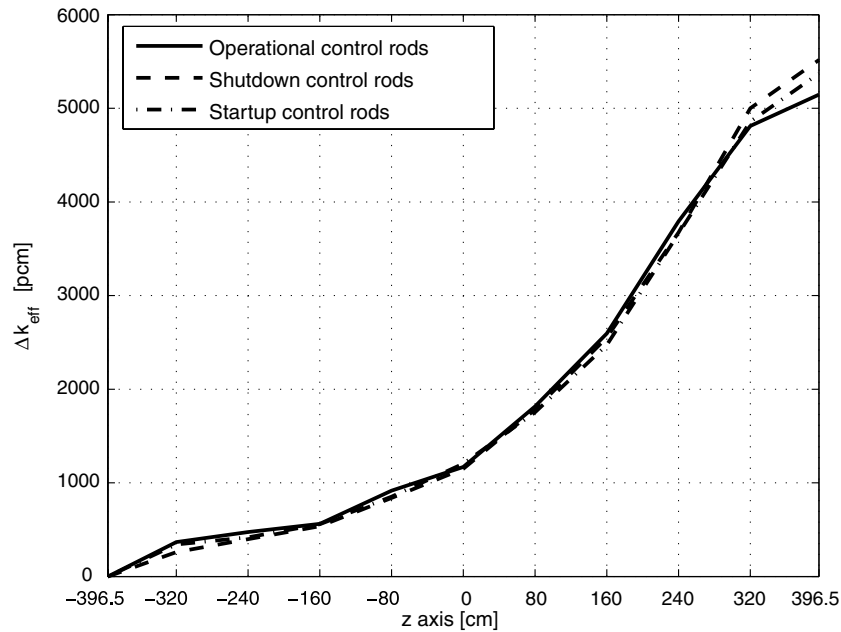


Fig. 7. Variation of  $k_{\text{eff}}$  with the progressive insertion of the control rods.

lye in the fuel ring with the highest flux. The slope of the curves changes after an insertion of 400 cm, from about 100 pcm to 1000 pcm per 80 cm; therefore, most of the reactivity feedback occurs when the insertion covers more than 50% of the rod length. Studies on the worth of six control rods for a pebble bed reactor indicated a value of 3500 pcm (Fig. 5 of Bernnat and Feltes, 2003).

Even if a quite large negative moderator CT is a benefit from the safety point of view, because it provides a strong passive reactivity feedback, it may arise some problem in the design of the control rods. In fact, the startup control rods must properly manage the excess of reactivity of the cold core, a configuration where all materials are at the room temperature of 300 K (including the scattering function  $S(\alpha, \beta)$  of graphite). Unfortunately, the present design of the startup control rods cannot manage an excess of reactivity of 8640 pcm, which corresponds to a cold core. Since we used a low BISO packing fraction, just 9.76%, we tested a higher packing fraction, about 39.09%, but we obtained a startup worth of only 6200 pcm, which still does not allow the reactor to reach criticality from the cold state. At the light of the above consideration, we retain boron a material unsuitable for the startup control rods and we suggest the use of a stronger absorber, e.g., europium. In fact, the reactivity worth of the startup control rods containing natural europium instead of enriched boron is 10970 pcm, enough to compensate the change in the  $k_{\text{eff}}$  during the startup operation.

The introduction of the control rods alters not only the reactivity of the reactor but also the neutron flux profile; therefore, we investigated the latter both radially and axially. We averaged the neutron flux in 11 radial hexagons, numbered according to the labels of Fig. 1, and in 10 equi-volume sub-blocks along the  $z$ -axis at different heights

of the core. Because of the symmetry, we plotted in Fig. 8, for each hexagon block, only the 5 upper axial sub-blocks, for we kept the operational control rods inserted and all the other types of rods withdrawn. We can note that the control rods depress the flux in the 8th hexagonal block, where they are located, and also twist the radial profile in the different fuel rings, compared to the configuration neglecting the presence of the control rods (Fig. 8 versus Fig. 3 of Talamo et al., 2004b). Moreover, the depression of the flux in the central and outer rings, due to the presence of the operational control rods, is counterbalanced by an increase in the inner ring because in both cases, with the rods inserted or withdrawn, the flux is normalized to the total power of the reactor. Consequently, the peak factor (intended as the maximum flux amid the fuel rings in the inner axial sub-block, at 35.15 cm, divided the average) reaches a value of 2.1. Fig. 8 reports, by a black circle, also the flux in the outer ring, which corresponds to the block 7a in the inner axial sub-block at 35.15 cm; we can note that the outer ring experiences a lower flux, comparing to the central ring, which corresponds to the block 7b, because of a more depleted fuel and the geometry location.

In order to investigate the effect of the partial insertion of the operational control rods on the axial neutron flux profile averaged in the fuel pins, we focused on three DF pins, each located in a different fuel ring and close to the center of the hexagonal block. We divided each of the three DF fuel pin into 10 equi-volume regions and we selected the set of insertions corresponding to: 0%, 25%, 50%, 75% and 100% of the control rod length. Fig. 9 confirms the neutron flux cosine shape obtained by our previous studies (Fig. 5 of Talamo et al., 2004b) where the reactor had been modeled without control rods and burnable poison. The inner ring, due to the loading of fresh fuel and the

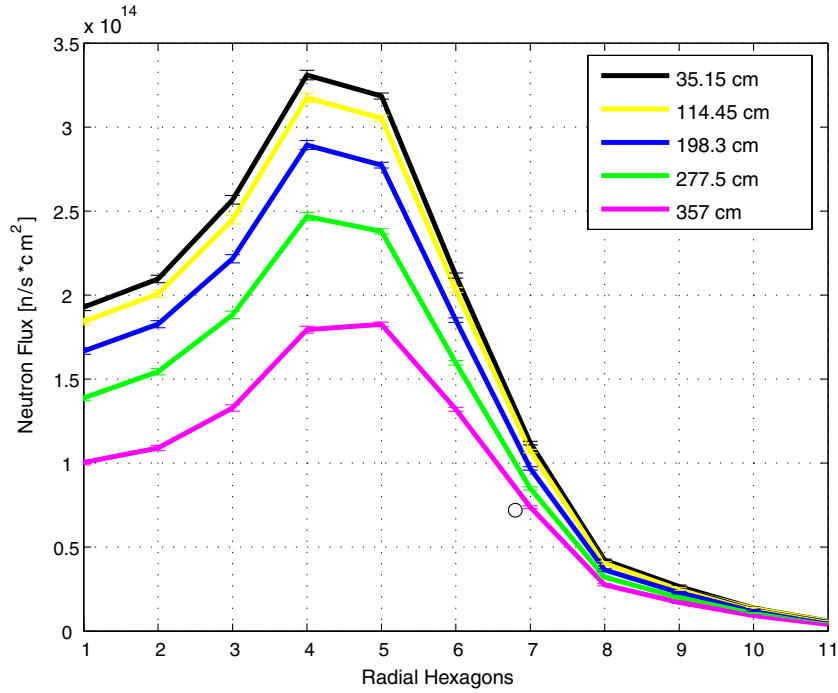


Fig. 8. Neutron flux profile at the equilibrium of the fuel composition. Neutron flux has been averaged in 10 axial sub-blocks and 11 radial hexagonal blocks from the center of the reactor, the index follows the numeration illustrated in Fig. 2. Curves refer to the upper 5 axial sub-blocks. Ticks on the curves represent the SD with a 95% confidence. The small black circle is the value in the block 7a at 35.15 cm whereas the curves report the values in the block 7b.

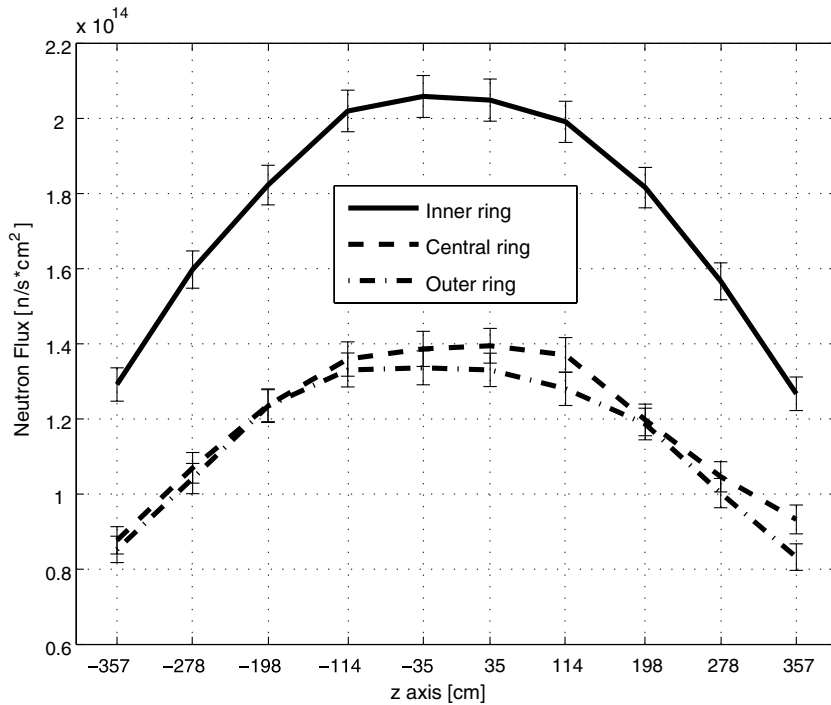


Fig. 9. Neutron flux axial profile averaged in a DF pin at the center of the hexagonal block with all operational control rods withdrawn. The SD is indicated by the small horizontal ticks and it is given with 95% confidence.

geometry location which enhance moderation, has a higher flux than the other two rings, whose curves cross each other. The insertion of 50% of the control rods (Fig. 10) alters the symmetry of the neutron flux and the peaking fac-

tor (defined as the maximum flux amid the axial regions in the same ring divided the average) increases from 1.17, when the rods are withdrawn, to 1.8–2. As shown in Fig. 11, the peaking factor decreases when the control rods



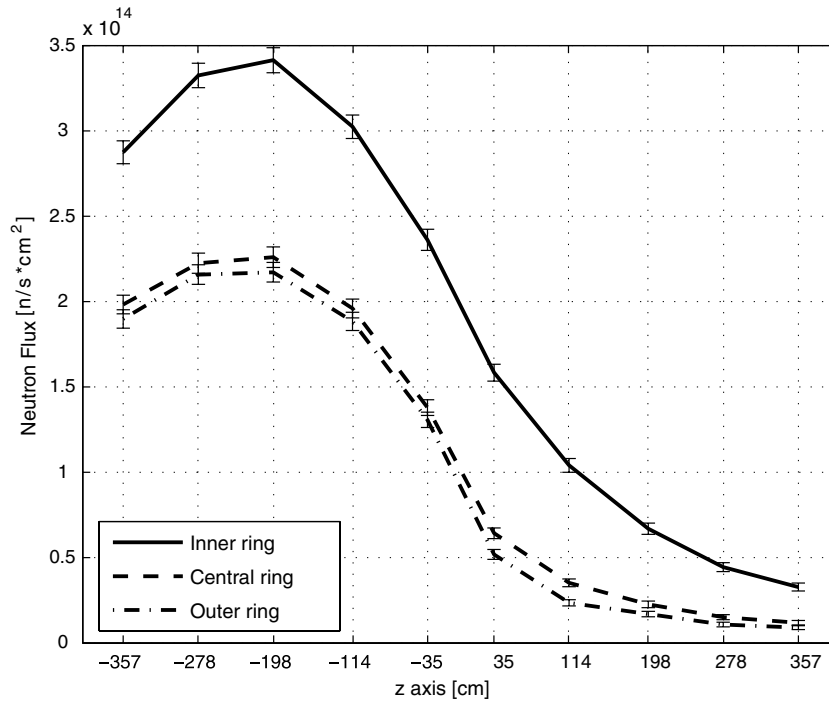


Fig. 10. Neutron flux axial profile averaged in a DF pin at the center of the hexagonal block with all operational control rods 50% withdrawn. SD is indicated by the small horizontal ticks and it is given with 95% confidence.

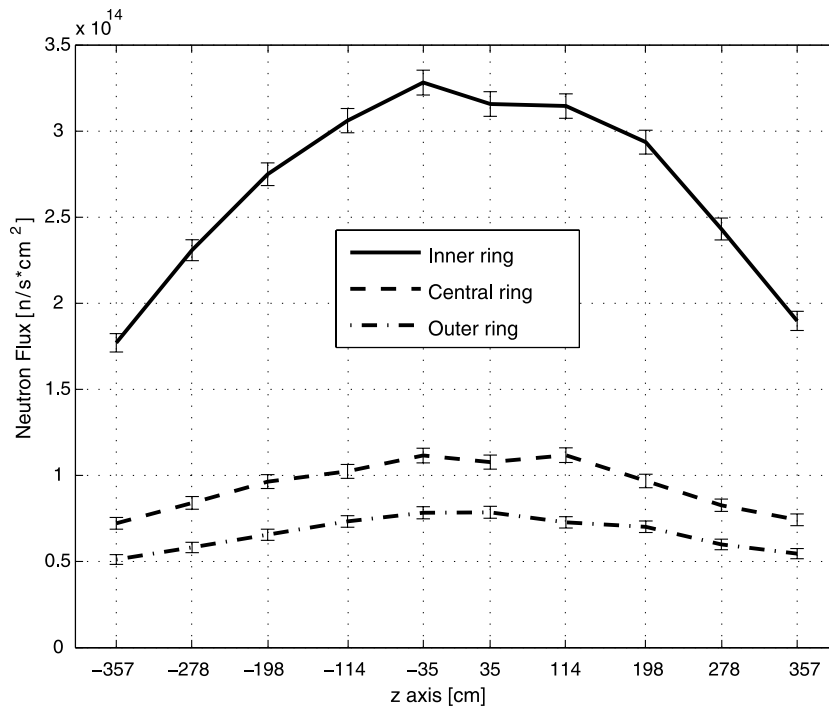


Fig. 11. Neutron flux axial profile averaged in a DF pin at the center of the hexagonal block with all operational control rods inserted. SD is indicated by the small horizontal ticks and it is given with 95% confidence.

are full inserted, compared to the configuration where the rods are 50% inserted; in fact, the peaking factor value ranges from 1.19 to 1.22. Fig. 12 proves that even a relatively small insertion of the control rods, 25% of the rod length, is enough to perturb the axial neutron flux shape;

however, the peaking factor remains limited to 1.48–1.54. A different scenario occurs while the rods are inserted up to 75% of their length, illustrated in Fig. 13, for the variation of the flux becomes much larger and it generates a peaking factor of 1.94–2.89.

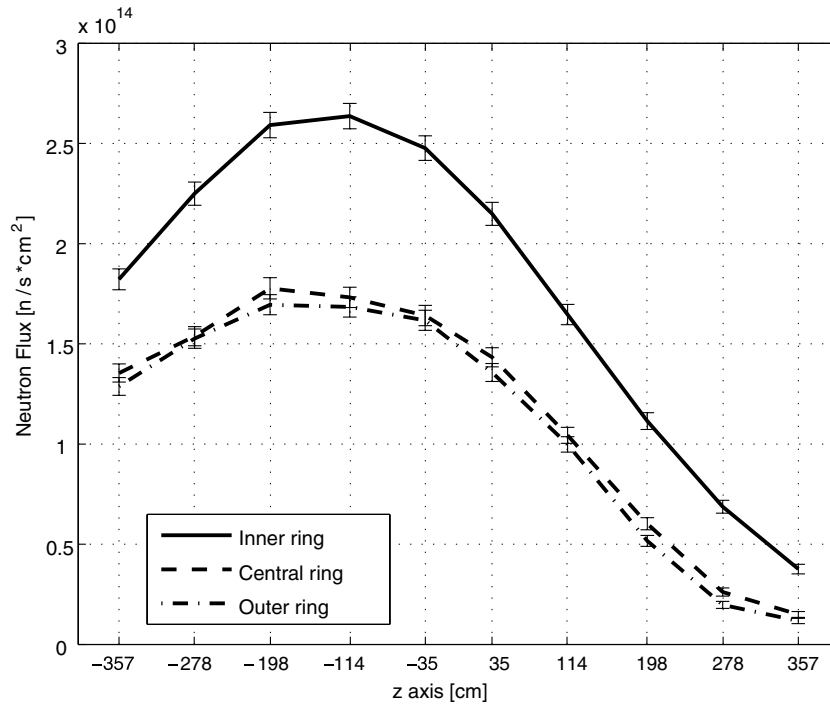


Fig. 12. Neutron flux axial profile averaged in a DF pin at the center of the hexagonal block with all operational control rods 75% withdrawn. SD is indicated by the small horizontal ticks and it is given with 95% confidence.

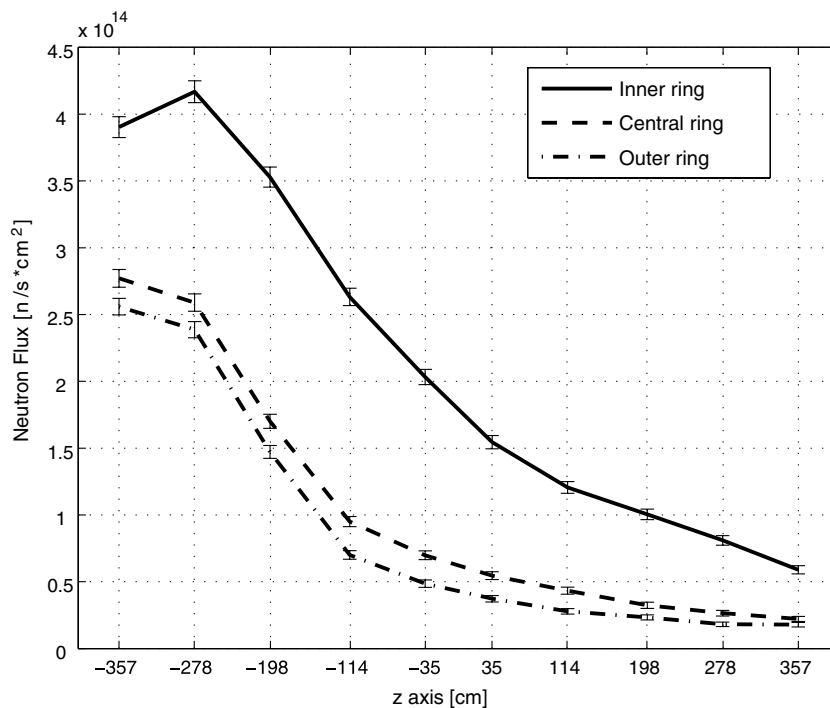


Fig. 13. Neutron flux axial profile averaged in a DF pin at the center of the hexagonal block with all operational control rods 25% withdrawn. SD is indicated by the small horizontal ticks and it is given with 95% confidence.

The control rods produce a different axial neutron flux shape according to the insertion length. When the rods are fully extracted or inserted the flux axial profile resembles a cosine shape of amplitude  $\pi$ . When the rods are

50% inserted the flux axial profile reminds a sine shape but asymmetric because the neutron leakage effect is visible only in the side which is not covered by the control rods. When the insertion corresponds to 25% or 75% of the

rod length the sinusoidal shape is lost and the curves assume a shape convex or concave, respectively; also in these two cases we can note that the diminishing of the flux, at the edge of the core along the z-axis, due to neutron leakage, is present only in the side not covered by the control rods.

The comparison of the spectra in the erbium and boron kernels, illustrated in Fig. 14, reveals that the neutron flux

in the control rods is over one order of magnitude lower than in the burnable poison, especially at the thermal energies, where the difference reaches a factor of 16. This phenomenon is due to two major factors: the 2.6 times larger width of the control rod comparing to the burnable poison pin, which enhances the flux depression inside the control rod, and the position of the burnable poison pins, for they are inserted close to the fuel pins where neutron flux is

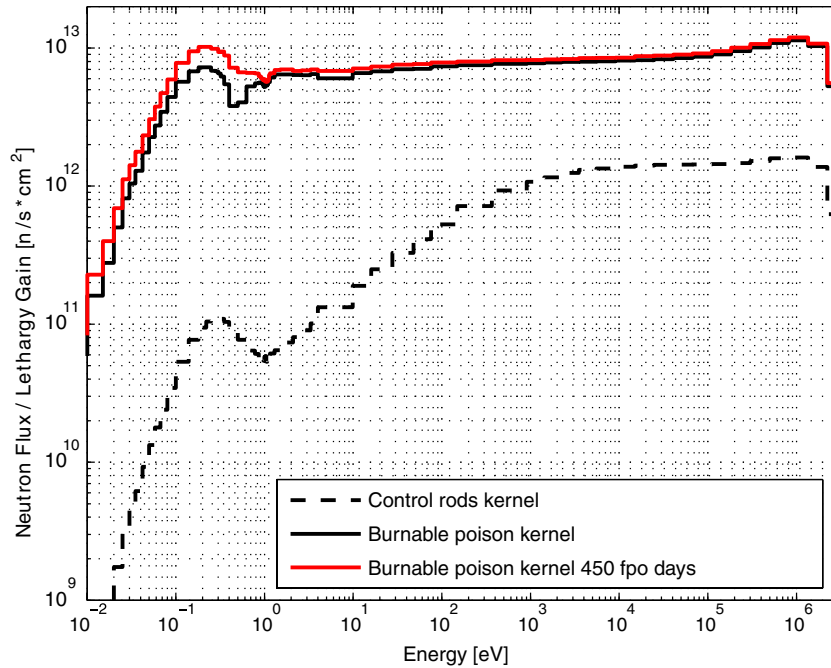


Fig. 14. Neutron spectrum averaged in the burnable poison and operational control rods BISO kernels. The energy groups have been tallied according to the WIMS library (Kim et al., 1989; Taubman, 1975) in a continuous energy Monte Carlo calculation.

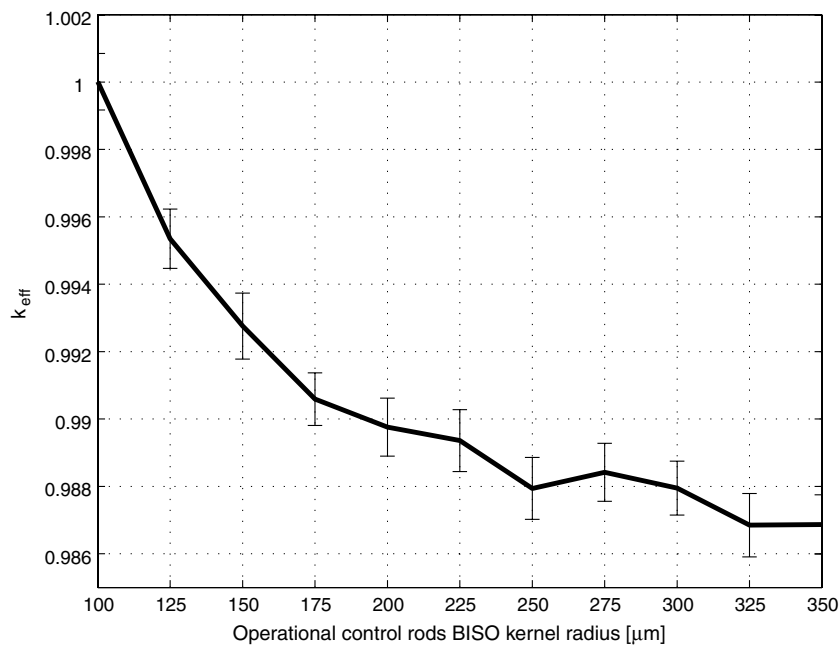


Fig. 15. Variation of the initial  $k_{eff}$  with different radii of the operational control rods BISO kernels. SD is indicated by the small horizontal ticks and it is given with 95% confidence.

Table 5  
 $k_{\text{eff}}$  for different MCNP treatment of delayed neutrons and different JEF-2.2 neutron data library sets

| MCNP cards             | JEF-2.2 library sets at 1500 K |         |
|------------------------|--------------------------------|---------|
|                        | 15c                            | 85c     |
| totnu; phys:n jjj -1   | 1.03884                        | 1.04498 |
| totnu no; phys:n jjj 0 | 1.03548                        | 1.04206 |

The maximal SD, with 68% confidence, of  $k_{\text{eff}}$  is lower than 14 pcm.

higher; by contrast, the controls rods are located in the outside reflector, where the flux is lower (Fig. 8). Of course, in both spectra the dips of the resonances of  $^{239}\text{Pu}$  and  $^{240}\text{Pu}$  are absent; while, they were clearly visible in the fuel spectra (Figs. 11–16 of Talamo et al., 2004b). The wide unresolved resonances of  $^{167}\text{Er}$ , at 0.46 and 0.58 eV, of 10,274 and 6478 b (Fig. 1), generate in that energy range a quite large depression of the spectrum (Fig. 14). The peak of the spectrum around 0.2 eV is higher for the burnable poison (Fig. 14) comparing to the fuel (Figs. 11–16 of Talamo et al., 2004b). Other independent studies did not accurately describe the spectrum depression, due to the low energy wide unresolved resonances of erbium, because of coarse neutron energy groups which caused a quite spiky profile (Fig. 7(a) of Plukiene and Ridikas, 2003a). After 450 full power operation (fpo) days, 73% of  $^{167}\text{Er}$  is transmuted and therefore the spectrum of the burnable poison visibly increases in the thermal neutron energy range; moreover, the depression due to the  $^{167}\text{Er}$  resonances disappears.

The variation of the radius of the operational control rods BISO kernel, shown in Fig. 15, indicates that after the threshold of 200  $\mu\text{m}$  the reactivity worth of the control rods increases little with the increase of the kernel radius; whereas, up to 200  $\mu\text{m}$ , an increase of 25  $\mu\text{m}$  in the kernel lowers the  $k_{\text{eff}}$  of 200 pcm.

Finally, we evaluated the  $\beta_{\text{eff}}$  of the reactor by applying a different MCNP treatment to the delayed neutrons in the JEF-2.2 neutron data library sets, as reported in Table 5. If one assumes as total  $k_{\text{eff}}$  ( $k_p$ ) that obtained with the *totnu* card and as prompt  $k_{\text{eff}}$  ( $k_p$ ) that obtained with the *totnu no* card, both calculated with the 85c data set, which contains also data for the delayed neutrons, the following formulas:

$$k_p = (1 - \beta_{\text{eff}})k \quad (2)$$

provides a  $\beta_{\text{eff}}$  of 280 pcm. In spite the value of  $\beta_{\text{eff}}$  is small, the safety of the reactor is granted by the large moderator CT, which gives a feedback of 280 pcm for a temperature raise of 29 K. Let us conclude that the use of the 15c data set, which neglects information about delayed neutrons, generates a value of  $k_{\text{eff}}$  600 pcm lower than that one obtained by the 85c data set.

## 6. Conclusions

The utilization of the burnable poison reduces the initial reactivity excess down to 4000 pcm and at the same time it also grants an operation longer than one year; during 450

full power operation days, the reactor burns most of  $^{167}\text{Er}$ , about 73%. The feedback due to a variation of 25  $\mu\text{m}$  in the radius of the burnable poison kernel is 700–1000 pcm.

Each group of rods has a worth of about 5100–5500 pcm while they are fully inserted; the worth of the rods changes after an insertion of 400 cm, from about 100 pcm to 1000 pcm per 80 cm. Of course, the rods depress the flux in the 8th hexagonal block, where they are located; the variation of the flux becomes quite large when they are inserted up to 75% of their length and that generates a peaking factor of 1.94–2.89. The startup control rods must contain europium instead of boron to manage the excess of criticality of the cold core. The variation of the radius of the operational control rods TRISO kernel indicates that, after the threshold of 200  $\mu\text{m}$ , the reactivity worth of the control rods increases little; whereas, up to 200  $\mu\text{m}$ , an increase of 25  $\mu\text{m}$  in the kernel lowers the  $k_{\text{eff}}$  of 200 pcm.

After 450 full power operation days the spectrum averaged in the burnable poison kernels, about one order of magnitude larger than that one averaged in the control rods kernels, visibly increases in the thermal neutron energy range and the depression due to the  $^{167}\text{Er}$  low energy wide unresolved resonances disappears.

The  $\beta_{\text{eff}}$  of the core is small, only 280 pcm; nevertheless, the safety of the reactor is granted by the large moderator CT, which is six times larger than the fuel one and equal to 9 pcm/K.

## References

- Ando, Y., et al., 2003. Development and verification of Monte Carlo burnup calculation system. In: Proceedings of the Conference on “Nuclear Criticality Safety”, Tokaimura (Japan).
- Baxter, A., Fikani, M., 2002. Reactor-based transmutation – physics studies of the gas-cooled graphite-moderated deep burn reactor. General Atomic, GA-501-0-TRT-000140.
- Baxter, A., Rodriguez, C., 2001. The application of gas-cooled reactor technologies to the transmutation of nuclear waste. Progress in Nuclear Energy 38, 81–105.
- Bernnat, W., Feltes, W., 2003. Models for reactor physics calculations for HTR pebble bed modular reactors. Nuclear Engineering and Design 222, 331–347.
- Briesmeister, J.F., 2002. A general Monte Carlo N-Particle transport code—version 4c. LANL, LA-13709-M.
- Brown, F.B., Martin, W.R., 2004. Stochastic geometry capability in MCNP5 for the analysis of particle fuel. Annals of Nuclear Energy 31, 2039–2047.
- Cetnar, J., Gudowski, W., Wallenius, J., 1999. MCB: a continuous energy Monte Carlo burnup simulation code, in actinide and fission product partitioning and transmutation. EUR 18898 EN, OECD/NEA 523.
- Cetnar, J., Gudowski, W., Wallenius, J., Tucek, K., 2001. Simulation of nuclide transmutation with Monte Carlo Continuous Energy Burnup Code (MCBIC). In: Proceedings of the Accelerator Application 2001 and ADTTA 2001 Nuclear Application in the New Millennium, Reno, USA.
- Gauld, I.C., 2003. MOX cross sections libraries for ORIGEN-ARP. ORNL/TM-2003/2, Oak Ridge National Laboratory, USA.
- General Atomics, 2002. GT-MHR conceptual design description report. GA/NRC-337-02.

- Grisell, A., 2004. Validation of the Monte Carlo continuous energy burnup code MCB on light water reactor fuel. Master of Science Thesis, Royal Institute of Technology, Stockholm, ISBN 91-7283-093-1.
- Kim, J.J., Lee, J.T., Kim, H.R., 1989. Generation and benchmarking of a 69 Group Cross Section Library for thermal reactor applications. *Journal of the Korean Nuclear Society* 21, 245.
- Kim, T.K., et al., 2004. Preliminary Assessment of Lattice Physics Capabilities for VHTR Analysis. ANS Winter Meeting, Transactions of the ANS no. 91, Washington, USA.
- Kiryushin, A.I., Kodochigov, N.G., Kouzavkov, N.G., et al., 1997. Project of the GT-MHR high temperature helium reactor with gas turbine. *Nuclear Engineering and Design* 173, 119–129.
- Kodochigov, N., Sukharev, Y., et al., 2003. Neutronic features of the GT-MHR. *Nuclear Engineering and Design* 222, 161–171.
- Kunitomi, K. et al., 2004. Japan's future HTR – the GTHTR300. *Nuclear Engineering and Design* 233, 309–327.
- Heinisch, H.L. et al., 2004. Displacement damage in silicon carbide irradiated in fission reactors. *Journal of Nuclear Materials* 327, 175–181 <http://jsekhon.fas.harvard.edu/macosex/>.
- Ohashi, K., Okamoto, F., Hayakawa, H., 2000. Modular high temperature reactor contributing the global environmental protection. *Progress in Nuclear Energy* 37, 307–312.
- Plukiene, R., Ridikas, D., 2003a. Modeling of HTRs with Monte Carlo: from a homogeneous to an exact heterogeneous core with microparticles. *Annals of Nuclear Energy* 30, 1573–1585.
- Plukiene, R., Ridikas, D., 2003b. Monte Carlo modeling of the GT-MHR with military and spent nuclear fuel plutonium isotopic composition. In: *Proceedings of the Workshop on “Neutron Measurements and Evaluations for Applications”*, Budapest, Hungary.
- Rodriguez, C. et al., 2003. Deep-Burn: making nuclear waste transmutation practical. *Nuclear Engineering and Design* 222, 299–317.
- Shiozawa, S. et al., 2004. Overview of the HTTR design features. *Nuclear Engineering and Design* 233, 11–21.
- Talamo, A., Gudowski, W., Venneri, F., 2004a. The burnup capabilities of the deep burn modular helium reactor analyzed by the Monte Carlo continuous energy code MCB. *Annals of Nuclear Energy* 31/2, 173–196.
- Talamo, A., Gudowski, W., Cetnar, J., Venneri, F., 2004b. Key physical parameters and temperature reactivity coefficients of the deep burn modular helium reactor fueled with LWRs waste. *Annals of Nuclear Energy* 31/16, 1913–1937.
- Talamo, A., Gudowski, W., Cetnar, J., 2004c. Comparative studies of ENDF/B-6.8, JEF-2.2 and JENDL-3.2 Data Libraries by Monte Carlo modeling of high temperature reactors on plutonium based fuel cycles. *Journal of Nuclear Science and Technology* 41/12, 1228–1236.
- Talamo, A., Gudowski, W., 2004d. Studies on the possibility to replace the burnable poison with the transmutation fuel in the deep burn fuel management strategy for the gas turbine modular helium reactor, American Nuclear Society, Winter Meeting, Washington, USA.
- Talamo, A., Gudowski, W., 2005a. A Deep Burn Fuel Management Strategy for the Incineration of Military Plutonium in the Gas Turbine-Modular Helium Reactor Modeled in a Detailed 3D Geometry by the Monte Carlo Continuous Energy Burnup Code. Internal report.
- Talamo, A., Gudowski, W., 2005b. Performance of the gas turbine-modular helium reactor fuelled with different types of fertile TRISO particles. *Annals of Nuclear Energy* 32/16, 1719–1749.
- Talamo, A., Gudowski, W., 2005c. Adapting the deep burn in-core fuel management strategy for the gas turbine-modular helium reactor to a uranium–thorium fuel. *Annals of Nuclear Energy* 32/16, 1750–1781.
- Taubman, C.J., 1975. The WIMS 69-Group Library Tape 166259. Report AEEW-M1324, U.K. Atomic Energy Authority, Winfrith, Great Britain.
- Xu, Y., Zuo, K., 2002. Overview of the 10 MW high temperature gas cooled reactor – test module project. *Nuclear Engineering and Design* 218, 13–23.

# NEUTRONIC AND SAFETY ASPECTS OF A GAS-COOLED SUBCRITICAL CORE FOR MINOR ACTINIDE TRANSMUTATION

THERMAL HYDRAULICS

**KEYWORDS:** *accelerator-driven systems, helium cooling, minor actinide fuel*

DANIEL WESTLÉN\* and JANNE WALLENIUS

*Royal Institute of Technology, Department of Nuclear and Reactor Physics  
S-10691 Stockholm, Sweden*

Received June 18, 2004

Accepted for Publication July 20, 2005

*We have designed a gas-cooled accelerator-driven system dedicated to transmutation of minor actinides. Thanks to the excellent neutron economy of the uranium-free fuel employed, the pin pitch to diameter ratio ( $P/D$ ) could be increased to 1.8. The increased coolant fraction allows for decay heat removal at ambient pressure. The large coolant fraction further results in a low pressure loss—26 kPa over the core, 35 kPa in total. Thanks to the large  $P/D$ , the elevation of the heat exchanger necessary to remove decay heat by natural circulation is just more than 1 m. The absence of uranium in conjunction with the presence of 35% (heavy atom) americium in the fuel results in a low effective delayed neutron fraction and a vanishing Doppler feedback, making subcritical operation mandatory.*

## I. INTRODUCTION

Transuranium elements in spent light water reactor (LWR) fuel remain radiotoxic at a level above that of uranium in nature for more than 100 000 yr. By separation and subsequent transmutation of these elements, the required time for storing the residual waste may be reduced to >1000 yr (Refs. 1 and 2). Plutonium may be multirecycled in fast reactors or in existing LWRs using mixed-oxide (MOX) fuel with the support of enriched uranium.<sup>3</sup> However, if one does not transmute americium and curium, the reduction in radiotoxic inventory becomes marginal. Recycling of americium and curium in LWRs, however, leads to an increase of neutron emission rates during reprocessing by three orders of magnitude.<sup>2</sup> Therefore, higher actinides should be recycled in a fast neutron spectrum.

\*E-mail: daniel@neutron.kth.se

Introducing americium into the fuel of fast critical reactors leads to safety concerns; since the Doppler feedback is reduced, the effective delayed neutron fraction decreases and the coolant void coefficient becomes more positive.<sup>4</sup> These three effects in combination limit the potential for transmuting americium in fast reactors. Transmutation of americium-rich fuels might be accomplished, however, by the implementation of fast neutron accelerator-driven systems (ADSs), as first suggested by Foster et al.<sup>5</sup> Several designs of such systems have been proposed.<sup>6–8</sup>

The main difference between a critical reactor and an ADS is that a spallation source driven by a proton accelerator is used to supply source neutrons. Spallation targets for high-power ADSs are typically suggested to consist of liquid lead-bismuth alloy. The design of the core itself is more of an open issue being subject to intense research efforts. Candidates for fuel composition are oxides, nitrides, and metals.

Lead-bismuth eutectic (LBE) or sodium have been considered as coolants.<sup>6,7</sup> The main reason to use a liquid metal as a coolant is because of the high thermal conductivity found in most metals. Among drawbacks pertaining to liquid-metal coolants are the incompatibility with water of sodium and the corrosion problems associated with lead and lead alloys.

Gas cooling is therefore an interesting alternative to the liquid-metal coolants. Among the possible gases, helium features the most suitable characteristics.<sup>9</sup> Helium provides a hard neutron spectrum, which is beneficial for limiting buildup of curium and other heavier elements. A low chemical reactivity of the coolant—as in the case of helium—is a prerequisite if high temperature operation is to be feasible. Further, the optical transparency allows for visual inspection of the core, which is not possible in metal-cooled systems.

However, the main disadvantage of using helium coolant is the low density, which implies that high pressure operation is necessary to ensure heat removal. Typically fast helium-cooled reactors are designed to operate at

pressures between 8 and 12 MPa (Ref. 9). A loss-of-pressure or loss-of-flow accident might consequently lead to severe difficulties in removing decay heat. Several approaches have been suggested to address this issue.<sup>10,11</sup>

We suggest utilizing the excellent neutron economy of uranium-free plutonium-based fuels to increase the coolant mass flow through the core by increasing the pin pitch to diameter ratio (P/D). An increased P/D may relieve issues related to loss-of-pressure and loss-of-flow accident scenarios.

In what follows we will account for a design of a gas-cooled ADS that guarantees decay heat removal at ambient pressure or under natural circulation conditions. We start by showing how the introduction of americium into the fuel of gas-cooled reactors reduces Doppler feedback and effective delayed neutron fractions. We then present the fuel composition and core geometry assumed in this study. We continue by showing how the core proposed is expected to behave during a severe loss-of-pressure accident and during a loss-of-flow accident. Finally, we conclude by giving some preliminary results concerning neutronic properties of the system, evaluating the transmutation capability of the proposed design.

**II. IMPACT OF AMERICIUM ON SAFETY PARAMETERS**

The safety of critical fast reactors relies on negative feedbacks that compensate for potential reactivity insertions. The negative feedback from radial expansion of the core diagrid typically is larger than the positive feedback from coolant expansion and manages to stabilize the core in the case of slow transients like loss of flow and loss of heat sink. For rapid excursions, which in fast reactors always may occur as a result of core compaction, it is important that prompt negative feedbacks like Doppler broadening and/or axial expansion of the fuel have a significant magnitude. Further, the effective delayed neutron fraction may not be too small.

When introducing americium into the fuel of fast reactors, the magnitude of the Doppler feedback and beta effective is reduced. This is because americium has a much higher cross section for capture than <sup>238</sup>U, <sup>240</sup>Pu, or <sup>232</sup>Th. Thus, neutrons under moderation are captured by americium in the unresolved resonance range, where Doppler broadening is much more inefficient than for captures in resolved resonances at lower energies. Similarly, the large cross section for capture in americium means that delayed neutrons, being born with an average energy of 0.5 MeV, have a smaller probability of inducing fission than in an americium-free fuel. Figure 1 displays the capture cross section of <sup>241</sup>Am and <sup>238</sup>U. Even though there is an uncertainty in the evaluated data sets, it is clear that even a relatively small fraction of Am in the fuel will have a significant impact on the capture rate in different nuclides.

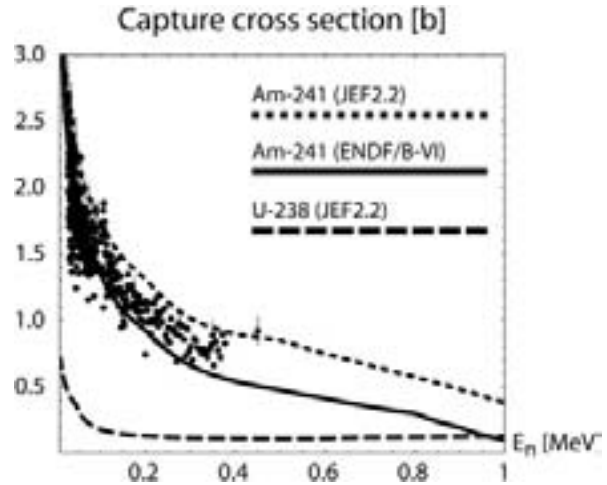


Fig. 1. Evaluated (JEFF3.0) capture cross section of <sup>241</sup>Am and <sup>238</sup>U.

In order to quantify this impact, we have calculated beta effective and the Doppler constant for a simplified pin cell model of the gas-cooled fast reactor (GCFR) design developed in the United States during the 1960s (Ref. 12). The model consists of a radially infinite pin lattice with P/D = 1.45. The calculation was made with the Monte Carlo code MCB1C, using the JEFF3.0 cross-section library Doppler broadened at temperatures of 1200 and 1800 K, including probability tables for absorption in the unresolved resonance region. Table I compares the Doppler constant  $K_D = T dk/dT$  and  $\beta_{eff}$  of the reference oxide fuel with fuels where part or all of the uranium has been substituted with americium or zirconium. As expected, the Doppler constant of the reference fuel is smaller than for liquid-metal-cooled fast breeder reactors but corresponds to a feedback comparable to that of axial

TABLE I  
Change in Doppler Effect and  $\beta_{eff}$  with Increasing Fuel Am Content\*

| U                             | Pu | Am | Zr | $K_D = T dk/dT$ | $\beta_{eff}$ |
|-------------------------------|----|----|----|-----------------|---------------|
| 80                            | 20 | —  | —  | -285 (11)       | 503 (25)      |
| 70                            | 20 | 10 | —  | -88 (11)        | 473 (23)      |
| 50                            | 20 | 30 | —  | 0 (14)          | 356 (32)      |
| —                             | 20 | 30 | 50 | +10 (16)        | 227 (38)      |
| Reference value <sup>13</sup> |    |    |    | -320            | —             |
| Calculated reference value    |    |    |    | -388 (13)       | —             |

\*The Doppler effect is significantly weakened and the value of  $\beta_{eff}$  diminishes when Am is introduced in the fuel. Values in parentheses indicate one standard deviation. The geometry of the reference core is assumed for all cases.

expansion of ceramic fuels, i.e.,  $-0.2$  pcm/K. The value obtained in our simplified model is in good agreement with full core calculations for the GCFR design.<sup>13</sup> When introducing americium into the fuel, one sees that the Doppler constant is dramatically reduced, even in the presence of  $^{238}\text{U}$ . This is well in line with calculations previously made by one of the present authors for sodium-cooled systems.<sup>14</sup> Thus, for fast neutron cores dedicated to transmutation of the higher actinides, it will only be possible to regain a significant Doppler feedback if the ratio of Am to  $^{238}\text{U}$  in the fuel is less than  $\sim 1$  to  $7$ . The effective delayed neutron fraction also decreases. The reduction is not as large as for the Doppler, but it does mean that any reactivity insertion has a considerably higher worth than in the case of an americium-free fuel.

One may thus conclude that burning of the minor actinide waste of present LWR parks in fast spectra requires a relatively large dilution of americium in uranium and therefore a large fraction of fast neutron reactors in the system operating on advanced fuels. Therefore, it is of interest to investigate the option of minor actinide burning in subcritical reactors, which may be loaded with a much higher fraction of americium.

### III. GAS-COOLED ADS CORE AND FUEL DESIGN

In conventional fast reactor designs, achieving a high breeding ratio has been the primary concern. Consequently, the reduction of neutron leakage has been an important design parameter. In contrast, uranium-free fuels dedicated to waste transmutation feature a neutron surplus that may be used to improve transmutation performance and core safety.

We have based our ADS design on the GCFR (Ref. 12). Seven of the central fuel assemblies are removed to make place for the spallation target. As in the GCFR, four fuel zones with different ratios between fertile and fissile nuclides are used to minimize the radial power peaking factor. At beginning of life (BOL), the reflector is loaded with boron carbide assemblies that batchwise are replaced with steel pin assemblies in order to manage reactivity losses. The corresponding core map is shown in Fig. 2. The active height of the core was decreased from 1.15 to 1.0 m to minimize the axial power peaking factor. This leads to increased axial neutron leakage, which, however, may be afforded because of a better neutron economy. We have adopted fuel clad dimensions identical to that of the GCFR, that is, an inner/outer diameter of 7.1/7.8 mm. The P/D has been increased as much as possible in order to maximize the coolant flow area. Thus, the working pressure as well as the pressure loss over the core are reduced, mitigating consequences of loss-of-pressure and loss-of-pumping-power accidents.

In line with recent studies of GCFRs in France,<sup>15</sup> we have selected nitride fuel for the present design because

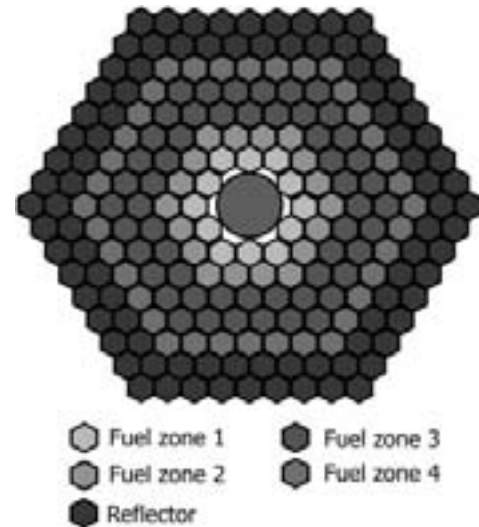


Fig. 2. Core map for the present design. Fuel zones distinguished by different shades of gray correspond to plutonium concentrations of 28, 34, 45, and 100%, respectively.

of its high power to melt and the relative ease of reprocessing. A fuel porosity of 15% was adopted to allow for solid fission product swelling. Nitrogen enriched in  $^{15}\text{N}$  is assumed to be used in order to avoid the production of  $^{14}\text{C}$ . A  $^{15}\text{N}$  content of 98% has been shown to be sufficient for the  $^{14}\text{C}$  production in minor actinide-burning ADS cores to be less than the production of  $^{14}\text{C}$  in the oxide fuel of LWRs (Refs. 16 and 17). The main disadvantage of nitride fuels, however, is the high vapor pressure of americium, which requires the use of a stabilizing inert matrix like zirconium nitride.<sup>18</sup> Recent tests of (Pu,Zr)N fabrication by nitridation of metals at relatively low temperature have shown that a solid solution is only obtained for matrix volume fractions above 60 at.% (Ref. 19). We therefore fix the ZrN fraction in the fuel to 60% in the entire core and adjust the ratio between plutonium and higher actinides in the fuel to obtain a  $k$  eigenvalue of 0.97 at BOL. Further, the Pu/minor actinide ratio is differentiated over the fuel zone in order to achieve a radial power peaking factor  $< 1.2$ . Increasing P/D, the relative fraction of plutonium must thus be raised.

Neutronics calculations were performed using the Monte Carlo continuous energy burnup code MCB (Refs. 20 and 21), which is based on MCNP4C and allows for a complete treatment of fuel burnup. All core design calculations were performed using a fully three-dimensional pin by pin model, including axial and radial reflectors. Assuming an actinide vector corresponding to that of spent LWR MOX fuel (see Table II), we find that the plutonium content in the outermost fuel zone becomes 100% for P/D  $\approx 1.8$ .

The core geometry parameters are summarized in Table III. As we have a larger P/D, the number of fuel



TABLE II

Isotopic Compositions of Actinides in the Fuel

|                   |       |                   |       |
|-------------------|-------|-------------------|-------|
| $^{238}\text{Pu}$ | 5.1%  | $^{241}\text{Am}$ | 66.6% |
| $^{239}\text{Pu}$ | 37.9% | $^{243}\text{Am}$ | 33.4% |
| $^{240}\text{Pu}$ | 30.3% |                   |       |
| $^{241}\text{Pu}$ | 13.2% | $^{244}\text{Cm}$ | 87.3% |
| $^{242}\text{Pu}$ | 13.5% | $^{245}\text{Cm}$ | 12.7% |

TABLE III

Core Geometry Parameters

| Property                               | Present Design |
|--|----------------|
| Core height (m)                        | 1.00           |
| Fuel pin inner/outer diameter (mm)     | 7.1/7.8        |
| Fuel-clad gap (mm)                     | 0.05           |
| Pellet diameter (mm)                   | 7.0            |
| P/D                                    | 1.7806         |
| Assembly wall thickness (mm)           | 4.0            |
| Assembly spacing (mm)                  | 2.0            |
| Assembly inner flat to flat (FTF) (mm) | 178.4          |
| Assembly outer FTF (mm)                | 185.3          |
| Number of fuel assemblies              | 120            |
| Number of rods                         | 20 280         |

pins per subassembly (169) as well as in the entire core (20 280) is lower than for the GCFR design. We have chosen not to increase the linear rating of the fuel in order to keep down the working pressure. Hence, the total core power will be reduced.

Figure 3 is an example of the shape of the power distribution at BOL for plutonium concentrations of 28/34/45/100% actinide atoms in the four fuel zones. These fractions correspond to a core-averaged composition of 58% Pu, 35% Am, and 7% Cm. Considering that spent LWR MOX fuel contains Pu and higher actinides in a proportion of 4 to 1 (Ref. 22), 30% of the Pu produced in LWRs could be incinerated in the present ADS, the remaining 70% being multirecycled in LWRs.

The contribution of neptunium to the radiotoxic inventory of spent LWR fuel is less than the radiotoxicity in natural uranium<sup>22</sup> (ingestion dose 20 mSv/g) and is hence not significant. For this reason, we chose not to include neptunium in our transmutation strategy.

#### IV. THERMAL-HYDRAULIC ANALYSIS

Having fixed P/D to 1.8 from neutronic considerations, we should settle on a linear rating and a total core power. While a low rating is beneficial from the safety

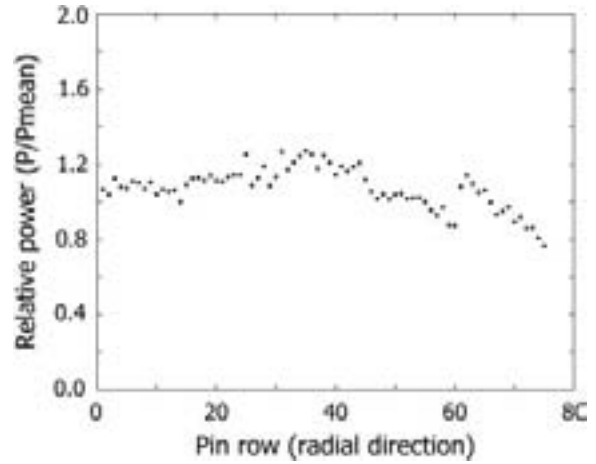


Fig. 3. Example of radial power profile in the core. Each dot corresponds to the calculated profile in a single rod. The estimated error of the Monte Carlo calculation is 3%.

viewpoint, economy drives toward higher power densities. We have chosen to require that decay heat should be possible to remove at ambient pressure (one atmosphere) for a coolant velocity of 70 m/s. The coolant temperature in an arbitrary axial position  $z_1$  is given by the sum of the inlet temperature and the integral of the heat flux,  $q(z)$ , from the pin to the coolant:

$$T_{cool} = T_0 + \int_0^{z_1} \frac{q(z)}{\dot{m} \cdot c_p} dz . \quad (1)$$

The cladding temperature is given by the relation

$$q(z) = h[T_{clad}(z) - T_{cool}(z)] = \frac{\chi(z)}{2\pi R_{clad}} , \quad (2)$$

where  $\chi(z)$  is the linear power. The heat transfer coefficient  $h$  is expressed as

$$h = \frac{k}{D_h} \cdot \text{Nu} \cdot \text{SR} \cdot C , \quad (3)$$

where  $D_h$  is the hydraulic diameter. The thermal conductivity  $k$  varies by about a factor of 3 for helium over the temperatures of interest. The geometry of the ribs on the cylindrical rods is chosen so that the surface roughening factor  $\text{SR}$  equals 2 (Refs. 9 and 23).  $C$  is a boundary layer correction factor, which we chose to put to unity.<sup>23</sup> In our case, the main contribution to the Nusselt number  $\text{Nu}$  is convection. We have adopted the Dittus-Boelter correlation for the Nusselt number:

$$\text{Nu} = 0.023\text{Re}^{0.8}\text{Pr}^{0.4} . \quad (4)$$

Thermophysical data for helium as a function of temperature and density were taken from the literature.<sup>24,25</sup>

For P/D = 1.8, a pressure of one atmosphere, a velocity of 70 m/s, and a decay heat power of 1.4 kW, we allow a maximum cladding temperature of 1300 K, the inlet temperature adjusted to meet this condition. Transient tests of D9 cladding tubes irradiated up to 100 displacements per atom (dpa) have been performed at heating rates of 110 K/s, showing that a hoop stress of 120 MPa leads to clad burst at 1300 K (Ref. 26). Such a hoop stress corresponds to a differential pressure of 11 MPa at 1300 K. As will be shown later, the internal gas pressure in the hottest fuel pin will not exceed 6.0 MPa under normal operation. Hence, it is likely that D9, or similar steels like the 15-15Ti clad developed for use in Phenix, would survive the here postulated loss-of-pressure accident at the given decay heating rate. Eventually, the grace time to failure would depend on thermal creep rates. Data on D9 indicate that the clad may survive up to 10 min at 1300 K and up to 1 h at 1200 K (Ref. 27). Since the decay heating rate decreases by more than a factor of 2 within a few minutes, it appears the clad would remain intact.

Having fixed the operating pressure, P/D, and the upper cladding temperature during a potential accident, the average linear power of the hottest fuel pin is given by the assumption that the decay heat corresponds to 5% of full power. We have chosen to limit it to 28 kW/m (axial average), considerably lower than that of the GCFR design. Our postulated loss-of-pressure scenario thus appears to be more restrictive than that assumed for GCFR.

We may now calculate the core working pressure. As will be shown later, the full release of all fission gases and helium generated in the fuel leads to an internal gas pressure of <6.0 MPa at end of life (EOL). The corresponding hoop stress is 64 MPa, which is just below one-third of the tensile yield strength for 15-15Ti cladding tubes at a temperature of 1000 K (Ref. 28). Abiding thus to the Règles d'Analyse Mécaniques des Structures criterion of the Commissariat à l'Energie Atomique<sup>29</sup> indicates that 1000 K should be taken as the temperature limit for our clad under normal operation. We chose, however, to stay conservative and have adopted 900 K as the limit. As shown in Fig. 4, the hot spot temperature in the core remains below 900 K for a coolant pressure exceeding 4.3 MPa. As the maximum linear power of our design, 28 kW/m, is lower than for the GCFR reference design, the inlet temperature may be somewhat higher without exceeding the temperature limits for core damage. The inlet temperature is 577 K as compared to 560 K for the GCFR. We summarize the thermal characteristics of the core in Table IV.

Concerning the core performance under a loss-of-pumping-power event, one needs to show that natural circulation can achieve decay heat removal. We have assumed turbulent flows as Reynolds numbers exceed 2500, the Reynolds number given from

$$Re = \frac{\rho U D_h}{\mu} \quad (5)$$

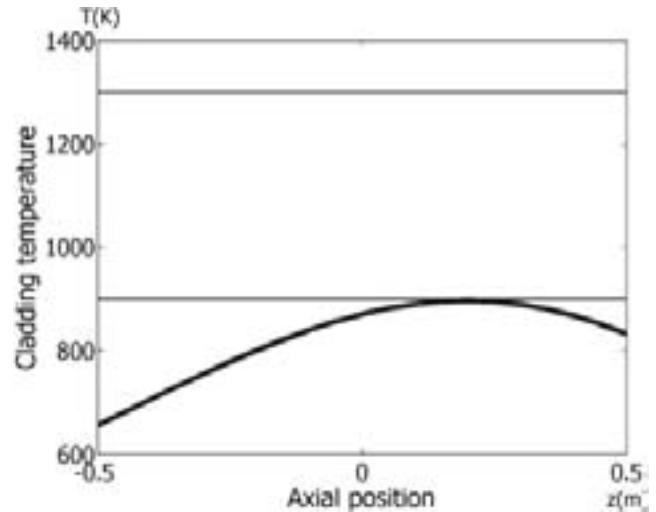


Fig. 4. Under normal operation at 4.3 MPa and a coolant velocity of 70 m/s, the hot spot temperature never exceeds 900 K.

TABLE IV  
Core Thermal-Hydraulics Characteristics

|  |                   |
|--|-------------------|
| Total core power [MW(thermal)]                       | 570               |
| Average linear power (kW/m)                          | 28                |
| Operating pressure (Pa)                              | $4.3 \times 10^6$ |
| Coolant flow speed (m/s)                             | 70                |
| Max cladding temperature—operation <sup>29</sup> (K) | 900               |
| Max cladding temperature—accident <sup>37</sup> (K)  | 1330              |
| Coolant inlet temperature (K)                        | 577               |
| Surface roughening factor <sup>23</sup>              | 2                 |

The coolant density, velocity, and viscosity are denoted by  $\rho$ ,  $U$ , and  $\mu$ , respectively.

The frictional pressure drop over the core is given by<sup>30</sup>

$$\Delta p_f = 2(f_r L_r + f_s L_s) \frac{1}{D_h} \cdot \frac{G^2}{\rho} \quad (6)$$

where  $L_r = 1.0$  m and  $L_s = 1.5$  m are the heights of the roughened and smooth parts of the coolant channel, respectively.  $G = \rho U$  is the mass flux. The rough channel friction factor is given by Melese-d'Hospital as  $f_r = 0.05 \cdot Re^{-0.1}$  (Ref. 30). According to Todreas and Kazimi, the Darcy smooth channel factor friction factor  $f$  satisfies  $f \cdot Re^{0.18} = 0.17$  for P/D = 1.8 and turbulent flow.<sup>31</sup> The average density of the helium coolant in our design is 3.5 kg/m<sup>3</sup> at normal operation. With a mass flux of  $G = 243$  kg·m<sup>-2</sup>·s<sup>-1</sup>, this gives a pressure drop over the coolant channel of  $2.6 \times 10^4$  Pa. This pressure drop is low compared to other gas-cooled designs, e.g.,

the GA-GCFR design, where the pressure drop over the core was  $1.83 \times 10^5$  Pa (Ref. 32). The main difference is that our core operates at a lower pressure and that the large P/D in our design reduces coolant channel friction significantly.

We are not concerned that the fuel pin spacers will produce hot spots on the cladding. Hassan and Rehme<sup>33</sup> showed that for high Reynolds numbers, the heat transfer properties are not affected much by the spacers. The effect that actually is seen is a somewhat increased heat transfer around the spacers due to an increase in flow velocity. In any case, we assume the spacers to be located away from the hottest part of the fuel pins.

The flow velocity at natural circulation (denoted by primed variables) is given by<sup>30</sup>

$$U' = \frac{Q'}{c_p A (T'_{out} - T'_{in}) \rho'} \quad (7)$$

The inlet and outlet temperatures are denoted by  $T_{in}$  and  $T_{out}$ , respectively. For a standard pin in a triangular lattice, the channel area  $A$  is expressed by

$$A = 2 \cdot \left( \frac{\sqrt{3}}{4} \left( \frac{P}{D} \right)^2 - \frac{\pi}{8} \right) D^2 \quad (8)$$

Natural circulation is governed by the difference in coolant density arising from temperature differences and from the vertical distance  $\Delta L$  between the thermal centers of the heat exchanger and core, according to

$$\Delta p = g \Delta L (\rho'_{in} - \rho'_{out}) = g \Delta L M_A \frac{p}{R} \frac{\Delta T'}{T'_{in} \cdot T'_{out}} \Rightarrow$$

$$\Delta L_t = \frac{\Delta p R}{g M_A p} \cdot \frac{T'_{in} \cdot T'_{out}}{\Delta T'} \quad (9)$$

The difference between inlet and outlet temperatures is denoted by  $\Delta T$ , where  $Z$  is a factor relating the pressure drop in the entire system to the pressure drop over the core. Following the GCFR design we have assumed  $Z = 4/3$  (Ref. 30).

At the large P/D we propose the pressure drop at low coolant velocities is small. If we assume a loss-of-flow situation without the pressure being lost, the  $\Delta L$  required is slightly above 1 m. Figure 5 shows how  $\Delta L$  varies with P/D.

The GCFR design uses 1000 K as the upper cladding temperature during normal operation. We believe this might be somewhat optimistic and have thus assumed 900 K. To achieve a lower top cladding temperature, a lower inlet temperature is necessary. A lower inlet temperature is beneficial for the natural circulation conditions as more heat is removed by the same mass flow when the temperature difference over the core increases.  $\Delta L$  for the GCFR was 10.4 m (Ref. 30). Our design would require a  $\Delta L$  of 2.5 m once the 1000 K temperature

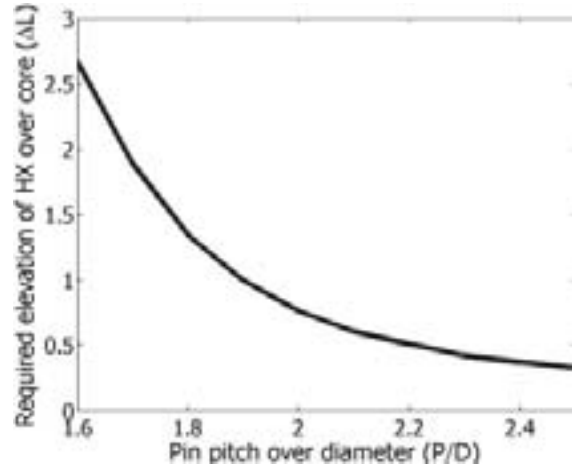


Fig. 5. The elevation of the heat exchanger over the core required for heat removal by natural circulation decreases considerably as P/D is increased.

limit, and the GCFR assumption of a decay heat corresponding to 6% of full power, were to be applied. For smaller P/D we calculate values corresponding to the values given by the reference.<sup>30</sup>

The pumping power  $W_p$  required at normal operation is given by

$$W_p = \Delta p_{tot} \cdot A \cdot U \quad (10)$$

For the present design,  $W_p = 5.9$  MW, which roughly corresponds to 3% of the electrical output from the system.

## V. NEUTRONIC SAFETY PARAMETERS

As mentioned previously, both the effective delayed neutron fraction and the Doppler feedback are reduced when americium is introduced in any significant amount.  $\beta_{eff}$  was calculated for the present core using MCNP in two consecutive runs, one with and one without delayed neutrons. The effective delayed neutron fraction was found to be  $140 (\pm 20)$  pcm. As expected from the pin cell calculations, the Doppler feedback is completely insignificant for the present fuel. Even when comparing  $k$  eigenvalues at fuel temperatures of 300 and 1800 K, the calculated difference is merely  $-0.02 (\pm 0.01)$  pcm/K. In a similar vein, the coolant void worth was calculated in two subsequent runs, the first one with He density corresponding to the core average temperature and pressure and the second with a He density relevant for ambient pressure. The  $k$  eigenvalue increases by  $870 (\pm 40)$  pcm at a pressure drop accident. The combination of a 6 \$ positive void worth, zero Doppler, and the low  $\beta_{eff}$  should make subcritical operation of this system mandatory.

## VI. BURNUP

Transmutation efficiency is governed by the burnup during irradiation and the losses during reprocessing and fuel fabrication. High burnup reduces the number of reprocessing cycles required, thereby reducing actinide losses, costs, and the time needed to transmute the waste. In a spallation source-driven subcritical core, the reactivity loss due to burnup of the fuel is compensated for by increasing the power of the accelerator beam. Initially, the beam current is  $\sim 24$  mA. We allow the current to double, but further increase is prohibited because of safety reasons.<sup>14</sup> This means the  $k$  eigenvalue drops from 0.97 to 0.94 before we take any action to increase the reactivity. Allowing for large variations in beam power and consequently in neutron source strength could result in erroneously large power insertions leading to fuel damage. In order to compensate for reactivity loss, boron carbide absorber assemblies in the reflector are replaced with steel pin assemblies as burnup proceeds. Consequently, the radial power profile changes with burnup. While the power decreases in the core center, it increases in the periphery.

The factor ultimately limiting burnup in fast neutron systems is irradiation-induced swelling of the fuel cladding. Titanium stabilized cladding steels like 15-15Ti have shown acceptable swelling rates up to irradiation doses of 150 dpa, the expectation being that 180 dpa will be possible with minor optimization.<sup>34</sup> The peak radiation dose rate anywhere in the present core is 44 dpa/yr. Hence, there is a potential for operation under 1500 effective power days. We are able to increase reactivity of our core four times by substituting absorbers in the reflector with steel, each time raising the  $k$  eigenvalue from 0.94 back to 0.97. This gives five burnup periods totaling 1400 days and a maximum dose of 170 dpa. The core-averaged actinide burnup is 19.1% at EOL.

The actinide inventory at BOL and EOL is shown in Table V. The decay of  $^{238}\text{Pu}$  ( $t_{1/2} = 87.7$  yr) and  $^{244}\text{Cm}$  ( $t_{1/2} = 18.1$  yr) out of pile gives rise to ( $\alpha, n$ ) reactions. Their concentrations at EOL are therefore likely to be the main cost drivers for fuel reprocessing and manufacturing. Curium-242 with a half-life of 162.8 days is the main source of helium production in the fuel, causing either fuel swelling or pin pressurization. A core design that minimizes the production of these three nuclides is hence favorable. Figures 6, 7, and 8 show how the buildup of these isotopes varies as a function of core position. Thanks to the hard spectrum achievable with helium cooling, the buildup of curium is insignificant, indicating that the Am/Cm ratio in the start-up fuel composition is similar to that in the equilibrium state. The softening of the spectrum in the outer fuel zone as boron carbide absorber elements in the reflector are removed leads to an increased production rate of curium when approaching EOL. Considering the very small initial concentration of Am and Cm in zone 4, the overall contribution to curium

TABLE V

Actinide Inventory at the Beginning and at the End of the Fuel Cycle\*

| Isotope           | 0 Days | 1400 Days | $\Delta_{tot}$ (%) |
|-------------------|--------|-----------|--------------------|
| $^{238}\text{Pu}$ | 117    | 182       | 56                 |
| $^{239}\text{Pu}$ | 880    | 587       | -33                |
| $^{240}\text{Pu}$ | 706    | 649       | -8.2               |
| $^{241}\text{Pu}$ | 309    | 187       | -40                |
| $^{242}\text{Pu}$ | 318    | 312       | -0.76              |
| $^{241}\text{Am}$ | 934    | 625       | -33                |
| $^{243}\text{Am}$ | 472    | 344       | -27                |
| $^{244}\text{Cm}$ | 248    | 248       | 0.03               |
| $^{245}\text{Cm}$ | 36.2   | 36.4      | 0.68               |
| All actinides     | 4020   | 3250      | -19                |

\*Unit: kg.

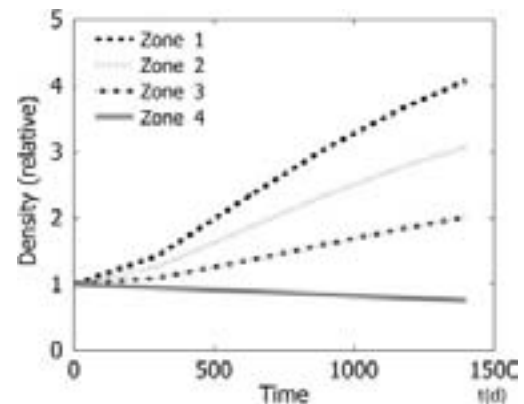


Fig. 6.  $^{238}\text{Pu}$  density evolution in the different fuel zones of the core. The production of  $^{238}\text{Pu}$  is largest in zone 1, having the largest americium concentration.

production in zone 4 is insignificant. Still, this is a good illustration of the benefits of a hard spectrum for transmutation of americium. During 1400 days of operation, 0.27 g of helium are produced per rod in fuel zone 1 closest to the spallation target. In zone 4 only 0.01 g are produced per rod.

One-group fission and capture cross sections for the nuclides of major interest are displayed in Tables VI and VII. The removal of the boron carbide absorber in the reflector leads to a decrease of the fission cross sections for the even neutron number nuclides, being most evident in zone 4. For the same reason, capture cross sections increase toward EOL. In Table VIII, the corresponding fission probability  $\sigma_f/(\sigma_c + \sigma_f)$  is shown. A high fission probability of americium results in a lower production rate of curium.

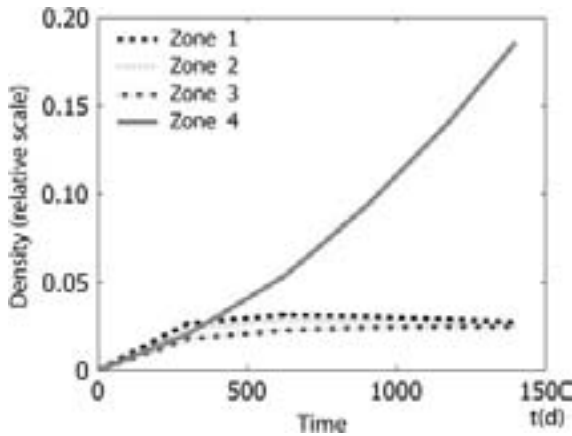


Fig. 7. <sup>242</sup>Cm density evolution. Note the effect of the spectrum softening in zone 4. In absolute numbers the core-averaged Cm production is negligible.

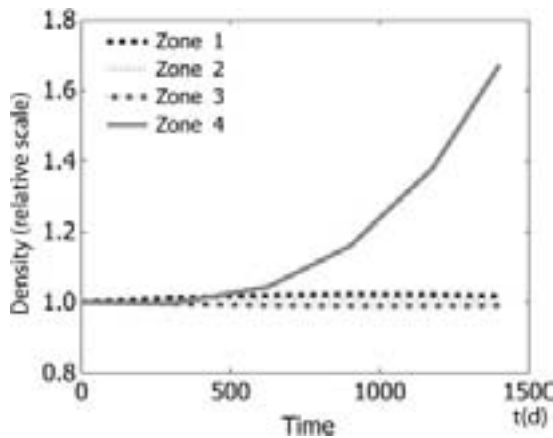


Fig. 8. <sup>244</sup>Cm density evolution. Note the effect of the spectrum softening in zone 4. In absolute numbers the core-averaged Cm production is negligible.

In order to compare the neutron spectrum in the present design with that resulting from use of liquid-metal coolants, we tabulate core-averaged cross sections for the sodium-cooled European fast reactor<sup>35</sup> (EFR) and the lead-bismuth-cooled accelerator transmutation of waste (ATW) design of Yang and Khalil<sup>36</sup> in Table IX. From the figures given in Table IX, one may expect that the use of helium coolant reduces the production of curium, as compared to transmutation of americium in sodium- or lead-bismuth-cooled systems. This is highlighted in Fig. 9, displaying the neutron spectrum in our core on top of that in the LBE-cooled ATW system.<sup>36</sup> The softer spectrum in the ATW design does have the advantage of increasing the burnup over fast fluence ratio. Accordingly, one may reach a higher burnup in the ATW design, reducing the number of reprocessing cycles.

TABLE VI  
One-Group Cross Sections for Fission

| Isotope           | $\sigma_f$ (b)<br>Zone 1 |      | $\sigma_f$ (b)<br>Zone 2 |      | $\sigma_f$ (b)<br>Zone 3 |      | $\sigma_f$ (b)<br>Zone 4 |      |
|-------------------|--------------------------|------|--------------------------|------|--------------------------|------|--------------------------|------|
|                   | BOL                      | EOL  | BOL                      | EOL  | BOL                      | EOL  | BOL                      | EOL  |
| <sup>237</sup> Np | 0.56                     | 0.48 | 0.59                     | 0.35 | 0.61                     | 0.24 | 0.66                     | 0.15 |
| <sup>238</sup> Pu | 1.32                     | 1.25 | 1.34                     | 1.13 | 1.36                     | 1.02 | 1.41                     | 0.96 |
| <sup>239</sup> Pu | 1.67                     | 1.66 | 1.67                     | 1.66 | 1.68                     | 1.71 | 1.68                     | 1.89 |
| <sup>240</sup> Pu | 0.61                     | 0.52 | 0.63                     | 0.40 | 0.66                     | 0.29 | 0.71                     | 0.21 |
| <sup>241</sup> Pu | 1.92                     | 1.98 | 1.90                     | 2.10 | 1.89                     | 2.32 | 1.88                     | 2.85 |
| <sup>242</sup> Pu | 0.47                     | 0.39 | 0.49                     | 0.29 | 0.52                     | 0.19 | 0.55                     | 0.12 |
| <sup>241</sup> Am | 0.48                     | 0.37 | 0.51                     | 0.26 | 0.54                     | 0.17 | 0.58                     | 0.11 |
| <sup>243</sup> Am | 0.39                     | 0.29 | 0.41                     | 0.20 | 0.43                     | 0.13 | 0.47                     | 0.07 |
| <sup>244</sup> Cm | 0.78                     | 0.62 | 0.75                     | 0.46 | 0.78                     | 0.32 | 0.83                     | 0.22 |
| <sup>245</sup> Cm | 2.07                     | 2.10 | 2.06                     | 2.21 | 2.06                     | 2.43 | 2.05                     | 3.01 |

TABLE VII  
One-Group Cross Sections for Capture

| Isotope           | $\sigma_c$ (b)<br>Zone 1 |      | $\sigma_c$ (b)<br>Zone 2 |      | $\sigma_c$ (b)<br>Zone 3 |      | $\sigma_c$ (b)<br>Zone 4 |      |
|-------------------|--------------------------|------|--------------------------|------|--------------------------|------|--------------------------|------|
|                   | BOL                      | EOL  | BOL                      | EOL  | BOL                      | EOL  | BOL                      | EOL  |
| <sup>237</sup> Np | 0.79                     | 0.89 | 0.76                     | 1.07 | 0.74                     | 1.36 | 0.70                     | 1.97 |
| <sup>238</sup> Pu | 0.27                     | 0.30 | 0.26                     | 0.37 | 0.26                     | 0.47 | 0.24                     | 0.69 |
| <sup>239</sup> Pu | 0.23                     | 0.25 | 0.22                     | 0.31 | 0.21                     | 0.42 | 0.20                     | 0.64 |
| <sup>240</sup> Pu | 0.28                     | 0.31 | 0.27                     | 0.37 | 0.26                     | 0.48 | 0.25                     | 0.67 |
| <sup>241</sup> Pu | 0.38                     | 0.41 | 0.38                     | 0.44 | 0.37                     | 0.50 | 0.36                     | 0.64 |
| <sup>242</sup> Pu | 0.23                     | 0.26 | 0.23                     | 0.32 | 0.22                     | 0.41 | 0.21                     | 0.58 |
| <sup>241</sup> Am | 1.12                     | 1.24 | 1.09                     | 1.45 | 1.06                     | 1.76 | 1.01                     | 2.37 |
| <sup>243</sup> Am | 0.90                     | 1.01 | 0.87                     | 1.20 | 0.85                     | 1.50 | 0.81                     | 2.17 |
| <sup>244</sup> Cm | 0.32                     | 0.35 | 0.31                     | 0.41 | 0.30                     | 0.50 | 0.29                     | 0.76 |
| <sup>245</sup> Cm | 0.16                     | 0.18 | 0.16                     | 0.22 | 0.15                     | 0.28 | 0.15                     | 0.41 |

TABLE VIII  
Fission Probability  $\sigma_f/(\sigma_f + \sigma_c)$

| Isotope           | Zone 1 |      | Zone 2 |      | Zone 3 |      | Zone 4 |      |
|-------------------|--------|------|--------|------|--------|------|--------|------|
|                   | BOL    | EOL  | BOL    | EOL  | BOL    | EOL  | BOL    | EOL  |
| <sup>237</sup> Np | 0.42   | 0.35 | 0.44   | 0.25 | 0.45   | 0.15 | 0.48   | 0.07 |
| <sup>238</sup> Pu | 0.83   | 0.80 | 0.84   | 0.75 | 0.84   | 0.68 | 0.85   | 0.58 |
| <sup>239</sup> Pu | 0.88   | 0.87 | 0.88   | 0.84 | 0.89   | 0.80 | 0.89   | 0.75 |
| <sup>240</sup> Pu | 0.69   | 0.63 | 0.70   | 0.52 | 0.72   | 0.38 | 0.74   | 0.24 |
| <sup>241</sup> Pu | 0.83   | 0.83 | 0.84   | 0.83 | 0.84   | 0.82 | 0.84   | 0.82 |
| <sup>242</sup> Pu | 0.67   | 0.60 | 0.68   | 0.48 | 0.70   | 0.32 | 0.73   | 0.17 |
| <sup>241</sup> Am | 0.30   | 0.23 | 0.32   | 0.15 | 0.34   | 0.09 | 0.37   | 0.04 |
| <sup>243</sup> Am | 0.30   | 0.23 | 0.32   | 0.14 | 0.34   | 0.08 | 0.37   | 0.03 |
| <sup>244</sup> Cm | 0.69   | 0.64 | 0.71   | 0.53 | 0.72   | 0.39 | 0.74   | 0.23 |
| <sup>245</sup> Cm | 0.93   | 0.92 | 0.93   | 0.91 | 0.93   | 0.90 | 0.93   | 0.88 |

TABLE IX

Comparison of Cross Sections in Different Core Designs\*

| Isotope           | This Design |            | ATW<br>(Ref. 36) |            | EFR<br>(Ref. 35) |            |
|-------------------|-------------|------------|------------------|------------|------------------|------------|
|                   | $\sigma_c$  | $\sigma_f$ | $\sigma_c$       | $\sigma_f$ | $\sigma_c$       | $\sigma_f$ |
| <sup>237</sup> Np | 0.74        | 0.61       | 0.85             | 0.39       | 1.58             | 0.31       |
| <sup>238</sup> Pu | 0.26        | 1.36       | 0.29             | 1.15       | 0.66             | 1.03       |
| <sup>239</sup> Pu | 0.21        | 1.68       | 0.23             | 1.61       | 0.51             | 1.85       |
| <sup>240</sup> Pu | 0.26        | 0.66       | 0.29             | 0.44       | 0.41             | 0.37       |
| <sup>241</sup> Pu | 0.37        | 1.90       | 0.40             | 1.92       | 0.59             | 2.63       |
| <sup>242</sup> Pu | 0.22        | 0.51       | 0.24             | 0.32       | 0.57             | 0.26       |
| <sup>241</sup> Am | 1.06        | 0.53       | 1.23             | 0.30       | 1.84             | 0.28       |
| <sup>243</sup> Am | 0.85        | 0.43       | 0.97             | 0.23       | 1.50             | 0.24       |
| <sup>244</sup> Cm | 0.30        | 0.77       | 0.35             | 0.51       | 0.67             | 0.43       |
| <sup>245</sup> Cm | 0.16        | 2.06       | 0.17             | 2.01       | —                | —          |

\*At BOL in barns.

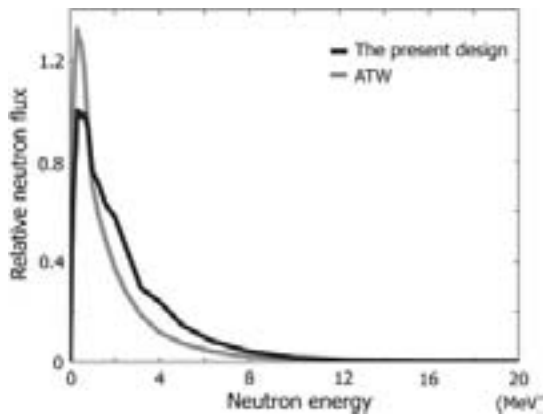


Fig. 9. Neutron flux spectrum in the present core. Comparison is made with the spectrum of the lead-bismuth-cooled core like in the ATW concept.<sup>36</sup> As expected, the spectrum of the gas-cooled core is harder.

## VII. CONCLUSIONS

The excess of neutrons in a plutonium-fueled uranium-free fast reactor may be used to increase the P/D. By doing this it is possible to design a gas-cooled fast core with P/D = 1.8, providing sufficient cooling for decay heat removal during a postulated loss-of-pressure accident, while achieving efficient transmutation of minor actinides. At normal operation, a helium coolant pressure of 4.3 MPa is enough to keep cladding temperatures below 900 K, respecting limits of yield strength for irradiated cladding steels like 15-15Ti. The unusually small pressure drop of our core enables decay heat removal under natural circulation conditions with a heat exchanger ele-

vation just more than 1 m above the core. The pumping power in the system under normal operation is as low as 5.9 MW, thanks to the low pressure drop. The calculated value of beta effective for this fuel type equals 140 pcm, which in conjunction with a vanishing Doppler feedback and a positive void worth of 6 \$ makes subcritical operation mandatory. During 1400 days of full-power operation, 19.1% of the initial actinide mass is fissioned, and the most exposed fuel pin receives a dose of 170 dpa.

In summary, the present core design achieves the combined benefits of a hard spectrum and low pressure losses, allowing minimization of curium production while ensuring decay heat removal under a loss-of-flow or a postulated loss-of-pressure accident.

## ACKNOWLEDGMENTS

The authors would like to thank W. Gudowski for providing Doppler-broadened cross-section files and M. Schikorr for clarifying discussions. This work was financially supported by SKB.

## REFERENCES

1. EUROPEAN TECHNICAL WORKING GROUP ON ADS, "A European Roadmap for Developing Accelerator Driven Systems (ADS) for Nuclear Waste Incineration," ISBN 88-8286-008-6, ENEA (2001).
2. J. P. GROUILLER, S. PILLON, C. DE SAINT JEAN, F. VARAINE, L. LEYVAL, G. VAMBENEPE, and B. CARLIER, "Minor Actinides Transmutation Scenario Studies with PWRs, FRs and Moderated Targets," *J. Nucl. Mater.*, **320**, 163 (2003).
3. A. VASILE, P. DUFOUR, H. GOLFIER, J. P. GROUILLER, J. L. GUILLET, C. POINOT, G. YOUINO, and A. ZAETTA, "Advanced Fuels for Plutonium Management in Pressurized Water Reactors," *J. Nucl. Mater.*, **319**, 173 (2003).
4. J. WALLENIUS and M. ERIKSSON, "Neutronics of Minor-Actinide Burning Accelerator-Driven Systems with Ceramic Fuel," *Nucl. Technol.*, **152**, 367 (2005).
5. "Review of PNL Study on Transmutation Processing of High Level Waste," D. G. FOSTER, Ed., LA-UR-74-74, Los Alamos National Laboratory (1974).
6. T. TAKIZUKA, H. TAKADA, I. KANNO, T. NISHIDA, M. AKABORI, and Y. KANEKO, "Conceptual Design of Transmutation Plant," *Proc. Specialist Mtg. Accelerator-Driven Transmutation Technology for Radwaste and Other Applications*, Stockholm, Sweden, June 24–28, 1991.
7. K. TSUJIMOTO, T. SASA, K. NISHIHARA, H. OIGAWA, and H. TAKANO, "Neutronics Design for Lead-Bismuth Cooled Accelerator-Driven System for Transmutation of Minor Actinide," *J. Nucl. Sci. Technol.*, **41**, 1, 21 (2004).

8. B. CARLUEC and P. ANZIEU, "Proposal for a Gas Cooled ADS Demonstrator," *Proc. 3rd Int. Conf. Accelerator Driven Transmutation Technologies and Applications (ADTTA'99)*, Praha, Czech Republic, June 7–11, 1999.
9. G. B. MELESE-D'HOSPITAL, "Review of Gas Cooled Reactors Thermal Hydraulics," *Proc. ANS/ASME/NRC Int. Topl. Mtg. Nuclear Reactor Thermal-Hydraulics*, Saratoga Springs, New York, October 5–8, 1980.
10. J. P. GAILLARD, G. MIGNOT, and A. CONTI, "Thermal-Hydraulic Design of a Gas Cooled Fast Reactor," *Proc. 2003 Int. Congress Advances in Nuclear Power Plants (ICAP '03)*, Córdoba, Spain, May 4–7, 2003, American Nuclear Society (2003) (CD-ROM).
11. E. E. FELDMAN and T. Y. C. WEI, "Cold-Finger Concept for Passive Decay Heat Removal in Gas-Cooled Reactors," *Trans. Am. Nucl. Soc.*, **88**, 681 (2003).
12. P. FORTESCUE, G. B. MELESE-D'HOSPITAL, J. PEAK, and L. MEYER, "A Developmental Gas-Cooled Fast Breeder Reactor Plant," *Proc. Nucl. 69*, Basel, Switzerland, October 6–11, 1969.
13. J. B. DEE and G. B. MELESE-D'HOSPITAL, "Part 1—The 300 MW(e) GCFR Demonstration Plant," *Mech. Eng.*, **94**, 18 (1972).
14. M. ERIKSSON, J. WALLENIUS, M. JOLKKONEN, and J. E. CAHALAN, "Inherent Safety of Fuels for Accelerator-Driven Systems," *Nucl. Technol.*, **151**, 314 (2005).
15. N. CHAUVIN, J. C. GARNIER, J. L. SERAN, P. MARTIN, and P. BROSSARD, "Requirements for Fuel and Structural Materials for Gas Cooled Fast Reactor (GFR), Preliminary Design," *Proc. Global 2003*, New Orleans, Louisiana, November 16–20, 2003, American Nuclear Society (2003) (CD-ROM).
16. J. WALLENIUS, "Neutronic Aspects of Inert Matrix Fuels for Application in ADS," *J. Nucl. Mater.*, **320**, 142 (2003).
17. J. WALLENIUS, K. MINATO, and Y. ARAI, "Influence of  $^{15}\text{N}$  Enrichment on Neutronics, Costs and  $^{14}\text{C}$  Production in Nitride Fuel Cycle Scenarios," *J. Nucl. Mater.* (submitted for publication).
18. R. THETFORD and M. MIGANELLI, "The Chemistry and Physics of Modelling Nitride Fuels for Transmutation," *J. Nucl. Mater.*, **320**, 44 (2003).
19. L. ZABOUDKO, "Status of CEA-Minatom Collaborative Experiment Bora-Bora: Fuels with High Plutonium Content," *Proc. ANL Transmuter Fuel Development Workshop*, Idaho Falls, Idaho, November 19–21, 2001.
20. J. CETNAR, J. WALLENIUS, and W. GUDOWSKI, "MCB: A Continuous Energy Monte-Carlo Burnup Simulation Code, Actinide and Fission Product Partitioning and Transmutation," *Proc. 5th Int. Information Exchange Mtg.*, Mol, Belgium, November 25–27, 1998, p. 523, Organization for Economic Cooperation and Development/Nuclear Energy Agency (1998).
21. "NEA-1643 MCBIC," available on the Internet at (<http://www.nea.fr/abs/html/nea-1643.html>) (Feb. 15, 2005).
22. "Actinide and Fission Product Partitioning and Transmutation—Status and Assessment Report," Organization for Economic Cooperation and Development/Nuclear Energy Agency (1999).
23. M. DALLE DONNE and L. MEYER, "Turbulent Convective Heat Transfer from Rough Surfaces with Two-Dimensional Rectangular Ribs," *Int. J. Heat Mass Transfer*, **20**, 583 (1977).
24. M. KAVIANY, *Principles of Heat Transfer in Porous Media*, Springer-Verlag, New York (1999).
25. *CRC Handbook of Chemistry and Physics*, 73rd ed., D. R. LIDE, Ed., CRC Press, Boca Raton, Florida (1992).
26. N. SCOTT CANNON, F. H. HUANG, and M. L. HAMILTON, "Transient and Static Mechanical Properties of D9 Fuel Pin Cladding and Duct Material Irradiated to High Fluence," *Proc. 15th ASTM Int. Symp. Effects of Radiation on Materials*, Nashville, Tennessee, 1992, ASTM STP 1125, American Society for Testing and Materials (1992).
27. R. J. PUGH and M. L. HAMILTON, "In-Reactor Creep Rupture Behavior of the D19 and 316 Alloys," *Proc. Influence of Radiation on Material Properties: 13th Int. Symp. (Part II)*, Seattle, Washington, June 23–25, 1986, American Society for Testing and Materials (1987).
28. J. L. SÉRAN et al., "Behaviour Under Neutron Irradiation of the 15-15 Ti and Em10 Steels Used as Standard Materials of the PHÉNIX Fuel Subassembly," *Proc. 15th ASTM Int. Symp. Effects of Radiation on Materials*, Nashville, Tennessee, 1992, ASTM STP 1125, American Society for Testing and Materials (1992).
29. GROUPE DE TRAVAIL RAMSES 2, "Règles d'analyse mécaniques des structures irradiées," CEA R.5618, Commissariat à l'Énergie Atomique.
30. G. B. MELESE-D'HOSPITAL, "Natural Circulation Cooling Potential of CO<sub>2</sub> and He for GCFR's," *Proc. ANS/ASME/NRC Int. Topl. Mtg. Nuclear Reactor Thermal-Hydraulics*, Saratoga Springs, New York, October 5–8, 1980.
31. N. E. TODREAS and M. S. KAZIMI, *Nuclear Systems I—Thermal Hydraulic Fundamentals*, Hemisphere Publishing Company, New York (1989).
32. A. E. WALTAR and A. B. REYNOLDS, *Fast Breeder Reactors*, Pergamon Press, New York (1981).
33. M. A. HASSAN and K. REHME, "Heat Transfer near Spacer Grids in Gas-Cooled Rod Bundles," *Nucl. Technol.*, **52**, 401 (1981).

34. *The Nuclear Fuel of Pressurized Water Reactors and Fast Reactors—Design and Behavior*, H. BAILLY, D. MÉNESIER, and C. PRUNIER, Eds., Commissariat à l’Energie Atomique (1999).
35. H. W. WIESE, “Actinide Transmutation Properties of Thermal and Fast Fission Reactors Including Multiple Recycling,” *J. Alloys Compounds*, **271**, 522 (1998).
36. W. S. YANG and H. S. KHALIL, “Blanket Design Studies of a Lead-Bismuth Eutectic-Cooled Accelerator Transmutation of Waste System,” *Nucl. Technol.*, **135**, 162 (2001).
37. C. W. HUNTER, R. L. FISH, and J. J. HOLMES, “Mechanical Properties of Unirradiated Fast Reactor Cladding During Simulated Overpower Transients,” *Nucl. Technol.*, **27**, 376 (1975).



# Accelerator-driven Systems: Safety and Kinetics

Marcus Eriksson

Doctoral Thesis  
Department of Nuclear and Reactor Physics  
Royal Institute of Technology  
Stockholm 2005

Akademisk avhandling som med tillstånd av Kungliga Tekniska Högskolan framlägges till offentlig granskning för avläggande av teknologie doktorsexamen fredagen den 18 mars 2004 kl. 10.00 i sal FA32, Albanova universitetscentrum, Roslagstullsbacken 21, Stockholm.

ISBN 91-7283-988-0

TRITA-FYS 2005:13

ISSN 0280-316X

ISRN KTH/FYS/--05:13—SE

Copyright Marcus Eriksson

Tryckeri: Universitetservice US-AB, Stockholm 2005

# Abstract

The accelerator-driven system (ADS) is recognized as a promising system for the purpose of nuclear waste transmutation and minimization of spent fuel radiotoxicity. The primary cause for this derives from its accelerator-driven, sub-critical operating state, which introduces beneficial safety-related features allowing for application of cores employing fuel systems containing pure transuranics or minor actinides, thereby offering increased incineration rate of waste products and minimal deployment of advanced (and expensive) partitioning and transmutation technologies. The main theme of the thesis is safety and kinetics performance of accelerator-driven nuclear reactors. The studies are confined to the examination of ADS design proposals employing fast neutron spectrum, uranium-free lattice fuels, and liquid-metal cooling, with emphasis on lead-bismuth coolant. The thesis consists of computational studies under normal operation and hypothetical accidents, and of evaluation and identification of safety design features.

By itself, subcritical operation provides a distinct safety advantage over critical reactor operation, distinguished by high operational stability and additional margins for positive reactivity insertion. For a uranium-free minor actinide based fuel important safety parameters deteriorate. Specific analyses suggest that operation of such cores in a critical state would be very difficult. The studies of unprotected transients indicate that lead-bismuth cooled accelerator-driven reactors can be effective in addressing the low effective delayed neutron fraction and the high coolant void reactivity that comes with the minor actinide fuel, but some supportive prompt negative feedback mechanism might be considered necessary to compensate for a weak Doppler effect in case of a prompt critical transient. Although lead-bismuth features a high boiling point, the work underlines the importance of maintaining a low coolant void reactivity value. The transient design studies identified a molybdenum-based Ceramic-Metal (CerMet) fuel with favourable inherent safety features. A higher lattice pitch is suggested to avoid mechanical failure during unprotected loss-of-flow. Detailed coupled neutron kinetics and thermal hydraulic analyses demonstrated that the point kinetics approximation is capable of providing highly accurate transient calculations of subcritical systems. The results suggest better precision at lower  $k_{\text{eff}}$  levels, which is an effect of the reduced sensitivity to system reactivity perturbations in a subcritical state resulting in small spatial distortions. In the course of a beam reliability study, the accelerator was identified as responsible for frequent beam interruptions. It is clear that extensive improvement in the mean-time between beam failures is required.

# List of Papers

The thesis is based on Papers I through VI. These papers are appended in the thesis and are referred to in the text by their Roman numerals.

- I. M. Eriksson, J. Wallenius, M. Jolkkonen, and J. E. Cahalan  
*Inherent Safety of Fuels for Accelerator-driven Systems*  
Accepted Nuclear Technology (January 2005).
- II. J. Wallenius and M. Eriksson  
*Neutronics of Minor Actinide Burning Accelerator Driven Systems with Ceramic Fuel*  
Accepted Nuclear Technology (January 2005).
- III. M. Eriksson, J. E. Cahalan, and W. S. Yang  
*On the Performance of Point Kinetics for the Analysis Accelerator-driven Systems*  
Nuclear Science and Engineering, 149, 298-311 (2005)
- IV. M. Eriksson, J. Wallenius, J. E. Cahalan, K. Tucek, and W. Gudowski  
*Safety Analysis of Na and Pb-Bi Coolants in Response to Beam Instabilities*  
Proc. 3<sup>rd</sup> International Workshop on Utilisation and Reliability of High Power Proton Accelerators, Santa Fe, May 12-16, NEA/OECD (2002).
- V. M. Eriksson and J. E. Cahalan  
*Inherent Shutdown Capabilities in Accelerator-driven Systems*  
Annals of Nuclear Energy, vol. 29/14 pp 1689-1706, (2002).
- VI. M. Eriksson and C. Piaszczyk  
*Reliability Assessment of the LANSCE Accelerator System*  
Proc. Workshop on Utilisation and Reliability of High Power Proton Accelerators, Mito, Japan, 13-15 October (1998)

## Author's contribution

With the exception for **paper II**, the author is the principal writer and bears the main responsibility for the papers included in the thesis. The author took active part in the discussions and preparation of **paper II**, but his contribution is primarily related to the subject reported in **Paper I**. **Paper III** consists mainly of computational studies and data interpretation, which were performed by the author, with important comments and suggestions by the co-authors. The author performed the main parts of **Papers IV** and **V** including the transient and thermal hydraulics calculations, data analysis and the writing of the manuscripts, supported with neutron transport data for **Paper IV**. **Paper VI** is the result of Diploma work performed by the author at the department.

# Acknowledgements

I owe thanks to many people who supported me in various different ways during the completion of this thesis. I wish to express my appreciation to friends and colleagues (past and present) of the reactor physics department (Royal Institute of Technology) for, among many other things, their helpful interactions and advice, and for providing a rich social life at the department as well as many memorable events outside work, including stimulating discussions on various topics covered, conference trips, unforgettable “fikas”, and so on. My sincere appreciation goes to W. Gudowski, who originally stimulated my interest in reactor physics and accepted me as graduate student, and to J. Wallenius, from whom I received much guidance and inspiration over the years and also for his efforts in reading the manuscript. It is also a pleasure to acknowledge the continued guidance of J. Cahalan of Argonne National Laboratory, for devoting so much time to me and for his untiring assistance on the topics of reactor safety analysis, whose thinking on the subject in many ways influenced my own. Also, thanks are due to numerous people working at Argonne National Laboratory at the former Reactor Analysis Division who provided considerable assistance and hospitality during my stay as visiting graduate student, in the year 2000-2001, and for their courtesy in allowing me to use their computing facilities. Sincere thanks are due to Svensk Kärnbränslehantering AB for supporting my research in transmutation systems for more than half a decade. I gratefully acknowledge The Swedish Centre for Nuclear Technology, for generously providing the extra resources to carry out part of my studies in the U.S., which I had the fortune to experience. Thanks are also due to the students and staff of the nuclear physics department not mentioned thus far for providing an enjoyable, friendly, and inspiring working environment.

Further, I wish to express my deep appreciation and love to my wife, Ellinor, for her continued support, encouragement, patience, and extraordinary understanding for my countless late returns and absent weekends throughout the many years of research, and for providing tasteful lunches (although I must confess I lost 9% of my initial body weight during the writing of this text!) and for her tending of the family during the trying period of writing. Without her support this task would have been impossible. I also extend my affectionate to my two daughters, Elvira and Lovisa, who truly provided the greatest inspiration of all, for their cheerful smile and loving company (understandably with varying degree of patience). Last but not least, special thanks must be given to my parents, Thomas and Elsy, who always followed my work with genuine interest, no matter what, and for their early stimulation on matters that finally brought me into academia.

*Marcus Eriksson*

Stockholm 2005

# Content

|  |           |
|--|-----------|
| <b>Chapter 1: Nuclear Waste</b>                        | <b>1</b>  |
| Introduction   | 1         |
| Classification of radioactive wastes                   | 1         |
| Spent nuclear fuel                                     | 3         |
| Options for spent fuel management                      | 11        |
| <b>Chapter 2: Partitioning &amp; Transmutation</b>     | <b>15</b> |
| Partitioning   | 15        |
| Transmutation  | 20        |
| <b>Chapter 3: Transmutation Strategies</b>             | <b>24</b> |
| Introduction   | 24        |
| Transmutation of plutonium                             | 25        |
| Transmutation of minor actinides                       | 27        |
| Transmutation of fission products                      | 31        |
| <b>Chapter 4: Accelerator-driven Systems</b>           | <b>33</b> |
| General principles                                     | 33        |
| Safety features of uranium-free cores                  | 36        |
| Motivation for subcritical operation                   | 42        |
| Responsiveness of the ADS                              | 44        |
| Accident performance                                   | 45        |
| Safety performance in super-prompt critical transients | 52        |
| Computational performance of the point kinetics method | 55        |
| Accelerator reliability                                | 60        |
| <b>Conclusions</b>                                     | <b>62</b> |
| <b>Appendix A: Reactor Kinetics Equations</b>          | <b>64</b> |
| <b>Appendix B: Short Summary of the SAS4A Code</b>     | <b>67</b> |
| <b>Bibliography</b>                                    | <b>68</b> |
| <b>Papers</b>  |           |

*“A grad student in procrastination tends to stay in procrastination unless an external force is applied to it”*

Also known as Newton's first law of graduation or the “Law of Inertia” originally discovered experimentally by Galileo when he threatened to cut his grad student's funding!  
(From <http://www.phdcomics.com>, originally published 2001)

# Chapter 1:

## Nuclear Waste

### ***Introduction***

Nuclear energy is used throughout the world and radioactive waste is an unavoidable by-product of its utilization. It is generated in every stage of the nuclear fuel cycle, but by far the largest amount of radioactivity is contained in the spent nuclear fuel produced in connection with nuclear power operation. Although the radioactive wastes arising from other steps of the nuclear fuel cycle are not to be neglected quantitatively, these wastes play only a minor role because of their low activity levels. The radioactivity contained in the spent fuel is typically several orders of magnitude higher than in wastes from other steps of the fuel cycle [1]. The radioactivity of the spent fuel after reactor service is due primarily to the radioisotopes generated by fission; however, because of the relatively short half-lives of many fission products, the activity levels of the fission products rapidly decrease with time. In comparison, a small amount of transuranic waste (~1 % of initial actinide loading) is generated by successive neutron capture in uranium. While the fission products are  $\beta$ - and  $\lambda$ -emitters, the transuranic elements are mainly  $\alpha$ -emitters. The transuranic waste raises special problems because of the high radiotoxicity and long half-life in comparison with the fission products. From a global radiotoxicity point of view, the transuranic waste presents the greatest obstacle, an aspect that suggests special waste management treatment. This chapter discusses the types, composition, and hazards involved in the spent nuclear fuel produced by light-water reactors, which serves as the reference case.

### ***Classification of radioactive wastes***

A reasonable starting point for discussions on nuclear waste management might be to try to define the term “radioactive waste”. The Swedish Radiation Protection Authority (SSI) [2] has a definition according to “a material which contains or is contaminated with radionuclides and for which there is no use”, which traces back to the definition considered in EU Directive 92/3/Euratom [3]. The Department of Energy [4] in the U.S. has a definition of radioactive waste as “Solid, liquid, or gaseous material that contains radionuclides regulated under the Atomic Energy Act of 1954, as amended, and of negligible economic value considering costs of recovery.” These definitions are quite ambiguous and subjective in nature, which open for different interpretations of the meaning of radioactive waste. What is considered as waste under one set of assumptions and in one place may be of use or value under another set of assumptions or in another place. For example, what is the appropriate declaration of spent nuclear fuel? If the fuel is disposed directly without reprocessing, spent nuclear fuel is considered to be radioactive waste. With reprocessing, spent nuclear fuel is considered to be a resource. With the latter definition the spent nuclear fuel is not ‘spent’ in a true sense. Dictionary meanings offer little further clarification on the interpretation of radioactive waste. While the Swedish Environmental Act [5], also known as “Miljöbalken”, defines “waste” as a material “that the owner disposes of or intends to, or is bound to dispose of” and this is regardless of whether the material has an economic value or can be reused, it does not clearly



specify the meaning of the term “radioactive waste”. So far the usefulness or the economic value of the waste material remain as our only definitions, yet the SSI has given consideration [6] to adopt a similar definition of radioactive waste as defined for general wastes under the Environmental Act. Nevertheless, from a radiation protection viewpoint, radioactive waste products are all products whose radioactivity exceeds certain levels, and which, for this reason must be managed in order to protect humans and the environment.

Radioactive waste may be classified in a variety of ways according to the specific radioactivity, half-life of the radionuclides, type of ionizing radiation emitted, physical state of the waste, i.e., whether it is in a gaseous, liquid, or solid form. With respect to the activity concentration, radioactive wastes are commonly classified as high-, intermediate-, and low-level wastes, but no strict distinction between these categories exists that is accepted worldwide. Low level waste (LLW) is generally characterized by low radioactivity levels that can be handled without shielding. It includes both short-lived and long-lived radionuclides. Intermediate level waste (ILW), however, requires special shielding measures but no cooling during handling, transportation, and storage. High-level waste (HLW), finally, generates a considerable amount of heat and requires cooling, as well as shielding because of its high intensity of ionizing radiation. Based on the decay heat emitted, a lower value of  $2 \text{ kW/m}^3$  is used to distinguish between high level radioactive wastes from other radioactive waste classes. Handling this waste requires special procedures to manage both the heat and the radioactivity. Based on the time required for the nuclei of the radioactive material to decay, the waste is often described as short-lived or long-lived. Short-lived radioactive waste usually includes radionuclides that have a half-life of less than thirty years. As noted in TABLE 1, the International Atomic Energy Agency (IAEA) suggests a set of 4 classes based on a combination of the activity concentration and the half-life [7]. Practically, HLW is produced only in connection with the operation of nuclear reactors and therefore it is often synonymous with the spent nuclear fuel. HLW also arises in the reprocessing of spent nuclear fuel in the form of concentrated liquid solutions containing fission products. In the process, transuranic radionuclides (also called the alpha-bearing waste) are extracted, which represents special problems because of its long half-life and high radiotoxicity, aspects that are very important with regard to waste management. These implications will be discussed furthermore in the following sections. Most nations apply a similar classification system as indicated by the IAEA, however, variations occur. In the U.S. [8], radioactive waste classes are source-defined (as in spent nuclear fuel, uranium mill tailings, transuranic waste, etc.) rather than defined by some measurable quality of the waste. In that classification, high-level waste is per definition the highly radioactive material created from the reprocessing of the spent fuel that contains the fission products. Irradiated reactor fuel is, however, for the purpose of the repository also regulated as high-level waste.

TABLE 1  
Classification of radioactive waste according to IAEA [7]

| Waste class               | Definition  |
|---------------------------|---|
| Low level                 | Contains enough radioactive material to require action for the protection of people, but not so much that it requires shielding during handling, storage or transportation. The activity clearance level is based on an annual dose to members of the public of less than 0.01 mSv. |
| Intermediate, short lived | Waste which requires shielding, but needs little or no provision for heat dissipation and contains low concentrations of long-lived radionuclides (less than 4000 Bq/g of alpha-emitters). The radionuclides generally have a half-life of less than 30 years.                      |
| Intermediate, long lived  | Waste that requires shielding, but needs little or no provision for heat dissipation. The radionuclides generally have a half life of more than 30 years.   |
| High level                | Waste which contains large concentrations of both short- and long-lived radionuclides and is sufficiently radioactive to require both shielding and cooling. The waste generates more than 2 kilowatts of heat per cubic metre.   |

### ***Spent nuclear fuel***

The bulk of all spent fuel results from the operation of light water reactors (LWR). The fuel material of LWRs consists of ceramic uranium dioxide (UO<sub>2</sub>) in the form of compacted (and sintered) pellets. The pellets are stacked inside metallic tubes, which are then bundled and collected in a metal case, referred to as an assembly or subassembly. The subassemblies are loaded into the reactor core and irradiated for a period of several years. During this period energy is released as the heavy atoms undergo fission and the fuel is said to be burned. After irradiation the spent fuel is removed from the core and stored in water pools for several months to allow the short-lived fission products to decay. Depending on national policy, the spent fuel is sent directly to storage facilities without reprocessing or shipped to reprocessing facilities in order to recycle plutonium and unused uranium. Today, a smaller fraction (20-30%) of the spent fuel is reprocessed while the majority is sent to direct disposal.

### ***Production facts***

As of October 2004, there were 440 nuclear reactors (commercial power producing) in operation worldwide with a total net installed capacity of 366 GWe [9]. Of these 207 are located in Europe (173 GWe), including Russia and Ukraine, and 104 (76 GWe) reactors in the Far East (mainly in Japan, South Korea, and China). The United States has 104 operating nuclear reactors that produce 98 GWe and 17 reactors (12 GWe) are in operation in Canada, the remaining 8 (6 GWe) reactors are located in South America (Brazil, Argentina, and Mexico) and South Africa. They provide about 2800 TWh of electricity in total, which correspond to approximately 16% of the global electricity supply [10]. TABLE 2 shows the operational reactors by type. Over 87% of the electricity production is produced by reactors of the light water reactor (LWR) type, i.e., PWR, BWR, ABWR, and VVER. It may be noted

that three fast breeder reactors (FBR) are in operation worldwide (BN-600 in Russia, Phenix in France, and Monju<sup>a</sup> in Japan) with a total electrical output of 1 GW.

A standard light water reactor generates 1 GW of electric power and produces some 23 tons HM (oxygen not accounted for) of spent nuclear fuel annually [11], assuming an average burnup of 40 MWdays/ton U. Based on this figure, together with electricity production data, a rough estimate of the annual production of spent fuel can be made. TABLE 3 gives an idea of the regional quantities involved. The estimated global spent nuclear fuel production is approximately 8,400 tons per year. This number does not include spent fuel of military origin (e.g. spent naval fuel, weapons production) or from research establishments. It should be kept in mind that the actual discharge rate of spent fuel (tons/year) depends on the burnup, which varies between reactors. Higher burnup essentially increases fuel utilization and generates less waste per unit electric capacity. According to a recent report by the IAEA [10], the global spent fuel generation is around 10,500 tons HM/year, which should then include spent fuel of all origins. According to the same report, the total amount of spent fuel cumulatively generated worldwide by the beginning of 2003 was close to 255,000 tons HM. The projected quantity for the year 2010 is close to 340,000 tons HM. By the year 2020, the time when most of the presently operated nuclear power reactors approach the end of their current licensed operational life time, the total amount of spent nuclear fuel will be around 445,000 tons HM. These figures are given in TABLE 4.

TABLE 2  
Operational reactors by type, according to the IAEA [9]

| Reactor type<br>(abbreviation) | No. of<br>units | Electric capacity<br>(GWe) | %-electric<br>capacity |
|--------------------------------|-----------------|----------------------------|------------------------|
| PWR                            | 214             | 204                        | 55.9%                  |
| BWR                            | 90              | 78                         | 21.3%                  |
| VVER                           | 52              | 35                         | 9.6%                   |
| PHWR                           | 39              | 20                         | 5.5%                   |
| LWGR                           | 17              | 13                         | 3.4%                   |
| AGR                            | 14              | 8                          | 2.3%                   |
| GCR                            | 8               | 2                          | 0.6%                   |
| ABWR                           | 3               | 4                          | 1.1%                   |
| FBR                            | 3               | 1                          | 0.3%                   |
| <b>Total:</b>                  | <b>440</b>      | <b>366</b>                 | <b>100.0%</b>          |

TABLE 3  
Estimated annual production (tons/year) of spent nuclear fuel. Based on production rate of 23 tons HM/GWe [10]

| Region                                      | Generating<br>capacity<br>(GWe) | Estimated production of spent<br>fuel from nuclear power plants<br>(tons HM) |
|---|---------------------------------|--|
| Europe (including Russia<br>and Ukraine)    | 173                             | 3990   |
| North America (U.S. and<br>Canda)           | 110                             | 2540   |
| Far East (mainly Japan, S.<br>Korea, China) | 76                              | 1740   |
| Others (South America,<br>South Africa)     | 6                               | 140  |
| <b>Worldwide</b>                            | <b>366</b>                      | <b>8410</b>  |

<sup>a</sup>Although Monju has been shutdown since an accident in 1995, it is categorized as ‘operational’ according to the IAEA since no permanent decision has been taken for its closure.

TABLE 4

Present and projected inventory (tons HM) of spent nuclear fuel accumulated worldwide [10].

| Year           | Worldwide inventory<br>(ktons HM) |
|----------------|-----------------------------------|
| 2003           | 255                               |
| 2010 projected | 340                               |
| 2020 projected | 445                               |

### Composition

The spent fuel is a multi-component system consisting of radionuclides with very different half-lives and toxicities. Besides the original components, i.e., uranium and oxygen, the spent fuel contains highly radioactive fission products, and transuranic elements. Fission products are created from the fission of heavy atoms (U,Pu) and transuranic elements (Pu, Am, Cm, etc.) are formed by capture reactions in heavy atoms. In addition, activation products are created by neutron capture in metal parts of the fuel element. There are many possible fission reactions, all producing different fission products. The amount of radioactivity and composition of the spent fuel is largely determined by the burnup and to limited degree on the burnup history, i.e., neutron spectrum, flux level, irradiation time, and cooling time after removal from the reactor. The term ‘burnup’ is a measure of the energy produced in the fuel (MWd per kg heavy atoms) or the fraction of heavy atoms that has fissioned. Increased burnup increases the concentration of fission products and transuranic elements. The local burnup depends on the position of the fuel rod in the core and varies also for each pin along its length. For this reason, burnup is usually reported as an average over local burnup levels. As a rule of thumb, 1% fission fraction corresponds to an energy production of 10 MWd per kg heavy atoms. Spectrum hardening in a LWR increases the formation of plutonium as it leads to more resonance capture. Although a higher neutron flux permits more secondary neutron capture reactions, the build-up of heavy actinides is less efficient. Since most actinides formed are fissile or fissionable but have a short lifetime relatively more will disappear by decay than will fission in a low flux. Long irradiation time tend to increase the proportion of long-lived products, while increased cooling time reduces the fraction of short-lived products. Because of these effects, the spent fuel varies in composition between reactor types but also between different fuel batches from the same reactor. TABLE 5 gives the composition of PWR fuel with an average burnup of 35 MWd/kg and 60 MWd/kg, three years after unloading [12]. The composition is normalized to the amount of initially present heavy atoms.

TABLE 5

Composition of spent PWR fuel in %-weight of initial heavy atoms (3 y of cooling) [12]

| Family           | Average burnup                                |   |
|------------------|---|---|
|                  | 35 MWd/kg U<br>3.25% initial <sup>235</sup> U | 60 MWd/kg U<br>4.95% initial <sup>235</sup> U |
| Uranium          | 95.3%   | 92.4%   |
| Plutonium        | 1.0%  | 1.3%  |
| Minor actinides  | 0.08%   | 0.16%   |
| Fission products | 3.6%  | 6.1%  |

One can see that the fission product content increases from 3.6% for 35 MWd/kg to 6.1% for 60 MWd/kg. The plutonium (TRU) content increases slightly with burnup, from 1.0% for 35 MWd/kg to 1.3% for 60 MWd/kg. In addition, the minor actinide (Np, Am, Cm) content increases with burnup, where the production of <sup>244</sup>Cm is problematic because of its neutron

emitting properties and its relatively short half-life of 18 years. The isotopic composition for plutonium changes with burnup [12], as shown in TABLE 6. The increase in burnup is accompanied by a decrease in fissile isotopes ( $^{239}\text{Pu}$  and  $^{241}\text{Pu}$ ) and build-up of even neutron numbered plutonium isotopes (which is well known from weapons plutonium production).  $^{240}\text{Pu}$  and  $^{242}\text{Pu}$  act as neutron absorbers.  $^{238}\text{Pu}$  is produced through neutron capture in  $^{237}\text{Np}$  and subsequent beta decay of  $^{238}\text{Np}$ . It is a neutron emitter (from spontaneous fission) and strong heat source because of alpha emission.  $^{240}\text{Pu}$  is also a neutron source because of its spontaneous fission. This has an adverse effect in handling high-burnup or multi-recycled spent fuel and also, reduces the fissile potential of the recycled fuel.

TABLE 6

Isotopic composition of plutonium in spent PWR fuel (in %-weight) 3 years of cooling [12].

| Burnup                                      | $^{238}\text{Pu}$ | $^{239}\text{Pu}$ | $^{240}\text{Pu}$ | $^{241}\text{Pu}$ | $^{242}\text{Pu}$ |
|---|-------------------|-------------------|-------------------|-------------------|-------------------|
| 33 MWd/kg<br>3.25% initial $^{235}\text{U}$ | 1.7%              | 57.2%             | 22.8%             | 12.2%             | 6.0%              |
| 60 MWd/kg<br>4.95% initial $^{235}\text{U}$ | 3.9%              | 49.5%             | 24.8%             | 12.9%             | 8.9%              |

In high burnup fuel, the irradiation time is usually limited by material stability, e.g., due to fuel swelling, embrittlement of cladding or structural materials, rather than by reactivity limitations. A typical LWR fuel reaches an average burnup level in the range 40-50 MWd per kg U., which implies that 4-5% of the heavy atoms, undergoes fission in standard LWR fuel. TABLE 7 lists the composition of the transuranic elements contained in spent fuel with an average burnup of 40 MWd/kg U after 15 years of decay [11]. The cooling time has an immediate effect on the content of the shorter lived isotopes, primarily  $^{241}\text{Pu}$ ,  $^{238}\text{Pu}$ , and  $^{244}\text{Cm}$ , and on the concentration of  $^{241}\text{Am}$ . The amount of  $^{241}\text{Am}$  increases with burnup because it is the daughter of  $^{241}\text{Pu}$  with a half-life of 14.4 years. Reduction of the inventory of  $^{238}\text{Pu}$  and  $^{244}\text{Cm}$  simplifies reprocessing and waste handling. Small amounts of elements heavier than curium are formed.

TABLE 7

TRU composition in LWR spent fuel (40 MWd/kg) 15 years after unloading [11]

| Nuclide                   | %-weight | Half-life (y)    |
|---------------------------|----------|------------------|
| $^{237}\text{Np}$         | 5.60%    | $2.1 \cdot 10^6$ |
| $^{238}\text{Pu}$         | 1.98%    | $8.8 \cdot 10^1$ |
| $^{239}\text{Pu}$         | 50.8%    | $2.4 \cdot 10^4$ |
| $^{240}\text{Pu}$         | 22.4%    | $6.6 \cdot 10^3$ |
| $^{241}\text{Pu}$         | 5.86%    | $1.4 \cdot 10^1$ |
| $^{242}\text{Pu}$         | 5.17%    | $3.8 \cdot 10^5$ |
| $^{241}\text{Am}$         | 6.63%    | $4.3 \cdot 10^2$ |
| $^{242\text{m}}\text{Am}$ | 0.02%    | $1.4 \cdot 10^2$ |
| $^{243}\text{Am}$         | 1.21%    | $7.4 \cdot 10^3$ |
| $^{244}\text{Cm}$         | 0.27%    | $1.8 \cdot 10^1$ |
| $^{245}\text{Cm}$         | 0.02%    | $8.5 \cdot 10^3$ |

### ***Radiotoxicity***

The activity of a radioactive substance is expressed in Bequerels (Bq) or Curies (1 Ci=3.7·10<sup>10</sup> Bq). It is simply the number of disintegrations in a sample per unit time without regard to the properties of the radiation or the induced biological effects. Although comparisons involving radioactivity sometimes appear in the literature, it is generally recognized as a poor measure of the hazard. The most common way of measuring the risk associated with a radioactive substance, that gives a better measure of the biological harm to the body, is through the concept of “radiotoxicity”. It takes into account the sensitivity of the human body to a particular radioisotope after intake. The radiotoxicity is determined by the product of the activity (Bq) and an effective dose coefficient,  $e$ , for a given isotope:

$$\text{Radiotoxicity} = e \cdot \text{Activity}$$

While the activity is given by the number of atoms present in the sample multiplied with the decay constant of the radioactive nuclei, the effective dose coefficient depends on the type and energy of emitted particle, mode of intake (inhalation or ingestion), metabolism of the substance in the body, and sensitivity of the exposed organs. The effective dose coefficient corresponds to the committed dose (integrated over the life expectancy) resulting from the intake of 1 Bq of the specific radionuclide. Relevant data are regularly published by the International Commission on Radiological Protection (ICRP) [13]. The dose coefficients depend on the mode of intake. Plutonium, for example, is far more hazardous if inhaled than if ingested, because it is more readily absorbed into the blood stream via the lungs than via the stomach and intestines [14]. Before being transported to other organs, inhaled plutonium will deliver a radiation dose to the lungs, increasing the risk for lung cancer; ingested plutonium will deliver a radiation dose to the walls of the intestines. The uptake fraction in the gut is low because plutonium is not very soluble in the body fluids. To evaluate the hazard risk of a radioactive substance it must also be taken into account the particular pathway by which the substance reaches man. The transportation of radionuclides in the environment is not explicitly considered in the concept of the effective dose coefficients. But, in comparing the radiotoxicity of buried wastes in a repository, the inhalation pathway is less likely. The principal route of intake for members of the public is through water or food. Thus, in most hazard comparisons ingestion toxicity is in favour for inhalation [15]. Effective Dose Coefficients for ingestion of radionuclides are listed in TABLE 8. The effective dose coefficient is age dependent as it corresponds to the committed dose per unit intake (Bq). The integration time depends on the time from intake to age 70 y; for an adult it is taken to be 50 years. Depending on the absorption fraction of radionuclides in the adult, the uptake fraction may be 2-10 times higher in the infant. This is reflected in the effective dose coefficients, as shown in TABLE 8.

TABLE 8

Effective dose coefficients,  $e$  (Sv/Bq), for ingestion of radionuclides and their associated half-life [13].

| Isotope           | Half-life (years) | Uptake fraction (adults) | Uptake fraction (infant) | $e$ , adults (Sv/Bq) | $e$ , infants (Sv/Bq) | Minimum amount for acquiring fatal cancer* (g) |
|-------------------|-------------------|--------------------------|--------------------------|----------------------|-----------------------|--|
| Actinides:        |                   |                          |                          |                      |                       |  |
| <sup>235</sup> U  | $7.0 \cdot 10^8$  | 0.02                     | 0.04                     | $4.7 \cdot 10^{-8}$  | $3.5 \cdot 10^{-7}$   | $5.3 \cdot 10^3$                               |
| <sup>238</sup> U  | $4.5 \cdot 10^9$  | 0.02                     | 0.04                     | $4.5 \cdot 10^{-8}$  | $3.4 \cdot 10^{-7}$   | $3.6 \cdot 10^4$                               |
| <sup>237</sup> Np | $2.1 \cdot 10^6$  | $5.0 \cdot 10^{-4}$      | $5.0 \cdot 10^{-3}$      | $1.1 \cdot 10^{-7}$  | $2.0 \cdot 10^{-6}$   | $6.8 \cdot 10^0$                               |
| <sup>238</sup> Pu | $8.8 \cdot 10^1$  | $5.0 \cdot 10^{-4}$      | $5.0 \cdot 10^{-3}$      | $2.3 \cdot 10^{-7}$  | $4.0 \cdot 10^{-6}$   | $1.4 \cdot 10^{-4}$                            |
| <sup>239</sup> Pu | $2.4 \cdot 10^4$  | $5.0 \cdot 10^{-4}$      | $5.0 \cdot 10^{-3}$      | $2.5 \cdot 10^{-7}$  | $4.2 \cdot 10^{-6}$   | $3.5 \cdot 10^{-2}$                            |
| <sup>240</sup> Pu | $6.6 \cdot 10^3$  | $5.0 \cdot 10^{-4}$      | $5.0 \cdot 10^{-3}$      | $2.5 \cdot 10^{-7}$  | $4.2 \cdot 10^{-6}$   | $9.6 \cdot 10^{-3}$                            |
| <sup>241</sup> Pu | $1.4 \cdot 10^1$  | $5.0 \cdot 10^{-4}$      | $5.0 \cdot 10^{-3}$      | $4.8 \cdot 10^{-9}$  | $5.6 \cdot 10^{-8}$   | $1.1 \cdot 10^{-3}$                            |
| <sup>242</sup> Pu | $3.8 \cdot 10^5$  | $5.0 \cdot 10^{-4}$      | $5.0 \cdot 10^{-3}$      | $2.4 \cdot 10^{-7}$  | $4.0 \cdot 10^{-6}$   | $5.8 \cdot 10^{-1}$                            |
| <sup>241</sup> Am | $4.3 \cdot 10^2$  | $5.0 \cdot 10^{-4}$      | $5.0 \cdot 10^{-3}$      | $2.0 \cdot 10^{-7}$  | $3.7 \cdot 10^{-6}$   | $7.8 \cdot 10^{-4}$                            |
| <sup>243</sup> Am | $7.4 \cdot 10^3$  | $5.0 \cdot 10^{-4}$      | $5.0 \cdot 10^{-3}$      | $2.0 \cdot 10^{-7}$  | $3.6 \cdot 10^{-6}$   | $1.4 \cdot 10^{-2}$                            |
| <sup>244</sup> Cm | $1.8 \cdot 10^1$  | $5.0 \cdot 10^{-4}$      | $5.0 \cdot 10^{-3}$      | $1.2 \cdot 10^{-7}$  | $2.9 \cdot 10^{-6}$   | $5.5 \cdot 10^{-5}$                            |
| <sup>245</sup> Cm | $8.5 \cdot 10^3$  | $5.0 \cdot 10^{-4}$      | $5.0 \cdot 10^{-3}$      | $2.1 \cdot 10^{-7}$  | $3.7 \cdot 10^{-6}$   | $1.5 \cdot 10^{-2}$                            |
| Fission products: |                   |                          |                          |                      |                       |  |
| <sup>90</sup> Sr  | $2.9 \cdot 10^1$  | 0.3                      | 0.6                      | $2.8 \cdot 10^{-8}$  | $2.3 \cdot 10^{-7}$   | $1.4 \cdot 10^{-4}$                            |
| <sup>99</sup> Tc  | $2.1 \cdot 10^5$  | 0.5                      | 1.0                      | $6.4 \cdot 10^{-10}$ | $1.0 \cdot 10^{-8}$   | $4.9 \cdot 10^1$                               |
| <sup>129</sup> I  | $1.6 \cdot 10^7$  | 1.0                      | 1.0                      | $1.1 \cdot 10^{-7}$  | $1.8 \cdot 10^{-7}$   | $2.8 \cdot 10^1$                               |
| <sup>135</sup> Cs | $2.0 \cdot 10^6$  | 1.0                      | 1.0                      | $2.0 \cdot 10^{-9}$  | $4.1 \cdot 10^{-9}$   | $2.0 \cdot 10^2$                               |
| <sup>137</sup> Cs | $3.0 \cdot 10^1$  | 1.0                      | 1.0                      | $1.3 \cdot 10^{-8}$  | $2.1 \cdot 10^{-8}$   | $4.8 \cdot 10^{-4}$                            |

\*Based on a dose of 20 Sv to acquire mortal cancer with 100% certainty (chemical toxicity not accounted for).

In terms of the level radiotoxicity per Bq, the plutonium isotopes belong to the most hazardous elements, despite that these are not easily absorbed from gastrointestinal tract. One may note that the effective dose coefficients are generally many times higher for the transuranic elements than for the fission products, which is principally due to their high alpha activity. One exception is <sup>241</sup>Pu, which is a  $\beta$ -emitter. Once transferred into the blood stream, the heavy elements are often concentrated in the bone, liver, and kidneys, where their  $\alpha$ -emissions provide essentially lifetime irradiation since the biological exchange-rate in these organs is low [15]. Once inside the body,  $\alpha$ -emitters are far more hazardous than  $\beta$ - and  $\lambda$ -emitters. The energy of the  $\alpha$ -particle is dissipated in a small volume where the radionuclide is located and considerably increases the local biological damage. Beta particles are generally much less energetic and dissipate their energy over a larger volume than that of the alpha-particles. Elements such as strontium, iodine and cesium are hazardous because they are readily absorbed and their body chemistry tends to localize them and retain them in a particular critical organ (strontium is incorporated in the bone and iodine is enriched in the thyroid gland).

An illustrative example can be made, which gives a relative measure of the intrinsic radiotoxic properties of a particular nuclide. According to the ICRP, the risk of fatal cancer induction is 5% per Sv (committed effective dose) [16]. This risk is on top of the natural lifetime risk of fatal cancer, which is around 24% for males and 20% for females in the U.S [17]. The usual assumption is that the risk of getting cancer is linearly related to the exposure [15]. Thus, based on this rule, there is a 100% chance for an individual to acquire (and die) of cancer if exposed to a dose of 20 Sv. For perspective, the average background dose is typically in the range 1-2 mSv per year, depending on the geographical location and ground properties (the largest contribution to the background radiation comes from the daughters of

radon). With this information it is possible to calculate the minimum ingested mass of a particular radionuclide to acquire fatal cancer with 100% probability. Results are shown in the last column in TABLE 8. It is seen that, among the listed elements, the most radiotoxic isotopes are  $^{244}\text{Cm}$  followed by  $^{238}\text{Pu}$ ,  $^{90}\text{Sr}$ , and  $^{137}\text{Cs}$ . The common property of these nuclides is that they are rather short-lived and hence, deliver the greatest activity per unit mass, in combination with a high effective dose coefficient.  $^{239}\text{Pu}$  is hazardous, but it is not immediately as hazardous as many other transuranic isotopes because of its long half-life. As outlined in TABLE 8, ingestion of about 35 mg of  $^{239}\text{Pu}$  would be necessary to result in the expectation of 100% risk of cancer mortality. The calculated amounts should not be regarded as a sharp line between death and survival as the actual lethal amount would depend on a variety of circumstances, e.g., the uptake fraction varies strongly with chemical form of the radionuclide. It is noted that ingestion of a radionuclide induces a long-term health-effect primarily, as cancer may take several years or decades to appear. Relatively high doses are required to deliver an acutely lethal dose. According to one report [18], ingestion of about 500 mg of plutonium would be necessary to produce acute sickness. (For comparison, the acute lethal dose of arsenic is around 100 mg). There are obviously all sorts of alternatives to this calculation; the values presented in TABLE 8 are intended to provide a frame of comparison about the hazard for a particular radionuclide as given by its radiotoxicity value. It is stressed that the ICRP dose limit apply to softly-ionizing radiation, i.e., primarily  $\beta$ - and  $\gamma$ -rays, administered to a person over a long time-period. In fact, there are several arguments for the assumption that the response to low dose-rates and softly-ionizing radiation may not be extrapolated to a high dose-rate and highly-ionizing radiation. For example, the value 20 Sv is twice as large as the lethal dose for instantaneous exposure [15], i.e., acute radiation sickness, which is a result of the fact that the biological harm is related to the dose-rate.

From the activity concentration and the effective dose coefficients, each radionuclide in the spent fuel can be assigned a radiotoxicity value. Fig. 1 shows the evolution of the ingestion radiotoxicity of spent uranium at a burnup of 40 MWd/kg as function of cooling time, where the results are grouped according to fission products and transuranic elements. The values are normalized to 1 g of initially present heavy metal (IHM). It is emphasized that the radiotoxicity corresponds to the committed dose that would be received over a time period of 50 years. This dose decreases over time as the radioactivity of the fission products and actinides decreases by time.



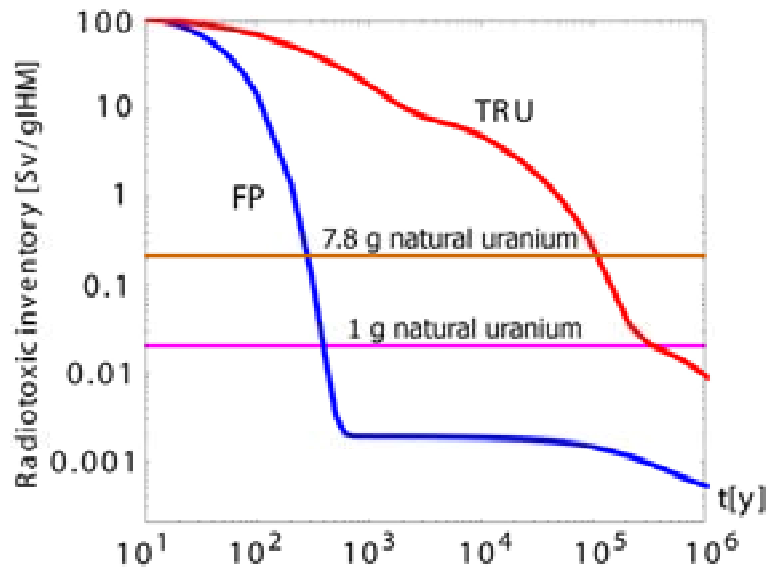


Fig. 1 Radiotoxic inventory of the fission products and transuranic elements in spent nuclear fuel (3.7%  $^{235}\text{U}$ , 42 MWd/kgIHM).

In the diagram, the horizontal lines refer to the total ingestion radiotoxicity for 7.8 g and 1 g of natural uranium, respectively. The 7.8 g of natural uranium correspond to the amount that must be recovered from the ore to produce 1 g of uranium fuel enriched to 4.2% in  $^{235}\text{U}$  (0.2% tails assay). Notice that these figures include not only the uranium isotopes but the uranium daughters that are in natural mixture with the uranium recovered from the mine. The use of the radiotoxicity value for an equal amount of natural uranium is easy to relate to in terms of the risk associated with the storage of spent fuel in an underground facility. It may be argued that when the radiotoxicity value for the spent fuel products crosses this reference level, it does not constitute a greater risk than natural uranium contained in the ore<sup>a</sup> (provided that the waste product is as equally fixed as the original ore). An alternative approach is to compare with the amount of uranium that must be recovered from the ore to produce the nuclear fuel. This way of comparison is often used by waste management people to provide a comparison with the risk if the wastes not been produced at all. The idea here is that disposal need not to provide any greater safety than if the uranium had never been mined in the first place.

Fig. 1 indicates the extreme difference in the long-term radiotoxicity associated with the fission products and the transuranic elements. During the first 20-30 years after discharge the fission products (primarily  $^{90}\text{Sr}$  and  $^{137}\text{Cs}$ ) determine the total radiotoxicity of the spent nuclear fuel. At later time the transuranic elements dominate the hazard. According to Fig. 1, it would take approximately 300,000 years before the radiotoxicity of the transuranic elements reaches natural levels. The cross over point for the fission products radiotoxicity curve is around 300 years. Obviously, if the transuranic elements could be eliminated, the long-term hazard would be considerably reduced. This is the basic motivation for partitioning and transmutation strategies, and for the deployment of dedicated reactor systems, which will be discussed in the following chapter.

<sup>a</sup>As Koplík [19] has pointed out, this analogy is not entirely satisfactory since the release probability for buried waste may be quite different to that of average material of the uranium-ore. Firstly, the nuclear waste form differ both chemically and physically from the ores and thus their mobility in the ground may be different. Secondly, it overlooks the fact that the nuclear wastes will be buried at great depths in a well-chosen location surrounded by engineered barriers, which suggests lower release probability than average material in an ore. The latter may be located at or near the surface with flowing ground water present.

It is also of interest to see how the individual transuranic elements contribute to the total TRU radiotoxicity. This is shown in Fig. 2. In the time span between 50 and 2000 years after unloading, the radiotoxicity is determined by  $^{241}\text{Am}$ . Beyond that,  $^{240}\text{Pu}$  and  $^{239}\text{Pu}$  dominates the radiotoxicity. Although  $^{241}\text{Am}$  has a half-life of 430 years, it is a very important contributor to the radiotoxicity during the first few thousand years because it is the radioactive daughter of  $^{241}\text{Pu}$ . It is understood that, in order to relax the time period over which the waste must be confined to a few hundreds of years rather than a few hundreds of thousands of years, the minor actinides must be eliminated together with the plutonium.

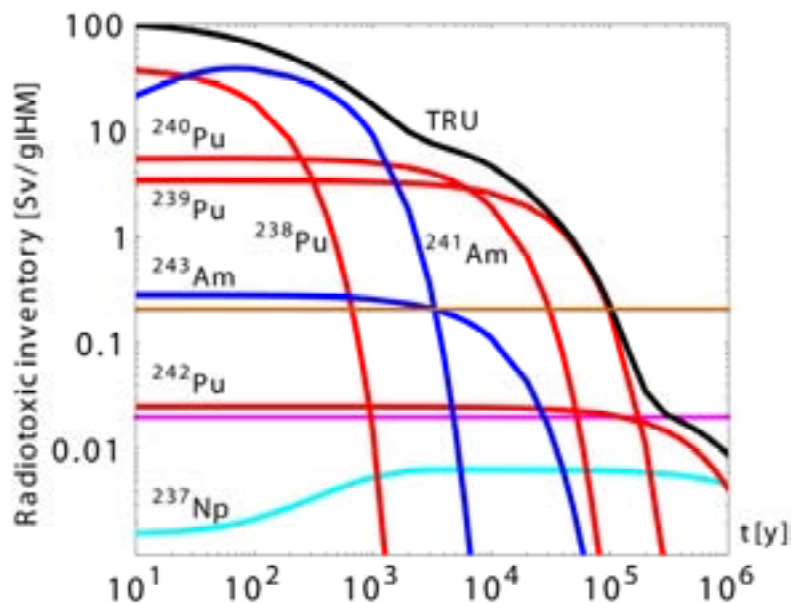


Fig. 2 Radiotoxic inventory of the main transuranic isotopes in spent nuclear fuel (3.7%  $^{235}\text{U}$ , 42 MWd/kgIHM).

### **Options for spent fuel management**

So far, the high-level wastes (reprocessing wastes or spent fuel) are stored in facilities above ground or shallow repositories, usually in close connection with the production site itself (nuclear power plants or reprocessing plants) and sometimes in a centralized storage. The idea is that these are interim procedures while awaiting a permanent solution. While the disposal issue is not urgent from a technical viewpoint, it is recognized that extended storage in the existing facilities is not acceptable since these facilities cannot provide sufficient isolation in the long term and neither is it ethical to leave the waste problem to future generations. No permanent waste disposal has yet occurred, but a number of methods have been proposed, a few which are listed below:

- Geologic repository
- Partitioning and transmutation
- Disposal in outer space
- Disposal in a remote place (e.g. in ocean floor or polar ice caps)
- Dispersion into air and sea

The most developed concept is emplacement in deep underground cavities, called repositories, in a suitable geologic media (e.g. granite, tuff, clay, salt bed). If the spent fuel is reprocessed, the wastes will emerge in a liquid form and the intention is then to solidify these

prior to disposal. The most commonly suggested solidification scheme is to vitrify the waste into an insoluble glass material. If the spent fuel is not reprocessed, the material to be disposed of is contained within the spent fuel itself (UO<sub>2</sub>). Before final deposition, the waste matrix (either the spent unprocessed fuel or the vitrified high-level waste) is encapsulated in a metal canister. The spent fuel elements may be placed as intact assemblies or the fuel rods may be removed from the assembly and framed inside the canister. The objective for rearranging the rods is to reduce the volume to be stored and improve heat removal characteristics. There is no essential difference between the repositories for vitrified high-level waste or spent fuel. Only the canisters differ somewhat between the two concepts.

Waste treatment by partitioning followed by transmutation is also being seriously considered. This is the subject of the remaining chapters. It may be added that partitioning and transmutation does not completely eliminate the need for a storage facility, but it may significantly reduce the risk of storing the remaining waste and also simplify the conditions for the final storage. Over the years, several other disposal methods have been suggested. These are mentioned here for completeness, but it should be noted that these are not being seriously considered at present. In theory, all radionuclides could be dispersed into the global air and sea volumes to reach acceptable concentrations, but the limitations are practical (no process for uniform dispersal exist), together with the social/moral and political difficulties involved. Another proposal is to launch the high-level waste into outer space, either by sending waste packages in an orbit around the earth or transportation to the sun or solar escape. The argument against this method is the obvious risk for an accident during launch (considering the large number of launches necessary) and the high cost. Other methods include: burial of waste containers under the ocean floor between tectonic plates, or placing them in deep bore holes in the ground, or even lowered into holes in the polar ice-sheet where they would begin propelling downwards through the melting ice. The problems shared by these proposals are the highly uncertain disposal processes (e.g. uncertain movement of canisters) and difficulty of inspection and retrievability/reversibility, which forecloses the possibility of future adjustments. It is possible that the environmental conditions changes which could motivate relocating the waste at a later stage or it could be decided to recover its resource value as a result of scientific progress.

### ***Safety performance of a geologic repository***

The principal safety issue of a repository is the risk of spread of radionuclides to the biosphere, where they can cause harm to humans. In the typical case in which the post-closure safety performance of the waste repository is analyzed [20], two distinct release scenarios can be identified (it should be noted that other definitions of “scenario” from that adopted here are in use, but essentially these can be grouped into the following two categories):

- Indirect release scenarios, via groundwater transport.
- Direct release to surface (by some natural event or human intrusion)

It is generally agreed, among waste management experts, that by a combination of physical barriers and environmental conditions, a carefully chosen repository can guarantee isolation for at least one thousand years and probably much longer. This conclusion is supported partly by the results of radioactive materials behaviour in natural analogues (e.g. Oklo) and findings of man-made objects which have withstood degradation since ancient times (e.g. The Egyptian pyramids and the bronze cannons of the Swedish warship Kronan which were found buried in seabed after the ship had been sunk in 1676). Beyond 10,000 years, however, it is recognized that the impact of major climate changes (e.g., glaciations) could affect the evolution of the repository system and canister containment cannot be guaranteed in general (although the SKB concludes that it is realistic to expect canister lifetime of 100,000 years or

even a million-year in the Swedish repository system [20]). For hazard assessment related to the natural break down of a canister, it is important to consider the processes involved in the pathway of the radioactive substance from the repository to man. Once the released from the repository, the waste products can only be carried to the surface via the groundwater. Under these circumstances, the solubility of the radionuclides in the groundwater, and their adhesion in the ground, and dispersion or buildup in the biosphere (food, water, background radiation) are the major factors determining the potential exposure to man. The actual transport rate of nuclides depend on many factors (geologic media, water composition, ground water velocity, etc.) and are site specific, but in general the actinide species move much slower in the ground water system compared with certain fission products (mainly technetium, iodine, cesium, and tin), and thus are not easily transported to the surface. Therefore, from the viewpoint of release scenarios associated with leakage through defective canisters, the risk is dominated by the long-lived fission products. The dominant contribution would then come from fission products such as  $^{99}\text{Tc}$ ,  $^{129}\text{I}$ ,  $^{135}\text{C}$ ,  $^{126}\text{Sn}$ , and  $^{79}\text{Se}$ .

As was shown in Fig. 1, some fission products ( $^{90}\text{Sr}$  and  $^{137}\text{Cs}$ ) dominate the radiotoxic inventory in the spent fuel during the first 30 years or so after discharge. However, after a few hundreds of years, the fission products are small contributors to the radiotoxicity being many orders of magnitude below that of the actinides ( $^{239}\text{Pu}$ ,  $^{240}\text{Pu}$ , and  $^{241}\text{Am}$ ). Thus, from the standpoint of the radiotoxicity contained in a repository, the risk is dominated by the transuranic elements. Considering their much lower mobility, release of actinides to the biosphere involves events that can bring some of the waste directly to the surface. Direct release to the surface, whether by natural phenomena or human activity, circumvents the pathway between the waste and the biosphere. Natural phenomena, such as earthquakes, volcanic eruptions, or impact of a giant meteorite, could lead to direct release of buried waste, but repeated studies have shown that the probability of these events (with the potential of lifting up the waste to the surface) is sufficiently low to be neglected [19, 21]. In the Swedish study of a granite repository [20], it was concluded that canister damage by seismic activity can be avoided in connection with the siting of the repository. Thus, causes for direct release of buried waste have focused on human intrusion scenarios.

Fig. 3 presents the calculated annual dose following the release from defective waste canisters for four repository cases of interest: 63,000 tons of spent fuel in oxidizing environment (volcanic rock in Yucca Mountain, U.S.), 2,600 tons of spent fuel in reducing environment (deep bedrock in Finland), 3,600 tons of vitrified high-level waste in granite (Switzerland), and 4,200 tons of vitrified high-level waste in clay (Belgium). The figure illustrates schematically the fact that the long-term risk is dominated by those nuclides that have high mobility in the ground ( $^{129}\text{I}$ ,  $^{99}\text{Tc}$ ,  $^{79}\text{Se}$ , and  $^{135}\text{Cs}$ ). The quality of the groundwater greatly influences the migration properties from the repository. An oxidizing environment increases the solubility of many radioactive substances (and promotes early deterioration of the canister). For example, Tc-99 is a major contributor to dose in the Yucca Mountain within the first 10,000 yr after closure. This is due in large part to its high mobility under the prevailing conditions. In a reducing environment, technetium is remarkably stable. With regards to the Swedish repository concept (granite repository containing spent fuel elements), the dominant isotopes for the release to the biosphere are  $^{129}\text{I}$  and  $^{79}\text{Se}$  and some activation products:  $^{36}\text{Cl}$ , and  $^{59}\text{Ni}$  [20]. The iodine, for example, has very high solubility and is not adhered in the granite. During reprocessing it is released to the off-gases and discharged into the sea and for that reason it is not present in any significant quantities in vitrified high-level waste. In general, the actinides have a negligible influence to the release to the biosphere for a canister break down scenario. An important exception is the mobility of  $^{237}\text{Np}$  in oxidising groundwater conditions, which makes it an important isotope for the long-term performance of Yucca Mountain. Groundwater release scenarios similar to the ones presented in Fig. 3 are

often used in repository safety analysis. In these scenarios the long-term risk is mainly associated with long-lived fission products not with the actinides. As a result, it has been reasoned [22, 23] that there is no real strong incentive for reducing the actinide inventory from the point of view repository performance. Yet, one should bear in mind that such account disregards human intrusion into the repository (malicious or accidental) and also overlooks the possibility for unanticipated natural events. These events are by their very nature extremely difficult to predict. A striking feature in the groundwater transportation scenarios is the complete absence of the most radiotoxic materials – plutonium, americium, and curium – since the retarding capacity of the repository is very good for these nuclides. Beyond 300 years the radiotoxicity of the transuranic elements is significantly higher than of the fission products. In a human intrusion scenario these elements are a major concern. We believe it is fair to consider the radiotoxicity of the spent fuel waste also from global point of view.

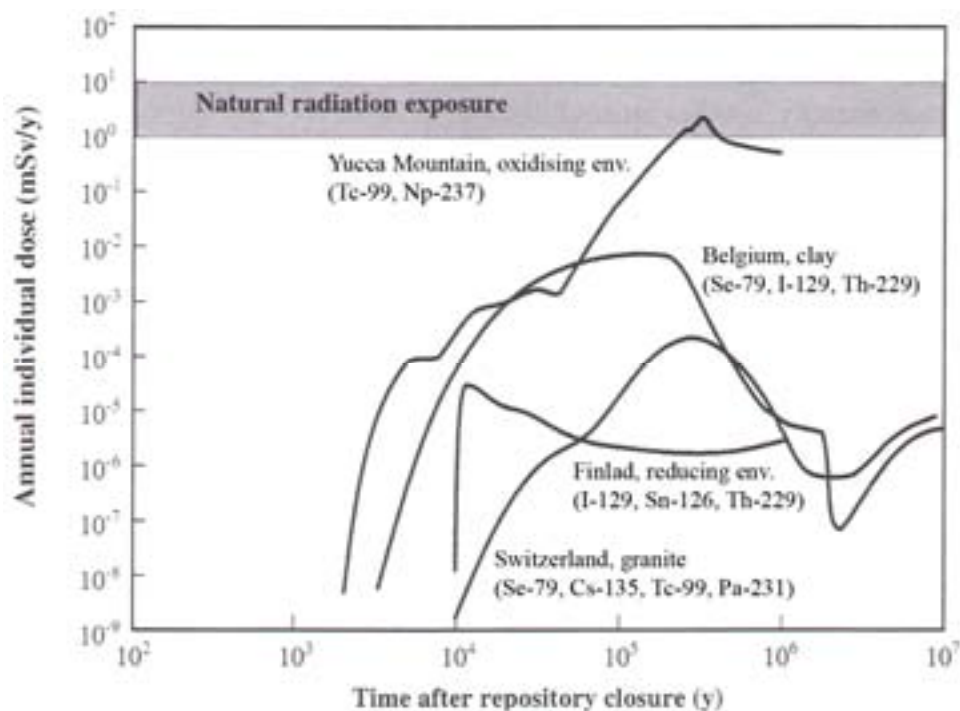


Fig. 3 Predicted annual individual dose from indirect release of defective waste canisters (adapted from OECD/NEA report [24]).

## Chapter 2:

# Partitioning & Transmutation

Partitioning and transmutation (P&T) is the general term for the techniques involved in the conversion process of long-lived radiotoxic isotopes into shorter-lived nuclides. In the following Chapter we will briefly describe the partitioning and transmutation operations considered with comments on their merits and limitations. The aqueous separation techniques, corresponding to the PUREX process, are briefly described together with the possible and desirable extensions to recover the minor actinides. Pyro-processing is another technique being investigated. The remainder of the chapter is devoted to describing the basic transmutation processes involved.

### ***Partitioning***

Partitioning refers to the chemical operations applied for the separation and extraction of selected elements from the spent nuclear fuel. It is closely related to the conventional reprocessing techniques of spent fuel, but embraces further separation operations to extract the minor actinides (MA) and the fission products (FP). Partitioning is a prerequisite for preparation of the spent nuclear fuel to realize further transmutation steps.

Plutonium separation technologies were developed in the United States during the Manhattan Project. Most plutonium reprocessing methods make use of the ‘oxidation-reduction principle’ in which plutonium is placed in different oxidation states whose chemical properties differ. The earliest attempts were based on “carrier” techniques, which were later replaced by the solvent extraction process that also forms the basis for the REDOX process and the PUREX process. The carrier technique was used to isolate the first amounts of plutonium to power the Fat Man bomb [25]. Today, all commercial reprocessing plants make use of the PUREX process, which is short for Plutonium Uranium Redox EXtraction. Major PUREX plants exist at La Hague, France, with a total capacity around 1600 tons IHM/y (two 800 t/yr units), the Magnox plant and the THORP reprocessing plant at Sellafield, United Kingdom, with capacities of 1500 and 850 tons IHM/y, respectively. At Marcoule in France one 400 t/yr reprocessing plant is operating for metal fuels from gas-cooled reactors. India has a 100 t/yr oxide fuel plant operating at Tarapur, and Japan is constructing a 800 t/y PUREX reprocessing plant at Rokkasho. Russia has a 400 t/yr oxide fuel reprocessing plant at Ozersk, Chelyabinsk. The worldwide annual capacity for civilian spent fuel reprocessing is around 5000 tons.

### ***PUREX***

According to a DOE historical overview [26], the solvent extraction processes (first the REDOX followed by the PUREX process) replaced the bismuth phosphate (carrier) method for plutonium production at the Hanford Site in the 1950s. The solvent extractions method is a wet (aqueous) process involving the dissolving of the fuel in nitric acid (nitric acid diluted with water). As it includes using a liquid-mixture of aqueous and organic solvents the

separations process is also known as liquid-liquid extraction. The solvent extraction process is adaptable to continuous operation, whereas the carrier technique operates in separate stages, meaning that only a limited amount of material can be treated in every stage. From an industrial production standpoint, processing a continuous stream of materials is generally preferred over batch processing. The solvent extraction processes make use of an alteration between the oxidation states of plutonium (IV, VI and III) whose chemical properties differ. Advantage is taken by the relative stability of the oxidation state of uranium and most fission products, while plutonium is easily reduced. Successive solvent extraction cycles are carried out until the desired decontamination and purification is achieved. The PUREX process was developed by Knolls Atomic Power Laboratory [26] in the United States and it is presented schematically in Fig. 4.

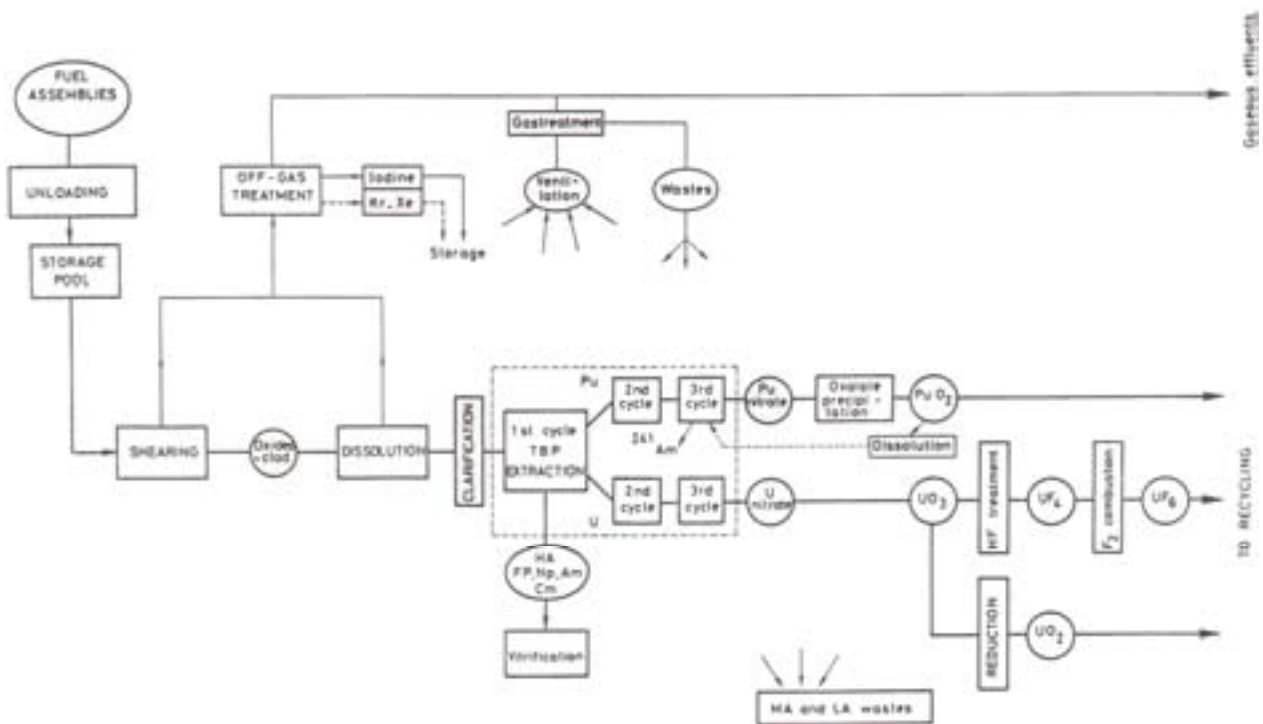


Fig. 4 Schematic flowsheet of the PUREX process. Adopted from textbook by G. Choppin, J. O. Liljenzin, and J. Rydberg [15].

As shown in Fig. 4, the first step of the PUREX process is to cut or saw the fuel pins into pieces, 3-5 cm long. This is usually done under water or inert gas. Gaseous fission products are collected and taken off in a separate stream. The chopped fuel pieces (oxide + cladding) are then dissolved in hot nitric acid. Remaining fission gas is released and transferred to the off-gas treatment. The cladding material is not dissolved in the nitric acid. The product solution is cooled and transferred to the separation section (the section enclosed in the dotted box in Fig. 4). At this point the uranium is in the hexavalent state, and plutonium in the tetravalent. Three purification cycles are conducted for both U and Pu. The first cycle consists of three solvent extraction stages (extraction stage, U-Pu partitioning stage, U stripping stage). In the first extraction stage, the aqueous fuel solution is contacted with an organic solution in special extraction columns. Presently, tributyl phosphate (TBP) is the chemical extractant used in all PUREX plants. It is normally used as a 30% solution in kerosene. The aqueous and the organic liquids will form separate layers in the extraction column with the aqueous flowing downward, while the organic flows up. This is the solvent extraction process and is the chemical basis for the PUREX method. The organic compound carries along the 4- and 6-

valent actinides (U, Np, Pu), leaving most fission products (I, II, III, V, and VII-valent species) and the trivalent actinides (Am and Cm) in the aqueous nitric acid solution. Thus, the uranium and plutonium are stripped out of the solution. More than 99.8% of the U and Pu are extracted into organic phase, leaving >99% of the fission products including most of the Am and Cm in the aqueous. Np exist in nitric medium in oxidation states V and VI, of which only the higher oxidation state (~60%) is extracted. The FP and MAs are transferred to the high-level waste residue. The HNO<sub>3</sub> concentration influences the extraction performance. In a second stage, plutonium is separated from the uranium by reducing it to its trivalent state which is insoluble in TBP. By adding fresh kerosene-TBP solvent, the plutonium is then stripped to a new aqueous phase and sent to the plutonium purification line. The uranium, which is in the tetravalent state, stays in the organic phase. In the third stage, the uranium is washed out of the TBP with dilute HNO<sub>3</sub>. The uranium and plutonium products are then subject to further purification cycles to reach higher purity. The 2<sup>nd</sup> and 3<sup>rd</sup> separation cycles are essentially based upon the same chemical reactions as in the first cycle. The separations process end with purified and separated plutonium and uranium in the form of nitrate paste, which is further refined into plutonium- and uranium-oxides or uranium hexafluorides. The high-level liquid waste contains the fission products including the Am, Cm, and some Np in nitric acid solution.

### ***Partitioning of Np, Am, and Cm***

As mentioned in Chapter 1, after plutonium, the minor actinides (Np, Am, and Cm) are the next most radiotoxic elements in the spent fuel. If they could be transmuted, the radiotoxic inventory would be considerably reduced. Transmutation of Am and Cm is a prerequisite for a significant reduction of the long-term radiotoxic inventory. The purpose for transmutation of Np is mainly to reduce the radiotoxic risk (mobility in the certain geological repository conditions) associated with the spent fuel repository in the very long term.

Before the minor actinides could be subject to transmutation operations, they must first be partitioned. In the conventional PUREX cycle, the minor actinides are left together with the fission products in the high-level waste. Neptunium is distributed between the oxidation states V and VI and is therefore partly discharged with the fission products and partly transferred with U and Pu. Recovery of separated neptunium is technically possible in a slightly modified version of the PUREX process. New processes are however necessary to separate Am and Cm. It is difficult to separate these from the lanthanides (Ln) as they have similar chemical properties (both are present in trivalent oxidation state). Depending on the burnup, the concentration of the lanthanides may be 30 times higher than Am and Cm in the high-level waste. A high purity of minor actinides is required in order to avoid neutron capture processes by the lanthanides in later reactor operations. The general scheme for separation of Am and Cm from the spent nuclear fuel is shown in Fig. 5. Firstly, the PUREX process is applied to recover U and Pu. Secondly, a process (e.g. TRUEX, DIAMEX, TALSPEAK/DIDPA) is used to co-extract the minor actinides and the lanthanides from the rest of the fission products. The processes require additional steps to extract the minor actinides from the Ln. A two step partitioning process is suggested, as described below. The techniques are not yet operational on an industrial scale.



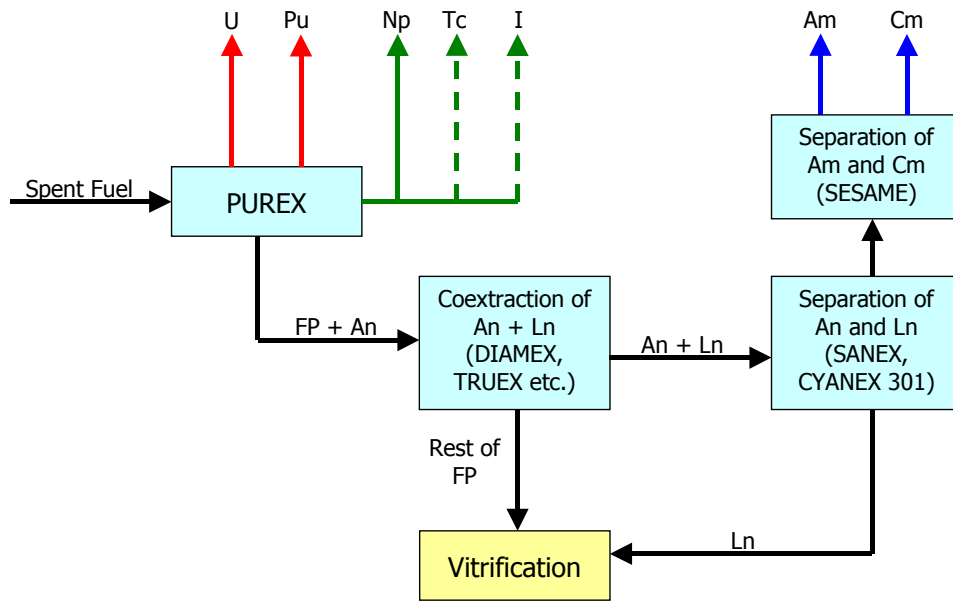


Fig. 5 General flow sheet for partitioning of Am and Cm from the spent nuclear fuel. (with permission by P. Seltborg [27])

The TRUEX (TransUranic Extraction) [28] process was developed by the U.S. Department of Energy (DOE) in the 1980s for separating actinides (and the lanthanides) from the high-level wastes generated by defence related reprocessing plant operations or during plutonium production and purification operations (at the Hanford, INEEL, Oak Ridge, and Savannah River Site sites). Complemented with the SREX (Strontium Extraction) process it can be used to remove strontium and cesium. An overall removal efficiency of 99.79% has been obtained for the actinides using TRUEX [29]. The CEA in France is developing the DIAMEX process (DIAMide EXtraction) as a method for combined extraction of actinides and lanthanides. It has been demonstrated on actual waste. In contrast to the TRUEX process, no secondary solid wastes are expected. The DIAMEX process has demonstrated recovery efficiencies of more than 99.9% of the Am and Cm, and very high decontamination factors were achieved for both Ln and An [30]. Difficulties are related to the partial co-extraction of palladium and ruthenium with the MAs. Subsequent separation of Am and Cm from lanthanides can be carried out in various versions of the SANEX processes (CYANEX 301, ALINA, BTP). Reasonably good separation efficiency of americium has been achieved (>99%), but further improvement is required for the recovery of curium (97.6% at present). Methods for selective separation of Am and Cm are under investigation. The current reference process is the SESAME process based on oxidation of Am(III) to Am(VI) and selective extraction of Am(VI) from Cm(III) by solvent extraction. In principle, a high extraction efficiency of Am is possible. But, it appears to be difficult to realize on a larger scale because of the instability of the higher oxidation states of Am in aqueous medium [31]. The use of stabilising agent increases the waste volume.

### ***Dry techniques***

The challenges anticipated by the aqueous partitioning processes with regards to MA-fuels include: 1) degradation of organic solvents at high radiation doses restricting the recycle potential, 2) Possibility of criticality which limits the concentrations which can be handled, and 3) Low solubility in nitric acid of many of the fuel forms considered.

As alternative to aqueous separation, dry fuel cycle processes have been investigated. These generally aim at pyroprocess methods. Opposite to conventional aqueous processing,

pyroprocessing does not involve dissolving the spent fuel in nitric acid. Refining is carried out in molten salt (fluorides, chlorides) and at high temperatures, around 500°C. As a result, these processes are often called “dry” processes. Instead of a solvent extraction principle, the recovery of individual actinides from the liquid mixture is achieved by electrorefining operation. The major advantages of pyrochemical techniques, in comparison to aqueous techniques, are that the materials used in the pyrochemical process are much more radiation resistant compared to the organic solutions used in the aqueous processes. Thus, pyrochemical techniques offer potential for the treatment of highly active spent fuel. This is a significant advantage when dealing with multi-recycled and high-burnup minor actinide fuels. In combination with the high solubility of most fuel forms in molten salts and less strict criticality constraints due to the absence of water, pyrochemical reprocessing can handle higher concentrations than aqueous solutions, and thus reduce the process volumes and also the size of the plant. Several process steps can be performed in a single vessel both reducing the size of equipments and the need for transportation of nuclear materials. It is often advocated that pyrochemistry is more economical than hydrochemical processes and that waste treatment is easier (small waste volumes and solid waste forms). Presently, actinide recovery in pyrochemical processing is limited to about 99% and thus multi-stage operation will be necessary.

Although several pyrochemical separations processes are known, two methods have been investigated extensively and developed up to industrial scale. One is the molten salt electrorefining method of metallic fuel developed by Argonne National Laboratory (ANL) for the treatment of spent EBR-II fuel and in connection with the Integral Fast Reactor (IFR) project [32]. The other route developed is the pyroelectrochemical method for oxide fuels (UOX and MOX) developed by the Research Institute for Atomic Reactors (RIAR), Russia [33].

The basic ANL method [34] was developed for the treatment of the sodium bonded U-Pu-Zr fuel. The first step is the dismantling of the fuel assemblies and removal of the cladding. The second step is dissolution of the fuel in a molten salt (LiCl-KCl) and molten metal (Cd) bath and the third step is the electrorefining of this liquid mixture. A schematic diagram of the electrorefining of U-Pu-Zr based minor actinide fuel involved using a molten eutectic of LiCl+KCl as electrolyte is shown in Fig. 6 [35]. The fuel is placed inside a basket where it is dissolved in the electrolyte. The uranium and transuranic elements are deposited on different cathodes. The fission products are not dissolved and remain in the basket or sink down to the bottom (although some remain dissolved in the molten salt). Uranium is partially deposited on a solid cathode (metal) and the transuranic elements together with the remaining uranium and a small amount of lanthanides are recovered into a liquid cadmium cathode. Whereas metallic alloy type fuel can be treated directly, oxide cycle must be first reduced to the metallic state before it can serve as feed material for the metal cycle. So far the oxide reduction technology has been experimentally demonstrated, but only at the laboratory level. Selective recovery of actinides beyond uranium and plutonium still needs to be demonstrated.

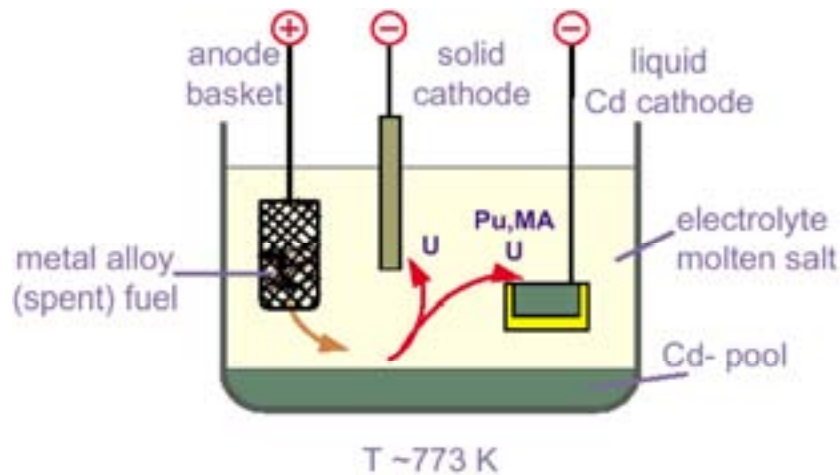


Fig. 6 Schematic picture of the pyroprocess treatment of U-Pu-Zr based minor actinide fuel [35]

## Transmutation

### *Physics of transmutation*

The term “transmutation” is used in reference to nuclear transformation processes in which one nuclide is converted into another. Transmutation of atomic nuclei can be artificially induced by collisions with neutrons, protons, alpha particles, and gamma quantum, or by natural disintegration processes such as  $\alpha$ - and  $\beta$ -decay, and spontaneous fission decay resulting in changes in the nuclear composition. In all cases, transmutation involves a change in the constitution of the atomic nuclei, i.e., change to the number of protons and/or neutrons, and is accompanied with a change to its properties.

In order to induce a nuclear reaction between charged particles, the incoming particle must possess sufficient kinetic energy to overcome the Coulomb barrier (there is a chance of tunnelling but the probability is very small unless the kinetic energy is close to the threshold energy). If the energy of the incoming nuclei is small, nuclear reaction is limited to elements of low atomic number. Nuclear reaction with heavy nuclei requires the largest kinetic energy. Nuclear interactions involving neutrons and photons are not subject to the coulomb repulsion, and hence may occur at any energy. In principle, a photon can transfer sufficient energy to a nucleus for a transmutation reaction to occur, but the energy required is still quite high and the probability for reaction is low in comparison with neutron-induced reactions. For example, the photofission threshold in uranium (around 6 MeV) is much higher than the neutron induced fission threshold (0-1 MeV), which is a consequence of the binding energy of the neutron added to the target nucleus. Such energetic gamma rays are rarely emitted in radioactive decay and even if they are the potential intensities are limited. As a result, large-scale transmutation by photonuclear reactions or bombardment by charged-particles can be dismissed on practical and economical grounds. Neutron induced transmutation is yet the only feasible means for transmutation at industrial scale. There are many ways of producing neutron sources of moderate intensity, but high neutron fluxes are most conveniently produced in a nuclear reactor.

Neutron induced transmutation encompasses two principle nuclear transformation processes<sup>a</sup>: fission and neutron capture. Besides the fission fragments, the reaction products of fission are several neutrons (between zero and five) as well as gamma radiation, beta particles, neutrinos, and of course energy. The exact identities of the two lighter nuclei vary from fission to fission, but a typical reaction can look like:

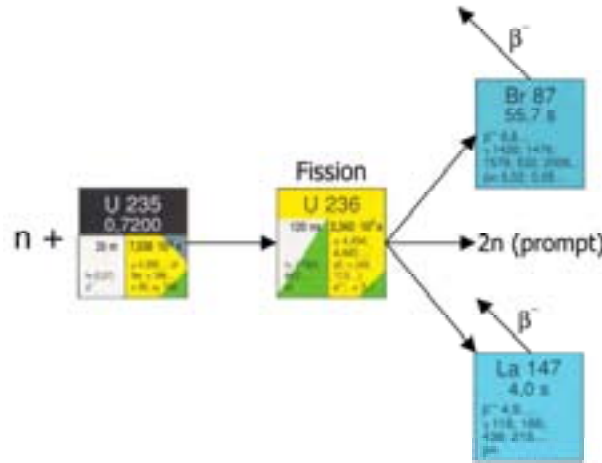


Fig. 7 Example of neutron-induced fission reaction in <sup>235</sup>U

The fission products are neutron-rich and will therefore decay mainly by beta particle emission. The half lives of the fission products are usually much shorter than the half life of the initial heavy nuclei. The second transmutation reaction is neutron capture, or “radiative capture” since the neutron is trapped inside the nucleus and only a gamma ray comes out ( $n,\gamma$ ). Neutron capture increases the mass number by one and the reaction is often accompanied by beta-decay. Neutron capture is the cause for build-up of transuranic elements from natural uranium. This is shown in Fig. 8.

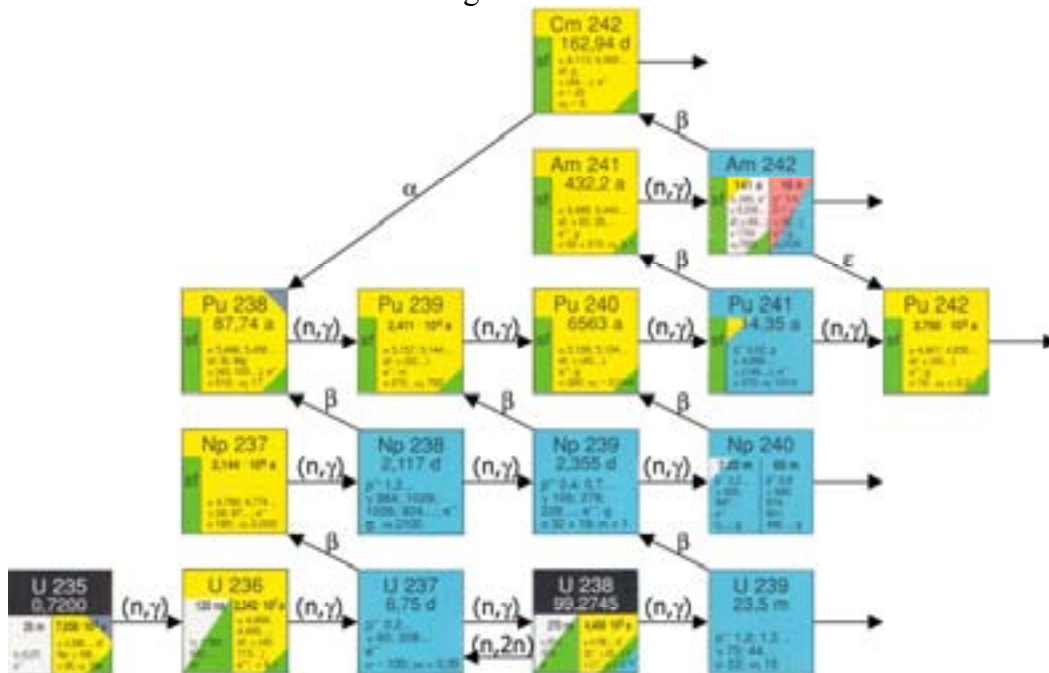


Fig. 8 Heavy-isotope build-up by neutron capture in natural uranium

<sup>a</sup>Although other transmutation reactions also occur, e.g., ( $n,p$ ), ( $n,2n$ ), and ( $n,\alpha$ ), these are of secondary importance for P&T purposes.

From the viewpoint of reducing the long-term radiotoxicity of the actinides, the most efficient reaction is fission since capture merely builds-up other heavier long-lived elements. It may be noted that fission results in higher radiotoxicity in the very short term (<100 years) because of the generation of the highly active fission products, but the resulting material will be much less radiotoxic in the long-term. In addition, a significant amount of energy is generated. However there is no guarantee that a neutron absorbed in a heavy nucleus causes fission. Both fission and capture take place simultaneously during irradiation. The probability of occurrence depends on the nucleus and on the energy of the incident neutron. The principal isotopes that are responsible for fission in a nuclear reactor are the heavy elements with odd number of neutrons, such as  $^{233}\text{U}$ ,  $^{235}\text{U}$ ,  $^{239}\text{Pu}$ ,  $^{241}\text{Pu}$ , and  $^{242\text{m}}\text{Am}$ . In these nuclides fission can be induced by neutrons of any energy. Such nuclides are referred to as fissile. Yet, it is still possible that the nuclei formed in the neutron absorption process in fissile isotopes will decay to its ground state by the emission of gamma, but it is less likely. For most heavy nuclides, however, absorption of low-energy neutrons is not likely to cause fission. Examples are the even-neutron numbered actinides ( $^{238}\text{U}$ ,  $^{237}\text{Np}$ ,  $^{238}\text{Pu}$ ,  $^{240}\text{Pu}$ ,  $^{242}\text{Pu}$ ,  $^{241}\text{Am}$ , etc.). These nuclides can only be fissioned by neutrons above a certain threshold (roughly 1 MeV). Such isotopes are referred to as fissionable. The fission probability upon neutron absorption is the ratio between the fission cross section and absorption cross section (fission + capture). It is of great importance in the discussion on transmutation. Its value depends on the properties of the reacting nucleus as well as on the energy of the incoming neutron. TABLE 9 compares this ratio for some actinides of particular interest, together with spectrum averaged cross-sections for fission and capture in a thermal spectrum and in a typical fast reactor spectrum. It can be seen that, for all nuclides the fission probability is higher in a fast spectrum than in a thermal spectrum, but the largest relative increase occurs for the even neutron numbered nuclei. It is further seen (Fig. 9) that the fission probability increases markedly for the even neutron numbered isotopes at energies above 0.1 MeV, which is a result of a significant energy variation of the fission cross section in this range. The conclusion to be drawn is that the spectrum should be as hard as possible to realize a high probability for direct fission. It ought to be mentioned that, in principle, transmutation of the minor actinides is possible in a thermal spectrum through breeding into fissile nuclides and successive build-up of heavier short-lived isotopes (Cm, Bk, Cf). However, limitations are set by the low burnup potential and insufficient neutron economy in a thermal spectrum, which require long irradiations, multiple-recycling, and high fissile loading. In practice, recycling is made difficult because of high neutron dose rates and the residence time is limited by helium generation in the fuel. This will later impact our choice for reactor system for transmutation purposes.

TABLE 9

Effective cross-sections of actinides for thermal systems and fast systems [31]

| Nuclide                   | Thermal spectrum (PWR) |            |                                | Fast spectrum (FBR) |            |                                |
|---------------------------|------------------------|------------|--------------------------------|---------------------|------------|--------------------------------|
|                           | $\sigma_f$             | $\sigma_c$ | $\sigma_f/(\sigma_f+\sigma_c)$ | $\sigma_f$          | $\sigma_c$ | $\sigma_f/(\sigma_f+\sigma_c)$ |
| $^{238}\text{U}$          | 0.10                   | 0.94       | 0.10                           | 0.04                | 0.30       | 0.12                           |
| $^{237}\text{Np}$         | 0.52                   | 33         | 0.02                           | 0.32                | 1.70       | 0.16                           |
| $^{238}\text{Pu}$         | 2.4                    | 27.7       | 0.08                           | 1.10                | 0.58       | 0.65                           |
| $^{239}\text{Pu}$         | 102                    | 58.7       | 0.63                           | 1.86                | 0.56       | 0.77                           |
| $^{240}\text{Pu}$         | 0.50                   | 110.6      | 0.00                           | 0.36                | 0.57       | 0.39                           |
| $^{241}\text{Pu}$         | 95                     | 36.7       | 0.72                           | 2.49                | 0.47       | 0.84                           |
| $^{242}\text{Pu}$         | 0.43                   | 29.0       | 0.01                           | 0.23                | 0.44       | 0.34                           |
| $^{241}\text{Am}$         | 1.10                   | 110        | 0.01                           | 0.27                | 2.00       | 0.12                           |
| $^{242\text{m}}\text{Am}$ | 595                    | 137        | 0.81                           | 3.30                | 0.60       | 0.85                           |
| $^{243}\text{Am}$         | 0.44                   | 49.0       | 0.01                           | 0.21                | 1.80       | 0.10                           |
| $^{244}\text{Cm}$         | 1.0                    | 16.0       | 0.06                           | 0.42                | 0.60       | 0.41                           |

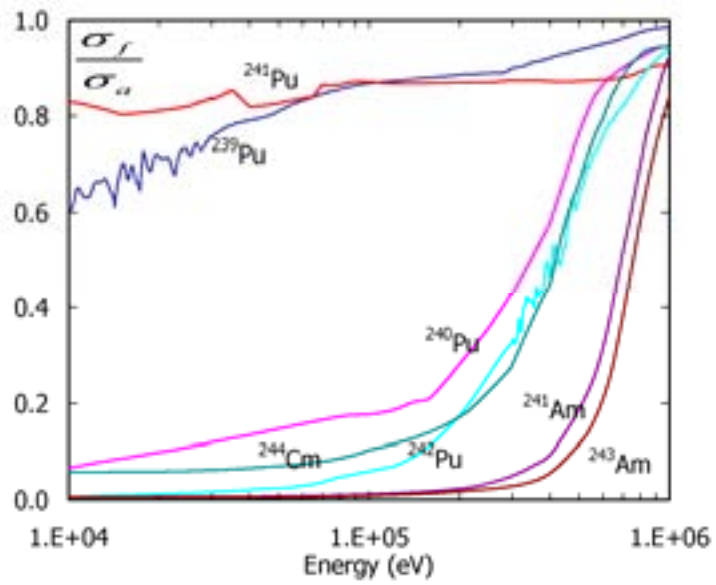


Fig. 9 Variation of fission probability ( $\sigma_f/\sigma_a$ ) with energy of some transuranic isotopes (ENDF/B-VI).

# Chapter 3:

## Transmutation Strategies

In this section we shall review the different P&T strategies and discuss their essential differences, mainly with respect to the achievable global waste radiotoxicity reduction. Numerous evaluations of transmutation scenarios have been performed. Much use has been made of available material on the subject with appropriate attribution. A comprehensive evaluation of P&T strategies was performed in a recent OECD/NEA study [24].

### ***Introduction***

The goal of P&T is to achieve a hundredfold reduction of the radiotoxicity in the medium- and long-term (beyond a few hundreds of years), which would considerably ease the performance requirements for an underground repository. Most likely an underground storage can provide confinement for at least 1000 years, during which the most radiotoxic fission products have decayed. The conditions for a hundredfold reduction require management of both plutonium and minor actinides. In addition a few long-lived fission products (mainly  $^{99}\text{Tc}$  and  $^{129}\text{I}$ ) are being considered for transmutation. Although their contribution to the global radiotoxicity is small some of them are mobile in the geosphere and may pose a radiological hazard under certain repository conditions. Various reactor concepts and fuel cycle strategies could be envisaged for transmutation purposes, incorporating both conventional light water reactors and fast fission reactors with conventional MOX-recycling and dedicated critical or sub-critical reactors with advanced reprocessing schemes. Fig. 10 provides an overview of the transmutation scenarios most commonly considered.

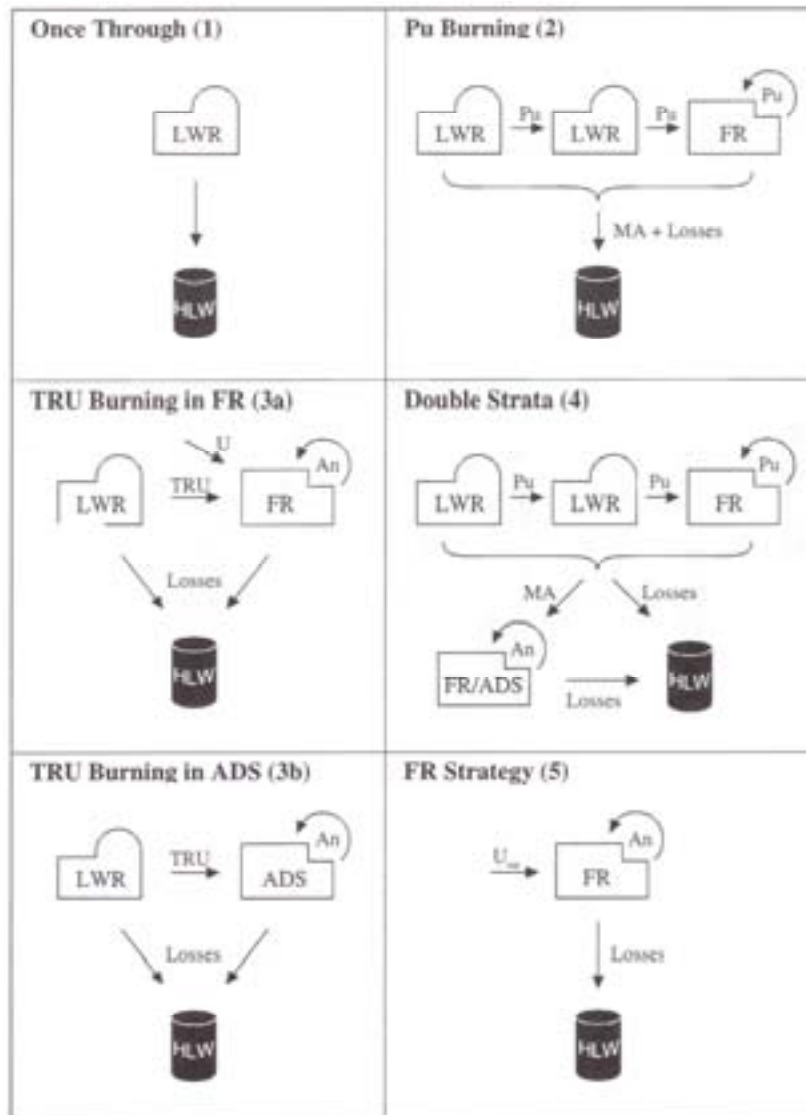


Fig. 10 Overview of principle fuel cycle scenarios (adapted from OECD/NEA report [24]).

### ***Transmutation of plutonium***

In the once-through cycle (scenario 1 in Fig. 10) the spent fuel is sent directly to long-term storage with no recycling (the once-through cycle is in fact not a cycle at all but an open-ended process). The fissile material content (approx. 1% Pu and 0.8% <sup>235</sup>U) and the remaining fertile material (<sup>238</sup>U) are considered as waste and excluded for further use. At present time, the once-through cycle is the main alternative for countries in which reprocessing is not practiced (for different reasons) such as Sweden, United States, Spain, and Canada. In the once-through cycle a geologic waste repository must be provided including demonstration of its long-term safety. In this scenario, the transuranic elements dominate the long-term radiotoxicity and it takes about 100,000-300,000 years (depending on the level of reference) before the radiotoxicity decays to natural levels.

In a LWR(MOX) recycling scenario, the spent fuel is reprocessed and the uranium and plutonium is recovered. In principle, both the uranium and plutonium could be recycled in LWRs but in practice, this is done only for plutonium. Nearly all of the uranium recovered



from reprocessing is sent into storage because fresh uranium is comparatively cheap and depleted uranium (from enrichment processes) is available in large quantities. Besides, the uranium recovered from reprocessing is less desirable for reactor use (higher neutron absorption and radiation levels) than fresh uranium because of the presence of troublesome isotopes like  $^{232}\text{U}$ ,  $^{234}\text{U}$ , and  $^{236}\text{U}$ , which necessitates re-enrichment and makes the reprocessed uranium more difficult to manage (due to radiotoxic daughter nuclides). Thus, nearly all of the uranium recovered from reprocessing remains in storage. After successive reactor cycles, the plutonium involved will become depleted in fissile isotopes ( $^{239}\text{Pu}$  and  $^{241}\text{Pu}$ ). Furthermore, the fuel will build-up minor actinides, especially  $^{244}\text{Cm}$ , as the irradiation increases because of the very low fission probability of fertile isotopes in a thermal spectrum. Obviously, this increases neutron emission rates and heat generation levels, which makes the fuel more difficult to reprocess with the PUREX method. The reduction of fissile plutonium also requires successively increased plutonium concentrations (or alternatively increased  $^{235}\text{U}$  enrichment) for reactivity compensation in subsequent cycles. But the amount of plutonium in the core is limited by reactor safety concerns (e.g., deterioration of moderator coefficient and lower delayed neutron fraction). According to one report [36], the plutonium content in a standard PWR core must not exceed 12 wt% on similar grounds. While the technical issues are important factors, they are not the only ones affecting decisions on plutonium recycling. Other subjects which have a critical impact include: environmental concerns, resource utilization, waste issues, cost, and proliferation aspects, and these are debated with considerable controversy. As of today, plutonium reprocessing operations has not kept pace with its use in reactors and this has led to a growing amount of separated civilian reactor-grade plutonium in storage around the world. According to the Washington based Institute for Science and International Security (ISIS) [37], roughly 235 tonnes of separated reactor-grade plutonium were available world-wide at the end of 2003, which may be compared with 155 tonnes of weapon-grade plutonium in military stocks. In the U.S., reprocessing of civilian nuclear fuel is not permitted because of proliferation concerns. It is advocated that as long as the plutonium remains in the spent fuel, it remains inaccessible and the risk of being used for weapons is reduced. On the other hand, this non-separated plutonium, while more proliferation resistant than separated, is not permanently inaccessible in the spent fuel. After a few hundreds of years, when the fission products have decayed, extraction processes are much easier to perform. In terms of cost, the advantages of reprocessing uranium and plutonium are reduced need for mining new uranium and decrease in enrichment works. However, there is the added cost for reprocessing and also increased cost for fabrication and transportation of MOX fuel compared to freshly mined uranium. According to a recent comparative study [38], reprocessing and recycling of plutonium in LWRs will be more expensive than direct disposal of spent fuel until the uranium price reaches over \$360 per kilogram of uranium (kgU), which is significantly higher than the current uranium price of \$40/kgU. From a waste management point of view, the volume of the residual high-level waste aimed for disposal is reduced since the uranium and plutonium are separated from the spent fuel, but the effect on the long-term radiotoxicity is marginal [35]. For reasons mentioned above, the number of cycles is limited to one or maybe two. In the first cycle around 25% of the recycled plutonium may be consumed and 10% is transformed into heavier nuclei (Am, Cm, and higher actinides) [24].

The use of fast reactors was discussed in the early days of nuclear energy. It deserves to be mentioned that the first fast reactor was Clementine, built at Los Alamos in 1946, and the first reactor to produce usable quantities of electricity from nuclear energy was the Experimental Breeder Reactor I (December 20, 1951). As early as 1944, the plan was to build reactors “to breed fissile materials from natural uranium or thorium”, according to minutes from the meetings of the “New Piles Committee”, which was formed to explore the peaceful uses of nuclear energy in the United States after the second-world war [39]. At that time the main

motivation was the limited supply of uranium. It was projected that the number of reactors would grow rapidly, and as a result the price of uranium would increase quickly. Since fast breeder reactors (FBR) could offer superior usage of uranium resources, representing a hundred-fold increase in utilization factor than that of thermal reactors, these were considered necessary not to run out of resources very soon. Undoubtedly, the early considerations lay the foundation for the nuclear energy research in the United States for many decades ahead and influenced the development in many other countries as well. However, uranium turned out to be abundant and inexpensive and mastering the fast reactor technology was more problematic than expected [40]. In the nineteen-sixties the FBRs were challenged by the cheap and technically attractive light-water reactors. Although much research work continued to be invested into the breeder technology, the expected transition to FBRs slowed considerably and in some cases even halted. In the 1990s, large-scale development programmes on FBRs essentially terminated in the United States, France, Britain, and Germany, though some longer-term research work continued. Plutonium recovered in reprocessing operations, which were initially intended for FBR use, became redundant and was reused in LWRs. More recently, as part of the transmutation strategies and the “Generation IV” initiative, and quite opposite to the initial purpose of breeding, it is the burning characteristic of fast neutron spectrum in which fast reactors see a possible future redeployment. In these new reactor strategies, the fast reactor can demonstrate a distinct advantage over the light water reactor. In contrast to plutonium recycling in LWRs, which is limited by safety concerns, complete plutonium burning is possible by integration of fast reactors. This option could be envisaged in special fast burner reactors (FBuR) operated in symbiosis with a park of LWRs. For example, in the French CAPRA project, MOX fuel with very high concentrations of plutonium oxide (up to 45%) and core designs without blanket region are investigated to achieve as high plutonium consumption as possible. However, aqueous reprocessing is valid only for MOX fuel with Pu-enrichment below 25%. Any higher Pu-concentrations would require the dissolution yield of the PUREX process to be improved or some other reprocessing scheme or alternative fuel material is required, e.g. nitride. Although recycling of plutonium in LWRs and FRs (with limited plutonium concentrations) is conceptually possible with current technology, rapid expansion of a large park of fast reactors is not a realistic scenario. It is estimated that 36% of the park power must be produced by fast reactors in order to achieve zero plutonium build-up at equilibrium conditions [41]. Capital costs are not in favor of FBRs. Traditionally, the estimated FBR/LWR plant capital cost ratio has been in the range 1.25-1.50 [42]. Theoretically, if all plutonium would be eliminated (without losses) from the spent fuel, the long-term radiotoxicity would decrease by a factor of ten relative to the once-through cycle. But in practice, due to the continuous build-up of Am and Cm, multi-recycling of plutonium in LWR/FR facilities only reduces the radiotoxicity by a factor of five (see Fig. 12) in the time frame >1000 years. Thus, from a radiotoxic point of view, multiple recycling of plutonium alone does not qualify as a transmutation strategy. In order to reduce further the radiotoxic inventory, it is necessary to recycle also the remaining TRU content, i.e. the minor actinides, which is the purpose of the advanced fuel cycle.

### ***Transmutation of minor actinides***

Recycling of the plutonium is a first, but not sufficient step in a transmutation strategy. Only by a fully closed fuel cycle, i.e., close the stream of all transuranic materials (plutonium + minor actinides) to the waste, is it possible to achieve a significant reduction (by a factor of one hundred or more) of the long-term radiotoxicity (>300 years), which is the main goal of a transmutation strategy. The minor actinides considered for transmutation are americium, curium, and neptunium. Americium is responsible for the second highest contribution to the

radiotoxicity in the spent fuel after plutonium, see Fig. 2. It dominates the radiotoxicity during the first 2000 years after discharge and it is produced in large amounts during multi-recycling of plutonium. Various types of reactors could be considered for transmutation of minor actinides, such as light-water reactors (LWR), fast reactors (FR), and dedicated critical or sub-critical reactors (ADS), either in homogeneous or heterogeneous mode. In the heterogeneous mode the minor actinides are diluted at low concentration in the standard fuel material. In the heterogeneous mode the MAs are separated from the conventional fuel and concentrated in special fuel elements known as “targets”.

Generally speaking, addition of minor actinides to the fuel leads to deterioration of the reactor safety parameters (less negative reactivity coefficients, lower delayed neutron fraction) and degradation of physical characteristics of the fuel (thermal properties, helium generation). The addition of americium also decreases the reactivity of the fuel due to higher capture losses and hence higher fissile enrichment is required. In a thermal system the introduction of minor actinides leads to a less negative moderator coefficient. In homogeneous mode, the MA content is restricted to 1% in a MOX-fuelled PWR [31]. Studies have shown that a somewhat higher MA content (2%) is possible in high moderation reactors (in which the ratio of moderator volume to fuel volume is greater than 3, compared to standard PWR with a ratio of 2). Heterogeneous recycling avoids dilution of nuclides with high alpha activity in the larger volume of spent LWR-MOX fuel, which later complicates chemical reprocessing and fuel fabrication operations. From fuel cycle point of view, it is advantageous to confine the treatment of the minor actinides to a separate side-stream. Moreover, in heterogeneous recycling, the negative effects on the reactor are somewhat reduced, if the targets are placed at the core periphery. However, transmutation of americium targets in a thermal spectrum leads to formation of  $^{242}\text{Cm}$  and  $^{244}\text{Cm}$  through neutron capture in  $^{241}\text{Am}$  and  $^{243}\text{Am}$ , see Fig. 11. Since  $^{242}\text{Cm}$  decays rapidly (162 days) into  $^{238}\text{Pu}$ , the proportion of  $^{238}\text{Pu}$  and  $^{244}\text{Cm}$  increases during successive recycles. Reprocessing and recycling of fuels containing high quantities of  $^{238}\text{Pu}$  and  $^{244}\text{Cm}$  is problematic because of their strong alpha activity and neutron emission rates. Multi-recycling is not possible with aqueous techniques because of the high density of radiation and fuel fabrication operations are made difficult by the need for remote control and cooling in shielded compartments. Because of these difficulties the so-called “once-through” recycling of americium targets in thermal systems has been suggested. Instead of multi-recycling, the targets would be subject to a single extended irradiation cycle and then sent for disposal. In this case, the incineration rate is limited by the residence time as the fertile actinides gradually convert into fissile nuclides. It has been shown that very long residence periods are required to achieve a significant americium destruction rate. Since the residence time is limited by fuel swelling and cladding irradiation damage, a high incineration fraction is not possible with once-through recycling. In principle a high incineration rate is achievable in a thermal system through secondary fission reactions [43,44], but in practice the transmutation capability is constrained by the performance and safety parameters, such as the reactivity swing during burn-up which require very high initial  $^{235}\text{U}$  enrichment. Transmutation in a thermal spectrum is generally not attractive from neutron-economics point of view (since most thermal neutrons are spent on conversion into higher TRU isotopes) and due to the much lower fluxes. In a recent IAEA report [35] it was concluded that neither conventional nor dedicated transmutation LWRs qualify for transmutation of minor actinides on the basis of the reasons mentioned above and other practical considerations. It should be noted that even a small amount (1%) of americium in the fuel produces sufficient curium in a thermal spectrum to cause serious transportation problems. Preferably, americium transmutation should be completed in a fast spectrum with its higher fission-to-capture probability, either in a dedicated fast burner or in symbioses with LWRs. It has also been suggested that transmutation in a thermal system could serve as an intermediate irradiation

step which is later finished in a fast reactor system. Another option, which has received some attention, is to use moderated zones of a fast reactor to take advantage of the high thermal cross section with the better economy and higher flux of a fast system.

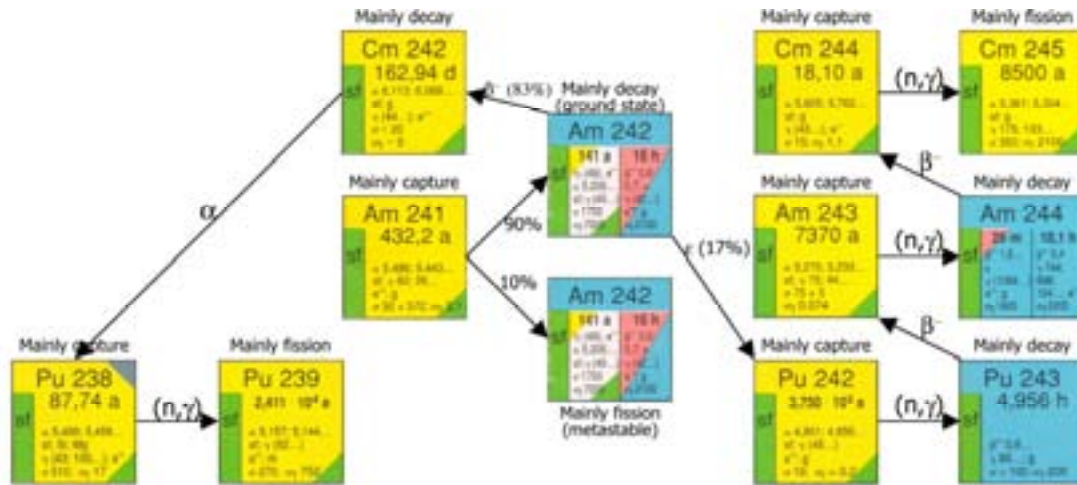


Fig. 11 Reaction path of  $^{241}\text{Am}$  and  $^{243}\text{Am}$  under thermal neutron irradiation. Of importance is the production of  $^{238}\text{Pu}$  and  $^{244}\text{Cm}$  which increases the radioactivity and decay heat of the fuel. The alpha-decay of  $^{242}\text{Cm}$  is a source for helium production and swelling of the fuel during irradiation. (Reaction path data from [44]).

It can be noted that all transmutation strategies recycling both MA and Pu in fast-spectrum systems (FR and/or ADS) could achieve high reductions (by a factor of one hundred) in the actinide radiotoxic inventory compared to the once-through cycle in the time frame of  $10^3$ - $10^5$  years. This is shown in Fig. 12. In that respect all the strategies are comparable. In practice, however, the selection needs to be balanced against the safety, cost-effectiveness, and technological feasibility of the systems. Central issues are the reactor safety aspects associated with MA-enrichment. Several studies have shown that the addition of minor actinides to the fuel leads to unfavourable reactor safety parameters. The effects of most immediate importance are:

- reduced effective delayed neutron fraction ( $\beta_{\text{eff}}$ )
- smaller Doppler coefficient
- larger positive coolant void- and density coefficient in a liquid-metal cooled reactor

The Doppler coefficient is of major importance for terminating reactivity driven accidents. The effective delayed neutron fraction establishes the margin to prompt criticality (in a critical system) and also determines the sensitivity to reactivity changes. The coolant void coefficient plays a crucial role in accidents involving coolant expulsion. Needless to say, they are fundamental factors in the design and safety evaluation of a nuclear reactor, and in particular vital for the safety performance of a critical reactor. Taking the deteriorated safety parameters of minor actinide cores into account, it is necessary to limit the MA-enrichment in critical reactor cores. With attention to the increase in void reactivity coefficient and decrease in the Doppler coefficient, a limit of 2.5%<sup>a</sup> of minor actinides in MA-MOX fuel is often used for sodium-cooled fast reactors [43, 45]. This necessarily calls for a very large power park of fast reactors (25-50%) for MA burning at equilibrium [35].

<sup>a</sup>This is by no means a closed subject. Many design parameters work in combination to make a reactor safe, and it is difficult to judge the safety performance simply based on the Doppler coefficient and void coefficient. These issues are further discussed in the next chapter (see also **Paper 2**). Besides the constraints deriving from reactor safety considerations, there are other problems related to MA-based fuels. The effect on fuel fabrication and reprocessing operations must also take into account the handling problems involved.

In order to overcome the safety issues associated with highly enriched MA cores (or MA and Pu), accelerator-driven systems (ADS) with a fast spectrum have been proposed. Since these systems would operate in a *sub-critical mode* they could more easily address the adverse safety characteristics of MA-based fuels. While a critical system requires a substantial fraction of fertile materials in the fuel to ensure acceptable core safety characteristics, accelerator-driven systems offer higher flexibility in fuel composition. In the extreme case an ADS could permit pure minor actinide fuels (or MA mixed with some Pu). The great advantage is that the MA transmutation rate per unit of power is maximised and so the fraction of specialised burners can be kept to a minimum. It would also confine the treatment of the MA to a small side-stream of the nuclear power park. Hence, the safety performance of the conventional reactors need not be affected and the effect on the fuel fabrication and reprocessing steps in the main cycle would be minimal. The cost analysis indicates that the ADS-based strategies can be made very competitive through minimal usage of innovative technology.

Various fuel cycle strategies could be foreseen involving ADS, FRs, and LWRs. ADSs could be used to burn transuranics in a two component strategy (3b in Fig. 10), “TRU burning in ADS” or as pure minor actinide burner in the so-called “double-strata scheme” (4 in Fig. 10). In the two-component strategy, the FR is replaced by an ADS and the transuranics are recycled in a sub-critical burner with a closed fuel cycle using pyrochemical reprocessing without MA-Pu separation. This approach was adopted in the USA [46], since it reduces the proliferation risk as the plutonium is always together with the minor actinides. Alternatively the ADS could operate in symbiosis with LWRs for Pu recycling (not shown specifically in Fig. 10). The capability of the latter to burn Pu reduces the LWR-to-ADS support ratio from 21% (no MOX recycling in LWRs) to 15%. In the double-strata cycle, first suggested in Japan in 1984 [47], the ADS would operate together with both LWRs and FRs. In the first stratum, plutonium is recycled in commercial LWRs and FRs using conventional reprocessing and MOX fuel technology. The MAs (mixture from LWRs and FRs) and some Pu (for reactivity management) are later transferred to the second stratum for final destruction. The double-strata scheme is sometimes considered to be an evolutionary approach as the fuel cycle is basically closed in successive steps, first Pu in LWRs and then in FRs, and last MA+Pu in ADS. Economically, it is more competitive since it reduces the number of ADSs by a factor of four relative to the TRU burning strategy (without MOX-recycling). The ADS support ratio in the double-strata scheme is around 5-10%. It is worth noticing that recycling of americium and curium alone could reduce the ADS support ratio even further, as we show in **Paper II**.

At first sight, the hazard of neptunium evaluated from its radiotoxicity value seems to be of little concern. However, the long half life ( $2.1 \cdot 10^6$  yr) and the build-up with time due to decay of  $^{241}\text{Am}$  and potential mobility of  $^{237}\text{Np}$  in groundwater is of concern for the long-term disposal of spent nuclear fuel under certain geological disposal conditions. This can to some extent counteract its far lower radiotoxicity and make it a greater risk in the overall risk assessment. For that reason many P&T strategies includes Np in the recycling scheme. From the global radiotoxicity point of view, however, Np is of little concern.

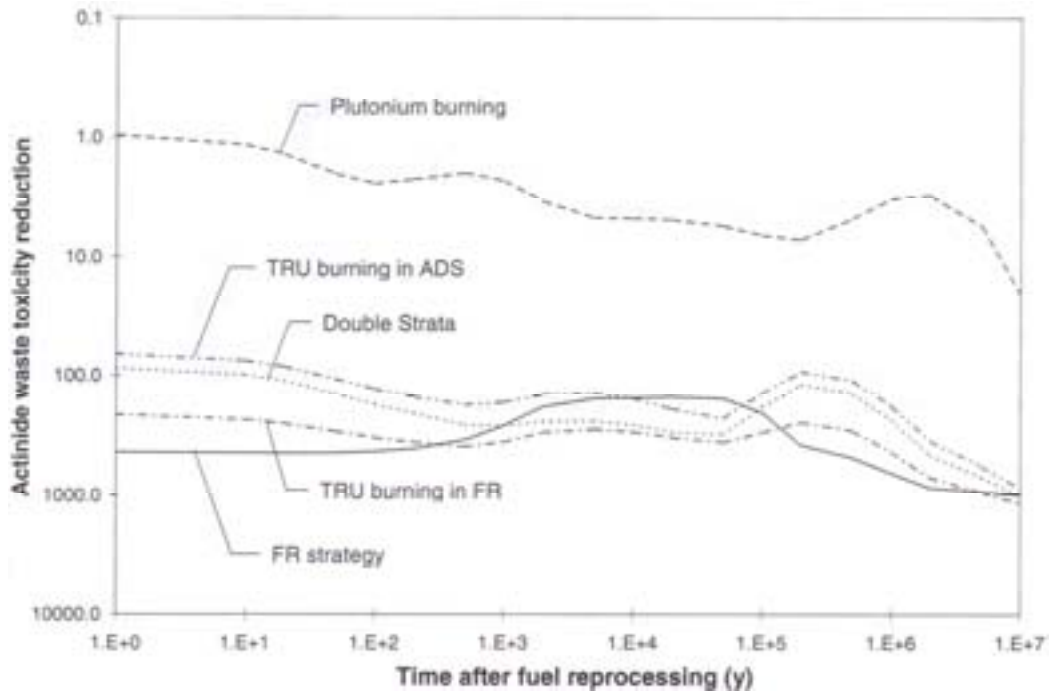


Fig. 12 Actinide waste radiotoxicity reduction relative to the once-through fuel cycle (adapted from OECD/NEA report [24]).

### **Transmutation of fission products**

The fission products are small contributors to the radiotoxicity contained in the spent fuel, being many orders of magnitude below that of the transuranic elements after a few hundreds of years. Thus, from the viewpoint of reducing radiotoxicity, transmuting fission products would appear to be of little interest. However, as mentioned before, some fission products are mobile in groundwater and therefore can contribute significantly to the surface dose rate under certain repository leakage conditions, i.e. groundwater release scenarios. The fission products that are relevant in this respect are primarily  $^{99}\text{Tc}$ ,  $^{129}\text{I}$ ,  $^{135}\text{Cs}$ ,  $^{79}\text{Se}$ , and possibly  $^{126}\text{Sn}$ , depending on the type of repository considered. It is theoretically possible to transmute fission products to shorter-lived or stable nuclides by means of neutron capture<sup>a</sup>. But, taking into account the small neutron capture cross sections for many of the long-lived fission products rather long irradiation times are required. Transmutation of fission products is only reasonable if the neutron capture cross-section of the targeted isotope is sufficiently high to allow transmutation rates which are high in relation to the natural decay [24]. This immediately excludes  $^{90}\text{Sr}$  and  $^{137}\text{Cs}$  for potential transmutation purposes because of their short half-life (~30 years) and limited transmutability. The only reasonable route for these nuclides appears to be disposal, special separation could be employed to reduce the heat load in the repository.

<sup>a</sup>It may be added that, in a quite opposite way to neutron capture, laser-driven gamma generation for photo-transmutation [49], through  $(\gamma, n)$  reactions, has been demonstrated for transmutation of  $^{129}\text{I}$  into  $^{128}\text{I}$  (with a half-life of 25 min). However, the technology is still at the fundamental level and considering the low transmutation rate achievable with present-day lasers it is not a realistic alternative for transmutation of industrial quantities.

$^{79}\text{Se}$  ( $T_{1/2}=6.5\cdot 10^4$  years) and  $^{126}\text{Sn}$  ( $T_{1/2}\sim 1\cdot 10^5$  years) are rather long-lived but their capture cross sections are very small, and thus the potential transmutation rate is limited.  $^{135}\text{Cs}$  is long-lived ( $T_{1/2}\sim 2.3\cdot 10^6$  years) and has moderate thermal capture cross-section, but Cs occurs in many isotopic forms in the high-level waste and would require isotopic separation to isolate  $^{135}\text{Cs}$  in order to prevent neutron capture in  $^{133}\text{Cs}$  and  $^{134}\text{Cs}$  [35]. This is an unrealistic undertaking from an economical and technical point of view. So far, the isotopes that have received the highest transmutation priorities, considering both their practical ability to transmute and in terms of their potential impact on the long-term radiological risk, are  $^{99}\text{Tc}$  ( $T_{1/2}\sim 2.1\cdot 10^5$  years) and  $^{129}\text{I}$  ( $T_{1/2}\sim 1.6\cdot 10^7$  years).  $^{99}\text{Tc}$  is present as single isotopic species and can be transmuted into  $^{100}\text{Tc}$ , which beta-decays rapidly ( $T_{1/2}\sim 16$  seconds) into stable  $^{100}\text{Ru}$ . Iodine separated from spent fuel is a mixture of  $^{127}\text{I}$  and  $^{129}\text{I}$ , but the former is present to an extent of 16%, which is tolerable [31]. Hence,  $^{129}\text{I}$  can be transformed to  $^{130}\text{I}$ , which decays with a half-life of 12 h to stable  $^{130}\text{Xe}$ . It is noteworthy that reactions involving successive neutron capture in  $^{99}\text{Tc}$  and  $^{129}\text{I}$  will still yield stable nuclides after beta-decay. Although the lower flux level in a thermal system is partly compensated by high capture cross sections, neutron economy requirements favor the use of fast systems. One must consider that fission products act as poisons without compensating neutron production. Fast systems offer better neutron economy which can be utilized for transmutation while a LWR system would require higher enrichment [31]. An optimal strategy, for transmutation of  $^{99}\text{Tc}$  and  $^{129}\text{I}$ , is to use moderated target assemblies of fast reactors, which could then combine the high flux of a fast system with the high cross-sections in a thermal system [48].

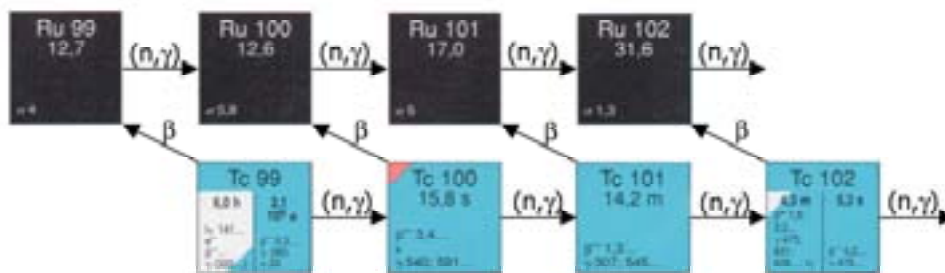


Fig. 13 Transmutation path of  $^{99}\text{Tc}$

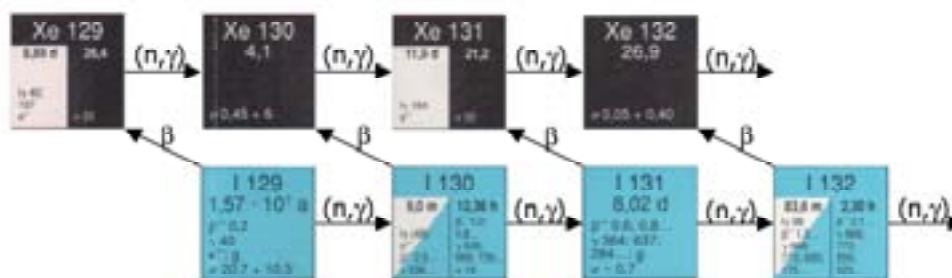


Fig. 14 Transmutation path of  $^{129}\text{I}$

# Chapter 4:

## Accelerator-driven Systems

In the previous chapters we have given brief accounts of the spent fuel composition, waste management strategies, chemical separation operations, and an overview of various transmutation strategies. The purpose was to provide background information on the general problems of spent fuel management and to explore possible means for reducing the radiotoxic inventory. It was found that the actinides, mainly plutonium, americium, and curium, are responsible for the majority of the radiotoxicity and the most efficient way to reduce the radiotoxic inventory is to fission them. Of the many transmutation schemes suggested, one is recognized as being the most promising: the accelerator-driven system. We shall now present the design principles upon which this system is based. The first part provides a brief description of the general principles, the remaining of the chapter deals with the safety and kinetics performance of ADS. A brief description will also be given of the reliability of the accelerator built to provide high-energy protons for the system.

### **General principles**

A vital feature of the fission reaction is that it generates neutrons that can cause further fission. If the fission reaction repeats itself the process that occurs is called a “chain reaction”. The fission chain-reaction is common to all nuclear reactors. If the neutrons from one fission cause on the average one more fission a “self-sustained chain reaction” is accomplished and the reactor is said to be “critical”. The neutrons in the first fission are said to belong to the first generation and the neutrons from the second fission which they caused belong to the next generation and so on. The effective multiplication factor<sup>a</sup>,  $k_{eff}$ , gives the ratio of the number of neutrons of one generation to the preceding generation (taking all losses into account):

$$k_{eff} = \frac{\text{number of neutrons in one generation}}{\text{number of neutrons in the previous generation}}$$

It is obvious that a self-sustained reactor will continue to operate at a constant fission rate as long as the effective multiplication factor remains unity. If  $k_{eff}$  is smaller than one, there are fewer neutrons produced in each generation than in the previous generation and the reactor is said to be subcritical. Without any help from an outside source of neutrons the chain-reaction will eventually die. In contrast, if  $k_{eff}$  is greater than 1, the neutron population will increase with or without the presence of an external source, and the reactor is supercritical. It should be realized that the value of  $k_{eff}$  depends solely upon the properties of the reactor core (size, shape, material composition, and temperature) not on the characteristics of the source. The material composition consists of a mixture of nuclear fuel, coolant, structural, and control material. To establish a self-sustained chain-reaction the material must be arranged in a suitable configuration of sufficient size and right shape.

<sup>a</sup>Static multiplication factor for a reactor in the eigenstate. The index “*eff*” refers to the multiplicative properties of a reactor of finite size as opposed to the infinite multiplication factor,  $k_{\infty}$ , assuming an infinite system. The latter neglects neutron leakage effects.



### **Source multiplication in a subcritical reactor**

In operator formulation, the steady-state Boltzmann neutron balance equation for a subcritical reactor including a neutron source reads:

$$(\mathbf{M} - \mathbf{F})\Phi_s = S \quad (1)$$

Where  $\mathbf{F}$  is the fission operator,  $\mathbf{M}$  is the migration and loss operator,  $\Phi_s(\mathbf{r}, E, \Omega)$  is the angle-dependent inhomogeneous neutron flux, and  $S(\mathbf{r}, E, \Omega)$  is the independent neutron source. From the above neutron balance formulation, it is seen that in a subcritical reactor, fewer neutrons are produced through fission ( $\mathbf{F}\Phi$ ) than lost ( $\mathbf{M}\Phi$ ), and the difference is compensated by neutrons from the outside source,  $S$ . The fundamental mode flux is defined as:

$$\left( \mathbf{M} - \frac{1}{k_{eff}} \mathbf{F} \right) \Phi = 0 \quad (1)$$

The subcritical multiplication factor,  $k_s$ , is defined as the ratio of the fission neutrons to the total neutron source as:

$$k_s = \frac{\langle \mathbf{F}\Phi_s \rangle}{\langle \mathbf{M}\Phi_s \rangle} = \frac{\langle \mathbf{F}\Phi_s \rangle}{\langle \mathbf{M}\Phi_s \rangle + \langle S \rangle} \quad (2)$$

where  $\langle \rangle$  denotes phase-space integration. Unlike the effective multiplication factor,  $k_{eff}$ , which is a characteristic of the core, the subcritical multiplication factor depends on the characteristics of the external source neutrons (spatial position, energy, angular distribution). It is a local multiplication factor in that sense that it describes the multiplication of source neutrons from the point of where they are inserted. Using the inhomogeneous flux in Eq. (1), the fission neutrons per external source neutron can be related according to:

$$\frac{\langle \mathbf{F}\Phi_s \rangle}{\langle S \rangle} = \frac{1}{1/k_s - 1} \quad (3)$$

The fission power of the inhomogeneous system can be represented as

$$P_{fission} = E_f \langle \Sigma_f \Phi_s \rangle \quad (4)$$

Where  $E_f$  is the energy recovered per fission. If we now combine Eq. (3) and (4), the fission power can be written as:

$$P_{fission} = \frac{E_f}{\bar{\nu}} \frac{k_s}{1 - k_s} \langle S \rangle \quad (4)$$

Where the average number of neutrons per fission is defined as

$$\bar{\nu} = \frac{\langle \mathbf{F}\Phi_s \rangle}{\langle \Sigma_f \Phi_s \rangle} \quad (5)$$

### **Definition of an accelerator-driven system**

Conventional power reactors generally do not require external neutron sources for normal operation. These reactors are based on the self-multiplication of neutrons in a critical state. In a critical reactor the fission reactions alone are able to maintain a steady-state. In contrast, the accelerator-driven system (ADS) is a subcritical reactor driven by an external neutron source. The external source is maintained by a spallation neutron target (as explained below) driven by a high power proton accelerator thereby the leading adjective ‘‘accelerator-driven’’. Taken by itself, critical or near-critical reactor operation would seem like the optimum solution, since it eliminates the need for an external source. But safety and controllability are the main

issues for the ADS. The main purpose is to minimize the risk for uncontrolled reactivity excursions. Among the advantages of subcritical operation is the stable nature of operation, increased margin to prompt criticality, and reduced influence of reactivity feedbacks.

### ***External neutron source intensity***

Spallation is a nuclear reaction that may occur when a high energy particle strikes a heavy element, in which the nucleon(s) struck by the incoming particle may collide with other nucleons inside the nucleus causing an “intra-nuclear cascade”. In the process, the incoming particle may “spall” the target nucleus, breaking it into smaller pieces, releasing protons, neutrons and other nuclear fragments. The incoming particle may be a proton, and the target material may, for example, be tungsten, lead or lead-bismuth. High-energy secondary particles (neutron, protons, or pions) may be knocked out in the initial collision. The remaining nucleus is left in an excited state. In the de-excitation process (evaporation stage) the nucleus may emit additional nucleons or it may fission. Most of the particles emitted in the de-excitation process are neutrons which are emitted isotropically. The neutron yield depends on the energy of the incident proton, as shown in Fig. 15. The yield increases almost linearly in the range 1-4 GeV.

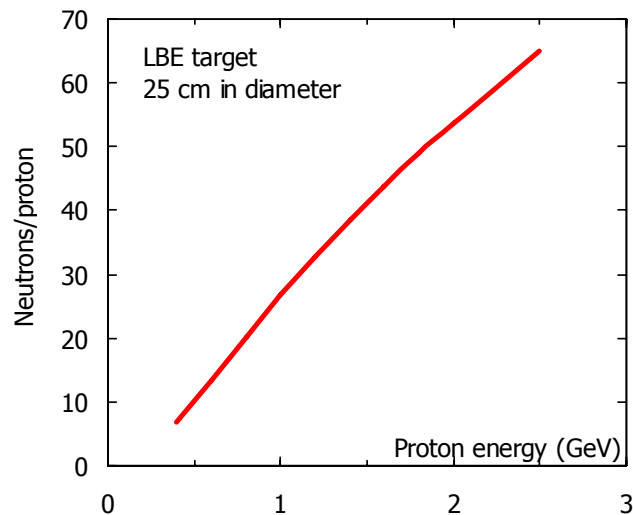


Fig. 15 Spallation neutron yield as function of incident neutron energy (by courtesy of P. Seltborg)

In order to produce a spallation neutron source of sufficient intensity the accelerator must be capable of delivering energetic protons at high current. As we saw in the previous paragraph, the total system power depends on both the source strength and the multiplication factor. Increasing the system power requires either reduced subcriticality or stronger source. To reduce the cost of the source it may seem desirable to increase the multiplication. This will, on the other hand, reduce reactivity safety margins. The degree of criticality offset is a fundamental design parameter of ADS systems. The choice of multiplication involves trade-off among various design goals such as reactor safety performance, core characteristics, and desired power rating, and at the same time remain consistent with current accelerator performance and cost goals. For typical industrial-scale ADS designs, it is envisioned that the thermal rating would be of the order of 500 MWth to 1500 MWth and employ  $k_{\text{eff}}$  values in the range 0.95-0.98. A legitimate question to ask then is what source intensity is required to drive this type of ADS? Consider a subcritical reactor operating at steady-state at 800 MWth with a  $k_{\text{eff}}=0.95$ . The required source intensity to maintain a fission power of 800 MWth is

given by the source multiplication formula (for the sake of simplicity let's assume that  $k_s$  is close  $k_{\text{eff}}$  which is almost true):

$$S = \frac{800 \cdot 10^6 [\text{W}] \cdot 2.5 [\text{neutrons/fission}]}{0.35 \cdot 10^{-10} [\text{W} \cdot \text{s/fission}]} \left( \frac{1-0.95}{0.95} \right) \approx 3 \cdot 10^{18} \text{ neutrons released per second}$$

Considering that the neutron production rate in  $^{252}\text{Cf}$  is  $2.3 \cdot 10^{12}$  n/s·gram, the required source intensity seems tremendous. The next question that comes to mind is whether an accelerator can produce a spallation neutron source of this intensity and what would the resulting beam power amount to? As we saw in Fig. 15, the spallation neutron yield depends on the incoming proton energy and the yield curve increases almost linearly in the range 1-4 GeV. However, most studies suggest optimum proton energy for an industrial ADS plant, in terms of cost and system efficiency, somewhere in the range 0.8-1 GeV. At 1 GeV each proton will on the average expel 25 neutrons, according to Fig. 15. Thus, the required proton intensity would roughly amount to  $1.2 \cdot 10^{17}$  protons/sec, which equals a beam current of roughly 20 mA ( $1.2 \cdot 10^{17}$  protons/sec  $\cdot 1.6 \cdot 10^{-19}$  C/proton) or expressed in different units, 20 MW of beam power ( $1 \cdot 10^9 \cdot 1.6 \cdot 10^{-19}$  J/proton  $\cdot 1.2 \cdot 10^{17}$  protons/sec). Although a beam power of 20 MW is an ambitious goal (such powerful machines do not exist today), it is not without reach with existing accelerator technology. Recent advances in accelerator technology have confirmed that a linear accelerator capable of delivering up to 100 MW at 1 GeV is a relatively direct extension of existing technology. Well-supported designs for this class of accelerator were completed several years ago at Los Alamos National Lab [50]. So the answer to the last question is: -Yes, high power proton accelerators can be built and they can be used to produce neutron sources of very high intensities, sufficient to drive an industrial sized ADS. The beam power required will be in the range 10-30 MW.

As a comparison, around one tonne of  $^{252}\text{Cf}$  would be necessary to deliver similar source intensities. The annual sales of  $^{252}\text{Cf}$  is less than 100 mg with a cost around \$60/ $\mu\text{g}$  (CRC Handbook, 2004-2005), and it would decay with a half-life 2.6 years. The heat generated in this source would be close to 30 MW. Thus, the neutron intensity required for an industrial ADS plant is well beyond the capabilities of any radioactive-decay type of source. It should be clear at this point that only a spallation neutron source driven by a high-power proton accelerator can produce neutron intensities of sufficient strength.

## **Safety features of uranium-free cores**

### ***Delayed neutron fraction***

Just as most fission neutrons appear instantaneously in the fission reaction, it happens that a few neutrons are released in the subsequent radioactive decay of certain fission products. These neutrons are referred to as delayed. Although the fraction of delayed neutrons in the reactor is small in comparison with the total number of neutrons, their presence is extremely important for the control of the chain reaction. The time delay for the delayed neutron emission is essentially determined by the time it took to undergo beta decay for the specific parent nuclei (e.g. delayed neutron precursor). The precursor nuclei usually disintegrates within a minute after fission (the longest-lived delayed neutron precursor has a 54-second half-life). If the delayed neutrons are considered along with the prompt neutrons, the weighted mean lifetime of all neutrons is considerably longer ( $\sim 10$  sec) than the prompt neutron lifetime ( $\sim 1 \cdot 10^{-6}$  sec in fast spectrum). Without the contribution from the delayed neutrons the reactor period following reactivity insertion (and removal) would be very small.

Since the isotopic fission yield will vary for different isotopes, the decay scheme leading to delayed neutron emission will be isotope-dependent. The two main delayed neutron

precursors are  $^{87}\text{Br}$  and  $^{137}\text{I}$ . One may recall that these nuclides have similar mass numbers as the two peaks in the fission-yield curve. The average number of prompt neutrons released in the fission event is denoted  $\nu_p$  and the corresponding yield of delayed neutrons is  $\nu_d$ . The delayed neutron fraction,  $\beta$ , then appears as:

$$\beta = \frac{\nu_d}{\nu_p + \nu_d}$$

In TABLE 10 we have tabulated prompt neutron yield, delayed neutron yield, and delayed neutron fraction characteristic for some principle fuel isotopes. The nuclides are listed in order of decreasing delayed neutron fraction. As noted by Keepin [51], the delayed neutron yield tends to increase with increasing number of neutrons for a given element, but decrease with increasing number of protons. This regularity is not that surprising since the fission yield of the most important delayed neutron precursor,  $^{87}\text{Br}$ , decreases with increasing mass number. The formation of  $^{137}\text{I}$  is roughly constant, however. Also the prompt neutron yield,  $\nu_p$ , tend to increase with increasing mass number, which lowers the  $\beta$  value even further. The effect is particularly pronounced in  $^{241}\text{Am}$  and  $^{244}\text{Cm}$ . The delayed neutron yield in  $^{238}\text{U}$  is about 7 times larger than  $^{239}\text{Pu}$  and for that reason it may contribute significantly in an FBR although its fission rate is lower ( $^{238}\text{U}$  may contribute with around 10% of the fissions). The dependence of the delayed neutron yield on the initiating neutron energy appears to be small up to 4 MeV [52]. The variation of the number of prompt neutrons emitted in fission is also small up to a few hundred keV, but increases thereafter. Therefore the energy dependence of the delayed neutron fraction is not very pronounced up to a few hundred keV. In general the isotope dependence of the delayed neutron precursor decay constants is not strong.

TABLE 10

Comparison delayed neutron yield ( $\nu_d$ ), prompt neutron yield ( $\nu_p$ ), and delayed neutron fraction ( $\beta$ ) for thermal induced fission (ENDF/B-VI.8).

| Nuclide             | $\nu_d^{th}$ | $\nu_p^{th}$ | $\beta$ |
|---------------------|--------------|--------------|---------|
| $^{238}\text{U}$    | 0.0440       | 2.45         | 1.77%   |
| $^{242}\text{Pu}$   | 0.0197       | 2.79         | 0.70%   |
| $^{235}\text{U}$    | 0.0167       | 2.42         | 0.69%   |
| $^{241}\text{Pu}$   | 0.0162       | 2.93         | 0.55%   |
| $^{237}\text{Np}$   | 0.0108       | 2.63         | 0.41%   |
| $^{240}\text{Pu}$   | 0.0090       | 2.79         | 0.32%   |
| $^{243}\text{Am}$   | 0.0080       | 3.26         | 0.24%   |
| $^{239}\text{Pu}$   | 0.0065       | 2.87         | 0.22%   |
| $^{245}\text{Cm}^*$ | 0.0064       | 3.59         | 0.18%   |
| $^{238}\text{Pu}$   | 0.0042       | 2.89         | 0.14%   |
| $^{244}\text{Cm}^*$ | 0.0044       | 3.24         | 0.13%   |
| $^{241}\text{Am}$   | 0.0043       | 3.23         | 0.13%   |

\*JENDL 3.3 data

Since the difference in the excitation energy and the neutron separation energy in the delayed neutron emitter is normally much smaller than in the prompt neutron emitter (i.e. direct fission product), the delayed neutrons are generally emitted with a much smaller average energy than prompt neutrons. Whereas the average fission neutron energy is roughly 2 MeV, the delayed neutrons are born at energies around ( $\sim 0.5$  MeV). This is illustrated in Fig. 16 for the thermal fission of  $^{239}\text{Pu}$ .

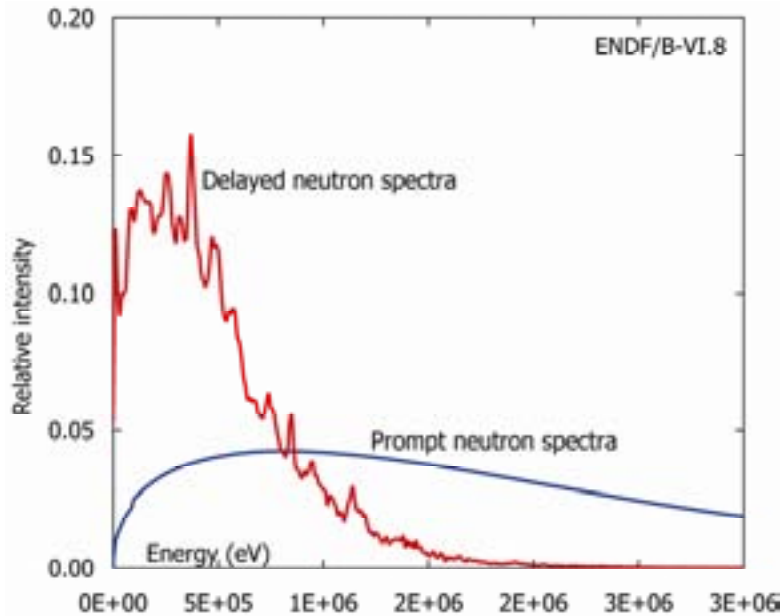


Fig. 16 Delayed neutron spectra vs. prompt neutron spectra for thermal neutron induced fission in  $^{239}\text{Pu}$ . Delayed neutron spectra is the weighted average of all six delay groups.

As the delayed neutrons emerge at lower energies than prompt neutrons, they are subject to different absorption, leakage, and neutron production properties. A more refined representation of the delayed neutron fraction, that takes into account the emission spectra influence, is the concept of the effective delayed neutron fraction,  $\beta_{\text{eff}}$ . The effective delayed neutron fraction can be interpreted as the number of delayed neutrons inducing fission in the system compared to the number of all neutrons inducing fission [53]. Depending on the core characteristics this value may be smaller or larger than the actual delayed neutron fraction. TABLE 11 gives the  $\beta$  and  $\beta_{\text{eff}}$  values for some oxide fuels of principle interest in a sodium cooled fast reactor. The table is extracted from **Paper II**. As can be observed, the effective delayed neutron fraction is 14% smaller than the delayed neutron fraction for the conventional fast reactor fuel ( $\text{U}_{0.8}\text{Pu}_{0.2}$ ). This is the usual situation in fast reactors as the delayed neutrons are emitted with average energies below the fast fission threshold in  $^{238}\text{U}$  ( $\sim 1$  MeV). The prompt neutron yield also decreases with energy, which further reduces the efficiency of delayed neutrons and suppresses the  $\beta_{\text{eff}}$ . Note that the relative drop in  $\beta_{\text{eff}}$  strongly increases with the addition of americium. For the fuels containing 30% Am, the effective  $\beta$  is 30-35% lower than the physical  $\beta$ . This is an effect of the higher capture probability of delayed neutrons in americium, as compared to prompt fission neutrons. Although the presence of uranium may contribute to some degree to the physical  $\beta$ , it has a limited effect on the effective delayed neutron fraction. TABLE 11 shows that even with 50%  $^{238}\text{U}$  in the fuel, the  $\beta_{\text{eff}}$  remains at 200 pcm. Not only does americium possess a low physical  $\beta$ , it reduces the advantage of adding uranium to the fuel. The effective delayed neutron fraction for the uranium-free zirconium-matrix fuel containing plutonium and americium is in the range 140 to 200 pcm, which is about half the value for the conventional FBR, and about a fifth the value for a LWR. Clearly, such a low beta value leaves a very small margin to prompt criticality. This feature combined with the enhanced neutron-kinetics response that follows with a small  $\beta_{\text{eff}}$  would make critical reactor control very difficult.

TABLE 11

The delayed neutron fraction ( $\beta$ ) and the effective delayed neutron fraction ( $\beta_{\text{eff}}$ ) for some oxide fuels in sodium cooled reactor. Results reproduced from **Paper II**.

| U [%] | Pu [%] | Zr [%] | Am [%] | $\beta$ [pcm] | $\beta_{\text{eff}}$ [pcm] |
|-------|--------|--------|--------|---------------|----------------------------|
| 80    | 20     | -      | -      | 399±11        | 342 ±10                    |
| 50    | 20     | -      | 30     | 307±10        | 204 ±11                    |
| -     | 20     | 80     | -      | 221±11        | 206 ±13                    |
| -     | 20     | 50     | 30     | 213±11        | 143 ±11                    |

### *Void reactivity*

Considerable attention is given to the reduction of the coolant void worth in current ADS designs. Coolant voiding could introduce reactivities that may override the subcritical reactivity for certain combinations of fuel and liquid-metal coolants [54]. It was shown in **Paper II** that the void reactivity effect increases with the americium content. The use of lead-bismuth yields lower void worths than sodium for a wide range of fuel types and core sizes [55, 56]. The low void worth and high boiling point in comparison with sodium are principal advantages that favour the selection of lead-bismuth, see **Paper IV**. The higher sodium void worth is partly due to its higher moderating power, which causes a larger spectrum shift during voiding. In general, hardening of the neutron spectrum and increased neutron leakage are the two dominating physical phenomena contributing to the void reactivity effect in liquid-metal cooled reactors [57]. Hardening of the spectrum leads to a positive reactivity effect due to an increase in the fission probability and an increase in the number of neutrons released per fission (see Fig. 9) while increased leakage gives rise to a reactivity loss since more neutrons may escape the core. Lead-bismuth void worths for a molybdenum-based Ceramic-Metal (CerMet) fuel, a magnesia-based Ceramic-Ceramic (CerCer) fuel, and a zirconium-nitride based fuel are reported in **Paper II**. For convenience, these results are tabulated in TABLE 12..

TABLE 12

Lead-bismuth void reactivity worth (in pcm) computed for the examined fuels in various lattice configurations. Results adapted from **Paper II**.

| Fuel    | P/D=1.50,<br>D <sub>o</sub> =5.7 mm |                 | P/D=1.75,<br>D <sub>o</sub> =5.7 mm |                 | P/D=1.50,<br>D <sub>o</sub> =6.8 mm |                 |
|---------|-------------------------------------|-----------------|-------------------------------------|-----------------|-------------------------------------|-----------------|
|         | Core                                | Core+<br>plenum | Core                                | Core+<br>plenum | Core                                | Core+<br>plenum |
| CerCer  | 4060                                | 1790            | 5300                                | 2300            | 4570                                | 2250            |
| CerMet  | 2460                                | 220             | 3580                                | 470             | 2990                                | 520             |
| Nitride | 2960                                | 680             | 4150                                | 880             | 3610                                | 1080            |

The effect of changing the core size and pin diameter is shown. The negative leakage component tends to decrease with increasing reactor size, while the spectrum hardening effect increases for higher coolant volume fractions. The net effect is that the void effect becomes more positive when the core size increases. The calculations indicate an increase in void worth for larger pin diameters. The effect of separately voiding the core region and plenum region was investigated. The spectral contribution to the void reactivity is closely related to the flux spatial distribution (and the spatial distribution of the adjoint flux) and is usually more positive near the center of the core, while the leakage component is more negative near the edges where the flux gradient is stronger. As a result, expulsion of coolant from the central region results in a positive reactivity gain. However, if the plenum region is voided simultaneously, the reactivity effect may decrease considerably. Evidently, the CerMet fuel

offers low void worths. For tight lattice configurations with this fuel, even central voiding can be accommodated. The void worth of the CerCer core is considerably higher than the CerMet and nitride. The reason is the larger core size (more fuel pins) of the CerCer core, which is an effect of the lower linear rating requirement of this fuel. It is noted, however, that all three fuels provide acceptable Lead-bismuth void values when the core and plenum is voided simultaneously.

### ***Doppler coefficient***

The presence of a strong Doppler effect produced by resonance absorption in  $^{238}\text{U}$  greatly contributes to the stability in thermal reactors as well as fast reactors. If in a power transient the temperature should increase, the Doppler feedback provides a prompt negative reactivity reduction. The Doppler broadening of resonances follows the fuel temperature instantaneously (increases as the temperature of the fuel rises, making fewer neutrons available to continue the chain-reaction). The Doppler effect is especially valuable under super prompt critical accidents, in which it will advance the shutdown process and thus reduce the energy release and limit the destructive force on the containment [58]. Its effectiveness in terms of “turning around” prompt-critical transients in the fast reactor was experimentally demonstrated in the SEFOR reactor tests [59]. The effect of uranium and americium content on the Doppler constant was investigated in **Paper II** for oxide fuels in a sodium-cooled core. It was found that the Doppler constant decreases drastically with increasing Am-content. The relatively high capture cross section of americium in the energy range of 10-500 keV leads to a decrease in Doppler feedback. As shown in figure 1, the capture cross section of  $^{241}\text{Am}$  is 10 times higher than that of  $^{238}\text{U}$  in the important energy range.  $^{241}\text{Am}$  exhibits no sharp resolved resonances above 100 eV and thus, in a fast spectrum there are few exposed resonances. Not only is  $^{241}\text{Am}$  a poor resonance absorber in itself, it prevents absorption in other possible resonant absorber nuclides, like  $^{238}\text{U}$  or  $^{240}\text{Pu}$ . Even with a large fraction of  $^{238}\text{U}$  in the fuel, most captures will take place in  $^{241}\text{Am}$ , at energies above the resolved resonance region. It is evident that the Doppler effect will be very small in fuels containing high concentrations of  $^{241}\text{Am}$ .

In the absence of a prompt negative reactivity feedback mechanism when passing through prompt criticality, the power will essentially continue to rise until the fuel vaporizes, which will disperse the core and eventually bring the reactor below critical. Consequent hazards are potential damage to the containment, internal structures, and heat-removal equipment. The absence of a significant negative Doppler effect requires greater care in the design to prevent accidents that might lead to prompt-critical conditions. For an ADS, the built-in subcritical margin is the first step in this direction. Other means include minimization of material reactivity potentials. To some degree thermal expansion of fuel can compensate for a small Doppler coefficient in a fast reactor, but it is not as reliable or as prompt as the Doppler effect.

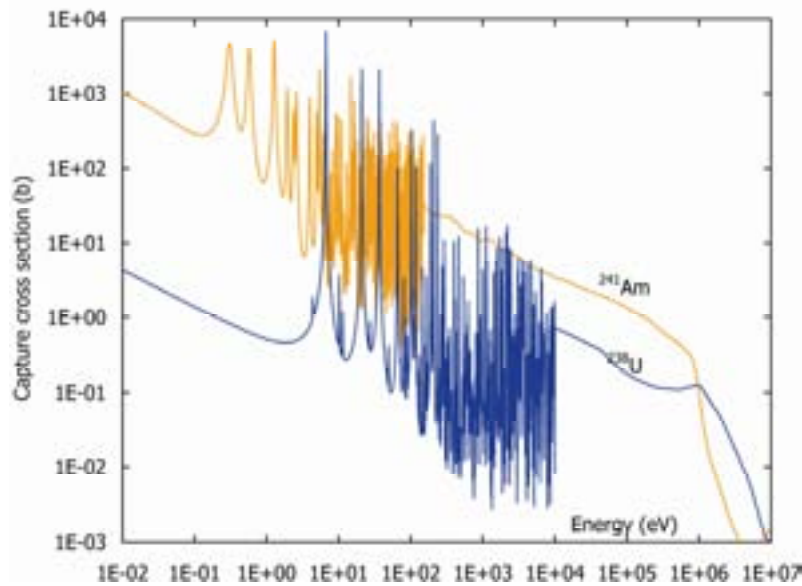


Fig. 17 Capture cross sections of  $^{238}\text{U}$  and  $^{241}\text{Am}$  as function of energy (ENDF/B-VI)

### *Clad reactivity*

Significant amounts of reactivity could be inserted if molten cladding would be ejected into the coolant and swept upwards out of the core. The effect is important if the cladding leaves the core ahead of the fuel. It is most likely to be associated with undercooling events if the cladding melts. Phenomenological studies of sodium systems [60] suggested that major clad relocation was not to be expected due to sodium-vapor streaming effects (which is the result of an alternating flooding and bypass process of sodium vapor in the channel). This may not be the case for a lead/bismuth-cooled reactor since clad melting will advance lead-bismuth boiling. On a longer timescale, positive reactivity could be inserted because of dissolution of structural materials in lead-bismuth. The reactivity effect of removing the cladding from the core is presented in **Paper I**. It was found that cladding removal leads to a net positive reactivity insertion around 3000 pcm. This value was more or less the independent of the fuel type. Use of a thinner cladding could further reduce the positive reactivity effect, but it would also degrade mechanical strength.

### *Fuel relocation and recriticality*

Reactivity might be introduced in a fast spectrum reactor if the fuel would collect in a denser configuration. Such redistribution of the fuel might result from a meltdown accident or structural collapse of the core. Fuel densification essentially allows fewer neutrons to leak out of the core. This is a fundamental distinction between reactors operating on a fast neutron spectrum and thermal systems. The latter is arranged in nearly an optimum configuration to maximize neutron multiplication and any change to the configuration will shut down the chain reaction. By comparison, if the core of an ADS melts the issue of recriticality must be addressed. The recriticality problem is aggravated by the lack of a negative Doppler effect. Neutronic calculations were performed in **Paper I** to determine critical fuel geometries. These results are shown TABLE 13. The critical mass is sensitive to the material composition (additions of steel, neutron absorbing materials, reflective conditions, etc.) and the fuel geometry. Calculations for standard fast reactor fuel ( $\text{U}_{0.8}\text{Pu}_{0.2}\text{O}_2$  surrounded by Na) were also performed to enable comparison. It is seen that the critical mass of the minor actinide fuels is quite small in comparison with standard fast reactor fuel, however, variations occur. The nitride fuel has the smallest critical mass (70 kg), which is approximately 20 times



smaller than classical MOX-fuel surrounded by sodium. This corresponds to the fuel mass contained in three subassemblies (127-pin bundles). The critical mass of the CerMet fuel is 340 kg, which is a factor of 5 larger than the nitride fuel. The critical mass of the CerCer fuel is somewhat smaller than for the CerMet. Clearly, an ADS core contains sufficient fuel to assemble several critical masses. About 69 critical masses were calculated for the nitride core while the oxide cores contain 18 critical masses each. By comparison, Super-Phénix held about 17 critical masses. Given that the total fuel mass in the French reactor is about 4 times larger than for the present ADS cores, a direct comparison is not appropriate. Based solely on the critical mass, it would seem desirable to use a neutron absorbing matrix material, such as molybdenum or magnesia. However, the recriticality question is complex and in comparison with fast reactors, the behavior of an ADS under these conditions is not well known. It is possible that the recriticality problem may be relaxed in lead-bismuth system where the fuel would tend to rise and possibly disperse at the surface rather than collect at the bottom. Moreover, the enhanced fission gas retention in americium based fuels may also provide a natural dispersive mechanism, although this remains to be demonstrated. The critical size of the fuel is merely one element affecting the recriticality potential.

TABLE 13

Critical mass studies for simple fuel geometry\*

| Fuel         | Critical mass<br>(kg) | Critical volume<br>(dm <sup>3</sup> ) | Reactor total<br>(critical masses) |
|--------------|-----------------------|---------------------------------------|------------------------------------|
| CerCer       | 290                   | 47                                    | 18                                 |
| CerMet       | 340                   | 33                                    | 18                                 |
| Nitride      | 70                    | 9                                     | 69                                 |
| Super-Phénix | 1370                  | 130                                   | 17**                               |

\*Cylindrical volume element (H/D=1) surrounded by lead-bismuth.

\*\*Based on (U<sub>0.8</sub>Pu<sub>0.2</sub>)O<sub>2</sub>, 3000 MWth (23 tons of fuel).

### **Motivation for subcritical operation**

The reactivity burnup swing influences the safety characteristics in many aspects. A low burnup reactivity swing lowers the power peaking during burnup and minimizes the built-in excess reactivity for burnup compensation. In an ADS it reduces the proton beam current capability. In a recent design study of a lead/bismuth-cooled ADS [61] it was shown that initial plutonium loading around 40% and 60% MA may provide optimum internal conversion and thus minimum reactivity swing when approaching equilibrium. It is then of interest to determine whether or not such a fuel could be operated in a critical mode. The previous analyses indicate that the addition of minor actinides to a fast spectrum reactor lowers the Doppler coefficient and reduces the effective delayed neutron fraction. Critical fast reactors rely heavily on the delayed neutrons and on the Doppler effects to achieve smooth power control during normal operation and protection against severe reactivity insertion accidents. In addition, the void reactivity effect becomes increasingly positive in uranium-free and liquid-metal cooled minor actinide cores, especially using sodium coolant.

The possibility of operating a uranium-free minor actinide oxide fuel in a sodium cooled fast reactor was investigated in **Paper II**. The analysis took advantage of a balance-of-reactivity approach<sup>a</sup> as suggested by Wade and Fujita [62] to determine the asymptotic core outlet temperature rise following unprotected transient events (loss-of-flow, loss-of-heat-sink, transient overpower). The method is useful to extract passive safety trends for slow transients (equilibrium conditions) from a quasi-static balance of all reactivity coefficients (Doppler, axial expansion, radial expansion, and sodium density). In the case of a total loss-of-heat sink accident, it was found that the minor actinide core featured a distinct positive inlet temperature coefficient. While structural expansion feedback was similar in the conventional core and the dedicated core, the dedicated core presented a marked positive void coefficient together with a non-existing Doppler effect. A positive inlet temperature coefficient is unacceptable from a passive safety viewpoint since it will eventually drive a sodium cooled core to boiling. The calculations also indicated a low value of the maximum acceptable reactivity insertion (dictated by the resulting increase in core outlet temperature), which effectively limits the control rod worth to a small value, a complication which is of practical importance. From these survey analyses it appears that operation of a critical uranium-free minor-actinide core would be difficult. It should be recognized that the survey analysis did not consider fast reactivity insertion transients, in which a critical minor actinide core would perform poorly due to the small effective delayed neutron fraction and weak Doppler effect, as discussed in a later section.

From an inherent safety standpoint, the Nuclear Regulatory Commission (NRC) requires [63] that “The reactor core and associated coolant systems shall be designed so that in the power operating range the net effect of the prompt inherent nuclear feedback characteristics tends to compensate for a rapid increase in reactivity.” In a conventional metal or oxide sodium-cooled design (\$3 to \$5 voiding worth) with a nominal Doppler coefficient (around -0.5 pcm/K), the Doppler feedback is sufficient to retard the reactivity addition to avoid super-prompt criticality for a boiling initiator [64]. Clearly, compensating reactivity at this level will be difficult to achieve in a sodium-cooled minor actinide based core. In the preliminary safety evaluation report of the PRISM design [65], the commission issued the following statement “The existence of a positive sodium void coefficient, or any reactivity feedback effect that tends to make a postulated accident more severe, is a significant concern”, which indicates the great importance attached to this issue.

With a subcritical reactor, one can adjust the initial level of subcriticality with regards to the void value and thus prevent progression into prompt critical conditions in voiding scenarios (one may note that there are other ways of voiding the reactor besides coolant boil-out). In that case the probability for core disruptive accidents could perhaps be made sufficiently low ( $<10^{-6}$  per reactor-year) to be excluded in the formal licensing process, similar to the approach adopted in the design and licensing of the FBRs [66].

<sup>a</sup>As cautioned by Wade and Fujita, the quasi-static reactivity balance approach is a blunt method to obtain precise safety data and cannot be used to extract transient effects. The list of design variables would also have to include power and flow distributions in the reactor, the pump flow coast-down characteristic, the reactivity feedback coefficients (Doppler, axial exp., radial exp., coolant density), the corresponding core pressure drop, and in the long term, the decay heat removal performance is important and the natural circulation capability. However, the conditions considered in the reactivity balance proved to be useful to evaluate safety trends in the frame of modular-sized liquid-metal cooled reactor concepts and the issue here is whether similar characteristics could be achieved in sodium-cooled minor actinide cores.

## **Responsiveness of the ADS**

The kinetics behaviour of an ADS differs substantially from a conventional (critical) reactor. The critical operating state represents a sensitive balance between the production rate of neutrons through fission and the neutron loss rate (through absorption and leakage) and a relatively small off-balance in these two quantities can lead to large deviations in the fission rate. In contrast, a subcritical reactor is inherently stable to reactivity changes within the subcritical range or changes in the external neutron source. If a subcritical reactor is subject to a change in the strength of the external source, or a change in reactivity within the subcritical range, the neutron population will adjust to a new stationary level. This is quite the contrary of critical reactors. In the absence of reactivity feedbacks the response in a critical reactor will either diverge exponentially or decay to zero depending on the sign of the reactivity disturbance. In the response to a reactivity insertion accident this feature provides to a distinct safety advantage over critical reactor operation, distinguished by high operational stability and additional margins for positive reactivity insertion. An example is shown in Fig. 18a for a linear reactivity-ramp-induced transient ( $\$1$  in 1 sec.) in a lead-bismuth cooled critical reactor and in similar reactors made subcritical by  $-1\beta$ ,  $-5\beta$ , and  $-10\beta$ . The cores (800 MWth,  $\beta_{\text{eff}}=0.19\%$ , MA-oxide fuel) are identical except for the initial reactivity. The reactivity feedbacks consist of coolant density (+0.53 pcm/K), axial fuel expansion (-0.28 pcm/K), radial core expansion (-1.0 pcm/K), and a small Doppler effect (-0.05 pcm/K). The increase in power is significantly weaker in the subcritical systems. The closer to criticality, the larger the power increase. For the power to double in a subcritical reactor, half of the reactivity required for criticality must be added. In response to negative reactivity feedbacks, however, subcritical operation is less favourable since the power will not drop as much as in a critical reactor. In Fig. 18b, an unprotected loss-of-flow is exercised for the same cores (featuring overall negative feedbacks) as in the previous example, which shows that the influence of such feedbacks will be much smaller in an ADS compared to any critical system.

Critical systems rely on delayed neutrons and smoothly varying feedbacks to level out reactivity disturbances. Since the operating point of a subcritical reactor is largely offset from prompt criticality both the delayed neutrons as well as reactivity feedbacks have a weak influence on the kinetics behaviour. The response is dominated by the prompt neutrons which follows the external neutron source. Hence, the time constant of change is essentially determined by the prompt period. Thus source changes and reactivity changes lead to abrupt power changes in the subcritical reactor. Delayed neutrons play an increasing role when the system approaches critical conditions. It should also be recognized that, an almost critical reactor behaves, for all practical purposes, nearly like a critical reactor. The essential difference is that for  $k_{\text{eff}} > 1$ , power continues to rise; for a reactivity increase that leaves  $k_{\text{eff}} < 1$  the power stops rising at a level that depends on reactivity.

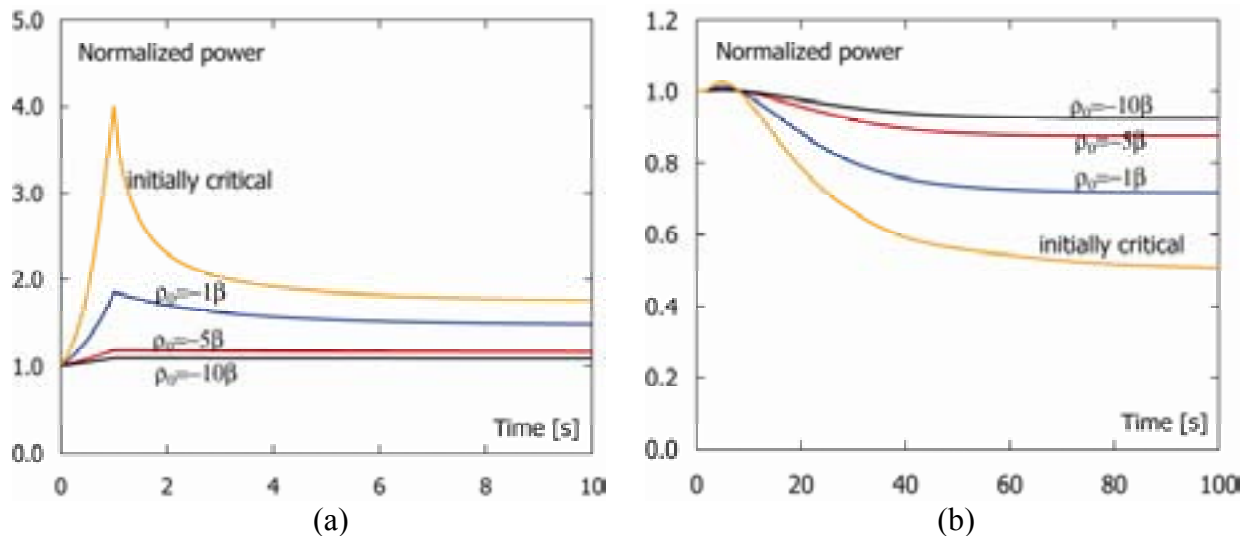


Fig. 18 Relative power vs. time following (a) linear reactivity-ramp insertion ( $\beta$  in 1 sec) and (b) unprotected loss-of-flow in subcritical systems and critical system.

## Accident performance

### Transient computational modelling

The SAS4A/SASSYS-1 [69] computer code is applied to the analysis of accident sequences. A detailed description of the SAS code is outside the scope. However, a brief background and overview of the basic features is provided in Appendix B. The primary system includes models of the core, primary pumps, shell side of the steam generators, connecting piping, and compressible pool volumes with cover-gas surfaces. Reactivity feedbacks are calculated for coolant expansion, fuel elongation, radial core expansion, and Doppler effect. Changes in power level are computed with point kinetics theory. The performance of the point kinetics approximation for transient analysis of ADS's is discussed in **Paper III** and found adequate for similar problems.

### Accelerator beam overpower

In an ADS, the traditional reactivity based shutdown system is replaced with a beam regulating system that controls the intensity of the external neutron source. The magnitude of the external neutron source is adjusted by changing the proton beam intensity. It is relevant to consider system disturbances in which the source strength suddenly changes. This could for example happen due to a control system failure, accelerator malfunction, or operator error. It may be noted that the source strength in an ADS may change abruptly while transients in a traditional reactor are limited by mechanical speeds. Since the prompt adjustment time in an ADS is very short (tens of  $\Lambda$ ), the power will instantaneously respond to any source variation, which permits accidents with very short initial ramp times in comparison with transients in critical reactors. No safety system can act instantaneously; there are always time delays involved. For a traditional safety rod based shutdown system, there is typically a 200 ms delay from detection to control rod motion [70], and then an insertion time of the order of a second. This is fast enough to detect all accident initiators identified for fast reactors [71], which always appear as gradual changes. A beam overpower accident, however, can produce a considerable power change before the malfunction has been detected. Hence, failure prevention should be precluded by the design, and not simply rely on proper control system action.

Fig. 19 compares the response in a sodium cooled and a lead-bismuth cooled ADS when the external source strength is multiplied by a factor of 2 (see **Paper IV**). The ramp is initiated at  $t=1$  second and halted at 1.001 seconds. The source is held constant thereafter. The fuel is diluted in zirconium oxide (Pu/TRU ratio is 0.4). The initial  $k_{\text{eff}}$  is 0.97 and the beta effective is 0.2%. The P/D ratio is 1.50 for the case shown. Following the initial jump the power changes as a result of reactivity feedbacks. The steam generators are assumed to remove heat at a rate of nominal power, resulting in increasing core inlet temperature as the transient proceeds. Coolant void reactivity feedbacks contribute to the course of the accident by adding reactivity. The void value for the sodium core is 6500 pcm (32.5) and in the case of Pb/Bi it is 3700 pcm (18.5). Differences in transient behaviour between lead/bismuth and sodium result primarily from the difference in boiling point and void reactivity effect. Coolant density changes provide modest changes in reactivity compared to the full void reactivity effect, which may introduce significant positive reactivity values. This causes the reactivity insertion rate to be considerable larger in the sodium-cooled core. Void generation, and thus positive reactivity insertion, is abrupt in the vicinity when boiling starts. Sodium boiling begins at the core outlet and develops axially downward. In the sodium-cooled core, the void effect adds enough reactivity to bring the reactor to a prompt critical state, with possible severe safety consequences. The small negative reactivity feedback associated with the Doppler effect does not influence the course of the accident, which is contrary to the situation in a boiling transient in a conventional FBR. Prompt critical conditions are established about 400 seconds after accident initiation. Large positive reactivity insertions are potentially possible due to lead/bismuth voiding as well. But the high boiling temperature for lead/bismuth (1943 K) compared to sodium (1154 K) makes voiding less probable even though there are other ways of voiding the coolant besides boiling, i.e. large scale steam generator failure or possibly sudden gas release from ruptured pins. The results point to a distinct advantage of using lead-bismuth as coolant.

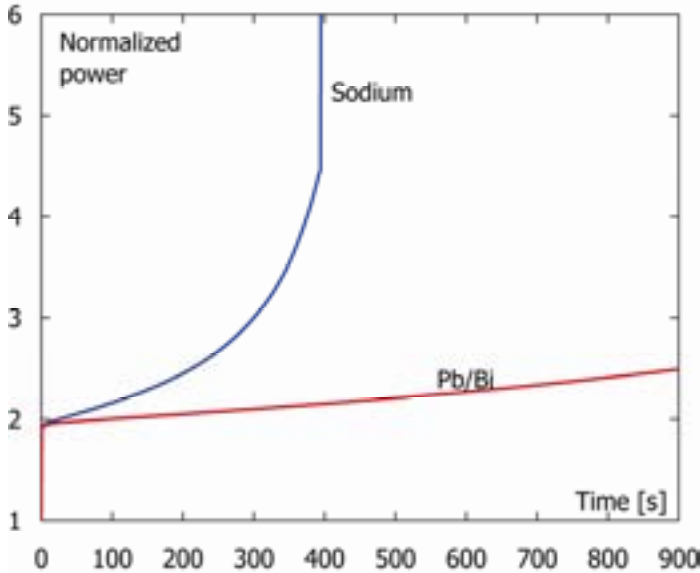


Fig. 19 Comparison of a beam overpower accident for sodium cooled and lead-bismuth cooled ADS.

### *Unprotected loss-of-flow*

The safety performance of a lead-bismuth cooled ADS in response to unprotected loss-of-flow is investigated in **Paper I**. The results are presented here in a condensed form. The studies encompass three inert matrix fuel systems: a molybdenum-based Ceramic-Metal (CerMet) fuel, a magnesia-based Ceramic-Ceramic (CerCer) fuel, and a zirconium-nitride based fuel. Major plant specifications are presented in TABLE 14. A pool system is used to take advantage of a simple tank design and to avoid any nozzles and pipes of a loop system. Due to high corrosion activity, coolant temperatures and velocities are limited. The coolant flow velocity in the pin bundle is limited to 2.5 m/s and the reactor inlet temperature is set at 573 K. Lead-bismuth is chemically inert with water/steam. Hence, a two-circuit system is utilized, with the steam generator located in the primary system, which simplifies the overall plant design and reduces the cost. The primary system includes four centrifugal pumps (two for each loop) and four steam generators (two for each loop). Based on a seismic analysis, a vessel height of 10 m is selected. The separation distance between the core midplane and the thermal center of the steam generators is 5.5 m. The pump design includes flywheels to prolong the coast-down time in the event of a loss of pumping power accident.

TABLE 14  
ADS plant specifications

| ADS plant specifications                          |                       |
|---|-----------------------|
| General   |                       |
| Type of plant                                     | Pool type             |
| Reactor power                                     | 800 MWth              |
| Coolant   | LBE (44.5%Pb+55.5%Bi) |
| Reactor inlet temperature                         | 573 K                 |
| Coolant inlet velocity                            | 2.5 m/s               |
| Reactor vessel                                    |                       |
| Height  | 10 m                  |
| Diameter  | 6 m                   |
| Wall thickness                                    | 13 cm                 |
| Weight (incl. coolant)                            | ~2500 ton             |
| Primary system                                    |                       |
| Steam generators                                  | 4 (integrated)        |
| No. of pumps                                      | 4                     |
| Pump mass of inertia                              | 400 kg·m <sup>2</sup> |
| Distance between thermal centers of core and SG's | 5.5 m                 |

It is assumed that all primary pumps are tripped in conjunction with failure of the shutdown system, i.e., the proton beam remains on. It is further assumed that the heat rejection system maintains core inlet temperature at the pre-transient value. During the transition to natural circulation condition, the flow rate is determined by the inertia of the pump and the thermal buoyant drive, which is counterbalanced by the system pressure losses. The pump moment of inertia has been optimized to soften the cladding-heating rate following pump trip. In principle, slower cladding heating rates and longer grace periods can be achieved with ever increasing pump inertia. There are, however, operational problems associated with high inertia pumps that impose an upper limit on the pump mass. Besides mechanical problems on the pump shaft, an adverse negative effect is sluggish speed control. In a controlled shutdown event, it is desirable to match the flow and power to avoid thermal cold shock in reactor components. This problem is of particular concern for ADS's because of the possibility for frequent beam interruptions, as discussed in **Paper VI**. Therefore, a balance must be struck in the selection of the flywheel size. The pitch-to-diameter (P/D) ratio and the pin diameter are

design parameters. The reference configuration uses a P/D equal 1.50 and a pin diameter of 5.72 mm. In a second configuration, the P/D value is increased to 1.75 by changing the pin pitch. In a third modification, the pin diameter is increased to 6.8 mm while holding the P/D ratio at 1.50. Matrix fractions are adjusted to obtain an initial  $k_{\text{eff}}$  equal 0.97 and a radial peak-to-average power ratio factor of 1.3. The  $\beta_{\text{eff}}$  is around 180 pcm for all three fuels. The plutonium fraction is fixed at 40% Pu and 50% MA. Because of lower thermal conductivity, the CerCer fuel is required to operate at lower linear powers; 25 kW/m compared to 35 kW/m for the CerMet and the nitride fuel. The calculational model used in this study employs two thermal-hydraulic channels. One channel represents an average pin within the core and a second channel represents the hottest pin in the core (with a power peaking factor of 1.3). The fuel-cladding gap conductance model accounts for gas conduction, radiative heat-transfer, surface roughness, and differential thermal expansion of fuel and cladding during transient conditions. Reactivity feedbacks are calculated for coolant expansion, fuel elongation, radial core expansion, and Doppler effect. Maximum temperatures during transients are determined and compared with design limits. Preliminary design limits are listed in TABLE 15, with detailed motivation given in **Paper I**. Si-modified 15-15Ti austenitic stainless steel (Phénix type) is the reference cladding material [72, 73].

TABLE 15

Summary of thermal limits for fuel and cladding.

| Component               | Failure temp. (K) | Failure mechanism  |
|-------------------------|-------------------|--------------------|
| Fuel                    |                   |                    |
| CerCer                  | 2200-2300         | Eutectic melt      |
| CerMet                  | 2640              | Oxide melting      |
| Nitride                 | 2400              | AmN dissociation   |
| Cladding (type 15-15Ti) |                   |                    |
| Surface (steady-state)  | 840               | Corrosive thinning |
| Midwall (steady-state)  | 920               | Creep rupture      |
| Midwall (transient)     | 1330              | Mech. burst limit  |

Fig. 20a shows the coolant flow rate and the power history for a core configuration with pitch-to-diameter ratio equal 1.75. It is seen that the natural circulation flow reaches a quasi-steady value of 23-27% of initial flow at 50-60 seconds after the pump trip. The power decreases steadily during the entire transition to natural circulation conditions. Reactivity feedbacks are illustrated in Fig. 20b. For simplicity only the case with CerCer fuel is shown. All three cores feature overall negative temperature-induced reactivity feedbacks. Reactivity feedback from radial expansion of the core is the dominant negative feedback mechanism – it contributes about minus one dollar at equilibrium conditions. Axial fuel expansion reactivity differs somewhat between the fuels. As the coolant temperature increases it produces a positive reactivity effect. The resulting reactivity increment due to coolant expansion amounts to +0.5\$ for the CerCer core and +0.4\$ for the nitride. The coolant reactivity is however exceeded by the reactivity losses due to radial expansion and fuel elongation. The positive coolant expansion effect is largely compensated by the negative feedback from fuel elongation. The Doppler effect is insignificant. The overall effect of the reactivity feedbacks is not great, however. The power falls to approximately 95% of the initial value of 800 MWth when equilibrium is reached. The power response behaviour is similar among the cores.

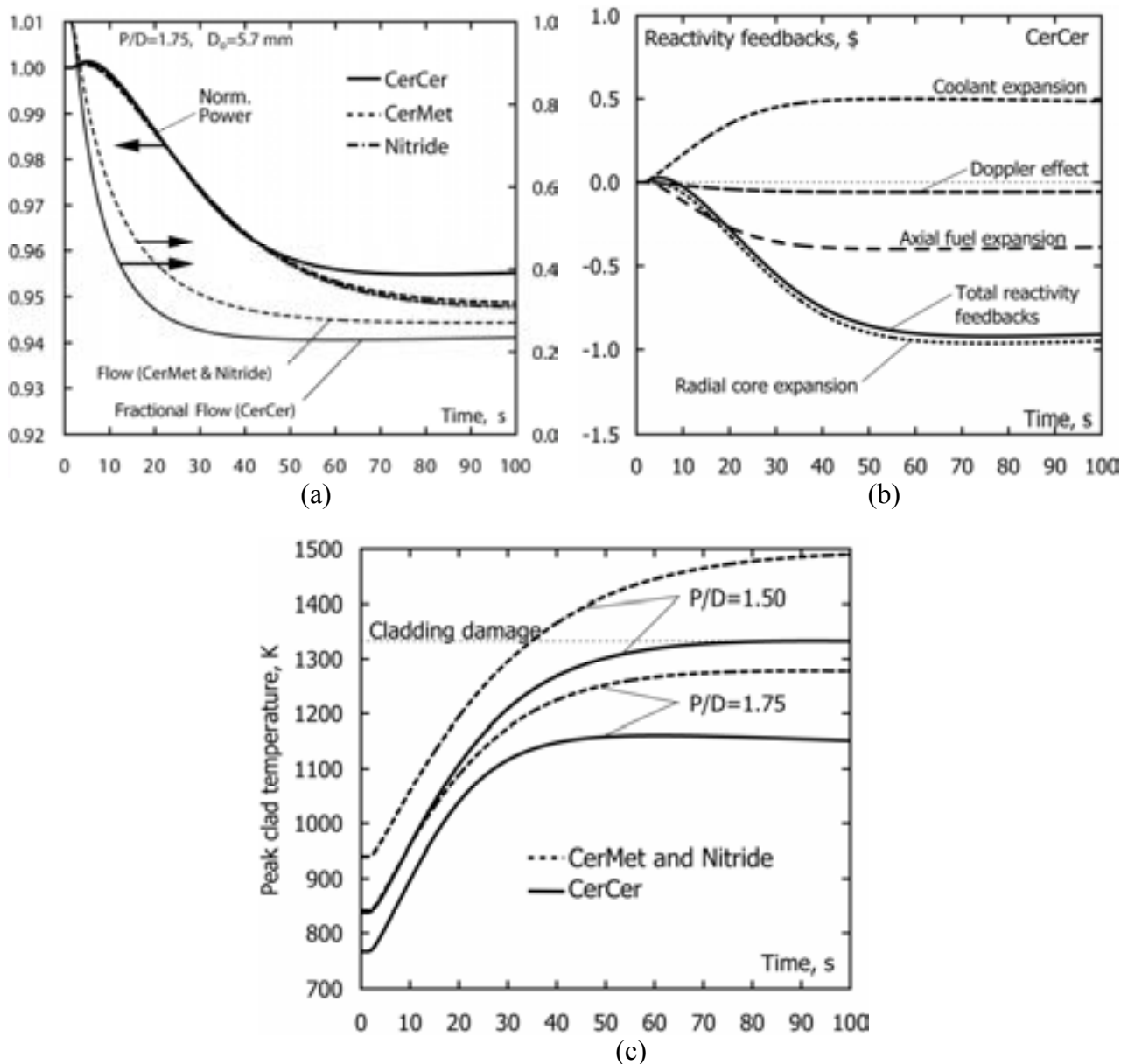


Fig. 20 Transient results for an ADS subject to unprotected loss-of-flow. (a) transient power and flow (b) associated reactivity feedbacks for the CerCer fuel (c) cladding temperatures.

The immediate effect of the flow reduction is a temperature rise in the coolant, and this in turn leads to higher cladding and fuel temperatures. Coolant boilout is not an issue with lead/bismuth. The primary concern is whether the cladding exceeds design limits. Lower cladding temperatures are promoted by higher coolant volume fractions. Larger distance between the fuel pins reduces the core pressure drop and in turn increases contribution from natural circulation. As a result, less forced flow is lost in a pump failure event. A comparison of cladding temperatures for these cores corresponding to  $P/D=1.50$  and  $P/D=1.75$  is shown in Fig. 20c. Cladding temperature is highest for the CerMet and nitride cores because of their higher power rating. The burst temperature for the cladding is 1330 K, as shown in TABLE 15. Thus, for the smaller pitch design, the cladding exceeds the failure point within 30-40 seconds after pump failure, which leaves small safety margins. On the other hand, increasing the  $P/D$  ratio to 1.75 reduces cladding temperatures by more than 200 degrees. In that case, early cladding failure can be avoided. It is noted however, that a safe state cannot be assured



indefinitely. The burst limit is applicable in transients in which the cladding is heated, without interruption, until failure. Thermal creep rates increase rapidly at high temperatures. Based on creep rupture data for D9 alloy [75], the lifetime at 1280 K is in the minute-scale. Thus, damage prevention will eventually require the need for shutdown and restored cooling capability. Maximum fuel and cladding temperatures as function of pitch-to-diameter ratio and pin diameter are presented in TABLE 16. Since the fuel temperature increases along with the coolant temperature, the potential for fuel damage must also be considered. The temperature of the CerMet fuel reaches 2120 K for the reference configuration (P/D=1.50 and  $D_o=5.7$  mm), which corresponds to a margin to melting of 500 degrees. The nitride fuel, which has lower thermal conductivity than the CerMet fuel but smaller gap size, is slightly colder (2080 K) leaving a margin to dissociation of 320 degrees. The CerCer temperature reaches close to the damage limit for the same configuration. Increasing the pin diameter should be considered in this case.

TABLE 16

Peak fuel and cladding temperatures at a time  $t=100$  seconds during unprotected loss-of-flow transient as function of P/D and pin diameter.

| Fuel    | P/D=1.50     |      | P/D=1.75     |      | P/D=1.50     |      |
|---------|--------------|------|--------------|------|--------------|------|
|         | $D_o=5.7$ mm |      | $D_o=5.7$ mm |      | $D_o=6.8$ mm |      |
|         | Fuel         | Clad | Fuel         | Clad | Fuel         | Clad |
| CerCer  | 2160         | 1330 | 2130         | 1160 | 1970         | 1200 |
| CerMet  | 2120         | 1490 | 2030         | 1280 | 1920         | 1340 |
| Nitride | 2080         | 1490 | 1980         | 1280 | 1920         | 1340 |

### ***Coolant voiding***

Extensive voiding in a liquid-metal reactor (LMR) may be caused by a leak in the primary system, sudden release of fission gases, failure in the heat-transport system that causes gas bubbles to enter the coolant, or coolant overheating and vaporization. Usually, LMR plant designs are arranged with backup protection to mitigate the impact of vessel leakage or rupture, to the degree that large-scale loss-of-coolant accidents (LOCA) are extremely unlikely. Pool systems typically have a second guard vessel, and loop systems are normally double pipe and tank designs. Since the liquid-metal coolant is not pressurized under normal operation, a leak in the primary system will not automatically result in coolant boiling, as opposed to the situation in LWR's. In a sodium-cooled reactor, voiding may arise due to boiling out of coolant. This is prevented in a lead-bismuth system. In order for the lead-bismuth to get hot enough to boil ( $T_b=1940$  K), temperatures have to be above the melting point of steel ( $T_m=1700$  K). In that case, much larger reactivity changes may become available due to fuel or cladding relocation. Coolant can be expelled by the rapid escape of fission gases from ruptured fuel pins. Fission gas release is of concern for unvented and high burnup ADS fuels. Another possible mechanism for coolant voiding, without the precondition of steel melting, is the possibility of entrainment of air into the core from the cover gas region or steam/water during a failure in the steam generator, i.e., a so-called steam generator tube rupture (SGTR) event. In sodium plants, intermediate sodium-loops are introduced as a second physical barrier to minimize the consequences of SGTRs and to avoid violent chemical reactions between water and sodium in the primary system. Because lead/bismuth is chemically inert with water/steam, two-circuit designs are suggested, with the steam generators located in the primary system. In such designs, there will only be one barrier to fail in order to get high-pressure steam into the primary system. It is noted that the pressure on the steam side can be as high as 100-150 bars and low pressure on the metal side, about 1 bar. Thus, a significant head is available to push steam into the primary system or cause

overpressurization in the circuit, which could open further leakage paths. Normally, steam generator tube failures have a high enough probability occurrence to be considered in the licensing procedure. It is noteworthy that a steam-generator failure was the cause of a LOCA and radioactive contamination in a Russian lead/bismuth-cooled nuclear submarine in 1982 [76].

Results for a transient test case study of a postulated steam generator tube rupture event leading to extensive cooling voiding were presented in **Paper I**. The core model and fuels are the same as the previous study of the unprotected loss-of-flow event. In the following analysis, it is assumed that the coolant is swept upwards through the core, beginning at the lower cold-leg region, and the void front moves at the average coolant velocity through the core (2.5 m/s). Since the total height of the core plus plenum regions is 2.5 m, the passage occurs in 1 second. The transient calculation uses a reactivity history based on progressive axial voiding of the core. It is assumed that the void spreads axially and simultaneously in all subassemblies. The reactivity effect, as function of axial void level, is illustrated in Fig. 21a. Note that the reactivity effect is strongest for the CerCer fuel and most positive when the core has been voided up to slightly below the top of the active fuel region. The reactivity insertion rate is highest at core midlevel. As a coincidence, the maximum reactivity insertion due to coolant void corresponded to the initial subcritical reactivity of the CerCer core.

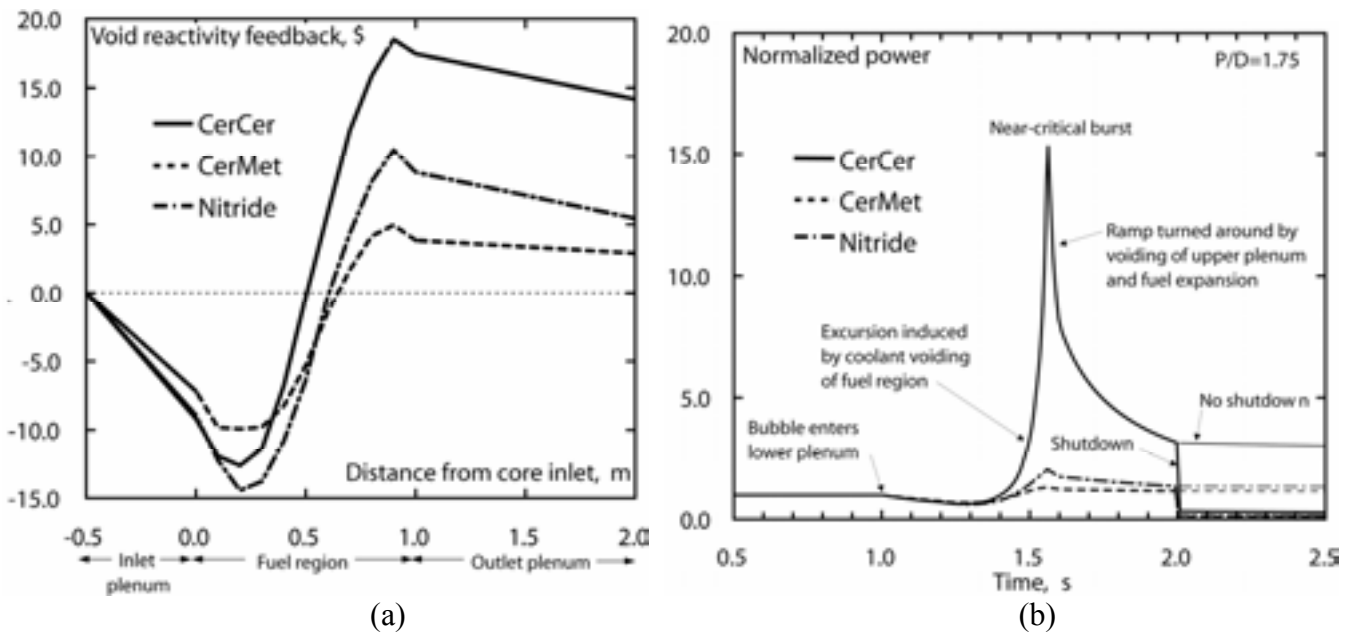


Fig. 21 Transient results for a postulated steam generator tube rupture accident. (a) shows the reactivity effect (\$) following progressive axial voiding of coolant beginning at the lower plenum. (b) Illustrates the transient power for the same accident.

The resulting power history is presented in Fig. 21b. The steam bubble reaches the lower plenum at 1 second after the steam generator failure. Initially, the bubble passage produces a negative reactivity effect due to increased neutron leakage, as the lower plenum is voided first. The power will find its peak as the reactivity reaches its maximum. The reactivity at peak power, is  $-0.2\%$ ,  $-12.3\%$ , and  $-6.8\%$ , respectively for the CerCer, CerMet, and nitride cores, the corresponding peak power is 15.3, 1.3, and 2.1, times the initial power. The power rise in the nitride and CerMet fueled cores is quite modest. The CerCer core, on the other hand, suffers from a sharp power peak. Except from coolant void, axial fuel expansion is the only feedback effect that has some impact on the transient. At peak conditions, the contribution from axial expansion provided an extra reactivity margin, which was sufficient to

maintain the reactor in the subcritical state, thereby limiting the magnitude of the peak. Radial core expansion is too slow to be of any significance. It was found that the flux shape in the voided state was similar to the initial shape, and power peaking factors were even lower. The power rise is halted when the void has extended to the top of the core and begins to void the upper plenum region. Judging from Fig. 21b, voiding of the upper plenum plays a vital role in reversing the accident. It is assumed that the beam is shutdown after 2 seconds.

Due to the strong positive reactivity effect, the CerCer system is subject to a sharp power peak, while the power rise in the nitride and CerMet fueled cores is quite modest, which simply confirms the importance of having a low coolant void reactivity value in a lead/bismuth system, despite of its high boiling temperatures.

### ***Safety performance in super-prompt critical transients***

Even if the probability for prompt critical transients can be made very low, the safety analyses usually require them to be investigated. Considering the high reactivity potentials available by core compaction (see TABLE 13) it is always possible to postulate an accident that will proceed into a prompt critical state. The resolution for the large FBR's was to demonstrate a low energetic potential (within the capabilities of the containment) of such accidents [66]. The large oxide cores relied on the presence of a strong Doppler effect to limit the energy yield (and pressure buildup) in a prompt critical reactivity transient. In such cores, the negative reactivity is provided by the Doppler broadening of resonances in primarily  $^{238}\text{U}$  resulting in a relative increase in resonance capture over resonance fission. Since the Doppler effect is inherent in the fuel, the feedback mechanism is completely passive. The resulting reactivity effect is applied immediately since the Doppler broadening occurs simultaneously with the temperature change. As is well-known, the Doppler effect is small for fuels dominated by MA. Hence, the prompt negative effects, might be insufficient to stop an excursion before energetic disassembly occurs. Here we treat a classical problem of reactor excursions, induced by a rapid reactivity ramp in systems with different prompt negative feedbacks. It may be postulated that the accident is caused by a loss-of-coolant (e.g. as a result of a major break in the primary system) and that some fuel is melted and the core collapses by gravity forming a supercritical configuration (traditional Bethe-Tait scenario).

Fig. 22 illustrates the essential characteristics of the transient in a MA-fueled ADS. The results are compared with calculations for a conventional sodium-cooled and MOX-fueled fast reactor ( $\text{U}_{0.8}\text{Pu}_{0.2}$ ) presented in the same graph. Consider at first the ADS with initial  $k_{\text{eff}}=0.97$ . The transient is driven by a linear reactivity insertion, 100  $\$/s$  (0.167  $\Delta k/s$ ), a value which is frequently related to core compaction/meltdown phenomena. It is further assumed that this reactivity ramp continues uninterminated. The value for the Doppler constant ( $T \cdot dk/dT$ ) as well as the effective delayed neutron fraction are chosen to simulate the conditions in the respective cores. The Doppler constant in the fast spectrum MA core ( $\text{Pu}_{0.4}\text{Am}_{0.6}$ ) is taken as  $2.0 \cdot 10^{-4}$  with a  $\beta_{\text{eff}}=0.167\%$ . The Doppler constant for the oxide fast reactor is  $8.1 \cdot 10^{-3}$  (see TABLE 11), which is about 40 times larger than the MA core. The corresponding ramp rate for the fast reactor is 50  $\$/s$  since the effective delayed neutron fraction ( $\beta_{\text{eff}}=0.34\%$ ) is about two times larger than the MA core. The Doppler effect contribution is assumed proportional to  $1/T$ , as in the case of large oxide-fueled fast reactor, where  $T$  is the average fuel temperature in the core. As comparison the Doppler coefficient decreases somewhat faster with temperature ( $T^{-3/2}$ ) in the smaller, highly enriched FR's. For the LWR's it approaches  $T^{-1/2}$ . The fuel heat-up is treated for the simple case of adiabatic boundary conditions for any additional heating above steady-state levels. This is a reasonable approximation considering the overall speed of the transient. The steady-state operational power density is  $\sim 1.3 \text{ W/mm}^3$ , which is fairly typical for the FBR as well an ADS employing

oxide fuel. During the transient, around 86% of the additionally produced fission energy is deposited in the fuel (~8% of the heat is deposited outside the fuel and 6% appears as decay heat which is not immediately affected by the transient). For simplicity, equal prompt neutron generations times ( $\Lambda=0.81 \mu\text{s}$ ) are applied for both cores. Reactivity contributions from core disassembly are not treated. The reactor behavior is described by the standard point kinetics equations with six delayed neutron groups coupled with a temperature dependent Doppler feedback.

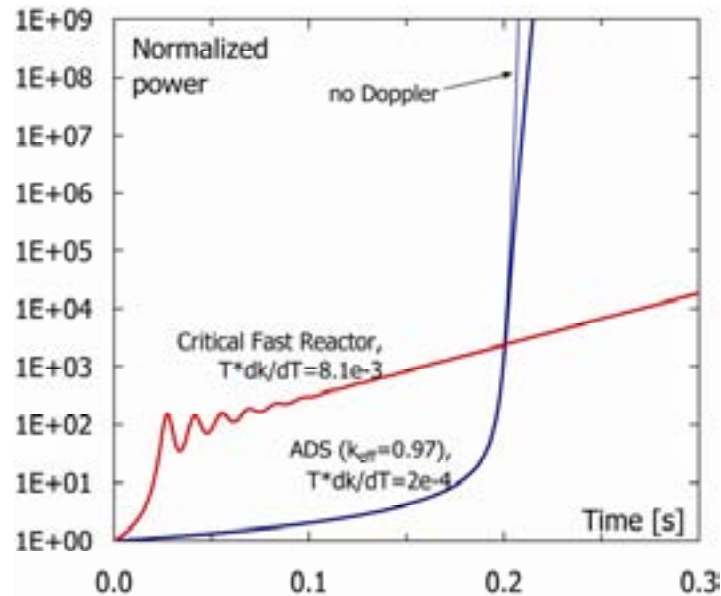


Fig. 22 Effect of Doppler feedback on prompt critical transients induced by a reactivity ramp insertion. Transients initiated from operating conditions in a conventional fast reactor with a large Doppler constant ( $T^*dk/dT=8.1 \cdot 10^{-3}$ ) and an ADS ( $k_{\text{eff}}=0.97$ ) with a small Doppler feedback ( $T^*dk/dT=2.0 \cdot 10^{-4}$ ). Core disassembly is neglected.

In the fast reactor the reactivity quickly reaches a prompt critical state. Prompt criticality is established around 20 ms after the onset of the transient. It follows that the power increases rapidly at first. However, as the temperature in the fuel increases, the negative Doppler feedback compensates the ramp-induced reactivity; this causes a decrease in reactivity and a corresponding power reduction. In the example given, the fast reactor is superprompt critical for 6 ms in connection with the first pulse. After the power is reduced, the rate of reactivity reduction by Doppler feedback slows down while the ramp drives the reactor to prompt criticality again, allowing for a second power surge. This causes the familiar damped oscillation in reactor power, where the maxima and minima occur when the reactivity passes through  $\beta$ . As the oscillations die-away, in the given example, the reactivity finds a balance at a level slightly below  $\beta$ . Since the Doppler effect contribution decreases with temperature ( $1/T$  dependence), the power tends to increase with time, but at a much slower rate than if the Doppler effect had not been present. It should be noted that progression with ever increasing power is physically unrealistic. At some point the ramp is terminated and the excursion is turned around by fuel displacement, possibly involving some vaporization. As first discussed by Bethe and Tait [67], rapid fuel motion is resisted by inertial effects and this may prolong the shutdown process, in which additional energy can be produced to enhance the very fast excursion. Under these conditions the Doppler effect is very effective [58], by reactivity reduction to subprompt critical values resulting in substantially lower energy releases.

The transient in the ADS is quite different according to the magnitude of the Doppler reactivity effect and the level of subcriticality. Since the reactivity in the ADS starts at a low

value (-\$18.5), the power increases slowly initially. Prompt criticality is reached at 195 ms. Because of the weak Doppler feedback the reactor settles on a fast period above prompt critical (\$1.4). As can be seen from the figure, the Doppler effect has an overall small effect on the transient. While no attempt has been made to calculate the disassembly process in this study, it is well-known [58] that a small Doppler can pose a serious threat to the containment structure in a maximum accident. At this point, it may be added that core disassembly generally starts when fuel boiling begins. The energy released during core disassembly is sensitive to the fuel boiling point [68], which may differ between the investigated fuels, but depends also on the fuel temperature at the start of the excursion. Higher starting temperature together with a low Doppler coefficient generally causes a reduction in the energy release as less reactivity is inserted [58]. One may realize that, starting from a highly subcritical state, the additionally produced heating during the subcritical reactivity insertion phase will cause higher fuel temperatures at the start of the excursion. Thus, subcriticality may in principle advance the shutdown process and limit the energy release. Nevertheless, it was found that for the rapid reactivity ramp (100 \$/s) the fuel temperature rise prior to approaching prompt criticality was rather small ( $\Delta\bar{T}_f \sim 170$  K). Hence, the majority of the temperature rise occurred in the prompt critical burst which suggests that the potential benefit may be small for rapid reactivity ramps ( $\sim 100$  \$/s). The subsequent fuel displacement would then mainly occur during the excursion phase and hence differences in the Doppler feedback plays a crucial role. It was found that the subcriticality is more effective in raising the starting temperature for slower reactivity ramps. For example, a reduction of the ramp rate from 100 \$/s to 10 \$/s increases the average fuel temperature by  $\sim 2700$  K at the onset of prompt criticality.

Longitudinal thermal expansion of the fuel column is a second feedback effect that may contribute with negative reactivity in a fast power excursion. This was not taken into account in the examples presented above. In most cases, fuel expansion may be considered as a prompt reactivity effect, although it is subject to certain time delay conceivably of some importance under disassembly conditions. It is a neutron leakage effect caused by a change in fuel density. Expansion coefficients for a standard MOX-fueled fast reactor and MA oxide-fueled ADS were calculated in **Paper II**. It was found to be similar for both cores and equal to  $-0.2 \cdot 10^{-5} \Delta k/T$ . This number refers to uniform temperature increase and axial expansion throughout the reactor. It is calculated for the intact core. Hence, it is well-defined during the startup period of the accident, but could be very misleading during the excursion phase involving partial melting. A partly melted core cannot be expected to possess the usual negative reactivity feedbacks from solid fuel expansion, so direct application to the meltdown problem may not be applicable. It is still of some interest to investigate the basic influence, partly due to its traditional usage in fast reactors. It may be noted that, thermal expansion effects were frequently included in the prompt excursion analyses of the early fast reactors (GODIVA, Fermi, EBR-I and EBR-II). These small and highly-enriched reactors essentially relied on this mechanism for early shutdown. Its effect on the present cores is illustrated in Fig. 23. Apparently, when axial expansion is included in the feedback description the characteristics of the transient are quite similar in the fast reactor core and the ADS. The essential difference is then the timing of the prompt critical burst. The results indicate that axial fuel expansion can stabilize a prompt critical accident in the ADS. But, a word of caution is added as the results are based on the simplified assumption of axial expansion reactivity feedback calculated for an intact core and as being proportional to the temperature rise during the entire accident.

To summarize, the analyses add to the statement that Doppler feedback in the typical minor actinide fueled ADS is too small to influence the development of a prompt critical accident. For slower reactivity insertions, subcriticality could possibly facilitate faster shutdown, but

may be less effective for fast insertions. To some degree axial expansion of the fuel can compensate for a small Doppler coefficient, but it cannot be considered as reliable as the Doppler effect in the general case. It depends on the engineering design and is subject to uncertainties in the thermo-mechanical behaviour of the fuel and overall conditions in the core.

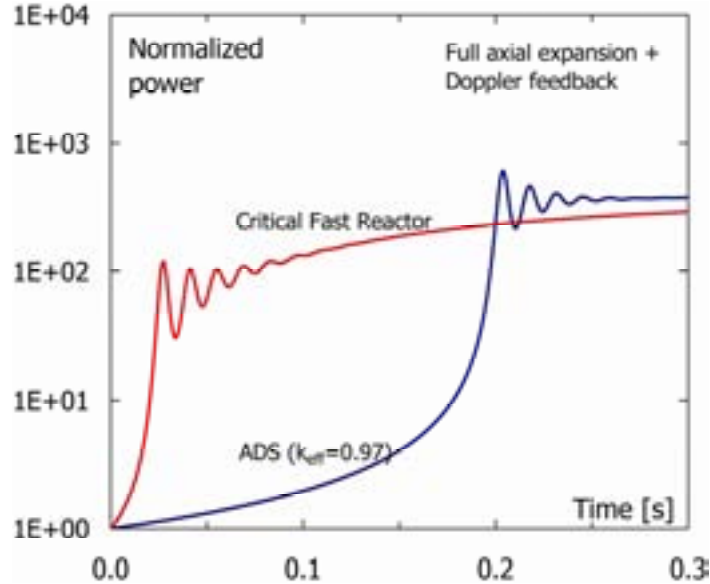


Fig. 23 Prompt critical transients in a conventional fast reactor and ADS ( $k_{\text{eff}}=0.97$ ) with axial expansion reactivity feedback included from the beginning through the entire transient.

### ***Computational performance of the point kinetics method***

The so-called “point kinetics approximation” is a widely used method for performing preliminary analyses of dynamic phenomena in nuclear reactors. It has been extensively applied for the transient design analysis of existing reactors and it forms the basis of many transient analysis computational codes. It is based on kinetics theory developed for critical reactor studies. While the utility of the point kinetics methodology for critical reactor analysis is well known, its applicability to source-driven subcritical systems is subject to investigation [77, 78]. Because the neutron balance equations that describe the response in source-driven reactors are fundamentally different from the problem characterizing critical reactors, it has been suggested [79] that the point kinetics technique may be inappropriate for ADS studies; it is nonetheless very popular and often used for analysing such systems. The computational performance of the point model in its application to ADS was investigated in **Paper III**.

#### ***Point kinetics theory***

The point kinetics equations were first derived by Henry [80]. Their limitations and capabilities for critical reactor analysis have been investigated in great detail [81-83]. The purpose behind the formulation of the kinetics equations is to derive a lumped model that describes the change in the average level of the flux, i.e., the integral of the neutron flux over the energy and the spatial domain. The point-kinetics equations for a source-driven system are derived in Appendix A. The equations are obtained by recasting the time-dependent diffusion (or transport) equation into:

$$\frac{dp(t)}{dt} = \frac{\rho(t) - \beta(t)}{\Lambda(t)} p(t) + \sum_k \lambda_k c_k(t) + s(t)$$

$$\frac{dc_k(t)}{dt} = \frac{\beta_k(t)}{\Lambda(t)} p(t) - \lambda_k c_k(t)$$

The above equations are usually referred to as the “point kinetics equations” or sometimes the “exact point kinetics equations” in a way to distinguish them from the simplifying assumptions applied in the point kinetics approximation. The new quantities,  $\beta$ ,  $\Lambda$ ,  $\rho$ ,  $s$ , and  $c_k$  that emerge in point kinetics equations are integral quantities and they arise only in the derivation of the point kinetics equations (more rigorous definitions of these quantities are given in Appendix A). This is realized since the basic time-dependent neutron diffusion equations do not involve these concepts. As pointed out by Ott [52], that as long as the exact definitions are applied in the calculation of the kinetics parameters (that implies full solution of the space-energy-time problem), the point kinetics equation is exact and completely equivalent to the basic, time-dependent diffusion (or transport) equation, but in a different form. This is true for critical as well as for subcritical systems. The error is introduced when an approximate representation of the time-dependent flux shape, e.g., the point kinetics approximation, is applied. In that case, a prefixed shape representation of the flux is used throughout the entire transient, only the “level” of that flux shape changes, i.e., first-order perturbation theory approach.

### ***Computational model***

Numerical testing was performed with coupled core dynamics calculations using the SAS4A/DIF3D-K code [84], see also Appendix B. The “exact” results are obtained from a direct numerical solution of the time-, space-, and energy-dependent multigroup diffusion equation. The direct solution is used as a standard of comparison for the point kinetics solution. One advantage of using the SAS4A/DIF3D-K program for the current task is that the direct solution method and the point kinetics procedure are implemented within the same code. This makes it straightforward to compare the underlying methods without worrying about consistency among different computational procedures and models. For example, the initial steady-state solutions, cross sections, thermal- and hydraulics treatments, and model specifications are all identical. More detailed specifications of the computational methods involved are given in **Paper III**.

The test model used in the present study is based on a previous OECD/NEA benchmark model [85]. The model pertains to an accelerator-driven, lead-bismuth cooled, and minor-actinide loaded transmuter core. The core consists of a central lead-bismuth target region and a homogenized fuel region surrounded by radial and axial reflectors (70% steel and 30% coolant). 114 fuel assemblies are included in the hexagonal-z representation; Fig 1 contains a plan view of a one-sixth symmetry section of the core. The height of the active core is 100 cm. The fuel consists of 2/3 minor actinides and 1/3 plutonium with a ZrN diluent;  $(\text{Pu}_{0.1}, \text{MA}_{0.2}, \text{Zr}_{0.7})\text{N}$ , where MA represents minor actinides such as Np, Am, and Cm. Fuel compositions correspond to plutonium discharge from UOX-fueled LWRs mixed with MA from a “double strata” strategy. Start-up core loading is used in the simulations. The fuel is further diluted with 71% ZrN.

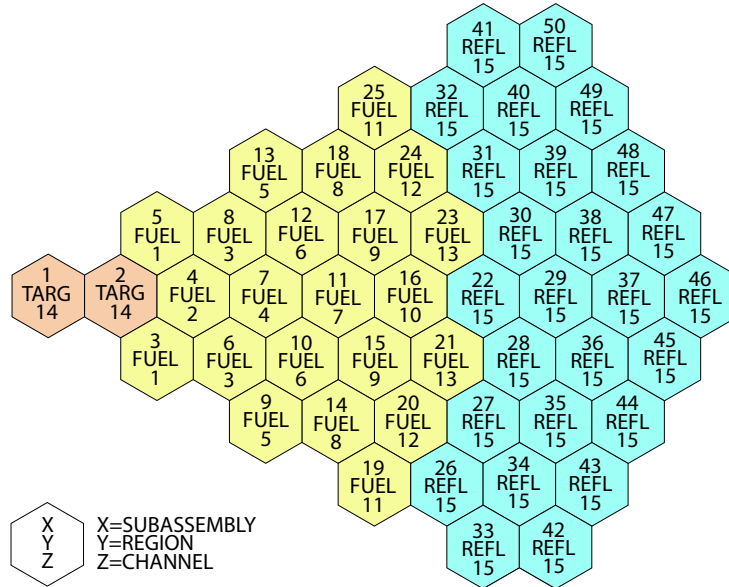


Fig. 24 One-Sixth Core Subassembly and Channel Assignment.

### Numerical results

Numerical solutions for three different categories of transients were analyzed. The test problems pertain to accident-type events in ADS's. The first category concerns alterations of the proton beam intensity, i.e., changes in the magnitude of the external neutron source (the spatial and energy distributions for the source neutrons are invariant). Secondly, localized reactivity insertions were examined. Finally, a flow reduction event is analyzed. The total power is extracted as a function of time, i.e., fission power plus decay power, as obtained in the direct solution and in the point kinetics solution. The transients are followed for 20.0 seconds. We further perform calculations at different subcritical levels, i.e.,  $k_{\text{eff}}$  values, to reveal any trends concerning performance characteristics. The initial effective multiplication constant is altered by changing the concentration of fuel diluents (ZrN). It will provide information on the numerical accuracy of the point kinetics solution as function of the level of subcriticality.

For accidents involving external source perturbations (both the source overpower transient and the source trip transient) the point method provided extremely accurate results. In fact, the results are indistinguishable as illustrated in Fig. 25a and Fig. 25b. The maximal deviations are 0.2% and 0.9% for the source overpowers and source trip transients, respectively. Maximum deviation occurs shortly after the source has been fully inserted/removed, followed by better agreement from that point and forward. Deviation from the point kinetics solution is an indication of flux shape changes. An external source perturbation, by itself, does not affect the reactivity. Hence, the only source for spatial distortion is due to reactivity feedbacks. The good agreement implies that the thermal feedbacks are small and/or distributed such that no noticeable flux deformation develops. Based on these results, it is expected that source disturbances can be described accurately by point kinetics.



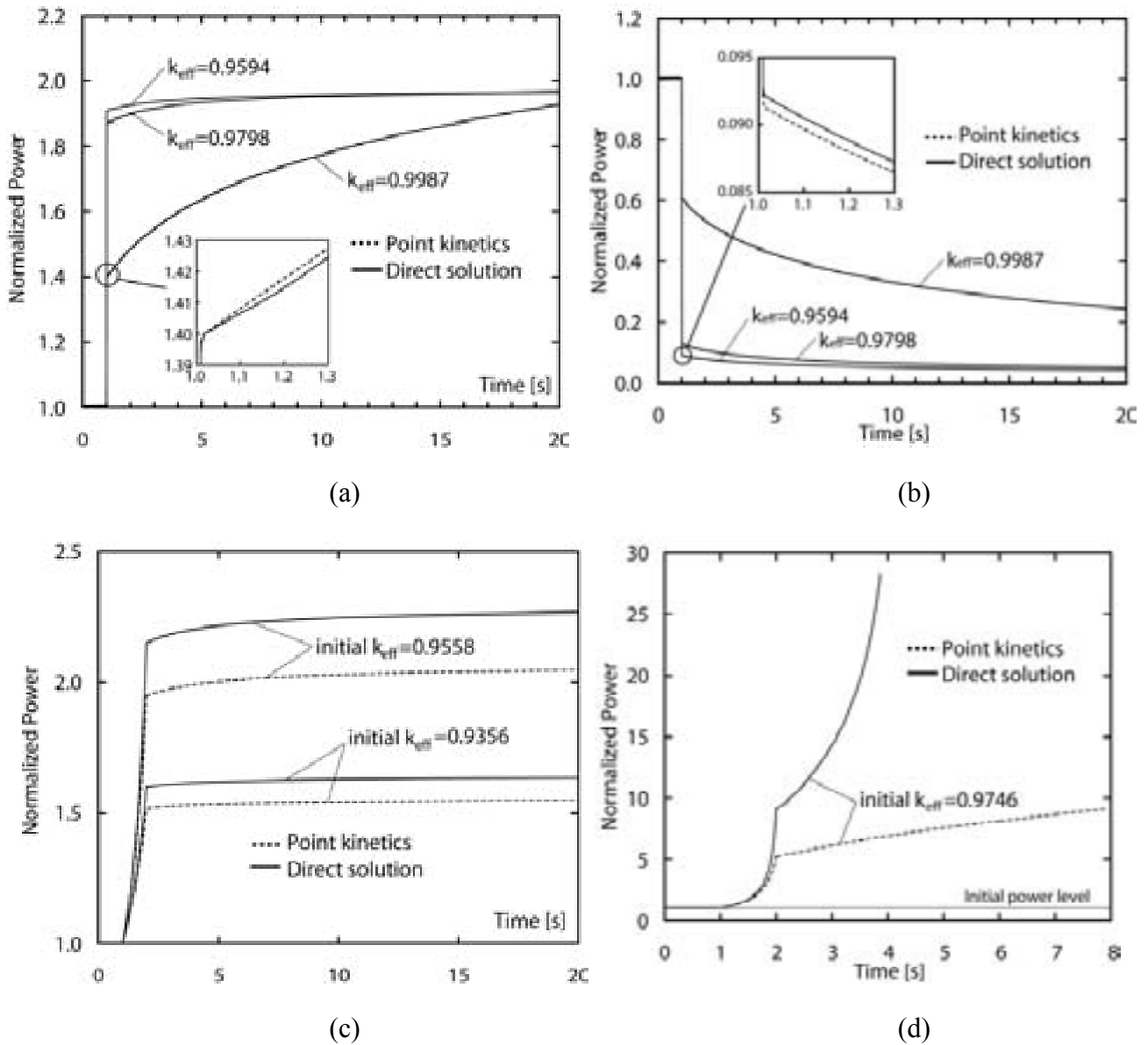


Fig. 25 Source overpower transient problem (a). Source trip transient (b). Reactivity insertion near core-center for cases with initial  $k_{\text{eff}}=0.9356$  (c) and  $k_{\text{eff}}=0.9558$  (c) and  $k_{\text{eff}}=0.9746$  (d).

Next, we consider the effect of local reactivity insertions, i.e., transients in which the point treatment is expected to be a poor approximation. It is assumed that a fuel subassembly is fully withdrawn at initial conditions and subsequently drops into the core during operation. Despite the somewhat remote likelihood of this scenario, it is useful for evaluating the performance of the underlying kinetics methods. The effect of reactivity insertion is investigated at two different positions; in one instant we move a subassembly close to core-center (subassembly no. 4 in accordance with the core map in Fig. 24) and in a second study it is inserted close to the core boundary (subassembly no. 16). The reactivity worth of the fuel subassembly near the core-center is approximately \$13 and \$4 for the subassembly at the core boundary. It is assumed that the region representing the absent subassembly is occupied with coolant at initial conditions. It is well known, from critical system analysis that for local reactivity insertion events, using the point kinetics technique to calculate the response can lead to significant errors. This is because the basic assumption is that the flux shape remains

constant. Comparison with the exact results shows that this is indeed the case. The point approximation severely underestimates the excursion for the case that is closest to the critical state, shown in Fig. 25d, but the results indicate better precision at lower  $k_{\text{eff}}$  levels, Fig. 25c. While the amount of reactivity insertion is essentially the same for all test configurations, it appears as if the flux spatial distortion decreases when the system is more subcritical. This behavior seems reasonable considering the reduced sensitivity to reactivity inputs in the subcritical state. When the fuel subassembly falls into the reactor, the neutron flux increases near this location due to a local increase in the fission rate. In the near-critical reactor, the neutrons are strongly multiplied, and the increase in the fission source produces a local deformation of the flux shape. In a deeply subcritical core, the neutrons are weakly multiplied therefore; the insertion of the subassembly has an overall smaller effect. Due to this lower sensitivity, flux distortions following a reactivity disturbance diminish as the  $k_{\text{eff}}$  decreases. In TABLE 17, the relative root-mean-square (*RelRMS*) deviation of the local peak-to-average flux (for all three-dimensional spatial nodes) with respect to the initial distribution is presented. Obviously, the *RelRMS* variation of the flux shape decreases as the core multiplication constant decreases, which gives further support to the previous argument.

TABLE 17

Relative root-mean-square (*RelRMS*) difference of the peak-to-average flux distribution with respect to the initial flux distribution following insertion of the subassembly near the core-center.

| Time [s] | RelRMS <sup>g</sup> peak-to-average flux |                         |                         |
|----------|--|-------------------------|-------------------------|
|          | Initial                                  | Initial                 | Initial                 |
|          | $k_{\text{eff}}=0.9356$                  | $k_{\text{eff}}=0.9558$ | $k_{\text{eff}}=0.9746$ |
| 1.2      | 0.9%                                     | 1.0%                    | 1.2%                    |
| 1.4      | 1.8%                                     | 2.2%                    | 2.6%                    |
| 1.6      | 2.8%                                     | 3.4%                    | 4.1%                    |
| 1.8      | 4.0%                                     | 4.7%                    | 5.7%                    |
| 2.0      | 5.2%                                     | 6.2%                    | 7.4%                    |
| 3.0      | 5.2%                                     | 6.3%                    | 7.8%                    |
| 20.0     | 5.4%                                     | 6.6%                    | -                       |

$$RelRMS = \sqrt{\frac{1}{N} \sum_{i=1}^N \left( \frac{p_i - p_{0_i}}{p_{0_i}} \right)^2}$$
 where N is the number of hex-Z nodes in the three-dimensional space and p is the local peak-to-average flux in each node. The subscript 0 denotes the initial state.

### ***Concluding remarks on the point kinetics approximation***

The results indicate that the point kinetics approximation is capable of providing highly accurate calculations in subcritical systems. The results suggest improved precision at lower  $k_{\text{eff}}$  levels. The reduced sensitivity to system reactivity perturbations in a subcritical state effectively mitigates any spatial distortions. Because a source-driven subcritical reactor approaches a stationary state (in response to source or reactivity changes), the error of the point kinetics method becomes essentially bounded. Prompt adjustment of the flux shape prevails since the delayed neutrons are less influential (in a critical reactor the delayed neutrons tend to retard the shape transition). In general, the flux shape in a fast neutron spectrum shows strong space-time coupling, i.e., local perturbations will quickly spread throughout the reactor. This is usually attributed to the relatively large mean free path of fast neutrons and to the comparatively compact core size of a fast reactor. All together these characteristics are favorable from a point kinetics view of application to fast spectrum ADS systems.

## **Accelerator reliability**

In accelerator-driven system designs, the neutron source is the controller of the chain reaction. Power fluctuations caused by accelerator beam interruptions (trips) enforces thermal transients to structures. Multiple shutdown events may result in thermal fatigue [86], which can cause premature failure. This problem is of particular concern for ADS's because of the possibility for frequent beam interruptions. ADS applications impose a new requirement on the design and operation of high-power proton accelerators, namely that of extremely high reliability of the beam.

**Paper VI** examines the reliability and availability of the proton accelerator facility at the Los Alamos Neutron Science Center (LANSCE). Beam trips and failure causes were collected based operational data records, accelerator logbook and beam monitor data. Mean Time Between Failure and Mean Down Time estimates are obtained for typical accelerator components. The availability is expressed as the ratio of the achieved beam time to the scheduled beam time. Reliability has to do with the number and durations of beam interrupts in that interval. It is typically determined by the mean time between failure and the mean down time of a trip. In the case of thermal cycling the reliability to beam trips and fluctuations has a critical influence. The LANSCE system is a linear proton accelerator. The accelerator delivers two proton beams at 800 MeV: the H<sup>+</sup> and the H<sup>-</sup> beam. The H<sup>+</sup> beam may deliver 1.25 mA current (routine operation is at 1 mA) and the H<sup>-</sup> beam delivers 70 μA. Each injector system includes a 750 keV Cockcroft-Walton type generator. Both ions are accelerated simultaneously in one and the same structure. The low energy section of the accelerator is an Alvarez Drift Tube Linac (DTL). The drift tube linac accelerate the protons from 750 keV to 100 MeV. The high energy section is a Side Coupled Linac (SCL). The SCL may accelerate protons up to 800 MeV. After acceleration the H<sup>+</sup> and H<sup>-</sup> beams are separated and divereted into different target areas.

Beam operational data is reported in Fig. 26. The reliability of the H<sup>+</sup> and the H<sup>-</sup> beams are investigated separately. The analysis considers scheduled accelerator operation of the H<sup>+</sup> beam for 1997 and of the H<sup>-</sup> beam for 1996 and 1997. From the figure it is obvious that the accelerator is exposed to many beam trips with short duration. The main cause for failure is electric breakdown in the high-voltage column of the injector. The characteristic of injector failure is short outage time, often in the order of 15-20 seconds, the time it takes to reset the trip and re-energize the generator. The annual interrupttion rate in the LANSCE linac is typically on the order of 10<sup>4</sup> per year. But that includes many interruptions of very short duration. Most of these trips are momentary effects, for which the beam has to be interrupted only for a very short period, while the offending system is restored to operation by automated recovery systems. Interruptions with duration shorter than 1 second are not detrimental because the thermal transients in the reactor are then very small. This leaves perhaps 10<sup>3</sup> annual interrupts of duration longer than 1 minut, which require some kind of operator intervention. What beam trip rate is the maximum acceptable limit for a high power subcritical reactor? If we compare the above performance data with an average of 2-3 unscheduled shutdowns per year in LWRs, the necessary reliability improvement appears to be tremendous. On the other hand, if the maximum acceptable trip rate can be relaxed to 10-100 trips/year, the goal seems to be more realistic. One should take into account that current operating proton linacs were designed with high beam availability as a key goal, but the frequency of beam interrupts was not a major issue.

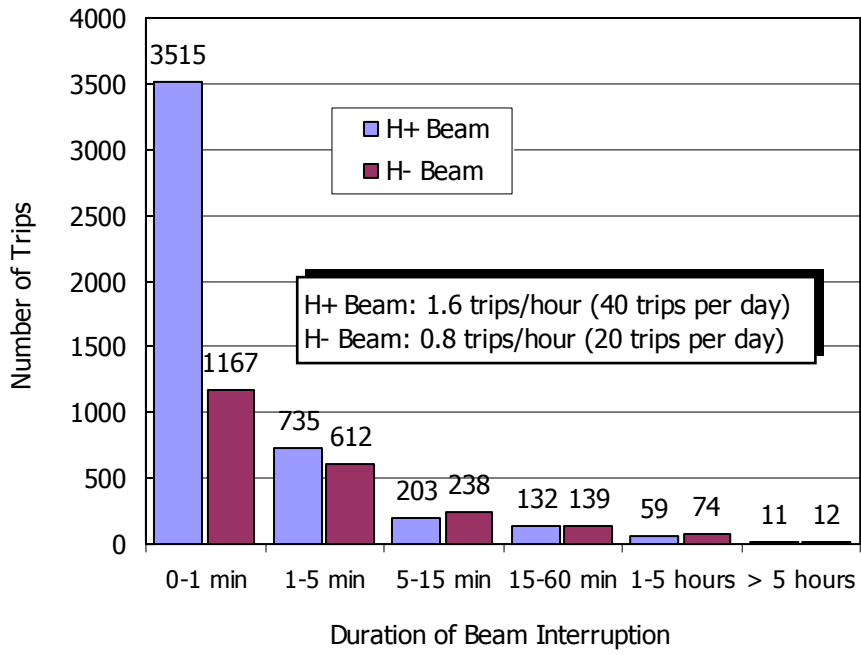


Fig. 26 Beam failure statistics of the LANSCE accelerator facility

# Conclusions

The thesis analysed and discussed the safety performance of accelerator-driven nuclear reactors, with emphasis on design features and safety characteristics under normal operation and hypothetical accident sequences. The studies concerned mainly lead-bismuth cooled accelerator-driven reactors operating on a fast neutron spectrum and employing transuranic fuel. Major consideration was given to the potential threat of coolant voiding. The thesis examined the performance of the point kinetics approximation in subcritical systems and also included a study of the proton beam reliability in accelerator facilities.

The ADS is a non-self-sustaining, subcritical reactor driven by an external neutron source, whose kinetics characteristics differ significantly from conventional (critical) nuclear reactors. The critical operating state represents a sensitive balance between the production rate of neutrons through fission and the neutron loss rate and a relatively small off-balance in these two quantities can lead to large deviations in power. In contrast, a subcritical reactor is inherently stable to reactivity changes within the subcritical range or changes in the external neutron source. Under such conditions, the neutron population will adjust to a new stationary level. In the response to a reactivity insertion accident this feature leads to a distinct safety advantage over critical reactor operation, distinguished by high operational stability and additional margins for positive reactivity insertion. In response to accidents featuring negative reactivity feedbacks, however, subcritical operation is less favourable since the power will not drop as much as in a critical reactor.

Given a uranium-free fuel based on minor actinides, the inherent core safety characteristics deteriorate. Parametric analyses indicate that the addition of minor actinides to a fast spectrum reactor lowers the Doppler coefficient and reduces the effective delayed neutron fraction. Critical fast reactors rely heavily on the delayed neutrons and the Doppler effect to achieve smooth power control during normal operation and protection against severe reactivity insertion accidents. In addition, the void reactivity effect becomes increasingly positive in uranium-free and liquid-metal cooled minor actinide cores, especially using sodium coolant. It thus appears that operation of such cores in a critical state would be very difficult. The specific studies of transient operating characteristics and unprotected accident sequences indicate that lead-bismuth cooled accelerator-driven reactors can be effective in addressing the low effective delayed neutron fraction and the high coolant void reactivity that comes with the minor actinide fuel. Here, the elementary factor in preventing supercritical excursion is the built-in subcritical margin. Adjustment of the initial level of subcriticality with regards to the magnitude of the inserted reactivity provides an effective means to overcome the deteriorated effective delayed neutron fraction and the high void value.

The situation with the absent prompt negative Doppler feedback is more complicated. In a conventional fast reactor, the Doppler effect is especially valuable under super prompt critical accidents, in which it will advance the shutdown process and thus reduce the energy release and limit the destructive force on the containment. The first counteractive measure would be to somehow preclude accidents that might lead to prompt-critical conditions from beginning. Obviously, adjustment of initial subcriticality is a step in the right direction. Minimization of the intrinsic reactivity potentials is a second step to preclude prompt critical conditions. Other means could involve adjustment of the fuel design and composition or changes in the

geometrical arrangement of the core to minimize the risk for core compaction and accommodate early dispersal mechanisms. But even beyond such measures, a large negative Doppler effect or some other inherent prompt negative feedback mechanism might ultimately be considered necessary to assure public safety even in the extremely unlikely event of core disruptive accident. Considering the large reactivity vested in a minor actinide core it is always possible to postulate an accident that will proceed into prompt critical conditions, that is a principal difficulty.

The thesis further underlined the importance of a having a low coolant void reactivity value in a lead-bismuth system, despite the high boiling temperature of the coolant. A steam generator tube rupture event was identified as a potential threat, which could lead to extensive voiding in current accelerator-driven design proposals. The design studies found favorable inherent safety features for a molybdenum-based Ceramic-Metal (CerMet) fuel. Detailed analyses found that the point kinetics approximation is capable of providing highly accurate transient calculations of subcritical systems. The results suggest better precision at lower  $k_{\text{eff}}$  levels, which is an effect of the reduced sensitivity to system reactivity perturbations in a subcritical state. It is recognized that the accelerator is responsible for frequent beam interruptions and this is of concern for accelerator-driven nuclear reactors because of the risk for thermal cycling and premature failure. It is clear that extensive improvement in the mean-time between beam failures is required.

# Appendix A:

## Reactor Kinetics Equations

Here we review shortly the derivation of the conventional kinetics equations. These were first derived by Henry [80]. The derivation is presented here to serve as a basis for discussion of applications to source-driven systems. For convenience, the derivation proceeds along the lines suggested by Henry [87] with minor modification. An independent source term is incorporated to include neutrons supplied by the external source. The starting-point is the time-dependent continuous energy diffusion equation<sup>1</sup>. In shorthand operator notation it can be written as:

$$\frac{1}{v} \frac{\partial \Phi}{\partial t} = (\mathbf{F}_p - \mathbf{M})\Phi + \sum_k \lambda_k C_k \chi_{dk} + S \quad (1a)$$

and completed with the balance equation for the delayed-neutron precursors

$$\frac{\partial C_k}{\partial t} = -\lambda_k C_k + \int_0^\infty v_{dk} \Sigma_f(\mathbf{r}, E', t) \phi(\mathbf{r}, E', t) dE' \quad (1b)$$

$\Phi = \phi(\mathbf{r}, E, t)$  is the time-dependent neutron flux. For simplicity of notation, the functional dependence in Eq (1a) and (1b) has been suppressed.  $\mathbf{M}$  and  $\mathbf{F}_p$  are the usual “migration and loss operator” and the “prompt neutron production operator”, respectively. These correspond to:

$$\begin{aligned} \mathbf{F}_p \Phi &= \chi_p(E) \int_0^\infty v_p \Sigma_f(\mathbf{r}, E', t) \phi(\mathbf{r}, E', t) dE' \\ \mathbf{M} \Phi &= -\nabla \cdot D(\mathbf{r}, E, t) \nabla \phi(\mathbf{r}, E, t) + \Sigma_t(\mathbf{r}, E, t) \phi(\mathbf{r}, E, t) \\ &\quad - \int_0^\infty \Sigma_s(\mathbf{r}, E' \rightarrow E, t) \phi(\mathbf{r}, E', t) dE' \end{aligned}$$

<sup>1</sup>In his original work, Henry derived the reactor kinetics equations starting from the time dependent neutron transport equation, we chose not to proceed along this path, but rather to utilize the diffusion approach as outlined in his textbook.

The purpose behind the formulation of the kinetics equations is to derive a lumped model that describes the change in the average level of the flux, i.e., the integral of  $\phi(\mathbf{r}, E, t)$  over the energy and the spatial domain. For that reason, the neutron flux is factorized in the form  $\phi(\mathbf{r}, E, t) = p(t) \cdot \psi(\mathbf{r}, E, t)$ . It is noted that flux factorization is not an approximation, in contrast to separation of variables. In the former case, the neutron spatial and energy distributions may still depend on time. However, it is necessary to impose a constraint condition to define precisely the two new functions,  $p(t)$  and  $\psi(\mathbf{r}, E, t)$ , that arise in the factorization procedure:

$$\int_V \int_0^\infty \frac{w(\mathbf{r}, E) \psi(\mathbf{r}, E, t)}{v(E)} dEdV = 1 \quad (2)$$

The constraint condition states that the shape function,  $\psi(\mathbf{r}, E, t)$ , is normalized, for all  $t$ , in such a manner that the integral, Eq. (2), over all energy and space is held constant (normally taken as unity) in time. Prior to integration over space and energy, Eq. (1a) and (1b) is multiplied with a weight function,  $w(\mathbf{r}, E)$ . Introducing a weight function is not a requirement, but it allows manipulation of the kinetics equations in a way that simplifying assumptions (such as the point kinetics approximation) can be applied more effectively. It is emphasized, that the weight function can be any function that is defined over the same energy and spatial domain as the flux. To preserve generality, the following derivation will not employ a specific weight function.

$p(t)$  is sometimes called the amplitude function and it is defined according to:

$$p(t) = \int_V \int_0^\infty \frac{w(\mathbf{r}, E) \phi(\mathbf{r}, E, t)}{v(E)} dEdV \quad (3)$$

Thus, under the constraint condition given in Eq. (2),  $p(t)$  can be represented as in Eq. (3) and hence it is proportional to the total number of neutrons present in the reactor at any time.

Next, Eq. (1a) and (1b) are multiplied with the weight function and the neutron flux is substituted with the factorized functions. The equations are then integrated with respect to space and energy. After some manipulations, we arrive at the conventional point kinetics equations:

$$\frac{dp(t)}{dt} = \frac{\rho(t) - \beta(t)}{\Lambda(t)} p(t) + \sum_k \lambda_k c_k(t) + s(t) \quad (4a)$$

$$\frac{dc_k(t)}{dt} = \frac{\beta_k(t)}{\Lambda(t)} p(t) - \lambda_k c_k(t) \quad (4b)$$

The new quantities,  $\rho$ ,  $\beta$ ,  $\Lambda$ ,  $\lambda_k$ ,  $s$ , and  $c_k$  that emerge in Eqs. (4) are the integral quantities identified with the following definitions:

$$\beta(t) = \sum_k \beta_k(t)$$

$$\beta_k(t) = \frac{1}{F(t)} \int \int w \sum_k \mathbf{F}_{dk} \psi dEdV$$



$$\rho(t) = \frac{\int \int w(\mathbf{F}_p - \mathbf{M})\psi dEdV}{F(t)}$$

$$\Lambda(t) = \frac{1}{F(t)} \int \int \frac{w\psi}{v} dEdV$$

$$s(t) = \frac{\int \int wSdEdV}{\int \int \frac{w\psi}{v} dEdV}$$

$$c_k(t) = \frac{\int \int wC_k \chi_{dk} dEdV}{\int \int \frac{w\psi}{v} dEdV}$$

The definition of  $F(t)$  is:

$$F(t) = \int \int w(\mathbf{F}_p + \sum_k \mathbf{F}_{dk})\psi dEdV$$

where the delayed neutron production operators  $\mathbf{F}_{dk}$  are defined similar to the prompt neutron production operator.

Henry [80], called Eqs. (4) the “conventional kinetics equations”. Today they are usually referred to as the “point kinetics equations” or sometimes the “exact point kinetics equations” in a way to distinguish them from the simplifying assumptions applied in the point kinetics approximation.

## **Appendix B:**

### **Short Summary of the SAS4A Code**

The SAS4A/SASSYS-1 [69] code is an integrated safety analysis computer code for the analysis of reactor plant transients in liquid-metal cooled reactors. The development of the SAS family of computer codes began at Argonne National Laboratory in the middle of the 1960's. The acronym SAS is an abbreviation for the Safety Analysis Section of the Reactor Analysis Division at Argonne. Over the years, SASSYS-1 has been employed extensively in the U.S. liquid metal reactor development programs. It has been the principal tool for the analysis of accidents in the licensing of the Fast Flux Test Facility (FFTF) and the Clinch River Breeder Reactor Plant (CRBRP) and in the passive safety design evaluation of the Integral Fast Reactor (IFR). Traditionally, the SAS code is used to track the initial phase of a core disruptive accident, through coolant heat-up and boiling, fuel element failure, and fuel melting and relocation. The information obtained can then be used to determine whether a noncritical and permanently cooled configuration could be established or whether there is a remote possibility for recriticality, and in that case provide the initial conditions for the disassembly phase.

The SAS4A code is built on a multiple-channel thermal-hydraulics core treatment coupled with a point kinetics neutronics model with reactivity feedbacks. Reactivity feedbacks are calculated from each channel. A channel contains a fuel pin, its associated coolant, and a fraction of the structure of the subassembly casing. Usually a channel represents an average pin within a subassembly or a group of similar subassemblies. The SASSYS-1 core treatment is built on the same models as SAS4A. In addition, SASSYS-1 is combined with detailed thermal-hydraulic models of the primary system and secondary coolant circuits and balance-of-plant steam/water circuit, including pumps, plena, pipes, valves, heat exchangers and steam generators. Models for two-phase coolant thermal-hydraulics, fuel and clad melting and relocation events were developed for sodium-cooled reactors with oxide fuel and stainless steel clad or specialized metallic fuel. Many of these models were validated with experimental test data from the EBR-II, FFTF, and TREAT reactors [88-90]. More recently, the code has been adapted to enable the analysis of heavy liquid-metal cooled reactor designs and accelerator-driven systems. The SAS4A has been coupled to the DIF3D-K [91] and VARIANT-K [92, 93] nodal spatial kinetics codes to provide accurate analysis of coupled spatial kinetics and thermal-hydraulics problems [94].

# Bibliography

- 1 R. G. Cochran and N. Tsoulfanidis, *The Nuclear Fuel Cycle: Analysis and Management*, Publ. American Nuclear Society, La Grange Park, IL (1990).
- 2 Statens strålskyddsinstitutets föreskrifter om kontroll vid in- och utförsel av radioaktivt avfall (SSI FS 1995:4).
- 3 EU Directive 92/3/Euratom on the supervision and control of shipments of radioactive waste between Member States and into and out of the Community.
- 4 DOE Order 5820.2 (1984) and replaced by 5820.2A in 1988, both titled "Radioactive Waste Management"
- 5 Miljöbalk (1998:808) 15 kap., 1§.
- 6 Statens strålskyddsinstitutets föreskrifter om hantering av radioaktivt avfall och kärnavfall vid kärntekniska anläggningar - bakgrund och kommentarer (SSI FS 2001:18).
- 7 IAEA Classification of radioactive waste. A safety guide. Safety Series No. 111-G-International Atomic Energy Agency.
- 8 M. D. Lowenthal, "Radioactive-Waste Classification in the United States: History and Current Predicaments," Lawrence Livermore National Laboratory Report, 1997, UCRL-CR-128127.
- 9 Power Reactor Information System (PRIS), Operational & Under construction Reactors by Type as of 21<sup>st</sup> Oct. 2004.
- 10 K. Fukuda, et al., "IAEA Overview of global spent fuel storage," IAEA-CN-102/60, International Conference on Storage of Spent Fuel from Power Reactors, Vienna, 2-6 June (2003).
- 11 "A European Roadmap for Developing Accelerator Driven Systems (ADS) for Nuclear Waste Incineration", ENEA, April 2001, ISBN 88-8286-008-6.
- 12 H. Bailly, D. Menessier, and Prunier C, *The Nuclear Fuel of Pressurized Water Reactors and Fast Neutron Reactors*, p. 167, Lavoisier Publishing, Paris (1999).
- 13 International Commission on Radiological Protection (ICRP), "Age-dependent dose to members of the public from intake of radionuclides: Part 5 compilation of ingestion and inhalation dose coefficients," *Annals of the ICRP*, Volume 26, Issue 1, Pages 1-91 (1996). Also included in ICRP Publication 72.
- 14 W. G. Sutcliffe, et al., "A Perspective on the Dangers of Plutonium," Lawrence Livermore National Laboratory, Livermore, CA, UCRL-JC-118825 (1995).
- 15 G. Choppin, J. O. Liljenzin, and J. Rydberg, *Radiochemistry and Nuclear Chemistry*, 2nd edition, Butterworth-Heinemann, Oxford, 1995.
- 16 International Commission on Radiological Protection (ICRP), ICRP Publication 60, 1990.
- 17 U.S. National Cancer Institute, "Lifetime Risk of Dying From Cancer, U.S. Total 1999-2001"

- 18 D. S. Myers, "The Biological Hazard and Measurement of Plutonium," Lawrence Livermore National Laboratory, Livermore, CA, UCRL-76571 (1975).
- 19 C. M. Koplik, M. F. Kaplan, and B. Ross, "The safety of repositories for highly radioactive wastes," *Reviews of Modern Physics*, Vol. 54, No. 1, January 1982.
- 20 SR 97 - Deep repository for spent nuclear fuel. SR 97 - Post-closure safety. SKB Technical Report TR-99-06, November 1999.
- 21 B. L. Cohen, "High-level radioactive waste from light-water reactors," *Reviews of Modern Physics*, Vol. 49, No. 1, January 1977.
- 22 A.G. Croff et al., A Preliminary Assessment of Partitioning and Transmutation as a Radioactive Waste Management Concept, ORNL/TM-5808, September 1977.
- 23 A.G. Croff and J.O. Blomeke, Actinide Partitioning-Transmutation Program Final Report. I. Overall Assessment, ORNL-5566, (1980).
- 24 OECD/NEA report, Accelerator-driven Systems (ADS) and Fast Reactors (FR) in Advanced Nuclear Fuel Cycles – A Comparative Study, OECD 2002.
- 25 T. E. Marceau, et al., Hanford Site Historic District: History of the Plutonium Production Facilities, 1943-1990. Columbus: Battelle Press, 2003.
- 26 U.S. Department of Energy, Linking Legacies: Connecting the Cold War Nuclear Weapons Production Processes to Their Environmental Consequences. DOE/EM-0319, Washington, D.C (1997).
- 27 P. Seltborg, "External Source Effects and Neutronics in Accelerator-driven Systems," Licentiate Thesis, Royal Inst. of Technology (2003).
- 28 E. P. Horwitz, W. W. Schulz, "The TRUEX Process: A vital tool for disposal of US defense nuclear waste in New separation chemistry for radioactive waste and other specific applications," *Elsevier Applied Science* (1991) 21-29.
- 29 Innovative Technology Summary Reports, *TRUEX/SREX Demonstration*, Prepared for the U.S. Department of Energy, DOE/EM-0419, OST Reference #347, December 1998.
- 30 D. Serrano-Purroy, et al., "Development of a DIAMEX process using high active concentrate," *Proceedings of the International Workshop on P&T and ADS development 2003*, SCK-CEN Club-House, Belgium, October 6-8, 2003.
- 31 OECD/NEA Status and Assessment Report on Actinide and Fission Product Partitioning and Transmutation, May 1999.
- 32 Y. I. Chang, "The Integral Fast Reactor", *Nucl. Technol.*, 88, 129 (1989).
- 33 A. V. Bychkov, et al., "Pyro-electrochemical reprocessing of irradiated FBR-MOX fuel, III. Experiment on high burn-up fuel for the BOR-60 reactor," *GLOBAL'97* (Proc. Int. Conf. Yokohama, Japan, 1997) pp 912-917 (1997).
- 34 C. E. Stevens, *The EBR-II Fuel Cycle Story*, American Nuclear Society, La Grange Park, Ill. (1987).
- 35 IAEA-TECDOC, Implications of Partitioning and Transmutation in Radioactive Waste Management, in publication (2004).
- 36 W. Bernnat, et al., PWR benchmarks from OECD working party on physics of plutonium recycling, in *Proceedings of the International Conference on Evaluation of Emerging Nuclear Fuel Cycle Systems*, GLOBAL'95, page 627, ANS, Versailles, France, September 11-14, 1995.
- 37 D. Albright and K. Kramer, "Plutonium Watch -- Tracking Civil Plutonium Inventories," Institute for Science and International Security, June 2004

- 38 M. Bunn, S. Fetter, J. P. Holdren, B. van der Zwaan, "The Economics of Reprocessing vs. Direct Disposal of Spent Nuclear Fuel," Project on Managing the Atom, Belfer Center for Science and International Affairs, John F. Kennedy School of Government, Harvard University, December 2003.
- 39 Article by C. G. Lawson and C. Krause, "Nuclear Documenting history: Minutes of the New Piles Committee meetings," Nuclear News, November 2004.
- 40 E. Teller, "Fast Reactors: Maybe," Nuclear News, August 1967.
- 41 M. Cometto, Standardisation des outils de calcul pour les ADS et leur application à différents scénarios de transmutation de déchets, Doctoral theses EPFL Lausanne (2002).
- 42 A. E. Waltar and A. B. Reynolds, Fast Breeder Reactors, Pergamon Press, New York (1981).
- 43 T. Wakabayashi, et al., "Feasibility studies of plutonium and minor actinide burning in fast reactors," Nuclear Technology 118 (1997) 14.
- 44 V. Berthou a, C. Degueldre, J. Magill, "Transmutation characteristics in thermal and fast neutron spectra: application to americium," Journal of Nuclear Materials 320 (2003) 156–162.
- 45 J. Tommasi, M. Delpech, J.-P. Grouiller, and A. Zaetta, Nuclear Technology 111, (1995) 133.
- 46 W. Yang and H. Khalil, "Neutronics design studies of an LBE cooled ATW blanket," IAEA-TECDOC--1356, Proc. of the Technical Committee Meeting on Core Physics and Engineering Aspects of Emerging Nuclear Energy Systems for Energy Generation and Transmutation, Argonne (IL), 28 Nov - 1 Dec. (2000).
- 47 H. Murata and T. Mukaiyama, "Fission reactor studies in view of reactor waste programmes," Atomkernenergie – Kerntechnik, 45 (1984) 23-29.
- 48 W. S. Yang, Y. Kim, R. N. Hill, T. A. Taiwo, H. S. Khalil, "Long-Lived Fission Product Transmutation Studies," Nuclear Science and Engineering, 146, 291-318 (2004).
- 49 J. Magill, H. schwoerer, F. Ewald, J. Galy, R. Schenkel, R. Sauerbrey, "Laser transmutation of iodine-129," Appl. Phys. B 77, 387–390 (2003).
- 50 APT Conceptual Design Report, LANL Report LA-UR-97-1329, April 1997.
- 51 G. R. Keeping, Physics of Nuclear Reactors, p. 99, Addison-Wesley Publishing Co., Reading Massachusetts (1965).
- 52 K. O. Ott and R. J. Neuhold, Introductory Nuclear Reactor Dynamics, American Nuclear Society, LaGrange Park, Illinois, USA (1985).
- 53 K. Tucek, Neutronic and Burnup Studies of Accelerator-driven Systems Dedicated to Nuclear Waste, Ph. D. Thesis, Royal Institute of Technology (2004).
- 54 W. Maschek, et al., "Safety Improvements for ADS Transmuters with dedicated Fuel," Proc. of the AccApp/ADTTA 2001 Meeting, Reno, November 11-15, American Nuclear Society (2001).
- 55 K. Tucek, J. Wallenius, and W. Gudowski, "Coolant void worths in fast breeder reactors and accelerator driven transuranium and minor actinide burners," Annals of Nuclear Energy, accepted for publication (2004).
- 56 J. Wallenius, K. Tucek, and W. Gudowski, "Safety analysis of nitride fuels in cores dedicated to waste transmutation," Proc. 6<sup>th</sup> Information Exchange Meeting on Actinide and Fission Product Partitioning and Transmutation, Madrid, December 11-13, OECD/NEA (2000).

- 57 H.H. Hummel and D. Okrent, *Reactivity Coefficients in Large Fast Power Reactors*, p. 82, American Nuclear Society (1970).
- 58 R. A. Meyer, B. Wolfe, and N. F. Friedman, "A Parameter Study of Large Fast Reactor Meltdown Accidents," Proc. Conf. on Safety, Fuels, and Core Design in Large Fast Power Reactors, ANL-7120, Argonne Natl. Lab., Oct. 11-14 (1965).
- 59 D. D. Freeman, "SEFOR Experimental Results and Applications to LMFBR's," GEAP-13929, General Electric Co., 1973.
- 60 H. K. Fauske, "Some Comments on Cladding and Early Fuel Relocation in LMFBR Core Disruptive Accidents," *Trans. Amer. Nucl. Soc.*, 21 (1975) 322-323.
- 61 K. Tsujimoto, T. Sasa, K. Nishihara, H. Oigawa, and H. Takano. "Neutronics design for lead-bismuth cooled accelerator-driven system for transmutation of minor actinides," *J. Nucl. Sci. Tech.*, 41:21, 2004.
- 62 D. C. Wade and E. K. Fujita. "Trends Versus Reactor Size of Passive Reactivity Shutdown and Control Performance," *Nucl. Sci. Eng.*, 103:182, 1989.
- 63 Nuclear Regulatory Commission, General Design Criterion 11 - Reactor inherent Protection, Appendix A to Part 50--General Design Criteria for Nuclear Power Plants.
- 64 J. Cahalan, Argonne Natl. Lab, Personal communication (January, 2005).
- 65 NUREG-1368, "Preapplication Safety Evaluation Report for the Power Reactor Innovative Small Module (PRISM) Liquid-Metal Reactor," February 1994.
- 66 H. K. Fauske, "The Role of Core-Disruptive Accidents in Design and Licensing of LMFBRs," *Nuclear Safety*, Vol. 17, No. 5 (1976).
- 67 H. A. Bethe and J. H. Tait, "An Estimate of the Order of Magnitude of the Explosion when the Core of a Fast Reactor Collapses," *British Report UKAEA-RHM (56)/113*, 1956.
- 68 H. K. Fauske, "Assessment of Accident Energetics in LMFBR Core-Disruptive Accidents," *Nuclear Engineering and Design* 42 (1977) 19-29.
- 69 J. E. Cahalan, A. M. Tentner, and E. E. Morris, "Advanced LMR Safety Analysis Capabilities in the SASSYS-1 and SAS4A Computer Codes," Proc. of the International Topical Meeting on Advanced Reactors Safety, Pittsburgh, April 17-21 (1994)
- 70 Y. S. Tang, R. D. Coffield, and R. A. Markley, *Thermal Analysis of Liquid Metal Fast Breeder Reactors*, p. 277, American Nuclear Society, LaGrange Park, Illinois (1978).
- 71 A. E. Waltar and A. B. Reynolds, *Fast Breeder Reactors*, p. 260 and 540, Pergamon Press, New York (1981).
- 72 J. L. Séran, et al., "Behavior under Neutron irradiation of the 15-15Ti and EM10 Steels Used as Standard Materials of the Phénix Fuel Subassembly," *Effects of Radiation on Materials: 15th Int. Symposium*, ASTM STP 1125, R. E. Stoller, A. S. Kumar, and D. S. Gelles, Eds., American Society for Testing and Materials, p. 1209-1233, Philadelphia (1992).
- 73 A. Fissolo, "Tensile Properties of Neutron Irradiated 316Ti and 15-15Ti Steels," *Effects of Radiation on Materials: 16th Int. Symposium*, ASTM STP 1175, A. S. Kumar, D. S. Gelles, R. K. Nanstad, and E. A. Little, Eds., American Society for Testing and Materials, p. 646-663, Philadelphia (1993).
- 74 N. S. Cannon, F. R. Huang, and M. L. Hamilton, "Transient and Static Mechanical Properties of D9 Fuel Pin Cladding and Duct Material Irradiated to High Fluence," *Effects of Radiation on Materials: 15th Int. Symposium*, ASTM STP 1125, R. E. Stoller, A. S. Kumar, and D. S. Gelles, Eds., American Society for Testing and Materials, p. 1071-1082, Philadelphia (1992).

- 75 R. J. Puigh and M. L. Hamilton, Influence of Radiation on Materials Properties: 13th Int. Symposium (Part II), ASTM STP 956, F. A. Garner, C. H. Henager, N. Igata, Eds., American Society for Testing Materials, p. 22-29 (1987).
- 76 B. F. Gromov, et al., "The Analysis of Operating Experience of Reactor Installations Using Lead-Bismuth Coolant and Accidents Happened," Proc. Heavy Liquid Metal Coolants in Nuclear Technology, Vol. 1, Obninsk, October 5-9, p. 60-66, State Scientific Center of Russian Federation Institute for Physics and Power Engineering (1998).
- 77 A. Rineiski and W. Maschek, "On Application of Quasistatic and Point-Kinetics Schemes for Subcritical Systems With External Neutron Source," Nuclear Mathematical and Computational Sciences: A Century in Review - A Century Anew, M&C 2003, Gatlinburg, Tennessee, USA, April 6-11 (2003).
- 78 S. Dulla, P. Ravetto, M. M. Rostagno, G. Bianchini, M. Carta, A. D'Angelo, "Some Features of Spatial Neutron Kinetics for Multiplying Systems," 149, 88-100 (2005).
- 79 D. G. Cacuci, "On the Neutron Kinetics and Control of Accelerator-Driven Systems," Nuclear Science and Engineering, 148, 55-66 (2004)
- 80 A. F. Henry, "The Application of Reactor Kinetics to the Analysis of Experiments," Nuclear Science and Engineering, 3, 52-70 (1958).
- 81 E. P. Gyftoploulos, Chapter on "General Reactor Dynamics," in The Technology of Nuclear Reactor Safety, Vol. 1, p. 175-204, T. J. Thomson and J. G. Beckerly, Eds., The MIT Press, Cambridge, Massachusetts, USA (1964).
- 82 J. B. Yasinsky and A. F. Henry, "Some Numerical Experiments Concerning Space-Time Reactor Kinetics Behavior," Nuclear Science and Engineering, 22, 171-181 (1965).
- 83 K. O. Ott and D. A. Meneley "Accuracy of the Quasistatic Treatment of Spatial Reactor Kinetics," Nuclear Science and Engineering, 36, 402-411 (1969).
- 84 J. E. Cahalan, T. Ama, G. Palmiotti, T. A. Taiwo, and W. S. Yang, "Development of a Coupled Dynamics Code with Transport Theory Capability," PHYSOR 2000, Pittsburgh, USA, 7-11 May (2000).
- 85 "Comparison Calculations for an Accelerator-driven Minor Actinide Burner," OECD/NEA Nuclear Science Committee, NEA/NSC/DOC(2001)13, OECD (2002). Benchmark prepared by P. WYDLER and H. TAKANO, NEA/NSC/DOC(99)13, Revised 27 Aug. 1999.
- 86 F. E. Dunn and D.C. Wade, "Estimates of Thermal Fatigue Due to Beam Interruptions for an ALMR-Type ATW," Proc. 2nd International Workshop on Utilisation and Reliability of High Power Proton Accelerators, Aix-en-Provence, November 22-24, NEA/OECD (1999).
- 87 A. F. Henry, Nuclear-Reactor Analysis, p. 300-329, The MIT Press, Cambridge, Massachusetts, USA (1975).
- 88 D. J. Hill, "SASSYS Validation Studies," Proc. of the International Topical Meeting on Safety of Next Generation Power Reactors, Seattle, WA, May 1-5, American Nuclear Society, (1988).
- 89 J. P. Herzog, "SASSYS Validation with the EBR-II Shutdown Heat Removal Tests," Trans. Am. Nucl. Soc., 60, 730, 1989.
- 90 F. E. Dunn, "Validation of Detailed Thermal Hydraulic Models Used for LMR Safety and for Improvement of Technical Specifications," Proc. of the American Nuclear Society International Topical Meeting on Safety of Operating Reactors, Seattle (Bellevue), WA, September 17-20, American Nuclear Society (1995).

- 91 T. A. Taiwo, DIF3D-K: A Nodal Kinetics Code for Solving the Time-Dependent Diffusion Equation in Hexagonal-Z Geometry, ANL/NPR-92/17, Argonne National Laboratory, Reactor Analysis Division, October, 1992.
- 92 G. Palmiotti, E. E. Lewis, and C. B. Carrico, VARIANT: VARIational Anisotropic Nodal Transport for Multidimensional Cartesian and Hexagonal Geometry Calculation, ANL-95/40, Argonne National Laboratory, Reactor Analysis Division, October, 1995.
- 93 A. Rineiski, KIN3D: Module de cinetique spatiale et de perturbations pour TGV2, Note technique SPRC/LEPh 97-203, CEA/Cadarache, May, 1997.
- 94 J. E. Cahalan, et al., "Development of a Coupled Dynamics Code with Transport Theory Capability and Application to Accelerator-Driven Systems Transients," Proc. of the ANS International Topical Meeting on Advances in Reactor Physics and Mathematics and Computation into the Next Millennium, PHYSOR 2000, Pittsburgh, Pennsylvania, May 7-12, 2000.



# Paper I

# INHERENT SAFETY OF FUELS FOR ACCELERATOR-DRIVEN SYSTEMS

M. ERIKSSON\*, J. WALLENIUS, M. JOLKKONEN  
Royal Institute of Technology (KTH), AlbaNova University Center,  
Dep. Nuclear & Reactor Physics, 10691 Stockholm, Sweden.

J. E. CAHALAN  
Argonne National Laboratory, Nuclear Engineering Division,  
9700 South Cass Ave., IL 60439, USA.

Submitted *Nuclear Technology* (Oct, 2004)

Accepted (Jan, 2005)

*Transient safety characteristics of accelerator-driven systems (ADS) using advanced minor actinide fuels have been investigated. Results for a molybdenum-based Ceramic-Metal (CerMet) fuel, a magnesia-based Ceramic-Ceramic (CerCer) fuel, and a zirconium-nitride based fuel are reported. The focus is on the inherent safety aspects of core design. Accident analyses are carried out for the response to unprotected loss-of-flow and accelerator beam-overpower transients, and coolant voiding scenarios. An attempt is made to establish basic design limits for the fuel and cladding. Maximum temperatures during transients are determined and compared with design limits. Reactivity effects associated with coolant void, fuel- and structural-expansion, and cladding relocation are investigated. Design studies encompass variations in lattice pitch and pin diameter. Critical mass studies*

*are performed. The studies indicate favorable inherent safety features of the CerMet fuel. Major consideration is given to the potential threat of coolant voiding in accelerator-driven design proposals. Results for a transient test case study of a postulated steam generator tube rupture event leading to extensive cooling voiding are presented. The study underlines the importance of a having a low coolant void reactivity value in a lead-bismuth system, despite the high boiling temperature of the coolant. It was found that the power rise following a voiding transient increases dramatically near the critical state. The studies suggest that a reactivity margin of a few dollars in the voided state is sufficient to permit significant reactivity insertions.*

## I. INTRODUCTION

Accelerator-driven systems (ADS) have been proposed for reducing the long-term hazards of spent nuclear fuel disposition [1,2]. The primary objective is to minimize the inventory of americium and curium that, besides plutonium, are responsible for the majority of the long-term radiotoxicity in nuclear waste. If successful, the technology could enable a reduction of the mass and radioactivity of the spent nuclear fuel by a factor of 100, and reduce the required storage time from  $\sim 100\,000$  years to  $\sim 1000$  years.

Studies of ADS neutronics and thermal hydraulics have been accomplished, leading to the selection of LBE as main choice for the coolant [3,4]. Concerning the selection of a suitable fuel material, investigations are made in connection with the joint European research programs [5,6]. While some of the originally suggested fuels did not fulfill basic safety and/or design criteria, three fuels have been selected for detailed examination, namely: two composite oxide fuels and one solid solution nitride fuel. The detailed motivation for

selecting these fuels has been outlined in a recent article [7]. In this paper, attention is directed to their inherent safety characteristics and performance during reactor transient conditions. Various accident events of interest in accelerator-driven systems are considered. Reactivity sources are examined with regard to their influence on reactor safety.

## II. INHERENT SAFETY

The term “inherent safety” is in widespread use, particularly in discussions of advanced nuclear reactors. Generally, it is used without further definition and sometimes with inconsistent meaning. In most cases, it is meant to denote an applied design approach or to describe a particular system feature and often to indicate a possible safety advantage. According to the IAEA [8], an inherent safety characteristic is a “fundamental property of a design concept that results from the basic choices in the materials used or in other aspects of the design which assures that a particular potential hazard can not become a safety concern in any way”. The potential hazards include the radioactive materials, decay heat, excess reactivity, high temperatures, high pressures, and energetic

\*Email: marcus@neutron.kth.se

chemical reactions. An “inherently safe” reactor would require all these hazards to be eliminated, which is impossible for all practical reactor purposes. Nevertheless, a reactor may possess inherent safety characteristics with respect to a particular eliminated hazard and for specific events. To avoid the potential of being misleading, this does not imply absolute safety for all possible situations.

In the following studies, we seek to investigate the inherent safety characteristics of an ADS with respect to specific accident-initiating events. Inherent safety characteristics associated with reactor transients translates into reactor performance when the protective shutdown devices do not perform their function. Studying this specific class of transients is of considerable importance since they describe the fundamental response of the reactor in the absence of safety system intervention. These so-called “unprotected” transients are potentially of the worst kind. Despite their extremely low probability of occurrence, reactor designs must still be protected against such events to assure the health and safety of the general public. Lessons learned from commercial nuclear power operation and reactor accidents recognize that safety should not rest solely on proper operation of the control and safety systems, or even on ideal performance of plant operators. Every mechanical system, electric power supply, instrumentation system, etc., has a non-vanishing probability of failure, and humans make mistakes. Hence, the reactor should be designed such that there is no undue risk for the environment outside the reactor building even in the hypothetical situation that the shutdown system should fail when needed. That implies that the energy releases, reactivities, pressures, and temperatures for critical reactor elements be kept within safe limits under all conditions.

### III. FUEL SELECTION PROCESS

The overall mission of the ADS is to maximize the destruction rate of transuranic elements, primarily americium (Am) and curium (Cm). While plutonium is recyclable in fast reactors and to some extent in commercial light water reactors, the amount of Am that can be charged into a critical reactor is limited by safety concerns. The Doppler feedback coefficient and effective delayed neutron fractions decline when americium is added to the fuel [7] and the reactivity effect associated with loss-of-coolant becomes more positive. The ADS is a nuclear reactor operating in a subcritical mode, which provides for the added safety margin to allow for high concentration of Am. With ADS, transmutation of the minor actinides (Am, Cm, and Np) may be confined to a single process, which will improve the operation of critical reactors and ease the burden on recycling in the overall process. Different fuel cycle strategies could be foreseen. The Japan Atomic Energy Research Institute (JAERI) has proposed the double-strata concept [9], utilizing both commercial light-water reactors and fast reactors for plutonium recycling and energy production and ADS's for MA consumption.

The MA based ADS fuel does not require  $^{238}\text{U}/^{232}\text{Th}$  for normal operation, but a certain amount of plutonium is necessary for reactivity management. A support material is needed to reduce the power density, and in some cases,

improve thermal properties. The support material constitutes an “inert matrix” in which the fuel particles are embedded (“inert” in this context refers to an inactive material with a high transparency to neutrons). These fuels are then referred to as “inert matrix fuels”. The inert matrix fuel may be of homogeneous (solid solution) and heterogeneous (composite) type and the fuel may be a Ceramic-Ceramic (CerCer) mixture or a combined Ceramic-Metal (CerMet) mixture. CerCer fuels of interest utilize a metal oxide matrix such as magnesia (MgO), spinel ( $\text{MgAl}_2\text{O}_4$ ), and alumina ( $\text{Al}_2\text{O}_3$ ). CerMet fuels are attractive because of high thermal conductivity. The refractory metals such as molybdenum, chromium, tungsten, and vanadium are of particular interest because of their high melting point. During a pre-selection phase [3], a number of inert matrices have been considered and examined. Among them, the magnesia (MgO) and molybdenum ( $^{92}\text{Mo}$ ) matrices were singled out as potential materials for use with oxide fuels and these are studied in the some more detail in the current paper. The major reason for this selection is a combination of good thermal properties, acceptable neutronics, and solubility in nitric acid. For a detailed account, see ref. [3,7].

Nitride fuel is an alternative to oxide fuels, yet the knowledge on nitride fuels is limited compared to the extensive experience available on oxide fuel. Nitride fuels offer relatively high thermal conductivity and dissolution rate in nitric acid, which makes it compatible with the PUREX reprocessing technique. The nitride fuels of potential use are of the solid solution type; composite nitride fuels are of little interest. Previous studies [10] have indicated that there are a limited number of inert matrices suitable for nitride fuels. So far, the diluents that have been considered are zirconium nitride (ZrN), hafnium nitride (HfN), and yttrium nitride (YN). At this stage of development, ZrN is the primary choice. HfN has high neutron absorption cross-section, and YN is difficult to handle, as it reacts chemically with air and water. ZrN offers relatively high thermal conductivity and high melting point [11]. It forms a solid solution with plutonium nitride [12], has a stabilizing effect on americium nitride [13] and is itself stable in air. Furthermore, it has a high transparency to neutrons, good chemical compatibility with steel, and is soluble in nitric acid. A disadvantage of the nitride fuel is the need for using nitrogen enriched in  $^{15}\text{N}$  [14], in order to minimize the production of radioactive  $^{14}\text{C}$  during neutron irradiation [by (n, p) reaction in  $^{14}\text{N}$ ].

In summary, two oxide fuels, one MgO-CerCer and one Mo-CerMet, and one solid solution ZrN-nitride fuel are examined in this article. The materials are listed in TABLE I.

TABLE I.  
Minor actinide fuels investigated in this study.

| Fuel*                         | Composition | Form           |
|-------------------------------|-------------|----------------|
| $\text{AnO}_{2-x}\text{-MgO}$ | Oxide       | CerCer         |
| $\text{AnO}_{2-x}\text{Mo}$   | Oxide       | CerMet         |
| $(\text{An,Zr})\text{N}$      | Nitride     | Solid solution |

\*“An” denotes a mixture of actinides (Pu, Am, and Cm). The oxide fuels are hypostoichiometric and the chemical formula is referred to as  $\text{AnO}_{2-x}$ , where x is the deviation from stoichiometry.

## IV. FUEL MATERIAL PROPERTIES

Material property data for the minor actinide fuels is limited, particularly at high temperature. Thermophysical properties of minor actinide oxide fuel [15] and nitride fuel [16] were recently reviewed by Thetford and Mignanelli. We have applied their recommendations with minor modification. It is assumed that the correlations depend on temperature, matrix fraction, and porosity. In the case of oxide fuels, the influence of stoichiometry is considered. These are the most important variables. While other parameters also have an effect, these are not reliably established yet. Correlations are based on unirradiated properties (see section IV.B for discussion on irradiation effects). Selected physical properties are presented in TABLE II. Material properties for standard MOX-fuel are included for reference purposes. The values are given at 1000°C and for the fully dense and fresh material. Fuel and matrix proportions correspond to an average fuel pin in the core, as explained later. The fuels contain 40% plutonium, 50% americium, and 10% curium. A more detailed account on this composition is given in later sections. It is seen that the CerCer has considerably lower thermal conductivity, lower density, and much higher specific heat than the nitride and CerMet fuels. It also has a higher coefficient of thermal expansion, which tends to increase the negative reactivity feedback associated with fuel expansion, but may also increase the risk for fuel-cladding mechanical interaction, thermal stresses, and cracking.

TABLE II.  
Selected fuel material properties at 1000°C.

| Fuel                 | Properties at 1000°C (100% TD) |             |                 | $\alpha^*$<br>1e+6/K |
|----------------------|--------------------------------|-------------|-----------------|----------------------|
|                      | $\rho$<br>g/cm <sup>3</sup>    | $k$<br>W/mK | $c_p$<br>kJ/kgK |                      |
| CerCer <sup>a</sup>  | 6.6                            | 4.7         | 0.90            | 14.0                 |
| CerMet <sup>b</sup>  | 10.6                           | 51.2        | 0.33            | 9.2                  |
| Nitride <sup>c</sup> | 9.3                            | 17.0        | 0.43            | 9.0                  |
| MOX <sup>d</sup>     | 10.7                           | 2.8         | 0.33            | 12.1                 |

\*Mean linear coefficient of thermal expansion (300 to 2100 K).

<sup>a</sup>0.42(Pu<sub>0.4</sub>,Am<sub>0.5</sub>,Cm<sub>0.1</sub>)O<sub>1.9</sub>+0.58MgO

<sup>b</sup>0.51(Pu<sub>0.4</sub>,Am<sub>0.5</sub>,Cm<sub>0.1</sub>)O<sub>1.9</sub>+0.49Mo

<sup>c</sup>(Pu<sub>0.13</sub>,Am<sub>0.17</sub>,Cm<sub>0.03</sub>,Zr<sub>0.67</sub>)N

<sup>d</sup>Standard MOX, U<sub>0.8</sub>Pu<sub>0.2</sub>, 95% TD, O/M=2.0.

### IV.A. Effect of diluent and porosity

The effect of the diluent on the material properties is approximated using Vegard's law, i.e., sum of the properties of the fissile fuel and diluent phases weighted by their respective atomic fractions. This is a rather crude approximation, but one which we need to accept in the absence of experimental data. Consequently, the fuel thermal conductivity becomes a linear and increasing function of the matrix content. The effect of fuel porosity on the thermal conductivity is modeled with the classical Maxwell-Eucken formula. For oxides and nitrides a pore shape factor of  $\beta=2$  has been recommended and is used in our analyses. However, it is noted that the pore geometry depends on the fabrication process and different correction models are in use. The CerCer fuel has a bulk density of 95% of the theoretical value. Hence, the correction factor for the thermal conductivity is 0.86. For the CerMet fuel, the as-fabricated porosity of the

oxide inclusions has a limited effect on the overall conductivity since it is mainly determined by the metallic component, which is fully dense. The porosity has a significant effect on the conductivity of the low-density nitride fuel. The effective thermal conductivity of the nitride fuel is reduced to 65% of the fully dense material. Fig 1 shows the effective thermal conductivity of the investigated fuels as function of temperature. Values are given for the porous material. The CerMet fuel has excellent thermal conductivity. The thermal conductivity of the nitride fuel is quite high, about 4-6 times higher than classical MOX-fuel in the typical reactor operating temperature range. The CerCer fuel has the lowest thermal conductivity of the fuels, however, it is still higher than the standard MOX-fuel (between 1.5 to 3 times higher). The thermal conductivity of the CerCer fuel has a minimum around 1500 K.

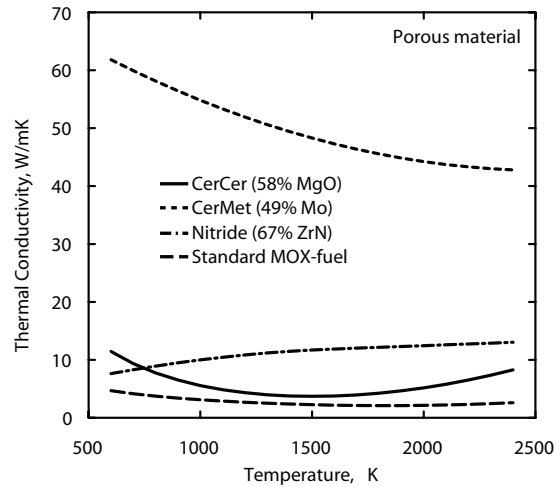


Fig. 1. Effective thermal conductivity of the examined fuels.

### IV.B. Effect of irradiation

Fuel properties change during irradiation as a result of restructuring, cracking, chemical redistribution, and introduction of fission products. Such differences play an important role in establishing safety margins as function of temperature and burnup history – both for steady-state operation and during thermal upset conditions. Restructuring (grain growth and pore migration) affects thermal conductivity, void formation, density, volumetric heat generation levels, and hence operating temperatures. An analysis of all the governing processes is beyond the scope of this article. Suffice it to say that restructuring and development of thermal stresses (cracking) depend strongly upon thermal gradients and operating temperatures and is usually small for high-thermal conductivity fuels [17], which suggest limited thermal restructuring for the CerMet and nitride fuels, whereas significant changes may occur in the CerCer fuel. Cracking is further aggravated by a high coefficient of thermal expansion, which suggests more severe cracking for the CerCer fuel. For oxide fuel, decrease in the thermal conductivity due to the introduction of fission products is small in comparison with the larger effects of restructuring. The development of a central void in typical fast reactor mixed-oxide fuel and densification of the restructured regions tend to reduce the maximum fuel

temperature with irradiation time even though the local linear power is constant [18]. Yet, very little in-pile data is available upon which to judge the irradiation behavior for the minor actinide dispersal fuels. Studies have been performed on a  $\text{UO}_2+64\%\text{Mo}$  composite fuel irradiated to a burnup of 5 atom% [19]. Post-irradiation examination revealed little or no signs of restructuring, which indicates that molybdenum is a potentially stable matrix material. The reduction of the thermal conductivity with burnup is probably larger for the CerMet fuel because of higher fission gas retention and less pore migration, but it is expected that the net effect of irradiation is to reduce maximum fuel temperatures because of fuel-cladding gap closure early in life. We presume that such a displacement of the fuel surface act to reduce centre line temperatures in the nitride case too, but to a lesser extent as compared to the CerMet fuel. Fission gas (xenon and krypton) mixture effects on the fill gas (helium) conductivity are largely offset by reduced fuel-cladding gap thickness and higher gas pressure. Although restructuring and swelling phenomena may improve fuel thermal performance, for reasons explained above, it is possible that higher burnup negatively affects fuel melting temperatures, fuel-pin mechanical performance as well as power peaking factors. It is apparent that an assessment of the variation of safety margins (power-to-melt, thermo-mechanical limits, etc.) as function of irradiation time would require examination of a wide range of phenomena, each suffering from large uncertainties and, consequently, we find it speculative to extract such limits at this stage.

## V. DESIGN LIMITS

We attempt to establish design limits for the fuel and cladding. The fuel failure limit is prescribed by accident conditions and has little constraints on normal operation, whereas the cladding failure limits are defined for steady-state and transient conditions. It should be noted that the design studies are yet in a pre-conceptual stage and it is not meant to imply that the indicated limits are complete. The objective at this point is to describe the analysis methodology involved and to provide a framework for guiding further design work, not to spell out elaborate details on the design criteria or particular failure processes. Inevitably, there are many uncertainties regarding potential failure mechanisms (e.g. mechanical and chemical interactions between fuel components, fission products, and cladding constituents), and, as discussed in Chapter IV.B, further research is required to establish reliable design limits based on in-pile experimental data.

To this end, we have selected Si-modified 15-15Ti austenitic stainless steel as reference cladding material. This class of alloy has demonstrated favourable performance up to 150 dpa [20] and has good high temperature mechanical properties [21].

### V.A. Oxide melting

Complications arise in describing the melting behavior of the present oxide fuels. Due to a low solid solubility of the oxide fuel particles in the diluents (MgO and Mo), the two constituents will melt at different temperatures. In addition, eutectic melting may appear at temperatures below the

melting points of the individual materials. The melting point of the mixed actinide oxide,  $\text{AnO}_{1.9}$ , is estimated to 2640 K, based on the melting points of  $\text{PuO}_{2-x}$  [22],  $\text{AmO}_{2-x}$  and  $\text{CmO}_{2-x}$  [23], and applying Vegard's law. We have assumed a melting point dependence on the oxygen content similar to the recommendations for  $(\text{U,Pu})\text{O}_{2-x}$  [24]. It appears that no eutectic reaction occurs between molybdenum and  $\text{UO}_2$  [25] If a similar behavior is assumed for  $\text{AnO}_{1.9}\text{-Mo}$ , then the first sign of melting will occur in the oxide phase (the melting point of pure Mo is 2900 K). The oxygen content may affect the potential for eutectic formation and oxidization of Mo into  $\text{MoO}_2$ , however, these effects are not sufficiently known to be taken into account. For the CerCer fuel, complication arises due to the possibility for eutectic reaction below the melting points of  $\text{AnO}_2$  and pure MgO ( $T_m=3100$  K). Laboratory measurements [26] found no eutectic reaction up to  $\sim 1923$  K, while theoretical calculations [27] predicted that an eutectic may start to form at temperatures as low as 1930 K for low oxygen contents. The same study also estimated that the melting point stabilizes around 2300 K for oxygen-to-metal ratios above 1.62. Keeping low oxygen content, however, is desirable because it reduces corrosion of the cladding. The melting point of  $\text{PuO}_{2-x}\text{-MgO}$  [28] ranges from 2341 to 2503 K when the oxygen content changes from 1.61 to 2. Following these results, we estimate the failure limit of the  $\text{AnO}_{1.9}\text{-MgO}$  fuel somewhere in the range 2200-2300 K.

### V.B. Nitride dissociation

The main concern about nitrides is the dissociation of AmN into metal and nitrogen gas at temperatures around 1600 K [29], which is too low to meet safety requirements under overpower conditions. To investigate this problem, thermo-chemical modeling has been performed on minor actinide nitride compounds in various environments. In this study, an updated version of the ALCHYMY database [30] for Thermo-Calc [31] was used to model the dissociation of AmN in  $(\text{Pu}_{0.2}\text{Am}_{0.3}\text{Zr}_{0.5})\text{N}$  heated in a constant-volume system mimicking the dimensions and materials proportions of an actual fuel pin with and without a stabilising addition of 1%  $\text{N}_2$  to the filling gas. The assumed pin pressure is that of the bonding gas at the corresponding temperature plus 1.5 times that of americium vapour ( $\text{AmN} \rightarrow \text{Am(g)} + 0.5 \text{N}_2$ ). Up to 2400 K, the contribution from dissociation of PuN is smaller by three orders of magnitude and can be ignored. In the same range, the increase in pressure arising from AmN dissociation is only a few percent of the total pressure and should not be an issue from a purely mechanical point of view. The depletion of Am from the fuel is in itself very small during uniform heating, below 0.01% even in pure helium. Based on these results, we estimate the failure point for the nitride fuel at 2400 K. This failure criteria should be considered applicable only during rapid overpower excursion. For slow transients, one may expect transport effects, with nitride continuously dissociating in hot zones and reforming on colder surfaces, if the overheating would persist for longer time. As the model contains several other simplifications (congruent vaporisation of AmN at stoichiometric composition, ideal solid solution of nitrides) and considering that thermodynamical parameters for AmN are based on

some reasonable but unverified assumptions [32], the results must not be interpreted too literally.

### V.C. Cladding transient burst limit

Thermal limits relevant for cladding during thermal upset conditions were established based on transient burst test data. These tests, called Fuel Cladding Transient Test (FCIT), duplicate reactor transient conditions in which the cladding (irradiated or unirradiated) is heated (out-of-pile) until failure occurs. The failure temperature is recorded as function of hoop stress and often related to a particular thermal ramp rate. The FCIT tests are typically carried out for relatively fast ramp rates, in the range 0.5-100 K/s. In our estimates, we have assumed an internal pin pressure of 14 MPa (equivalent to a membrane stress of 100 MPa) and a thermal ramp rate of 5 K/s. This thermal ramp rate was selected because it is similar to the heating rates involved in loss-of-flow conditions. Temperature limits for 15-15Ti are estimated using data for unirradiated D9 pin cladding [33]. The D9 alloy is a titanium modified 316 austenitic stainless steel, which has similar composition as 15-15Ti steel. Tension tests [21] show that the mechanical properties of irradiated 15-15Ti is better than Ti-stabilized 316, indicating that transient/mechanical properties should be no worse than for D9. The failure temperature of irradiated cladding specimens is comparable to the unirradiated cladding [34], as the fuel adjacency effect (FAE) [35] may be negligible in the actual fuel pin environment [36]. Based on these studies, we estimate a failure temperature for 15-15Ti cladding equal to 1330 K.

### V.D. Cladding creep rupture limit

For long-term operation, nominal temperatures are limited by thermo-mechanical creep rates. Stress rupture data is scarce for 15-15Ti steels. However, a reasonable amount of data is available for D9. The better tensile properties of 15-15Ti suggest that the thermal creep performance of CW 15-15Ti could be comparable or better than D9. Ongoing studies show that silicon modified CW 15-15Ti stainless steel possesses even better tensile properties, indicating that further improvement might be possible. Tests conducted on 20% CW D9 cladding [37], showed that the in-pile rupture lifetime is lower compared to out-of-pile data, indicating that the pin cladding might fail sooner than predictions based on out-of-core test results. The maximum operating temperature for the CW 15-15Ti cladding, with respect to thermal creep, was estimated to be 920 K (maximum midwall temperature). This limit was determined for a constant plenum pressure loading of 10 MPa (equivalent to a hoop stress of 74 MPa) and an expected in-pile service of 3 years (exposure time 30,000 h).

### V.E. Cladding corrosion limit

Corrosive attack by the coolant imposes additional constraints. The effect of LBE corrosion is manifest as wall thinning, as structural material dissolves in the coolant, and higher stresses, which altogether leads to reduced cladding lifetime. The corrosion rate shows a strong dependence on temperature and some correlation with fluid velocity. It has been demonstrated that, for non-protected stainless steels, nominal temperatures must not exceed 670 K for austenitic steels and 720 K for ferritic steels [38]. In an oxygen-controlled environment, however, a protective oxide film may

form on the surface of the structure, which may slow down the dissolution rate. The protective film is formed by oxidation reactions between the oxygen dissolved in the coolant and steel alloy elements (Fe, Cr, Si, and others with high affinity to O<sub>2</sub>). Using this technique, operating temperature can be raised by 150-200 degrees. In Russia, where most corrosion studies with Pb/Bi have been carried out, the results indicate that the ferritic/martensitic steels offer the best performance. This appears to be due to the low nickel content of the ferritic steels compared to the austenitic steels [38]. Nickel shows high solubility in Pb/Bi alloy, which has an impairing effect on the stability of the oxide film and increases the corrosion rate. At this stage of development, long-term operation ( $\geq 30,000$  hours) at temperatures above 890 K appears to be difficult [38], even for the most promising corrosion resistant steel, i.e., Russian type silicon-alloyed ferritic-martensitic steel (EP823). With reference to austenitic 15-15Ti steels, we assume that the operating clad temperature is to be kept below 840 K (surface temperature). TABLE III summarizes the current estimates of the design limits for the investigated fuels and cladding materials. It is cautioned that these limits are preliminary estimates and may change in the light of further testing.

TABLE III.  
Summary of thermal limits for fuel and cladding.

| Component               | Failure temp. (K) | Failure mechanism  |
|-------------------------|-------------------|--------------------|
| Fuel                    |                   |                    |
| CerCer                  | 2200-2300         | Eutectic melt      |
| CerMet                  | 2640              | Oxide melting      |
| Nitride                 | 2400              | AmN dissociation   |
| Cladding (type 15-15Ti) |                   |                    |
| Surface (steady-state)  | 840               | Corrosive thinning |
| Midwall (steady-state)  | 920               | Creep rupture      |
| Midwall (transient)     | 1330              | Mech. burst limit  |

## VI. COMPUTATIONAL METHODS

The continuous energy Monte Carlo code MCNP4C [39] together with the JEF2.2 nuclear data library is used for neutronic calculations. A three-dimensional pin-by-pin model is employed. The MCNP code is used to calculate neutronics input data required for transient modeling (kinetics parameters, reactivity coefficients, power distributions, and gamma heating).

The SAS4A/SASSYS-1 computer code [40] is used for thermal- and hydraulic calculations at steady-state and transient conditions. The SASSYS-1 code is an integrated safety analysis computer code for the analysis of reactor plant transients in liquid-metal cooled reactors. A detailed description of the SAS code is outside the scope of this paper. The code has been adapted to enable the analysis of heavy liquid-metal cooled reactor designs and accelerator-driven systems. The calculational model used in this study employs two thermal-hydraulic channels. One channel represents an average pin within the core and a second channel represents the hottest pin in the core (with a power peaking factor of 1.3). The primary system includes models of the core, primary pumps, shell side of the steam generators, connecting piping,

and compressible pool volumes with cover-gas surfaces. The fuel-cladding gap conductance model accounts for gas conduction, radiative heat-transfer, surface roughness, and differential thermal expansion of fuel and cladding during transient conditions. Reactivity feedbacks are calculated for coolant expansion, fuel elongation, radial core expansion, and Doppler effect. Changes in power level are computed with point kinetics theory. The performance of the point kinetics approximation for transient analysis of ADS's was considered in a previous assessment [41] and found adequate for similar problems.

## VII. CORE MODEL

A reference core was constructed largely based on previous parametric studies. The core model pertains to a LBE-cooled accelerator-driven system with a thermal rating of 800 MW. The core consists of a central lead-bismuth spallation target surrounded by a fuel region. The active core is 1 m high with a diameter of 1.6 to 2.2 m, depending on the core configuration. The core is surrounded by axial and radial reflectors 0.5 m thick. The reflectors consist of subassemblies filled with coolant and empty cladding tubes. The pitch-to-diameter (P/D) ratio and the pin diameter are design parameters. The reference configuration uses a P/D equal 1.50 and a pin diameter of 5.72 mm. In a second configuration, the P/D value is increased to 1.75 by changing the pin pitch. In a third modification, the pin diameter is increased to 6.8 mm while holding the P/D ratio at 1.50. In all the cases the flat-to-flat distance is fixed while the number pins per subassembly is either 91 or 127. A summary of design parameters is given in TABLE IV.

TABLE IV.  
Core lattice configurations

|                            |                       |
|----------------------------|-----------------------|
| SA pitch                   | 10.2 cm               |
| FTF outer                  | 10.0 cm               |
| FTF inner                  | 9.6 cm                |
| P/D                        | 1.50/1.75             |
| Pins per SA (1.50/1.75)    | 127/91                |
| Volume fractions           | 27/16/52 % (P/D=1.50) |
| (fuel/steel/coolant)       | 19/14/63 % (P/D=1.75) |
| Cladding o.d.              | 5.7/6.8               |
| Cladding i.d.              | 5.0/6.0               |
| Active core height         | 1.0 m                 |
| Core diameter              | ~1.6-2.2 m            |
| Spallation target diameter | 0.4 m                 |
| Gas plenum height          | 1.50 m                |

The core is partitioned into three regions of different matrix fractions. The purpose is to level out the radial power distribution. Matrix fractions are adjusted to obtain an initial  $k_{\text{eff}}$  equal 0.97 and a radial peak-to-average power ratio factor of 1.3. Matrix contents drop towards the edges, as shown in TABLE V. The poorer neutron economy of the oxides result in matrix contents lower compared to the nitride, which has an adverse effect on the fuel performance. A high volume fraction of diluents is favorable from the viewpoint of thermal performance, stability, and fuel fabrication. Increasing the P/D ratio requires lower concentration of diluents while increasing the pin diameter enables a slightly larger fraction of

matrix to be used. The plutonium fraction is fixed at 40%, which is similar to the initial Pu loading in the double-strata cycle studied by JAERI. It was shown that this plutonium content provides minimal burnup reactivity swing over a large number of irradiation cycles [42]. The fuel has total americium content of 50% and 10% curium. Neptunium is not considered because it is not an important contributor to the long-term radiotoxicity. The americium vector consists of two thirds  $^{241}\text{Am}$  and one third of  $^{243}\text{Am}$ . Curium is composed of 87%  $^{244}\text{Cm}$  and 13%  $^{245}\text{Cm}$ . The isotopic vector of plutonium (5%  $^{238}\text{Pu}$ , 38%  $^{239}\text{Pu}$ , 30%  $^{240}\text{Pu}$ , 13%  $^{241}\text{Pu}$ , and 14%  $^{242}\text{Pu}$ ) corresponds to discharged MOX fuel from LWRs after 7 years cooling. The isotopic composition of americium and curium derives from a mixture of spent UOX and MOX fuel. Burnup reactivity losses are compensated by increasing the proton beam current by a factor of 1.5 at end-of-life. Delayed neutron parameters and prompt neutron generation times are shown in TABLE VI. Clearly, there is a large difference between the effective delayed neutron fraction ( $\beta_{\text{eff}}$ ) and the actual delayed neutron fraction ( $\beta$ ). The  $\beta_{\text{eff}}$  is around 180 pcm, while the corresponding  $\beta$  value is in the range of 230-280 pcm. The reason for this variation is that delayed neutrons are emitted with much smaller average energy ( $\sim 0.5$  MeV) and thus with lower chance of causing fission in the even neutron numbered nuclei ( $^{241}\text{Am}$ ,  $^{243}\text{Am}$ ,  $^{240}\text{Pu}$ , and  $^{242}\text{Pu}$ ) than prompt neutrons. The prompt neutron generation time ( $\Lambda$ ) varies between 0.5-0.8  $\mu\text{s}$  and increases for higher P/D.

TABLE V.  
Inert matrix volume fractions.

| Fuel    | $D_{\text{clad}}$ | P/D  | Zone 1 | Zone 2 | Zone 3 |
|---------|-------------------|------|--------|--------|--------|
| CerCer  | 5.7               | 1.50 | 0.65   | 0.58   | 0.42   |
|         | 5.7               | 1.75 | 0.56   | 0.51   | 0.41   |
|         | 6.8               | 1.50 | 0.68   | 0.62   | 0.52   |
| CerMet  | 5.7               | 1.50 | 0.54   | 0.48   | 0.37   |
|         | 5.7               | 1.75 | 0.47   | 0.41   | 0.31   |
| Nitride | 6.8               | 1.50 | 0.60   | 0.54   | 0.45   |
|         | 5.7               | 1.50 | 0.73   | 0.67   | 0.54   |
|         | 5.7               | 1.75 | 0.66   | 0.61   | 0.50   |
|         | 6.8               | 1.50 | 0.76   | 0.71   | 0.60   |

TABLE VI.  
Delayed neutron fractions ( $\beta$  and  $\beta_{\text{eff}}$ ) and neutron generation times ( $\Lambda$ ).

| Fuel    | $D_{\text{clad}}$ | P/D  | $\beta$ (pcm) | $\beta_{\text{eff}}$ (pcm) | $\Lambda$ ( $\mu\text{s}$ ) |
|---------|-------------------|------|---------------|----------------------------|-----------------------------|
| CerCer  | 5.7               | 1.50 | 250           | 180                        | 0.65                        |
|         | 5.7               | 1.75 | 250           | 190                        | 0.81                        |
|         | 6.8               | 1.50 | 250           | 190                        | 0.76                        |
| CerMet  | 5.7               | 1.50 | 240           | 170                        | 0.50                        |
|         | 5.7               | 1.75 | 230           | 180                        | 0.67                        |
|         | 6.8               | 1.50 | 270           | 190                        | 0.60                        |
| Nitride | 5.7               | 1.50 | 280           | 180                        | 0.55                        |
|         | 5.7               | 1.75 | 240           | 180                        | 0.71                        |
|         | 6.8               | 1.50 | 260           | 170                        | 0.67                        |

Additional fuel pin specifications are given in TABLE VII. Because of lower thermal conductivity, the CerCer fuel is required to operate at lower linear powers; 25 kW/m compared to 35 kW/m for the CerMet and the nitride fuel.

The initial gap thickness is chosen so that direct solid-to-solid contact is prevented during transients (assuming unirradiated geometry). As oxide fuels have a high plasticity and low swelling characteristics, pellet cladding mechanical interactions (PCMI) are less acute, and hence a rather small pre-fabricated porosity is sufficient. In the case of the nitride and the CerMet, PCMI cannot be tolerated, and hence a larger porosity of the nitride and a larger fuel-cladding gap of the CerMet have been adopted. The smear density for the CerCer, CerMet, and the nitride fuels are 91%, 88%, and 82%, respectively.

TABLE VII.

Fuel pin description (at operating condition).

| Fuel                               | CerCer | CerMet | Nitride |
|------------------------------------|--------|--------|---------|
| Average linear power, kW/m         | 25     | 35     | 35      |
| Smear density (%)                  | 91     | 88     | 82      |
| Fuel-clad gap width, $\mu\text{m}$ | 50     | 100    | 50      |

### VII.A. Temperature profile

The temperature distribution in structural components and fuel elements depend on the surface heat transfer conditions. Following recommendations by the IPPE (Obninsk), the heat-transfer coefficient between element and lead-bismuth coolant is determined using the following Lyon-Martinelli correlation [43]:

$$Nu = 5 + 0.025Pe^{0.8}$$

In Fig. 2, the steady-state temperature profile in the fuel rod is shown. The plot reproduces the profile for the hottest pin at core midplane and for the configuration using a pin diameter of 5.7 mm. Because of the low thermal conductivity, the CerCer fuel suffers from a steep temperature gradient (more than 300 K/mm). Despite that the CerCer fuel is operating with a lower specific power, it is the hottest of the three fuels. The CerMet fuel remains relatively cold, reaching a maximum temperature of 1690 K. The margin to melting is 950 K. The larger gap size for the CerMet eliminates some of the advantage of its high conductivity. Use of a liquid-metal bonding material could reduce fuel surface temperatures further, but at the risk of introducing additional problems, e.g., compatibility issues with fuel and cladding, bond vaporization, practical problems associated with manufacturing and reprocessing. Considering the small temperature gradient in the CerMet fuel (approaching 50 K/mm) suggests lower tendency for thermal restructuring and cracking, and the relatively low operating temperature implies lower fission gas release rates. Peak fuel and cladding temperatures as function of P/D and pin diameter are tabulated in TABLE VIII. It is seen that the reference case, with a tight pin lattice and thin pin diameter, is not consistent with a permissible cladding surface temperature of 840 K as dictated by long-term cladding corrosion damage. Cladding temperatures reported in TABLE VIII refer to the cladding midpoint. The surface temperature, which is of interest for the corrosion rate, is approximately 10-20 degrees lower. Maximum cladding temperatures occur at the outlet where coolant temperatures are highest. To maintain the cladding temperature within the given limit, a higher coolant mass flow rate is desirable. This may be achieved by increasing the P/D ratio. The reason the steady-state temperatures are lower for

the cases with larger pin diameter is twofold: coolant temperatures are lower because the coolant flow area is larger and the thermal conductivity of the fuel is better because matrix fractions are generally higher.

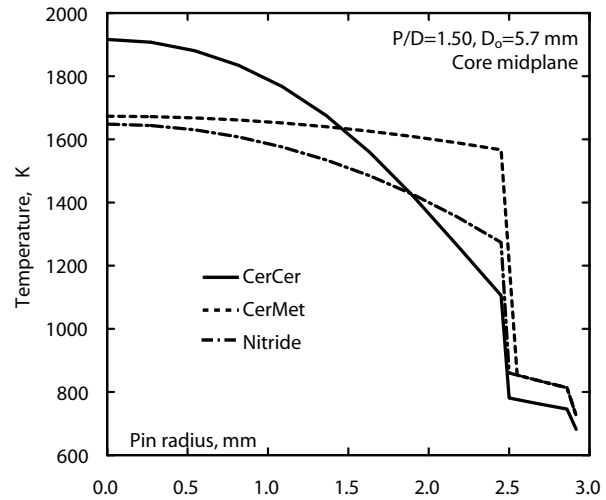


Fig. 2 Steady-state temperature profile at core midplane.

TABLE VIII.

Peak fuel and cladding (midpoint) temperatures in the hottest channel at normal operating conditions.

| Fuel    | P/D=1.50, D <sub>o</sub> =5.7 mm |      | P/D=1.75, D <sub>o</sub> =5.7 mm |      | P/D=1.50, D <sub>o</sub> =6.8 mm |      |
|---------|----------------------------------|------|----------------------------------|------|----------------------------------|------|
|         | Fuel                             | Clad | Fuel                             | Clad | Fuel                             | Clad |
| CerCer  | 1920                             | 840  | 1920                             | 770  | 1740                             | 770  |
| CerMet  | 1690                             | 940  | 1690                             | 840  | 1530                             | 850  |
| Nitride | 1660                             | 940  | 1650                             | 840  | 1540                             | 850  |

### VIII. REACTOR PLANT SYSTEM

TABLE IX contains major specifications of the lead-bismuth cooled ADS plant. The primary system is of pool type design. Due to high corrosion activity, coolant temperatures and velocities are limited. The coolant flow velocity in the pin bundle is limited to 2.5 m/s and the reactor inlet temperature is set at 573 K. LBE is chemically inert with water/steam. Hence, a two-circuit system is utilized, with the steam generator located in the primary system, which simplifies the overall plant design and reduces the cost. The primary system includes four centrifugal pumps (two for each loop) and four steam generators (two for each loop). Based on a seismic analysis, as discussed in the next section, a vessel height of 10 m is selected. The elevation difference between the core midplane and the thermal center of the steam generators should be as large as possible to increase natural circulation contribution. To allow room for cover gas and bottom support, however, the separation distance is limited to 5.5 m. The pump design includes flywheels to prolong the coast-down time in the event of a loss-of-flow accident. The size of the flywheel was optimized to provide a smooth transition to natural circulation. A pump inertia (pump, motor, and flywheel) equal to 400 kg m<sup>2</sup> was found appropriate. As a



comparison, the FFTF reactor, which is a sodium-cooled 400 MWth reactor, had a primary pump inertia of 700 kg m<sup>2</sup> [44].

### VIII.A. Seismic analysis

A tall vessel is desirable to promote natural circulation. On the other hand, a large vessel increases the cost and decreases seismic stability. The vessel thickness increases with the vessel size and weight of the contained liquid. According to one report [45], wall thickness for type 316SS is limited to 130 mm by manufacturing capability. Thus, to ensure acceptable stress levels under a seismic event, it is necessary to limit the size of the vessel. A rough estimate of the allowable vessel height was calculated based on a seismic model suggested by Buongiorno [46]. We assume that the vessel has an outer diameter of 6 m and contains lead-bismuth with an average density of 10.2 g/cm<sup>3</sup>. The vessel is made of grade 316 stainless steel with a steady-state operating temperature of 693 K. Following Buongiorno's example, the vessel is subject to an earthquake with a peak ground acceleration of 0.5g (horizontal motion). This criterion is adequate for licensing purposes of most sites in the U.S. The calculated peak stress intensity is compared with limits specified by the ASME code for 316SS. The analysis suggests an allowable vessel height in the range 10-12 m. It should be noted that this estimate is based on a tentative maximum wall thickness of 130 mm for a vessel made of 316SS, as compared to thicknesses around 200-250 mm for PWR systems (utilizing carbon steels). It is found that, a wall thickness of 250 mm should admit a vessel height around 15-16 m, which indicates a rather high sensitivity of the stress level on the vessel height. The dependence on the vessel diameter is not strong, however. The study also depends on seismic load conditions, which are site dependent. Use of bottom horizontal structure support and/or base isolation could enhance seismic performance. The effect of seismic isolation is a reduction of the natural frequency of the structure, which may lead to significant reduction of building accelerations in an earthquake. This was recently shown in the application to an ADS plant [47].

TABLE IX.  
Plant specification

|   |                       |
|---|-----------------------|
| General   |                       |
| Type of plant                                     | Pool type             |
| Reactor power                                     | 800 MWth              |
| Coolant   | LBE (44.5%Pb+55.5%Bi) |
| Reactor inlet temperature                         | 573 K                 |
| Coolant inlet velocity                            | 2.5 m/s               |
| Reactor vessel                                    |                       |
| Height  | 10 m                  |
| Diameter  | 6 m                   |
| Wall thickness                                    | 13 cm                 |
| Weight (incl. coolant)                            | ~2500 ton             |
| Primary system                                    |                       |
| Steam generators                                  | 4 (integrated)        |
| No. of pumps                                      | 4                     |
| Pump mass of inertia                              | 400 kg·m <sup>2</sup> |
| Distance between thermal centers of core and SG's | 5.5 m                 |

### VIII.B. Thermal- and hydraulics analysis

Plant thermal-hydraulics data are presented in TABLE X. Because of different linear power ratings, the exit temperature for the CerCer core is lower than the CerMet and nitride cores. It is noted that the coolant mass flow rate is higher and the exit temperatures are lower for the configurations using a pin diameter of 6.8 mm, which is a geometrical effect of maintaining a constant P/D ratio while the pin diameter is increased. Friction factors for the calculation of the pressure drop in the rod bundle are determined from the Blasius relation for turbulent flow:

$$f = 0.316 \text{Re}^{-0.25}$$

The pressure drop through the core depends on the pitch-to-diameter ratio and on the cladding diameter. It is found that for P/D=1.50 it accounts for 90% of the total system pressure loss at normal forced flow operation; at P/D=1.75 it is responsible for about 60% of the pressure loss.

TABLE X  
Thermal-hydraulics data during steady-state.

| Fuel                          | $D_{\text{clad}}$ | P/D  | CerCer           | CerMet           | Nitride          |
|-------------------------------|-------------------|------|------------------|------------------|------------------|
| Coolant exit temp. (K)        | 5.7               | 1.50 | 740              | 810              | 810              |
|                               | 5.7               | 1.75 | 680              | 720              | 720              |
|                               | 6.8               | 1.50 | 690              | 740              | 740              |
| Hot channel exit temp. (K)    | 5.7               | 1.50 | 790              | 880              | 880              |
|                               | 5.7               | 1.75 | 710              | 760              | 760              |
|                               | 6.8               | 1.50 | 730              | 790              | 790              |
| Mass flow rate (kg/s)         | 5.7               | 1.50 | 0.96             | 0.96             | 0.96             |
|                               | 5.7               | 1.75 | 1.61             | 1.61             | 1.61             |
|                               | 6.8               | 1.50 | 1.33             | 1.33             | 1.33             |
| SA friction, $\Delta p$ (Pa)  | 5.7               | 1.50 | $2.8 \cdot 10^5$ | $2.8 \cdot 10^5$ | $2.8 \cdot 10^5$ |
|                               | 5.7               | 1.75 | $1.6 \cdot 10^5$ | $1.6 \cdot 10^5$ | $1.6 \cdot 10^5$ |
|                               | 6.8               | 1.50 | $2.4 \cdot 10^5$ | $2.4 \cdot 10^5$ | $2.4 \cdot 10^5$ |
| Primary loop, $\Delta p$ (Pa) | 5.7               | 1.50 | $3.1 \cdot 10^5$ | $3.1 \cdot 10^5$ | $3.1 \cdot 10^5$ |
|                               | 5.7               | 1.75 | $2.5 \cdot 10^5$ | $2.5 \cdot 10^5$ | $2.5 \cdot 10^5$ |
|                               | 6.8               | 1.50 | $3.0 \cdot 10^5$ | $3.0 \cdot 10^5$ | $3.0 \cdot 10^5$ |

## IX. REACTIVITY SOURCES

Identification of potential reactivity sources is an important element influencing the inherent safety characteristics of the reactor. These sources may come into play because of temperature changes during normal operation or as a result of displacement of core materials under accident conditions. Because of the built-in subcritical margin, reactivity feedbacks involving only temperature changes have a limited role in ADS's [48]. We have chosen to include them in the discussion for completeness.

### IX.A. Temperature coefficients

The main reactivity feedback mechanisms and their numerical values are shown in TABLE XI. These coefficients are whole core values and reflect the effect of changes in temperature about the normal operating point. The reactivity coefficients are calculated through two successive eigenvalue calculations, one for the initial state, and one for a perturbed state (involving a certain change in density, temperature, or geometric configuration around the operating point). The coefficient for thermal expansion of the associated material (fuel, coolant, steel) is used to define the appropriate relationship with the temperature coefficient of reactivity. The radial expansion reactivity is calculated by expanding the core grid in the horizontal direction. The fuel expansion reactivity effect is determined based on elongation of the fuel column; any contact between the fuel and the cladding is ignored. It is seen that the coolant density coefficient is somewhat stronger in the CerCer core than in the CerMet and nitride cases. Literature values for the typical sodium-cooled and MOX-fueled fast breeder reactor (FBR) are included for comparison. It is noteworthy that the positive reactivity effect due to sodium expansion in the FBR is about twice the LBE-expansion coefficient in the investigated cores. The Doppler coefficient is around 0.05 pcm/K for the studies cores, which is an order of magnitude smaller than in the FBR. The integrated effect (up to fuel failure) due to Doppler feedback is in the range  $-0.2$ - $0.3\%$ , which is unimportant for transients in ADS's. Reactivity feedback due to axial expansion is

approximately 5 times the Doppler coefficient, but usually it has a small effect. It may be compared with subcriticality levels around 16-18 dollars for the examined cores. All cores feature a net negative temperature coefficient, assuming isothermal heatup. Radial core expansion is by far the most important feedback effect in this respect. However, radial core expansion effect is determined by temperature changes of the grid support structure and heating of the duct walls at the above-core load pads, so the overall effect depends on the heating rate and local temperature distribution.

TABLE XI.

Whole-core temperature reactivity coefficients for reference core P/D=1.5, D=5.7 mm (as calculated around the operating point).

| Reactivity coefficients | $\Delta k / \Delta T \cdot 10^5$ (pcm) |        |         |                    |
|-------------------------|--|--------|---------|--------------------|
|                         | CerCer                                 | CerMet | Nitride | FBR                |
| Coolant expansion       | +0.43                                  | +0.32  | +0.35   | +0.80 <sup>a</sup> |
| Axial fuel expansion    | -0.28                                  | -0.18  | -0.25   | -0.18 <sup>b</sup> |
| Radial core expansion   | -0.94                                  | -0.97  | -1.01   | -1.10 <sup>a</sup> |
| Doppler effect          | -0.05                                  | -0.05  | -0.05   | -0.40 <sup>a</sup> |
| Net (isothermal heatup) | -0.84                                  | -0.88  | -0.96   | -0.88              |

<sup>a</sup>Super-Phénix, sodium cooled, UO<sub>2</sub>-PuO<sub>2</sub> fuel.

<sup>b</sup>FFTF, sodium cooled, UO<sub>2</sub>-PuO<sub>2</sub> fuel.

### IX.B. Coolant void

Considerable attention is given to the reduction of the coolant void worth in current ADS designs. It has been shown that coolant voiding could introduce reactivities that may override the subcritical reactivity for certain combinations of fuel and liquid-metal coolant [3,4,49]. A parametric study of the effect of americium content on the void worth was made by Tucek, et al. [50]. It was found that the void reactivity effect increases with the americium content. LBE yields lower void worths than sodium for a wide range of fuel types and core sizes [3,51]. The low void worth and high boiling point in comparison with sodium are principal advantages that favour the selection of LBE. The higher sodium void worth is partly due to its higher moderating power, which causes a larger spectrum shift during voiding. The void worths associated with the present fuels were calculated in a previous paper [7]. For convenience, these results are listed in TABLE XII. The effect of changing the core size and pin diameter is shown. The negative leakage component tends to decrease with increasing reactor size, while the spectrum hardening effect increases for higher coolant volume fractions. The net effect is that the void effect becomes more positive when the core size increases. The calculations indicate an increase in void worth for larger pin diameters. The effect of separately voiding the core region and plenum region was investigated. The spectral contribution to the void reactivity is usually more positive near the center of the core, while the leakage component is more negative near the edges where the flux gradient is stronger. As a result, expulsion of coolant from the central region results in a positive reactivity gain. However, if the plenum region is voided simultaneously, the reactivity effect may decrease considerably. Evidently, the CerMet fuel offers low void worths. For tight lattice configurations with this fuel, even central voiding can be accommodated. The void worth of the CerCer core is considerably higher than the

CerMet and nitride. The reason is the larger core size (more fuel pins) of the CerCer core, which is an effect of the lower linear rating requirement of this fuel. It is noted, however, that all three fuels provide acceptable void values when the core and plenum is voided simultaneously.

TABLE XII.

Coolant void reactivity worth (in pcm) computed for the examined fuels in various lattice configurations.

| Fuel    | P/D=1.50,<br>D <sub>o</sub> =5.7 mm |                 | P/D=1.75,<br>D <sub>o</sub> =5.7 mm |                 | P/D=1.50,<br>D <sub>o</sub> =6.8 mm |                 |
|---------|-------------------------------------|-----------------|-------------------------------------|-----------------|-------------------------------------|-----------------|
|         | Core                                | Core+<br>plenum | Core                                | Core+<br>plenum | Core                                | Core+<br>plenum |
| CerCer  | 4060                                | 1790            | 5300                                | 2300            | 4570                                | 2250            |
| CerMet  | 2460                                | 220             | 3580                                | 470             | 2990                                | 520             |
| Nitride | 2960                                | 680             | 4150                                | 880             | 3610                                | 1080            |

### IX.C. Cladding relocation

Theoretically, molten cladding could be ejected into the coolant and swept upwards with a consequent positive reactivity effect. Such a scenario has been suggested by Maschek et al. [52] in a previous paper. The effect is important if the cladding leaves the core ahead of the fuel. For transient events, it is likely to be associated with coolant overheating, e.g., due to a reduction in flow. On a longer timescale, positive reactivity could be inserted because of dissolution of structural materials in the coolant. In this study, we calculated the reactivity effect assuming all cladding is removed from core, which enables a rough estimate of the reactivity values involved. The results are presented in TABLE XIII. It can be seen that cladding removal leads to a net positive reactivity insertion around 3000 pcm. Note that this value is more or less the same for all fuels. It is further seen that the cladding reactivity worth is largely insensitive to the size of the pin, but decreases for larger pitches as the volume fraction of cladding is lower. Evidently, a larger core size may reduce the cladding worth, but at the cost of a higher void worth. Use of a thinner cladding could further reduce the positive reactivity effect, but it would also degrade mechanical strength.

TABLE XIII.

Reactivity changes (in pcm) following removal of the cladding from the core.

| Fuel    | P/D=1.50,<br>D <sub>o</sub> =5.7 mm | P/D=1.75,<br>D <sub>o</sub> =5.7 mm | P/D=1.50,<br>D <sub>o</sub> =6.8 mm |
|---------|-------------------------------------|-------------------------------------|-------------------------------------|
|         | CerCer                              | 3170                                | 2610                                |
| CerMet  | 3360                                | 2750                                | 3310                                |
| Nitride | 3350                                | 2790                                | 3400                                |

### IX.D. Fuel relocation

Reactivity might be introduced in a fast reactor if the fuel would collect in a denser configuration. This is a fundamental distinction between reactors operating on a fast neutron spectrum and thermal systems. The latter is arranged in nearly an optimum configuration to maximize neutron multiplication and any change to the configuration is likely to shut down the chain reaction. By comparison, if the fuel in an ADS melts or the structure collapses, it is possible that criticality would occur. Neutronic calculations have been

performed to determine critical fuel geometries. TABLE XIV shows critical mass, critical volume, and theoretical number of critical assemblies available. The critical mass is sensitive to the material composition (additions of steel, neutron absorbing materials, reflective conditions, etc.) and the fuel geometry. The calculations were carried out for a cylinder containing pure fuel material (fresh fuel) at its normal density. The height-to-diameter (H/D) ratio of the cylinder is 1. It was further assumed that the cylinder is surrounded by LBE on all surfaces. Of course, the assumed critical geometry is an idealized form of the actual configuration of a hypothetical core melt. Calculations for standard fast reactor fuel (U<sub>0.8</sub>Pu<sub>0.2</sub>O<sub>2</sub> surrounded by Na) were also performed to enable comparison. It is seen that the critical mass of the minor actinide fuels is quite small in comparison with standard fast reactor fuel, however, variations occur. The nitride fuel has the smallest critical mass (70 kg), which is approximately 20 times smaller than classical MOX-fuel surrounded by sodium. This corresponds to the fuel mass contained in three subassemblies (127-pin bundles). The critical mass of the CerMet fuel is 340 kg, which is a factor of 5 larger than the nitride fuel. The critical mass of the CerCer fuel is somewhat smaller than for the CerMet. Clearly, an ADS core contains sufficient fuel to assemble several critical masses. About 69 critical masses were calculated for the nitride core while the oxide cores contain 18 critical masses each. By comparison, Super-Phénix held about 17 critical masses. Given that the total fuel mass in the French reactor is about 4 times larger than for the present ADS cores, a direct comparison is not appropriate. Based solely on the critical mass, it would seem desirable to use a neutron absorbing matrix material, such as molybdenum or magnesia. However, the recriticality question is complex and in comparison with fast reactors, the behavior of an ADS under these conditions is not well known. The critical size of the fuel is merely one element affecting the recriticality potential.

TABLE XIV.

Critical mass studies.

| Fuel         | Critical mass*<br>(kg) | Critical volume<br>(dm <sup>3</sup> ) | Reactor total<br>(critical masses) |
|--------------|------------------------|---------------------------------------|------------------------------------|
| CerCer       | 290                    | 47                                    | 18                                 |
| CerMet       | 340                    | 33                                    | 18                                 |
| Nitride      | 70                     | 9                                     | 69                                 |
| Super-Phénix | 1370                   | 130                                   | 17**                               |

\*Cylindrical volume element (H/D=1) surrounded by LBE.

\*\*Based on (U<sub>0.8</sub>Pu<sub>0.2</sub>)O<sub>2</sub>, 3000 MWth (23 tons of fuel).

## X. UNPROTECTED LOSS-OF-FLOW

This section presents results for a flow coastdown transient. It is assumed that all primary pumps are tripped in conjunction with failure of the shutdown system, i.e., the proton beam remains on. It is further assumed that the heat rejection system maintains core inlet temperature at the pre-transient value. This is a reasonable assumption, since negligible changes in the inlet temperature typically occur during a loss-of-flow event. During the transition to natural circulation condition, the flow rate is determined by the inertia of the pump and the thermal buoyant drive, which is

counterbalanced by the system pressure losses. It was mentioned earlier that the pump moment of inertia was optimized to soften the cladding-heating rate following pump trip. The cladding-heating rate gradually decreases for longer flow coast-down time, which implies longer grace periods with ever increasing pump inertia. There are, however, operational problems associated with high inertia pumps that impose an upper limit on the pump mass. Besides mechanical problems on the pump shaft, an adverse negative effect is sluggish speed control. In a controlled shutdown event, it is desirable to match the flow and power to avoid thermal cold shock in reactor components (mainly in upper internal structures and heat exchangers). In that case, a large rotating mass is a drawback. Multiple shutdown events may result in thermal fatigue [53], which can cause premature failure. This problem is of particular concern for ADS's because of the possibility for frequent beam interruptions [54]. Therefore, a balance must be struck in the selection of the flywheel size.

### X.A. Transient results

Examination of Fig. 3, which shows the coolant flow rate in the average channel for the case with  $P/D=1.75$ , reveals that the natural circulation flow reaches a quasi-steady value of 23-27% of initial flow at 50-60 seconds after the pump trip. From this data plus the thermal response for the cladding shown later, it is apparent that the transition to natural circulation is smooth. Because the CerCer system operates with a lower coolant  $\Delta T$ , the fluid density difference between the hot leg and the cold leg is smaller, which provides for a lower circuit buoyant head. As a result, the natural circulation flow level is lower in the CerCer reactor. Fig. 3 shows the power history. All three cores feature overall negative temperature-induced reactivity feedbacks. The power decreases steadily during the entire transition to natural circulation conditions. The overall effect of the reactivity feedbacks is not great, however. The power falls to approximately 95% of the initial value of 800 MWth when equilibrium is reached. The power response behavior is similar among the cores.

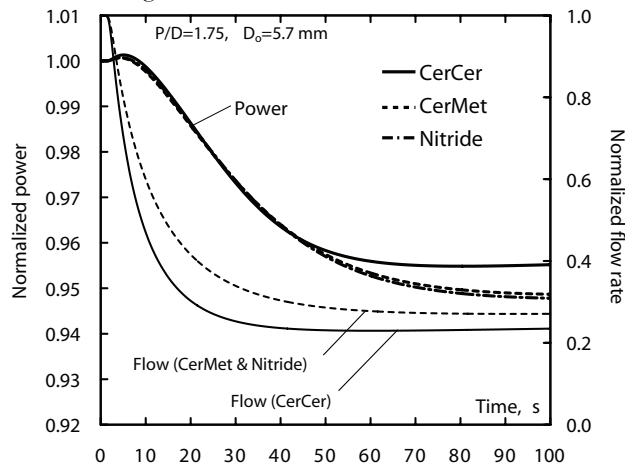


Fig. 3. Transient power and flow conditions for unprotected loss-of-flow transient.

Reactivity feedbacks are illustrated in Fig. 4. For simplicity only the case with CerCer fuel and  $P/D=1.75$  is shown. Reactivity feedback from radial expansion of the core is the

dominant negative feedback mechanism – it contributes about minus one dollar at equilibrium conditions. A brief description on the radial expansion reactivity model is in place. The radial growth of the core is determined by the expansion of the grid support structure and by the expansion of the hexcan duct walls and the above-core load pads. The model does not explicitly account for subassembly bowing or for subassembly clearance at the upper load pads. Since the coolant inlet temperature is constant during the transient, the reactivity feedback is determined solely by the temperature rise of duct walls and the structure in the upper load pad region. Axial fuel expansion reactivity differs somewhat between the fuels, where the coefficient of thermal expansion for the CerCer fuel is larger by a factor 1.6 in comparison with the CerMet and nitride. The smaller axial expansion reactivity coefficient for the CerMet fuel tends to reduce the reactivity effect associated with this feedback. As the coolant temperature increases it produces a positive reactivity effect. The resulting reactivity increment due to coolant expansion amounts to +0.5\$ for the CerCer core and +0.4\$ for the nitride. The coolant reactivity is however exceeded by the reactivity losses due to radial expansion and fuel elongation. The positive coolant expansion effect is largely compensated by the negative feedback from fuel elongation. The Doppler effect is insignificant.

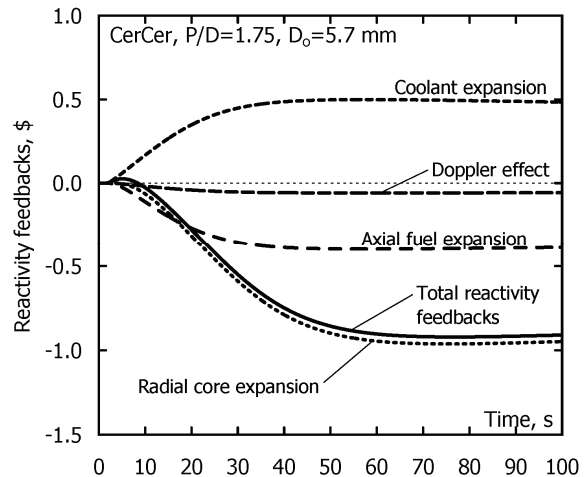


Fig. 4. Reactivity feedback contributions plotted for unprotected loss-of-flow transient.

The immediate effect of the flow reduction is a temperature rise in the coolant, and this in turn leads to higher cladding and fuel temperatures. Coolant boilout is not an issue with lead/bismuth. The major concern is whether the cladding exceeds design limits. Lower cladding temperatures are promoted by higher coolant volume fractions. Larger distance between the fuel pins reduces the core pressure drop and in turn increases contribution from natural circulation. As a result, less forced flow is lost in a pump failure event. Cladding temperature is highest for the CerMet and nitride cores because of their higher power rating. A comparison of cladding temperatures for these cores corresponding to  $P/D=1.50$  and  $P/D=1.75$  is shown in Fig. 5. The burst temperature for the cladding is 1330 K, as discussed previously. Thus, for the smaller pitch design, the cladding exceeds the failure point within 30-40 seconds after pump

failure, which leaves small safety margins. On the other hand, increasing the P/D ratio to 1.75 reduces cladding temperatures by more than 200 degrees. In that case, early cladding failure can be avoided. It is noted however, that a safe state cannot be assured indefinitely. The burst limit is applicable in transients in which the cladding is heated, without interruption, until failure. Thermal creep rates increase rapidly at high temperatures. Based on creep rupture data for D9 alloy [37], the lifetime at 1280 K is in the minute-scale. Thus, damage prevention will eventually require the need for shutdown and restored cooling capability.

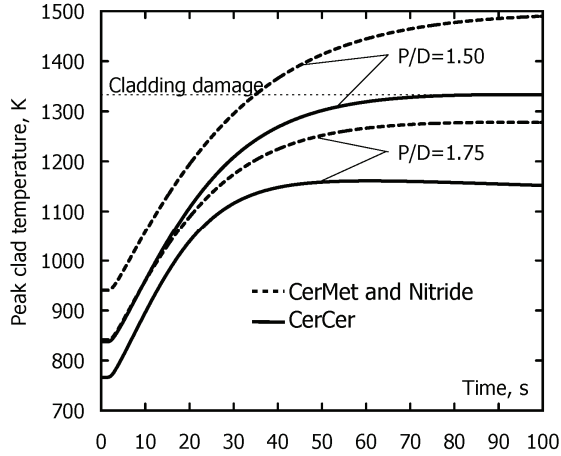


Fig. 5. Peak cladding temperatures for unprotected loss-of-flow transient. Effect of P/D is illustrated.

Maximum fuel and cladding temperatures as function of pitch-to-diameter ratio and pin diameter are presented in TABLE XV. Since the fuel temperature increases along with the coolant temperature, the potential for fuel damage must also be considered. The CerCer temperature reaches close to the damage limit for the cases of the smaller pins. Increasing the pin diameter should be considered in this case.

TABLE XV.

Peak fuel and cladding temperatures at a time  $t=100$  seconds during unprotected loss-of-flow transient as function of P/D and pin diameter.

| Fuel    | P/D=1.50               |      | P/D=1.75               |      | P/D=1.50               |      |
|---------|------------------------|------|------------------------|------|------------------------|------|
|         | D <sub>o</sub> =5.7 mm | Clad | D <sub>o</sub> =5.7 mm | Clad | D <sub>o</sub> =6.8 mm | Clad |
| CerCer  | 2160                   | 1330 | 2130                   | 1160 | 1970                   | 1200 |
| CerMet  | 2120                   | 1490 | 2030                   | 1280 | 1920                   | 1340 |
| Nitride | 2080                   | 1490 | 1980                   | 1280 | 1920                   | 1340 |

## XI. BEAM OVERPOWER

In accelerator-driven system designs, fission reactions are maintained through multiplication of neutrons from a spallation neutron source, which is driven by a proton accelerator. In such systems, the neutron source is the controller of the chain reaction [55]. Thus, it is appropriate to consider transients in which the source intensity suddenly changes. This could for example happen due to a control system failure, accelerator malfunction, or operator error. In the study, it is assumed that the source intensity increases by a factor of 1.5 times the initial strength, which corresponds to

the beam output capability at end-of-cycle. The ramp is initiated at  $t=1$  second and halted at 1.001 seconds. The source is held constant thereafter. It is noted that the source strength in an ADS may change rapidly while transients in a traditional reactor are limited by mechanical speeds. Since the prompt adjustment time in an ADS is very short (tens of  $\Lambda$ ), the power will instantaneously respond to any source variation, which permits accidents with very short initial ramp times in comparison with transients in critical reactors. No safety system can act instantaneously; there are always time delays involved. For a traditional safety rod based shutdown system, there is typically a 200 ms delay from detection to control rod motion [56], and then an insertion time of the order of a second. This is fast enough to detect all accident initiators identified for fast reactors [17], which always appear as gradual changes. A beam overpower accident, however, can produce a considerable power change before the malfunction has been detected. Hence, failure prevention should be precluded by the design, and not simply rely on proper control system action.

### XI.A. Transient results

Power variation and fuel hot-channel temperatures are illustrated in Fig. 6. It shows the case with a pin diameter of  $D=6.8$  mm. Beam overpower transients are characterized by higher fuel temperatures and the primary concern is fuel melting. As indicated in TABLE XVI, the configuration with the smaller P/D and smaller pin diameter is unacceptable for the CerCer fuel. The melting point is reached at 3 seconds after the beam insertion, which leaves little room for control action. Transient temperatures drop when a larger pin diameter is used because steady-state temperatures are lower with this configuration, for reasons discussed previously. It seems that the CerCer fuel needs to employ a larger pin diameter to avoid premature fuel failure. The temperature of the CerMet fuel reaches 2130 K for the same configuration, which corresponds to a margin to melting of 500 degrees. The nitride fuel, which has lower thermal conductivity than the CerMet fuel but smaller gap size, is slightly colder (2080 K) leaving a margin to dissociation of 320 degrees. As seen in TABLE XVI, the cladding remains well below the damage limit for all three fuel-systems and core configurations.

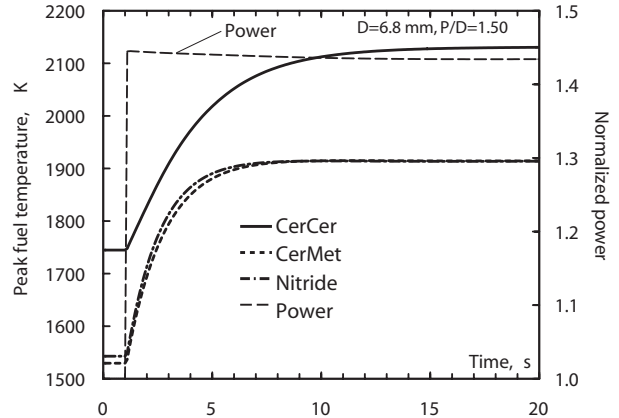


Fig. 6. Transient power and fuel temperatures for beam overpower transient.

TABLE XVI.

Peak fuel and cladding temperatures at a time  $t=20$  seconds during beam overpower accident.

| Fuel    | P/D=1.50               |      | P/D=1.75               |      | P/D=1.50               |      |
|---------|------------------------|------|------------------------|------|------------------------|------|
|         | D <sub>o</sub> =5.7 mm |      | D <sub>o</sub> =5.7 mm |      | D <sub>o</sub> =6.8 mm |      |
|         | Fuel                   | Clad | Fuel                   | Clad | Fuel                   | Clad |
| CerCer  | 2290                   | 950  | 2300                   | 850  | 2130                   | 860  |
| CerMet  | 2130                   | 1090 | 2130                   | 950  | 1920                   | 970  |
| Nitride | 2080                   | 1090 | 2070                   | 950  | 1910                   | 970  |

## XII. COOLANT VOIDING

The purpose is to investigate transient response associated with coolant voiding. Extensive voiding in a liquid-metal reactor (LMR) may, for example, be caused by a leak in the primary system, sudden release of fission gases, failure in the heat-transport system that causes gas bubbles to enter the coolant, or coolant overheating and vaporization. Usually, LMR plant designs are arranged with backup protection to mitigate the impact of vessel leakage or rupture, to the degree that large-scale loss-of-coolant accidents (LOCA) are extremely unlikely. Pool systems typically have a second guard vessel, and loop systems are normally double pipe and tank designs. Since the liquid-metal coolant is not pressurized under normal operation, a leak in the primary system will not automatically result in coolant boiling, as opposed to the situation in LWR's. In a sodium-cooled reactor, voiding may arise due to boiling out of coolant. This is prevented in a LBE system. In order for the LBE to get hot enough to boil ( $T_b=1940$  K), temperatures have to be above the melting point of steel ( $T_m=1700$  K). In that case, much larger reactivity changes may become available due to fuel or cladding relocation. Coolant can be expelled by the rapid escape of fission gases from ruptured fuel pins. Such an accident has been analyzed by Maschek in a previous study [57]. Fission gas release is of concern for unvented and high burnup ADS fuels. Significant amounts of helium are produced due to production of  $^{242}\text{Cm}$  through neutron capture in  $^{241}\text{Am}$ , and its subsequent alpha-decay into  $^{238}\text{Pu}$ . Another possible mechanism for coolant voiding, without the precondition of steel melting, is the possibility of entrainment of air into the core from the cover gas region or steam/water during a failure in the steam generator, i.e., a so-called steam generator tube rupture (SGTR) event. In sodium plants, intermediate sodium-loops are introduced as a second physical barrier to minimize the consequences of SGTRs and to avoid violent chemical reactions between water and sodium in the primary system. Because lead/bismuth is chemically inert with water/steam, two-circuit designs are suggested, with the steam generators located in the primary system. In such designs, there will only be one barrier to fail in order to get high-pressure steam into the primary system. It is noted that the pressure on the steam side can be as high as 100-150 bars and low pressure on the metal side, about 1 bar. Thus, a significant head is available to push steam into the primary system or cause overpressurization in the circuit, which could open further leakage paths. Normally, steam generator tube failures have a high enough probability occurrence to be considered in the licensing procedure. It is noteworthy that a steam-generator failure was the cause of a LOCA and

radioactive contamination in a Russian LBE-cooled nuclear submarine in 1982 [58].

### XII.A. Modeling approach

The steam transfer in the circuit and the rate of coolant removal depends on the hydraulic design of the reactor and the size of leak (i.e. number of ruptured steam generator tubes). In this study, we have assumed that the coolant is swept upwards through the core, beginning at the lower cold-leg region, and that the void front moves at the average coolant velocity through the core (2.5 m/s). Since the total height of the core plus plenum regions is 2.5 m, the passage occurs in 1 second. The transient calculation uses a reactivity history based on progressive axial voiding of the core. It is assumed that the void spreads axially and simultaneously in all subassemblies. The reactivity effect, as function of axial void level, is pre-calculated using the MCNP code. The results are illustrated in Fig. 7. Based on this information, a time pattern for the reactivity change is constructed, which is applied in the transient calculation. The configuration employing P/D=1.75 is investigated, which poses the largest positive void reactivity effect. Note that the reactivity effect is strongest for the CerCer fuel and most positive when the core has been voided up to slightly below the top of the active fuel region. The reactivity insertion rate is highest at core midlevel. As a coincidence, the maximum reactivity insertion due to coolant void corresponded to the initial subcritical reactivity of the CerCer core.

The model is intended for scoping evaluations on a shorter time scale. It is noted that the coolant could not be removed from the channel in a physical sense; only the associated reactivity effect is reproduced. As a result, the insulating effect of the gas is neglected. This will affect fuel pin temperatures. The cladding will be subject to the largest uncertainty since it has the shortest time response to changes in convective conditions. The effect on the fuel is expected to be limited during the time frame studied. Power estimates are not affected since all thermal feedback effects are small in comparison with the void reactivity.

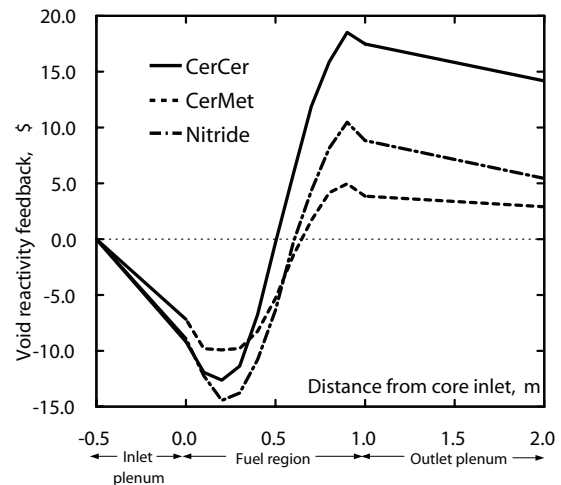


Fig. 7. Reactivity effect (\$) following progressive axial voiding of coolant beginning at the lower plenum.

## XII.B. Transient results

The resulting power history is presented in Fig. 8. It is assumed that the steam bubble reaches the lower plenum at 1 second after the steam generator failure. Initially, the bubble passage produces a negative reactivity effect due to increased neutron leakage, as the lower plenum is voided first. The power will find its peak as the reactivity reaches its maximum. The reactivity at peak power, is  $-0.2\%$ ,  $-12.3\%$ , and  $-6.8\%$ , respectively for the CerCer, CerMet, and nitride cores, the corresponding peak power is 15.3, 1.3, and 2.1, times the initial power. The power rise in the nitride and CerMet fueled cores is quite modest. The CerCer core, on the other hand, suffers from a sharp power peak. Except from coolant void, axial fuel expansion is the only feedback effect that has some impact on the transient. At peak conditions, the contribution from axial expansion provided an extra reactivity margin, which was sufficient to maintain the reactor in the subcritical state, thereby limiting the magnitude of the peak. Radial core expansion is too slow to be of any significance. It was found that the flux shape in the voided state was similar to the initial shape, and power peaking factors were even lower. The power rise is halted when the void has extended to the top of the core and begins to void the upper plenum region. Judging from Fig. 8, voiding of the upper plenum plays a vital role in reversing the accident. It is assumed that the beam is shutdown after 2 seconds. After shutdown, heat is generated by fissions produced by delayed neutrons plus the reactor decay heat. The delayed neutron source dies away in about 80 seconds (which is the mean life of the longest living precursor  $^{87}\text{Br}$ ).

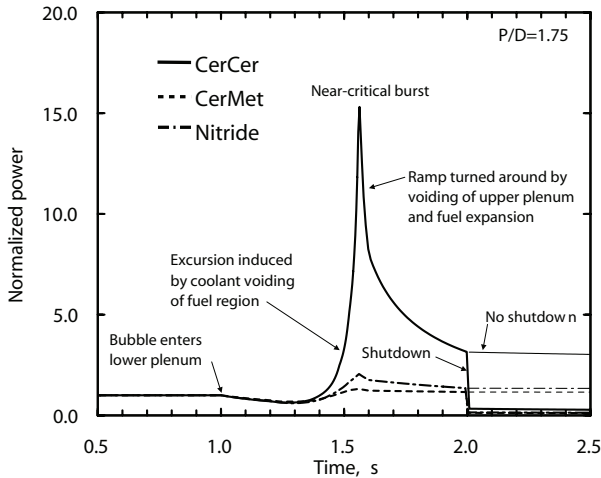


Fig. 8. Transient power for coolant voiding transient.

It is interesting to see that the power in the CerMet and nitride cases is only slightly affected, despite that the reactivity input is of the order of 5-10 dollars. This is a consequence of the fact that these two systems maintain a considerable margin to criticality during the entire transient. The power following a reactivity insertion in a subcritical reactor is inversely proportional to the reactivity in the perturbed state, which tends to zero as the reactor approaches the critical state. Thus, in the presence of an external source, the power approaches infinity as the reactor approaches critical conditions (a  $1/\rho$  approach). As a result, the majority of the

power rise will occur near the critical state. The analysis shows that it can be extremely productive to adjust the initial multiplication constant even by a relatively small amount. For example, if the CerCer core would be designed with an initial  $k_{\text{eff}}=0.96$  instead of  $k_{\text{eff}}=0.97$ , then the same voiding scenario (subject to an equivalent reactivity input) would cause a mild peak of approximately 3 times the initial value, instead of 15.

Fig. 9 illustrates the maximum fuel temperature during the accident. The temperature of the CerCer fuel rises considerably; reaching over 2500 K at the time when the reactor is shutdown (the thicker curve represents the temperature evolution after shutdown takes place). The temperature exceeds the assumed melting point of 2200 K at 1.6 seconds. Unless shutdown is initiated, fuel temperatures would continue to rise according to the thinner curve depicted in Fig 9. The temperature of the CerMet and nitride fuels is well below their failure limits. In these systems, the main effect of the coolant expulsion is the loss in heat removal capability on the surface, which presents greatest hazard to the cladding. The temperature rise in the CerCer fuel is overshadowed by the power rise caused by the positive void reactivity insertion. When the power falls during the shutdown phase, the temperature profile tends to level out across the fuel rod. Thus, fuel centerline temperatures decrease, according to Fig 9. Nevertheless, the average temperature of the core continues to rise even after the reactor has been shutdown since the core is deprived of cooling (assuming no coolant reentry). Beam shutdown alone does not prevent the reactor from reaching a failure point, as it would require restored cooling capability. Because of the limited power rise in the nitride and CerMet cores, it is predicted that cladding failure will occur prior to fuel failure.

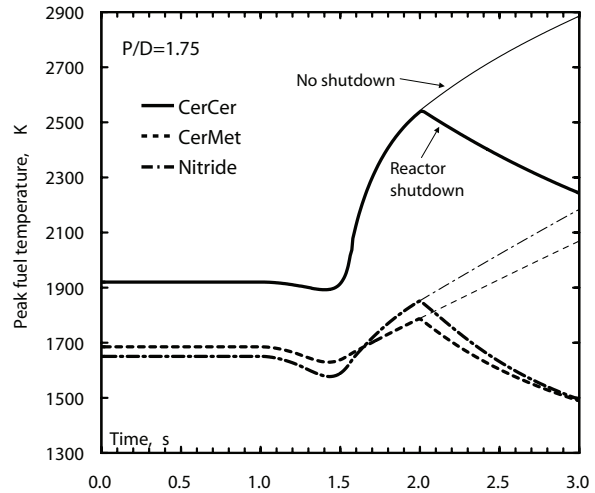


Fig. 9. Peak fuel temperatures for coolant voiding transient.

## XIII. CONCLUSIONS

The objective was to study transient safety characteristics of lead-bismuth cooled accelerator-driven systems (ADS) with CerCer-, CerMet-, or nitride-fueled cores. Major consideration was given to the inherent safety aspects of core design. Analyses were carried out for the short-term transient response to unprotected loss-of-flow and accelerator beam-overpower accidents, and a coolant voiding scenario. The

effect of design changes involving variations in the lattice pitch and pin diameter was investigated. Design limits for the fuel and selected cladding materials were compiled. Fuel thermophysical properties were updated according to recently published review articles. Maximum temperatures were determined and compared with design limits. Reactivity effects associated with the relocation of core materials were investigated.

In summary, the better thermal conductivity, higher melting point, and lower coolant void worth of the CerMet fuel combine to contribute to better inherent safety features. In none of the studied transients was the CerMet fuel close to melting. The swelling behavior and hardness of the molybdenum metal raise safety concerns regarding fuel-cladding mechanical interactions. The approach so far has been to increase the initial fuel-cladding gap to accommodate fuel swelling. Although, the results indicate favorable safety performance of the CerMet fuel, many questions still need to be answered and irradiation performance remains to be demonstrated. The CerCer fuel suffers from low thermal conductivity and uncertain melting behavior, which limits both the achievable power density and predicted performance during overpower conditions. Even though the fuel is set to operate at a lower linear power, hot channel fuel temperatures are fairly high, leaving a limited margin to melting. This margin is easily exceeded in an overpower accident and the fuel reaches close to melting during unprotected loss-of-flow conditions. Further measures must be taken to lower the fuel temperature, e.g., increasing the coolant flow area. Increasing the pin diameter will enable lower operating temperature as it allows larger matrix fractions to be used. In addition, the reactivity void worth of this fuel is relatively high in comparison with the other fuels, which is a safety dilemma. It is noted that the specific power density has a critical impact on the achievable burnup level, recycling requirements, overall transmutation efficiency, etc., and, thus, has a strong influence on the economics of the entire fuel cycle. The lower power rating capability of the CerCer fuel leads to obvious performance penalties. The principal problem with the nitride fuel, with regards to the safety performance, is its tendency to dissociate at low temperatures. However, recent studies have shown that decomposition could be suppressed in a nitrogen atmosphere. Whether this is an effective solution under accident conditions, is subject to further investigation. Efforts to increase the understanding of nitride dissociation phenomena are underway. The cladding reactivity worth was essentially the same for all fuels and comparable to the maximum void reactivity available. The study showed that the fuels possess smaller critical masses in comparison with classical fast reactor fuel, but significant variations were observed. The studies point to a particular small critical mass for the low absorbing nitride fuel, about 70 kg, which corresponds to the fuel inventory contained in three individual subassemblies. The critical mass is much larger for the oxide fuel versions, by a factor of ~5. The higher melting point of the CerMet fuel in combination with its larger critical mass is favorable characteristics from the recriticality point of view.

Standard type 316 stainless steel is excluded as potential cladding material because of unacceptable radiation swelling.

HT-9 cladding, which has excellent irradiation performance, is rejected because of unsatisfactory high-temperature mechanical performance. At this point, type 15-15Ti austenitic stainless steel is the suggested cladding material. While previous studies indicate high reliability for this material, experimental confirmation of corrosion stability and transient mechanical performance is necessary. For a lead/bismuth-cooled reactor, cladding corrosion leading to wall thinning is a major life-limiting factor. The corrosion rate is strongly dependent on temperature. Cladding temperatures during normal operation are essentially determined by the coolant outlet temperature, which is given by the linear power and the coolant mass flow rate. For a given geometrical arrangement, the coolant mass flow rate is the same for all three fuels; only the linear power rating varies. It was found that the higher rated CerMet and nitride fuels required a higher coolant mass flow rate in order to achieve acceptable cladding temperatures for normal operation. This suggests the use of a higher pin pitch. A higher lattice pitch is also necessary to avoid mechanical failure during unprotected loss-of-flow.

Finally, a steam generator tube rupture event was identified as a potential threat, which could lead to extensive voiding in current accelerator-driven design proposals. A preliminary transient test case study was performed. Due to the strong positive reactivity effect, the CerCer system was subject to a sharp power peak, while the power rise in the nitride and CerMet fueled cores was quite modest, which simply confirms the importance of having a low coolant void reactivity value in a lead/bismuth system, despite of its high boiling temperatures.

## REFERENCES

1. D. G. FOSTER, et al., "Review of PNL Study on Transmutation Processing of High Level Waste," LA-UR-74-74, Los Alamos Scientific Laboratory (1974).
2. T. TAKIZUKA, et al., Proc. 5th Int. Conf. Emerging Nuclear Energy Systems 1989, ICENES '89, Karlsruhe, July 3-6 (1989).
3. J. WALLENIUS, "Neutronic aspects of inert matrix fuels for application in ADS," J. Nucl. Mater. **320** (2003) 142-146.
4. M. ERIKSSON, J. WALLENIUS, J. E. CAHALAN, K. TUCEK, and W. GUDOWSKI, "Safety analysis of Na and Pb-Bi coolants in response to beam instabilities," Proc. 3rd International Workshop on Utilisation and Reliability of High Power Proton Accelerators, Santa Fe, May 12-16, NEA/OECD (2002).
5. J. WALLENIUS, "CONFIRM: Collaboration on Nitride Fuel Irradiation and Modelling," Proc. of the AccApp/ADTTA 2001 Meeting, Reno, November 11-15, American Nuclear Society (2001).
6. S. PILLION and J. WALLENIUS, "Oxide and nitride TRU-fuels: lessons drawn from the CONFIRM and FUTURE projects of the 5th European framework



- programme,” Nucl. Sci. Eng., Accepted for publication (2004).
7. J. WALLENIS and M. ERIKSSON, “Neutronic design of minor actinide burning accelerator driven systems,” Nucl. Technol., Submitted (2004).
  8. “Safety related terms for advanced nuclear plants,” IAEA-TECDOC-626, September (1991).
  9. H. MURATA and T. MUKAIYAMA, “Fission reactor studies in view of reactor waste programmes,” Atomkernenergie – Kerntechnik, **45** (1984) 23-29.
  10. H. KLEYKAMP, “Selection of materials as diluents for burning of plutonium fuels in nuclear reactors,” J. Nucl. Mater. **275** (1999) 1-11.
  11. M. BURGHARTZ, G. LEDERGERBER, H. HEIN, R. R. VAN DER LAAN, and R. J. M. KONINGS, “Some aspects of the use of ZrN as an inert matrix for actinide fuels,” J. Nucl. Mater. **288** (2001) 233-236.
  12. K. MINATO, M. AKABORI, M. TAKANO, Y. ARAI, K. NAKAJIMA, A. ITOH, and T. OGAWA, “Fabrication of nitride fuels for transmutation of minor actinides,” J. Nucl. Mater. **320** (2003) 18-24.
  13. M. TAKANO, “Study on The Stability of AmN and (Am,Zr)N,” Proc. GLOBAL 2003, New Orleans, Louisiana, November 16-20 (2003).
  14. J. WALLENIS and S. PILLON, “N-15 Requirement for 2nd Stratum ADS Nitride Fuels,” Proc. of the AccApp/ADTTA 2001 Meeting, Reno, November 11-15, American Nuclear Society (2001).
  15. M. A. MIGNANELLI and R. THETFORD in Proc. on Advanced Reactors with Innovative Fuels, ARWIF-2001, Chester, October 22-24 (2001).
  16. R. THETFORD and M. MIGNANELLI, “The chemistry and physics of modeling nitride fuels for transmutation,” J. Nucl. Mater. **320** (2003) 44-53.
  17. A. E. WALTAR and A. B. REYNOLDS, Fast Breeder Reactors, p. 260 and 540, Pergamon Press, New York (1981).
  18. D. R. OLANDER, Fundamental Aspects of Nuclear Reactor Elements, p. 131-135, Published by Technical Information Center, Office of Public Affairs, Energy Research and Development Administration, Springfield, VA (1976).
  19. Ph. DEHAUDT, A. MOCELLIN, G. EMINET, L. CAILLOT, G. DELETTE, M. BAUER, and I. VIALLARD, “Composite Fuel Behaviour Under and After Irradiation,” IAEA Technical Committee Meeting on Research of Fuel Aimed at Low Fission Gas Release, Moscow, October 1-4 (1996).
  20. J. L. SÉRAN, V. LÉVY, P. DUBUISSON, D. GILBON, A. MAILLARD, A. FISSOLO, H. TOURON, R. CAUVIN, A. CHALONY, and A. LE BOULBIN, “Behavior under Neutron irradiation of the 15-15Ti and EM10 Steels Used as Standard Materials of the Phénix Fuel Subassembly,” Effects of Radiation on Materials: 15th Int. Symposium, ASTM STP **1125**, R. E. Stoller, A. S. Kumar, and D. S. Gelles, Eds., American Society for Testing and Materials, p. 1209-1233, Philadelphia (1992).
  21. A. FISSOLO, V. LÉVY, J. L. SÉRAN, A. MAILLARD, J. ROYER, and O. ARBOUILLE, “Tensile Properties of Neutron Irradiated 316Ti and 15-15Ti Steels,” Effects of Radiation on Materials: 16th Int. Symposium, ASTM STP **1175**, A. S. Kumar, D. S. Gelles, R. K. Nanstad, and E. A. Little, Eds., American Society for Testing and Materials, p. 646-663, Philadelphia (1993).
  22. E. H. P. CORDFUNKE and R. J. M. KONINGS, Thermochemical Data for Reactor Materials and Fission Products, North-Holland, Amsterdam (1990).
  23. J. J. KATZ, G. T. SEOBORG, and L. R. MOSS, The chemistry of the actinide elements, 2<sup>nd</sup> ed., Vols. 1 and 2, Chapman and Hall, London (1986).
  24. J. EDWARDS, et al., “Fast Reactor Manual,” Fast Reactor European Collaboration report (1990).
  25. R. KONINGS, Personal Communication (January, 2004).
  26. S. CASALTA, HJ. MATZKE, and C. PRUNIER, Proc. Int. Conf. On Evaluation of Emerging Nuclear Fuel Cycle Systems, GLOBAL’95, Versailles, September 11-14, p. **1725** (1995).
  27. H. ZHANG, R. J. M. KONINGS, M. E. HUNTELAAR, and E. H. P. CORDFUNKE, “Melting behaviour of oxide systems for heterogeneous transmutation of actinides. III. The system Am-Mg-O,” J. Nucl. Mater. **250** (1997) 88-95.
  28. H. ZHANG, R. J. M. KONINGS, M. E. HUNTELAAR, and E. H. P. CORDFUNKE, “Melting behaviour of oxide systems for heterogeneous transmutation of actinides. I. The systems Pu-Al-O and Pu-Mg-O,” J. Nucl. Mater. **249** (1997) 223-230.
  29. M. TAKANO, A. ITOH, M. AKABORI, et al., “Synthesis of americium mononitride by carbothermic reduction method,” Proc. Int. Conf. On Future Nuclear Energy Systems, GLOBAL’99, Jackson Hole, Wyoming, Aug. 29 – Sep. 3, p. 110, American Nuclear Society (1999).
  30. M. JOLKKONEN, M. STREIT, and J. WALLENIS, “Thermo-chemical modelling of uranium-free nitride fuels,” J. Nucl. Sci. Technol. **41**(4), 457 (2004).
  31. J.-O. ANDERSSON, et al., “Thermo-Calc and DICTRA, computational tools for materials science,” Calphad **26**, 273 (2002).
  32. T. OGAWA, T. OHMACHI, A. MAEDA, et al., “Vaporization behaviour of (Pu,Am)N,” J. Alloys and Compounds, **224**, 55 (1995).
  33. N. S. CANNON, F. R. HUANG, and M. L. HAMILTON, “Transient and Static Mechanical Properties of D9 Fuel Pin Cladding and Duct Material Irradiated to High Fluence,” Effects of Radiation on Materials: 15th Int.

- Symposium, ASTM STP 1125, R. E. Stoller, A. S. Kumar, and D. S. Gelles, Eds., American Society for Testing and Materials, p. 1071-1082, Philadelphia (1992).
34. I. SHIBAHARA, T. OMORI, Y. SATO, S. ONOSE, and S. NOMURA, "Mechanical Property Degradation of Fast Reactor Fuel Cladding During Thermal Transients," Effects of Radiation on Materials: 16th Int. Symposium, ASTM STP 1175, A. S. Kumar, D. S. Gelles, R. Nanstad, and E. A. Little, Eds., American Society for Testing and Materials, p. 664-678, Philadelphia (1994).
35. M. G. ADAMSON, E. A. AITKEN, and S. VAIDYANATHAN, "Synergistic tellurium-caesium embrittlement of Type 316 stainless steel", Nature, **295**, 49 (1982).
36. S. TANI, S. NOMURA, and I. SHIBAHARA, "Fuel Cladding Mechanical Property Degradation Mechanisms and Fuel Reliability Under Transient Conditions," Int. Conf. on Reliable Fuels for Liquid Metal Reactors, Sep. 7-11, Tucson (1986).
37. R. J. PUGH and M. L. HAMILTON, Influence of Radiation on Materials Properties: 13th Int. Symposium (Part II), ASTM STP 956, F. A. Garner, C. H. Henager, N. Igata, Eds., American Society for Testing Materials, p. 22-29 (1987).
38. G. S. YACHMENYOV, A. YE. RUSANOV, B. F. GROMOV, YU. S. BELOMYTSEV, N. S. SKVORTSOV, and A. P. DEMISHONKOV, "Problems of structural materials' corrosion in lead-bismuth coolant," Proc. Heavy Liquid Metal Coolants in Nuclear Technology, Vol. 1, Obninsk, October 5-9, p. 133-140, State Scientific Center of Russian Federation Institute for Physics and Power Engineering (1998).
39. J. F. BRIESMEISTER, "MCNP - A general Monte Carlo N-Particle transport code," LA-13709-M, Los Alamos National Laboratory (2000).
40. J. E. CAHALAN, A. M. TENTNER, and E. E. MORRIS, "Advanced LMR Safety Analysis Capabilities in the SASSYS-1 and SAS4A Computer Codes," Proc. of the International Topical Meeting on Advanced Reactors Safety, Pittsburgh, April 17-21 (1994).
41. M. ERIKSSON, J. E. CAHALAN, and W. S. YANG, "On the Performance of Point Kinetics for the Analysis of Accelerator Driven Systems," Accepted for publication in the March Issue of Nucl. Sci. Eng. (2005).
42. K. TSUJIMOTO, T. SASA, K. NISHIHARA, H. OIGAWA, and H. TAKANO, "Neutronics Design for Lead-Bismuth Cooled Accelerator-Driven System for Transmutation of Minor Actinides," J. Nucl. Sci. & Technology, **41** (2004) 21.
43. P. A. USHAKOV, "Hydrodynamics and Heat Transfer in Reactor Cooled by Lead-Bismuth Alloy," Proc. Heavy Liquid Metal Coolants in Nuclear Technology, Vol. 2, Obninsk, October 5-9, p. 612-626, State Scientific Center of Russian Federation Institute for Physics and Power Engineering (1998).
44. F. E. DUNN and D. J. MALLOY, "LMR Centrifugal Pump Coastdowns," Proc. Anticipated and Abnormal Transients In Nuclear Power Plants, Vol. 1, American Nuclear Society Topical Meeting, Atlanta, Georgia, April 12-15 (1987).
45. H. TAKANO, et al., "A Design for Inherent Safety Core, Aseismicity and Heat Transport System in Lead-Cooled Nitride-Fuel Fast Reactor," Proc. Int. Topical Meeting on Advanced Reactor Safety, Pittsburgh, April 17-21 (1994).
46. J. BUONGIORNO and B.D. HAWKES, "Seismic analysis of heavy-liquid-metal-cooled reactor vessels", Nuclear Engineering and Design **228** (2004) 305-317.
47. I. MICHELI, S. CARDINI, A. COLAIUDA, P. TURRONI, "Investigation upon the dynamic structural response of a nuclear plant on aseismic isolating devices," Nuclear Engineering and Design **228** (2004) 319-343.
48. M. ERIKSSON and J. E. CAHALAN, "Inherent shutdown capabilities in accelerator-driven systems," Annals of Nuclear Energy, vol. 29/14 pp 1689-1706, (2002).
49. W. MASCHKEK, et al., "Safety Improvements for ADS Transmuters with dedicated Fuel," Proc. of the AccApp/ADTTA 2001 Meeting, Reno, November 11-15, American Nuclear Society (2001).
50. K. TUCEK, J. WALLENIUS, and W. GUDOWSKI "Coolant void worths in fast breeder reactors and accelerator driven transuranium and minor actinide burners," Annals of Nuclear Energy, accepted for publication (2004).
51. J. WALLENIUS, K. TUCEK, and W. GUDOWSKI, "Safety analysis of nitride fuels in cores dedicated to waste transmutation," Proc. 6th Information Exchange Meeting on Actinide and Fission Product Partitioning and Transmutation, Madrid, December 11-13, OECD/NEA (2000).
52. W. MASCHKEK, T. SUZUKI, X. CHEN, MG. MORI, C. M. BOCCACCINI, M. FLAD, K. MORITA, "Behavior of Transmuter Fuels of Accelerator Driven Systems under Severe Accident Conditions," GENES4/ANP2003, Kyoto, September 15-19 (2003).
53. F. E. DUNN and D.C. WADE, "Estimates of Thermal Fatigue Due to Beam Interruptions for an ALMR-Type ATW," Proc. 2nd International Workshop on Utilisation and Reliability of High Power Proton Accelerators, Aix-en-Provence, November 22-24, NEA/OECD (1999).
54. M. ERIKSSON, "Reliability Assessment of the LANSCE Accelerator System," M.Sc. Thesis, Royal Institute of Technology, Dep. Nuclear and Reactor Physics (Nov. 1998).
55. J. E. CAHALAN and M. ERIKSSON, "Active and Passive Safety Control Performance in Sub-critical, Accelerator-Driven Nuclear Reactors," Proc. 3rd International Workshop on Utilisation and Reliability of High Power Proton Accelerators, Santa Fe, May, NEA/OECD (2002).
56. Y. S. TANG, R. D. COFFIELD, and R. A. MARKLEY, Thermal Analysis of Liquid Metal Fast Breeder Reactors, p.

277, American Nuclear Society, LaGrange Park, Illinois (1978).

57. W. MASCHKEK, et al., "Safety Analyses for ADS Cores with Dedicated Fuel and Proposals for Safety Improvements," IAEA-TECDOC-1356, IAEA (2000).

58. B. F. GROMOV, O. G. GRIGORIEV, A. V. DEDOUL, G. I. TOSHINSKY, V. S. STEPANOV, "The Analysis of Operating Experience of Reactor Installations Using Lead-Bismuth Coolant and Accidents Happened," Proc. Heavy Liquid Metal Coolants in Nuclear Technology, Vol. 1, Obninsk, October 5-9, p. 60-66, State Scientific Center of Russian Federation Institute for Physics and Power Engineering (1998).

# Paper II

# Neutronics of minor actinide burning accelerator driven systems with ceramic fuel

J. Wallenius and M. Eriksson

Department of Nuclear and Reactor Physics, Royal Institute of Technology, Stockholm, Sweden

(Dated: February 2, 2005)

We have investigated neutronic properties of lead-bismuth cooled accelerator driven systems (ADS) with different minor actinide based ceramic fuels (two composite oxides and one solid solution nitride). Adopting a TRU composition with 40% plutonium in the initial load, transmutation rates of higher actinides (americium and curium) equal to 265-285 kg per  $GWth \times y$  are obtained. The smallest reactivity swing is provided by the magnesium oxide based cercer fuel. The cercer cores however exhibit large coolant void worths, which is of concern in case of gas bubble introduction into the core. Nitride and cermet cores are more stable with respect to void formation. The poorer neutron economy of the molybdenum based cermet makes it however difficult to accommodate an inert matrix volume fraction exceeding 50 percent, a lower limit for fabricability. Higher plutonium fraction is thus required for the cermet, which would lead to lower actinide burning rates. The nitride core yields high actinide burning rates, low void worths and acceptable reactivity losses.

## I. INTRODUCTION

Separating plutonium and minor actinides from spent nuclear fuel, these elements may be recycled in fission reactors. If the amount of these elements destined for geological repository can be reduced by more than a factor of 100, the time needed to store the residual waste until it reaches the toxicity of uranium ore is shortened to less than 1000 years [1]. Multi-recycling of americium and curium, in addition to plutonium, is necessary in order to obtain such reduction factors [2]. The introduction of americium into the fuel of critical reactors however leads to deterioration of safety parameters [3]. Hence, already in 1974, it was suggested by Los Alamos that the higher actinides should be recycled in accelerator driven systems (ADS) [4]. Later, JAERI proposed the Double Strata fuel cycle, where the management of minor actinides would take place in dedicated facilities, separated from the commercial fuel cycle [5, 6]. Adopting fast reactors for recycling of plutonium, such a strategy would allow for a very small fraction of the nuclear power park to be penalised by the handling of strong alpha and neutron emitters, as shown in a study by CEA [7].

Previous design studies of accelerator driven systems were made using a fixed core concept, with coolant and fuel selected on the basis of chemical and physical properties, choice of reprocessing method or fast reactor experience [6, 8–11]. To our knowledge, no consistent comparison between different fuel options for ADS has been published. It is the purpose of the present paper to perform such a comparison. The focus will be on neutronic characteristics, while thermo-hydraulic studies are presented in forthcoming paper [12].

In what follows we will show why a uranium matrix does not significantly improve the neutronic safety parameters of americium bearing fuels, corroborating the selection of inert matrix fuels and sub-critical operation for minor actinide burning. We will briefly motivate the selection of lead-bismuth coolant and recapitulate a scoping study leading to selection of three fuel

form/compositions to be investigated in detail. Then we account for detailed calculations of neutronic properties for 800 MWth cores with two composite oxide fuels and one solid solution nitride fuel, as function of core geometry. Finally we discuss the relative performance and safety characteristics pertaining to the fuels.

## II. FERTILE VS INERT MATRIX

When designing a dedicated minor actinide burner a small reactivity swing is desired for reasons of safety and economy, irrespective of whether the reactor is operated in critical or sub-critical mode. Therefore some plutonium should be present in the fuel. For a uranium free core, a ratio of americium to plutonium of about 3:2 was shown to provide a minimum reactivity swing when approaching equilibrium [13]. The question then may be raised whether such a core can be operated in a critical mode, or if sub-criticality is an absolute requirement. A complete answer can only be given by time-dependent analysis of all relevant accident conditions. However, an indicator of the potential for critical operation may be provided by quasi-static analysis.

Among the neutronic parameters of importance for the safety of critical reactors are

- The effective delayed neutron fraction  $\beta_{\text{eff}}$
- The fuel Doppler coefficient  $\alpha_D = \left(\frac{\Delta k}{\Delta T}\right)_{\text{Doppler}}$
- The coolant temperature coefficient  $\alpha_c = \left(\frac{\Delta k}{\Delta T}\right)_{\text{cool}}$

When introducing minor actinides into the fuel, these parameters are deteriorated, and margins to failure under design extension conditions decrease. Wade and Fujita defined the following safety indicators for passive shutdown behavior in sodium-cooled fast reactors [14]:

$$\begin{aligned} A &= (\alpha_D + \alpha_l) \overline{\Delta T_{\text{fuel}}} \\ B &= (\alpha_D + \alpha_l + \alpha_c + 2\alpha_R) \Delta T_{\text{cool}} / 2 \\ C &= \alpha_D + \alpha_l + \alpha_c + \alpha_R \end{aligned} \quad (1)$$

where  $\alpha_l$  and  $\alpha_r$  are axial and radial expansion coefficients, respectively.  $\overline{\Delta T_{\text{fuel}}}$  is the difference between the average fuel and coolant temperature and  $\Delta T_{\text{cool}}$  is the difference between coolant inlet and outlet temperatures.

In the quasi static approximation, the asymptotic rise in coolant outlet temperature is then given by

$$\Delta T_{\text{out}} = \frac{A}{B} \Delta T_{\text{cool}} \quad (2)$$

for the un-protected loss of flow (LOF) event. In the case of a total loss of heat-sink (LOHS), the maximum temperature increase in core inlet temperature is given by  $(A + B)/C$ , which may be rewritten as

$$\Delta T_{\text{out}} = \left( \frac{1 + A/B}{C \Delta T_{\text{cool}}/B} - 1 \right) \Delta T_{\text{cool}} \quad (3)$$

An estimate for the asymptotic increase in core outlet temperature during a control rod runout transient over power event (TOP) is given by

$$\Delta T_{\text{out}} = \left( \frac{-\Delta \rho_{\text{TOP}}/B}{1 + A/B} \right) \Delta T_{\text{cool}} \quad (4)$$

where  $\Delta \rho_{\text{TOP}}$  is the reactivity worth of the most efficient control rod. To preclude coolant boiling and ensure integrity of the cladding and structural materials during passive shutdown, the following set of conditions may be derived from (2), (3) and (4), under the assumption that  $\Delta T_{\text{out}} \leq M \Delta T_{\text{cool}}$ :

$$\frac{A}{B} \leq M \quad (5)$$

$$\frac{C \Delta T_{\text{cool}}}{B} \geq 1 \quad (6)$$

$$\frac{\Delta \rho_{\text{TOP}}}{|B|} \leq M \quad (7)$$

where  $A$ ,  $B$  and  $C$  are all negative. The margin to clad failure is thus  $M \Delta T_{\text{cool}}$ . In a conventional sodium cooled reactor we have  $\Delta T_{\text{cool}} \simeq 150$  K. Ferritic steels like HT-9, have a 24 hour creep limit of about 950 K [15], giving  $M \simeq 1$ . The corresponding limit for austenitic steels is 1100 K [16], leading to  $M \simeq 2$ .

Values of axial expansion coefficients range from  $-0.2$  pcm/K for oxide to  $-0.6$  pcm/K for metal fuel. Radial expansion coefficients are independent of fuel type, but vary with core size between  $-1.1$  pcm/K for large reactors like Super-Phenix to  $-1.4$  pcm/K for smaller cores, assuming that austenitic steels are used for the diagrid. [14, 17, 18]. A ferritic diagrid would yield 30% smaller radial expansion coefficients.

For a conventional sodium cooled reactor with oxide fuel we have  $\Delta T_{\text{cool}} \simeq 150$  K and  $\overline{\Delta T_{\text{fuel}}}/\Delta T_{\text{cool}} \simeq 5$ . Temperature coefficients calculated for Super-Phenix:  $\alpha_D = -0.6$  pcm/K,  $\alpha_c = +0.8$  pcm/K,  $\alpha_l = -0.2$  pcm/K and  $\alpha_r = -1.1$  pcm/K yields  $C \Delta T_{\text{coolant}}/B = 1.0$  and

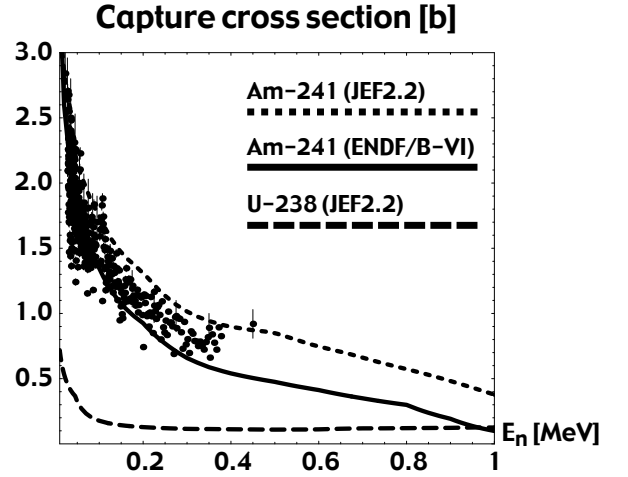


FIG. 1: Capture cross section of  $^{241}\text{Am}$ . Solid line: ENDF/B-VI, dotted line JEF2.2. Experimental data from EXFOR are denoted with error bars. The capture cross section of  $^{238}\text{U}$  (dashed line) is included for comparison.

$A/B = 1.8$ . These numbers indicate that clad and structural material have to be made from austenitic steels if a Super-Phenix core is to survive an un-protected LOF.

The negative temperature coefficients (Doppler plus expansion) must compensate for the magnitude of the positive coolant void coefficient for the total inlet temperature coefficient  $C$  to be negative. This is typically the case for reactors with  $(\text{U}, \text{Pu})\text{O}_2$  fuel. As we shall see, it may not be so for americium based fuels. Further, the magnitude of  $B$  is drastically reduced, leading to very small upper limits for control rod worths.

The relatively high capture cross section of americium in the energy range of 10-500 keV leads to a decrease in Doppler feedback. As shown in Fig. 1, the capture cross section of  $^{241}\text{Am}$  is 10 times higher than that of  $^{238}\text{U}$  at  $E = 100$  keV. Even with a large fraction of  $^{238}\text{U}$  in the fuel, most captures will take place in americium, at energies above the resolved resonance region.

In order to quantify the impact, we have calculated the fuel Doppler constant  $K_D$  with the Monte Carlo code MCNP4C, for an hexagonal pin cell with oxide fuel and sodium coolant. Clad inner/outer diameters of 5.8/6.6 mm and  $P/D = 1.20$  were assumed. Fitting the function  $k = c + K_D \times \log(T)$  to k-eigenvalues obtained with cross sections Doppler broadened with NJOY at 900, 1200, 1500 and 1800 Kelvin, the statistical error could be minimised. Probability tables were used above the resolved resonance region. Table I shows how the Doppler constant vanishes with large fractions of americium present in the core.

It can be seen that the addition of 30% americium in the fuel completely suppresses the Doppler feedback, even in the presence of uranium. This fact is reflected in the average neutron flux energy, increas-

TABLE I: Fuel Doppler constant  $K_D$  ( $\partial k/\partial T = -K_D/T$ ) for oxide fuels in a sodium cooled hexagonal pin cell with P/D = 1.20. ENDFB/VI data were used.

| U [%] | Pu [%] | Zr [%] | Am [%] | $K_D$ [pcm]   |
|-------|--------|--------|--------|---------------|
| 80    | 20     | -      | -      | $-810 \pm 20$ |
| 50    | 20     | -      | 30     | $-20 \pm 20$  |
| -     | 20     | 80     | -      | $-420 \pm 20$ |
| -     | 20     | 50     | 30     | $-20 \pm 20$  |

TABLE II: Sodium temperature coefficient in an oxide fuel hexagonal pin cell with P/D = 1.20.  $\Delta k/\Delta T$  was calculated as an average between 700 and 900 K, using the ENDFB/VI library. The statistical error corresponds to one standard deviation.

| U [%] | Pu [%] | Zr [%] | Am [%] | $\Delta k/\Delta T$ |
|-------|--------|--------|--------|---------------------|
| 80    | 20     | -      | -      | $+1.07 \pm 0.02$    |
| 50    | 20     | -      | 30     | $+1.79 \pm 0.02$    |
| -     | 20     | 80     | -      | $+0.72 \pm 0.03$    |
| -     | 20     | 50     | 30     | $+2.02 \pm 0.02$    |

ing from 480 keV in the americium free fuels to above 620 keV in the americium bearing fuels. Note that fertile plutonium nuclides may provide a substantial negative Doppler feedback, if americium is absent. The plutonium vector used in the pin cell calculation was  $238/239/240/241/242 = 1.0/69.0/25.0/3.0/2.0$ , corresponding to that of fast spectrum equilibrium in IFR [19].

Table II displays the coolant temperature coefficient in the pin cell model, obtained using perturbation techniques, as function of uranium and americium content. We see a strong increase in the coolant temperature coefficient with americium content. The pure plutonium fuel, on the other hand, gives a smaller temperature coefficient.

The presence of  $^{238}\text{U}$  in the fuel of FBRs has been thought to be a major contributor to  $\beta_{\text{eff}}$  [20]. It is true that the use of  $^{238}\text{U}$  as matrix for an americium bearing fuel increases the production of delayed neutrons, comparing to an inert (non-fissionable) matrix. However,

TABLE III: Delayed and effective delayed neutron fractions for fresh oxide fuels in a sodium cooled hexagonal pin cell with P/D = 1.20. The ENDF/B-VI library was used. The statistical error corresponds to one standard deviation.

| U [%] | Pu [%] | Zr [%] | Am [%] | $\beta$ [pcm] | $\beta_{\text{eff}}$ [pcm] |
|-------|--------|--------|--------|---------------|----------------------------|
| 80    | 20     | -      | -      | $399 \pm 11$  | $342 \pm 10$               |
| 50    | 20     | -      | 30     | $307 \pm 10$  | $204 \pm 11$               |
| -     | 20     | 80     | -      | $221 \pm 11$  | $206 \pm 13$               |
| -     | 20     | 50     | 30     | $213 \pm 11$  | $143 \pm 11$               |

the *effective* delayed neutron fraction will not be raised by the same magnitude. The reason is that the spectrum of the delayed neutrons has a median energy below the fast fission threshold and hence leads to a higher probability for absorption of delayed neutrons in americium, as compared to prompt fission neutrons.

In order to quantify the impact, we have calculated  $\beta$  (the fraction of delayed neutrons emitted in an average fission) and  $\beta_{\text{eff}}$  using the same pin cell model. As can be seen,  $\beta_{\text{eff}}$  is reduced more than  $\beta$  when substituting 3/8 of the initial uranium with americium. Note further that  $\beta_{\text{eff}}$  for a uranium free fuel may be of the same magnitude as a fuel with 50%  $^{238}\text{U}$ , as long as americium is not present.

Safety indicators estimated on the basis of the above pin cell calculations are shown in Table IV. The axial and radial expansion coefficients were taken to be  $\alpha_l = -0.2 \text{ pcm/K}$  and  $\alpha_R = -1.2 \text{ pcm/K}$ .

The first thing to note is the very small absolute value of  $B$  for the americium bearing fuels. Condition (7) means that the individual control rod worth should be less than  $|B|$ . To achieve a similar total control bank worth one would need 2.5 times more control rods in the  $(U_{0.5}, Pu_{0.2}, Am_{0.3})O_2$  fueled core than in a standard FBR.

Second, the inlet temperature coefficient  $C$  is positive for the americium loaded cores. This is clearly unacceptable if passive shutdown capability is a required feature.

It thus appears that a uranium free, americium based fuel should not be used in a oxide fueled critical reactor with sodium coolant. The use of a uranium matrix does not provide us with a Doppler feedback sufficient to compensate for the increase in coolant temperature coefficient caused by the fast fission in even neutron number nuclides. In addition, absorption of delayed neutrons in americium quenches the effective delayed neutron fraction. We thus conclude that for core configurations and fuel compositions similar to the ones here investigated, the use of a fertile matrix for minor actinide burning does not improve safety indicators to the extent that such cores may be operated in a critical mode. Plutonium fuels (or fuels with high Pu/Am ratios) might be operated in critical configurations without support of uranium. Their large reactivity loss however leads to problem with condition (7). Inert matrix supported americium based fuels, on the other hand, may provide acceptable safety parameters during sub-critical operation. In the following sections we will discuss conditions for selection of coolant and fuel composition of a sub-critical system operating on americium based fuels.

### III. CHOICE OF COOLANT FOR THE ACCELERATOR DRIVEN REACTOR

As seen in Table II, the sodium temperature coefficient becomes very large for americium bearing fuels.

TABLE IV: Safety indicators estimated for a sodium cooled oxide fuel pin channel with P/D = 1.2.

| U [%] | Pu [%] | Zr [%] | Am [%] | A [pcm] | B [pcm] | C [pcm/K] | A/B | $\Delta T_{\text{cool}}C/B$ |
|-------|--------|--------|--------|---------|---------|-----------|-----|-----------------------------|
| 80    | 20     | -      | -      | -280    | -160    | -0.88     | 1.8 | +0.8                        |
| 50    | 20     | -      | 30     | -80     | -60     | +0.38     | 1.3 | -0.9                        |
| -     | 20     | 80     | -      | -180    | -160    | -0.97     | 1.1 | +0.9                        |
| -     | 20     | 50     | 30     | -80     | -40     | +0.64     | 2.0 | -2.3                        |

The probability of reaching the boiling point of sodium during a LOHS event grows if the inlet temperature coefficient is positive. In a previous study, we have shown that the sodium void worth exceeds 4000 pcm for several kinds of inert matrix fuels [21]. We further found that certain accelerator over power transients in cores with such fuels result in sodium boiling followed by a prompt excursion [22]. An alternative coolant providing a fast neutron spectrum should thus be chosen for the system under consideration. While lead and gas cooling have been suggested [8, 23], problems related to clad durability during transients (He) and extended operation at high temperature (Pb) lead us to adopt lead-bismuth eutectic (LBE) as the reference coolant. LBE features a combination of relatively low melting temperature and high boiling point that makes it suitable for application in ADS. Corrosion control is more delicate than in sodium. A core melt due to corrosion product blockage of the coolant occurred in the first LBE cooled submarine reactor put into operation. Subsequently, oxygen control systems were developed and 80 years of reactor operation were accumulated in Soviet sub-marines without any incident related to corrosion problems [24]. Finally, synergy effects with the spallation target are evident.

#### IV. CHOICE OF FUEL

Having selected lead-bismuth as coolant, we need to find an inert matrix fuel that provides us with the following features:

- A high linear rating, in order to achieve a high burnup within the short residence time set by LBE induced corrosion.
- At least 50 percent inert matrix volume fraction, to ensure fabricability and/or stability at high temperature.
- A low void worth, in order to ensure that the core remains sub-critical during steam blow down or fission and helium gas leakage events.
- Reasonable solubility rate in nitric acid, to retain compatibility with existing industrial scale reprocessing facilities in Europe.

Recently, americium bearing metal alloy fuels have successfully been fabricated [25]. Metallic fuels feature a large solid fission product swelling rate, and are thus fabricated with a large pellet clad gap, that is filled with sodium [26]. Consequently, aqueous reprocessing is not applicable. We therefore consider metal alloys to be out of scope of the present work, and focus on ceramic fuels.

##### A. Oxide fuels

The condition of high linear rating directly excludes solid solution oxide fuels from our list of candidates. Not only do most oxides have low conductivity. The oxygen to metal ratio of compounds with americium and curium must be considerably less than 2.0, in order to ensure stability at high temperatures [27, 28]. Consequently, the thermal conductivity will be lower than for standard oxide fuels. Composite oxide fuels, where the matrix provides heat conduction is however a relevant option. The host phase may be either ceramic (cercer) or metallic (cermet).

Several ceramic matrices with high thermal conductivity have been investigated, like MgO and MgAl<sub>2</sub>O<sub>4</sub> (spinel). Low temperature irradiation tests of AmO<sub>2-x</sub> micro-dispersed in spinel have however shown that this matrix is prone to radiation damage [29, 30]. PuO<sub>2</sub>-MgO fuels have successfully been irradiated at linear ratings up to 165 kW/m [31]. AmO<sub>1.6</sub>-MgO targets have been fabricated and are currently under irradiation in Phenix [32]. Some concerns for a possible formation of a low melting eutectic between americium oxide and magnesia were raised [27], but the issue remains to be clarified experimentally.

At first glance, one may consider all metals with high melting temperature as candidates for cermet fuels; the possible choices are however limited by the cross section for neutron absorption of the matrix.

In the present design study, we assume that the Pu-fraction in the actinide vector is 40%, in order to minimise the reactivity swing. It has been shown that 20% burnup of this type of fuel can be achieved with a reactivity swing less than 2000 pcm [13, 33]. Consequently, it will be possible to avoid any fuel shuffling during irradiation, which is an important advantage in liquid metal cooled systems, both for safety and cost. In any case, the content of plutonium in the oxide phase is limited to less than 40% by the solubility of plutonium oxide in



nitric acid. Therefore, we may not compensate a high cross section for absorption in the matrix by increasing the fissile content of the fuel too much.

In a scoping study performed by one of the present authors, it was shown that for a Pu fraction of 40%, the matrix fraction of tungsten and natural molybdenum must be less than 50 volume percent, to achieve a k-eigenvalue of 0.97 in 800 MWth cores with LBE coolant [21]. Tungsten is thus of less interest for application in the present context. Molybdenum, on the other hand, may be enriched in  $^{92}\text{Mo}$ , which has a full neutron shell, and hence a lower cross section for neutron absorption.

Among the metallic matrices with high melting temperature that satisfy the matrix volume fraction condition, chromium appears to be most interesting from the neutronic viewpoint, yielding a very low void worth. Recent fabrication tests however indicate that a low melting eutectic may form between Cr and rare earth oxides [34].

Hence two composite oxide fuel candidates remain that fulfill the above listed criteria, one cermet and one cermet:

- $(\text{Pu,Am,Cm})\text{O}_{2-x}\text{-MgO}$
- $(\text{Pu,Am,Cm})\text{O}_{2-x}\text{-}^{92}\text{Mo}$

Irradiation experience of Mo based cermet fuels is limited to  $\text{UO}_2\text{-Mo}$  [35]. Pure molybdenum has been irradiated under a wide variety of conditions in the context of fusion, and has shown to exhibit the classical increase of ductile to brittle transition temperature of BCC metals.

## B. Nitride fuels

Nitride fuels intrinsically have a high thermal conductivity, but are more complex to fabricate. Nitrogen enriched to 98% in  $^{15}\text{N}$  is required for the fabrication, in order to limit production of  $^{14}\text{C}$  in the fuel during irradiation [36].

Actinide nitrides unfortunately tend to dissociate into metal and nitrogen at temperatures below their melting point [37, 38]. Especially americium nitride is unstable under sintering conditions [39–42]. Hence, a stabilizing matrix is necessary, and it has been shown that UN in solid solution with ZrN remains stable up to melting [38].

$(\text{Pu,Zr})\text{N}$  has successfully been fabricated by several methods [43, 44]. When performing sintering of  $(\text{Pu,Am,Zr})\text{N}$  under inert gas, considerable vapourisation of Am was reported [40]. Such losses may be avoided by sintering under nitrogen [42], and recent sintering tests of  $(\text{Am,Zr})\text{N}$  performed at JAERI showed that the losses of Am could be reduced by an order of magnitude [41].

Nitrides are in general more easily soluble in nitric acid than corresponding oxides, and the above mentioned scoping study showed that a molar fraction of

ZrN in excess of 50% can be maintained even for relatively large pin pitches.

$(\text{Pu,Zr})\text{N}$  has been irradiated at low rating (25 kW/m) up to 11% burnup in BOR-60 [45]. Similar ratings are used for JAERI's irradiation of  $(\text{Pu,Zr})\text{N}$  in JMTR [43]. Recently irradiation of  $(\text{Pu,Am,Zr})\text{N}$  started in ATR [46]. Irradiation of  $(\text{Pu,Zr})\text{N}$  at high linear rating (40-50 kW/m) is planned to take place in Studsvik [44].

Other nitride matrices could be considered, like YN and HfN. YN is however extremely hygroscopic, and hafnium nitride has a much higher cross section for absorption than zirconium nitride. The solid solution fuel candidate best suited for application in ADS thus appears to be

- $(\text{Pu,Am,Cm,Zr})^{15}\text{N}$

the main question-mark being loss of clad integrity leading to un-inhibited dissociation of the ceramic phase.

## V. METHOD

The core design was made in a series of iterative steps. First, the core power was chosen on the basis of the heat removal capacity of the spallation target and an assumed maximum level of the source multiplication factor. Then, a rough estimation of the maximum linear rating of each fuel was made, based on assessments of the effective thermal conductivity for the three selected fuel candidates. The approximate number of fuel pins in the core was obtained from the ratio of core to pin power, assuming that a radial power peaking factor of 1.3 would be achievable by dividing the core into three fuel zones with different inert matrix fraction. Adopting a spallation target radius of 20 cm, the dimensions of the fuel sub-assembly was fixed by fitting the spallation target into the empty space left by removing 19 central sub-assemblies. For a fixed pin diameter and sub-assembly FTF, only discreet values of P/D are possible. A small pin diameter is preferred in order to provide a short residence time to reach a target burnup of 20%. We decided to study two different values of P/D resulting from the selected pin diameter, each P/D corresponding to a different average inert matrix fraction in the fuel. Finally, the inert matrix fraction in the three fuel zones was adjusted to yield a radial power peaking factor smaller than 1.3, while maintaining a k-eigenvalue of 0.97 at BOL. A more detailed description of each step taken is given below. The resulting core geometry and fuel composition is displayed in Tables VI, VII and VIII.

### A. Core power

The thermal power of an ADS is limited by the source strength and multiplication. A heavy liquid metal spallation target would allow for dissipation of a proton

beam power of the order of 10 MW. Lead bismuth eutectic has been selected as the reference material in the ADS programs in Europe, Unites States and Japan. Using a beam window in contact with the molten LBE, the lifetime of the window material however becomes very short [47, 48]. A "windowless" solution, where a cold window is separated by vacuum from a free surface of LBE, appears thus to be the best solution for a high power target. With a windowless design, the heat deposition  $P_{\text{dep}}$  possible to remove may be estimated from the temperature rise in the molten metal:

$$\Delta T = \frac{P_{\text{dep}}}{\rho C_p \bar{v} A}. \quad (8)$$

For LBE we have  $\rho \simeq 10^4 \text{ kg/m}^3$ ,  $C_p \simeq 150 \text{ J/(kg} \times \text{K)}$  and  $\bar{v} \leq 2.5 \text{ m/s}$ , the velocity being limited by erosion rates of structural material [49]. For long term durability of these components, we would like to keep LBE temperatures below 720 K. Assuming that  $\Delta T$  should not exceed 100 K and that the effective flow area equals  $350 \text{ cm}^2$ , we find that  $P_{\text{dep}} \leq 13 \text{ MW}$ . As about 50% of the proton beam energy is consumed by the spallation process, this corresponds to a proton beam power of 26 MW. Hence we adopt  $P_{\text{beam}}^{\text{max}} = 26 \text{ MW}$  for the present design.

The fission power  $P_f$  in the core of an accelerator driven sub-critical system is a function of the proton source efficiency  $\psi^*$  [50]:

$$P_f = \langle S_p \rangle \frac{\bar{E}_f}{\bar{v}} \frac{k}{1-k} \psi^* \quad (9)$$

where  $S_p = P_{\text{beam}}/E_p$  is the proton current,  $\bar{E}_f$  and  $\bar{v}$  are the average energy and number of neutrons released in a fission, and  $k$  is the  $k$ -eigenvalue of the core. Safety considerations will lead us to demand  $k \leq 0.97$ . With a reactivity loss of 2000 pcm, the maximum proton beam current (at EOL) is inserted for  $k \simeq 0.95$ . For a proton energy of 1000 MeV, an average fission energy of 200 MeV, and  $\bar{v} = 3.0$ , we thus get at EOL

$$P_f \simeq P_{\text{beam}} 1.3 \psi^* \quad (10)$$

The LBE cooled cores here studied yield EOL proton source efficiencies of about 25. A maximum beam power of 30 MW then corresponds to a core fission power of 800 MW. We hence fix the core power to 800 MWth for all fuels.

## B. Linear Power

Having selected three fuel candidates to be used in detailed design studies, the linear rating of each fuel was assessed. In deeply sub-critical systems, feedbacks are not able to reduce power as they are in critical reactors [51]. Hence, beam over-current accidents may have severe consequences in ADSs. Further, if the core power

is regulated by adjusting the proton source strength, the possible overpower insertion is given by

$$\Delta P \simeq \frac{1 - k_s^{\text{max}}}{1 - k_s^{\text{min}}} \quad (11)$$

where  $k_s$  is the source multiplication eigenvalue. If  $k_s$  varies between 0.967 and 0.95, an overpower insertion of 50% is theoretically possible. Therefore, one should set the operational rating lower than 2/3 of the maximum permissible power density.

The failure temperatures of americium bearing inert matrix fuels are unfortunately not precisely known. The cercer fuel here studied is expected to undergo eutectic melting. Eutectic melting of  $\text{PuO}_2\text{-MgO}$  has been detected at  $T = 2530 \pm 30 \text{ K}$  [52], in good agreement with theoretical assessments [53]. Decreasing the oxygen to metal ratio lowers the melting temperature, and  $\text{PuO}_{1.61}\text{-MgO}$  melts at  $T \simeq 2300 \pm 80 \text{ K}$  [53, 54]. With americium in the fuel, a certain degree of hypo-stoichiometry is mandatory to ensure sufficiently vapour pressure of oxygen at operating temperature. No measurements on the eutectic melting temperature of  $\text{AmO}_{2-x}\text{-MgO}$  have been reported. The assessment of Zhang and Konings indicates that the melting temperature would vary between 1930 K for  $\text{AmO}_{1.5}\text{-MgO}$  and 2360 K for  $\text{AmO}_{1.8}\text{-MgO}$  [27]. The  $(\text{Pu,Am})\text{O}_{2-x}\text{-MgO}$  fuel of interest in the present context will be fabricated with  $x \simeq 0.10$  [55]. Judging from the data for its components, we adopt a failure temperature of  $2300 \pm 100 \text{ K}$  for this composite fuel.

Concerning the molybdenum based cermet, the failure temperature may be identified with the melting temperature of the oxide inclusions. As in the case of the cercer, these will be hypostoichiometric, lowering their melting temperature. Using Vegard's law, the melting point of  $(\text{Pu}_{0.4}\text{,Am}_{0.5}\text{,Cm}_{0.1})\text{O}_{1.9}$  is estimated to 2640 K.

In the case of the nitride, it is known that  $\text{AmN}$  dissociates in inert gas atmosphere when temperatures exceed 1600 K [40]. In a closed volume, the nitrogen pressure buildup will however stabilise the solid phase [41, 42]. At  $T = 2200 \text{ K}$ , the vapour pressure of americium in a fuel pin is negligible and there should be little concern about material transport to cold spots [12, 42]. Although the fuel most likely could survive transients to higher temperature, we use 2200 K at upper limit for the nitride in the present study.

In order to arrive at an operative rating for the three fuels, we need to make assumptions about clad temperature, gap conductance and fuel thermal conductivity.

An upper limit for the clad outer temperature is set by LBE corrosion rates. Using oxygen control techniques, the performance of austenitic stainless steels seems to be satisfactory up to 820 K [56, 57]. Ferritic steels with high silicon content developed in Russia feature good corrosion resistance up to 870-890 K [58]. Ferritic steels unfortunately have poorer mechanical properties under transient conditions [59, 60]. Standard stainless steels

(e.g. SS316) on the other hand have a low incubation threshold for swelling. Austenitics with composition especially tailored for high radiation resistance were therefore developed in the fast reactor programs, and Si-modified 15-15Ti have been shown to withstand doses up to 150 DPA. We therefore select Si-modified 15-15Ti as reference material, leading to an upper temperature limit of the clad equal to 820 K.

The biggest uncertainty in the fuel temperature calculation at BOL is the gap conductance. While the contribution from heat conduction in helium for a well defined open gap can be calculated with a small error, radiative contributions may be of significance. In Fig. 2, temperature gradients over the gap resulting from neglecting radiative heat transport and surface roughness are plotted as function of radial gap size and linear power.

In the absence of thermo-mechanical calculations of pellet-clad mechanical interaction, we adopt a hot radial gap of 50 microns at BOL for the oxide cercer and the nitride fuel. In the case of cermet fuel a larger initial gap is required to allow for swelling. As the fuel failure temperature is comparatively high, we settle for a radial gap of 100 microns for the cermet.

For the composite fuels, the effective thermal conductivity of a matrix with spherical inclusions having negligible conductivity, was estimated using the standard formula for a material with spherical porosity  $P$ :

$$\lambda_{\text{eff}} = \lambda(1 - P)^{3/2} \quad (12)$$

For a matrix volume fraction of 50%, we get  $\lambda_{\text{eff}} = 0.35\lambda$ .

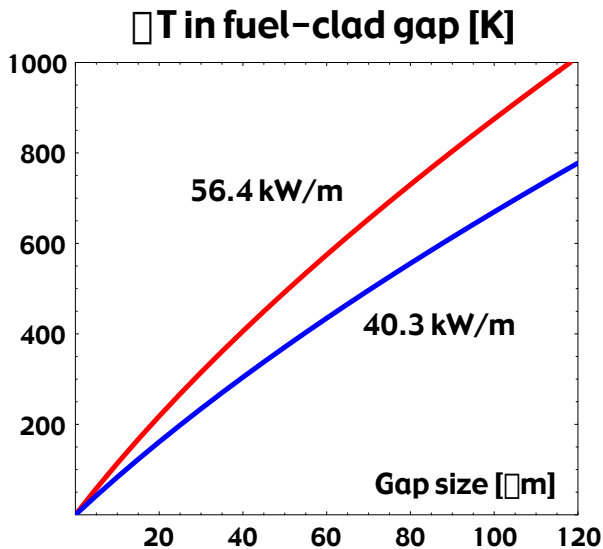


FIG. 2: Temperature gradient in the fuel clad gap as function of radial gap size, for a pellet diameter of 4.9 mm. Radiative contributions to heat transport are neglected.

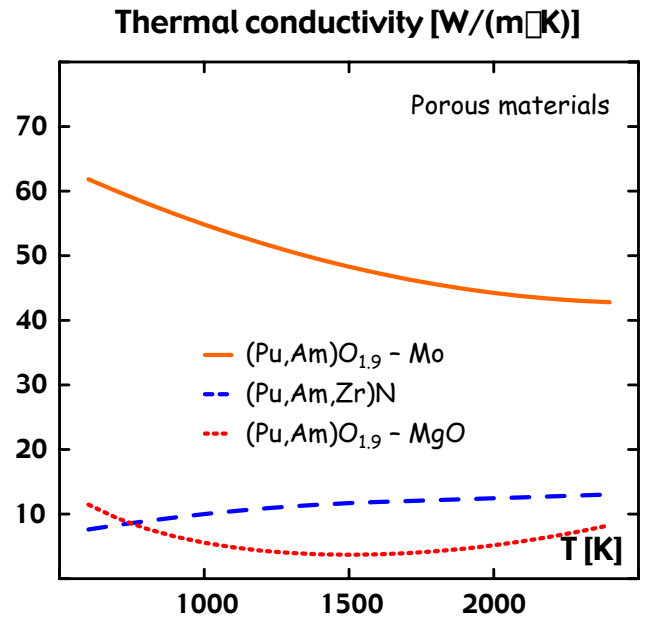


FIG. 3: Effective thermal conductivity for the three inert matrix fuels here investigated. The porosity of the ceramic phase was assumed to be 5% for the Cercer fuel, 10% for the Cermet and 15% for the nitride.

The metallic matrix in the Cermet fuel will be 100% dense. For magnesia, we assume that a density of 95% TD is possible to achieve. For the nitride fuel, a porosity of 15% was adopted to allow for solid fission product swelling. The resulting effective conductivity in a fuel pin with 50 volume percent inert matrix is displayed in Fig. 3, for each of the fuel candidates.

From the above data, the temperature gradient  $\Delta T_{\text{fuel}}$  over a solid fuel pellet as function of linear rating can be evaluated in terms of the conductivity integral. If we make the rough approximation that temperature gradients scale linearly with power, we may set the condition that the temperature difference between coolant inlet and fuel temperature during normal operation should be less than 2/3 of the allowed difference during a transient. Doing so, we may estimate an upper limit for the linear power during normal operation. With an inlet coolant temperature of 570 K, this limit becomes 1660 K for the nitride fuel, 1730 K for the cercer and 1950 K for the cermet fuel. In table V linear ratings yielding these steady state temperatures for fuels with 50 volume percent inert matrix fraction are tabulated. With a total power peaking factor of 1.6, these number correspond to average pin powers of 24, 36 and 40 kW/m.

More detailed temperature calculations, including transient performance, will be provided in a forthcoming paper [12].

TABLE V: BOL fuel temperatures at core mid-plane for the maximum linear ratings of the fuels here investigated. A coolant inlet temperature of 570 K. was assumed. For the nitride and cermet fuels a clad outer diameter of 5.7 mm and  $P/D = 1.75$  was used. For the Cercec fuel 6.8 mm and  $P/D = 1.50$  was adopted. Temperatures are given in Kelvin, ratings in  $kW/m$ .

| Fuel type    | $\chi$ | $\Delta T_{\text{clad}}$ | $\Delta T_{\text{gap}}$ | $\Delta T_{\text{fuel}}$ | $T_{\text{max}}$ |
|--------------|--------|--------------------------|-------------------------|--------------------------|------------------|
| Nitride      | 58     | 65                       | 495                     | 350                      | 1660             |
| Oxide Cercec | 38     | 45                       | 310                     | 600                      | 1730             |
| Oxide Cermet | 65     | 75                       | 970                     | 145                      | 1950             |

While the molybdenum based Cermet fuel would appear to be outstanding from the terms of linear rating, it will be evident that this potential cannot be fully utilised in an ADS, as the relatively high neutron absorption cross section of molybdenum cripples the neutron balance. Thus a larger actinide inventory is required in the Cermet core to achieve similar reactivity. In the present study, we therefore adopt identical linear rating for the nitride and the Cermet fuels (35  $kW/m$  core average), letting the margin to melt of the Cermet fuel increase by several hundred degrees.

### C. Core geometry

In the present study, we adopt a classical hexagonal fuel bundle geometry. Due to sub-criticality, three fuel zones are required to achieve an acceptable radial power peaking factor, as compared to two zones in a standard FBR. Hence we choose a comparatively small wrapper tube flat to flat (FTF) distance, of the order of 10 cm. 19 central fuel assemblies are removed to make space for the spallation target, having an outer radius of 21 cm. The impact of the proton beam is set to 18 cm above core mid plane to make the axial power profile symmetric, and the radius of beam guide tube is set to 15 cm to allow for spreading of the beam.

In order to reduce the reactivity potential related to core compaction, the fuel pin pitch to diameter ratio ( $P/D$ ) should ideally be set to the smallest value ensuring sufficient heat removal under transient conditions. As the detailed accident analysis will be presented in another paper [12], we here choose to investigate the neutronic performance for two limiting cases, one *small* pitch ( $P/D = 1.50$ ), expected to yield higher inert matrix fraction and lower void worth [21], and one *large* pitch ( $P/D = 1.75$ ), providing better coolability under design extension conditions [22].

For a fixed linear rating, the burnup rate of the fuel increases with decreasing pellet diameter. Since the fuel residence time is limited by LBE corrosion rates, small pellet diameters are preferable. On the other hand, neutron leakage increases with decreasing pellet radius,

TABLE VI: Core geometry parameters used for the present study. A total core power of 800 MWth is assumed. The higher number of fuel pins in the Cercec core is thus due to the lower linear rating of this fuel. The combination of a large pin diameter with a large pin pitch is not investigated.

|  |             |
|--|-------------|
| Spallation target radius                   | 21 cm       |
| Proton beam impact (relative to mid plane) | 18 cm       |
| Beam tube radius                           | 15 cm       |
| Sub-assembly inner flat to flat            | 96 mm       |
| Sub-assembly outer flat to flat            | 100 mm      |
| Sub-assembly pitch                         | 102 mm      |
| Pin pitch to diameter ratio                | 1.50/1.75   |
| Clad outer diameter                        | 5.7/6.8 mm  |
| Clad inner diameter                        | 5.0/6.0 mm  |
| Pins per sub-assembly                      | 91/127      |
| Nitride/Cermet core fuel sub-assemblies    | 180/246     |
| Nitride/Cermet core fuel pins              | 22386/22860 |
| Cercec core fuel sub-assemblies            | 252/348     |
| Cercec core fuel pins                      | 32004/31668 |
| Active core height                         | 100 cm      |
| Upper gas plenum height                    | 100 cm      |
| Lower gas plenum height                    | 50 cm       |

making it more difficult to meet the requirement of at least 50 volume percent matrix fraction set by fabricability. Especially for oxide fuels, this becomes an issue of concern. Thus, beside making core calculations for a small diameter pellet, we also investigate the case of a larger pellet combined with the smaller  $P/D$ .

Since the FTF distance of the sub-assemblies has been fixed by the spallation target radius, only discrete combinations of fuel clad diameters and pin pitches are possible.  $D_{\text{clad}} = 5.7 \text{ mm}$  and  $D_{\text{clad}} = 6.8 \text{ mm}$  may be combined with the selected  $P/D$  ratios for an inner FTF of 96 mm. Assuming that the 15-15Ti clad should be thick enough to withstand an internal gas pressure of 20 MPa at a temperature of 1000 K, the corresponding inner clad diameters become 5.0  $mm$  and 6.0  $mm$ , respectively.

Table VI summarises the geometrical parameter of the cores here investigated. Note that a relatively large gas plenum is present to provide space for release of helium arising from decay of  $^{242}\text{Cm}$ .

The radial reflector was assumed to consist of two sub-assembly rows filled with steel pins, cooled by lead bismuth. The LBE fraction in the radial reflector was set to 10 volume percent. In Fig. 4, a core map for the nitride/cermet configuration with 246 sub-assemblies is displayed.

## VI. COMPUTATIONAL MODEL

Beginning of life (BOL) core calculations were made with the continuous energy Monte Carlo code

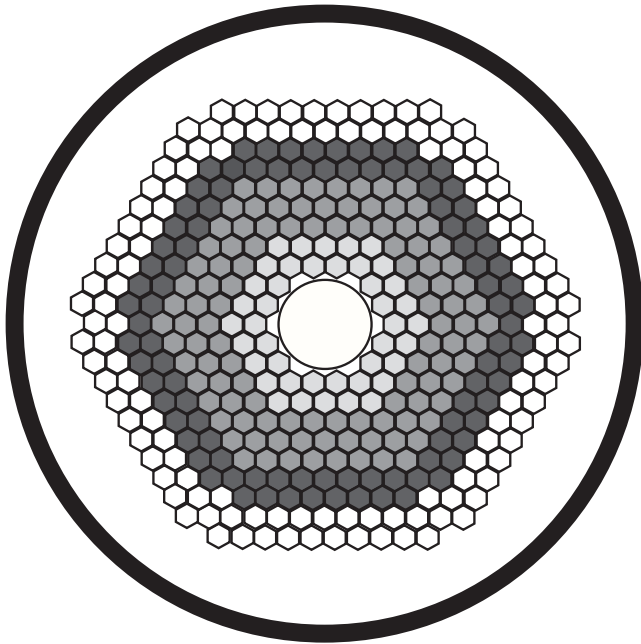


FIG. 4: Example of core map with 246 sub-assemblies for the cermet and nitride cores here studied. Around the central spallation target, the three fuel zones are distinguished by different shades of grey. Outside of the fuel, two sub-assembly rows filled with steel pins function as radial shield/reflector.

MCNP4C, using the JEF2.2 nuclear data library. Fully three dimensional, pin by pin models were constructed. The plutonium, americium and curium vectors used are shown in Table VII. The Pu vector is that of spent light water reactor MOX fuel after seven years of cooling. The higher actinide vectors represent a mixture of Am and Cm deriving from spent UOX and MOX fuel.

The relative fractions of Am and Cm was set to 5/1, corresponding to their concentration in spent LWR fuel. The plutonium fraction in these start-up cores was set to 40% in order to minimise the burnup reactivity swing

TABLE VII: Isotope vectors used for the present design study. The Pu vector is that of spent LWR MOX fuel after seven years of cooling. The higher actinide vectors represent a mixture of Am and Cm deriving from spent UOX and MOX fuel.

| Nuclide           | Atom fraction |
|-------------------|---------------|
| $^{238}\text{Pu}$ | 0.050         |
| $^{239}\text{Pu}$ | 0.379         |
| $^{240}\text{Pu}$ | 0.303         |
| $^{241}\text{Pu}$ | 0.132         |
| $^{238}\text{Pu}$ | 0.135         |
| $^{241}\text{Am}$ | 0.666         |
| $^{243}\text{Am}$ | 0.334         |
| $^{244}\text{Cm}$ | 0.873         |
| $^{245}\text{Cm}$ | 0.127         |

over a large number of irradiation cycles where the plutonium feed comes from spent ADS fuel, starting with the second core load [13].

Burnup simulations of the first irradiation cycle were made using the Monte Carlo burnup code MCB, for cores with  $P/D = 1.75$ . The accumulation and decay heat of about 300 fission products was taken into explicit account. For source calculations, the high energy particle transport code MCNPX was used to write a neutron source on the surface of the target with a cut-off at 20 MeV, which then was used for neutron transport in MCB. The statistical uncertainty for the major transmutation rates was calculated to be less than 0.1% in each burnup step, indicating less than 1% uncertainty in the final composition averaged over each burnup zone.

## VII. RESULTS

Inert matrix volume fraction in the inner, middle and outer fuel zones yielding a radial power peaking factor less than 1.3 at BOL are given in Table VIII.

One may note the following: In the case of the nitride core, all geometries are compatible with an inert matrix fraction above 50 volume percent in all fuel zones. The poorer neutron economy pertaining to the composite oxide fuels results in matrix fractions below this limit with exception for the small pitch, large pin cermet core. Especially the cermet has a too high neutron absorption cross section, in spite of the use of depleted Molybdenum. In the latter case, one would either have to increase the relative concentration of plutonium in the fuel, or increase the actinide inventory in the core. Neither of these solutions are optimal. Increasing the Pu concentration in the feed stream would lead to a larger reactivity swing, which could require the introduction of fuel shuffling to reach the target burnup. The economic penalty related to shuffling of fuel elements in liquid metal cooled reactors is significant. Concerning an increase of fuel inventory, example given by increasing the number of fuel assemblies, the operating power

TABLE VIII: Inert matrix volume fractions yielding a radial power peaking factor less than 1.3 at BOL.

| Fuel type    | $D_{\text{clad}}$ [mm] | P/D  | Zone 1 | Zone 2 | Zone 3 |
|--------------|------------------------|------|--------|--------|--------|
| Oxide Cermet | 5.7                    | 1.50 | 0.65   | 0.58   | 0.42   |
|              | 6.8                    | 1.75 | 0.56   | 0.51   | 0.41   |
| Oxide Cermet | 5.7                    | 1.50 | 0.68   | 0.62   | 0.52   |
|              | 6.8                    | 1.50 | 0.68   | 0.62   | 0.52   |
| Oxide Cermet | 5.7                    | 1.50 | 0.54   | 0.48   | 0.37   |
|              | 6.8                    | 1.75 | 0.47   | 0.41   | 0.31   |
| Nitride      | 5.7                    | 1.50 | 0.60   | 0.54   | 0.45   |
|              | 6.8                    | 1.50 | 0.60   | 0.54   | 0.45   |
| Nitride      | 5.7                    | 1.50 | 0.73   | 0.67   | 0.54   |
|              | 6.8                    | 1.75 | 0.66   | 0.61   | 0.50   |
| Nitride      | 5.7                    | 1.50 | 0.76   | 0.71   | 0.60   |
|              | 6.8                    | 1.50 | 0.76   | 0.71   | 0.60   |

density of the cermet fuel would go down, as the total core power is limited by the source strength. An even higher margin to failure would result, but also a longer residence time. The ultimate limit for the fuel burnup would then be set by corrosion damage to the clad, rather than by irradiation induced swelling. These conclusions are however preliminary, as the absorption cross section of molybdenum appears to differ significantly from one evaluation to the other.

### A. Power profiles

In Fig. 5, the radial power profile for the nitride core with small pins and large pitch is shown. The number of sub-assembly rows in each fuel zone was set to minimise the difference in power between adjacent assemblies on the interface between the fuel zones. Between zone two and three, twenty percent difference in power density remains, which roughly translates into forty degrees temperature difference between neighbouring hot and cold channels. Thermal striping should thus not be an issue. The axial peaking factor remains modest (less than 1.22), thanks to the better reflective properties of LBE, as compared to sodium.

### B. Safety parameters

Neutronic safety parameters calculated for each of the core configurations are tabulated in Table IX. The coolant core void worth  $W_{core}$  was calculated by removing the

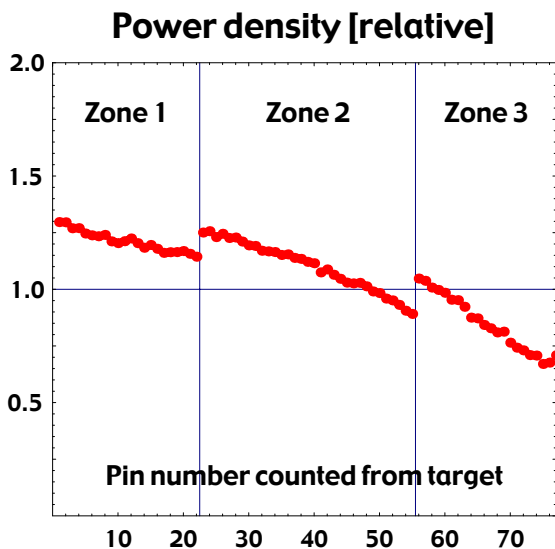


FIG. 5: Radial power profile (relative to the average pin power) in the nitride core with small pin diameter and large pitch. Each point corresponds to a single fuel pin. The radial peaking factor equals 1.29.

coolant from the active zone only, while the total void worth  $W_{tot}$  was calculated by removing the coolant from the active zone and the upper plenum. As expected, the effective delayed neutron fraction is very small. If these cores were to be operated in a critical mode, they would be extremely sensitive to any reactivity perturbation. Example given, the coolant void worths vary between 15 and 25 dollars, which may be compared to the upper limit of 3-4 dollars usually considered to be appropriate for critical sodium cooled reactors. Judging from the quoted numbers only, it would appear that a sub-criticality margin of 3000 pcm is sufficient to ensure that the cores could not go prompt critical, as long as the coolant density in the plenum is reduced proportionally to the density in the active zone. However, a localised void, potentially arising from introduction of gas bubbles into the core, could yield a reactivity insertion in excess of 3000 pcm, especially in the case of the oxide cermet fuel. Here, one should keep mind that the nuclear data libraries yield significantly different values of LBE void worths, mainly due to differences in the inelastic scattering of lead [61]. The ENDF/B-VI evaluation, for instance, yield about 1000 pcm higher void worths for the present cases.

The variation of  $\beta_{eff}$  between different core configurations appears to be insignificant, considering the estimated statistical uncertainty. Neutron generation times are slightly larger than typically found for classical FBRs, which may be attributed to the larger pin pitch.

The coolant and fuel temperature coefficients are of much less significance in a sub-critical system than in a critical reactor [51]. Still, they might play a role to mitigate excursions into the prompt critical regime. Table X gives core averaged values for coolant and fuel expansion coefficients for each of the configurations here studied. The coolant expansion was calculated assuming a uniform temperature rise in the active zone and upper plenum. The fuel grid radial expansion coefficient was calculated by increasing pin P/D and the sub-

TABLE IX: BOL neutronic safety parameters. Delayed neutron fractions and void worths are given in pcm, neutron generation times in  $\mu s$ . The estimated uncertainty arising from the Monte Carlo procedure is  $\pm 15$  pcm for the delayed neutron fractions and  $\pm 25$  pcm for the void worths.

| Fuel    | $D_{clad}$ | P/D  | $\beta$ | $\beta_{eff}$ | $\Lambda$ | $W_{core}$ | $W_{tot}$ |
|---------|------------|------|---------|---------------|-----------|------------|-----------|
| Cermet  | 5.7        | 1.50 | 250     | 180           | 0.65      | 4060       | 1790      |
|         | 5.7        | 1.75 | 250     | 190           | 0.81      | 5300       | 2300      |
|         | 6.8        | 1.50 | 250     | 190           | 0.76      | 4570       | 2250      |
| Nitride | 5.7        | 1.50 | 240     | 170           | 0.50      | 2460       | 220       |
|         | 5.7        | 1.75 | 230     | 180           | 0.67      | 3580       | 470       |
|         | 6.8        | 1.50 | 270     | 190           | 0.60      | 2990       | 520       |
| Cermet  | 5.7        | 1.50 | 280     | 180           | 0.55      | 2960       | 680       |
|         | 5.7        | 1.75 | 240     | 180           | 0.71      | 4150       | 880       |
|         | 6.8        | 1.50 | 260     | 170           | 0.67      | 3610       | 1080      |

TABLE X: BOL temperature coefficients of coolant, fuel and grid, given in  $pcm/K$ . The fuel Doppler coefficient was estimated to be negligible (i.e. less than 0.05 pcm/K) for all core configurations. The estimated uncertainty arising from the Monte Carlo procedure is  $\pm 0.02$  pcm/K.

| Fuel    | $D_{\text{clad}}$ | P/D  | $(\frac{\Delta k}{\Delta T})_{\text{LBE}}$ | $(\frac{\Delta k}{\Delta T})_{\text{fuel}}^{\text{axial}}$ | $(\frac{\Delta k}{\Delta T})_{\text{grid}}^{\text{radial}}$ |
|---------|-------------------|------|--|--|---|
| Cercer  | 5.7               | 1.50 | +0.43                                      | -0.28  | -0.94   |
|         | 5.7               | 1.75 | +0.59                                      | -0.28  | -0.99   |
|         | 6.8               | 1.50 | +0.53                                      | -0.26  | -0.97   |
| Cermet  | 5.7               | 1.50 | +0.32                                      | -0.18  | -0.97   |
|         | 5.7               | 1.75 | +0.46                                      | -0.17  | -1.04   |
|         | 6.8               | 1.50 | +0.36                                      | -0.18  | -1.05   |
| Nitride | 5.7               | 1.50 | +0.35                                      | -0.25  | -1.01   |
|         | 5.7               | 1.75 | +0.50                                      | -0.24  | -1.11   |
|         | 6.8               | 1.50 | +0.42                                      | -0.23  | -0.99   |

assembly FTF and pitch uniformly. As expected, the coolant temperature coefficient increases with increasing coolant volume fraction. Still the calculated LBE expansion reactivity coefficient is significantly smaller for all pitches than corresponding sodium expansion coefficients, approaching +2 pcm/K even for small pitches, as shown in Table II. The fuel axial expansion coefficient is smallest for the cermet fuel, due to the relatively small thermal expansion coefficient of metallic molybdenum. The fuel grid radial expansion coefficient has a magnitude similar to that of critical cores, as expected.

### C. Burnup simulations

Table XI compares the accumulated burnup, higher actinide transmutation rate, damage fluence, reactivity loss and proton beam power after 300 full power days for the three different fuels. The spread in burnup is less than one might expect from the variation in linear rating. This can be attributed to the different inert matrix fractions and light atom content, leading to roughly equal actinide inventories in the three cores.

TABLE XI: Burnup characteristics after 300 EFPD for cores with outer clad diameter of 5.7 mm and P/D = 1.75. The burnup  $B$  is given in percent TRU. The higher actinide transmutation rate  $R_{\text{Am+Cm}} = \Delta M_{\text{Am+Cm}} / \Delta M_{\text{TRU}}$  is given relative to the TRU consumption of the core. The damage fluence  $F_{\text{dam}}$  is estimated for the most exposed pin.

| Fuel    | $B$ [%] | $R_{\text{Am+Cm}}$ | $F_{\text{dam}} [m^{-2}]$ | $\Delta k/B$ | $P_{\text{beam}}$ |
|---------|---------|--------------------|---------------------------|--------------|-------------------|
| Cercer  | 9.1     | 0.77               | $1.2 \times 10^{27}$      | -70 pcm/%    | 16 MW             |
| Cermet  | 9.3     | 0.82               | $1.7 \times 10^{27}$      | -290 pcm/%   | 25 MW             |
| Nitride | 9.6     | 0.81               | $1.6 \times 10^{27}$      | -250 pcm/%   | 23 MW             |

The higher actinide transmutation rate  $R_{\text{Am+Cm}} = \Delta M_{\text{Am+Cm}} / \Delta M_{\text{TRU}}$  equals about 80%, being slightly higher for cores with harder spectrum. In terms of mass, the cores are capable of transmuted 265-285 kg higher actinides per  $GWth \times y$ , which may be compared to the theoretical maximum of 345 kg per  $GWth \times y$ . Assuming a capacity factor of 80%, 14-15 of these cores may then consume the entire higher actinide production of the 130 GWe European LWR park, being about 2.5 tons per year (after four years of cooling). The corresponding fraction of nuclear electricity produced in the accelerator driven reactors would be about three percent.

Note the lower damage fluence of the cercer core. The reason is the considerably softer spectrum of this oxygen rich core, also being reflected in a remarkably small reactivity loss. At BOL, the number averaged neutron energy in zone 2 of the cercer core is 115 keV, which may be compared with 169 keV for the nitride and 187 keV for cermet core. The corresponding fission probabilities of  $^{243}\text{Am}$  are 13, 17 and 20%, respectively. Consequently, the curium build-up in the magnesia supported oxide fuel is larger, leading to higher heat loads.

Assuming a damage fluence limit for 15-15Ti of  $3.2 \times 10^{27} n/m^2$ , the core averaged dose limitation to burnup for the cercer fuel would be about 25 %, even without fuel shuffling. The corresponding limits for the nitride and cermet fuels are 19% and 18%, respectively. The ultimate limitation to burnup may however be corrosion damage rather than radiation damage. With typical LBE corrosion damage rates of 20 microns per year [56, 57], more than 10% of the clad thickness would be oxidised after 700 full power days. It remains to be seen whether this is acceptable or not.

The reactivity loss for cercer core may remain within 1500 pcm for 20% burnup. The concomitant increase in proton beam power would in this case remain below 50%. For the other fuels the reactivity swing and increase in proton beam power becomes too large when the burnup exceeds 10%. It is however known that the reactivity swing is reduced in consecutive core loads, as to the poorer Pu quality of recycled ADS fuel comes into play [13]. Hence it should be possible to reach 20% burnup with a source strength increase less than 50% also for the cermet and the nitride cores, starting from the second core load.

## VIII. CONCLUSIONS

We have presented detailed neutronic studies of lead-bismuth cooled, sub-critical minor actinide burners with different inert matrix ceramic fuels. Assuming an TRU composition with 40% Pu in the initial load, higher actinide transmutation rates of 265-285 kg per  $GWth \times y$  are obtained, being about 80% of the theoretical maximum. The fraction of nuclear power that has to be produced in such cores in order to fission the entire higher actinide production from present LWR fleets is about

three percent.

The reactivity swing for the initial load varies between 70 and 300 pcm per percent burnup. The smallest reactivity loss was provided by the magnesium oxide based cermet fuel, which also featured the softest spectrum and lowest damage rate.

Among neutronic safety indicators, the coolant void worth proves to be the most delicate issue. Even though coolant boiling is virtually excluded in LBE cooled systems, fission and helium gas release or steam blow down from failing heat exchangers may lead to void formation in cores of the present type. In this case, the cermet fuel exhibits the least benign characteristics, with core and upper plenum combined void worth exceeding 2000 pcm due to a combination of softer spectrum and larger core size. Recently we have shown that such void worths may produce a sharp power increase followed by fuel failure within a few seconds after an introduction of a gas bubble through the core, even if the core remains sub-critical [12]. The bubble scenario is also the main reason why these cores should not be operated in a critical mode, even though they fulfill the A-B-C criteria (5,6 & 7). A conventional FBR with a nominal Doppler feedback around  $-0.5 \text{ pcm/K}$  is designed to avoid superprompt criticality for a boiling initiator, delivering reactivity ramp rates in the neighbourhood of  $1\$/s$  to  $5\$/s$  [62]. Thus it appears that a prompt temperature feedback coefficient of less than  $-0.2 \text{ pcm/K}$  is not sufficient to avoid a prompt super-excursion for ramp rates exceeding  $10\$/s$ . Reactivity potentials of such magnitude

violate the NRC requirement that the reactor core and associated coolant systems should be designed so that in the power operating range the net effect of the prompt inherent nuclear feedback characteristics tends to compensate for a rapid increase in reactivity [63].

The nitride and the cermet cores are more stable with respect to coolant void formation. The poorer neutron economy of the composite oxide fuels makes it however difficult to combine an inert matrix volume fraction exceeding 50 volume percent with the suggested plutonium concentration (40% of actinides) for the molybdenum based cermet. Since fabrication of composite fuel requires an inert matrix fraction of at least 50 volume percent, a higher plutonium fraction may be required for the cermet, leading to larger reactivity losses and lower performance in terms of actinide burning rates.

The nitride core yields high actinide burning rates, low void worths and acceptable reactivity losses.

## IX. ACKNOWLEDGEMENTS

The authors would like to thank P. Smith and J. Cahalan for fruitful discussions and advice, and W. Gudowski for providing cross section libraries in MCNP format. Financial support from SKB and the European Commission CONFIRM and FUTURE projects is acknowledged.

- 
- [1] A roadmap for developing accelerator transmutation of waste (ATW) technology: A report to congress, US DOE, 1999.
- [2] M. Delpech. The Am and Cm transmutation, physics and feasibility. In *Proc. Int. Conf. Future Nuclear Systems, GLOBAL 99*. American Nuclear Society, 1999.
- [3] J. Tommasi, M. Delpech, J-P. Grouiller, and A. Zaetta. Long-lived waste transmutation in reactors. *Nucl. Tech.*, 111:133, 1995.
- [4] D.G. Foster, editor. Review of PNL study on transmutation processing of high level waste. Technical Report LA-UR-74-74, Los Alamos Scientific Laboratory, 1974.
- [5] H. Murata and T. Mukaiyama. Fission reactor studies in view of reactor waste programs. *Atomkernenergie-Kerntechnik*, 45:23, 1984.
- [6] T. Takizuka, I. Kanno, H. Takada, T. Ogawa, T. Nishida, and Y. Kaneko. A study on incineration target system. In *Proc. 5th Int. Conf. Emerging Nuclear Energy Systems, ICENES 89*, page 70. World Scientific, 1989.
- [7] M. Salvatores, I. Slessarev, G. Ritter, P. Fougeras, A. Tchistiakov, G. Youinou, and A. Zaetta. Long-lived radioactive waste transmutation and the role of accelerator driven (hybrid) systems. *Nucl. Inst. Meth. A*, 414:5, 1998.
- [8] C. Rubbia. Fast neutron incineration in the energy amplifier as alternative to geologic storage. Technical Report LHC/97-01 (EET), CERN, 1997.
- [9] K. Tsujimoto, T. Sasa, K. Nishihara, T. Takizuka, and H. Takano. Accelerator-driven system for transmutation of high-level waste *Prog. Nucl. Energy.*, 37:339, 2000.
- [10] J. Wallenius, K. Tucek, J. Carlsson, and W. Gudowski. Application of burnable absorbers in an accelerator driven system. *Nucl. Sci. Eng.*, 137:96, 2001.
- [11] W. Yang and H. Khalil. Blanket design studies of a lead-bismuth eutectic-cooled accelerator transmutation of waste system. *Nucl. Tech.*, 135:162, 2001.
- [12] M. Eriksson, J. Wallenius, M. Jolkkonen, and J.E. Cahalan. Safety properties of minor actinide bearing inert matrix fuels. *Nucl. Tech.*, 2005. accepted for publication.
- [13] K. Tsujimoto, T. Sasa, K. Nishihara, H. Oigawa, and H. Takano. Neutronics design for lead-bismuth cooled accelerator-driven system for transmutation of minor actinides. *J. Nucl. Sci. Tech.*, 41:21, 2004.
- [14] D.C. Wade and E.K. Fujita. Trends Versus Reactor Size of Passive Reactivity Shutdown and Control Performance. *Nucl. Sci. Eng.*, 103:182, 1989.
- [15] T.H. Bauer, G.R. Fenske, and J.M. Kramer. Cladding failure margin for metallic fuel in the integral fast reactor. In *9th Int. Conf. on structural mechanics in reactor technology*, volume C, 1987.
- [16] R.J. Puigh and M.L. Hamilton. In *Influence of Radiation on Materials Properties: 13th Int. Symposium, ASTM STP*, volume 956. ASTM, 1987.
- [17] Y.S. Tang. *Thermal analysis of liquid metal fast breeder reactors*. ANS, 1978.



- [18] M.A. Smith, E.E. Morris, and R.N. Hill. Physics and safety studies of low conversion ratio sodium cooled fast reactors. In *Proc. Int. Conf. Future Nuclear Systems, GLOBAL 03*. American Nuclear Society, 2003.
- [19] D.C. Wade and R.N. Hill. The design rationale of the IFR. *Prog. Nucl. Energy.*, 31:27, 1997.
- [20] A. Waltar and A. Reynolds. *Fast Breeder Reactors*. Pergamon Press, 1981.
- [21] J. Wallenius. Neutronic aspects of inert matrix fuels for application in ADS. *J. Nucl. Mat.*, 320:142, 2003.
- [22] M. Eriksson, J. Wallenius, J. Cahalan, K. Tucek, and W. Gudowski. Safety analysis of Na and Pb-Bi coolants in response to beam instabilities. In *Proc. 3rd Int. workshop on utilisation and reliability of high power proton accelerators, HPPA02*. American Nuclear Society, 2002.
- [23] B. Carluec and P. Anzieu. Proposal for a gas cooled ADS demonstrator. In *Proc. Int. Conf. Accelerator Driven Transmutation Technologies and Application, ADTTA 99*, 1999.
- [24] B.F. Gromov, Yu. S. Belomitcev, E. I. Yefimov, M. P. Leonchuk, P. N. Martinov, Yu. I. Orlov, D. V. Pankratov, Yu. G. Pashkin, G. I. Toshinsky and V. V. Chekunov. Use of lead-bismuth coolant in nuclear reactors and accelerator-driven systems. *Nucl. Eng. Des.*, 173:207, 1997.
- [25] M. K. Meyer. Development and testing of metallic fuels with high minor actinide content. In *Proc. 11th International Conference on Nuclear Engineering, ICONE-11*, 2003.
- [26] G.L. Hofman, L.C. Walters, and T.H. Bauer. Metallic fast reactor fuels. *Prog. Nucl. Energy.*, 31:83, 1997.
- [27] R.J.M. Konings, H. Zhang, M.E. Huntelaar, and E.H.P. Cordfunke. Melting behaviour of oxide systems for heterogeneous transmutation of actinides. III. the system Am-Mg-O. *J. Nucl. Mat.*, 250:88, 1997.
- [28] R.J.M. Konings. Thermochemical and thermophysical properties of curium and its oxides. *J. Nucl. Mat.*, 298:255, 2001.
- [29] F. Klaassen, K. Bakker, R.P.C. Schram, R. Klein Meulekamp, R. Conrad, J. Somers, and R.J.M. Konings. Post irradiation examination of irradiated americium oxide and uranium dioxide in magnesium aluminate spinel. *J. Nucl. Mat.*, 319:108, 2003.
- [30] T. Wiss, R.J.M. Konings, C.T. Walker, and H. Thiele. Microstructure characterisation of irradiated am-containing  $MgAl_2O_4$  (EFTTRA-T4). *J. Nucl. Mat.*, 320:85, 2003.
- [31] M.D. Freshley and D.F. Carroll. The irradiation performance of  $PuO_2/MgO$  fuel material. In *Trans. Amer. Nucl. Soc.*, volume 6, page 396. ANS, 1963.
- [32] Y. Croixmarie, E. Abonneau, A. Fernandez, R.J.M. Konings, F. Desmouliere, and L. Donnet. Fabrication of transmutation fuels and targets: the ECRIX and CAMIX-COCHIX experience. *J. Nucl. Mat.*, 320:11, 2003.
- [33] P. Smith. Detailed core design of a reference ADT for safety analyses. In S. Pillon, editor, *2nd annual report of the FUTURE project*. CEA, 2004.
- [34] A. Fernandez. Institute of Transuranium Elements, Personal communication (2003).
- [35] P. Dehaut. Composite fuel behaviour under and after irradiations. In *Studies on fuels with low fission gas release*. IAEA-TECDOC-970, 1996.
- [36] J. Wallenius and S. Pillon. N-15 requirement for 2nd stratum ADS fuels. In *Proc. ANS Meeting on Accelerator Applications/ Accelerator Driven Transmutation Technology Applications, AccApp/ADTTA01*. ANS, 2001.
- [37] K. Richter and C. Sari. Investigation of the operational limits of uranium-plutonium nitride fuels. *J. Nucl. Mat.*, 184:167, 1991.
- [38] R. Thetford and M. Mignanelli. The chemistry and physics of modelling nitride fuels for transmutation. *J. Nucl. Mat.*, 320:44, 2003.
- [39] T. Ogawa, T. Ohmichi, A. Maeda, Y. Arai, and Y. Suzuki. Vaporization behaviour of (Pu,Am)N. *J. Alloys and Compounds.*, 224:55, 1995.
- [40] R. Margevicius. AFC fuels development update. Technical Report LA-UR-03-0415, Los Alamos National Laboratory, 2003.
- [41] M. Takano, A. Itoh, M. Akabori, K. Minato, and M. Numata. Study on the stability of AmN and (Am,Zr)N. In *Proc. Int. Conf. Future Nuclear Systems, GLOBAL 03*. American Nuclear Society, 2003.
- [42] M. Jolkkonen, M. Streit, and J. Wallenius. Thermochemical modelling of uranium-free nitride fuels. *J. Nucl. Sci. Tech.*, 41, 2004.
- [43] K. Minato, M. Akabori, M. Takano, Y. Arai, K. Nakajima, A. Itoh, and T. Ogawa. Fabrication of nitride fuels for transmutation of minor actinides. *J. Nucl. Mat.*, 320:18, 2003.
- [44] J. Wallenius. CONFIRM: status and perspectives. In *Proc. Int. Conf. Future Nuclear Systems, GLOBAL 03*. American Nuclear Society, 2003.
- [45] A. Mayorshin. Irradiation of oxide and nitride fuels in BOR-60. In *Proc. Int. Conf. Future Nuclear Systems, GLOBAL 03*. American Nuclear Society, 2003.
- [46] B. Hilton, S. Hayes, M.K. Meyer, D. Crawford, G.S. Chang, and R.G. Ambrosek. The AFC-1 and AFC-1F irradiation tests of metallic and nitride fuels for actinide transmutation. In *Proc. Int. Conf. Future Nuclear Systems, GLOBAL 03*. American Nuclear Society, 2003.
- [47] Y. Dai, X.J. Dia, and K. Farrell. Mechanical properties of modified 9Cr1Mo (T91) irradiated at 300 C in SINQ target-3. *J. Nucl. Mat.*, 318:192, 2003.
- [48] C. Fazio, R. Stieglitz, J. Knebel, F. Groeschel, W. Wagner, A. Strinning, H. Heyck, Y. Dai, B. Smith, W. Leung, G. Laffont, T. Kirchner, A. Guertin, P. Agostini, D. Gorse, T. Auger, J. Vogt, and A. Al Mazouzi. The MEGA-PIE test project. In *InWor03*. SCK-CEN, 2003.
- [49] N.N. Novikova, Y. Pashkin, and V.V. Chekunov. Some features of sub-critical blankets cooled with lead-bismuth. In *Proc. Int. Conf. on Accelerator Driven Transmutation Technologies and Applications, ADTTA99*, 1999.
- [50] P. Seltborg, J. Wallenius, K. Tucek, and W. Gudowski. Definition and application of proton source efficiency in accelerator driven systems. *Nucl. Sci. Eng.*, 145:390, 2003.
- [51] M. Eriksson and J.E. Cahalan. Inherent shutdown capabilities in accelerator driven systems. *Ann. Nucl. Energy*, 29:1689, 2002.
- [52] A. Hough and J.A.C. Marples. The pseudo binary phase diagrams of  $PuO_2$  with alumina, beryllia and magnesia and the pseudo ternary  $PuO_2-ThO_2-BeO$ . *J. Nucl. Mat.*, 15:298, 1965.
- [53] R.J.M. Konings, H. Zhang, M.E. Huntelaar, and E.H.P. Cordfunke. Melting behaviour of oxide systems for heterogeneous transmutation of actinides. I. the systems Pu-Al-O and Pu-Mg-O. *J. Nucl. Mat.*, 249:223, 1997.
- [54] D.F. Carroll. *J. Am. Ceram. Soc.*, 47:650, 1964.
- [55] R. Konings. Institute of Transuranium Elements, Personal communication (2003).
- [56] F. Barbier, G. Benamati, C. Fazio, and A. Rusanov. Compatibility tests of steels in flowing liquid lead-bismuth. *J. Nucl. Mat.*, 295:149, 2001.

- [57] N. Li. Corrosion tests of US steels in lead-bismuth eutectic (LBE). In *Proc. ANS Meeting on Accelerator Applications/ Accelerator Driven Transmutation Technology Applications, AccApp/ADTTA01*. ANS, 2001.
- [58] A. Rusanov. Developing and studying the cladding steels for the fuel elements of NPLs with heavy coolant. In *Heavy liquid metal coolants in Nuclear technology, HLMC98*. IPPE, 1998.
- [59] N.S. Cannon, F.H. Huang, and M.L. Hamilton. Simulated transient behaviour of HT-9 cladding. In *Effects on radiation on materials: 14th Int. Symposium*, volume 2. ASTM STP 1046, 1990.
- [60] N.S. Cannon, F.H. Huang, and M.L. Hamilton. Transient and static mechanical properties of D9 fuel pin cladding and duct material irradiated to high fluence. In *Effects on radiation on materials: 15th Int. Symposium*. ASTM STP 1125, 1992.
- [61] M. Embid, R. Fernandez, and E. Gonzales. In *Proc. 5th Int. Information Exchange Meeting on Actinide and Fission Product Partitioning and Transmutation*. OECD/NEA, 1998.
- [62] J. Cahalan. Argonne National Laboratory, Personal communication (2005).
- [63] NRC general design criterion 11 - reactor inherent protection, appendix a to part 50 - general design criteria for nuclear power plants, 1999.

# Paper III

# On the Performance of Point Kinetics for the Analysis of Accelerator Driven Systems

M. Eriksson\*

Royal Institute of Technology (KTH), AlbaNova University Center,  
Dep. Nuclear & Reactor Physics, 10691 Stockholm, Sweden.  
and

J. E. Cahalan and W. S. Yang

Argonne National Laboratory, Nuclear Engineering Division,  
9700 South Cass Ave., IL 60439, USA.

Accepted *Nuclear Science and Engineering* (2004).

**Abstract** – *The ability of point kinetics to describe dynamic processes in accelerator-driven systems (ADS) is investigated. Full three-dimensional energy-space-time dependent calculations, coupled with thermal- and hydraulic feedback effects, are performed and used as a standard of comparison. Various transient accident sequences are studied. Calculations are performed in the range of  $k_{\text{eff}} = 0.9594$  to  $0.9987$ , to provide insight into the dependence of the performance on the subcritical level. Numerical experiments are carried out on a minor-actinide loaded and lead-bismuth cooled ADS. It is shown that the point kinetics approximation is capable of providing highly accurate calculations in such systems. The results suggest better precision at lower  $k_{\text{eff}}$ -levels. It is found that subcritical operation provides features that are favorable from a point kinetics view of application. For example, reduced sensitivity to system reactivity perturbations effectively mitigates any spatial distortions. If a subcritical reactor is subject to a change in the strength of the external source, or a change in reactivity within the subcritical range, the neutron population will adjust to a new stationary level. Therefore, within the normal range of operation, the power predicted by the point kinetics method and the associated error in comparison with the exact solution tends to approach an essentially bounded value. It was found that the point kinetics model is likely to underestimate the power rise following a reactivity insertion in an ADS, which is similar to the behavior in critical systems.*

## I. INTRODUCTION

In recent years, there has been an increasing interest in the application of accelerator-driven systems (ADS) for the purpose of incinerating long-lived radionuclides in high-level waste. The ADS is a non-self-sustaining, subcritical reactor driven by an external neutron source that is maintained by a charged-particle accelerator. Appropriate neutron kinetics models are required for predicting the consequences of operational disturbances and accidents in these systems. The so-called “point kinetics approximation” is a widely used method for performing preliminary analyses of dynamic phenomena. It has been extensively applied for the transient design analysis of existing reactors and it forms the basis of many transient analysis computational codes. It is based on kinetics theory developed for critical reactor studies. While the utility of the point kinetics methodology for critical reactor analysis is well known, its applicability to source-driven

subcritical systems is subject to investigation<sup>1</sup>. Because the neutron balance equations that describe the response in source-driven reactors are fundamentally different from the problem characterizing critical reactors, it has been suggested<sup>2</sup> that the point kinetics technique may be inappropriate for ADS studies; it is nonetheless very popular and often used for analysing such systems.

In the present paper, we investigate the precision of the point model in its application to ADS in some more detail. The objective is to estimate the magnitude of the errors encountered in the analysis of certain accidents under physically realistic conditions, i.e., including thermal- and hydraulic feedbacks. The basic approach is by comparison with an “exact” numerical solution. Results are obtained as function of the subcritical level. First, we make a short review of point kinetics theory and discuss its implications in a source-driven, subcritical operating mode. We then describe the test models and the computational techniques involved in the study. Problems and results are then summarized, followed by a brief conclusion in the last section.

---

\*E-mail: marcus@neutron.kth.se

## II. REACTOR KINETICS EQUATIONS

In this section, we review shortly the derivation of the conventional kinetics equations. These were first derived by Henry<sup>3</sup>. Their limitations and capabilities for critical reactor analysis have been investigated in great detail<sup>4,6</sup>. The derivation is presented here to serve as a basis for discussion of applications to source-driven systems. For convenience, the derivation proceeds along the lines suggested by Henry<sup>7</sup> with minor modification. An independent source term is incorporated to include neutrons supplied by the external source. The starting-point is the time-dependent continuous energy diffusion equation<sup>a</sup>. In shorthand operator notation it can be written as:

$$\frac{1}{v} \frac{\partial \Phi}{\partial t} = (\mathbf{F}_p - \mathbf{M})\Phi + \sum_k \lambda_k C_k \chi_{dk} + S \quad (1a)$$

and completed with the balance equation for the delayed-neutron precursors

$$\frac{\partial C_k}{\partial t} = -\lambda_k C_k + \int_0^\infty v_{dk} \Sigma_f(\mathbf{r}, E', t) \phi(\mathbf{r}, E', t) dE' \quad (1b)$$

$\Phi = \phi(\mathbf{r}, E, t)$  is the time-dependent neutron flux. For simplicity of notation, the functional dependence in Eq (1a) and (1b) has been suppressed.  $\mathbf{M}$  and  $\mathbf{F}_p$  are the usual “migration and loss operator” and the “prompt neutron production operator”, respectively. These correspond to:

$$\mathbf{F}_p \Phi = \chi_p(E) \int_0^\infty v_p \Sigma_f(\mathbf{r}, E', t) \phi(\mathbf{r}, E', t) dE'$$

$$\mathbf{M}\Phi = -\nabla \cdot D(\mathbf{r}, E, t) \nabla \phi(\mathbf{r}, E, t) + \Sigma_t(\mathbf{r}, E, t) \phi(\mathbf{r}, E, t) - \int_0^\infty \Sigma_s(\mathbf{r}, E' \rightarrow E, t) \phi(\mathbf{r}, E', t) dE'$$

The purpose behind the formulation of the kinetics equations is to derive a lumped model that describes the change in the average level of the flux, i.e., the integral of  $\phi(\mathbf{r}, E, t)$  over the energy and the spatial domain. For that reason, the neutron flux is factorized in the form  $\phi(\mathbf{r}, E, t) = p(t) \cdot \psi(\mathbf{r}, E, t)$ . It is noted that flux factorization is not an approximation, in contrast to separation of variables. In the former case, the neutron spatial and energy distributions may still depend on time. However, it is necessary to impose a constraint condition to define precisely the two new functions,  $p(t)$  and  $\psi(\mathbf{r}, E, t)$ , that arise in the factorization procedure:

$$\int_V \int_0^\infty \frac{w(\mathbf{r}, E) \psi(\mathbf{r}, E, t)}{v(E)} dEdV = 1 \quad (2)$$

The constraint condition states that the shape function,  $\psi(\mathbf{r}, E, t)$ , is normalized, for all  $t$ , in such a manner that the integral, Eq. (2), over all energy and space is held constant (normally taken as unity) in time. Prior to integration over space and energy, Eq. (1a) and (1b) is multiplied with a weight function,  $w(\mathbf{r}, E)$ . Introducing a weight function is not a requirement, but it allows manipulation of the kinetics equations in a way that simplifying assumptions (such as the point kinetics approximation) can be applied more effectively. It is emphasized, that the weight function can be any function that is defined over the same energy and spatial domain as the flux. To preserve generality, the following derivation will not employ a specific weight function.

$p(t)$  is sometimes called the amplitude function and it is defined according to:

$$p(t) = \int_V \int_0^\infty \frac{w(\mathbf{r}, E) \phi(\mathbf{r}, E, t)}{v(E)} dEdV \quad (3)$$

Thus, under the constraint condition given in Eq. (2),  $p(t)$  can be represented as in Eq. (3) and hence it is proportional to the total number of neutrons present in the reactor at any time.

Next, Eq. (1a) and (1b) are multiplied with the weight function and the neutron flux is substituted with the factorized functions. The equations are then integrated with respect to space and energy. After some manipulations, we arrive at the conventional point kinetics equations:

$$\frac{dp(t)}{dt} = \frac{\rho(t) - \beta(t)}{\Lambda(t)} p(t) + \sum_k \lambda_k c_k(t) + s(t) \quad (4a)$$

$$\frac{dc_k(t)}{dt} = \frac{\beta_k(t)}{\Lambda(t)} p(t) - \lambda_k c_k(t) \quad (4b)$$

The new quantities,  $\rho$ ,  $\beta$ ,  $\Lambda$ ,  $s$ , and  $c_k$  that emerge in Eqs. (4) are the integral quantities identified with the following definitions:

$$\beta(t) = \sum_k \beta_k(t)$$

$$\beta_k(t) = \frac{1}{F(t)} \int \int w \sum_k \mathbf{F}_{dk} \psi dEdV$$

$$\rho(t) = \frac{\int \int w(\mathbf{F}_p - \mathbf{M}) \psi dEdV}{F(t)}$$

$$\Lambda(t) = \frac{1}{F(t)} \int \int \frac{w \psi}{v} dEdV$$

$$s(t) = \frac{\int \int w S dEdV}{\int \int \frac{w \psi}{v} dEdV}$$

$$c_k(t) = \frac{\int \int w C_k \chi_{dk} dEdV}{\int \int \frac{w \psi}{v} dEdV}$$

<sup>a</sup>In his original work<sup>3</sup>, Henry derived the reactor kinetics equations starting from the time dependent neutron transport equation, we chose not to proceed along this path, but rather to utilize the diffusion approach as outlined in his textbook<sup>7</sup>, mainly to be in better accordance with the terms of our computational exercises and to avoid the potential of being misleading. In general, the reactor kinetics equations involve angular dependence and as shown by Henry, the equations may be extended to a transport formulation in a straightforward manner.

The definition of  $F(t)$  is:

$$F(t) = \int \int w(\mathbf{F}_p + \sum_k \mathbf{F}_{dk}) \psi dE dV$$

where the delayed neutron production operators  $\mathbf{F}_{dk}$  are defined similar to the prompt neutron production operator. It is in the cross sections (that depend on temperature, material density, and composition) in the operators  $\mathbf{F}_p$  and  $\mathbf{M}$  that thermal and hydraulic feedbacks are accounted for during a transient.

Henry<sup>3</sup>, called Eqs. (4) the ‘‘conventional kinetics equations’’. Today they are usually referred to as the ‘‘point kinetics equations’’ or sometimes the ‘‘exact point kinetics equations’’ in a way to distinguish them from the simplifying assumptions applied in the point kinetics approximation.

It is stressed that Eqs. (4) are exact and completely equivalent to Eqs. (1), but in a different form. The basic, time-dependent equations, Eqs. (1), are recast into Eqs. (4) without simplifying approximations. Henry<sup>7</sup> clearly states that as long as the rigorous definitions of the kinetics parameters are used, i.e., the actual time-dependent flux shape is calculated, the solution of Eqs. (4) for  $p(t)$  with any arbitrary weighting function will be *exactly* the same as the solution of Eqs. (1) for  $\phi(\mathbf{r}, E, t)$  and then the application of Eq. (3). This is true for critical as well as for subcritical systems. The error is introduced when we modify the equations to better cope with an approximate representation of the time-dependent flux shape, e.g., the point kinetics approximation. In that case, the weight function becomes useful because it leaves us with the possibility of freely choosing  $w(\mathbf{r}, E)$  in a manner to better suit a point kinetics approximation. Within a perturbation theory approach it is shown<sup>7</sup> for a critical reactor, that adjoint flux weighting eliminates the influence of first-order flux shape changes on the reactivity, and therefore also reduces the error in the approximation of  $p(t)$ . Consequently, the estimation for  $p(t)$  may tolerate a less precise description of the flux shape. This fact facilitates the use of the initial flux shape throughout the entire transient, i.e., first-order perturbation theory approach. In first-order perturbation theory, the weight function corresponds to the initial adjoint flux,  $\Phi_{\lambda_0}^*$ , i.e., the solution of the initial adjoint eigenvalue problem:

$$(\mathbf{M}_0^* - \lambda_0 \mathbf{F}_0^*) \Phi_{\lambda_0}^* = 0 \quad (5)$$

Where  $\mathbf{F}_0^*$  and  $\mathbf{M}_0^*$  are the adjoint operators of the total neutron production operator,  $\mathbf{F}_0 = \mathbf{F}_{p0} + \sum_k \mathbf{F}_{dk0}$ , and the loss operator  $\mathbf{M}_0$ . In the point kinetics approximation, the basic assumption is that the time dependence is separable from the  $(\mathbf{r}, E)$  dependence, i.e., the space-energy flux shape is fixed at all times. For a critical reactor, it permits the use of first-order perturbation theory to calculate the reactivity changes. The neutron balance equation for a reactor with an independent source is mathematically an inhomogeneous problem. In strict terms, separation of variables is not

possible for such cases. Thus, the point kinetics approximation becomes questionable. Moreover, the adjoint flux is not uniquely defined for a source-driven system. This invalidates the use of the standard first-order perturbation formula. The usual procedure for generating a weight function for a source-driven reactor is to employ an artificial initial  $\lambda$ -mode adjoint weighting function, i.e., the solution to the source-free adjoint equation, Eq. (5). As was shown by Ott<sup>8</sup>, the error cancellation property of the first-order perturbation formula is preserved in a source-driven system if the real flux shape is calculated from the initial inhomogeneous problem and not the initial  $\lambda$ -mode shape.

The integral kinetics parameters  $\rho$ ,  $\beta$ , and  $\Lambda$  arise only in the derivation of lumped models such as the kinetics equations. This is realized since Eqs. (1) do not involve these concepts. It is noted that the point kinetics parameters depend on the weighting function and for that reason their definition is entirely arbitrary. Therefore, the kinetics parameters do not necessarily correspond to any physically meaningful quantities. According to Henry<sup>3</sup>, the kinetics parameters have a meaningful interpretation only when the reactor is on a constant reactivity level and when the independent source term is negligible in comparison with the fission rate. These conditions are fulfilled automatically in a critical reactor when the time dependence is separable from the  $(\mathbf{r}, E)$  dependence. If the weighting function is unity then a clear physical interpretation can be defined. If  $w(\mathbf{r}, E) \neq 1$  then the kinetics parameters correspond to some weighted physical value. Using the adjoint flux as weighting function,  $w(\mathbf{r}, E) = \phi(\mathbf{r}, E)^*$ , has the benefit of producing ‘‘importance’’ weighted kinetics parameters. These can sometimes be interpreted as ‘‘effective’’ values. Since a source-free adjoint weighting function does not correspond to the actual state of a source-driven system the physical meaning of the point kinetics parameters is not clear. However, according to Becker<sup>9</sup>, a complication also arises in a critical system because the weighting function employed in the point kinetics equations is time-independent, nevertheless the adjoint function might change during a transient. In that case, it might not correspond to the actual physical state.

### III. TEST MODEL

The model used in the present study is based on a previous OECD/NEA benchmark model<sup>10</sup> with some minor modifications<sup>b,c</sup>. The original benchmark was not intended as a transient case study, but adopting this system as the basis for the current tests has the benefit that initial static results could be compared with previous studies.

<sup>b</sup>The  $r$ - $z$  geometry specification prescribed in the benchmark was converted to a three-dimensional hexagonal- $z$  representation.

<sup>c</sup>To avoid computational artefacts due to the treatment of void regions with a diffusion theory approach, the current model assumes that the coolant fills the full extent of the target and the beam duct region.

The model pertains to an accelerator-driven, lead-bismuth cooled, and minor-actinide loaded transmuter core. The core consists of a central lead-bismuth target region and a homogenized fuel region surrounded by radial and axial reflectors (70% steel and 30% coolant). 114 fuel assemblies are included in the hexagonal-z representation; Fig 1 contains a plan view of a one-sixth symmetry section of the core. The height of the active core is 100 cm. The fuel consists of 2/3 minor actinides and 1/3 plutonium with a ZrN diluent;  $(\text{Pu}_{0.1}, \text{MA}_{0.2}, \text{Zr}_{0.7})\text{N}$ , where MA represents minor actinides such as Np, Am, and Cm. Fuel compositions correspond to plutonium discharge from UOX-fueled LWRs mixed with MA from a “double strata” strategy<sup>11</sup>. Start-up core loading is used in the simulations. The fuel is further diluted with 71% ZrN. Core material compositions are summarized in TABLE I. Additional lattice parameters are included in TABLE II.

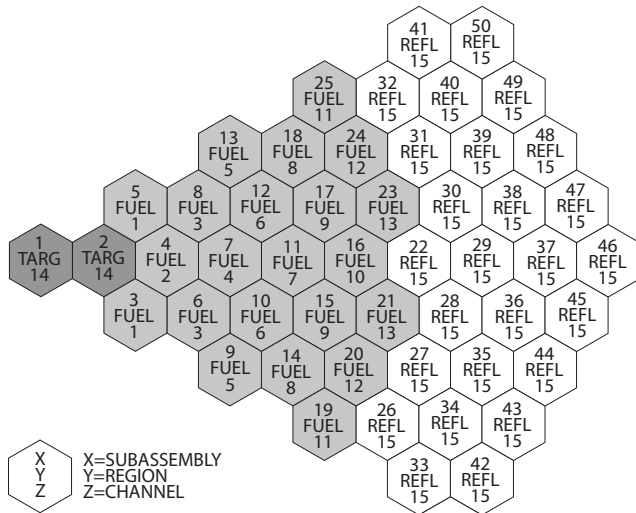


Fig 1. One-Sixth Core Subassembly and Channel Assignment.

TABLE I  
Material Specification of the Reference Core Configuration

|  |                                    |
|--|------------------------------------|
| Core Volume Fractions:   |                                    |
| 30 vol%  | Fuel                               |
| 48 vol%  | Coolant (Pb/Bi eutectic)           |
| 22 vol%  | Clad + Structure (stainless steel) |
| Reflector Volume Fractions:  |                                    |
| 30 vol%  | Coolant                            |
| 70 vol%  | Stainless Steel                    |
| Fuel:  |                                    |
| Fuel Material: $(\text{Pu}_{0.1}, \text{MA}_{0.2}, \text{Zr}_{0.7})\text{N}$ |                                    |
| Theoretical density (300°C): 9.19 g/cm <sup>3</sup>                          |                                    |
| Fuel smear density: 84 % of theoretical                                      |                                    |
| 68% MA/TRU ratio   |                                    |
| 71% molar fraction ZrN   |                                    |

TABLE II  
Lattice parameters

|                                  |        |
|----------------------------------|--------|
| Number of pins per assembly      | 217    |
| Pitch/diameter ratio             | 1.6    |
| Pin diameter [mm]                | 7.366  |
| Cladding thickness [mm]          | 0.787  |
| Ducts flat-to-flat distance [cm] | 15.956 |

#### IV. COMPUTATIONAL MODELING TECHNIQUES

Numerical testing was performed with coupled core dynamics calculations using the SAS4A/DIF3D-K<sup>12</sup> code. The “exact” results are obtained from a direct numerical solution of the time-, space-, and energy-dependent multigroup diffusion equation. The direct solution is used as a standard of comparison for the point kinetics solution. One advantage of using the SAS4A/DIF3D-K program for the current task is that the direct solution method and the point kinetics procedure are implemented within the same code. This makes it straightforward to compare the underlying methods without worrying about consistency among different computational procedures and models. For example, the initial steady-state solutions, cross sections, thermal- and hydraulics treatments, and model specifications are all identical.

Thirty-three energy groups are employed in the multi-group treatment. Composition-, temperature- and region-dependent broad group microscopic cross sections were generated based on JEF2.2 data and further processed using the MC<sup>2</sup>-2<sup>13</sup> and TWODANT<sup>14</sup> codes. With MC<sup>2</sup>-2, a homogeneous, ultra-fine group (2082 groups), zero-dimensional spectrum calculation (infinite medium assumption) is first performed for each composition. Individual material microscopic cross sections are reduced to the fine group level (230 groups) by averaging the ultra-fine-group data over the flux and current spectra. Full-core fine group calculations are then carried out with TWODANT. The spectra obtained from TWODANT are used to spatially collapse the fine-group data to a broad group level (33 groups). The broad-group microscopic cross sections are composition-, region- and temperature dependent, i.e., different sets of cross sections for different regions and temperatures (500 K, 980 K, 1580 K, and 2500 K). Local cross sections used in the transient flux calculations are obtained through interpolation in these sets to fit a particular temperature.

Data for delayed neutrons and their precursors were generated based on the ENDF/B-VI library. Delayed neutron data for fissioned curium isotopes was not available in ENDF/B-VI. The missing curium isotopes adopted the delayed neutron yield of <sup>239</sup>Pu.

An external neutron source distribution was supplied in the specification of the benchmark<sup>10</sup>. The neutrons are produced by spallation nuclear reactions induced by high-energy protons impinging on a lead-bismuth target. The target has a height of 100 cm and a radius of 20 cm. The

energy of the incident protons is 1 GeV and the beam has a radius of 10 cm. The fine group source (122 groups) is collapsed to a broad group level (33 groups) and the r-z representation was converted to hexagonal-z geometry. The source neutrons are presumed to enter the system at the target meshes. The temporal dependence of the external source intensity enters the SAS4A/DIF3D-K code as one of the system driving functions. For transients involving alterations of the source strength, it is assumed that the neutron spatial and energy distributions are maintained during the transients; i.e., only the magnitude of the external neutron source is adjusted. This is a reasonable assumption since the spatial and energy distributions of the source neutrons depend on the proton beam energy and the target and core configuration, which are fixed during the transients.

The spatial flux solutions are based on a three-dimensional nodal diffusion theory method<sup>15</sup>. The core is partitioned into assembly-sized hexagonal unit cells in the horizontal planar direction and axially subdivided into twenty-one axial nodes, each with a mesh spacing of 4.76 cm. In reflector regions, axial mesh sizes of 12.5 cm are employed. The radial distance between the assembly vertical centerlines is 16 cm. The solution takes advantage of one-sixth core symmetry by solving for a single sextant section of the core. Uniform nuclear cross sections are used within each node. In the direct method, the time-dependent component is solved using a fully implicit finite-difference approximation (the DIF3D-K<sup>16</sup> code uses a specified  $\theta$ -method<sup>17</sup> of time differencing). The theta ( $\theta=1$ ) method consists of representing the time differential operators with their implicit finite-difference formulation. Thermal- and hydraulic calculations are performed for 13 channels, each representative of an average pin within individual subassemblies (See Fig 1 for channel to subassembly assignments). Feedback effects (due to Doppler and coolant density variations) are included as necessary to reproduce the physical situation as closely as possible. Both the direct solution and the point kinetics method account for thermal feedbacks through node-dependent microscopic and macroscopic cross sections. The cross sections are updated with time as local temperatures and densities changes. In the point kinetics solution, the initial flux shape is used throughout the entire transient calculation. Time-dependent point kinetics parameters are computed by means of first-order perturbation theory. The initial flux shape, determined with a given external source distribution, and the initial  $\lambda$ -mode adjoint flux are used along with macroscopic cross sections to compute time-dependent point kinetics parameters, especially the reactivity parameter which reflects the thermal feedbacks. The reactivity is found by summing contributions from local changes in temperature and material densities (as opposed to the use of core-average reactivity coefficients). The adjoint flux is required in the evaluation of the scalar products used in the calculation of the time-dependent kinetics parameters. It corresponds to the initial source-free mathematical nodal adjoint solution<sup>18</sup>. The direct solution technique does not

require the formulation of kinetics parameters and adjoint fluxes. The great advantage of the direct solution is that an unambiguous and “exact” solution of the inhomogeneous time-dependent group diffusion equation is obtained, in that sense that no approximations is introduced other than space nodalization and time differencing.

Transient solutions are obtained using a fixed time step size<sup>d</sup> of  $\Delta t=10$  ms (results for test problems employing smaller time steps suggested that a time increment of 10 ms is adequate for the current set of problems). At the end of each time step, new cross sections are calculated. Heat-transfer and hydraulics time-steps are on separate sub-steps.

## V. NUMERICAL RESULTS

Numerical solutions for three different categories of transients were analyzed. The test problems pertain to accident-type events in ADS’s. The first category concerns alterations of the proton beam intensity, i.e., changes in the magnitude of the external neutron source. Secondly, localized reactivity insertions are examined. Finally, a flow reduction event is analyzed. The total power is extracted as a function of time, i.e., fission power plus decay power, as obtained in the direct solution and in the point kinetics solution. The transients are followed for 20.0 seconds.

We further perform calculations at different subcritical levels, i.e.,  $k_{eff}$  values, to reveal any trends concerning performance characteristics. It will provide information on the numerical accuracy of the point kinetics solution as function of the level of subcriticality. The multiplication constant is altered by changing the concentration of fuel diluents (ZrN), everything else is unchanged, initial  $k_{eff}$  values are given in TABLE III. Unless the source strength is adjusted, an increase in  $k_{eff}$  would lead to a higher power output. Thus, the intensity of the external source is adjusted to maintain the initial power at 377 MWth. Results from the calculation of the initial effective multiplication constant, shown in TABLE III, proved to be in good agreement with previous results<sup>10</sup>.

TABLE III  
Initial effective multiplication constant (hot condition)

| Case          | Fraction ZrN | $k_{eff}$ |
|---------------|--------------|-----------|
| Case 1 (ref.) | 70.7%        | 0.9594    |
| Case 2        | 69.4%        | 0.9798    |
| Case 3        | 68.2%        | 0.9987    |

<sup>d</sup>It ought to be clarified that the time-dependent flux solution in DIF3D-K employs an automatic time-step selection algorithm, which monitors the rate of change of the fission source and constrains the time-step based on a user-specified value. However, the specified time step was sufficiently small that it prevailed in all test cases.



### V.A. Variations in Source Strength

In an ADS, the traditional reactivity based shutdown system is replaced with a beam regulating system that controls the intensity of the external neutron source. The magnitude of the external neutron source is adjusted by changing the proton beam intensity. It is relevant to consider system disturbances in which the source strength suddenly changes. This could for example happen due to a control system failure, accelerator malfunction, or operator error. The first transient is initiated by ramping the source intensity to double strength while keeping the spatial and energy distribution fixed. The ramp is initiated at  $t=1$  second and halted at 1.001 seconds. The source is held constant thereafter. The reactor is initially at full power; so the disturbance causes a strong overpower condition. In a second transient, the external source neutrons are completely removed, i.e., a source trip.

Fig 2 and Fig 3, display the results for the source overpowers and the source trip events, respectively. The power responds with a prompt jump followed by a slower adjustment when the delayed neutrons establish a balance with the new flux level. In the source removal transient, the power is reduced to a level determined by fissions induced by delayed neutrons plus the release of decay heat. The fission power dies away faster in cores with larger subcriticality because the multiplication of delayed neutrons is lower. The decay power is given by the fission product inventory and its change requires longer time intervals. The effective delayed neutron fraction is 0.186%. The delayed neutrons typically have a small effect in subcritical reactors<sup>20</sup>. Note that case 3 ( $k_{eff}=0.9987$ ) is very close to criticality (less than  $\beta$ ). Consequently the delayed neutrons are much more influential in that case.

It is seen that the point kinetics method, employing no flux shape recalculations, yields extremely accurate solutions for both the source overpower transient and the source trip transient and at all  $k_{eff}$ -levels. In fact, the results are indistinguishable as illustrated in Fig 2 and Fig 3. Numerical performance results are presented in TABLE IV and TABLE V. The maximal deviations are 0.2% and 0.9% for the source overpowers and source trip transients, respectively. Maximum deviation occurs shortly after the source has been fully inserted/removed, followed by better agreement from that point and forward. Deviation from the point kinetics solution is an indication of flux shape changes. The good agreement suggests that spatial effects are less important. Since the only source for spatial distortion is due to reactivity feedbacks, the good agreement implies that these are small and/or distributed such that no noticeable flux deformation develops. The effect of neglecting the system feedbacks is shown in Fig 4. Evidently, the current ADS features inherent positive reactivity feedbacks. This is attributed to a positive coolant density feedback component, characteristic of a minor-actinide loaded reactor operating on a fast neutron spectrum, whereas the Doppler effect is negligible. As a comparison, it is seen that the error of the point kinetics method is much smaller than the error due to the neglect of

thermal feedbacks, even in the deeply subcritical case 2 ( $k_{eff}=0.9798$ ). In the near-critical reactor, this is not so surprising since the feedbacks have a much stronger effect.

The flux shape that develops following a change in the source strength in a subcritical system without feedback is identical to the initial steady-state distribution (except in the case of complete source removal). The adjustment will occur almost instantaneously (within a few tens of prompt periods). A prompt adjustment of the flux shape prevails since the delayed neutrons are less influential; in a critical reactor the delayed neutrons tend to retard the shape transition. Since an external source perturbation, by itself (feedbacks excluded), does not affect the reactivity<sup>21</sup> the point kinetics results typically become quite accurate. In case strong feedbacks occur, the point kinetics approach may not necessarily provide correct results.

In the source trip transient the feedbacks cause the reactivity to decrease. As shown in TABLE V, the point kinetics method has a tendency to overpredict the negative reactivity insertion in the source trip transient. It also appears as if the numerical performance of the point method is improving slightly as the subcriticality decreases. However, it is difficult to draw any firm conclusions on that behavior; all results are very close together. It could be related to the nature and the interplay of the feedbacks in this particular problem. The source overpower transient does not seem to exhibit the same behavior.

Test calculations confirmed that a time step of 10 ms was adequate suggested by the fact that employing time increments of 1 ms and 0.1 ms provided essentially identical results (not shown).

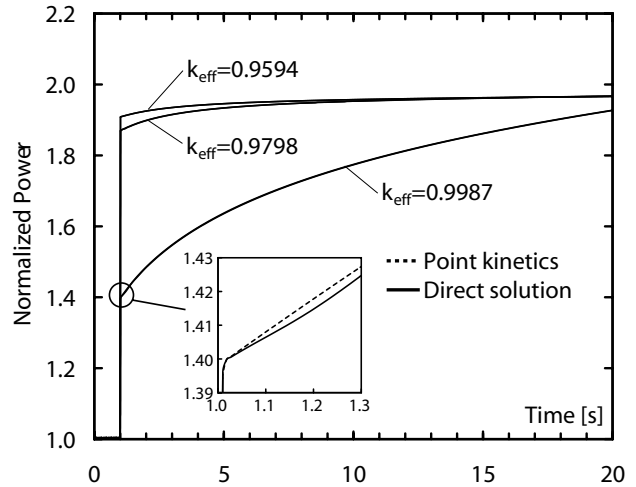


Fig 2. Source overpower transient problem.

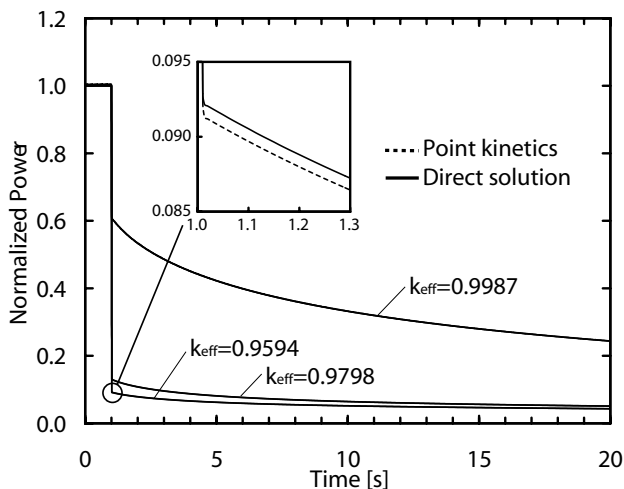


Fig 3. Source trip transient problem.

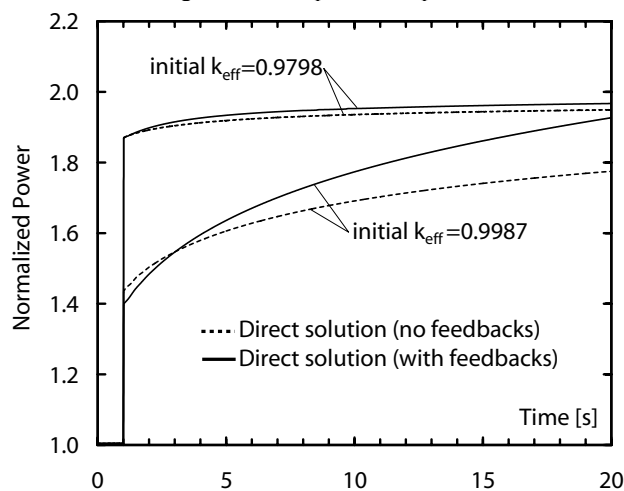


Fig 4. Source overpower transient with and without reactivity feedbacks.

TABLE IV

Comparison of results for the source overpower transient problem<sup>e</sup>

| Time [s]          | Initial $k_{eff}=0.9594$ |        |                | Initial $k_{eff}=0.9798$ |        |                | Initial $k_{eff}=0.9987$ |        |                |
|-------------------|--------------------------|--------|----------------|--------------------------|--------|----------------|--------------------------|--------|----------------|
|                   | Direct                   | PK     | $\epsilon$ (%) | Direct                   | PK     | $\epsilon$ (%) | Direct                   | PK     | $\epsilon$ (%) |
| 2.0               | 1.9245                   | 1.9251 | 0.03           | 1.8981                   | 1.8988 | 0.04           | 1.4837                   | 1.4853 | 0.10           |
| 5.0               | 1.9454                   | 1.9458 | 0.02           | 1.9336                   | 1.9339 | 0.01           | 1.6357                   | 1.6372 | 0.10           |
| 10.0              | 1.9570                   | 1.9572 | 0.01           | 1.9528                   | 1.9530 | 0.01           | 1.7734                   | 1.7746 | 0.06           |
| 15.0              | 1.9626                   | 1.9626 | 0.00           | 1.9613                   | 1.9617 | 0.02           | 1.8612                   | 1.8620 | 0.05           |
| 20.0              | 1.9663                   | 1.9662 | 0.00           | 1.9671                   | 1.9673 | 0.01           | 1.9268                   | 1.9274 | 0.03           |
| Max deviation (%) |                          | 0.05   |                | 0.08                     |        | 0.22           |                          |        |                |

<sup>e</sup>Direct numerical solution (Direct), point kinetics solution (PK),  $\epsilon$  (%) is relative error in calculated power:  $(P_{PK}-P_{direct})/P_{direct}$ , max deviation is maximum relative error over a 20 sec. time period.

TABLE V

Comparison of results for the source trip transient problem.

| Time [s]          | Initial $k_{eff}=0.9594$ |        |                | Initial $k_{eff}=0.9798$ |        |                | Initial $k_{eff}=0.9987$ |        |                |
|-------------------|--------------------------|--------|----------------|--------------------------|--------|----------------|--------------------------|--------|----------------|
|                   | Direct                   | PK     | $\epsilon$ (%) | Direct                   | PK     | $\epsilon$ (%) | Direct                   | PK     | $\epsilon$ (%) |
| 2.0               | 0.0791                   | 0.0784 | -0.84          | 0.1084                   | 0.1077 | -0.64          | 0.5342                   | 0.5337 | -0.09          |
| 5.0               | 0.0626                   | 0.0622 | -0.68          | 0.0816                   | 0.0811 | -0.60          | 0.4228                   | 0.4223 | -0.11          |
| 10.0              | 0.0521                   | 0.0518 | -0.54          | 0.0647                   | 0.0644 | -0.50          | 0.3323                   | 0.3319 | -0.09          |
| 15.0              | 0.0468                   | 0.0466 | -0.45          | 0.0565                   | 0.0562 | -0.43          | 0.2797                   | 0.2797 | -0.01          |
| 20.0              | 0.0433                   | 0.0432 | -0.40          | 0.0512                   | 0.0510 | -0.39          | 0.2439                   | 0.2436 | -0.11          |
| Max deviation (%) |                          |        | -0.94          |                          |        | -0.73          |                          |        | -0.36          |

### V.B. Localized Reactivity Insertion

In this section, we consider the effect of local reactivity insertions. It is assumed that a fuel subassembly is fully withdrawn at initial conditions and subsequently drops into the core during operation. Despite the hypothetical nature of this scenario, it is useful for evaluating the performance of the underlying kinetics methods. An idealized model of the subassembly movement is employed, in which the volume fraction of materials representing the control subassembly increases uniformly over its axial distance with time. It is further assumed that the subassembly is inserted in a ramp fashion over a time interval of 1 second. The transient is initiated during operation at full power (the external source strength is initially adjusted so that the steady-state reactor power corresponds to the nominal power).

We investigate the effect of reactivity insertion at two different positions; in one instant we move a subassembly close to core-center (subassembly no. 4 in accordance with Fig 1) and in a second study it is inserted close to the core boundary (subassembly no. 16 in accordance with Fig 1). It is assumed that the region representing the absent subassembly is occupied with coolant at initial conditions. In TABLE VI, the initial  $k_{eff}$ -values of the various configurations are shown. The  $\Delta k_{eff}$  given in TABLE VI corresponds to the increase in effective multiplication constant when the subassembly is completely inserted, when thermal feedback effects are not included, i.e. it is the numerical difference in the initial  $k_{eff}$  when the core is fully loaded (values tabulated in TABLE III) and for the case when one subassembly is absent from start. It is seen that the reactivity worth of the fuel subassembly near the core-center is approximately 13\$ and 4\$ for the subassembly at the core boundary. It should be noted, however, that starting from normal power and temperature the coolant expansion reactivity coefficient will contribute with some additional reactivity insertion.

TABLE VI

Calculations of the core configurations aimed at studying subassembly movement.  $\Delta k_{eff}$  is the corresponding change in  $k_{eff}$  when the subassembly is inserted into the core. The value given in parenthesis is the reactivity insertion quoted in dollars ( $1\$\text{=}0.00186$ ).

| Core configuration | Insertion close to core-center |                    | Insertion close to core boundary |                    |
|--------------------|--------------------------------|--------------------|----------------------------------|--------------------|
|                    | Initial $k_{eff}$              | $\Delta k_{eff}^f$ | Initial $k_{eff}$                | $\Delta k_{eff}^f$ |
| Case 1             | 0.9356                         | +0.0238 (+12.8)    | 0.9519                           | +0.0075 (+4.0)     |
| Case 2             | 0.9558                         | +0.0240 (+12.9)    | 0.9722                           | +0.0076 (+4.1)     |
| Case 3             | 0.9746                         | +0.0241 (+13.0)    | 0.9910                           | +0.0077 (+4.1)     |

<sup>f</sup>Change in  $k_{eff}$  when feedbacks are not taken into account. The amount of reactivity inserted in cases 2 and 3 is slightly higher because of a higher reactivity worth of individual fuel subassemblies.

It is well known, from critical system analysis that for local reactivity insertion events, using the point kinetics technique to calculate the response can lead to significant errors. This is because the basic assumption is that the flux shape remains constant. Comparison with the exact results shows that this is indeed the case. The point approximation severely underestimates the excursion for the case that is closest to the critical state (initial  $k_{eff}$ =0.9746), shown in Fig 5. However, it is seen that point kinetics is a much better approximation for the deeply subcritical cores, illustrated in Fig 6. In TABLE VII, the relative root-mean-square (*RelRMS*) deviation of the local peak-to-average flux (for all three-dimensional spatial nodes) with respect to the initial distribution is shown. Comparing the *RelRMS* values for the various subcritical test cases provide an indication of the flux spatial distortion sensitivity as function reactor  $k_{eff}$ . While the amount of reactivity insertion is essentially the same for all test configurations, the *RelRMS* variation of the flux shape decreases, as the core multiplication constant decreases. Thus, it appears that for a fixed reactivity change the flux spatial distortion decreases when the system is more subcritical. This behavior seems reasonable considering the reduced sensitivity to reactivity inputs in the subcritical state. As the subcritical margin increases, the total (negative) reactivity of the system increases and a given reactivity change will constitute a smaller fraction of the overall reactivity. The net effect is lower reactivity sensitivity as the subcriticality increases. When the fuel subassembly falls into the reactor, the neutron flux increases near this location due to a local increase in the fission rate. In the near-critical reactor, the neutrons are strongly multiplied, and the increase in the fission source produces a local deformation of the flux shape. In a deeply subcritical core, the neutrons are weakly multiplied therefore; the insertion of the subassembly has an overall smaller effect. Due to this lower sensitivity, flux distortions following a reactivity disturbance diminish as the  $k_{eff}$  decreases.

In the second problem, the subassembly is inserted at the outer end of the core (subassembly no. 16 according to Fig. 1). Given the lower importance in the outer core regions, the magnitude of the reactivity disturbance is lower. The spatial location of the initiating perturbation is

expected to influence the resulting flux deformation. The point method showed a slight improvement, however, the basic trends were the same, producing better results at lower subcriticality levels. The *RelRMS* deviation in the flux spatial distribution is summarized in TABLE VIII.

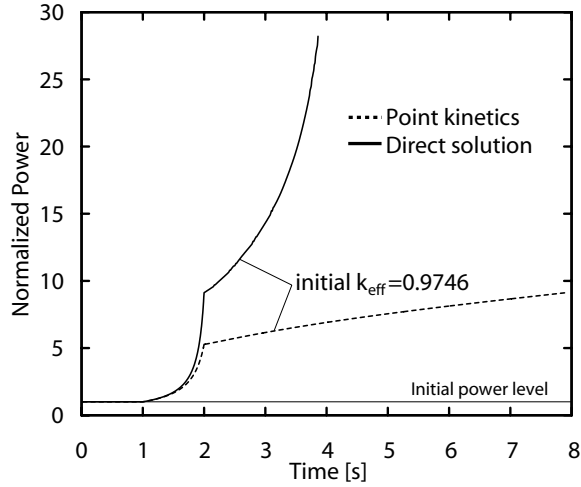


Fig 5. Reactivity insertion near core-center (initial  $k_{eff}$ =0.9746).

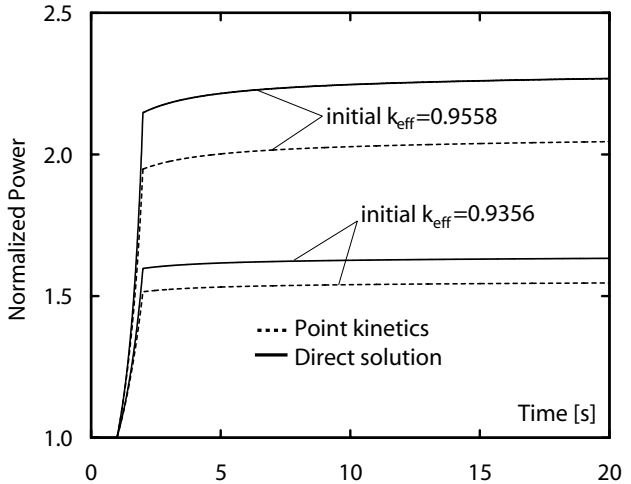


Fig 6. Reactivity insertion near core-center (initial  $k_{eff}$ =0.9356 and  $k_{eff}$ =0.9558).

TABLE VII

Relative root-mean-square (*RelRMS*) difference of the peak-to-average flux distribution with respect to the initial flux distribution following insertion of the subassembly near the core-center.

| Time [s] | RelRMS <sup>g</sup> peak-to-average flux |                         |                         |
|----------|--|-------------------------|-------------------------|
|          | Initial                                  | Initial                 | Initial                 |
|          | $k_{\text{eff}}=0.9356$                  | $k_{\text{eff}}=0.9558$ | $k_{\text{eff}}=0.9746$ |
| 1.2      | 0.9%                                     | 1.0%                    | 1.2%                    |
| 1.4      | 1.8%                                     | 2.2%                    | 2.6%                    |
| 1.6      | 2.8%                                     | 3.4%                    | 4.1%                    |
| 1.8      | 4.0%                                     | 4.7%                    | 5.7%                    |
| 2.0      | 5.2%                                     | 6.2%                    | 7.4%                    |
| 3.0      | 5.2%                                     | 6.3%                    | 7.8%                    |
| 20.0     | 5.4%                                     | 6.6%                    | -                       |

$$^g \text{RelRMS} = \sqrt{\frac{1}{N} \sum_{i=1}^N \left( \frac{p_i - p_0}{p_0} \right)^2}$$

where N is the number of hex-Z nodes

in the three-dimensional space and p is the local peak-to-average flux in each node. The subscript 0 denotes the initial state.

TABLE VIII

Relative root-mean-square (*RelRMS*) difference of the peak-to-average flux distribution with respect to the initial flux distribution following insertion of the subassembly near the core boundary.

| Time [s] | RelRMS peak-to-average flux |                         |                         |
|----------|-----------------------------|-------------------------|-------------------------|
|          | Initial                     | Initial                 | Initial                 |
|          | $k_{\text{eff}}=0.9519$     | $k_{\text{eff}}=0.9722$ | $k_{\text{eff}}=0.9910$ |
| 1.2      | 0.7%                        | 0.8%                    | 0.9%                    |
| 1.4      | 1.4%                        | 1.6%                    | 1.8%                    |
| 1.6      | 2.2%                        | 2.6%                    | 2.9%                    |
| 1.8      | 3.0%                        | 3.6%                    | 4.0%                    |
| 2.0      | 4.0%                        | 4.7%                    | 5.3%                    |
| 3.0      | 4.0%                        | 4.7%                    | 5.5%                    |
| 20.0     | 4.1%                        | 4.8%                    | -                       |

Numerical performance data are summarized in TABLE IX for the case when the subassembly is inserted close to core-center and in TABLE X for the case when the subassembly is inserted at the core boundary. Ideally (stripped of reactivity feedbacks), all cases should remain in the subcritical state even after the subassembly has been fully inserted. However, due to positive thermal feedbacks additional reactivity is inserted, which for the case with initial  $k_{\text{eff}}=0.9746$  (subassembly inserted close to core-center) leads to an excursion in the range above critical (but below prompt critical). The direct space-time solution predicts that the reactor in that case becomes supercritical at  $t=3.3$  seconds and the calculation is subsequently terminated at  $t=3.9$  seconds due to reaching excessive temperatures. The point solution, on the other hand, underpredicts the reactivity insertion and the reactor remains in the subcritical range, which leads to considerable discrepancies since it is in the supercritical range where most of the power rise occurs. The cases  $k_{\text{eff}}=0.9356$  and  $k_{\text{eff}}=0.9558$  are predicted to stay in the subcritical state, therefore the power approaches a stationary level and the error is essentially bounded at the value already accumulated. It is seen that the point kinetics

calculations underestimate the exact space-time solution in all cases. The same non-conservative behavior is observed in critical systems.

The fuel is calculated to reach the melting point at approximately 2.6 sec. into the transient. In reality, the nature of the accident might change significantly from that point. Fuel dispersal may act to terminate the accident prior to reaching supercritical conditions, however, reactivity could also be added due to fuel relocation and expulsion of lead-bismuth. Therefore, current predictions beyond core damaging levels are highly uncertain from a physical point of view, but nonetheless it permits comparison of the basic methods under extreme conditions.

TABLE IX

Comparison of results for the insertion of a fuel subassembly near the core-center (subassembly no. 9 according to the core map in Fig. 1).

| Time [s]          | Initial $k_{\text{eff}}=0.9356$ |       |                | Initial $k_{\text{eff}}=0.9558$ |       |                | Initial $k_{\text{eff}}=0.9746$ |       |                |
|-------------------|---------------------------------|-------|----------------|---------------------------------|-------|----------------|---------------------------------|-------|----------------|
|                   | Direct                          | PK    | $\epsilon$ (%) | Direct                          | PK    | $\epsilon$ (%) | Direct                          | PK    | $\epsilon$ (%) |
| 1.2               | 1.073                           | 1.072 | -0.1           | 1.108                           | 1.106 | -0.2           | 1.191                           | 1.187 | -0.3           |
| 1.4               | 1.163                           | 1.156 | -0.6           | 1.250                           | 1.238 | -0.9           | 1.493                           | 1.464 | -1.9           |
| 1.6               | 1.274                           | 1.255 | -1.5           | 1.442                           | 1.408 | -2.4           | 2.034                           | 1.920 | -5.6           |
| 1.8               | 1.415                           | 1.372 | -3.0           | 1.719                           | 1.633 | -5.0           | 3.282                           | 2.807 | -14.5          |
| 2.0               | 1.598                           | 1.515 | -5.2           | 2.148                           | 1.948 | -9.3           | 9.112                           | 5.270 | -42.2          |
| 3.0               | 1.607                           | 1.523 | -5.2           | 2.182                           | 1.975 | -9.5           | 14.314                          | 6.157 | -57.0          |
| 20.0              | 1.633                           | 1.546 | -5.3           | 2.268                           | 2.045 | -9.8           | -                               | -     | -              |
| Max deviation (%) |                                 |       | -5.3           |                                 |       | -9.8           |                                 |       | -75.9          |

TABLE X

Comparison of results for the insertion of a fuel subassembly near the core-boundary (subassembly no. 16 according to the core map in Fig. 1).

| Time [s]          | Initial $k_{\text{eff}}=0.9519$ |       |                | Initial $k_{\text{eff}}=0.9722$ |       |                | Initial $k_{\text{eff}}=0.9910$ |       |                |
|-------------------|---------------------------------|-------|----------------|---------------------------------|-------|----------------|---------------------------------|-------|----------------|
|                   | Direct                          | PK    | $\epsilon$ (%) | Direct                          | PK    | $\epsilon$ (%) | Direct                          | PK    | $\epsilon$ (%) |
| 2.0               | 1.136                           | 1.106 | -2.63          | 1.290                           | 1.223 | -5.18          | 3.382                           | 2.380 | -29.6          |
| 4.0               | 1.138                           | 1.108 | -2.66          | 1.302                           | 1.232 | -5.44          | 4.687                           | 2.734 | -41.7          |
| 6.0               | 1.140                           | 1.109 | -2.71          | 1.307                           | 1.235 | -5.50          | 6.058                           | 2.941 | -51.5          |
| 8.0               | 1.141                           | 1.110 | -2.72          | 1.311                           | 1.237 | -5.58          | 7.980                           | 3.082 | -61.4          |
| 10.0              | 1.141                           | 1.110 | -2.72          | 1.312                           | 1.239 | -5.56          | 12.815                          | 3.188 | -75.1          |
| 20.0              | 1.143                           | 1.111 | -2.75          | 1.317                           | 1.243 | -5.65          | -                               | -     | -              |
| Max deviation (%) |                                 |       | -2.77          |                                 |       | -5.65          |                                 |       | -78.2          |

### V.C. Flow Reduction

Finally, kinetics performance characteristics were compared for a flow coastdown event. Complete loss of forced flow in the primary system is assumed. The analysis further assumes that the shutdown system is inoperable, which in an accelerator-driven system corresponds to a “beam-on” situation. Constant coolant inlet temperature is specified.

The power traces for the cases with initial  $k_{\text{eff}}=0.9594$  and  $k_{\text{eff}}=0.9798$  are presented in Fig 7 and for  $k_{\text{eff}}=0.9987$  in Fig 8; the scale on the left is for the normalized power, and the scale on the right is for the normalized flow. The accident is initiated by gradually reducing the inlet driving

pressure, starting at  $t=1$  sec. The pump driving pressure approaches zero at 10 sec. The transient is dictated by coolant reactivity feedback. Coolant heat-up occurs at a rate determined by the flow coastdown. The resulting density reduction of the coolant has a positive effect. For the deeply subcritical cores, i.e. cases  $k_{eff}=0.9594$  and  $k_{eff}=0.9798$ , the power peaks (with some delay) as the flow drops to a minimum. Eventually, the coolant flow balances at a flowrate sustained by natural circulation alone. Given the small reactivity effects, the power settles at a level slightly above the initial state. For the near-critical core, shown in Fig 8, the power trace is different. The feedback-induced reactivity has a much stronger effect in this case. This is because the response is more sensitive near the critical state. At approximately 13.8 seconds into the transient, the reactor becomes supercritical. Continued coolant heat-up causes gradual insertions of reactivity, leading to an essentially unbounded power excursion. The calculation was terminated when the cladding in the hottest channel exceeded the melting point.

In TABLE XI, the numerical error versus time is presented. The point kinetics results were found to be in excellent agreement with the exact solution for the deeply subcritical cases (initial  $k_{eff}=0.9594$  and  $k_{eff}=0.9798$ ), indicating that coolant feedbacks did not alter the initial flux shape. For the near-critical reactor (initial  $k_{eff}=0.9987$ ), the direct solution predicts a somewhat higher power than does the point approximation.

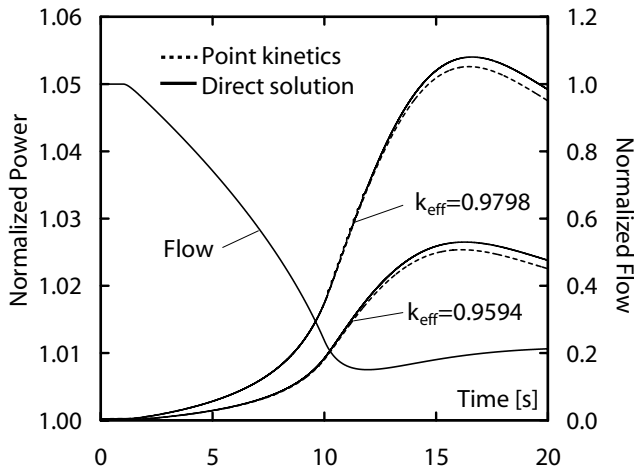


Fig 7. Unprotected Loss-of-flow transient (initial  $k_{eff}=0.9594$  and  $k_{eff}=0.9798$ ).

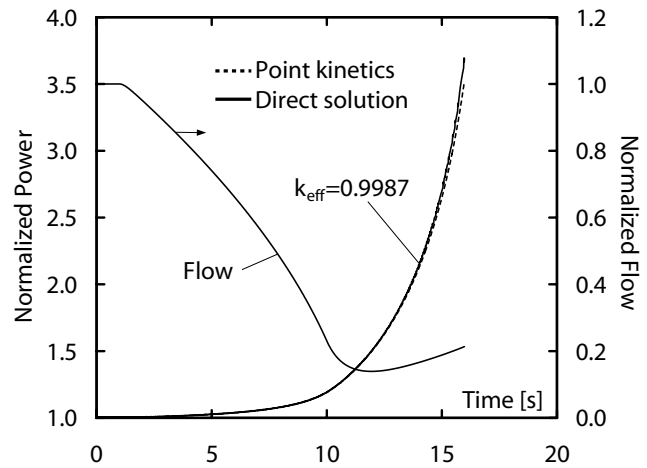


Fig 8. Unprotected Loss-of-flow transient (initial  $k_{eff}=0.9987$ ).

TABLE IX

Comparison of results for the Unprotected Loss-of-Flow transient.

| Time [s]          | Initial $k_{eff}=0.9594$ |        |                | Initial $k_{eff}=0.9798$ |        |                | Initial $k_{eff}=0.9987$ |        |                |
|-------------------|--------------------------|--------|----------------|--------------------------|--------|----------------|--------------------------|--------|----------------|
|                   | Direct                   | PK     | $\epsilon$ (%) | Direct                   | PK     | $\epsilon$ (%) | Direct                   | PK     | $\epsilon$ (%) |
| 2.0               | 1.0002                   | 1.0002 | 0.00           | 1.0004                   | 1.0005 | 0.01           | 1.0036                   | 1.0058 | 0.22           |
| 5.0               | 1.0014                   | 1.0014 | 0.01           | 1.0030                   | 1.0028 | -0.01          | 1.0244                   | 1.0267 | 0.23           |
| 10.0              | 1.0093                   | 1.0090 | -0.03          | 1.0176                   | 1.0175 | -0.02          | 1.1908                   | 1.1915 | 0.06           |
| 15.0              | 1.0259                   | 1.0249 | -0.10          | 1.0521                   | 1.0509 | -0.11          | 2.6999                   | 2.6493 | -1.87          |
| 20.0              | 1.0238                   | 1.0225 | -0.12          | 1.0492                   | 1.0475 | -0.16          | -                        | -      | -              |
| Max deviation (%) |                          |        | -0.14          |                          |        | -0.19          |                          |        | -4.56          |

## VI. CONCLUSIONS

The purpose of this paper was to investigate the ability of point kinetics to predict the transient behavior in accelerator-driven systems (ADS) under accident conditions. Numerical experiments were carried out in a minor-actinide loaded and lead-bismuth cooled ADS. The precision of the point approximation was compared in the subcritical range from  $k_{eff}=0.9594$  to 0.9987. A full three-dimensional nodal energy-space-time solution, coupled with feedback effects, was provided and used as a standard of comparison. The numerical tests suggest that point kinetics is capable of producing very good predictions of certain types of accidents in ADS's. For transients involving external source perturbations the point method provided extremely accurate results. Such changes are associated with spatially uniform reactivity feedbacks that produce little flux deformation. This may not be the case in severe source disturbances, involving strong reactivity feedbacks, but for most practical situations, it is expected that source disturbances be rather well described by point kinetics. When applied to the analysis of localized reactivity perturbations - a condition when the point treatment is expected to be a poor approximation - the results indicated better precision at lower  $k_{eff}$ -levels. This behavior appears to be due to the lower reactivity sensitiveness in the subcritical operating state, which effectively weakens the response and mitigates any spatial distortions. If a subcritical reactor is subject to a change in

the strength of the external source, or a change in reactivity within the subcritical range, the neutron population will adjust to a new stationary level. Therefore, within the normal range of operation, the power predicted by the point kinetics method and the associated error in comparison with the exact solution tends to approach an essentially bounded value. This is quite the contrary of critical reactors, in the absence of reactivity feedbacks the response will either diverge exponentially or decay to zero depending on the sign of the reactivity disturbance. In general, the flux shape in a fast neutron spectrum shows strong space-time coupling, i.e., local spatial disturbances are rapidly distributed to the remaining parts of the core, which softens spatial variations in a transient. This is usually attributed to the relatively large mean free path of fast neutrons and to the comparatively compact core size of a fast reactor. Due to the overall smaller influence of delayed neutrons in the subcritical operating state a prompt adjustment of the flux shape prevails. For a critical reactor, the delayed neutrons tend to retard the shape transition for certain transients. All together these characteristics are favorable from a point kinetics view of application to fast spectrum ADS systems. A non-favorable feature is that proposed ADS designs have large reactivity potential vested in the core<sup>22</sup>. Changes in lattice geometry or coolant density<sup>23</sup> may contribute with significant reactivity values. Such feedbacks are potential sources of spatial effects, and therefore, possible deviation from the point kinetics model. The essential requirements for an accurate point kinetics treatment are the same in subcritical reactors, i.e., symmetric reactivity insertion, small and tightly coupled core. Thus, favorable point kinetics performance in an ADS appears to be possible as long as the transient does not involve significant shape distortions. Similar conclusions have been drawn by other authors<sup>24</sup>. While the current study suggests that subcritical operation may provide for improved point kinetics performance and enhanced tolerance to system reactivity perturbations, the results showed that it is not feasible for local reactivity perturbation studies and it should still be used with care in situations involving strong feedback phenomena.

The situation in a loss-of-flow scenario was also studied. Here again, the point method was capable of very accurate calculations. The reasons are similar to those previously discussed. It was also found that the point kinetics model has a tendency to underestimate the severity of reactivity insertion accidents. The same nonconservative behavior is observed in critical systems, but it ought to be recognized for subcritical systems as well because of its overriding importance in reactor safety considerations.

## VII. ACKNOWLEDGMENTS

This research was supported by the Swedish Nuclear Fuel and Waste Management Co. (SKB). The calculations reported here were performed on the ANL-NE computer network.

## REFERENCES

1. A. RINEISKI and W. MASCHKEK, "On Application of Quasistatic and Point-Kinetics Schemes for Subcritical Systems With External Neutron Source," *Nuclear Mathematical and Computational Sciences: A Century in Review - A Century Anew*, M&C 2003, Gatlinburg, Tennessee, USA, April 6-11 (2003).
2. D. G. CACUCI, "On Perturbation Theory and Reactor Kinetics: From Wigner's Pile Period to Accelerator Driven Systems," *PHYSOR 2002*, Seoul, Korea, October 7-10 (2002).
3. A. F. HENRY, "The Application of Reactor Kinetics to the Analysis of Experiments," *Nuclear Science and Engineering*, **3**, 52-70 (1958).
4. E. P. GYFTOPOULOS, Chapter on "General Reactor Dynamics," in *The Technology of Nuclear Reactor Safety*, Vol. 1, p. 175-204, T. J. THOMPSON and J. G. BECKERLY, Eds., The MIT Press, Cambridge, Massachusetts, USA (1964).
5. J. B. YASINSKY and A. F. HENRY, "Some Numerical Experiments Concerning Space-Time Reactor Kinetics Behavior," *Nuclear Science and Engineering*, **22**, 171-181 (1965).
6. K. O. OTT and D. A. MENELEY, "Accuracy of the Quasistatic Treatment of Spatial Reactor Kinetics," *Nuclear Science and Engineering*, **36**, 402-411 (1969).
7. A. F. HENRY, *Nuclear-Reactor Analysis*, p. 300-329, The MIT Press, Cambridge, Massachusetts, USA (1975).
8. K. O. OTT and R. J. NEUHOLD, *Introductory Nuclear Reactor Dynamics*, p. 69, American Nuclear Society, LaGrange Park, Illinois, USA (1985).
9. M. BECKER, "A Generalized Formulation of Point Nuclear Reactor Kinetics Equations," *Nuclear Science and Engineering*, **31**, 458-464 (1968).
10. "Comparison Calculations for an Accelerator-driven Minor Actinide Burner," OECD/NEA Nuclear Science Committee, NEA/NSC/DOC(2001)13, OECD (2002). Benchmark prepared by P. WYDLER and H. TAKANO, NEA/NSC/DOC(99)13, Revised 27 Aug. 1999.
11. M. SALVATORES, et al., "Long-lived radioactive waste transmutation and the role of accelerator driven (hybrid) systems," *Nucl. Instrum. Methods Phys. Res., Sect. A*, **414**, 5-20 (1998).
12. J. E. CAHALAN, T. AMA, G. PALMIOTTI, T. A. TAIWO, and W. S. YANG, "Development of a Coupled Dynamics Code with Transport Theory Capability," *PHYSOR 2000*, Pittsburgh, USA, 7-11 May (2000).
13. H. HENRYSON II, B. J. TOPPEL, and C. G. STENBERG, "MC<sup>2</sup>-2: A Code to Calculate Fast Neutron Spectra and Multigroup Cross Sections," ANL-8144, Argonne National Laboratory (1976).

14. R. E. ALCOUFFE, F. W. BRINKLEY, D. R. MARR, and R. D. O'DELL, "User's Guide for TWODANT: A Code Package for Two-Dimensional, Diffusion-Accelerated, Neutral-Particle Transport," LA-10049-M, Los Alamos National Laboratory (1990).
15. R. D. LAWRENCE, "The DIF3D Nodal Neutronics Option for Two- and Three-Dimensional Diffusion Theory Calculations in Hexagonal Geometry," ANL-83-1, Argonne National Laboratory (1983).
16. T. A. TAIWO, "DIF3D-K: A Nodal Kinetics Code for Solving the Time-Dependent Diffusion Equation in Hexagonal-Z Geometry," ANL/NPR-92/17, Argonne National Laboratory (1992).
17. W. M. STACEY, Jr., *Space-Time Nuclear Reactor Kinetics*, p. 43-46, Academic Press, New York, USA (1969).
18. R. D. LAWRENCE, "Perturbation Theory Within the Framework of a Higher-Order Nodal Method," *Trans. Am. Nucl. Soc.*, **46**, 402 (1984).
19. T. A. TAIWO, H. S. KHALIL, J. E. CAHALAN, and E. E. MORRIS, "Time-Step Selection Considerations in the Analysis of Reactor Transients with DIF3D-K," *Trans. Am. Nucl. Soc.*, **68**, 429-430 (1993).
20. R. A. RYDIN and M. L. WOOSLEY, JR., "Evidence of Source Dominance in the Dynamic Behavior of Accelerator-Driven Systems," *Nuclear Science and Engineering*, **126**, 341-344 (1997).
21. Y. KIM, W. S. YANG, T. A. TAIWO, and R. N. HILL, "Reactivity Estimation for Source-Driven Systems Using First-Order Perturbation Theory," PHYSOR 2002, Seoul, Korea, October 7-10 (2002).
22. W. MASCHEK, A. RINEISKI, K. MORITA, M. FLAD, "Inherent and Passive Safety Measures in Accelerator Driven Systems: A Safety Strategy for ADS," GLOBAL 2001, Paris, France, Sep 9-13 (2001).
23. M. ERIKSSON, J. WALLENIUS, J. E. CAHALAN, K. TUCEK, and W. GUDOWSKI, "Safety analysis of Na and Pb-Bi coolants in response to beam instabilities," Proc. 3<sup>rd</sup> International Workshop on Utilisation and Reliability of High Power Proton Accelerators, Santa Fe, USA, May (2002).
24. A. AMIONE, et al., "Dynamics of Accelerator-Driven Systems by the Quasi-static Method," 6<sup>th</sup> International Meeting on Nuclear Applications of Accelerator Technology (AccApp'03), June 1-5, San Diego (2003).

# Paper IV



# Safety Analysis of Na and Pb-Bi Coolants in Response to Beam Instabilities

*M. Eriksson, J. Wallenius, J. E. Cahalan\*, K. Tucek, and W. Gudowski*

Royal Institute of Technology, Dep. Nuclear & Reactor Physics  
10691 Stockholm, Sweden.

\*Argonne National Laboratory, Reactor Analysis & Engineering Division  
9700 South Cass Ave., IL 60439, USA.

Presented at the Third International Workshop on Utilisation and Reliability of High Power  
Proton Accelerators, Santa Fe, New Mexico, USA, May 12-16, 2002.

## Abstract

A comparative safety study has been performed on sodium vs. lead/bismuth as coolant for accelerator-driven systems. Transient studies are performed for a beam overpower event. We examine a fuel type of recent interest in the research on minor actinide burners, i.e. uranium-free oxide fuel. A strong positive void coefficient is calculated for both sodium and lead/bismuth. This is attributed to the high fraction of americium in the fuel. It is shown that the lead/bismuth-cooled reactor features twice the grace time with respect to fuel or cladding damage compared to the sodium-cooled reactor of comparable core size and power rating. This accounts to the difference in void reactivity contribution and to the low boiling point of sodium. For improved safety features the general objective is to reduce the coolant void reactivity effect. An important safety issue is the high void worth that could possibly drive the system to prompt criticality.

## Introduction

Both sodium and lead/bismuth are considered as coolant candidates in accelerator-driven systems. At RIT a global safety study of accelerator driven systems is performed to investigate neutronic and transient characteristics of lead/bismuth vs. sodium as primary coolant and the performance of oxide, nitride, and metallic fuels for various accident initiators and core sizes. In the present analysis we benchmark the two coolants for oxide fuel in the response to a sudden beam excursion. This type of accident initiator is unique to accelerator-driven systems and is open to considerable question. One of the most questionable items is the nature of the initiating circumstances; for example; what is the maximum beam load change that could possibly occur and at what speed can this transition materialize? The outcome will depend strongly on the details of these conditions as well as on the time over which the beam remains on. In the following paper, the beam is presumed to double in strength in an instant and remain on for an unspecified time. The extreme nature of this assumption is subject to debate. However, the analysis of accidents that appear incredible is an important part of the design of a safe reactor. Much can be learned from simulated severe accidents. The purpose of the present paper is to measure the strengths and weaknesses of two particular coolants, independent of probability, or even possibility, of occurrence.

## Model and assumptions

The benchmark is performed using a common design, set of assumptions, and computational methods. The continuous energy MCNP simulation code is applied to the neutronics analysis. A three-dimensional pin-by-pin model is defined. Oxide fuel is adopted being diluted with zirconium dioxide. In order to flatten the power distribution, the core is subdivided into two regions with varying content of  $\text{ZrO}_2$ . We have adopted a Pu to TRU ratio of 40% at BOL since this composition minimizes reactivity losses over a large number burnup cycles [1]. The Pu/TRU ratio is kept constant. The plutonium isotopic vector corresponds to the discharge from spent MOX fuel (5%  $^{238}\text{Pu}$ , 38%  $^{239}\text{Pu}$ , 30%  $^{240}\text{Pu}$ , 13%  $^{241}\text{Pu}$ , and 14%  $^{242}\text{Pu}$ ). The americium composition consists of two thirds  $^{241}\text{Am}$  and one third of  $^{243}\text{Am}$ . The analysis aimed at increasing the core diameter through an increase in pin pitch while holding the pin diameter and core height constant. Pitch-to-diameter ratios are varied in the range from  $P/D=1.25$  to  $2.25$  (constant  $D=8$  mm). To compensate the reactivity loss when  $P/D$  is increased the fraction of  $\text{ZrO}_2$  is adjusted (from core average of 30% at  $P/D=2.25$  to 70% at  $P/D=1.25$ ) in order to preserve  $k_{\text{eff}}=0.97$ . A summary of design parameters is presented in Table 1.

Transient analysis is performed with the aid of the SAS4A safety code [2]. A primary heat transport system is defined and represented by the core, primary pumps, the shell side of the heat exchangers, connecting piping, and compressible pool volumes with cover-gas surfaces. Coolant passage through the core is modelled by a single thermal and hydraulics channel. The feedwater system is assumed to remove heat at 100% for all time. Thus, when the power increases above nominal, there will be a mismatch in heat production and heat removal and the net effect is core inlet temperature rising with time. The point kinetics approximation is used for calculating transient power. A value of  $\beta_{\text{eff}}$  equal to 0.20% is assumed, a representative value for a minor actinide burner. The coolant flow rate in a lead/bismuth-cooled reactor is limited by erosion/corrosion damage of structural material. At present the flow rate of lead/bismuth is taken to be 2.5 m/s. No such limitation exists for the sodium-cooled reactor where the main concern in the past has been to limit pumping power requirement. For that reason a sodium flow rate of 5 m/s is adopted. Transient response is calculated assuming intact core geometry; i.e., fuel pins and coolant channels are well defined, precluding the possibility for insertion of large reactivity values by core compaction. Temporal and spatial void distributions are calculated. Reactivity feedbacks are modelled by coolant density changes and an assumed Doppler constant of  $T_{\text{dk}}/dT=-38$  pcm. As will be seen, the Doppler coefficient has negligible influence on the operational behavior. The void reactivity coefficient and the prompt neutron lifetime are determined from static neutronic analysis, as discussed in the next section. In a preliminary study, a uniform void coefficient is used. Structural reactivity feedback phenomena (e.g. radial and axial core expansion) have been excluded considering the low responsiveness of a source-driven system to reactivity changes [3]. Under the present conditions, structural expansion introduces reactivity changes that are small with respect to the void effect. It is recognized, however, that such reactivity feedback effects may affect the calculated performance values.

**Table 1.** Design parameters

| Characteristic                 | Value   |
|--------------------------------|---|
| Core power                     | 800 MWth  |
| Average linear power           | 16 kW/m   |
| Core coolant inlet temperature | 573 K (Pb/Bi and Na)  |
| Coolant flow rate              | 2.5 m/s (Pb/Bi) and 5.0 m/s (Na)  |
| Fuel composition               | (Pu <sub>0.6</sub> Am <sub>0.4</sub> )O <sub>2</sub> + ZrO <sub>2</sub> |
| Fuel porosity                  | 10 %  |
| Core height                    | 1.0 m   |
| Fission gas plenum height      | 1.50 m  |
| Outer fuel radius              | 3.45 mm   |
| Inner cladding radius          | 3.50 mm   |
| Outer cladding radius          | 4.00 mm   |
| P/D                            | Varied from 1.25 to 2.25  |
| Doppler constant (Tdk/dT)      | -38 pcm   |
| k_eff (eigenvalue)             | 0.97  |
| β_eff                          | 0.20 %  |

### Neutronics analysis

Following coolant voiding there is hardening of the spectrum caused by a decrease in neutron scattering. Removal of coolant also results in higher neutron leakage. Hardening of the neutron spectrum and increased neutron leakage are the two dominating physical phenomena contributing to the void reactivity effect. In general, hardening of the spectrum leads to a positive reactivity component due to an increase in the number of neutrons released per neutron absorbed in the fuel while increased leakage gives rise to a reactivity loss since more neutrons may escape the core. The void reactivity effect has been calculated for the present system and is illustrated in Figure 1. The void coefficient is expressed as a function of pitch-to-diameter ratio. The void coefficient is obtained by calculating the k-eigenvalue at a given density and then performing a second calculation but with a density corresponding to a temperature increase of 200 degrees Celsius. The density is changed uniformly over the core and the upper plenum. Figure 1 indicates that the negative reactivity effect associated with increased neutron leakage is not sufficient to offset the positive reactivity contribution of a harder spectrum. The spectrum effect becomes more positive as P/D increases. As a result, the void reactivity coefficient becomes increasingly positive at higher P/D. It is observed that both coolants possess a significant positive void reactivity coefficient. However, the void coefficient tends to be more positive for sodium because of higher moderating power and an influential scattering resonance in <sup>23</sup>Na at 3 keV. In the energy region above 100 keV, the fission-to-capture ratio for <sup>241</sup>Am rises more rapidly than for <sup>239</sup>Pu. For that reason, the void coefficient becomes more positive if the fraction of americium is increased and the fraction of plutonium is correspondingly decreased.

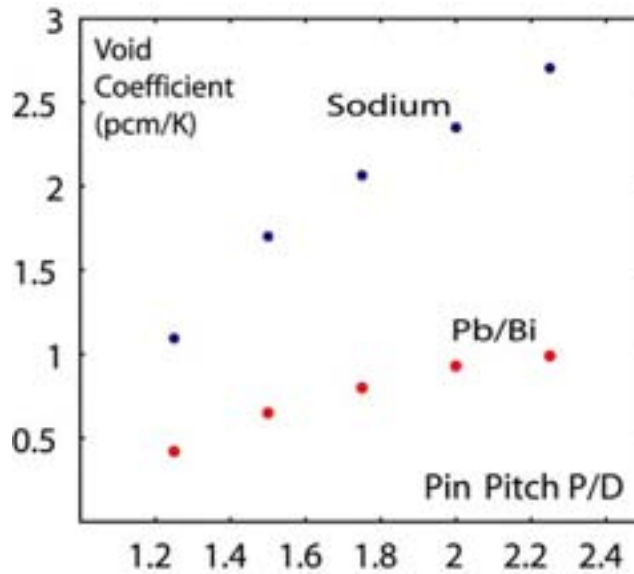


**Figure 1.** Void reactivity coefficient [pcm/K]

The prompt neutron lifetime was calculated using MCNP. As expected, the prompt neutron lifetime increases with increasing P/D, corresponding to a softer spectrum and longer distance travelled by neutrons up to their point of absorption. Note that the average neutron lifetime in the lead/bismuth-cooled core exceeds  $1\mu\text{s}$  for high pin pitches ( $P/D > 2.0$ ).

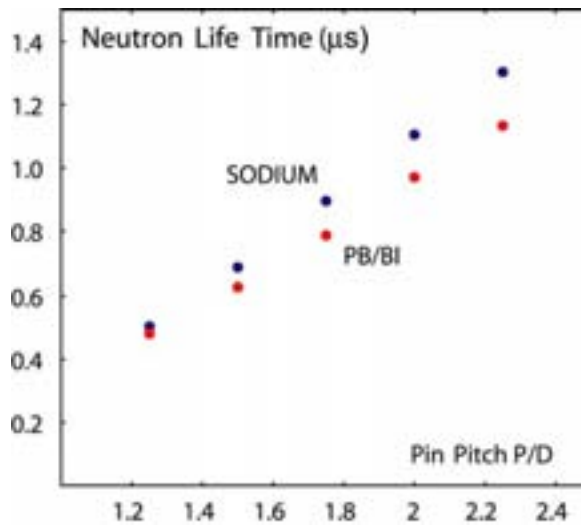


**Figure 2.** Prompt neutron lifetimes

### Failure criteria

In order to predict core damage a set of failure criteria has been postulated, those are listed in Table 2. Several difficulties exist in attempting to provide failure criteria for the existing system. The principal difficulty is the uncertainty in the operating performance of the fuel and structural materials. Chemical and mechanical interactions between the fuel, cladding, and coolant, as well as irradiation performance, etc. are not well known. Validation of failure criteria will require the availability of experimental test data. Nonetheless, preliminary safety margins can be established as a first estimate to envelop worst-case conditions. The fuel is assumed to be stable up to the melting point, which is a reasonable assumption for sub-

stoichiometric oxide fuel. The fuel melting point as well as thermophysical properties vary with the stoichiometry. Present fuel properties correspond to an oxygen-to-metal ratio of 1.93. The failure temperature is based on the melting point of PuO<sub>2</sub> [4] and AmO<sub>2</sub> [5] together with the melting point of diluent ZrO<sub>2</sub>, applying Vegard's law. The maximum cladding temperature is constrained by mechanical considerations. The primary cladding loading is the internal gas pressure; fuel-cladding mechanical interaction is neglected. We have assumed a maximum internal pin pressure of 10 MPa in steady-state as a result of pressure build-up by the continuous release of fission gases. Under transient conditions the pressure may increase even further causing an increase in the loading of the cladding. Simultaneously, the cladding loses its strength at elevated temperatures. The cladding failure temperature is determined from correlations based on the calculated hoop stress and the failure temperature measured in cladding burst tests (20% cold-worked type 316 austenitic stainless steel) [6]. The transient burst temperature is representative for fast transients where the temperature is rapidly increasing until the cladding fails, providing less time for creep-type deformation.

**Table 2.** List of failure temperatures

| Failure mechanism          | Failure temperature | Comment   |
|----------------------------|---------------------|---|
| Melting of oxide fuel      | 2886 K              | 0.11(Pu <sub>0.6</sub> Am <sub>0.4</sub> )O <sub>2</sub> + 0.89ZrO <sub>2</sub> |
| Cladding burst temperature | 1333 K              | 20% CW SS316, 5.56 °C/sec, hoop stress 100 MPa.                                 |

### Transient analysis

Transient response has been examined for an unprotected transient overpower (UTOP) event. It is assumed that the intensity of the external neutron source is *promptly increased by twice the initial value*. Reactor shutdown is disregarded. It is possible to imagine that a control system failure or simply inadvertent operation of the accelerator could lead to an accidental increase of beam power. However, it is important to acknowledge the highly hypothetical nature of the accident under discussion.

Transient power is displayed in Figure 3. For the case displayed the pitch-to-diameter ratio is 1.50. The magnitude of the initial burst is the same, independent of the coolant. The steady-state power will multiply by a factor of S/S<sub>0</sub> if the source strength is stepped from S<sub>0</sub> to S. The speed of the transition is determined by the prompt period. Delayed neutrons do not appreciably slow the response. Following the prompt jump, the power changes as a result of reactivity feedbacks. Coolant void reactivity feedbacks contribute to the course of the accident by adding reactivity. The small negative reactivity feedback associated with the Doppler effect does not influence the course of the accident. Differences in transient behaviour between lead/bismuth and sodium result primarily from the difference in boiling point and void reactivity effect. Coolant density changes provide modest changes in reactivity compared to the full void reactivity effect, which may introduce significant positive reactivity values. This causes the reactivity insertion rate to be considerable larger in the sodium-cooled core. Void generation, and thus positive reactivity insertion, is abrupt in the vicinity when boiling starts. Sodium boiling begins at the core outlet and develops axially downward. In the sodium-cooled core, the void effect adds enough reactivity to bring the reactor to a prompt critical state, with possible severe safety consequences. Prompt critical conditions are established about 400 seconds after accident initiation. Large positive reactivity insertions are potentially possible due to lead/bismuth voiding as well. However, it is seen that the high boiling temperature for lead/bismuth (1943 K) compared to sodium (1154 K) makes voiding less probable even though

there are other ways of voiding the coolant besides boiling, i.e. large scale steam generator failure or possibly sudden gas release from ruptured pins. Voiding could possibly occur in severe loss of coolant accidents, such as tank rupture, however this must be regarded as extremely unlikely. It should be recognized that structural damage most likely occurs before boiling is encountered in a lead/bismuth-cooled reactor.

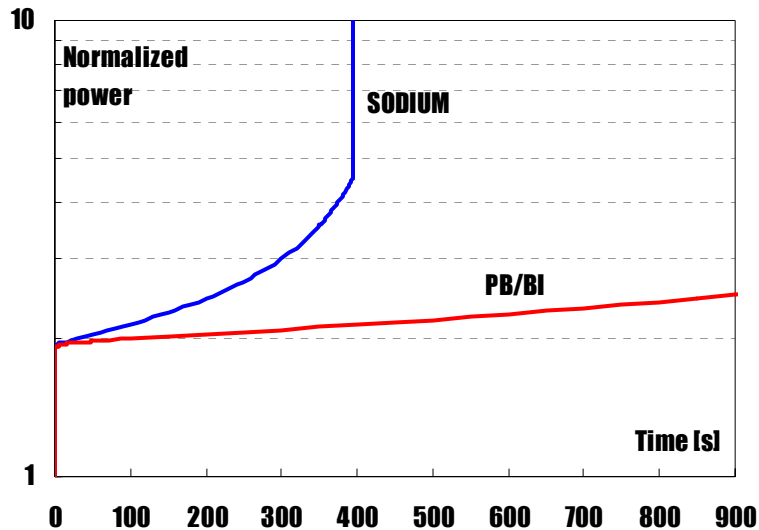
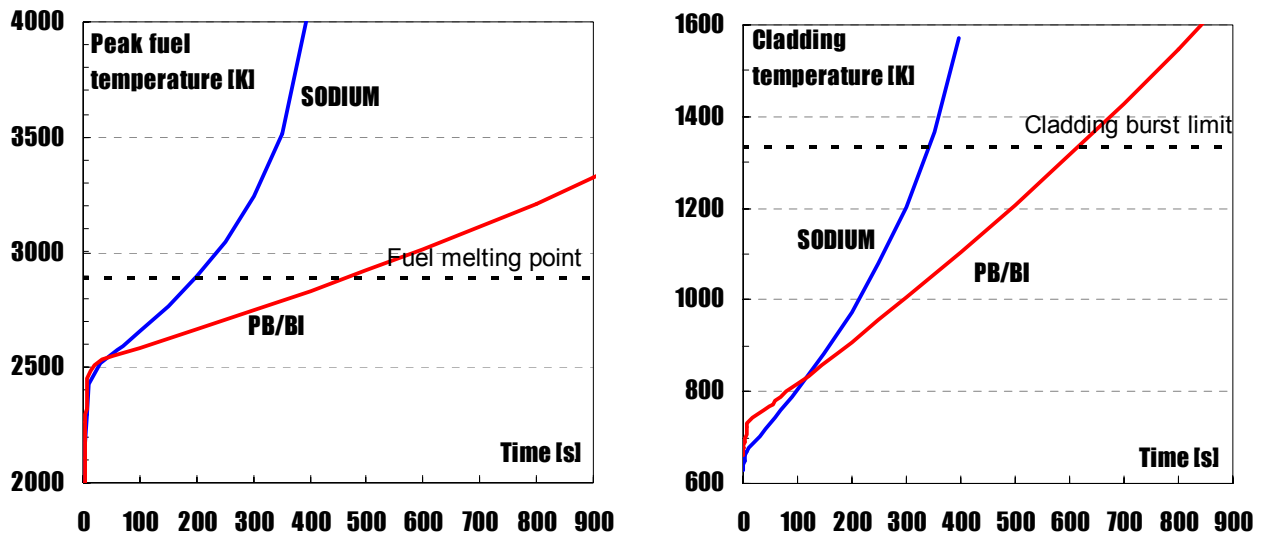


Figure 3. Normalized reactor power.  $P/D=1.50$ .

In Figure 4 peak fuel and cladding temperatures are shown for the case  $P/D=1.50$ . Since no time is required for heat transport, the fuel suffers a rapid temperature rise. The amount of beam input determines whether there is immediate fuel damage or not. Subsequent heat-up occurs as a result of positive feedback from voiding and insufficient heat removal capability. The steam generators are assumed to remove heat at a rate of nominal power, resulting in increasing core inlet temperature as the transient proceeds. Sharp fuel temperature increase is calculated in the sodium case, as a result of a significant void reactivity insertion. The failure criterion for the fuel is exceeded in 200 seconds and the cladding is expected to reach its burst temperature in 350 seconds. The fuel fails prior to the initiation of sodium boiling (~350 sec) and this might disable the reactor before boiling and prompt criticality occurs. However, it is difficult to determine the consequences of fuel melting. In the sodium case, cladding failure is predicted to occur by burnout. Cladding failure occurs simultaneously with sodium boiling. It is recognized that a substantial change in the nature of the accident may occur at the onset of fuel or cladding damage. Therefore, extrapolation beyond the actual failure points is subject to considerable uncertainty.

The assumption of constant heat rejection rate is conservative. In an overpower accident it is likely there will be some increase in the heat removal above 100%. Taking this into account would yield less pessimistic results. In reality, the feedwater system would try to maintain the correct coolant temperature returning to the core, and if it is not able to do so, the feedwater system would trip and issue reactor shutdown. It should be recognized that for both coolants considered the grace period is in the order of several minutes, which, in principle, provides considerable time for a well-designed safety system to act.



**Figure 4.** Peak fuel temperature (left) and peak cladding temperature (right). P/D=1.50.

The calculation is repeated for a range of pitch-to-diameter ratios. In Figure 5, the grace period is calculated for different P/D's. The grace period is measured in seconds. The grace time decreases somewhat at large pitches, a consequence of higher void coefficient for larger P/D. From the very basis of the assumptions, the choice of coolant does not change the inevitability of reaching a failure point; the timing of failure is different, however. The Pb/Bi cooled core features twice the grace time compared to the sodium-cooled core with the same P/D and power rating. The calculation revealed a small margin to prompt criticality at large pitches (sodium case). It was found that rapid sodium vaporization and expulsion occurred at the onset of boiling. Prompt criticality could possibly occur in less than 1 sec ( $P/D > 1.50$ ) once sodium boiling is initiated.

Oxide fuel temperatures are sensitive to linear power ratings. The allowable linear power is limited by the melting point. The low thermal conductivity of oxide fuel is compensated somewhat by a high melting point. Figure 6 illustrates the sensitivity of grace time on linear power. The calculation was performed for P/D=1.50. It should be recognized that different power ratings correspond to different core total powers in Figure 6. The number of fuel pins is fixed while the steady-state linear power is varied. In the reference case the linear power is 16 kW/m corresponding to a total reactor power of 800 MWth. The mode of failure differs; fuel failure dominates at high linear powers while cladding failure supersedes as the mode of failure at low linear power (<14 kW/m). The grace period provides an indication of the time available for a safety system to act. It was found that the safety performance of oxide fuel deteriorates rapidly with increasing pin power rating. At high linear power immediate fuel damage may occur, providing little time for a protection system to respond. It is possible to extend the grace period by derating the oxide fuel, but it has some obvious penalties.

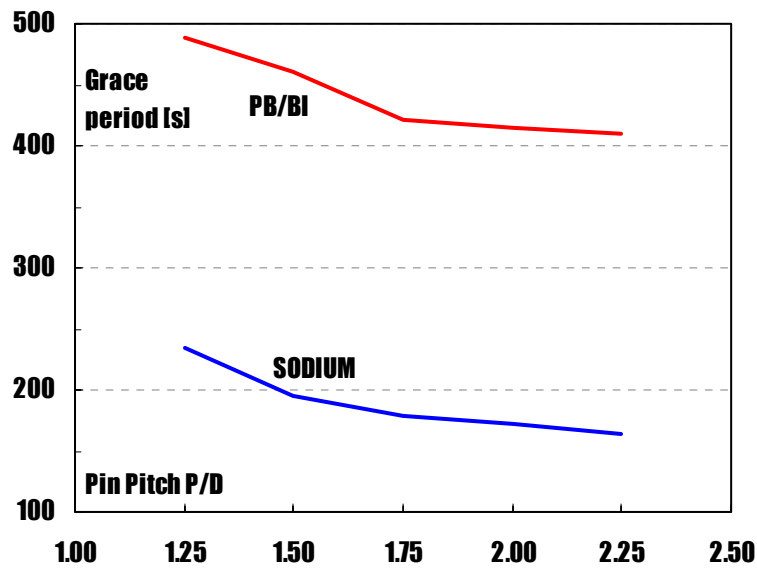


Figure 5. Grace period as a function of pin pitch. Linear power=16 kW/m.

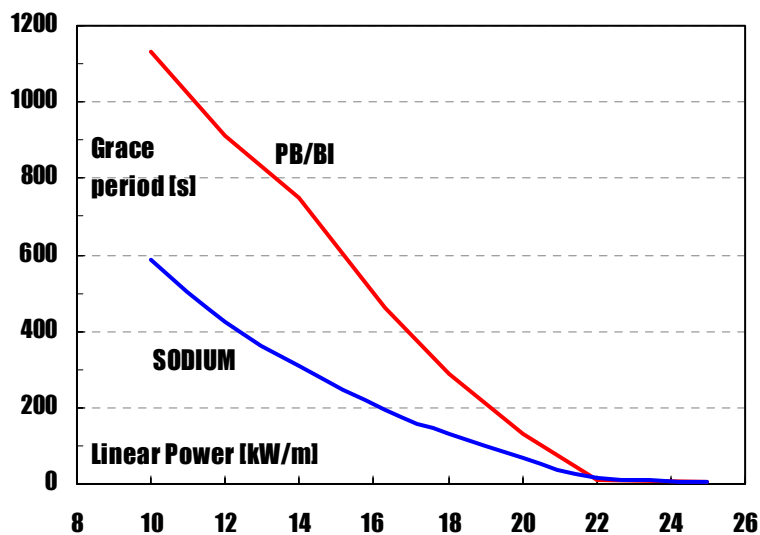
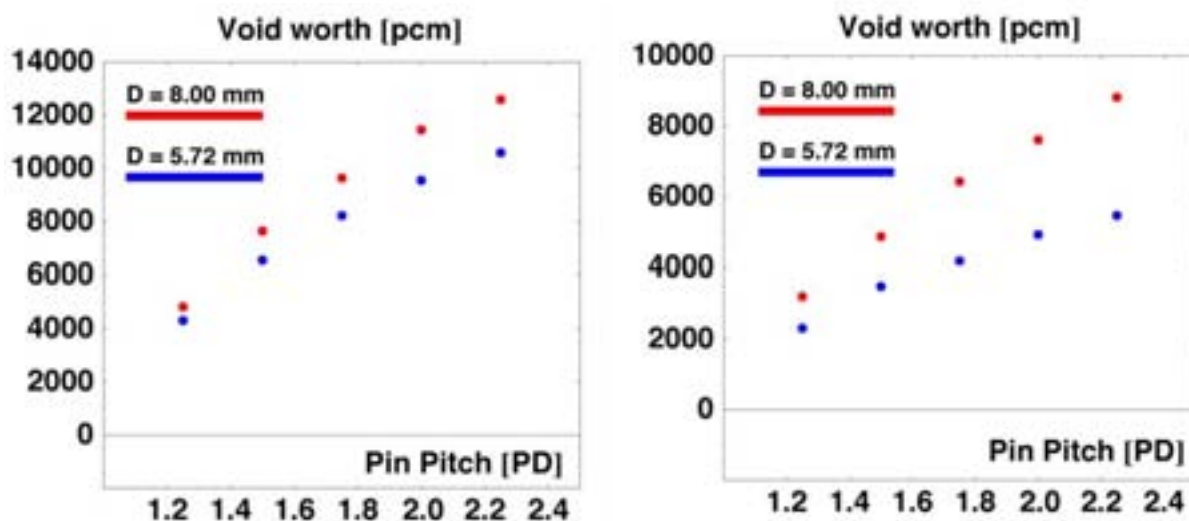


Figure 6. Grace period as a function of linear power rating. P/D=1.50.

The characteristics that have the greatest effect in the present analysis are the differences in boiling point and void coefficient. While the boiling temperature is fixed, the void coefficient can change significantly with design parameters. The void reactivity effect is the result of several physical phenomena and various methods have been proposed for reducing the void worth by design [7]. One possible way of void worth reduction is to reduce the pin size. The net result is shown in Figure 7, where the void worth of lead/bismuth and sodium, respectively, is calculated as a function of P/D. The coolant void worth is determined by removing all coolant from the core and the upper plenum. The results suggest that a significant reduction in the void worth is achievable using smaller pin diameter. Reducing the void worth is an essential design objective. Large values of the void worth may present a difficulty in the licensing of minor actinide burners because of the risk for severe damage to the plant and public safety.





**Figure 7.** Sodium (left) and lead/bismuth (right) void worth as a function of P/D. Pin diameter is a parameter.

## Summary

Comparison was made of the safety performance of sodium vs. lead/bismuth as primary coolant in a minor actinide burner reactor. The systems were benchmarked for oxide fuel. Neutronic investigations were made on the void reactivity effect for a range of pitch-to-diameter ratios. Transient behavior for a beam overpower event and the time-to-failure were compared.

A strong positive void coefficient was found for both sodium and lead/bismuth. The considerable void effect is attributed to a high fraction of americium (60%) in the fuel. It was found that void reactivity insertion rates increases with P/D. In response to the particular accident under discussion, the Pb/Bi-cooled core featured twice the grace time compared to the sodium-cooled core. The essential difference is attributed to the difference in boiling point and void reactivity contribution. An important safety issue is the high void worth that could possibly drive the system to prompt criticality. The problem is the result of the present fuel composition and it exists in both the sodium-cooled reactor and the lead/bismuth-cooled reactor. To some degree, this may be counter-balanced with proper core design, e.g. smaller pitch and pin diameter. For improved safety features, the general objective is to reduce the coolant void reactivity effect. The sodium-cooled core was found to have a smaller safety margin to prompt criticality. The high boiling temperature of lead/bismuth makes voiding less probable. The low effective thermal conductivity of oxide fuel results in high fuel temperatures and imposes constraints on the allowable linear power. Derating the oxide fuel could enhance the safety performance, but it has some obvious penalties.

## References

- [1] T. Takizuka et al., Studies on accelerator-driven transmutation systems, Proc. 5<sup>th</sup> information exchange meeting on actinide and fission product partitioning and transmutation, EUR 18898 EN, OECD/NEA 1998.
- [2] J. E. Cahalan, A. M. Tentner, and E. E. Morris, "Advanced LMR Safety Analysis Capabilities in the SASSYS-1 and SAS4A Computer Codes," Proc. of the International Topical Meeting on Advanced Reactors Safety, Pittsburgh, April 17-21, 1994.
- [3] M. Eriksson and J. E. Cahalan, "Inherent shutdown capabilities in accelerator-driven systems," *Annals of Nuclear Energy*, vol 29/14 pp 1689-1706, (2002).

- [4] E. H. P. Cordfunke, R. J. M. Konings, G. Prins, P. E. Potter, and M. H. Rand, "Thermochemical Data for Reactor Materials and Fission Products," Elsevier Science, Amsterdam, 1990.
- [5] J. J. Katz, G. T. Seaborg, L. R. Morss, The Chemistry of actinide elements, 2nd Ed., Vol. 1 and 2, Chapman and Hall, London, 1986.
- [6] Hunter, C. W., Fish, R. L., Holmes, J. J., 1975. Mechanical properties of unirradiated fast reactor cladding during simulated overpower transients. *Nucl. Technol.* 27(3), pp. 376-388 (Nov 1975).
- [7] H. S. Khalil and R. N. Hill, "Evaluation of Liquid-Metal Reactor Design Options for Reduction of Sodium Void Worth," *Nucl. Sci. Eng.*, 109, 221-266 (1991).

# Paper V



PERGAMON

Annals of Nuclear Energy 29 (2002) 1689–1706

---

---

annals of  
NUCLEAR ENERGY

---

---

www.elsevier.com/locate/anucene

# Inherent shutdown capabilities in accelerator-driven systems

M. Eriksson<sup>a,\*</sup>, J.E. Cahalan<sup>b</sup>

<sup>a</sup>Royal Institute of Technology, Stockholm Center for Physics, Astronomy and Biotechnology,  
Department of Nuclear and Reactor Physics, S-106 91 Stockholm, Sweden

<sup>b</sup>Argonne National Laboratory, Reactor Analysis and Engineering Division, 9700 South Cass Avenue,  
IL 60439, USA

Received 16 October 2001; accepted 3 December 2001

---

## Abstract

The applicability for inherent shutdown mechanisms in accelerator-driven systems (ADS) has been investigated. We study the role of reactivity feedbacks. The benefits, in terms of dynamics performance, for enhancing the Doppler effect are examined. Given the performance characteristics of source-driven systems, it is necessary to manage the neutron source in order to achieve inherent shutdown. The shutdown system must be capable of halting the external source before excessive temperatures are obtained. We evaluate methods, based on the analysis of unprotected accidents, to accomplish such means. Pre-concepted designs for self-actuated shutdown of the external source suggested. We investigate time responses and evaluate methods to improve the performance of the safety system. It is shown that maximum beam output must be limited by fundamental means in order to protect against accident initiators that appear to be achievable in source driven systems. Utilizing an appropriate burnup control strategy plays a key role in that effort. © 2002 Elsevier Science Ltd. All rights reserved.

---

## 1. Introduction

In the design process of a nuclear reactor, important consideration is given to the utilization of passive safety systems and inherent safety features. There is a consensus among reactor designers, supporting the value of passive safety designs. Passive safety systems rely on natural physical phenomena, such as thermal expansion, fundamental nuclear properties, gravity, and heat-transfer by natural convection, to perform essential safety functions. The laws of physics dictate such properties and their effectiveness is not influenced by human action. In the ideal case, passive safety

---

\* Corresponding author. Tel.: +46-8-5537-8197; fax: +46-8-5537-8465.

E-mail address: marcus@neutron.kth.se (M. Eriksson).

design does not require the action of any mechanical or electrical device, making safety functions less dependent on active components. The incentives for employing such designs are improved reliability and simplified operation, both resulting in better safety performance. Inherent features are valuable means for minimizing public concern and gaining public perception on new reactor concepts.

Most work on passive safety in the past has been related to the study of the innovative use of natural convection, decay heat removal, and inherent negative reactivity feedbacks. Such schemes have been successfully implemented in many reactor designs, including water-cooled reactors, gas-cooled reactors, and liquid metal-cooled reactors.

In this paper, we explore the use of passive safety mechanisms to accelerator-driven systems (ADS). While an intrinsic heat-transport path and sufficient natural convection are necessary to achieve passive safety in any reactor system, those requirements are of a general character and are treated elsewhere e.g. (Karlsson and Wider, 2000). Our attention is focused on inherent shutdown capabilities. We evaluate the applicability for such schemes and we suggest some concepts for that purpose.

## **2. Reference design and modelling**

In the assessment, we employ a reference design of an ADS to obtain operating performance data. Accident analysis is performed with the aid of the SAS4A safety code (Cahalan et al., 1994).

The reference design is a model of an ADS that has evolved at the Royal Institute of Technology, Sweden (Wallenius et al., 2001a,b). The core has a nominal power of 800 MWth. It is cooled by liquid lead-bismuth eutectic (LBE) and the fuel is based on a nitride matrix. Fuel pins are configured in an open pin lattice with core average volume fractions of 8/12/80% (fuel/structure/coolant). The fuel consists of (core average): 58% plutonium, 12% minor actinides, 14% boron carbide, 10% uranium-238, and 6% zirconium nitride. Uranium-238 is used in the inner zones to compensate for burnup and poisoning effects (Tucek et al., 2001). Boron carbide is utilized to increase fission-to-absorption probabilities in even neutron number americium isotopes. Radial zoning is applied with an optimized distribution of minor actinides, plutonium, burnable absorbers, and diluents to mitigate power peaking factors and reduce long-term reactivity swing. Taking advantage of a multi-batch fuel loading strategy (Yang and Khalil, 2000), where some fuel sub-assemblies are added to the perimeter of the core on an intermediate time schedule (150 days), the required beam insertion capacity can be reduced. In the present design, it is necessary to ramp the beam by a factor of 1.8 to maintain constant power through an irradiation period of 510 days. Basic design parameters are listed in Table 1.

The primary circuit is illustrated in Fig. 1. The core, heat exchangers, and primary pumps are immersed in a single pool containing LBE. Coolant temperatures, in steady state, range from 573 K at inlet to 702 K at the outlet. In the present design, the inlet flow velocity is set to 2.5 m/s. Deterioration of the protective oxide film

Table 1  
Reference ADS design parameters

|  |                               |
|--|-------------------------------|
| Core power, MWth                               | 800                           |
| Coolant  | LBE                           |
| Core inlet temperature, K                      | 573                           |
| Core outlet temperature, K                     | 702                           |
| Flow velocity, m/s                             | 2.50                          |
| Volume hot pool, m <sup>3</sup>                | 435                           |
| Volume cold pool, m <sup>3</sup>               | 197                           |
| Volume inlet plenum, m <sup>3</sup>            | 20                            |
| Fuel composition (core average)                | Nitrides: 12%MA/73%Pu/15%U238 |
| Inner radius, mm                               | 1.00                          |
| Outer radius, mm                               | 2.40                          |
| Cladding                                       | HT-9                          |
| Inner radius, mm                               | 2.49                          |
| Outer radius, mm                               | 2.94                          |
| P/D  | 1.83 and 2.33                 |
| $k_{\text{eff}}$ eigenvalue, BOL, steady-state | 0.954                         |
| $\beta_{\text{eff}}$ , %                       | 0.160                         |
| Doppler constant, $T_f dk/dT_f$                | $-3.87 \cdot 10^{-4}$         |
| Coolant density reactivity feedback, $dk/dT_c$ | $-2.28 \cdot 10^{-6}$         |

layer on structural material imposes an upper limit on the flow velocity. The actual limit depends on the temperature and is not well known, however, it is estimated to be in the range of 2–3 m/s (Novikova et al., 1999). The reactor vessel is filled with LBE to a prescribed level, with the remainder of the vessel being occupied by an inert cover gas. The steam generators are elevated well above the core to promote natural convection.

A primary system model is set-up in SAS4A, including a detailed multi-channel model of the core, heat exchangers, pumps, compressible pool volumes, etc. Point kinetics is used for calculating transient power. The neutronic response between core regions is strongly coupled and space-time effects may be neglected for our purposes.

### 3. Applicability of reactivity feedbacks in ADS

Intelligent use of inherent reactivity feedbacks (e.g. Doppler effect, coolant density effect, structural expansion, etc.) has provided excellent safety characteristics to advanced, critical, reactor. In the design process of a new reactor, it is simply good engineering practice to utilize the inherent nuclear properties of the reactor to ensure optimal safety performance. In particular, operating experience and experiments on liquid metal reactors have demonstrated that better use of the inherent nuclear properties may provide a high level of safety even in severe accidents where the shutdown system fails completely (Lucoff et al., 1992). Nowadays, because of design efforts and increased understanding, the safety characteristics of critical, liquid metal

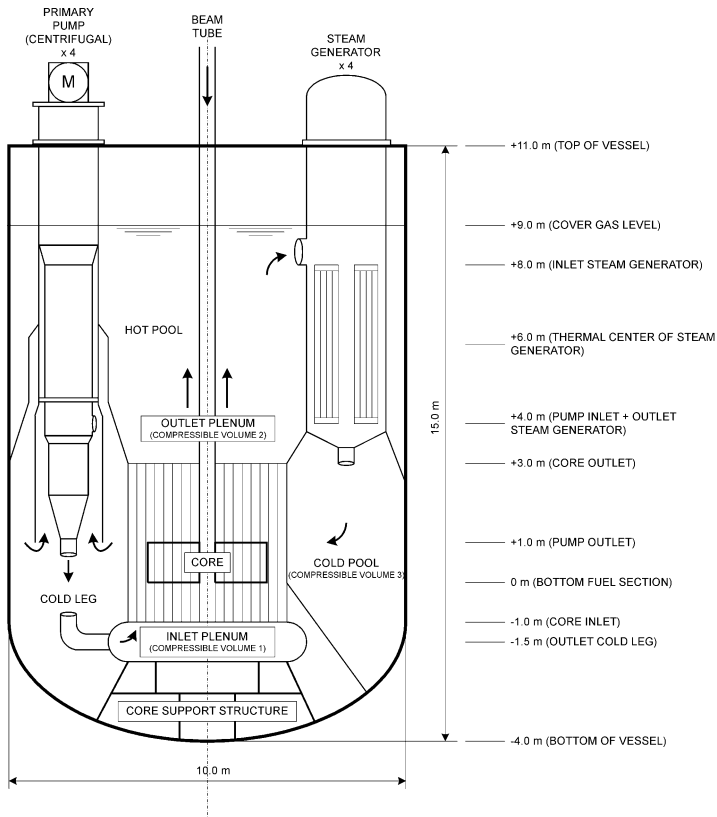


Fig. 1. Primary circuit of reference ADS design.

reactors, are considered as a principal advantage. In that context, it may seem natural to use a similar strategy for ADS's. However, an ADS does not respond to reactivity feedbacks like a critical reactor. While the critical reactor is sensitive to reactivity feedbacks, the ADS is not. The ADS is largely offset from criticality. The net effect is a substantially reduced sensitivity to reactivity changes. This feature diminishes the practical use of reactivity feedbacks as a means for natural safety mechanisms in accelerator-driven systems.

To study these features we exposed the reference design to an unprotected transient overpower (UTOP) event. The initiator for the accident is a sudden increase in source intensity. The intensity of the external neutron source is promptly increased by a factor of 1.8, corresponding to the insertion of maximum beam power at begin-of-life. It represents a strong transient, integral power increases by a factor of 1.8 within a few hundred prompt periods. In Fig. 2, the impact of subcriticality on the combined reactivity effect from Doppler feedback ( $Tdk/dT = -3.87 \times 10^{-4}$ ) and coolant density feedback ( $dk/dT = -2.28 \times 10^{-6}$ ) is illustrated. The unconstrained response, when no feedbacks are accounted for, is also shown to facilitate comparison.

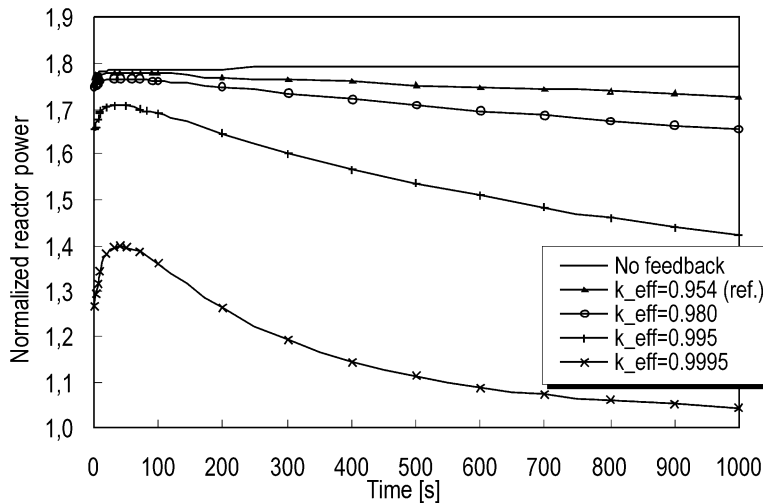


Fig. 2. Impact of reactivity feedbacks in a source-driven system. Accident initiator by sudden increase in source intensity ( $S = 1.8 \cdot S_0$ ). Subcriticality is a parameter.

The response is calculated for a varying degree of subcriticality,  $k_{\text{eff}} = 0.954$  (reference design),  $k_{\text{eff}} = 0.98$ ,  $k_{\text{eff}} = 0.995$ , and  $k_{\text{eff}} = 0.9995$ . Structural reactivity feedback phenomena (e.g. radial and axial core expansion) are not incorporated into the model. Nevertheless Fig. 2 is instructive in the sense that it demonstrates the general characteristics of a source-driven system subject to reactivity feedbacks.

The reference ADS ( $k_{\text{eff}} = 0.954$ ) experiences minor influence from Doppler and coolant density feedback whereas the close-to-critical system ( $k_{\text{eff}} = 0.9995$ ) exhibits strong feedback effects. Approaching criticality, at the expense of reducing the margin to prompt criticality, results in a stronger reactivity feedback coupling. Thus the significance of reactivity feedback depends on the specific design and in particular the choice of the subcritical level. Taking advantage of reactivity feedbacks calls for a careful balance between the desired feedback performance and the subcritical margin. It is clear, however, that reactivity feedbacks will not be as effective a means in source-driven systems as they are in critical systems. Much stronger reactivity effects, from what is experienced in critical reactors, are necessary to impact on the source driven system. Therefore, it is not practical to implement reactivity feedbacks, by physics or engineering design, as the sole means to bring an ADS to safe shutdown condition. Inherent shutdown must be reinforced by other means.

### 3.1. Doppler effect

There has been considerable interest in the use of so-called “dedicated” fuels as to achieve maximum transmutation rate in accelerator-driven systems. The dedicated fuels contain large amounts of minor actinides (Np, Am, and Cm) and plutonium, but lack the classical fertile isotopes (i.e.  $^{238}\text{U}$  and  $^{232}\text{Th}$ ). Subsequent deterioration



of safety parameters, when using such fuels, is well known (Maschek et al., 2000). While Doppler broadening of capture resonances is the most important inherent shutdown mechanism in a liquid–metal reactor, the effect is vanishing in accelerator-driven systems using dedicated fuels. The reduction of the fertile inventory and the spectrum hardness are the main reasons for this impairment (Maschek et al., 1999, 2000). It has been argued that a typical ADS core, based on dedicated fuels, contains several critical masses, which in principle provides the potential for criticality if the fuel is rearranged in a more dense configuration. In the absence of the Doppler effect, such accidents may occur without any restraining prompt negative reactivity feedback. Provisions for increasing the Doppler effect in dedicated cores have been proposed (Tommasi and Massara, 1999). In Table 2, values of the Doppler constant are listed for various heavy-metal cooled reactors. The Doppler constant for a sodium-cooled reactor is also included.

The Doppler constant for the dedicated cores (cases 1 and 2) are an order of magnitude lower than those of the mixed U–Pu fuels (cases 4 and 5) with their large Doppler constant. Tommasi and Massara (1999) enhanced the Doppler effect in a fertile-free core by adding some amount of hydrogenated moderator. The Doppler effect obtained in the sodium design (case 6), by Hill et al. (1999), surpasses the Doppler values in the lead-based designs by a factor of two. The argument is that the softer spectrum of the sodium design allows more neutrons to appear in the resonance region. Practically all the Doppler effect occurs below about 25 keV, where cross section variations with temperature are large (Hummel and Okrent, 1978).

We have investigated the merits; in terms of safety performance of the core, of increasing the Doppler effect in an ADS. By explicitly taking into account the Doppler feedback, we studied the response following a sudden “source jump” (same as previous transient). The source transient was chosen because it results in high fuel temperatures, which is the driver for reactivity input by the Doppler effect. Different values for the Doppler constant were modelled,  $Tdk/dT = -3.87 \times 10^{-4}$  and  $Tdk/dT = -2.71 \times 10^{-3}$ , representing a core containing dedicated fuels and a core containing large amounts of fertile material, respectively. The results are presented in Fig. 3.

The dynamics response, including Doppler reactivity feedback in the reference ADS ( $k_{\text{eff}} = 0.954$ ) with dedicated fuel is tiny. Even if the Doppler constant is increased by a

Table 2  
List of Doppler constants in various LMR designs

| Case | $Tdk/dT$              | Fuel composition  | Coolant | Comment            | Reference                  |
|------|-----------------------|---|---------|--------------------|----------------------------|
| 1    | $-3.87 \cdot 10^{-4}$ | (U <sub>0.1</sub> Pu <sub>0.7</sub> MA <sub>0.2</sub> ) | PbBi    | Mostly MA and Pu   | Present design             |
| 2    | $-1.50 \cdot 10^{-4}$ | (Pu <sub>0.5</sub> MA <sub>0.5</sub> )                  | Pb      | Very hard spectrum | Tommasi and Massara (1999) |
| 3    | $-2.03 \cdot 10^{-4}$ | (Pu <sub>0.5</sub> MA <sub>0.5</sub> )                  | Pb      | Added moderator    | Tommasi and Massara (1999) |
| 4    | $-1.63 \cdot 10^{-3}$ | (U <sub>0.8</sub> Pu <sub>0.2</sub> )                   | PbBi    | Compact design     | Hill et al. (1999)         |
| 5    | $-2.71 \cdot 10^{-3}$ | (U <sub>0.9</sub> Pu <sub>0.1</sub> )                   | PbBi    | Derated design     | Hill et al. (1999)         |
| 6    | $-4.89 \cdot 10^{-3}$ | (U <sub>0.9</sub> Pu <sub>0.1</sub> )                   | Na      | Derated design     | Hill et al. (1999)         |

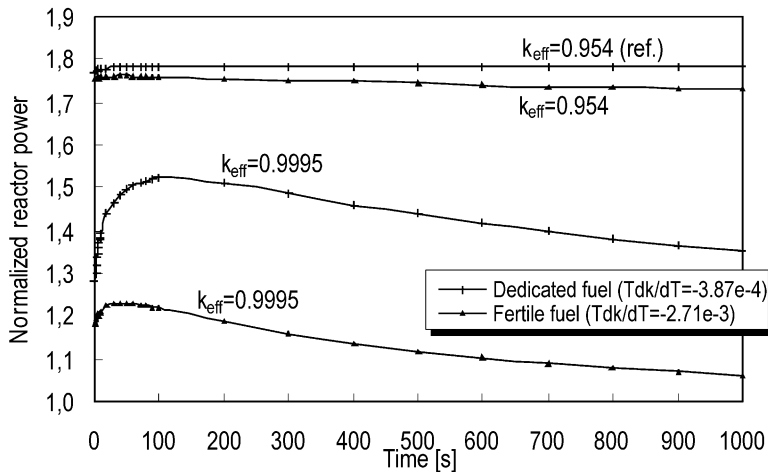


Fig. 3. Issue of enhancing the Doppler effect in ADS's. Lower Doppler value representing a dedicated core, higher Doppler value representing a core containing a large fraction of  $^{238}\text{U}$ . Two different subcritical levels are considered. Accident initiator by sudden increase in source intensity ( $S = 1.8 \cdot S_0$ ).

factor of seven, by introducing massive amounts of fertile material, the gain in feedback effect is small. There seems to be little benefit for increasing the Doppler effect in an effort to obtain a more benign response to accidents that remain in the subcritical state. In general, the importance of the Doppler effect in an ADS is strongly related to the level of subcriticality. In a close-to-critical system an equivalent increase of the Doppler effect would result in a significant improvement (see Fig. 3) ( $k_{\text{eff}} = 0.9995$ ). The role of Doppler feedback in hypothetical accidents exceeding the critical margin must be further evaluated.

#### 4. Time response

The thermal response of core constituents and the time to reach failure in various accidents influences the requirements on the shutdown device. Knowledge of the grace period, as defined by IAEA (1991), is essential in the evaluation of such devices. The plant must survive long enough for a passive safety action to be initiated in time to prevent core damage.

The numerical value of the grace period is necessarily specific to the particular design and is of less interest, but the time responses of accidents. Our intention is to study the response in order to assess the requirements on the safety system and to evaluate possible safety actions to enhance the performance. We may express response times defined by time constants rather than by absolute values, which has a broader range of applicability.

We subjected the reference design to three representative sequences of unprotected (i.e. no shutdown or plant protection system action) accidents, namely:

- (a) *Unprotected transient overpower (UTOP)* by a prompt insertion of maximum beam current. It is assumed that the steam generators remove heat at a rate of nominal power (constant temperature drop in steam generators).
- (b) *Unprotected loss-of-flow (ULOF)* by a loss of primary pump power. Feed-water flow is assumed to remain at its initial value and coolant inlet temperature is constant (constant outlet temperature in steam generator).
- (c) *Unprotected loss-of-heat-sink (ULOHS)* by a sudden inability of the steam generators to remove heat (zero temperature drop in steam generators).

Constant steam generator boundary conditions are assumed. The actual boundary condition depends on the particular accident (see above). Safety margins that are applicable to the reference design are indicated in the figures. These are based on postulated transient failure temperatures (listed in Table 3).

The dissociation temperature of minor actinide nitride fuel (NpN, AmN, CmN) is not well known (Suzuki and Arai, 1998). However, it is known that stable AmN has been fabricated at 1573 K (Takano et al., 1999). Mechanical failure limits, used to evaluate cladding failure, are those for 20% cold-worked 316 stainless steel due to lack of reliable data on HT-9. Mechanical strength properties are based on transient burst tests conducted on unirradiated and internally pressurized cladding specimens (Hunter et al., 1975).

In Figs. 4 and 5, peak fuel temperatures and peak cladding temperatures, respectively, are displayed as a function of time.

In the source transient (UTOP), the power “jumps” by a factor of 1.8, see Fig. 2. Since no time is required for heat flow, the fuel suffers a rapid, almost adiabatic thermal excursion, Fig. 4. Coolant and structure are heated at a rate determined by the characteristic time constant of the fuel element. The fuel itself, has the shortest time response and is most sensitive to source transients. After a few seconds, the fuel pins have adjusted to the new power level and temperatures temporarily settle in a quasi-equilibrium (not visible in the figure). For an extended period, mainly determined by the primary loop circulation time and the coolant heat capacity, the coolant inlet temperature remains at its initial value. The steam generators are assumed to remove heat at a rate of nominal power, resulting in a mismatch in the heat production and heat removal. The net effect is increasing inlet temperature, which causes the reactor core, coolant, and other components to overheat, inevitably leading to core damage unless the reactor is shut down.

Table 3  
List of failure temperatures for the reference design

| Failure mechanism          | Failure temperature | Comment  |
|----------------------------|---------------------|--|
| Dissociation of AmN        | 1573 K              | Conservative assumption (Takano et al., 1999)                      |
| Cladding burst temperature | 1333 K              | 20% CW SS316, 5.56 °C/s, hoop stress 100 MPa (Hunter et al., 1975) |
| Cladding/coolant corrosion | 946 K               | Extended operation (Novikova et al., 1999)                         |

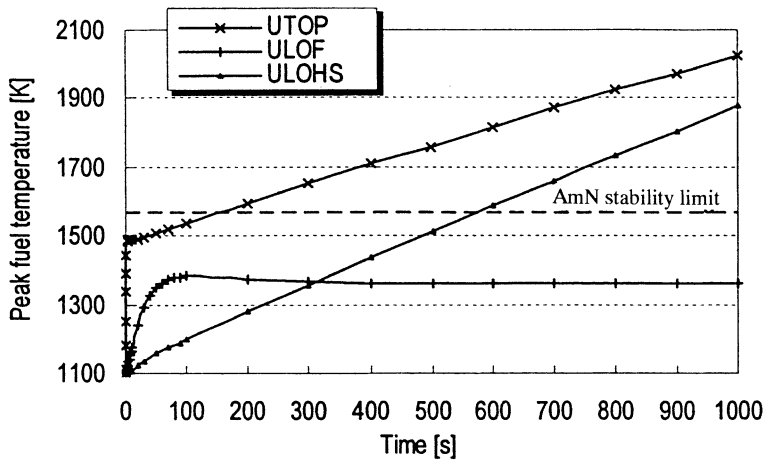


Fig. 4. Peak fuel temperatures in unprotected TOP, LOF, and LOHS.

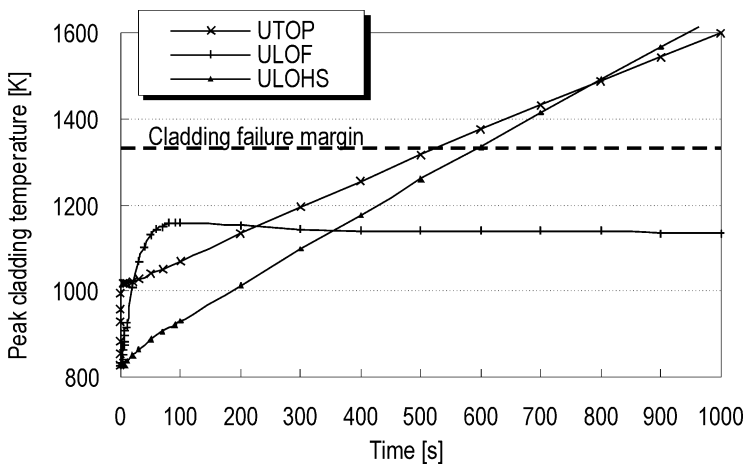


Fig. 5. Peak cladding temperature in unprotected TOP, LOF, and LOHS.

In the loss-of-flow (ULOFS) accident, core heat-up occurs at a rate determined by the flow coast-down. Inertial forces help to push the coolant through the primary system for an extended period. Peak temperatures occur as the pump impeller comes to a complete rest. Core temperatures and buoyancy forces eventually balance. In the asymptotic state, flow is sustained by natural convection alone. Reactivity feedbacks have negligible effect on the transient. For this particular system, an unprotected loss-of-flow accident should result in little or no damage. The integrity of the fuel and the cladding is not compromised. The protective oxide film layer on the cladding may suffer some damage that potentially could harm the cladding in the long run.

The loss-of-heat-sink (ULOHS) accident tends to be a more slowly evolving accident than the source transient and the loss-of-flow accident. The accident manifests as rising inlet temperature, which accompanies loss of primary heat sink. Response time is determined by the primary loop circulation time and coolant heat capacity. The prolonged grace period in a ULOHS accident facilitates successful performance of the safety system. Core damage is inevitable unless safety measures are taken to shut down the reactor.

In the unprotected LOHS accident shown in Fig. 4, we assumed that the primary pumps continued to operate. We also studied the response to a combination of loss-of-heat-sink and malfunctioning primary pumps. The temperature increased much more rapidly as the initial response, in that case, is mainly determined by the flow coast-down. It turned out that the grace period in a combined ULOHS and ULOF accident for this specific system was reduced by 50% compared to an isolated ULOHS. It should be taken into account, however, that it is likely that a loss-of-heat-sink accident will be in the form of impairment rather than a sudden and complete loss of heat rejection capability.

In Fig. 6, the thermal response of the coolant in the hot pool is displayed. The coolant temperature is an important safety system parameter since it is related to the heat production in the core. It can be used to sense power excursions and reduction in coolant flow rate. The coolant temperature may be used as an actuator in a passive safety device.

The thermal response of the coolant in the hot pool following a change in power or flow is delayed by the heat capacity of the coolant and transport lags. Therefore, it must be ascertained whether the time response of the coolant is sufficient to serve as an accident indicator and protect against the fastest transients conceivable in an ADS. Rapid coolant response is advantageous since it promotes prompt action of the safety system. In general, UTOP caused by insertion of maximum beam power, is likely to exert the fastest transient. The absence of any moveable control rods, that may rather quickly add or remove large amounts of reactivity, diminishes the

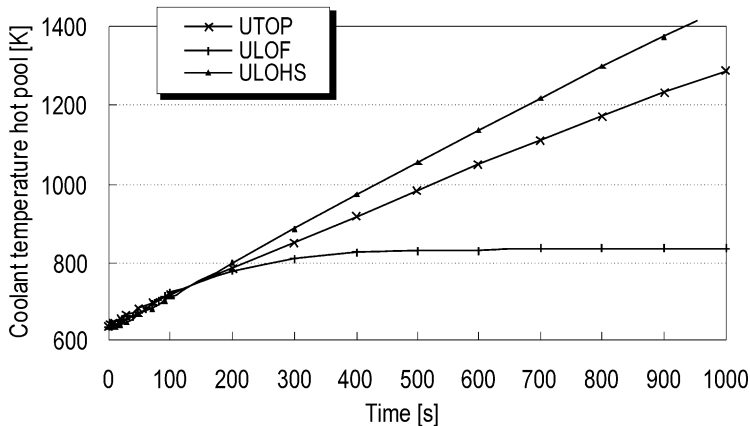


Fig. 6. Coolant temperature in the hot pool.

potential for fast transients caused by reactivity insertion. Significant reactivity is potentially available in core compaction or voiding phenomenon, but such sequences stretch over a longer period. It is noticeable in Fig. 6, that the initial response (<200 s) is more or less the same for all transients. However, source transients introduce the shortest grace period (with respect to fuel damage), while the temperature rise in the coolant is modest. In that sense, source transients impose the highest demands on a passive device that relies on the thermal response of the coolant.

## 5. An approach to inherent shutdown

Compared to reactivity changes, variations in source strength or source importance have a strong influence on the ADS. The power is linearly proportional to the source, 10% reduction in source strength yields 10% reduction of power, and so on. Shutdown of the external source effectively halts the fission process in the entire core.

Our approach is to design a passive system for the primary purpose to shut down the source in an emergency. The passive device would be comprised in an overall plant control system strategy similar to (Table 4): (a) use an active, regulating system that adjusts the source during normal operation. The regulating system function is to meet the power demand rather than to shut the reactor down if an accident occurs. (b) Use an active plant protection system (PPS) as a first level of protection to shut off the beam in an accident. The PPS would signal on excess temperature levels, low coolant flows, high neutron flux levels, etc. (c) Use the passive, self-actuated, shutdown system providing the second line of protection whenever the PPS function is not properly carried out. The passive system must be inherently independent of the normal beam control system.

It should be recognized that system redundancy makes the assumption of PPS failure highly unlikely. In fact, actual activation of the passive shutdown system must be regarded as hypothetical. Indeed, it affects the requirements on the device.

The shutdown system must be capable of halting the external source before excessive temperatures are obtained. This may be accomplished by reducing the time required for the shutdown system to act and by limiting the thermal response by design considerations. As mentioned previously, the fastest credible transient in an ADS is a source insertion transient. Worst conditions occur when the maximum

Table 4  
Plant control system strategy

| Control system                | Classification | Action  |
|-------------------------------|----------------|---|
| Regulating system             | Active         | Source regulation. Online usage during normal operation |
| Plant protection system (PPS) | Active         | Beam/source shutdown. Actuated in an off-normal event   |
| Passive shutdown system       | Passive        | Source shutdown. Actuated when PPS malfunctions         |

beam power is inserted in a step fashion at the begin-of-life. Source transients result in a rapid, but bounded power excursion. Consequently, it is unsafe to rely on a safety system to assure protection in the early phase of a source transient. Instead, protection must be accomplished through safety-by-design principles, e.g. minimizing the beam output capability by utilizing an appropriate burnup control strategy. While the speed of the beam controller may be limited by fundamental means, the capacity of the accelerator (beam power) is dictated by reactivity losses governed by fuel burnup. Various options exist, for example, shorter irradiation-cycle time and multi-batch fuel loading strategy (Yang and Khalil, 2000), lower power density and higher transuranic inventory (Hill and Khalil, 2000), optimal distribution of plutonium and minor actinides (Gonzalez et al., 2000), use of burnable absorbers (Wallenius et al., 2001a, b). Safety-by-design relaxes the requirements on the shutdown system.

In UTOP and ULOHS accidents, the grace period may be prolonged by the primary loop circulation time and the coolant heat capacity. Typical accidents where the coolant inventory has an appreciable effect on the thermal response involve situations when there is a net change in internal energy (primary system). Loss-of-flow accidents do not necessarily involve any accumulation of internal energy in the primary system, as the heat-removal rate may be unaffected. For loss-of-flow transients, the initial response is determined by the flow coast-down. It may be influenced by changing the moment of inertia of the pump and by increasing natural convection.

Taking these circumstances in consideration, our approach is to prolong grace periods, increase safety margins, and utilize safety-by-design principles, all easing the demands on the safety system. Prolonged grace periods do not only improve our chances for successful safety performance but reduces the probability for false actuation and interference of the passive system during normal operation. The second objective, in order to achieve high reliability, is to design simple, redundant and diverse shutdown systems, and to use components of proven high reliability. Greater complexity generally means reduced reliability.

## **6. Inherent shutdown mechanisms**

In this section, we suggest some concepts for inherent beam shutdown. The intention is to demonstrate the basic working principle. Appropriate references are included for strategies suggested by separate authors.

### *6.1. Flooding of the beam tube*

Shutdown of the external source can be accomplished by flooding the beamtube with coolant. The main purpose for filling the beamtube is to shift the axial position of beam impact, which in principle reduces the importance of source neutrons. Actuation may be based on thermal expansion of coolant or use of bursting disk devices. Several authors have proposed designs that utilize such principles.

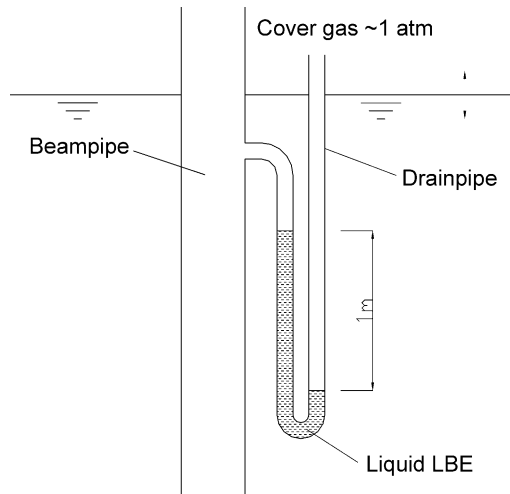


Fig. 7. Basic scheme for filling the beamtube with coolant through a U tube. Concept relies on a working moving fluid (class B device).

Rubbia et al. (1995) proposed a technique for the “energy amplifier” in which coolant rising above a prescribed level activates an overflow path and floods the cavity in the beam tube.

To fill the beamtube, we suggest installing a drainpipe in the shape of a U tube, shown in Fig. 7.

One side of the U tube is open to the cover gas region while the other side is connected to the beamtube. A portion of the coolant is retained in the U bend, forming a liquid seal that separates the beamtube from the cover gas region. A liquid column is supported by the pressure difference. A pressure difference of 1 atm is equivalent to a column height of LBE of 1 m (11 m for sodium). The inlet is located at a certain height above the surface. As the coolant expands, it would rise to the inlet, flood the drainpipe, and subsequently spill into the beamtube. The intake to the drainpipe must be elevated high enough to reduce the risk for false actuation. Difficulties may exist if the surface is seriously disturbed by turbulence and vapor bubbles.

In our reference design, the coolant level rises at a rate of 10 cm/100 K. In Fig. 8, the coolant surface elevation is calculated for unprotected TOP, LOF, and LOHS accidents. Zero level is the surface elevation at steady-state. The points at which the fuel and the cladding exceed their safety margins are also indicated. For the source transient (UTOP), the surface rises approximately 10 cm before fuel failure, corresponding to the smallest level change yet leading to core damage. In a loss-of-flow accident there is a gradual loss of pressure head why the coolant level actually drops during pump coast-down. The rate at which the coolant rises can be affected by the geometry of the vessel.

The basic design only relies on the integrity of the components and a moving working fluid. It does not require signals, external power, moving mechanical parts.



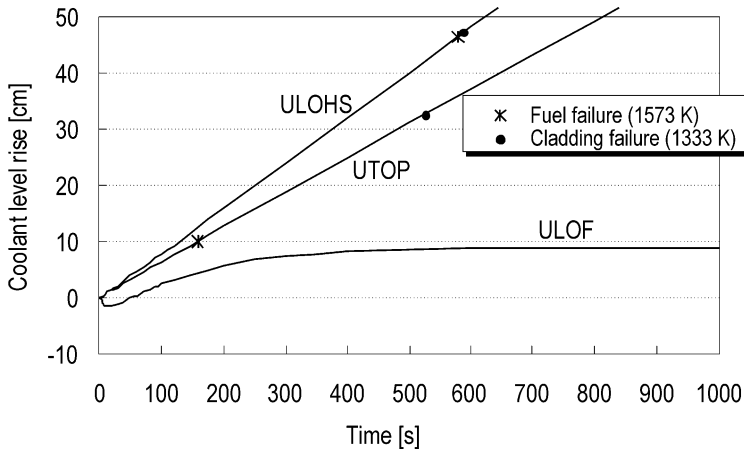


Fig. 8. Rise of coolant level in hot pool in unprotected accidents.

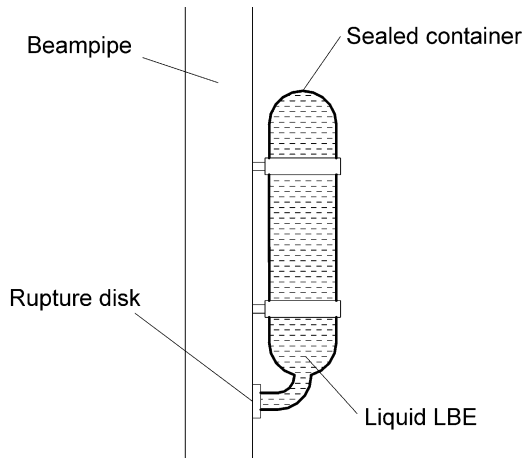


Fig. 9. Scheme for filling the beamtube using a pressurized container. Concept relies on a bursting disk device (class C device).

In that case, it is classified as a passive device in category B, in compliance with IAEA's categorization of passive systems (IAEA, 1991).

A straightforward method was proposed by Wider et al. (1999), in which a melt-rupture disk is installed in the side-wall of the beam tube. The membrane is in contact with the coolant. Source shutdown is actuated as the disk fails and the vacuum tube is flooded with coolant.

Another option is to have a liquid, e.g. LBE, completely fill a sealed container of fixed volume, see Fig. 9. The container is placed in thermal contact with the coolant and it is sealed off to the beamtube by a rupture disk. When excessive pressures occur then the rupture disk fractures releasing the liquid to the beamtube.

In general, bursting disk devices tend to be less accurate. The burst pressure or temperature is unpredictable. The problem is accentuated due to ageing and when used in a hostile environment. A drawback is that the disk is destroyed in the action, thus eliminating the possibility of testing the device prior to its installation or when it is in service. In order to attain a short time response, the disk must be operated close to its bursting point, which increases the possibility for false actuation. Passive safety based on bursting disk devices is classified in category C, in accordance with IAEA regulation.

Beam chambers typically require high vacuums and chemically clean surfaces to prevent proton interaction with trapped gas. Filling the beamtube with coolant may cause serious contamination of the accelerator tunnel. One option is to install a second beam window at the top of the tube to separate the beamtube from the accelerator tunnel. If the passive system provokes a shutdown, it may require replacing the beamtube, however, it is likely the plant needs correction anyhow, to assure its integrity and to reinstate the original safety function. In that perspective, filling of the beam tube could possibly serve as a last resort. False actuation, however, must be eliminated.

## 6.2. *Alternative methods*

In most pre-conceptual ADS designs, the beam is subject to some bending action before entering the vessel. Bending of a charged particle beam is normally carried out by magnets. In principle, a bending magnet could serve as an on/off switch for the external source. If the magnet is de-energized, the beam would safely end-up in a beamstop, otherwise the beam is diverted to the target.

For such a device switching is necessary, e.g. an electrical circuit must open/close, which limits the safety level achievable by this principle. Preferably, the passive switch is of a fail-safe type, i.e. unless connection is established the magnet is off. Possible agencies for actuating such a switch include:

- A ferromagnetic Curie-point-operated device. Above the Curie temperature, the magnetization of a permanent magnet vanishes. Such a device could either be used for switching or in a lock-release function acting on safety rods. Similar devices showed considerable promise for application in self-actuated shutdown systems in liquid-metal fast breeder reactors (Sowa et al., 1976). The Curie temperature of carbon steel is 1043 K.
- Elongation of a metal rod that is submerged in the coolant or bending of a bi-metallic component could be used as a temperature-sensitive switch.
- Rising coolant levels could elevate a float device that is connected to an electrical circuit. Alternatively, the medium itself could act as a conductor and establish connection.
- Pressure build-up in the cover gas region (or some other compartment), due to thermal expansion of the medium could actuate a switch that operates at a predetermined pressure. A weighted lever or a spring could set the limiting pressure. Alternatively, thermal expansion of a fixed mass of a fluid (LBE) in a confined space could perform a similar task.

- A generator that is connected to the coolant flow may supply power to the bending magnet. The generator may be driven by mechanical forces or as a reversed electromagnetic pump. However, the drawbacks include, obstruction of flow in a free-convection mode, need for significant pumping power, and lack of temperature feedback.
- Liquid metal coolants feature temperature-dependent resistivity. Increasing the temperature will increase the resistivity. Resistivity rising above a limiting value could trigger an electrical or magnetic switch.

## 7. Conclusions

The applicability for passive safety to accelerator-driven systems was studied. The current study focused on means for inherent shutdown. The usefulness for reactivity feedbacks was evaluated and some schemes for inherent source shutdown were suggested.

It seems that inherent shutdown based solely on reactivity feedbacks is fruitless in accelerator-driven systems. Inherent shutdown must be reinforced by other means. It was shown that increasing the Doppler effect, by introducing massive amounts of fertile material, have limited effect on transients that remain in the subcritical state. Doppler feedback may be important for accidents exceeding criticality. The significance of reactivity feedbacks, in general, depends on the specific design and in particular on the choice of the subcritical level. Taking advantage of reactivity feedbacks calls for a careful balance between the desired feedback performance and the subcritical margin.

Safety analysis indicated that transient overpower accidents, caused by insertion of the maximum beam power, is likely to exert the fastest transients conceivable in an ADS. In that perspective, source transients have profound impact on the requirements for a shutdown device. Safety-by-design principles must be utilized to assure protection to source transients.

Some concepts to accomplish passive source shutdown were presented. Two methods that seek to block the beam by filling the beamtube with coolant were proposed. Actuation is caused by thermal expansion of coolant. Other options include shutdown of beam bending magnets or insertion of shutdown rods by passive means.

Shutdown of the beam by passive means can provide an important additional safety feature for accelerator-driven systems. Such systems may contribute significantly to the reliability of the overall plant protection system. At this point, however, considering the premature nature and the lack of experimental validation, further work is necessary in order to determine the practicability of the present design concepts.

## Acknowledgements

Sincere appreciation is expressed to the SKB AB and The Swedish Center for Nuclear Technology who financially supported the project.

## References

- Cahalan, J.E., Tentner, A.M., Morris, E.E., 1994. Advanced LMR safety analysis capabilities in the SASSYS-1 and SAS4A computer codes. Proceedings of the International Topical Meeting on Advanced Reactors Safety, Pittsburgh.
- Gonzalez, E., et al. 2000. Transuranics on fertile and inert matrix lead-bismuth cooled ADS. 6th Information Meeting on Actinide and Fission Product Partitioning and Transmutation, Madrid.
- Hill, R.N., Cahalan, J.E., Khalil, H.S., Wade, D.C., 1999. Development of small, fast reactor core designs using lead-based coolant. Proceedings of the International Conference On Future Nuclear Energy Systems, GLOBAL'99, Jackson Hole.
- Hill, R., Khalil, H., 2000. Physics studies for a Na-cooled ATW design. IAEA Technical Committee Meeting on Core Physics and Engineering Aspects of Emerging Nuclear Energy Systems for Energy Generation and Transmutation, Argonne.
- Hummel, H.H., Okrent, D., 1978. Reactivity coefficients in large fast power reactors. American Nuclear Society, Illinois, pp. 133.
- Hunter, C.W., Fish, R.L., Holmes, J.J., 1975. Mechanical properties of unirradiated fast reactor cladding during simulated overpower transients. *Nucl. Technol* 27 (3), 376–388.
- IAEA, 1991. Safety Related Terms for Advanced Nuclear Power Plants. TECDOC-626.
- Karlsson, J., Wider, H., 2000. New aspects of emergency decay heat removal from a Pb/Bi-cooled ADS by auxiliary cooling. Proceedings of the ICONE 8, 8th International Conference on Nuclear Engineering, Baltimore.
- Lucoff, D.M., Waltar, A.E., Sackett, J.I., Aizawa, K., 1992. Experimental and design experience with passive safety features of liquid metal reactors. International Conference on Design and Safety of Advanced Nuclear Power Plants, Tokyo.
- Maschek, W., Rineiski, A., Morita, K., Muhling, G., Flad, M., 2000. Safety analysis for ADS cores with dedicated fuel and proposals for safety improvements. Proceedings of the IAEA Technical Committee Meeting on Core Physics and Engineering Aspects of Emerging Nuclear Energy Systems for Energy Generation and Transmutation, Argonne.
- Maschek, W., Thiem, D., Heusener, G., 1999. Safety features of a reactor core with minor actinide transmutation and burning capabilities. Proceedings of the International Conference On Future Nuclear Energy Systems, GLOBAL'99, Jackson Hole.
- Novikova, N., Pashkin, Y., Chekunov, V., 1999. Some features of sub-critical blankets cooled with lead-Bismuth. Proceedings of the International Conference on Accelerator-driven Technologies and Applications, ADTTA'99, Praha.
- Sowa, E.S., et al., 1976. LMFBR Self-actuated Shutdown Systems, Vol. II. Proceedings of the International Meeting of fast Reactor Safety and Related Physics, Chicago.
- Rubbia, C., et al., 1995. Conceptual Design of a Fast Neutron Operated Energy Amplifier. Cern publication, CERN/AT/95-44.
- Suzuki, Y., Arai, Y., 1998. Thermophysical and thermodynamic properties of actinide mononitrides and their solid solutions. *J. Alloys Comp.* 271–273, 577–582.
- Takano, M., et al., 1999. Synthesis of americium mononitride by carbothermic reduction method. Proceedings of the International Conference on Future Nuclear Energy Systems, GLOBAL'99, ANS, Jackson Hole.
- Tommasi, J., Massara, S., 1999. L.M.F.R dedicated cored for transmutation critical vs. subcritical systems comparison. Proc. International Conf. On Future Nuclear Energy Systems, GLOBAL'99, Jackson Hole.
- Tucek, K., Wallenius, J., Gudowski, W., 2001. Source efficiency in an accelerator-driven system with burnable absorbers. GLOBAL 2001, International conference on the Back-end of the Fuel Cycle: from Research to Solutions, Paris.
- Wallenius, J., Tucek, K., Carlsson, J., Gudowski, W., 2001a. Application of burnable absorbers in an accelerator-driven system. *Nucl. Sci. Eng.* 137, 96–106.
- Wallenius, J., Tucek, K., Eriksson, M., Gudowski, W., 2001. The Sing Sing core: a sub-critical TRU burner with low reactivity losses. Proceedings of the International Conference on Accelerator

Applications/Accelerator Driven Transmutation Technology and Applications '01. AccApp/ADTTA '01, Reno.

Wider, H., Karlsson, J., Jones, A. V., 1999. Safety considerations of heavy metal-cooled accelerator-driven systems. Proceedings of the International Conference on Future Nuclear Energy Systems, GLOBAL'99, Jackson Hole.

Yang, W. S., Khalil, H. S., 2000. Reduction in burnup reactivity loss in accelerator driven transmutation systems. Proceedings of the 4th Topical Meeting on Nuclear Applications of Accelerator Technology, Washington.

# Paper VI

# RELIABILITY ASSESSMENT OF THE LANSCE ACCELERATOR SYSTEM

**Marcus Eriksson**

Royal Institute of Technology, Sweden

**Christopher Piasczyk**

Northrop Grumman Corporation, USA

## Abstract

This paper describes the reliability analysis of the accelerator facility at Los Alamos Neutron Science Center (LANSCE)[1]. The goal of the analysis is to present beam failure statistics of LANSCE and identify the root cause of a beam failure. Beam trips and failure causes are assembled using operational data records, accelerator logbook and beam monitor data. Mean Time Between Failure and Mean Down Time estimates are obtained for typical accelerator components. The results are useful in accelerator reliability modelling and identifying development issues in high power accelerators.

## Introduction

The reliability and availability of the accelerator in an accelerator driven system is an important issue. New applications for high power proton accelerators such as the production and destruction of radioactive elements demand high availability, reliability and maintainability. Persistent beam power fluctuations have a negative influence on a hybrid system. In order to estimate and improve the availability and reliability of future accelerator designs, data from existing accelerators are being analyzed. The accelerator facility at Los Alamos Neutron Science Center (LANSCE) is the most powerful linear proton accelerator in the world. The accelerator offers enough operating history to supply meaningful reliability data.

The objective of the present data collection and analysis effort is to understand the behavior of existing operating accelerator facilities so that better, more reliable systems can be designed and built in the future. Previous work has identified the current state of the art lacking in the area of reliability database information for components typically used in rf accelerator systems, such as rf stations, rf drives, rf transport, cooling, vacuum systems, magnets, and magnet power supplies. Thus, while it is possible to use the reliability theory to model accelerator systems, the input data currently available for such analyses lacks credibility. This led to the initiation of an effort of data collection and analysis of which this study is one of the tasks. The present work examines the data set of failure events for the LANSCE 800 MeV accelerator facility.

## The LANSCE Accelerator Facility

The LANSCE accelerator delivers two proton beams at 800 MeV: the H<sup>+</sup> and the H<sup>-</sup> beam. The H<sup>+</sup> beam may deliver 1.25 mA current (routine operation is at 1 mA) and the H<sup>-</sup> beam delivers 70  $\mu$ A. Each injector system includes a 750 keV Cockcroft-Walton type generator. Both ions are accelerated simultaneously in one and the same structure. After acceleration the H<sup>+</sup> and H<sup>-</sup> beams are separated. The H<sup>-</sup> beam is injected into a Proton Storage Ring for accumulation and delivery to the neutron scattering center or weapons neutron research.

| Beamline | Energy  | Current    | Injector<br>(High Voltage Generator) | Proton Storage Ring |
|----------|---------|------------|--------------------------------------|---------------------|
| H+ beam  | 800 MeV | 1.25 mA    | Cockcroft-Walton                     | No                  |
| H- beam  | 800 MeV | 70 $\mu$ A | Cockcroft-Walton                     | Yes                 |

Table 1. The LANSCE accelerator delivers two ion beams

The low energy section of the accelerator is an Alvarez Drift Tube Linac (DTL). The drift tube linac accelerate the protons from 750 keV to 100 MeV. The high energy section is a Side Coupled Linac (SCL). The SCL may accelerate protons up to 800 MeV. Different rf systems are used for the drift tube linac and for the side coupled linac. In the DTL, triode power tubes are used for the generation of rf power while in the side coupled linac klystrons are used. The rf system for the DTL is sometimes referred to as the 201 system since the rf frequency in the drift tube linac is 201.25 MHz. The rf system for the SCL is called the 805 rf system since the rf frequency is 805 MHz.

| Linac Section      | Energy region   | RF Power           | RF Frequency |
|--------------------|-----------------|--------------------|--------------|
| Drift Tube Linac   | 750 keV-100 MeV | Triode power tubes | 201.25 MHz   |
| Side Coupled Linac | 100 MeV-800 MeV | Klystrons          | 805 MHz      |

Table 2. Different rf systems are used in the DTL and the SCL

Ahead of time a beam schedule has been organized with respect to time-sharing between experiments, beam intensity, and beam energy. An overall schedule of commissioned beam time for each beamline is set out. Scheduled operation at LANSCE is divided into run cycles. During scheduled operation, the accelerator is operated almost 24 hours per day for an entire run cycle with only a few scheduled breaks. A run cycle is maintained for approximately 5-6 weeks (800-1000 hours). A large fraction of the year the accelerator is not scheduled due to maintenance activities. Scheduled operation is usually in the region of 2000-3000 hours per year, which is about 30 % of the year. In reliability assessment of LANSCE the total scheduled beam time is an important factor **-beam trips are only analyzed if they occur within scheduled accelerator operation.**

## Input Data

Beam delivery is measured by current monitors near the targets. If the beam current for some reason is below half the scheduled current the beam is considered as interrupted. This event/trip generates loss of scheduled beam time, commonly called down time. The operator assigns a failure cause, or down time assignment, to each trip. The down time assignment is recorded in the logbook. The failures and down time assignments are also entered into operational data records. Separate data records are maintained for each beam line or target area. In this investigation beam trips associated with the H+ beam and the H- beam are analyzed. The records obtained cover run cycles 71 through 76, over the period 1996-97.

The first, and most time intensive task of this effort was collecting the input data. Thanks to the cooperation of the LANSCE Operations Group, a large amount of data was collected. This included the:

- 1) Operational data records
- 2) Central Control Room Logbook
- 3) Operations Shift Supervisor's Summary Reports
- 4) Beam Monitor data for 1997

## Overall LANSCE Reliability

In this section, the distribution of beam trips and down time for the entire LANSCE accelerator facility is presented. The analysis considers scheduled accelerator operation of the H+ beam for 1997 and of the H- beam for 1996 and 1997. The H+ and the H- beams are investigated separately. All



calculations are based on operational data records or indirectly accelerator logbook data. A histogram of beam trips that occur in the H+ and the H- beam is presented in figure 1.

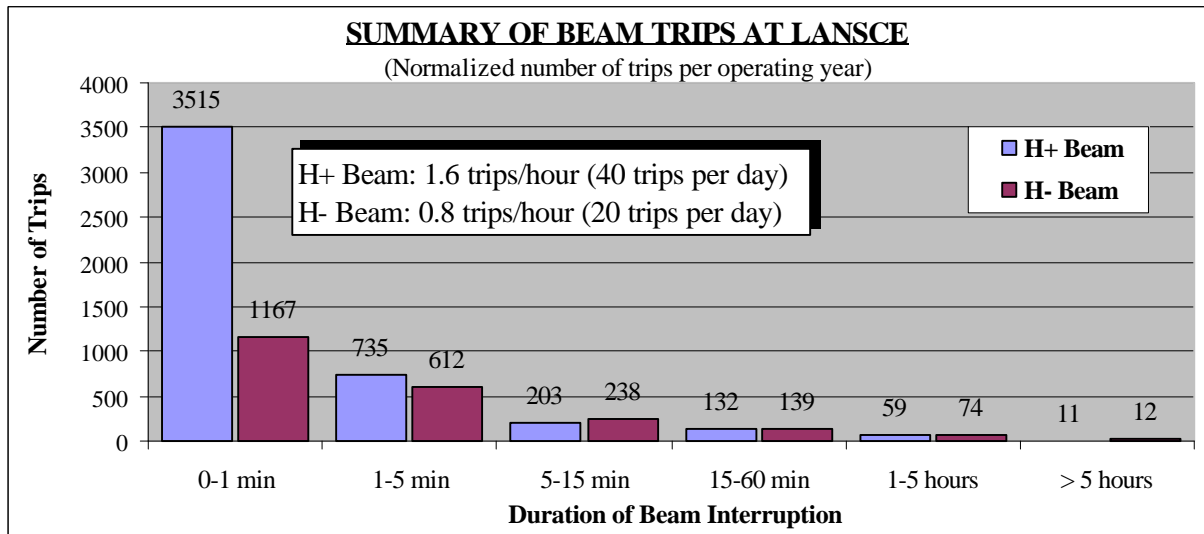


Figure 1. Beam failure statistics of the LANSCE accelerator facility

From figure 1 it is obvious that the H+ beam is exposed to many beam trips with short duration. 76% of all trips in the H+ beam are 0-1 minute long. When comparing the total number of trips in the H+ and H- beams, the conclusion is that twice as many trips occur in H+ beam. When operating, the H+ beam is exposed to 1.6 trips/hour and the H- beam 0.8 trips/hour. The main reason is the larger number of short trips in the H+ beam. For long down times (> 5 minutes), almost the same number of trips occur in the H+ and the H- beams. This makes sense since both beamlines utilize, for most of their length, the same accelerating structure. At a closer look, a slightly larger number of long trips occur in the H- beam. The reason is that the H- beamline is more complex. It includes the Proton Storage Ring and hence more components are subject to failure.

In figure 2, the most frequent causes for beam failure and beam downtime in the H+ beam are presented. Two columns are displayed for each individual system. The leftmost column in each system shows the fraction of total number of H+ trips the system is responsible for. The rightmost column shows the equivalent fraction of total downtime. It is a good thing to separate trips and downtime. Trips affect beam stability and produce power fluctuations. Downtime has a negative influence on the overall beam availability.

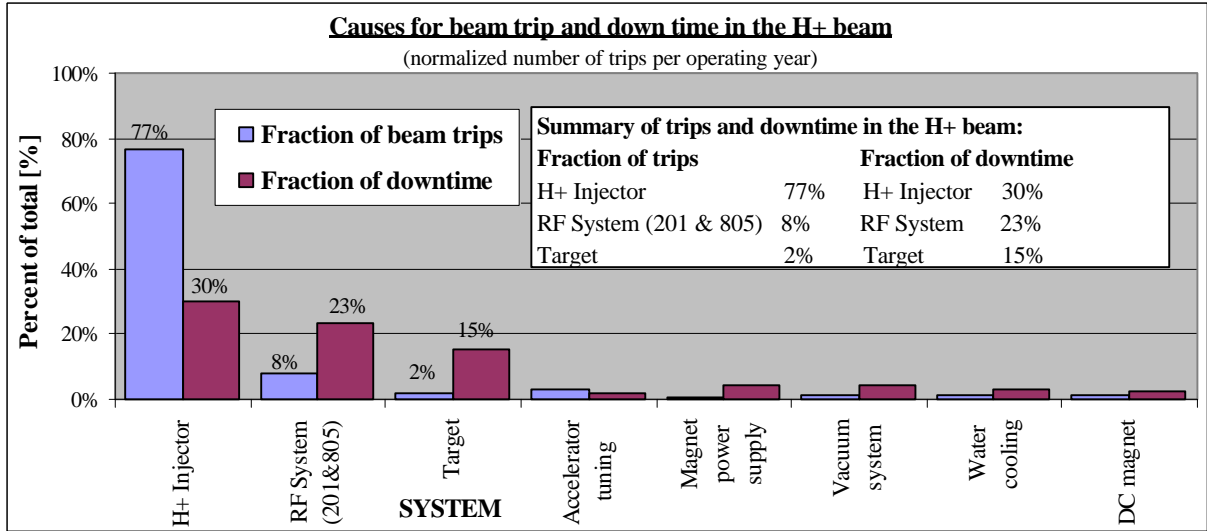


Figure 2. Systems responsible for trips and downtime in the H+ beam

From figure 2, it is obvious that an injector failure is the most frequent cause for beam trip. In the H+ beam 77% of all trips are caused by a failure in the H+ injector. The characteristic of the injector failure is the interruption length. It is usually shorter than 1 minute, often in the order of 15-20 seconds, the time it takes to reset the trip and re-energize the Cockcroft-Walton generator. An injector failure is usually caused by electric breakdown in the high voltage column. Since a typical injector failure is short, the injector is not as dominating when it comes to the generation of downtime. While the H+ injector is responsible for 77% of the trips it is "only" responsible for 30% of the downtime. In other words, the injector is the main reason for beam current fluctuations but it has a significantly smaller influence on the overall beam availability. The rf system, including the rf system for the DTL and the SCL, is generating 8% of the trips but is accountable for 23% of the downtime. Hence, a failure in the rf system usually results in a long downtime (> 5 minutes).

In figure 3, historical data on overall beam availability and beam schedule for the years 1979-97 is presented [2]. The line graph represents beam availability and the column bars represent the scheduled beamtime. It is important to remember that the availability only measures the availability of the accelerator during scheduled operation. A common misunderstanding is that the availability of the machine gives the year round availability.

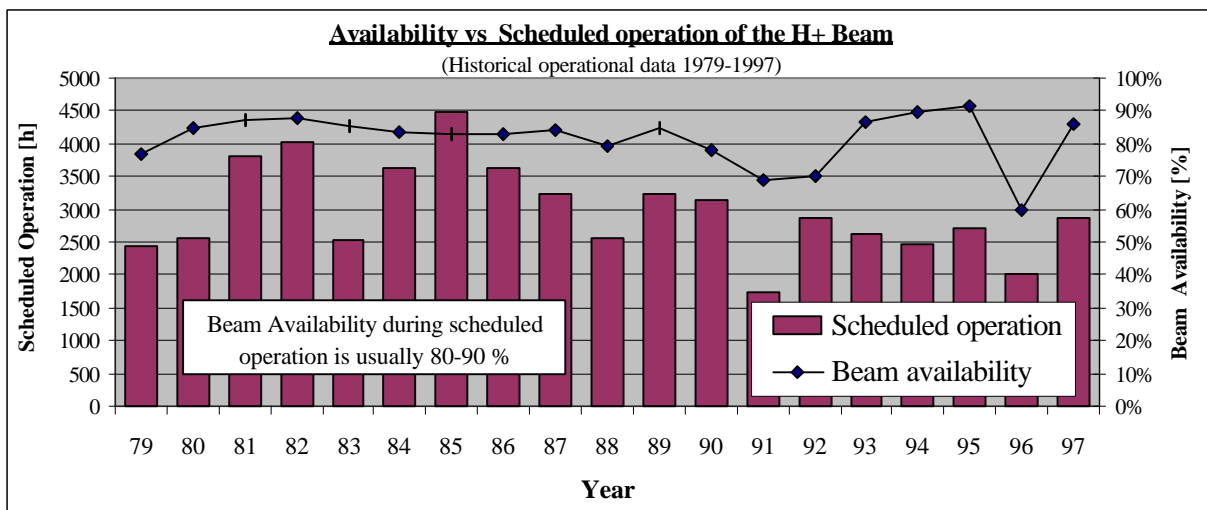


Figure 3. Historical availability and scheduled beamtime of the H+ beam [2]

Figure 3 is interesting in that sense it shows the relation between beam availability and the length of the operating period. Since a short scheduling period is usually followed by a longer maintenance period figure 3 also gives information on the affect of accelerator maintenance on overall availability. When examining figure 3, the conclusion is that **the scheduled beamtime seems to have little influence on the availability**. It means that a long schedule does not have to imply lower beam availability. This is not all true but one obvious example occurred in 1985. In 1985, the longest schedule ever was practiced. The accelerator was commissioned for 4500 hours (50% of the year) and it operated with normal availability (83%). In some years the availability actually drops when the accelerator is operated for less time! In 1996, the availability experienced a decline due to a single water leak in one of the targets, otherwise the standard availability of LANSCE is in the region of 80-90%. This level of availability is similar to the availability experienced in other accelerator facilities.

### Analysis of beam current

Previous calculations and diagrams presented in this paper were all based on data originating from the accelerator logbook. Similar beam reliability analysis is performed for data originating from beam current monitors. The H+ beam current has been analyzed during scheduled operation of 1997. The beam current at the end of the H+ beamline is inspected and interruptions are registered. A total of 163,000 beam current recordings are included in the analysis. The current analysis will verify previous results and it will present the "true" beam performance. When analyzing beam current data it is not possible to investigate the failure cause. Results of the beam current analysis are presented in figure 4. The histogram includes the total number of beam trips detected in the beam current and the corresponding down time. For comparison, the total number of trips registered in the logbook during the same time period are also included in the histogram.

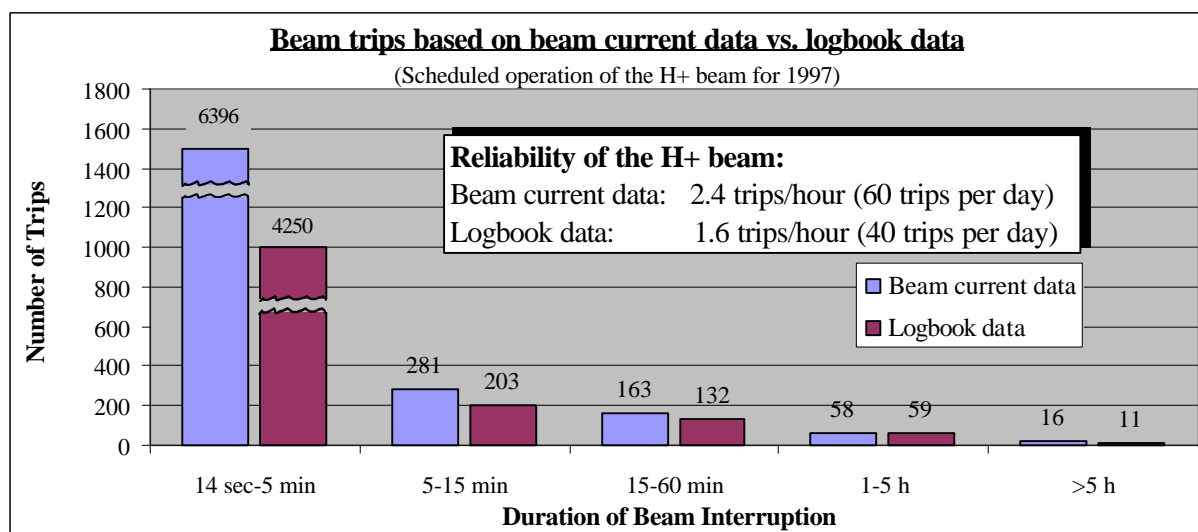


Figure 4. Reliability of the H+ beam at LANSCE

The trips occurred during scheduled operation of the H+ beam for 1997. When analyzing the beam current a total of 6914 beam trips are detected. This number is larger than the number of trips recorded in the logbook (4655 trips) under the same period of time. From figure 4 it is clear that the main reason is that a large number of short interruptions (15-20 seconds) are detected in the beam current which are not included in the logbook. This is also confirmed by operating personnel. For example, in difficult periods when the injector is tripping frequently all short beam trips are not recorded in the logbook, instead comments like "continuous arcing in the injector column" are used.

For trips with long downtime (>5 minutes) it is remarkable how well the results agree even though the underlying data origins from two completely different sources. That is a strong evidence for the correctness of the results from both analyses. When analyzing the beam current it is also evident that practically no interruptions with downtime shorter than 10 seconds occur. In other words, if an interruption occurs it is likely it will last for at least 10 seconds.

## Reliability of subsystems & components

In this section the reliability of major LANSCE subsystems and components are investigated. A first cut analysis of the available LANSCE data is performed. Mean Time Between Failure (MTBF) and Mean Down Time (MDT) for individual subsystems are studied to obtain input data for accelerator reliability modelling (RAMI). Individual failures are thoroughly investigated with the help of logbooks, operational reports, operators, maintenance personnel. In case the cause of a trips is uncertain, experts in particular field are consulted to correctly classify the event. The aim is to detect the root cause, down to components level, of each failure. For this purpose, the raw data is divided into categories corresponding to individual subsystems and subsequently estimates of failure and repair rates are obtained. These categories are listed in table 2.

| MAIN SYSTEM                  | SUBSYSTEMS   |  |                       |
|------------------------------|--|--|-----------------------|
| <b>805 RF</b>                | Klystron assembly<br>High Voltage system<br>805 Tank | Phase and Amplitude Control<br>Resonance Control<br>Module Control | Other<br>Unknown      |
| <b>DC Magnets</b>            | Magnet Hardware<br>Interlocks                        | Water cooling  | Vacuum                |
| <b>Magnet Power Supplies</b> | Electronics<br>Capacitors                            | Transformers<br>Water cooling                                      | Interlocks<br>Unknown |
| <b>Pulsed Power</b>          | Harmonic Buncher<br>Deflector                        | Chopper  | Kicker                |
| <b>Water System</b>          | Water Pump<br>Other                                  | Piping   | Unknown               |
| <b>Vacuum System</b>         | Ion Pump   | Piping   | Unknown               |

Table 2. Classification of subsystems

Failures corresponding to each subsystem are merged and classified into individual databases. In table 3, an illustration of the database format for failures in the Klystron Assembly of the 805 RF System is presented. Similar databases are compiled for each subsystem. The database contain trips that affect both the H+ and the H- beams. Failures are only recorded if they occur within scheduled operation.

| DURATION OF BEAM INTERRUPTION |                            |                   | LOCATION OF FAILURE |        |           | CAUSE OF FAILURE                  |   |
|-------------------------------|----------------------------|-------------------|---------------------|--------|-----------|-----------------------------------|---|
| Date & Time of Outage         | Date & Time of restoration | Down Time [h:min] | Area                | System | Subsystem | Component failure or other reason | Comment   |
| <b>Klystron Assembly</b>      |                            |                   |                     |        |           |                                   |   |
| 11/01/96 02:09                | 11/01/96 02:29             | 0:20              | LINAC               | 805    | Klystron  | Flow switch                       | Module 21 Klystron water not okay. Mechanically agitated flow switch and it made up.  |
| 11/23/96 09:43                | 11/23/96 09:56             | 0:13              | LINAC               | 805    | Klystron  | Water flow                        | Sector D off. Module 21 klystron water flow trip. The klystron magnet supply valve has been opened 1/8 of a turn.   |
| 11/23/96 23:17                | 11/23/96 23:32             | 0:15              | LINAC               | 805    | Klystron  | Water flow                        | Module 21 klystron water flow trip  |
| 03/17/97 07:25                | 03/17/97 07:40             | 0:15              | LINAC               | 805    | Klystron  | Ion Pump                          | Module 46 (Sector H) Klystron ion pump supply failed. It was replaced.  |
| 05/24/97 07:24                | 05/24/97 13:14             | 5:50              | LINAC               | 805    | Klystron  | Klystron                          | Module 36 Main Amplitude crowbar. Sector F tripped a second time and the fire alarm went off. Acrid smell from the capacitor room. Module 36 klystron was replaced. |

Table 3. Illustration of final database format

The database is for practical reasons divided into three major sections: One section deals with the Duration of the Interruption. It contains the date and time of the beam outage and restoration. It also includes the Down Time of each interruption. The second section considers the Location of the Failure. The Area defines the geographical location of the failure [3]. The System and Subsystem columns specify in what System and Subsystem the failure is located. The third section gives detailed information on the Cause of the Failure. The cause may be a component failure that needs replacement, a bad condition such as a water flow problem or an adjustment failure that needs to be tuned. In the comment column, extra text has been added to explain the failure.

The main objective of the analyses is to obtain estimates for the MTBF and MDT for typical accelerator components, such as RF amplifiers, HV power supplies, magnets, magnet power supplies, vacuum system components, or water cooling components. For illustration the mean down time estimate as a function of time for the magnet power supplies is presented in figure 5. Each dot marks a failure in the magnet power supply. Spaces in between dots is the time between failure. The diagram shows the Mean Down Time estimate at a certain number of failures. The final Mean Down Time estimate for the magnet power supplies is obtained at the last failure in the diagram.

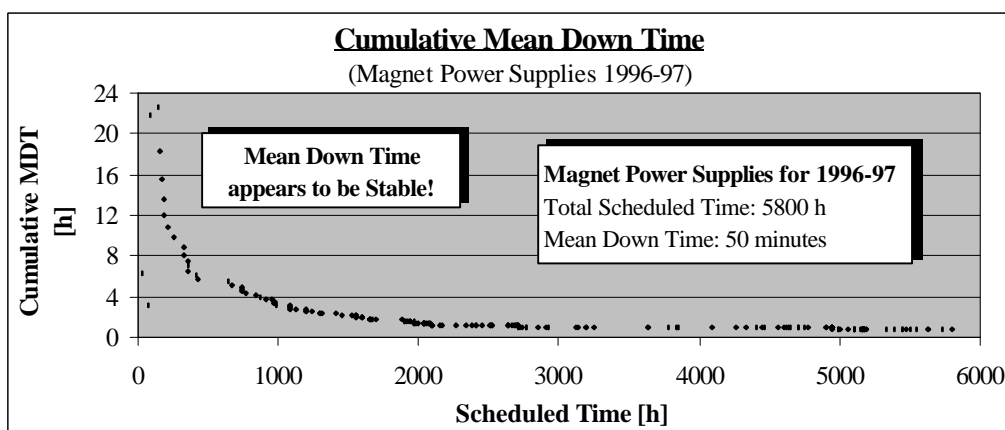


Figure 5. Cumulative Mean Down Time for Magnet Power Supplies

One indication of sufficient number of entries in the data set is the asymptotic behavior of the statistical estimators for the desired quantities, such as the Cumulative Mean Downtime which is calculated as the ratio of the cumulative downtime to the cumulative number of events as shown in figure 5. The conclusion in this case is that further data collection is not necessary, Mean Down Time estimate appears to be stable at approximately 50 minutes. A similar plot is made for the cumulative Mean Time Between Failure in figure 6.

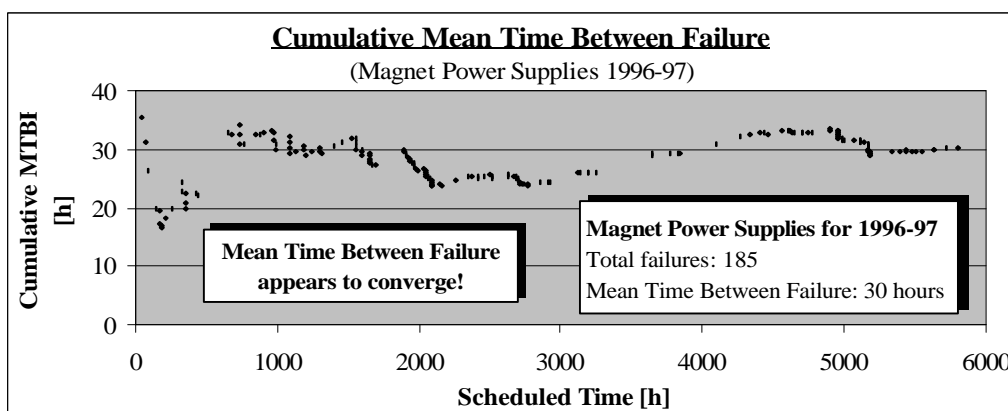


Figure 6. Cumulative Mean Time Between Failure for a single Magnet Power Supply

Cumulative Mean Time Between Failure is calculated as the ratio of the cumulative number of failures to the cumulative up time (scheduled time - downtime). As illustrated in figure 6, the MTBF behavior for the magnet power supplies is not as smooth as for the cumulative downtime but it appears to converge somewhere in the region of 30 h. With 278 magnet power supplies total in the system, the MTBF estimate for an individual magnet power supply is 8445 hours, assuming that all supplies have the same failure rate and can be treated as a series system of independent power supplies.

The results obtained via similar analyses for the other subsystems at LANSCE are summarized in table 4.

| <b>RESULTS OF RELIABILITY STUDY AT LANSCE</b> |                     |                      |                                    |  |
|---|---------------------|----------------------|------------------------------------|--|
| <b>Main System</b>                            | <b>Subsystem</b>    | <b>MDT</b><br>[h:mm] | <b>MTBF for all devices</b><br>[h] | <b>MTBF for a single device</b><br>[h] |
| <b>805 RF</b>                                 | Klystron Assembly   | 0:44                 | 262                                | 11560                                  |
|   | High Voltage System | 0:18                 | 137                                | 960                                    |
| <b>DC Magnets</b>                             |                     | 0:53                 | 290                                | 232280                                 |
| <b>Magnet Power Supplies</b>                  |                     | 0:50                 | 30                                 | 8445                                   |
| <b>Pulsed Power</b>                           | Harmonic Buncher    | 0:09                 | 44                                 | 44                                     |
|   | Chopper magnet      | 0:08                 | 291                                | 291                                    |
|   | Deflector magnet    | 0:10                 | 342                                | 684                                    |
|   | Kicker magnet       | 1:58                 | 185                                | 557                                    |
| <b>Water System</b>                           |                     | 1:20                 | 120                                |  |
|   | Water pump          | 0:29                 | 245                                | 29506                                  |
| <b>Vacuum System</b>                          |                     | 0:48                 | 77                                 |  |
|   | Ion pump            | 0:29                 | 101                                | 25308                                  |

Table 4. Some results of the reliability investigation of subsystems and components

The MTBF for the klystron assembly calculated from the raw data corresponds to the entire 805 RF system consisting of 44 klystron assemblies. An estimate of the MTBF for an individual klystron assembly was obtained by multiplying this value by 44 as 11560 hours. This value is not unreasonable when compared with the 20-50,000 hours commonly quoted for the typical klystron tube by itself. A total of 800 dc magnets exist in the LANSCE facility. MTBF for a single magnet is 232280 hours ( $\approx 26$  years). The dc magnets at LANSCE are very reliable. This is also confirmed by maintenance personnel at LANSCE. 50% of the magnet failures are water cooling problems inside the magnet. The most frequent failure cause in a magnet power supply is malfunctioning electronic equipment. Most of the power supplies at LANSCE are controlled by manual electronics. Modern power supplies are computer controlled and proves to be much more reliable. MDT for a water pump is 29 minutes and MTBF is 29500 hours ( $\approx 3$  years). MDT for an ion pump is 29 minutes and MTBF is 25300 hours ( $\approx 3$  years).

**Failure analysis**

Analysis of failure causes is performed for all major systems. In this section the failure analysis of the rf system is illustrated. In figure 7, the distribution of trips in the rf system is presented. In figure 8, on a deeper level, the distribution of trips in the klystron assembly is presented.

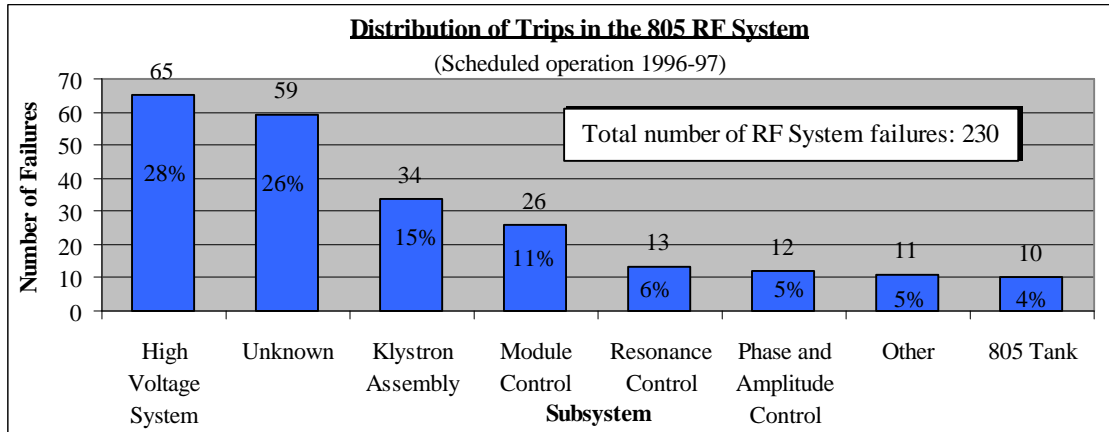


Figure 7. Distribution of trips in the 805 rf system

All subsystems of the 805 rf system are represented in figure 7. The High Voltage System causes many short interruptions. Usually the High Voltage system causes phase or amplitude disturbances to the beam. 26% of the failures in the rf system are unknown. Sometimes when a failure occurs in the rf system it is not possible to point out any specific subsystem (but it is known that the failure occurred in the rf system!). 15% of the failures in the rf system are caused by the klystron assembly. In figure 8, typical failure causes in the klystron assembly are presented.

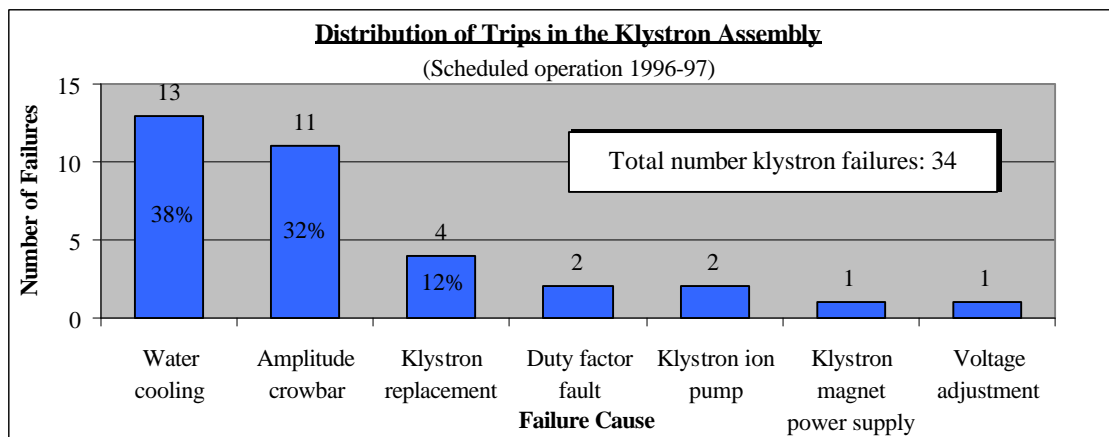


Figure 8. Failure causes in the Klystron Assembly

The klystron assembly includes some other components beside the klystron tube, for example an ion pump, a klystron magnet etc. 38% of all failures in the klystron assembly are water cooling problems and 32% are amplitude crowbars. Amplitude crowbars are usually electric sparking in the klystron tube or switchtube (and this may be due to an old switchtube). Most of the downtime occurs when klystron replacement is necessary. During scheduled operation of 1996-97, four klystron replacements occurred.

## Conclusions

Operational statistics of the powerful 1.25 mA H<sup>+</sup> beam at LANSCE has been obtained using the accelerator logbook and beam monitor data. When the beam current is inspected over a long period of time (2800 hours), on average 2.4 trips/hour or 60 trips per day are registered. Approximately 75% of all trips are 0-1 minute long. The typical down time of a beam trip is 15-20 seconds.

In the overall reliability balance of the entire LANSCE accelerator, the injector is responsible for most of the trip events. The injector is accountable for 77 % of all trips in the H<sup>+</sup> beam. The injector is primarily generating short trips. For long down times (>5 min) the rf system is the largest producer of trips. Upgrading the injector will result in a more stable beam with less interruptions, especially short ones. Upgrading the rf system will result in a better beam availability.

In summary, as a result of the investigation of individual systems, estimates for both MTBF and MDT were obtained for several typical accelerator components: DC magnet power supplies, DC magnets, klystron assemblies, HV power supplies, vacuum system, and water system. The results will be useful in developing preliminary estimates for reliability, availability, and maintainability of high power accelerator systems planned in the future. However, before we can fully trust them, they have to be corroborated through comparison with statistics obtained from other facilities. The impact of maintenance activities outside of the scheduled production time needs to be tracked down and included in the estimates as well.

## Acknowledgement

The generous assistance of many LANSCE Operations Personnel in performing this work is greatly appreciated. Special thanks are due to Michael Oothoudt and Tim Callaway of LANSCE-6. Also, special thanks are due to Stan Cohen of LANSCE-6 for valuable help with magnet power supplies and John Lyles of LANSCE-5 for help with RF Technology.

## References

- [1] Marcus Eriksson, "Reliability Assessment of the LANSCE Accelerator System", M.Sc. thesis at the Royal Institute of Technology, Stockholm, 1998.
- [2] Olin van Dyck, "LAMPF Reliability History and Program", International Conference on Accelerator-driven Transmutation Technologies and Applications, Las Vegas, 1994.
- [3] Michael Oothoudt, "Availability for cycle 75", LANSCE-6 Technical Report LANSCE-6-97-51-TR, 1997





**KTH Engineering Sciences**

# **Source efficiency and high-energy neutronics in accelerator-driven systems**

**Per Seltborg**

**Doctoral Thesis**

**Department of Nuclear and Reactor Physics  
Royal Institute of Technology  
Stockholm 2005**

Akademisk avhandling som med tillstånd av Kungl Tekniska Högskolan framlägges till offentlig granskning för avläggande av teknisk doktorexamen fredagen den 30 september 2005 kl 14.00 i sal FA32, Albanova universitetscentrum, Roslagstullsbacken 21, Stockholm.

ISBN 91-7178-147-1

TRITA-FYS 2005:46

ISSN 0280-316X

ISRN KTH/FYS/--05:46--SE

© Per Seltborg, September 2005

Universitetsservice US-AB  
Stockholm 2005

# Abstract

Transmutation of plutonium and minor actinides in accelerator-driven systems (ADS) is being envisaged for the purpose of reducing the long-term radiotoxic inventory of spent nuclear reactor fuel. For this reason, the physics of sub-critical systems are being studied in several different experimental programs across the world. Three of these experiments have been studied within the scope of the present thesis; the MUSE experiments in France, the Yalina experiments in Belarus and the SAD experiments in Russia.

The investigations of the MUSE experiments have focused on three different neutronic parameters; the neutron energy spectrum, the external neutron source efficiency and the dynamic neutron source response. It has been shown that the choice of external neutron source has negligible effect on the neutron energy spectrum in the core. Therefore, from this point of view, the MUSE experiments can be considered representative of an ADS. From the analyses of different reactivity determination methods in the Yalina experiments, it can be concluded that the slope fit method gives results in good agreement with the results obtained by the Monte Carlo method MCNP. Moreover, it was found that the Sjöstrand method underestimates  $k_{eff}$  slightly, in comparison with MCNP and the other investigated methods. In the radiation shielding studies of the SAD experiments, it was shown that the entire part of the effective dose detected at the top of the biological shielding originates from the proton-induced spallation reactions in the target. Thus, it can be concluded that the effective dose is directly proportional to the proton beam power, but independent of the reactivity of the sub-critical core.

In order to study the energy gain of an ADS, i.e., the core power divided by the proton beam power, the proton source efficiency,  $\psi^*$ , has been studied for various ADS models.  $\psi^*$  is defined in analogy with the neutron source efficiency,  $\varphi^*$ , but relates the core power directly to the source protons instead of to the source neutrons.  $\varphi^*$  is commonly used in the physics of sub-critical systems, driven by any external neutron source (spallation source, (D,D), (D,T),  $^{252}\text{Cf}$  spontaneous fission etc.). On the contrary,  $\psi^*$  has been defined only for ADS studies, where the system is driven by a proton-induced spallation source. The main advantages of using  $\psi^*$  instead of  $\varphi^*$  are that the way of defining the external source is unique and that  $\psi^*$  is proportional to the energy gain. An important part of this thesis has been devoted to studies of  $\psi^*$  as a function of different system parameters, thereby providing a basis for an ADS design with optimal properties for obtaining a high core power over beam power ratio. For instance,  $\psi^*$  was found to decrease considerably with increasing spallation target radius.

# List of Publications

The following papers are included in this thesis;

- I. P. Seltborg and R. Jacqmin, “Investigation of neutron source effects in sub-critical media and application to a model of the MUSE-4 experiments”, International Meeting on Mathematical Methods for Nuclear Applications, Mathematics and Computation, September 9-13, 2001, Salt Lake City, Utah, USA (2001).
- II. P. Seltborg, J. Wallenius, K. Tucek and W. Gudowski, “Definition and application of proton source efficiency in accelerator driven systems”, *Nuclear Science and Engineering*, **145**, 390-399 (2003).
- III. P. Seltborg, A. Polanski, S. Petrochenkov, A. Lopatkin, Waclaw Gudowski and V. Shvetsov, “Radiation shielding of high-energy neutrons in SAD”, *Nuclear Instruments and Methods in Physics Research*, **A550**, 313-328, (2005).
- IV. P. Seltborg and Jan Wallenius, “Proton source efficiency for heterogeneous distribution of actinides in the core of an accelerator-driven system”, *Nuclear Science and Engineering*, submitted for publication (2005).
- V. C-M Persson, P. Seltborg et al., ”Analysis of reactivity determination methods in the sub-critical experiment Yalina”, *Nuclear Instruments and Methods in Physics Research, A*, accepted for publication (2005).
- VI. D. Westlén and P. Seltborg, “Source efficiency studies in gas- and lead-bismuth-cooled sub-critical accelerator-driven cores”, *Annals of Nuclear Energy*, submitted for publication (2005).

## Author’s contribution

The author of the thesis is the principal author and has had the main responsibility for **Papers I-IV**. He took active part in **Paper V** as a direct supervisor, assisting in the development of the theoretical framework, the computer simulations, the results analyses and the writing of the manuscript. In **Paper VI**, the author participated mainly in the theoretical preparations and the interpretations of the results.

The following papers are not included in this thesis;

- VII. P. Seltborg and R. Jacqmin, “Spallation neutron source effects in a sub-critical system”, International Meeting AccApp'01, November 11-15, 2001, Reno, Nevada, USA (2001).
- VIII. P. Seltborg and J. Wallenius, “Proton source efficiency for inert matrix fuels in accelerator-driven systems”, International Meeting AccApp'03, June 1-5, 2003, San Diego, California, USA (2003).
- IX. P. Seltborg and J. Wallenius, “Impact of heterogeneous Cm-distribution on proton source efficiency in accelerator-driven systems”, International Meeting PHYSOR'04, April 25-29, 2004, Chicago, Illinois, USA (2004).
- X. P. Seltborg, A. Lopatkin, Waclaw Gudowski, V. Shvetsov and A. Polanski, “Investigation of radiation fields outside the sub-critical assembly in Dubna”, International Conference on Radiation Shielding ICRS-10, May 9-14 2004, Funchal, Madeira Island, Portugal (2004).
- XI. C-M Persson, P. Seltborg et al., ”Comparison of neutron kinetic parameters of the sub-critical ADS experiments Yalina and Yalina Booster”, International Meeting ICENES 2005, August 21-26, Brussels, Belgium (2005).
- XII. D. Westlén, P. Seltborg and J. Wallenius, “Source efficiency in gas- and lead-bismuth-cooled subcritical cores”, International Meeting AccApp'05, August 29 – September 1, Venice, Italy (2005).
- XIII. P. Seltborg, A. Polanski, S. Petrochenkov, A. Lopatkin, Waclaw Gudowski and V. Shvetsov, “Radiation shielding design studies of the accelerator-driven System demonstrator SAD”, International Conference GLOBAL'05, October 9-13, Tsukuba, Japan (2005).

# Abbreviations

|            |   |
|------------|---|
| ABWR       | Advanced Boiling Water Reactor  |
| AC         | Alternating Current   |
| ACER       | Calculational routine in the NJOY code, also nuclear data format for Monte Carlo codes  |
| ADS        | Accelerator-Driven Systems  |
| AGR        | Advanced Gas-cooled Reactor   |
| ALINA      | Reprocessing technique for separating actinides from lanthanides  |
| ATALANTE   | ATelier Alpha et Laboratoires pour ANalyses, Transuraniens et Etudes de retraitement  |
| ATW        | Accelerator-driven Transmutation of Waste   |
| BISTRO     | Two-dimensional transport code, used by ERANOS  |
| BTP        | Bis-Triazinyl-Pyridine, an organic extractant   |
| BWR        | Boiling Water Reactor   |
| CEA        | Commissariat à l’Energie Atomique (The French Atomic Energy Commission)   |
| CEM        | Cascade Exciton Model   |
| CERCER     | CERamic-CERamic composites  |
| CERMET     | CERamic-METal composites  |
| CERN       | Centre Européen pour la Recherche Nucléaire (The European Organisation for Nuclear Research)  |
| CIEMAT     | Centro de Investigaciones Energéticas, Medioambientales y Tecnológicas (The Spanish Research Centre for Energy, Environment and Technology) |
| CNRS       | Centre National de la Recherche Scientifique (The French National Council for Scientific Research)  |
| CYANEX 301 | Bis-(2,4,4-trimethylpentyl) dithiophosphinic acid, an organic extractant  |
| DIAMEX     | DIAMide EXtraction process  |
| DIDPA      | Di-IsoDecylPhosphoric Acid  |
| DPA        | Displacement Per Atom   |
| DTL        | Drift Tube Linac  |
| ECCO       | European Cell COde  |
| ECR        | Electron Cyclotron Resonance  |
| EDC        | Effective Dose Coefficient  |
| EFTTRA     | Experimental Feasibility for Targets and TRAnsmutation  |
| ENDF       | Evaluated Neutron Data File   |

|         |  |
|---------|--|
| ERALIB1 | ERAnos LIBrary   |
| ERANOS  | European Reactor ANalysis Optimized System   |
| ESS     | European Spallation Source   |
| FBR     | Fast Breeder Reactor   |
| FEAT    | First Energy Amplifier Test  |
| FLUKA   | FLUctuating KAscade simulation program   |
| FR      | Fast Reactor   |
| FZK     | Forschungszentrum Karlsruhe  |
| GCR     | Gas-cooled Reactor   |
| GENEPI  | GEnerateur de NEutrons Pulsés Intenses   |
| GSI     | Gesellschaft für SchwerIonenforschung (Institute for Heavy Ion Research in Darmstadt, Germany) |
| HETC    | High Energy Transport Code   |
| HLLW    | High Level Liquid Waste  |
| HLM     | Heavy Liquid Metal   |
| HPPA    | High Power Proton Accelerator  |
| IAEA    | International Atomic Energy Agency   |
| ICRP    | International Commission on Radiological Protection  |
| ICRU    | International Commission on Radiation Units  |
| INC     | IntraNuclear Cascade model   |
| INCL    | IntraNuclear Cascade Liege   |
| INL     | Idaho National Laboratory  |
| INL     | Idaho National Laboratory  |
| ISABEL  | An INC model   |
| ISN     | Institut des Sciences Nucléaires (The French National Institute for Nuclear Physics)           |
| ITU-JRC | Institute for Transuranium Elements - Joint Research Centre (European Commission)              |
| JAERI   | Japan Atomic Energy Research Institute   |
| JEF     | Joint Evaluated File   |
| JEFF    | Joint Evaluated Fission and Fusion file  |
| JENDL   | Japanese Evaluated Nuclear Data Library  |
| JINR    | Joint Institute for Nuclear Research   |
| KEK     | High-energy accelerator research organization (Japan)  |
| KTH     | Kungliga Tekniska Högskolan (Royal institute of Technology, Sweden)                            |
| LA150   | Los Alamos 150, High-energy data file  |
| LAHET   | Los Alamos High Energy Transport code system   |
| LANL    | Los Alamos National Laboratory   |
| LANSCE  | Los Alamos Neutron Science Center  |
| LBE     | Lead-Bismuth Eutectic  |
| LEDA    | Low Energy Demonstration Accelerator   |
| LINAC   | LINear ACcelerator   |
| LWGR    | Light-Water Graphite Reactor   |

|              |   |
|--------------|---|
| LWR          | Light-Water Reactor   |
| MA           | Minor Actinide  |
| MASURCA      | MAquette SURgénératrice de CAdarache  |
| MCNP         | Monte Carlo N-Particle transport code   |
| MCNPX        | Monte Carlo N-Particle Extended   |
| MEGAPIE      | MEGAWatt PIlot Experiment   |
| MOX          | Mixed Oxide fuel  |
| MPM          | Multistage Pre-equilibrium Model  |
| MSM          | Modified Source Method  |
| MUSE         | MULTiplication of External Source   |
| MYRRHA       | Multi-purpose hYbrid Research Reactor for High-tech Applica-<br>tions                               |
| NJOY         | A nuclear data processing computer code   |
| OECD         | Organization for Economic Cooperation and Development (Paris,<br>France)                            |
| ORNL         | Oak Ridge National Laboratory (USA)   |
| PDS-XADS     | Preliminary Design Studies of an XADS   |
| PHTLIB       | PHoTon LIBrary  |
| PHWR         | Pressurised Heavy Water Reactor   |
| PSI          | Paul Scherrer Institute   |
| PUREX        | Plutonium and Uranium Recovery by EXtraction  |
| PWR          | Pressurised Water Reactor   |
| RAL          | Rutherford Appleton Laboratory  |
| RF           | Radio-Frequency   |
| RFQ          | Radio-Frequency Quadrupole  |
| SAD          | Sub-critical Assembly in Dubna  |
| SANEX        | Selective ActiNides(III) EXtraction   |
| SCRF         | Super-Conducting Radio-Frequency  |
| SESAME       | Selective Extracting Separation of Americium by Means of Elec-<br>trolysis                          |
| SINQ         | Schweizer Institut für Nuklearforschung Quelle (Swiss spallation<br>neutron source)                 |
| SNR300       | Schneller Natriumgekühlter Reaktor (German fast sodium-cooled<br>reactor)                           |
| SNS          | Spallation Neutron Source   |
| SODERN/GENIE | 14 MeV Neutron Generator, using the (D,T)-reaction  |
| SPX          | SuperPheniX   |
| TALSPEAK     | Trivalent Actinide-Lanthanide Separation by Phosphorus reagent<br>Extraction from Aqueous Complexes |
| TBP          | Tri-Butyl-Phosphate   |
| TIERCE       | A high-energy particle transport code system  |
| TRASCO       | TRASmutazione SCORie (a research project for the design of an<br>ADS)                               |
| TRPO         | TRialkyl Phosphine Oxide  |



|       |   |
|-------|---|
| TRU   | TRansUranic elements  |
| TRUEX | TRansUranium EXtraction                                     |
| UOX   | Uranium OXide fuel  |
| WWER  | Water-cooled Water-moderated power Reactor (Russian design) |
| XADS  | Experimental Accelerator-Driven System                      |
| XADT  | Experimental Accelerator-Driven Transmuter                  |

# Acknowledgements

I am indebted to several people for their contributions to this thesis. I should like to particularly express my gratitude to some of them here. I thank;

Waclaw Gudowski, for his encouragement, support and supervision, and for always providing prompt and straight answers and advice.

Jan Wallenius, for his skilful guidance and many productive technical ideas.

Robert Jacqmin for his proficient supervision during my one-year stay at CEA/Cadarache.

Mikael Jolkkonen, Daniel Westlén and Carl-Magnus Persson for proofreading the thesis manuscript, as well as my brother-in-law, Alan, for his linguistic advice.

Everybody in the Reactor Physics group for providing a friendly and stimulating daily working environment.

My dear parents, Hans and Margaretha, for supporting me in all situations and for providing me with such propitious genes.

My beloved wife, Sara, for being on my side and for continuously captivating me with her cleverness, beauty and kindness.

My two adorable daughters, Lea and Ella, for their warm, searching hearts and their vivid zest for life.

I also acknowledge the financial support for this thesis project from the Swedish Centre for Nuclear Technology (SKC), SKB AB (Swedish Nuclear Fuel and Waste Management Co), CEA/Cadarache (France) and the European Commission (Project MUSE: FIKW-CT-2000-00063).

*Per Seltborg*

Stockholm 2005

# Contents

|          |  |           |
|----------|--|-----------|
| <b>1</b> | <b>Introduction</b>  | <b>1</b>  |
| <b>2</b> | <b>Transmutation of nuclear waste</b>                              | <b>5</b>  |
| 2.1      | Nuclear waste .....  | 5         |
| 2.2      | Partitioning and transmutation.....                                | 8         |
| 2.3      | Reprocessing technologies .....                                    | 18        |
| <b>3</b> | <b>Accelerator-driven systems</b>                                  | <b>23</b> |
| 3.1      | Introduction .....   | 23        |
| 3.2      | Fuel options .....   | 24        |
| 3.3      | Coolant options.....   | 26        |
| 3.4      | The spallation target .....  | 27        |
| 3.5      | Accelerator technology.....  | 30        |
| 3.6      | The European Roadmap for the development of ADS technologies ..... | 35        |
| <b>4</b> | <b>The simulation tools</b>  | <b>37</b> |
| 4.1      | The Monte Carlo method.....  | 37        |
| 4.2      | MCNP and MCNPX.....  | 38        |
| 4.3      | ERANOS .....   | 38        |
| 4.4      | High-energy codes and models.....                                  | 39        |
| <b>5</b> | <b>Neutron transport theory</b>                                    | <b>41</b> |
| 5.1      | The neutron transport equation.....                                | 41        |
| 5.2      | Criticality .....  | 42        |
| 5.3      | The adjoint equation .....   | 43        |
| 5.4      | Neutron importance .....   | 45        |
| 5.5      | Definition of $k_{eff}$ and $k_s$ .....                            | 46        |
| <b>6</b> | <b>Source efficiency and energy gain</b>                           | <b>49</b> |
| 6.1      | Neutron source efficiency.....                                     | 49        |
| 6.2      | Proton source efficiency .....                                     | 53        |
| 6.3      | Energy gain.....   | 55        |
| <b>7</b> | <b>The MUSE experiments</b>  | <b>61</b> |
| 7.1      | The MUSE experiments .....   | 61        |
| 7.2      | Neutron energy spectra.....  | 67        |
| 7.3      | Neutron source efficiency.....                                     | 73        |
| 7.4      | Reactivity determination.....                                      | 74        |

|           |  |            |
|-----------|--|------------|
| 7.5       | Replacement of sodium coolant by lead coolant.....                           | 76         |
| <b>8</b>  | <b>The Yalina experiments</b>  | <b>79</b>  |
| 8.1       | The Yalina facility.....   | 79         |
| 8.2       | Dynamic experiments performed at Yalina.....                                 | 81         |
| 8.3       | Other reactivity determination methods.....                                  | 85         |
| 8.4       | Conclusions.....   | 87         |
| <b>9</b>  | <b>The SAD experiments</b>   | <b>89</b>  |
| 9.1       | The SAD experiments.....   | 89         |
| 9.2       | Core simulations.....  | 93         |
| 9.3       | Radiation shielding of high-energy neutrons in SAD.....                      | 96         |
| <b>10</b> | <b>Summary of studies of proton source efficiency</b>                        | <b>103</b> |
| 10.1      | Model I.....   | 103        |
| 10.2      | Model II.....  | 111        |
| 10.3      | Model III.....   | 113        |
| <b>11</b> | <b>Abstracts of papers</b>   | <b>117</b> |
| 11.1      | Paper I.....   | 117        |
| 11.2      | Paper II.....  | 117        |
| 11.3      | Paper III.....   | 118        |
| 11.4      | Paper IV.....  | 118        |
| 11.5      | Paper V.....   | 119        |
| 11.6      | Paper VI.....  | 119        |
| <b>12</b> | <b>Conclusions</b>   | <b>121</b> |
|           | <b>Appendix A: Production facts of nuclear power</b>                         | <b>123</b> |
|           | <b>Appendix B: Derivation of an equation for the total core power in ADS</b> | <b>125</b> |
|           | <b>Appendix C: Fluence-to-effective dose conversion coefficients</b>         | <b>127</b> |
|           | <b>References</b>  | <b>129</b> |

# Chapter 1

## Introduction

The growing stockpiles of radiotoxic nuclear waste accumulated over the years by the operation of existing nuclear reactors are a matter of public concern. Different options of how to deal with this growing problem are investigated, transmutation in accelerator-driven systems (ADS) being one of them [1,2,3,4]. In principle, the sub-criticality of ADS allows for much higher concentrations of minor actinides (MA) in the core than is acceptable in critical reactors. In combination with appropriate reprocessing of the spent fuel, the use of ADS could become an efficient mean for reducing the long-term radiotoxicity of the nuclear waste. Calculations show that by recycling of plutonium, americium and curium, a reduction factor of about 100 is theoretically possible [5].

In an ADS, a sub-critical core is coupled to a high-power proton accelerator. The high-energy protons ( $E \sim 1000$  MeV) impinge on a target of heavy metal, generating a large number of neutrons via spallation reactions. The produced spallation neutrons leak out from the target, thus providing the surrounding sub-critical core with a strong external neutron source. The new and advanced technologies of accelerator-driven systems are being thoroughly investigated worldwide and the optimal choices among many design options are still open questions. Several independent areas, such as core coolant studies, the spallation module, the accelerator technology and the reprocessing and fuel fabrication technologies will need many years of development before they could be implemented in a large-scale industrial ADS. A general introduction to transmutation of nuclear waste and accelerator-driven systems, as well as a description of the status of some of the related research areas under development are presented in Chapter 2 and Chapter 3. In Chapter 4, a brief description of the simulation tools used in this thesis, primarily the Monte Carlo codes MCNP [6] and MCNPX [7], is given.

One of the objectives when designing an ADS is to strive for as high power as possible to be produced in the core, using as low proton beam power as possible. Since the construction of a reliable high-power proton accelerator is an extremely difficult technical task and its operation is very expensive, the optimisation of the energy gain could have an important impact on the overall design of a future ADS and on the economy of its operation. Naturally, this optimisation must be achieved in conjunction with the various safety constraints as well as other technical and physical conditions. The neutron source efficiency parameter [8,9],  $\phi^*$ , is related to

the total energy released by fission in the core and, for constant neutron source intensity and a fixed reactivity level, it is proportional to the core power. Therefore,  $\phi^*$  is commonly used to study the ratio of the core power over the external source power. The source efficiency is dependent on several different system parameters, such as target radius, coolant material, fuel composition and proton energy.

In an ADS, the source particles are protons, which produce neutrons in the target via spallation reactions. In order to calculate  $\phi^*$  in such a system, the external neutron source first has to be defined and then the efficiency of this neutron source can be determined. A problem associated with  $\phi^*$  in this context is that the external neutron source can be defined in different ways, leading to different results. Indeed, different groups in the ADS field studying  $\phi^*$  do use different source definitions [**Paper VII**,10,11,12], which in many cases makes results from different studies difficult to compare. Another drawback with  $\phi^*$  may appear when it is studied as a function of different system parameters. If a certain system parameter, e.g., the target radius, is changed, the neutron source distribution and the number of source neutrons per incident proton,  $Z$ , may also change, which consequently would alter the initial conditions for the study. In order to represent the energy gain in this case,  $\phi^*$  needs to be multiplied by  $Z$ .

In contrast to the source neutrons, which have no uniquely defined beginning of life, the appearance of the source protons can only be approached in one way. For the purpose of studying the source efficiency and the energy gain in ADS, a new parameter,  $\psi^*$ , which refers to the source *protons* instead of to the source *neutrons*, has been introduced [**Paper II**].  $\psi^*$  thus relates the core power directly to the proton beam. The advantages of using the proton source efficiency instead of the neutron source efficiency is that there is no ambiguity in how to define the external source and that it is proportional to the energy gain, without the need of a weighting factor ( $Z$ ). In Chapter 5, the basics of neutron transport theory providing the underlying theoretical framework for the concepts of source efficiency in an ADS is presented. The definitions of the neutron source efficiency and the proton source efficiency are then described and discussed in Chapter 6.  $\psi^*$  has been studied as a function of several different system parameters, such as target radius, coolant material, axial proton beam impact, proton energy, fuel composition, geometrical distribution of actinides and choice of inert matrix. In the end of the present thesis, in Chapter 10, a summary of the most important investigations of the proton source efficiency of an ADS, performed within the scope of this thesis, is given.

Several different experimental programs around the world are devoted to the development of ADS, one of them being the MUSE (MULTiplication of External Source) experiments carried out in Cadarache, France. The recently completed phase of this project was the MUSE-4 program [13,14], which started in 2000 via the 5th Framework Programme of the European Community and where detailed analyses of the neutronics of a source-driven sub-critical system were performed. The accurate measurements that have been carried out were made possible by the coupling of the (D,D)- and (D,T)-neutron generator GENEPI [15] and the zero-power MASURCA facility, in which different sub-critical configurations could be loaded. One of the

objectives of the present thesis has been to investigate, by Monte Carlo simulation, different neutronic aspects of the sub-critical fast neutron MUSE-4 core, coupled to the external neutron source. Apart from the presence of the (D,D)- and the (D,T)-sources, a spallation source has also been simulated in order to compare some of the source characteristics of the MUSE experiments with a future spallation-driven ADS. In Chapter 7, the MUSE experiments are described and the investigations of the neutronic properties of the MUSE-4 core, in terms of energy spectrum, neutron source efficiency and dynamic neutron source response, are presented.

Another experimental program devoted to the studies of sub-critical systems, similar to MUSE, is the Yalina experiments [16,17], carried out at Minsk, Belarus. The Yalina facility consists of a thermal zero-power sub-critical core, which is also driven by a (D,D)- or a (D,T)-neutron generator. In Chapter 8, the Yalina facility and the dynamic experiments performed are presented, together with the investigations of different reactivity determination methods.

The third ADS-related experimental program that the author of this thesis has been involved in is the upcoming SAD (Sub-critical Assembly in Dubna) experiments in Dubna, Russia, which is currently in its late preparation phase [18,19]. SAD is the first medium-power (maximum 100 kWth) facility in the world coupling a high-energy proton accelerator to a sub-critical core, and with the realisation of these experiments, one step further will be taken towards the development of a large-scale industrial ADS. The numerical studies of the SAD system performed within the scope of this thesis have been focused on core neutronics, source efficiency and radiation shielding of high-energy neutrons. The SAD experimental program and some of the investigations performed for it are presented in Chapter 9.

## Chapter 2

# Transmutation of nuclear waste

## 2.1 Nuclear waste

### 2.1.1 Composition of the nuclear waste

According to the Code of Practice issued by the International Atomic Energy Agency (IAEA) [20], “radioactive waste is any material that contains or is contaminated with radionuclides at concentrations or radioactivity levels greater than the exempt quantities established by the competent authorities and for which no use is foreseen”. In the world, there are 441 operating nuclear reactors producing a total power of about 368 GW electric power, which annually generates about 8500 tons of spent fuel [21]. The estimated annual production of waste was based on a production rate of 23 tons per GWe [22]. In Appendix A, production facts of global nuclear power, sorted by reactor type and by country, are given [23]. Most of the produced nuclear waste still consists of the original uranium (~95%), while about 4% has been converted to fission products and about 1% to transuranic elements (TRU, the elements with atomic number higher than 92). The relative composition, together with the half-lives and the effective ingestion dose coefficients (EDC) [24], of uranium and the transuranic elements in representative spent light-water reactor (LWR) uranium oxide (UOX) fuel after four years of cooling are listed in Table 1. The exact amount and composition of the spent fuel varies somewhat between different discharged spent fuel assemblies, depending on the initial uranium enrichment and on the discharge burn-up. However, the magnitudes are similar for all LWR fuels, except for those containing recycled plutonium (MOX fuels).

There are mainly two families of nuclear waste that have to be disposed of; fission products and the transuranic elements. The transuranic elements are produced in nuclear reactors by neutron absorption in heavy nuclides, primarily in  $^{238}\text{U}$ . All transuranic nuclides are unstable and will disintegrate via alpha, beta or gamma decay. Further neutron captures and successive disintegrations during reactor operation generate a wide spectrum of nuclides. As an example,  $^{239}\text{Pu}$  is produced by the absorption of a neutron in  $^{238}\text{U}$ , followed by two successive  $\beta^-$ -decays. An example of a chain of reactions starting with  $^{238}\text{U}$  and producing plutonium and americium is



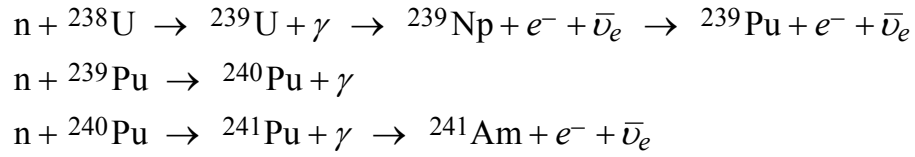


**Table 1.** Relative mass abundances of uranium, the main transuranic elements and the most important fission products in a UOX-fuel (41.2 GWd/tHM and 3.7% initial enrichment of  ${}^{235}\text{U}$ ) after 4 years of cooling [25], together with the half-lives and the effective ingestion dose coefficients for each nuclide [24].

| Element/Nuclide         | Relative mass | Half-life<br>[Years] | Effective ingestion<br>dose coefficient<br>[ $10^{-8}$ Sv/Bq] |
|-------------------------|---------------|----------------------|---|
| <b>Uranium</b>          | <b>94.6%</b>  |                      |   |
| ${}^{235}\text{U}$      | 0.8%          | $7.04 \cdot 10^8$    | 4.7   |
| ${}^{236}\text{U}$      | 0.6%          | $2.34 \cdot 10^7$    | 4.7   |
| ${}^{238}\text{U}$      | 98.6%         | $4.47 \cdot 10^9$    | 4.5   |
| <b>Neptunium</b>        | <b>0.06%</b>  |                      |   |
| ${}^{237}\text{Np}$     | 100%          | $2.14 \cdot 10^6$    | 11  |
| <b>Plutonium</b>        | <b>1.1%</b>   |                      |   |
| ${}^{238}\text{Pu}$     | 2.5%          | 87.7                 | 23  |
| ${}^{239}\text{Pu}$     | 54.2%         | $2.41 \cdot 10^4$    | 25  |
| ${}^{240}\text{Pu}$     | 23.8%         | $6.56 \cdot 10^3$    | 25  |
| ${}^{241}\text{Pu}$     | 12.6%         | 14.4                 | 0.47  |
| ${}^{242}\text{Pu}$     | 6.8%          | $3.75 \cdot 10^5$    | 24  |
| <b>Americium</b>        | <b>0.05%</b>  |                      |   |
| ${}^{241}\text{Am}$     | 63.8%         | 432                  | 20  |
| ${}^{243}\text{Am}$     | 36.0%         | $7.37 \cdot 10^3$    | 19  |
| <b>Curium</b>           | <b>0.01%</b>  |                      |   |
| ${}^{243}\text{Cm}$     | 1.0%          | 29.1                 | 15  |
| ${}^{244}\text{Cm}$     | 92.2%         | 18.1                 | 12  |
| ${}^{245}\text{Cm}$     | 5.7%          | $8.50 \cdot 10^3$    | 21  |
| ${}^{246}\text{Cm}$     | 1.1%          | $4.76 \cdot 10^3$    | 21  |
| <b>Fission products</b> | <b>4.2%</b>   |                      |   |
| ${}^{93}\text{Zr}$      | 30.6%         | $1.53 \cdot 10^6$    | 0.11  |
| ${}^{99}\text{Tc}$      | 35.2%         | $2.11 \cdot 10^5$    | 0.078   |
| ${}^{107}\text{Pd}$     | 9.5%          | $6.50 \cdot 10^6$    | 0.004   |
| ${}^{126}\text{Sn}$     | 1.1%          | $\sim 1 \cdot 10^5$  | 0.47  |
| ${}^{129}\text{I}$      | 7.4%          | $1.57 \cdot 10^7$    | 11  |
| ${}^{135}\text{Cs}$     | 16.2%         | $2.30 \cdot 10^6$    | 0.2   |

The transuranic nuclides constituting the most hazardous part of the spent fuel in the long term are generally long-lived with half-lives of up to several hundred thousand years.

The fission products, on the other hand, are created when a heavy nucleus undergoes fission and is disintegrated into two fission fragments, also releasing two or three (up to six) prompt neutrons. These fission products are generally short-lived and most of them disappear rapidly after the reactor has been shut off. However, a number of them has relatively long half-lives and remain toxic for an extended period of time.  $^{90}\text{Sr}$  and  $^{137}\text{Cs}$  have half-lives of about 30 years and are the most radiotoxic isotopes of the spent fuel during the first decades after discharge.  $^{99}\text{Tc}$ ,  $^{129}\text{I}$  and  $^{135}\text{Cs}$  have half-lives longer than 100 000 years and, although much less toxic, might possibly turn out to be a potential problem in the very long run. The half-lives and effective ingestion dose coefficients of the most hazardous fission products are listed in Table 1.

### 2.1.2 Radiotoxic inventory

The activity of an unstable isotope is defined as the number of disintegrations per second and is measured in units of Becquerel (Bq). However, in order to better express the harmful potential of the uptake of certain isotopes by humans, the concept of radiotoxicity is used. To convert the activity of the inhaled or ingested radionuclide, it has to be multiplied by a so-called effective dose coefficient (EDC), expressed in Sieverts per Becquerel (Sv/Bq), where Sv is the unit describing the biological effect of radiation deposited in an organism. The EDC is thus a measure of the damage a radionuclide would do to the body, taking into account factors such as the metabolism of the nuclides in the organism, the type and energy of the radiation emitted in the body, tissue-weighting factors etc. In general, the EDC are several orders of magnitude higher for the actinides than for the fission products. The EDC are published and regularly updated by the International Commission on Radiological Protection (ICRP) [24].

The overall radiotoxicity of the spent fuel obviously decreases with time, as the radioactive nuclides decay. The evolution over time of the radiotoxic inventory is depicted in Fig. 1, showing the different contributions from the transuranic nuclides and the fission products. It is seen that the contribution from the fission products dominates the radiotoxicity during the first 30 or 40 years after discharge. Thereafter, it decreases relatively rapidly, along with the decay of  $^{90}\text{Sr}$  and  $^{137}\text{Cs}$ , and becomes negligible after a few hundred years. For time periods longer than that, the transuranic elements govern completely the radiotoxicity, with the largest contribution coming from the plutonium isotopes and  $^{241}\text{Am}$ .  $^{241}\text{Am}$  is the decay product of  $^{241}\text{Pu}$  and represents the major part of the radiotoxic inventory in the time span between about 50 and 2000 years. After that,  $^{239}\text{Pu}$  and  $^{240}\text{Pu}$  are the main contributors to the radiotoxicity.

As a reference, the radiotoxicity of the spent fuel can be compared with the radiotoxicity of the amount of material in a uranium ore needed to produce the fuel. In order to produce 1 g of 3.7%  $^{235}\text{U}$ -enriched uranium oxide, approximately 7.8 g of

natural uranium is typically needed, which corresponds to a radiotoxicity level of about 20 mSv/g [25]. When deriving this number, not only the uranium isotopes have been included, but also their radioactive daughters in equilibrium concentrations. It is seen in Fig. 1 that it would take about 300 000 years for the spent fuel to decay to this level. It should be noted, though, that the abovementioned reference level of 20 mSv/g is only one of several possible ways of defining a reference radiotoxicity level and that it should not be used as an absolute measure of how long the waste will be “dangerous”. Nevertheless, it may provide a useful mean when making estimations and comparisons of the risks associated with the nuclear waste at different times. It is also indicated that the radiotoxicity of the very long-lived fission products, e.g.,  $^{99}\text{Tc}$ ,  $^{129}\text{I}$  and  $^{135}\text{Cs}$ , is well below the reference level at all times. However, while the solubility of the actinides in water is generally very low (except for  $^{237}\text{Np}$ ), these fission products show relatively high mobilities in the geosphere and therefore need to be taken into account in the study of the nuclear waste disposal.

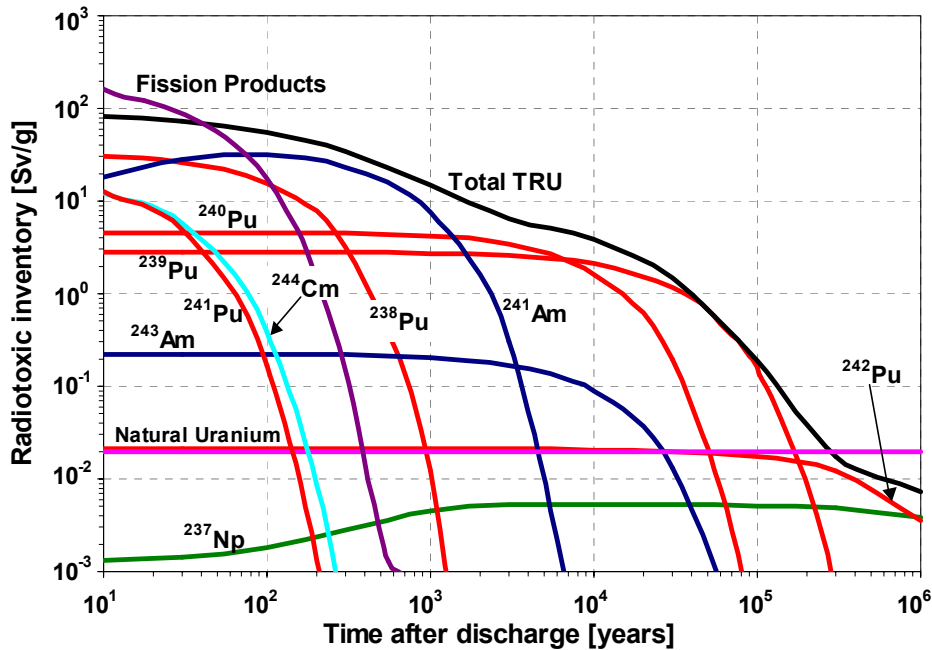


**Fig. 1.** Radiotoxic inventory, in Sv per gram spent fuel, of the most important actinides, compared with the radiotoxicity of the amount of natural uranium needed to produce 1 g of 3.7%  $^{235}\text{U}$ -enriched uranium oxide ( $\sim 20$  mSv/g).

## 2.2 Partitioning and transmutation

A prerequisite for transmutation is partitioning of the spent nuclear fuel. Partitioning means handling and separation of the actinides that are subject to transmutation, and fabrication of new fuels that will be dedicated to transmutation. Transmutation refers to the transformation of a long-lived radiotoxic nuclide into one or more short-lived

or stable products. As the transuranic elements (Np, Pu, Am and Cm) represent the largest part of the radiotoxic inventory in the long term, these elements are the main subjects of most transmutation studies. The transmutation of waste is relevant, both in the case of the continuous use of nuclear power as an important contributor to a country's electricity production, as well as in the scenario of a nuclear power phase-out.

### 2.2.1 Requirements for efficient actinide-burning

The best way to transmute the actinides is to fission them. This can be done efficiently and on a large-scale only in nuclear reactors. In principle, all types of nuclear reactors (thermal and fast, critical and sub-critical) can be used to burn the actinides, although fast reactors (FR) have some fundamental advantages over thermal reactors. The main purpose of a transmutation reactor is to reduce as much as possible the net radiotoxic inventory of the spent fuel in the long-time perspective. The basic requirements for such a reactor to be efficient are therefore maximal fissioning of actinides combined with minimal production of new actinides (via neutron capture reactions). This can be achieved by adapting the following two objectives;

- The amount of fertile material, e.g.,  $^{238}\text{U}$ , should be minimised in order to limit further TRU breeding.
- The neutron energy spectrum should be as hard as possible in order to favour fission over capture for the actinides.

Many of the actinides to be transmuted, those with even number of neutrons (even-N), have very low fission cross-sections for slow neutrons. This is due to the absence of the pairing binding energy effect in odd-N nuclides, which is the intermedi-

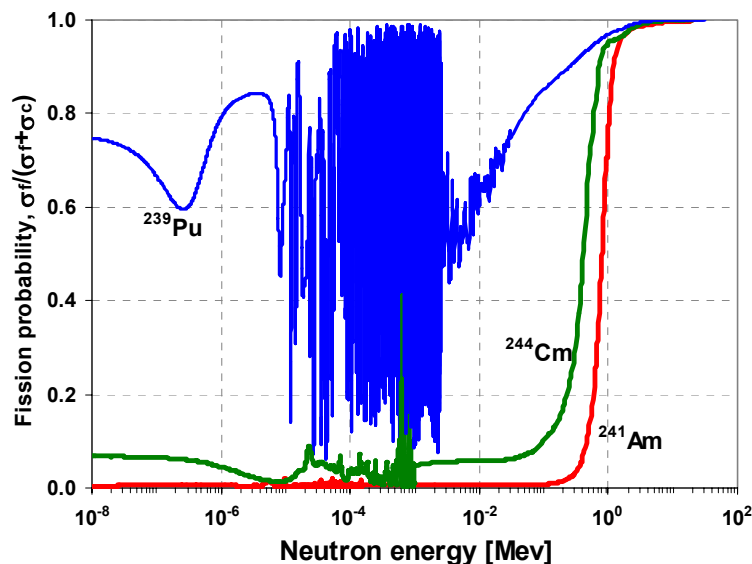


**Fig. 2.** Fission probability, i.e., microscopic fission cross-section over total microscopic absorption cross-section,  $\sigma_f/(\sigma_f + \sigma_c)$ , as a function of neutron energy for  $^{239}\text{Pu}$ ,  $^{241}\text{Am}$  and  $^{244}\text{Cm}$  (JEFF-3.0 [26]).

ate step when an even-N nuclide is fissioned by a neutron. This means that the fission probability is essentially zero for these nuclides for thermal and epi-thermal neutrons and capture is thus strongly favoured over fission. However, in the energy range between about 0.1 and 1.0 MeV, the fission cross-sections for these isotopes increase drastically, which is illustrated in Fig. 2, where the fission over absorption cross-section is displayed for  $^{239}\text{Pu}$  (even number of neutrons),  $^{241}\text{Am}$  and  $^{244}\text{Cm}$  (odd number of neutrons). The obvious conclusion from this is that fast neutron reactors enhance the burning of the transuranic elements, while thermal reactors favour the breeding of them. Another important advantage of fast reactor systems over thermal reactors is that the neutron economy is improved as the fission probability increases.

### 2.2.2 Adverse safety effects for minor actinide fuel

The removal of uranium from the fuel and the adding of minor actinides have serious negative impacts on several safety parameters. This is true for most reactor types, in particular for fast reactors. Firstly, the negative Doppler feedback, which is essential for the power control of a reactor, is significantly reduced. Secondly, the effective fraction of delayed neutrons,  $\beta_{eff}$ , is much lower for uranium-free fuels, in particular for those containing high fractions of MA. This parameter is crucial for the safe operation of a reactor, since it establishes the margin to prompt criticality. A third adverse effect, an increase in void worth, arises when the coolant material (lead, sodium or gas) in an FR is combined with high fractions of americium in the fuel.

#### Doppler feedback

It is of vital importance for the safe operation of a nuclear reactor that the fuel temperature reactivity feedback, which acts with immediate response to a power increase, is negative. All reactors existing today do have negative fuel temperature coefficients, due to the Doppler reactivity feedback. The Doppler feedback is caused by the broadening of the resonance peaks in the neutron capture cross-sections as the temperature increases and the average energy of the fuel nuclei increases. A broadening of the capture resonances leads to an altogether higher probability for capture. Thus, an increase in fuel temperature due to an increase in fission heating will cause an increase in the capture rate, which will reduce the reactivity. The Doppler feedback is primarily due to the epithermal capture resonances in the non-fissionable fuel nuclides, and it is particularly important in  $^{238}\text{U}$  (Fig. 3). Consequently, it decreases when uranium is removed from the fuel.

To solve this problem, it has been proposed to add materials with absorbing resonances in the fast neutron energy spectrum in order to restore, to some extent, the negative Doppler effect. However, if the fraction of americium is significant, this will have limited effect, even with the addition of  $^{238}\text{U}$ . The explanation of this is that, due to the high absorption cross-sections of both  $^{241}\text{Am}$  and  $^{243}\text{Am}$  for fast neutrons, most of the neutrons would be absorbed by the americium before they reach the absorption resonances in  $^{238}\text{U}$  [27], which is illustrated in Fig. 3.

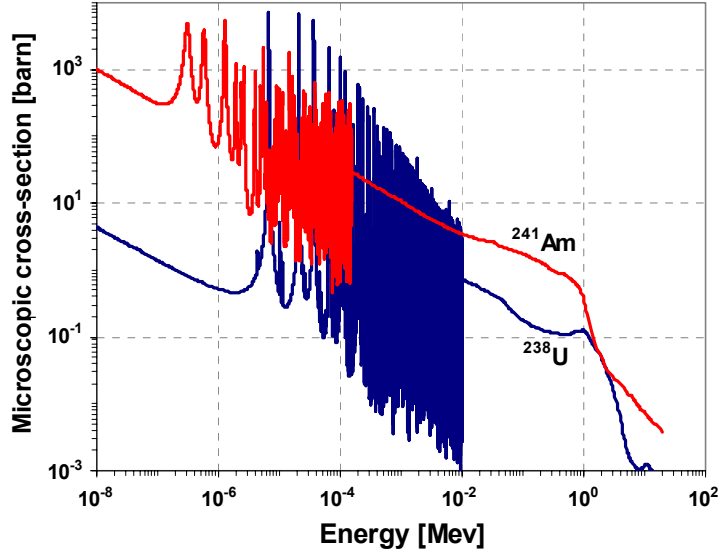


**Fig. 3.** Microscopic cross-section for neutron capture in  $^{238}\text{U}$  and  $^{241}\text{Am}$  (JEFF-3.0).

### Delayed neutrons

A small fraction of the neutrons produced in a multiplying medium comes from the decay of certain fission products, the delayed neutron precursors. These neutrons are emitted with a significant delay, compared to the prompt neutrons emitted in the fission process itself, and are therefore called delayed neutrons. Due to this delay, the dynamics of a reactor in normal operation is determined primarily by the delayed neutrons. For instance, when the fission product  $^{87}\text{Br}$  decays to  $^{87}\text{Kr}$ , the latter will immediately release one of its neutrons, which appears to be emitted with a delay of the 55.7-second half-life of  $^{87}\text{Br}$ . The delayed neutron precursors are usually divided into 6 different groups, each with its own characteristic half-life. In Table 2, the half-lives, the delayed neutron yield (per fission) for each neutron precursor group,  $\nu_{d,g}$ , and the delayed neutron fractions for each group,  $\beta_g$ , for thermal fission in  $^{235}\text{U}$  are listed.  $\beta_g$  is defined as the fraction of all neutrons released in fission that appear as delayed neutrons in group  $g$ , i.e., the absolute delayed neutron yield in group  $g$  ( $\nu_{d,g}$ ) divided by the total neutron yield,  $\nu_t$ .

The fraction of delayed neutrons over the total number of neutrons for an individual nuclide,  $\beta_i$ , is defined as

$$\beta_i = \frac{\nu_{d,i}}{\nu_{t,i}}, \quad (1)$$

where  $\nu_{d,i}$  is the average number of delayed neutrons emitted after a fission event in a specific nuclide and  $\nu_{t,i}$  is the total number of neutrons emitted ( $\nu_t = \nu_p + \nu_d$ ). In Table 3,  $\nu_{d,i}$ ,  $\nu_{t,i}$  and  $\beta_i$  for thermal neutrons are displayed for the most important actinide nuclides. It can be observed that the delayed neutron yield increases with

the atomic mass of a specific element, whereas it decreases with increasing proton number. Moreover, the average number of neutrons emitted in a fission reaction,  $\nu$ , is a nearly linearly increasing function of the energy of the incident neutron for all fissile nuclides and can in general be described by the following relation;

$$\nu(E) = \nu_0 + aE, \quad (2)$$

where  $\nu_0$  and  $a$  are constants determined experimentally for each nuclide. In Fig. 4,  $\nu$  is plotted for  $^{239}\text{Pu}$ ,  $^{241}\text{Am}$  and  $^{244}\text{Cm}$  as a function of neutron energy.

**Table 2.** Delayed neutron data for thermal fission in  $^{235}\text{U}$  [28] for each delayed neutron precursor group  $g$ . The total average neutron yield,  $\nu_t$ , for  $^{235}\text{U}$  is 2.43.

| Group | Half-life<br>[sec] | Yield <sup>a</sup><br>( $\nu_{d,g}$ ) | Fraction<br>( $\beta_g$ )     |
|-------|--------------------|---------------------------------------|-------------------------------|
| 1     | 55.72              | 0.00052                               | 0.000215                      |
| 2     | 22.72              | 0.00346                               | 0.001424                      |
| 3     | 6.22               | 0.00310                               | 0.001274                      |
| 4     | 2.30               | 0.00624                               | 0.002568                      |
| 5     | 0.610              | 0.00182                               | 0.000748                      |
| 6     | 0.230              | 0.00066                               | 0.000273                      |
|       |                    | Total yield<br>( $\nu_d$ )            | Total fraction<br>( $\beta$ ) |
|       |                    | 0.0158                                | 0.0065                        |

<sup>a</sup> Delayed neutron yield per fission.

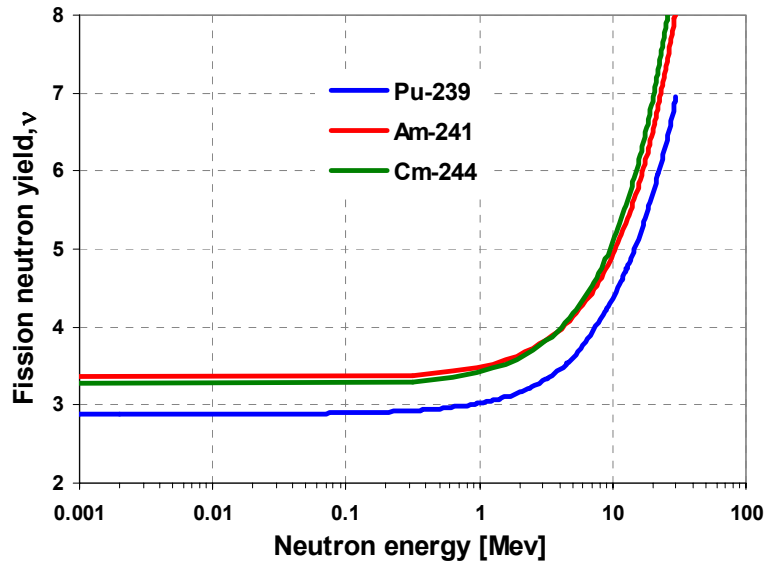


**Fig. 4.** Average number of neutrons emitted in a fission reaction,  $\nu$ , as a function of neutron energy for  $^{239}\text{Pu}$ ,  $^{241}\text{Am}$  and  $^{244}\text{Cm}$  (JEFF-3.0).

**Table 3.** Thermal delayed and total neutron yields together with delayed neutron fractions for the most important nuclides. The data are taken from the evaluated nuclear data libraries ENDF/B-6.8, JEFF-3.0 and JENDL-3.3 [29].

| Nuclide            | $\nu_{d,i}$ |        |        | $\nu_{t,i}$ |       |       | $\beta_i$ [pcm] |      |       |
|--------------------|-------------|--------|--------|-------------|-------|-------|-----------------|------|-------|
|                    | ENDF        | JEFF   | JENDL  | ENDF        | JEFF  | JENDL | ENDF            | JEFF | JENDL |
| <sup>232</sup> Th  | 0.0527      | -      | -      | 1.949       | -     | -     | 2704            | -    | -     |
| <sup>235</sup> U   | 0.0167      | 0.0167 | 0.0159 | 2.437       | 2.437 | 2.436 | 685             | 685  | 651   |
| <sup>238</sup> U   | 0.0440      | 0.0478 | 0.0463 | 2.492       | 2.489 | 2.488 | 1766            | 1920 | 1863  |
| <sup>237</sup> Np  | 0.0108      | 0.0108 | 0.0120 | 2.636       | 2.636 | 2.601 | 410             | 410  | 461   |
| <sup>238</sup> Pu  | 0.0042      | 0.0047 | 0.0047 | 2.895       | 2.895 | 2.845 | 144             | 163  | 165   |
| <sup>239</sup> Pu  | 0.0065      | 0.0065 | 0.0062 | 2.881       | 2.880 | 2.884 | 224             | 224  | 216   |
| <sup>240</sup> Pu  | 0.0090      | 0.0091 | 0.0091 | 2.803       | 2.784 | 2.784 | 321             | 327  | 327   |
| <sup>241</sup> Pu  | 0.0162      | 0.0160 | 0.0160 | 2.945       | 2.931 | 2.931 | 550             | 546  | 546   |
| <sup>242</sup> Pu  | 0.0197      | 0.0183 | 0.0183 | 2.810       | 2.860 | 2.859 | 701             | 640  | 640   |
| <sup>241</sup> Am  | 0.0043      | -      | 0.0049 | 3.239       | 3.330 | 3.060 | 132             | -    | 160   |
| <sup>242m</sup> Am | 0.0069      | 0.0069 | 0.0065 | 3.264       | 3.264 | 3.271 | 211             | 211  | 199   |
| <sup>243</sup> Am  | 0.0080      | -      | 0.0085 | 3.273       | 3.062 | 3.209 | 243             | -    | 265   |
| <sup>242</sup> Cm  | 0.0014      | 0.0014 | 0.0021 | 3.440       | 3.440 | 3.252 | 40              | 40   | 64    |
| <sup>243</sup> Cm  | 0.0030      | 0.0030 | 0.0030 | 3.432       | 3.433 | 3.432 | 88              | 88   | 88    |
| <sup>244</sup> Cm  | -           | -      | 0.0044 | 3.460       | 3.240 | 3.244 | -               | -    | 134   |
| <sup>245</sup> Cm  | 0.0064      | 0.0063 | 0.0064 | 3.596       | 3.531 | 3.596 | 178             | 178  | 178   |
| <sup>246</sup> Cm  | 0.0092      | 0.0092 | 0.0092 | 3.614       | 3.614 | 3.614 | 253             | 253  | 253   |

Moreover, the fraction of delayed neutrons averaged over the whole reactor is defined as the ratio of the number of all delayed neutrons emitted in the core,  $N_{n,d}$ , over the number of all neutrons emitted,  $N_{n,t}$  ( $N_{n,t} = N_{n,p} + N_{n,d}$ ), according to

$$\beta = \frac{N_{n,d}}{N_{n,t}} . \quad (3)$$

As  $\beta_i$  is different for different nuclides, it is evident that  $\beta$  in a reactor core can vary considerably for different nuclide compositions. For instance, replacing the uranium in a core by americium may reduce  $\beta$  by a factor of about 2 to 3.

The prompt neutrons produced in fission reactions are emitted with a Watt-distributed energy spectrum, with the maximum density at about 0.7 MeV and the mean energy at about 2 MeV. The typical prompt neutron fission spectrum, illustrated in Fig. 5, can be represented by a simple empirical expression, which, for <sup>235</sup>U, is given by [30]

$$\chi(E) = 0.453e^{-1.036E} \cdot \sinh\sqrt{2.29E} . \quad (4)$$



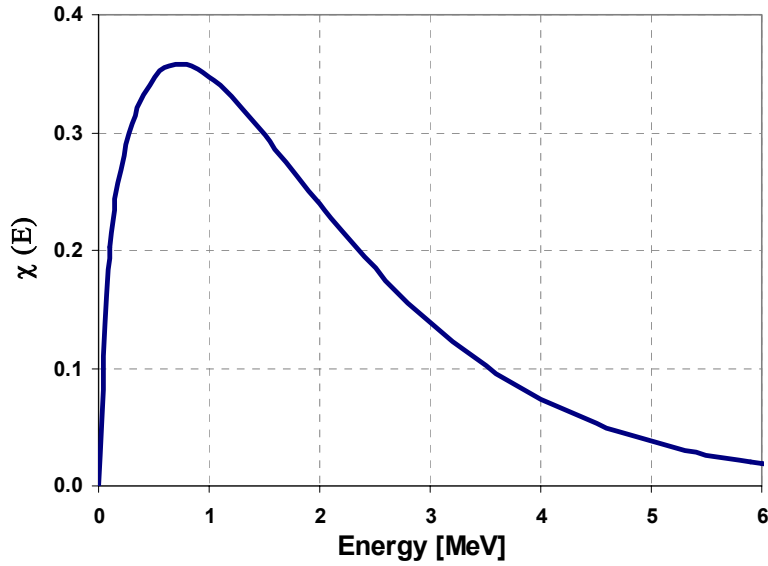


**Fig. 5.** Prompt neutron fission spectrum,  $\chi(E)$ , for  $^{235}\text{U}$  induced by thermal neutrons.

However, the energy spectrum of the delayed neutrons is considerably softer than that of the prompt fission neutrons, the maximum being located at about one or a few hundred keV, depending on the precursor energy group [31]. Since the microscopic cross-sections for all nuclides are highly energy-dependent, this may have a significant effect on the probabilities for the neutrons to induce fission. For this reason, it becomes necessary to introduce the effective delayed neutron fraction,  $\beta_{eff}$ , which is defined as the number of fission events induced by delayed neutrons,  $N_{f,d}$ , over the total number of fission events in the reactor,  $N_{f,t}$  ( $N_{f,t} = N_{f,p} + N_{f,d}$ ), i.e.,

$$\beta_{eff} = \frac{N_{f,d}}{N_{f,t}} . \quad (5)$$

In a thermal reactor, the delayed neutrons have higher probabilities to induce fission than the prompt fission neutrons, since they are emitted with energies closer to the thermal region and, thus, have smaller probability of being captured before becoming thermalised. Therefore, in that case,  $\beta_{eff}$  is larger than  $\beta$ . On the other hand, in a fast reactor, the situation may be the inversed, primarily due to the fact that the fission probability of the even-N nuclides increases considerably in the energy region between about 0.1 and 1.0 MeV. In order to analyse, by a more mathematical approach, the efficiency of the delayed neutrons relative to the efficiency of the prompt fission neutrons, one may introduce the importance function,  $\Phi^+(\mathbf{r}, \mathbf{\Omega}, E)$ , which is a measure of the probability that a neutron emitted at position  $\mathbf{r}$  with direction  $\mathbf{\Omega}$  and energy  $E$  will eventually result in a fission. The importance function, or the adjoint function, will be further treated in Chapter 5.

### 2.2.3 Different transmutation strategies

The dedicated reactors envisaged to burn the plutonium and the minor actinides could be either critical fast reactor systems or sub-critical accelerator-driven systems. However, in a critical fast reactor, even for innovative systems, the maximum fraction of MA would be limited to a few percent, the limit being determined by the safety margins. This implies that a large part of the nuclear reactor park would have to be contaminated by minor actinides. In order to overcome the safety deterioration for minor actinide-burning cores and to minimise the number of required dedicated reactors, the ADS concept has been proposed. In an ADS, a sub-critical reactor core is coupled to an intense external neutron source [1,2,3]. The fact that the reactor is sub-critical, without the self-sustained neutron multiplication chain reaction, increases considerably the margin to prompt criticality and, hence, the safety of the reactor. Thanks to the sub-criticality, the safe operation of the reactor is less dependent on the reactivity feedbacks and the delayed neutron fraction, and this allows for a much higher flexibility in choosing the desired proportions of actinides in the fuel. As the fraction of minor actinides in the fuel is more or less unlimited, the number of dedicated MA-burning reactors in the reactor park can be kept relatively small. Accelerator-driven systems will be further treated in Chapter 3.

Several different concepts concerning the handling of the nuclear waste have been proposed [22]. Six of them, depicted in Fig. 6, are briefly treated here. Some countries, including Sweden, have adopted the “once-through” cycle (Strategy 1), in which all of the discharged spent fuel is considered as waste and must be disposed of in geological repositories, although the possibility to transmute the waste at a later time, if the national policies are changed, may remain. Other countries, such as France and Japan, reprocess their spent fuel and recycle the plutonium and the uranium in LWR-reactors. Only the minor actinides and the fission products are considered as waste, which is planned to be deposited in geological repositories, or, alternatively, to be transmuted. An extension of this strategy is the plutonium-burning concept (Strategy 2), where the plutonium reprocessed from the MOX-LWR cycle is recycled indefinitely in a closed loop in fast reactors.

Concerning the transmutation of also the minor actinides, two major types of strategies have emerged. In the “mono-stratum” fuel cycle (Strategy 3), all of the waste is recycled and transmuted in conventional, albeit modified and possibly innovative, critical reactors. The other alternative is to burn the minor actinides in dedicated transmutation reactors, e.g., ADS, as in the “double strata” concept (Strategy 4). The main advantage of the double-strata fuel cycle is that only a limited number of dedicated MA-burning reactors would be needed, as low as 5-10% of an entire nuclear power plant population, whereas a significantly higher fraction of conventional critical reactors would be needed to burn the waste in the mono-stratum concept.

In the original double-strata concept, initially proposed by JAERI in 1984 [32], the plutonium (and uranium) alone is recycled in critical reactors (LWR and FR) in the first stratum, while the minor actinides are directed to the second stratum to be

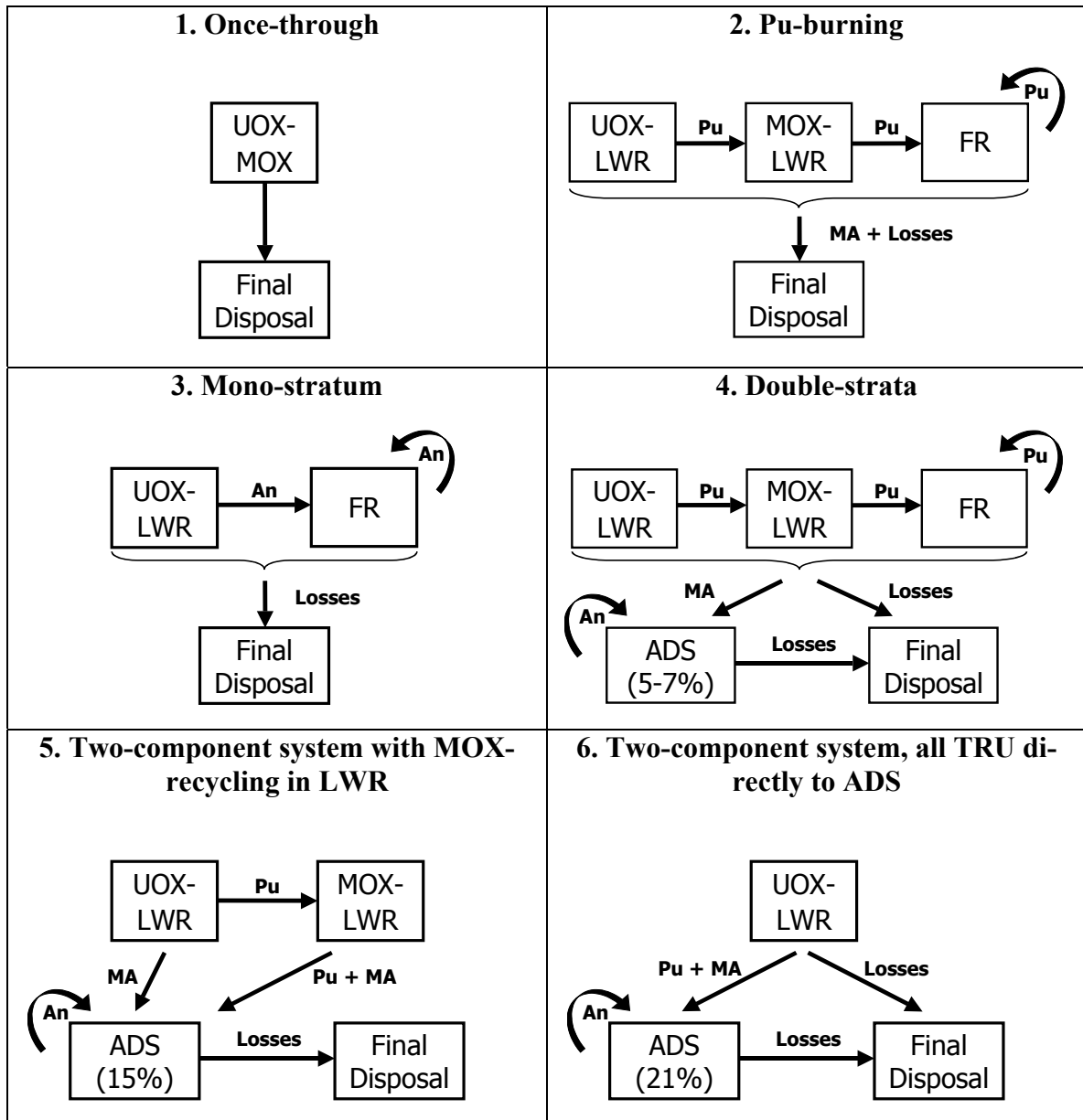


**Fig. 6.** Different fuel cycle strategies. Percentage in parentheses indicates the fraction of a nuclear power park corresponding to ADS.

burned in dedicated reactors. Stated simply, the first stratum would be dedicated mainly to electricity production and waste mass reduction, while the primary objective of the second stratum would be radiotoxicity reduction. Moreover, the first stratum is based both on conventional types of reactors and well-known reprocessing technologies. The second stratum, on the other hand, has to deal with far more complicated challenges, such as the development of the dedicated MA-burners (ADS or advanced FR), as well as the techniques of reprocessing americium and curium (involving preferably pyrochemical methods). As depicted in Fig. 6, the plutonium from the standard LWR-UOX reactors is first reprocessed and recycled (once or twice) in conventional LWR-MOX reactors. In the final stage of the first stratum,

the plutonium is recycled indefinitely in fast reactor systems in a closed cycle. All the minor actinides reprocessed in the first stratum are transferred to the second stratum, where they are recycled indefinitely. All losses from the reprocessing are considered as high-level waste and are sent to geological repositories. Calculations show that, if accelerator-driven systems are used in the second stratum, only about 5-7% of the reactor park will have to consist of dedicated MA-burning systems [1]. In the first stratum, approximately 70% of the electricity produced would be generated by conventional UOX-LWR, whereas ~11% by MOX-LWR and ~19% by FR.

Alternatively, the possibility of recycling neptunium together with plutonium in FR in the first stratum has also been considered [1]. Neptunium is a less problematic fuel material than americium and curium and could probably be burned in critical reactors. It is also more easily reprocessed and can be separated in the well-established PUREX process [33] together with plutonium. However, as the radiotoxicity of neptunium is very low (Fig. 1) (although the mobility of neptunium is higher than for the other actinides), it could also be omitted and directly disposed of. Several variations of the double-strata concept have been considered, diverging somewhat from the original proposal, depending on factors such as national policies and interests. The following two-component strategies, employing ADS in the second stratum, are possible scenarios [22];

- The plutonium produced in the LWR could be recycled once in MOX-LWR and then sent to the ADS together with the MA (Strategy 5). In this case, a fraction of 15% ADS of the reactor park would be required. As approximately 6 UOX-LWR produce the necessary actinide inventory to fabricate 1 MOX-LWR, about 12% of the reactor park would be of MOX type and the rest (~73%) of UOX type.
- All of the plutonium and the MA produced in the conventional LWR are transferred directly to the ADS (Strategy 6). This scenario would require a slightly higher fraction of ADS (~21%) than the previous scenario.

Apart from choosing the type of reactor in which to transmute the radiotoxic inventory of the spent fuel, the options of how the elements to be transmuted should be added to the rest of the fuel have to be considered. Generally, two ways to incinerate the actinides into the reactor core are investigated. Either they could be dispersed homogeneously with the rest of the fuel (homogeneous mode) or they could be isolated in specialised fuel assemblies (targets) positioned in strategic places throughout the core (heterogeneous mode). In the former case, the actinides are mixed with standard fuels. In a dedicated ADS burner, the fuel would consist of mainly (or only) TRU, which would probably be distributed homogeneously. If a strategy of the mono-stratum type is chosen, using FR to burn all TRU, the heterogeneous mode offers the advantage of reprocessing the standard fuel and the TRU-fuel separately. As a result, the target fuels could reach very high burn-up, since they do not have to be recycled with the rest of the core.

## 2.2.4 Radiotoxicity reduction

The transmutation efficiency of a nuclide is determined mainly by two basic factors, namely the burn-up in each fuel cycle and the losses from the reprocessing of the spent fuel. Assuming a maximum burn-up of 10-20% implies that, on average, each waste atom has to pass through 5-10 transmutation cycles. If, for example, a separation loss of 0.1% is assumed, which is realistic for plutonium, this means that the total cumulative losses amount to 0.5-1.0%. Consequently, the mass is reduced by a factor of 100-200. For americium and curium, the reprocessing methods are more complicated and larger separation losses can be expected.

Many different studies on transmutation scenarios have been performed, assuming different types of reactors and different fuel cycle strategies. When plutonium is recycled in LWR, as in the first step of the double-strata fuel cycle, a large amount of minor actinides are built up. Therefore, the radiotoxicity is actually increased. Considering also the indefinite recycling of plutonium in FR (but without the recycling of MA), a total radiotoxicity reduction factor of 3-6 can be achieved [5]. Hence, the plutonium recycling in the first stratum is, apart from the economical utilisation of the initial uranium resources, mainly an efficient way to reduce the mass of the spent fuel, and thus to keep the number of required MA-burning ADS low.

Recycling of also americium reduces the total radiotoxicity by a factor of about 10, but produces significant amounts of plutonium and curium. The curium production is the reason why the radiotoxicity reduction is limited by a factor of 10. In order to reach reduction factors of up to 100, curium also has to be transmuted [5]. However, the main problem with recycling of curium is that it is strongly radioactive and very hot, which complicates the reprocessing and the fuel fabrication methods. When deriving the estimated reduction factor of 100, reprocessing losses of 0.1% for plutonium and 1.0% for the MA were assumed. The radiotoxicity reduction is strongly dependent on the reprocessing losses and if they could be decreased for the MA, a reduction factor of a few hundred could possibly be achieved.

## 2.3 Reprocessing technologies

Reprocessing of nuclear spent fuel is being carried out on an industrial basis in several countries, e.g., France, United Kingdom, Japan, India and Russia. The purpose of the reprocessing is to extract the uranium and the plutonium from the discharged UOX-fuel and to recycle it as MOX-fuel. The remaining elements, the minor actinides, the fission products and the reprocessing losses, are incorporated into the vitrified high-level waste, destined for interim storage or final disposal. Discharged MOX fuel can also be reprocessed if it is diluted with standard UOX fuel. The technique used in all industrial reprocessing plants existing today is the PUREX process, which is a hydrochemical method. However, in order to recover also the minor actinides, and possibly also some of the fission products, new reprocessing technologies are required. Generally, there are two types of processes that can be applied to the reprocessing of nuclear waste; hydrochemical methods, also referred to as aqueous

or wet methods, and pyrochemical methods, also referred to as molten salt or dry methods [25,34,35].

### **2.3.1 Hydrochemical methods**

#### **The PUREX process**

The most important hydrochemical reprocessing technique to separate uranium and plutonium, and the only one used today on a commercial basis, is the PUREX process. It applies the organic extractant molecule, tri-butyl-phosphate (TBP) to extract uranium and plutonium from the spent fuel, which has been dissolved in nitric acid ( $\text{HNO}_3$ ). The TBP molecule has the property of extracting actinides with even oxidation states IV and VI from an acidic medium. The stable oxidation states in nitric acid of uranium and plutonium are VI and IV, respectively, and they are thus separated into the organic phase, while the rest of the dissolved nuclear waste remains in the aqueous phase. By changing the oxidation state of plutonium from IV to III, it can then be separated from uranium in a second purification cycle. This process is referred to as the “standard PUREX process”. The recovery yield of uranium and plutonium is high, close to 99.9%.

Neptunium has similar chemical properties to those of uranium and plutonium, but it exists in the nitric acid as a mixture of oxidation states V and VI, of which only the latter can be extracted by TBP. Hence, neptunium is only partly separated (~60%) together with the uranium and plutonium stream. This fraction is then separated from the uranium and the plutonium in the second purification cycle and added to the rest of the high-level liquid waste (HLLW). The “improved PUREX process”, on the other hand, is based on the standard process, but with improved separation of neptunium. One method of recovering all neptunium consists of using an oxidising reagent to change the oxidation state of the whole neptunium inventory to VI, allowing it to be extracted by TBP. Neptunium recovery yields of 95% have been demonstrated and improvements towards 99% are under development. Research has also shown that it is possible to extract the long-lived fission products iodine and technetium in the PUREX process.

#### **Separation of americium and curium**

Americium and curium are both trivalent ions, their stable oxidation state being III, and since they cannot be extracted by TBP in the standard PUREX process, they remain in the aqueous phase. In order to separate these elements using hydrochemical methods, new extractant molecules are needed and several innovative processes are under development. The current approach to recover americium and curium is usually divided into a three-stage process, also called the “extended PUREX process”. A flow sheet including the different processes separating the individual actinides is shown in Fig. 7. The first stage is based on the co-extraction of actinides (An) and lanthanides (Ln) from the rest of the fission products in the PUREX waste stream. One way of doing this is by using extractant agents of diamide type, which has been applied in the DIAMEX process [36], developed by CEA (France). It has been dem-

onstrated that recovery yields of 99.9% can be achieved in this process. Other processes developed (or under development) for this purpose are TALSPEAK (USA), DIDPA (Japan), TRUEX (USA) and TRPO (China).

The second stage aims at separating the actinides from the lanthanides. This separation is difficult for two main reasons. Firstly, the chemical properties of the two series of elements are very similar; importantly, they exist in nitric acid in the same oxidation state (III). Secondly, the mass ratio of Ln/An is high (in the order of 20 or higher), which indicates the need for a strongly selective mechanism in order to keep the Ln contamination low. One of the methods that has been developed to separate An from Ln is the SANEX process [37]. It utilises the fact that An(III) ions present a slightly larger extension of their electron clouds than do Ln(III) ions. It has been found that bis-triazinyl-pyridine (BTP) molecules are among the most suitable extractants for the An-Ln separation. BTP has an affinity for An(III) ions of more than a hundred times larger than that for Ln(III) ions, and the SANEX process has demonstrated a recovery yield of the actinides of up to 99.9%. Other extractants with high selectivity for actinides are used in the CYANEX 301 [38] and the ALINA processes.

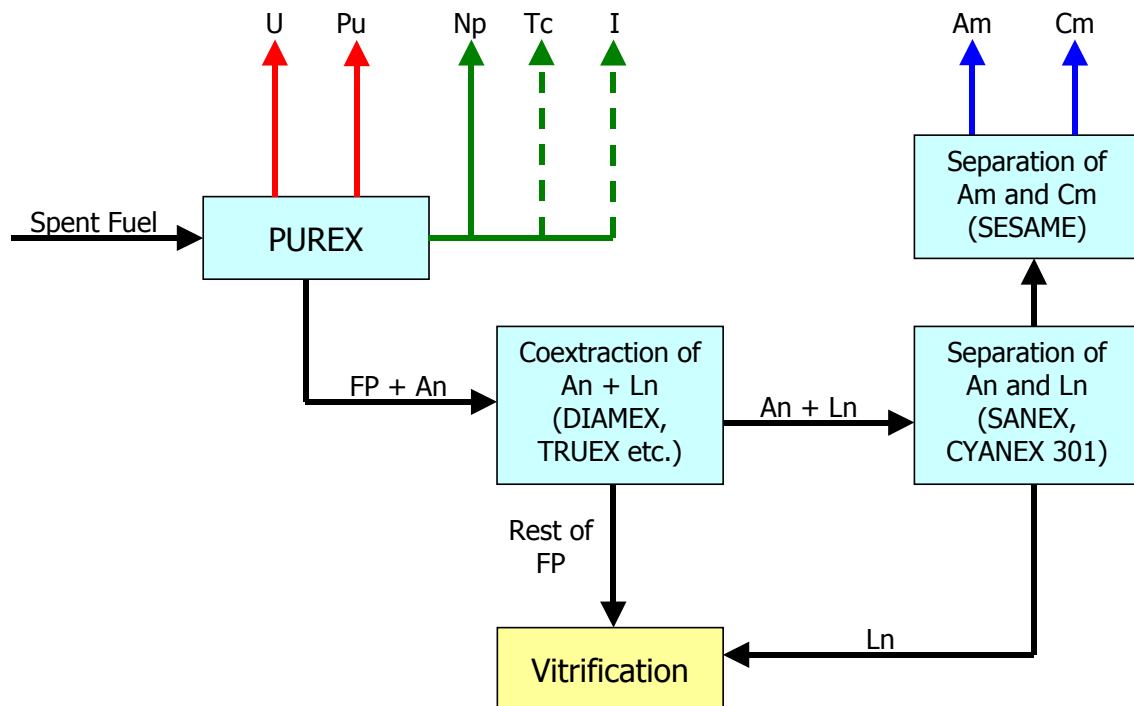


**Fig. 7.** Flow sheet of advanced hydrochemical reprocessing [34].

The separation of americium from curium can be accomplished in the third stage, if it is intended to manage these elements separately. The separation is based on the fact that americium can exist in nitric solutions in several different oxidation states, whereas this property is not shared by curium, which exists only as a trivalent ion. In the SESAME process [39], americium is oxidised to IV or VI by an electrochemical method, after which it can be selectively extracted by the TBP molecule (same ex-

tractant as in the standard PUREX process). Alternatively, the SESAME process could be used to extract americium directly from the PUREX waste stream or after the co-extraction of An and Ln. This is technically more complicated, due to the larger quantities of waste and the larger amount of different elements that have to be managed.

### **Advantages and disadvantages of hydrochemical reprocessing**

Hydrochemical reprocessing is particularly suited for large quantities of standard LWR-UOX fuels, where long cooling times are allowed. Indeed, it is being successfully used worldwide on an industrial basis, utilising the PUREX process to separate the uranium and plutonium from the nuclear waste. Moreover, the recovery yield of the other transuranic elements, using the different processes described above, have been demonstrated to be as high as up to 99.9% for both americium and curium.

However, there are some important drawbacks connected to the hydrochemical reprocessing of MA-containing fuels. The first is the limited solubility in nitric acid for many fuel forms. This is especially the case for fuels dispersed with a non-fissile metal, such as zirconium, but also for oxide fuels with high fractions of plutonium. It has been shown that the solubility for plutonium-containing fuels starts to deteriorate for concentrations higher than about 30%. On the other hand, nitride fuels pose no problems for the PUREX reprocessing technique, which also enables the recovery of  $^{15}\text{N}$ . The other shortcoming of the hydrochemical methods is the low radiation stability of the organic extractant molecules used in the processes. This is particularly unfavourable when dealing with highly radioactive TRU fuels and when multi-recycling is required, implying the need for short cooling times.

### **2.3.2 Pyrochemical methods**

A promising alternative to hydrochemical reprocessing is the pyrochemical method, in which molten salts are used as solvents in the waste refining. Pyrochemistry has been used within the metallurgical industry for several decades and has also been investigated for the purpose of nuclear waste reprocessing, mainly in the USA, Japan and Russia. The high radiation resistance of the molten salts and the absence of neutron-moderating water make the solvent suitable for spent fuel separation. Pyrochemical methods for fast reactor fuel reprocessing are applied on a pilot scale at the Idaho National Laboratory (INL) (U.S.) and in Dimitrovgrad (Russia).

In the pyrochemical processes, the spent fuel is dissolved at high temperatures (500-800°C) in molten salt, preferably fluorides or chlorides. Separation of the actinides by electro-refining is the process that is primarily considered for nuclear waste reprocessing, although several different pyrotechnical methods are under development. One of the major advantages of pyrochemical reprocessing, compared to hydrochemical methods, is the much higher radiation resistance of the inorganic reactants used in the process. This allows for the possibility to reprocess high-burnup ADS fuels, including large fractions of minor actinides, with minimum cooling time, possibly as short as one or two years to allow for the decay of  $^{242}\text{Cm}$ . In addition to this, pyrochemical methods offer good solubility for most types of fuels. Another



advantage, thanks to the radiation stability, is the higher compactness of equipment and the possibility of forming an integrated system between the irradiation and the reprocessing facilities. This would considerably reduce the expenses and the difficulties associated with the transport of the highly radioactive fuel. Finally, the absence of water in the solvent reduces the criticality risks during separation and pyrochemical processes are also more proliferation-resistant than hydrochemical methods.

Due to the advantages of the pyrochemical processes stated above, these methods are considered to be well suited for the second stratum fuel cycles, dedicated to the recycling of minor actinides. The hydrochemical methods, on the other hand, seem to offer the best solutions for uranium and plutonium recycling in the first stratum. However, pyrochemical methods involve far more complex challenges, in terms of theory and technical implementation, than hydrochemical methods. Several decades of research will probably be required before they can be implemented on an industrial scale as a mature technology. Among the drawbacks of pyrochemical methods are the difficulty of separating the individual actinides and the somewhat higher degree of fission product contamination. If the reprocessed fuel is planned to be recycled in a fast reactor spectrum, however, the contamination is of less importance. Another challenge is the management of the very hot and highly corrosive processing medium.

## Chapter 3

# Accelerator-driven systems

### 3.1 Introduction

The basic idea of accelerator-driven systems is to operate a sub-critical reactor driven by an intense high-power proton accelerator. The fact that the reactor core is sub-critical compensates for the several adverse effects on the safety that the uranium-free MA-containing fuel introduces. In most cases, a sub-criticality level in the order of  $k_{eff} = 0.95$  is assumed to be sufficient to compensate for the deteriorated safety, caused mainly by the loss in Doppler reactivity feedback, the decrease in delayed neutron fraction and the positive void worth. Since the fission multiplication chain reaction in a sub-critical core is not self-sustained, an external neutron source must be supplied to the core. This neutron source is sought to be produced by an intense proton beam impinging on a heavy-metal target, thereby generating a large number of neutrons via spallation reactions. A high-power proton accelerator is used to accelerate the protons to energies in the order of 1000 MeV and to guide them towards the spallation target, as depicted in Fig. 8. The spallation neutrons leak out from the target, after different kinds of interactions with the target nuclei, and are subsequently multiplied in the surrounding sub-critical core.

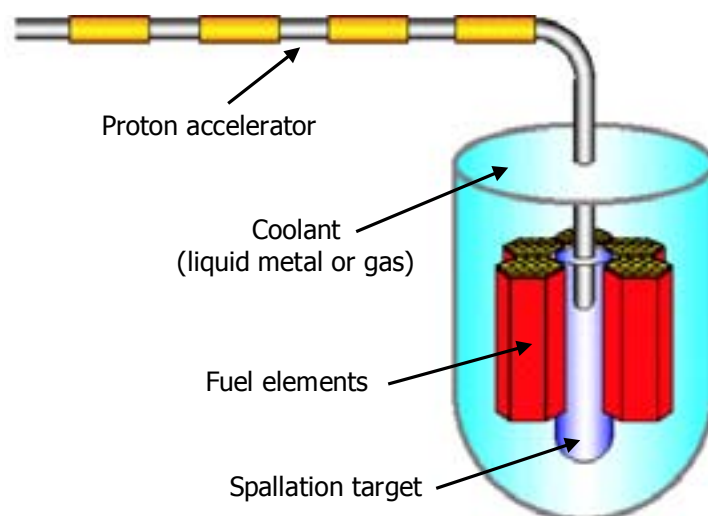


**Fig. 8.** Schematic picture of an accelerator-driven system.

As was mentioned earlier, a fast neutron spectrum is needed in order to achieve high fission rates. For this purpose, liquid metals, such as sodium, lead or lead-bismuth eutectic (LBE), or gas are eligible candidates as coolant materials. The most promising materials for the spallation target are liquid lead and LBE, due to their favourable spallation-neutron production characteristics and their suitable thermal properties. Several different fuel forms are also being studied, of which some of the most promising are oxides, nitrides and metal fuels. These different design options will be further treated below.

## 3.2 Fuel options

The choice of fuel form envisaged for the transmutation of spent fuel in accelerator-driven systems is still an open question. These fuels, preferably uranium-free, will contain high fractions of plutonium and minor actinides and will be irradiated to high burn-up in order to achieve a high degree of transmutation. These new circumstances, compared to conventional reactors, imply the need for evaluating and developing alternative fuel materials. There is much experience and know-how about uranium-based fuel forms, but much less about the characteristics and fabrication technology of the corresponding plutonium- and MA-based ones. Several different options of advanced fuels are being investigated, oxides, nitrides and possibly metal fuels being the most promising [35]. Other fuel forms under investigation (not presented here) are carbide fuels, composite fuels and coated particle fuels.

There are currently two facilities in Europe that can be used for the handling and fabrication of americium- and curium-containing fuels; ATALANTE in Marcoule, France (CEA), and the MA-laboratory at the Institute for Transuranium Elements (ITU-JRC) in Karlsruhe, Germany. The capacity is currently limited to a few grams of curium and to about 150 g of americium (at the MA-lab). Other facilities also exist in the U.S., Japan and in Russia.

### 3.2.1 Oxide fuels

Compared to other advanced fuel options, oxide fuels have the advantage that their characteristics are known from the current industrial MOX fuel operation and fabrication technology. This advantage is limited, however, due to the significant differences that can be expected for MA-containing oxide fuels. The physico-chemical properties of uranium-free fuels are generally inferior to the corresponding uranium-based fuel forms. Among the negative consequences of going from a uranium-based fuel to fuels containing high fractions of plutonium and MA are lower melting point (decreases with increasing atom number, from  $\text{UO}_2$  (3113 K) to  $\text{AmO}_2$  (2448 K)), lower thermal conductivity and poorer chemical stability. Moreover, a general problem for all fuel forms with high MA content is the helium gas production, leading to intolerable swelling of the fuel. This has been demonstrated in the EFTTRA experiment, where uranium-free MA-containing fuels have been irradiated. The helium is produced primarily as  $^{242}\text{Cm}$  (created from  $^{241}\text{Am}$ ) disintegrates via alpha-decay.

Despite the degradation of the transuranium oxide fuel properties, compared to standard UOX or MOX fuels, they still exhibit the important advantage over other advanced fuel options of having comparatively high chemical stability. This implies relatively simple handling and fuel fabrication, which is very important when dealing with MA-containing materials. Oxide fuels are also stable in air, which makes the safety requirements for the fabrication process less demanding. The major drawback connected to oxide fuels is the low thermal conductivity, leading to high operating temperatures. Therefore, a shift of emphasis towards CERMET (ceramic-metal) oxides has recently been made, where the actinide oxide is dispersed in a metallic matrix, e.g., molybdenum. Two different types of oxide fuels are currently being considered in Europe as candidates for the ADS fuel cycle; CERCER (ceramic-ceramic) oxides (e.g., (Pu,MA)O<sub>2</sub>-MgO) and CERMET oxides (e.g., (Pu,MA)O<sub>2</sub>-Mo).

### 3.2.2 Nitride fuels

The major advantage of nitride fuels is their favourable thermal properties (up to five times higher thermal conductivity for UN than for UO<sub>2</sub>), whereas the melting temperatures are similar. This implies lower operating temperature, and/or higher linear power rating. The actinide nitrides also show good mutual miscibility and it is therefore expected that the solid solution (Np, Pu, Am, Cm)N exists over a wide range of compositions. Other advantages associated with nitride fuels are the compatibility with the PUREX reprocessing method, which has some limitations for oxide fuels, and the reasonable chemical compatibility with water, air and stainless steel cladding materials.

However, nitride fuels exhibit poorer chemical and thermal stability, which makes them more difficult to fabricate and which may lead to safety problems during power-temperature excursions, such as pressurisation of the reactor vessel (caused by dissociation of the nitride and production of N<sub>2</sub> gas). Further, the addition of an inert matrix, e.g., ZrN, is expected to improve the thermal stability of nitride fuels. Another disadvantage of nitride fuels is the production of <sup>14</sup>C from <sup>14</sup>N. This may require the enrichment of <sup>15</sup>N [40], which has been proven feasible, but which will make the fuel fabrication process more difficult and more expensive.

### 3.2.3 Metal fuels

The main advantage of metallic fuels is that the thermal conductivity is high. For uranium-based alloys, the melting temperature is also reasonably high, about 1620 K. However, moving to uranium-free fuels with high contents of plutonium and minor actinides, the thermal properties are considerably deteriorated, both with respect to the melting point and the thermal conductivity. Consequently, in order to increase the margin to melting, the addition of an inert matrix is required, of which the most promising candidate is zirconium with a melting point of 2128 K. Another disadvantage of metallic fuels is their incompatibility with LBE.

### 3.3 Coolant options

Since the neutron energy spectrum in an ADS must be hard in order to achieve high transmutation rates, the choice of core coolant is restricted to liquid metals (e.g., Pb, LBE or Na) or gas (e.g., He or CO<sub>2</sub>) [22,41]. Water, for instance, cannot be used, because of its strong moderating properties. The main advantages of liquid metals are their attractive thermal properties and the possibility of operating close to atmospheric pressure, while the major drawbacks are the opacity (makes inspections and repair more difficult), the positive void worth [42] and the adverse chemical properties. Gas, on the other hand, is not chemically reactive and allows easy in-service, but needs very high pressure for efficient cooling. The molten salt concept, which exhibits many attractive properties, is also being investigated. However, this technique lies well beyond the state of the art and is not a realistic option for a demonstrator ADS within the near future.

#### 3.3.1 Lead or lead-bismuth eutectic

Lead or lead-bismuth eutectic as coolant medium may have the advantage of being the same material as the spallation target, which will most probably consist of one of these two materials. This would avoid the physical separation of the spallation target and the sub-critical system. Moreover, the very high boiling point (~1700 °C) is favourable in order to prevent or delay the core cooling problems that may arise in the unlikely event of a loss of heat removal accident (loss of coolant due to boiling is thus very unlikely). Lead and bismuth also possess comparatively good neutronic properties, such as very low capture cross-sections, which is favourable for the neutron economy of the multiplying system. The physical properties of lead, LBE and sodium are listed in Table 4. Their relatively high melting point, on the other hand, places constraints on the operating temperatures during shutdown and refuelling in order to avoid solidification of the coolant. Using pure lead with a melting point of 327 °C would require operating temperatures of 400-600 °C, with no drop below 400 °C at any time. These high temperatures also further aggravate the structural material corrosion problems. However, using LBE as coolant, with a melting point of only 123.5 °C, would enable the operating temperature to be reduced by about 200 °C, facilitating the shutdown procedure and relaxing the corrosion strains. The presence of bismuth, however, leads to the production of the alpha emitter <sup>210</sup>Po (half-life of 138 days) and the related radioactivity confinement concerns need to be

**Table 4.** Physical properties of the main liquid metal coolant options.

|     | $\rho$<br>[g/cm <sup>3</sup> ]<br>(~400 °C) | $T_{\text{melt}}$<br>[°C] | $T_{\text{boil}}$<br>[°C] | $k$<br>[W/m·K]<br>(~400 °C) | $C_p$<br>[J/kg·K] |
|-----|---|---------------------------|---------------------------|-----------------------------|-------------------|
| Pb  | 11.07                                       | 327.5                     | 1749                      | 16                          | 150               |
| LBE | 10.24                                       | 123.5                     | 1670                      | 12.9                        | 147               |
| Na  | 0.857                                       | 97.7                      | 883                       | 71.6                        | 1300              |

managed. Moreover, the availability of bismuth is limited and would probably allow only a smaller number of ADS cooled with LBE. Experience of LBE-cooled reactors is available in Russia (submarines), although the application in ADS needs more thorough research.

### **3.3.2 Sodium**

Sodium is the most well-known liquid metal coolant for fast reactor systems. There is extensive experience and knowledge from system design and operation of fast critical sodium-cooled reactors, e.g., Phenix, Superphenix, Bor-60 and BN600, and most of the required compatible reactor components are available. Sodium has very good thermal properties, e.g., high thermal inertia and thermal conductivity, leading to efficient cooling and reducing the core cooling problems in the case of a loss of heat removal accident. Drawbacks connected to this choice of coolant are the violent chemical reactivity with air and water as well as the positive void worth, which is particularly high when combined with a minor actinide-containing fuel [42].

### **3.3.3 Gas**

One of the main advantages of gas is the hard neutron spectrum it induces. Using gas (He or CO<sub>2</sub>) as coolant would facilitate in-service inspection and repair of the reactor core significantly, due to its transparency. Another advantage is that the void worth is close to zero, as the gases are more or less transparent to neutrons. Moreover, helium is inert and does therefore not exhibit adverse effects concerning chemical compatibility with structural materials. The major drawback associated with gas as coolant is that the system needs high pressure, in the order of 50-70 bars, with the related consequences on vessel loading and increased risk of failures, possibly leading to loss of coolant. In the event of loss of coolant, the decay heat removal is expected to be more troublesome than with liquid metal cooling. Finally, as the core is pressurised, the physical separation of the spallation target and the sub-critical system is a disadvantage.

## **3.4 The spallation target**

The design of the spallation target module should be based on the optimisation of neutronic efficiency (maximum neutron yield), while ensuring the removal of the heat released in the spallation process as well as the physical and chemical integrity of the structural and target materials. The spallation target, for which only limited experience exists, constitutes the physical interface between the proton accelerator and the sub-critical core and it is one of the most innovative components of the ADS. It will be subject to severe radiation and thermal stresses, induced both by the high power gradients generated by the intense proton beam (possibly up to 30 MW for a future commercial ADS) and by the material damage caused by high-energy particles and spallation products. The neutron production in the spallation process is most efficient for large nuclei and several heavy metals, e.g., Ta, W, Hg, Pb, LBE and U, have been considered as possible target material candidates.

### 3.4.1 Heavy liquid metal target

Two main options for the spallation target material are being considered; solid or liquid metal. While all current spallation sources operate with a solid metal target, the heavy liquid metal (HLM) choice appears to be the only realistic one for a large-scale ADS, due to the extremely high power densities. The main advantages of liquid metals are the superior heat removal capabilities and the significant reduction of the radiation damage to the target. However, the corrosion and erosion of the structural materials, the risk for release of volatile spallation products and the possible need for a beam window separating the beam tube from the target region are associated problems that have to be dealt with.

Among the studied heavy liquid metals, lead and LBE have emerged as the primary candidates. LBE has the clear advantage of having a low melting temperature, which would simplify the heating of the system before operation, as well as reducing the risk of target solidification in case of beam interruption or reactor shutdown. If LBE is chosen as core coolant material, full compatibility between the target loop and the core coolant primary loop could also be achieved. The main drawback with LBE, as mentioned in the previous section, is the production of the alpha emitter,  $^{210}\text{Po}$ .

A third target material that is being considered is mercury, with the main advantages being the absence of  $^{210}\text{Po}$ -activity and the possibility of not having to heat up the system before operation. Mercury is studied in the frame of the Spallation Neutron Source (SNS) [43], currently under construction at Oak Ridge, U.S. The spallation experiments are based on a pulsed proton beam of 1.4 MW (1.4 mA and 1000 MeV proton beam) impinging on a target of liquid mercury. However, the high volatility of mercury imposes very strict requirements on the integrity of the system and the boiling point of 356 °C is probably not high enough for the operation temperatures required for a large-scale ADS. Another disadvantage of mercury is the high neutron absorption cross-section.

### 3.4.2 Window or windowless option

Another major choice that has to be made concerning the spallation target module is whether to connect the accelerator channel to the spallation target via a solid window, or to let the beam impinge directly on the HLM (windowless option). If a window is used, it has to consist of a material of high strength and high radiation resistance, as it will be exposed to very high proton irradiation doses and high temperatures. Only limited experience from window irradiation is currently available, but it is estimated that the window would have a life-time not longer than 6 months, due to the heavy radiation damage. In the MEGAPIE project, carried out at the PSI, an LBE target will be irradiated by the SINQ proton beam (590 MeV and 1.8 mA) [44]. The beam and the target will be separated by a beam window, which is expected to reach an irradiation dose of about 10 DPA (displacement per atom) during a period of six months. While a neutron dose of 10 DPA usually not constitutes a problem,

the concomitant production of hydrogen and helium in proton irradiation causes increased embrittlement of the window.

A windowless design avoids the problems associated with high-temperature window stresses (although there has to be a cold window higher up in the accelerator channel), but involves other technical difficulties. The main challenge is to manage the metal and the spallation product evaporation contaminating the beam line vacuum. This option will be experimentally investigated in the MYRRHA project [45,46], where a windowless LBE target will be irradiated by a 350 MeV and 5 mA proton beam. The proton beam will drive a sub-critical core of about 30 MW thermal power.

### 3.4.3 The spallation process

The nuclear process of spallation can be divided into two stages, which is illustrated in Fig. 9. In the first stage, called the “intranuclear cascade”, a high-energy particle impinging on a target nucleus interacts directly with the individual nucleons inside the nucleus, the interactions being described by particle-particle cross-sections. High-energy neutrons, protons and pions may be emitted as a result of this interaction. The nucleus is left in a highly excited state, the energy being distributed throughout all the nucleons of the nucleus. In the second stage, which is much slower, the highly excited nucleus undergoes “evaporation”, releasing nucleons or light ions with an energy of typically about 1 MeV. The nucleus might also undergo fission in this stage. When the nucleus reaches an energy level that is less than about 8 MeV above its ground state, further de-excitation occurs by gamma ray emission.

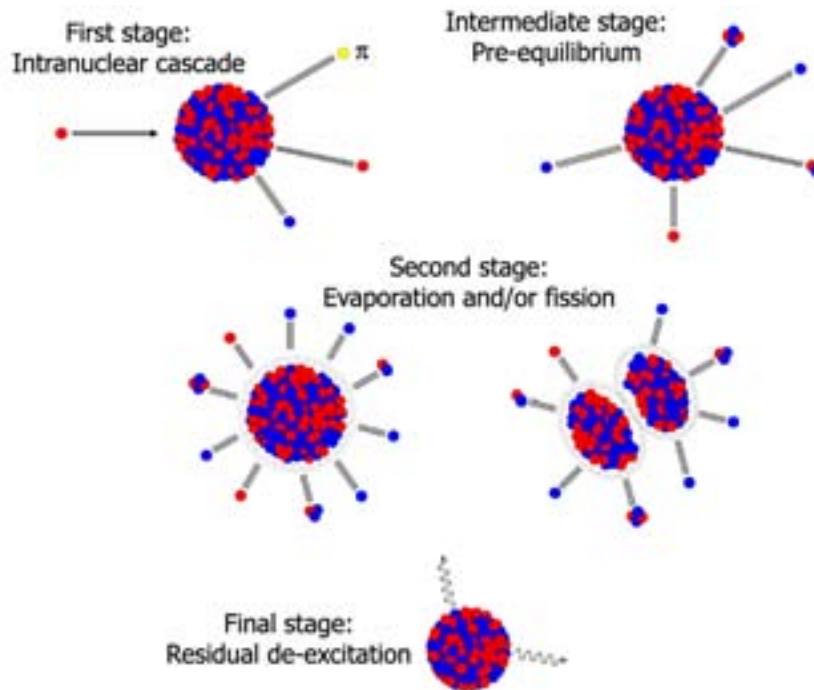


**Fig. 9.** The different stages of the spallation process.



In a single spallation reaction, about 15 neutrons are created from a 1000 MeV proton impinging on a lead nucleus. However, some of these emitted neutrons are energetic enough to induce further spallation reactions or (n,xn)-reactions in other target nuclei. This multiplication thus gradually leads to a larger number of neutrons leaving the spallation target. In a large lead spallation target, typically about 30 neutrons are created altogether for each 1000 MeV proton.

### **3.5 Accelerator technology**

The operation of an ADS will require a high-power proton accelerator (HPPA) and the two types of accelerators that are being considered are linacs and cyclotrons [22,47,48]. The most powerful linac existing today is the LANSCE accelerator at the Los Alamos National Laboratory (LANL), U.S., operating with a maximum proton energy of 800 MeV and a mean beam current of 1 mA, whereas the biggest cyclotron is the separated sector unit at the Paul Scherrer Institute (PSI), Switzerland, with maximum 590 MeV and an average current of 1.8 mA. There are also several large accelerators that are currently being planned or are under construction, some of the most important projects being the Spallation Neutron Source (SNS) (1.4 mA and 1.0 GeV pulsed linac) [43], the KEK/JAERI project (600 MeV linac coupled to a 3 GeV and a 50 GeV synchrotron) and the European Spallation Source (ESS) (1.33 GeV pulsed linac) [49,50]. Furthermore, the LEDA (Low Energy Demonstration Accelerator) accelerator in Los Alamos, U.S., which has operated without beam trips at a current of about 100 mA for many hours [51], is an important proof that an accelerator of such strength can be built.

However, all of these accelerators are far from meeting the requirements that will be imposed by the operation of a future large-scale ADS. The most important areas for accelerators envisaged for ADS application, where significant development and technological improvement are needed, concern performance, reliability and availability, as well as operation and safety.

#### **3.5.1 Accelerator performance**

##### **The proton beam characteristics**

A proton energy in the order of about 1 GeV combined with an accelerator current of 20-30 mA (20-30 MW power) will probably be required for a large-scale industrial ADS with a power in the order of 1000 MWth, while about 5 mA using 600 MeV protons (~3 MW power) is estimated to be enough for an experimental facility with a power of about 100 MWth, such as the XADS demonstrator [22]. The required proton energy lies well within the present capabilities of accelerator technology, but the high currents require significant improvement. Using super-conducting linacs, it has been shown that accelerator powers of up to 100 MW (100 mA, 1 GeV) are feasible, constructional costs being the main limiting factor. On the other hand, 1 GeV and a few mA (possibly up to 10 mA) are considered as the upper limits of what is achievable for cyclotrons. Consequently, both linacs and cyclotrons could be

used for a 100 MW experimental facility, while only linacs can be eventually upgraded to a future commercial ADS.

One of the main characteristics of the proton beam, that is, its energy, will be determined mainly by two physical quantities; the number of neutrons produced per proton and per GeV and the amount of energy deposited in the target window. The first quantity is an approximate measure of the efficiency of the proton beam, in terms of number of produced spallation neutrons for a given amount of accelerator power. This is an increasing function of proton energy and reaches its optimum level at about 1000-1500 MeV, which is illustrated in a later chapter (Fig. 14). The second quantity, the energy deposited in the target window, which is due to ionisation losses, is a decreasing function of proton beam energy. Since the required current is also lower for higher proton energies, the window damage is significantly reduced by increasing the proton energy. Hence, considering the physical properties of the beam-window-target interactions, a proton energy in the order of 1 GeV or higher is clearly favoured.

### **Reliability and availability**

The reliability and continuity of the accelerator beam is a new and challenging constraint on the accelerator technology and will require considerable improvement of a large number of accelerator components. A reduction of beam interruptions of a few orders of magnitude is needed in order to meet the requirements for the coupling of an accelerator to an industrial sub-critical reactor [52].

The beam trips are generally divided into two categories; those shorter and those longer than one second. Current research shows that the beam interruptions shorter than about one second do not significantly affect the thermodynamics of the reactor or other plant parameters, e.g., thermal power, temperature, primary flow and pressure. Therefore, no specific limit on the frequency of trips is required for this category. On the contrary, beam trips longer than one second will lead to a variation of these parameters or even to a plant shutdown and a frequent repetition of such trips can significantly damage the reactor structures. The number of allowable long-duration beam trips depends on the properties of the structural components, but it is generally considered that some hundreds per year would be acceptable. However, considering the availability and the cost-efficiency of the reactor operation, the limit of beam trips long enough to cause a shutdown will be much lower, maybe in the order of 10 per year. This value, which is still significantly higher than the average number of shutdowns for present industrial nuclear power plants, is acceptable, since the main purpose of ADS is transmutation rather than electricity production. Hence, the major challenge within accelerator technology, in terms of improving reliability and availability, is the reduction of long-term beam interruptions.

### **Operation and safety**

The control of the power and the monitoring of the reactivity level of the core pose other challenges for the operation of a source-driven sub-critical reactor. Concerning the time structure of the proton beam, a pulsed mode operation may be advantageous

for this purpose, since it allows for a repeated beam interruption ( $\sim 1$  ms). For instance, using different reactivity determination methods, the sub-criticality can be determined by monitoring the prompt neutron flux decay subsequent to a source pulse. As long as the frequency is high enough, no penalties in terms of thermal stresses are expected. Different methods for determining the reactivity are treated in Chapter 8. Other safety functions that have to be taken into account are the containment of radioactive materials and the radiological protection of the working personnel under normal operating conditions.

### 3.5.2 Linear accelerators

#### Basic technology

The basic principle of a linear accelerator, commonly called linac, is that the charged particles are accelerated, either by electrostatic fields or oscillating radio-frequency (RF) fields, along a straight line. The particles travel through a series of hollow “drift tubes”, alternately connected to the opposite poles of an AC voltage source (Fig. 10). The energy transfer to the particles occurs in the electric field between the tubes, whereas the inside of the tubes are field-free (hence the name, “drift tube”). The polarity of the voltage is reversed while the particles are travelling inside the tubes and the lengths of the tubes are chosen so that the particles reach the gap between the tubes at the moment when the electric field is accelerating. As the velocity of the particles increases, the length of the tubes must also increase, approaching a constant value as the particles become relativistic. In order to reach high energies, since the final energy of the particles is equal to the sum of the voltages to which they have been exposed, either the number of tube segments or the voltage of the RF-source may be increased. As the velocity of the particles quickly becomes high, it is desirable that the RF-frequency is high in order to keep the tube lengths reasonably short.

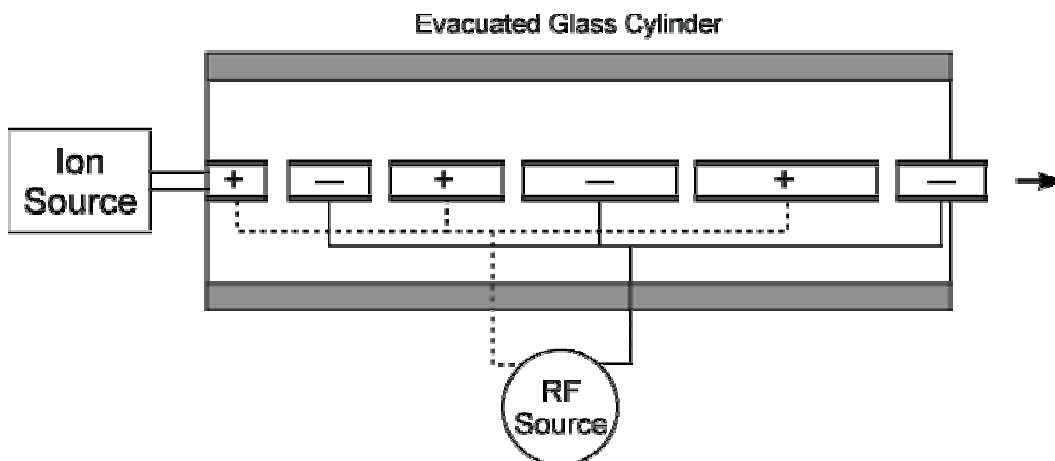


**Fig. 10.** Principle design of a linear accelerator.

## The linac envisaged for ADS

The HPPA linac envisaged for ADS can schematically be divided into three different parts; the injector, the intermediate section and the super-conducting high-energy section. In a typical design proposal, depicted in Fig. 11 [53], the injector consists of three parts with the first stage being the ion source, producing a high-intensity proton beam. The ECR (electron-cyclotron resonance) ion sources have proved very suitable for producing intense proton beams and to be highly reliable. The source is followed by an RFQ (radio-frequency quadrupole), accelerating (to 5 MeV), focusing and bunching the beam, and a DTL (drift tube linac) accelerating the protons to about 10 MeV.

The intermediate section consists of a number of classical normal-conducting copper structure DTL, in which the particles reach an energy of about 85 MeV. At higher energies, in the last section of the linac, super-conducting cavities and focusing quadrupoles are needed. This is the longest section and brings the protons up to their final energy, possibly 450-600 MeV for a demonstrator or about 1000 MeV for a prototype ADS. In addition to the first 100 m of the two first parts, approximately 180 m are needed to reach 450 MeV, while about 300 m are needed to reach 1000 MeV. Alternatively, a transition to super-conducting technology at lower energies ( $\sim 20$  MeV) has been considered, e.g., in the TRASCO project and in the US road-map for ATW [54].

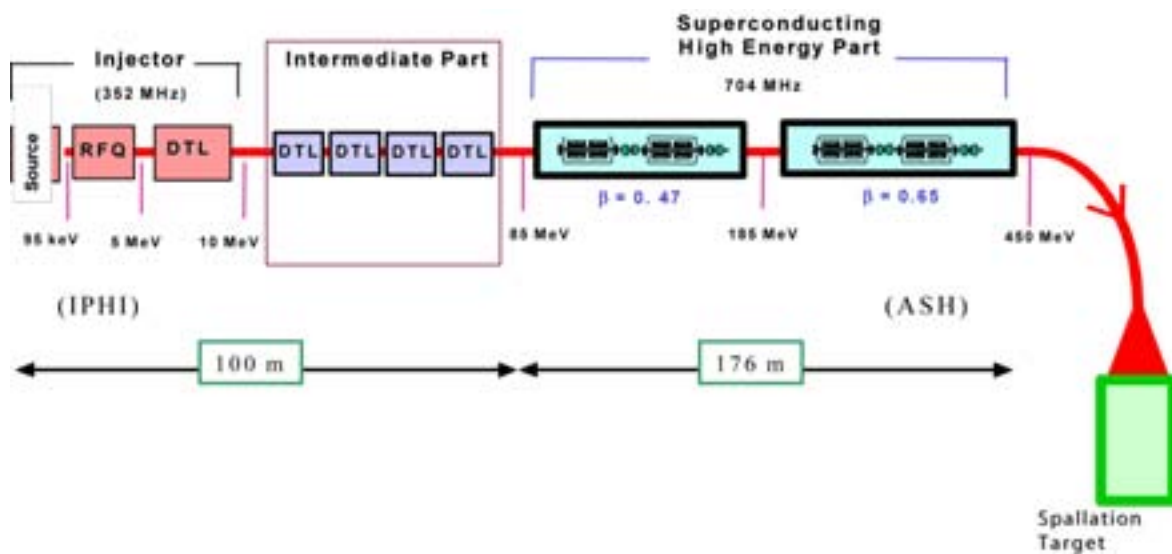


**Fig. 11.** Typical layout for a super-conducting HPPA linac [53].

The main advantage of super-conducting radio-frequency-cavities (SCRF) compared to normal-conductors is the very high efficiency of the power transferred from the RF-transmitters to the proton beam. Using classical copper structure cavities, about half of the power is dissipated in the walls, while for SCRF cavities almost 100% efficiency can be obtained. This leads to considerable economical advantages as well as relaxed constraints on the construction of the RF-source. Besides this obvious economical impetus for using SCRF cavities, they are also favoured for several

technical reasons. One is that large beam openings, not achievable in classical linacs, drastically reduce the problems associated with the activation in the structural components induced by beam halo. Another reason is that stronger accelerating fields are possible (10 MeV/m is foreseen, compared to 1.6 MeV/m for classical copper cavities), which considerably reduces the length (and costs) of the high-energy section.

### 3.5.3 Cyclotron accelerators

A cyclotron is a circular accelerator consisting of two large dipole magnets and two semi-circular metal chambers, called Dee:s because of their shape, in which the particles orbit (Fig. 12). The Dee:s are connected to an oscillating voltage, generating an alternating electric field in the gap between the two Dee:s, in which the particles are accelerated. When they are inside the Dee:s, however, they sense no electric field and follow a circular path until they reach the gap and are accelerated again. In this way, the particles that are emitted at the centre of the device follow a spiral path, gaining a certain amount of energy each cycle, until they become energetic enough to leave the accelerator.

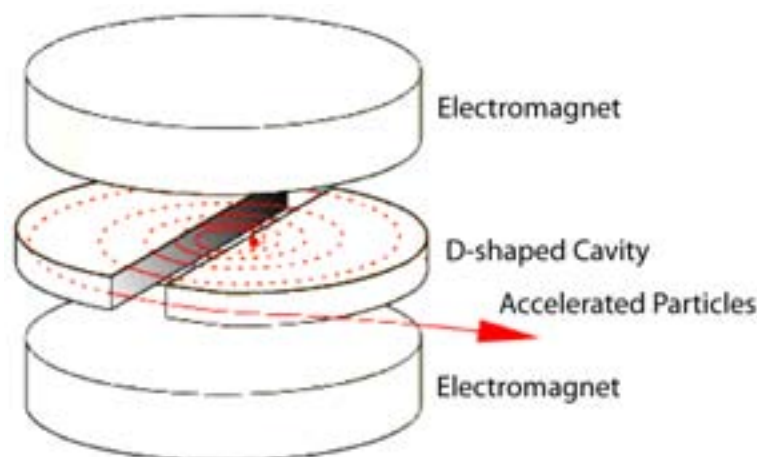


**Fig. 12.** Schematic design of a cyclotron.

A difficulty with this type of classical cyclotron arises when the particles become relativistic, which causes them to become out of phase with the alternating voltage. For protons, the maximum achievable energy due to this effect is about 40 MeV ( $\gamma = 1.04$ ). In order to overcome this problem, either the frequency must be modulated or the magnetic field must increase with the orbital radius. This has been accomplished, for example, by the development of the frequency-modulated synchro-cyclotron. On the other hand, increasing the magnetic field by increasing the radius has the undesirable effect of defocusing the beam. However, focusing can be restored by dividing the dipole magnets into sectors with alternating high and low magnetic fields (isochronous cyclotron). The strongest focusing effect is obtained in a separated sector cyclotron. This is the principle for the 590 MeV PSI cyclotron, which is constructed using 8 separate magnet sectors.

Cyclotrons may be a realistic alternative to linacs as the accelerator to drive an ADS, provided that a relatively small reactor is envisaged. The maximum achievable beam power is estimated to be 5-10 MW, so a thermal output power of about 100-200 MW appears to be the upper limit for a cyclotron-driven ADS. An alternative that has been considered is to operate several independent cyclotrons. In this scenario, a 500 MW core could possibly be managed. This would also increase the reliability of the proton beam and, given the lower unit cost of a cyclotron compared to a linac, it could equally be an economically favourable option. Most of the conceptual design proposals of ADS cyclotrons are based on a version of the PSI ring cyclotron upgraded to about 1 GeV and 10 mA, thus yielding a maximum power of 10 MW.

### **3.6 The European Roadmap for the development of ADS technologies**

The main goals of the European Roadmap are to propose a technological route for the transmutation of nuclear waste in accelerator-driven systems and to prepare a detailed plan for its first phase; the realisation of an experimental ADS (XADS) [22,55] of thermal power in the order of 100 MW. The XADS program, which is envisaged to cover the time-period of the 6th and the 7th European Framework Programs, is the first step in the European Roadmap for the development towards a large-scale and industrial application of ADS. During the operation of the XADS, which will use conventional MOX fuel, the basic physical principles of an accelerator-driven system, mainly the coupling between the proton accelerator and the sub-critical core, will be studied and demonstrated. The MOX fuel could be either existing fuels from the SNR300 or Superphenix (SPX) reactors, or new MOX fuels specifically constructed for the XADS. The latter choice has the advantage that the fuel design can be adapted to the design of the reactor system.

It has been agreed that a thermal power of about 30-100 MW is suitable for the XADS. A power level of 100 MW would require a maximum accelerator current of about 2-5 mA and an accelerator power in the order of 2-3 MW, assuming a proton beam energy between 600 and 1000 MeV. It has also been agreed that the spallation module should be separated from the primary coolant, whereas the choices of many other system parameters, such as coolant and spallation target materials, are still unresolved. For the spallation module, the choice between the window and windowless concept will be based on the results from the MEGAPIE and the MYRRHA preliminary experiments, respectively. The XADS will also have the role of an irradiation tool and a limited number of dedicated MA-based fuel assemblies will be inserted in the reactor for irradiation studies. These advanced fuels, characterised by a high content of plutonium and minor actinides and preferably uranium-free, will be irradiated to relatively high burn-up in order to achieve high transmutation rates.

The preparations for the development of the XADS have been carried out during the European 5th Framework Program within the frame of the PDS-XADS program (Preliminary Design Studies of an XADS) [56]. The following three different ADS

concepts, developed by different EU member countries, have been comprised by the program;

- The Ansaldo design (~80 MWth), cooled by LBE.
- The Framatome design, cooled by gas.
- MYRRHA (~30 MWth), windowless and cooled by LBE.

In the second phase of the roadmap for ADS development, the MOX fuel is planned to be replaced by dedicated fertile-free fuel, thereby allowing full demonstration of the transmutation process. This may be realised either by converting the XADS to an experimental accelerator-driven transmuter (XADT) or, should this not be feasible, by constructing a new facility. A high priority with the XADS design phase will be to provide the maximum practical flexibility in order to make it possible to convert the plant to XADT without major modifications.

Possibly around 2030, the construction of a prototype ADS, which should be based on the same technology as the XADT, except that it would be larger, could be started. This prototype must have all the features of an industrial ADS deployed at a later stage (power, coolant, fuel, spallation module etc.). Until this time, a spallation module, including an accelerator of about 20 to 30 MW power and with availability far beyond its current status, must be developed and constructed. Apart from the accelerator technology, the realisation of a large-scale ADS will also rely on several other independent factors, such as the development and construction of advanced processing and fabrication plants, various safety issues and many different technological challenges. Eventually, if the operation of the prototype is successful, accelerator-driven transmutation systems could possibly be applied on a large and industrial scale from around 2040.

## Chapter 4

# The simulation tools

The major part of the numerical simulations performed within the scope of this thesis was performed with the Monte Carlo codes MCNP [6] and MCNPX [7]. For comparison, the deterministic fast reactor code ERANOS [57] was used as modelling tool in some of the studies [**Paper VII**].

### 4.1 The Monte Carlo method

The Monte Carlo method is a stochastic process, which allows for simulating particle transport in any arbitrary geometry. While deterministic codes solve the neutron transport equation for an *average* particle, Monte Carlo obtains a solution by simulating *individual* particles and then inferring their *average* behaviour. It is particularly useful for complex problems that cannot be modelled by deterministic codes. The problem description is often relatively short and easily constructed. The method consists of following each particle, created somewhere in the geometry, throughout its life (from birth to death, e.g., via absorption or escape) and its interactions with other particles (fission, capture, scattering etc.). The process is run for a large number of source particles to obtain a statistically reliable result and the program records the average behaviour of the simulated particles.

To simulate the particle interaction with matter using a Monte Carlo method, such as MCNP, nuclear data libraries, e.g., JEFF, JENDL, ENDF/B, containing cross-section information for all relevant isotopes and processes, are used. This data is then processed into a format appropriate for MCNP (so-called ACER format) by the code, NJOY [58], which produces new data files and a “directory” file, XSDIR, which is directly used by MCNP. A flow sheet describing the nuclear data treatment procedure is depicted in Fig. 13.

The basic advantage of Monte Carlo codes over deterministic codes is that they require no averaging approximations in space, energy and time. One disadvantage of Monte Carlo, however, is that the solution contains statistical errors. All results in Monte Carlo represent estimates with associated uncertainties and the calculations can be rather time consuming as the required precision of the results increases.



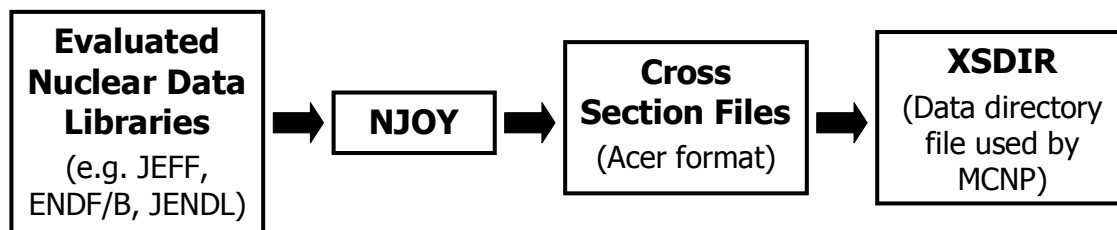


**Fig. 13.** Flow sheet of nuclear data treatment, finally applied by a simulation tool such as MCNP.

## 4.2 MCNP and MCNPX

MCNP has the capability of transporting neutrons, electrons and photons, the neutron energy range being limited to 20 MeV. These features are sufficient for classical reactor simulations and most other neutron transport problems. However, this limitation is a problem when simulating an accelerator-driven system involving high-energy transport of both neutrons and protons, and high-energy interactions, such as proton-induced spallation.

MCNPX on the other hand, is an extended version of MCNP, in which the major capabilities of the high-energy transport code, LAHET [59], and MCNP have been merged together. In MCNP, particle transport relies entirely on nuclear data contained in externally supplied cross-section tables, which are derived from evaluated nuclear data files. In LAHET, on the other hand, particle transport is accomplished by using various theoretical physical models embedded in the code, covering the energy range up to several GeV. In MCNPX, the table-based data are used whenever they exist, as such data are known to yield the best results. When they do not exist, the code built-in physical models are used. LAHET and MCNPX also have the possibility to transport many particles other than neutrons, the most important in the context of ADS simulations being protons. The nuclear data libraries used by MCNP and MCNPX have traditionally been limited to 20 MeV. However, progress is underway with the development of cross-section tables covering the important energy range from 20 up to 150 or 200 MeV, e.g., LA150 [60].

## 4.3 ERANOS

ERANOS is a deterministic fast reactor code system using cross-section libraries based on the JEF-2.2 [61] or the JEFF-3.0 evaluated files. ERANOS is well validated for classical sodium-cooled fast reactors. This validation has recently been extended to plutonium-burning cores with steel-sodium reflectors and high plutonium content. However, the code is not yet fully validated for systems characterised by large sub-criticalities and the presence of high-energy neutrons from spallation.

In ERANOS, 1D cell or 2D sub-assembly calculations are performed with the ECCO code, while core calculations can be performed with different 2D, e.g., BISTRO [62], or 3D diffusion or transport theory modules. Two basic sets of nuclear data libraries are available with ERANOS, both of them based on the JEFF evaluated file. The first one is directly derived from JEFF, whereas the other one,

called ERALIB1 [63], has been generated in a nuclear data statistical adjustment procedure. The energy range in ERANOS is limited to 20 MeV and it thus needs to be combined with a high-energy code in order to be able to simulate high-energy spallation-driven systems.

## **4.4 High-energy codes and models**

High-energy particle transport, e.g., in spallation interactions, is usually performed by a high-energy Monte Carlo code, based on several different physical models. For reactor problems, these codes are generally coupled, below a certain cut-off energy (usually 20 MeV), to a neutron transport code, such as MCNP. There are presently a number of different models and computation codes for simulating high-energy particle transport, of which HETC [64,65] and LAHET are two of the most widely used. The physical models used for high-energy interactions are in most codes divided into the following different categories; intranuclear cascade models (INC), multi-stage pre-equilibrium models (MPM) [66], evaporation and break-up models and high-energy fission models.

### **4.4.1 Intranuclear cascade and pre-equilibrium models**

The concept of the INC model was developed several decades ago in the early stages of high-energy nuclear interaction modelling. It is a relatively fast model, in terms of computation speed, and within some energy ranges it is the only available tool for simulating hadron-nucleus interactions. As a result, several different INC models have emerged and have become more and more refined and widespread.

In the INC models, the incoming particle interacts directly with individual nucleons inside the nucleus. The nucleus is assumed to be a cold, free gas of nucleons, confined within a potential that describes the nucleon binding energies and the nuclear density as a function of the radius. Standard Wood-Saxon potentials are used and the quantum effects of Pauli blocking are generally taken into account. Some of the INC models available today are Bertini [67,68], ISABEL [69,70], the Cugnon INCL models [71,72], CEM (Cascade-Exciton Model) [73] and FLUKA [74]. Bertini is the oldest and most widely used INC model and it is the default in MCNPX. Nevertheless, the Bertini model has shown some disagreement with experimental results, obtained at the SATURNE accelerator at Saclay (France) [75]. For instance, it was found to over-predict the low-energy neutron production resulting from high-energy protons impinging on different heavy-metal targets. The Cugnon INCL model used by the TIERCE code [76], on the other hand, yields neutron production rates in good agreement with the experiments, although this model has some other deficiencies that have yet to be overcome.

After the termination of the INC model, a multistage pre-equilibrium model may optionally be applied for sub-sequent de-excitation of the residual nucleus. During this intermediate stage, the excited nucleus may emit nucleons or light nuclei. When the Bertini INC model is used in the LAHET code system, the use of this pre-equilibrium model is recommended for most cases. It was also shown in the

SATURNE experiments that the Bertini model followed by the MPM clearly improves the performances.

#### **4.4.2 Evaporation and breakup models**

At the completion of the INC model (and the MPM, if used), an evaporation model or, for lighter nuclei, the Fermi-breakup model may be applied for the de-excitation of the nucleus. The energy of the highly excited residual nucleus is dissipated by evaporation of neutrons, protons, deuterons, tritons,  $^3\text{He}$ - and  $^4\text{He}$ -particles. The most widely used evaporation model is the Dresner model [77], usually associated with the Atchison fission model [78], but the GSI model [79], for example, also appears to be a promising alternative.

For the disintegration of light nuclei ( $A \leq 22$ ), the Fermi-breakup model [80] has replaced the evaporation model. The de-excitation process is treated as a sequence of simultaneous breakups of the nucleus into two or more products. The products may be a stable or unstable nucleus, or a nucleon. Any unstable nucleus is subject to further breakups until all products are stable.

#### **4.4.3 High-energy fission models**

Instead of undergoing evaporation after the intranuclear cascade, the highly excited nucleus may also fission. There are two main models for fission induced by high-energy interactions; the Rutherford Appleton Laboratory (RAL) model [81] and the ORNL model [82]. The RAL model, which is the default in MCNPX, covers fission for nuclei larger than  $Z=71$ , whereas the ORNL model only treats actinides.

# Chapter 5

## Neutron transport theory

A major part of this thesis has been devoted to the study of source efficiency in accelerator-driven systems. In this chapter, the basic theoretical framework of neutron transport theory, providing the basis for the source efficiency concepts, is briefly presented.

### 5.1 The neutron transport equation

The neutron transport equation, when no distinction is made between prompt and delayed neutrons, can be expressed as [83]

$$\frac{1}{v} \frac{\partial \Phi}{\partial t} + \boldsymbol{\Omega} \cdot \nabla \Phi + \Sigma \Phi = \int_0^{\infty} \int_{4\pi} \Sigma' f \Phi' d\boldsymbol{\Omega}' dE' + S, \quad (6)$$

where  $\Phi(\mathbf{r}, \boldsymbol{\Omega}, E, t)$  is the neutron angular flux. The following short-notations have been introduced in order to simplify the representation;

$$\begin{aligned} \Phi &= \Phi(\mathbf{r}, \boldsymbol{\Omega}, E, t) \\ \Phi' &= \Phi(\mathbf{r}, \boldsymbol{\Omega}', E', t) \\ \Sigma &= \Sigma(\mathbf{r}, E) \\ \Sigma' f &= \Sigma(\mathbf{r}, E') \cdot f(\mathbf{r}, \boldsymbol{\Omega}', E' \rightarrow \boldsymbol{\Omega}, E) \\ S &= S(\mathbf{r}, \boldsymbol{\Omega}, E, t) \end{aligned}$$

The five different terms in Eq. (6), counted from the left, have the following physical meanings;

1. Time rate of change of the neutron angular density at the fixed position  $\mathbf{r}$ .
2. Rate of change of the neutron angular density at the position  $\mathbf{r}$  due to streaming of the neutrons, i.e., motion of the neutrons in a straight line without any collisions.
3. Number of neutrons disappearing as a result of interactions with the background medium.  $\Sigma$  is the total macroscopic cross-section.

4. Number of neutrons appearing as a result of interactions with the background medium.
5. Number of neutrons appearing from the source term  $S$ .

Moreover, by separating the fission cross-section from the total transfer probability, the neutron transport equation can also be expressed as

$$\frac{1}{v} \frac{\partial \Phi}{\partial t} + \mathbf{\Omega} \cdot \nabla \Phi + \Sigma \Phi = \int_0^\infty \int_{4\pi} \sum_{x \neq f} \Sigma'_x f_x \Phi' d\mathbf{\Omega}' dE' + \frac{\chi(E)}{4\pi} \int_0^\infty \int_{4\pi} \nu \Sigma'_f \Phi' d\mathbf{\Omega}' dE' + S, \quad (7)$$

where the normalised fission spectrum,  $\chi(E)$ , was expressed by Eq. (4). In order to guarantee a unique solution, a boundary condition must be specified. From now on, we assume the free surface boundary condition

$$\Phi(\mathbf{r}, \mathbf{\Omega}, E) \Big|_{\mathbf{n} \cdot \mathbf{\Omega} < 0} = 0. \quad (8)$$

It should be noted that the homogeneous transport equation (source free) is linear, which implies that if  $\Phi_1$  and  $\Phi_2$  are solutions, then  $\Phi_1 + \Phi_2$  is also a solution. For the inhomogeneous equation we have that, if  $\Phi_1$  corresponds to a source  $S_1$  and a solution  $\Phi_2$  to a source  $S_2$ , then, provided that the appropriate boundary conditions are satisfied,  $\Phi_1 + \Phi_2$  is the solution for the source  $S_1 + S_2$ . Moreover, it can be shown that unique time-independent solutions to the transport equation exist for a critical system without a source and for a sub-critical system with the presence of a source.

## 5.2 Criticality

Physically, the concept of criticality can be described by the following descriptions. If the neutron population in a system will die out at late times unless it is sustained by a neutron source, the system is said to be sub-critical. Similarly, if it diverges at late times, the system is described as being super-critical. Finally, the system is defined to be critical if the neutron population remains constant in the absence of a neutron source or any other external influence.

### 5.2.1 The $\alpha$ -eigenvalue

Since  $\Phi = vN$ , the homogeneous neutron transport equation, Eq. (6) with  $S = 0$ , is equivalent to

$$\frac{\partial N}{\partial t} = -v\mathbf{\Omega} \cdot \nabla N - v\Sigma N + \int_0^\infty \int_{4\pi} \Sigma' f v' N' d\mathbf{\Omega}' dE' \equiv \hat{\mathbf{L}}N, \quad (9)$$

where the operator  $\hat{\mathbf{L}}$  has just been defined. Now we consider the solution to the equation

$$\frac{\partial N}{\partial t} = \hat{\mathbf{L}}N \quad (10)$$

of the following form

$$N(\mathbf{r}, \boldsymbol{\Omega}, E, t) = N_\alpha(\mathbf{r}, \boldsymbol{\Omega}, E) e^{\alpha t} .$$

It then follows that

$$\alpha N_\alpha(\mathbf{r}, \boldsymbol{\Omega}, E) = \hat{\mathbf{L}}N_\alpha(\mathbf{r}, \boldsymbol{\Omega}, E) . \quad (11)$$

It can be shown that, at late times, the solution is determined by the eigenvalue having the largest real part,  $\alpha_0$ , i.e.,  $N(\mathbf{r}, \boldsymbol{\Omega}, E, t) = N_0(\mathbf{r}, \boldsymbol{\Omega}, E) e^{\alpha_0 t}$ . It can thus be concluded that, when  $\alpha_0 < 0$  the system is sub-critical, when  $\alpha_0 = 0$  it is critical and when  $\alpha_0 > 0$  it is super-critical.

## 5.2.2 The $k$ -eigenvalue

From a physical understanding of criticality, any system containing fissile material could be made critical by arbitrarily varying the number of neutrons emitted in fission,  $\nu$ . In particular,  $\nu$  may be replaced by  $\nu/k$  and  $k$  could then be varied to obtain the criticality condition  $\alpha_0 = 0$  with  $k = k_{eff}$ . It will therefore be assumed, on physical grounds, that for such a system, there will always exist a unique positive eigenvalue,  $k_{eff} > 0$ . By definition,  $k_{eff}$  is the unique positive eigenvalue of the neutron transport equation

$$\nu \boldsymbol{\Omega} \cdot \nabla N_k + \Sigma \nu N_k = \int_0^\infty \int_{4\pi} \sum_{x \neq f} \Sigma'_x f_x \nu' N'_k d\boldsymbol{\Omega}' dE' + \frac{1}{k} \int_0^\infty \int_{4\pi} \frac{1}{4\pi} \nu \Sigma'_f \nu' N'_k d\boldsymbol{\Omega}' dE' , \quad (12)$$

where  $\nu = \nu(\mathbf{r}, E' \rightarrow E)$  and where  $N_k$  and  $N'_k$  are the corresponding eigenfunctions.

## 5.3 The adjoint equation

### 5.3.1 Self-adjoint and adjoint operators

Let  $\psi(\xi)$  and  $\phi(\xi)$  be functions of the same variables. The inner product of these two functions is then defined by

$$(\psi, \phi) = \int \psi(\xi) \phi(\xi) d\xi . \quad (13)$$

In the case of the transport equation, the phase variable  $\xi$  stands for  $\xi = (\mathbf{r}, \boldsymbol{\Omega}, E)$  and  $d\xi = dr d\boldsymbol{\Omega} dE$ . For a hermitian, or self-adjoint operator,  $\hat{\mathbf{M}}$ , we have that

$$(\psi, \hat{\mathbf{M}}\phi) = (\hat{\mathbf{M}}\psi, \phi) . \quad (14)$$

The eigenfunctions of hermitian operators are orthogonal and the eigenvalues are always real. However, in neutron transport theory, the operator associated with the transport equation,  $\hat{\mathbf{L}}$ , is not self-adjoint, which requires the introduction of an operator,  $\hat{\mathbf{L}}^+$ , that is adjoint to  $\hat{\mathbf{L}}$ . The adjoint operator  $\hat{\mathbf{L}}^+$  will operate on adjoint functions  $\psi^+$  and  $\phi^+$ , and is defined by the requirement that

$$(\phi^+, \hat{\mathbf{L}}\phi) = (\hat{\mathbf{L}}^+\phi^+, \phi) . \quad (15)$$

The eigenfunctions of  $\hat{\mathbf{L}}^+$  are orthogonal to those of  $\hat{\mathbf{L}}$ . Indeed, if

$$\hat{\mathbf{L}}\phi = \lambda\phi \text{ and } \hat{\mathbf{L}}^+\phi^+ = \lambda^+\phi^+ ,$$

then, Eq. (15) gives

$$(\lambda - \lambda^+)(\phi^+, \phi) = 0 . \quad (16)$$

Hence, if  $\lambda \neq \lambda^+$ , then  $(\phi^+, \phi) = 0$ , i.e., eigenfunctions of  $\hat{\mathbf{L}}$  and  $\hat{\mathbf{L}}^+$  corresponding to the different eigenvalues,  $\lambda$  and  $\lambda^+$ , are orthogonal. On the other hand, if  $(\phi^+, \phi) \neq 0$ , then  $\lambda = \lambda^+$ .

### 5.3.2 The transport operator

The transport operator  $\hat{\mathbf{L}}$  can be defined by writing the inhomogeneous and time-independent transport equation (Eq. 6) as

$$\hat{\mathbf{L}}\Phi(\mathbf{r}, \mathbf{\Omega}, E) + S(\mathbf{r}, \mathbf{\Omega}, E) = 0 , \quad (17)$$

where

$$\hat{\mathbf{L}}\Phi = -\mathbf{\Omega} \cdot \nabla\Phi - \Sigma\Phi + \int_0^\infty \int_{4\pi} \Sigma'f\Phi' d\mathbf{\Omega}' dE' . \quad (18)$$

In this expression, the short-notation

$$f = f(\mathbf{r}, \mathbf{\Omega}', E' \rightarrow \mathbf{\Omega}, E)$$

was used. As  $\hat{\mathbf{L}}$  is not self-adjoint, we have that

$$(\psi, \hat{\mathbf{L}}\phi) \neq (\hat{\mathbf{L}}\psi, \phi) .$$

### 5.3.3 The adjoint to the transport operator

The direct operator  $\hat{\mathbf{L}}$  operates on the neutron angular flux,  $\Phi(\mathbf{r}, \mathbf{\Omega}, E)$ . In contrast, the adjoint operator  $\hat{\mathbf{L}}^+$  operates on adjoint functions,  $\Phi^+(\mathbf{r}, \mathbf{\Omega}, E)$ . By definition,  $\hat{\mathbf{L}}^+$  obeys

$$(\Phi^+, \hat{\mathbf{L}}\Phi) = (\hat{\mathbf{L}}^+\Phi^+, \Phi) , \quad (19)$$

where  $\Phi^+(\mathbf{r}, \mathbf{\Omega}, E)$  is the adjoint angular flux. Similarly to Eq. (18),  $\hat{\mathbf{L}}^+$  is proved to be defined as

$$\hat{\mathbf{L}}^+\Phi^+ = \mathbf{\Omega} \cdot \nabla \Phi^+ - \Sigma \Phi^+ + \int_0^\infty \int_{4\pi} \Sigma f \Phi' d\mathbf{\Omega}' dE' . \quad (20)$$

Here,

$$f = f(\mathbf{r}, \mathbf{\Omega}, E \rightarrow \mathbf{\Omega}', E') .$$

The following two differences between the direct operator  $\hat{\mathbf{L}}$  (Eq. 18) and the adjoint operator  $\hat{\mathbf{L}}^+$  (Eq. 20) should be noted;

- The gradient terms,  $\mathbf{\Omega} \cdot \nabla \Phi$  and  $\mathbf{\Omega} \cdot \nabla \Phi^+$ , have opposite signs.
- The before-state and the after-state of the scattering function  $f$  have been interchanged, i.e.,  $(\mathbf{\Omega}, E \rightarrow \mathbf{\Omega}', E')$  in  $\hat{\mathbf{L}}$  becomes  $(\mathbf{\Omega}', E' \rightarrow \mathbf{\Omega}, E)$  in  $\hat{\mathbf{L}}^+$ .

The boundary condition of no incoming neutrons for the direct flux results in no outgoing neutrons for the adjoint flux, i.e.,

$$\begin{aligned} \Phi(\mathbf{r}, \mathbf{\Omega}, E)|_{\mathbf{n} \cdot \mathbf{\Omega} < 0} &= 0 \\ \Phi^+(\mathbf{r}, \mathbf{\Omega}, E)|_{\mathbf{n} \cdot \mathbf{\Omega} > 0} &= 0 . \end{aligned}$$

## 5.4 Neutron importance

It can be shown that the adjoint function can be used as a measure of neutron importance. Consider a steady-state sub-critical system containing a steady source  $S(\mathbf{r}, \mathbf{\Omega}, E)$  and suppose that there is a neutron detector present with a response proportional to the macroscopic cross-section,  $\Sigma_d(\mathbf{r}, E)$ , of the detector material. The inhomogeneous time-independent transport equation can be written as

$$\hat{\mathbf{L}}\Phi = -S \quad (21)$$

with the boundary condition of no incoming neutron flux. Consider also an inhomogeneous adjoint equation with the source  $\Sigma_d(\mathbf{r}, E)$ , i.e.,

$$\hat{\mathbf{L}}^+\Phi^+ = -\Sigma_d \quad (22)$$

with the boundary condition of no outgoing adjoint flux. By multiplying Eq. (21) by  $\Phi^+$  and Eq. (22) by  $\Phi$ , subtracting the resulting expressions and integrating the difference over all variables, the following expression can be obtained;



$$\iiint S(\mathbf{r}, \boldsymbol{\Omega}, E) \Phi^+(\mathbf{r}, \boldsymbol{\Omega}, E) d\mathbf{r} d\boldsymbol{\Omega} dE = \iiint \Sigma_d(\mathbf{r}, \boldsymbol{\Omega}, E) \Phi(\mathbf{r}, \boldsymbol{\Omega}, E) d\mathbf{r} d\boldsymbol{\Omega} dE . \quad (23)$$

In the last step, the definition of the adjoint operator in Eq. (19) was used. The right-hand side of Eq. (23) is proportional to the response of the detector to the source  $S$ . Assuming a steady state unit source,  $S$ , at the location  $\mathbf{r}_0$  emitting one neutron per second with energy  $E_0$  in the direction  $\boldsymbol{\Omega}_0$ , i.e.,

$$S(\mathbf{r}, \boldsymbol{\Omega}, E) = \delta(\mathbf{r} - \mathbf{r}_0) \delta(\boldsymbol{\Omega} - \boldsymbol{\Omega}_0) \delta(E - E_0) ,$$

the left-hand side of Eq. (23) reduces to the adjoint flux. We thus obtain the following useful representation;

$$\Phi^+(\mathbf{r}_0, \boldsymbol{\Omega}_0, E_0) = \iiint \Sigma_d(\mathbf{r}, \boldsymbol{\Omega}, E) \Phi(\mathbf{r}, \boldsymbol{\Omega}, E) d\mathbf{r} d\boldsymbol{\Omega} dE . \quad (24)$$

Hence,  $\Phi^+(\mathbf{r}_0, \boldsymbol{\Omega}_0, E_0)$  is proportional to the detector response to the unit source  $S$  and the adjoint flux is thus a measure of the importance of a neutron in contributing to the response of the detector. From this, it can also be understood that the adjoint flux with the values  $\mathbf{r}_0$ ,  $\boldsymbol{\Omega}_0$  and  $E_0$  may be defined to be proportional to the average flux in the system, as well as to the total power produced.

## 5.5 Definition of $k_{eff}$ and $k_s$

The time-independent neutron transport equation can also be expressed using the fission production operator,  $\hat{\mathbf{F}}$ , and the net neutron loss operator,  $\hat{\mathbf{A}}$ , according to

$$\hat{\mathbf{A}}\Phi = \hat{\mathbf{F}}\Phi + S . \quad (25)$$

Here,

$$\hat{\mathbf{A}}\Phi = \boldsymbol{\Omega} \cdot \nabla \Phi + \Sigma \Phi - \int_0^\infty \int_{4\pi} \sum_{x \neq f} \Sigma'_x f_x \Phi' d\boldsymbol{\Omega}' dE' \quad (26)$$

$$\hat{\mathbf{F}}\Phi = \frac{\chi(E)}{4\pi} \int_0^\infty \int_{4\pi} \nu \Sigma'_f \Phi' d\boldsymbol{\Omega}' dE' . \quad (27)$$

For the corresponding homogeneous system, we have for the direct and the adjoint fluxes that

$$\hat{\mathbf{A}}\Phi = \frac{1}{\lambda} \hat{\mathbf{F}}\Phi \quad (28)$$

$$\hat{\mathbf{A}}^+\Phi^+ = \frac{1}{\lambda^+} \hat{\mathbf{F}}^+\Phi^+ . \quad (29)$$

By multiplying Eq. (28) by  $\Phi^+$  and integrating over all variables, multiplying Eq. (29) by  $\Phi$  and integrating, and then using the definition of the adjoint operator (Eq. 19), it can also be shown that the two eigenvalues,  $\lambda$  and  $\lambda^+$ , are identical, i.e.,

$$\lambda = \frac{\langle \Phi^+, \hat{\mathbf{F}}\Phi \rangle}{\langle \Phi^+, \hat{\mathbf{A}}\Phi \rangle} = \frac{\langle \hat{\mathbf{F}}^+\Phi^+, \Phi \rangle}{\langle \hat{\mathbf{A}}^+\Phi^+, \Phi \rangle} = \lambda^+ . \quad (30)$$

Assuming that  $\Phi_0$  is the solution corresponding to the largest eigenvalue, i.e.,  $\lambda_0 = k_{eff}$ , the direct and the adjoint balance equations become

$$\hat{\mathbf{A}}\Phi_0 = \frac{1}{k_{eff}} \hat{\mathbf{F}}\Phi_0 \quad (31)$$

$$\hat{\mathbf{A}}^+\Phi_0^+ = \frac{1}{k_{eff}} \hat{\mathbf{F}}^+\Phi_0^+ . \quad (32)$$

Thus,

$$k_{eff} = \frac{\hat{\mathbf{F}}\Phi_0}{\hat{\mathbf{A}}\Phi_0} = \frac{\hat{\mathbf{F}}^+\Phi_0^+}{\hat{\mathbf{A}}^+\Phi_0^+} . \quad (33)$$

Here, the both ratios do not depend on the phase point  $(\mathbf{r}, \mathbf{\Omega}, E)$ . If we now multiply Eq. (31) by  $\Phi_0^+$ , integrating and recalling Eq. (19), we obtain

$$k_{eff} = \frac{\langle \Phi_0^+, \hat{\mathbf{F}}\Phi_0 \rangle}{\langle \Phi_0^+, \hat{\mathbf{A}}\Phi_0 \rangle} . \quad (34)$$

Moreover, by using the orthogonality relation between eigenmodes,

$$\langle \Phi_i^+, \Phi_j \rangle = 0 \quad i \neq j , \quad (35)$$

and assuming that the solution to Eq. 25 may be cast into a series,

$$\Phi = \sum_n \Phi_i = \Phi_0 + \Phi_1 + \dots + \Phi_n , \quad (36)$$

$\Phi_0$  in Eq. (34) can be replaced by  $\Phi$ . We thus have that

$$k_{eff} = \frac{\langle \Phi_0^+, \hat{\mathbf{F}}\Phi \rangle}{\langle \Phi_0^+, \hat{\mathbf{A}}\Phi \rangle} = \frac{\langle \Phi_0^+, \hat{\mathbf{F}}\Phi \rangle}{\langle \Phi_0^+, \hat{\mathbf{F}}\Phi \rangle + \langle \Phi_0^+, S \rangle} . \quad (37)$$

We can also define a source multiplication factor,  $k_s$ , as

$$k_s = \frac{\langle \hat{\mathbf{F}}\Phi \rangle}{\langle \hat{\mathbf{A}}\Phi \rangle} = \frac{\langle \hat{\mathbf{F}}\Phi \rangle}{\langle \hat{\mathbf{F}}\Phi \rangle + \langle S \rangle}, \quad (38)$$

which represents the ratio of fission neutrons produced over the total neutrons produced (fission plus external source). This also allows us to introduce the parameter,  $\rho_s$ , as

$$\rho_s = \frac{k_s - 1}{k_s} = -\frac{\langle S \rangle}{\langle \hat{\mathbf{F}}\Phi \rangle}, \quad (39)$$

which is sometimes called the inhomogeneous reactivity or the source reactivity, because of the analogy to the homogeneous reactivity,  $\rho_{eff} = (k_{eff} - 1)/k_{eff}$ . When  $k_{eff}$  approaches unity ( $k_{eff} \rightarrow 1$ ), we also note that  $\Phi \rightarrow \Phi_0$ ,  $k_s \rightarrow k_{eff}$  and that  $\rho_s \rightarrow \rho_{eff}$ .

## Chapter 6

# Source efficiency and energy gain

### 6.1 Neutron source efficiency

#### 6.1.1 Definition of $\varphi^*$

The neutron source efficiency [8,9], usually denoted  $\varphi^*$ , represents the average importance of external source neutrons over the average importance of fission neutrons. It can be defined as

$$\varphi^* = \frac{\frac{\langle \Phi_0^+, S \rangle}{\langle S \rangle}}{\frac{\langle \Phi_0^+, \hat{\mathbf{F}}\Phi \rangle}{\langle \hat{\mathbf{F}}\Phi \rangle}}, \quad (40)$$

where

$$\frac{\langle \Phi_0^+, S \rangle}{\langle S \rangle} = \frac{\int S \Phi_0^+ dr d\Omega dE}{\int S dr d\Omega dE} \quad (41)$$

is the average importance of source neutrons, and

$$\frac{\langle \Phi_0^+, \hat{\mathbf{F}}\Phi \rangle}{\langle \hat{\mathbf{F}}\Phi \rangle} = \frac{\int \hat{\mathbf{F}}\Phi \Phi_0^+ dr d\Omega dE}{\int \hat{\mathbf{F}}\Phi dr d\Omega dE} \quad (42)$$

is the average importance of fission neutrons in the fundamental mode. Using Eq. (25) and Eq. (37), Eq. (40) can be decomposed and reformulated, according to

$$\frac{\langle \Phi_0^+, S \rangle}{\langle \Phi_0^+, \hat{\mathbf{F}}\Phi \rangle} = \frac{\langle \Phi_0^+, (\hat{\mathbf{A}} - \hat{\mathbf{F}})\Phi \rangle}{\langle \Phi_0^+, \hat{\mathbf{F}}\Phi \rangle} = \frac{\langle \Phi_0^+, \hat{\mathbf{A}}\Phi \rangle}{\langle \Phi_0^+, \hat{\mathbf{F}}\Phi \rangle} - 1 = \frac{1 - k_{eff}}{k_{eff}}$$

and

$$\frac{\langle S \rangle}{\langle \hat{\mathbf{F}}\Phi \rangle} = \frac{\langle \hat{\mathbf{A}}\Phi \rangle - \langle \hat{\mathbf{F}}\Phi \rangle}{\langle \hat{\mathbf{F}}\Phi \rangle} = \frac{\langle \hat{\mathbf{A}}\Phi \rangle}{\langle \hat{\mathbf{F}}\Phi \rangle} - 1 = \frac{1 - k_s}{k_s} .$$

Consequently,  $\varphi^*$  can also be expressed as

$$\varphi^* = \frac{\left( \frac{1 - k_{eff}}{k_{eff}} \right)}{\left( \frac{1 - k_s}{k_s} \right)} = \frac{\rho_{eff}}{\rho_s} , \quad (43)$$

or equivalently, as [84]

$$\varphi^* = \left( \frac{1 - k_{eff}}{k_{eff}} \right) \cdot \frac{\langle \hat{\mathbf{F}}\Phi \rangle}{\langle S \rangle} . \quad (44)$$

The expression for  $\varphi^*$  is valid in the range  $0 < k_{eff} < 1$ . Eq. (44) is the expression that has been used for all calculations determining the source efficiency.  $\langle \hat{\mathbf{F}}\Phi \rangle$  is the total production of neutrons by fission and  $\langle S \rangle$  is the total production of neutrons by the external source. In the above formula, the brackets imply integration over space, angle and energy. Eq. (44) shows that, for given values of  $k_{eff}$  and the external source intensity, the larger  $\varphi^*$  is, the larger is the fission power produced in the system. The quantities on the right hand side of Eq. (44) are standard outputs in the Monte Carlo codes MCNP and MCNPX.

### 6.1.2 Estimation of the statistical error in $\varphi^*$

In order to estimate the statistical uncertainty of  $\varphi^*$ , the formula for ‘‘propagation of error’’ was applied (Eq. 45), assuming that the errors of  $\langle \hat{\mathbf{F}}\Phi \rangle$  and  $\langle S \rangle$  are  $\Delta\langle \hat{\mathbf{F}}\Phi \rangle$  and  $\Delta\langle S \rangle$ .

$$\Delta f(x_1, x_2, \dots) = \sqrt{\left( \frac{\partial f}{\partial x_1} \Delta x_1 \right)^2 + \left( \frac{\partial f}{\partial x_2} \Delta x_2 \right)^2 + \dots + \rho_{12} \cdot \frac{\partial f}{\partial x_1} \Delta x_1 \cdot \frac{\partial f}{\partial x_2} \Delta x_2 + \dots} . \quad (45)$$

The correlation constant  $\rho$  could be either positive or negative; negative if  $k_{eff}$  and  $\langle \hat{\mathbf{F}}\Phi \rangle$  are correlated and positive if they are anti-correlated. However, as a first approximation,  $\rho$  was assumed to be zero. With the derivatives  $\partial\varphi^*/\partial k_{eff}$ ,  $\partial\varphi^*/\partial\langle \hat{\mathbf{F}}\Phi \rangle$  and  $\partial\varphi^*/\partial\langle S \rangle$  inserted in Eq. (45), the following expression for the relative error in  $\varphi^*$  can be obtained;

$$\left( \frac{\Delta\varphi^*}{\varphi^*} \right)^2 \approx \left( \frac{1}{1 - k_{eff}} \cdot \frac{\Delta k_{eff}}{k_{eff}} \right)^2 + \left( \frac{\Delta\langle \hat{\mathbf{F}}\Phi \rangle}{\langle \hat{\mathbf{F}}\Phi \rangle} \right)^2 + \left( \frac{\Delta\langle S \rangle}{\langle S \rangle} \right)^2 . \quad (46)$$

Eq. (46) was used in all calculations presented in this thesis to estimate the statistical uncertainty of  $\varphi^*$ .

### 6.1.3 Definition of the external neutron source in ADS

Since the actual source particles in a system coupled to a proton-induced spallation source are protons rather than neutrons, it is not obvious which is the most appropriate way to define the external neutron source. The procedure to calculate  $\varphi^*$  in an ADS is usually divided into two steps, the first one generating the source neutrons produced as the incident protons interact with the target nuclei and the second step determining the efficiency of these source neutrons. Different source definitions are possible and they will result in different values and meanings of  $\varphi^*$  [Paper VII,11,12]. A brief summary of four different definitions of the external neutron source that have been used in the ADS field is given by Klein Meulekamp and Hogenbirk [10]. Among these, the two most frequently used definitions, the target neutron leakage source and the energy cut-off source, as well as the primary neutron source, are described in the following. The fourth definition is the fission source, consisting of the first generation of fission neutrons.

#### The target neutron leakage source

In the approach of the target neutron leakage source, the neutrons that leak out radially from the target are defined as source neutrons [11,85]. The method consists of, in the first step, transporting, with a high-energy code (e.g., MCNPX), the high-energy protons and the secondary particles that they produce in the target. The neutrons that leak out from the target are defined as the source and their properties, in terms of position, direction and energy, are written to a source file. Only the target is present in the first simulation, so no once-leaked neutrons reentering the target are included in the source definition. In the second step, the leakage neutrons are re-emitted as fixed source neutrons in a separate run and the efficiency of them, i.e.,  $\varphi^*$ , is determined. Since the target neutron leakage spectrum includes a high-energy tail, both step 1 and step 2 should preferably be simulated with a high-energy transport code, which has the capability of transporting neutrons with energy up to the incident proton energy.

#### The energy cut-off neutron source

Another way to define the neutron source is to collect the neutrons that fall below a certain cut-off energy, usually 20 or 150 MeV [12,86,87]. In the first step, a high-energy code is used to transport the incident protons and the secondary high-energy particles. The neutrons that are produced are either killed if they are born below the cut-off energy or transported until they fall below this energy. The properties of the killed neutrons are written to a source file, which is followed by their reemission in the second-step run and the calculation of  $\varphi^*$ . An advantage of this approach is that the second step can be simulated with a low-energy transport code. The cut-off energy is set to the upper energy limit of the cross-section library that will be used in

the second-step calculation. This is desirable since many reactor code systems are limited to the energy range covered by the cross-section data library (generally 20 or 150 MeV).

### **The primary neutron source**

The source neutrons produced from spallation are in this case defined as the neutrons produced directly in a spallation reaction induced by a proton, or by any other particle, except neutrons [Paper VII]. These neutrons are called “primary neutrons”, in contrast to “secondary” neutrons, which are the neutrons created by the primary neutrons, e.g., via neutron-induced spallation or (n,xn)-reactions. In this approach, the starting point for the chain of neutron multiplication is the moment when a neutron is born in a non-neutron-induced reaction. The primary neutron may be multiplied, if its energy is sufficiently high, by secondary spallation and/or (n,xn)-reactions in the lead target, followed by fission reactions in the fuel. The end point of the neutron multiplication chain is the absorption or escape of the last neutron originating from the initial primary source neutron.

In the computational procedure, the properties of the neutrons that are created directly in the spallation interactions are recorded. After that, the neutron trajectories are immediately terminated. This procedure produces a spectrum of primary spallation neutrons, i.e., no secondary neutrons are included. In the second step, these primary spallation neutrons are supplied to the computation code as fixed source neutrons for separate simulations determining  $\varphi^*$ .

### **6.1.4 Neutron importance**

The importance of a neutron in a system can be described analytically by determining the adjoint flux,  $\Phi^+(\mathbf{r}, \boldsymbol{\Omega}, E)$ , which is dependent on the position, direction and energy of the neutron. The adjoint flux is a measure of the importance of a neutron in contributing to the response of a detector located somewhere in the core, and consequently also to the neutron flux in the core. Considering the source neutrons that leak out radially from the spallation target and enter into the core, it can therefore be assumed that the average importance of these neutrons will be different from the average importance of the fission neutrons, since they are emitted at different positions, in different directions and with different energy distributions than are the fission neutrons. Thus, the efficiency of the source neutrons can be expected to differ from unity, i.e.,  $\varphi^* \neq 1$ .

When changing some of the properties of the inner part of the core, e.g., the composition of nuclides, the multiplicative conditions for both the source neutrons and the fission neutrons may change, mainly due to the differences in the microscopic cross-sections between different nuclides. The change in the source efficiency is dependent on whether the nuclide substitution in the core changes the importance of the source neutrons more than the importance of the fission neutrons, or not. If the importance of the source neutrons increases more than that of the fission neutrons, the source efficiency will increase, and vice versa. Since the cross-sections are affected mainly by the energy of the neutrons, the major cause for the source effi-

ciency to change is therefore if the spectra of the source neutrons and/or that of the fission neutrons change.

## 6.2 Proton source efficiency

An important factor when designing an ADS is to optimise the energy gain of the system, i.e., the core power over the accelerator power, given that the reactor is operating at a certain sub-critical reactivity level. Optimising the source efficiency and thereby minimising the proton beam requirements can have an important impact on the overall design of an ADS and on the economy of its operation. The neutron source efficiency is commonly used to study this quantity, since it is related to the energy production in the core induced by an average external source neutron.

However, calculating  $\varphi^*$  for an ADS introduces some complications. Since the neutron source is generated by a proton beam/target simulation, the distribution of the source neutrons is dependent on the target properties and the proton beam properties. Apart from the drawback that the neutron source can be defined in different ways, another complication associated with  $\varphi^*$  is that varying certain system parameters, when studying  $\varphi^*$ , may change the neutron source distribution and, thus,  $Z$ . If a change in the studied system parameter changes the distribution of the neutron source,  $\varphi^*$  has to be weighted by  $Z$ . Adopting the target neutron leakage definition, examples of parameters affecting the source distribution are the target dimension, the proton beam energy and the axial proton beam impact position. Other system parameters, such as the core coolant material, the fuel composition and the core dimensions, are independent of the target region and do not affect the neutron source. In contrast to the target neutron leakage source, it has been shown that using the energy cut-off definition, the neutron source distribution is rather insensitive to changes in the target radius [12]. However, substituting the coolant material or changing the fuel composition in this case might affect the distribution of the neutron source, in particular for small target radii.

With the aim of providing a simple mean for studying the core power over the beam power, a new parameter, the proton source efficiency,  $\psi^*$ , has been introduced [Paper II].  $\psi^*$  refers to the number of fission neutrons produced in the system by each source proton. The advantages of using the proton source efficiency instead of the neutron source efficiency is that there is no ambiguity in how to define the external source and that it is proportional to the energy gain. Extensive MCNPX calculations of  $\psi^*$  as a function of many different target/core properties have been performed in order to provide a basis for the optimisation of the energy gain of an ADS. A summary of these studies is given in Chapter 10.

### 6.2.1 Definition of $\psi^*$

The proton source efficiency is defined in analogy with the definition of  $\varphi^*$  and can be expressed in terms of the k-eigenvalue,  $k_{eff}$ , and the total number of neutrons produced by fission in the core for each source proton,  $\langle \hat{\mathbf{F}}\Phi \rangle / \langle S_p \rangle$ , according to



$$\psi^* = \left( \frac{1 - k_{eff}}{k_{eff}} \right) \cdot \frac{\langle \hat{\mathbf{F}}\Phi \rangle}{\langle S_p \rangle} . \quad (47)$$

Since  $\langle \hat{\mathbf{F}}\Phi \rangle$  is approximately proportional to the total power produced in the core, for a given  $k_{eff}$ ,  $\psi^*$  is thus proportional to the core power divided by the proton beam power. Since  $\psi^*$  is also equal to the product of  $\varphi^*$  and the number of source neutrons generated per source proton,  $Z$ , we have the following relation between the proton source efficiency and the neutron source efficiency;

$$\psi^* = \varphi^* \cdot Z . \quad (48)$$

Here,  $Z = \langle S \rangle / \langle S_p \rangle$ , and  $\langle S \rangle$  and  $\langle S_p \rangle$  are the total numbers of emitted source neutrons and source protons, respectively. For a fixed system, i.e.,  $Z$  is constant, it follows that  $\psi^*$  is proportional to  $\varphi^*$ . However, when studying a change in a system design,  $Z$  may change. Therefore, in such a case, only  $\psi^*$  (not  $\varphi^*$ ) remains proportional to the ratio between the core power and the proton beam power.

## 6.2.2 Comparison of $\psi^*$ and $\varphi^*$

Investigating  $\psi^*$  and  $\varphi^*$  as functions of the target radius and of coolant material illustrates the differences between system parameters that affect and do not affect the neutron source distribution. Using the target neutron leakage definition as an example and changing the coolant material, the target and the neutron source distribution are unaffected and  $Z$  does not change, so  $\psi^*$  and  $\varphi^*$  vary in exactly the same way. Hence, for a fixed target radius, but with different coolant materials (LBE and Na), it follows from Eq. (48) that

$$\frac{\psi^*_{LBE}}{\psi^*_{Na}} = \frac{\varphi^*_{LBE}}{\varphi^*_{Na}} . \quad (49)$$

When varying the target radius, on the other hand,  $Z$  changes, so  $\psi^*$  and  $\varphi^*$  vary in different ways. For a fixed coolant material, but with different target radii ( $R_1$  and  $R_2$ ), we thus have that

$$\frac{\psi^*_{R_1}}{\psi^*_{R_2}} \neq \frac{\varphi^*_{R_1}}{\varphi^*_{R_2}} . \quad (50)$$

Consequently, if one wants to use the  $\varphi^*$  parameter, it needs to be multiplied by  $Z$  when studying the energy gain as a function of the target radius, whereas this is not necessary when comparing different coolant materials. However, applying the proton source efficiency and always referring to  $\psi^*$ , none of this has to be considered.

## 6.3 Energy gain

Calculations determining some different energy-related parameters have been performed with the high-energy Monte Carlo code MCNPX for an LBE-cooled ADS-model similar to the model described in **Paper II** and in Section 10.1. The data library ENDF/B-6.8 and the Bertini intranuclear cascade model were used in the simulations.

### 6.3.1 Relationship between the source efficiency and the energy gain

Assuming that the proton beam current needed to drive the sub-critical core,  $i_p$ , and the reactivity of the sub-critical core have been fixed, the total core power,  $P_{tot}$ , can be determined, according to [88]

$$P_{tot} = \frac{k_{eff}}{1 - k_{eff}} \cdot \frac{i_p \bar{E}_f}{\bar{\nu}} \cdot Z\varphi^* , \quad (51)$$

where  $\bar{\nu}$  is the average neutron yield per fission,  $\bar{E}_f$  is the average recoverable energy released in a fission and  $Z$  is the number of source neutrons produced in the target per incident proton. Eq. (51) is valid in the range  $0 < k_{eff} < 1$ . If  $i_p$  is expressed in mA and  $\bar{E}_f$  in MeV in Eq. (51),  $P_{tot}$  is given in kW. For the model studied in this section, it was found that  $\bar{\nu} = 2.97$  and  $\bar{E}_f = 187$  MeV. The source efficiency is treated in more detail in a later chapter and Eq. (51) is derived in Appendix B. Eq. (51) shows that, apart from the strong dependence on the reactivity level, the core power is proportional to the product of the number of neutrons per proton ( $Z$ ) and the efficiency of these neutrons ( $\varphi^*$ ).

Let us now define the energy gain,  $G$ , as the ratio between the total power produced in the core and the power of the accelerator beam,  $P_{acc}$ . Since  $i_p = P_{acc} / E_p$ , where  $E_p$  is the proton energy,

$$G = \frac{P_{tot}}{P_{acc}} = \frac{k_{eff}}{1 - k_{eff}} \cdot \frac{\bar{E}_f}{\bar{\nu}} \cdot \frac{Z\varphi^*}{E_p} . \quad (52)$$

For a given fuel composition,  $\bar{E}_f$  and  $\bar{\nu}$  can be considered to be constant. Even though there are high-energy neutrons entering into the fuel (the neutron yield  $\nu$  is not constant with respect to neutron energy), the fraction of fissions in the core that are induced by high-energy neutrons is very small. Therefore, a change in the neutron yield for these fission events will have very little impact on  $\bar{\nu}$ . The variations of  $\bar{E}_f$  and  $\bar{\nu}$  have been calculated for the series of different studies presented in this thesis and were found to be much smaller than the statistical errors in the simulations (except in the case where the fuel composition was modified). When the fuel composition changes,  $\bar{\nu}$  might also change, which should be kept in mind if different fuel types are compared.

Moreover, replacing  $\varphi^* \cdot Z$  by  $\psi^*$  in Eq. (51) and Eq. (52), the following relations between the total core power and  $\psi^*$ ;

$$P_{tot} = \frac{k_{eff}}{1 - k_{eff}} \cdot \frac{i_p \bar{E}_f}{\bar{v}} \cdot \psi^* \quad (53)$$

and between the energy gain and  $\psi^*$ ;

$$G = \frac{P_{tot}}{P_{acc}} = \frac{k_{eff}}{1 - k_{eff}} \cdot \frac{\bar{E}_f}{\bar{v}} \cdot \frac{\psi^*}{E_p}, \quad (54)$$

can also be obtained.

### 6.3.2 Varying the proton energy

In Fig. 14, the number of neutrons produced in the target per proton, divided by the proton energy,  $Z/E_p$ , is plotted as a function of proton energy. It is shown that  $Z/E_p$  increases rapidly with increasing proton energy up to about 1000 MeV and that the maximum is reached at about 1400 MeV. The values of  $Z$  and  $Z/E_p$  are also listed in Table 5. According to Eq. (52), it appears that, in order to obtain the exact relationship between the neutron production and the energy gain,  $Z/E_p$  should be multiplied by  $\varphi^*$ , which can vary considerably for different target and core designs. However, when varying only the proton energy, as is the case in Fig. 14, the change in  $\varphi^*$  is relatively small, 1.41 for 600 MeV protons compared to 1.47

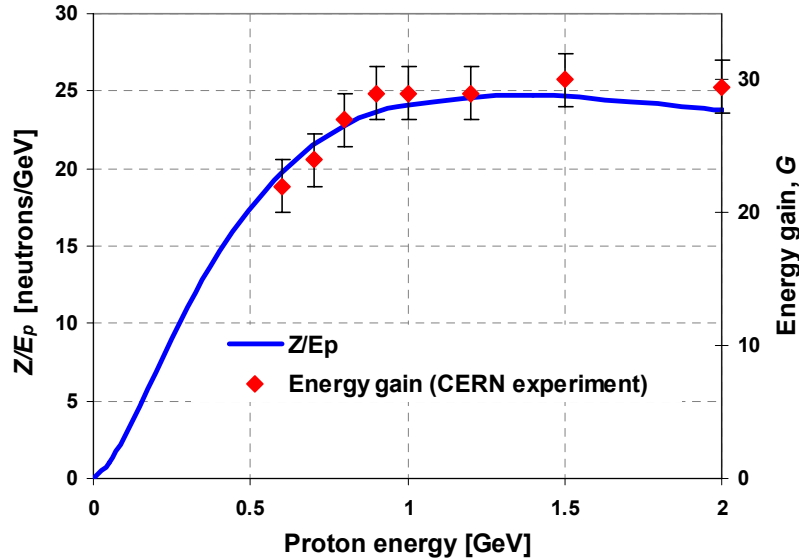


**Fig. 14.** Neutron yield per proton energy,  $Z/E_p$ , as function of proton energy for proton beams impinging on a LBE target with radius 20 cm. For comparison, the energy gain,  $G$ , determined in the FEAT experiments performed at CERN [89] for a set-up configuration of  $k_{eff} = 0.895$  is also displayed.

**Table 5.** Different neutronic parameters computed for different proton beam energies for an LBE-cooled ADS with target radius of 20 cm and  $k_{eff} = 0.95$ .

| Proton energy | $Z$  | $Z/E_p$ | $\varphi^*$ <sup>a</sup> | $\psi^*$ | $G$ |
|---------------|------|---------|--------------------------|----------|-----|
| 400           | 5.9  | 14.7    | 1.37                     | 8.1      | 25  |
| 600           | 11.8 | 19.7    | 1.41                     | 16.8     | 35  |
| 800           | 18.2 | 22.7    | 1.42                     | 25.8     | 41  |
| 1000          | 24.2 | 24.2    | 1.47                     | 35.5     | 45  |
| 1400          | 34.6 | 24.7    | 1.47                     | 50.9     | 46  |
| 2000          | 47.6 | 23.8    | 1.47                     | 69.8     | 44  |

<sup>a</sup>  $\varphi^*$  was calculated according to the target neutron leakage definition.

for 1000 MeV protons, as is shown in Table 5. Thus, the energy gain appears to be fairly well represented by the  $Z/E_p$  ratio. The reason why  $\varphi^*$  is only weakly dependent on the proton energy is that the energy spectrum of the neutrons leaking out from the target changes only marginally with the proton energy, which is shown in Fig. 15. The product of  $Z$  and  $\varphi^*$ ,  $\psi^*$ , is also displayed in Table 5.

In the FEAT experiments performed at CERN [89], the energy gain was studied as function of the proton beam energy for a sub-critical multiplying medium consisting of depleted uranium. The results are re-plotted in Fig. 14. We see in the figure that the MCNPX-simulated values of  $Z/E_p$  have similar relative dependence on the proton energy as the results from the CERN experiments. The small deviation at higher proton energies is a result of the limited height of the target in the MCNPX simulations. This comparison confirms that  $Z/E_p$  (provided that  $\varphi^*$  does not change significantly), as well as  $\psi^*$ , represent well the energy gain of an ADS. The  $k_{eff}$  of the sub-critical assembly in the CERN experiments was 0.895. In order to obtain  $G$  for  $k_{eff} = 0.95$ , the values have to be multiplied by  $(1-0.895)/(1-0.95) = 2.1$ . For  $E_p = 1000$  MeV, the energy gain thus becomes 61.

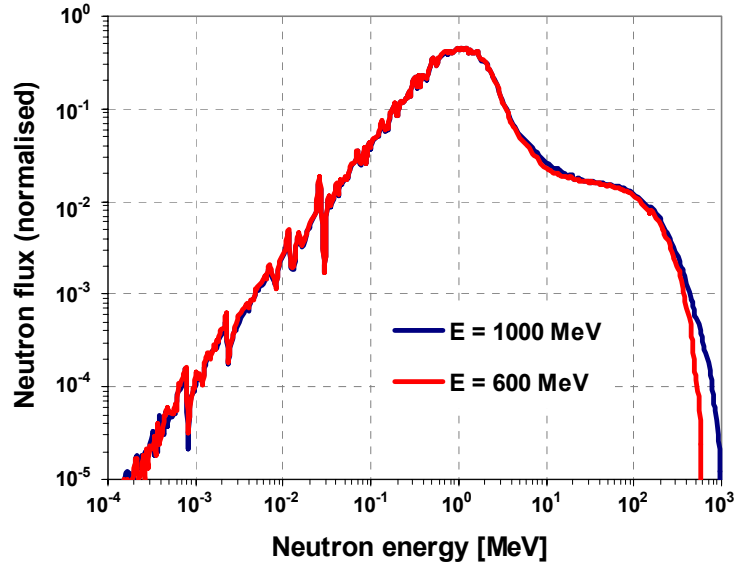


**Fig. 15.** Energy spectra for the source neutrons leaking out into the core, for proton energies of 600 and 1000 MeV.

### 6.3.3 Varying the target radius

Both  $Z$  and  $\varphi^*$  are dependent on the system design, in particular on the target dimensions. In this section,  $Z$  has been defined as the number of neutrons leaking out radially from the spallation target and entering into the fuel. This definition is somewhat different to the one applied in Section 10.1 and in **Paper II**, where all neutrons leaking out radially, i.e., also those leaving the target above and below the core and never enter into the fuel, are included. In particular for large target radii ( $R > 10$  cm), the difference becomes large, since the axial leakage increases with increasing target radius. In Fig. 16 and in Table 6, where  $Z$  and  $\varphi^*$  are displayed for different target radii, it is seen that  $Z$  increases when the target radius increases from 10 cm to 20 cm, as the high-energy neutrons are multiplied on their way out into the fuel. At about 20-30 cm target radius, the increasing effect on  $Z$  from the neutron multiplication in the target is cancelled out by the increasing axial leakage of the source neutrons and increasing the radius further decreases  $Z$ .

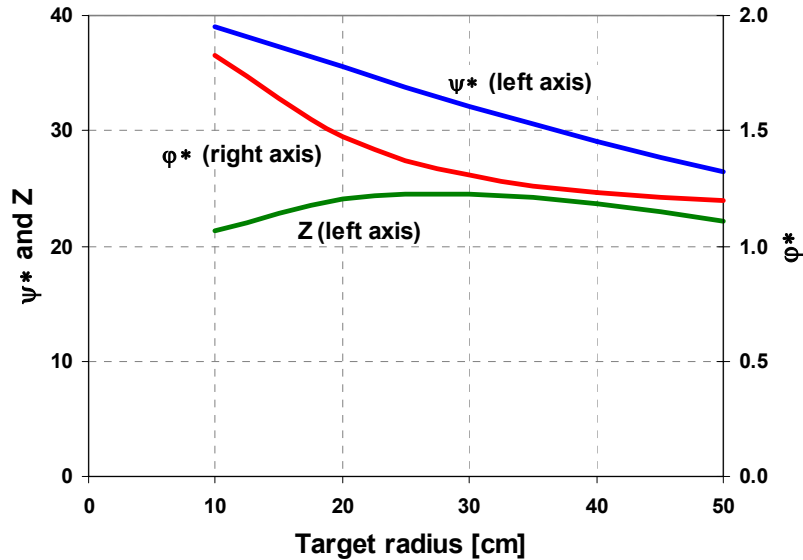


**Fig. 16.** Proton source efficiency,  $\psi^*$ , neutron source efficiency,  $\varphi^*$ , (calculated according to the target neutron leakage definition) and number of source neutrons per incident proton,  $Z$ , for different target radii.

**Table 6.** Different neutronic parameters computed for different target radii for an ADS of  $k_{eff} = 0.95$ , driven by proton beams of energy 600 and 1000 MeV.

| Target radius | $E_p = 600$ MeV |                |          |     | $E_p = 1000$ MeV |                |          |     |
|---------------|-----------------|----------------|----------|-----|------------------|----------------|----------|-----|
|               | $Z$             | $\varphi^{*a}$ | $\psi^*$ | $G$ | $Z$              | $\varphi^{*a}$ | $\psi^*$ | $G$ |
| 10            | 10.9            | 1.75           | 19.1     | 40  | 21.3             | 1.82           | 39.0     | 49  |
| 20            | 11.8            | 1.41           | 16.8     | 35  | 24.2             | 1.46           | 35.6     | 45  |
| 30            | 11.9            | 1.29           | 15.4     | 32  | 24.5             | 1.31           | 32.1     | 41  |
| 40            | 11.4            | 1.24           | 14.2     | 30  | 23.6             | 1.22           | 29.1     | 37  |
| 50            | 10.7            | 1.19           | 12.7     | 27  | 22.1             | 1.19           | 26.5     | 34  |

<sup>a</sup>  $\varphi^*$  was calculated according to the target neutron leakage definition.

Moreover,  $\varphi^*$  decreases considerably as the target radius increases, which is due to the softening of the energy spectrum of the source neutrons entering into the target. The probability for neutrons to induce fission decreases with decreasing energy, in particular when the core is loaded with even-N nuclides (Fig. 2). The dependence of the source neutron spectrum on the target radius is illustrated in Fig. 17. The maximum of the neutron spectrum is located at about 1.7, 1.1 and 0.7 MeV for the 10 cm, the 20 cm and the 40 cm target radii, respectively. The differences in energy spectrum are also quantified by calculating the fraction of source neutrons above some energy thresholds (Table 7). We can thus conclude that, with increasing target radius, the efficiency of the source neutrons is strongly reduced. Accordingly,  $\psi^*$ , which is equal to  $Z \cdot \varphi^*$ , as well as the energy gain, which is, for a given proton energy and reactivity, proportional to  $Z \cdot \varphi^*$ , decrease considerably with increasing target radius.

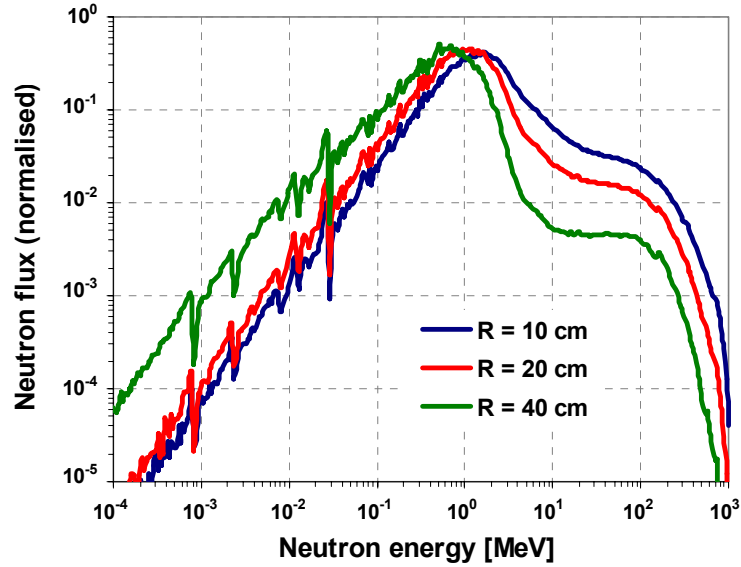


**Fig. 17.** Energy spectra for the source neutrons leaking out into the core, for target radii of 10, 20 and 40 cm.

**Table 7.** Fraction of source neutrons with energy higher than 1, 20 and 150 MeV, together with the location of the maximum of the energy spectrum.

| Target radius | >1 MeV | >20 MeV | >150 MeV | Spectrum peak at [MeV] |
|---------------|--------|---------|----------|------------------------|
| 10            | 64%    | 6.9%    | 1.1%     | 1.7                    |
| 20            | 48%    | 3.3%    | 0.5%     | 1.1                    |
| 30            | 34%    | 1.8%    | 0.25%    | 0.9                    |
| 40            | 23%    | 1.0%    | 0.14%    | 0.7                    |
| 50            | 16%    | 0.6%    | 0.08%    | 0.5                    |

### 6.3.4 Required proton beam current

Rearranging Eq. (53), we can also express the proton beam current as

$$i_p = \frac{P_{acc}}{E_p} = \frac{1 - k_{eff}}{k_{eff}} \cdot \frac{\bar{v}}{\bar{E}_f} \cdot \frac{P_{tot}}{\psi^*} \quad (55)$$

Assuming a total core power of 1000 MWth, a  $k_{eff}$  of 0.95 and a proton energy of 1000 MeV, and using the values of  $\psi^*$  listed in Table 6, a required proton beam current of 22 mA is obtained, which corresponds to a beam power of 22 MW. Such large beam powers will be possible to achieve only with a super-conducting linac. The required proton current, the beam power and the energy gain for some different reactivity levels of a 1000 MWth core are given for 600 MeV and 1000 MeV proton energies in Table 8.

**Table 8.** Required proton beam current,  $i_p$ , proton beam power,  $P_{acc}$ , and energy gain,  $G$ , for a 1000 MWth core.

| $k_{eff}$ | $E_p = 600 \text{ MeV}$ |                   |     | $E_p = 1000 \text{ MeV}$ |                   |     |
|-----------|-------------------------|-------------------|-----|--------------------------|-------------------|-----|
|           | $i_p$<br>[mA]           | $P_{acc}$<br>[MW] | $G$ | $i_p$<br>[mA]            | $P_{acc}$<br>[MW] | $G$ |
| 0.90      | 100                     | 60                | 17  | 47                       | 47                | 21  |
| 0.95      | 47                      | 28                | 35  | 22                       | 22                | 45  |
| 0.98      | 18                      | 11                | 91  | 9                        | 9                 | 116 |

## Chapter 7

# The MUSE experiments

## Investigation of core neutronics

As a step towards the development of a future ADS, the MUSE experiments have provided a valuable mean for investigating the physics of sub-critical systems in the presence of an external neutron source, and for validating experimentally the theoretical methods and calculation tools developed to characterise such a system. An important part of this thesis has been devoted to numerical Monte Carlo simulations investigating the neutronics and the neutron source effects for a model representative of the sub-critical MUSE-4 experiments. Most of the results from these studies have been presented in **Paper I** and **Paper VII**.

### 7.1 The MUSE experiments

#### 7.1.1 The MASURCA facility

MASURCA is the experimental reactor at CEA/Cadarache that has been dedicated to neutronic studies of sub-critical systems in the framework of the MUSE program. The MASURCA core has a height of about 60 cm and a width of about 100 cm. The reactor power is low (maximum 5 kW) and the core cooling is provided by air.

The MASURCA reactor has a flexible design and several different core configurations are possible. The core can be loaded with different fuels, e.g., thorium, uranium and plutonium, different coolants can be simulated, e.g., sodium, lead and gas, and different reactivity levels are possible, both critical and sub-critical. The core of MASURCA is composed of a number of quadratic sub-assemblies (10.6×10.6 cm), each of them being composed of 32 (U,Pu)O<sub>2</sub> rodlets and 32 sodium rodlets (simulating the coolant medium) with a diameter of 1.27 cm. A schematic view of MASURCA, coupled to the GENEPI neutron generator [15], is shown in Fig. 18.

#### 7.1.2 The MUSE experimental programs

In order to validate experimentally the main physical principles of a sub-critical reactor, the basic idea in the MUSE experiments has been to separate the sub-critical



multiplication process from the external source characteristics. This can be done by using a well-defined, in terms of energy and position, neutron source to drive the sub-critical core. The methodology is a step-wise approach, starting from a known and tested critical reference configuration. In the first step, the characterisation of the multiplying medium alone is performed, after which the insertion of an external source and the investigation of the response in the medium is accomplished.

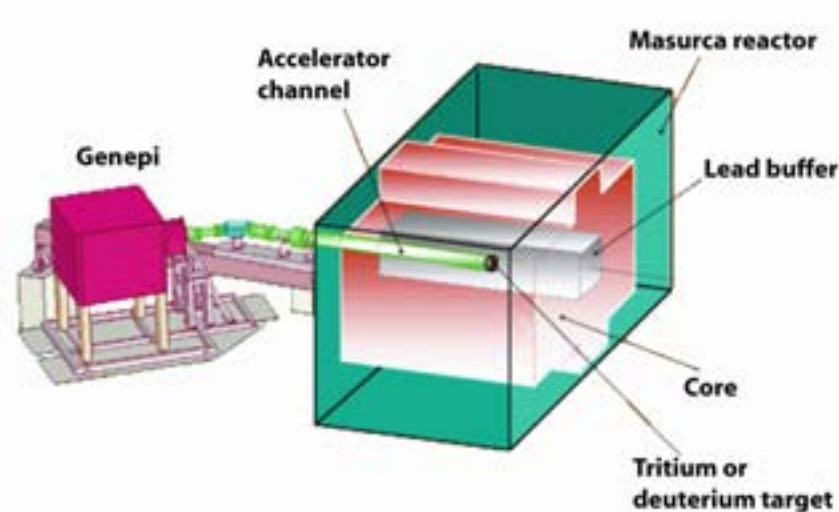


**Fig. 18.** Schematic view of the MASURCA reactor, coupled to the GENEPI neutron generator.

The MUSE program started at CEA/Cadarache in 1995 with the short MUSE-1 experiment [90]. In MUSE-2 (1996) [9], diffusing materials (sodium and stainless steel) were placed around the external source in order to modify its neutron importance and to study the effects from it. In both MUSE-1 and MUSE-2, an intense  $^{252}\text{Cf}$  neutron source was used as the external source. In MUSE-3 (1998) [91], the californium source was replaced by the neutron generator, SODERN/GENIE26, producing 14 MeV neutrons by (D,T)-reactions. Several levels of reactivity were investigated and experiments with different buffer zones, consisting of sodium, stainless steel or lead, were performed.

In the recently completed MUSE-4 experiments [13], which started in 2000 in international collaboration via the 5th Framework Program of the European Community, the neutron generator, GENEPI, especially developed for the MUSE-4 experiments, was introduced. With its improved performances, in terms of source intensity and quality of the neutron pulse, and the use of both (D,D)- and (D,T)-reactions, it extended the range of experimental possibilities and considerably improved the accuracy of the measurements. For example, the accurate dynamic measurements, based on the pulsed mode operation of GENEPI, have enabled experimental reactivity determination of the sub-critical multiplying media. Some of the techniques that were investigated [14,92] for this purpose were the slope fit method (pulsed neutron source method), the inverse kinetics method, the Sjöstrand method (area method), the Rossi- $\alpha$  method and the Feynman- $\alpha$  method. One of the objectives of the

MUSE-4 experiments was to propose a validated experimental technique, including experimental uncertainties, for the development of a reactivity meter that can be envisaged for a future ADS. The conclusions from these investigations were that the method based on the ratio between the source intensity and the neutron flux in the core appears to be the most promising technique for on-line reactivity monitoring. This method, called the current-to-flux reactivity indicator, is briefly described in Section 7.4.2. The other reactivity determination methods are further treated in Section 7.4 and in Chapter 8.

The horizontal cross-sectional geometry of the second sub-critical configuration of MUSE-4 (SC2) is shown in Fig. 19. The GENEPI deuteron accelerator tube is introduced horizontally at the core mid-plane and the deuterium or tritium target is located at the core centre. The neutron source is surrounded by a lead buffer medium in order to achieve a spectrum of the source neutrons similar to the spectrum of spallation neutrons. The fuel is MOX fuel with 72%  $^{238}\text{U}$ , 21%  $^{239}\text{Pu}$  and 5%  $^{240}\text{Pu}$ , with the addition of small amounts of some other actinides. The simulated coolant medium is sodium. A more detailed description of MUSE-4 is given by Soule et al. [93].

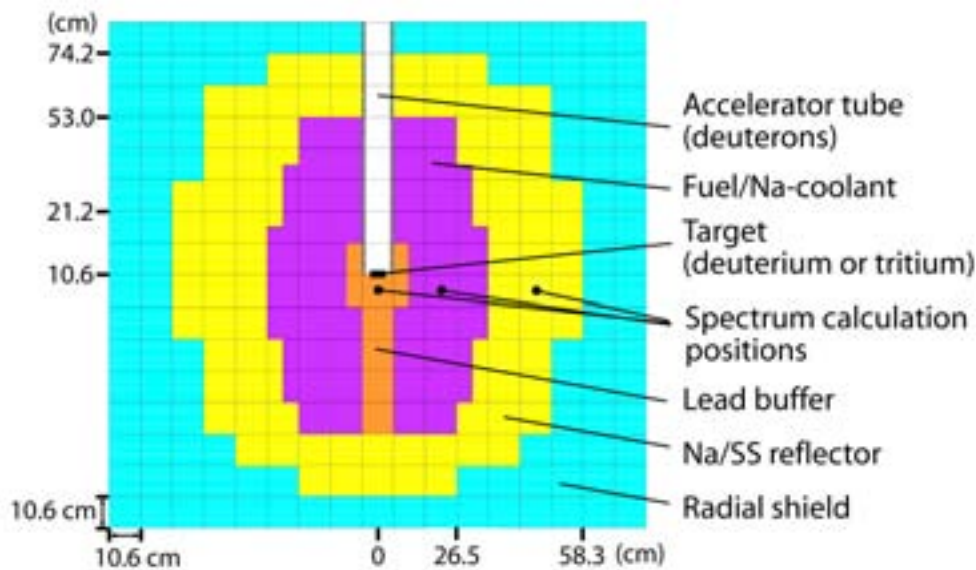


**Fig. 19.** Horizontal cross-sectional view of the second sub-critical configuration, SC2 ( $k_{eff} \sim 0.97$ ) of the MUSE-4 experiments. The core is composed of a number of sub-assemblies with the dimension  $10.6 \times 10.6$  cm. The black dots indicate the positions where the neutron energy spectra have been calculated (Section 7.2.2).

The following experimental configurations, all of them with sodium as coolant medium, were studied in the MUSE-4 experiments;

- One critical reference configuration (GENEPI shut off). The reactivity was experimentally determined by classical pilot rod shutdown measurements.

- Three sub-critical configurations, SC0 with  $k_{eff} \sim 0.994$ , SC2 with  $k_{eff} \sim 0.97$  and SC3 with  $k_{eff} \sim 0.95$ .
- Two complementary asymmetrical configurations with  $k_{eff}$  of about 0.95 and 0.93, obtained from the reference configuration and SC1, by complete insertion of one of the safety rods.

It was also decided to include, in an extended phase of MUSE-4, a configuration partially cooled by lead.

Most neutron transport computational tools and most data libraries existing today have not yet been sufficiently validated for accelerator-driven systems coupled to an intense external neutron source. In the MUSE-4 collaboration, relatively large discrepancies between various codes used to compute the reactivity of a MUSE-type core have been observed. However, the MASURCA reactor used in the MUSE experiments, together with the introduction of GENEPI, has offered a good opportunity for tests and validation of available standard and new reactor codes. For this purpose, a benchmark on computer simulation of MASURCA critical and sub-critical experiments, particularly concentrated on the MUSE-4 experiments, was proposed by the OECD Nuclear Energy Agency [94] and performed by the MUSE-4 collaboration partners. One of the objectives of the benchmark was to define a reference calculation route, including nuclear data, methods and calculation codes, for the prediction of various neutronic parameters of an ADS.

### 7.1.3 The GENEPI neutron generator

GENEPI (GEnérateur de NEutrons Pulsés Intenses), schematically depicted in Fig. 20, is a high-intensity pulsed neutron generator constructed by CNRS/ISN in Grenoble that has been especially developed for the MUSE experiments in the MASURCA facility. A duo-plasmatron providing short pulses of deuterons and a high-intensity electrostatic accelerator are combined to create the 240 keV deuteron beam, which is guided towards either a deuterium or a tritium target at the centre of the core. The (D,D)- and the (D,T)-reactions produce neutrons of, on average, 2.67 MeV and 14.1 MeV, respectively. The main characteristics of GENEPI in the (D,T)-mode are given in Table 9. The special features of GENEPI are the rather high intensity ( $\sim 50$  mA peak) and a pure and very short (1  $\mu$ s) and sharp-edged pulse. This is desirable in order to be able to study the pure neutron propagation out into the fuel of the reactor, independently of the influence of the neutron source. The frequency can be varied from 10 Hz to 5 kHz and each pulse comprises 25 million neutrons, which corresponds to about  $10^{11}$  neutrons per second for the maximum frequency. GENEPI can be operated in either continuous or pulsed mode. The beam has a Gaussian profile with a diameter of 20 mm at half maximum. In order to keep the deuterons together while they are propagating the distance of 2-3 m into the centre of the core, electrostatic planar electrodes are placed in the beam tube, creating effective focusing of the beam. The target consists of a thin layer of deuterium/tritium dissolved in titanium, placed on a 1.5 mm thick cylindrical plate ( $\phi = 30$  mm) of natural copper.

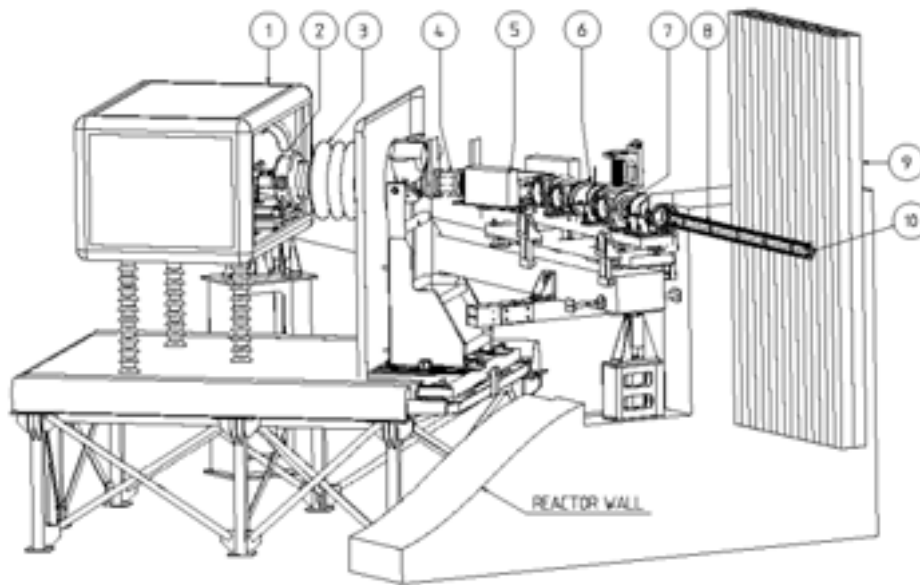


**Fig. 20.** The GENEPI neutron generator. The HV terminal (1), the duoplasmatron (2), the accelerating tube (3), three electrostatic quadrupoles (4,6,7), the dipole (5), the beam line (8) inside the reactor (9) towards the tritium target (10).

**Table 9.** Characteristics of the GENEPI neutron generator in the (D,T)-mode.

|                           |                                 |
|---------------------------|---------------------------------|
| Peak current              | ~50 mA                          |
| Mean current              | < 200 $\mu$ A                   |
| Pulse length              | 1 $\mu$ s                       |
| Deuteron energy           | 240 keV                         |
| Frequency                 | 10-5000 Hz                      |
| Beam diameter             | 20 mm (half max)                |
| Target                    | Tritium + titanium              |
| Activity of target        | 12 Ci ( $4.4 \cdot 10^{11}$ Bq) |
| Neutron energy (mean)     | 14.1 MeV                        |
| Neutron production (peak) | $\sim 25 \cdot 10^6$ n/pulse    |
| Neutron production (mean) | $\sim 10^9$ - $10^{11}$ n/sec   |

#### 7.1.4 The GENEPI-generated external neutron sources

The reaction induced by the GENEPI generator, in the (D,T)-mode, is a deuterium-tritium nuclear reaction, creating a neutron and an alpha particle. The energy released is 17.6 MeV, of which the neutron obtains on average 14.1 MeV. The Coulomb barrier for this reaction is about 400 keV and the deuterons thus have to tunnel through this barrier. The probability for this kind of reaction to occur is a combination of the penetration probability and the cross-section of the (D,T)-interaction, and in this case it is maximal at about 100 keV. If the incoming deuteron energy is low, the angular distribution of neutrons is essentially isotropic and the neutrons will

have energy close to 14.1 MeV. However, with increasing deuteron energy, the neutron density and the neutron energy are higher in the forward direction than in the backward direction.

In the MUSE-4 studies presented in this thesis, the (D,D)- and the (D,T)-reactions themselves have not been simulated. Instead, the double-differential cross-section and the energy dependence of the neutron emission angle are taken from the Handbook on nuclear activation data [95]. These distributions are plotted in Fig. 21 and Fig. 22. The energy of the emitted neutrons in the laboratory system ranges from

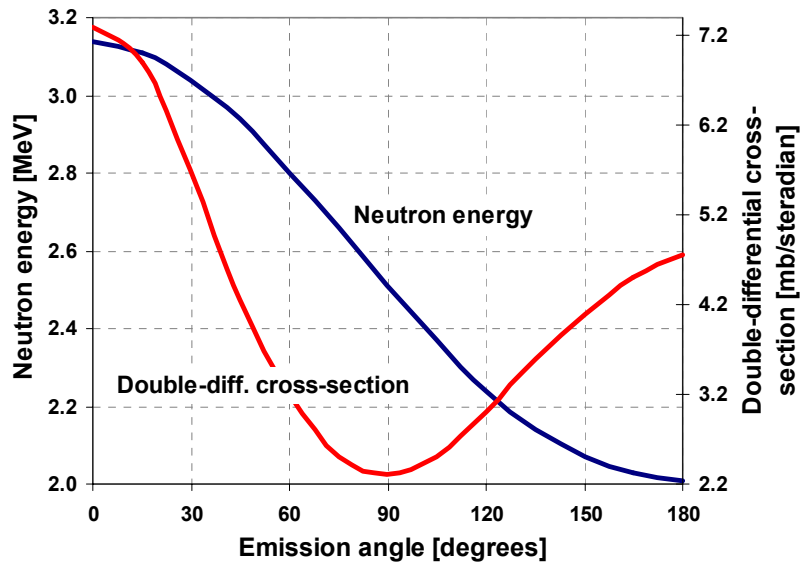


**Fig. 21.** Energy dependence and double-differential cross-section as functions of neutron emission angle for the (D,D)-reaction.

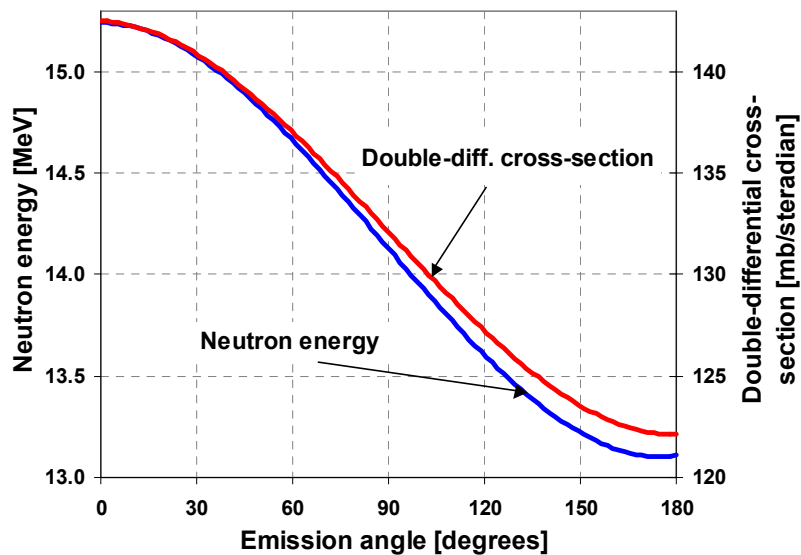


**Fig. 22.** Energy dependence and double-differential cross-section as functions of neutron emission angle for the (D,T)-reaction.

about 2.0 to 3.1 MeV for the (D,D)-neutrons and from about 13.1 to 15.2 MeV for the (D,T)-neutrons, with a maximum emission probability density peaking in the forward direction (0 degrees). For the (D,T)-reaction, the double-differential cross-section has similar shape as the energy dependence, with the maximum at 0 degrees and minimum at 180 degrees. For the (D,D)-reaction, however, the double-differential cross-section has a minimum at 90 degrees. The reason for this behaviour is a quantum effect from the interference of the incoming and outgoing wave functions of the particles involved in the reaction.

## 7.2 Neutron energy spectra

One of the objectives of the studies presented in this section was to compare the effects from the GENEPI-generated (D,D)- and (D,T)-neutron sources with the effects from a spallation source, representative of a future ADS. All of the sources were coupled to the same sub-critical MUSE-4 core. MCNP was used for all calculations with the (D,D)- and the (D,T)-sources, while MCNPX was used to simulate the configurations involving the 1000 MeV proton-induced spallation source.

### 7.2.1 Neutron leakage spectra from the lead buffer

One way to investigate the neutron source effects is to first study the sources without the multiplicative medium present and to compare the different spectra of the neutrons leaking out from the target. For this purpose, the surrounding fuel and shielding were temporarily removed, as shown in Fig. 23. For the simulation of the spallation source, the lead buffer/target in the model was extended by one extra sub-assembly towards the proton beam, replacing part of the accelerator tube.

The energy spectra of the neutrons exiting the lead buffer are displayed in Fig. 24 and it is seen that the spectrum from the (D,D)-source has a large peak between 2 and 3 MeV, which is the energy range with which the neutrons are emitted by the GENEPI generator. Hence, only a limited fraction of the source neutrons have lost their initial energy. This is an expected result, since the energy loss by elastic scattering of neutrons in lead is quite small. However, for the (D,T)-source, the average energy of the neutron spectrum has decreased a little more, which is explained by the (n,2n)-reactions in the lead buffer, induced by the 14 MeV neutrons. The (n,2n)-reaction in lead has a threshold at about 7 MeV (Fig. 25), explaining why there is no such effect for the (D,D)-source. Nevertheless, about 35% of the neutrons exiting the lead buffer have not interacted with the lead and are still in the 14 MeV peak. In the case of the spallation source, most of the source neutrons have rather low energy compared to the initial proton energy, with the maximum density at a little less than 2 MeV. This is a typical neutron leakage spectrum for 1000 MeV protons impinging on a lead target of this size. About 7% of the spallation neutrons, however, still have energy higher than 20 MeV. The comparison of the neutron leakage spectra shows that the neutrons originating from the (D,T)-source in MUSE-4 have a rather similar energy spectrum below ~10 MeV as those originating from the spallation source,

and can from this point of view be considered more representative for a spallation-driven system than the (D,D)-source.

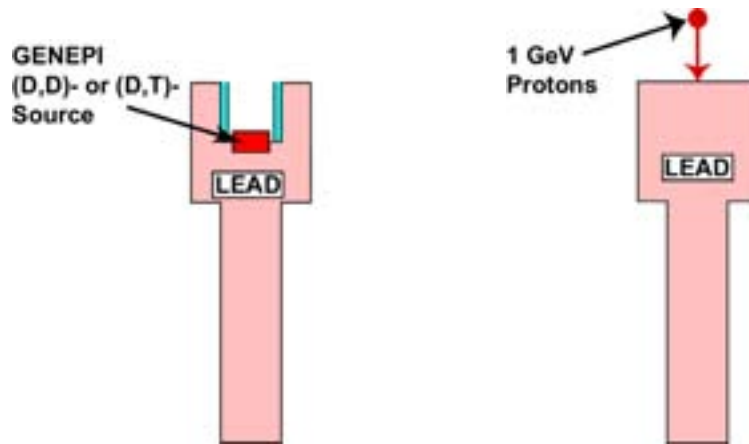


**Fig. 23.** Configurations of only the lead buffer region. To the left; (D,D)- or (D,T)-source neutrons emitted at the centre of the core. To the right; 1000 MeV protons accelerated towards the extended lead buffer.

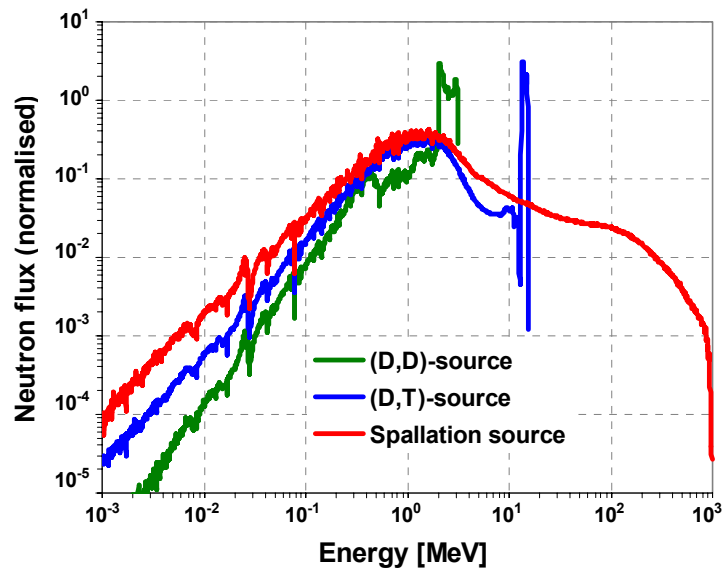


**Fig. 24.** Neutron leakage spectrum from the lead buffer/target for a (D,D)-source, a (D,T)-source and a spallation source (1000 MeV protons).

## 7.2.2 Neutron spectra in the core

The neutron energy spectra for the three different sources have been computed with the entire core present, including target, fuel, reflector and shields. The three positions where the spectra have been calculated, one in the target, one in the fuel and one in the reflector, are marked with the black dots in Fig. 19. The calculations were performed for the second sub-critical state of MUSE-4, SC2 ( $k_{eff} \sim 0.97$ ). The spectra

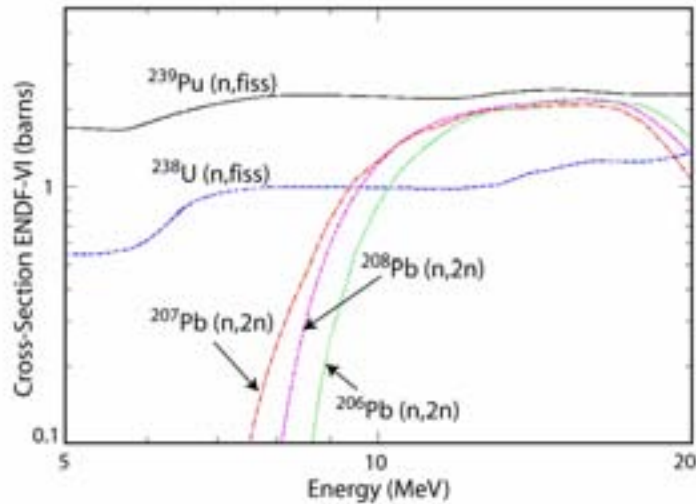


**Fig. 25.** Neutron microscopic cross-sections for (n,2n)-reactions in  $^{206}\text{Pb}$ ,  $^{207}\text{Pb}$  and  $^{208}\text{Pb}$ , compared to fission cross-sections in  $^{238}\text{U}$  and  $^{239}\text{Pu}$  (ENDF/B-VI).

for the other sub-critical states, SC0 ( $k_{eff} \sim 0.994$ ) and SC3 ( $k_{eff} \sim 0.95$ ) are not shown here, since they are very similar to the spectra of SC2. However, as there is less fission multiplication for larger sub-criticalities, the origin of the sources becomes a little more pronounced in SC3 and vice versa in SC0.

In Fig. 26, the neutron energy spectra for the three different sources calculated in the lead buffer are plotted. The spectra below  $\sim 10$  MeV are very similar to each other, the neutron density being maximal at about 500 keV. Several spectrum characteristics of the multiplying fuel can be recognised, for example, the dip in the neutron flux at  $\sim 3$  keV, caused by a large scattering resonance in sodium. This indicates that the neutron spectrum at this position is dominated by the fission multiplication in the fuel. However, a small fraction of the neutrons have energies different from the average behaviour and the two peaks representing the origins of the GENEPI-generated neutron sources, as well as the high-energy tail of the spallation source, are very clear. It should be noted, though, that the position in the lead buffer where the energy spectra have been calculated is only about 5 cm from the position where the GENEPI source neutrons are emitted.

In Fig. 27, the neutron spectra in the fuel, at a point located 21 cm from the centre of the core and about 10 cm into the fuel, are depicted. Naturally, the fuel spectrum characteristics in this case are even more pronounced than in the lead buffer. The three different curves are very similar and merely minor traces from the origins of the external neutron sources can be observed. Only about 0.15% of the (D,T)-source neutrons are still in the 14 MeV peak and about 0.04% of the neutrons in the spallation-driven system have energies higher than 20 MeV. Finally, the spectra in the reflector have been calculated (Fig. 28) and, as expected, they are considerably softer than in the target and in the fuel.



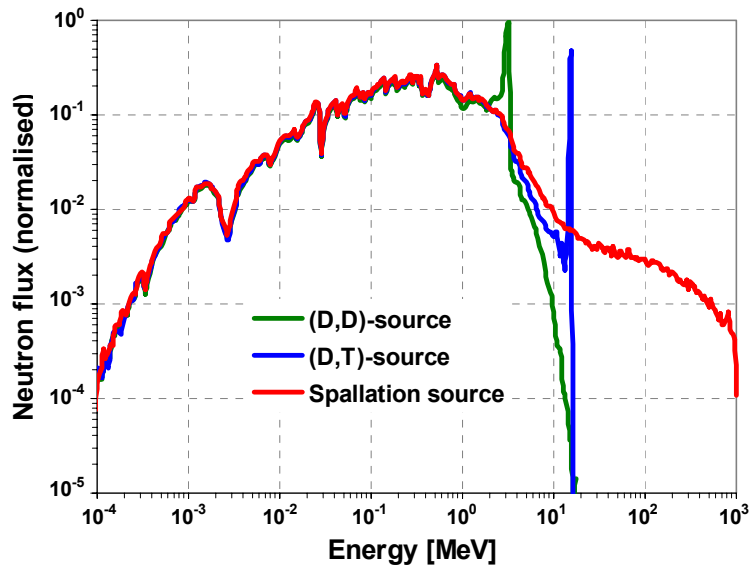


Fig. 26. Neutron energy spectra in the lead buffer.

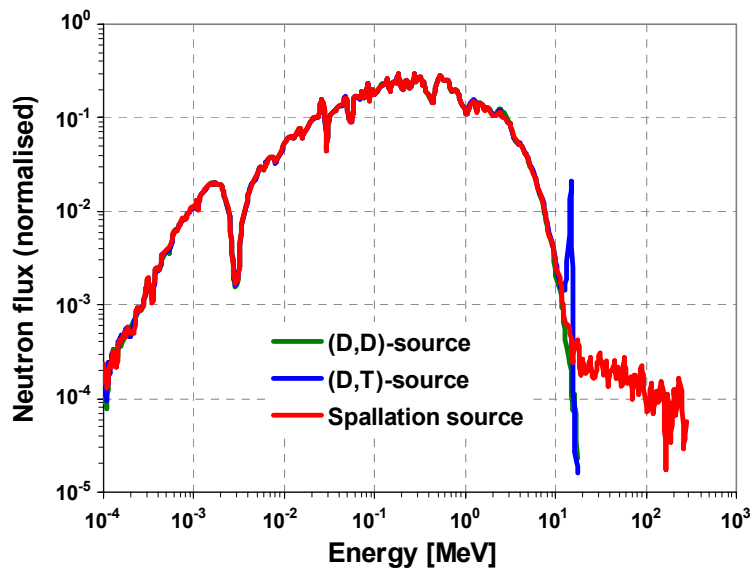


Fig. 27. Neutron energy spectra in the fuel.

The computed neutron spectra show that the spectra in the core, originating from the three different external sources, are very similar to each other. These results indicate the validity of one of the basic hypotheses of the MUSE experiments, namely that the choice of using a spallation source or the source neutrons produced by the (D,D)- or the (D,T)-reactions, will affect only marginally the neutron spectrum in the fuel. Only inside the lead buffer and at the buffer/core interface some significant differences are observed. We therefore conclude that, for the purpose of computing neutron spectrum-weighted quantities, the properties of the external source can be ne-

glected beyond a few centimetres into the fuel, whatever the neutron source energy distribution.

Finally, in Fig. 29, the energy spectra for the system driven by the spallation source, calculated in the target, the core and the reflector have been displayed together. It appears that the spectra in the target and the core are very similar, except for the much stronger contribution from the high-energy source neutrons in the target.

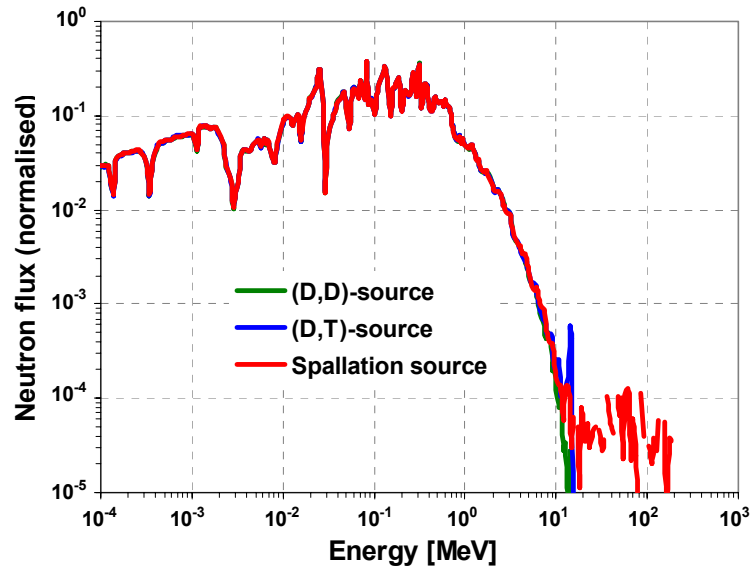


Fig. 28. Neutron energy spectra in the reflector.

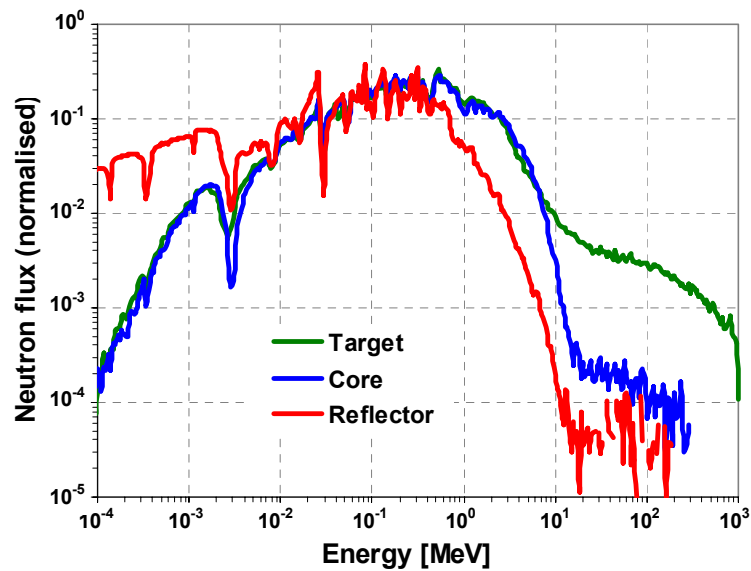
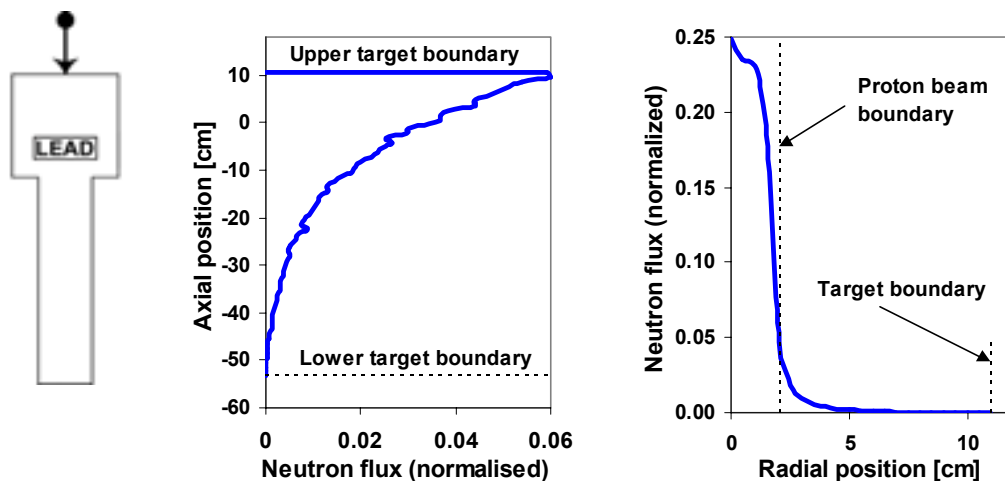


Fig. 29. Neutron energy spectra for the spallation source calculated in the target, the core and the reflector.

### 7.2.3 Distribution of the spallation neutrons

The distribution of the neutrons produced in the spallation target was calculated for 1000 MeV protons impinging on the extended MUSE-4 target. The properties, in terms of energy and space, of the neutrons emerging from the proton-induced spallation reactions were recorded. These emitted neutrons have been called “primary neutrons”, as they include only the first neutron in each neutron chain reaction. No neutrons generated in reactions induced by other neutrons (secondary neutrons) are included. The definition of primary neutrons has been further treated in Section 6.1 and in **Paper VII**.

The spatial distribution of the positions where the primary neutrons were created was found to be rather limited. Axially, most of the neutrons were created in the upper part of the lead target (77% within the first 20 cm), as shown in Fig. 30. It was also found that the neutron density, which in addition to the primary neutrons include also secondary neutrons, has a different shape with its maximum about 10 cm below the top of the target. The radial distribution was found to be very peaked around the axis of the incident proton beam, about 98% of the neutrons were created within a 3 cm radius. In this case, the radius of the uniformly distributed proton beam was 2 cm. The energy distribution of the primary neutrons produced by the 1000 MeV protons is displayed in Fig. 31 and, as expected, it is considerably harder than the spectrum of the neutrons leaking out from the target. For instance, it can be noted that 16.8% of the neutrons have energies higher than 20 MeV, compared to ~7% for the target leakage neutrons, and 3.3% of them higher than 150 MeV. Moreover, the maximum of the energy spectra are located at ~3.5 MeV for the primary spallation neutrons, whereas at ~1.4 MeV for the target leakage neutrons. The neutrons with very high energy were mainly emitted in the forward direction of the proton beam.



**Fig. 30.** To the left; 1000 MeV protons impinging on the extended MUSE-4 lead buffer/target. In the middle; Axial distribution of the primary spallation neutrons. To the right; Radial distribution of the primary spallation neutrons.

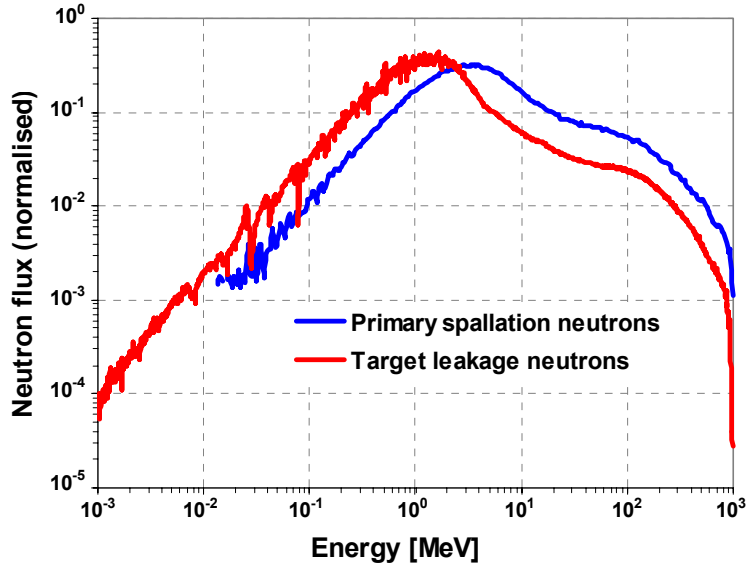


**Fig. 31.** Energy spectrum of the primary spallation neutrons created by the 1000 MeV protons, compared to the spectrum of the neutrons leaking out from the target.

On average, there were about 14.5 primary neutrons produced in each proton-induced spallation reaction. This value may be compared with the total number of neutrons produced in the lead target, i.e., about 21 neutrons per incident proton. Thus, almost a third of the neutrons that exit the lead target and enter into the fuel are secondary neutrons, most of them created in neutron-induced spallation reactions and (n,xn)-reactions. In a large cylindrical target, this fraction is about 50%, the total number of neutrons created per proton being about 25-30, while the number of primary spallation neutrons is the same, independently of the target size.

### 7.3 Neutron source efficiency

The neutron source efficiency,  $\varphi^*$ , was determined for the GENEPI-generated neutron sources and for the spallation source, all of them coupled to SC2 of the MUSE-4 experiments. The multiplication factor  $k_{eff}$  and the total number of neutrons produced by fission in the core,  $\langle \hat{\mathbf{F}}\Phi \rangle$ , were calculated for the three different sources. Knowing these two parameters,  $\varphi^*$  can be determined, according to Eq. (44).  $\langle \hat{\mathbf{F}}\Phi \rangle$  is automatically normalised per source neutron in MCNP, as well as in MCNPX if the source particles are neutrons, so  $\langle S \rangle$  was always equal to 1 in the calculations. The corresponding statistical errors ( $\pm 1$  standard deviation) were calculated using Eq. (46). The results, including error estimates, are listed in Table 10. For the calculations of the spallation source, the primary neutron source definition was used.

The energy of the emitted (D,D)-source neutrons (2-3 MeV) is only slightly larger than the average energy of a neutron produced by fission. Since  $\varphi^*$  is 1.0 for an average fission neutron, the value for the (D,D)-source is therefore expected to be

equal or slightly larger than 1, which is indeed the case. For the (D,T)-source, the reason for the higher values of  $\varphi^*$  is the larger fission rate, part of which coming from fissions induced by the neutrons multiplied by (n,2n)-reactions in the lead buffer. It is seen in Table 10 that the number of fission neutrons per source neutron is large, approximately 59% larger than for the (D,D)-source. The (n,2n)-multiplication of the 14 MeV neutrons increases the number of neutrons leaking out into the fuel and inducing fission chain reactions, thus enhancing the neutron source efficiency. On average, about 1.5 neutrons per initial 14 MeV neutron leave the lead buffer, compared to about 1 neutron for each 2.7 MeV (D,D)-source neutron.

Concerning the spallation source neutrons, the values of  $\varphi^*$  obtained in the simulations are somewhat higher than for the (D,T)-source. This is due to the fraction of primary neutrons having very high energy (Fig. 31). Most of the neutrons from the spallation process are born with an energy lower than the (n,2n)-cross-section threshold in lead (i.e., no (n,2n)-multiplication occurs), but the neutrons with very high energy contribute significantly to  $\varphi^*$ . Additional calculations investigating the contribution to  $\varphi^*$  by the high-energy fraction of the spallation source show that the primary source neutrons with energies higher than 20 MeV (16.8% of all source neutrons) contribute for about 50% to the total  $\varphi^*$  [Paper VII]. The explanation for this is that most of the high-energy neutrons from the spallation source have already been multiplied in the lead (most of them via secondary neutron spallation and (n,xn)-reactions) *before* they enter into the fuel. Each of them gives birth to a number of lower-energy neutrons, which then leak out of the lead and induce fission chain reactions in the fuel.

**Table 10.** Neutron source efficiency,  $\varphi^*$ , and the total number of neutrons produced by fission in the core for each source neutron,  $\langle \hat{\mathbf{F}}\Phi \rangle$ , for the MUSE-4 SC2 configuration.

| Source            | $k_{eff}$       | $\langle \hat{\mathbf{F}}\Phi \rangle$ | $\varphi^*$                       |
|-------------------|-----------------|--|-----------------------------------|
| (D,D)-Source      | 0.97285         | 48.8 ( $\pm 0.4\%$ )                   | 1.36 ( $\pm 0.010$ )              |
| (D,T)-Source      | ( $\pm 18$ pcm) | 77.6 ( $\pm 0.5\%$ )                   | 2.17 ( $\pm 0.020$ )              |
| Spallation Source |                 | 80.6 ( $\pm 1.0\%$ )                   | 2.25 <sup>a</sup> ( $\pm 0.030$ ) |

<sup>a</sup> Calculated according to the primary neutron source definition.

## 7.4 Reactivity determination

Different techniques to monitor the sub-criticality level during operation in a source-driven sub-critical system were studied within the MUSE-4 program. With the introduction of GENEPI into MASURCA, it was possible to perform accurate dynamic measurements, allowing for experimental reactivity determination of the sub-critical multiplying medium. The dynamic measurements were based on the pulsed mode operation of GENEPI.

In the experiments, after the reactivity calibration by the rod drop technique, the sub-critical level of the different configurations was first precisely determined by the well-known static modified source method (MSM) [14,96]. In the next step, based

on reactor kinetics and neutron noise theory, different dynamic techniques were applied in order to determine the reactivity level. The studied methods, as well as results and interpretations from the dynamic experiments, have been presented in several documents [13,14,92,97,98,99].

### 7.4.1 Dynamic neutron source response

The time response in one of the detectors in MASURCA has been simulated with MCNP for a GENEPI-generated (D,T)-neutron source pulse for the three sub-critical states, SC0, SC2 and SC3 of the MUSE-4 experiments. It is clear from Fig. 32 that the more sub-critical the core is, the faster is the prompt decay rate.

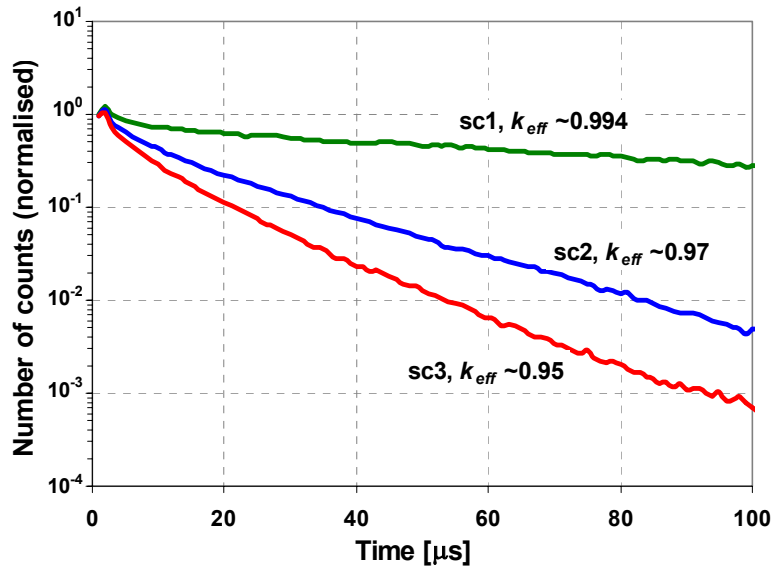


**Fig. 32.** Neutron source response after a (D,T)-source pulse for the three different sub-critical configurations in MUSE-4, SC0, SC2 and SC3.

### 7.4.2 The current-to-flux reactivity indicator

In the profound study of different measurement techniques for reactivity monitoring in an ADS performed within the MUSE-4 program, the method based on the current-to-flux reactivity indicator has appeared to be the major candidate for on-line monitoring [14]. The ratio between the neutron flux,  $\phi$ , monitored in a detector in the core and the proton beam current,  $i_p$ , can be expressed by the relation;

$$\frac{\phi}{i_p} \propto \frac{\psi^*}{\rho} \quad (56)$$

According to Eq. (56), assuming that the reactor is operating at a constant reactivity,  $\psi^*$  is the proportionality factor between the monitored neutron flux and the proton beam current. By studying the dependence of  $\psi^*$  on different possible variations of the target-core properties, a good estimation of the stability of the current-to-flux

reactivity indicator can be obtained. Possible transients that might affect  $\psi^*$  are, for instance, a change in the beam direction or the beam impact location, the proton energy or the target temperature. Over longer periods, the change in isotopic composition of the fuel due to burnup, or the modification of the core geometry during re-loading, might change the source efficiency. In order to assure the reliability of the reactivity indicator, these factors, potentially able to affect the proton source efficiency, should be monitored continually or calibrated on a regular basis.

## 7.5 Replacement of sodium coolant by lead coolant

It was decided within the MUSE community to include, in an extended phase of the MUSE-4 experiments, a new configuration, in which 22 of the central sodium-cooled fuel sub-assemblies were replaced by lead-cooled sub-assemblies. Three parameters;  $k_{eff}$ , the source neutron efficiency and the dynamic neutron source response were studied for this centrally lead-cooled configuration. The neutron source used in the study comparing this configuration with the original sodium-cooled configuration was the GENEPI-generated (D,T)-source.

When calculating  $k_{eff}$  for the new lead-cooled configuration, it was found that it increases with about 1600 pcm. The reason for this is that there is less absorption in lead and that the energy spectrum is different. In order to maintain the same reactivity for the two configurations, which is particularly important for the comparison of the neutron source response, some of the peripheral fuel sub-assemblies were removed.  $k_{eff}$  was approximately 0.974 in both cases (Table 11).

### 7.5.1 Neutron source efficiency

The results from the comparison of  $\varphi^*$  for the two configurations are listed in Table 11. As is shown, the value for the lead-cooled configuration is significantly higher than for the sodium-cooled configuration, 2.39 compared to 2.13. The reason for this difference is again the (n,2n)-multiplicative effect in lead, the same effect that caused the large difference in  $\varphi^*$  between the (D,D)- and the (D,T)-source. Since there is more lead in the central part of the core in the lead-cooled configuration, where there are still many neutrons with energy higher than about 7 MeV, there is more (n,2n)-reactions. These circumstances enhance the neutron multiplication, as well as  $\varphi^*$ . Since the source efficiency relates the source intensity to the power produced in the system, it can be concluded that the replacement of sodium coolant by lead coolant in the 22 central fuel sub-assemblies increases the energy gain by approximately 12%.

**Table 11.** Neutron source efficiency,  $\varphi^*$ , for the sodium-cooled and the centrally lead-cooled MUSE-4 configurations.

| Configuration         | $k_{eff}$               | $\varphi^*$         |
|-----------------------|-------------------------|---------------------|
| Sodium-cooled         | 0.97428 ( $\pm 20$ pcm) | 2.13 ( $\pm 0.02$ ) |
| Centrally lead-cooled | 0.97382 ( $\pm 27$ pcm) | 2.39 ( $\pm 0.03$ ) |

## 7.5.2 Dynamic neutron source response

Finally, the neutron source response from a pulse insertion from the (D,T)-source, registered by a detector in the core, was calculated and it is seen in Fig. 33 that the intensity is somewhat higher (~15%) for the lead-cooled configuration. The explanation for this is the same as for the difference in  $\varphi^*$ , namely the multiplicative effect of the (n,2n)-reactions in the lead. Since the neutron multiplication is higher in the second case, the intensity registered by the detector will also be higher. It was also observed that the prompt decay rate is more or less the same for the two systems.

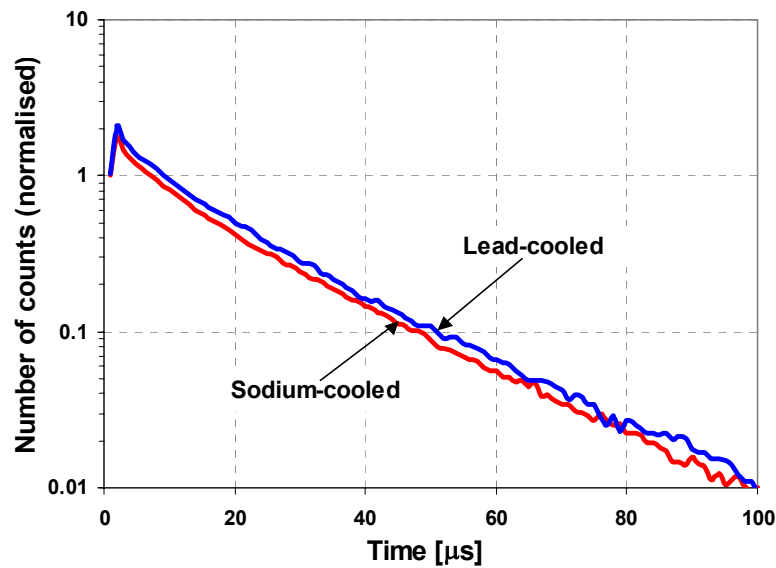


**Fig. 33.** Neutron source response in one of the detectors for the sodium-cooled and the partially lead-cooled configuration.



## Chapter 8

# The Yalina experiments

### Investigation of reactivity determination methods

In addition to the MUSE experiments, another similar European experimental program devoted to ADS studies has been performed at the Yalina facility outside Minsk, Belarus [16,17]. Yalina is based on the same principles as MUSE, i.e., an external neutron generator, based on the (D,D)- and the (D,T)-fusion reactions, coupled to a zero-power sub-critical core. The major difference between Yalina and MUSE, however, is that the neutron energy spectrum in Yalina is thermal.

There are several different techniques available for reactivity determination and they can be divided into three different types of methods; static methods, dynamic methods and noise methods. In the present study, only the dynamic methods, based on the pulsed neutron source experiments and the source jerk experiments, have been investigated. The dynamic methods are all based on the point kinetic equations. The idea is to investigate the time-dependent flux and to find different parameters derived from the point kinetics. The dynamic methods studied within the scope of this thesis are the slope fit method [100], the Sjöstrand method [101] and the source jerk method [100]. The basic principles of the static methods; the rod drop method [100] and the modified source method (MSM) [14,96], and the noise methods; the Rossi- $\alpha$  method [100,102] and the Feynman- $\alpha$  method [100], are briefly presented in the end of this chapter.

### 8.1 The Yalina facility

The external neutron generator used in the Yalina experiments, coupled to the sub-critical core, is similar to the GENEPI generator devoted to the MUSE experiments, as it also consists of a beam of deuterons impinging on a target of Ti-D or Ti-T, thereby creating spectra of neutrons characteristic of the (D,D)- and the (D,T)-fusion reactions. In the experiments performed, only the tritium target was used. The main characteristics of the neutron generator in the (D,T)-mode are presented in Table 12.

The fuel that was used in the experiments is of oxide fuel type, with 10% enriched uranium. The fuel rods were placed in a lattice of polyethylene blocks, which have the purpose of moderating the neutrons to thermal energies. However, in the region around the target, the polyethylene lattice was replaced by a lead lattice. The

purpose of the lead is to diffuse the energy spectrum of the (D,T)-neutrons so that it resembles a spallation spectrum. In the nominal design, the core is loaded with 280 fuel rods, but this number can easily be modified in order to alter the reactivity level. The low power of the core makes the natural convection of the surrounding air sufficient for cooling. The core is surrounded by a graphite reflector with a thickness of approximately 40 cm. Five axial experimental channels (EC) with a diameter of 25 mm are located inside the core and the reflector [103]. A schematic view of the sub-critical assembly is depicted in Fig. 34.

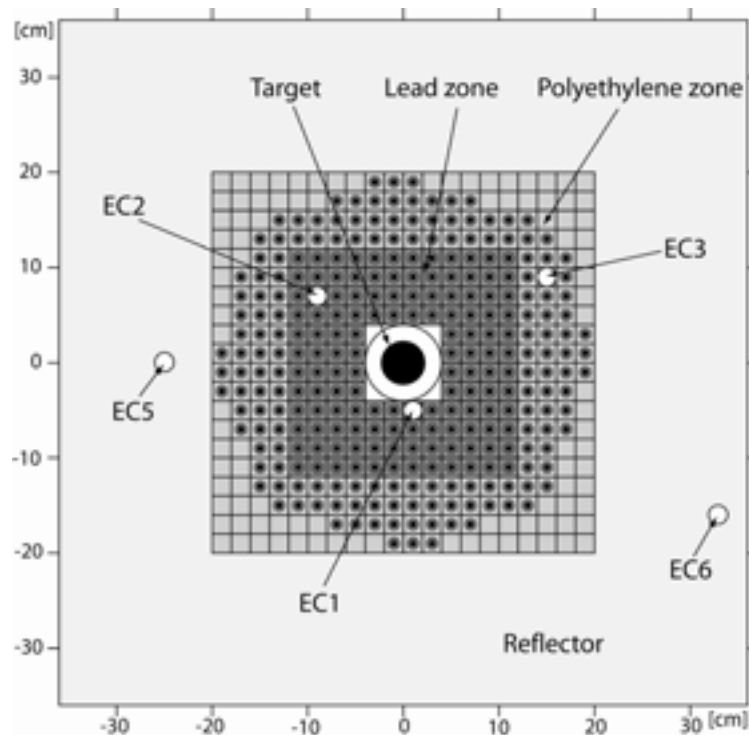


**Fig. 34.** Vertical cross-sectional view of the Yalina core. The deuteron beam is entering the core from the side (into the paper).

**Table 12.** Main characteristics of the neutron generator in the (D,T)-mode.

|                       |                              |
|-----------------------|------------------------------|
| Beam current          | 1-12 mA                      |
| Pulse length          | 0.5-100 $\mu$ s              |
| Deuteron energy       | 100-250 keV                  |
| Frequency             | 1-10 000 Hz                  |
| Beam diameter         | 20 mm (half max)             |
| Target                | Tritium + titanium           |
| Neutron energy (mean) | 14.1 MeV                     |
| Maximum neutron yield | $\sim 1 \cdot 10^{11}$ n/sec |

## 8.2 Dynamic experiments performed at Yalina

### 8.2.1 Pulsed neutron source experiments

By studying the prompt neutron decay after a neutron pulse insertion, it is possible to determine the reactivity of the core. This can be done in two different ways, either by applying the slope fit method or the Sjöstrand method. These two methods have been used to analyse the data collected from the pulsed neutron source experiment. In Fig. 35, the accumulated detector counts in the five different detectors after 40 000 source pulses injected at the Yalina core are displayed. During the experiment, the neutron generator was operating at 43 Hz, thus corresponding to a pulse period of about 23 ms. The intensity of the inherent source was negligible compared to the external neutron source.

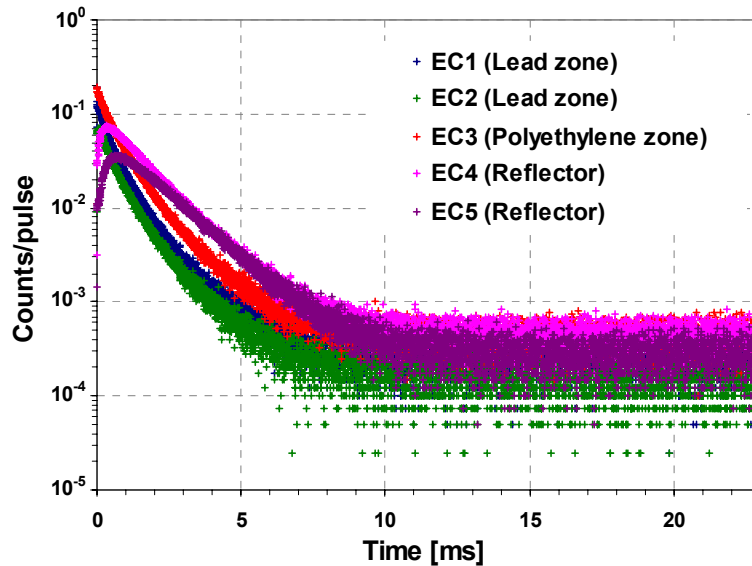


**Fig. 35.** Data collected from the pulsed neutron source experiments. The counts were accumulated in the five different detectors from 40 000 pulse insertions.

#### The slope fit method

When a multiplying medium is sub-critical, the neutron density will decay exponentially and the pulse response will quickly disappear, according to basic point-kinetic theory. Neglecting the delayed neutrons, the point-kinetic equation, for a reactor without sources, can be expressed as [100,104]

$$\frac{dn(t)}{dt} = \alpha n(t) , \quad (57)$$

where  $n(t)$  is the neutron density and  $\alpha$  is the prompt neutron decay constant, given by

$$\alpha = \frac{\rho - \beta_{eff}}{\Lambda} . \quad (58)$$

Eq. (57) has an exponential solution of the following form;

$$n(t) = n_0 e^{\alpha t} . \quad (59)$$

In a sub-critical reactor,  $\alpha$  is negative and the neutron flux thus decays exponentially. In the short time-scale, there is no contribution from the delayed neutrons and the decay is mainly described by the prompt neutron decay constant. By measuring  $\alpha$  experimentally, the reactivity,  $\rho$ , can be determined, provided that the mean neutron generation time,  $\Lambda$ , and the effective delayed neutron fraction,  $\beta_{eff}$ , are known.

The neutron flux transient induced by a neutron pulse injection, which is illustrated in Fig. 35, can be decomposed into a number of time periods with different characteristics. In the present case, the following four periods were identified; the injection period, the adjustment period, the fundamental decay period and the delayed neutron period. When a neutron pulse is injected into a sub-critical multiplying medium, the source neutrons initialise fission chain reactions. As a result, the neutron flux is suddenly increased. This rapid increase of the neutron flux is called the injection period. In the three detectors located in the core, the injection period is very short and cannot be identified in Fig. 35. Naturally, it takes a longer time for the neutrons to reach the reflector and in the two detectors located there, the injection period is in the order of 1 ms. Subsequent to the injection period, the adjustment period follows, where the neutron flux adjusts its shape and approaches the prompt fundamental decay rate. After a few ms, the neutron flux reaches the prompt fundamental decay mode, characteristic of the inherent reactor properties and approximately described by the point-kinetic equations. During this process, the decay rate of the neutron flux is the same for all positions in the system and Eq. (59) can be applied. Finally, the neutron flux reaches a nearly constant level (within the studied time-scale), determined by the delayed neutron background.

Due to the exponential behaviour of the neutron flux transient, it is appropriate to describe the transient mathematically by a series of exponentials. By fitting a function of the form

$$f(t) = \sum_{i=1}^{\infty} A_i e^{\alpha_i t} \quad (60)$$

to all data points, it is possible to determine the exponential component that represents the fundamental decay mode, which is described by the prompt neutron decay constant  $\alpha$ . It turns out that four terms are necessary to describe the response function with satisfactory statistical agreement. Two fast exponential terms are required for the injection and adjustment periods, one exponential term for the fundamental decay mode and one constant term for the delayed neutron background. The prompt

fundamental decay rate, determined by the  $\alpha$ -value obtained for EC3, is displayed together with the fitted function in Fig. 36. The results from the analyses of the experimental data, including the obtained values of  $k_{eff}$ ,  $\Lambda$ , and  $\beta_{eff}$  in the different experimental channels, are presented in **Paper V**.

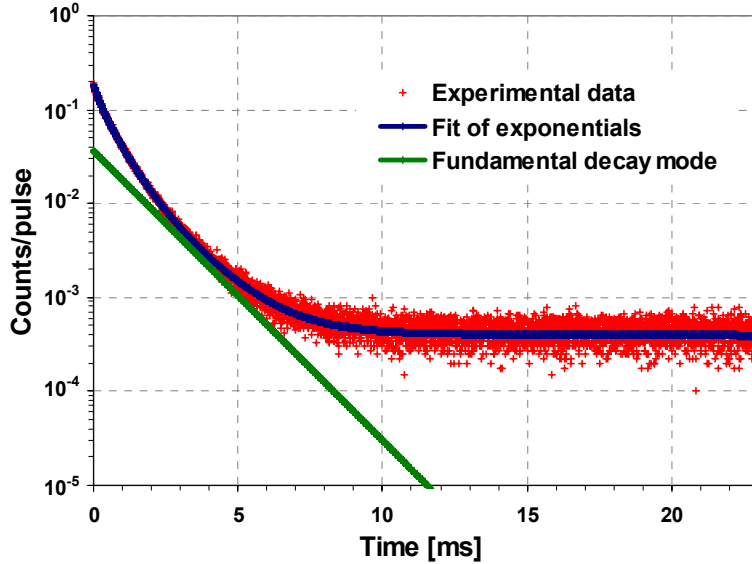


**Fig. 36.** Fit of exponentials to the experimental data in the experimental channels in the core (EC3). The straight line represents the fundamental decay mode.

### The Sjöstrand method

The Sjöstrand method, also called the area method, is based on the decomposition of the neutron flux transient into two components; the prompt part and the delayed part, which is illustrated in Fig. 37. The delayed neutrons are represented by the “delayed area”,  $A_d$ , and the prompt neutrons by the “prompt area”,  $A_p$ . Starting with the point kinetics equations for the prompt neutrons, the delayed neutrons and the delayed neutron precursors, the reactivity of the sub-critical system can after some algebraic manipulation be expressed as

$$\frac{\rho}{\beta_{eff}} = -\frac{A_p}{A_d} . \quad (61)$$

This method has the advantage that the involved parameters are integrals, which reduces the statistical errors. The approximation that the prompt and the delayed neutrons are emitted with the same energy spectrum was made in the derivation of Eq. (61), which may affect the accuracy of the results somewhat. The results of the analyses are presented in **Paper V**.

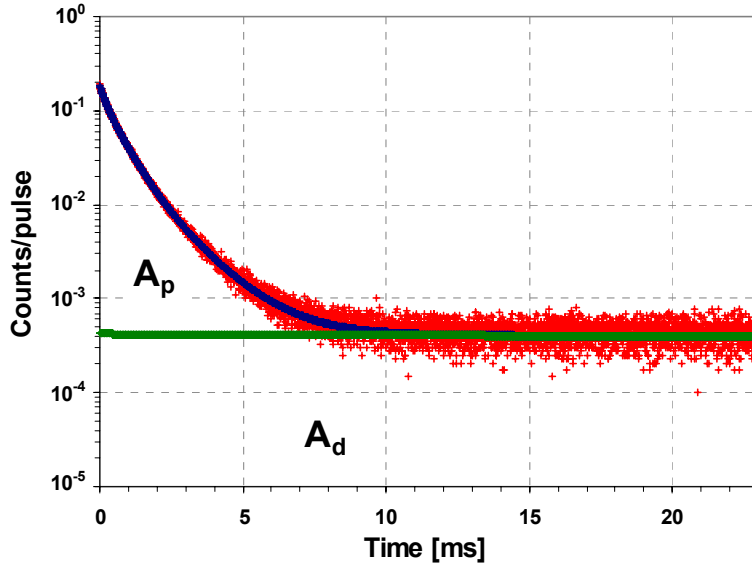


**Fig. 37.** Illustration of the prompt ( $A_p$ ) and the delayed ( $A_d$ ) neutron areas used in the Sjöstrand method.

## 8.2.2 The source jerk experiments

### The source jerk method

Consider a sub-critical system that is maintained at equilibrium neutron density,  $n_0$ , and equilibrium delayed neutron precursor population,  $C_{i,0}$ , by an external source,  $S$ , when the source is suddenly removed. The neutron balance equation of the system before the source removal is

$$\left(\frac{\rho - \beta}{\Lambda}\right)n_0 + \sum_{i=1}^6 \lambda_i C_{i,0} + S = 0 . \quad (62)$$

Within a few prompt neutron lifetimes after the removal of the source, the system will adjust to a lower level,  $n_1$ , determined by the multiplication of the delayed neutrons. However, immediately after the source jerk, the delayed neutron precursor population will still be the same as before the source jerk. Thus, the neutron balance equation after the source removal will be expressed by

$$\left(\frac{\rho - \beta}{\Lambda}\right)n_1 + \sum_{i=1}^6 \lambda_i C_{i,0} = 0 . \quad (63)$$

Using Eq. (62) and Eq. (63), together with the relation between the delayed precursor concentrations and the delayed neutron fractions,  $C_{i,0} = \beta_i / \lambda_i$ , the reactivity of the sub-critical system can be expressed as

$$\frac{\rho}{\beta_{eff}} = \frac{n_1 - n_0}{n_1} . \quad (64)$$

The neutron levels  $n_0$  and  $n_1$  can be obtained from the measurements. The collected data from the source jerk experiments are displayed in Fig. 38. The results of the analyses are presented in **Paper V**.

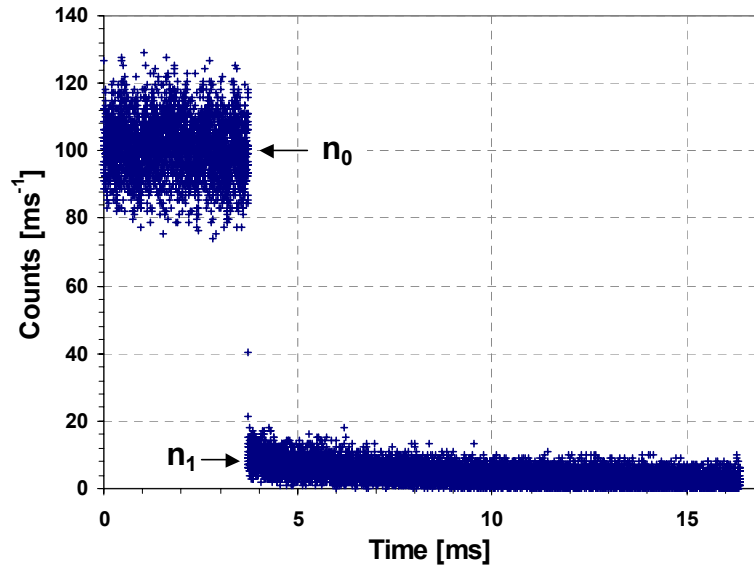


**Fig. 38.** Data collected from the source jerk experiments at Yalina.

## 8.3 Other reactivity determination methods

### 8.3.1 Static methods

#### The rod drop method

The static methods are based on the fact that, close to criticality, the inverse of the neutron count rate is proportional to the multiplication constant. In a first step, the rod drop method [100] may be used to calibrate the control rod worth in order to determine a reference reactivity level. This should be done at a near-critical level. By using a point kinetics relation for the reactivity and determining the source term by a linear fit to the measured data, the absolute reactivity of the reference level can be determined.

#### The modified source method

In a second step, using the value of the reference reactivity determined by the rod drop method, all other sub-critical states can be determined by the modified source method, which is based on inverse kinetics. In a sub-critical system, the source neutrons will be multiplied according to  $S/(1 - k_{eff})$ . Thus, the number of counts,  $C$ , that a detector will record can be expressed as [14]

$$C = \frac{\varepsilon S}{1 - k_{eff}} . \quad (65)$$

Hence, taking the ratio of count rates between two sub-critical states, any other sub-critical state can be determined according to [88]

$$\frac{C_1}{C_2} = \frac{\varepsilon_1 S_1 (1 - k_{eff,2})}{\varepsilon_2 S_2 (1 - k_{eff,1})} . \quad (66)$$

The fact that the detector efficiency  $\varepsilon$  and the effective source strength  $S$  may change when the reactivity level is changed, can be compensated for by determining the so-called MSM correction factor [14].

### 8.3.2 Noise methods

The noise methods are statistical methods used to analyse the inherent statistical behaviour of the reactor, based on the fact that the number of radioactive decays emitted by a radioactive medium per unit time is Poisson distributed. However, when a neutron is emitted in a fission process in a reactor, a number of chain-related neutrons will follow due to the multiplicative properties of the fuel. This implies that the Poisson distribution is disturbed. By investigating the deviation from the pure Poisson distribution, it is possible to obtain information about the sub-criticality of the core.

#### The Rossi- $\alpha$ method

The Rossi- $\alpha$  method [100,102] is based on the statistical probability of detecting neutrons originating from the same fission chain reaction, using a coincidence acquisition system. Assuming that a neutron count from a decay chain is observed at  $t = 0$ , the probability of another neutron count being observed in a small time interval at a later time  $t$  can be expressed as the sum of the probability of a count from a chain-related neutron,  $Qe^{-\alpha t} \Delta t$ , plus the probability of a count of a neutron from another chain,  $C \Delta t$ , where  $C$  is the average counting rate, according to

$$P(t) dt = C dt + Q e^{-\alpha t} dt . \quad (67)$$

In a Rossi- $\alpha$  experiment,  $P(t)$  is measured by a time analyser and the random count rate  $C dt$  is subtracted.  $\alpha$  can then be determined from the remaining chain-correlated term  $Q e^{-\alpha t} dt$ .

#### The Feynman- $\alpha$ method

The Feynman- $\alpha$  method [100], or the variance-to-mean method, is based on the statistical fluctuations of neutron counts during a fixed counting interval. If the number of counts during  $\Delta t$  in a multiplying system, critical or sub-critical, is determined repeatedly, the result will deviate somewhat from a Poisson distribution. The reason



for this is the fluctuations of the neutron population driven by the fission chain reactions. Applying the Feynman- $\alpha$  method, one determines the ratio of variance of the number of counts to the mean,  $\bar{C}$ , according to

$$\frac{\overline{C^2} - \bar{C}^2}{\bar{C}} \equiv 1 + Y . \quad (68)$$

For a pure Poisson distribution,  $Y$  is zero. Hence,  $Y$  is a measure of the additional fluctuations corresponding to the fission chain process. Moreover,  $Y$  is related to  $\alpha$  by the following equation;

$$Y(\Delta t) = \frac{\varepsilon D}{\alpha^2 \Lambda^2} \left( 1 - \frac{1 - e^{-\alpha \Delta t}}{\alpha \Delta t} \right) , \quad (69)$$

where  $D$  is the Diven factor.

## 8.4 Conclusions

From the analyses of the experiments performed at the Yalina facility, it can be concluded that the slope fit method is somewhat inconvenient to apply to deep sub-critical configurations, such as Yalina, but gives reliable results in comparison with those results obtained by MCNP. Moreover, it was found that the Sjöstrand method underestimates  $k_{eff}$  slightly, in comparison with MCNP and the other methods. This tendency was also observed in the MUSE experiments [98,99]. The probable reason for these discrepancies is that when analysing the experimental data with the Sjöstrand method, all data from the pulse insertion to the end of the pulse response are used. However, only the data representative for the fundamental decay mode, used in the slope fit method analysis, is valid according to the point-kinetics. Since the fundamental decay mode will be more and more dominating closer to criticality, the gap between the two methods is expected to decrease when approaching criticality, which was indeed observed in the MUSE-4 experiments [99]. Finally, it was found that the source jerk method overestimates  $k_{eff}$ , in comparison with MCNP and the other methods. However, due to the large uncertainty of the lower neutron flux level, these results are connected with large statistical errors and must therefore be considered less reliable than the results obtained with the other methods.

None of the methods investigated in this study have the capability of determining the reactivity satisfactorily during on-line operation of a system. However, the methods can be used to estimate the sub-criticality during loading and for calibration of other possible measurement techniques, for instance, the current-to-flux reactivity indicator, which appears to be the major candidate for on-line reactivity measurements.

## Chapter 9

# The SAD experiments

## Investigation of core neutronics and high-energy neutron radiation shielding

The SAD (Sub-critical Assembly in Dubna) experimental reactor system is composed of the three main components characteristic of an accelerator-driven system; a proton accelerator, a spallation target and a sub-critical core, which makes it the first prototype of a medium-power ADS in the world. The project will be a natural step on the way from the zero-power experiments, e.g., MUSE and Yalina, where the sub-critical assemblies are driven by an external neutron generator, to the large-scale semi-industrial installations driven by proton beams, e.g., MYRRHA, which are now in the conceptual design phase in Europe.

### 9.1 The SAD experiments

#### 9.1.1 System design

In the upcoming SAD experiments [18,19], set up at the Joint Institute for Nuclear Research (JINR) in Dubna in collaboration with CEA (Cadarsache), CIEMAT (Madrid), FZK (Karlsruhe) and KTH (Stockholm), the various concepts and the basic physical principles of accelerator-driven systems will be studied extensively. In these experiments, a 660 MeV proton accelerator is coupled to a sub-critical core, loaded with fast reactor MOX fuel assemblies.

The protons are generated by the JINR phasotron proton accelerator, in which they reach an energy of 660 MeV. The maximum current of the accelerator is 3.2  $\mu\text{A}$  ( $2.0 \cdot 10^{13}$  protons/s). The protons are guided into the core from below, where they impinge on a target of heavy metal. The target is replaceable, with two possible materials; lead and tungsten. In the present study, lead was used as reference target material. The target consists of 19 hexagonal rods, each with a distance between two opposite sides of 3.6 cm, and the height of the target is 60 cm. However, in order to obtain a maximal neutron density in the centre of the core and therefore maximising the proton source efficiency, the impact position of the proton beam is located 10 cm

above the bottom of the active part of the fuel. The radius of the radially uniform proton beam is 1.5 cm. A cross-sectional view of the SAD core is given in Fig. 39.

MOX fuel assemblies, based on experimental fuel elements used in the Russian fast reactor type BN-600, will be used as fuel for the SAD assembly. The fuel contains about 30% PuO<sub>2</sub> and 70% UO<sub>2</sub>, with the average fuel density of 10.4 g/cm<sup>3</sup>. The fraction of <sup>239</sup>Pu in the plutonium vector is in the order of 95%. The active part of the core consists of about 141 hexagonal sub-assemblies, the exact number depending on the desired reactivity level, adding up to a total core radius of about 25 cm. The height of the active core is 51 cm. The core is surrounded by a lead reflector, which is covered with a thick biological shielding of heavy concrete. The sub-critical level of the SAD core can be easily changed by adding or removing some of the fuel sub-assemblies. The Russian licensing regulations allow sub-critical experiments without control rods provided that  $k_{eff}$  does not exceed 0.98. The main characteristics of the SAD facility are listed in Table 13.

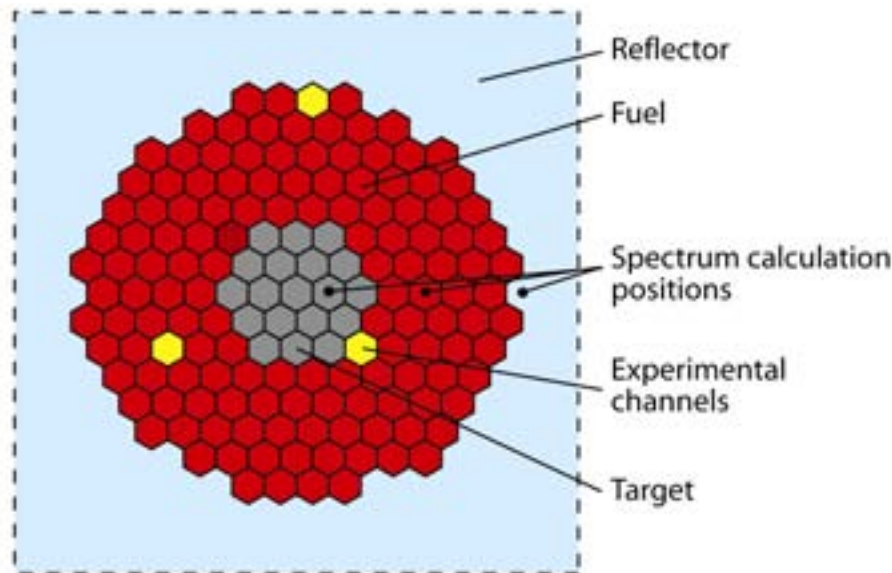


**Fig. 39.** Horizontal cross-sectional view of SAD core. The distance between two opposite sides of the hexagonal sub-assemblies is 3.6 cm. The black dots indicate the positions where the neutron energy spectra have been calculated (Section 9.2.3).

### 9.1.2 Experimental program

The main objective of the SAD experiments is to investigate the basic physical principles of an ADS and thereby validating the theoretical predictions and estimations of the technological features of such systems. The most important issues to be addressed are the following;

**Table 13.** The main design characteristics of SAD.

|  |  |
|--|--|
| Thermal core power (maximum)             | Up to 100 kW                                     |
| Proton energy                            | 660 MeV  |
| Proton current (maximum)                 | 3.2 $\mu\text{A}$ ( $2 \cdot 10^{13}$ protons/s) |
| Proton beam power (maximum)              | 2.0 kW   |
| Multiplication coefficient, $k_{eff}$    | 0.95 – 0.98                                      |
| Fuel composition                         | MOX (30% $\text{PuO}_2$ + 70% $\text{UO}_2$ )    |
| $^{239}\text{Pu}$ fraction in Pu vector  | > 95%  |
| Number of fuel sub-assemblies            | ~141   |
| Flat-to-flat thickness of sub-assemblies | 3.6 cm   |
| Number of fuel pins in one sub-assembly  | 18   |
| Core radius                              | ~25 cm   |
| Core height                              | 51 cm  |
| Pin pitch/pin diameter                   | 7.95/6.9 mm (P/D = 1.15)                         |
| Target radius                            | ~8.5 cm  |
| Spallation target                        | Pb or W  |
| Reflector                                | Pb   |
| Coolant                                  | Air  |
| Biological shielding                     | Heavy concrete                                   |

### 1. Development of reliable methods for reactivity monitoring

The operation of an ADS will require novel methods for monitoring the reactivity of the sub-critical core. Experience from previous experimental programs, such as MUSE and Yalina, has been accumulated and will provide the basis for the present studies. The already developed techniques for studying the various reactivity determination methods will be directly transferred to the SAD facility and applied in an early stage of the experiments. Some of the methods that will be investigated are the slope fit method, the Sjöstrand method and the source jerk method. Other methods, such as Rossi- $\alpha$  and Feynman- $\alpha$ , will also be studied and evaluated.

### 2. Validation of the core power and the proton beam current relationship

The current-to-flux reactivity indicator, which appeared to be the most promising method for on-line monitoring of the reactivity level during the MUSE experiments [14], will be validated experimentally. The beam current and beam shape will be monitored at different locations with high precision using inductive sensors, ionisation chambers and profilemeters. The power level will be monitored in two channels with three different neutron sensors.

### 3. Validation of nuclear data and calculation codes

The SAD experiments offer a good opportunity to validate and benchmark the various reactor simulation tools, the nuclear data and the available high-energy physical models relevant for the modelling of an ADS. An important activity will thus be to prepare and carry out the relevant benchmark specifications. Extensive computer modelling will also be performed in order to predict and to help interpreting the ex-

perimental results. Experience from the computer simulation benchmark performed within the MUSE program will be taken advantage of.

#### 4. Radiation shielding

The presence of the 660 MeV proton accelerator in SAD introduces a new dimension to the radiation shielding concerns, compared to the operation of conventional critical reactors. The cause of this is the long range in the biological shielding of the high-energy neutrons created in the spallation reactions. Extensive simulations have been performed to estimate the radiation fields and the radiation doses at various places outside the biological shielding [**Paper III**] in order to verify that they do not exceed the maximal allowed doses. In the experiments, the radiation doses will be measured at some of these locations. In particular, the contribution from the high-energy neutrons ( $E > 10$  MeV), which is the determining factor for the constraints on the biological shielding, should be measured and studied.

#### 5. Thermal reactivity feedbacks

In the original SAD design, with a nominal power of about 15-20 kW, the thermal reactivity feedbacks would have been negligible, due to the low power densities and the low temperatures. However, the upgrade of the power to about 100 kW is expected to allow for some limited measurements of the reactivity feedbacks.

#### 6. Measurements of the neutron core physics characteristics

Various neutronic parameters characteristic of the sub-critical core, such as spectral flux densities, prompt neutron lifetimes and effective fraction of the delayed neutrons, will be measured.

#### 7. Design choices

The experiments will provide valuable knowledge concerning the different design options of the construction of a future large-scale ADS, for instance, the choice of fuel type, coolant material, target material and reflector material.

#### 8. Calculation and measurements of the power gain

The energy gain of the SAD facility will be determined by monitoring the total core power and the accelerator power. Some of the performed pre-calculations will be validated.

#### 9. Start-up and shutdown procedures

The start-up and shutdown procedures will be investigated, including testing of specific dedicated equipment and instrumentation.

#### 10. Qualification of the reliability of the proton beam and the spallation target

The qualification of the reliability of the proton beam, the beam transport line and the spallation target will be assessed.

## 9.2 Core simulations

Calculations determining different core parameters have been performed with MCNPX for a model of the SAD experiments. The data libraries ENDF/B-6.8 and LA150 in combination, and the Bertini intranuclear cascade model were used in the simulations.

### 9.2.1 Energy gain

By calculating the power deposition in the core and the target for a configuration with  $k_{eff} = 0.95$ , it was found that about 22.0 GeV was deposited for each 660 MeV proton, of which about 98% in the core and the rest in the target. We have the following relation for the total power produced in the core,  $P_{tot}$ ;

$$P_{tot}(kW) = i_p(\mu A) \cdot E_{dep}(GeV), \quad (70)$$

where  $i_p$  is the proton current and  $E_{dep}$  is the energy deposited in the system for each source proton. Hence, assuming a proton beam power and current of 2.0 kW and 3.0  $\mu A$ , the total power deposited in the system is 67 kW and the energy gain, i.e.,  $G = P_{tot}/P_{acc}$ , is thus about 33. The total power and the energy gain have been calculated for some different reactivity levels, the results being displayed in Table 14 and in Fig. 40. The energy gain as a function of  $k_{eff}$  is approximately described by the known relation  $k_{eff}/(1 - k_{eff})$ , according to Eq. (52).

**Table 14.** Total core power,  $P_{tot}$ , and energy gain,  $G$ , for a proton beam power of 2.0 kW, calculated for the 660 MeV proton beam coupled to the SAD core. For comparison, the same parameters were also calculated for a proton beam of 1000 MeV, coupled to the same core. The power of 2.0 kW corresponds to a proton current of 3.0  $\mu A$  for the 660 MeV protons and of 2.0  $\mu A$  for the 1000 MeV protons.

| $k_{eff}$ | $E_p = 660 \text{ MeV (SAD)}$ |     | $E_p = 1000 \text{ MeV}$ |     |
|-----------|-------------------------------|-----|--------------------------|-----|
|           | $P_{tot}$ [kW]                | $G$ | $P_{tot}$ [kW]           | $G$ |
| 0.90      | 32                            | 16  | 35                       | 18  |
| 0.95      | 67                            | 33  | 74                       | 37  |
| 0.98      | 172                           | 86  | 190                      | 96  |

### 9.2.2 Proton source efficiency

The proton source efficiency,  $\psi^*$ , as well as the neutron source efficiency,  $\varphi^*$ , has been calculated for the reference SAD design.  $\varphi^*$  was calculated according to the target leakage source definition (Section 6.1.3). The number of source neutrons leaking out radially from the target,  $Z$ , was found to be about 12.5, which is also the ratio between  $\psi^*$  and  $\varphi^*$ . For comparison, the same parameters were also calculated for a proton beam of 1000 MeV, coupled to the same sub-critical system. The values of

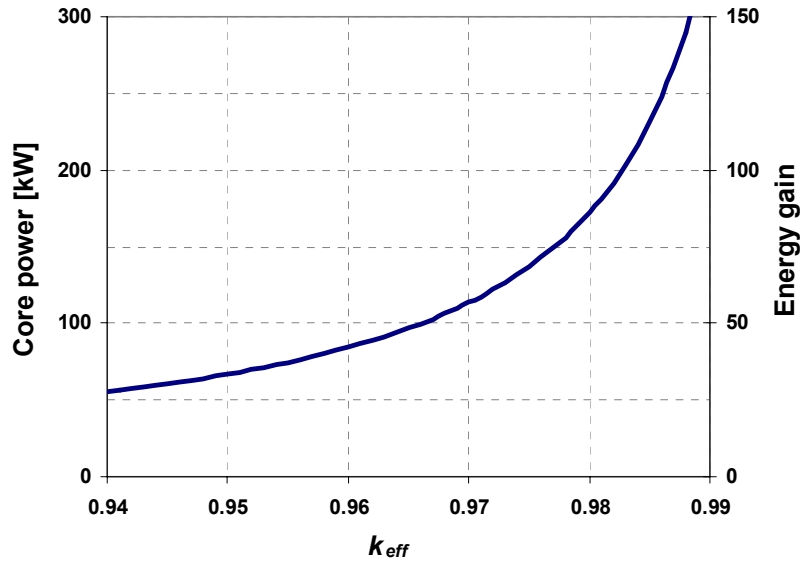


**Fig. 40.** Total core power and energy gain as functions of  $k_{eff}$  for a proton beam power and current of 2.0 kW and 3.0  $\mu$ A, calculated for the 660 MeV proton beam coupled to the SAD core.

$\psi^*$ ,  $\phi^*$  and  $Z$  are displayed in Table 15. It was found that  $\psi^*$  was higher for the 1000 MeV protons than for the 660 MeV protons by about 70%. This corresponds to a difference of about 11% in  $\psi^*/E_p$ , which is identical to the difference observed for the energy gain, since  $\psi^*/E_p$  is proportional to  $G$  for a given  $k_{eff}$  (Eq. 52). Worth noting is also that  $\phi^*$  is the same for the two different proton energies. The reason why  $\phi^*$  is almost independent of the proton energy is that the energy spectrum of the target leakage neutrons changes only marginally with the proton energy, which is shown in Fig. 41.

$\psi^*$  has also been studied as a function of the proton beam impact position, which has been varied from the bottom of the target ( $Z = 0$  cm), to 30 cm above the bottom of the target ( $Z = 30$  cm). It is seen in Fig. 42 that it has a maximum at about 10 cm above the bottom of the core, which is indeed where the impact position has been located in the current SAD design. This location of the beam impact position thus gives an energy gain higher by about 12% than an impact position at the bottom of the target.

**Table 15.** Proton source efficiency,  $\psi^*$ , number of source neutrons per incident proton,  $Z$ , and neutron source efficiency,  $\phi^*$ , for proton energies of 660 MeV (SAD) and 1000 MeV.

| $E_p$ (MeV) | $\psi^*$ | $Z$  | $\phi^*$ <sup>a</sup> |
|-------------|----------|------|-----------------------|
| 660         | 17.1     | 12.5 | 1.38                  |
| 1000        | 28.8     | 21.0 | 1.38                  |

<sup>a</sup>  $\phi^*$  was calculated according to the target leakage source definition.

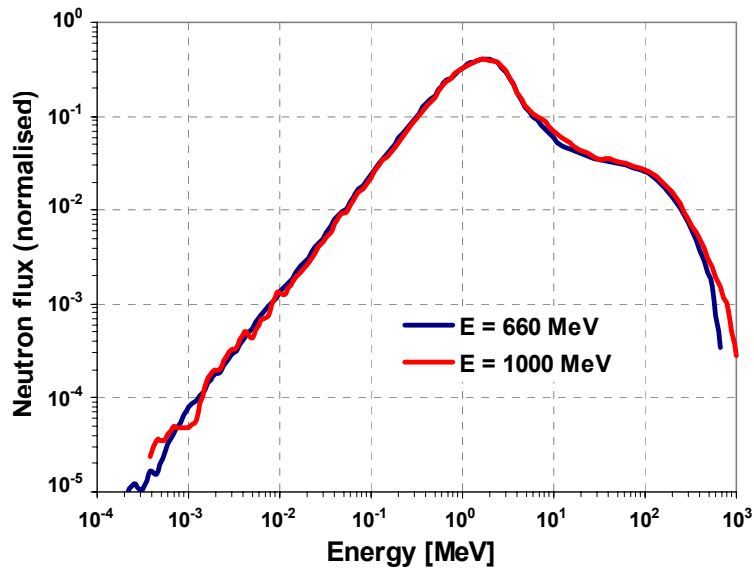


**Fig. 41.** Energy spectrum of the source neutrons leaking out from the target, for proton energies of 660 MeV (SAD) and 1000 MeV.

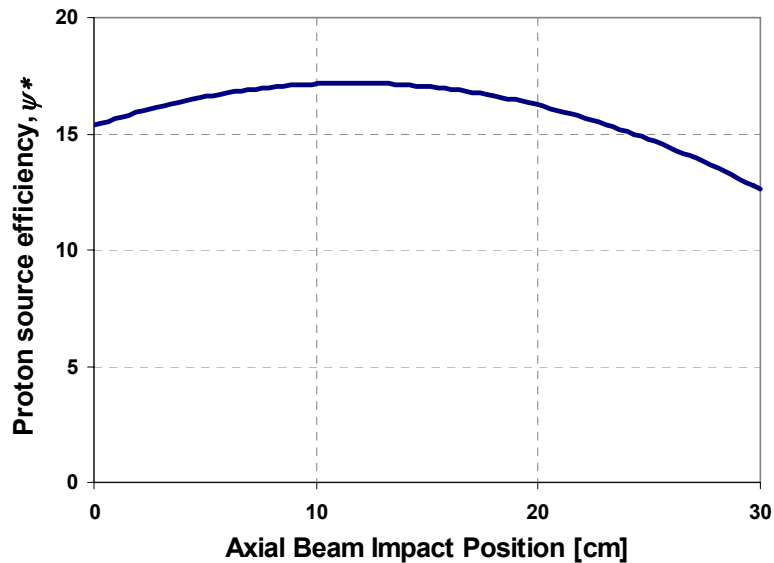


**Fig. 42.** Proton source efficiency,  $\psi^*$ , versus axial proton beam impact position (cm above the bottom of the core).

### 9.2.3 Core energy spectra

The neutron energy spectrum has been calculated at three positions in the SAD system, one in the target, one in the core and one in the reflector, these positions being indicated by the black dots in Fig. 39. The three spectra displayed in Fig. 43 are typical for a fast reactor, with the maximum flux located slightly below 1 MeV. The spectra are also similar to the spectra calculated for the MUSE experiments (Fig.



29). As expected, it appears that the high-energy spallation source neutrons constitute a non-negligible fraction of the total neutron flux inside the target. In the core and in the reflector, on the other hand, their intensity is about an order of magnitude lower.

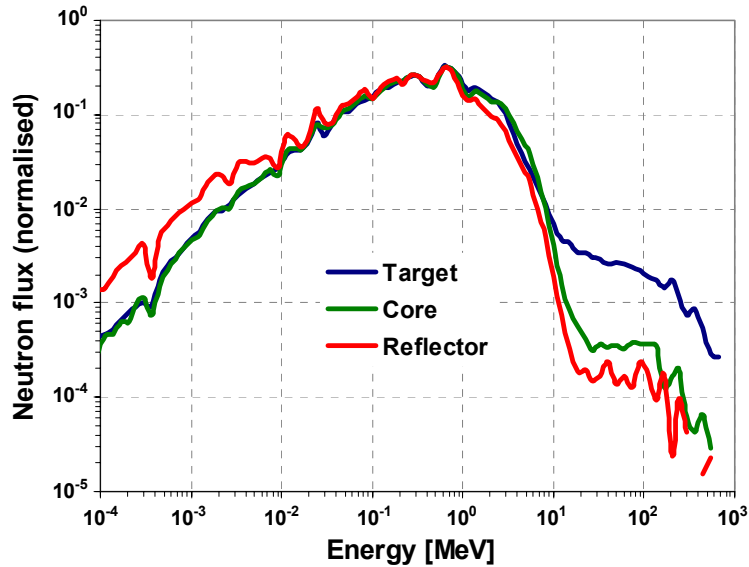


**Fig. 43.** Neutron energy spectra calculated in the target, the core and the reflector.

### 9.3 Radiation shielding of high-energy neutrons in SAD

A major concern before licensing the operation of SAD is to accurately determine the radiation fields outside the reactor system. The surrounding building is shielded from the radiation emerging from the accelerator beam and the reactor by thick walls of concrete. In the present work, the effective dose induced in the rooms above the reactor, i.e., in the direction of the incident proton beam, have been determined in order to verify that they do not exceed the limits determined by the Russian radiation protection regulations. The studies have been quantified by first calculating, with the Monte Carlo code MCNPX, the flux of the particles leaking out through the shielding and then by converting the obtained fluxes to effective dose. The effective doses have been obtained by using fluence-to-effective dose conversion coefficients, provided mainly by the International Commission for Radiological Protection (ICRP) [105] and the International Commission on Radiation Units (ICRU) [106].

The shielding problems in a system coupled to a high-energy proton beam are mainly connected to the deeply penetrating high-energy neutrons. These neutrons, released in the spallation process by direct head-on collisions between the source protons and the target nuclei (the intranuclear cascade phase), have a strong angular dependence and can, in the forward direction, reach energies up to the level of the incident protons [107,108]. The lower-energy neutrons, on the other hand, created in the subsequent evaporation stage and emitted nearly isotropically, constitute only a

minor shielding concern, due to their comparatively short range in most shielding materials. For this reason, the largest radiation doses will appear in the forward direction of the incident proton beam [**Paper X**] and the design of the biological shielding in this direction will generally be of largest importance. The issues treated in this section have been analysed in detail in **Paper III**.

### 9.3.1 Conversion coefficients for use in radiological protection

#### Radiological protection quantities

There are three principal protection quantities currently recommended for use in radiological protection [105,106]; the mean absorbed dose in an organ or tissue,  $D_T$ , the equivalent dose in an organ or tissue,  $H_T$ , and the effective dose,  $E$ .

The absorbed dose,  $D_T$  [J/kg or Gy], in a particular organ or tissue,  $T$ , in the human body is given by

$$D_T = \frac{1}{m_T} \cdot \int_T D \cdot dm , \quad (71)$$

where  $m_T$  is the mass of the organ or tissue and  $D$  is the absorbed dose in the mass element  $dm$ .

In order to calculate the equivalent dose in an organ or tissue,  $H_T$ , the radiation field in which the organ is present must be divided into energy bins and into the different types of radiation that the field consists of. The absorbed dose in the organ of each radiation bin,  $D_{T,R}$ , must then be multiplied by a radiation-weighting factor,  $w_R$ , and summed over the different radiations,  $R$ , i.e.,

$$H_T = \sum_R w_R \cdot D_{T,R} . \quad (72)$$

The effective dose,  $E$ , was introduced for the quantification of the medical risk from a given radiation exposure.  $E$  is defined as the sum of the tissue-weighted equivalent doses in all the tissues and organs of the body,

$$E = \sum_T w_T \cdot H_T , \quad (73)$$

where  $w_T$  is the tissue-weighting factor for tissue  $T$ . For the purpose of radiological protection calculations, the human body is in the ICRP Publication 60 [109] defined by 12 designated tissues and organs plus the remainder, which consists of 10 additional tissues and organs.

#### Fluence-to-effective dose conversion coefficients

In order to calculate the effective dose induced by any particle flux, the fluence-to-effective dose conversion coefficients for all energies of all particle types that may be present in the radiation field should be known. Using this set of conversion coef-

ficients together with the specific particle flux that a person may be exposed to, the effective dose received by that person could be determined. The fluence-to-effective dose conversion coefficients are determined by calculating the total effective dose in an anthropomorphic model representing the human body, for mono-energetic fields of all particles of interest. The resulting effective dose for each energy bin is then divided by the total fluence of each radiation.

A number of studies determining these conversion coefficients have been performed by different research groups, using different simulation tools (mainly Monte Carlo codes) and different anthropomorphic models for the radiation transport calculations. In the ICRU Report 57, the results from many of the relevant studies are summarised. Most of the calculations of protection quantities reviewed were made with an adult model using either hermaphrodite models [110] or models with sex-specific differences, e.g., ADAM and EVA [111]. The data points from each group of authors were combined into one data set for each organ as a function of particle energy, resulting in one combined data set for each organ and for each gender. The conversion coefficients for the effective dose per unit fluence for whole-body irradiation by neutrons in isotropic irradiation geometry (ISO), recommended by the ICRU Report 57, cover the range from thermal energies up to 20 MeV. However, for dose calculations around an ADS driven by high-energy protons, such as the SAD experiments, conversion coefficients up to the energy of the incident protons are needed.

In the present study, the fluence-to-effective dose coefficients for neutrons from thermal neutrons up to 20 MeV are taken from the ICRU Report 57. For neutrons with energy from 20 up to 500 MeV, as well as for photons and protons of all energies, the coefficients are taken from a study by V. Mares and H. Schraube [112]. The results from Mares and Schraube were found to be in good agreement with the overview of fluence-to-effective dose conversion coefficients for high-energy radiation performed by M. Pelliccioni [113]. All fluence-to-effective dose conversion coefficients used in the study were based on the ISO geometry and are listed in Appendix C.

### 9.3.2 System modelling

In Fig. 44, a schematic view of the target, the core, the reflector and the upper part of the biological shielding is depicted. The core is surrounded by a lead reflector, which is 30 cm thick in the axial directions. In the present SAD design, the biological shielding above the reactor consists of a 100 cm thick section of heavy concrete, followed by 340 cm of standard concrete. Since the particles that leak out radially from the reflector do not contribute significantly to the effective dose at the top of the shielding, the radial and the lower sections of the shielding have been neglected in the simulations.

In order to determine the total effective dose, the flux of the particles that leak out at the detector area at the top of the biological shielding was calculated with MCNPX, with the energy spectrum divided into the appropriate energy bins. Knowing the flux,  $\phi_{E,P}$ , and the fluence-to-effective dose conversion coefficients,

$(E/\phi)_{E,P}$ , for each energy bin and each particle type, the total effective dose per unit time,  $\dot{E}$ , can then be determined as

$$E = \sum_P \left( \sum_E (E/\phi)_{E,P} \cdot \phi_{E,P} \right). \quad (74)$$

The summation is over all energy bins and all particles. MCNPX (version 2.5.e) was used in coupled neutron, proton and photon mode and the evaluated nuclear data library used in the simulations was LA150 [60] for those isotopes included in this library and ENDF/B-6.8 for the remaining isotopes. The high-energy physics package used by MCNPX was the Bertini model [67,68].

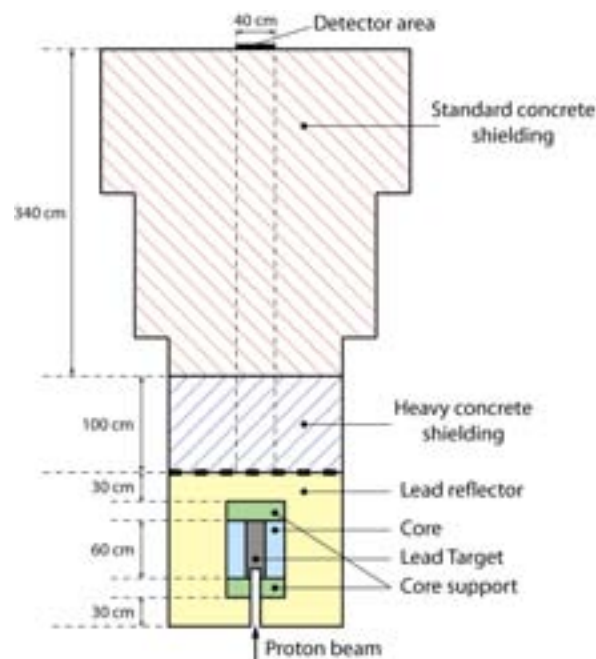


**Fig. 44.** Vertical cross-sectional view of the present design of the SAD reactor system, including the target, the core, the lead reflector and the upper part of the biological shielding. The shielding consists of a 100 cm thick section of heavy concrete plus 340 cm of standard concrete. The effective dose was calculated at the detector area at the upper surface of the biological shielding.

### 9.3.3 Attenuation

#### Effective dose

The separate fluxes for neutrons, photons and protons calculated at the detector area at the top of the biological shielding, as well as the corresponding effective doses and the total effective dose, are displayed in Table 16. The total effective dose was found to be about 190  $\mu\text{Sv/h}$ , with a statistical uncertainty of about 5%. According to radiation protection rules in Russia, the maximal allowed effective dose for civil

personnel is 12  $\mu\text{Sv/h}$ . However, provided that access for working personnel to the rooms above the shielding will be prohibited during operation, the radiation dose obtained for the present design of the biological shielding is in agreement with the radiation regulations.

**Table 16.** Separate flux,  $\phi$ , and effective dose,  $E$ , of neutrons, photons and protons, together with the total effective dose, at the detector area at the top of the biological shielding.

| Neutrons                        |                    | Photons                         |                    | Protons                         |                    | Total              |                   |
|---------------------------------|--------------------|---------------------------------|--------------------|---------------------------------|--------------------|--------------------|-------------------|
| $\phi$                          | $E$                | $\phi$                          | $E$                | $\phi$                          | $E$                | $E$                | 1 $\sigma$ -error |
| $[\text{cm}^{-2}\text{s}^{-1}]$ | $[\mu\text{Sv/h}]$ | $[\text{cm}^{-2}\text{s}^{-1}]$ | $[\mu\text{Sv/h}]$ | $[\text{cm}^{-2}\text{s}^{-1}]$ | $[\mu\text{Sv/h}]$ | $[\mu\text{Sv/h}]$ | $[\%]$            |
| 174                             | 172                | 114                             | 1.9                | 2.0                             | 18                 | 192                | $\sim 5$          |

Apparently, the neutrons contribute for the major part of the effective dose,  $\sim 89\%$ , but, a non-negligible part of the effective dose is also induced by photons and protons, which contribute for  $\sim 1\%$  and  $\sim 10\%$ , respectively. The reason why the contribution from photons is only 1%, although the fluxes of neutrons and photons are in the same order of magnitude, is that the conversion coefficients of the photons, of which the major part have energy between 0.1 and 10 MeV, are about 100 times smaller than those of the neutrons, of which an important fraction have energy around 100 MeV. Similarly, the conversion coefficients for the protons, which all have energy in the order of 100 MeV, are about 10 times higher than those for the neutrons, which explains the relatively high contribution to the effective dose induced by the much lower flux.

The explanation to why there is such a considerable flux of photons and protons detected, although it has been found that they have comparatively short range in the shielding, and that those entering into the concrete are not expected to penetrate the entire shielding, is that the high-energy neutrons create, apart from secondary neutrons with lower energy, also secondary photons and protons. The high-energy neutrons will thus be followed through the concrete by cascades of neutrons, photons and protons. Hence, all protons and photons detected at the top of the shielding have been created by neutrons inside the standard concrete. The minimum energy of neutrons required to create protons is in the order of a few MeV, while thermal neutrons have the highest probability to create photons. Since both photons, protons and low-energy neutrons have limited range in the concrete, it can moreover be assumed that the major part of the detected particles have been created nearby the detector area.

## Attenuation

In the following sub-section, the effective dose in the SAD biological shielding as a function of the distance from the reflector-shielding boundary has been studied. In Fig. 45, it is shown that, during the first  $\sim 50$  cm in the heavy concrete, the decay of the effective dose is very fast and cannot be described by a single exponential. The reason for this is that the effective dose close to the reflector is induced mainly by

the low-energy neutrons leaking out from the reflector, which have a large variety in energy. Since neutrons with different energy are attenuated at different rates, the total decay can be described by the sum of many exponentials. However, all of these low-energy neutrons are efficiently attenuated in the heavy concrete and, beyond about half a meter, the decay of the effective dose is largely dominated by the attenuation of the high-energy neutrons. The particle spectra have almost reached their equilibrium and the decrease of the effective dose is very close to exponential. However, entering into the standard concrete, the decay switches into another mode, with less efficient attenuation. Since the energy spectra of the transported particles changes at this boundary, some distance is required before the decay curve becomes single-exponential again.

In order to determine the linear attenuation coefficients and the attenuation lengths in the two shielding materials, two exponential curves have been fitted to the calculated data points, one for the heavy concrete and one for the standard concrete. In the heavy concrete, the purely exponential decay appears first after about 150 cm (although it is close to exponential already after 50 cm), so additional simulations, extending the heavy concrete, had to be performed to determine the attenuation coefficient (data points from 150 to 250 cm were used for the curve fitting). In the standard concrete, the equilibrium of the particle spectra is reached after a few tens of cm from the boundary and the data points from 150 to 400 cm were used for the curve fitting. The tenth-valued attenuation lengths,  $\lambda_{10}$ , i.e., the thickness required to reduce the effective dose by a factor of 10, obtained from the exponential fits were found to be about 58 cm in heavy concrete and 93 cm in standard concrete.

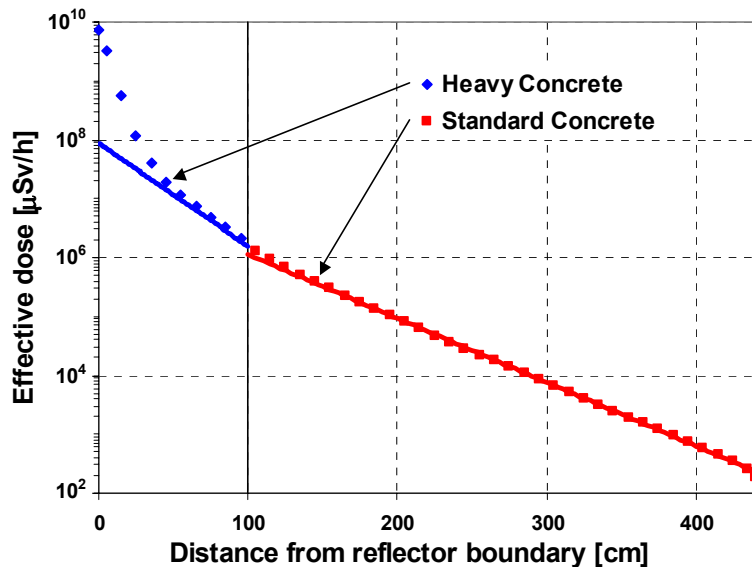


**Fig. 45.** Total effective dose induced by the particles leaking out from the SAD reactor system as a function of the distance from the reflector-shielding boundary. Exponential curves have been fitted to the MCNPX-calculated values; one in the heavy concrete and one in the standard concrete.

## High-energy contribution

As was shown above, low-energy neutrons have very short attenuation lengths in concrete compared to high-energy neutrons, which indicates that only the high-energy neutrons have long enough range to penetrate the full length of the shielding and to induce any significant effective dose at the top of it. In order to calculate the separate contributions to the effective dose from neutrons of different energies, the flux of the neutrons entering into the biological shielding from the reflector was divided into four energy bins (0-1, 1-10, 10-100 and 100-660 MeV). As expected, the relative contribution from the two low-energy bins is zero ( $<10^{-14}$ ). The contribution from the third energy bin (10-100 MeV) is also limited ( $\sim 0.3\%$ ), whereas the last energy bin (100-660 MeV) contributes for nearly the entire part of the effective dose. It was also found that the contributions from photons and protons are negligible. The small contribution originating from the source protons is induced by the secondary neutrons created as the incident high-energy protons are moderated in the heavy concrete.

The maximal energy of the neutrons released in the fission processes in the reactor core is in the order of 10 MeV. It can therefore be assumed that the entire part of the effective dose detected at the top of the shielding originates from the proton-induced spallation reactions in the target and practically nothing from the fission multiplication in the core. Thus, it can be concluded that the effective dose is directly proportional to the proton beam power and that it is completely independent of the reactivity of the sub-critical core.

**Table 17.** Relative contribution to the total effective dose originating from the source particles that enter into the biological shielding from the reflector. The neutrons were divided into four different energy intervals.

| Source particle | Energy interval<br>[MeV] | Relative contribution to $E$ |
|-----------------|--------------------------|------------------------------|
| Neutrons        | 0-1                      | 0                            |
|                 | 1-10                     | 0                            |
|                 | 10-100                   | 0.3%                         |
|                 | 100-660                  | 99.7%                        |
| Photons         | All                      | 0                            |
| Protons         | All                      | 0.01%                        |

# Chapter 10

## Summary of studies of proton source efficiency

In order to find an optimal system design that maximises the energy gain, and thereby minimises the proton current needs, the proton source efficiency,  $\psi^*$ , was studied as a function of several different system parameters for a large-scale ADS. In the following chapter, a brief summary of the most important studies of  $\psi^*$  performed within the framework of this thesis is given. Three different basic ADS-models have been used.

### 10.1 Model I

#### 10.1.1 Model design

A homogenised model representing a nitride-fuelled and LBE-cooled ADS (maximum 800 MWth) was first studied. The height of the active core in the reference model (Fig. 46) was 100 cm and the outer radius was 70 cm. The inner radius was 20 cm, which was also the boundary of the LBE target. The accelerator tube had a radius of 15 cm and the axial position of the proton beam impact was 25 cm below the top of the core. The radius of the radially uniform 1000 MeV proton beam was 7.5 cm. The actinide nitride fuel was in solid solution with ZrN with a volume fraction adjusted to 83% in order to obtain a  $k_{eff}$  of about 0.95. The relative fraction of actinides was 80% plutonium and 20% americium. The Monte Carlo code MCNPX (Version 2.3.0) in coupled neutron and proton mode was used for all simulations, relying on the evaluated nuclear data library ENDF/B-VI.8. The intranuclear cascade model used by MCNPX was the Bertini package.  $\psi^*$  was studied for the following parameters; target radius, coolant material, axial beam impact position, proton beam energy, fuel composition and inert matrix material. The studied model and the analyses performed are presented in detail in **Paper II, VIII and IX.**



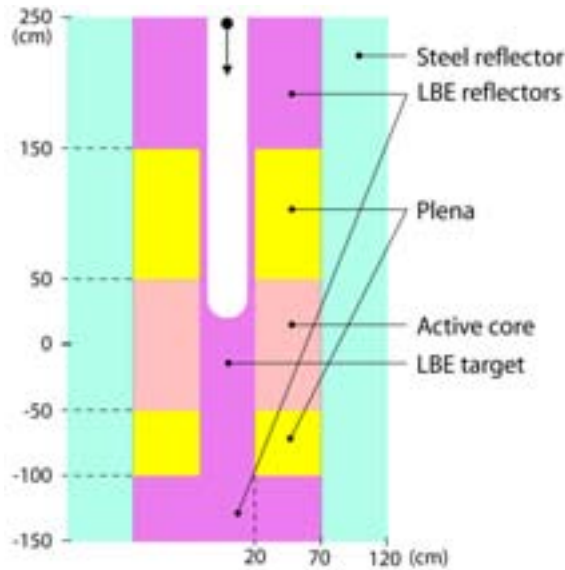


**Fig. 46.** Vertical cross-sectional view of the studied homogeneous LBE-cooled ADS reference model (Model I). The radius of the spallation target is 20 cm.

### 10.1.2 $\psi^*$ as function of target radius

$\psi^*$ , as well as  $\phi^*$ , was computed for the LBE-cooled ADS model for different target radii. The results are listed in Table 18, together with the number of source neutrons per incident proton,  $Z$ , and the energy gain,  $G$ .  $\psi^*$ ,  $\phi^*$  and  $Z$  are also plotted as functions of target radius in Fig. 47 and Fig. 48.  $\phi^*$  was calculated using the target neutron leakage definition (Section 6.1.3), although applied in a slightly different way than it was in Section 6.3. In this section, the source neutrons were defined as all neutrons leaking out radially from the target from the height of 150 cm below to 250 cm above the core mid-plane. Hence, also those neutrons leaving the target above and below the core and never entering the fuel were included. This modification in source definition results in a larger value of  $Z$  and a smaller value of  $\phi^*$ , the differences being particularly large for large target radii. Of course,  $\psi^*$  is unaffected by the choice of neutron source definition.

**Table 18.** Computed values of  $\psi^*$ ,  $\phi^*$ ,  $Z$  and  $G$  for different target radii, determined for the LBE-cooled ADS model of  $k_{eff}$  0.95.

| Target Radius   | $\phi^*$ <sup>a</sup> | $Z$  | $\psi^*$ | $G$ |
|-----------------|-----------------------|------|----------|-----|
| 10 <sup>b</sup> | 1.81                  | 21.9 | 39.6     | 50  |
| 20              | 1.35                  | 26.8 | 35.9     | 45  |
| 30              | 1.13                  | 29.0 | 32.4     | 41  |
| 40              | 0.99                  | 30.0 | 29.5     | 37  |
| 50              | 0.89                  | 30.2 | 27.0     | 34  |

<sup>a</sup>  $\phi^*$  was calculated according to the target neutron leakage definition.

<sup>b</sup> For the 10 cm target radius, the radius of the accelerator tube was decreased to 10 cm.

Concerning the dependence on the target radius, it is seen that  $\psi^*$  decreases considerably when the radius increases. There are mainly two reasons for this behaviour, one of them being the softening of the radial neutron leakage spectrum from the target as the target is enlarged (Fig. 17). The probability to induce fission for the neutrons entering the active part of the core drastically decreases with decreasing energy, in particular when the core is loaded with even-N nuclides. The other reason for the decrease in  $\psi^*$  is that the axial target neutron leakage increases with increasing target radius.

On the other hand, increasing the target radius increases the neutron multiplication inside the lead target, which leads to a higher number of neutrons created per source proton, i.e.,  $Z$  increases. The multiplicative effect of (n,xn)-reactions and secondary spallation in the lead target thus enhances  $\psi^*$ . Consequently, with increasing target radius, there are more neutrons for each source proton entering into the fuel, although the efficiency of these neutrons is strongly reduced. Accordingly, it is shown in Table 18 that  $\psi^*$  decreases less rapidly with increasing target radius than  $\varphi^*$  does, due to the increase in  $Z$ . These two competing factors in  $\psi^*$  are thus well represented by Eq. (48). Since the reactivity and the proton energy were fixed in this study, it follows that the energy gain is proportional to  $\psi^*$  (Eq. 54), which was indeed found to be the case.

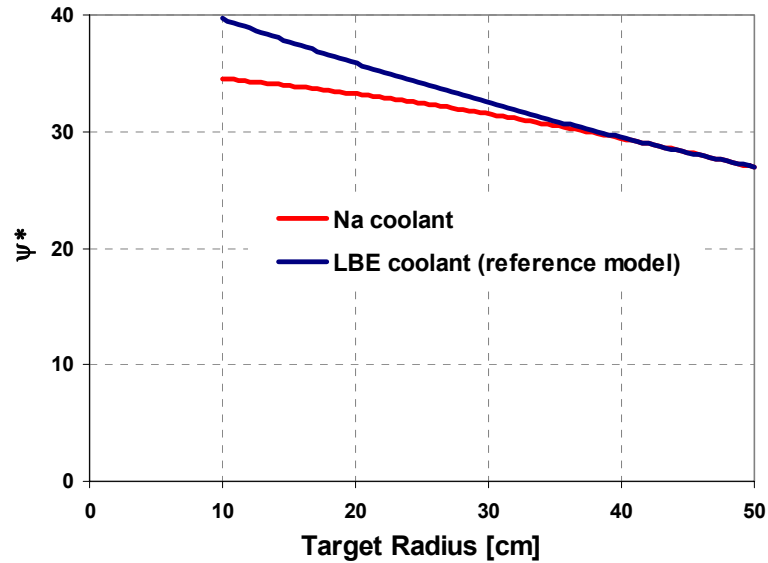


**Fig. 47.** Proton source efficiency,  $\psi^*$ , as function target radius for the LBE-cooled (reference model) and the sodium-cooled model.

Replacing the LBE coolant with sodium, it is shown in Fig. 47 that  $\psi^*$  decreases for small target radii, while it remains about the same for large radii. For the 20 cm target radius, the difference is about 8%. The main reason for this is that there is no neutron multiplication in the sodium coolant, in contrast to LBE. The differences between the two curves indicate that the contribution from (n,xn)-multiplication in the LBE coolant is significant for target radii smaller than about 30 cm. As long as

there is a fraction of leakage neutrons with energy higher than about 7 MeV, which is the (n,2n)-threshold in lead and bismuth, there will be (n,xn)-neutron multiplication in LBE. When the target radius is small, this high-energy fraction is rather high (6.1% have energies higher than 7 MeV for R=20 cm, compared to 0.8% for R=50 cm). When the target radius increases, the fraction of high-energy leakage neutrons decreases and at radii above 40 cm, the  $\psi^*$  values are essentially the same. The difference between the LBE and the sodium coolant are further illustrated in Fig. 48, where the values of  $\varphi^*$  are depicted together with those of  $Z$ .

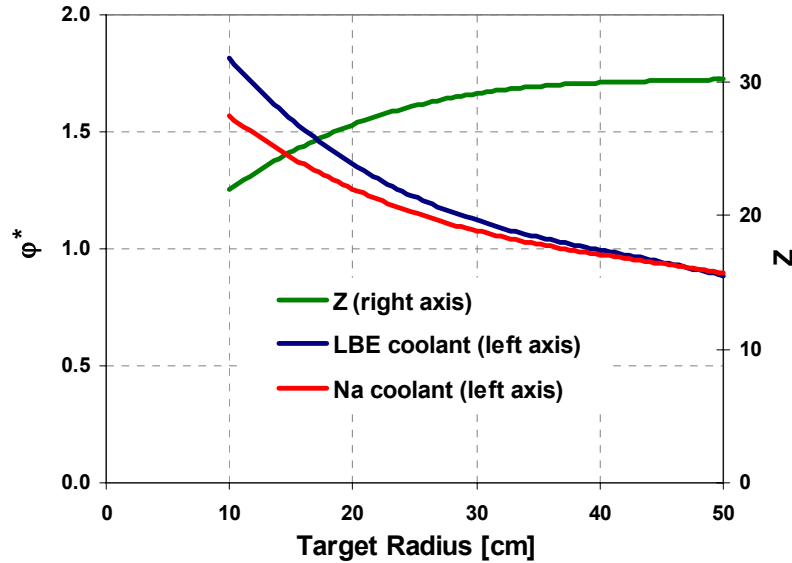


**Fig. 48.** Neutron source efficiency,  $\varphi^*$ , (calculated according to the target neutron leakage definition) for the LBE-cooled and the sodium-cooled model, together with the number of source neutrons per incident proton,  $Z$ , as functions of target radius.

We conclude that, in order to optimise the proton source efficiency and the energy gain, a target radius as small as possible should be chosen. For instance, increasing the radius from 20 cm to 50 cm decreases  $\psi^*$  by about 25% for the LBE-cooled core. These results are in good agreement with other similar studies [12]. However, it has also been shown that reducing the target radius has some undesirable effects, for example, higher fluence/burn-up ratio (lower maximum burn-up) and more severe high-energy neutron damage. Moreover, for a large-scale ADS, the target must be sufficiently large to be able to remove the massive heat deposited by the high-power accelerator beam.

### 10.1.3 $\psi^*$ as function of axial beam impact position

It was found that the axial position of the proton beam impact that maximises  $\psi^*$  was located approximately 20 cm above the core centre for the reference model (accelerator tube radius = 15 cm), the variations between 0 and about 35 cm being relatively small (Fig. 49). However, the dependence of  $\psi^*$  on the impact position is sen-

sitive to the accelerator tube radius and for a tube radius of 10 cm the maximum was found at about 13 cm above the core centre. Reducing the tube radius from 15 to 10 cm also increases the maximum of  $\psi^*$  by 3%.

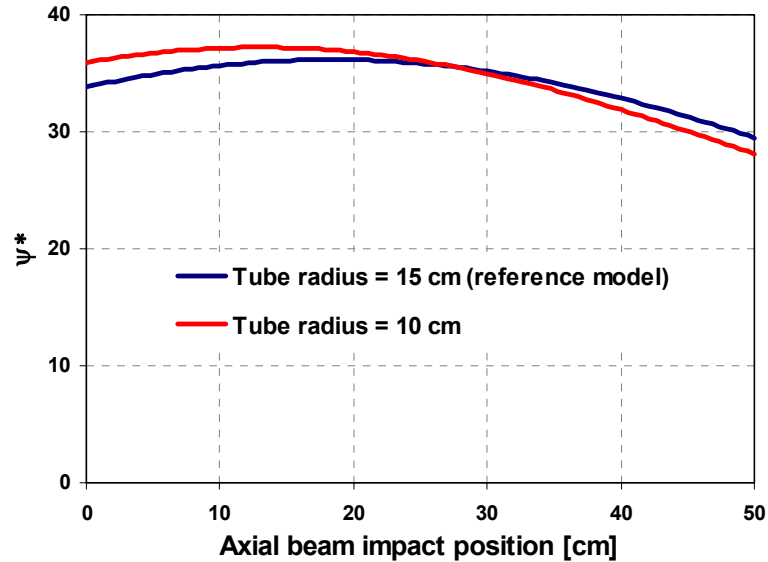


**Fig. 49.** Proton source efficiency,  $\psi^*$ , as function of axial beam impact position (cm above the core centre) for a tube radius of 15 cm and of 10 cm ( $1\sigma$ -error  $\sim 0.50\%$ ).

#### 10.1.4 $\psi^*$ as function of proton beam energy

Investigating the proton source efficiency divided by the proton energy,  $\psi^*/E_p$ , as a function of the proton energy showed that a maximal core power over beam power ratio is obtained for proton energies of about 1200 to 1400 MeV, but with relatively small changes in the region between 1000 and 2000 MeV (Fig. 50). These results are in good agreement with those presented in Fig. 14, where  $Z/E_p$  was plotted as a function of the proton energy. The comparison of the relative dependence of  $\psi^*/E_p$  with that of the energy gain,  $G$ , obtained in the FEAT experiments performed at CERN [89], confirms the relationship between  $\psi^*/E_p$  and  $G$  expressed by Eq. (54).

#### 10.1.5 $\psi^*$ for an americium-based fuel

Increasing the americium content in the fuel from 20% to 60% decreases  $\psi^*$  considerably, in particular for larger target radii (Fig. 51). Due to the sharp decrease in fission cross-section below 1 MeV, americium is more sensitive than plutonium to the softening of the energy spectrum of the neutrons that enter into the fuel, which appears when the target radius increases. The smaller fission probability directly inhibits the fission multiplication and, thus, decreases  $\psi^*$ .

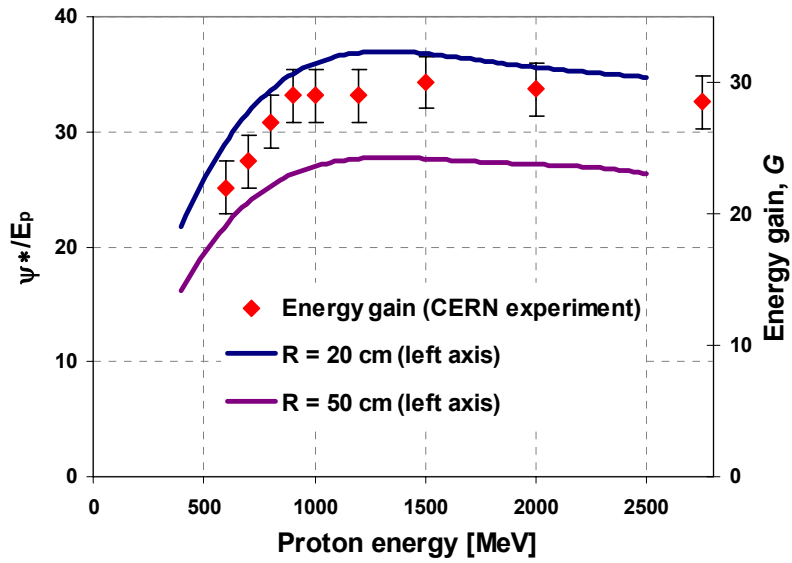


**Fig. 50.** Proton source efficiency divided by the proton energy in GeV,  $\psi^*/E_p$ , as function of proton beam energy, for target radii of 20 cm and 50 cm. The energy gain,  $G$ , determined in the FEAT experiments performed at CERN [89] for a set-up configuration of  $k_{eff} = 0.895$  was also displayed.

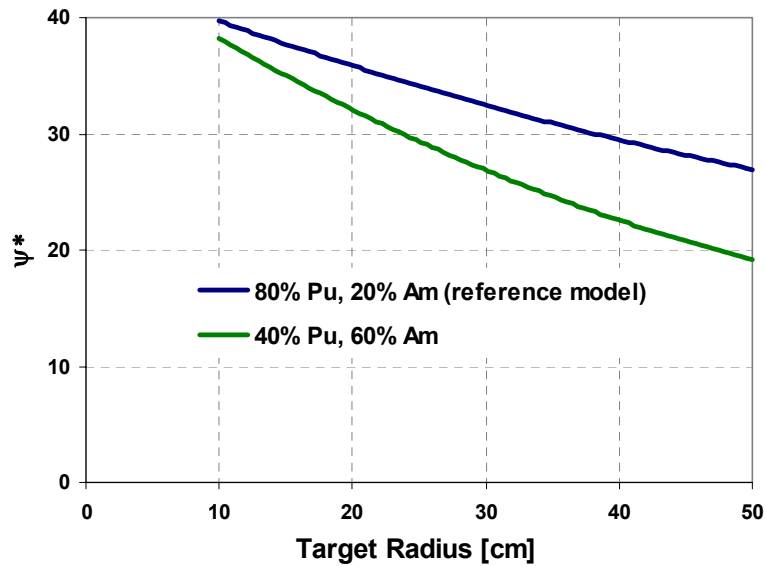


**Fig. 51.** Proton source efficiency,  $\psi^*$ , as function of target radius for an americium-based fuel, compared with the plutonium-based reference model.

### 10.1.6 $\psi^*$ as function of inert matrix material

In order to guarantee the stability of uranium-free fuels at high temperatures, the use of inert matrices is foreseen. Different safety parameters of several possible inert matrix fuels have been studied [42]. In **Paper VIII**, three inert matrices, ZrN, YN and HfN, dispersed with a plutonium- and americium-mixed nitride fuel have been investigated in terms of  $\psi^*$ .  $\psi^*$  has been studied as a function of target radius (Fig. 52) and has been compared for a single-zone core and a power-flattened double-zone core (Table 19). It was found that the HfN matrix fuel yields a lower  $\psi^*$  than the ZrN and the YN matrix fuels. However, for the americium-based fuel and in particular for small target radii, the difference is relatively small. Due to other favourable properties of HfN, e.g., the combination of a hard neutron spectrum with an acceptable void worth, it is still an interesting option of inert matrix material, despite the loss in proton source efficiency. It was also shown that  $\psi^*$  is lower for a power-flattened double-zone core, compared to a single-zone core. The differences are about 5% for the ZrN matrix fuels, while about 10% for the HfN matrix fuels. Comparing the ZrN matrix with the HfN matrix, assuming a double-zone core, the difference in  $\psi^*$  is larger for the plutonium-based fuel (~12%) than for the americium-based fuel (~8%).

**Table 19.**  $\psi^*$  calculated for a single-zone core (1Z) and a double-zone core (2Z). Target radius = 20 cm.

| Fuel          | Matrix | $\psi^*$ |      |            |
|---------------|--------|----------|------|------------|
|               |        | 1Z       | 2Z   | Rel. diff. |
| Pu/Am = 80/20 | ZrN    | 36.0     | 34.3 | -4.8%      |
|               | HfN    | 34.0     | 30.3 | -10.7%     |
| Pu/Am = 40/60 | ZrN    | 32.0     | 30.1 | -5.9%      |
|               | HfN    | 30.7     | 27.6 | -9.9%      |

### 10.1.7 $\psi^*$ as function of actinide distribution in the core

$\psi^*$  has been studied for two different double-zone core configurations. In the first configuration, americium and curium were distributed homogeneously together with plutonium over the entire core, while in the second one, all of the curium was concentrated to the inner zone and the americium to the outer zone. It is seen in Fig. 53 that, heterogenising the fuel distribution by moving curium to the inner zone and americium to the outer zone, increases  $\psi^*$ , compared to when the two materials are homogeneously mixed with each other. The relative increase ranges from ~5% for the 10 cm target radius to ~16% for the 50 cm target radius.

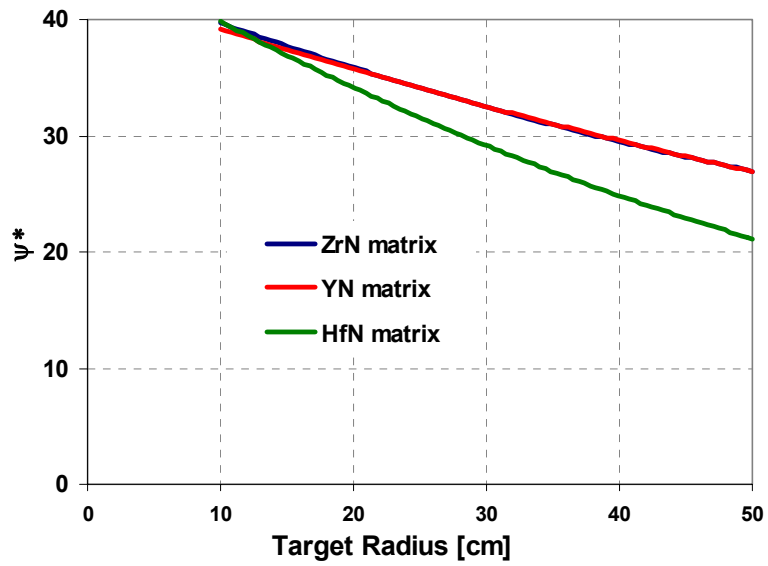


**Fig. 52.** Proton source efficiency,  $\psi^*$ , as function of target radius for different inert matrices (80% Pu + 20% Am).

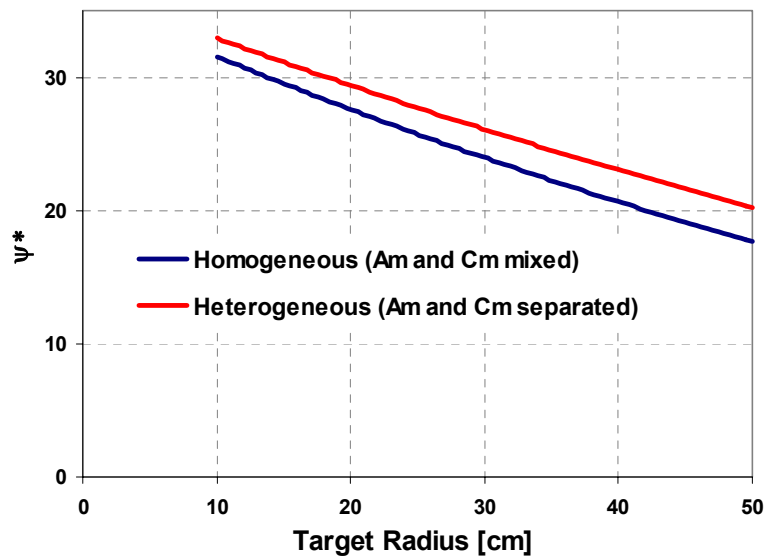


**Fig. 53.** Proton source efficiency,  $\psi^*$ , as function of target radius of the homogeneous and the heterogeneous configurations.

## 10.2 Model II

### 10.2.1 Model design

In order to investigate the possibilities of increasing  $\psi^*$  by distributing the actinides heterogeneously over the core, four different heterogeneous triple-zone configurations of an ADS model were studied (Fig. 54). The ADS model used in the simulations was defined in a previous work, where different neutronic properties of an LBE-cooled ADS with minor actinide-based fuels were investigated [27]. The different configurations were geometrically identical, but had the actinides distributed in different ways over the three core zones. In the first configuration, the same relative fractions of the actinides, Pu/Am/Cm = 0.4/0.5/0.1, in all three zones were used. In the second configuration, all of the americium in zone 1 was moved to the two outer zones and was replaced by curium. In the last two configurations, zone 1 was loaded with one element only, plutonium in configuration III and curium in configuration IV. All simulations performed in the present study were made with MCNPX (version 2.5.e), using the JEFF-3.0 nuclear data library. The high-energy physics package used by MCNPX was the cascade-exciton model (CEM). The studied model and the analyses are presented in detail in **Paper IV**.

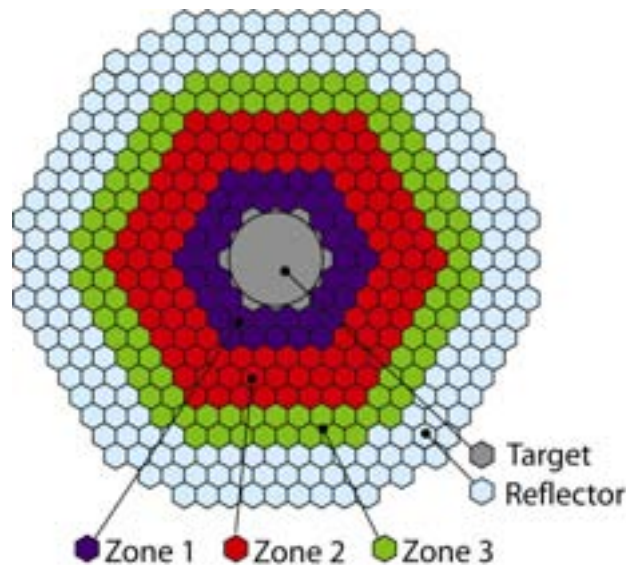


**Fig. 54.** Horizontal cross-sectional view of the studied heterogeneous LBE-cooled ADS model (Model II). The target radius is 21 cm and the subassembly pitch is 10 cm.

### 10.2.2 $\psi^*$ for heterogeneous distribution of actinides

It was found that, compared to the first configuration, where the plutonium, americium and curium were distributed homogeneously in the core, loading the inner zone with only curium increases  $\psi^*$  by about 7% (Table 20).



**Table 20.** Proton source efficiency,  $\psi^*$ , for the four studied configurations, together with the relative differences of configuration II, III and IV compared to configuration I.

| Configuration | $\psi^*$ | Relative difference |
|---------------|----------|---------------------|
| I             | 31.2     |                     |
| II            | 32.0     | 3%                  |
| III           | 30.8     | -1%                 |
| IV            | 33.4     | 7%                  |

The neutron energy spectrum in zone 1 was found to be harder for the source neutrons than for the average fission neutrons in the fundamental mode, as is shown in Fig. 55. This spectrum difference affects several parameters that are directly connected to the magnitude of  $\psi^*$  and is the underlying reason for the differences in  $\psi^*$  that were observed for the different configurations. Three parameters, the average macroscopic fission and capture cross-sections,  $\bar{\Sigma}_f$  and  $\bar{\Sigma}_c$ , and the average fission neutron yield in zone 1,  $\bar{\nu}_z$ , which are affected in different ways for the source neutrons and the fission neutrons by the substitution of actinides in zone 1, have been identified as mainly responsible for the differences in  $\psi^*$ .

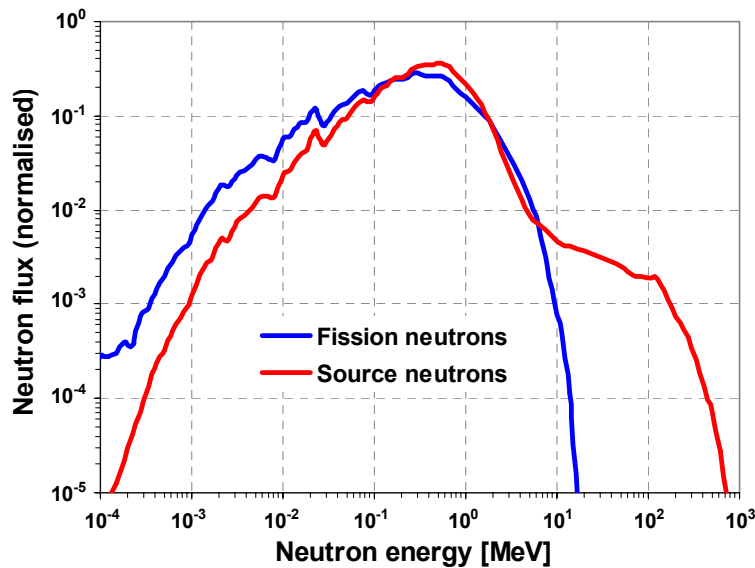


**Fig. 55.** Energy spectra for the source neutrons and the fission neutrons in zone 1 for configuration I.

It was shown that the even-N nuclides in general and  $^{241}\text{Am}$  and  $^{244}\text{Cm}$  in particular are the most favourable nuclides in respect of improving  $\psi^*$ . The reasons for the better properties of the even-N nuclides than those of the odd-N nuclides are the following. Firstly, the harder spectrum in zone 1 for the source neutrons than for the fission neutrons leads to a larger flux-weighted average microscopic fission cross-section,  $\bar{\sigma}_f$ , for the even-N nuclides, whereas a smaller one is obtained for the odd-N nuclides. The second effect of the harder spectrum is a considerably higher aver-

age fission neutron yield for separate nuclides in zone 1,  $\bar{\nu}_n$ , for the even-N nuclides, while it is only marginally higher for the odd-N nuclides. Both these effects enhance the neutron multiplication in zone 1 as well as  $\psi^*$ . On the other hand, the effect on  $\bar{\sigma}_c$  is that it decreases considerably for all nuclides, but more strongly for  $^{239}\text{Pu}$  than for the remaining nuclides. This property of  $^{239}\text{Pu}$  compensates partly for the negative effects from  $\bar{\sigma}_f$  and  $\bar{\nu}_n$ .

Comparing the different configurations, it can be concluded that a larger relative increase in  $\bar{\Sigma}_f$  and in  $\bar{\nu}_z$  for the source neutrons than for the fission neutrons can be expected to enhance  $\psi^*$ , while the opposite effect can be expected for changes in  $\bar{\Sigma}_c$ . Consequently, when loading zone 1 with plutonium only (configuration III),  $\psi^*$  changes only marginally, compared to configuration I, while loading zone 1 with only curium increases it considerably (configuration IV). It can thus be concluded that plutonium, in particular that of high quality consisting mainly of  $^{239}\text{Pu}$  and  $^{241}\text{Pu}$ , is a source inefficient material, compared to curium. The minor increase in  $\psi^*$  when substituting the americium in zone 1 by curium (configuration II) indicates that curium is a slightly better element than americium from this point of view.

The idea of concentrating all of the curium in zone 1 only (comprising 17% of the subassemblies) has both advantages and disadvantages. The fabrication and handling of a fuel consisting of curium only (32% CmN and 68% ZrN) would involve serious technical problems due to intense radiation and heat generation. On the other hand, only a minor fraction of the fuel subassemblies would have to be contaminated by curium, as the remaining 83% would consist of plutonium and americium only. Hence, there is a trade-off between these factors and the gain in  $\psi^*$ .

Finally, one of the general assumptions of the study, that the actinide composition of the innermost zone is of much larger importance for the magnitude of  $\psi^*$  than the two outer zones, was confirmed. By studying the neutron balance in zone 1, it was shown that  $\psi^*$  is directly connected to the neutron multiplication in this zone. The conclusions that the differences in  $\psi^*$  between the different configurations are the results of changes in the ratios of  $\bar{\Sigma}_f$ ,  $\bar{\Sigma}_c$  and  $\bar{\nu}_z$  between the source neutrons and the fission neutrons, were also confirmed.

## 10.3 Model III

### 10.3.1 Model design

$\psi^*$  has been studied for two heterogeneous models based on the PDS-XADS LBE- and gas-cooled concepts [114,115]. For both models, the radius of the target was 21 cm and the outer radii of the cores were adjusted, to 64.5 cm for the helium model and to 83 cm for the LBE model, in order to obtain a  $k_{eff}$  close to 0.97. The core heights were 150 cm and 87 cm, respectively. Two different fuel types were studied for each of the two core designs. The first one was based on the MOX fuel used in the PDS-XADS design, whereas the second one represented a TRU-based fuel with a Pu/Am/Cm relative ratio of 0.4/0.5/0.1. This fuel was chosen as a possible candidate for use in a future full-scale accelerator-driven transmutation reactor.

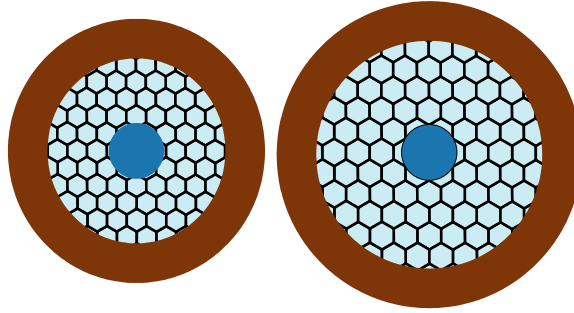


**Fig. 56.** Horizontal cross-sectional views of the studied heterogeneous PDS-XADS core models (Model III). The helium-cooled core is displayed to the left, the LBE-cooled core to the right. The target radius is 21 cm in both cases.

### 10.3.2 LBE-cooled versus gas-cooled core

Comparing the coolant materials, it was found that, for the MOX case, LBE yields a value of  $\psi^*$  lower by about 13% than for helium (Table 21). For the TRU-based fuel, the corresponding difference is about 10%. The main reason for the lower proton source efficiency in LBE-cooled cores is that the relative difference in macroscopic capture cross-section,  $\bar{\Sigma}_c$ , between source neutrons and fission neutrons is higher, which inhibits the fission multiplication and therefore decreases  $\psi^*$ . The differences in the cross-sections arise from differences in the energy spectra of the source neutrons and of the fission neutrons. The dominating contributors to the observed changes in macroscopic capture cross-sections are  $^{238}\text{U}$  in MOX-fuel and  $^{241}\text{Am}$  and  $^{243}\text{Am}$  in the TRU fuel. These nuclides have the common property that the microscopic capture cross-sections decrease rapidly with neutron energy in the 1 MeV range. The conclusion is that the increased moderation in the LBE-coolant reduces the average neutron energy of the source neutrons more than of the fission neutrons, which increases the capture cross-sections more for the former. The results of this study are in line with a previous study by Pelloni [116], where a considerably lower source efficiency was observed for the LBE-cooled core than for the helium-cooled core.

**Table 21.**  $\psi^*$ , calculated for the four studied models and the relative differences to the He-MOX-case.

|                 | He-cooled<br>MOX-fuel | LBE-cooled<br>MOX | He-cooled<br>TRU | LBE-cooled<br>TRU |
|-----------------|-----------------------|-------------------|------------------|-------------------|
| $\psi^*$        | 19.4                  | 16.8              | 16.8             | 15.2              |
| Rel. difference |                       | -13%              | -13%             | -22%              |

Comparing the two different fuel types, it appears that  $\psi^*$  decreases when replacing the MOX fuel by the TRU-fuel, by 13% for the helium-cooled model and by 10% for the LBE-cooled model. In this case, the main reason for the observed differences in  $\psi^*$  is that the relative difference in macroscopic fission cross-section,  $\bar{\Sigma}_f$ , be-

tween source neutrons and fission neutrons, decreases for the TRU-based fuel, which results in a decrease in  $\psi^*$ . The explanation of this behaviour is that the fission probability of the americium isotopes in the fast energy region ( $\sim 0.1$  to  $\sim 1$  MeV) is very sensitive to a softening of the neutron spectrum.

# Chapter 11

## Abstracts of papers

### 11.1 Paper I

Monte Carlo simulations have been performed to investigate the neutron source effects in a sub-critical media successively coupled to a (D,D)-source, a (D,T)-source and a spallation source. The investigations have focused on the neutron energy spectra in the fuel and on the source relative efficiency  $\varphi^*$ . The calculations have been performed for three sub-critical configurations, representative of the coming MUSE-4 experiments.

The Monte Carlo codes MCNP and MCNPX have been used to compute  $\varphi^*$ .  $\varphi^*$  has been found to be low for the (D,D)-source ( $\sim 1.35$  compared to 1.0 for an average fission neutron), while considerably higher for the (D,T)-source ( $\sim 2.15$ ) and the spallation source ( $\sim 2.35$ ). The high value of  $\varphi^*$  for the spallation source has been shown to be due to the fraction of high-energy neutrons (17 % of total source with  $E_n > 20$  MeV) born from spallation, which contribute for 50 % to the total number of fission neutrons produced in the core. The variations of  $\varphi^*$  with neutron importance have also been studied for some spherical configurations with a (D,D)- and a (D,T)-source. For the class of variations considered here,  $\varphi^*$  was found to remain constant or increase only slightly in the interval  $0.70 < k_{eff} < 0.996$ .

### 11.2 Paper II

In order to study the energy gain of an accelerator driven system (ADS), a new parameter, the proton source efficiency,  $\psi^*$ , is introduced.  $\psi^*$  represents the average importance of the external proton source, relative to the average importance of the eigenmode production, and is closely related to the neutron source efficiency,  $\varphi^*$ , which is frequently used in the ADS field.  $\varphi^*$  is commonly used in the physics of sub-critical systems driven by any external source (spallation source, (D,D), (D,T), Cf-252 spontaneous fissions etc.). On the contrary,  $\psi^*$  has been defined in this paper exclusively for ADS studies, where the system is driven by a spallation source. The main advantage of using  $\psi^*$  instead of  $\varphi^*$  for ADS is that the way of defining the external source is unique and that it is proportional to the core power divided by the proton beam power, independently of the neutron source distribution.

Numerical simulations have been performed with the Monte Carlo code MCNPX in order to study  $\psi^*$  as a function of different design parameters. It was found that, in order to maximise  $\psi^*$ , and therefore minimising the proton current needs, a target radius as small as possible should be chosen. For target radii smaller than about 30 cm, LBE is a better choice of coolant material than sodium, regarding the proton source efficiency, while for larger target radii the two materials are equally good. The optimal axial proton beam impact was found to be located approximately 20 cm above the core centre. Varying the proton energy,  $\psi^*/E_p$  was found to have a maximum for proton energies between 1200 and 1400 MeV. Increasing the americium content in the fuel decreases  $\psi^*$  considerably, in particular when the target radius is large.

### 11.3 Paper III

The radiation fields and the effective dose at the Sub-critical Assembly in Dubna (SAD) have been studied with the Monte Carlo code MCNPX. The effective dose above the shielding, i.e., in the direction of the incident proton beam of 3.0  $\mu\text{A}$ , was found to be about 190  $\mu\text{Sv/h}$ . This value meets the dose limits according to Russian radiation protection regulations, provided that access to the rooms in this area is not allowed for working personnel during operation.

By separating the radiation fields into a spallation-induced and a fission-induced part, it was shown that the neutrons with energy higher than 10 MeV, originating exclusively from the proton-induced spallation reactions in the target, contribute for the entire part of the radiation fields and the effective dose at the top of the shielding. Consequently, the effective dose above the SAD reactor system is merely dependent on the proton beam properties and not on the reactivity of the core.

### 11.4 Paper IV

The distribution of actinides in the core of an accelerator-driven system (ADS) loaded with plutonium, americium and curium has been studied in order to optimise the proton source efficiency,  $\psi^*$ . One of the basic assumptions of the study, that the actinide composition in the inner part of the core is of much larger importance for the magnitude of  $\psi^*$  than in the rest of the core, has been confirmed. It has been shown that the odd-N nuclides in general and  $^{241}\text{Am}$  and  $^{244}\text{Cm}$  in particular have favourable properties in respect of improving  $\psi^*$  if they are placed in the innermost part of the core. The underlying reason for this phenomenon is that the energy spectrum of the source neutrons in the inner part of the core is harder than that of the average fission neutrons. Moreover, it has been shown that loading the inner part of the core with only curium increases  $\psi^*$  by about 7%. Plutonium, on the other hand, in particular high-quality plutonium consisting mainly of  $^{239}\text{Pu}$  and  $^{241}\text{Pu}$ , was found to be a comparatively source inefficient element and is preferably located in the outer part of the core. The differences in  $\psi^*$  are due to combined effects from relative changes in the average fission and capture cross-sections and in the average fission neutron yield.

## 11.5 Paper V

Different reactivity determination methods have been investigated, based on experiments performed at the sub-critical assembly Yalina in Minsk, Belarus. The knowledge about on-line monitoring of the reactivity level in a future accelerator-driven system (ADS) is of major importance for safe operation. Since an ADS is operating in a sub-critical mode, the safety margin to criticality must be sufficiently large. The investigated methods are the slope fit method, the Sjöstrand method and the source jerk method. The results are compared with Monte Carlo simulations performed with different nuclear data libraries. The slope fit method compares well with the Monte Carlo simulation results, whereas the Sjöstrand method underestimates the criticality somewhat. The source jerk method is subject to inadequate statistical accuracy.

## 11.6 Paper VI

The efficiency of a spallation neutron source, in an accelerator-driven system (ADS) dedicated to actinide transmutation, is dependent on a series of variables, one of them being the nature of the coolant, another one being the composition of the fuel. In the present study, the proton source efficiency,  $\psi^*$ , has been studied with the Monte Carlo code MCNPX for two heterogeneous models based on the PDS-XADS LBE- and gas-cooled concepts. Minor actinide fuels have also been studied. The main conclusion from the study is that there are important variations in the source efficiency arising both from the choice of fuel and from the choice of coolant. Replacing the MOX-fuel in the core by MA-containing fuel decreases  $\psi^*$  by more than 10% for both coolant options. The explanation for this behaviour is the large difference in fission cross-sections for neutrons in americium, resulting in low macroscopic cross-sections for source neutrons in americium rich fuels. The spectrum change resulting from a substitution of coolant has a large impact on the macroscopic cross-sections of even-N nuclides, leading to a lower  $\psi^*$  for LBE than for helium coolant. Utilising simplified homogenous models yield significantly different results in the helium-cooled case. The result of changing the coolant found in this study is in agreement with a previous study by Pelloni.

# Chapter 12

## Conclusions

Accelerator-driven systems have been proposed as an important component in a nuclear reactor park optimised for reducing the large amount of the radiotoxic nuclear waste produced by the many nuclear power plants in operation over the world. The chief of the work presented in this thesis has been devoted to Monte Carlo simulations investigating the neutronics and various source effects in sub-critical systems, driven by an external neutron source.

In order to estimate the ratio between the total power produced in the core and the power supplied by the external source in a sub-critical system, the neutron source efficiency parameter,  $\varphi^*$ , is commonly used. However, with the aim of studying the energy gain in an ADS, i.e., the core power over beam power, the proton source efficiency,  $\psi^*$ , has been introduced. For different reasons,  $\psi^*$  is better suited than  $\varphi^*$  for this purpose when the external source consists of protons, which is indeed the case in an ADS. Importantly, using  $\psi^*$  instead of  $\varphi^*$  avoids ambiguities connected to the definition of the external neutron source. When studying  $\psi^*$  as a function of different system parameters it becomes clear that, choosing a system design that optimises  $\psi^*$  may increase significantly the energy gain and can thus have an important impact on the performance of an ADS. One of the results from the simulations of an ADS model with the high-energy Monte Carlo code MCNPX was that  $\psi^*$  decreases strongly with increasing target radius. Hence, in order to maximise the energy gain, and thereby minimising the proton current needs, a target radius as small as possible should be chosen, without exceeding the limits determined by safety constraints, thermal hydraulics and other target-core characteristics.  $\psi^*$  was also studied as a function of many other system parameters for different models of an ADS. From these studies, we conclude that, in order to optimally design an efficient ADS with high fuel performances, there is a trade-off arising between several different aspects. Various system parameters, e.g., target radius, axial beam impact position, proton beam energy, choice of coolant medium, fuel composition and inert matrix material, together with other target-core characteristics and different safety limitations, have to be weighted against the advantage of optimising  $\psi^*$  and the energy gain.

Calculations have been performed with MCNP and MCNPX for a model representative of the recently completed MUSE-4 experiments. Neutronic parameters, such as neutron energy spectrum, neutron source efficiency and dynamic neutron



source response have been investigated for different sub-critical configurations. The effects from the (D,D)- and the (D,T)-sources produced by the GENEPI neutron generator have been studied and compared with the effects from a 1000 MeV proton-induced spallation source, coupled to the same sub-critical core. The computed neutron spectra show that fission multiplication dominates at distances past a few centimetres into the fuel. This implies that, for the purpose of ADS core studies, the properties of the source may be ignored when calculating spectrum-weighted quantities, except possibly in the immediate vicinity of the external source. The calculations of  $\varphi^*$  for the different sources yield a much higher value for the (D,T)-source ( $E \sim 14$  MeV) than for the (D,D)-source ( $E \sim 2.7$  MeV), which is explained by the (n,2n)-multiplications of the 14 MeV neutrons in lead. In the case of the spallation source, the possibility of choosing different neutron source definitions and the consequences of this choice have been emphasised.

In the Yalina experiments, accurate dynamic measurements have enabled investigations of different techniques for reactivity determination in sub-critical systems. Three dynamic methods were investigated; the slope fit method, the Sjöstrand method and the source jerk method. It was found that the results of  $k_{eff}$  obtained with the slope fit method are in good agreement with those obtained by MCNP simulations. The Sjöstrand method, on the other hand, appears to underestimate  $k_{eff}$  slightly, in comparison with MCNP and the slope fit method. Finally, the results of  $k_{eff}$  obtained with the source jerk method were found to be higher than those of the other methods, although this method is connected with large uncertainties.

The main objective of the MCNPX-based investigations of the upcoming SAD experiments was to determine the radiation doses above the biological shielding covering the upper part of the core. It was found that the shielding concerns are mainly caused by the deeply penetrating high-energy neutrons created in the spallation process. The fact that 100% of the dose originates from neutrons with energy higher than 10 MeV, which are exclusively produced in the spallation target, shows that the effective dose at the top of the SAD shielding is directly proportional to the proton beam current and that it is independent of the reactivity of the sub-critical core.

## Appendix A

# Production facts of nuclear power

**Table A1.** Production facts for operational reactors and reactors under construction, sorted by reactor type (last updated on 2005/08/17) [23].

| Country      | Operational  |                      | Under construction |                      |
|--------------|--------------|----------------------|--------------------|----------------------|
|              | No. of units | Total power<br>[GWe] | No. of units       | Total power<br>[GWe] |
| PWR          | 214          | 205                  | 2                  | 2.5                  |
| BWR          | 89           | 78                   | 1                  | 1.1                  |
| WWER         | 53           | 36                   | 10                 | 9.5                  |
| PHWR         | 40           | 20                   | 7                  | 2.6                  |
| LWGR         | 16           | 11                   | 1                  | 0.9                  |
| AGR          | 14           | 8.4                  | -                  | -                    |
| GCR          | 8            | 2.3                  | -                  | -                    |
| ABWR         | 4            | 5.3                  | 2                  | 2.6                  |
| FBR          | 3            | 1.0                  | 1                  | 0.5                  |
| <b>Total</b> | <b>441</b>   | <b>368</b>           | <b>24</b>          | <b>19.7</b>          |

**Table A2.** Production facts for operational reactors and reactors under construction, sorted by country (last updated on 2005/08/17) [23].

| Country        | Operational  |                      |                           | Under construction |                      |
|----------------|--------------|----------------------|---------------------------|--------------------|----------------------|
|                | No. of units | Total power<br>[GWe] | Share <sup>a</sup><br>[%] | No. of units       | Total power<br>[GWe] |
| USA            | 104          | 99.2                 | 19.9                      | -                  | -                    |
| France         | 59           | 63.4                 | 78.1                      | -                  | -                    |
| Japan          | 55           | 46.8                 | 29.3                      | 2                  | 1.9                  |
| Russia         | 31           | 21.7                 | 15.6                      | 4                  | 3.8                  |
| United Kingdom | 23           | 11.9                 | 19.4                      | -                  | -                    |
| Korea, Rep. of | 20           | 16.8                 | 37.9                      | -                  | -                    |
| Canada         | 17           | 12.1                 | 15.0                      | -                  | -                    |
| Germany        | 17           | 20.3                 | 32.1                      | -                  | -                    |
| India          | 15           | 3.0                  | 2.8                       | 8                  | 3.6                  |
| Ukraine        | 15           | 13.1                 | 51.1                      | 2                  | 1.9                  |
| Sweden         | 10           | 8.9                  | 51.8                      | -                  | -                    |
| China          | 9            | 6.6                  | 2.2                       | 2                  | 2.0                  |
| Spain          | 9            | 7.6                  | 22.9                      | -                  | -                    |
| Belgium        | 7            | 5.8                  | 55.1                      | -                  | -                    |
| Czech Rep.     | 6            | 3.5                  | 31.2                      | -                  | -                    |
| Slovak Rep.    | 6            | 2.4                  | 55.2                      | -                  | -                    |
| Taiwan/China   | 6            | 4.9                  |                           | 2                  | 2.6                  |
| Switzerland    | 5            | 3.2                  | 40.0                      | -                  | -                    |
| Bulgaria       | 4            | 2.7                  | 41.6                      | -                  | -                    |
| Finland        | 4            | 2.7                  | 26.6                      | 1                  | 1.6                  |
| Hungary        | 4            | 1.8                  | 33.8                      | -                  | -                    |
| Argentina      | 2            | 0.9                  | 8.2                       | 1                  | 0.7                  |
| Brazil         | 2            | 1.9                  | 3.0                       | -                  | -                    |
| Mexico         | 2            | 1.3                  | 5.2                       | -                  | -                    |
| Pakistan       | 2            | 0.4                  | 2.4                       | -                  | -                    |
| South Africa   | 2            | 1.8                  | 6.6                       | -                  | -                    |
| Armenia        | 1            | 0.4                  | 38.8                      | -                  | -                    |
| Lithuania      | 1            | 1.2                  | 72.1                      | -                  | -                    |
| Netherlands    | 1            | 0.4                  | 3.8                       | -                  | -                    |
| Romania        | 1            | 0.7                  | 10.1                      | 1                  | 0.7                  |
| Slovenia       | 1            | 0.7                  | 38.8                      | -                  | -                    |
| Iran           | 0            | 0.0                  |                           | 1                  | 0.9                  |
| <b>Total</b>   | <b>441</b>   | <b>368</b>           | <b>16</b>                 | <b>24</b>          | <b>19.7</b>          |

<sup>a</sup> Nuclear share of electricity production

## Appendix B

# Derivation of an equation for the total core power in ADS

The total recoverable energy produced by fission in the core,  $W$ , can be approximately expressed as the product of the total number of fission events and the average available energy released in a fission, according to the following relation;

$$W = \frac{\langle \hat{\mathbf{F}}\Phi \rangle}{\bar{\nu}} \cdot \bar{E}_f, \quad (\text{B.1})$$

where  $\langle \hat{\mathbf{F}}\Phi \rangle$  is the total production of neutrons by fission,  $\bar{\nu}$  is the average neutron yield per fission and  $\bar{E}_f$  is the average recoverable energy released in a fission. The neutron source efficiency,  $\varphi^*$ , can be expressed according to [84]

$$\varphi^* = \left( \frac{1}{k_{eff}} - 1 \right) \cdot \frac{\langle \hat{\mathbf{F}}\Phi \rangle}{\langle S_n \rangle}, \quad (\text{B.2})$$

where  $\langle S_n \rangle$  is the total production of source neutrons. Inserting Eq. (B.2) into Eq. (B.1), an expression for the energy produced per source neutron is obtained,

$$\frac{W}{\langle S_n \rangle} = \frac{\bar{E}_f}{\bar{\nu}} \cdot \frac{k_{eff}}{1 - k_{eff}} \cdot \varphi^*. \quad (\text{B.3})$$

Now defining the number of source neutrons produced per incident source proton as

$$Z = \frac{\langle S_n \rangle}{\langle S_p \rangle}, \quad (\text{B.4})$$

where  $\langle S_p \rangle$  is the total number of source protons, we obtain

$$\frac{W}{\langle S_p \rangle} = \frac{\bar{E}_f}{\bar{\nu}} \cdot \frac{k_{eff}}{1 - k_{eff}} \cdot Z\varphi^*. \quad (\text{B.5})$$

Eq. (B.5) expresses the energy produced per incident source proton, which can also be expressed as

$$\frac{W}{\langle S_p \rangle} = \frac{P_{tot}}{i_p} . \quad (\text{B.6})$$

We thus finally obtain the following expression for the total power produced in the core,  $P_{tot}$ , as

$$P_{tot} = \frac{k_{eff}}{1 - k_{eff}} \cdot \frac{i_p \bar{E}_f}{\bar{v}} \cdot Z\varphi^* , \quad (\text{B.7})$$

which is valid in the range  $0 < k_{eff} < 1$ .

## Appendix C

# Fluence-to-effective dose conversion coefficients

**Table C1.** Effective dose per unit fluence,  $E/\phi$ , for neutrons, photons and protons (ISO geometry) used in the present study. The conversion coefficients for neutrons in the energy range from  $1 \cdot 10^{-9}$  MeV to 20 MeV are taken from [106], while the coefficients for neutrons from 30 to 500 MeV, as well as all coefficients for photons and protons, are taken from [112].

| Neutrons            |                                    | Photons         |                                    | Protons         |                                    |
|---------------------|------------------------------------|-----------------|------------------------------------|-----------------|------------------------------------|
| Energy<br>[MeV]     | $E/\phi$<br>[pSv·cm <sup>2</sup> ] | Energy<br>[MeV] | $E/\phi$<br>[pSv·cm <sup>2</sup> ] | Energy<br>[MeV] | $E/\phi$<br>[pSv·cm <sup>2</sup> ] |
| $1 \cdot 10^{-9}$   | 2.40                               | 0.02            | 0.093                              | 10              | 20.6                               |
| $1 \cdot 10^{-8}$   | 2.89                               | 0.05            | 0.21                               | 20              | 173.9                              |
| $2.5 \cdot 10^{-8}$ | 3.30                               | 0.1             | 0.31                               | 30              | 423.8                              |
| $1 \cdot 10^{-7}$   | 4.13                               | 0.2             | 0.61                               | 50              | 1346.0                             |
| $2 \cdot 10^{-7}$   | 4.59                               | 0.5             | 1.65                               | 100             | 2953.8                             |
| $5 \cdot 10^{-7}$   | 5.20                               | 1               | 3.30                               | 150             | 4648.0                             |
| $1 \cdot 10^{-6}$   | 5.63                               | 2               | 6.02                               | 200             | 4577.4                             |
| $2 \cdot 10^{-6}$   | 5.96                               | 5               | 12.15                              | 300             | 3445.6                             |
| $5 \cdot 10^{-6}$   | 6.28                               | 10              | 20.63                              | 500             | 2965.6                             |
| $1 \cdot 10^{-5}$   | 6.44                               | 20              | 32.40                              |                 |                                    |
| $2 \cdot 10^{-5}$   | 6.51                               | 50              | 62.16                              |                 |                                    |
| $5 \cdot 10^{-5}$   | 6.51                               | 100             | 96.63                              |                 |                                    |
| $1 \cdot 10^{-4}$   | 6.45                               | 200             | 133.5                              |                 |                                    |
| $2 \cdot 10^{-4}$   | 6.32                               | 500             | 190.2                              |                 |                                    |
| $5 \cdot 10^{-4}$   | 6.14                               |                 |                                    |                 |                                    |
| $1 \cdot 10^{-3}$   | 6.04                               |                 |                                    |                 |                                    |
| $2 \cdot 10^{-3}$   | 6.05                               |                 |                                    |                 |                                    |
| $5 \cdot 10^{-3}$   | 6.52                               |                 |                                    |                 |                                    |
| 0.01                | 7.70                               |                 |                                    |                 |                                    |
| 0.02                | 10.2                               |                 |                                    |                 |                                    |
| 0.03                | 12.7                               |                 |                                    |                 |                                    |
| 0.05                | 17.3                               |                 |                                    |                 |                                    |
| 0.07                | 21.5                               |                 |                                    |                 |                                    |

**Table C1 (cont.)**

| Neutrons        |                                    | Photons         |                                    | Protons         |                                    |
|-----------------|------------------------------------|-----------------|------------------------------------|-----------------|------------------------------------|
| Energy<br>[MeV] | $E/\phi$<br>[pSv·cm <sup>2</sup> ] | Energy<br>[MeV] | $E/\phi$<br>[pSv·cm <sup>2</sup> ] | Energy<br>[MeV] | $E/\phi$<br>[pSv·cm <sup>2</sup> ] |
| 0.1             | 27.2                               |                 |                                    |                 |                                    |
| 0.15            | 35.2                               |                 |                                    |                 |                                    |
| 0.2             | 42.4                               |                 |                                    |                 |                                    |
| 0.3             | 54.7                               |                 |                                    |                 |                                    |
| 0.5             | 75.0                               |                 |                                    |                 |                                    |
| 0.7             | 92.8                               |                 |                                    |                 |                                    |
| 0.9             | 108                                |                 |                                    |                 |                                    |
| 1.0             | 116                                |                 |                                    |                 |                                    |
| 1.2             | 130                                |                 |                                    |                 |                                    |
| 2               | 178                                |                 |                                    |                 |                                    |
| 3               | 220                                |                 |                                    |                 |                                    |
| 4               | 250                                |                 |                                    |                 |                                    |
| 5               | 272                                |                 |                                    |                 |                                    |
| 6               | 282                                |                 |                                    |                 |                                    |
| 7               | 290                                |                 |                                    |                 |                                    |
| 8               | 297                                |                 |                                    |                 |                                    |
| 9               | 303                                |                 |                                    |                 |                                    |
| 10              | 309                                |                 |                                    |                 |                                    |
| 12              | 322                                |                 |                                    |                 |                                    |
| 14              | 333                                |                 |                                    |                 |                                    |
| 15              | 338                                |                 |                                    |                 |                                    |
| 16              | 342                                |                 |                                    |                 |                                    |
| 18              | 345                                |                 |                                    |                 |                                    |
| 20              | 343                                |                 |                                    |                 |                                    |
| 30              | 356                                |                 |                                    |                 |                                    |
| 50              | 389                                |                 |                                    |                 |                                    |
| 100             | 412                                |                 |                                    |                 |                                    |
| 150             | 527                                |                 |                                    |                 |                                    |
| 200             | 526                                |                 |                                    |                 |                                    |
| 500             | 791                                |                 |                                    |                 |                                    |

# References

- 1 M. Salvatores et al., “Long-Lived Radioactive Waste Transmutation and the Role of Accelerator Driven (Hybrid) Systems”, *Nucl. Inst. Meth. A*, **414**, 5 (1997).
- 2 D. G. Foster et al., “Review of PNL Study on Transmutation Processing of High Level Waste”, LA-UR-74-74, Los Alamos National Laboratory (1974).
- 3 T. Takizuka et al., “Conceptual Design of Transmutation Plant”, Proc. Specialist Mtg. Accelerator Driven Transmutation Technology for Radwaste, LA-12205-C, p. 707, Los Alamos National Laboratory (1991).
- 4 D. G. Cacuci, “On the Neutron Kinetics and Control of Accelerator-driven Systems”, *Nucl. Sci. Eng.*, **148**, 55-66 (2004).
- 5 M. Delpech et al., “The Am and Cm Transmutation – Physics and Feasibility”, Int. Conf. Future Nuclear Systems, GLOBAL’99, August 30-September 2, 1999, Jackson Hole, Wyoming, American Nuclear Society (1999).
- 6 J. F. Briesmeister, “MCNP<sup>TM</sup> – A General Monte Carlo N-Particle Transport Code – Version 4C”, LANL/Los Alamos, LA-13709-M, March, 2000.
- 7 L. S. Waters, “MCNPX<sup>TM</sup> User’s Manual – Version 2.1.5”, Los Alamos National Laboratory, November 14, (1999).
- 8 M. Salvatores et al., “The Potential of Accelerator-Driven Systems for Transmutation or Power Production Using Thorium or Uranium Fuel Cycles”, *Nucl. Sci. Eng.*, **126**, 333 (1997).
- 9 R. Soule, M. Salvatores, R. Jacqmin, “Validation of Neutronic Methods Applied to the Analysis of Fast Sub-Critical Systems: The MUSE-2 Experiments”, Int. Conf. GLOBAL’97, page 639 (1997).
- 10 R. Klein Meulekamp and A. Hogenbirk, “The Neutron Source in ADS applications”, PDS-XADS D23 App. D, NRG report /I 20782 / 02.50727, Petten (2002).
- 11 J. Wallenius et al., “Application of burnable absorbers in an accelerator driven system”, *Nucl. Sci. Eng.*, **96**, 137 (2001).
- 12 W. S. Yang and L. Mercatali et al., “Effects of Buffer Thickness on ATW Blanket Performances”, Int. Meeting AccApp’01, November 11-15, 2001, Reno, Nevada, USA (2001).



- 13 R. Soule, “Neutronic Studies in Support to ADS: The MUSE Experiments in the MASURCA Facility”, PHYSOR’02, Seoul, Korea, October 7-10, (2002).
- 14 F. Mellier (coordinator) et al., “The MUSE Experiments for Sub-critical Neutronics Validation”, Deliverable No 8 (Final report) of the EU 5th FP contract No FIKW-CT-2000-00063, Cadarache, France, (2005).
- 15 J. M. De Conto et al., “GENEPI: A high intensity deuteron accelerator for pulsed neutron production”, Proc. EPAC 1998, Stockholm.
- 16 A. I. Kievitskaia et al., “Experimental and theoretical research on transmutation of long-lived fission products and minor actinides in a subcritical assembly driven by a neutron generator”, Int. Meeting ADTTA’99, Czech Republic, Praha, June (1999).
- 17 I. G. Serafimovich et al., “A small-scale set-up for research of some aspects of accelerator driven transmutation technologies”, Int. Meeting ADTTA’99, Czech Republic, Praha, June (1999).
- 18 W. Gudowski, A. Polanski, I. V. Puzynin, V. Shvetsov, “Monte Carlo modelling of a sub-critical assembly driven with the existing 660 MeV JINR Proton Accelerator”, Int. Meeting AccApp’01, November 11-15, 2001, Reno, Nevada, USA (2001).
- 19 ISTC Project 2267 (SAD). <http://www.sad.dubna.ru/>
- 20 International Atomic Energy Agency, “Code of Practice on the Transboundary Movement of Radioactive Waste”; [http://www.mint.gov.my/policy/treaty\\_nuclear/iaea90code\\_waste.htm](http://www.mint.gov.my/policy/treaty_nuclear/iaea90code_waste.htm)
- 21 K. Fukuda et al., “IAEA Overview of global spent fuel storage”, IAEA-CN-102/60, Int. Conf. on Storage of Spent Fuel from Power reactors, Vienna, 2-6 June (2003).
- 22 “A European Roadmap for Developing Accelerator Driven Systems (ADS) for Nuclear Waste Incineration”, ENEA, April 2001, ISBN 88-8286-008-6.
- 23 Power Reactor Information System (PRIS), “Nuclear power plants information”, last updated on 2005/08/17; <http://www.iaea.org/programmes/a2/>
- 24 International Commission on Radiological Protection (ICRP), “Dose Coefficients for Intakes of Radionuclides by Workers”, ICRP Publication 68, 1994.
- 25 OECD Nuclear Energy Agency, “Actinide and Fission Product Partitioning and Transmutation; Status and Assessment Report”, Paris, France, (1999).
- 26 OECD Nuclear Energy Agency, “The JEFF-3.0 Nuclear Data Library”, JEFF Report 19, (2005).
- 27 J. Wallenius and M. Eriksson, “Neutronics of minor actinide burning accelerator-driven systems with ceramic fuel”, *Nucl. Tech.* **152** (2005).

- 28 J. R. Lamarsh and A. J. Baratta, "Introduction to Nuclear Engineering", Prentice Hall Inc, Upper Saddle River, NJ (2001).
- 29 OECD/NEA Data Bank, "Janis 2.1"; <http://www.nea.fr/janis/> (2004).
- 30 J. J. Duderstadt and L. J. Hamilton, "Nuclear Reactor Analysis", John Wiley & Sons, Inc (1976).
- 31 International Atomic Energy Agency, "Delayed Fission Neutrons", IAEA, Vienna (1968).
- 32 H. Murata and T. Mukaiyama, "Fission Reactor Studies in View of Reactor Waste Programs", *Atomkernenergie-Kerntechnik*, 45:23, 1984.
- 33 G. Kock, "Existing and projected reprocessing plants: a general review", *Atomkernenergie./Kerntech.* **33**, 241, 1979.
- 34 Commissariat à l'Énergie Atomique (CEA), "Clefs: Radioactive Waste management Research", Clefs CEA No 46, Spring 2002.
- 35 R. J. M. Konings, (ED). "Advanced fuel cycles for accelerator-driven systems: fuel fabrication and reprocessing", Prepared by The Fuel Fabrication and Processing Subgroup of the Technical Working Group on ADS. *EUR 19928*. 2001.
- 36 C. Madic et al., "Actinide partitioning from high-level waste using the DIAMEX process", Int. Conf., RECOD'94, London, UK, 24-28 April (1994).
- 37 C. Hill et al., "SANEX-BTP process development studies", 7th Inf. Exch. Meeting on Actinide and Fission Product Partitioning and Transmutation, 14-16 October 2002, Jeju, Korea (2002).
- 38 Y. J. Zhu, "Extraction of Am(III) and Eu(III) from nitrate solution with purified Cyanex 301", *Solv. Extr. & Ion Exch.* **14**, pp 61, 1996.
- 39 J. M Adnet et al., "The development of the SESAME process", Int. Conf., GLOBAL'97, October 5-10, Yokohama, Japan (1997).
- 40 J. Wallenius and S. Pillon, "N-15 Requirements for 2nd Stratum ADS Nitride Fuels", Int. Meeting AccApp'01, November 11-15, 2001, Reno, Nevada, USA (2001).
- 41 S. Monti et al., "Interim Report of the Technical Working Group on Accelerator Driven Sub-critical Systems", October 12, 1998.
- 42 J. Wallenius, "Neutronic Aspects of Inert Matrix Fuels for Application in ADS", *J. Nucl. Mat.* **320**, 142 (2003).
- 43 Review of the Spallation Neutron Source (SNS), DOE/ER-0705 (June 1997).
- 44 Y. Dai, "Summary on the Preliminary Assessment of the T91 Window Performance in the MEGAPIE Conditions", Int. Meeting AccApp'05, August 29 – September 1, Venice, Italy (2005).

- 45 H. A. Abderrahim, P. Kuoschus, MYRRHA-team, "MYRRHA - A Multipurpose Accelerator Driven System (ADS) for Research & Development", March 2002 Pre-Design Report", R-3595, March 2002.
- 46 H. A. Abderrahim et al., "MYRRHA: A Multipurpose Accelerator-driven system for Research and Development", *Nucl. Inst. and Meth. in Phys. Res.* **A463**, 487-494, (2001).
- 47 OECD Nuclear Energy Agency, "Accelerator-driven Systems (ADS) and Fast Reactors (FR) in Advanced Nuclear Fuel Cycles; A Comparative Study", Paris, France, (2002).
- 48 B. Carlucci et al., "Report of the TWG sub-group on Accelerators for ADS", March 2001.
- 49 G. S. Bauer, 2nd Int. Conf. on Accelerator Driven Transmutation Technologies, Kalmar, Sweden, June 3-7, 159 (1996).
- 50 K. N. Clausen, "ESS – The European Spallation Source", 16th Meeting on the International Collaboration on Advanced Neutron Sources, May 12-15, 2003, Düsseldorf-Neuss, Germany (2003).
- 51 H. V. Smith, Jr. et al., "Status Report on the Low-Energy Demonstration Accelerator (LEDA)", *ibid.*, pp. 581-583.
- 52 M. Eriksson and C. Piaszczyk, "Reliability Assessment of the LANSCE Accelerator System", Workshop on Utilisation and Reliability of High-power Proton Accelerators, Mito, Japan, 13-15 October, 1998.
- 53 H. Safa, J.M. Lagniel, T. Junquera and A.C. Mueller, "A Superconducting Proton Linear Accelerator for Waste Transmutation", Proc. Int. Conf. ADTT'99, Praha, Czech Rep. April (1999).
- 54 Department of Energy (DOE), "A Roadmap for Developing Accelerator Transmutation of Waste (ATW) Technology", DOE/RW-0519, U.S., Department of Energy, Washington, DC, October (1999).
- 55 H. Safa, "Requirements for the XADS Accelerator & the Technical Answers", Internal Report under the E.C. Contract N°: FIKW-CT-2001-00179.
- 56 PDS-XADS, Preliminary Design Studies of an Experimental Accelerator-driven System", EU 5th FP FIKW-CT-2001-00179.
- 57 J.Y. Doriath et al, "ERANOS 1: The Advanced European System of Codes for Reactor Physics Calculation", Int. Conf. on Mathematical Methods and Super Computing in Nuclear Application, 19-23 April 1993, Kongresszentrum, Karlsruhe, Germany (1993).
- 58 R. E. Macfarlane and D. W. Muir, "The NJOY Nuclear Data Processing System", Los Alamos National Laboratory, LA-12740-M (1992).
- 59 R. E. Prael and H. Lichtenstein, "User Guide to LCS: The LAHET Code System", LA-UR-89-3014, Los Alamos National Laboratory (1989).

- 60 M. B. Chadwick et al., *Nucl. Sci. Eng.* (submitted 1998, Los Alamos National Laboratory LA-UR-98-1825 (1998)).
- 61 OECD Nuclear Energy Agency, “The JEF-2.2 Nuclear Data Library”, JEFF Report 17, (2000).
- 62 G. Palmiotti et al, “BISTRO Optimized Two Dimensional Sn Transport Code”, *Nucl. Sci. Eng.* **104**, 26 (1990).
- 63 E. Fort, et al., “Realisation and Performance of the adjusted Nuclear Data Library ERALIB1 for Calculating Fast Reactor Neutronics”, PHYSOR’96, Mito, Japan, September 1996.
- 64 T. W. Armstrong and K. C. Chandler, “HETC Monte Carlo High Energy Nucleon Meson Transport Code”, ORNL-4744, Oak Ridge National Laboratory (1972).
- 65 Radiation Shielding Information Centre, “HETC Monte Carlo High-Energy Nucleon-Meson Transport Code”, Report CCC-178, Oak Ridge National Laboratory (August 1977).
- 66 R. E. Prael and M. Bozoian, “Adaptation of the Multistage Pre-equilibrium Model for the Monte Carlo Method (1)”, LA-UR-88-3238, Los Alamos National Laboratory Report, (September 1988).
- 67 H. W. Bertini, *Phys. Rev.* **131** (1963) pp 1801.
- 68 H. W. Bertini, *Phys. Rev.* **188** (1969) pp 1711.
- 69 Y. Yariv and Z. Fraenkel, *Phys. Rev.* **C20** (1979), pp 2227.
- 70 Y. Yariv and Z. Fraenkel, *Phys. Rev.* **C24** (1981), pp 488.
- 71 J. Cugnon, *Nucl. Phys.* **A462**, 751 (1987)
- 72 J. Cugnon, C. Volant and S. Vuillier, *Nucl. Phys.* **A620**, 475 (1997).
- 73 S. G. Mashnik and V. D. Toneev, “Modex – The Program for Calculation of Energy Spectra of Particles Emitted in the Reactions of Preequilibrium Statistical Decays”, JINR P4-8417, Dubna, 1974.
- 74 A. Fasso et al., “FLUKA 92” Proc. Of the Workshop on Simulating Accelerator Radiation Environments, Santa Fe, Jan. 11-15, 1993.
- 75 S. Leray et al., “Spallation Neutron Production by 0.8, 1.2, and 1.6 GeV Protons on various Targets”, *Phys. Rev.*, **C65** (2002).
- 76 O. Bersillon et al., “TIERCE: A Code System for Particles and Radiation Transport in Thick Targets”, Proceedings of International Conference on Nuclear Data for Science and Technology, 19-24 May 1997, Trieste, Italy (1997), 257.
- 77 L. Dresner, Oak Ridge report ORNL-TM-196 (1962).

- 78 F. Atchison, Proc. of a Specialists' Meeting, OECD/NEA, Issy-le-Moulineaux, France, May 30 - June 1 (1994) 199.
- 79 A.R. Junghans et al., *Nucl. Phys.* **A629** 635 (1998).
- 80 D. J. Brenner et al., "Improved Calculations of Energy Deposition from fast Neutrons", in *Proceedings Fourth Symposium on Neutron Dosimetry*, EUR-7448, Munich-Neuherberg (1981).
- 81 F. Atchison, "Spallation and Fission in Heavy Metal Nuclei under Medium Energy Proton Bombardment", in *Targets for Neutron Beam Spallation Source*, Jül-Conf-34, Kernforschungsanlage Jülich GmbH (January 1980).
- 82 J. Barish et al., "HETFIS High-Energy Nucleon-Meson Transport Code with Fission", ORNL/TM-7882, Oak Ridge National Laboratory (1981).
- 83 G. I. Bell and S. Glasstone, "Nuclear Reactor Theory", Litton Educational Publishing, Inc, (1970).
- 84 G. Aliberti et al., "Analysis of the MUSE-3 Subcritical Experiment", Int. Conf. GLOBAL'01, France, Paris, September (2001).
- 85 K. Tucek et al., "Source Efficiency in an Accelerator-Driven System with Burnable Absorbers", Int. Conf. on Back-End of the Fuel Cycle: From Research to Solutions, GLOBAL 2001, Paris, France (2001).
- 86 S. Atzeni et al., "Statistical Fluctuations in Monte Carlo Simulations of a Sub-Critical System", CERN-LHC-97-012-EET, CERN (1997).
- 87 K. W. Burn, "A Decoupled Approach to the Neutronics of subcritical configurations: Evaluating the Neutron Source", RT/ERG/99/2, ENEA, Bologna, Italy (1999).
- 88 A. Gandini and M. Salvatores: "The Physics of Subcritical Multiplying Systems", *Journal of Nuclear Science and Technology*, Vol. 39, No. 6, pp. 673-686 (June 2002).
- 89 S. Andriamonje et al., "Experimental determination of the energy generated in nuclear cascades by a high-energy beam", *Physics Letters B*, **348**, 697-709, (1995).
- 90 M. Salvatores, M. Martini and I. Slessarev, "MUSE-1: A first Experiment at MASURCA to Validate the Physics of Sub-Critical Multiplying Systems Relevant to ADS", Kalmar, Sweden, June 3-7 (1996).
- 91 J. F. Lebrat et al., "Experimental Investigation of Multiplying Sub-Critical Media in Presence of an External Source Operating in Pulsed or Continuous Mode: The MUSE-3 Experiment", ADTTA'99 (1999).
- 92 C. Jammes et al., "First MUSE-4 Experimental Results based on Time Series Analysis", PHYSOR'02, Seoul, Korea, October 7-10, 2002.

- 93 R. Soule et al., “Geometrical and Physical Data Associated to the MUSE 4 Reference Configuration”, CEA/Cadarache (2001).
- 94 D. Villamarin, R. Soule and E. Gonzalez-Romero, “Benchmark on Computer Simulation of MASURCA Critical and Sub-critical Experiments (MUSE-4 Benchmark)”, NEA/SEN/NSC/WPPT (2001)5, 2001.
- 95 “Handbook on Nuclear Activation Data”, Technical Reports Series No. 273, IAEA, Vienna, 1987, pp. 116, 132, 181.
- 96 S. Carpenter, “Measurements of control rod worths using ZPPR”, Specialists Meeting on Control Rod Measurements Techniques, April 1976, Cadarache, France, NEACRP-U-75 (1997).
- 97 D. Villamarin and E. Gonzalez-Romero, “First CIEMAT Measurements of the MUSE-4 Kinetic Response”, PHYSOR’02, Seoul, Korea, October 7-10, 2002.
- 98 R. Soule et al., “Neutronic Studies in Support of Accelerator-driven Systems: The MUSE Experiments in the MASURCA Facility”, *Nucl. Sci. Eng.* **148**, 124-152, (2004).
- 99 D. Villamarin, “Análisis dinámico del reactor experimental de fisión nuclear MUSE-4”, Doctoral Thesis, Universidad Complutense de Madrid, Departamento de Física Atómica, Molecular y Nuclear, 2004.
- 100 G. R. Keepin, “Physics of Nuclear Kinetics”, Addison-Wesley Publishing Company, Inc (1965).
- 101 N. G. Sjöstrand, “Measurements on a sub-critical reactor using a pulsed source”, *Arkiv för Fysik*, 11, 13, (1956).
- 102 W. M. Stacey, “Nuclear Reactor Physics”, John Wiley & Sons, Inc. (2001).
- 103 S. E. Chigrinov and I. G. Serafimovich, “Experimental and Theoretical Research of the Peculiarities of Transmutation of Long-lived Fission Products and Minor Actinides in Sub-critical Assembly Driven by a Neutron Generator”, Technical report, Joint Institute of Power and Nuclear Research, National Academy of Sciences of Belarus, Minsk, Sosny, ISTC Project B-070-98.
- 104 K. O. Ott and R. J. Neuhold, “Introductory Nuclear Reactor Dynamics”, American Nuclear Society, La Grange Park, Illinois, USA, (1985).
- 105 International Commission on Radiation Protection, “Conversion coefficients for use in radiological protection against external radiation”, ICRP Publication 74, Pergamon Press, Oxford (1997).
- 106 International Commission on Radiation Units and Measurements, “Conversion coefficients for use in radiological protection against external radiation”, ICRU Report 57, Bethesda, Maryland (1998).
- 107 S. Leray et al., “Spallation Neutron Production by 0.8, 1.2, and 1.6 GeV Protons on various Targets”, *Phys. Rev.* **C65** (2002).

- 108 I. Koprivnikar, E. Schachinger, “The biological shield of a high-intensity spallation source: a Monte Carlo design study”, *Nucl. Instr. Meth. In Phys. Res.* **A487**, 571-584, (2002).
- 109 International Commission on Radiation Protection, “Recommendations of the international commission on radiological protection”, ICRP Publication 60, Pergamon Press, Oxford (1991).
- 110 W. S. Snyder et al., “Estimates of absorbed fractions for monoenergetic photon sources uniformly distributed in various organs of a heterogeneous phantom”, MIRD Pamphlet No. 5. Society of Nuclear Medicine, New York (1969).
- 111 R. Kramer et al., “The calculation of dose from external photon exposures using reference human phantoms and Monte Carlo methods. Part I: the male (ADAM) and female (EVA) adult mathematical phantoms”, GSF-Bericht S-885. Gesellschaft für Strahlen-und Umweltforschung mbH, Munich, Germany, (1982).
- 112 V. Mares and H. Schraube, “The effect of the fluence to dose conversion coefficients upon the dose estimation to cosmic radiation”, Expert Group on Shielding Aspects of Accelerators, Targets and Irradiation Facilities (Sixth Meeting - SATIF-6), April 10-12, 2002, Menlo Park, USA (2002).
- 113 M. Pelliccioni, “Overview of fluence-to-effective dose and fluence-to-effective dose equivalent conversion coefficients for high-energy radiation calculated using the FLUKA code”, *Radiat. Prot. Dosim.* **88**, 279-297 (2000).
- 114 ANSALDO NUCLEARE, “Core Design Summary Report for the LBE-Cooled XADS”, XADS 41 TNIX 064 Rev. 0 (2004).
- 115 NNC LTD, “PDS-XADS Work Package 4.2 Deliverable 65: Core Design Summary”, C6862/TR/0028 (2004).
- 116 S. Pelloni, “Static analysis of the PDS-XADS LBE and gas-cooled concepts”, *Annals of Nuclear Energy*, **32**, 13 (2004).

# INVESTIGATION OF NEUTRON SOURCE EFFECTS IN SUB-CRITICAL MEDIA AND APPLICATION TO A MODEL OF THE MUSE-4 EXPERIMENTS

P. Seltborg<sup>1</sup>, R. Jacqmin  
CEA/Cadarache - DER/SPRC/LEPh – Bat. 230  
13 108 Saint-Paul-Lez-Durance, France  
[per@neutron.kth.se](mailto:per@neutron.kth.se), [Robert.Jacqmin@cea.fr](mailto:Robert.Jacqmin@cea.fr)

**Keywords:** MUSE-4, Neutron Source, Spallation, MCNP, MCNPX

## ABSTRACT

Monte Carlo simulations have been performed to investigate the neutron source effects in a sub-critical media successively coupled to a  $(d,d)$ -source, a  $(d,t)$ -source and a spallation source. The investigations have focused on the neutron energy spectra in the fuel and on the source relative efficiency  $\varphi^*$ . The calculations have been performed for three sub-critical configurations, representative of the coming MUSE-4 experiments.

The Monte Carlo codes MCNP and MCNPX have been used to compute  $\varphi^*$ .  $\varphi^*$  has been found to be low for the  $(d,d)$ -source ( $\sim 1.35$  compared to 1.0 for an average fission neutron), while considerably higher for the  $(d,t)$ -source ( $\sim 2.15$ ) and the spallation source ( $\sim 2.35$ ). The high value of  $\varphi^*$  for the spallation source has been shown to be due to the fraction of high-energy neutrons (17 % of total source with  $E_n > 20$  MeV) born from spallation, which contribute for 50 % to the total number of fission neutrons produced in the core. The variations of  $\varphi^*$  with neutron importance have also been studied for some spherical configurations with a  $(d,d)$ - and a  $(d,t)$ -source. For the class of variations considered here,  $\varphi^*$  was found to remain constant or increase only slightly in the interval  $0.70 < k_{eff} < 0.996$ .

## 1 INTRODUCTION

Accelerator Driven Systems (ADS) (Salvatores, 1999) are being investigated as a possible means for reducing the long-term radiotoxicity in the spent fuel from the nuclear industry. In principle, the sub-criticality of ADS allows for dedicated cores with a much higher concentration of minor actinides than what is acceptable in critical reactors. Those dedicated cores could achieve high transmutation rates. Research done on ADS indicates that a waste reduction factor of 50 to 100 is theoretically possible (Delpech et al, 1999).

---

<sup>1</sup> Permanent affiliation:  
Department of Nuclear and Reactor Physics  
Royal Institute of Technology  
100 44 Stockholm, Sweden



The basic idea of ADS is to supply a sub-critical reactor core with neutrons generated by an intense external neutron source, usually from spallation reactions in a heavy metal target. This idea is being investigated in the MASURCA experimental facility at CEA Cadarache in the framework of the MUSE experiments (Multiplication avec Source Externe). Different configurations and several different sub-critical levels are being studied (Salvatores, 1996; Soule, 1997; Lebrat, 1999).

The planned MUSE-4 experiments will not use a spallation source. Instead, a high-intensity pulsed neutron generator GENEPI, constructed by CNRS/ISN/Grenoble, will be used to accelerate a 250 keV deuteron beam towards either a deuterium target ( $d,d$ ) or a tritium target ( $d,t$ ) to produce well-characterized neutron sources *via* fusion reactions. ( $d,d$ )-reactions produce neutrons with energies between 2 and 3 MeV, while the ( $d,t$ )-reactions produce neutrons between 13 and 15 MeV.

The objective of the present study is to investigate neutron source effects in a MUSE-4-type sub-critical core coupled to a well-known ( $d,d$ )- or ( $d,t$ )-source, and to compare the results with those that would be obtained for a hypothetical spallation source coupled to the same core.

This investigation relies entirely on numerical simulations performed with the MCNP (Briesmeister, 2000) and MCNPX (Waters, 1999) Monte Carlo software packages. The two codes are essentially equivalent for neutron transport below 20 MeV. MCNP is used to simulate the production of the ( $d,d$ )- and ( $d,t$ )-sources, as well as neutron transport below 20 MeV. MCNPX is used to simulate the production of spallation neutrons and particle transport at all energies.

MCNP and MCNPX Monte Carlo models were set up in which a ( $d,d$ )-source, a ( $d,t$ )-source and a spallation source were successively coupled to three sub-critical configurations (Sc1, Sc2 and Sc3) representative of the upcoming MUSE-4 experiments.

A description of the MUSE-4 model, the calculation codes and the neutron sources used in this study is given in Section 2. In Section 3, the computed neutron energy spectra in the fuel are compared for the three different sources. In Section 4, we describe investigations of the neutron source efficiency  $\varphi^*$ . The specific procedure used for calculating  $\varphi^*$  with MCNP and MCNPX is described. The differences in the computed values of  $\varphi^*$  are analysed, as well as the variations of  $\varphi^*$  with neutron importance and reactivity.

## **2 DESCRIPTION OF THE MUSE-4 MODEL, CALCULATION TOOLS AND NEUTRON SOURCES USED IN THIS STUDY**

### **2.1 The Muse-4 Model**

Three homogeneous sub-critical configurations have been studied (Sc1, Sc2 and Sc3 with  $k_{eff} = 0.99, 0.97$  and  $0.95$  respectively) representing three configurations planned in the MUSE-4 experiments. The geometry of the Sc2 model is shown in Fig. 1 below. The material compositions of the different regions are listed in Appendix A. The axial ( $z$

direction) dimension of the fuel is 60.96 cm, except in a 21.2 cm wide channel above and below the lead buffer and the accelerator tube (in the y direction), where it was extended by 10.16 cm. The Na/SS reflector (Region 2) ends at  $z = \pm 61.76$  cm. There is also a 10.16 thick axial shield (Region 3) above and below the Na/SS reflector. The overall dimensions of the whole model, including the reflector and the shields, are 159\*169.6\*143.84 cm.

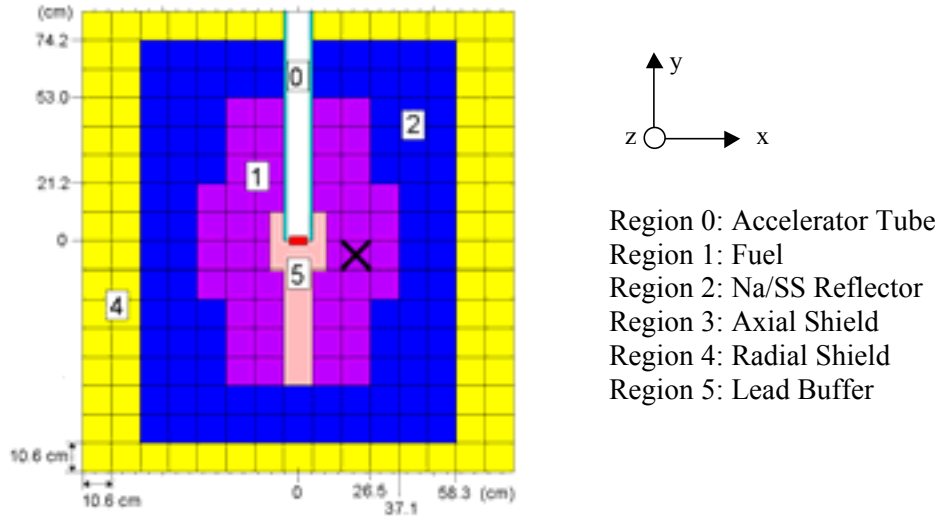


**Fig. 1** *x-y Cross-sectional View of the MUSE-4 Sc2 Sub-Critical Configuration ( $k_{eff} = 0.97$ ). The cross shows the position where the neutron spectra have been calculated, see Section 3.*

To obtain the two other sub-critical levels, Sc1 and Sc3, fuel cells were added or removed at the core periphery.

## 2.2 Description of the Calculation Codes

Calculations have been performed with MCNP-4C for models of the three MUSE-4 sub-critical configurations with the  $(d,d)$ - and  $(d,t)$ -sources. MCNPX was used to simulate the system with the spallation source. All simulations relied on the same evaluated nuclear data library, namely ENDF/B-VI.4.

MCNPX is the extended version of MCNP where the major capabilities of LAHET (Prael and Lichtenstein, 1989) and MCNP-4B (Briesmeister, 1997) have been merged together. In MCNP, particle transport relies entirely on nuclear data contained in externally supplied cross section tables ( $E_n < 20$  MeV), which are derived from evaluated nuclear data files. In LAHET, on the other hand, particle transport is accomplished by using various theoretical physics models embedded in the code, covering the energy range up to several GeV. In MCNPX, the table-based data are used whenever they exist, as such data are known to yield the best results. When they do not exist, the code built-in physics models are used.

Several physics models are available for high-energy transport in MCNPX. In the first stage, in which the incident particles interact with the individual nucleons via particle-particle cross sections, the Intranuclear Cascade (INC) and Multistage Pre-

equilibrium (Prael, 1998) Models are used. The INC model used in this study is the Bertini package (Bertini, 1963). In the second stage the nucleus undergoes either evaporation (emitting neutrons and light ions) or fission, while in the final stage the excited nucleus decays by gamma emission, with energies described by a decay library (PHTLIB).

### 2.3 Description of the Sources

Three different neutron sources have been considered in this study: a  $(d,d)$ -, a  $(d,t)$ - and a spallation source. It should be noted that  $(\alpha,n)$ - or spontaneous fission sources in the fuel have not been considered here.

#### 2.3.1 The Fusion Sources used in MUSE-4

Two different fusion sources can be produced by the GENEPI neutron generator. 250 keV-deuterons are accelerated through the accelerator tube towards either a deuterium or a tritium target. The neutrons are emitted (the fusion reactions themselves are not simulated) from a point at the centre of the core (Fig. 2A). The energy of the emitted neutrons in the laboratory system (derived from basic kinematics) ranges from 2 to 3 MeV for the  $(d,d)$ -neutrons and from about 13 to 15 MeV for the  $(d,t)$ -neutrons, with a maximum emission probability density peaked in the forward direction. The source neutron energy spectrum and angular distribution used in this study are listed in Appendix B.

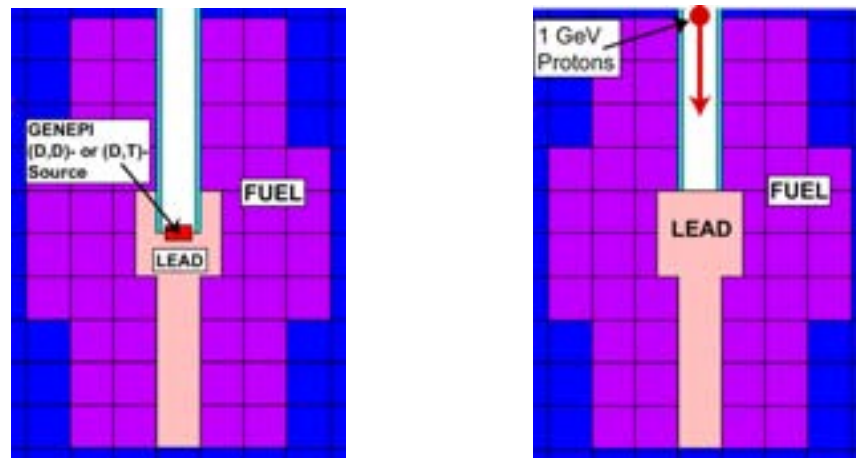


**Fig. 2** A)  $(d,d)$ - or  $(d,t)$ -Source Emitted from the GENEPI Neutron Generator at the Centre of the Core. B) 1 GeV Protons Accelerated Towards the Lead Buffer Creating Neutrons via Spallation Interactions. The generated neutrons are “frozen” and emitted as fixed source neutrons in a separate simulation.

#### 2.3.2 The Spallation Source

For the purpose of producing the spallation source for the numerical simulations, the lead buffer/target in the model was extended by one extra subassembly towards the proton beam, replacing part of the accelerator tube (Fig. 2B). This was done in order to

maximize neutron production near the centre of the core (the same position where the  $(d,d)$ - and the  $(d,t)$ -source neutrons are emitted).

The simulations with the spallation source were divided into two steps. A first simulation with the 1000 MeV proton beam (the protons were uniformly distributed across the beam of diameter 4 cm) impinging on the lead target, was performed with MCNPX. The properties, in terms of angular, energy and spatial distribution, of the primary neutrons born from the spallation interactions were recorded. In the second step, these primary neutrons were supplied to the MCNPX code as fixed source neutrons for separate simulations.

The spatial range of the primary neutrons was found to be rather limited, most neutrons being emitted within a 3 to 4 cm radius around the z-axis and within the first 30 cm axially, i.e., in the direction of the proton beam. The energy distribution of the neutrons produced from the 1000 MeV protons, integrated over all angles, is shown in Fig. 3 (neutrons created from secondary protons will have a slightly softer spectrum). We note that 17.3 % of the neutrons have energies higher than 20 MeV and 3.6 % of them higher than 150 MeV, and that these are mainly emitted in the forward direction of the incident proton beam. The effect of this high-energy fraction of neutrons on  $\rho^*$  will be discussed in Section 4.5.

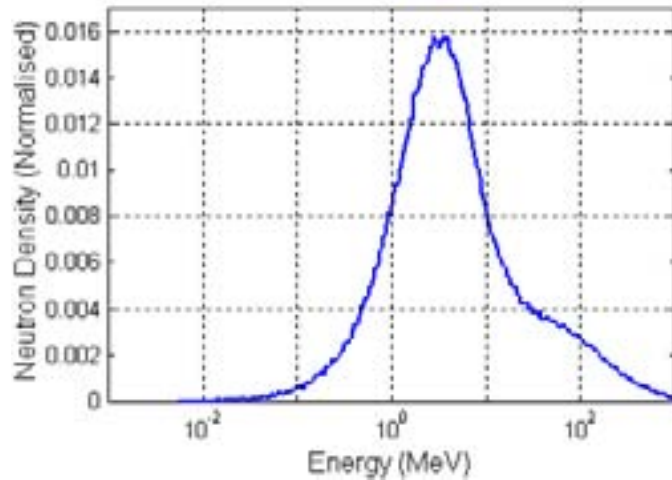


*Fig. 3 Spectrum of Primary Neutrons (Integrated over all Angles) born from 1000 MeV Protons Impinging on a very thin Target of Lead (Single Reaction).*

### 3 NEUTRON SPECTRA IN THE MUSE-4 CORE

The Sc3 sub-critical configuration of the MUSE-4 model with  $k_{eff} = 0.95$  was simulated. The neutron energy spectra resulting from the three different sources were calculated in the subassembly centred at 21.2 cm from the centre of the core, indicated with a cross in Fig. 1. The neutron spectra of the other sub-critical states (Sc1 and Sc2) are not shown here, since they are very similar to the spectra of Sc3.

It is seen in Fig. 4 that the three spectra at this position are very similar to each other and that they are largely dominated by the fission multiplication in the fuel. The

two dips in the neutron fluxes caused by the resonances in sodium ( $\sim 3$  keV) and oxygen ( $\sim 0.4$  MeV) can be seen. The fraction of neutrons still having their initial (source) energy is very small (but should not automatically be disregarded) – about 0.2 % of the  $(d,t)$ -neutrons are still in the 14 MeV peak and 0.1 % of the spallation neutrons have energies above 20 MeV. Hence, we conclude that, for the purpose of computing neutron spectrum weighted quantities, the presence of the external sources can be considered “forgotten” beyond a few centimetres into the fuel.

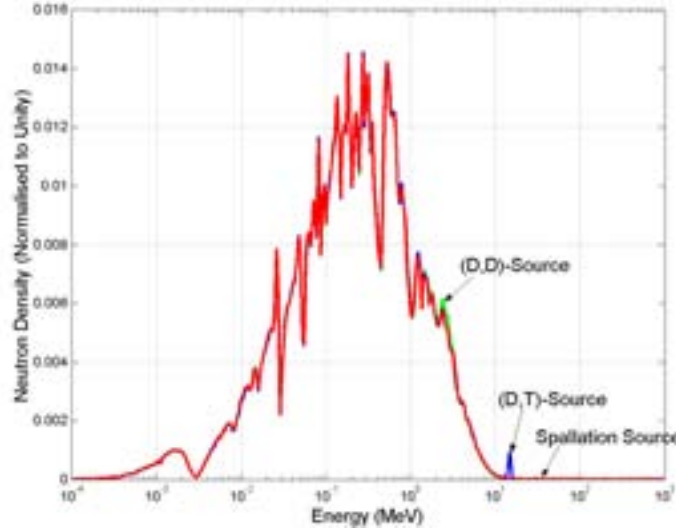


**Fig. 4** MUSE-4 Neutron Energy Spectra in the Subassembly Centred at  $x=21.2$  cm,  $y=-5.3$  cm, Resulting from the three Different External Sources.

## 4 SOURCE EFFICIENCY

The relative efficiency ( $\varphi^*$ ) of the source neutrons was determined for the three different sources and for the three different sub-critical configurations of the MUSE-4 model.

### 4.1 Definition of $\varphi^*$

The neutron flux distribution in a sub-critical core is the solution of the inhomogeneous balance equation:

$$A\phi_s = F\phi_s + S \quad (1)$$

where  $F$  is the fission production operator,  $A$  is the net neutron loss operator and  $S$  is the external source. The quantity  $\varphi^*$ , which represents the relative efficiency of external source neutrons, is defined as the ratio of the average importance of the external source neutrons to the average importance of the fission neutrons (Salvatores, 1999), i.e.:

$$\varphi^* = \frac{\frac{\langle \phi_0^*, S \rangle}{\langle S \rangle}}{\frac{\langle \phi_0^*, F\phi_s \rangle}{\langle F\phi_s \rangle}} \quad (2)$$

where  $\phi_0^*$  = The adjoint flux (the everywhere positive solution of

$$A^* \phi_0^* = \frac{1}{k_{eff}} F^* \phi_0^*) \text{ which provides a measure of neutron importance.}$$

$\langle F \phi_s \rangle$  = Total production of neutrons by fission.

$\langle S \rangle$  = Total production of neutrons by the external source.

In the above formula, the brackets imply integration over space, angle and energy.

As some of the integrals in Eq. (2) cannot be directly calculated with MCNP and MCNPX, another procedure was sought to compute  $\varphi^*$ . By using the balance equation (Eq. 1), the properties of the adjoint flux  $\phi_0^*$ , the  $A$ ,  $F$  operators and their adjoints  $A^*$ ,  $F^*$ , the source efficiency can be expressed equivalently as

$$\varphi^* = \left( \frac{1}{k_{eff}} - 1 \right) \cdot \frac{\langle F \phi_s \rangle}{\langle S \rangle} \quad (3)$$

Eq. (3) is a simple formula relating the total fission neutron production  $\langle F \phi_s \rangle$  to the external source,  $\varphi^*$  and reactivity  $(1 - 1/k_{eff})$ . It shows that, for given values of  $k_{eff}$  and  $\langle S \rangle$ , the larger  $\varphi^*$  the larger the fission power produced in the system.

The quantities in the right hand side of Eq. (3) are standard outputs from MCNP and MCNPX. For simplicity, the production terms will be labelled only  $F$  and  $S$  in the sequel.

## 4.2 Estimation of the Statistical Error in $\varphi^*$

To get an estimate of the statistical uncertainty in the source efficiency, assume that the errors of  $F$  and  $S$  are  $\Delta F$  and  $\Delta S$  and apply the formula for ‘‘propagation of error’’ (Eq. 4)

$$\Delta f(x_1, x_2, \dots) = \sqrt{\left( \frac{\partial f}{\partial x_1} \Delta x_1 \right)^2 + \left( \frac{\partial f}{\partial x_2} \Delta x_2 \right)^2 + \dots + \rho_{12} \cdot \frac{\partial f}{\partial x_1} \Delta x_1 \cdot \frac{\partial f}{\partial x_2} \Delta x_2 + \dots} \quad (4)$$

The correlation constant  $\rho$  could be either positive or negative – negative if  $k_{eff}$  and  $F$  are correlated and positive if they are anti-correlated. However, as a first approximation,  $\rho$  may be assumed to be zero. With the derivatives  $\frac{\partial \varphi^*}{\partial k_{eff}}$ ,  $\frac{\partial \varphi^*}{\partial F}$  and  $\frac{\partial \varphi^*}{\partial S}$  inserted in Eq.

(4) an expression for the relative error in  $\varphi^*$  can be obtained:

$$\left( \frac{\Delta \varphi^*}{\varphi^*} \right)^2 \approx \left( \frac{1}{1 - k_{eff}} \cdot \frac{\Delta k_{eff}}{k_{eff}} \right)^2 + \left( \frac{\Delta F}{F} \right)^2 + \left( \frac{\Delta S}{S} \right)^2 \quad (5)$$

Eq. 5 will be used in the subsequent sections to estimate the statistical uncertainty in  $\varphi^*$ .

### 4.3 Calculations of $\phi^*$ for the MUSE-4 Model

The multiplication factor  $k_{eff}$  and the total number of neutrons produced by fission ( $F$ ) were calculated for the three different sources and the three different sub-critical configurations.  $F$  was automatically normalised per source neutron, so  $S$  was always equal to 1. The source efficiency was calculated according to Eq. (3) and the corresponding statistical errors ( $\pm 1$  standard deviation) according to Eq. (5). All results including error estimations are listed in Table 1.

**Table 1** MCNP/MCNPX Results for the MUSE-4 Sc1, Sc2 and Sc3 Configurations.

|     | Source            | $k_{eff}$                  | $F$                  | $\phi^*$             |
|-----|-------------------|----------------------------|----------------------|----------------------|
| Sc1 | (D,D)-Source      | 0.99045                    | 140.2 ( $\pm 1.6$ %) | 1.35 ( $\pm 0.024$ ) |
|     | (D,T)-Source      | ( $\pm 8$ pcm)             | 223.2 ( $\pm 1.7$ %) | 2.15 ( $\pm 0.040$ ) |
|     | Spallation Source | 0.99040<br>( $\pm 8$ pcm)  | 248.6 ( $\pm 1.8$ %) | 2.41 ( $\pm 0.047$ ) |
| Sc2 | (D,D)-Source      | 0.97007                    | 44.2 ( $\pm 0.9$ %)  | 1.36 ( $\pm 0.015$ ) |
|     | (D,T)-Source      | ( $\pm 14$ pcm)            | 69.9 ( $\pm 1.0$ %)  | 2.16 ( $\pm 0.024$ ) |
|     | Spallation Source | 0.96992<br>( $\pm 15$ pcm) | 76.6 ( $\pm 1.1$ %)  | 2.37 ( $\pm 0.028$ ) |
| Sc3 | (D,D)-Source      | 0.94982                    | 25.4 ( $\pm 0.6$ %)  | 1.34 ( $\pm 0.009$ ) |
|     | (D,T)-Source      | ( $\pm 14$ pcm)            | 40.1 ( $\pm 0.5$ %)  | 2.12 ( $\pm 0.013$ ) |
|     | Spallation Source | 0.94993<br>( $\pm 15$ pcm) | 44.2 ( $\pm 0.7$ %)  | 2.33 ( $\pm 0.018$ ) |

The energy of the  $(d,d)$ -source neutrons (2-3 MeV, see Appendix B) is only slightly larger than the average energy of a neutron produced by fission. The  $\phi^*$  value for the  $(d,d)$ -source is therefore expected to be equal or slightly larger than 1, which is indeed the case.

In the case of the  $(d,t)$ -source, the reason for the higher values of  $\phi^*$  is the larger fission rate, part of which coming from fissions induced by the neutrons multiplied by  $(n,2n)$ -reactions in the lead buffer. It is seen in Table 1 that the number of fission neutrons per source neutron is large, approximately 58 % larger than for the  $(d,d)$ -source. It is also seen in Fig. 5 that the  $(n,2n)$ -cross section in lead has a threshold at about 7 MeV, which is the reason why this reaction is insensitive to the  $(d,d)$ -source neutrons. At 14 MeV the value of the lead  $(n,2n)$ -cross section is about 2 barns, which is comparable to the fission cross section in Pu-239 and in U-238.

Concerning the spallation source neutrons, the values of  $\phi^*$  obtained in the simulations are somewhat higher than for the  $(d,t)$ -source. This is due to the fraction of neutrons having a very high energy (see Section 2.3.2). Most of the neutrons from the spallation process are born with an energy lower than the  $(n,2n)$ -cross section threshold in lead, but the neutrons with very high energy contribute significantly to  $\phi^*$ , as will be shown in Section 4.5.

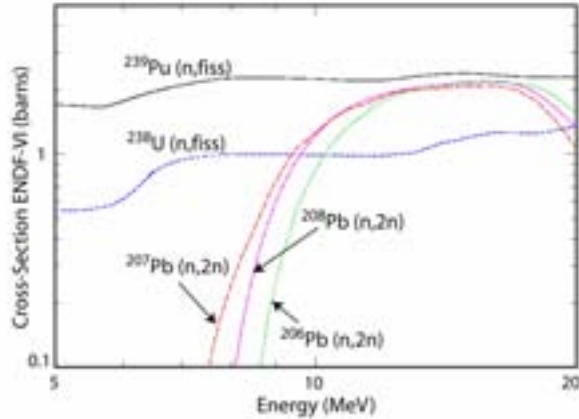


**Fig. 5** Neutron Microscopic Cross Sections for Pu-239 Fission, U-238 Fission and (n,2n)-Reactions in Pb-206, -207, -208. (ENDF/B-VI.4)

It is also seen in Table 1 that, for all three sources,  $\phi^*$  remains approximately constant or increases slightly as  $k_{eff}$  increases. This trend will be further discussed in the following section.

#### 4.4 Dependence of $\phi^*$ on Neutron Importance and $k_{eff}$

The dependence of the source efficiency on neutron importance  $\phi_0^*$  was investigated for a wider range of sub-criticality ( $k_{eff} = 0.70$  to  $0.996$ ), for a (d,d)- and a (d,t)-source, using a spherical model consisting of a buffer core (lead or U-238 with  $r=10$  cm) and MUSE-4 type fuel. Only a limited class of importance variations was considered. The results are plotted in Fig. 6.

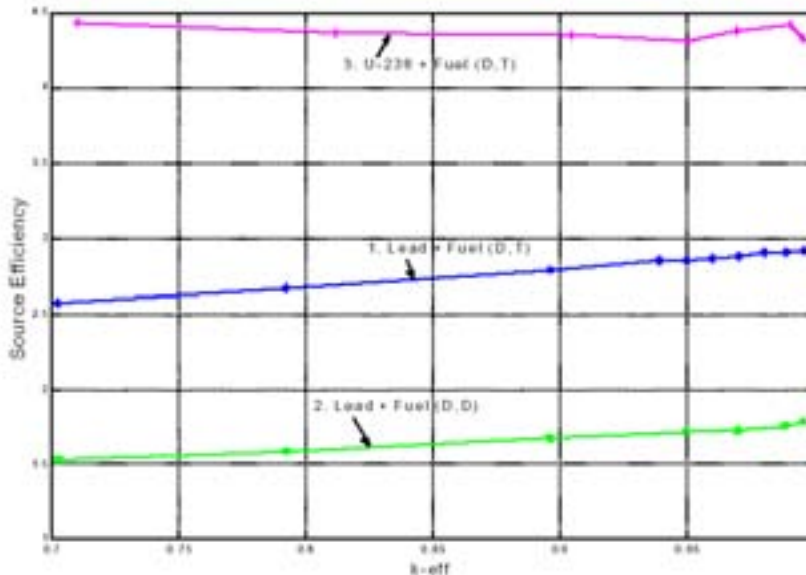


**Fig. 6**  $\phi^*$  versus  $k_{eff}$  for Spherical Configurations with a Buffer of Lead or U-238 ( $r=10$  cm) and MUSE-4 type Fuel, Coupled to a (d,d)- and a (d,t)-Source. The neutron importance and  $k_{eff}$  were changed by varying the fuel radius from about 48 cm ( $k_{eff} \approx 0.70$ ) to 68 cm ( $k_{eff} \approx 0.996$ ).



Instead of plotting the ratio  $\varphi^* / (1/k_{eff} - 1)$  versus  $k_{eff}$  which would reflect the rapid increase of  $\langle F\phi_s \rangle / \langle S \rangle$  (and therefore of the fission power) as  $k_{eff}$  approaches unity, we focused instead on the behaviour of  $\varphi^*$  versus  $k_{eff}$ . The neutron importance (and therefore  $k_{eff}$ ) was varied by changing the outer radius of the fuel from approximately 48 to 68 cm. It is seen in Fig. 6 that  $\varphi^*$  shows the same almost constant or slightly increasing trend in the interval  $k_{eff} = 0.95$  to  $0.99$ , for the spherical configurations with the lead buffer, as already observed for the MUSE-4 model.

The first case (Case 1) is a sphere consisting of a lead core surrounded by fuel with approximately the same material composition as listed in Table 3.  $\varphi^*$  increases slightly but constantly in the interval  $k_{eff} = 0.70$  to  $0.996$ . The importance of the  $(n,2n)$ -effect is also demonstrated by replacing the  $(d,t)$ -source by a  $(d,d)$ -source (Case 2), which results in significantly lower values of  $\varphi^*$ . The curve shows the same increasing trend as for the  $(d,t)$ -source.

In Case 3, when the lead buffer at the centre of the sphere is replaced by U-238, a large increase in  $\varphi^*$  occurs at all sub-criticality levels because of U-238 fissions. The same increasing trend as with the lead buffer is not observed here as  $\varphi^*$  remains nearly constant.

The statistical errors of the  $\varphi^*$  values are rather small in the range  $0.70 \leq k_{eff} \leq 0.99$  – less than 1 % ( $\pm 1$  standard deviation), while around 2.5 % for the very last point ( $k_{eff} = 0.996$ ). In the absolute vicinity of criticality ( $k_{eff} \geq 0.996$ ) the computation time for calculating  $\varphi^*$  grows too large to obtain reliable results.

We conclude that the variations of  $\varphi^*$  with neutron importance are rather small in the investigated range  $0.70 \leq k_{eff} \leq 0.996$ .

#### 4.5 Decomposition of the Spallation Source

Most reactor code simulations only take into account neutrons with energies lower than 20 MeV. However, a significant fraction of the neutrons produced by spallation have energies higher than 20 MeV (see Fig. 3). The contribution of those high-energy neutrons to the source efficiency needs to be investigated. For this, the spallation source was artificially split into two “low-energy” bins ( $S_1$  from 0 to 5 MeV and  $S_2$  from 5 to 20 MeV) and two “high-energy” bins ( $S_3$  from 20 to 150 MeV and  $S_4$  from 150 to 1000 MeV). The study was performed for the third sub-critical level Sc3 ( $k_{eff} = 0.95$ ) of the MUSE-4 model.

In order to derive a formula for the low- and high-energy contributions to the source efficiency, we start from Eq. (3), applied to each source bin

$$\varphi_i^* = \left( \frac{1}{k_{eff}} - 1 \right) \cdot \frac{\langle F\phi_i \rangle}{\langle S_i \rangle} \quad (6)$$

where  $\phi_i$  = Flux resulting from each source bin ( $S_1 \rightarrow \phi_1, S_2 \rightarrow \phi_2$  etc.).

Since  $\langle F\phi_T \rangle = \sum_{i=1}^4 \langle F\phi_i \rangle$ , the following relationship for the decomposition of  $\varphi^*$  is readily obtained

$$\varphi_T^* = \sum_{i=1}^4 \varphi_i^* \cdot \frac{\langle S_i \rangle}{\langle S_T \rangle} \quad (7)$$

where  $\varphi_T^*$  = Efficiency of the total source.

$\varphi_i^*$  = Efficiency of each source bin alone.

The  $\varphi_i^*$  results obtained from the Monte Carlo simulations are listed in Table 2. As expected, for the first low-energy bin,  $\varphi_1^*$  is low ( $\varphi_1^*=1.25$ ) and close to the value obtained for the  $(d,d)$ -source. For the second bin, it is found to be higher ( $\varphi_2^*=1.71$ ) since many of the neutrons have energies above the lead  $(n,2n)$ -cross section threshold. For the two high-energy parts,  $\varphi_i^*$  is very high ( $\varphi_3^*=4.58$  and  $\varphi_4^*=14.4$ ), which is the consequence of fissions induced by neutrons born from  $(n,xn)$ -reactions and spallation interactions.

**Table 2** MCNPX Results for the Sc3 MUSE-4 Model ( $k_{eff} = 0.94993$ ) Obtained from the Decomposition of the Spallation Source.

| Source Bin                  | Energy limits (MeV) | $\frac{\langle S_i \rangle^A}{\langle S_T \rangle}$ | $\frac{\langle F\phi_i \rangle^B}{\langle S_i \rangle}$ | $\varphi_i^*$ | $\varphi_i^* \cdot \frac{\langle S_i \rangle^C}{\langle S_T \rangle}$ |
|-----------------------------|---------------------|---|---|---------------|---|
| S <sub>1</sub>              | 0 - 5               | 0.559   | 23.7  | 1.25          | 0.699 (30 %)  |
| S <sub>2</sub>              | 5 - 20              | 0.268   | 32.5  | 1.71          | 0.458 (20 %)  |
| S <sub>3</sub>              | 20 - 150            | 0.137   | 86.9  | 4.58          | 0.627 (27 %)  |
| S <sub>4</sub>              | 150 - 1000          | 0.036   | 273.1   | 14.4          | 0.518 (23 %)  |
|                             |                     |   |   |               | Sum = 2.30  |
| S <sub>T</sub> <sup>D</sup> | 0 - 1000            | 1.0   | 44.2  | 2.33          |   |

The superscripts A, B, C and D in Table 2 stand for:

A: Fraction of the total number of source neutrons in each energy bin (compare Fig. 3).

B: Neutrons produced by fission in the core.

C: Contribution to total  $\varphi^*$  (Product of column 3 and 5).

D: Simulation with the total source, identical as for Sc3 in Table 1.

It is also seen in Table 2 that the two high-energy parts (17.3 % of the total number of source neutrons), contribute for about 50 % of the total  $\varphi^*$ , and the highest energy part alone (3.6 % of the total number of source neutrons) for more than 20 %. The sum of the contributions to  $\varphi^*$  from the four different parts in the rightmost column, according to Eq. (7), is 2.30, which is in good agreement with the value obtained from the simulation with the total source ( $\varphi_T^*=2.33$ ). The statistical  $1\sigma$  error estimates in the  $\varphi^*$  values are less than 1 %.

The rather high average number of fission neutrons produced per source neutron for the two high-energy bins (87 and 273 respectively) might seem surprising at first. The explanation for this is that most of the high-energy neutrons from the spallation source

have already been multiplied in the lead (via secondary spallation and  $(n,xn)$ -reactions) *before* they enter into the fuel. Each of them gives birth to a number of lower-energy neutrons, which then leak out of the lead and induce fission chain reactions in the fuel. Additional simulations in which the lead target alone was kept showed that only about 5 % of the neutrons leaking out of the lead have energies higher than 20 MeV and about 1 % of them higher than 150 MeV.

We conclude that, although neutron transport in the fuel is largely dominated by neutrons with low energy ( $E_n < 20$  MeV) which can be well simulated with a number of classical calculation codes such as MCNP, the importance of the high-energy contribution to  $\varphi^*$  indicates the need for further investigating the effects from high-energy spallation neutrons. This could be made easier by extending the capabilities of existing neutronics codes, in particular deterministic codes, for studying high-energy (20-150 MeV) neutron transport.

## 5 CONCLUSIONS

Numerical simulations have been performed with MCNP and MCNPX to investigate the neutronic properties of a sub-critical core representative of the up-coming MUSE-4 experiments, alternatively coupled with a  $(d,d)$ -source, a  $(d,t)$ -source and a spallation source. The source-plus-core systems have been studied in terms of neutronic spectra and efficiency ( $\varphi^*$ ) in three different sub-critical configurations ( $k_{eff} = 0.99, 0.97, 0.95$ ).

The computed neutron spectra in all cases show that fission multiplication dominates at distances past a few centimetres into the fuel. This implies that, for the purpose of ADS core studies, the presence of the source may be ignored in the calculation of spectrum-weighted quantities, except possibly in the immediate vicinity of the external source.

The relative efficiency of the  $(d,d)$ -source is somewhat higher than 1 ( $\sim 1.35$ ). For the  $(d,t)$ -source, it is much larger, around 2.15. This significantly larger value is due to the  $(n,2n)$ -multiplication in lead (with an energy threshold at about 7 MeV) and the induced fissions. To analyse the high value of  $\varphi^*$  obtained for the spallation source ( $\sim 2.35$ ), the source was artificially split into four different energy bins and the efficiency of each bin was determined. It was found that these two high-energy bins ( $E_n > 20$  MeV) contribute for about 50 % to  $\varphi^*$  and to the total number of fission neutrons produced in the core. This can be explained by the fact that primary neutrons born with high energy from spallation give birth to a large number of lower-energy neutrons, which in turn induce fissions. This rather high fraction indicates the need for extending reactor analysis code capabilities above 20 MeV for more detailed investigations of high-energy spallation neutron effects.

The variations of  $\varphi^*$  with neutron importance (and reactivity) was also investigated for different spherical configurations. It was found that  $\varphi^*$  remains approximately constant or increases slightly in the interval  $0.70 < k_{eff} < 0.996$ .

## AKNOWLEDGEMENTS

This research work is supported and partly funded by SKB AB, Sweden, the Swedish Centre of Nuclear Technology, and the European Commission, DGRTD, under Contract # FIKW-CT-2000-00063.

## REFERENCES

**Bertini**, H. W., 1969. Phys. Rev. 131, 1801.

**Briesmeister**, J.F. MCNP<sup>TM</sup> – A General Monte Carlo N-Particle Transport Code – Version 4B. LANL/Los Alamos, LA-12625-M, March, 1997.

**Briesmeister**, J.F. MCNP<sup>TM</sup> – A General Monte Carlo N-Particle Transport Code – Version 4C. LANL/Los Alamos, LA-13709-M, April 10, 2000.

**Delpech**, M. et al., 1999. The Am and Cm Transmutation – Physics and Feasibility. Global'99.

**Lebrat**, J.F. et al., 1999. Experimental investigation of multiplying sub-critical media in presence of an external source operating in pulsed or continuous mode: The MUSE-3 experiment. ADTTA'99.

**Prael** R.E., Lichtenstein H. User Guide to LCS: The LAHET Code System. Los Alamos National Laboratory, LA-UR-89-3014, September 15, 1989.

**Prael** R.E., Bozoian M. Adaptation of the Multistage Pre-equilibrium Model for the Monte Carlo Method (I). Los Alamos National Laboratory Report LA-UR-88-3238, September 1998.

**Salvatores**, M., Martini, M., Slessarev, I. MUSE-1: A first experiment at MASURCA to validate the physics of sub-critical multiplying systems relevant to ADS. Kalmar, Sweden, June 3-7, 1996.

**Salvatores**, M., 1999. Accelerator Driven Systems (ADS), Physics Principles and Specificities. J. Phys. IV France 9, pp. 7-17 –7-33.

**Soule**, R., Salvatores, M., Jacqmin, R., 1997. Validation of neutronic methods applied to the analysis of fast sub-critical systems: The MUSE-2 experiments. Global'97, page 639.

**Waters**, L.S. MCNPX<sup>TM</sup> User's Manual – Version 2.1.5. Los Alamos National Laboratory, November 14, 1999.

## APPENDIX A

**Table 3** *Material Composition for the Different Homogeneous Regions of the MUSE-4 Model.*

| Isotope       | Atomic Density of Materials [ $10^{24}$ atoms/cm <sup>3</sup> ] |                 |              |               |             |                  |
|---------------|---|-----------------|--------------|---------------|-------------|------------------|
|               | Fuel  | Na/SS Reflector | Axial Shield | Radial Shield | Lead Buffer | Accelerator Tube |
| <b>C</b>      | 2.75e-05  | 1.90e-05        | 1.64e-05     | 1.47e-03      | 1.64e-05    | 9.32e-05         |
| <b>O-16</b>   | 1.44e-02  | -               | -            | -             | -           | -                |
| <b>Na-23</b>  | 9.32e-03  | 4.66e-03        | -            | -             | -           | -                |
| <b>Al-27</b>  | -   | -               | -            | -             | -           | 1.46e-02         |
| <b>Si</b>     | 1.00e-05  | 1.18e-03        | 1.54e-03     | 2.98e-05      | 2.98e-05    | 1.15e-04         |
| <b>Cr-52</b>  | 1.62e-03  | 1.02e-02        | 1.30e-02     | 8.00e-04      | 7.58e-04    | 1.75e-03         |
| <b>Cr-53</b>  | 1.84e-04  | 1.15e-03        | 1.47e-03     | 9.07e-05      | 8.59e-05    | 1.98e-04         |
| <b>Mn-55</b>  | 1.24e-04  | 8.33e-04        | 1.07e-03     | 5.83e-04      | 3.61e-05    | 1.75e-04         |
| <b>Fe-54</b>  | 4.16e-04  | 2.74e-03        | 3.50e-03     | 4.70e-03      | 1.97e-04    | 4.58e-04         |
| <b>Fe-56</b>  | 6.47e-03  | 4.26e-02        | 5.45e-02     | 7.30e-02      | 3.06e-03    | 7.01e-03         |
| <b>Ni-58</b>  | 6.49e-04  | 3.48e-03        | 4.42e-03     | 7.43e-04      | 2.64e-04    | 6.78e-04         |
| <b>Ni-60</b>  | 2.50e-04  | 1.34e-03        | -            | 2.86e-04      | 1.02e-04    | 2.61e-04         |
| <b>Pb-206</b> | -   | -               | -            | -             | 7.72e-03    | 4.09e-03         |
| <b>Pb-207</b> | -   | -               | -            | -             | 6.69e-03    | 3.54e-03         |
| <b>Pb-208</b> | -   | -               | -            | -             | 1.59e-02    | 8.40e-03         |
| <b>Bi-209</b> | -   | -               | -            | -             | 1.50e-06    | -                |
| <b>U-235</b>  | 1.75e-05  | -               | -            | -             | -           | -                |
| <b>U-238</b>  | 5.26e-03  | -               | -            | -             | -           | -                |
| <b>Pu-239</b> | 1.52e-03  | -               | -            | -             | -           | -                |
| <b>Pu-240</b> | 3.71e-04  | -               | -            | -             | -           | -                |
| <b>Pu-241</b> | 2.84e-05  | -               | -            | -             | -           | -                |
| <b>Pu-242</b> | 1.33e-05  | -               | -            | -             | -           | -                |
| <b>Am-241</b> | 4.95e-05  | -               | -            | -             | -           | -                |

## APPENDIX B

**Table 4** *Laboratory-system Angular and Energy Dependence (Derived from Basic Kinematics) of the (d,d)- and the (d,t)-Source Neutrons Emitted at the Centre of the Core, Resulting from the GENEPI 250 keV Deuterons Impinging on a Deuterium/Tritium Target.*

| Angle | (D,D)-reaction |                              | (D,T)-reaction |                              |
|-------|----------------|------------------------------|----------------|------------------------------|
|       | Energy         | Emission probability density | Energy         | Emission probability density |
| 0     | 3.050          | 5.250%                       | 15.12          | 4.924%                       |
| 9     | 3.042          | 5.243%                       | 15.10          | 4.922%                       |
| 18    | 3.020          | 5.223%                       | 15.07          | 4.916%                       |
| 27    | 2.984          | 5.192%                       | 15.00          | 4.906%                       |
| 36    | 2.935          | 5.150%                       | 14.92          | 4.893%                       |
| 45    | 2.876          | 5.098%                       | 14.82          | 4.876%                       |
| 54    | 2.808          | 5.038%                       | 14.70          | 4.856%                       |
| 63    | 2.734          | 4.970%                       | 14.57          | 4.834%                       |
| 72    | 2.656          | 4.899%                       | 14.43          | 4.811%                       |
| 81    | 2.576          | 4.825%                       | 14.28          | 4.786%                       |
| 90    | 2.496          | 4.750%                       | 14.13          | 4.760%                       |
| 99    | 2.419          | 4.676%                       | 13.98          | 4.735%                       |
| 108   | 2.346          | 4.605%                       | 13.83          | 4.711%                       |
| 117   | 2.279          | 4.538%                       | 13.70          | 4.688%                       |
| 126   | 2.219          | 4.478%                       | 13.58          | 4.667%                       |
| 135   | 2.167          | 4.425%                       | 13.47          | 4.648%                       |
| 144   | 2.123          | 4.380%                       | 13.37          | 4.632%                       |
| 153   | 2.089          | 4.344%                       | 13.30          | 4.619%                       |
| 162   | 2.064          | 4.318%                       | 13.25          | 4.610%                       |
| 171   | 2.049          | 4.302%                       | 13.21          | 4.604%                       |
| 180   | 2.044          | 4.297%                       | 13.20          | 4.602%                       |

# Definition and Application of Proton Source Efficiency in Accelerator Driven Systems

Per Seltborg<sup>\*</sup>, Jan Wallenius, Kamil Tuček, Waclaw Gudowski

*Department of Nuclear and Reactor Physics  
Royal Institute of Technology, Stockholm, Sweden*

**Abstract** – In order to study the beam power amplification of an accelerator driven system (ADS), a new parameter, the proton source efficiency ( $\psi^*$ ) is introduced.  $\psi^*$  represents the average importance of the external proton source, relative to the average importance of the eigenmode production, and is closely related to the neutron source efficiency ( $\phi^*$ ), which is frequently used in the ADS field.  $\phi^*$  is commonly used in the physics of sub-critical systems driven by any external source (spallation source, (d,d), (d,t), Cf-252 spontaneous fissions etc.). On the contrary,  $\psi^*$  has been defined in this paper exclusively for ADS studies, where the system is driven by a spallation source. The main advantage with using  $\psi^*$  instead of  $\phi^*$  for ADS is that the way of defining the external source is unique and that it is proportional to the core power divided by the proton beam power, independently of the neutron source distribution.

Numerical simulations have been performed with the Monte Carlo code MCNPX in order to study  $\psi^*$  as a function of different design parameters. It was found that, in order to maximize  $\psi^*$ , and therefore minimizing the proton current needs, a target radius as small as possible should be chosen. For target radii smaller than about 30 cm, lead-bismuth is a better choice of coolant material than sodium, regarding the proton source efficiency, while for larger target radii the two materials are equally good. The optimal axial proton beam impact was found to be located approximately 20 cm above the core center. Varying the proton energy,  $\psi^*/E_p$  was found to have a maximum for proton energies between 1200 and 1400 MeV. Increasing the americium content in the fuel decreases  $\psi^*$  considerably, in particular when the target radius is large.

---

<sup>\*</sup> E-mail: per@neutron.kth.se

## I. INTRODUCTION

Accelerator Driven Systems (ADS) [1, 2, 3, 4] are being investigated as a possible mean for reducing the long-term radiotoxicity of spent reactor fuel. In principle, the sub-criticality of ADS allows for dedicated cores with a much higher concentration of minor actinides than what is acceptable in critical reactors. Such dedicated cores enable multi-recycling of americium and curium, providing thus a potential for reducing the radio-toxicity by a factor of 50 to 100 [5].

In ADS, a high-power particle accelerator is used to accelerate protons to energies of the order of 1000 MeV. The protons impinge on a heavy metal target, generating a large number of neutrons via spallation. The spallation neutrons leak out from the target, after different kinds of interactions with the target nuclei, and are subsequently multiplied in the surrounding sub-critical blanket.

An important factor when designing an ADS is to optimize the beam power amplification, given that the reactor is operating at a certain sub-critical reactivity (with sufficient safety margins to criticality). Optimizing the source efficiency, and thereby minimizing the proton current needs, can have an important impact on the overall design of an ADS and on the economy of its operation. The neutron source efficiency parameter  $\varphi^*$  is commonly used to study this quantity, since it is related to the number of fissions produced in the core (which is closely related to the core power), by an average external source neutron.

However, calculating  $\varphi^*$  for an accelerator driven system introduces some complications, since the actual source particles are protons, and not neutrons. In order to determine  $\varphi^*$ , the external neutron source first has to be defined and then the efficiency of this neutron source can be determined. A drawback with using  $\varphi^*$  is that the neutron source can be defined in several different ways, and the results are directly dependent on the choice of definition. Therefore, completely different values of  $\varphi^*$  are often observed [6, 7, 8], due to different choices of external neutron source definition. Another complication associated to the neutron source efficiency is that, studying  $\varphi^*$  as a function of a certain system parameter might change the neutron source distribution and the number of neutrons produced per source proton. In this case, in order to represent the beam power amplification,  $\varphi^*$  needs to be weighted with the number of source neutrons produced per source proton.

With the motivation of simplifying the concept of source efficiency, we introduce in this paper a new parameter  $\psi^*$ , which refers to the number of fission neutrons produced in the system by each source **proton**. The advantages with using the proton source efficiency instead of the neutron source efficiency is that there is no ambiguity

in how to define the external source, and that it is proportional to the beam power amplification, without the need of a weighting factor.

In this paper,  $\psi^*$  has been studied as a function of different system parameters, in order to find the optimal design conditions for maximum proton beam amplification, within the given safety constraints. For this purpose, a model of a nitride fuelled and lead-bismuth cooled ADS was used. First, the neutron source efficiency is defined and discussed (Section II) and then the proton source efficiency parameter is introduced (Section III). Section IV describes the reference model used in this study. In Section V.A,  $\psi^*$  and  $\varphi^*$  are studied as functions of the target radius and coolant material. In the following sections,  $\psi^*$  is studied as a function of the axial proton beam impact (V.B) and the proton beam energy (V.C). Finally, an americium based fuel has been compared with the plutonium based reference fuel (V.D).

## II. NEUTRON SOURCE EFFICIENCY $\varphi^*$

### II.A. Definition of the Neutron Source Efficiency

The neutron flux distribution  $\phi_s$  in a sub-critical core is the solution to the inhomogeneous steady-state neutron transport equation

$$\mathbf{A}\phi_s = \mathbf{F}\phi_s + S_n \quad (1)$$

where  $\mathbf{F}$  is the fission production operator,  $\mathbf{A}$  is the net neutron loss operator and  $S_n$  is the external neutron source.

The neutron source efficiency [9, 10], usually denoted  $\varphi^*$ , represents the efficiency of the external source neutrons and can be expressed according to the following equation [11]:

$$\varphi^* = \left( \frac{1}{k_{eff}} - 1 \right) \cdot \frac{\langle \mathbf{F}\phi_s \rangle}{\langle S_n \rangle} \quad (2)$$

which is valid in the range  $0 < k_{eff} < 1$ .  $\langle \mathbf{F}\phi_s \rangle$  is the total production of neutrons by fission and  $\langle S_n \rangle$  is the total production of neutrons by the external source. In the above formula, the brackets imply integration over space, angle and energy. Eq. (2) relates the total fission neutron production  $\langle \mathbf{F}\phi_s \rangle$  to the external neutron source,  $\varphi^*$  and the reactivity  $(1 - 1/k_{eff})$ . It shows that, for given values of  $k_{eff}$  and  $\langle S_n \rangle$ , the larger  $\varphi^*$  the larger the fission power produced in the system.

### II.B. Definition of the External Neutron Source

Since the actual source particles in an accelerator driven system are protons and not neutrons, it is not obvious which



is the best way to define the neutron source. The procedure to calculate  $\phi^*$  is usually divided into two steps – the first generating the source neutrons, produced from the proton beam interacting with the target, and the second one determining the efficiency of these source neutrons. Different source definitions are possible and they will result in different values and meanings of  $\phi^*$ . A brief summary of four different definitions of the external neutron source that have been used in the ADS field is given in [12]. Among these, the two most frequently used definitions, the target neutron leakage source and the energy cut-off source, will be discussed in the two following sections. The other two definitions are the fission source, consisting of the first generation of fission neutrons, and the primary neutron source, which is the collection of neutrons that are created directly from proton induced spallation (primary spallation neutrons) [8].

### II.B.1. The Target Neutron Leakage Source

This approach uses the neutrons that leak out radially from the target as source neutrons [6, 13]. The method consists of, in the first step, transporting the high-energy protons and the secondary particles that they produce in the target. The neutrons that leak out from the target are defined as the source, and their properties, in terms of position, direction and energy, are written to a source file. Only the target is present in the first simulation, so no once-leaked neutrons re-entering the target are included in the source definition. In the second step, the leakage neutrons are reemitted as fixed source neutrons in a separate run and the efficiency ( $\phi^*$ ) of them is determined. Since the target neutron leakage spectrum includes a high-energy tail, both step 1 and 2 need to be simulated with a high-energy transport code (which can simulate neutrons with energy up to the incident proton energy).

Since the neutron source is generated by a proton beam/target simulation, the distribution of the source neutrons is dependent on the target properties and the proton beam properties. This might induce complications when trying to optimize  $\phi^*$  and the beam power amplification, by varying different system parameters. If a change in the studied system parameter changes the distribution of the source neutrons,  $\phi^*$  has to be weighted by the number of neutrons produced per source proton. With the target neutron leakage definition, examples of these parameters are the target dimension, the proton beam energy or the axial proton beam impact position. Other system parameters, such as the core coolant material, the fuel composition or the core dimensions, are independent of the target region and do not affect the neutron source.

### II.B.2. The Energy Cut-off Neutron Source

The other way to define the neutron source is to collect the neutrons that fall below a certain cut-off energy (usually 20 or 150 MeV) [7, 14, 15]. In the first step, a high-energy code is used to transport the accelerated protons and the secondary high-energy particles. The neutrons that are produced are either killed if they are born below the cut-off energy or transported until they fall below this energy. The properties of the killed neutrons are written to a source file. In the second step, these neutrons are reemitted as fixed source neutrons in a separate run and  $\phi^*$  is determined.

An advantage of this approach is that the second step can be simulated with a low-energy transport code. The cut-off energy is set to the upper energy of the cross section library that will be used in the second step calculation. This is desirable since many reactor codes systems are limited to the upper energy limit of the cross-section data library (e.g. 20 or 150 MeV).

It has been shown in [7] that, in contrast to the target neutron leakage source, the neutron source distribution in this case is rather insensitive to changes in the target radius. However, substituting the coolant material or changing the fuel composition will affect the distribution of the neutron source.

## III. PROTON SOURCE EFFICIENCY $\psi^*$

### III.A. Introduction of the Proton Source Efficiency

In order to simplify the concept of source efficiency, a new parameter, called “proton source efficiency” and denoted  $\psi^*$ , which represents the product of  $\phi^*$  and the number of source neutrons generated per source proton ( $S_n/S_p$ ), is introduced in this paper. We thus have the following relation between the **proton** source efficiency  $\psi^*$  and the **neutron** source efficiency  $\phi^*$ :

$$\psi^* = \phi^* \cdot \frac{\langle S_n \rangle}{\langle S_p \rangle} \quad (3)$$

This parameter could also, in analogy with  $\phi^*$ , be expressed in terms of  $k_{eff}$  and the total number of neutrons produced by fission in the core, for each source **proton**. Inserting Eq. (2) in Eq. (3) it is expressed in the same way as  $\phi^*$ , only with the replacement of  $S_n$  by  $S_p$ ,

$$\psi^* = \left( \frac{1}{k_{eff}} - 1 \right) \cdot \frac{\langle F\phi_s \rangle}{\langle S_p \rangle} \quad (4)$$

$\langle F\phi_s \rangle / \langle S_p \rangle$  is the total production of neutrons by fission over the total number of source protons.

Considering  $\psi^*$  and  $\phi^*$  (according to the target neutron leakage definition) as functions of the target radius and of coolant material illustrates the discussion in the previous section about which design parameters that affect and do not affect the neutron source distribution. Changing the coolant material,  $S_n/S_p$  does not change, so  $\psi^*$  and  $\phi^*$  vary in exactly the same way. When varying the target radius, on the other hand,  $S_n/S_p$  changes, so  $\psi^*$  and  $\phi^*$  varies in different ways. Consequently, if one wants to use the neutron source efficiency parameter  $\phi^*$ , it needs to be weighted with  $S_n/S_p$  when it is studied as a function of the target radius, whereas this is not necessary when comparing different core coolant materials. However, with the introduction of the proton source efficiency and always referring to  $\psi^*$ , none of this has to be considered, and the procedure is simplified.

### III.B. Relationship between $\psi^*$ and the Core Power

The total power produced by fission in the core ( $P_f$ ) can be expressed as the product of the total number of fission events and the average available energy released in a fission, according to the following relation;

$$P_f = \frac{\langle F\phi_s \rangle}{\bar{\nu}} \cdot \bar{E}_f \quad (5)$$

Inserting Eq. (4) in Eq. (5), we obtain

$$\frac{P_f}{\langle S_p \rangle} = \frac{\bar{E}_f}{\bar{\nu}} \cdot \frac{k_{eff}}{1 - k_{eff}} \cdot \psi^* \quad (6)$$

For a given fuel composition,  $\bar{E}_f$  and  $\bar{\nu}$  can, for the purpose of this study, be considered to be constant. Even though there are high-energy neutrons entering into the fuel (the neutron yield  $\bar{\nu}$  is not constant with respect to neutron energy), the fraction of fissions in the core that are induced by high-energy neutrons is very small. Therefore, a change in the neutron yield for these fission events will have very little impact on  $\bar{\nu}$ . The variations of  $\bar{E}_f$  and  $\bar{\nu}$  have been calculated for the series of different studies presented in this paper and were found to be much smaller than the statistical errors in the simulations (except in the case where the fuel composition was modified). When the fuel composition changes,  $\bar{\nu}$  might also change, which should be kept in mind in Section V.D, where two different fuels are compared.

If we further make the approximation that the energy produced by fission is proportional to the total core power produced in the core, we find that  $\psi^*$  is proportional to the total power divided by the source intensity (output/input power).

## IV. SYSTEM MODELING

A homogenized model representing a nitride fuelled and lead-bismuth cooled ADS (maximum 800 MWth) has been studied. The height of the active core in the reference model (Fig. 1) is 100 cm and the outer radius is 70 cm. The inner radius is 20 cm, which is also the boundary of the lead-bismuth target. The accelerator tube has a radius of 15 cm and the axial position of the proton beam impact is 25 cm below the top of the core. The radius of the radially uniform 1000 MeV proton beam is 7.5 cm. Above and below the active zone of the core, plena for accommodation of gas release are included, having lengths of 100 and 50 cm, respectively. The radial reflector is assumed to consist of 90 % steel and 10 % lead-bismuth.

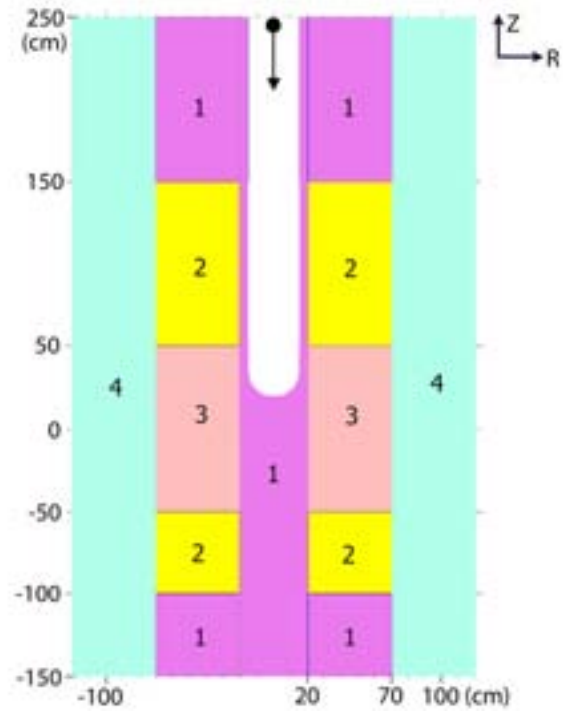


Fig. 1. RZ-view of the homogenised reference model. The 1000 MeV protons are guided through the accelerator tube and impinge on the Pb-Bi target. The different regions in the model are pure Pb-Bi (1), the plena (2), the active core (3) and the reflector (4).

The relative fraction of fuel, cladding and coolant material used in the homogenized model correspond to a pin radius of 2.5 mm and  $P/D = 1.72$ . The nitride actinide fuel is in solid solution with ZrN. The volume fraction of ZrN was adjusted to 83 %, in order to obtain a  $k_{eff}$  of about 0.95. The fuel consists of 80% plutonium and 20% americium (the actinide vectors are listed in Table I). The spallation target and the core coolant consist of lead-bismuth eutectic and the fuel pin cladding of 10% chromium and 90% iron.

TABLE I

Relative Fraction of Actinides in the Reference Fuel. The Pu vector corresponds to that of spent LWR MOX fuel after 7 years of cooling and the Am vector to a mixture of spent UOX (Uranium Oxide Fuel) and MOX (Mixed Oxide Fuel) fuel.

| Plutonium | 80 % | Americium | 20 % |
|-----------|------|-----------|------|
| Pu-238    | 5 %  | Am-241    | 67 % |
| Pu-239    | 38 % | Am-243    | 33 % |
| Pu-240    | 30 % |           |      |
| Pu-241    | 13 % |           |      |
| Pu-242    | 14 % |           |      |

The Monte Carlo code MCNPX [16] (Version 2.3.0), in coupled neutron and proton mode, was used for all simulations, relying on the evaluated nuclear data library ENDF/B-VI.8 (limited to 20 MeV). The Intranuclear Cascade model used by MCNPX was the Bertini package [17].

#### V. THE PROTON SOURCE EFFICIENCY AS A FUNCTION OF DIFFERENT SYSTEM PARAMETERS

The proton source efficiency  $\psi^*$  has been studied as a function of a number of system parameters, such as the target radius, coolant material, axial proton beam impact position, proton beam energy and fuel composition. The starting point for each parameter study is the reference model. In each case when a parameter has been changed, the reactivity has been re-adjusted in order to keep  $k_{\text{eff}}$  constant at about 0.95.

##### V.A. $\psi^*$ as function of Target Radius

In this section,  $\psi^*$  has been computed for different target radii, for the reference lead-bismuth cooled core and for a sodium cooled core. The neutron source efficiency  $\phi^*$ , using the target neutron leakage definition, has also been determined.  $k_{\text{eff}}$  was kept constant at 0.95 by adjusting the outer radius of the core.

Since changing the geometry of the core might affect the results,  $\psi^*$  has also been studied as a function of the outer core radius, varying from 60 to 90 cm. It was found that an increase of the core radius leads to a slight increase of  $\psi^*$ , on average 0.26% per cm. The explanation for this is that the radial neutron leakage into the reflectors decreases as the core radius increases. This dependence of  $\psi^*$  (rather small but not automatically negligible) on the core radius should be kept in mind in the parameter studies where the core radius is varying.

##### V.A.1. The Lead-Bismuth Cooled Reference Model

$\psi^*$  was computed for the reference model for different target radii, both as the product of  $\phi^*$  and  $S_n/S_p$  (Eq. 3) and directly according to Eq. (4), in order to verify the consistency between the two different expressions.  $\phi^*$  was calculated using the target neutron leakage definition. The results are listed in Table II and we see that they are in good agreement with each other, the differences being within the statistical uncertainty. Hence, using a two-step simulation procedure,  $\psi^*$  can be obtained according to Eq. (3), independently of the choice of neutron source definition. If MCNPX is used,  $\psi^*$  can be obtained directly according to Eq. (4).  $\psi^*$ ,  $\phi^*$  and  $S_n/S_p$  are also plotted as functions of target radius later on in this section.

TABLE II

Computation of  $\psi^*$  according to Eq. (3) and Eq. (4) ( $1\sigma$ -error  $\sim 0.75\%$ ). For the 10 cm target radius, the radius of the accelerator tube was decreased to 10 cm. The results are also plotted below.

| Target Radius | $\phi^*$ | $\frac{\langle S_n \rangle}{\langle S_p \rangle}$ | $\phi^* \cdot \frac{\langle S_n \rangle}{\langle S_p \rangle}$ | $\psi^*$ |
|---------------|----------|---|--|----------|
| 10            | 1.81     | 21.9  | 39.8   | 39.6     |
| 20            | 1.35     | 26.8  | 36.3   | 35.9     |
| 30            | 1.13     | 29.0  | 32.9   | 32.4     |
| 40            | 0.99     | 30.0  | 29.6   | 29.5     |
| 50            | 0.89     | 30.2  | 26.7   | 27.0     |

Concerning the dependence on target radius, we see that  $\psi^*$  decreases considerably when the radius increases. There are mainly two reasons for this behaviour. One of them is the softening of the radial neutron leakage spectrum from the target (the spectrum of the neutrons that enter into the fuel), when the target is enlarged. The probability to induce fission for the source neutrons strongly decreases with decreasing energy, especially when the core is loaded with even-neutron number actinides, as will be shown below. Lower neutron energy also inhibits other possible neutron multiplication reactions, such as (n,xn)-reactions and secondary spallation. The number weighted mean energy of the radial neutron leakage spectrum decreases by a factor of four when the target radius is increased from 20 cm to 50 cm and the fraction of neutrons above 20 MeV is only 0.5% for a radius of 50 cm, while 3.2% for a 20 cm radius. The radial neutron leakage spectra for different target radii are plotted in Fig. 2 and the fraction of leakage neutrons above some energy thresholds are listed in Table III.

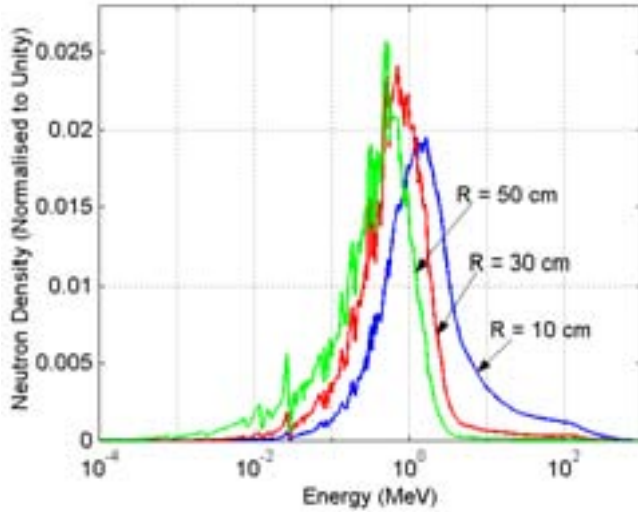


Fig. 2. Radial neutron leakage spectra from the target for different target radii.

TABLE III

Fraction of Neutrons Leaking out Radially from the Target that have Energies above 1, 7, 20 and 150 MeV.

| Target Radius | >1 MeV | >7 MeV | >20 MeV | >150 MeV |
|---------------|--------|--------|---------|----------|
| 10            | 62.4%  | 13.4%  | 6.9%    | 1.1%     |
| 20            | 45.2%  | 6.1%   | 3.2%    | 0.45%    |
| 30            | 31.0%  | 3.0%   | 1.7%    | 0.22%    |
| 40            | 20.7%  | 1.6%   | 0.9%    | 0.12%    |
| 50            | 13.5%  | 0.8%   | 0.5%    | 0.07%    |

The other reason for the decrease in  $\psi^*$  is that the axial target neutron leakage (the neutrons that leak out from the target axially and never enter the active core) increases significantly with increasing target radius. The fraction of axial target leakage neutrons relative to the total number of neutrons exiting the target is approximately 5 % for the 20 cm radius target while about 28 % for the 50 cm radius target. The major part of the axial leakage is in the backward direction, through the accelerator tube.

On the other hand, increasing the target radius increases the neutron multiplication inside the lead target, which leads to a higher number of neutrons created per source proton ( $S_n/S_p$  increases from 26.8 for  $r=20$  cm to 30.2 for  $r=50$  cm). The multiplicative effect of  $(n,xn)$ -reactions and secondary spallation in the lead target enhances the proton source efficiency. Consequently, with increasing target radius, there are more neutrons for each source proton that enter into the fuel, though the efficiency of these neutrons is strongly reduced. Accordingly, we see in Table II that  $\psi^*$  decreases less rapidly than  $\phi^*$  with increasing target radius, due to the increase in  $S_n/S_p$ . These two competing factors in  $\psi^*$  are thus well represented by Eq. (3).

We conclude that, in order to optimize the proton source efficiency and the output/input power, a target radius as small as possible should be chosen (increasing the radius from 20 cm to 50 cm decreases  $\psi^*$  by about 25%). These results are in good agreement with other similar studies [7]. However, it has also been shown that, reducing the target radius has some undesirable effects, for instance higher fluence/burnup ratio (lower maximum burnup) and more severe high-energy damages. Moreover, for a large-scale ADS, the target must be sufficiently large to be able to remove the heat from the high-power accelerator beam. It is thus clear that, in order to optimally design a cost-efficient ADS with high fuel performances, a trade-off between several different aspects arises.

#### V.A.2. A Sodium Cooled Model

Replacing the lead-bismuth coolant with sodium reduces the reactivity by about 5000 pcm, so in order to maintain a  $k_{\text{eff}}$  of 0.95, the outer core radius was increased by 11 cm. As is shown in Fig. 3, the proton source efficiency for small target radii is lower for the sodium cooled core than with the lead-bismuth coolant (approximately 7% lower for  $r = 20$  cm).

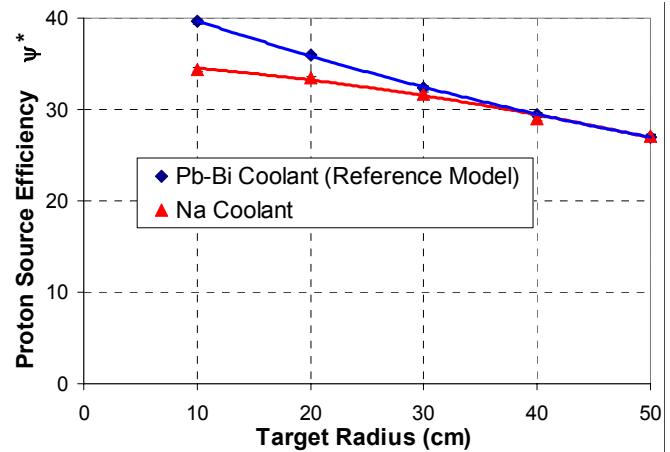


Fig. 3. Proton source efficiency  $\psi^*$  versus target radius for a Pb-Bi cooled and a Na cooled model ( $1\sigma$ -error  $\sim 0.75\%$ ).

The main reason for this is that there is no neutron multiplication in the sodium coolant, in contrast to lead-bismuth. The differences between the two curves indicate that the contribution from  $(n,xn)$ -multiplication in the Pb-Bi coolant is significant for target radii smaller than about 30 cm. As long as there is a fraction of neutrons with energy higher than about 7 MeV (the  $(n,2n)$ -threshold in lead) there will be  $(n,xn)$ -neutron multiplication in lead. When the target radius is small, this high-energy fraction is rather high (6.1% have energies higher than 7 MeV for  $r=20$  cm).

compared to 0.8% for  $r=50$  cm). When the target radius increases, the fraction of high-energy neutrons decreases, and at radii above 40 cm the  $\psi^*$  values are essentially the same. Another difference between the two coolant materials is that lead-bismuth has better spallation-neutron production characteristics. This enhances  $\psi^*$  for small target radii, in which cases there are still a significant fraction of very energetic neutrons leaking out into the fuel region. The difference between the Pb-Bi and the Na coolant are further illustrated in Fig. 4, where the neutron source efficiencies are depicted, together with the number of neutrons per source proton.

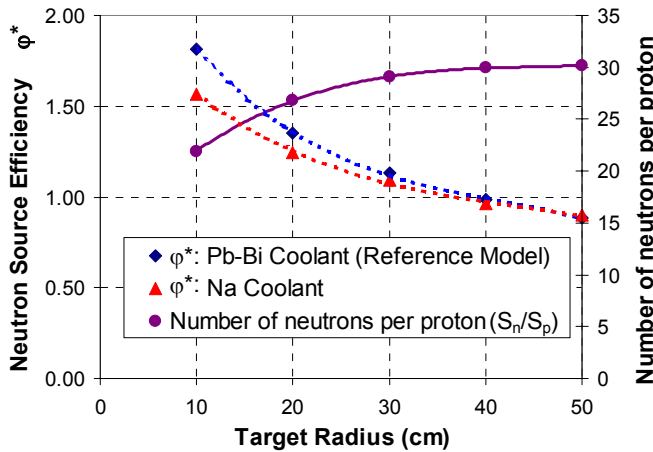


Fig. 4. Neutron source efficiency  $\phi^*$  (according to the target neutron leakage definition) and number of neutrons per source proton ( $S_n/S_p$ ), versus target radius for the Pb-Bi cooled and the Na cooled model ( $1\sigma$ -error  $\sim 0.75\%$ ).

#### V.B. $\psi^*$ as function of Axial Beam Impact Position

The proton source efficiency has been studied as a function of the axial beam impact position, varying from the center of the core ( $z = 0$ ) to the top of the core ( $z = 50$  cm). It is seen in Fig. 5 that, for the reference model (with an accelerator tube radius of 15 cm) the maximum in  $\psi^*$  is obtained at about 20 cm above the core center. Moving away from the optimum impact position,  $\psi^*$  decreases, due to increasing axial neutron leakage from the target.

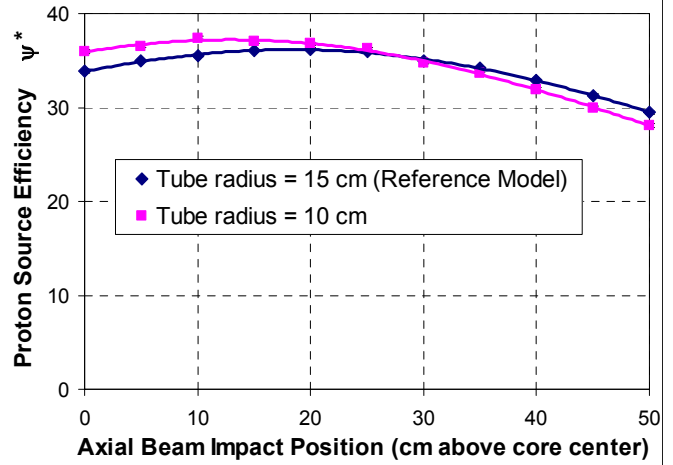


Fig. 5. Proton source efficiency  $\psi^*$  versus axial beam impact position (cm above the core center) for a tube radius of 15 cm and of 10 cm ( $1\sigma$ -error  $\sim 0.50\%$ ).

As is shown in Fig. 5,  $\psi^*$  and its dependence of the axial beam impact is rather sensitive to the accelerator tube radius. For a tube radius of 10 cm, the beam impact position that maximizes  $\psi^*$  is moved downwards in the core, with the optimum at about 13 cm above the core center. The maximum value of  $\psi^*$  also increases somewhat ( $\sim 3\%$ ) when the tube radius is changed from 15 cm to 10 cm.

When the tube radius decreases there are mainly two effects appearing. One is that the axial neutron leakage in the backward direction decreases (increasing  $\psi^*$ ) and the other one is that the energy spectrum of the neutrons entering into the fuel is softened (decreasing  $\psi^*$ ). When the beam impact is close to the core center, the impact of the leakage on the neutron balance is more pronounced than the softening of the neutron spectrum. On the contrary, when the beam impact is close to the top of the core, the softening effect is dominant and  $\psi^*$  is lower for the 10 cm tube radius.

An accidental scenario that has been considered in an ADS is that the accelerator tube is filled (partially or fully) with the target material [18], which would increase  $k_{\text{eff}}$ . For the reference model, filling the tube from 20 cm above the core center till the top of the core, this increase is about 600 pcm. For an initial reactivity level of  $k_{\text{eff}} = 0.95$ , and not taking the variations in  $\psi^*$  into account, this would increase the core power by 14%. For the 10 cm tube radius, the change in  $k_{\text{eff}}$  is smaller and also the effect on the power. However, the rapid decrease in  $\psi^*$  above  $z = 20$  cm will tend to reduce the core power. Adding these two opposite effects together, according to Eq. (6), it is found that the core power decreases when the tube channel is filled with lead-bismuth coolant. Filling the tube from  $z = 20$  cm to  $z = 50$  cm decreases the core power by 7% for the 15 cm tube radius and by 20% for the 10 cm tube radius.

However, if the reactor is operating at a reactivity level closer to criticality, the effect on the core power from a reactivity insertion will be higher and might be more important than the decrease in  $\psi^*$ . One way to increase the safety margins to prompt criticality, is to set the proton beam impact at the top of the core ( $z = 50$  cm). However, the loss in proton source efficiency, by moving the impact from the optimal position to the top of the core would be large - about 18 % for the 15 cm tube radius and 24 % for the 10 cm tube radius.

#### V.C. $\psi^*$ as function of Proton Beam Energy

The proton source efficiency was calculated for different proton beam energies, varying from 400 MeV to 2.5 GeV, for a 20 cm and a 50 cm radius target. The  $\psi^*$  values divided by the proton energy ( $\psi^*/E_p$ ) are displayed in Fig. 6.

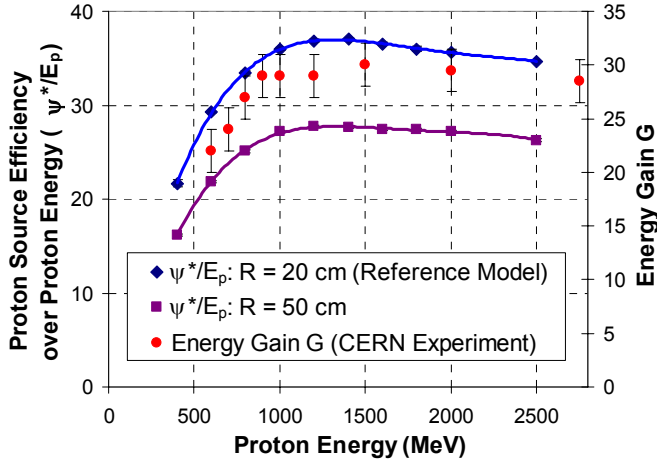


Fig. 6. Proton source efficiency divided by proton energy in GeV ( $\psi^*/E_p$ ) versus proton beam energy, for target radii of 20 cm and 50 cm ( $1\sigma$ -error  $\sim 0.50$  %). Energy gain  $G$  from CERN experiments [19] for a set-up configuration of  $k_{\text{eff}} = 0.895$ .

In coherence with Fig. 3,  $\psi^*$  is higher for the 20 cm radius than for the 50 cm radius, for all proton energies. However, the shape of the two curves is very similar.  $\psi^*/E_p$  increases strongly with increasing proton energy up to about 1000 MeV. The maximum is reached at about 1200-1400 MeV. Above 1400 MeV the curves decrease slightly. The reason for this is that the range of the protons increases with increasing energy and a larger fraction of the spallation induced neutrons will be created far away from the center of the core (or even below the core). This increases the axial neutron leakage from the target in the downward direction. For instance, the range of 1 GeV protons impinging on a lead target is about 53 cm, while about 95 cm for 2 GeV

protons [18]. The distance from the top of the target to the bottom of the core was 75 cm (Fig. 1).

The proton source efficiency divided by the proton energy ( $\psi^*/E_p$ ) is closely related to the energy gain (beam power amplification) of a source driven sub-critical system. The energy gain ( $G$ ), as defined in [19], represents the total power produced in the core over the accelerator power

$$G = \frac{P_{\text{tot}}}{P_{\text{acc}}} = \frac{G_0}{1 - k_{\text{eff}}} \quad (7)$$

where  $G_0$  relates to the efficiency of the spallation regime. Similarly, using Eq. (6) and the fact that  $P_{\text{acc}} \ll \langle S_p \rangle \cdot E_p$ ,

$P_{\text{tot}}/P_{\text{acc}}$  can be expressed as

$$\frac{P_{\text{tot}}}{P_{\text{acc}}} = \frac{P_{\text{tot}}}{\langle S_p \rangle \cdot E_p} \propto \frac{k_{\text{eff}}}{1 - k_{\text{eff}}} \cdot \left( \frac{\psi^*}{E_p} \right) \quad (8)$$

Hence, for given  $k_{\text{eff}}$ ,  $\psi^*/E_p$  is proportional to the energy gain  $G$ . In the experiments performed at CERN [19], the energy gain was studied as function of the proton beam energy. The results are re-plotted in Fig. 6. We see in the figure that the MCNPX simulated values of  $\psi^*$  have similar relative dependence on the proton energy, as the results from the CERN experiments. This comparison confirms that the  $\psi^*$  parameter represents well the beam power amplification of an ADS.

The  $k_{\text{eff}}$  of the sub-critical assembly in the CERN experiments was 0.895. In order to obtain  $G$  for  $k_{\text{eff}} = 0.95$ , the values have to be multiplied by  $(1 - 0.895)/(1 - 0.95) = 2.1$ . For  $E_p = 1000$  MeV the energy gain becomes 61.

#### V.D. $\psi^*$ for an Americium Based Fuel

Finally,  $\psi^*$  has been studied for an americium based fuel (40% Pu and 60% Am), as a function of the target radius. The volume fraction of the ZrN matrix was re-adjusted to 63%, in order to keep a  $k_{\text{eff}}$  of about 0.95. The results are displayed, together with the results for the reference model, in Fig. 7. We see that the introduction of americium decreases the source efficiency significantly and makes it more sensitive to the target radius.

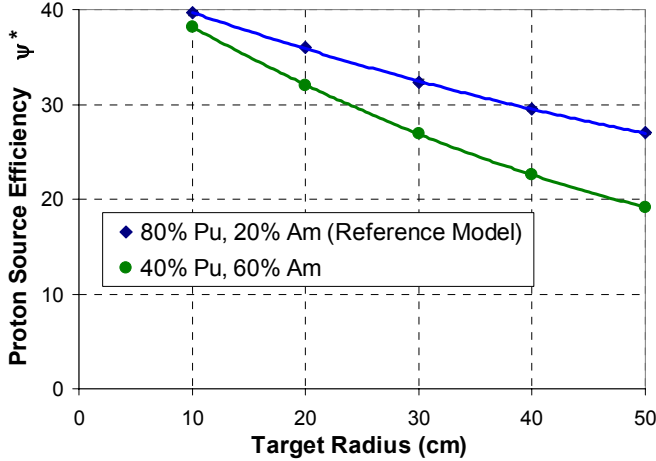


Fig. 7. Proton source efficiency  $\psi^*$  versus target radius for an americium based fuel, compared with the plutonium based reference model ( $1\sigma$  error  $\sim 0.75\%$ ).

This is expected, since the fission cross-section of Am-241 and Am-243 decreases rapidly for neutron energies below 1 MeV. Fig. 8, where the fission cross-section over the absorption cross section is plotted for Am-241 and Pu-239, shows that the fission probability of Am-241 is very sensitive to neutron energies between 0.1 and 1 MeV, whereas for Pu-239, it is high everywhere in this energy range. Above 1 MeV the fission probability for plutonium and americium are of the same order of magnitude. The other even-neutron number actinides, Pu-238, Pu-240, Pu-242 and Am-243, have similar cross-section dependence as Am-241, while the Pu-241 cross-section is similar to that of Pu-239.

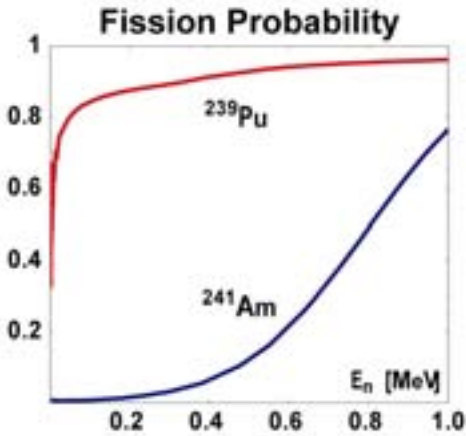


Fig. 8. Fission cross-section over absorption cross-section for Pu-239 and Am-241 (ENDF/B-VI).

Hence, the neutrons entering into the fuel with energy below 1 MeV will have less probability to induce fission in the fuel, when the core is loaded mainly with americium. As

was shown in Fig. 2 and in Table III, the energy distribution of the radial target leakage neutrons is very sensitive to the target radius. For a 10 cm radius, only 38% of the leakage neutrons are below 1 MeV and  $\psi^*$  is not so sensitive to the americium/plutonium ratio, which is also seen in Fig. 7. However, with increasing target radius, the fraction of neutrons above 1 MeV decreases rapidly, with a corresponding loss in proton source efficiency. Thus, increasing the americium concentration from 20% to 60%, reduces  $\psi^*$  by 11% for the 20 cm target radius and by 29% for the 50 cm target radius.

In Section III.B, it was shown that, for a fixed fuel composition,  $\psi^*$  is approximately proportional to the core power divided by the source intensity. However, increasing the fraction of americium in the fuel increases  $\bar{\nu}$  by about 5%. Therefore, normalising to the same core power, the difference between the two curves would be slightly larger (by 5%) than in Fig. 7.

## VI. CONCLUSIONS

Instead of using the neutron source efficiency parameter  $\phi^*$ , in order to study the beam power amplification, a new parameter  $\psi^*$ , representing the efficiency of the source protons, has been introduced. The proton source efficiency  $\psi^*$  is related to the number of fissions produced in the system, which in its turn is approximately proportional to the total core power. By introducing  $\psi^*$ , ambiguities in defining the external neutron source when calculating the source efficiency are avoided. Another advantages with  $\psi^*$  over  $\phi^*$  is that it is proportional to the core power divided by the proton beam power, independently of the neutron source distribution. Maximizing the proton source efficiency minimizes the proton current needs and relaxes the constraints on the construction of the high-power accelerator. Studying  $\psi^*$  when optimising different system parameters therefore becomes an important factor in the overall design of an ADS.

Studying the radius of the spallation target, it was found that  $\psi^*$  decreases strongly with increasing target radius (by 25% when the radius is changed from 20 cm to 50 cm). The two main reasons for this behaviour is that, the axial neutron leakage from the target increases and that the energy spectrum of the neutrons that enter into the fuel is softened, when the target is enlarged. These effects are only partly compensated by the increased neutron multiplication inside the target. Hence, in order to maximize the beam power amplification, a target radius as small as possible should be chosen, without exceeding the limits determined by safety constraints and other target-core characteristics (e.g. high-energy particle fuel damages and beam power heat removal). Substituting the lead-bismuth coolant by sodium decreases  $\psi^*$  for target radii smaller than 30 cm, whereas

for larger target radii, the two coolant options perform equally good.

The axial position of the proton beam impact that maximizes  $\psi^*$  was, for the reference model (tube radius = 15 cm), located approximately 20 cm above the core centre, but with relatively small variations between 0 and about 35 cm. However, the dependence of  $\psi^*$  on the impact position is sensitive to the accelerator tube radius, and for a tube radius of 10 cm, the maximum was found at about 13 cm above the core centre. Reducing the tube radius from 15 to 10 cm also increases the maximum of  $\psi^*$  by 3 %.

Investigating the proton source efficiency divided by the proton energy ( $\psi^*/E_p$ ) as a function of the proton energy showed that a maximal accelerator power amplification is obtained for proton energies of about 1200 to 1400 MeV, but with rather small changes between 1000 and 2000 MeV. Finally, increasing the americium content in the fuel from 20% to 60%, decreases  $\psi^*$  considerably, especially for larger target radii. Due to the sharp decrease in fission cross-section below 1 MeV, americium is more sensitive than plutonium to the softening of the energy spectrum of the neutrons that enter into the fuel.

#### ACKNOWLEDGEMENTS

This work was financially supported by the Swedish Centre for Nuclear Technology, SKB AB (Swedish Nuclear Fuel and Waste Management Co) and the European Commission (Project MUSE: FIKW-CT-2000-00063). The authors would like to thank J. Cetnar, R. Klein Meulekamp and R. Jacqmin for useful discussions.

#### REFERENCES

1. M. SALVATORES et al., "Long-Lived Radioactive Waste Transmutation and the Role of Accelerator Driven (Hybrid) Systems," *Nucl. Instrum. Methods A*, **414**, 5 (1997).
2. D. G. FOSTER et al., "Review of PNL Study on Transmutation Processing of High Level Waste," LA-UR-74-74, Los Alamos National Laboratory (1974).
3. T. TAKIZUKA et al., "Conceptual Design of Transmutation Plant," Proc. Specialist Mtg. Accelerator Driven Transmutation Technology for Radwaste, LA-12205-C, p. 707, Los Alamos National Laboratory (1991).
4. D. G. CACUCI, "On Perturbation Theory and Reactor Kinetics: From Wigner's Pile Period to Accelerator Driven Systems," *Int. Meeting*, PHYSOR2002, Korea, Seoul (2002).
5. M. DELPECH et al., "The Am and Cm Transmutation – Physics and Feasibility," *Proc. Int. Conf. Future Nuclear Systems, GLOBAL '99*, August 30-September 2, 1999, Jackson Hole, Wyoming, American Nuclear Society (1999).
6. J. WALLENIUS et al., "Application of burnable absorbers in an accelerator driven system", *Nuclear Science and Engineering*, **96**, 137 (2001).
7. W. S. YANG, L. MERCATALI et al., "Effects of Buffer Thickness on ATW Blanket Performances", *Int. Meeting Accelerator Applications/Accelerator Driven Transmutation Technology and Applications ADTTA/AccApp'01*, November 11-15, 2001, Reno, Nevada, USA (2001).
8. P. SELTBORG, R. JACQMIN, "Spallation Neutron Source Effects in a Sub-Critical System," *Int. Meeting Accelerator Applications/Accelerator Driven Transmutation Technology and Applications, ADTTA/AccApp'01*, November 11-15, 2001, Reno, Nevada, USA (2001).
9. M. SALVATORES et al., "The Potential of Accelerator-Driven Systems for Transmutation or Power Production Using Thorium or Uranium Fuel Cycles," *Nucl. Sci. Eng.*, **126**, 333 (1997).
10. R. SOULE, M. SALVATORES, R. JACQMIN, "Validation of Neutronic Methods Applied to the Analysis of Fast Sub-Critical Systems: The MUSE-2 Experiments," *GLOBAL '97*, page 639 (1997).
11. G. ALIBERTI et al., "Analysis of the MUSE-3 Subcritical Experiment", *Int. Conf. Global 2001*, France, Paris, September (2001).
12. R. KLEIN MEULEKAMP, A. Hogenbirk, "The Neutron Source in ADS applications", PDS-XADS D23 App. D, NRG report /I 20782 / 02.50727, Petten (2002).
13. K. TUCEK et al., "Source Efficiency in an Accelerator-Driven System with Burnable Absorbers," *Int. Conf. on Back-End of the Fuel Cycle: From Research to Solutions, GLOBAL 2001*, Paris, France (2001).
14. S. ATZENI et al., "Statistical Fluctuations in Montecarlo Simulations of the Energy Amplifier," *CERN/LHC/97-12 (EET)*, CERN (1997).
15. K. W. BURN, "A Decoupled Approach to the Neutronics of subcritical configurations: Evaluating the Neutron Source", RT/ERG/99/2, ENEA, Bologna, Italy (1999).



16. L. S. WATERS, "MCNPX<sup>TM</sup> User's Manual – Version 2.1.5," Los Alamos National Laboratory, November 14, (1999).
17. H. W. BERTINI, Phys. Rev. 131, 1801, (1969).
18. L. MONSANT et al., "Proposed Sub-criticality level for an 80 MWth Lead-Bismuth Cooled ADS, 7th Information Exchange Meeting on Actinide and Fission Product Partitioning & Transmutation, October 14-16 2002, Jeju, Korea.
19. S. ANDRIAMONJE et al., "Experimental determination of the energy generated in nuclear cascades by a high energy beam", Physics Letters B 348, 697-709 (1995).
20. S. BUONO, "Beam Target Design in Accelerator Driven Systems", Frederic Joliot/Otto Hahn Summer School '2002, August 21-30, 2002, Cadarache, France.



ELSEVIER

Available online at [www.sciencedirect.com](http://www.sciencedirect.com)

SCIENCE @ DIRECT®

Nuclear Instruments and Methods in Physics Research A 550 (2005) 313–328

NUCLEAR  
INSTRUMENTS  
& METHODS  
IN PHYSICS  
RESEARCH  
Section A

[www.elsevier.com/locate/nima](http://www.elsevier.com/locate/nima)

# Radiation shielding of high-energy neutrons in SAD

P. Seltborg<sup>a,\*</sup>, A. Polanski<sup>b</sup>, S. Petrochenkov<sup>b</sup>, A. Lopatkin<sup>c</sup>,  
W. Gudowski<sup>a</sup>, V. Shvetsov<sup>b</sup>

<sup>a</sup>Department of Nuclear and Reactor Physics, Albanova University Centre, Royal Institute of Technology, S-106 91 Stockholm, Sweden

<sup>b</sup>Joint Institute for Nuclear Research, 141 980, Joliot-Curie 6, Dubna, Russia

<sup>c</sup>Research and Development Institute of Power Engineering, 101 000, PB78, Moscow, Russia

Received 4 April 2005; accepted 29 April 2005

Available online 27 June 2005

## Abstract

The radiation fields and the effective dose at the Sub-critical Assembly in Dubna (SAD) have been studied with the Monte Carlo code MCNPX. The effective dose above the shielding, i.e. in the direction of the incident proton beam of  $3.0 \mu\text{A}$ , was found to be about  $190 \mu\text{Sv h}^{-1}$ . This value meets the dose limits according to Russian radiation protection regulations, provided that access to the rooms in this area is not allowed for working personnel during operation.

By separating the radiation fields into a spallation- and a fission-induced part, it was shown that the neutrons with energy higher than 10 MeV, originating exclusively from the proton-induced spallation reactions in the target, contribute for the entire part of the radiation fields and the effective dose at the top of the shielding. Consequently, the effective dose above the SAD reactor system is merely dependent on the proton beam properties and not on the reactivity of the core.

© 2005 Elsevier B.V. All rights reserved.

PACS: 28.50

Keywords: SAD; Effective dose; MCNPX; High-energy neutrons; Sub-critical; ADS

## 1. Introduction

In the up-coming SAD experiments [1,2], set up at the Joint Institute for Nuclear Research in Dubna (JINR) in collaboration with CEA (Cadar-

ache), CIEMAT (Madrid), FZK (Karlsruhe) and KTH (Stockholm), the various concepts and the basic physical principles of accelerator-driven systems (ADS) [3–5] will be studied extensively. In these experiments, a 660 MeV proton accelerator is coupled to a sub-critical core, loaded with fast reactor MOX (Mixed Oxide) fuel assemblies. The proton beam impinges on a target of lead, which generates a large number of neutrons via

\*Corresponding author. Tel.: +46 8 55 37 82 04;  
fax: +46 8 55 37 84 65.

E-mail address: [per@neutron.kth.se](mailto:per@neutron.kth.se) (P. Seltborg).

spallation reactions. The produced spallation neutrons leak out from the target, thus providing the sub-critical core with a strong external neutron source.

A major concern before licensing the operation of SAD is to accurately determine the radiation fields outside the reactor system. The surrounding building is shielded from the radiation emerging from the accelerator beam and the reactor by thick walls of concrete. In the present paper, the effective dose induced in the rooms above the reactor, i.e. in the direction of the incident proton beam, have been determined in order to verify that they do not exceed the limits determined by the Russian radiation protection regulations. The studies have been quantified by first calculating, with the Monte Carlo code MCNPX [6], the flux of the particles leaking out through the shielding and then by converting the obtained fluxes to effective dose. The effective doses have been obtained by using fluence-to-effective dose conversion coefficients, provided mainly by the International Commission for Radiological Protection (ICRP) [7] and the International Commission on Radiation Units (ICRU) [8].

The shielding problems in a system coupled to a high-energy proton beam are mainly connected to the deeply penetrating high-energy neutrons. These neutrons, released in the spallation process by direct head-on collisions between the source protons and the target nuclei (the intranuclear cascade phase), have a strong angular dependence and can, in the forward direction, reach energies up to the level of the incident protons [9,10]. The lower-energy neutrons, on the other hand, created in the subsequent evaporation stage and emitted nearly isotropically, constitute only a minor shielding concern, due to their comparatively short range in most shielding materials. For this reason, the largest radiation doses will appear in the forward direction of the incident proton beam [11] and the design of the biological shielding in this direction will generally be of largest importance. The objective of the present paper has been to study the radiation fields and the effective dose where they are maximal, i.e. above the reactor.

In the following section, a brief introduction to the quantities and conversion coefficients used for

radiological protection against external radiation is first given, followed by a description of the SAD experiments and the calculation method that was applied in the study. In Section 4, the results from the simulations are presented and analysed, with special focus given to the effects coming from the high-energy neutrons. First, the particles entering into the biological shielding are studied in terms of flux and energy spectra. The effective dose and the energy spectra of the particles detected at the top of the shielding are then determined. The next subsection addresses the transport and the attenuation of the particles in the shielding. Then, the relative contribution to the effective dose from high-energy neutrons and low-energy neutrons are studied and finally, the design of the biological shielding is optimised in order to reduce the dose to the Russian radiation limits for working personnel.

## 2. Conversion coefficients for use in radiological protection

### 2.1. Radiological protection quantities

There are three principal protection quantities currently recommended for use in radiological protection [7,8]; the mean absorbed dose in an organ or tissue ( $D_T$ ), the equivalent dose in an organ or tissue ( $H_T$ ) and the effective dose ( $E$ ).

#### 2.1.1. Absorbed dose

The absorbed dose,  $D_T$  [J/kg or Gy], in a particular organ or tissue, T, in the human body is given by

$$D_T = \frac{1}{m_T} \cdot \int_T D \cdot dm \quad (1)$$

where  $m_T$  is the mass of the organ or tissue and  $D$  is the absorbed dose in the mass element  $dm$ .

#### 2.1.2. Equivalent dose

In order to calculate the equivalent dose,  $H_T$ , in an organ or tissue, the radiation field in which the organ is present must be divided into energy bins and into the different types of radiation that the

field consists of. The absorbed dose in the organ of each radiation bin,  $D_{T,R}$ , must then be multiplied by a radiation-weighting factor,  $w_R$ , and summed over the different radiations,  $R$ , i.e.,

$$H_T = \sum_R w_R \cdot D_{T,R}. \quad (2)$$

### 2.1.3. Effective dose

The effective dose,  $E$ , was introduced for the quantification of the medical risk from a given radiation exposure.  $E$  is defined as the sum of the tissue-weighted equivalent doses in all the tissues and organs of the body,

$$E = \sum_T w_T \cdot H_T \quad (3)$$

where  $w_T$  is the tissue-weighting factor for tissue  $T$ . For the purpose of radiological protection calculations, the human body is in the ICRP Publication 60 [12] defined by 12 designated tissues and organs plus the remainder, which consists of 10 additional tissues and organs.

## 2.2. Fluence-to-effective dose conversion coefficients

In order to calculate the effective dose induced by any particle flux, the fluence-to-effective dose conversion coefficients for all energies of all particle types that may be present in the radiation field should be known. Using this set of conversion coefficients together with the specific particle flux that a person may be exposed to, the effective dose received by that person could be determined. The fluence-to-effective dose conversion coefficients are determined by calculating the total effective dose in an anthropomorphic model representing the human body, for mono-energetic fields of all particles of interest. The resulting effective dose for each energy bin is then divided by the total fluence of each radiation.

A number of studies determining these conversion coefficients have been performed by different research groups, using different simulation tools (mainly Monte Carlo codes) and different anthropomorphic models for the radiation transport calculations. In the ICRU Report 57, the results from many of the relevant studies are summarised.

Most of the calculations of protection quantities reviewed were made with an adult model using either a hermaphrodite MIRD-5 phantom [13] or modified MIRD-based phantoms, e.g. ADAM and EVA [14], with sex-specific differences. The data points from each group of authors were combined into one data set for each organ as a function of particle energy, resulting in one combined data set for each organ and for each gender. The conversion coefficients for the effective dose per unit fluence for whole-body irradiation by neutrons in isotropic irradiation geometry (ISO), recommended by the ICRU Report 57, cover the range from thermal energies up to 20 MeV. However, for dose calculations around an ADS driven by high-energy protons, such as the SAD experiments, conversion coefficients up to the energy of the incident protons are needed.

In the present study, the fluence-to-effective dose coefficients for neutrons from thermal neutrons up to 20 MeV are taken from the ICRU Report 57. For neutrons with energy from 20 up to 500 MeV, as well as for photons and protons of all energies, the coefficients are taken from a study by Mares and Schraube [15]. The calculations presented in Ref. [15] were performed with the high-energy Monte Carlo code MCNPX, using the ADAM and EVA anthropomorphic models. The results from Mares and Schraube were also found to be in good agreement with the overview of fluence-to-effective dose conversion coefficients for high-energy radiation performed by Pelliccioni [16]. All fluence-to-effective dose conversion coefficients used in the study were based on the ISO geometry and are listed in Table A.1.

## 3. System modelling

### 3.1. The SAD design

The design of the SAD facility is based on a sub-critical highly enriched MOX-loaded core, driven by a 660 MeV proton beam impinging on a target of lead. The protons are generated by the JINR Phasotron proton accelerator, which can provide a current of maximum 3.2  $\mu$ A. In the following study, a beam power of 2.0 kW, corresponding to a

current of  $3.0 \mu\text{A}$  ( $1.9 \times 10^{13}$  protons/s), was assumed in all simulations. For the calculated effective multiplication coefficient ( $k_{\text{eff}} \sim 0.95$ ), this proton beam induces a total core power of about 60 kW. In Fig. 1, a schematic view of the target, the core, the reflector and the upper part of the biological shielding is depicted. The core is surrounded by a lead reflector, which is 30 cm thick in the axial directions. In the present SAD design, the biological shielding above the reactor consists of a 100 cm thick section of heavy concrete, followed by 340 cm of standard concrete (the elementary compositions of the concrete materials are displayed in Table 1). Since the particles that leak out radially from the reflector do not contribute significantly to the effective dose at the top of the shielding, the radial and the lower sections of the shielding have been neglected in the simulations.

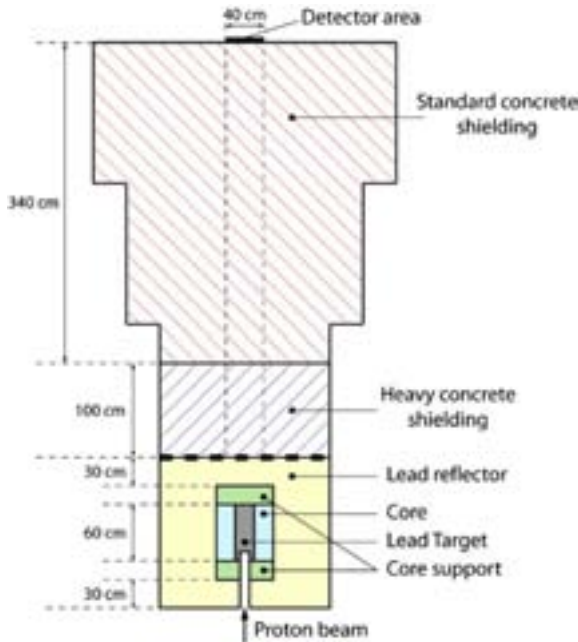


Fig. 1. Schematic  $rz$ -view of the present design of the SAD reactor system, including the target, the core, the lead reflector and the upper part of the biological shielding. The shielding consists of a 100 cm thick section of heavy concrete plus 340 cm of standard concrete. The effective dose was calculated at the detector area at the upper surface of the biological shielding.

Table 1

Elementary composition of the standard and the heavy concrete used in the biological shielding above the SAD core [17]

| Element                        | Standard concrete (wt%) | Heavy concrete (wt%) |
|--------------------------------|-------------------------|----------------------|
| O                              | 53.0                    | 14.6                 |
| Si                             | 37.2                    | 4.4                  |
| Ca                             | 8.3                     | 4.6                  |
| H                              | 1.0                     | 0.6                  |
| Mg                             | 0.5                     | 2.7                  |
| Fe                             | —                       | 66.3                 |
| C                              | —                       | 2.5                  |
| S                              | —                       | 1.5                  |
| Ni                             | —                       | 0.7                  |
| Mn                             | —                       | 0.7                  |
| Cr                             | —                       | 0.5                  |
| Al                             | —                       | 0.5                  |
| P                              | —                       | 0.2                  |
| Density ( $\text{g cm}^{-3}$ ) | 2.30                    | 4.44                 |

### 3.2. Calculation method

In order to determine the total effective dose, the flux of the particles that leak out at the detector area at the top of the biological shielding was calculated with the high-energy Monte Carlo code MCNPX (version 2.5.e), with the energy spectrum divided into the appropriate energy bins. Knowing the flux,  $\Phi_{E,P}$ , and the fluence-to-effective dose conversion coefficients,  $(E/\Phi)_{E,P}$ , for each energy bin and each particle type, the total effective dose per unit time,  $E$ , can then be determined as

$$E = \sum_P \left( \sum_E (E/\Phi)_{E,P} \cdot \Phi_{E,P} \right). \quad (4)$$

The summation is over all energy bins and all particles. MCNPX was used in coupled neutron, proton and photon mode and the evaluated nuclear data library used in the simulations was LA150 [18] for those isotopes included in this library and ENDF/B-6.8 for the remaining isotopes. The high-energy physics package used by MCNPX was the Bertini model [19,20].

The main objective of the present study has been to determine the effective dose induced at the top of the biological shielding. For practical reasons, the simulations were divided into two steps. In the

first simulation, where the 660 MeV source protons impinge on the spallation target, only the target, the core and the reflector were present. The properties, in terms of position, direction and energy, of the particles that leak out from the upper surface of the reflector (marked with the thick dotted line in Fig. 1) were recorded and written in a source file. In the second step, in which only the shielding was present, these particles were re-emitted as fixed source particles in a separate run and transported through the shielding. The particle fluxes and the effective dose were then determined at the detector area at the top of the shielding (marked with the thick black line at the top of Fig. 1).

In Monte Carlo-based shielding calculations, different kinds of variance reduction techniques are generally needed in order to obtain reliable statistics within reasonable computing time. In the present study, the Geometry splitting with Russian roulette option in MCNPX was applied. The biological shielding was divided into separate layers with increasing splitting multiplicity, such that the particle populations remained approximately constant from the source point to the detection point. The thickness of each layer was 10 cm and, since the particle fluxes decrease approximately logarithmically with the distance travelled, the importance between two neighbouring layers was increased by a nearly constant factor.

#### 4. Results and discussion

##### 4.1. The radiation fields at the reflector surface

From the target-core-reflector simulation, it was found that the flux of the neutrons at the centre

(within 20 cm radius) of the upper reflector surface, is about  $3.5 \times 10^{10} \text{ cm}^{-2} \text{ s}^{-1}$  (Table 2). Most of these neutrons come from the fission multiplication in the core and have an energy distribution peaking at about 500 keV (Fig. 2). However, there is small fraction of the neutrons that comes directly from the spallation process in the target and carries very high energy. Although the fraction of neutrons with energy higher than 10 MeV is only  $\sim 0.12\%$ , it will be shown below that these high-energy neutrons contribute to the entire part of the radiation fields and the effective dose at the top of the shielding.

The fluxes of photons and protons at the reflector surface were, as expected, significantly lower than the neutron flux, in the order of  $8 \times 10^7$  and  $4 \times 10^5 \text{ cm}^{-2} \text{ s}^{-1}$ , respectively. The major part of the photons was found in the energy range

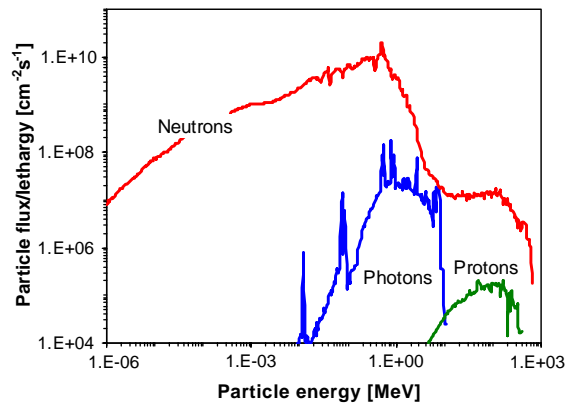


Fig. 2. Energy spectra of the neutrons, photons and protons that leak out through the centre (within 20 cm radius) of the upper reflector surface. The resolution of the spectra corresponds to a constant lethargy width of 0.05.

Table 2

Flux ( $\Phi$ ) of neutrons, photons and protons and the relative fractions of particles in different energy intervals, that leak out through the centre of the upper reflector surface (averaged over a 20 cm radius)

|          | $\Phi \text{ (cm}^{-2} \text{ s}^{-1}\text{)}$ | Fraction of particles in different energy bins (%) |          |            |             |
|----------|--|--|----------|------------|-------------|
|          |  | 0–1 MeV  | 1–10 MeV | 10–100 MeV | 100–660 MeV |
| Neutrons | $3.5 \times 10^{10}$                           | 95.4   | 4.4      | 0.08       | 0.04        |
| Photons  | $8.1 \times 10^7$                              | 57.2   | 42.8     | 0          | 0           |
| Protons  | $4.0 \times 10^5$                              | 0  | 5        | 60         | 35          |

between 0.1 and 10 MeV, while most of the protons had energy higher than 10 MeV.

#### 4.2. The radiation fields at the top of the biological shielding

##### 4.2.1. Effective dose

The separate fluxes for neutrons, photons and protons calculated at the detector area at the top of the biological shielding, as well as the corresponding effective doses and the total effective dose, are displayed in Table 3. The total effective dose was found to be about  $190 \mu\text{Sv h}^{-1}$ , with a statistical uncertainty of about 5%. According to radiation protection rules in Russia, the maximal allowed effective dose for civil personnel is  $12 \mu\text{Sv h}^{-1}$ . However, provided that access for working personnel to the rooms above the shielding will be prohibited during operation, the radiation dose obtained for the present design of the biological shielding is in agreement with the radiation regulations.

Apparently, the neutrons contribute for the major part of the effective dose,  $\sim 89\%$ , but, a non-negligible part of the effective dose is also induced by photons and protons, which contribute for  $\sim 1\%$  and  $\sim 10\%$ , respectively. The reason why the contribution from photons is only 1%, although the fluxes of neutrons and photons are in the same order of magnitude, is that the conversion coefficients of the photons (having energy between 0.1 and 10 MeV) are about 100 times smaller than those of the neutrons (a major fraction having energy around 100 MeV). Similarly, the conversion coefficients for the protons (with the major part having energy around 100 MeV) are about 10 times higher than those for the neutrons, which explains the relatively high

contribution to the effective dose induced by the much lower flux.

The explanation to why there is such a considerable flux of photons and protons detected, although only high-energy neutrons entering into the concrete are expected to penetrate the entire shielding, is that the high-energy neutrons create, apart from secondary neutrons with lower energy, also secondary photons and protons. The high-energy neutrons will thus be followed through the concrete by cascades of neutrons, photons and protons. Hence, all protons and photons detected at the top of the shielding have been created by neutrons inside the standard concrete. The minimum energy of neutrons required to create protons is in the order of a few MeV, while thermal neutrons have the highest probability to create photons. Since both photons, protons and low-energy neutrons have limited range in the concrete, it can moreover be assumed that the major part of the detected particles have been created nearby the detector area.

##### 4.2.2. Energy spectra

The energy distributions of the neutrons, photons and protons detected at the top of the biological shielding are displayed in Fig. 3. It was found that about half of the neutrons have energy above 10 MeV. Accordingly, since the neutrons contribute for the major part of the effective dose and since the conversion coefficients increases with energy, the major part of the total effective dose is induced by neutrons with energy higher than 10 MeV.

The energy spectrum of the detected neutrons is typical for a high-energy proton beam shielded by concrete. The shape of these spectra is generally characterized by a thermal peak, an evaporation

Table 3

Separate flux ( $\Phi$ ) and effective dose ( $E$ ) of neutrons, photons and protons, as well as the total effective dose, at the detector area at the top of the biological shielding

| Neutrons                                 |                               | Photons                                  |                               | Protons                                  |                               | Total                         |                      |
|--|-------------------------------|--|-------------------------------|--|-------------------------------|-------------------------------|----------------------|
| $\Phi$ ( $\text{cm}^{-2}\text{s}^{-1}$ ) | $E$ ( $\mu\text{Sv h}^{-1}$ ) | $\Phi$ ( $\text{cm}^{-2}\text{s}^{-1}$ ) | $E$ ( $\mu\text{Sv h}^{-1}$ ) | $\Phi$ ( $\text{cm}^{-2}\text{s}^{-1}$ ) | $E$ ( $\mu\text{Sv h}^{-1}$ ) | $E$ ( $\mu\text{Sv h}^{-1}$ ) | $1\sigma$ -error (%) |
| 174                                      | 172                           | 114                                      | 1.9                           | 2.0                                      | 18                            | 192                           | $\sim 5$             |

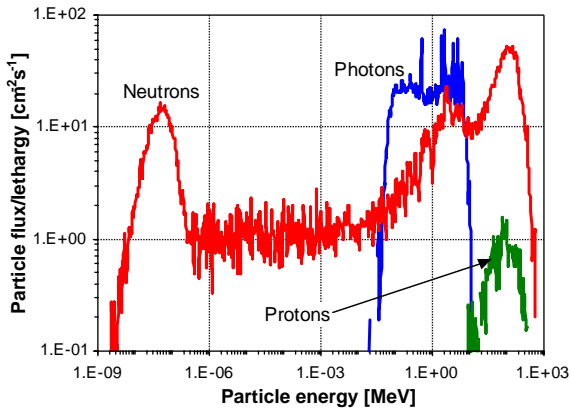


Fig. 3. Energy spectra of the neutrons, photons and protons detected at the top of the concrete shielding. The resolution of the spectra corresponds to a constant lethargy width of 0.05.

shoulder around a few MeV and a high-energy spallation peak, which is indeed the case. The high-energy peak with a maximum at about 100 MeV arises mainly from the deeply penetrating neutrons that were emitted in the intranuclear cascade reactions in the spallation target. The major part of these high-energy neutrons, formed in direct head-on collisions between the incident source protons and the individual target nucleons, were emitted in the forward direction and have been transported through the shielding without being significantly moderated. Since only the most energetic neutrons can be traced back to the shielding region of heavy concrete, the detected spectra below about 100 MeV is determined only by the isotopic composition of the standard concrete. The evaporation shoulder comes from the neutrons emitted in the neutron-induced spallation reactions on the heavier elements in the standard concrete (mainly oxygen and silicon). The narrow peak on top of this shoulder, located at 2.35 MeV, is the result of a deep minimum in the elastic scattering cross-section of  $^{16}\text{O}$ .

Most of the detected photons have been created in neutron-induced reactions, by either one of the two following types of reactions. In the first type, a high-energy neutron is scattered on one of the concrete nuclei and transfers a considerable amount of energy to it, leaving it in an excited state. When the nucleus is de-excited, photons of

various discrete energies are emitted. The second type of reaction that leads to photon production is a neutron-capture reaction. Examples of such reactions occurring in the concrete are  $^{16}\text{O}(n,\gamma)^{17}\text{O}$  and  $^{28}\text{Si}(n,\gamma)^{29}\text{Si}$  with  $Q$ -values of 4.1 and 8.5 MeV, respectively. Thermal neutrons have the highest probability of inducing this type of reaction. The overall photon energy spectrum, ranging mainly from about 0.1 to about 10 MeV, can be characterized by a Compton continuum on top on which is added hundreds of discrete photon peaks of varying intensity. Among the most distinct peaks can be mentioned those originating from electron–positron annihilation (0.511 MeV), the formation of  $^2\text{H}$  (fusion of a neutron and a proton emitting a photon carrying the released binding energy of 2.225 MeV), gamma emission following neutron capture in  $^{28}\text{Si}$  (4.935 MeV) and the de-excitation of  $^{16}\text{O}^*$  (6.130 MeV).

The shape of the proton energy spectrum is similar to that of the high-energy neutrons, the major part having energy higher than 10 MeV. The protons have been created in direct head-on reactions between the high-energy neutrons and the various nuclei in the standard concrete. In this type of reactions, a large fraction of the neutron energy is transferred to the released proton, which is emitted preferably in the forward direction.

#### 4.3. Attenuation in the biological shielding

In order to estimate the range of the particles transported in the biological shielding, the attenuation of parallel beams of neutrons, photons and protons of various discrete energies have been studied. The attenuation of a beam of non-charged monoenergetic particles in a homogeneous material can be expressed by the following relation [21]:

$$N/N_0 = B(x) \cdot e^{-\mu x} \quad (5)$$

where  $N/N_0$  refers to the relative intensity of the beam,  $B(x)$  is the build-up factor and  $\mu$  is the linear attenuation coefficient. The build-up factor represents the ratio of the intensity of the total radiation reaching a point, to the intensity of the primary radiation reaching the same point. If the incident beam, as well as the area one is trying to shield, would be very narrow, or, if the shielding material



would be very thin, only the unscattered primary particles would contribute to the effective dose and  $B$  would be equal to unity. However, since this is rarely the case,  $B$  will in general be larger than 1, as it accounts also for the contribution coming from those particles that have been scattered and from those that have been formed by the primary particles. It should be noted that, for beams of mixed energies, the decay of the total intensity have to be described by more than one exponential.

In this study, the attenuation length is defined as the thickness required to reduce the effective dose by a factor of 10 (the tenth-value thickness), and will be labelled  $\lambda_{10}$  ( $\lambda_{10} = \ln(10)/\mu$ ). The attenuation of the effective dose is approximately equal to the diminishing of the flux. The attenuation coefficients and the attenuation lengths, displayed in Table 4, were obtained by simulating the transport of parallel mono-energetic particle beams through a slab of concrete and calculating the effective dose at different distances from the incident point. All particles contributing to the effective dose were included, i.e., apart from the primary source particles, also the neutrons, photons and protons that are formed as the primary particles are moderated. An exponential function was then fitted to the data points and  $\mu$  was determined as the slope of the decay curve. The so-called attenuation factors have also been

determined for the mono-energetic particle beams impinging on the SAD shielding (100 cm of heavy concrete plus 340 cm of standard concrete), referring to the ratio of the effective dose at the incident point to the effective dose at the top of the shielding.

#### 4.3.1. Attenuation of mono-energetic neutron beams

It is shown in Table 4 and Fig. 4 that the attenuation length of neutrons transported in concrete increases considerably with increasing energy. For instance, the attenuation length of a 100 MeV neutron beam is about three times longer than for a 10 MeV neutron beam and the attenuation factor for the present SAD design is in the order of  $10^{17}$  for the 10 MeV neutrons, whereas only about  $10^5$  for the 100 MeV neutrons. These results indicate that the contribution to the effective dose above the SAD shielding from neutrons below 10 MeV will be negligibly small (this assumption will be verified below by direct MCNPX simulations). As can be seen in Fig. 4, the attenuation of the neutron beams does not decay exponentially during the first part of the concrete slab (the build-up factor is larger than 1 and increases with the thickness). As was explained above, the attenuation of the unscattered primary neutrons will be purely exponential (no build-up factor needed), but, in particular the

Table 4

Attenuation lengths ( $\lambda_{10}$ ) for the decay of the effective dose, induced by parallel mono-energetic beams of neutrons, photons and protons of different energies impinging on thick slabs of either heavy or standard concrete

| Particle type | Energy (MeV) | Attenuation length, $\lambda_{10}$ (cm) |                   | Attenuation factor   |
|---------------|--------------|---|-------------------|----------------------|
|               |              | Heavy concrete                          | Standard concrete |                      |
| Neutrons      | 1            | 13                                      | 16                | $2.4 \times 10^{23}$ |
|               | 10           | 18                                      | 29                | $1.4 \times 10^{17}$ |
|               | 100          | 54                                      | 92                | $2.6 \times 10^5$    |
|               | 500          | 74                                      | 135               | $3.3 \times 10^3$    |
| Photons       | 1            | 9                                       | 17                | $> 10^{30}$          |
|               | 10           | 21                                      | 49                | $1.5 \times 10^{12}$ |
| Protons       | 100          | 39                                      | 51                | $4.1 \times 10^{10}$ |
|               | 500          | 68                                      | 111               | $2.2 \times 10^5$    |

The so-called attenuation factors have been calculated for the mono-energetic particles impinging on the SAD shielding (100 cm of heavy concrete plus 340 cm of standard concrete) and refer to the ratio of the effective dose at the incident point to the effective dose at the top of the shielding.

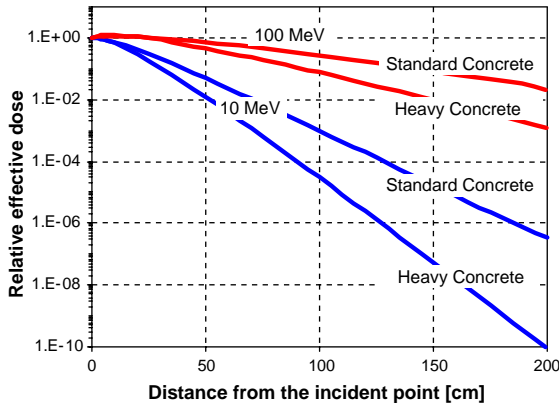


Fig. 4. Relative effective dose as a function of distance from the incident point, in standard and heavy concrete for parallel beams of 10 and 100 MeV neutrons. The effective dose includes the contributions from all secondary particles, i.e., the neutrons, photons and protons that are created when the incident high-energy neutrons are moderated.

100 MeV neutrons, will create secondary particles as they are moderated. These particles, mainly the neutrons, will contribute considerably to the effective dose close to the incident point. However, as they have comparatively low energy and limited range in the concrete, the primary high-energy neutrons will dominate the attenuation completely at longer distances. When the energy distributions of the particles contributing to the effective dose reach their equilibrium, i.e. only the amplitudes and not the shape of the spectra change, the total effective dose will decay with the same single exponential as the incident primary neutrons. For distances beyond about 50 and 100 cm, for the 10 MeV neutrons and the 100 MeV neutrons, respectively, the energy spectra are in equilibrium and the decay constants have reached their asymptotic value of a single exponential (the build-up factor is constant). The calculated data beyond these points have been used to determine the attenuation coefficients and the attenuation lengths of the neutron beams.

#### 4.3.2. Attenuation of mono-energetic photons beams

Photons in the energy range where most of the reflector leakage photons are found (0.1–10 MeV) have comparatively short range in the concrete, in the same order of magnitude as neutrons of similar

energy. Therefore, the photons that leak out through the reflector surface can be assumed to give zero contribution to the effective dose at the top of the shielding, which can also be understood from the large attenuation factors shown in Table 4. The build-up factors are closer to 1 than for the neutron beams, as the photons form less secondary particles, and the attenuation curves become purely exponential already very close to the impact position.

#### 4.3.3. Attenuation of mono-energetic proton beams

Opposite to neutrons and photons, protons carry electric charge. Therefore, the attenuation of a proton beam shows a more complicated behaviour than the exponential decay described by Eq. (5). When a high-energy proton is moderated in a material, the rate of energy loss increases as the proton energy decreases. Near the end of the path, when most of its energy has been lost, the energy loss per unit distance reaches a maximum (the Bragg peak), after which it drops to zero as the particle comes to rest. This abrupt slowing down enables a precise range of the incident protons to be defined. For instance, the typical range of 500 MeV protons in the heavy concrete in the SAD shielding was found to be about 35 cm, which is illustrated in Fig. 5. Hence, protons have very limited range in concrete, compared to neutrons of similar energy. The typical range of the 100 MeV protons is only a few cm.

However, the high-energy protons being transported in the concrete will create spectra of secondary particles as they interact with the concrete nuclei. Some of the created neutrons will be formed in direct head-on collisions and receive the major part of the proton energy. Since these high-energy neutrons have much longer range in the concrete than the primary protons, the dominant contribution to the effective dose will after a distance longer than the typical proton range actually be induced by these secondary neutrons (Fig. 5). Moreover, as was already explained, these high-energy neutrons will, in their turn, create spectra of both neutrons, photons and protons. Hence, at distances longer than the primary proton range, the attenuation of the effective dose directly induced by protons, as well

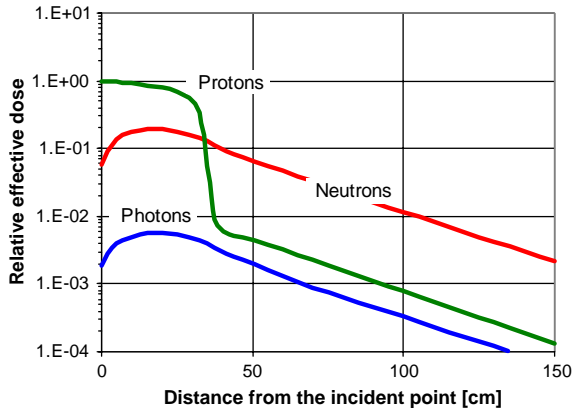


Fig. 5. Attenuation of the effective dose in heavy concrete for parallel beams of 500 MeV protons. The different curves represent the separate contributions to the effective dose from protons, neutrons and photons.

as that by photons, will decay with the same exponential as the neutrons. It can thus be concluded that the effective range of high-energy protons incident on a concrete shielding, in terms of inducing effective dose, is determined mainly by the attenuation of neutrons with similar energy and is much longer than can be expected from studying only the Bragg curve of the incident protons. This is also illustrated in Table 4, where the attenuation lengths for the protons have been determined from the exponential neutron decay beyond the Bragg peak. It is seen that the attenuation lengths for the protons are only slightly shorter than for the neutrons of the same energy.

However, despite the relatively long range of the proton-induced effective dose, the rapid decrease of the total effective dose at the Bragg point reduces the contribution to the dose at the top of the SAD shielding significantly. Moreover, the intensity of the proton flux at the reflector surface is very low (more than 100 times lower than for the high-energy neutrons), which makes the relative contribution to the effective dose from the protons negligible.

#### 4.3.4. Attenuation of the SAD-leakage particles in the biological shielding

In the following subsection, the effective dose induced by the particles leaking out from the SAD

reactor system has been studied in the biological shielding as a function of the distance from the reflector-shielding boundary. In Fig. 6, it is shown that, during the first  $\sim 50$  cm in the heavy concrete, the decay of the effective dose is very fast and cannot be described by a single exponential. The reason for this is that the effective dose close to the reflector is induced mainly by the low-energy neutrons leaking out from the reflector, which have a large variety in energy. Since neutrons with different energy are attenuated at different rates, the total decay will be described by the sum of many exponentials. However, all of these low-energy neutrons are efficiently attenuated in the heavy concrete and, beyond about half a meter, the decay of the effective dose is largely dominated by the attenuation of the high-energy neutrons. The particle spectra have almost reached their equilibrium and the decrease of the effective dose is very close to exponential. However, entering into the standard concrete, the decay switches into another mode, with less efficient attenuation. Since the energy spectra of the transported particles change at this boundary, some distance is required before the decay curve becomes single-exponential again.

In order to determine the linear attenuation coefficients and the attenuation lengths in the two

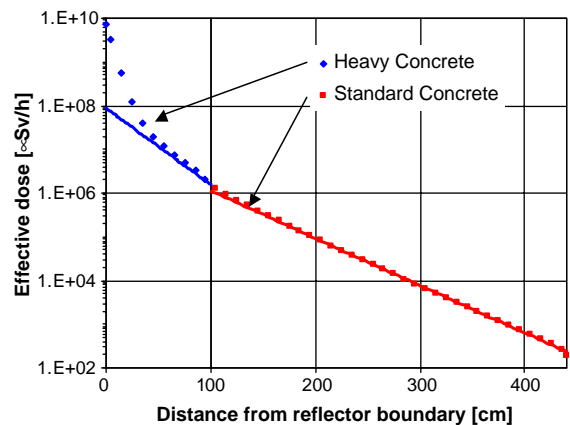


Fig. 6. Total effective dose induced by the particles leaking out from the SAD reactor system as a function of the distance from the reflector-shielding boundary. Exponential curves have been fitted to the MCNPX-calculated values; one in the heavy concrete and one in the standard concrete.

Table 5

Attenuation lengths ( $\lambda_{10}$ ) and attenuation factors for the decay of the effective dose induced by the particles leaking out from the SAD reactor system

| Attenuation length, $\lambda_{10}$ (cm) |                   | Attenuation factor |
|---|-------------------|--------------------|
| Heavy concrete                          | Standard concrete |                    |
| 58                                      | 93                | $3.9 \times 10^7$  |

shielding materials, two exponential curves have been fitted to the MCNPX-calculated data points, one for the heavy concrete and one for the standard concrete. In the heavy concrete, the purely exponential decay appears first after about 150 cm (although it is close to exponential already after 50 cm), so additional simulations, extending the heavy concrete, had to be performed to determine the attenuation coefficient (data points from 150 to 250 cm were used for the curve fitting). In the standard concrete, the equilibrium of the particle spectra is reached after a few tenths of cm from the boundary and the data points from 150 to 400 cm were used for the curve fitting. The attenuation lengths ( $\lambda_{10}$ ) of the effective dose obtained from the exponential fits were found to be 58 cm in heavy concrete and 93 cm in standard concrete (Table 5).

#### 4.4. Contribution to the effective dose from source neutrons in different energy intervals

As was shown above, low-energy neutrons have very short attenuation lengths in concrete, compared to high-energy neutrons, which indicates that only the high-energy neutrons have long enough range to penetrate the full length of the shielding and to induce any significant effective dose at the top of it. In order to calculate the separate contributions to the effective dose from neutrons of different energies, the flux of the neutrons entering into the biological shielding from the reflector was divided into four energy bins (0–1, 1–10, 10–100 and 100–660 MeV). As expected, the relative contribution from the two low-energy bins is zero (Table 6). The contribution from the third energy bin (10–100 MeV) is also

Table 6

Relative contribution to the total effective dose originating from the source particles that enter into the biological shielding from the reflector. The neutrons were divided into four different energy intervals

| Source particle | Energy interval (MeV) | Relative contribution to E (%) |
|-----------------|-----------------------|--------------------------------|
| Neutrons        | 0–1                   | 0 ( $\sim 10^{-18}$ )          |
|                 | 1–10                  | 0 ( $\sim 10^{-14}$ )          |
|                 | 10–100                | 0.3                            |
|                 | 100–660               | 99.7                           |
| Photons         | All                   | 0 ( $\sim 10^{-12}$ )          |
| Protons         | All                   | 0.01                           |

limited ( $\sim 0.3\%$ ), whereas the last energy bin (100–660 MeV) contributes for nearly the entire part of the effective dose. It was also found that the contributions from photons and protons are negligible. As was explained above, the dose originating from the source protons is induced by the secondary neutrons created as the protons are moderated in the heavy concrete.

The maximal energy of the neutrons released in the fission processes in the reactor core is in the order of 10 MeV. It can therefore be assumed that the entire part of the effective dose detected at the top of the shielding originates from the proton-induced spallation reactions in the target and practically nothing from the fission multiplication in the core. Thus, it can be concluded that the effective dose is directly proportional to the proton beam power and that it is independent of the reactivity and the total power of the sub-critical core.

#### 4.5. Optimising the design of the biological shielding

##### 4.5.1. Reducing the effective dose to Russian regulation limits for working personnel

As was mentioned above, the effective dose obtained for the present design of the biological shielding above the SAD core ( $\sim 190 \mu\text{Sv h}^{-1}$ ) meets the Russian regulations for radiation doses. However, if the access for working personnel in the rooms above the reactor would be required, the effective dose would have to be decreased to

$12 \mu\text{Sv h}^{-1}$ , which is about 15 times lower than for the present design. In such case, the shielding would have to be modified, for instance by increasing the fraction of heavy concrete in the shielding.

The amount of standard concrete that must be replaced by heavy concrete in order to obtain the desired dose can be determined in two ways, either by extrapolating the two exponential functions that were fitted to the MCNPX-calculated data (Fig. 6) or by direct MCNPX calculations. Applying the extrapolation method, it was found that the boundary between the heavy concrete and the standard concrete should be located at 316 cm from the reflector, in order to reduce the dose to  $12 \mu\text{Sv h}^{-1}$ . In the second method, the effective dose was calculated in different MCNPX-simulations with the boundary between the heavy concrete and the standard concrete varying. Interpolating between the obtained data points, it was found that the desired dose is obtained with the boundary located at 305 cm, which is in fairly good agreement with the first result. The main reason for the slight disagreement between the two results is that the attenuation is not purely exponential during the first tenths of cm in the standard concrete, which was not taken into account in the extrapolation method.

#### 4.5.2. Shielding thickness required for a large-scale ADS

The power of the proton beam in the SAD experiments is relatively low (maximum 2 kW) and not representative of a future large-scale ADS, which might require a beam power of several MW. The thickness of concrete required to maintain the dose at  $12 \mu\text{Sv h}^{-1}$  for different beam powers have been estimated by calculating the effective dose as a function of concrete thickness, for heavy concrete and standard concrete separately, and then extrapolating the results to the required thickness. Since the effective dose is linearly proportional to the beam power (given a fix proton energy), the amount of extra concrete required for an increase of the beam power by a factor of 10 is equal to the attenuation length,  $\lambda_{10}$  (58 cm for heavy concrete and 93 cm for standard concrete). In Table 7, the amount of standard

Table 7

Thickness of the biological shielding required to maintain the effective dose at  $12 \mu\text{Sv h}^{-1}$  for a proton beam power varying from 2 kW to 20 MW

| Beam power (kW)   | Heavy concrete (cm) |   | Standard concrete (cm) |
|-------------------|---------------------|---|------------------------|
| 2.0 <sup>a</sup>  | 305                 | + | 135                    |
|                   | 394                 |   | 591                    |
| 20                | 453                 |   | 684                    |
| 200               | 511                 |   | 777                    |
| $2.0 \times 10^3$ | 570                 |   | 869                    |
| $20 \times 10^3$  | 628                 |   | 962                    |

The shielding consisted of only heavy concrete or only standard concrete, except for the 2 kW proton beam, where the two materials were also combined.

<sup>a</sup>The desired effective dose for a proton beam power of 2 kW could be obtained either by combining 305 cm of heavy concrete plus 135 cm of standard concrete, or by using 394 cm of only heavy concrete or 591 cm of only standard concrete.

concrete and heavy concrete, respectively, required to maintain the effective dose at  $12 \mu\text{Sv h}^{-1}$  is displayed for the proton beam power varying from 2 kW to 20 MW.

#### 4.5.3. Lead or iron as high-energy neutron shield

Heavier elements, like lead, generally have high cross-sections for inelastic reactions of high-energy neutrons and can therefore be assumed to be an efficient shielding of high-energy neutrons. However, as the neutrons are attenuated, there is a considerable build-up of low-energy neutrons that will dominate the contributions to the effective dose. For this reason, lead could not be used as shielding alone, but might, if followed by a layer of some hydrogenous material, such as concrete, significantly improve the overall shielding properties. Iron is also a material known for having favourable shielding features, but with similar properties as lead of producing low-energy neutrons. The microscopic cross-sections for high-energy neutrons in iron are lower than in lead, but the atomic density is higher by a factor of 2.5. Therefore, iron can actually be expected to attenuate the high-energy neutrons more efficiently than lead.

In order to verify these assumptions and with the aim of providing a proposal of an improved

Table 8

Separate flux ( $\Phi$ ) and effective dose ( $E$ ) at the top of the biological shielding, with the 100 cm thick section of heavy concrete replaced by iron or lead. The 340 cm of standard concrete was not changed

|    | Neutrons                                   |                            | Photons                                    |                            | Protons                                    |                            | Total |
|----|--|----------------------------|--|----------------------------|--|----------------------------|-------|
|    | $\Phi$ (cm <sup>-2</sup> s <sup>-1</sup> ) | $E$ (μSv h <sup>-1</sup> ) | $\Phi$ (cm <sup>-2</sup> s <sup>-1</sup> ) | $E$ (μSv h <sup>-1</sup> ) | $\Phi$ (cm <sup>-2</sup> s <sup>-1</sup> ) | $E$ (μSv h <sup>-1</sup> ) |       |
| Fe | 21   | 21                         | 14   | 0.2                        | 0.2  | 1.9                        | 23    |
| Pb | 30   | 30                         | 18   | 0.3                        | 0.5  | 5.0                        | 36    |

biological shielding at the SAD facility, the effective dose was calculated with the 100 cm thick section of heavy concrete replaced by iron and lead, respectively. Indeed, it is shown in Table 8 that iron improves the shielding capacity more than lead, reducing the effective dose by more than a factor of 8, compared to the present shielding design. Other ways of improving the shielding capacity might be to combine layers of iron or lead with different types of hydrogenous materials.

## 5. Conclusions

The main objective of the present paper was to determine the effective dose above the biological shielding covering the upper part of the SAD core. The sub-critical core, loaded with fast-reactor MOX fuel, is driven by a 660 MeV proton beam of 3.0 μA current (2.0 kW), impinging on a spallation target of lead. The high-energy neutrons created in the spallation process are deeply penetrating in all shielding materials and constitute a major concern in shielding design studies. Consequently, the biological shielding around an ADS, even for those operating at comparatively low power, must be made thicker and much more efficient than those typically needed for critical reactors. In the present SAD design, the biological shielding consists of 100 cm of heavy concrete plus 340 cm of standard concrete.

In order to determine the effective dose, the fluxes of the particles leaking out through the top of the shielding were first calculated with the high-energy Monte Carlo code MCNPX. By combining appropriate fluence-to-effective dose conversion coefficients with the calculated fluxes, the effective

dose could then be obtained. The total effective dose at the centre of the top of the shielding was found to be about 190 μSv h<sup>-1</sup>. This dose is in agreement with the radiation protection regulations in Russia, provided that access by working personnel to this area is prohibited during operation. The major part of the dose is induced by neutrons (89%), whereas the rest by protons (10%) and photons (1%). The spectrum of the detected neutrons can be characterised by a thermal peak, an evaporation shoulder at a few MeV and a strong high-energy peak centred around 100 MeV. Since more than half of the neutrons have energy higher than 10 MeV and since the conversion coefficients increases with energy, the high-energy neutrons contribute for the major part of the effective dose.

The attenuation of the effective dose was studied as a function of shielding thickness. After the composite decay during the first tenths of cm in each concrete shielding material, the dose was found to decrease exponentially, following one exponential in the heavy concrete and one in the standard concrete. By fitting exponential functions to the calculated data points, the attenuation lengths were determined for the two concrete materials. These exponential functions were also used for estimating the extra amount of heavy and standard concrete needed to reduce the dose to the Russian limit for working personnel (12 μSv h<sup>-1</sup>) or to increase the proton beam power to values representative for a large-scale ADS without increasing the dose.

Moreover, the relative contributions to the effective dose from low-energy and high-energy neutrons that leak out from the reactor were determined. The fact that 100% of the dose

originates from neutrons with energy higher than 10 MeV, which are exclusively produced in the spallation target, shows that the effective dose at the top of the SAD shielding is directly proportional to the proton beam power and that it is independent of the total power and the reactivity of the sub-critical core. Finally, the heavy concrete in the biological shielding was replaced by lead and iron, in order to optimise the shielding of the high-energy neutrons. Of the two, it was found that iron is the most efficient shielding material, reducing the effective dose by a factor of 8, compared to the present shielding design.

## Acknowledgements

This work was partially supported by SKB AB (Swedish Nuclear Fuel and Waste Management Co) and the Swedish Centre for Nuclear Technology. The development of the SAD design is financed by the International Science and Technology Centre (ISTC).

## Appendix A

The dose conversion coefficients used in the study are shown in Table A.1

Table A.1

Effective dose per unit fluence ( $E/\Phi$ ) for neutrons, photons and protons (ISO geometry) used in the present study

| Neutrons     |                                 | Photons      |                                 | Protons      |                                 |
|--------------|---------------------------------|--------------|---------------------------------|--------------|---------------------------------|
| Energy (MeV) | $E/\Phi$ [pSv cm <sup>2</sup> ] | Energy (MeV) | $E/\Phi$ [pSv cm <sup>2</sup> ] | Energy (MeV) | $E/\Phi$ [pSv cm <sup>2</sup> ] |
| 1.E-09       | 2.40                            | 0.02         | 0.093                           | 10           | 20.6                            |
| 1.E-08       | 2.89                            | 0.05         | 0.21                            | 20           | 173.9                           |
| 2.5E-08      | 3.30                            | 0.1          | 0.31                            | 30           | 423.8                           |
| 1.E-07       | 4.13                            | 0.2          | 0.61                            | 50           | 1346.0                          |
| 2.E-07       | 4.59                            | 0.5          | 1.65                            | 100          | 2953.8                          |
| 5.E-07       | 5.20                            | 1            | 3.30                            | 150          | 4648.0                          |
| 1.E-06       | 5.63                            | 2            | 6.02                            | 200          | 4577.4                          |
| 2.E-06       | 5.96                            | 5            | 12.15                           | 300          | 3445.6                          |
| 5.E-06       | 6.28                            | 10           | 20.63                           | 500          | 2965.6                          |
| 1.E-05       | 6.44                            | 20           | 32.40                           |              |                                 |
| 2.E-05       | 6.51                            | 50           | 62.16                           |              |                                 |
| 5.E-05       | 6.51                            | 100          | 96.63                           |              |                                 |
| 1.E-04       | 6.45                            | 200          | 133.5                           |              |                                 |
| 2.E-04       | 6.32                            | 500          | 190.2                           |              |                                 |
| 5.E-04       | 6.14                            |              |                                 |              |                                 |
| 1.E-03       | 6.04                            |              |                                 |              |                                 |
| 2.E-03       | 6.05                            |              |                                 |              |                                 |
| 5.E-03       | 6.52                            |              |                                 |              |                                 |
| 0.01         | 7.70                            |              |                                 |              |                                 |
| 0.02         | 10.2                            |              |                                 |              |                                 |
| 0.03         | 12.7                            |              |                                 |              |                                 |
| 0.05         | 17.3                            |              |                                 |              |                                 |
| 0.07         | 21.5                            |              |                                 |              |                                 |
| 0.1          | 27.2                            |              |                                 |              |                                 |
| 0.15         | 35.2                            |              |                                 |              |                                 |
| 0.2          | 42.4                            |              |                                 |              |                                 |
| 0.3          | 54.7                            |              |                                 |              |                                 |
| 0.5          | 75.0                            |              |                                 |              |                                 |
| 0.7          | 92.8                            |              |                                 |              |                                 |
| 0.9          | 108                             |              |                                 |              |                                 |
| 1            | 116                             |              |                                 |              |                                 |
| 1.2          | 130                             |              |                                 |              |                                 |
| 2            | 178                             |              |                                 |              |                                 |
| 3            | 220                             |              |                                 |              |                                 |
| 4            | 250                             |              |                                 |              |                                 |
| 5            | 272                             |              |                                 |              |                                 |

Table A.1 (continued)

| Neutrons     |                                 | Photons      |                                 | Protons      |                                 |
|--------------|---------------------------------|--------------|---------------------------------|--------------|---------------------------------|
| Energy (MeV) | $E/\Phi$ [pSv cm <sup>2</sup> ] | Energy (MeV) | $E/\Phi$ [pSv cm <sup>2</sup> ] | Energy (MeV) | $E/\Phi$ [pSv cm <sup>2</sup> ] |
| 6            | 282                             |              |                                 |              |                                 |
| 7            | 290                             |              |                                 |              |                                 |
| 8            | 297                             |              |                                 |              |                                 |
| 9            | 303                             |              |                                 |              |                                 |
| 10           | 309                             |              |                                 |              |                                 |
| 12           | 322                             |              |                                 |              |                                 |
| 14           | 333                             |              |                                 |              |                                 |
| 15           | 338                             |              |                                 |              |                                 |
| 16           | 342                             |              |                                 |              |                                 |
| 18           | 345                             |              |                                 |              |                                 |
| 20           | 343                             |              |                                 |              |                                 |
| 30           | 356                             |              |                                 |              |                                 |
| 50           | 389                             |              |                                 |              |                                 |
| 100          | 412                             |              |                                 |              |                                 |
| 150          | 527                             |              |                                 |              |                                 |
| 200          | 526                             |              |                                 |              |                                 |
| 500          | 791                             |              |                                 |              |                                 |

The conversion coefficients for neutrons in the energy range from  $1 \times 10^{-9}$  to 20 MeV are taken from Ref. [8], while the coefficients for neutrons from 30 to 500 MeV, as well as all coefficients for photons and protons, are taken from Ref. [15].

## References

- [1] W. Gudowski, A. Polanski, I. V. Puzynin, V. Shvetsov, Monte Carlo modeling of a sub-critical assembly driven with the existing 660 MeV JINR proton accelerator, International Meeting AccApp'01, November 11–15, 2001, Reno, Nevada, USA, 2001.
- [2] ISTC Project 2267. <http://www.sad.dubna.ru>
- [3] M. Salvatores, et al., Nucl. Instr. and Meth. A 414 (1997) 5.
- [4] D. G. Foster, Review of PNL study on transmutation processing of high level waste, LA-UR-74-74, Los Alamos National Laboratory, 1974.
- [5] T. Takizuka, Conceptual design of transmutation plant, Proceedings of the Specialist Mtg. Accelerator Driven Transmutation Technology for Radwaste, LA-12205-C, Los Alamos National Laboratory, 1991, p.707.
- [6] L. S. Waters, MCNPX™ User's Manual—Version 2.1.5, Los Alamos National Laboratory, November 14, 1999.
- [7] International Commission on Radiation Protection, Conversion Coefficients for Use in Radiological Protection Against External Radiation, ICRP Publication 74, Pergamon Press, Oxford, 1997.
- [8] International Commission on Radiation Units and Measurements, Conversion coefficients for use in radiological protection against external radiation, ICRU Report 57, Bethesda, Maryland, 1998.
- [9] S. Leray, et al., Phys. Rev. C 65 (2002).
- [10] I. Koprivnikar, E. Schachinger, Nucl. Instr. and Meth. In Phys. Res. A 487 (2002) 571.
- [11] P. Seltborg, et al, Investigation of radiation fields outside the sub-critical assembly in Dubna, International Conference on Radiation Shielding ICRS-10, May 9–14, 2004, Funchal, Madeira Island, Portugal, 2004.
- [12] International Commission on Radiation Protection, Recommendations of the International Commission on Radiological Protection, ICRP Publication 60, Pergamon Press, Oxford, 1991.
- [13] W.S. Snyder, et al., Estimates of absorbed fractions for monoenergetic photon sources uniformly distributed in various organs of a heterogeneous phantom MIRD Pamphlet No. 5, Society of Nuclear Medicine, New York, 1969.
- [14] R. Kramer, et al., The Calculation of Dose from External Photon Exposures Using Reference Human Phantoms and Monte Carlo Methods. Part I: The Male (ADAM) and Female (EVA) Adult Mathematical Phantoms, GSF-Bericht S-885, Gesellschaft für Strahlen-und Umweltforschung mbH, 1982.
- [15] V. Mares, H. Schraube, The effect of the fluence to dose conversion coefficients upon the dose estimation to cosmic radiation, Expert Group on Shielding Aspects of Accelerators, Targets and Irradiation Facilities (Sixth Meeting—SATIF-6), April 10–12, 2002, Menlo Park, USA, 2002.
- [16] M. Pelliccioni, Radiat. Prot. Dosim. 88 (2000) 279.



- [17] Internal SAD document at the Joint Institute for Nuclear Research (JINR).
- [18] M. B. Chadwick, et al., Nucl. Sci. Eng., Los Alamos National Laboratory LA-UR-98-1825, 1998, submitted for publication.
- [19] H.W. Bertini, Phys. Rev. 131 (1963) 1801.
- [20] H.W. Bertini, Phys. Rev. 188 (1969) 1711.
- [21] J.K. Shults, R.E. Faw, Radiation Shielding, Prentice-Hall, PTR, Upper Saddle River, NJ, 1996.

# Proton Source Efficiency for Heterogeneous Distribution of Actinides in the Core of an Accelerator-driven System

Per Seltborg\* and Jan Wallenius  
Department of Nuclear and Reactor Physics  
Albanova University Centre, Royal Institute of Technology  
S-106 91 Stockholm, Sweden

**Abstract** – The distribution of actinides in the core of an accelerator-driven system (ADS) loaded with plutonium, americium and curium has been studied in order to optimise the proton source efficiency,  $\psi^*$ . One of the basic assumptions of the study, that the actinide composition in the inner part of the core is of much larger importance for the magnitude of  $\psi^*$  than in the rest of the core, has been confirmed. It has been shown that the odd-N nuclides in general and  $^{241}\text{Am}$  and  $^{244}\text{Cm}$  in particular have favourable properties in respect of improving  $\psi^*$  if they are placed in the innermost part of the core. The underlying reason for this phenomenon is that the energy spectrum of the source neutrons in the inner part of the core is harder than that of the average fission neutrons. Moreover, it has been shown that loading the inner part of the core with only curium increases  $\psi^*$  by about 7%. Plutonium, on the other hand, in particular high-quality plutonium consisting mainly of  $^{239}\text{Pu}$  and  $^{241}\text{Pu}$ , was found to be a comparatively source inefficient element and is preferably located in the outer part of the core. The differences in  $\psi^*$  are due to combined effects from relative changes in the average fission and capture cross-sections and in the average fission neutron yield.

## I. INTRODUCTION

Transmutation of plutonium and minor actinides in accelerator-driven systems (ADS)<sup>1-5</sup> is being envisaged for the purpose of reducing the long-term radiotoxic inventory of spent nuclear reactor fuel. In ADS, a sub-critical core is coupled to a high-power proton beam, impinging on a target of heavy metal and thereby generating a large number of neutrons via spallation reactions. The produced spallation neutrons leak out from the target, thus providing the surrounding sub-critical core with a strong external neutron source.

One of the objectives when designing an ADS, given that  $k_{\text{eff}}$  is fixed by safety limitations, is to try to attain as high power as possible to be produced in the core, using as low proton beam power as possible. Since the construction of a reliable high-power proton accelerator is a difficult technical task and its operation is very expensive, the optimisation of the efficiency of the source protons could have an important impact on the overall design of a future ADS. In order to study the beam power amplification, i.e. the core power divided by the proton beam power, a new parameter, the proton source efficiency,  $\psi^*$ , was introduced in a previous

study<sup>6</sup>.  $\psi^*$  represents the average importance of the external proton source, relative to the average importance of the fundamental mode fission neutrons. It is closely related to the neutron source efficiency  $\phi^{*7,8}$ , but connects the core power directly to the source protons instead of to the source neutrons.  $\phi^*$  is commonly used in the physics of sub-critical systems, driven by any external neutron source (spallation source, (d,d), (d,t),  $^{252}\text{Cf}$  spontaneous fission etc.).  $\psi^*$ , on the other hand, has been defined for systems driven by a proton-induced spallation source only. The main advantages with using  $\psi^*$  instead of  $\phi^*$  are that the way of defining the external source is unique and that  $\psi^*$  is directly proportional to the beam power amplification. It has been shown in previous studies that the source efficiency can vary considerably for different reactor cores<sup>6,9-10</sup>. Studying  $\psi^*$  for various system parameters is therefore of interest when designing an ADS.

In the following, it will be shown that the proton source efficiency is dependent on how the actinides are distributed in the core. In particular curium, if it is placed around the spallation target in the innermost part of the core, has some favourable properties that enhance  $\psi^*$ . Four different triple-zone configurations, with the actinides distributed differently, have been studied in terms of  $\psi^*$ . Three major factors

---

\* E-mail: per@neutron.kth.se

affecting  $\psi^*$  - the macroscopic fission and capture cross-sections and the average fission neutron yield - have been analysed in detail. Finally, one of the basic assumptions of the study, that  $\psi^*$  is sensitive to the actinide composition mainly in the innermost part of the core, has been confirmed.

## II. SOURCE EFFICIENCY

### II.A. Proton Source Efficiency

The proton source efficiency is defined in analogy with the definition of  $\phi^{*6,11}$  and can be expressed in terms of the k-eigenvalue,  $k_{eff}$ , and the total number of neutrons produced by fission in the core for each source proton,  $\langle F\phi_s \rangle / \langle S_p \rangle$ , according to

$$\psi^* = \left( \frac{1}{k_{eff}} - 1 \right) \cdot \frac{\langle F\phi_s \rangle}{\langle S_p \rangle}. \quad (1)$$

The brackets imply integration over space, angle and energy. Since  $\langle F\phi_s \rangle$  is approximately proportional to the total power produced in the core, for a given  $k_{eff}$ ,  $\psi^*$  is thus proportional to the core power divided by the proton beam power. Since  $\psi^*$  is also equal to the product of  $\phi^*$  and the number of source neutrons generated per source proton,  $Z$ , we have the following relation between the *proton* source efficiency and the *neutron* source efficiency;

$$\psi^* = \phi^* \cdot Z. \quad (2)$$

For a fixed system (constant  $Z$ ), it follows that  $\psi^*$  is proportional to  $\phi^*$ . However, when studying a change in a system design,  $Z$  may change. Therefore, in such a case, only  $\psi^*$  (not  $\phi^*$ ) remains proportional to the ratio between the core power and the proton beam power.

Nevertheless, in order to analyse the efficiency of the source protons, it is often useful to study also the efficiency of the source neutrons and their multiplication in the fuel. However, it is not always evident which way is the most appropriate to define the source neutrons in order to be able to determine  $\phi^*$ . Several different source definitions are possible and they will result in different meanings and values of  $\phi^{*10,12-13}$ . In the present paper, when referring to the source neutrons or the neutron source efficiency, the definition of the target neutron leakage source has been adopted<sup>6,14-15</sup>, which is the collection of the spallation neutrons that leak out radially from the target. In the following study, the properties of the proton beam and the spallation target are fixed, and consequently also the distribution of the source neutrons at the target surface. Thus,  $Z$  is constant and  $\psi^*$  will in all cases be proportional to  $\phi^*$ .

### II.B. Neutron Importance

In analogy with  $\psi^*$ , the neutron source efficiency represents the average importance of the source neutrons over the average importance of the fission neutrons in the k-eigenvalue fundamental mode. The importance of a neutron in a system can be described analytically by determining the adjoint function,  $\phi^*(\mathbf{r}, \boldsymbol{\Omega}, E)$ , which is dependent on the position, direction and energy of the neutron. The adjoint function, or the adjoint flux, is proportional to the response of a source neutron in a detector located at a certain position in the core. In other words, it is a measure of the importance of a neutron in contributing to the response of the detector, and consequently also to the total neutron flux in the core. Considering the source neutrons that leak out radially from the spallation target and enter into the core, it can therefore be assumed that the average importance of these neutrons will be different from the average importance of the fission neutrons, since they are emitted at different positions, in different directions and with different energy distributions than are the fission neutrons. Thus, the efficiency of the source neutrons can be expected to differ from unity, i.e.  $\phi^* \neq 1$ .

When changing the composition of actinides in the innermost part of the core, the multiplicative conditions for both the source neutrons and the fission neutrons will change, mainly due to the differences in the cross-sections and in fission neutron yield between different nuclides. The change in the source efficiency is dependent on whether the actinide substitution in the core changes the importance of the source neutrons more than the importance of the fission neutrons or not. If the importance of the source neutrons increases more than that of the fission neutrons, the source efficiency will increase, and vice versa. Since cross-sections and fission neutron yield are affected mainly by the energy of the neutrons, the major cause for the source efficiency to change is therefore if the energy distributions of the source neutrons and the fission neutrons differ, which is generally the case.

## III. SYSTEM MODELLING

In the present work, the proton source efficiency is studied using a core model from a previous work, where different neutronic properties of a lead-bismuth-cooled ADS with minor actinide-based fuels were investigated<sup>16</sup>. A map of the core model is displayed in Fig. 1. In order to achieve an acceptably flat radial power profile, the core was divided into three different fuel zones. The total amount of subassemblies, separated by a pitch of 10 cm, is 246, of which 42 are contained in zone 1, 108 in zone 2 and 96 in zone 3. Each fuel subassembly contains 91 fuel rods. 19 fuel subassemblies were removed to make room for the spallation target of

lead-bismuth-eutectic (LBE), having an outer radius of 21 cm. The axial impact position of the proton beam was set to 18 cm above the core mid-plane in order to make the density of the emerging neutrons maximal at the centre of the core, thereby optimising the efficiency of the source protons. The 1000 MeV proton beam, characterised by a Gaussian spatial distribution with a full-width half-maximum of 7.5 cm, was guided towards the spallation target through a vacuum beam tube of 15 cm radius. The core was designed to operate at a maximal power of 800 MWth. All simulations performed in the present study were made with the continuous high-energy Monte Carlo code MCNPX<sup>17</sup> (version 2.5.e), using the JEFF-3.0 nuclear data library. The high-energy physics package used by MCNPX was the Cascade-Exciton Model<sup>18</sup>.

Although the main purpose of an ADS is to transmute the minor actinides, a certain amount of plutonium has to be added to the fuel for reactivity management. Setting the plutonium fraction to 40% minimises the burnup reactivity swing when approaching equilibrium<sup>19</sup>. For the start-up core here studied, a plutonium vector corresponding to spent LWR/MOX fuel is adopted. The relative fractions of americium and curium were set to 5/1, corresponding to their concentration in spent LWR fuel<sup>20</sup>. The actinide vectors are listed in Table I.

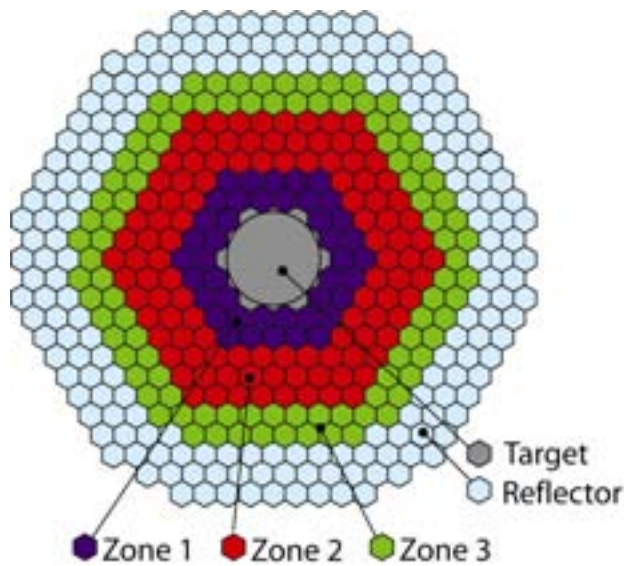


Fig. 1. Horizontal cross-sectional view of the studied model. The target radius is 21 cm and the subassembly pitch is 10 cm.

TABLE I  
Relative Atomic Fraction of Actinides in the Fuel.

| Relative Atomic Fraction of Actinides in the Fuel. |     |
|--|-----|
| Plutonium  | 40% |
| <sup>238</sup> Pu                                  | 5%  |
| <sup>239</sup> Pu                                  | 38% |
| <sup>240</sup> Pu                                  | 30% |
| <sup>241</sup> Pu                                  | 13% |
| <sup>242</sup> Pu                                  | 14% |
| Americium  | 50% |
| <sup>241</sup> Am                                  | 67% |
| <sup>243</sup> Am                                  | 33% |
| Curium   | 10% |
| <sup>244</sup> Cm                                  | 87% |
| <sup>245</sup> Cm                                  | 13% |

Four different configurations with different geometrical distributions of the actinides were studied. In the first configuration, the same relative fractions of the actinides (Pu/Am/Cm = 0.4/0.5/0.1) in all three zones were used. In the second configuration, all of the americium in zone 1 was moved to the two outer zones and was replaced by curium. In the last two configurations, zone 1 was loaded with one element only, plutonium in configuration III and curium in configuration IV. The relative fractions of actinides in the core in total were unchanged. The relative fractions of actinides in zone 1 for the four studied configurations are listed in Table II. As will be shown below, the actinide composition of the inner zone has the largest effect on the proton source efficiency, whereas the compositions in the middle and the outer zones are of minor importance from this point of view. For this reason, the analyses presented in this paper focus on zone 1.

The nitride fuels were mixed with an inert matrix consisting of ZrN. Both the fractions of inert matrix in the three zones and the relative compositions of the actinides in zone 2 and zone 3 were adjusted in order to obtain a level of sub-criticality ( $k_{eff} \sim 0.97$ ) and a radial core power profile similar for all four configurations. The relative fractions of inert matrix in zone 1 for all configurations are displayed in Table II. The obtained power peaking factors, i.e. the maximal pin power over the average pin power, in zone 1 and 2 were close to 1.3 ( $\pm 0.02$ ) for all configurations, whereas it was slightly lower in zone 3. The radial power profile, relative to the average pin power, for one of the configurations is depicted in Fig. 2. The fact that the radial power profile, in particular in zone 1, is the same for all configurations is an important criterion for this study, since the source efficiency is dependent on the fission rate in zone 1. A higher power peaking factor in the inner part of the core is directly con-

nected to an increase in  $\psi^*$ . Preliminary calculations show that increasing the power peaking factor in zone 1 by  $\sim 10\%$  increases  $\psi^*$  by  $\sim 5\%$ . The systematic errors of the  $\psi^*$ -results introduced by the small differences in the power profile between the different configurations are estimated to be in the order of 1%.

It is seen in Table II that, when the americium is removed from the fuel in zone 1, the relative fraction of inert matrix needs to be increased in order to avoid an increase of the power peaking factor in this zone. The explanation for this is the higher fission probability for plutonium and curium (in particular for plutonium) than for americium, which increases the fission rate for the americium-free zones. Since plutonium has the largest fission probability, the matrix fraction is the highest in configuration III, where zone 1 contains plutonium only.

TABLE II

Relative Atomic Fraction of Actinides and Relative Volume Fraction of Inert Matrix (ZrN) in Zone 1 for the Four Studied Configurations.

| Configuration                   | I   | II  | III  | IV   |
|---------------------------------|-----|-----|------|------|
| Atomic fraction of actinides    |     |     |      |      |
| Pu                              | 40% | 40% | 100% | 0%   |
| Am                              | 50% | 0%  | 0%   | 0%   |
| Cm                              | 10% | 60% | 0%   | 100% |
| Volume fraction of inert matrix |     |     |      |      |
| ZrN                             | 59% | 75% | 82%  | 68%  |

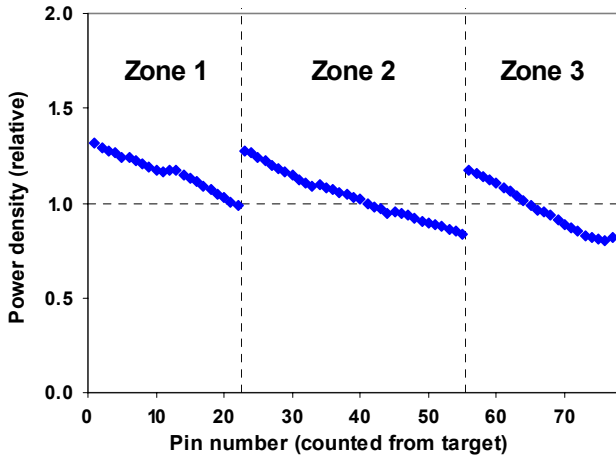


Fig. 2. Radial power profile relative to the average pin power for configuration III.

## IV. RESULTS

The main purpose of the present paper has been to investigate the impact on the proton source efficiency for different heterogeneous distributions of the actinides in the core. It has been found that, compared to configuration I, where the relative fractions of actinides were the same in all three zones, by removing all americium from zone 1 and replacing it by curium (configuration II),  $\psi^*$  increases slightly ( $\sim 3\%$ ). On the other hand, loading zone 1 with plutonium only (configuration III) tends to decrease  $\psi^*$  somewhat ( $\sim 1\%$ ), while loading it with curium only (configuration IV) increases  $\psi^*$  considerably ( $\sim 7\%$ ). The obtained values of  $\psi^*$  are displayed in Table III. The statistical uncertainty of the results, corresponding to  $1\sigma$ , was about 0.6% ( $\sim 0.20$ ) for all configurations. Including also the systematic error due to the small differences in the power profile, the total uncertainty is estimated to be in the order of 1-2%. Hence, the small decrease in  $\psi^*$  observed for configuration III is clearly within the statistical uncertainty.

Moreover, the number of source neutrons leaking out radially from the target (Z), i.e. the constant ratio between  $\psi^*$  and  $\phi^*$  was found to be 25.4.

TABLE III

Proton Source Efficiency,  $\psi^*$ , for the Four Studied Configurations, followed by the Relative Differences of Configuration II, III and IV Compared to Configuration I, i.e.  $(\psi^*_{i} - \psi^*_{I}) / \psi^*_{I}$ .

| Configuration | $\psi^*$ | Relative difference |
|---------------|----------|---------------------|
| I             | 31.2     |                     |
| II            | 32.0     | 3%                  |
| III           | 30.8     | -1%                 |
| IV            | 33.4     | 7%                  |

## V. ANALYSIS

### V.A. General Assumptions

#### V.A.1. Source Neutrons Relative Fission Neutrons

The basic reason for a substitution of actinides leading to a change in the source efficiency is that there is a difference in energy spectrum between the fission neutrons and the source neutrons. When the composition of nuclides in the inner part of the core changes, the spectrum differences may affect the neutronic properties in such a way that the change in importance is different for the source neutrons than for the fission neutrons. If the two energy spectra would be identical, on the other hand, the source neutrons and the fission

neutrons would experience the same change. Therefore, the substitution of actinides would change the importances in similar ways, thus not affecting the efficiency of the source neutrons. In the present analysis, the three main effects arising from the differences in energy spectrum that affect the source efficiency have been studied. The first two effects arise from changes in the flux-weighted average macroscopic fission and capture cross-sections,  $\bar{\Sigma}_f$  and  $\bar{\Sigma}_c$ , in zone 1 and the third effect arise from a change in the average fission neutron yield in zone 1,  $\bar{\nu}_z$ .

In order to analyse the reasons for the differences in  $\psi^*$  for the different configurations, the energy spectra of the fission neutrons and the source neutrons have first been compared. Then, the flux-weighted average macroscopic cross-sections have been determined for the different configurations. An increase in the relative difference in  $\bar{\Sigma}_f$  between the source neutrons and the fission neutrons would indicate an increase in source efficiency and vice versa for  $\bar{\Sigma}_c$ . A similar analysis has then been performed for  $\bar{\nu}_z$ . Also in this case, an increase in the relative difference between the values for the source neutrons and the fission neutrons would indicate an increase in source efficiency.

#### V.A.2. Emphasis on Zone 1

The source neutrons have been analysed by tracking the spallation neutrons from the moment they enter into the inner core zone until they are absorbed or leak out from this zone. Only the primary source neutrons, i.e. those neutrons entering into the core from the target surface, are tracked. Thus, those neutrons created inside zone 1 (mainly by fission) and those neutrons re-entering from zone 2 are not taken into account. The average properties of these primary source neutrons in zone 1 are registered, constituting the basis for the following analyses of the energy spectrum, the cross-sections and the neutron fission yield. Concerning the fission neutrons, they are studied by simulating the k-eigenvalue fundamental mode of the system and registering their average properties in zone 1.

The properties of the fission neutrons and the source neutrons have been studied and compared in zone 1 only. This assumption is intuitively justified for the source neutrons, as this is the zone where they enter into the core. Concerning the fission neutrons, on the other hand, in a formally correct analysis, the importance of the fission neutrons in all three zones should be taken into account. However, the average importance of the fundamental mode fission neutrons in the whole core will not change between the different configurations, since the reactivity of the system was fixed. Neither will the average importance of the fission neutrons in zone 1 vary between the studied configurations, since the spatial profile of the neutron flux and the core power in the fundamental mode were also fixed. In other words, the fission rate will be the same in zone 1 for all four configura-

tions. Therefore, a comparison of the properties of the source neutrons and the fission neutrons in zone 1 is an appropriate approach for estimating the effects on the source efficiency that changes in the actinide distribution may induce.

#### V.B. Energy Spectra

The neutron energy spectra in zone 1 have been calculated for the fission neutrons and the source neutrons for all configurations. The spectra in zone 1 for configuration II, III and IV, which are free from americium, are almost identical to each other, both for the fission neutrons and the source neutrons. For configuration I, the spectrum is slightly softer below  $\sim 10$  keV than for the other configurations, but otherwise also very similar. This difference arises because of the higher capture cross-sections for the americium isotopes in this energy range.

In Fig. 3, the spectra of the source neutrons and the fission neutrons in zone 1 are depicted for configuration I. It is seen that the source neutron spectrum is shifted towards higher energies in the entire energy range, except in a small region between about 2 and 6 MeV. Naturally, the high-energy tail is only present for the source neutrons. Comparing the different configurations, it can thus be expected that  $\bar{\Sigma}_f$ ,  $\bar{\Sigma}_c$  and  $\bar{\nu}_z$  in zone 1 will change in different ways for the source neutrons and the fission neutrons, which in turn may affect the magnitude  $\psi^*$ .

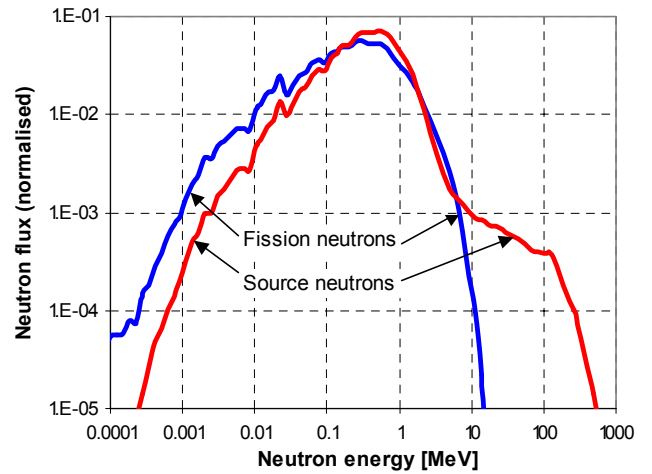


Fig. 3. Energy spectra for the source neutrons and the fission neutrons in zone 1 for configuration I.

#### V.C. Cross-sections

##### V.C.1. Microscopic Cross-sections

In order to study the effects induced by the differences in energy spectrum, the flux-weighted average microscopic

fission and capture cross-sections for individual nuclides,  $\bar{\sigma}_f$  and  $\bar{\sigma}_c$ , have been calculated, according to

$$\bar{\sigma}_{x,i} = \frac{\int \sigma_{x,i}(E) \cdot \phi(E) dE}{\int \phi(E) dE}, \quad (3)$$

where the indices  $x$  and  $i$  represent the type of reaction and the respective nuclide.  $\sigma_{x,i}(E)$  is the microscopic cross-section and  $\phi(E)$  is the neutron flux.  $\bar{\sigma}_f$  and  $\bar{\sigma}_c$  have been calculated for the source neutrons and for the fission neutrons in zone 1, for all nuclides and for all configurations. Since the neutron energy spectrum is harder for the source neutrons than for the fission neutrons,  $\bar{\sigma}_f$  is higher for the even-N nuclides (those nuclides with even number of neutrons) and vice versa for the odd-N nuclides, which is shown in Table IV. The typical energy dependence of  $\sigma_f$  for an

even-N nuclide is characterised by a rapid increase within the energy region between about 0.1 and 1 MeV. On the other hand, for the odd-N nuclides,  $\sigma_f$  is generally a decreasing function with energy, which explains the lower values for the source neutrons than for the fission neutrons. The typical energy dependence of  $\sigma_c$  for all fissile nuclides describes a continually decreasing function with energy. Therefore,  $\bar{\sigma}_c$  is considerably lower for the source neutrons than for the fission neutrons for all of the present nuclides. The largest relative difference is observed for  $^{239}\text{Pu}$ .

In Table IV, the values of  $\bar{\sigma}$  have been listed for configuration I only. However, these values are representative for all configurations, as there are only minor differences between the configurations.

TABLE IV

Flux-weighted Average Microscopic Fission and Capture Cross-sections,  $\bar{\sigma}_f$  and  $\bar{\sigma}_c$  [barn], for each Nuclide Present in the Core, in Zone 1 for Configuration I. The relative differences between the values for the source neutrons and the fission neutrons,  $(\bar{\sigma}^{source} - \bar{\sigma}^{fission}) / \bar{\sigma}^{fission}$ , are also displayed.

| Nuclide           | $\bar{\sigma}_f$ |                 |                     | $\bar{\sigma}_c$ |                 |                     |
|-------------------|------------------|-----------------|---------------------|------------------|-----------------|---------------------|
|                   | Fission neutrons | Source neutrons | Relative difference | Fission neutrons | Source neutrons | Relative difference |
| $^{238}\text{Pu}$ | 1.23             | 1.28            | 4%                  | 0.42             | 0.29            | -31%                |
| $^{239}\text{Pu}$ | 1.70             | 1.64            | -4%                 | 0.37             | 0.22            | -40%                |
| $^{240}\text{Pu}$ | 0.41             | 0.50            | 22%                 | 0.41             | 0.28            | -31%                |
| $^{241}\text{Pu}$ | 2.25             | 1.93            | -14%                | 0.39             | 0.29            | -25%                |
| $^{242}\text{Pu}$ | 0.31             | 0.40            | 27%                 | 0.38             | 0.25            | -35%                |
| $^{241}\text{Am}$ | 0.29             | 0.35            | 22%                 | 1.60             | 1.20            | -25%                |
| $^{243}\text{Am}$ | 0.22             | 0.27            | 24%                 | 1.36             | 0.96            | -30%                |
| $^{244}\text{Cm}$ | 0.48             | 0.61            | 27%                 | 0.44             | 0.33            | -25%                |
| $^{245}\text{Cm}$ | 2.37             | 2.06            | -13%                | 0.29             | 0.23            | -23%                |

### V.C.2. Macroscopic Cross-sections

The macroscopic cross-section represents the probability per unit path length for a reaction to occur in a medium and is of interest for the analysis of the source efficiency. In particular the fission probability in the inner part of the core is of large importance for the magnitude of  $\psi^*$ . Since the first fission reaction induced by a source neutron, generally occurring in the inner part of the core, is the starting point of each fission multiplication chain in the fuel, and since the source efficiency is proportional to the total number of neutrons produced by fission in the core, the larger probability of the first fission to occur, the larger is the expected value of  $\psi^*$ . After the first fission, on the other hand, the multiplication in the core is to a much higher extent determined by the fundamental mode of the core. The importance of the second-

dary source neutrons, i.e. those emitted in the fission reactions induced by the primary source neutrons, is similar to the average importance of all fission neutrons, which does not change between the different configurations. Analogously, a lower probability for capture of the primary source neutrons in zone 1 also enhances the overall neutron production, as well as the source efficiency. However, as was mentioned above, the effect on the source efficiency is not determined directly by the absolute macroscopic cross-sections for the source neutrons, but by the ratio of the reaction probabilities for the source neutrons over those for the fission neutrons.

The flux-weighted average macroscopic cross-sections,  $\bar{\Sigma}_x$ , have been calculated in zone 1 for each of the studied configurations, according to

$$\bar{\Sigma}_x = \sum_i (\bar{\sigma}_{x,i} \cdot n_i), \quad (4)$$

where  $n_i$  is the atomic density of nuclide  $i$ . It is seen in Table V that, in zone 1 in configuration I,  $\bar{\Sigma}_f$  is higher by about 4% for the source neutrons than for the fission neutrons. For configuration II, III and IV, the relative differences are about 0%, -7% and 6%, respectively. The reason for the significantly lower  $\bar{\Sigma}_f$  for the source neutrons for configuration

III, in which zone 1 consist of plutonium only, is that the major contribution to  $\bar{\Sigma}_f$  come from the odd-N nuclides  $^{239}\text{Pu}$  and  $^{241}\text{Pu}$ , which have lower  $\bar{\sigma}_f$  for the source neutrons. About 51% of the plutonium consists of those two isotopes, but as  $\sigma_f$  is much higher than for the other plutonium isotopes, they induce almost 80% of the fission events. On the contrary, for configuration IV, the mixture of  $^{244}\text{Cm}$  and  $^{245}\text{Cm}$  yields a clearly higher  $\bar{\Sigma}_f$  for the source neutrons than for the fission neutrons.

TABLE V  
Macroscopic Fission and Capture Cross-sections,  $\bar{\Sigma}_f$  and  $\bar{\Sigma}_c$  [ $10^{-3} \text{ cm}^{-1}$ ], in Zone 1 for all Configurations followed by the Relative Differences  $(\bar{\Sigma}^{\text{source}} - \bar{\Sigma}^{\text{fission}}) / \bar{\Sigma}^{\text{fission}}$ .

| Configuration | $\bar{\Sigma}_f$ |                 |                     | $\bar{\Sigma}_c$ |                 |                     |
|---------------|------------------|-----------------|---------------------|------------------|-----------------|---------------------|
|               | Fission neutrons | Source neutrons | Relative difference | Fission neutrons | Source neutrons | Relative difference |
| I             | 7.4              | 7.7             | 4%                  | 11.0             | 8.0             | -27%                |
| II            | 6.3              | 6.3             | 0%                  | 4.1              | 2.8             | -32%                |
| III           | 6.4              | 5.9             | -7%                 | 3.4              | 2.1             | -38%                |
| IV            | 6.1              | 6.5             | 6%                  | 4.7              | 3.4             | -28%                |

$\bar{\Sigma}_c$  was found to be considerably lower for the source neutrons than for the fission neutrons for all configurations, which is expected since the same differences were observed for  $\bar{\sigma}_c$  for all of the separate nuclides. The largest differences were observed for configuration II and III.

The fact that  $\bar{\Sigma}_f$  in zone 1 for configuration III is lower for the source neutrons than for the fission neutrons, while they are similar or higher for the other configurations, is one of the reasons contributing to the unchanged (or slightly lower)  $\nu^*$  for this configuration. Similarly, the highest relative difference for configuration IV partly explains the larger  $\nu^*$  observed in this case. On the other hand, there is also the effect from the smaller  $\bar{\Sigma}_c$  for the source neutrons in configuration III that compensates partially for the other two effects.

Comparing the absolute values of  $\bar{\Sigma}_f$  for the different configurations, it was found that it is somewhat lower for configuration II, III and IV than for configuration I, both for the fission neutrons and for the source neutrons. This is mainly due to the higher relative matrix fractions used in these cases.  $\bar{\Sigma}_c$ , on the other hand, decreases considerably for configurations II, III and IV. One of the reasons for this is again the higher relative matrix fractions. However, the main effect comes from the removal of americium. In configuration I, americium contributes for more than 75% of  $\bar{\Sigma}_c$  and  $^{241}\text{Am}$  alone for about 55%.

## V.D. Fission Neutron Yield

### V.D.1. Energy Dependence of the Fission Neutron Yield

A large fraction of the fission reactions in the even-N nuclides, particularly in  $^{241}\text{Am}$  and  $^{244}\text{Cm}$ , is induced by neutrons with comparatively high energy ( $\sim 1$  MeV or higher). The explanation is that  $\sigma_f$  for these nuclides is very low up to energies of  $\sim 0.1$  MeV, after which it increases rapidly to a maximum at about 1 MeV.  $\sigma_c$ , on the other hand, decreases continuously with the energy for all of the studied nuclides in this energy range. Thus, the relative fission probability, i.e.  $\sigma_f / (\sigma_f + \sigma_c)$ , for the even-N nuclides increase from close to zero below 0.1 MeV to close to 1 above 1 MeV, which is illustrated for  $^{241}\text{Am}$  and  $^{244}\text{Cm}$  in Fig. 4. For  $^{239}\text{Pu}$ , on the other hand, as for the other odd-N nuclides, the relative fission probability is high already at low energies and the major part of the fission events are induced by neutrons in the energy range where the neutron flux is maximal, i.e. between  $\sim 0.1$  MeV and  $\sim 1.0$  MeV.



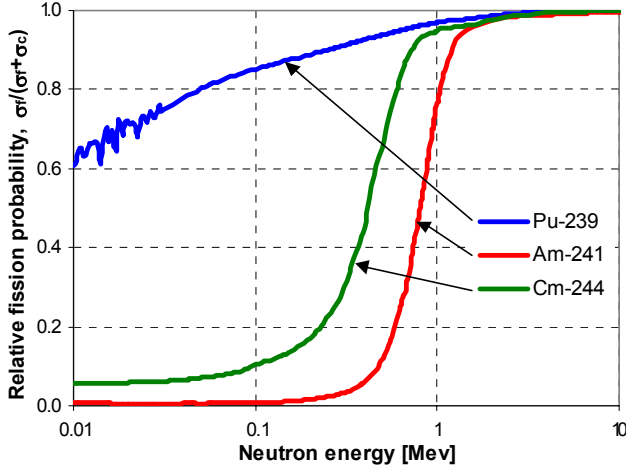


Fig. 4. Microscopic fission cross-section over total microscopic absorption cross-section,  $\sigma_f/(\sigma_f + \sigma_c)$ , as a function of neutron energy for  $^{239}\text{Pu}$ ,  $^{241}\text{Am}$  and  $^{244}\text{Cm}$  (JEFF-3.0).

The average number of neutrons emitted in a fission reaction,  $\nu$ , is a nearly linearly increasing function of the energy of the incident neutron for all fissile nuclides and can in general be described by the following relation;

$$\nu(E) = \nu_0 + aE, \quad (5)$$

where  $\nu_0$  and  $a$  are constants determined experimentally for each nuclide. In Fig. 5, where  $\nu$  is plotted for  $^{239}\text{Pu}$ ,  $^{241}\text{Am}$  and  $^{244}\text{Cm}$  as a function of neutron energy, it can be seen that the fissioning at higher energies of the even-N nuclides will lead to a higher average fission neutron yield,  $\bar{\nu}_n$ , for these nuclides.  $\bar{\nu}_n$  has been calculated as the average value of  $\nu$  for all fission reactions in zone 1 of a particular nuclide. The other nuclides, such as  $^{239}\text{Pu}$ , are apparently less sensitive to the energy dependence of  $\nu$ , since the major part of the fission reactions are induced by neutrons with energy lower than 1 MeV. This phenomenon can also be understood by comparing the values of  $\nu$  for fission reactions induced by thermal neutrons ( $\nu = \nu_0$ ) with the obtained values of  $\bar{\nu}_n$ . In Table VI, it is shown that, for most of the even-N nuclides,  $\bar{\nu}_n$  is considerably higher than  $\nu_0$ .  $\bar{\nu}_n$  is particularly high for  $^{241}\text{Am}$  and  $^{244}\text{Cm}$ , whereas the smallest differences are observed for the odd-N nuclides  $^{239}\text{Pu}$ ,  $^{241}\text{Pu}$  and  $^{245}\text{Cm}$ . The  $\bar{\nu}_n$ -values of 3.59 and 3.47 for  $^{241}\text{Am}$  and  $^{244}\text{Cm}$  for the fission neutrons correspond to the average energies of 1.65 MeV and 1.25 MeV, respectively, while  $\bar{\nu}_n = 2.95$  for  $^{239}\text{Pu}$  corresponds to 0.49 MeV. Thus, the assumption that the even-N nuclides are fissioned by neutrons with higher average energy than the odd-N nuclides is confirmed.

Since the spectrum of the source neutrons in zone 1 is harder than that of the fission neutrons,  $\bar{\nu}_n$  can moreover be expected to be higher for the former, which was indeed

found to be the case. In analogy with the discussion above, the hardening of the spectrum increases  $\bar{\nu}_n$  particularly much for  $^{241}\text{Am}$  and  $^{244}\text{Cm}$  (by 13% and 12%, respectively). The values of  $\bar{\nu}_n$  for the source neutrons for these two nuclides (4.05 and 3.89) correspond to energies as high as 4.5 MeV and 3.5 MeV, respectively, whereas for  $^{239}\text{Pu}$ ,  $\bar{\nu}_n = 2.99$  corresponds to the comparatively low energy of 0.77 MeV. Apart from the effect of the overall harder spectrum of the source neutrons, the high-energy tail above 10 MeV has a larger effect on the even-N nuclides than on the odd-N. Since only a minor fraction of all fission events is induced by neutrons below  $\sim 1$  MeV in this case, the relative fraction of fissions induced by neutrons with energy above  $\sim 10$  MeV is therefore considerably larger than for the odd-N nuclides.

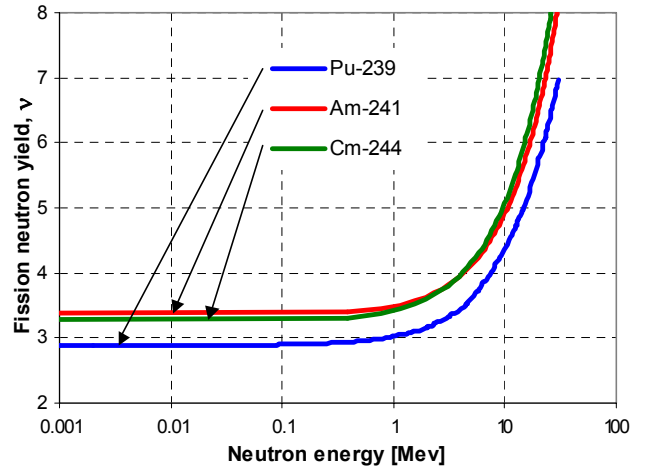


Fig. 5. Average number of neutrons emitted in a fission reaction,  $\nu$ , as a function of neutron energy for  $^{239}\text{Pu}$ ,  $^{241}\text{Am}$  and  $^{244}\text{Cm}$  (JEFF-3.0).

TABLE VI

Average Value of  $\nu$  for all Fission Reactions in Zone 1 of a Particular Nuclide,  $\bar{\nu}_n$ , for Configuration I, followed by the Relative Differences  $(\bar{\nu}_n^{source} - \bar{\nu}_n^{fission})/\bar{\nu}_n^{fission}$ . The values of  $\nu$  for thermal neutrons ( $\nu_0$ ) are also displayed (JEFF-3.0).

| Nuclide           | $\bar{\nu}_n$    |                 |                     | $\nu_0$ |
|-------------------|------------------|-----------------|---------------------|---------|
|                   | Fission neutrons | Source neutrons | Relative difference |         |
| <sup>238</sup> Pu | 2.99             | 3.05            | 2%                  | 2.89    |
| <sup>239</sup> Pu | 2.95             | 2.99            | 2%                  | 2.88    |
| <sup>240</sup> Pu | 2.97             | 3.04            | 3%                  | 2.78    |
| <sup>241</sup> Pu | 2.98             | 3.00            | 1%                  | 2.93    |
| <sup>242</sup> Pu | 3.10             | 3.18            | 3%                  | 2.86    |
| <sup>241</sup> Am | 3.59             | 4.05            | 13%                 | 3.33    |
| <sup>243</sup> Am | 3.36             | 3.53            | 5%                  | 3.06    |
| <sup>244</sup> Cm | 3.47             | 3.89            | 12%                 | 3.24    |
| <sup>245</sup> Cm | 3.58             | 3.62            | 1%                  | 3.53    |

#### V.D.2. Fission Neutron Yield Averaged over Zone 1

In Table VII, the average value of  $\nu$  for all fission reactions in zone 1,  $\bar{\nu}_z$ , are displayed for the fission neutrons and the source neutrons for all four configurations. The relative differences between the values in each configuration, 6%, 5%, 2% and 8% for configuration I, II, III and IV, respectively, are directly connected to the actinide compositions in zone 1 and the relative differences in  $\bar{\nu}_n$  for respective nuclide. Since zone 1 in configuration III consists of plutonium only, the change in  $\bar{\nu}_z$  is thus relatively small, while in configuration IV, where zone 1 consists of curium only, the change is larger, almost 8%.

The fact that the relative difference in  $\bar{\nu}_z$  between the source neutrons and the fission neutrons in zone 1 is considerably higher for configuration IV than for configuration III is one of the reasons for the higher  $\psi^*$  in this case.

TABLE VII

Average Value of  $\nu$  for all Fission Reactions in Zone 1,  $\bar{\nu}_z$ , for all Configurations, followed by the Relative Differences  $(\bar{\nu}_z^{source} - \bar{\nu}_z^{fission})/\bar{\nu}_z^{fission}$ .

| Configuration | $\bar{\nu}_z$    |                 |                     |
|---------------|------------------|-----------------|---------------------|
|               | Fission neutrons | Source neutrons | Relative difference |
| I             | 3.13             | 3.31            | 6%                  |
| II            | 3.22             | 3.39            | 5%                  |
| III           | 2.95             | 3.00            | 2%                  |
| IV            | 3.52             | 3.78            | 8%                  |

## V.E. Analyse of the Neutron Multiplication in Zone 1

### V.E.1. Decomposition of the Core Simulation

When the spallation neutrons leak out from the target and enter into the fuel, their first interactions, generally occurring in the inner part of the core, is a determining factor for the magnitude of  $\psi^*$ . In order to perform a more detailed study of the first generation of fission multiplication chains in the core, started by the primary source neutrons, the MCNPX simulation of the system were divided into three different calculation steps. Since the total neutron production in the core, as well as the source efficiency, to a large extent is determined by the multiplication properties in the innermost part of the core, it will be shown that the differences in  $\psi^*$  between the different configurations are closely connected to the neutron multiplication in zone 1. In the first calculation step, only the proton source,  $S_p$ , and the spallation target were simulated. The neutrons that leak out radially from the target, i.e. the primary source neutrons that would have entered into zone 1, were registered and their properties, in terms of position, direction and energy, were written to a source file, denoted by  $S_1$ . In the second step, where both the target and zone 1 were simulated, these primary source neutrons were then emitted into zone 1 from the surface boundary between the target and zone 1. In this calculation step, all neutrons that leaked out through the outer radius of zone 1, i.e. those neutrons that would have entered into zone 2, were written to another source file, denoted by  $S_2$ . Finally, in the third step, the entire system was included in the model, which was driven by the external source  $S_2$ , thus entering into zone 2 at the surface boundary between zone 1 and zone 2. The total number of neutrons produced in the whole core, induced by  $S_2$ , was then determined.

The total number of neutrons produced by fission in the core per initial source proton, which for a given reactivity is the factor that determines  $\psi^*$  (Eq. 1), can be expressed as

$$\frac{\langle F\phi_s \rangle}{\langle S_p \rangle} \approx \frac{\langle S_1 \rangle}{\langle S_p \rangle} \cdot \frac{\langle S_2 \rangle}{\langle S_1 \rangle} \cdot \frac{\langle F\phi_{s_2} \rangle}{\langle S_2 \rangle}, \quad (6)$$

where the factors on the right-hand side represent the first, the second and the third step of the decomposed calculation procedure.  $\langle S_1 \rangle / \langle S_p \rangle$  is the number of primary source neutrons per initial source proton that leak out from the target and enter into zone 1 (i.e.  $Z = 25.4$ ).  $\langle S_2 \rangle / \langle S_1 \rangle$  represents the number of neutrons leaking out radially from zone 1 per primary source neutron, while  $\langle F\phi_{s_2} \rangle / \langle S_2 \rangle$  is a measure of the total number of neutrons produced in the core induced by each source neutron in  $S_2$ . In Eq. (6), the relation that the total number of neutrons produced in the core is equal to the sum of the number of neutrons produced in each calculation step was used, which can be expressed by

$$\langle F\phi_s \rangle = \langle F\phi_{s_p} \rangle + \langle F\phi_{s_1} \rangle + \langle F\phi_{s_2} \rangle. \quad (7)$$

The terms on the right-hand side represents the first, the second and the third steps in the calculation procedure. Normalised per source proton, the first term equals zero, since no fission neutrons are born in the target. The second term is about 15, whereas the third term is in the order of 1000. Hence, since almost all fission neutrons are produced in the third step, the relation  $\langle F\phi_s \rangle \approx \langle F\phi_{s_2} \rangle$  is justified, which was the assumption used in Eq. (6).

Since only the target is modelled in the first simulation, the first factor in Eq. (6) is the same for all configurations. The third factor, as well, is nearly constant for the different configurations, which can be explained by the following arguments. Since  $S_2$  consists mainly of neutrons emitted in fission reactions in zone 1 or primary source neutrons that have been moderated, the energy distribution of the source neutrons in  $S_2$  is rather similar to that of the average fission neutrons. Therefore, the efficiency of  $S_2$  is expected not to differ significantly for the different configurations, thus inducing about the same total number of neutrons produced in the core for all configurations, since the reactivity was also the same. Consequently, since the first and the third factors in Eq. (6) are constant or nearly constant, the difference in  $\psi^*$  for the different configurations is nearly proportional to the difference in the second factor, i.e. the number of neutrons leaking out radially from zone 1 over the number of neutrons entering zone 1 from the target,  $\langle S_2 \rangle / \langle S_1 \rangle$ .

### V.E.2. Neutron Balance in Zone 1

In order to further investigate the close relationship between the neutron multiplication in zone 1 and the magnitude of  $\psi^*$ , the neutron balance in zone 1, determined from the second step of the decomposed calculation procedure, have been studied. Normalising the number of primary source neutrons entering into zone 1 to unity, i.e.  $S_1 = 1$ , the neutron balance in zone 1 can be described by

$$S_1 - A_c - A_f + P_f - A_x + P_x - S_2 - L = 0, \quad (8)$$

where  $A_c$  is the number of neutrons absorbed by capture,  $A_f$  the number of neutrons absorbed by fission and  $P_f$  the number of neutrons produced by fission. The terms  $A_x$  and  $P_x$  represent the absorption and production of neutrons by all other reaction types, e.g. (n,xn)-reactions and secondary spallation reactions, whereas  $L$  is the leakage out through all surfaces except the outer radial surface, which is represented by  $S_2$ . In Table VIII, the neutron balances in zone 1 for the different configurations are displayed. Since the terms  $A_x$  and  $P_x$  were found to be very similar for the different configurations and therefore of lesser interest, they have been merged into the leakage term  $L$ . It should be noted that the reason for the slightly lower values of  $\bar{v}_z$  in Table VIII than those for

the source neutrons listed in Table VII is that the former were averaged over all fission events in zone 1, whereas the latter were averaged only over those fission events induced by the primary source neutrons.

It is seen in Table VIII that, compared to configuration I,  $S_2$  increases slightly for configuration II, decreases marginally for configuration III, whereas it increases considerably for configuration IV. The relative differences in  $S_2$  are fairly similar to those obtained for the proton source efficiency, listed in Table III, which confirms the assumption that  $\psi^*$  is nearly proportional to  $S_2$ . As was explained above, it is also shown in Table VIII that when removing americium from zone 1 in configuration II, III and IV and compensating for the increased fission rate by increasing the relative fraction of inert matrix, the total probability for fission in zone 1 decreases slightly and the total probability for capture decreases considerably. The relative fission and capture rates in the neutron balance in zone 1 correspond well to the flux-weighted average macroscopic fission and capture cross-sections listed in Table V.

Comparing the neutron balance for the two first configurations, it is seen that the lower fission neutron production for configuration II (-0.09) is more than compensated by the lower neutron absorption by capture and fission (-0.14) so that  $S_2$  increases by about 4%. Similarly, for configuration III, the significantly lower neutron production (-0.20), which is due to lower probability for fission and lower  $\bar{v}_z$ , is almost fully compensated by the considerably lower neutron absorption (-0.17), so that  $S_2$  is lower only by 1%. Finally, for configuration IV, the number of neutrons absorbed by fission is only about 10% lower than for configuration I, which is more than compensated by the 12% higher  $\bar{v}_z$ , so that the neutron production actually increases slightly (+0.02). The significantly lower number of absorbed neutrons (-0.11) then leads to a value of  $S_2$  higher by about 9% (+0.09). The leakage term  $L$  is approximately proportional to  $S_2$ .

It should also be noted that the major part of the primary source neutrons, ~60% for configuration I and ~70% for configuration II, III and IV, actually leak directly into zone 2 without being absorbed in zone 1. Therefore, since a considerable fraction of the primary source neutrons induce their first fission in zone 2, it could be expected that the composition of actinides in zone 2 would have a more pronounced effect on the magnitude of  $\psi^*$ . However, at this point, most of these neutrons entering into zone 2 have been moderated and the difference in energy spectrum compared to that of the average fission neutrons is comparatively small. Therefore, the efficiency of these leakage neutrons will not differ significantly between the different configurations and the effect on  $\psi^*$  can therefore be assumed to be small.

The first conclusion that can be drawn from the decomposition of the core simulation and the study of the neutron balance in zone 1 is that the magnitude of  $\psi^*$  is very sensi-

tive to the composition of actinides in the inner core zone and that the differences between the different configurations are directly related to the neutron multiplication in this zone. Moreover, it was shown that the differences in the neutron multiplication arise from combined effects of the changes in

$\bar{\Sigma}_f$ ,  $\bar{\Sigma}_c$  and  $\bar{\nu}_z$ . These results are also in analogy with the conclusions drawn in Sections V.C and V.D, where the changes in the relative values between fission neutrons and source neutrons of the same quantities were studied.

TABLE VIII

Neutron Balance in Zone 1 in the Second Step of the Decomposed Calculation Procedure (only the target and zone 1 were simulated), according to Eq. (8). The relative differences in  $S_2$  of configuration II, III and IV compared to configuration I,  $(S_{2,i} - S_{2,I})/S_{2,I}$ , are also displayed.  $S_I$  is normalized to unity and  $\bar{\nu}_z$  is the average value of  $\nu$  for all fission reactions in zone 1.

| Configuration | $S_I$ | $A_c$ | $A_f$ | $P_f$ | $L$  | $S_2$ | Relative difference | $\bar{\nu}_z$ |
|---------------|-------|-------|-------|-------|------|-------|---------------------|---------------|
| I             | 1.00  | 0.17  | 0.19  | 0.62  | 0.29 | 0.97  |                     | 3.27          |
| II            | 1.00  | 0.06  | 0.16  | 0.53  | 0.30 | 1.00  | 4%                  | 3.34          |
| III           | 1.00  | 0.05  | 0.14  | 0.42  | 0.28 | 0.95  | -1%                 | 3.01          |
| IV            | 1.00  | 0.08  | 0.17  | 0.64  | 0.32 | 1.06  | 9%                  | 3.66          |

## VI. VARYING TARGET RADIUS

The properties of the source neutrons are directly dependent on the properties of the target and the proton beam. For instance, an increase of the target radius leads to a softening of the source neutrons entering into the core. On the other hand, the spectrum of the fission neutrons is unaffected by such a target change. The direct effect of this, which has been investigated in detail in Ref. 6, is that  $\psi^*$  decreases considerably with increasing target radius.

However, for the comparison of the different core configurations for a fixed target radius, the modified spectrum of the source neutrons may lead to different results than those presented in the present paper. In order to study this, preliminary calculations with energy spectra of source neutrons leaking out from targets of radius 10 cm and 50 cm have been performed. As expected, the spectrum of the primary source neutrons in zone 1 was found to be slightly harder for the 10 cm target radius than for the reference case analysed in Section V (radius = 21 cm) and vice versa for the 50 cm target radius. However, even for the 50 cm radius, the spectrum of the source neutrons is still harder than that of the fission neutrons in zone 1, except in the energy region between about 2-8 MeV. Therefore, the same trends in the differences between the different configurations as were already observed can be expected also for the 10 cm and the 50 cm target radius, which was indeed shown to be the case. However, the following minor changes were identified. In analogy with the analyses performed in Section V, the harder spectrum of the source neutrons for the 10 cm target radius, compared to the reference case, improves the properties of the americium isotopes somewhat and vice versa for most of the plutonium isotopes. The opposite effect was observed for

the softer spectrum of the 50 cm target radius. The favourable properties of curium identified for the reference case appears to be only marginally deteriorated by the spectrum softening in the case of the 50 cm target radius.

The relative differences in  $\psi^*$  between configuration II and III relative to configuration I, compared to the reference study, decreases by a few percent for the 10 cm target radius and vice versa for the 50 cm target radius. For configuration IV,  $\psi^*$  is larger than for configuration I by about 8% for both the 10 cm target and the 50 cm target. Generally, it can thus be concluded that the concentration of curium to the inner core zone is clearly favourable in respect of  $\psi^*$  for all realistic dimensions of the target radius.

## VII. CONCLUSIONS

In order to investigate the possibilities of increasing the proton source efficiency,  $\psi^*$ , by distributing the actinides heterogeneously over the core, four different configurations of an ADS model were studied. The different configurations were geometrically identical, but had the actinides distributed in different ways over the three core zones. It was found that, compared to the first configuration where the plutonium, americium and curium were distributed homogeneously in the core, loading the inner zone with only curium increases  $\psi^*$  by about 7%.

The neutron energy spectrum in zone 1 was found to be harder for the source neutrons than for the average fission neutrons in the fundamental mode. This spectrum difference affects several parameters that are directly connected to the magnitude of  $\psi^*$  and is the underlying reason for the differences in  $\psi^*$  that were observed for the different configura-

tions. Three parameters – the average macroscopic fission and capture cross-sections,  $\bar{\Sigma}_f$  and  $\bar{\Sigma}_c$ , and the average fission neutron yield,  $\bar{\nu}_z$  – which are affected in different ways for the source neutrons and the fission neutrons by the substitution of actinides in zone 1, have been identified as mainly responsible for the differences in  $\psi^*$ .

It was shown that the even-N nuclides in general and  $^{241}\text{Am}$  and  $^{244}\text{Cm}$  in particular are the most favourable nuclides in respect of improving  $\psi^*$ . The reasons for the better properties of the even-N nuclides than those of the odd-N nuclides are the following. First, the harder spectrum in zone 1 for the source neutrons than for the fission neutrons leads to a larger flux-weighted average microscopic fission cross-section,  $\bar{\sigma}_f$ , for the even-N nuclides, whereas a lower is obtained for the odd-N nuclides. The second effect of the harder spectrum is a considerably higher average fission neutron yield in zone 1,  $\bar{\nu}_n$ , for the odd-N nuclides, while it is only marginally higher for the even-N nuclides. Both these effects enhance the neutron multiplication in zone 1 as well as  $\psi^*$ . On the other hand, the effect on  $\bar{\sigma}_c$  is that it decreases considerably for all nuclides, but more strongly for  $^{239}\text{Pu}$  than for the remaining nuclides. This property of  $^{239}\text{Pu}$  compensates partly for the negative effects from  $\bar{\sigma}_f$  and  $\bar{\nu}_n$ .

Comparing the different configurations, it can be concluded that a larger relative increase in  $\bar{\Sigma}_f$  and in  $\bar{\nu}_z$  for the source neutrons than for the fission neutrons can be expected to enhance  $\psi^*$ , while the opposite effect can be expected for changes in  $\bar{\Sigma}_c$ . Consequently, when loading zone 1 with plutonium only (configuration III),  $\psi^*$  changes only marginally, compared to configuration I, while loading zone 1 with curium only increases it considerably (configuration IV). It can thus be concluded that plutonium, in particular that of high quality consisting mainly of  $^{239}\text{Pu}$  and  $^{241}\text{Pu}$ , is a source inefficient material, compared to curium. The minor increase in  $\psi^*$  when substituting the americium in zone 1 by curium (configuration II) indicates that curium is a slightly better element than americium from this point of view.

The idea of concentrating all of the curium in zone 1 only (comprising 17% of the subassemblies) has both advantages and disadvantages. The fabrication and handling of a fuel consisting of curium only (32% CmN and 68% ZrN) would involve serious technical problems due to intense radiation and heat generation. On the other hand, only a minor fraction of the fuel subassemblies would have to be contaminated by curium, as the remaining 83% would consist of plutonium and americium only. Hence, there is a trade-off between these factors and the gain in  $\psi^*$ .

Finally, one of the general assumptions of the study, that the actinide composition of the innermost zone is of much larger importance for the magnitude of  $\psi^*$  than the two outer zones, was confirmed. By studying the neutron balance in zone 1, it was shown that  $\psi^*$  is directly connected to the neutron multiplication in this zone. The conclusions that the differences in  $\psi^*$  between the different configurations are the

results of changes in the ratios of  $\bar{\Sigma}_f$ ,  $\bar{\Sigma}_c$  and  $\bar{\nu}_z$  between the source neutrons and the fission neutrons, were also confirmed.

## ACKNOWLEDGEMENTS

This work was financially supported by the Swedish Centre for Nuclear Technology, SKB AB (Swedish Nuclear Fuel and Waste Management Co) and the European Commission (Project MUSE: FIKW-CT-2000-00063).

## REFERENCES

1. M. SALVATORES et al., "Long-Lived Radioactive Waste Transmutation and the Role of Accelerator Driven (Hybrid) Systems," *Nucl. Instrum. Methods A*, **414**, 5 (1997).
2. D. G. FOSTER et al., "Review of PNL Study on Transmutation Processing of High Level Waste," LA-UR-74-74, Los Alamos National Laboratory (1974).
3. T. TAKIZUKA et al., "Conceptual Design of Transmutation Plant," Proc. Specialist Mtg. Accelerator Driven Transmutation Technology for Radwaste, LA-12205-C, p. 707, Los Alamos National Laboratory (1991).
4. D. G. CACUCI, "On the Neutron Kinetics and Control of Accelerator-Driven Systems," *Nucl. Sci. Eng.*, **148**, 55-66 (2004).
5. M. DELPECH et al., "The Am and Cm Transmutation – Physics and Feasibility," *Proc. Int. Conf. Future Nuclear Systems, GLOBAL '99*, August 30-September 2, 1999, Jackson Hole, Wyoming, American Nuclear Society (1999).
6. P. SELTBORG et al., "Definition and Application of Proton Source Efficiency in Accelerator Driven Systems," *Nucl. Sci. Eng.*, **145**, 390 (2003).
7. M. SALVATORES et al., "The Potential of Accelerator-Driven Systems for Transmutation or Power Production Using Thorium or Uranium Fuel Cycles," *Nucl. Sci. Eng.*, **126**, 333 (1997).
8. R. SOULE, M. SALVATORES, R. JACQMIN, "Validation of Neutronic Methods Applied to the Analysis of Fast Sub-Critical Systems: The MUSE-2 Experiments," *GLOBAL '97*, page 639 (1997).
9. P. SELTBORG and J. WALLENIUS, "Proton Source Efficiency for different Inert Matrix Fuels in Accelerator Driven Systems," Int. Meeting AccApp'03, June 1-5, 2003, San Diego, California, USA (2003).

10. W. S. YANG, L. MERCATALI et al., "Effects of Buffer Thickness on ATW Blanket Performances", *Int. Meeting Accelerator Applications/Accelerator Driven Transmutation Technology and Applications ADTTA/AccApp'01*, November 11-15, 2001, Reno, Nevada, USA (2001).
11. G. ALIBERTI et al., "Analysis of the MUSE-3 Subcritical Experiment", *Int. Conf. Global 2001*, France, Paris, September (2001).
12. J. WALLENIOUS et al., "Application of burnable absorbers in an accelerator driven system", *Nuclear Science and Engineering*, 96, 137 (2001).
13. P. SELTBORG, R. JACQMIN, "Spallation Neutron Source Effects in a Sub-Critical System," *Int. Meeting Accelerator Applications/Accelerator Driven Transmutation Technology and Applications*, ADTTA/AccApp'01, November 11-15, 2001, Reno, Nevada, USA (2001).
14. R. KLEIN MEULEKAMP, A. Hogenbirk, "The Neutron Source in ADS applications", *PDS-XADS D23 App. D*, NRG report /I 20782 / 02.50727, Petten (2002).
15. K. TUCEK et al., "Source Efficiency in an Accelerator-Driven System with Burnable Absorbers," *Int. Conf. on Back-End of the Fuel Cycle: From Research to Solutions, GLOBAL 2001*, Paris, France (2001).
16. J. WALLENIOUS and M. ERIKSSON, "Neutronic design of minor actinide burning accelerator driven systems," *Nucl. Tech.*, accepted for publication.
17. L. S. WATERS, "MCNPX<sup>TM</sup> User's Manual – Version 2.1.5," Los Alamos National Laboratory, November 14, (1999).
18. S. G. MASHNIK and A. J. SIERK, "Improved cascade-exciton model of nuclear reactions," *Proc. SARE4*, September 14–16, 1998, Knoxville, TN, USA (ORNL, USA, 1999) pp. 29–51; Eprint nucl-th/9812069.
19. K. TSUJIMOTO et al., "Neutronic design for Lead-bismuth cooled accelerator-driven system for transmutation of minor actinide", *J. Nucl. Sci. Tech.* **41**, 21-36 (2004).
20. OECD Nuclear Energy Agency, "Actinide and Fission Product Partitioning and Transmutation; Status and Assessment Report", Paris, France, (1999).



ELSEVIER

Available online at [www.sciencedirect.com](http://www.sciencedirect.com)

SCIENCE @ DIRECT®

Nuclear Instruments and Methods in Physics Research A ■ (■■■■) ■■■–■■■

---

**NUCLEAR  
INSTRUMENTS  
& METHODS  
IN PHYSICS  
RESEARCH**


---

 Section A
 

---

[www.elsevier.com/locate/nima](http://www.elsevier.com/locate/nima)

## Analysis of reactivity determination methods in the subcritical experiment Yalina

Carl-Magnus Persson<sup>a,\*</sup>, Per Seltborg<sup>a</sup>, Alexandra Åhlander<sup>a</sup>,  
Waclaw Gudowski<sup>a</sup>, Thomas Stummer<sup>b</sup>, Hanna Kiyavitskaya<sup>c</sup>, Victor Bournos<sup>c</sup>,  
Yurij Fokov<sup>c</sup>, Ivan Serafimovich<sup>c</sup>, Sergey Chigrinov<sup>c</sup>

<sup>a</sup>Department of Nuclear and Reactor Physics, Albanova University Centre, Royal Institute of Technology, S-106 91 Stockholm, Sweden

<sup>b</sup>Vienna University of Technology, Austria

<sup>c</sup>Joint Institute of Power and Nuclear Research, National Academy of Sciences of Belarus, Minsk, Sosny

Received 18 May 2005; received in revised form 18 July 2005; accepted 20 July 2005

---

### Abstract

Different reactivity determination methods have been investigated, based on experiments performed at the subcritical assembly Yalina in Minsk, Belarus. The development of techniques for on-line monitoring of the reactivity level in a future accelerator-driven system (ADS) is of major importance for safe operation. Since an ADS is operating in a subcritical mode, the safety margin to criticality must be sufficiently large. The investigated methods are the Slope Fit Method, the Sjöstrand Method and the Source Jerk Method. The results are compared with Monte Carlo simulations performed with different nuclear data libraries. The results of the Slope Fit Method are in good agreement with the Monte Carlo simulation results, whereas the Sjöstrand Method appears to underestimate the criticality somewhat. The Source Jerk Method is subject to inadequate statistical accuracy.

© 2005 Elsevier B.V. All rights reserved.

PACS: 28.50.Dr

Keywords: Yalina; Reactivity determination; Subcritical; MCNP; ADS

---

### 1. Introduction

In order to reduce the radiotoxic inventory of the nuclear waste, accelerator-driven systems

(ADS) have been suggested to transmute the accumulated transuranic elements [1]. In a subcritical core it is possible to use large fractions of “exotic” fuels, apart from plutonium also consisting of the minor actinides americium and curium. Intensive research programs investigating the physics and technology of proton accelerators, spallation targets and subcritical cores are required

---

\*Corresponding author. Tel.: +46 8 55 37 82 04;  
fax: +46 8 55 37 84 65.

E-mail address: [callem@neutron.kth.se](mailto:callem@neutron.kth.se) (C.-M. Persson).

for the development of full-scale ADS in the future. This present work is dedicated to the study of reactivity determination methods of a subcritical zero-power core. The development of reliable methods for reactivity determination is essential for the safe operation and for the licensing of a future ADS.

Recently, the comprehensive MUSE program (multiplication with an external source), performed at the MASURCA facility in Cadarache, France, was completed [2]. In the MUSE experiments, a neutron generator, mainly consisting of a deuteron accelerator and a tritium target, was coupled to a subcritical core operating with a fast neutron energy spectrum. A major part of the experiments in MUSE was devoted to the investigation of methods for reactivity determination of different subcriticality levels [2].

Parallel with the MUSE program, another European program devoted to ADS studies has been running at the Yalina facility outside Minsk, Belarus [3,4]. This facility has the same basic construction with a neutron generator coupled to a subcritical core, but the neutron spectrum of Yalina is thermal. The fact that the fission chain process relies mainly on reactions induced by thermal neutrons, implies that the neutronic time scales are in the order of a factor  $10^3$  larger than in a fast system. The methods used in this study, earlier evaluated in a fast spectrum in the MUSE experiments, will now be investigated in a thermal spectrum. A pulsed neutron source (PNS) experiment has been analyzed by the Slope Fit Method [5] and the Sjöstrand Method [6], and a source jerk experiment [5] has been performed and analyzed. The results have been compared with the results from the MUSE experiments and Monte Carlo simulations.

## 2. The Yalina facility

Yalina is a subcritical assembly operating with a thermal neutron energy spectrum. The external source coupled to the core is provided by a neutron generator consisting of a deuterium accelerator and a Ti-D or Ti-T target (Table 1). In the experiments, the Ti-T target was used, situated in the center of the core. As fuel, EK-10

type fuel rods with 10% enriched uranium oxide are used in polyethylene blocks for moderation. Under normal conditions, the core is loaded with 280 fuel rods, but this number can easily be modified. The very low power of the core makes the natural convection of the surrounding air sufficient for cooling.

The core (Fig. 1) consists of subassemblies surrounding the target and the ion channel up to the side dimensions of  $400 \times 400 \times 576$  mm. Each subassembly is made of nine blocks ( $80 \times 80 \times 63$  mm) of polyethylene (density  $0.927 \text{ g/cm}^3$ ) with 16 channels for the fuel rods, with a diameter of 11 mm. At the sides and behind the target, the polyethylene blocks are replaced by lead blocks of the same geometry. The purpose of these lead blocks is to diffuse the energy spectrum of the (D,T)-neutrons into a more spallation-like spectrum, by ( $n, xn$ )- and scattering reactions. The core is surrounded by a graphite reflector with a thickness of approximately 400 mm. Only at the side facing the accelerator, and its opposite side, no shielding or borated polyethylene is used, for ease of handling. Five axial experimental channels (EC) with 25 mm diameter are located inside the core and reflector [7].

## 3. Initial Monte Carlo simulation

The experimental setup has been analyzed using MCNP version 4c3 [8]. The effective multiplication factor,  $k_{\text{eff}}$ , and the effective delayed neutron

Table 1  
Main parameters of the neutron generator (NG-12-1)

|                            |                       |   |
|----------------------------|-----------------------|---|
| Deuteron energy            |                       | 100–250 keV                               |
| Beam current               |                       | 1–12 mA                                   |
| Pulse duration             |                       | 0.5–100 $\mu\text{s}$                     |
| Pulse repetition frequency |                       | 1–10 000 Hz                               |
| Spot size                  |                       | 20–30 mm                                  |
| Ti-T target                | Maximum neutron yield | $\sim 2.0 \times 10^{12} \text{ ns}^{-1}$ |
|                            | Reaction $Q$ -value   | 17.6 MeV                                  |
| Ti-D target                | Maximum neutron yield | $\sim 3.0 \times 10^{10} \text{ ns}^{-1}$ |
|                            | Reaction $Q$ -value   | 3.3 MeV                                   |



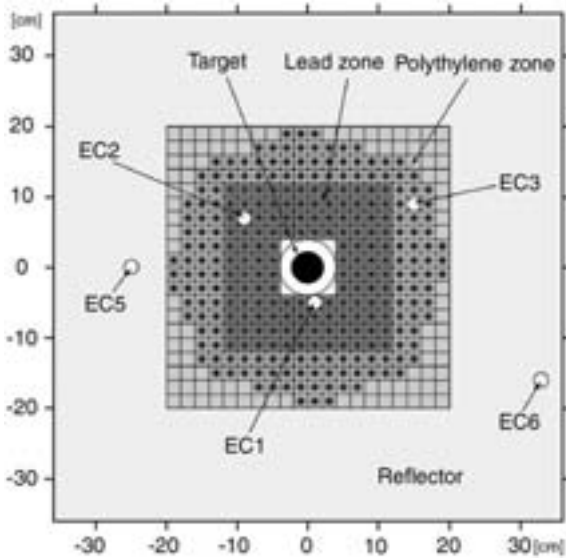


Fig. 1. Vertical cross-sectional view of the Yalina core.

fraction,  $\beta_{\text{eff}}$ , have been calculated for three different data libraries; ENDF/B-VI, JEFF3.0 and JENDL3.3 [9]. The effective delayed neutron fraction was calculated from the following relation:

$$\beta_{\text{eff}} = \frac{N_d}{N_{\text{Tot}}} \quad (1)$$

where  $N_d$  is the number of fissions induced by delayed neutrons and  $N_{\text{Tot}}$  is the total number of fissions [10]. The results for the different libraries are displayed in Table 2. For the following analysis, the mean generation time,  $\Lambda$ , is needed. Since MCNP calculates non-adjoint-weighted time parameters, not suitable for kinetic calculations, another approach must be adopted. This is described in the next section.

## 4. Reactivity determination

### 4.1. Pulsed neutron source experiment

When a neutron pulse enters a subcritical core, a number of fission chains start to propagate in the fuel. Because of the subcriticality, every fission chain will die out rapidly, which is characterized by a global exponential decay of the neutron flux.

Table 2

Effective multiplication factor,  $k_{\text{eff}}$ , and effective delayed neutron fraction,  $\beta_{\text{eff}}$ , calculated with MCNP

|           | $k_{\text{eff}}$      | $\beta_{\text{eff}}$ (pcm) |
|-----------|-----------------------|----------------------------|
| ENDF/B-VI | $0.91803 \pm 0.00005$ | $788 \pm 9$                |
| JEFF3.0   | $0.92010 \pm 0.00007$ | $793 \pm 9$                |
| JENDL3.3  | $0.92114 \pm 0.00006$ | $742 \pm 9$                |

By studying the prompt neutron decay after a neutron pulse, it is possible to determine the reactivity of the core in two different ways, either by applying the Slope Fit Method or the Sjöstrand Method, frequently also called the Area Method. These two methods have been used to analyze the data collected from the pulsed neutron source experiment. During the experiment, the neutron generator was operating at 43 Hz emitting deuterium pulses of duration  $2 \mu\text{s}$ . The  $^3\text{He}$ -detector was situated in different experimental channels at the core mid-plane. Fig. 2 shows the accumulated detector counts after 40,000 source pulses. The inherent source can in all experiments be neglected.

#### 4.1.1. Slope fit method

This method was first introduced already in Ref. [11], but the method has achieved increased interest during the last years, due to its possible applicability to ADS [2,12–14].

Neglecting the delayed neutrons, the point-kinetic equations take the following form for a reactor without sources [5,15]:

$$\frac{dn(t)}{dt} = \alpha n(t). \quad (2)$$

This equation has an exponential solution given by

$$n(t) = n_0 e^{\alpha t} \quad (3)$$

where  $\alpha$  is the prompt neutron decay constant:

$$\alpha = \frac{\rho - \beta_{\text{eff}}}{\Lambda}. \quad (4)$$

In a subcritical reactor,  $\alpha$  is negative, which gives rise to an exponential decrease of the neutron flux. In the short time-scale after a neutron pulse

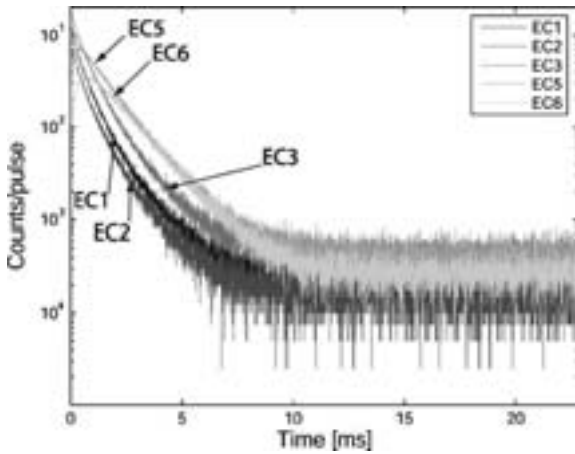


Fig. 2. Accumulated  $^3\text{He}$ -detector counts in different experimental channels after 40,000 pulse insertions.

injection, the neglecting of the delayed neutrons is legitimate and thus, the decay is mainly described by the prompt neutron decay constant. By measuring  $\alpha$  experimentally, the reactivity,  $\rho$ , can be found if  $\beta_{\text{eff}}$  and  $\Lambda$  are known.

From Fig. 2 it is evident that one single exponential is not enough to describe the complete behavior of the neutron flux decay after a neutron pulse insertion. During the first milliseconds, there is an injection and an adjustment period. During the injection period, the flux decreases rapidly in the three innermost experimental channels, located inside the core, and at the same time in the reflector channels, the neutron population is subject to a fast increase. After the injection period follows the adjustment period, when the neutron flux approaches a common decay rate in all channels. After approximately 4ms, the neutron flux reaches a fundamental decay mode, characteristic of the inherent reactor properties and described by the point-kinetic equations. During this process, the neutron flux decreases with approximately the same rate in all channels. Finally, the neutron flux reaches a constant level, due to the delayed neutron background.

Due to the exponential behavior of neutron flux changes in the reactor according to Eq. (3), it is appropriate to describe the neutron pulse response mathematically by a series of exponentials. By

Table 3  
Results from the slope fit method

|     | $\alpha$ ( $\text{s}^{-1}$ ) | $\rho$ (pcm)    |
|-----|------------------------------|-----------------|
| EC1 | $-675 \pm 13$                | $-8240 \pm 260$ |
| EC2 | $-722 \pm 19$                | $-9050 \pm 260$ |
| EC3 | $-711 \pm 11$                | $-8870 \pm 160$ |
| EC5 | $-634 \pm 21$                | $-8130 \pm 310$ |
| EC6 | $-653 \pm 2$                 | $-8560 \pm 30$  |

$\beta_{\text{eff}}$  and  $\Lambda$  were calculated using ENDF/B-VI.

fitting a function of the form

$$f(t) = \sum_{i=1}^{\infty} A_i e^{\alpha_i t} \quad (5)$$

to all data points, using the function fitting code MINUIT [16], it is possible to determine the exponential component which represents the fundamental decay mode. During the fitting procedure, all data points describing each pulse are used. It turns out that four terms are necessary to describe the response function with satisfactory statistical agreement. Two fast exponentials are required for the injection and adjustment periods, one exponential for the fundamental decay mode and finally, one constant for the delayed neutron background. The  $\alpha$ -values, describing the fundamental decay mode, are summarized in Table 3 and displayed visually for EC3 and EC5 in Fig. 3. The values are followed by a one standard deviation statistical error. Throughout this study, only statistical errors are considered.

The neutron pulse and the subsequent neutron flux have also been simulated with MCNP, relying on the nuclear data library ENDF/B-VI. The reaction rate with  $^3\text{He}$  has been tracked in each experimental channel during a period of 10ms after the neutron pulse. The results for EC 2, 3 and 5 are displayed in Fig. 4. These data can be analyzed in the same way as the experimental data, to find the  $\alpha$ -values. In this case, the reactivity is already known, through earlier simulations, which means that the mean generation time can be found from Eq. (4).

In the simulated case, three exponentials are sufficient to describe the response function with

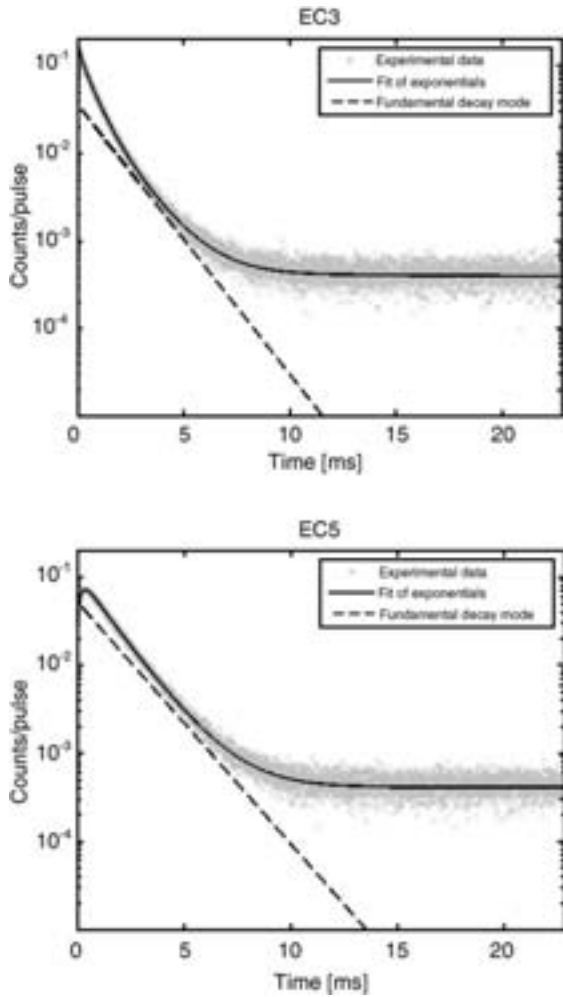


Fig. 3. Fit of exponentials to the experimental data in the experimental channels in the core (EC3) and in the reflector (EC5). The dashed lines represent the fundamental decay mode.

satisfactory statistical agreement, since the delayed neutrons are not included in the simulation. Two fast exponentials are required for the injection and adjustment periods and one exponential for the fundamental decay mode. The  $\alpha$ -values and their corresponding mean generation time, for each experimental channel, are summarized in Table 4.

By using the simulated values of the mean generation time in Table 4, it is possible to calculate the reactivity from the experimental values of  $\alpha$  (Table 3). The maximum difference between the experimental  $\alpha$ -values for different

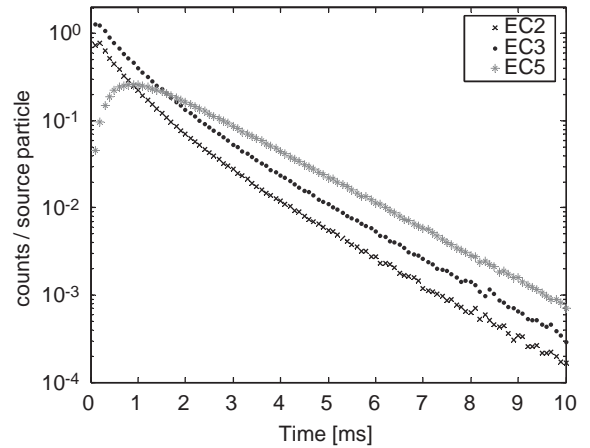


Fig. 4. MCNP-simulation of the pulsed neutron source experiment. The curves describe the reaction rate with  $^3\text{He}$  in EC2, EC3 and EC5.

Table 4

$\alpha$ -values and corresponding mean generation times,  $\Lambda$ , determined from the MCNP simulation of the PNS-experiment (ENDF/B-VI)

|     | $\alpha$ ( $\text{s}^{-1}$ ) | $\Lambda$ ( $\mu\text{s}$ ) |
|-----|------------------------------|-----------------------------|
| EC1 | $-726 \pm 16$                | $134 \pm 3$                 |
| EC2 | $-713 \pm 3$                 | $136.3 \pm 0.6$             |
| EC3 | $-716 \pm 2$                 | $135.7 \pm 0.5$             |
| EC5 | $-690 \pm 7$                 | $140.8 \pm 1.5$             |
| EC6 | $-679 \pm 1$                 | $142.2 \pm 0.3$             |

channels is approximately 10%. The differences are caused by statistical errors from the fitting procedure and different physical properties around the different experimental channels. The slope is found to be a little lower in the reflector channels. In Table 4, it can be seen that the simulated values deviate somewhat from the experimental values in Table 3, but they follow more or less the same pattern.

#### 4.1.2. Sjöstrand method

Considering the much shorter time scale of the decay of the prompt neutron flux compared to the delayed neutron precursor lifetimes, the delayed neutron flux contribution can be regarded as constant during the studied time interval. If the area under the response function is divided into a

prompt neutron area,  $A_p$ , and a delayed neutron area,  $A_d$ , as illustrated in Fig. 5, the reactivity in dollars can be expressed as [6]

$$\frac{\rho}{\beta_{\text{eff}}} = -\frac{A_p}{A_d}. \quad (6)$$

The prompt area is obtained by trapezoidal numeric integration and the delayed neutron area is obtained by averaging the values from the last milliseconds where the curve has flattened out. The results are listed in Table 5 and the maximal difference between the values is approximately 7%.

#### 4.2. Source jerk experiment

The idea behind the Source Jerk Method is to operate the subcritical reactor at steady state, at

flux level  $n_0$ , and then suddenly remove the neutron source. At this point, the system will make a prompt jump to a lower level,  $n_1$ , determined by the delayed neutron background. This level is only quasistatic and will decay according to the decay rate of the delayed neutron precursor groups [5]. The reactivity in dollars is given by

$$\frac{\rho}{\beta_{\text{eff}}} = \frac{n_1 - n_0}{n_1}. \quad (7)$$

During the source jerk experiment, the neutron flux is measured with a  $^3\text{He}$ -detector in EC2 (Fig. 6). The neutron flux levels are estimated by the flux values before and immediately after the prompt jump, which gives the reactivity  $\rho = -8.9 \pm 1.7\text{\$}$ . The statistical error is large due to the low count rate after the source jerk.

#### 4.3. Experimental estimation of the mean generation time

It is of interest to verify the Monte Carlo-based values of the mean generation time (Table 4) experimentally. An estimation of the ratio  $\lambda/\beta_{\text{eff}}$  can be found by rewriting Eq. (4) as

$$\frac{\lambda}{\beta_{\text{eff}}} = \frac{1}{\alpha} \left( \frac{\rho}{\beta_{\text{eff}}} - 1 \right) \quad (8)$$

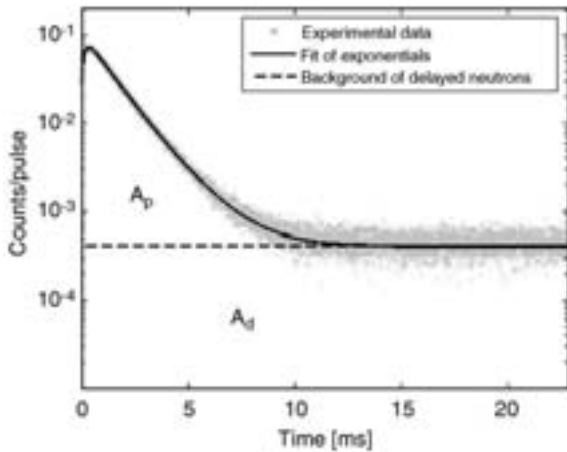


Fig. 5. Illustration of the prompt and the delayed neutron areas utilized in the Sjöstrand Method.

Table 5  
Results from the Sjöstrand Method

|     | $\rho$ (\$)     |
|-----|-----------------|
| EC1 | $-13.9 \pm 0.1$ |
| EC2 | $-13.7 \pm 0.1$ |
| EC3 | $-12.9 \pm 0.1$ |
| EC5 | $-13.0 \pm 0.1$ |
| EC6 | $-13.5 \pm 0.1$ |

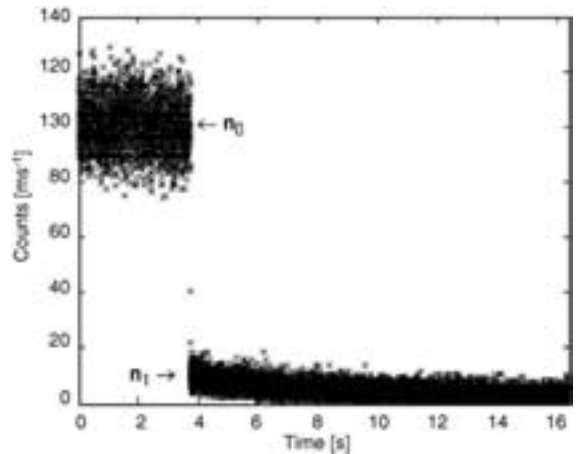


Fig. 6. Application of the Source Jerk Method in Yalina.

Table 6  
Experimental estimation of the mean generation time,  $\Lambda$

|                              | $\Lambda/\beta_{\text{eff}} (10^{-3} \text{ s})$ | $\Lambda (\mu\text{s})$ |             |             |
|------------------------------|--|-------------------------|-------------|-------------|
|                              |  | ENDF/B-VI               | JEFF3.0     | JENDL3.3    |
| <i>Slope Fit+Sjöstrand</i>   |  |                         |             |             |
| EC1                          | $22.1 \pm 0.4$                                   | $174 \pm 4$             | $175 \pm 4$ | $164 \pm 4$ |
| EC2                          | $20.3 \pm 0.6$                                   | $160 \pm 5$             | $161 \pm 5$ | $151 \pm 5$ |
| EC3                          | $19.5 \pm 0.3$                                   | $154 \pm 3$             | $155 \pm 3$ | $145 \pm 3$ |
| EC5                          | $22.1 \pm 0.7$                                   | $175 \pm 6$             | $175 \pm 6$ | $164 \pm 6$ |
| EC6                          | $22.2 \pm 0.2$                                   | $175 \pm 3$             | $176 \pm 3$ | $164 \pm 2$ |
| <i>Slope Fit+Source Jerk</i> |  |                         |             |             |
| EC2                          | $14.5 \pm 1.1$                                   | $114 \pm 9$             | $115 \pm 9$ | $108 \pm 8$ |

and combining the values of  $\alpha$  obtained from the Slope Fit Method with the values of  $\rho/\beta_{\text{eff}}$  obtained from the Sjöstrand Method or the Source Jerk Method. By using the calculated values of  $\beta_{\text{eff}}$  (Table 2), it is possible to find an estimate for  $\Lambda$ . From the results listed in Table 6, obtained by combining the Slope Fit Method and the Sjöstrand Method, it can be expected that the true value of  $\Lambda$  is in the range 140–180  $\mu\text{s}$ . The combination of the Slope Fit Method and the Source Jerk Method gives a lower value. The results diverge since the different methods give different values of the reactivity. However, this simple method shows that the values obtained by simulation (Table 4) should be good estimations of the real value. As a comparison, it can be mentioned that the non-adjoint-weighted mean generation time<sup>1</sup> calculated by MCNP, which is a very poor estimation of the true value, is approximately 370  $\mu\text{s}$ .

#### 4.4. Validity of the point-kinetic model

Since all three methods used in this study are based on the point-kinetic model, the validity of the model when applied to this system has been investigated.

<sup>1</sup>The (non-adjoint-weighted) neutron mean generation time is not given explicitly by MCNP. It must be calculated as the ratio between the prompt removal lifetime,  $l$ , and  $k_{\text{eff}}$ , or as the ratio between the prompt fission lifetime,  $\tau$ , and the number of prompt neutrons per fission,  $\nu_p$  [15,17,18].

The point-kinetic equations were developed for critical reactor calculations, and do not describe a subcritical system driven by an external neutron source strictly mathematically correct [19]. In a critical reactor, reactivity changes can be described by perturbation of an equilibrium state around criticality, where spatial flux shapes change slowly [20]. A subcritical facility, such as Yalina, with its driving point-like source, cannot be described in the same manner [21]. Thereby, the use of the point-kinetic approximation becomes questionable and its applicability to ADS is subject to investigation [20–22]. However, in the experiments of this study, the source is shut down and the decay of a well-established neutron population is studied. During this process, the reactor is not driven by an external source and the only driving source is the decaying fission source. Moreover, all points in the reactor are subject to the same time dependence. These circumstances make the use of the point-kinetic approximation acceptable, at least for a compact subcritical core, such as Yalina. In a large core, the spatial effects are worse, which make the point-kinetic approximation difficult or inappropriate to apply.

One basic assumption when deriving the point-kinetic equations is that the time-part of the solution can be separated from the energy and spatial part [15]. In other words, if the spatial one-energy group flux profile is constant in time, the assumption is valid. By using MCNP, the radial flux profile as a function of time after a neutron pulse has been simulated. Since the core relies mainly on thermal fissions, a one-energy group assumption should be well founded. Similar studies have been performed in Ref. [23]. The simulation has shown that after approximately 4 ms after the pulse, the relative values of the radial flux profile do not change in time. At this point, the injection and adjustment periods have past and all points in the system are subject to the same time-dependence (the fundamental decay mode). These results indicate that the point-kinetic model is applicable as an appropriate approximation of the time behavior of the neutron flux decay.

## 5. Discussion of results

### 5.1. Comparison between the methods

The Slope Fit Method, the Sjöstrand Method and the Source Jerk Method have been applied to the same configuration of the Yalina experiments. In comparison with the MCNP calculations, the Slope Fit Method shows similar results, whereas the Sjöstrand Method and the Source Jerk Method underestimates and overestimates  $k_{\text{eff}}$ , respectively. Both the Sjöstrand Method and the Slope Fit Method produce results with low statistical errors. The Source Jerk Method, on the other hand, is connected with larger errors due to the large uncertainty in the lower neutron flux level, which makes it difficult to make comparisons with the other methods. All results are summarized in Table 7 and Fig. 7.

When applying the Slope Fit Method on deep subcritical configurations, as in the present case, it can sometimes be difficult to find the correct slope through a fitting procedure. The effects from the injection and adjustment periods have disappeared after about 4ms, as mentioned in the previous

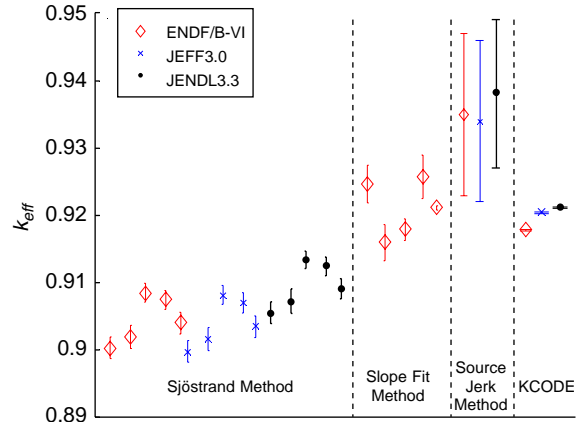


Fig. 7. Summary of all  $k_{\text{eff}}$  obtained through different methods applied on data from five experimental channels (Sjöstrand Method and Slope Fit Method). The error bars correspond to one standard deviation in each direction. The different libraries refer to the chosen value of  $\beta_{\text{eff}}$ .

Table 7

Summary of all  $k_{\text{eff}}$  obtained through the utilized methods and for different values of  $\beta_{\text{eff}}$  from different libraries

|                           | $k_{\text{eff}}$ |                 |                 |
|---------------------------|------------------|-----------------|-----------------|
|                           | ENDF/B-VI        | JEFF3.0         | JENDL3.3        |
| <i>Sjöstrand Method</i>   |                  |                 |                 |
| EC1                       | 0.9012±0.0013    | 0.9008±0.0013   | 0.9065±0.0013   |
| EC2                       | 0.9027±0.0013    | 0.9022±0.0013   | 0.9079±0.0013   |
| EC3                       | 0.9076±0.0011    | 0.9072±0.0011   | 0.9126±0.0011   |
| EC5                       | 0.9069±0.0011    | 0.9064±0.0011   | 0.9119±0.0011   |
| EC6                       | 0.9040±0.0013    | 0.9036±0.0013   | 0.9091±0.0012   |
| <i>Slope Fit Method</i>   |                  |                 |                 |
| EC1                       | 0.9239±0.0022    | —               | —               |
| EC2                       | 0.9170±0.0022    | —               | —               |
| EC3                       | 0.9185±0.0013    | —               | —               |
| EC5                       | 0.9248±0.0026    | —               | —               |
| EC6                       | 0.9211±0.0002    | —               | —               |
| <i>Source Jerk Method</i> |                  |                 |                 |
| EC2                       | 0.935±0.012      | 0.934±0.012     | 0.938±0.011     |
| MCNP                      |                  |                 |                 |
|                           | 0.91803±0.00005  | 0.92010±0.00007 | 0.92114±0.00006 |

section, and the delayed neutron background starts to influence the shape after approximately 7ms (Fig. 3). Consequently, the fundamental decay mode is the dominating mode during a relatively short time period. The situation is most problematic in the experimental channels in the core, where it is very difficult to visually distinguish a single slope. In the reflector, on the other hand, the fast exponentials have opposite sign, due to the fast increase in neutron flux during the injection period, which makes the fundamental decay mode evident.

According to the results, the Sjöstrand Method has a tendency to give lower values of  $k_{\text{eff}}$  than other methods. Especially the difference between the Sjöstrand Method and the Slope Fit Method is worth to notice, since they are based on the same measurement. The same tendency was also observed in the MUSE-4 experiments [2,12]. The main probable reason for the discrepancies is the use of the point-kinetic approximation. When analyzing the experimental data with the Sjöstrand Method, all data from the pulse insertion to the end of the pulse response are used. However, only the data representative for the fundamental decay mode, used in the Slope Fit Method analysis, is valid according to the point-kinetics. Since the fundamental decay mode will be more and more

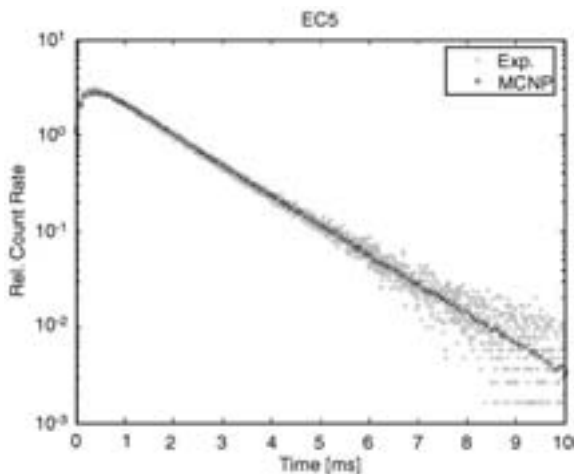


Fig. 8. Comparison between PNS experiment and Monte Carlo simulation for EC5.

dominating closer to criticality, the gap between the two methods is expected to decrease when approaching criticality. This effect was also observed in the MUSE-4 experiments [12].

The differences between the calculations based on the different nuclear data libraries are small; approximately 4% for the reactivity and 6% for  $\beta_{\text{eff}}$ . In comparison, the data library ENDF/B-VI gives a somewhat lower value of  $k_{\text{eff}}$  and JENDL3.3 gives a lower value of  $\beta_{\text{eff}}$ . However, the choice of nuclear data library does not induce prominent effects on the result.

### 5.2. Comparison between the PNS experiment and MCNP

As mentioned before, there is no delayed neutron background when simulating the pulsed neutron source experiment in MCNP. In order to compare the simulation with the experiment, this background must be subtracted from the experimental data. The result for EC5 is depicted in Fig. 8 and indicates good agreement.

## 6. Conclusions

Three reactivity determination methods, the Slope Fit Method, the Sjöstrand Method and the

Source Jerk Method, have been investigated by applying them to the Yalina experiments. Two types of experiments were performed at the facility; a pulsed neutron source experiment (PNS) and a source jerk experiment. The PNS experiment has also been simulated with MCNP. The simulations provided parameters, such as effective delayed neutron fraction and mean generation time, which were necessary for the evaluation of the reactivity and the effective multiplication constant from the experiments.

From the measurements it can be concluded that:

- The Sjöstrand Method underestimates the criticality slightly in comparison with MCNP and the other methods, but gives low statistical error.
- The Slope Fit Method is inconvenient to apply to deep subcritical configurations, but gives reliable results in comparison with MCNP. The cleanest response functions are achieved in the reflector channels.
- The Source Jerk Method is connected with large uncertainties.
- Although the neutron spectrum of Yalina is thermal and has different kinetic parameters than in MUSE, the results show many similarities.

Moreover, from the simulations it can be concluded that:

- MCNP gives reliable results, which was shown by the simulations in comparison with the experiments. However, care must be taken when calculating time parameters.
- The point-kinetic approximation describes the system well under the studied circumstances.

In this work, differences between different reactivity levels were not studied. Even if the methods do not predict the absolute value of the reactivity absolutely correct, they may be able to predict reactivity changes with good precision.

None of the methods investigated in this study have the capability of measuring the reactivity without disturbing a running system. However, the

methods can be used to estimate the subcriticality during loading and for calibration of other possible measurement techniques, for example the current-to-flux reactivity indicator. In the profound study of different measurement techniques for reactivity monitoring in an ADS performed within the MUSE-4 program, the method based on the current-to-flux reactivity indicator has appeared to be the major candidate for on-line monitoring [24].

### Acknowledgements

This work was financially supported by SKB AB (Swedish Nuclear Fuel and Waste Management Co) and SKI (Swedish Nuclear Power Inspectorate). The authors would like to thank R. Klein Meulekamp for calculations of effective delayed neutron fractions and for useful discussions.

### References

- [1] M. Salvatores, et al., Nucl. Instr. and Meth. A 414 (1998) 5.
- [2] R. Soule, et al., Nucl. Sci. Eng. 148 (2004) 124.
- [3] A.I. Kievitskaia, et al., Experimental and theoretical research on transmutation of long-lived fission products and minor actinides in a subcritical assembly driven by a neutron generator, in: The Third International Conference on Accelerator Driven Transmutation Technologies and Applications, ADTTA'99, Praha, Czech Republic, June, 1999.
- [4] I.G. Serafimovitch, et al., A small-scale set-up for research of some aspects of accelerator driven transmutation technologies, in: The Third International Conference on Accelerator Driven Transmutation Technologies and Applications, ADTTA'99, Praha, Czech Republic, June 1999.
- [5] G.R. Keepin, Physics of Nuclear Kinetics, Addison-Wesley, Reading, MA, 1965.
- [6] N.G. Sjöstrand, Ark. Fys. 11 (1956) 13.
- [7] S.E. Chigrinov, I. G. Serafimovich, Experimental and theoretical research of the peculiarities of transmutation of long-lived fission products and minor actinides in subcritical assembly driven by a neutron generator, Technical report, Joint Institute of Power and Nuclear Research, National Academy of Sciences of Belarus, Minsk, Sosny, ISTC Project B-070-98.
- [8] J.F. Briesmeister (Ed.), MCNP—A general Monte Carlo N-Particle Transport Code, Version 4c, LA-13709-M, Los Alamos National Laboratory, USA, 2000.
- [9] OECD/NEA www.nea.fr.
- [10] S.C. Van Der Marck, R. Klein Meulekamp, Calculating the Effective Delayed Neutron Fraction Using Monte Carlo Techniques, PHYSOR, Chicago, IL, USA, 2004 (April).
- [11] B.E. Simmons, J.S. King, Nucl. Sci. Eng. 3 (1958) 595.
- [12] D. Villamarin, Análisis dinámico del reactor experimental de fisión nuclear MUSE-4, Doctoral Thesis, Universidad Complutense de Madrid, Departamento de Física Atómica, Molecular y Nuclear, 2004.
- [13] M. Rosselet, et al., Nucl. Sci. Eng. 135 (2000) 33.
- [14] S. Dulla, et al., Kerntechnik 67 (2002).
- [15] K.O. Ott, R.J. Neuhold, Introductory Nuclear Reactor Dynamics, American Nuclear Society, 1985.
- [16] F. James, M. Winkler, MINUIT User's Guide, CERN, Geneva, 2004.
- [17] G.D. Spriggs, et al., On the definition of neutron lifetimes in multiplying and non-multiplying systems, LA-UR-97-1073, Brazilian Meeting on Reactor Physics and Thermo hydraulics, Pocos de Caldas Springs, MG, Brazil, 1997.
- [18] R.D. Busch, et al., Definition of neutron lifespan and neutron lifetime in MCNP4B, LA-UR-97-222, American Nuclear Society Meeting, Orlando, FL, June 1997.
- [19] D.G. Cacuci, Nucl. Sci. Eng. 148 (2004) 55.
- [20] D.G. Cacuci, On Perturbation Theory and Reactor Kinetics: From Wigner's Pile Period to Accelerator Driven Systems, PHYSOR, Seoul, Korea, 2002.
- [21] A. Rineiski, W. Maschek, Ann. Nucl. Energy 32 (2005) 1348.
- [22] A. Rineiski, W. Maschek, On application of quasistatic and point-kinetics schemes for subcritical systems with external neutron source, Nuclear Mathematical and Computational Sciences: A Century in Review—A Century Anew, M&C 2003, Gatlinburg, TN, USA, 6–11 April 2003.
- [23] M. Eriksson, et al., Nucl. Sci. Eng. 149 (2005) 298.
- [24] EU Project FIKW-CT-2000-00063, Final report—The MUSE experiments for subcritical neutronics validation, unpublished.





---

---

Journal logo

---

---

# Source efficiency studies in gas- and lead-bismuth-cooled subcritical accelerator-driven cores

Daniel Westlén,<sup>a\*</sup> Per Seltborg<sup>a</sup>

<sup>a</sup>*Department of nuclear and reactor physics, Albanova university centre, Royal institute of technology, Stockholm, Sweden*

**Elsevier use only:** Received date here; revised date here; accepted date here

---

## Abstract

The efficiency of a spallation neutron source, in an accelerator-driven system (ADS) dedicated to actinide transmutation, is dependent on a series of variables, one of them being the nature of the coolant, another one being the composition of the fuel. In the present study, the proton source efficiency,  $\psi^*$ , has been studied with the Monte Carlo code MCNPX for two heterogeneous models based on the PDS-XADS LBE- and gas-cooled concepts. Minor actinide fuels have also been studied. The main conclusion from the study is that there are important variations in the source efficiency arising both from the choice of fuel and from the choice of coolant. Replacing the MOX-fuel in the core by minor actinide (MA) containing fuel decreases  $\psi^*$  by more than 10% for both coolant options. The explanation for this behavior is the large difference in fission cross-sections for neutrons in americium, resulting in low macroscopic cross-sections for source neutrons in americium rich fuels. The spectrum change resulting from a substitution of coolant has a large impact on the macroscopic cross-sections of even-N nuclides, leading to a lower  $\psi^*$  for LBE than for helium coolant. Utilizing simplified homogenous models yield significantly different results in the helium-cooled case. The result of changing the coolant found in this study is in agreement with a previous study by Pelloni.

*Keywords:* source efficiency; proton source efficiency; ADS; transmutation; actinide nitrides; minor actinides, XADS, MCNPX

*PACS-2003:* 28.50.Dr Research reactors

---

\* Corresponding author. Tel.: +46 70 631 54 08; e-mail: daniel@neutron.kth.se.

## 1. Introduction

Subcritical cores dedicated to transmutation of nuclear waste require a continuous supply of external neutrons for their operation. Usually an accelerator-driven spallation source is considered to supply these neutrons in future full-scale systems [1][2][3]. Protons are accelerated towards a liquid metal target, where neutrons are produced through spallation. The neutrons multiply through subsequent spallation reactions in the target and, once in the fuel, (primarily) through fission reactions.

The number of neutrons produced in the spallation target depend on a number of variables, such as proton energy and target size. Also the design of the core surrounding the spallation target has a large influence on the multiplication.

When performing studies on the neutronics of subcritical cores, the impact of the coolant on the source efficiency is a returning question. The purpose of this paper is to compare the source efficiency in two subcritical cores, based on the designs proposed in the PDS-XADS project, out of which one is cooled by helium and the other by lead-bismuth eutectic (LBE).

We begin by explaining some theory regarding source efficiency. Then, the core designs and fuel options studied are described. The results are provided and discussed. The discussion is concentrated on the causes for the differences in source efficiency observed. Some analysis is provided that deals with possible causes of changes in  $\psi^*$  other than the changes regarding fuels and coolants. Finally we conclude our discussion.

## 2. Source efficiency

In order to study the beam power amplification in a sub-critical core, i.e. the core power divided by the proton beam power, a new parameter, the proton source efficiency,  $\psi^*$ , was introduced in a previous study [4].  $\psi^*$  represents the average importance of the external proton source, relative to the average importance of the fundamental mode fission neutrons. It is closely related to the neutron source

efficiency,  $\phi^*$  [5][6], but connects the core power directly to the source protons instead of to the source neutrons. The main advantages of using  $\psi^*$  instead of  $\phi^*$  are that the way of defining the external source is unique and that  $\psi^*$  is directly proportional to the beam power amplification. It has been shown in previous studies that the source efficiency can vary considerably for different reactor cores [1][4][7][8][10]. Therefore, studying  $\psi^*$  for various system parameters is of interest when designing an accelerator driven system (ADS).

The proton source efficiency is defined in analogy with the definition of  $\phi^*$  [1][9] and can be expressed in terms of the k-eigenvalue,  $k_{eff}$ , and the total number of neutrons produced by fission in the core for each source proton,  $\langle F\phi_s \rangle / \langle S_p \rangle$ , according to

$$\psi^* = \left( \frac{1}{k_{eff}} - 1 \right) \cdot \frac{\langle F\phi_s \rangle}{\langle S_p \rangle} . \quad (1)$$

Since  $\langle F\phi_s \rangle$  is approximately proportional to the total power produced in the core, for a given  $k_{eff}$ ,  $\psi^*$  is thus proportional to the core power divided by the proton beam power.

## 3. System descriptions

Two core designs were proposed by the PDS-XADS-project, funded within the European fifth framework program [1][2]. Both are 80 MW<sub>th</sub> experimental core designs. They are of similar size and consequently they have similar power densities. The main difference is the choice of coolant. One of the cores is helium-cooled, the other is cooled by LBE.

We have constructed models of the two cores in the Monte Carlo code MCNPX 2.5e. The models follow the original designs on the level of pin design, but are somewhat simplified as displayed in Figure 1. A main simplification in the core models is that they are limited by cylinders cutting straight through assemblies rather than encircling the assemblies. This will give a minor underestimation of the coolant fraction close to the target and close to the blanket. The simplification makes it possible to adjust  $k_{eff}$  by varying the core radius though. For both the helium- and LBE-cores, the radii of the outer cylinders were

adjusted to give a  $k_{eff}$  close to 0.97. The radius of the inner cylinder is directly given by the target size. The reflector surrounding the core is simplified in the sense that it consists of a smear-material corresponding to the fraction of steel and coolant adopted in the two XADS-designs.

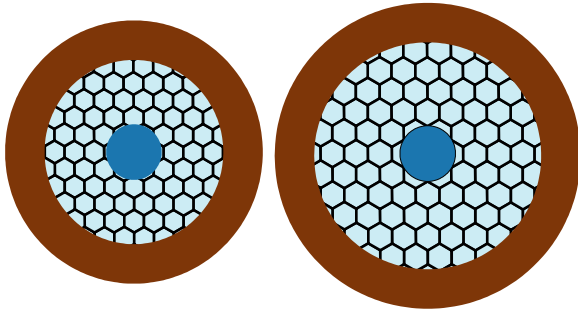


Figure 1: The two core models, the helium-cooled core is displayed to the left, the LBE-cooled to the right.

Two different fuel types have been used for each of the two core designs. In the reference case, MOX-fuel has been used. In a more innovative setup, an actinide nitride fuel, with a Pu/Am ratio corresponding to the equilibrium nuclide vector expected in a transmutation fuel cycle, has been assumed. This fuel was chosen as a more probable candidate for fuel in a full-scale transmutation reactor. The fuel compositions are summarised in Table 1.

|                   | MOX (%) | AcN (%) |
|-------------------|---------|---------|
| <sup>235</sup> U  | 0.42    | -       |
| <sup>238</sup> U  | 76.47   | -       |
| <sup>238</sup> Pu | 0.09    | 2.00    |
| <sup>239</sup> Pu | 16.00   | 15.16   |
| <sup>240</sup> Pu | 5.64    | 12.14   |
| <sup>241</sup> Pu | 0.60    | 5.29    |
| <sup>242</sup> Pu | 0.27    | 5.40    |
| <sup>241</sup> Am | 0.51    | 33.30   |
| <sup>243</sup> Am | -       | 16.68   |
| <sup>244</sup> Cm | -       | 8.74    |
| <sup>245</sup> Cm | -       | 1.30    |

Table 1: Nuclide compositions of the two fuels examined. MOX refers to the mixed oxide fuel proposed in the XADS project. AcN refers to the equilibrium actinide composition in a core dedicated to actinide transmutation. ZrN is used as matrix in the latter case.

At radii 64.5 and 83.0 cm for the helium- and LBE-cooled cores respectively,  $k_{eff}$  equals 0.97 for the MOX-loaded core. In the actinide nitride-loaded cores, the geometry was kept the same as in the reference cases. The reactivity was adjusted by altering the fuel inert matrix fraction. In the helium case, the ZrN mass fraction was 45%, in the LBE case, the corresponding figure was 41%.

The two XADS-designs have somewhat different geometries. The pin-pitch over diameter is 1.58 in the LBE-cooled core models and 1.29 in the helium cores. This enhances neutron leakage to the outer parts of the core, but is, as we shall see, not enough to compensate for the larger scattering cross-sections in LBE, which counter-act this effect. Both cores utilise annular pins. The dimensions are slightly different though. Hexagonal fuel assemblies are used in both cases, however with different dimensions, the most important difference being that the helium-core is much higher. Some important geometrical parameters of the two models are summarised in Table 2.

|                   | He      | LBE     |
|-------------------|---------|---------|
| Assemblies        | 90      | 120     |
| Pins              | 3330    | 10800   |
| Pin P/D           | 1.29    | 1.58    |
| Pin diameter      | 13.0 mm | 8.50 mm |
| Pellet internal d | 3.2 mm  | 1.8 mm  |
| Core radius       | 645 mm  | 830 mm  |
| Core height       | 1500 mm | 870 mm  |

Table 2: Basic geometrical parameters for the LBE-cooled and the gas-cooled models.

A spallation target radius of 20 cm was assumed in both models. To examine the effects of the target size, the radius was varied from 20 to 40 cm for the LBE-MOX case as a separate part of the study.

The radial power profiles of the four fuel-coolant combinations studied show similar behaviour. This is a criterion for this study, since  $\psi^*$  is affected by the power profile as was shown in a previous study [10].

## 4. Results

The proton source efficiencies have been calculated for the four different cores, yielding the  $\psi^*$  listed in Table 3. For the comparison,  $Z$  and  $\phi^*$  are also given. The variations in  $\phi^*$  are different from those in  $\psi^*$ . The different heights of the cores give a significant contribution to  $\phi^*$  through  $Z$ .

|                  | He-<br>MOX | LBE-<br>MOX | He-<br>AcN | LBE-<br>AcN |
|------------------|------------|-------------|------------|-------------|
| $\psi^*$         | 19.4       | 16.8        | 16.8       | 15.2        |
|                  |            | -13%        | -13%       | -22%        |
| $Z$              | 13.5       | 12.5        | 13.5       | 12.5        |
| $\phi^*$         | 1.43       | 1.35        | 1.24       | 1.22        |
|                  |            | -6%         | -13%       | -15%        |
| $\phi^*$<br>[11] | 1.212      | 0.986       | -          | -           |
|                  |            | -19%        |            |             |

Table 3:  $\psi^*$  for the four cores studied and the relative difference to the He-MOX case.  $Z$  is the number of neutrons leaving the target per source proton.  $\phi^*$  is a measure of the multiplication of the source neutrons in the core, source neutrons here being defined as neutrons leaving the target, entering the fuel region. The variations in  $\psi^*$  and  $\phi^*$  are different. The cause is the variation in  $Z$  arising from the different core geometries. Pelloni [11] uses a different definition of  $\phi^*$ , but the change in  $\phi^*$  when going from helium- to LBE-cooling is in agreement with the present study.

As displayed in Table 3, there are significant differences in the proton source efficiency in the four cases considered, both with respect to fuel and coolant. Values for  $\phi^*$  are given both for the present study and for a previous study by Pelloni [11]. Pelloni use a different definition of  $\phi^*$  though. Thus, the results are not directly comparable, however the changes in  $\phi^*$  in the two studies are in agreement.

## 5. Analysis

### 5.1. Main observations

Looking at how the macroscopic cross-sections for fission and capture vary for fission and source neutrons respectively gives important clues to why

$\psi^*$  changes. Table 4 shows how, in all cases, the probability for fission is higher for neutrons originating from fission reactions than for source neutrons. In the case of capture, the opposite situation is valid. In all four coolant-fuel combinations studied, the macroscopic capture cross-sections are higher for neutrons originating from the source.

These two observations combined are directly coupled to the variations in  $\psi^*$ . A high capture cross-section for source neutrons together with a low fission cross-section results in a low proton source efficiency.

### 5.2. Replacing the coolant

Looking closer into the effects on the cross-sections from changing coolant, leads to the observation that the differences in macroscopic fission cross-sections between fission and source neutrons decrease when substituting helium by LBE, from 7% to 4% for MOX-fuel and from 13% to 11% for actinide fuel. For the capture cross-sections, the opposite is valid. The differences grow from 2% to 9% for MOX-fuel and from 5% to 12% for the actinide-fuel. Since we observe lower proton source efficiencies for the LBE-cooled models, the explanation should be sought for in the capture cross-sections. The dominating contributors to the observed changes in macroscopic capture cross-sections are  $^{238}\text{U}$  in MOX-fuel and the americium nuclides  $^{241}\text{Am}$  and  $^{243}\text{Am}$  in the actinide fuel. These nuclides have the common property that the microscopic capture cross-sections increase by almost an order of magnitude when lowering the incident neutron energy somewhat from the 1 MeV region. Figure 2 shows how the cross-sections are strongly dependent on neutron energy in this energy region. The conclusion is that the increased moderation in the LBE-coolant reduces the average neutron energy of the source neutrons more than of the fission neutrons, increasing the capture cross-sections more for the former. The results of this study are in line with a previous study by Pelloni [11], who showed a large drop in source efficiency following a change of coolant from helium to LBE.

| Core    | $\bar{\Sigma}_f$ |                 |                     | $\bar{\Sigma}_c$ |                 |                     |
|---------|------------------|-----------------|---------------------|------------------|-----------------|---------------------|
|         | Fission neutrons | Source neutrons | Relative difference | Fission neutrons | Source neutrons | Relative difference |
| He-MOX  | 37.0             | 34.2            | - 7 %               | 37.8             | 38.6            | 2 %                 |
| LBE-MOX | 28.9             | 27.7            | - 4 %               | 33.2             | 36.4            | 9 %                 |
| He-AcN  | 53.5             | 46.7            | -13 %               | 71.7             | 74.9            | 5 %                 |
| LBE-AcN | 35.5             | 31.5            | - 11 %              | 48.9             | 54.7            | 12 %                |

Table 4: Macroscopic Fission and Capture Cross-sections,  $\bar{\Sigma}_f$  and  $\bar{\Sigma}_c$  [ $10^{-3} \text{ cm}^{-1}$ ], for the four cores, followed by the Relative Differences  $(\bar{\Sigma}_{source} - \bar{\Sigma}_{fission}) / \bar{\Sigma}_{fission}$ . The relative differences show clear parallels to the values of  $\psi^*$ . Lower macroscopic cross-sections for fission for source neutrons combined with increasing cross-sections for capture result in lower values of  $\psi^*$ .

Further, the average fission neutron yield -  $\nu$ , is of interest for the analysis. A high  $\nu$  for source neutrons result in a high source efficiency, since the number of fission neutrons in the system will be high. The total neutron economy of the core is governed by the reactivity management, however  $\nu$  affects the relative abundance of fission and source neutrons. It appears that the behaviour of  $\nu$  is very similar in the four cases.  $\nu$  is higher for the source neutrons, but the variations between the four cases are small,  $\nu$  for the source neutrons are 1-3% higher than for the fission neutrons. The variations in  $\nu$  do not in themselves supply sufficient explanation to

the changes in  $\psi^*$  observed. However, since they act in the same direction as the other possible causes of changes in  $\psi^*$  it is an important part of the explanation.

### 5.3. Replacing the fuel

Isolating the effect of replacing MOX for actinide nitride fuel leads to a similar chain of effects as does the replacement of the coolant. In this case, the situation is somewhat clearer, since now the differences in fission and capture cross-sections act in the same direction (Table 4).

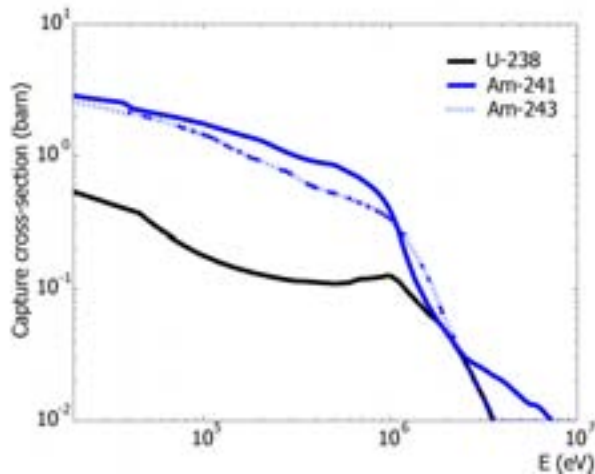


Figure 2: The microscopic capture cross-sections change drastically with energy in the 1 MeV region for both  $^{238}\text{U}$  and the even-N americium nuclides.

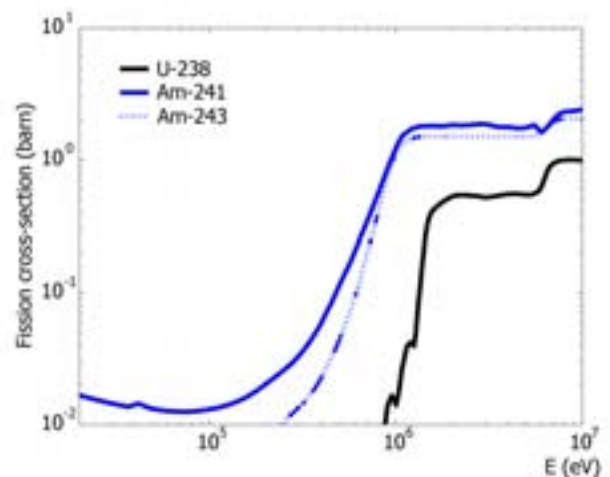


Figure 3: The microscopic cross-sections for fission in the most important nuclides also change significantly with energy. However the changes occur at somewhat different energies being an important part of the explanation of the behaviour of  $\psi^*$  when changing the fuel.

In MOX-fuel the dominating nuclide is  $^{238}\text{U}$ , whereas in the actinide nitride fuel uranium is replaced by minor actinides. The main contributor to fission in the MOX-fuel is  $^{239}\text{Pu}$ . However, the fission cross-section for  $^{239}\text{Pu}$  in the energy region of interest is rather constant. Small changes in energy do not change the importance of fission in  $^{239}\text{Pu}$  very much.

Instead, the causes of the increasing differences in macroscopic fission cross-sections for fission and source neutrons are due to other nuclides, whose cross-sections vary more with energy. In the MOX-fuelled models,  $^{238}\text{U}$  is the nuclide mainly responsible for the fact that source neutrons have lower cross-sections for capture. In the actinide fuel, this role is taken over by the even-N americium nuclides  $^{241}\text{Am}$  and  $^{243}\text{Am}$ , where fission cross-sections differ more for the fission and source neutron spectra than they do for  $^{238}\text{U}$ . Figure 3 shows how both  $^{238}\text{U}$  and the americium nuclides have very energy dependent fission cross-sections, although the large steps in fission probability occur at somewhat different energies in uranium and americium.

As mentioned, the differences in capture cross-sections are larger when LBE-coolant is used. The same three nuclides appear to be the cause of this.  $^{238}\text{U}$  is responsible for almost the entire difference in the MOX-fuelled cores. In the actinide-fuelled cores, americium has overtaken this role. However, the change in cross-section following the energy shift is larger in americium, resulting in larger relative differences in macroscopic capture cross-sections between fission and source neutrons for the actinide-fuelled models.

The shift in fission and capture cross-sections resulting from the uranium being replaced by americium explain the change in  $\psi^*$  observed when changing fuel in the models.

#### 5.4. Effects of varying radii

Since the spallation target size is expected to have an impact on  $\psi^*$ , three different target diameters have been examined. The resulting  $\psi^*$  are listed in Table 5.

| Target radius (cm) | 20   | 30   | 40   |
|--------------------|------|------|------|
| $\psi^*$           | 16.8 | 15.1 | 12.8 |
| Rel. diff.         | -    | -11% | -24% |

Table 5:  $\psi^*$  varies with the spallation target radius.

As is clearly seen in Table 5, the spallation target radius has a large impact on the source efficiency as it affects the mean energies of the source neutrons and thus the cross-sections for fission and capture. Generally  $\psi^*$  is expected to drop when the target radius increases. The simple reason for this is that the source neutron spectrum is softer at larger distances from the spallation target, where as the fission neutron spectrum is unchanged [4][5].

Changes in target geometry have a large effect on the final value of  $\psi^*$ . These are of similar magnitude to the effects arising from fuel and coolant changes. Hence, it is vital that the target geometry is kept constant throughout the study.

#### 5.5. Effects of homogenising the core model

As was previously mentioned, the power profile is important for the magnitude of the proton source efficiency. Moreover, the distribution of source neutrons in the core has a large impact. In the helium-cooled core studied, the leakage of source neutrons to the core periphery is larger than in the LBE-cooled core.

In order to produce some first results, simplified geometries are often used in core models in order to shorten calculation times. Mixing fuel, coolant and construction materials in one modeled material smeared out over the entire core region is a way of making the geometry significantly simpler. However, such an approach may give misleading results, which is especially true in helium-cooled designs. The scattering cross-sections of helium are small, which means that straight paths between pins and assemblies allow source neutrons to spread – uncollided – far from the target. Naturally, in a homogenised model, paths are not modeled. The behaviour of the neutrons will be quite different in such a case since neutrons are scattered at an early stage in fuel and structure materials

Table 6 shows how the differences in  $\psi^*$  observed in helium- and LBE-cooled cores disappear in a homogenous core model.

|               | He-MOX | LBE-MOX | He-AcN | LBE-AcN |
|---------------|--------|---------|--------|---------|
| Heterogeneous | 18.5   | 16.8    | 16.8   | 15.2    |
| Homogeneous   | 16.8   | 16.9    | 15.2   | 15.3    |
|               | -15%   | 1%      | -10%   | 1%      |

Table 6:  $\psi^*$  for the four cases in heterogeneous and homogenous core models. The homogenous model is too simplified to model helium-cooled cores accurately, while giving accurate results for LBE-cooled cores. The last row indicates the deviation of the results from using a homogenous core model to using a heterogeneous model.

### 5.6. Effects of changing the coolant fraction

The geometrical distribution of source neutrons in the fuel is dependent on the coolant fraction, especially for gas-cooled cores. To examine whether this has an impact on  $\psi^*$ , cores with different pin-pitch over diameter (P/D) were modeled for the He-MOX case. The level of subcriticality was kept constant by altering the radius. The results are displayed in Table 7.

| P/D      | 1.291 | 1.4  | 1.5  | 1.7  | 1.9  |
|----------|-------|------|------|------|------|
| $\psi^*$ | 16.8  | 18.6 | 18.5 | 20.1 | 20.1 |
|          | -     | 10%  | 10%  | 19%  | 19%  |

Table 7:  $\psi^*$  for the He-MOX case, when P/D and consequently the coolant fraction is varied. A larger coolant fraction leads to higher proton source efficiency.

When P/D is increased, the helium-filled paths to the outer parts of the core are widened, increasing the probability of source neutrons reaching further away from the spallation target leading to higher source efficiency. These observations confirm the results found when comparing the heterogeneous and homogenous core models.

## 6. Conclusions

Americium introduction in the fuel of a subcritical core decreases  $\psi^*$ . This is why  $\psi^*$  is around 10% lower in a core loaded with americium based fuels than in a core fuelled by MOX-fuel.  $\psi^*$  is reduced by another 10% when helium is replaced by LBE.

Both of these effects are due to the strong dependence of fission and capture cross-sections on incident neutron energy in the 1 MeV region in even-N nuclides and to their appearance in slightly shifted energy bands.

## Acknowledgments

This work was financially supported by the Swedish Centre for Nuclear Technology and by SKB AB (Swedish Nuclear Fuel and Waste Management Co).

## References

- [1] ANSALDO NUCLEARE, "Core Design Summary Report for the LBE-Cooled XADS", XADS 41 TNIX 064 Rev. 0 (2004).
- [2] NNC LTD, "PDS-XADS Work Package 4.2 Deliverable 65: Core Design Summary", C6862/TR/0028 (2004).
- [3] "A EU roadmap for developing accelerator driven systems (ADS) for nuclear waste incineration", Technical report, The European Technical Working Group on ADS, ENEA (2001).
- [4] P. SELTBORG et al., "Definition and Application of Proton Source Efficiency in Accelerator Driven Systems," *Nucl. Sci. Eng.*, 145, 390 (2003).
- [5] M. SALVATORES et al., "The Potential of Accelerator-Driven Systems for Transmutation or Power Production Using Thorium or Uranium Fuel Cycles," *Nucl. Sci. Eng.*, 126, 333 (1997).
- [6] R. SOULE, M. SALVATORES, R. JACQMIN, "Validation of Neutronic Methods Applied to the Analysis of Fast Sub-Critical Systems: The MUSE-2 Experiments," GLOBAL'97, page 639 (1997).
- [7] P. SELTBORG and J. WALLENIUS, "Proton Source Efficiency for different Inert Matrix Fuels in Accelerator Driven Systems," Int. Meeting AccApp'03, June 1-5, 2003, San Diego, California, USA (2003).
- [8] W. S. YANG, L. MERCATALI et al., "Effects of Buffer Thickness on ATW Blanket Performances", Int. Meeting Accelerator Applications/Accelerator Driven Transmutation Technology and Applications ADTTA/AccApp'01, November 11-15, 2001, Reno, Nevada, USA (2001).

- [9] G. ALIBERTI et al., "Analysis of the MUSE-3 Subcritical Experiment", Int. Conf. Global 2001, France, Paris, September (2001).
- [10] P. SELTBORG and J. WALLENUS, "Proton Source Efficiency for Heterogeneous Distribution of Actinides in the Core of an Accelerator-driven System", *Nucl. Sci. Eng.*, submitted for publication (2005).
- [11] S. PELLONI, "Static analysis of the PDS-XADS LBE and gas-cooled concepts", *Ann. Nucl. Energy* 32, 13 (2004).





**KTH Engineering Sciences**

**Transmutation of nuclear waste in gas-cooled  
sub-critical reactors**

DANIEL WESTLÉN

Licentiate Thesis  
Stockholm, Sweden 2005

TRITA-FYS 2005:60  
ISSN 0280-316X  
ISRN KTH/FYS/--05:60--SE  
ISBN 91-7178-196-X

KTH  
School of Engineering Sciences  
SE-106 91 Stockholm  
SWEDEN

Akademisk avhandling som med tillstånd av Kungl Tekniska högskolan framläggas till offentlig granskning för avläggande av Technologie licentiatexamen i fysik fredagen den 2005-11-25 klockan 14.00 i FA32, Albanova Universitetscentrum, Roslagstullsbacken 21, Stockholm.

© Daniel Westlén, October 2005

Tryck: Universitetsservice US AB

**Abstract**

The actinides in spent nuclear fuel constitute the main radiotoxic hazard in the long time perspective. Most of the fission products are short-lived and do not contribute significantly to the radiotoxicity after about 300 years after the fuel is discharged from the reactor. Transmuting the actinides into fission products may ease the task of designing geological repositories by drastically reducing the time scale during which these have to remain intact. Efficient transmutation requires hard neutron spectra. The hardest spectra are found in helium-cooled cores. The present work investigates the feasibility of utilising helium-cooled sub-critical cores for the task of transmuting actinides. High transmutation efficiencies are shown to be achievable. The risk of losing coolant pressure in the system does require innovative solutions for fuel design, which to some extent reduce the transmutation efficiency. The efficiency of the neutron spallation source coupled to the sub-critical system has been found to be 10% higher in a helium-cooled core compared to a lead-bismuth-cooled core.

# List of publications

## Included papers

The following papers are included in this thesis:

- I. D. Westlén and J. Wallenius, Neutronic and safety aspects of a gas-cooled sub-critical core for minor actinide transmutation, to be published in Nuclear Technology, April 2006
- II. D. Westlén and J. Wallenius, On TiN-particle fuel based helium-cooled transmutation systems, manuscript
- III. D. Westlén and P. Seltborg, Source efficiency studies in gas- and lead-bismuth-cooled subcritical accelerator-driven-cores, under review by Annals of Nuclear Energy

## The authors contribution

The author has performed all of the calculations for the three papers included in the thesis. The responsibility for writing paper I was shared with the coauthor. The general ideas of the designs presented in papers I and II have been worked out by the author together with the coauthor, where as the technical details are the work of the author. Paper III was written mainly by the author, the analysis of the calculations for this paper was performed together with the coauthor.

## Papers not included

The following papers have not been included in the thesis:

- IV D. Westlén, P. Seltborg and J. Wallenius, Source efficiency in gas- and lead-bismuth-cooled subcritical cores, International conference on accelerator applications (AccApp'05), Venice, Italy (2005)
- V D. Westlén and J. Wallenius, Achieving decay heat removal in a sub-critical fast gas cooled reactor, International Conference on Future Nuclear Systems, (GLOBAL'03), New Orleans, USA (2003)

- VI D. Westlén, J. Cetnar and W. Gudowski, Performance of transmutation assemblies in the gas-cooled XADS, International conference on accelerator applications (AccApp'03), San Diego, USA (2003)
- VII D. Westlén, W. Gudowski, J. Wallenius, K. Tuček, A Cost Benefit Analysis of an Accelerator Driven Transmutation System, (AccApp'01), Reno, USA (2001)

# List of abbreviations

|                         |   |
|-------------------------|---|
| ATW                     | accelerator-driven transmutation of waste                             |
| ADS                     | accelerator-driven system   |
| BN-350, BN-600, BN-800  | Soviet prototype fast reactors  |
| BR-1, BR-2, BR-5, BR-10 | Soviet experimental fast reactors                                     |
| BOC                     | beginning of cycle  |
| CAPRA                   | Consommation Accrué de Plutonium en Réacteur rApide                   |
| CEFR                    | China Experimental Fast Reactor                                       |
| CERN                    | Centre Européen pour la Recherche Nucleaire                           |
| CPF                     | coated particle fuel  |
| DFR                     | Dounreay Fast Reactor   |
| dpa                     | displacements per atom  |
| EBR-I, EBR-II           | Experimental breeder reactor<br>(American experimental fast reactors) |
| EFR                     | European Fast Reactor (design project)                                |
| EOC                     | end of cycle  |
| FAUST                   | German fast reactor test facility                                     |
| FBTR                    | Fast Breeder Test Reactor (India)                                     |
| FFTF                    | Fast Flux Test Facility (USA)   |
| FR-0                    | Swedish fast critical assembly  |
| GA                      | General Atomics   |
| GCFR                    | Gas-Cooled Fast Reactor (GA design project)                           |
| GFR                     | Gas-cooled Fast Reactor (Gen IV concept)                              |
| IAEA                    | International Atomic Energy Agency                                    |
| IFR                     | Integral Fast Reactor (American fast reactor design project)          |
| JAERI                   | Japan Atomic Energy Research Institute                                |
| JNC                     | Japan Nuclear Cycle Development Institute                             |
| JOYO                    | Japanese experimental fast reactor                                    |
| kgHM                    | kilogram heavy metal  |
| KNK-2                   | German fast reactor design project                                    |
| LBE                     | lead-bismuth eutectic   |
| LFR                     | Lead-cooled Fast Reactor (Gen IV concept)                             |
| LWR                     | light water reactor (thermal reactor)                                 |
| MK-I, MK-II, MK-III     | Joyo-core configurations  |

|                  |   |
|------------------|---|
| MONJU            | Japanese experimental fast reactor                                      |
| MOX              | mixed oxide (mixed U and Pu oxides used in LWR fuel)                    |
| MW <sub>el</sub> | megawatt electric   |
| MW <sub>th</sub> | megawatt thermal  |
| MWd/kg           | megawatt-days per kilo gram   |
| OECD             | Organisation for Economic Corporation and Development                   |
| OMEGA            | Options Making Extra Gains from Actinides                               |
| P&T              | partitioning and transmutation  |
| pcm              | 1/100 000   |
| PFBR             | Prototype Fast Breeder Reactor (India)                                  |
| PFR              | Prototype Fast Reactor (United Kingdom)                                 |
| PUREX            | plutonium uranium redox extraction                                      |
| PWR              | pressurised water reactor (LWR)   |
| SFR              | Sodium-cooled Fast Reactor (Gen IV concept)                             |
| SPX              | Superphénix   |
| TBP              | tributyl phosphate  |
| TMI              | Three Mile Island   |
| UOX              | uranium oxide   |
| XADS             | experimental accelerator-driven system<br>(European ADS design project) |

# Contents

|   |           |
|---|-----------|
| Contents  | vii       |
| <b>1 Burdening future generations</b>                     | <b>1</b>  |
| 1.1 Pioneering . . . . .                                  | 1         |
| 1.2 A change in attitude . . . . .                        | 2         |
| 1.3 High-level radioactive waste . . . . .                | 2         |
| 1.4 Transmutation . . . . .                               | 8         |
| <b>2 Nuclear reactions</b>                                | <b>9</b>  |
| 2.1 Cross-sections . . . . .                              | 9         |
| <b>3 Fast reactors</b>                                    | <b>13</b> |
| 3.1 Fast reactor development . . . . .                    | 13        |
| 3.2 Design projects . . . . .                             | 17        |
| 3.3 Gas-cooled fast reactors . . . . .                    | 18        |
| <b>4 Partitioning and transmutation</b>                   | <b>23</b> |
| 4.1 The development of transmutation techniques . . . . . | 23        |
| 4.2 Fuel cycle strategies . . . . .                       | 27        |
| <b>5 Fast sub-critical cores</b>                          | <b>33</b> |
| 5.1 Motives for sub-criticality . . . . .                 | 34        |
| 5.2 Spallation . . . . .                                  | 38        |
| 5.3 Reactor safety parameters . . . . .                   | 39        |
| 5.4 Fuel . . . . .  | 41        |
| 5.5 Coolants . . . . .                                    | 42        |
| 5.6 Material damage . . . . .                             | 45        |
| <b>6 Designing a gas-cooled transmutation core</b>        | <b>47</b> |
| 6.1 General design concerns . . . . .                     | 47        |
| 6.2 Decay heat removal . . . . .                          | 48        |
| 6.3 Calculation methods . . . . .                         | 49        |
| 6.4 Summary of the first paper . . . . .                  | 49        |



|          |                                       |           |
|----------|---------------------------------------|-----------|
| 6.5      | Summary of the second paper . . . . . | 56        |
| 6.6      | Summary of the third paper . . . . .  | 60        |
| <b>7</b> | <b>Concluding remarks</b>             | <b>67</b> |
|          | <b>Bibliography</b>                   | <b>69</b> |

# Chapter 1

## Burdening future generations

### 1.1 Pioneering

The possibility of releasing the enormous amounts of energy bound in atomic nuclei was terrifyingly demonstrated to the world on August the sixth in 1945 when a nuclear bomb destroyed Hiroshima. The atomic age had begun, threatening mankind with weapons never before imaginable, but also promising a new source of cheap energy.

In the early days the pioneering spirit grew strong. Large efforts were invested in designing nuclear power plants, nuclear propelled ships, aeroplanes and spacecrafts. Even nuclear weapons were suggested to be used for civilian purposes such as building canals, harbours and caves for storing oil [1]. Nuclear energy was to become an obliging servant of mankind. Reactors desalinating seawater would turn deserts into prospering gardens. Comfort would be brought to everyone's daily life.

The development accelerated and energy producing reactors were rapidly constructed, especially in the seventies. However, the fuel for the new energy source - uranium - was known to be a scarce metal. Already early in the development of nuclear power it was realised that reactors breeding their own fissile fuel were a necessity if the nuclear industry was to play a role in supplying energy on a large scale in the long perspective. Due to the high pace in reactor construction, uranium prices were expected to start rising rather soon. This would lead to a massive demand for breeder reactors. In this perspective, plutonium production arose as a concern, since all of the breeder reactors foreseen had to be supplied with their initial fuel loadings. The radioactive nuclides in the spent nuclear fuel - most of all plutonium - was at this time considered valuable resources. Fast breeder reactor development was focused on the design of breeders that would turn uranium into fissile plutonium as efficiently as possible. The foreseen rising uranium prices had to be met, but also nuclear power should phase out the fossil fuels as the worlds primary energy source [2]. Reactor designers were concentrating on achieving high *breeding ratios* giving as large plutonium production as possible. Short *doubling*

*times* were generally desired, doubling time being the time needed to double the fissile inventory of a certain core. The doubling time limits the pace at which new fast reactors may be started, since each core is initially loaded with fissile material produced in another core.

Soon however, more uranium resources were discovered and the number of nuclear reactors worldwide ceased to increase as fast as it used to. Together, this kept uranium prices at rather low and stable levels [3]. In this new situation the need for breeder reactors was no longer urgent and, consequently, the need for plutonium was no longer as stressed as it had seemed.

## 1.2 A change in attitude

After the accident at the Three Mile Island (TMI) nuclear power station in the end of March and beginning of April in 1979, an awareness of the potential dangers of nuclear power awoke, not only among the public, but also within the nuclear industry. The physical effects of the TMI accident outside of the reactor containment were very limited [4]. Even though the accident was quite severe, involving a partial core melt down, the releases of radioactivity from the plant were small. However, the accident had a tremendous impact since it showed that accidents in commercial nuclear power plants was a possibility. Before TMI, large scale nuclear accidents had been considered too unlikely to be given any serious consideration, especially not in the communication with the public.

Since the accidents at TMI, and seven years later in Chernobyl, the attitude towards the nuclear industry has gradually improved in many countries. However, even though the operation of the power plants is today considered safe by large groups of the public, the issue of the radioactive nuclides produced in the nuclear fuel remains. Today the exotic nuclides are regarded as a major problem due to their radioactivity and since they pose a potential health threat, whereas they were regarded as a valuable resource only two decades ago. Nowadays, the production of long-lived radio-toxic nuclides is a main argument against nuclear power.

In the eighties, the development of fast reactors was close to commercialisation with the construction of the BN-600 and the Superphénix demonstration reactors (Chapter 3). However, in France, technical difficulties in Superphénix, in combination with the unexpectedly low uranium prices, lead to a change in fast reactor policy. The fall of the Soviet Union lead to economical problems delaying the fast reactor programme there. In some countries, like Germany and Italy, the Chernobyl accident had a major impact on fast reactor policy and lead to closing down of the programmes.

## 1.3 High-level radioactive waste

The spent nuclear fuel can be divided into three main groups of nuclides; uranium, fission products and transuranic elements. The three groups pose waste manage-

ment issues of different characteristics and time scales. In order to compare the health hazards, the concept of radiotoxicity has been introduced.

### Radiotoxicity

It is well known that the health effects of different kinds of ionising radiation vary considerably. Alpha activity is rather harmless as long as the source of the radiation stays outside the body. Once inside the body it becomes very harmful. Gamma radiation penetrates the body, however the track of ions left in the tissue where the gamma radiation have passed is sparse, resulting in less harmful damage in the cells compared to the dense ion tracks produced by heavy, charged particles. The hazard of neutrons vary with energy. Each high energy neutron cause much more damage than do the average low energy neutron, however radiation induced damage is generally normalised per energy. With such a normalisation, thermal neutrons are quite harmful. Also, the residence time for sources of radioactivity in the body varies considerably. Some stay very long, some are of no use to the body and pass quickly through the digestion system. This, of course, has a major impact on the harmfulness of the radiation source.

Of course, the estimations of the hazard of different kinds of radiation are in no way exact. Instead, coefficients interrelating different ionising radiation are issued by the International Commission on Radiological Protection (ICRP) [5]. Using these guidelines, radiation from one nuclide may be weighted against another. Knowing the activity from each nuclide and the weighting coefficient for, i.e., ingestion, these can be summed up to give what will be refereed to as radiotoxicity. The radiotoxicity for inhalation would be somewhat differing.

The concept of radiotoxicity will be used to compare different kinds of spent nuclear fuel as well as to discuss the development of health hazards of the fuel over time. The problem with this approach is that it does not take transport processes in geological formations into account. The accuracy of comparing different waste forms for example in geological storage with regard to their respective radiotoxicities only, may be debated. In the end, the dose to the biosphere is the parameter of interest. The dose is dependent on more than the radiotoxicity. Transport processes are important, but also e.g. the integrity of the storage canisters over time. However, including such parameters makes the entire issue very scenario dependent.

### Uranium

In today's commercial reactors the main part of the uranium remains in the fuel after use in the core. Of the fissile nuclide  $^{235}\text{U}$ , some is left since the nuclear chain reaction stops before all of it is consumed. The most abundant nuclide in both the fresh and the spent fuel is  $^{238}\text{U}$ , which is not fissile. Fresh nuclear fuel for commercial reactors is usually enriched only to a few percent of  $^{235}\text{U}$ , the rest being  $^{238}\text{U}$ . Most of the  $^{238}\text{U}$  is not affected during irradiation in the reactor, but

a fraction of it is turned into  $^{239}\text{Pu}$  through neutron capture reactions. Higher nuclides are produced through subsequent neutron capture in  $^{239}\text{Pu}$ .

### **Fission products**

Heavy elements such as uranium and plutonium, are relatively neutron rich. For nuclear stability reasons they contain around 1.5 neutrons per proton, whereas most of the lightest elements contain about one neutron per proton. When a heavy nucleus undergoes fission, it also releases free neutrons. The number of neutrons released varies between none and about ten, the most probable being the release of two or three neutrons. However, since stable elements in the lower mass regions, where most of the fission products are found contain less neutrons per proton compared to the heavy nuclides, the newly born fission products are in general comparatively neutron rich, and therefore unstable. Through subsequent radioactive decays, the fission products lower their neutron content until stable nuclei are formed.

Most of the fission products have rather short half-lives, which leads to a very intense radioactivity immediately after discharge from the core. However, during the first minutes and hours after that the reactor is shut down, the activity level decreases rapidly. In the case of an accident in a nuclear reactor, the short-lived nuclides are hazardous due to their high activity, which is also the cause of a significant heat production in the reactor core right after shutdown. Ensuring the removal of this decay heat is a main issue in designing safe reactors.

Some fission products have half-lives in the order of decades, the most abundant of them being  $^{90}\text{Sr}$  and  $^{137}\text{Cs}$ . These nuclides would cause problems if they were released since they remain harmful to humans for a few hundred years. Also, the decay of  $^{90}\text{Sr}$  and  $^{137}\text{Cs}$  contributes for the main heat production in the spent nuclear fuel after the very short-lived fission products have decayed. The heat raises waste management concerns since there are physical limits to the maximum temperatures allowed when storing radioactive waste.

A few of the fission products have very long half-lives, in the order of millions of years. However, the radioactivity of these is so small that their contribution to the total radiotoxicity is negligible. This is illustrated in Figure 1.1, which shows the radiotoxic inventory of spent light water reactor fuel as function of time. The figure also shows how the contribution from the fission products becomes nearly constant after the decay of  $^{90}\text{Sr}$  and  $^{137}\text{Cs}$ . In conclusion, there will be traces of radioactivity, originating from the fission products virtually forever. However, the immediate danger to humans disappears during the first three hundred years. After that, only the few very long lived fission products remain in the waste. Their contribution to the radiotoxicity is lower than the radiotoxicity in uranium found in nature - as was discussed in Section 1.3. It may be concluded that, in the long time perspective, another group of nuclides constitute the main radiological hazard - the transuranic elements.

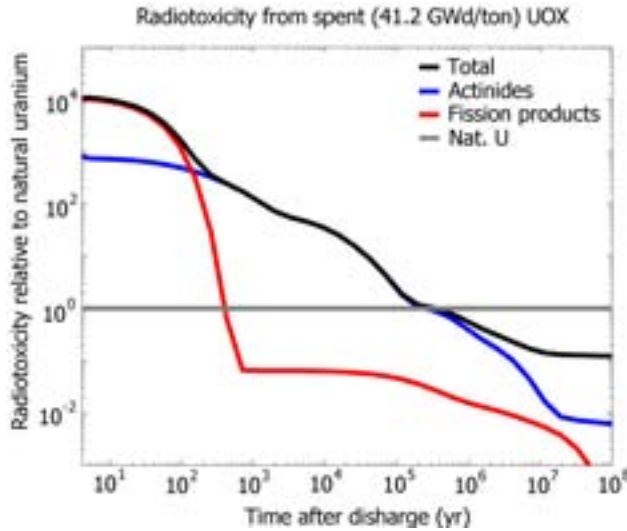
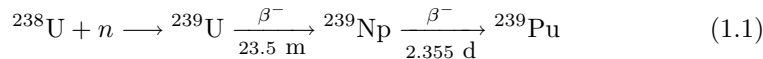


Figure 1.1: Radiotoxic inventory in spent fuel from light water reactors. The reference level represents the radiotoxicity in the amount of uranium originally used to produce the fuel.

### Transuranic elements

Apart from inducing fission reactions in heavy nuclei, the neutrons in the reactor are captured in all kinds of nuclei turning them into heavier isotopes of the same element. These reactions, together with the fission reactions, are the main sources of radioactive nuclides in a nuclear reactor.

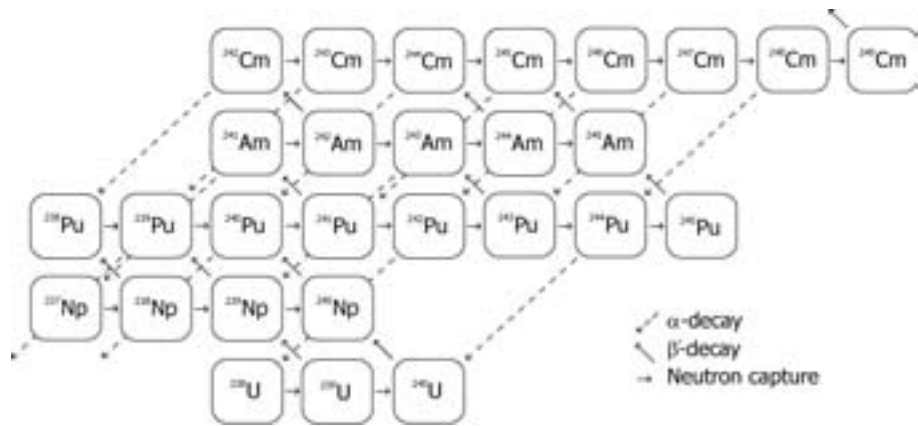
The probability of neutron capture is determined by the *capture cross-section*, as is further discussed in Chapter 2.1. Cross-sections are energy dependent and they show very different behaviour for different nuclides.  $^{238}\text{U}$  is abundant in the reactor core and significant amounts of heavier nuclides are built from this nuclide through successive neutron capture reactions and decays. The most abundant among the transuranic nuclides is  $^{239}\text{Pu}$ , which is produced according to expression 1.1, when a neutron is captured in  $^{238}\text{U}$ , creating  $^{239}\text{U}$ , which beta-decays with a half-life of 23.5 minutes to  $^{239}\text{Np}$ , that in turn beta-decays to  $^{239}\text{Pu}$  within days.



Starting from  $^{239}\text{Pu}$ , even heavier nuclides are produced in subsequent neutron capture reactions. In this way, americium is produced from plutonium and curium is built from americium. We refer to elements containing more protons than uranium as transuranic elements. Most of these have long half-lives compared to the fission

| Nuclide           | Half-life           | Nuclide            | Half-life |
|-------------------|---------------------|--------------------|-----------|
| $^{235}\text{U}$  | $7.04 \cdot 10^6$ y | $^{241}\text{Am}$  | 432 y     |
| $^{238}\text{U}$  | $4.47 \cdot 10^9$ y | $^{242m}\text{Am}$ | 141 y     |
| $^{237}\text{Np}$ | $2.14 \cdot 10^6$ y | $^{242}\text{Am}$  | 16.0 h    |
| $^{238}\text{Np}$ | 2.12 d              | $^{243}\text{Am}$  | 7370 y    |
| $^{238}\text{Pu}$ | 87.7 y              | $^{242}\text{Cm}$  | 163 d     |
| $^{239}\text{Pu}$ | 24100 y             | $^{243}\text{Cm}$  | 29.1 y    |
| $^{240}\text{Pu}$ | 6560 y              | $^{244}\text{Cm}$  | 18.1 y    |
| $^{241}\text{Pu}$ | 14.4 y              | $^{245}\text{Cm}$  | 8500 y    |
| $^{242}\text{Pu}$ | $3.73 \cdot 10^5$ y |                    |           |
| $^{243}\text{Pu}$ | 4.96 h              |                    |           |

Table 1.1: Half-lives of important actinide nuclides

Figure 1.2: The most important actinide nuclides and their relations, via  $\alpha$ -decay,  $\beta$ -decay and neutron capture reactions.

products. The half-lives of the most important transuranic nuclides are displayed in Table 1.1. The most important paths for build-up of transuranium nuclides are displayed in Figure 1.2. The most abundant of the nuclides produced through neutron capture in  $^{238}\text{U}$  rich fuels is  $^{239}\text{Pu}$ , with a half-life of 24100 years. Other important nuclides are  $^{240}\text{Pu}$ ,  $^{242}\text{Pu}$ ,  $^{241}\text{Am}$  and  $^{243}\text{Am}$ , all with long half-lives. About a thousand years after discharge from the reactor, these nuclides alone are responsible for almost the entire radiotoxicity of the radioactive waste, which is shown in Figure 1.3.

As may be seen in Figure 1.1, the contribution to radiotoxicity from neptunium is much below the reference level. However, in some geological environments, e.g.,

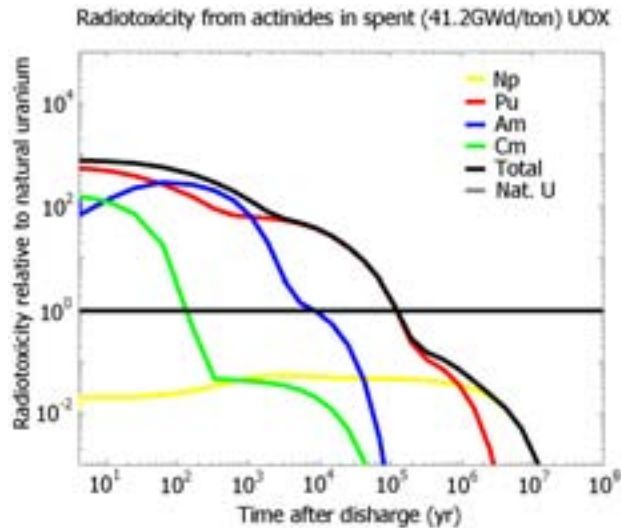


Figure 1.3: Actinide inventory in spent fuel from light water reactors.

the Yucca Mountain, where the American spent fuel repository is planned to be built, neptunium is mobile and may contribute significantly to the dose that people might receive from the spent fuel in the very long run. It should be noted that the dose people are expected to receive from leaking repositories in many years from now are well below the level of background radiation. In the Swedish granite bedrock, neptunium is not very mobile. This in combination with the relatively low radiotoxicity contribution from neptunium is the reason why it is not considered in the transmutation strategy adopted in this work.

Determining the hazard of long-lived radioactive nuclides is a complex question. The parameters judging the risk of an individual nuclides are several. Half-life and activity is of course important. The choice of repository technology in combination with transport processes for the nuclides in the environment surrounding the repository are also important. Finally, the scenario chosen is has quite an impact on the analysis. In case human activity does not interfere with the repository, low releases of radioactive materials should be expected. However, if human intrusion, deliberate or undeliberate, is part of the scenario, the assessment of the hazards to life changes completely. All of this should be considered when settling the strategy for the spent fuel.



## 1.4 Transmutation

Due to the long half-life and relatively high abundance of  $^{239}\text{Pu}$ , the spent fuel from today's nuclear fuel cycle will have to be kept separated from the biosphere for many hundreds of thousands of years. Since fission products in general have far shorter half-lives than the transuranic elements, it is tempting to fission the heavy elements, to turn them into fission products. This would completely change the timescale of the nuclear waste issue. All heavy nuclides are fissionable, but some of them only by neutrons with energies in the order of 1 MeV or higher.

Any process changing one nuclide into another nuclide is a *transmutation process*. In the following, the term transmutation will usually refer to the destruction of heavy transuranic nuclides through fission reactions or through subsequent capture and fission reactions.

The main demand on a reactor dedicated to the transmutation of heavy nuclides is a high transmutation efficiency. The actinides should optimally be fissioned directly rather than after a series of neutron capture reactions. Achieving this minimises the production of americium, curium and even heavier elements, that are responsible for the main fraction of the neutron radiation dose during reprocessing and fuel manufacturing. Further, the amount of plutonium needed to supply neutrons for capture reactions in the transmutation reactor is lowered, the more efficient the transmutation. More efficient transmutation implies quicker and cheaper incineration of the long-lived radioactive nuclides. This thesis presents an attempt of designing a nuclear reactor with highest possible transmutation efficiency.

The term *transmutation efficiency* refers to the amount of transuranic nuclides fissioned per gigawatt of thermal power ( $\text{GW}_{\text{th}}$ ) produced. For a core loaded with transuranic elements only, this term would then imply the theoretical maximum. Here we have used the term referring to the fraction of the transuranic elements fissioned per resource assigned to the task. The resource consumption is intimately connected to the number of fuel cycles. This also applies to the time needed to complete the task.

## Chapter 2

# Nuclear reactions

Among all of the nuclear reactions occurring in a nuclear reactor, two are of special interest when discussing the buildup and transmutation of heavy nuclides. Of course, the fission reaction is of interest since it is responsible for the production of the fission products, it consumes the heavy nuclides and it is the main source of neutrons and energy in the nuclear reactor. The capture reaction is interesting to us since it builds heavy long-lived nuclides, starting from uranium. In this chapter, these reactions will be studied more in detail.

### 2.1 Cross-sections

The probability for a nuclear reaction to occur is described by the cross-section. Cross-sections have the unit of area and may be understood as an effective intersection area between the target nucleus and the incident particle. The basic unit for cross-sections is one *barn*, which equals  $10^{-28} \text{ m}^2$

Neutron cross-sections are energy dependent. The distribution of neutron energies in a reactor is dependent on a series of variables, the most important being the moderating properties of the reactor. Neutrons lose energy when interacting with nuclei in scattering reactions. Therefore, the probability of interaction and the masses of nuclei in the reactor determine how much the neutrons are moderated.

Fission neutrons are born with a broad spectrum of energies. The energy distribution is slightly dependent on the mother nucleus. However, all of the actinides exhibit a Watt-distributed fission energy spectrum peaking at a neutron energy of about 0.7 MeV, with a mean energy around 2 MeV. The rate of different neutron interactions are given by the cross-section, the neutron flux and the density of the reacting nuclei. The cross-section for the individual nucleus is referred to as the microscopic cross-section ( $\sigma$ ). When multiplied by the number density of the reacting nucleus ( $N$ ), one gets the macroscopic cross-section ( $\Sigma$ ) at some position,  $\mathbf{r}$ , for some energy,  $E$ , as in Equation 2.1.

$$\Sigma(\mathbf{r}, E) = \sigma(E) \cdot N(\mathbf{r}) \quad (2.1)$$

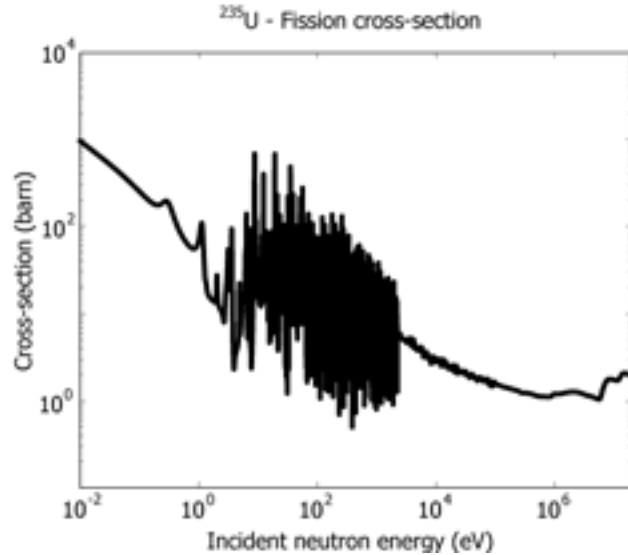


Figure 2.1: Microscopic fission cross-section in  $^{235}\text{U}$  as function of incident neutron energy.

The reaction rate in some position  $\mathbf{r}$  is given by the integral of the neutron flux and the cross-section for the reaction over all energies, according to Equation 2.2.

$$R(\mathbf{r}) = N(\mathbf{r}) \int_0^{\infty} \sigma(E) \Phi(\mathbf{r}, E) dE \quad (2.2)$$

Reaction cross-sections vary over several orders of magnitude with neutron energy. This is the case both for fission and capture cross-sections. The fissile nuclides  $^{235}\text{U}$  and  $^{239}\text{Pu}$  have rather large probabilities for fission for low-energy neutrons. This is because their fission cross-sections are significantly larger than their capture cross-sections in the thermal energy region. Thermal neutrons have approximately the same velocities as the surrounding medium, which typically corresponds to an energy of about 0.025 eV. Figure 2.1 displays the cross-section for fission in  $^{235}\text{U}$ . It is seen that it is much larger at thermal energies than at higher energies. The fluctuating behavior of the cross-section in the epi-thermal energy region are resonances. For some neutron energies in this region, the cross-sections are very much larger than for neighboring energies. These resonances will turn out to be very important for the safety parameters of reactors. This is further discussed in Chapter 5.3. Also for the fissile nuclide  $^{239}\text{Pu}$ , the cross-section is the highest for low energies as shown in Figure 2.2. Both for  $^{235}\text{U}$  and for  $^{239}\text{Pu}$  there are resonances in the fission cross-sections above the thermal neutron energies. For the higher neutron energies, the cross-sections stabilise again around about one barn

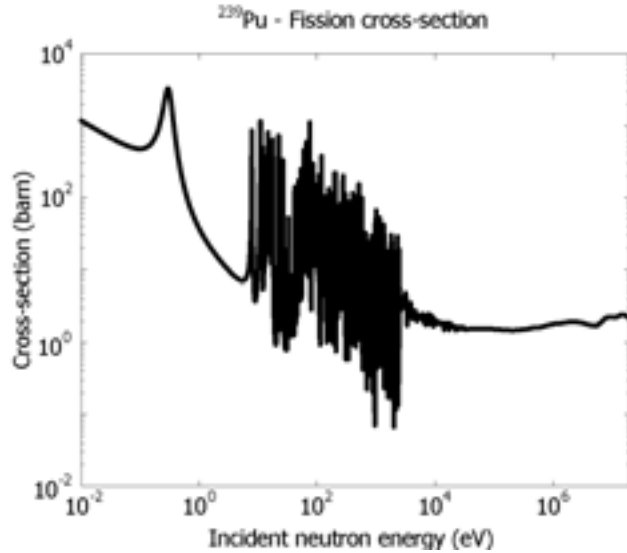


Figure 2.2: Microscopic fission cross-section in  $^{239}\text{Pu}$  as function of incident neutron energy.

for both nuclides. The even- $N$  nuclides (containing an even number of neutrons) are not fissile in interactions with thermal neutrons. However, when the incident neutron carries enough energy to excite the nucleus above the fission barrier, they may fission. Figure 2.3 shows how, for energies around 1 MeV, the probability for fission in  $^{238}\text{U}$  raises several orders of magnitude as the energy of the incident neutron carries enough energy to raise the nucleus over the fission barrier. The increasing fission probabilities make fission reactions more probable than capture reactions at high enough energies. Figure 2.3 clearly shows why a fast neutron spectrum is necessary to fission the even- $N$  nuclides. For low incident neutron energies, the capture process dominates completely over fission in  $^{238}\text{U}$ ,  $^{239}\text{Pu}$  as well as  $^{241}\text{Am}$ . However at higher energies the fission is the dominating process. Especially, this is the case for  $^{238}\text{U}$  and  $^{241}\text{Am}$ . The improved fission to capture probability is the reason a transmutation core is efficient only when designed to give a fast neutron spectrum. In a thermal neutron spectrum more heavy isotopes would be built up, than fissioned. It should be noted that  $^{245}\text{Cm}$  is fissile in the thermal spectrum. Successive buildup of heavy nuclides eventually leads to the production of this nuclide. In theory it would thus be possible to transmute the actinides in a thermal spectrum. However, the production of  $^{245}\text{Cm}$  requires quite a few capture reactions. Starting with  $^{242}\text{Pu}$ , three neutrons are needed to produce  $^{245}\text{Cm}$  via  $^{243}\text{Am}$  and  $^{244}\text{Cm}$ . Starting at  $^{241}\text{Am}$  instead requires three neutrons to produce fissile  $^{239}\text{Pu}$ , via  $^{242}\text{Cm}$  and  $^{238}\text{Pu}$ . The eventual fission of  $^{245}\text{Cm}$  produces

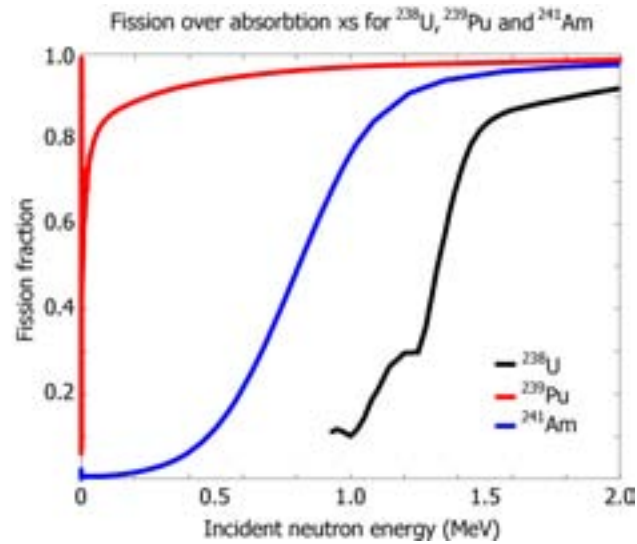


Figure 2.3: Fission over absorption cross-sections ratios for  $^{238}\text{U}$ ,  $^{239}\text{Pu}$  and  $^{241}\text{Am}$ .

in average 3.5-3.6 neutrons [6] [7]. A large part of the fission neutrons produced would be needed to maintain the chains of capture reactions building the fissile nuclide, leaving very few left for e.g. parasitic capture in construction materials and for leakage. It is a demanding task to design a core that may operate under such a poor neutron economy. The conclusion is that efficient transmutation of the even-N nuclides does in practice require a fast reactor.

## Chapter 3

# Fast reactors

### 3.1 Fast reactor development

Fast reactors have been a prime interest to reactor physicists ever since the early days of the atomic age. The first fast neutron spectrum core to be constructed was Clementine at Los Alamos in 1946, which had a power of 25 kW. The first electricity ever produced by a nuclear reactor was generated by the fast reactor EBR-I, USA in 1951 [9].

Several countries followed and constructed fast reactors, the Soviets started BR-1 in 1958. The Dounreay Fast Reactor (DFR) in Britain went critical in 1959. Both France and Germany constructed fast reactors during the sixties and seventies (Rapsodie, KNK-2). Later, also China and India have constructed fast reactors. Sweden had a zero-power fast reactor, FR-0. It was located in Studsvik and achieved criticality for the first time in 1964 [10].

Larger plants were constructed. In the eighties the belief that fast reactors are necessary to supply energy to society was still strong. The fast reactor development reached the demonstration phase with the construction of BN-600 in Russia in 1980 and Superphénix in France in 1985. Several countries had serious plans to construct commercial breeders. Milestones of the world-wide fast reactor development are summarised in Table 3.1.

In the following the fast reactor programmes still running will be studied somewhat more in detail. There will also be an overview of some interesting design projects, where nothing have been built so far.

Two concepts will be given particular attention. The *burnup* is a measure of how much energy is taken out of the fuel. It is given in megawatt days per kilogram or sometimes in gigawatt days per ton. The radiation damage induced in materials in the core is proportional to the radiation dose and is measured in displacements per atom - dpa.

| Reactor       | Country     | Critical | MW <sub>th</sub> | MW <sub>el</sub>     | Coolant |
|---------------|-------------|----------|------------------|----------------------|---------|
| Clementine    | USA         | 1946     | 0.025            | -                    | Hg      |
| EBR-I         | USA         | 1951     | 1.2              | 0.2                  | NaK     |
| BR-1 (BR-2)   | USSR        | 1956     | 0.1              | -                    | Hg      |
| BR-5 (BR-10)  | USSR        | 1958     | 5 (10)           | -                    | Na      |
| DFR           | UK          | 1959     | 60               | 15                   | NaK     |
| LAMPRE        | USA         | 1961     | 1                | -                    | Na      |
| Fermi (EFFBR) | USA         | 1963     | 200              | 65                   | Na      |
| Rapsodie      | France      | 1967     | 40               | -                    | Na      |
| BOR-60        | USSR        | 1968     | 60               | 12                   | Na      |
| EBR-II        | USA         | 1968     | 62               | 20                   | Na      |
| SEFOR         | USA/Germany | 1969     | 20               | -                    | Na      |
| KNK-2         | Germany     | 1972     | 58               | 21                   | Na      |
| BN-350        | USSR        | 1972     | 1000             | 150+H <sub>2</sub> O | Na      |
| Phénix        | France      | 1973     | 560              | 250                  | Na      |
| PFR           | UK          | 1974     | 600              | 250                  | Na      |
| JOYO          | Japan       | 1977     | 100              | -                    | Na      |
| BN-600        | USSR        | 1980     | 1470             | 600                  | Na      |
| FFTF          | USA         | 1980     | 200              | 61                   | Na      |
| Superphénix   | France      | 1985     | 3000             | 1200                 | Na      |
| FBTR          | India       | 1985     | 40               | 13                   | Na      |
| MONJU         | Japan       | 1995     | 714              | 300                  | Na      |
| BN-800        | Russia      | ?        | 2100             | 880                  | Na      |
| PFBR          | India       | 2010?    | 1210             | 500                  | Na      |
| CEFR          | China       | 2005?    | 65               | 23.4                 | Na      |

Table 3.1: Important fast reactor projects [2][8]

### France - Rapsodie, Phénix and Superphénix (SPX)

The fast reactor programme in France started with the experimental reactor Rapsodie in 1967. In 1973, the power reactor Phénix was completed. Initially, Phénix was loaded with fifty percent uranium oxide (UOX) fuel and fifty percent mixed uranium and plutonium oxide fuel (MOX), but since 1977 the core is loaded with pure MOX [2]. In Phénix, the burnup reached 90 MWd/kg in the centre and 115 MWd/kg in the periphery, corresponding to 13.5% burnup of the heavy atoms. In some experimental assemblies, the burnup was even higher. The BOITIX 9 experimental sub-assembly reached 144 MWd/kg. Individual pins have reached higher burnups, the record holder being the CZAR 1 experimental pins, which reached a burnup of over 151 MWd/kg. At 90 MWd/kg, the radiation dose to the structural material in sub-assemblies was 90 dpa [11].

The full-scale prototype Superphénix (SPX) achieved criticality for the first time

in 1985. Electricité de France (EdF) had at this time plans to build two commercial 1500 MW<sub>el</sub> sodium-cooled breeder reactors during the eighties. However, the plans were changed for several reasons.

Three incidents caused long periods of outage in Superphénix. In May 1987 there was a sodium leak in the fuel storage drum. Brittle carbon steel had been used for constructing the drum. Using stainless steel instead would probably have prevented the accident. Operation could be resumed after two years. In July 1990, SPX was shut down again after a three week air leak. There were no instruments for monitoring impurities in the atmosphere above the sodium surface, which meant no one discovered the leak at first. The purification of the sodium lasted for eight months. The third incident occurred in the heat-exchanger where there was an argon leak. None of the incidents implied any serious threat to reactor safety, two of them were graded as ones and one as a two on the reactor incident scale, INES [12].

Apart from its operational difficulties, SPX was an expensive project. The cost of installed capacity in SPX was between 2.2 and 2.7 times the cost of installed capacity in PWRs constructed at the same time [13]. The BN-600 project in Russia, as a comparison, was much cheaper, where the cost of installed capacity was 1.3 times the cost of a VVER-1000 constructed at the same time [14]. Compared to the Russian BN-600, SPX was a more complex design with a much larger sodium inventory and a technically more advanced building.

Superphénix produced its last power in December 1996. In 1997, the French government decided to shut down the reactor.

### Japan - Joyo and Monju

Japan started its fast reactor Joyo in 1977. Initially, it had a core configuration called MK-I, with a power of 50 MW<sub>th</sub>. MK-I was upgraded to 75 MW<sub>th</sub>. Later, reconfigurations of the core were made, resulting in the 100 MW<sub>th</sub> MK-II core [8]. In a recent upgrade, the thermal power was raised to 140 MW<sub>th</sub> [15]. After this reconstruction, the core is referred to as the MK-III core. Joyo (MK-III) has reached a burnup of 71 MWd/kg.

In April 1994, the prototype core Monju went critical. Monju is a 714 MW<sub>th</sub>, 280 MW<sub>el</sub> core loaded with mixed oxide (MOX) fuel. In December 1995, there was a sodium leak in the inactive loop at Monju. Monju has not yet been restarted after the repairs [9].

### Russia - BN-350, BN-600 and BN-800

The Soviet fast reactor BN-350, in Aktau on the shores of the Caspian sea in Kazakhstan, attained criticality in November 1972, making the Soviet Union the first country to build a prototype fast reactor. At full power, BN-350 produced 150 MW electricity and about 120 000 tonnes of desalinated water per day. The



reactor had a loop-type sodium-cooled core, fuelled with  $\text{UO}_2$ . It was closed in 1999 [2][9].

BN-600 at the Beloyarsk nuclear power plant was connected to the grid on April 8, 1980. A compact design with a low sodium inventory, based on BN-350, was chosen. Due to cladding damage caused by high linear powers (54 kW/m), the core design was modified in 1986 and 1987. Initially, the fuel was divided into two zones with different enrichment of  $^{235}\text{U}$ . After the modification, the core got three zones with lower enrichment - 17%, 21% and 26% instead of 21% and 33%. This was compensated for by increasing the core height from 750 mm to 1000 mm. Also the structural materials were changed. In the new core configuration, the peak linear power was 47.2 kW/m. The design work on the core has continued aiming at increasing the burnup of the core [16].

BN-800 is a commercial fast reactor being constructed in Russia. It will be the fourth block at the Beloyarsk nuclear power station. The construction work began at both the Beloyarsk and South-Ural power plants in the mid-eighties, but were put on hold due to the fall of the Soviet Union and due to the Chernobyl accident. However, construction work has started again in Beloyarsk, after being relicensed in 1997.

### China - CEFBR

In China an experimental fast reactor (CEFBR), (65  $\text{MW}_{\text{th}}$ /23.4  $\text{MW}_{\text{el}}$  [8]) is under construction at the China Institute of Atomic Energy (40 km from Beijing). Criticality is planned in 2005. China's fast reactor programme is aimed at deploying commercial fast reactors around 2030. Sodium-cooled, pool-type reactors are foreseen.

### India - FBTR and PFBR

In October 1985 India commissioned a 13  $\text{MW}_{\text{el}}$  [8] fast spectrum research reactor at the Kalpakkam site known as the Fast breeder test reactor (FBTR). Carbide fuels are used in the FBTR. The original intention was to use highly enriched uranium oxide. However because of the embargo on such material on India following its weapons programme, that was not possible. The carbide fuels have been irradiated to just over 140  $\text{MWd/kgHM}$ . It is believed that the burnup may be further increased to around 150  $\text{MWd/kgHM}$  [17].

As a next step in its fast reactor programme, India is constructing a 500  $\text{MW}_{\text{el}}$  prototype fast reactor - PFBR - at Kalpakkam. The PFBR will be a MOX fuelled sodium-cooled pool type reactor. The maximum linear power is 45 kW/m, with an average of 32 kW/m [18].

## 3.2 Design projects

### The European Fast Reactor

In 1988, the European Fast Reactor collaboration was formed. Initially, the aim was to design a reactor that would be safe, in comparison to light water reactors, while being an economically competitive fast reactor. As experience was gained from Superphénix, additional demands were added to the EFR design, including a high load factor, better inspection and repair possibilities compared to Superphénix and better fuel cycle flexibility. In order to meet the economical condition, the targeted plant lifetime was 60 years.

A special core was designed within the EFR project for the incineration of plutonium - CAPRA (Consommation Accrué de Plutonium en Réacteur rApide). The difference in design to the breeder fuel assemblies is that the CAPRA core has smaller pin diameter and a larger distance between subassemblies, pitch. Further, the plutonium content of the MOX fuel is higher, in order to increase plutonium incineration [19][20].

### Integral Fast Reactor

The Integral Fast Reactor (IFR) project was undertaken at Argonne National Laboratory, USA, from 1984 to 1994. IFR was a reactor designed to be able to either burn fissile material, keep the inventory constant or breed more fissile material. One of the main ideas behind IFR was to close the nuclear fuel cycle by reprocessing the spent fuel and by incinerating all of the actinides. Other design criteria were a strong resistance to proliferation of fissile material and a high tolerance to errors and mistakes, all at a competitive cost [21].

The concluding design was a metal fuel sodium-cooled design. The fuel design was in the form of a metal alloy with ten weight percent zirconium, 15 to 25 weight percent recycled transuranic elements and the rest depleted uranium. Extensive fuel irradiation tests were performed in the EBR-II core from 1983 to 1994. Peak burnup levels of 20 atom percent (200 MWd/kg) and linear ratings up to 50 kW/m were reached. The upper core temperature was limited by the cladding to 550 °C to 600 °C [9].

Reprocessing of the fuel was suggested to take place on site in a pyrochemical process capable of handling highly radioactive fuel, thereby shortening the required cooling period between discharge and reprocessing, see also Chapter 4.2. By keeping the transuranic nuclides admixed in every reprocessing step the fuel cycle would be resistant to plutonium proliferation [21].

The IFR programme was cancelled in September 1994, following a change in American nuclear policy [9].

## Generation IV

The *Generation IV* project includes the study of six different reactors which all meet fifteen criteria in the areas of sustainability, economics, safety and proliferation resistance. Three of the six chosen reactor concepts are fast reactors, one gas-cooled (GFR), one lead-cooled (LFR) and one sodium-cooled (SFR).

The gas-cooled reactor is based on a 600 MW<sub>th</sub>/288 MW<sub>el</sub> helium-cooled core. The outlet temperature of the helium is 850 °C, which allows for a high thermal efficiency. Generation IV ranks its reactors after a list of criteria. The GFR has achieved a high ranking in sustainability because of the efficient transmutation of actinides. In the rest of the classes, it is ranked as a good reactor.

The LFR is foreseen to be cooled by either lead or lead bismuth eutectic (LBE). Several designs are suggested in different power intervals. The coolant outlet temperature is much lower than in the GFR, mainly due to corrosion concerns emanating from the use of lead coolant. The LFR is ranked the same as the GFR except for the sustainability, where the LFR is even higher ranked.

The sodium-cooled concept is much like the LFR, both in design, use, temperature and ranking. However, Generation IV assumes that SFR may be deployed in 2015 since there exists already considerable experience on sodium technology, whereas there is less experience concerning the GFR and LFR. These could possibly be deployed in 2025. [22]

However, keeping in mind that the selection of a suitable site and especially the licensing process for new reactors takes quite a long time, 2015 seems like an unrealistic date for deploying the first Generation IV reactor.

### 3.3 Gas-cooled fast reactors

The idea of gas-cooled reactors is old. In 1945, a helium cooled, BeO moderated high temperature reactor was suggested. However, the priority at the time was the construction of high power density submarine reactors. Water-cooled reactors were chosen, which were later to develop into the pressurised water reactors. [23] But the idea of gas cooling was not forgotten, and soon it came into use again in new innovative core designs.

#### GCFR

During the 1960s, a major design study was performed on gas-cooled fast reactors (GCFR). The study was lead by the Gulf General Atomics company (GA) and was financed by more than 40 utilities [24].

Two designs were presented, one 300 MW<sub>el</sub> [25] and one 1000 MW<sub>el</sub> [26] plant. Both designs were helium-cooled. The main benefit of helium cooling shown in the design studies was the much improved breeding ratio of the proposed cores compared to sodium-cooled cores. The breeding ratio of a reactor is the number of fissile nuclides produced, by neutron capture in nonfissile (fertile) nuclides and

radioactive decay, per nuclide fissioned. When it is higher than one, the core produces more fissile material than it consumes. The *doubling time* - the time needed to double the fissile inventory - for the 1000 MW<sub>e1</sub> GA-GCFR design is seven years at 16 percent fuel enrichment. For the sodium-cooled designs, the irradiation time required to double the fissile inventory is around ten years [26].

Both of the designs have steam generators. Using steam super-heaters to improve the performance, would, using the technology available at the time, have given an efficiency of 37.6% for the small plant and somewhat higher, depending on configuration, for the larger plant. The GCFR designers pointed out that the use of direct-cycle gas turbines, omitting the steam generators, would improve the efficiency in electricity production and ease the demands on secondary cooling [26]. However, in the 1960s, direct-cycle gas turbines needed further development before they could manage this task. A more extensive discussion on this is given in Section 5.5.

### Recent Japanese gas-cooled fast reactor development

In Japan, fast reactors are a main focus for the future energy system. Since 1999, the Japan Nuclear Fuel Cycle Development Institute (JNC) and the Japan Atomic Energy Research Institute (JAERI) are conducting feasibility studies on commercial fast reactors in cooperation with the nuclear industry. Sodium, heavy metal and gas-cooled concepts have been studied. Three gas-cooled concepts were chosen for further studies to find one main alternative. These were; a carbon dioxide-cooled pin type core, a helium-cooled pin type core and a helium-cooled coated particle fuel type core. Both the steam turbine (550 °C) and the direct-gas (850 °C) turbine power generation alternative have been considered. The steam alternative is not compatible with coated particles since the combination of introducing both steam and titanium nitride particle coatings moderates the neutron spectrum too much. Carbon dioxide cause corrosion concerns above 650 °C, that have not been solved, and thus, it is not compatible with the direct-gas turbine alternative [27].

A comparative study showed that construction costs would be at the same level both for the carbon dioxide-cooled concept and the helium-cooled particle fuel concept. The helium system was found to be superior in thermal efficiency as it is operating at much higher temperatures. Also, the safety analysis showed that: *"In a CPF (coated particle fuel) type, core melt could be avoided without any active component actuations even under depressurized accident conditions, namely, coolable geometries of the core would be kept and the core would be cooled only with passive components and natural circulations under the condition of a depressurized accident, without scram and without active component actuation."* [27] According to the study, the fission products that would be released, would stay in the containment.

Based on the safety analysis and on the thermal efficiency being 46.7%, the coated particle design was chosen from the three alternatives studied [27].

Two entirely different fuel geometries have been investigated. One is based on hexagonal blocks of fuel particles hosted in a silicon carbide matrix. The blocks have vertical coolant tubes. In this way, the helium is never in direct contact with the fuel particles. This reduces the risk of contamination of the helium by leakages of gaseous fission products from damaged particles.

The second fuel geometry was designed after an idea presented by Gratton et al [28]. Their design is based on the idea of horizontal flow. The particle fuel is contained in between an inner tube and an outer tube. Both tubes are made of silicon carbide and are porous. The design gives an efficient cooling and a homogenous temperature. In Gratton's original design, the gas flows from the bottom, upward at the outside of the fuel, through the fuel and then upwards and out through the inner tube [28]. Konomura et al. suggests a similar design but proposes to lead the helium to the inner tube first, letting it exit on the outside [27]. The original design by Gratton is displayed in Figure 3.1.

### Properties of gas-cooled reactors

Helium and carbon dioxide has historically been the main candidates for gas reactor coolants. In early gas-cooled reactors,  $\text{CO}_2$  was a common gas coolant. Helium might have been preferred, but at the time it was both expensive and difficult to buy commercially. Heat transport is determined by the mass flow, the heat capacity and the temperature increase of the transporting medium. For helium and  $\text{CO}_2$ , it is more or less equal at equal pressure and temperature increase, the excellent heat capacity of helium compensating for the lower density. The main thermo-hydraulic advantage of using helium rather than  $\text{CO}_2$  is the much better heat conductivity of helium, which gives a more homogenous temperature and, thus, more efficient heat transport.

Gas cooling of a reactor core possesses some important advantages to liquid metal cooling. The possibility of visual inspection of the core makes both operation and repairs easier. Chemical reactivity of the coolant is not a source of serious concern for helium-cooled reactors, whereas this is a main issue for metal-cooled reactors. Sodium reacts violently with both air and water. Lead-bismuth eutectic cause both corrosion and erosion concerns.

Moreover, the neutronic properties are less favourable for metals, than for gases. Both sodium and bismuth will be activated by the neutron flux in the reactor environment. Helium, is inert to neutron radiation and is not activated. Avoiding activation of the coolant simplifies maintenance work considerably. Since the cross-section for neutron interactions with helium is low, helium cooling allows for hardening of the neutron spectrum, i.e., shifting the spectrum to higher energies, yielding higher fission to capture ratios as compared to metal-cooled cores, where scattering reactions soften the spectrum and capture reactions consume neutrons. In the case of a transmutation core, which is a fast reactor dedicated to the incineration of heavy actinides, which leads to improved transmutation efficiency. In a fast reactor dedicated to breeding, the improved neutron economy from using helium instead of

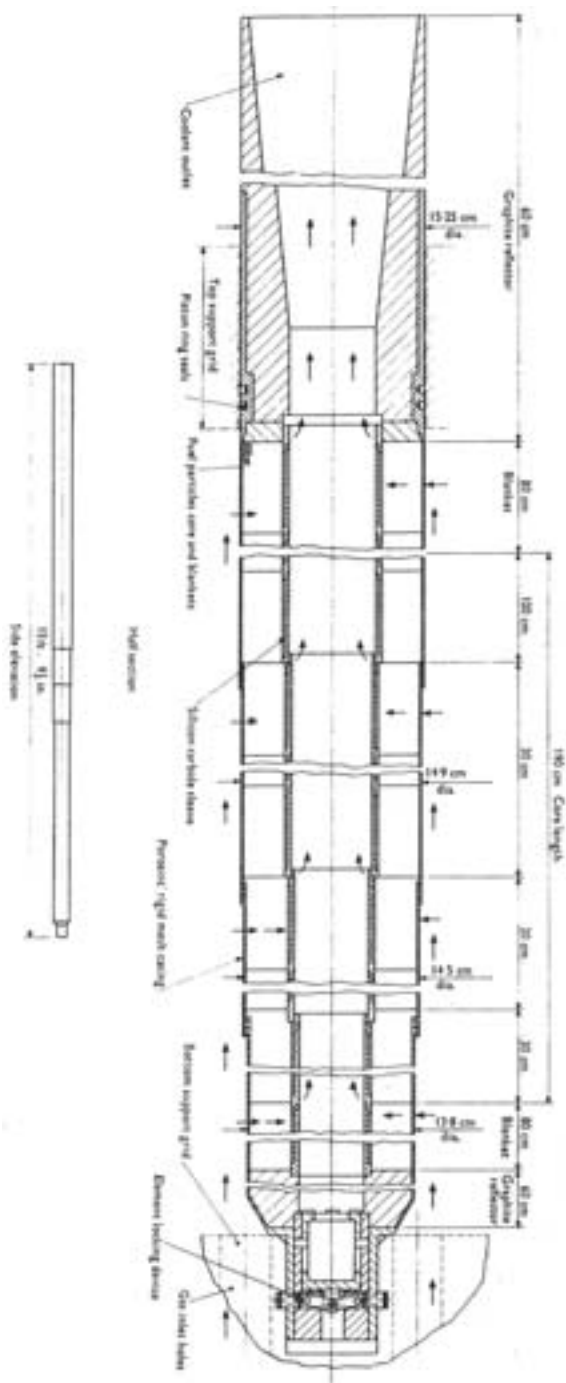


Figure 3.1: Gratton et al [28] have proposed a tube type fuel assembly with an upward flow fuel design. Figure 6.2 gives a schematic view of the principle of the tube assembly. (This picture was taken from the paper by Gratton et al.)

a liquid metal coolant means that the breeding ratio is improved and the doubling time is reduced.

The main disadvantage of gas coolants is their low density at normal pressure. In order to achieve a sufficiently high mass flow to ensure cooling of the core, the gas pressure is raised to several tens of atmospheres. A pressure drop following a damage in the coolant system may result in severe consequences. A main task for the reactor designer is to show that such accidents can be handled safely under all conditions.

In order to assure sufficient mass flow, gas cooling requires high gas velocity. Pumping power is strongly dependent on the coolant velocity. This usually leads to higher pumping powers when gases are used as coolants as compared to, e.g., liquid metals. For core designs utilising pin fuel, the demand on pumping power is further raised by the poor heat transfer implying a need for roughed fuel pin surfaces which increase friction, and consequently pumping power [29].

Low scattering cross-sections are beneficial for achieving a hard neutron spectrum. However, utilising a coolant transparent to neutrons means the axial leakage of neutrons increase. The higher neutron leakage from gas-cooled cores means that only large gas-cooled cores, where the relative leakage is minimised, are candidates for efficient commercial reactors.

## Chapter 4

# Partitioning and transmutation

### 4.1 The development of transmutation techniques

#### Early transmutation proposals

Already in 1964 Steinberg et al [30] proposed that some of the long-lived fission products might pose future problems. Especially  $^{85}\text{Kr}$  was pointed out as a potential hazard, since it was released in the atmosphere at reprocessing. Steinberg calculated the background radiation and found that it would have increased by 4.2% in the year 2000 based on the prognoses for plant construction valid at the time [30]. In the paper from 1964, Steinberg suggests that  $^{85}\text{Kr}$  and  $^{90}\text{Sr}$  should be transmuted, for example, in the reactors at Hanford, being decommissioned at the time. He is more sceptical to the transmutation of  $^{137}\text{Cs}$ , since transmuting  $^{137}\text{Cs}$  would imply a cost penalty to of about ten percent of the 1964 price of electricity. In 1967, however, Gregory and Steinberg proposed a reactor designed to burn caesium and strontium [31].

Claiborne, of the Oak Ridge national laboratory, stated in 1972 that transmutation suggested by Gregory and Steinberg seems unattractive due to the high cost and the significant research needs. Claiborne regards the alpha emitters of the spent fuel as a larger concern than caesium and strontium. His suggestion is to transmute the heavy nuclides in thermal reactors. He shows how it is possible to reduce the radiotoxicity of spent nuclear fuel in the very long time scale by over a factor of 200 through recycling in standard pressurised water reactors (PWR) [32]. The reduction of the radiotoxicity after 1000-10 000 years is only about a factor 20. In this time scale, the main contributor to the radiotoxicity is the considerable amounts of  $^{245}\text{Cm}$  produced by the soft spectrum in the PWRs. Claiborne pinpoints something important however, namely that, in thermal spectrum it is not possible to transmute all of the actinide nuclides.



### First evaluation of transmutation techniques

In 1974, a group of scientists from Los Alamos wrote an important paper edited by Foster [33]. The paper is a summary of a chapter in a report in preparation. The authors have read and given their comments on the chapter on transmutation of radioactive material.

Foster et al. discuss several techniques for transmutation, including fission and fusion reactors and nuclear explosives. The authors point out two technically and economically promising methods for reducing the radiotoxicity; transmutation in dedicated accelerator-driven cores and transmutation by exposure to the intense neutron flux from underground nuclear explosions.

In the case of actinide incineration in fission reactors, the authors draw attention to the aspect that in a nuclear economy in equilibrium, it might just not be possible to transmute all actinides in standard cores since the process requires neutrons which would be needed to breed more fuel. It is stated that it might be worth enriching the uranium fuel to a very high  $^{235}\text{U}$  content in order to postpone the build-up of actinides (emanating from  $^{238}\text{U}$ ) until sufficiently cheap transmutation techniques are available. That is when transmutation costs are competitive with the cost for highly enriched fuel. Eventually, the  $^{238}\text{U}$  would be needed for breeding plutonium to secure the supply of fissile material. During the breeding, production of actinides heavier than plutonium is unavoidable [33].

There are three main arguments against the idea of highly enriched  $^{235}\text{U}$ -fuel, the main being that such a fuel would lead to a quickly falling reactivity in the core. Further, the Doppler feedback is significantly reduced when  $^{238}\text{U}$  is removed. Also the delayed neutron fraction of  $^{238}\text{U}$  is very high. Even though the fraction of the fission reactions in  $^{238}\text{U}$  is small, large amounts of  $^{238}\text{U}$  has an impact on the possibility to control the chain reaction.

Foster et al. also suggests the use of cores fuelled with uranium-free actinide fuel. It is pointed out that the neutron spectrum need to be hard, that is, the average neutron energy need to be high, for transmutation to be efficient. Further, the issue of a potentially low delayed neutron fraction is stressed. The authors suggest source-driven subcritical cores to manage the transmutation task. The source should be either a thermal nuclear reactor, that is controllable due to its relatively large fraction of delayed neutrons, or an accelerator-driven spallation source. The latter is considered to be the safer option. A  $k$ -eigenvalue of 0.97 is suggested for the accelerator-driven core based on rough calculations. In such a reactor 97% of the neutrons are supplied by the fission reactions, the rest emanating from the external neutron source. Foster et al. write that the thermal power output from the dedicated transmutation systems would range in the order of a few to ten percent of the thermal reactor park output.

The authors are optimistic towards the idea of transmuted mainly long-lived fission products in the neutron flux from an underground nuclear explosion. The use of "clean", low fission-yield 100 kiloton devices exploded at a depth of 1.5 km is suggested. According to Foster et al., it would be possible to recover the transmuted

material for recycling and further transmutation cycles. The same cavity would be used repeatedly for the operations. If the energy from the explosion is used to produce steam for electricity production, the technique would be promising also from an economical perspective [33]

### Japanese transmutation research

In Japan, JAERI started studying transmutation systems in the mid 1970s. Also France and Germany had some initial activities in the field in the late 1970s.

In the beginning of the 1980s, both an Oak Ridge report [34] and an IAEA report [35] drew pessimistic conclusions about partitioning and transmutation (P&T). However, work continued around the world and later in the 1980s the interest for P&T was renewed as more and more difficulties around licensing geological repositories were emerging.

In 1989, Takizuka et al. presented two designs of accelerator-driven transmutation cores [36]. Both designs were based on a 1.5 GeV proton beam impinging on a liquid metal spallation target. The target is surrounded by alloyed actinide fuel manufactured from spent PWR fuel (33 GWd/ton) which was reprocessed 90 days after discharge. The materials suggested for the spallation target are liquid Na and LBE, respectively. The authors show how the LBE-cooled design allow incineration of the actinides produced in eight and a half PWR cores, while in the Na-cooled case, the corresponding number is two and a half. In both cases, the subcritical cores are able to supply their own electricity consumption.

More recent designs, like the one by Takahashi et al. [37] and the one by Wallenius et al. [38] have much in common with the early design suggested by Takizuka et al. in 1989.

The Japanese OMEGA (Options Making Extra Gains from Actinides) partitioning and transmutation programme was announced in 1988 [39]. The programme assumes that plutonium is an important future nuclear fuel. The aim is to address issues related to plutonium and the higher actinides, to allow the utilisation of these in the nuclear fuel cycle. Three areas of research are covered; properties of minor actinides and fission products, reprocessing and transmutation [40].

An accelerator-driven subcritical core for demonstrating the engineering feasibility of actinide transmutation is planned for the late 2010s. The intention is to use MOX fuel to start with, gradually replacing it for minor actinide nitride fuel [40].

### The Energy amplifier

A group of particle physicists from CERN suggested in 1993 that a strong particle accelerator, inducing spallation reactions in a thorium target, should be utilised to supply the neutrons needed to sustain a constant power production in a core loaded mainly with  $^{233}\text{U}$  [41]. The main idea is the construction of a subcritical reactor, called the "Energy amplifier" that does not produce large amounts of long-lived radioactive waste. The authors suggest the use of a 1.5 GeV proton accelerator

producing about 42 neutrons per incident proton. The k-eigenvalue is considered to be optimal in the 0.9-0.95 range meaning 10-20 neutrons are produced through fission reactions in the fuel for each source neutron. The arguments for the choice of  $^{233}\text{U}$ -fuel bred from  $^{232}\text{Th}$  are that this cycle does not produce large amounts of the higher actinides, that are built from  $^{238}\text{U}$ . Proliferation of fissile material is only a minor concern since there does not exist isotopically clean fissile material anywhere in the cycle. The uranium nuclides are mixed at all instances, as well as the plutonium nuclides, the latter being present only in insignificant amounts. The main importance of the report was that it gained a large interest in society and directed interest to sub-critical accelerator-driven nuclear systems in the research society.

The Energy amplifier is not primarily a transmutation core. However, the project directed focus to accelerator-driven sub-critical cores. By doing so, the Energy amplifier project has been of importance for later transmutation research.

### **American transmutation efforts**

In the USA, *A Roadmap for Developing Accelerator Transmutation of Waste ATW Technology* was published in 1999 [42]. It describes a path to industrial transmutation facilities, describing what issues should be addressed along the way. There are also estimations of the time needed for the research and economical estimations.

Apart from the goal of reducing the overall radiotoxicity of the spent fuel, the American interest in partitioning and transmutation is also to a large extent political. There is a political ambition to avoid constructing geological repositories. The background of this is the political difficulties of the planned repository under Yucca Mountain in Nevada. Also, there is a political will to reduce the stockpiles of fissile material, mainly  $^{239}\text{Pu}$  to make sure this, potential weapons material does not end up in the wrong hands.

### **Recent European transmutation efforts**

The European commission showed an increased interest in P&T with the fifth framework programme that started in 1998. In 2001, the European working group on ADS (accelerator-driven systems) published its "roadmap" for ADS development in Europe [43]

#### **France**

In France, the parliament passed a law (Loi n° 91-1381) on radioactive wastes on the 30th of December 1991. The law states that the French government should report to the parliament every year concerning the progress on research in three fields: partitioning and transmutation of long-lived nuclides in nuclear waste, studies on geological repository and studies on surface repositories. After fifteen years, i.e. in

2007, the methods are to be evaluated and the parliament is to decide on a strategy for waste handling.

In the frame of the transmutation programme, studies have been performed on both liquid metal-cooled and gas-cooled sub-critical transmutation cores [44].

### Myrrha and XADS

An accelerator-driven experimental system, Myrrha, is planned to be constructed in Mol in Belgium. The design work is well under way, however, the funding of the project is still uncertain.

Within the European Union fifth framework research programme, the XADS-project was undertaken. The aim of the project was to perform conceptual studies on both a LBE- and a helium-cooled accelerator-driven core in the scale of a research reactor. XADS and Myrrha are separate projects, but they have a lot in common.

## 4.2 Fuel cycle strategies

Several strategies are possible for the nuclear fuel cycle. These include cycles based on the fissioning of  $^{235}\text{U}$ , the breeding of  $^{239}\text{Pu}$  from  $^{238}\text{U}$  and the breeding of  $^{233}\text{U}$  from  $^{232}\text{Th}$ . In the following chapter only uranium fuelled cycles will be discussed, since these are the primary choice in most countries with India as the main exception, where thorium is foreseen as the main candidate for nuclear fuel.

In order to utilise the uranium resources as efficiently as possible, the neutron surplus in fast reactors should be used to breed plutonium from  $^{238}\text{U}$ . In this way, all uranium may be used as nuclear fuel instead of only the small fraction of  $^{235}\text{U}$ . With the once-through fuel cycle, the known, conventional resources of uranium are sufficient to provide the same electrical production as in 2002 for another 85 years. With a pure fast reactor fuel cycle, this figure changes to 2500 years. If the resources expected to exist also are included, the figures increase about three times [3].

### Reprocessing

A prime divisor between different fuel cycle strategies is the choice whether to reprocess the spent fuel or not. Reprocessing is the process of chemically separating elements in the spent fuel. Since the spent fuel is highly radioactive, reprocessing is both complicated and costly. It includes complicated technology that has to be controlled remotely.

All advanced nuclear fuel cycles, including those foreseen in transmutation scenarios include reprocessing. In order to utilise the material, the spent fuel has to be chemically separated. In the MOX strategy, remaining uranium and plutonium are separated, since they may be reused in fuel for light water reactors. Would one want to manufacture fuel for a transmutation core, the minor actinides would also have to be separated. In such a fuel, no  $^{238}\text{U}$  is allowed since, this nuclide is

the source of building the higher actinides. Further, the fission products should be removed in both the case of MOX fuel and more advanced fuels.

There are two main branches of reprocessing methods; aqueous reprocessing, also referred to as *hydrochemical* or *wet* reprocessing, and the methods using molten salt processes, known as *pyrochemical* or *dry* reprocessing methods.

### Wet reprocessing

The most widely spread aqueous reprocessing method is PUREX, which is a solvent extraction process for uranium and plutonium. PUREX gives a clean product and is very efficient in extracting uranium and plutonium from the spent fuel.

All of the aqueous separation methods use a two phase system and an extraction solution. In PUREX, the two phases are nitric acid as aqueous phase and kerosene as organic phase. Tributyl phosphate (TBP) is used as extracting agent. The spent fuel is dissolved in the nitric acid, where uranium and plutonium form neutral nitrate complexes. These complexes bind to the TBP-molecule. TBP is soluble in both the aqueous and the organic phase. In the organic phase, TBP forms complexes with the kerosene, releasing the uranium and plutonium nitrates.

By repeating the process in many subsequent separation steps, uranium and plutonium is transferred to the organic phase, while the fission products and the rest of the actinides remain in the aqueous phase. Using other extraction agents, separation of the minor actinides is also possible.

The main disadvantage of the aqueous separation methods is the radiation sensitivity of the extracting agent. Including large amounts of americium and curium in the waste stream, which would be the case in an equilibrium transmutation scenario, destroys the organic extractant unless the process is performed very quickly. The way to resolve this issue is to allow the spent fuel to cool for a longer time. This, however, significantly extends the time needed to transmute the actinides.

### Dry reprocessing

An alternative to using aqueous separation methods is the use of pyrochemical methods. These methods were developed for recycling spent fast reactor fuel. Extensive research efforts were undertaken within the IFR project [45].

The pyrochemical processes work at high temperatures. Chopped fuel is inserted into an anode basket, which is submerged in a molten salt. Lithium or potassium chlorides have been considered. In the salt melt, there are two cathodes, one solid and one liquid. When a voltage is applied over the system, uranium will deposit on the solid cathode. The transuranic elements, some rare earths and some of the uranium will deposit in the liquid cadmium cathode. The fission products, the noble metals and some of the rare earths will sink through the molten salt, ending up in a layer of molten cadmium at the bottom of the process vessel. By gradually increasing the voltage, it is to some extent possible to separate different elements based on their electronegativities.

Pyrochemical reprocessing gives a clean product, but it has not been able to show as good separation efficiency as the aqueous methods.

### The once-through strategy

The simplest of the nuclear fuel cycles is the *once-through* strategy. No reprocessing is involved in this cycle. After discharge from the core, the spent fuel is placed in long-term storage, without further action. The spent fuel remain radiotoxic on a level above that of uranium in nature for many hundreds of thousands of years.

The once-through strategy is widely used today. One of the main reasons is that uranium prices are low, and have been so for a long time [3]. Today, it is more expensive to reprocess the spent fuel, and thereby make better use of the uranium resource, than it is to manufacture fuel from virgin ore. Apart from the economical consideration, there are also historical, political reasons for adopting this fuel strategy. Production of plutonium bombs require reprocessing, since the plutonium produced in nuclear reactors is always mixed with other elements. The presence of a reprocessing industry lowers the threshold for producing nuclear weapons. Some countries have avoided reprocessing to assure that there is no political option at hand of producing nuclear weapons.

In countries where nuclear power is to be phased out, the once-through cycle may provide the most cost efficient alternative regardless of uranium prices, since reprocessing plants imply an investment with a long pay-back time.

### Plutonium recycling in light water reactors

In some countries, reprocessing was developed early to serve the foreseen fast breeder reactor park. Especially in France a huge effort was invested in getting the reprocessing industry running in time for the massive introduction of fast reactors that was expected. The key issue was to ensure a large enough Pu-separation to supply the initial fuel loads.

However, the fast reactor introduction was delayed, mainly due to the uranium price development. The reprocessing plants were already built and were delivering separated plutonium. Today, this plutonium is used for fabrication of MOX fuel. MOX fuel is more expensive than fuel fabricated from virgin uranium, due to the comparatively costly reprocessing.

An efficient way of reducing the actinide mass inventory is to burn plutonium in thermal reactors. However, neutron capture in the plutonium isotopes, in particular in  $^{242}\text{Pu}$ , leads to buildup of americium isotopes, which exhibit low probabilities of fission in the thermal spectrum of light water reactors. Further neutron capture in the americium isotopes leads to increasing curium inventories. The presence of americium and curium in spent fuel complicates the radiation issue, which will be further discussed in Section 5.1. Special care has to be taken concerning curium, which is a source of neutron radiation originating from  $(\alpha, n)$ -reactions and spontaneous fission reactions. After a few cycles of reprocessing and irradiation in the

core, the radiation from the MOX fuel makes both the handling and reprocessing cumbersome. The rising radiation levels efficiently prohibits total incineration of plutonium in a thermal neutron spectrum. Furthermore, large introduction of plutonium and americium into the core has an impact on the reactor safety parameters, and thus has to be limited for that reason as well.

Even if all plutonium produced in the light water reactors would be incinerated, the uranium demand would only decrease by 17 % [46]. The real potential of nuclear power to become a long term, global source of energy lies in breeding fissile material from  $^{238}\text{U}$ .

### Current uranium situation

A report, known as the 'Red book', summarizing the uranium resources and demand projections is published biannually by the OECD. In the 2001 edition [47], three scenarios of long term nuclear development are analysed. Three levels of uranium demand result from the scenarios. In the middle demand scenario, the cheap (less than 52 USD/kg uranium) uranium production is expected to be unable to meet the demand in 2021. The known high cost resources are expected to be sufficient to meet the demand for another 13 years. Beyond that, uranium resources not yet discovered, will be needed.

However, in the 2003 edition [3], the projections are far more careful. It is stated that the present uranium production is insufficient to meet the demand. Moreover, the report from 2003 do not foresee the uranium price to rise significantly until after 2020, when the deposits of cheaply available uranium are expected to start getting depleted. It is stated though, that a main driver for the uranium price the coming fifteen years will be the size of uranium inventories being held around the world. As today, the inventories are decreasing, which compensates for the insufficient production. A change in that policy could increase the prices. The report concludes that it is hard to predict the future uranium price because of the uncertainty of inventories and because rising prices are expected to lead to increases in production.

In 2002, 66 815 tons of uranium was consumed world wide. The uranium mining provided 36 042 tons, corresponding to 54 percent of the total consumption. The rest of the uranium originated from decreasing stockpiles, dismantling of nuclear weapons, recycling and re-enrichment of depleted uranium [3].

### The fast reactor economy

As mentioned, cheap uranium is a scarce resource. Using nuclear reactors to supply a major part of the worlds energy is only possible for a very limited period assuming the once-through fuel cycle is used. Fast neutron spectrum breeder reactors are necessary if nuclear is to play of role of importance in world energy supply in the long run.

A pure fast reactor nuclear park has been suggested as the long term goal for the nuclear development [9]. The benefits of such a nuclear park are several. For instance, the uranium resource is utilised efficiently and the waste issue is eased since closed fuel cycles are possible for all of the actinides. The pure fast reactor economy further implies a fuel cycle with only one type of reactors, simplifying reprocessing and fuel fabrication.

However, apart from being very distant, the pure fast reactor economy is expensive. Fast reactors are complex in comparison to light water reactors. In combination with a fuel cycle heavily dependent on expensive reprocessing, this implicates that a higher cost of electricity should be expected from a fast reactor park than from the light water reactor park [9].

### Double strata

Even though fast reactors may incinerate their own production of actinides, they can not simultaneously take care of the actinide stream from the existing light water reactor park. Introduction of americium in the breeder reactors reduces the effective delayed neutron fraction. The reason for this is that americium capture neutrons in the intermediate neutron energy region, as described in Section 5.3, which deteriorates the reactor safety, since the delayed neutrons are essential for the control of the chain reaction. As the americium content rises too high, it must be separated from the plutonium to assure safe fast reactor operation. The excess americium must thus be incinerated in dedicated cores. These cores should be designed for sub-critical operation in order to cope with the deteriorated safety. This is further discussed in Chapter 5.

The *double strata* fuel cycle strategy, based on light water reactors and transmutation of the minor actinides in dedicated reactors, was first suggested by Murata and Mukaiyama in 1984 [48]. Their idea was to divide the nuclear fuel cycle into two strata. The first stratum contains conventional reactors. The fuel cycle is 'clean', in the sense that the material streams contain fairly low amounts of heavier nuclides. The minor actinides produced in the light water reactors are directed, together with sufficient amounts of plutonium to fabricate transmuter fuel, to the second stratum, where they are recycled indefinitely until they have fissioned completely.

Later, the original idea have been modified by the introduction of breeder reactors in the first stratum [49]. In this way, the  $^{238}\text{U}$  is utilised to breed more fissile nuclides. The fuel material is recycled in the first stratum until all uranium and almost all plutonium is consumed. Following this fuel cycle concept, the mined uranium is used far more efficiently than in a once-through cycle. Since the long-lived transuranic elements are almost completely removed from the final waste form, the demand on geological storage of the waste from the double strata cycle is reduced to being sealed for about 1000 years.

In the double strata fuel cycle, light water reactors produce the main part of the electricity from the nuclear park. This electricity is cheap [9] and thus, the mean electricity cost from a double strata economy is significantly lower than from



the pure fast reactor economy. Still, however, the fuel cycle is closed for all of the actinides. Also the double strata is the natural phase in between today's nuclear park and the pure fast breeder economy. At least, this is true if a serious attempt to incinerate the existing high-level waste is to be undertaken. Considering the double strata as a natural development indicates that the pure fast breeder economy is a very distant goal. However, the further into the future it does become implemented, the more important the development of transmutation cores seems, since the stocks of plutonium and higher actinides from the light water reactors is increasing. Double strata is a promising fuel cycle since it is a link between today's once-through cycle and the fast breeder nuclear economy eventually necessary because of shrinking uranium resources.

### **Phase-out with transmutation**

Some countries, like Sweden, have decided to phase out nuclear energy. Even in these countries strategies, involving transmutation of the spent fuel may play a role, the main motive being to lessen the potential hazard to coming generations from the spent fuel repositories. However, transmutation in a phase-out scenario will be an expensive strategy since the revenue from selling useful energy from the transmutation reactors can not cover the expense of constructing them. Also, the need for a waste repository remains [50]. Consequently, the main incentive to follow this strategy is the idea that every generation should do what is possible, not to pass on problems to the forthcoming generations. The decision is ethical rather than technical or economical.

Some material is inevitably lost in each recycle due to limitations in the recycling processes. As long as the losses in each recycle are less than 0.1 percent, transmutation of the spent fuel is considered to be an attractive option [42]. Below this level of losses, the remaining waste from a transmutation core will remain radiotoxic at a level above that of the uranium originally used to manufacture the fuel for about 1000 years. Fission products dominate the radiotoxicity for 300 years, transuranic elements lost to waste in the fuel cycle will keep the radiotoxicity over the uranium reference level for another 700 years. Minimising the losses in reprocessing and fuel fabrication would thus further reduce the storage times.

## Chapter 5

### Fast sub-critical cores

A nuclear reactor is said to be *critical* when the nuclear reaction is exactly self-sustained, meaning the number of fission reactions is constant over time. The neutrons produced in each fission induce, in average, one subsequent fission reaction.

Each fission yields around three neutrons on average depending on the incident neutron energy and the fissioning nuclide. As a rule of thumb, the number of neutrons released is larger for the heavy nuclides as shown in Table 5.1. A large fraction of these do not induce further fission reactions as they are either captured in nuclei or leak out of the core. The neutron captures are important in breeder reactors, since captures in fertile nuclides build fissile nuclides, which by definition is breeding. Some of the captures occur in construction materials, which is generally not desired. These are referred to as parasitic captures. When, in average, more than one of the released fission neutrons induce new fission reactions, the core is *super-critical*. In such a core, the power produced increases exponentially. The opposite is a *sub-critical* core, where the power decreases in each fission generation unless neutrons are added to the system by a source. With such an arrangement, the nuclear reaction stops if the source is removed.

For a large core, an intense neutron source is needed. In the case of power reactors a *spallation* neutron source (Section 5.2) is the option available. Core power is limited by the source strength, together with the level of sub-criticality. Since the neutron source implies an extra cost to the system, sub-critical cores will be more expensive than critical cores producing the same power. Thus, sub-critical cores will not be competitive economically if used for power production. However, for some purposes like transmutation of transuranic elements they are still attractive because of their safety characteristics and because transmutation itself may be seen as a benefit that motivates the higher cost.

## 5.1 Motives for sub-criticality

### Delayed neutrons

Delayed neutrons are emitted in radioactive decays in fission products, succeeding the fission reaction. They are important to assure safe operation of the reactor since they give the operator time to react on disturbances in the reactor behavior. In the case when the prompt neutrons by themselves are in sufficient number to sustain the nuclear reaction, the reactor is *prompt critical*. A prompt critical core has a *neutron generation time*, that is orders of magnitude shorter than in the case when also delayed neutrons are needed for criticality. The neutron generation time is given as the weighted average of the neutron lifetimes. Even though the delayed neutrons only constitute a small fraction of the total neutron population, they have a large impact on the generation time due to their very long life time in comparison to the prompt neutrons. In the prompt situation even a small reactivity insertion leads to a rapid power increase. In the worst case scenario the power keeps increasing until rapid changes in the geometry of the system interrupt the chain reaction.

| Nuclide            | $\nu_{th}$ |        | $\nu_d$  |         | $\beta$  |        |
|--------------------|------------|--------|----------|---------|----------|--------|
|                    | ENDFB6.8   | JEF3.0 | ENDFB6.8 | JEFF3.0 | ENDFB6.8 | JEF3.0 |
| <sup>235</sup> U   | 2.44       | 2.44   | 0.0167   | 0.0167  | 0.69%    | 0.68%  |
| <sup>238</sup> U   | 2.49       | 2.49   | 0.0440   | 0.0478  | 1.77%    | 1.92%  |
| <sup>237</sup> Np  | 2.64       | 2.64   | 0.0108   | 0.0108  | 0.41%    | 0.41%  |
| <sup>238</sup> Np  | 2.79       | 2.79   | 0.0216   | 0.0216  | 0.77%    | 0.77%  |
| <sup>238</sup> Pu  | 2.90       | 2.89   | 0.0042   | 0.0047  | 0.14%    | 0.16%  |
| <sup>239</sup> Pu  | 2.88       | 2.88   | 0.0065   | 0.0065  | 0.22%    | 0.22%  |
| <sup>240</sup> Pu  | 2.80       | 2.78   | 0.0090   | 0.0091  | 0.32%    | 0.33%  |
| <sup>241</sup> Pu  | 2.95       | 2.93   | 0.0162   | 0.0160  | 0.55%    | 0.55%  |
| <sup>242</sup> Pu  | 2.81       | 2.86   | 0.0197   | 0.0183  | 0.70%    | 0.64%  |
| <sup>241</sup> Am  | 3.24       | 3.33   | 0.0043   | -       | 0.13%    | -      |
| <sup>242m</sup> Am | 3.26       | 3.26   | 0.0069   | 0.0069  | 0.21%    | 0.21%  |
| <sup>243</sup> Am  | 3.27       | 3.06   | 0.0080   | -       | 0.24%    | -      |
| <sup>242</sup> Cm  | 3.44       | 3.44   | 0.0014   | 0.0014  | 0.04%    | 0.04%  |
| <sup>243</sup> Cm  | 3.43       | 3.43   | 0.0030   | 0.0030  | 0.09%    | 0.09%  |
| <sup>244</sup> Cm  | 3.46       | 3.24   | 0.0044   | -       | 0.13%    | -      |
| <sup>245</sup> Cm  | 3.60       | 3.53   | 0.0059   | 0.0063  | 0.16%    | 0.18%  |

Table 5.1: Prompt neutrons, delayed neutrons and delayed neutron fractions for important transuranic nuclides (data from JENDL3.3 was used for the delayed neutrons in <sup>244</sup>Cm)

The delayed neutron fraction is dependent on the fission products produced in the core and thus of the fuel composition. As displayed in Table 5.1 the fraction

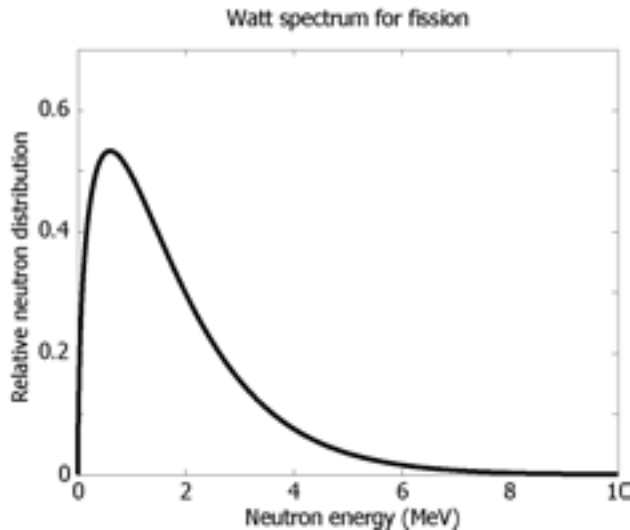


Figure 5.1: Watt-spectrum, typical for fission neutron energy distribution

of delayed neutrons from fissioning  $^{235}\text{U}$  is high compared to e.g. the plutonium nuclides. This means fuel containing large amounts of  $^{235}\text{U}$  give the reactor larger margins to prompt criticality than is the case with other fuels. In a reactor, there are several processes which supply reactivity feedback to temperature changes. Generally, negative temperature feedbacks are beneficial for reactor safety since they will decrease reactivity in the case of a power excursion. However apart from feedbacks acting to reduce power, the time scale is important. The feedbacks have to be given enough time to affect the state of the core. In a prompt critical situation, the neutron generation length is too short for this.

To include plutonium and americium in the fuel, implies lowering the delayed neutron fraction. One consequence of this is the introduction of an upper limit to the plutonium fraction that may be loaded into a light water reactor for example as MOX fuel.

### $\beta$ and $\beta_{\text{eff}}$

The prompt neutrons are produced in fission-,  $(n, xn)$ - and  $(\gamma, n)$ -reactions. Fission neutrons constitute the main part. These have a Watt-spectrum-distributed energy, where the most probable energy is around 0.7 MeV and the average energy is around 2 MeV, varying for different nuclides. Almost all of the fission neutrons are born at energies in between 0.1 MeV and 10 MeV. A typical fission energy spectrum is displayed in Figure 5.1. Delayed neutrons on the other hand show a completely different energy spectrum since they are born in a radioactive decay rather than in a

fission reaction. Since the fission cross-sections are strongly dependent on the energy of the incident neutron, a delayed neutron does not have the same probability of causing fission as a prompt neutron does. In thermal cores a delayed neutron gives a larger contribution to reactivity compared to the average fission neutron since it is born closer to the thermal fission energy region and thus have a smaller chance of being captured before inducing the fission reaction. In cores working operating in fast neutron spectrum, especially when the fuel is rich in even-N nuclides, the opposite occur since the heavy even-N nuclei have very small fission cross-sections in the energy region where delayed neutrons are born.

In critical cores, the delayed neutron emission is geometrically distributed more or less like the prompt neutrons. In a sub-critical core, this is not the case. Here, the source gives a contribution to the prompt neutron spectrum only. Since the source is usually not distributed in the core, this results in a difference in the geometrical distribution of prompt and delayed neutrons in sub-critical cores.

Taken together, the energy and geometry effects cause, in some cases a significant discrepancy in reactivity contribution between the average delayed and the average prompt neutron.

The delayed neutron fraction for some fuel is the weighted average of delayed neutrons released by the individual nuclides in the fuel over the weighted average of the total neutron release through fission. It is denoted  $\beta$  and is given by Equation 5.1. The delayed neutron fraction weighted for its effect on reactivity is denoted  $\beta_{\text{eff}}$ , as in Equation 5.2.

$$\beta = \frac{\bar{\nu}_d}{\bar{\nu}_d + \bar{\nu}_p} \quad (5.1)$$

$$\beta_{\text{eff}} = \frac{n_d}{n_d + n_p} \quad (5.2)$$

$\bar{\nu}_d$  and  $\bar{\nu}_p$  denote the delayed and the prompt neutron fractions averaged over all nuclides. The number of delayed and of prompt neutrons causing fission is given by  $n_d$  and  $n_p$  respectively.

The parameter  $\beta_{\text{eff}}$  will show to be very important in core design since it is a measure of the allowed margin in off-normal behaviour allowed in the core.

## Criticality

Understanding the behavior of the neutron flux in a nuclear reactor is fundamental since it is proportional to the power density of the core. Some expressions are of special interest [51]. The *neutron angular density* is a measure of the expected number of neutrons in a position  $r$  of some energy  $E$  travelling in a direction  $\Omega$  at some time  $t$ .

$$N = N(r, \Omega, E, t) \quad (5.3)$$

The *neutron density* -  $n$ , is the density of neutrons of some energy  $E$  in some position  $\mathbf{r}$ , is given by the integral of the angular density over all angles.

$$n(r, E, t) \equiv \int_{4\pi} N(r, \Omega, E, t) d\Omega \quad (5.4)$$

The *angular flux* is the product of the neutron angular density and neutron speed -  $v$ , ( $\mathbf{v} = v\mathbf{\Omega}$  denoting the neutron velocity).

$$\Phi(\mathbf{r}, \mathbf{\Omega}, E, t) \equiv vN(\mathbf{r}, \mathbf{\Omega}, E, t) \quad (5.5)$$

This gives the *total flux* as the integral of the angular flux over all angles.

$$\phi(\mathbf{r}, E, t) \equiv \int_{4\pi} \Phi(\mathbf{r}, \mathbf{\Omega}, E, t) d\Omega \quad (5.6)$$

A reactor is critical exactly when the chain reaction is self-sustained. The amount of neutrons produced through fission ( $\mathbf{F}\phi$ ) is exactly consumed or lost ( $\mathbf{A}\phi$ ), the loss term including, as negative terms, other contributions to the neutron creation e.g. (n,xn)-reactions.

$$(\mathbf{A} - \mathbf{F})\phi_S = 0 \quad (5.7)$$

Introducing an eigenvalue  $k_{eff}$  gives a solution to 5.7.

$$\mathbf{A}\phi_0 = \frac{1}{k_{eff}} \mathbf{F}\phi_0 \quad (5.8)$$

In a critical reactor the neutron distribution is described by the fundamental mode  $\phi_0$ . However when the flux is disturbed by a source, the neutron distribution will be described by the *source mode* -  $\phi_S$  given as the sum of several core eigenmodes.

$$\phi_S = \sum_n \phi_i = \phi_0 + \phi_1 + \phi_2 + \dots + \phi_n \quad (5.9)$$

In subcritical reactors, fewer neutrons are created than lost. A source term,  $S$  has to be introduced to sustain a chain reaction, i.e.

$$(\mathbf{A} - \mathbf{F})\phi_S = S \quad (5.10)$$

where,

$$\mathbf{F}\phi_S = \iint \frac{1}{4\pi} \sigma_f \nu(\mathbf{r}; E' \rightarrow E) \cdot \phi'_S d\mathbf{\Omega}' dE' \quad (5.11)$$

$$\mathbf{A}\phi_S = \mathbf{\Omega} \cdot \nabla \phi_S + \sigma \phi_S - \sum_{i \neq f} \iint \sigma'_{i} f_i \phi'_S d\mathbf{\Omega}' dE' \quad (5.12)$$

The terms within the sum describe all neutrons emerging in the system except from fission.

Equation 5.10 may be solved in source mode by the introduction of a source-eigenvalue  $k_S$ .

$$k_S = \frac{\langle \mathbf{F}\phi_S \rangle}{\langle \mathbf{A}\phi_S \rangle} \quad (5.13)$$

The reactivity inserted by the source is

$$\rho_S = \left( \frac{1}{k_S} - 1 \right) = \frac{\langle S \rangle}{\langle \mathbf{F}\phi_S \rangle} \quad (5.14)$$

Close to criticality  $k_S$  approaches  $k_{eff}$ .

In a commercial light water reactor, the fuel composition may be optimised to minimise the cost of the electricity or to adjust parameters of importance to the reactor safety. In reactors dedicated to transmutation, the main incentive is to incinerate radiotoxic nuclides rather than to produce cheap electricity. The fuel composition is determined by the waste composition from the reactors dedicated to power production. The composition is neither optimised for easy handling nor for safe operation. It is a fuel producing far less delayed neutrons than  $^{235}\text{U}$ -rich fuels. Also the inherent safety parameters of light water reactor fuels are much different in the transmuter fuel, as will be further discussed in Section 5.3. Together this makes sub-critical operation mandatory to ensure controllable reactor operation. Deciding the level of sub-criticality implies guaranteeing the possibility to shut the reactor down before prompt criticality is reached in any case of disturbance. However it is desirable to operate the core as close to criticality as possible to minimise the neutron source strength.  $k_S$  equal to 0.97 at the beginning of the fuel cycle (BOC) is a common level chosen to meet both demands. However, this figure is dependent on fuel and coolant characteristics and has to be chosen based on design choices. Throughout the fuel cycle, the fuel nuclides are consumed and  $k_S$  diminishes. This is compensated for by increasing the source strength. Consequently, the length of the fuel cycle is limited by the source strength, which is never allowed to increase to a level above twice its initial value. Allowing further increase in flux would jeopardise the reactor safety at BOC, as introduction of the full source strength into the fresh fuel would threaten safe operation. Reducing the upper source strength eases this threat.

## 5.2 Spallation

Since the source should supply three to six percent of the neutron flux, the sub-critical reactor power is limited by the source strength. The strongest sources available for sub-critical reactors are spallation neutron sources.

In the spallation process, a target of some heavy element such as lead, tungsten or uranium are bombarded by highly energetic particle projectiles, e.g. protons. If the energy of the incident particle is high enough, the nuclei are fragmented. Different light particles are produced in the spallation reaction, among them neutrons.

The particles produced have high energies themselves and may induce subsequent spallation reactions in other nuclei.

For subcritical cores accelerators producing a proton current of up to 40 mA at an energy of about 1 GeV are suggested [42]. The beam power is limited by material damage in the spallation window separating the evacuated accelerator from the molten metal spallation target, and by the heat production in the target. The accelerator delivers between 20 and 40 MW to the system. Hence, the heat production in the beam window and the spallation target is intense and efficient cooling of the target is a necessity. Spallation target design is one of the main research areas connected to the development of a working transmutation system. One of the suggested solutions is to design a windowless target based on clever flow of the liquid metal.

### 5.3 Reactor safety parameters

Increasing the power in a nuclear reactor leads to an increasing temperature in the short time scale. When temperature increases are modest, the cooling system will be able handle the situation and stabilise the temperature, if not, the temperature might keep increasing and eventually damage the core.

In order to ensure safe reactor operation, it is important that there are natural phenomena which are able to decrease the reactivity in a situation where the temperature starts increasing. There are several effects that come into play with temperature changes, which affect the reactivity. Among those are geometrical changes due to thermal expansion, Doppler feedback and density changes of the coolant.

#### Doppler

The Doppler effect is caused by resonance peaks in the neutron capture cross-sections broadening when the nuclei vibrations intensify with increasing temperature. Figure 5.2 shows how there are large resonances in the capture cross-section in the epithermal energy region for  $^{238}\text{U}$ . When these peaks broaden to cover a larger energy region, the neutron capture rate increase and the reactivity drops. The Doppler effect is found also in other nuclei, however it is extraordinarily strong in  $^{238}\text{U}$ .

A major introduction of americium in the fuel, has been shown to decrease the Doppler effect despite the presence of  $^{238}\text{U}$  [52]. Americium has large non-resonant capture cross-sections in an energy region above the resonant region in  $^{238}\text{U}$ . This means, the neutrons are captured in americium during slow down, never reaching the resonance region where the Doppler effect in  $^{238}\text{U}$  starts. Figure 5.2 shows the capture cross-sections in americium  $^{241}\text{Am}$  and in  $^{238}\text{U}$ . The cross-sections are particularly large in  $^{241}\text{Am}$  for energies ranging from some hundred eV to about 1 MeV. Even rather small americium fractions in the fuel reduce the importance of the Dop-



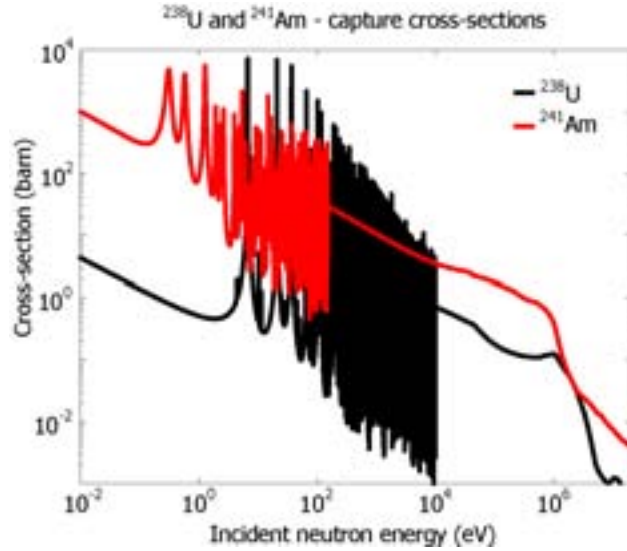


Figure 5.2: Cross-section for neutron capture in  $^{241}\text{Am}$  and in  $^{238}\text{U}$  as function of incident neutron energy

pler effect significantly. Table 5.2 displays the results of calculations performed for a helium cooled core loaded with fuels of different americium content. Already when ten percent of the fuel is americium, the Doppler feedback to reactivity is reduced to less than one third. In reactors dedicated for transmutation of heavy

| U  | Pu | Am | Zr | $K_D = Tdk/dT$ | $\beta_{\text{eff}}$ |
|----|----|----|----|----------------|----------------------|
| 80 | 20 | -  | -  | -285 (11)      | 505 (25)             |
| 70 | 20 | 10 | -  | -88 (11)       | 473 (23)             |
| 50 | 20 | 30 | -  | 0 (14)         | 356 (32)             |
| -  | 20 | 30 | 50 | -10 (16)       | 227 (38)             |

Table 5.2: Doppler feedback and delayed neutron fraction for four different fuels. Values are given in pcm ( $10^{-5}$ ). The standard deviations are given in parenthesis.

actinides, a key issue is to minimise the buildup of heavy nuclides. Removing  $^{238}\text{U}$  from the fuel, in combination with the introduction of americium, removes most of the Doppler reactivity feedback. This means that one of the most important mechanisms for negative feedback in conventional reactors will be unavailable in transmutation cores.

### $\beta_{\text{eff}}$ and americium

Just as the Doppler effect is decreased by the presence of americium, so is the effective delayed neutron fraction -  $\beta_{\text{eff}}$ . The delayed neutrons are emitted distributed in a soft spectrum at energies where the americium isotopes have relatively high capture cross-sections. A significant fraction of the neutrons are captured in americium and thus do not contribute to the effective delayed neutron fraction [52]. Table 5.2 shows how americium introduction in a helium cooled core reduces the effective delayed neutron fraction. Sodium cooled cores show similar results [53].

## 5.4 Fuel

Among the options for nuclear fuels, a few are of special interest for this study - especially nitride fuels. Oxide fuels are the most common in today's reactors and will also be given attention below. Some general concerns are always valid when making the choice of the nuclear fuel:

- Thermal properties - The thermal properties of the fuel sets the limit for the power density in the core and consequently for the fuel burnup rate. In power reactors the power density has economical implications, in transmutation reactors the burnup rate is of interest since it determines the number of recycles necessary to incinerate the long-lived nuclides, which in turn has impacts on both the time necessary for actinide incineration and on the economics of the process.
- Geometrical stability - When irradiated, the fuel geometry is affected. Generally, swelling of the fuel due to fission product and helium production, is undesired and should be avoided.
- Chemical compatibility - The fuel material should be compatible with the surrounding materials. If it does react with e.g. the coolant following a cladding fracture, this reaction should be slow enough to allow for removal of the damaged fuel assembly. An example of such a situation is when uranium oxide fuel is used in sodium cooled reactors. In case of a cladding break leading to sodium intrusion in the fuel, the oxide starts reacting with the coolant. However, the reaction is slow enough to have limited consequences before the damaged fuel element can be removed [54]
- Heavy atom density - In some cases the actinides are dispersed in the fuel for reasons of chemical stability or for neutronic reasons. The fraction of heavy metal nuclides in the fuel may in some cases be an issue. Especially this is important in thermal reactors with a low fuel enrichment in combination with a poor moderator, e.g. graphite.

- Economics - The limits for fuel design are often not set by engineering difficulties, rather they are determined by the cost of mass production of the fuel.

Oxide fuels are the most wide spread today, being used in most of the thermal reactor designs. The operating experience of oxide fuels - especially  $\text{UO}_2$  - is vast. The main reason for the popularity of the oxide fuels is their high compatibility with water [54]. This makes oxide fuels the primary option in water cooled reactors, where metallic, carbide and nitride fuels are ruled out for water compatibility reasons.

For transmutation cores, the demands on fuels differ somewhat from those that apply to power reactor fuels. In conventional cores the prime interest is to produce cheap energy. In transmutation cores, the idea is to reduce the radiotoxicity of the fuel material as efficiently as possible, efficiently meaning more than just doing it cheap. The Japan Atomic Energy Research Institute, JAERI have set up fuel selection criteria for actinide burners [55]:

- High heavy metal density - The higher the heavy metal density, the harder neutron flux is possible. Hard neutron fluxes is beneficial for actinide transmutation, since it facilitates fission of the actinides over build-up of heavier nuclides.
- Compatibility with recycling and fuel fabrication - Efficient transmutation requires multi-recycling with small losses in each cycle. Thus, the fuel chosen has got to be compatible with efficient recycling and fuel manufacturing methods.
- Material stability - It is important that the fuel is relatively stable as the material composition changes following burnup.
- Irradiation database requirements - Collecting the information for an irradiation database implies a large and expensive effort. Thus it is beneficial to choose a fuel candidate that has a well known irradiation behavior. This requirement is the strongest argument for choosing oxides as actinide burner fuels.

Based on this, oxides and nitrides are the most probable candidates for fuels for transmutation systems.

## 5.5 Coolants

The coolant in a fast neutron spectrum core must meet three important requirements. In order to preserve the fast spectrum, neutron moderation should be minimised. Fast reactors allow for high power densities and compact designs. Typically the fast reactor produces a power per volume four times higher than the

thermal reactor [2]. High power densities require a coolant with the ability to remove this high specific power. The third criterion is that the neutron absorption in the coolant should be minimised in order to avoid build up of radioactive isotopes and to avoid deterioration of the neutron economy.

Water is ruled out as a fast reactor coolant based on its moderating properties. Also, organic coolants are impossible for the same reason. Liquid metals and gas coolants remain as potential coolants.

### **Liquid metal coolants**

Liquid metals were proposed as coolant candidates since they in general feature both high thermal capacities and allow for high mass flow rates. Sodium, sodium-potassium (NaK), mercury, lead and lead-bismuth-eutectic (LBE) have all been given serious consideration as fast reactor coolants.

#### **Sodium**

Sodium has been the main coolant candidate in the breeder reactor development programmes (table 3.1). A main reason for its popularity among reactor designers is that it allows for high power densities, making a high breeding ratio possible. Using a light metal like sodium, eases the requirements on pumping power compared to using heavy metal coolants such as lead. Sodium-cooled reactors have shown hard to decommission as they contain large amounts of frozen activated sodium. Serious incidents have occurred when trying to remove sodium residues with alcohol (ethycarbitol), both in the French reactor Rapsodie and in the German test facility FAUST [56].

The boiling temperature of sodium is only 880 °C. In accelerator-driven cores this is a clear disadvantage to using sodium as coolant, since an accidental increase of the beam power may cause boiling and voiding of the core, voiding implying that the coolant density is reduced.

#### **Sodium-potassium**

The primary reason to add potassium to the sodium coolant is that NaK, is liquid at room temperature. The demand on coolant heating during low power periods is thus released. However the introduction of potassium increases the parasitic neutron capture. The last fast reactor that used NaK was the Dounreay fast reactor. Since then, pure sodium has been the main metal coolant option for fast reactors [9].

#### **Lead and lead-bismuth eutectic**

In the breeder programmes, lead and lead-bismuth were no prime coolant candidates. The two main reasons being the high pumping power and the corrosion issue associated with these coolants.

When lead is mixed to form an eutectic with bismuth, the melting temperature is reduced from 328 °C to 123 °C. This allows a lower operating temperature, which decreases corrosion. The risk of blocking coolant circulation due to freezing is reduced. However  $^{209}\text{Bi}$  forms the beta emitter  $^{210}\text{Po}$  with a half-life of 138 days through the capture of a neutron. Despite the activation of bismuth, lead-bismuth eutectic is considered as the primary choice for liquid metal-cooled ADS-cores [42].

Voiding of a lead-bismuth-cooled core leads to a reactivity insertion to the core. For sodium, the reactivity insertion is even larger. One consequence of this is that subcritical LBE-cooled cores may be operated with a smaller margin to criticality, leading to a lower demand on the neutron source strength in LBE-cooled sub-critical cores.

Lead-bismuth-cooled reactors have been used in the Soviet Alpha-class submarines. The aim was to construct a very fast submarine to attack American aircraft-carriers. A fast submarine requires a high-power-density engine. Combustion engines are out of the question and even light water reactors have too low power density. A fast reactor could do the job though. Sodium was considered as coolant, but lead-bismuth was chosen because of its very high boiling temperature and its low chemical reactivity. The Americans also made work on LBE-cooled naval reactors, but they did not succeed in solving the corrosion issue [57].

In total seven Alpha-class submarines were constructed in between 1971 and 1981. Several incidents occurred with the LBE-reactors including frozen coolant and coolant leakage [57].

## Gas-coolants

Using gas reactor coolants raises completely different issues than do the liquid metals. The benefits are several, visual inspection of the core is possible, there will not be any frozen coolant blocking flow or contaminating the spent fuel. No heating of the coolant is necessary and the reactivity issues are eased, especially in the case of helium-coolant. However, gases have low densities, meaning high pressures are required to assure sufficient mass flow through the core. Gas-cooled cores have thus got to be designed in such a way that a loss of pressure accident does not lead to any severe consequences.

## Helium

Helium interacts only slightly with neutrons. Consequently, helium-cooled cores have hard neutron spectra, where the neutrons are moderated by the construction materials only. Moreover, helium is not chemically reactive. As with other gas coolants, the pressure loss issue is the main disadvantage for helium. In order to improve the situation somewhat,  $\text{N}_2$  may be used to replace the helium coolant in the case of a severe pressure loss accident.  $\text{N}_2$  has a heat capacity per volume about 40 percent higher than helium and consequently removes 40 percent more heat.

### Carbon dioxide

Carbon dioxide has been used in past reactor design e.g. the British Magnox reactors. Carbon dioxide ( $\text{CO}_2$ ) is corrosive and has a lower heat transfer capability compared to helium. The main reason to use carbon dioxide is that it is cheap. Helium used to be scarce when the Magnox reactors were constructed and the gas-leakage from these reactors would have led to unacceptably high costs if helium would have been used.

### Power conversion with gas-coolants

With helium as the primary choice of gas coolant, two choices are available for the power conversion system. Utilising a direct helium gas-turbine cycle is the simpler choice. The second option is to separate the reactor coolant from the power turbine by introducing a second coolant cycle connected to the reactor coolant by a heat exchanger. Many options are available as medium for the second part of the cycle. Some, like e.g. steam should be avoided however in order to minimise the risk of water intrusion into the core leading to positive reactivity effects resulting from a moderated neutron spectrum.

Helium cycles are, in many ways, simpler than steam cycles. Maybe the most important difference is the size of the helium turbine. In comparison to a steam turbine of the same output the helium turbine weighs roughly one third. In helium turbines, the peripheral speed of the blades is limited by material strength rather than by the sonic velocity, which is high in helium. In steam on the other hand, the sonic velocity is lower. This means, the peripheral speed of the turbine blades may approach the sonic velocity, which is not desired. The heat exchanger part of the coolant cycle is expected to be cheaper for helium than for steam, since there is no phase shift in the helium case. Also, helium regenerators are expected to be cheaper than feed water heaters [58]. Together this suggests that the power conversion system for a helium-cooled core would be cheaper than for a LWR.

## 5.6 Material damage

Neutron radiation cause damage in materials, through nuclear reactions and, mainly, through energy deposition. In reactor design the expected material damage in construction materials is important, since the properties of many materials change following radiation. Radiation damage in metals is of particular interest. When neutrons strike a metal, atoms are knocked out of their lattice positions. Subsequent reactions knock out more atoms, causing a cascade effect. The atoms knocked out are called *interstitials*, the empty lattice positions formed are referred to as *vacancies*. Collectively we refer to a vacancy and an interstitial as a point defect or a Frenkel pair. Most of the interstitials and vacancies will eventually recombine, leading to a self-healing of the material. However some defects will remain, as free point defects or as clusters of vacancies or interstitials. Clusters of interstitials

are referred to as *dislocations* and clusters of vacancies as *cavities*. In theory, the neutron need to carry only very low energy to induce a Frenkel pair. However, it is the high energy neutrons that cause the cascades of vacancies and interstitials. This is why, in a thermal reactor the issue of radiation damage is not as severe as in fast reactors. After many years of exposure, radiation induced material damage appear also in thermal reactors.

Radiation damage in materials is usually measured in units of *displacements per atom* (dpa). One dpa is equal to N defects in a population of N atoms. Since self-healing occurs in materials, all of these defects do not remain.

### Swelling

The production of vacancies and interstitials increase the volume of steels. Helium produced through high energy neutron induced  $(n, \alpha)$ -reactions in the steel collect in the cavities formed by clustered interstitials, forming *bubbles*. The pressure of helium in the bubbles accelerate the swelling process. Swelling is temperature dependent. At temperatures around 40% of the steel melting temperature, the conditions for formation of large helium bubbles is optimal. The swelling of steels accelerate at some radiation dose. At the optimal temperature this accelerated swelling start earlier than for other temperatures.

### Embrittlement

An important change in metals is embrittlement. The metal hardens when irradiated, implying an increased yield strength, but reducing the plastic deformation possible before a break occurs. These effects remain as the radiation ceases. The embrittlement effect is caused by helium bubbles migrating to the boundaries of grains in the microstructure of the steel. As helium collects there, the bonds between neighbouring grains weakens.

## Chapter 6

# Designing a gas-cooled transmutation core

### 6.1 General design concerns

Designing a nuclear reactor dedicated to transmuting long lived isotopes raises somewhat different issues than when designing a power reactor. In the power reactor case, optimisation is focused on economical parameters such as the efficiency in electricity production and the consumption of fissile material. Avoiding the buildup of exotic nuclides is of less concern. In some special cases such as burning MOX fuel, the actinide production is a limiting parameter. Introducing large amounts of plutonium and the minor actinides changes the core parameters considerably, leading to decreased safety margins.

The design incentives for a transmutation core are different. Here, the main objective is to decrease the radiotoxicity of the material stream in the long term perspective. The freedom for the reactor designer to tailor the fuel composition is drastically reduced. The nuclide composition of the transmuter fuel is dictated by the conditions in the original radiation environment in the power reactor rather than by engineering and optimisation. There are several consequences arising from this fact. The material composition in the core may no longer be optimised to maximise core safety parameters or fuel cycle economy.

In order to achieve a high burnup of transuranic nuclides, a hard neutron spectrum is beneficial. The fission to absorption ratio is much higher in a fast spectrum than at lower energies. The material choices in the transmutation core will be of importance as some materials moderate the spectrum much more than others. In helium cooled cores, the moderation in the coolant is rather modest. Very hard neutron spectra may be achieved in such cores, allowing for high actinide burnup.

As was discussed in Chapter 5, introduction of americium deteriorates the most important neutronic safety parameters of the core. The Doppler effect vanishes, the effective delayed neutron fraction is reduced and the void coefficient, which



typically is positive in fast reactors, is further increased.

The reduced Doppler effect in combination with the reduced delayed neutron fraction, results in such a poor margin to prompt criticality that sub-critical operation becomes mandatory. A core working close to criticality would be cheaper to operate since a smaller fraction of the energy produced would be needed to support the neutron source. On the other hand the designer must assure a large enough margin to prompt criticality to guarantee that the chain reaction is controllable under all conditions which is an argument of increasing the margin to criticality.

The aim of this work is to examine the possibility to utilise gas cooling in transmutation cores. Traditional design proposals for transmutation systems [37][38] have been based on the use of liquid metal cooled cores. While the promising transmutation efficiency is the main advantage of a gas-cooled transmutation core, the high pressure operation necessary and the resulting risk of a loss of coolant accident is the main disadvantage. This issue will be addressed below.

## 6.2 Decay heat removal

The purpose of a power reactor is to produce heat, for electricity production, district heating or industrial applications. Keeping the heat production under control is the main engineering task concerning a nuclear reactor. Unless the heat is removed, the temperature will rapidly start rising, inevitably leading to core damage. Core damage generally leads to the release of gaseous fission products, into the containment and in the worst case outside of the reactor building.

In the case of an off normal core behavior caused by e.g. some insertion of reactivity, the main design demand is assuring that the chain reaction may be stopped before core damage occurs. Failure to succeed in stabilising the fission process in time leads - in the worst scenario - to a rapid exponential growth of core power, and eventually to core disassembly. In a core fuelled mainly by plutonium and americium, where there is a low fraction of delayed neutrons, the margin to prompt criticality is decreased in comparison to uranium fuelled cores.

Assuming the fission reaction can always be stopped on a time-scale sufficiently short, the second design issue is to guarantee that the heat from the radioactive decay can be removed. Right after the fission process is stopped, decay heat production is quite significant, accounting several percent of full power. For a large power reactor, this means over one hundred megawatts. The power production diminishes with the radioactivity in the core. But, cooling is required for a long time.

Heat removal in a gas-cooled core is in a sense somewhat more complicated than in liquid cooled cores. To achieve a high enough coolant mass-flow through the core, the gas is pressurised during normal operation. Loosing the high pressure implies a potentially severe accident scenario. In such a situation the mass flow through the core, and subsequently the cooling performance, falls linearly with the pressure loss.

Another potential situation is the loss of cooling of the core due to loss of pumping, even though with out loss of the operating pressure. In case that would happen, the cooling of the core is dependent on the natural circulation of the coolant. The designer should take this into account, designing the coolant loop in such a way, that the natural circulation is sufficient to remove at least the decay heat. Two main parameters determine this, the pressure drop in the coolant loop and the elevation of the cold side of the loop over the hot side.

However, in order to avoid core damage, the equilibrium temperature should be below the temperature limits set by the material parameters of the fuel and, by the structure materials. Evidently, this means that the success of the core design is highly dependent on material choices, since rising core temperatures established at natural circulation should be expected following accidents in gas cooled cores.

Three papers are included in this work. The first two address different approaches in assuring safe operation of helium cooled transmutation cores. Core safety is an important part of both papers, however they also include calculations of core performance and the transmutation efficiency in the two systems studied. The third paper addresses the issue of spallation source efficiency in a helium cooled sub-critical core. It shows that source neutrons behave somewhat differently depending on whether the core is helium- or liquid-metal-cooled.

### 6.3 Calculation methods

The main calculations carried out in the scope of this work have been statistic calculations of the neutronics of the core designs proposed. Two codes have been used.

MCB, the Monte Carlo continous Burn up code [59] was used for the calculations concerning neutronics in the first and second paper. MCB is based on MCNP4C [60] and calculates the changes in nuclide composition continuously. Neutron data have been taken from the JEFF3.0 library compiled for temperature steps of 300 K [6]. The neutron spectra are recalculated at each time step.

In the paper on source efficiency, MCNPX2.5e [61] was used for the neutronics calculations. MCNPX has the benefit over MCNP of treating high energy particle transport, which is necessary for a correct modelling of the source neutrons.

Calculations, other than the neutronics calculations, have been simplified. As an example, the thermal hydraulics calculations were performed for the hottest pin rather than for a model of the entire core.

### 6.4 Summary of the first paper

Knowing the decay heat removal capability is the key safety issue for cores cooled by helium, any design proposal of such a system has to address this issue. Utilising plutonium rich fuels in a fast core gives a very good neutron economy. The hypothesis in the first paper is that this would make it possible to ease the decay

heat removal issue enough for safe operation simply by maximising the coolant to fuel ratio in the core, thus allowing for a lower operating pressure at the expense of higher neutron leakage.

The core suggested is based on an original helium cooled fast reactor design by General Atomics (GA), the GCFR-design [62]. This design was adopted since the GCFR-project led to rather detailed studies on helium cooled fast reactors. A large part of the work performed by GA has been useful, especially for bench-marking results.

The two reactors suggested within the GCFR-project are both helium cooled. The fuel is introduced into clad pins, gathered in fuel assemblies. The main difference between the two cores is the power - 330 MW<sub>el</sub> and 1000 MW<sub>el</sub> for the smaller and larger versions respectively.

Increasing the coolant fraction in the core allows for decreasing the working pressure of the coolant, while maintaining the same mass flow rate through the core. The decrease in working pressure makes the relative drop in coolant performance smaller in the case of a severe loss of pressure accident. An increased coolant fraction may be achieved by increasing the distance in between fuel pins. In a uranium fuelled core the resulting increased leakage deteriorates the neutron economy to much to maintain criticality and is hence not an option. When the plutonium fraction of the fuel is raised though, the neutron economy is much improved. The excess neutrons allow for an increased neutron leakage and an increased coolant fraction.

### Core and fuel design

A nitride fuel consisting of in average 58% plutonium, 35% americium and seven percent curium dispersed in a zirconium nitride matrix is employed. The fuel region is divided into four zones in order to achieve as flat a radial power profile as possible. Reactivity in the four zones is regulated by altering the plutonium content of the fuel. At the beginning of the burnup cycle (BOC), the plutonium fractions are set to 28, 34, 45 and 100% respectively for the four zones. The relation between the distance between adjacent pins, and the pin diameter, the *pin pitch to diameter ratio* (P/D) can be increased to 1.8 at a level of sub-criticality corresponding to  $k_{eff}=0.97$ . The resulting operating pressure is 4.3 MPa as compared to around 10 MPa in the GCFR-design. The maximum P/D, and hence the minimum pressure is given by the situation where the fuel in the outermost zone consists of pure plutonium.

The nitride is enriched to 98% <sup>15</sup>N in order to prevent the build-up of <sup>14</sup>C from (n,p)-reactions in <sup>14</sup>N. At that enrichment, the production of <sup>14</sup>C is less than in a LWR of the same size [63][64].

The fuel dimensions are the same as in the GCFR-design, the fuel pellet diameter is 7.1 mm, the outer diameter is 7.8 mm. Each assembly contains 169 pins resulting in a total of 20280 pins, which is less than in the GCFR reference case. The pins are arranged in a triangular lattice in the assemblies, which are in turn arranged in a

triangular lattice, making up the core. Table 6.1 summarises some core parameters. *Flat to flat* is the measure across a hexagonal fuel assembly.

| Property                      | Present design |
|-------------------------------|----------------|
| Core height                   | 1.00 m         |
| Fuel pin inner/outer diameter | 7.1/7.8 mm     |
| Fuel-clad gap                 | 0.05 mm        |
| Pellet diameter               | 7.0 mm         |
| P/D                           | 1.7806         |
| Assembly wall thickness       | 4.0 mm         |
| Assembly spacing              | 2.0 mm         |
| Assembly inner flat to flat   | 178.4 mm       |
| Assembly outer flat to flat   | 185.3 mm       |
| Number of fuel assemblies     | 120            |
| Number of rods                | 20 280         |

Table 6.1: Properties of the core proposed.

### Thermal-hydraulics

An important thermo-hydraulic trade-off in nuclear core design is the one between safety and economics when settling for the pin linear power. The main safety requirement being the possibility of removing decay heat at ambient pressure. In the loss of pressure scenario, the pumps are assumed to be circulating the helium at 70 m/s. With the coolant fraction given by the neutronics, the mass flow is known.

There are limits to temperatures in the core. Especially the cladding temperature is limited for material concerns. The cladding temperature is given by

$$q(z) = h[T_{clad}(z) - T_{cool}(z)] = \frac{\chi(z)}{2\pi R_{clad}} \quad (6.1)$$

where  $q(z)$  is the heat flux from the pin to the coolant,  $\chi(z)$  is the linear power  $R_{clad}$ , is the radius of the cladding and the coolant temperature is given by

$$T_{cool} = T_0 + \int_0^{z_1} \frac{q(z)}{\dot{m} \cdot c_p} \quad (6.2)$$

The mass flux is denoted by  $\dot{m}$ ,  $c_p$  denotes the coolant heat capacity and  $T_0$  is the inlet temperature. The heat transfer coefficient  $h$  is given by

$$h = \frac{k}{D_h} \cdot Nu \cdot SR \cdot C \quad (6.3)$$

The thermal conductivity is denoted by  $k$  and varies with temperature, the hydraulic diameter is denoted by  $D_h$ . SR is a factor describing the increase in heat

|   |                        |
|---|------------------------|
| Total core power                          | 570 MW <sub>th</sub>   |
| Average linear power                      | 28 kW/m                |
| Operating pressure                        | 4.3·10 <sup>6</sup> Pa |
| Coolant flow speed                        | 70 m/s                 |
| Max cladding temperature - operation [67] | 900 K                  |
| Max cladding temperature - accident [68]  | 1330 K                 |
| Coolant inlet temperature [62]            | 577 K                  |

Table 6.2: Thermal properties of the pin type gas-cooled design suggested in the first paper

transfer arising from roughening of the fuel pins. In this case it was set to two.  $C$  is a constant describing the influence of the boundary layer. It is set to one. Since the main contribution to the Nusselt,  $Nu$ , number is in this case convection, the Dittus-Boelter correlation is assumed to be valid

$$Nu = 0.023Re^{0.8}Pr^{0.4} \quad (6.4)$$

$Re$  and  $Pr$  denote the Reynolds and Prandtl numbers respectively. Optimised austenitic steels such as D9 or 15-15Ti are likely to stand rather high temperatures even in an intense radiation environment. D9-data [65] indicate that this steel survives for ten minutes at 1300 K and for one hour at 1200 K. The power level - 5% of full power - assumed as decay heat power, is valid only for a very short time since the power production drops rapidly due to the short half lives of many of the nuclides being the source of the heat. Thus, it is reasonable to assume 1300 K as temperature limit for D9-steel in an accident scenario.

With decay heat assumed to equal five percent of full power, the upper temperature and the mass flow during an accident give the maximum pin power allowed. For the design proposed the average linear power is 28 kW/m. With 20280 one metre long pins, this gives a total core power of 570 MW<sub>th</sub>. The operating pressure of 4.3 MPa is given by the cladding temperature limit at normal operation - 900 K, which is based on the thermal creep limit for such steels [66]. Some thermal data for the core proposed have been collected in Table 6.2.

### Natural circulation

Having designed the thermal hydraulic parameters of the core to handle the consequences of a loss of pressure situation, the scenario of loosing the pumps remain. In case all pumping of the coolant fails, the core cooling must rely on natural circulation only. In the same way as for the loss of pressure accident, the demand will be to assure decay heat removal.

Natural circulation is driven by the density differences occurring between the hot and the cold side of the coolant cycle. If the cold side, where the coolant is heavier,

lies higher than the heat source, natural circulation starts once the difference in elevation is high enough to overcome the frictional pressure drop of the system given by

$$\Delta p_f = 2(f_r L_r + f_s L_s) \frac{1}{D_h} \cdot \frac{G^2}{\rho} \quad (6.5)$$

Indexes  $r$  and  $s$  denote *rough* and *smooth* respectively. The friction factors  $f$  for the two cases are quite different. In the present core, the rough part of the channel is 1 m and the smooth 1.5 m.  $G$  is the mass flux given by the density  $\rho$  multiplied by the velocity  $U$ . The flow velocity at natural circulation is given by

$$U' = \frac{Q'}{c_p A (T'_{out} - T'_{in}) \rho'} \quad (6.6)$$

where primed variables denote natural circulation conditions.  $Q'$  denotes the power produced at the hot side and  $A$  is the coolant channel area. The required vertical distance between the hot and the cold side is given by

$$\Delta L_t = \frac{\Delta p R}{g M_A p} \cdot \frac{T'_{in} \cdot T'_{out}}{\Delta T'} \quad (6.7)$$

The density has been expressed in terms of temperature, using the general gas law, introducing the general gas constant  $R$  and the mole-mass  $M_A$ . The temperature difference between hot and cold side is denoted  $\Delta T'$ . In the present core, the resulting  $\Delta L$  is just over 1 m thanks to the large P/D. The variation of  $\Delta L$  is displayed in Figure 6.1 In line with the approach adopted in the GCFR thermal calculations [69] the pressure drop over the rest of the coolant loop, outside of the core is assumed to be one third of the pressure drop over the core. This is a rough simplification, however the true value is in that range. Last of all an estimation of the pumping power required at normal operation of the system may be calculated as

$$W_P = \Delta p_{tot} \cdot A \cdot U \quad (6.8)$$

The resulting pumping power is 5.9 MW, which roughly corresponds to three percent of the electrical output of the system.

### Neutronic parameters

As already mentioned the neutronic parameters in a core loaded with uranium free, minor actinide bearing fuel, is very different to uranium fuelled cores. The delayed neutron fraction is low. On top of that, capture in the energy regions where delayed neutrons are emitted is strong in the americium nuclides. Removal of  $^{238}\text{U}$  is one of the reasons for the disappearance of the Doppler effect, non-resonant capture in americium at energies above the  $^{238}\text{U}$  resonance region being the other cause. Nevertheless, changes in reactivity due to changes in temperature, geometry or coolant pressure have impact on control and safety of the core.

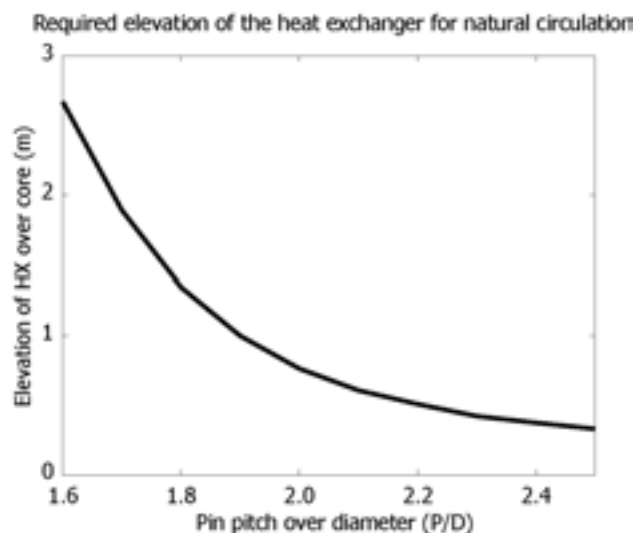


Figure 6.1: The figure shows the required elevation of the cold side of the coolant loop over the core for natural circulation to remove decay heat as a function the distance between fuel pins in units of pin diameter.

Neutronic parameters are typically calculated in consecutive runs where the parameter of interest, e.g. the coolant density, the temperature or the geometry is varied. Table 6.3 shows the most important neutronic parameters for the core design of the present paper. The loss of coolant pressure in a helium-cooled core gives a positive feedback, however, it is much smaller than the reactivity insertion usually expected following the voiding of a liquid metal cooled core with a similar fuel. The Doppler feedback is totally negligible. The delayed neutron fraction  $\beta$  is about one third of what is expected in a standard LWR, fuelled by uranium oxide. However, the impact of the delayed neutrons,  $\beta_{\text{eff}}$  is smaller since the delayed neutrons are captured in americium to a higher extent than the average neutron. In a typical 1200 MW<sub>th</sub> uranium-plutonium fuelled, sodium cooled fast reactor  $\beta_{\text{eff}}$  is expected to be about 420 pcm [2]. For this type of reactor  $\beta_{\text{eff}}$  is generally about 10% lower than  $\beta$  [2].

### Irradiation cycle

The main incentive for helium cooling of a core dedicated to transmutation of trans-uranium nuclides is the hard neutron spectrum resulting in high burnup even of the even-N nuclides. The core studied is run for five cycles, between which the reactivity is altered. Each cycle is limited by the neutron multiplication decreasing as fuel is consumed. During the irradiation period, this is compensated for by increasing

|                      |                   |
|----------------------|-------------------|
| Coolant void worth   | 870 (40) pcm      |
| Doppler feedback     | -0.02(0.01) pcm/K |
| $\beta$              | 240(20) pcm       |
| $\beta_{\text{eff}}$ | 140(20) pcm       |

Table 6.3: Neutronic parameters

the proton beam power, leading to an increased source neutron production. For safety reasons the beam power is not allowed to increased to much. In this study the beam is allowed to double.

After each of the five irradiation periods, the reactivity is altered by making adjustments to the core blanket. No changes are made to the fuel. In the beginning of the first cycle, the blanket has a large content of boron carbide assemblies, absorbing neutrons. These are gradually replaced for steel assemblies, reflecting neutrons back into the fuel region. Ultimately, the burnup is limited by fast neutron induced radiation damage in core structure material. The peak radiation dose anywhere in the core is 44 dpa per effective power year. With a limiting dose for the steels used of 180 dpa [54], this gives a potential for 1500 days of full power operation. In this study, the irradiation was terminated after 1400 effective power days.

Table 6.4 displays the changes in mass inventory for the most interesting nuclides. Keeping in mind that the fuel used in this study is spent MOX, where the americium and curium fractions are rather low and would be expected to increase towards a higher equilibrium level during radiation, the figures should draw the readers attention. After a few recycles of the transmuter fuel the relation between nuclides with even and odd neutron numbers changes. Even-N nuclides are built by capture reactions in the odd-N nuclides. However, as the fractions of the even-N nuclides increases, fission in these become more dominating, and an equilibrium eventually settles. Interestingly, the figures show how the curium production and consumption are more or less balanced already in the first recycle. In liquid metal cooled cores several cycles would be needed before such a balance would be reached, naturally the curium fraction would be higher in that case.

In the present core, there is almost a net consumption already in this first fuel cycle step even for the curium nuclides. Overall, the net consumption of actinides is just over 19%. This figure includes all nuclides heavier than uranium, not only those listed in the table. Further discussion on these burnup figures will be found in Section 6.5 where a comparison between different core designs is made.

## Conclusion

Though the burnup figures presented for this core look very promising there are safety concerns that deserves further attention. Two accident events have been



| Nuclide           | BOC  | EOC (1400 days) | $\Delta_{tot}$ |
|-------------------|------|-----------------|----------------|
| $^{238}\text{Pu}$ | 117  | 182             | 56 %           |
| $^{239}\text{Pu}$ | 880  | 587             | -33 %          |
| $^{240}\text{Pu}$ | 706  | 649             | -8.2 %         |
| $^{241}\text{Pu}$ | 309  | 187             | -40 %          |
| $^{242}\text{Pu}$ | 318  | 312             | -0.76 %        |
| $^{241}\text{Am}$ | 934  | 625             | -33 %          |
| $^{243}\text{Am}$ | 472  | 344             | -27 %          |
| $^{244}\text{Cm}$ | 248  | 248             | 0.03 %         |
| $^{245}\text{Cm}$ | 36.2 | 36.4            | 0.68 %         |
| All actinides     | 4020 | 3250            | -19 %          |

Table 6.4: Evolution of the actinide vector during the first recycle. The net burnup is 19% in 1400 days. Note that the sum includes all actinides heavier than uranium, not only the above listed. The actinide inventory is given in kg.

discussed above; the loss of pressure and the loss of flow scenario. Even though these two scenarios are to be regarded as very serious and highly unlikely, there is always the possibility of both of them occurring simultaneously. This design would have serious problems to manage these two scenarios in combination.

Obviously, a different approach, allowing for much higher temperatures is necessary if helium is to be an option as coolant. The second paper presents a design using an entirely different core design to find a solution to the cumbersome issues arising from the high pressure operation required in gas-cooled cores.

## 6.5 Summary of the second paper

The first paper above shows that a pin fuel design is barely adequate to meet, and safely manage, the serious accident scenarios discussed above. Despite the design being optimised from a safety perspective in the first place, the measures taken are insufficient to meet the most severe accident scenarios imaginable.

### Core and fuel design

The second paper takes a completely different approach. The main idea in this design is to allow very high temperatures in the core, thus easing the demand on heat transport under severe accidents, ultimately making radiation the dominating means of heat transfer. To achieve this, a titanium nitride particle fuel is used, as proposed by Ogawa [70]. The fuel particles contains a kernel of fissile material, surrounded by several layers of titanium nitrite. The inner layer is porous to allow for gas release from the fuel. The outermost layer is gas-tight to assure containment of the fission products. Thus, gases released exit the fuel, but stay in the particle.

An other type of particles, filled with hafnium nitride rather than fuel is used to manage criticality and to give a harder neutron spectrum. Hafnium is a poison for low energy neutron, exhibiting rather high capture cross-sections for those, while exhibiting low capture cross-sections for high energy neutrons. Each particle is small, having a diameter just under 2 mm.

Millions of fuel particles are contained within the fuel assemblies. Each fuel assembly consists of two silicon carbide tubes, between which the fuel particles are located. Both tubes are porous to helium. Inside the inner tube, cold helium rises, eventually passing through the SiC-tube, through the fuel region, out through the outer SiC-tube. Finally, the helium flow upwards in the gap between the assemblies and exits the core in the upper part. All structure materials are either ceramic or covered by ceramics to withstand very high temperatures. Utilising tube-assemblies is an old idea originally presented by Gratton et al. [28]. The tube type assemblies give a very large intersection area between fuel and coolant. No fuel is more than 1 mm distant from the coolant. Figure 6.2 shows the principle of the tube type assemblies. The peak power at any time in an assembly is around 9 MW. The core consists of 156 assemblies implying an average assembly power just over  $5 \text{ MW}_{\text{th}}$ . These are arranged in a hexagonal lattice. Seven positions in the centre of the lattice are reserved for the spallation target.

This design uses the same seven year cooled spent MOX as do the core proposed in paper one. The favourable neutron economy of the plutonium bearing transuranium fuel gives a requirement for the plutonium fraction as low as 25 percent. A main reason to raise the americium and curium fractions in the transmuter fuel as much as possible is to limit the number of expensive accelerator-driven systems. The bottle-neck of the fuel cycle is the incineration of the minor actinides.

## Thermal-hydraulics

The design philosophy behind the Japanese helium-cooled fast critical core, upon which this design is based, is to rely on radiation and natural convection for emergency cooling [71]. Thanks to the coated particle fuel and ceramic coating of core structures, the temperatures may rise high enough to manage a loss of pressure accident without scram or forced convection. The temperature limit was set to  $2200 \text{ }^\circ\text{C}$ , given by the upper temperature allowed to maintain a coolable geometry in SiC-structures [27][71].

Outside the core region there are emergency cooling systems to act as heat sink for the core.

In the gas cooled cores in general, and especially in this design, the outlet temperature of the coolant during normal operation is much higher than for the liquid-metal-cooled systems, leading to an increased thermal efficiency compared to liquid-metal-cooled systems.

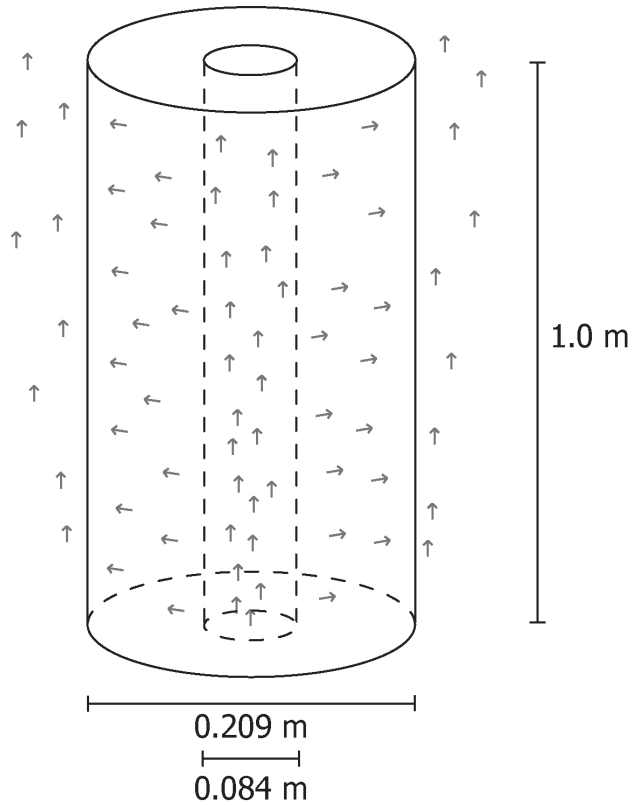


Figure 6.2: Drawing of the tube type assembly principle: Helium enters from below in the centre tube, rises, passes through the porous SiC-wall to the fuel region, passes through the outer wall and exits upwards.

### Cross-sections and burnup results

Taking a look at the neutron cross-sections in the two helium-cooled transmutation cores presented here and comparing them to other fast reactors gives some useful information on the performance of the designs. Table 6.5 shows the probability for fission as compared to the total probability of a reaction absorbing a neutron. Four cores are compared, TiN denotes the present core, GCADS denotes the core presented in paper one, ATW [42] is the American accelerator-driven transmutation of waste concept and EFR is the acronym for the European Fast Reactor [20]. The harder the neutron spectra, the higher the fission probabilities. It is obvious from Table 6.5, that the GCADS gives the hardest energy spectrum of the four cores compared. The present core shows similar characteristics to the ATW. The EFR

| Nuclide           | TiN  | GCADS | ATW  | EFR  |
|-------------------|------|-------|------|------|
| <sup>237</sup> Np | 0.36 | 0.45  | 0.31 | 0.16 |
| <sup>238</sup> Pu | 0.80 | 0.84  | 0.80 | 0.61 |
| <sup>239</sup> Pu | 0.86 | 0.89  | 0.88 | 0.78 |
| <sup>240</sup> Pu | 0.64 | 0.71  | 0.60 | 0.47 |
| <sup>241</sup> Pu | 0.87 | 0.84  | 0.83 | 0.82 |
| <sup>242</sup> Pu | 0.61 | 0.70  | 0.57 | 0.31 |
| <sup>241</sup> Am | 0.27 | 0.33  | 0.20 | 0.13 |
| <sup>243</sup> Am | 0.26 | 0.33  | 0.19 | 0.14 |
| <sup>244</sup> Cm | 0.66 | 0.72  | 0.59 | 0.39 |
| <sup>245</sup> Cm | 0.90 | 0.93  | 0.92 | -    |

Table 6.5: Fission to absorption cross-section ratios at BOC for four different fast cores. TiN denotes the present core, GCADS the core presented in paper one, ATW denotes the accelerator-driven transmutation of waste concept and EFR the European fast reactor.

| Nuclide           | BOC  | EOC (600 d) | $\Delta_{tot}$ |
|-------------------|------|-------------|----------------|
| <sup>238</sup> Pu | 39   | 130         | 233%           |
| <sup>239</sup> Pu | 295  | 193         | -34.5%         |
| <sup>240</sup> Pu | 237  | 228         | -3.9%          |
| <sup>241</sup> Pu | 104  | 69          | -34.0%         |
| <sup>242</sup> Pu | 107  | 134         | 25.7%          |
| <sup>241</sup> Am | 1307 | 876         | -33.0%         |
| <sup>243</sup> Am | 661  | 482         | -27.1%         |
| <sup>244</sup> Cm | 347  | 379         | 9.3%           |
| <sup>245</sup> Cm | 51   | 52          | 3.4%           |
| All actinides     | 3146 | 2671        | -15.1 %        |

Table 6.6: Actinide mass reduction in the tube type transmutation assemblies suggested in the second article. The masses are in kg. The figure for the total reduction includes all actinides heavier than uranium, not only those displayed in the table.

gives a much softer spectrum leading to lower fission probabilities, neutron capture being a more important process. The softer neutron spectrum of the present core compared to the pin-design of paper one is visible also in the burnup achieved after 700 days of operation. The total burnup is very high in the present core. Over 15% of the actinide mass is fissioned in 600 days as compared to 19% in 1400 days in the GCADS. This is because the power density in the present core is much higher, which in turn is a direct consequence of the higher temperature limits during accident conditions easing the demands to limit the assembly peak power. But,

when looking at individual nuclides as in Table 6.6, it is obvious that the spectrum is softer in the present design. Instead of remaining constant, the mass of curium and  $^{242}\text{Pu}$  increases, especially the increase in  $^{238}\text{Pu}$  inventory is significant. Even though the spectrum is softer, the inventory of curium is almost constant already at the first fuel cycle. In liquid metal cooled cores, such an equilibrium is reached eventually, after several recycles, as the composition of the actinide vector changes. Keeping the curium inventory low is important, since curium is a main cost driver for reprocessing and fuel manufacturing.

The reason for the softer spectrum in the present core is the massive introduction of titanium in the particle fuel, which leads to moderation of the spectrum thus enhancing capture reactions, building heavy nuclides.

## Conclusion

This second article concludes that it is most possible to design a gas-cooled transmutation core, which is both safe and efficient compared to the liquid metal cooled alternatives. The very hard spectrum, is to some extension lost when the core is redesigned to deal better with safety issues. The softer spectrum means the fractions of the cumbersome americium and curium nuclides will be higher in the equilibrium fuel composition. However, the increased safety performance allows for a much faster burnup though in the present core than in the one presented in paper one.

## 6.6 Summary of the third paper

### Background

Sub-critical cores require an external neutron source to supply the extra neutrons required to keep the power constant. For the large cores considered for the task of transmuting the nuclear waste, spallation neutron sources is the option available. The source neutrons are produced in a spallation reaction induced by a high energy charged particle e.g. a proton hitting a heavy target. After impact, a series of consecutive reactions follow. Some neutrons, born in the spallation process, have very large energies and induce further spallation reactions. Naturally, the geometry of the spallation target has an impact on the total number of neutrons produced. The radius of the target is an important parameter for the secondary reactions, but it is also important for the mean energy of the source neutrons. The fuel region, surrounding the target, gives an important influence depending on both geometry and material choices. This is where the coolant comes in to the picture. The efficiency of the spallation source depends on the choice of coolant. The aim of the third paper is to examine what consequences should be expected when changing the ADS coolant from LBE to helium.

### Proton source efficiency

In the third paper, the *proton source efficiency* -  $\psi^*$  is examined.  $\psi^*$  is closely related to the neutron source efficiency  $\phi^*$ . Both concepts describe the neutron production in the core,  $\psi^*$  being normalised to source protons,  $\phi^*$  to source neutrons. The benefit of using  $\psi^*$  is that that it is directly proportional to the beam power amplification. Further, there are several ways of defining  $\phi^*$ , whereas the definition of  $\psi^*$  is unique.  $\psi^*$  is expressed as

$$\psi^* = \left( \frac{1}{k_{eff}} - 1 \right) \cdot \frac{\langle \mathbf{F}\Phi_S \rangle}{\langle S_p \rangle} \quad (6.9)$$

As shall be seen, there are large variations in  $\psi^*$  following changes in core and target geometry and following material changes.

### Model descriptions

Two core models are studied, one helium-cooled and one LBE-cooled. In each model, two kinds of fuel are used; MOX and minor actinide fuel with the nuclide composition from spent MOX cooled for seven years as in the first and second papers. Table 6.7 gives the material compositions used. The models for the two different coolants require somewhat different geometries. These follow the designs developed within the PDS-XADS project funded within the fifth European framework programme. Both designs are 80 MW<sub>th</sub> and of similar size [72][73]. Table 6.8 gives some important geometrical parameters for the two different core models used.

The reflector was simplified in the models and was replaced with a homogenous material with density and composition corresponding to the lattice of steel pins making up the real reflector. In the base cases the target radius was kept at 20 cm. However the effect of variations in the radius was examined in the 20 - 40 cm range.

All core setups have  $k_{eff}$  close to 0.97. In the MOX fuelled cores this is achieved by adjusting the core outer radius. For the actinide fuel models, the radii used in the corresponding MOX cores were kept. The reactivity was managed by altering the inert matrix fraction of the actinide fuel. In the helium-cooled core the matrix mass fraction was 45%, in the LBE case 41% was enough to achieve the desired level of sub-criticality. Figure 6.3 show the two simplified models used for the calculations.

### Results

The cases modelled yield quite different proton source efficiencies. Both changes in fuel and coolant result in significant effects. The calculated values of  $\psi^*$  are collected in Table 6.9.

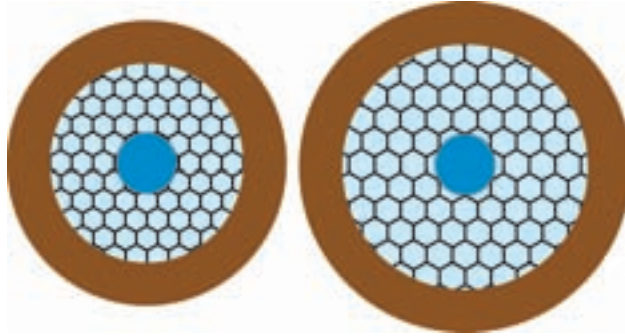


Figure 6.3: Two cores were modelled, the helium-cooled core (left) has a smaller radius, but is higher. The fuel assemblies are larger in the LBE-cooled core (right). Both models are based on the designs developed within the PDS-XADS-project. However, the core radii have been adjusted to give the desired level of sub-criticality.

|                   | BOC (%) | AcN (%) |
|-------------------|---------|---------|
| $^{235}\text{Pu}$ | 0.42    | -       |
| $^{238}\text{U}$  | 76.47   | -       |
| $^{238}\text{Pu}$ | 0.09    | 2.00    |
| $^{239}\text{Pu}$ | 16.00   | 15.16   |
| $^{240}\text{Pu}$ | 5.64    | 12.14   |
| $^{241}\text{Pu}$ | 0.60    | 5.29    |
| $^{242}\text{Pu}$ | 0.27    | 5.40    |
| $^{241}\text{Am}$ | 0.51    | 33.30   |
| $^{243}\text{Am}$ | -       | 16.68   |
| $^{244}\text{Cm}$ | -       | 8.74    |
| $^{245}\text{Cm}$ | -       | 1.30    |

Table 6.7: Nuclide compositions of the two fuels examined. MOX refers to the mixed oxide fuel proposed in the XADS project. AcN refers to the equilibrium actinide composition in a core dedicated to actinide transmutation. ZrN is used as matrix in the latter case.

|                          | He      | LBE     |
|--------------------------|---------|---------|
| Assemblies               | 90      | 120     |
| Pins                     | 3330    | 10800   |
| Pin P/D                  | 1.29    | 1.58    |
| Pin diameter             | 13.0 mm | 8.50 mm |
| Pellet internal diameter | 3.2 mm  | 1.8 mm  |
| Core radius              | 645 mm  | 830 mm  |
| Core height              | 1500 mm | 870 mm  |

Table 6.8: The two XADS-designs differ in geometry, the most important difference being that P/D is larger in the LBE cooled core.

|          | He-MOX | LBE-MOX      | He-AcN       | LBE-AcN      |
|----------|--------|--------------|--------------|--------------|
| $\psi^*$ | 19.4   | 16.8<br>-13% | 16.8<br>-13% | 15.2<br>-22% |
| Z        | 13.5   | 12.5         | 13.5         | 12.5         |
| $\phi^*$ | 1.43   | 1.35<br>-6%  | 1.24<br>-13% | 1.22<br>-15% |

Table 6.9:  $\psi^*$  for the four cases studied and the relative difference to the He-MOX case.

## Analysis

Table 6.10 shows the macroscopic cross-sections for fission and capture in the four cases studied for fission and source neutrons respectively. The relative differences in the cross-sections for fission and source neutrons are very important for the proton source efficiency. Generally, high fission cross-sections and low capture cross-section for the source neutrons in comparison with the fission neutrons result in high proton source efficiency.

Several interesting observations can be made from the table. By looking at the changes in cross-sections when changing the fuel and coolant, the reasons for the observed changes in  $\psi^*$  may be traced.

When the coolant is changed from helium to LBE, the cross-sections for fission induced by fission neutrons increases in comparison with the cross-sections for source neutrons. This suggests that  $\psi^*$  would increase when changing the coolant. However, the observed changes are the opposite,  $\psi^*$  decreases by around 10%. The reason for this is found in the cross-sections for capture. When LBE is utilised as coolant, the capture cross-sections for source neutrons are significantly higher than in the helium-cooled cases relative to the fission neutron capture cross-sections. For the MOX fuelled core, the difference increases from 2% to 9%, for the actinide case, from 5% to 12%. Apparently, this effect is large enough to counter act the change



| Model   | $\bar{\Sigma}_f$ |                 |                     | $\bar{\Sigma}_c$ |                 |                     |
|---------|------------------|-----------------|---------------------|------------------|-----------------|---------------------|
|         | Fission neutrons | Source neutrons | Relative difference | Fission neutrons | Source neutrons | Relative difference |
| He-MOX  | 37.0             | 34.2            | - 7%                | 37.8             | 38.6            | 2%                  |
| LBE-MOX | 28.9             | 27.7            | - 4%                | 33.2             | 36.4            | 9%                  |
| He-AcN  | 53.5             | 46.7            | -13%                | 71.7             | 74.9            | 5%                  |
| LBE-AcN | 35.5             | 31.5            | - 11%               | 48.9             | 54.7            | 12%                 |

Table 6.10: The macroscopic cross-sections for fission and source neutrons for the four cores and the relative differences. There is a pattern in the figures corresponding to the variations in  $\psi^*$  observed. High cross-sections for source neutron capture in combination with low fission cross-sections result in poor source efficiency as displayed in Table 6.9.

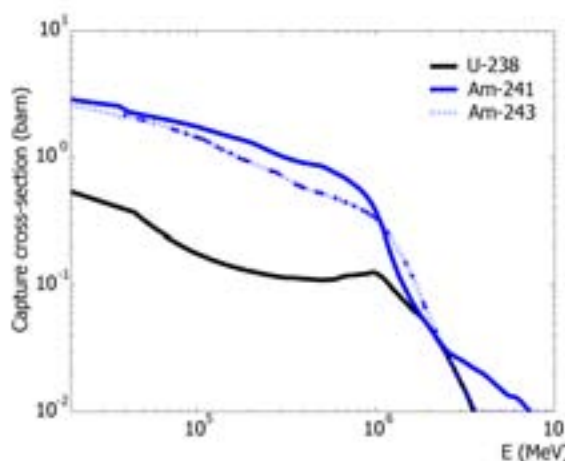


Figure 6.4: Capture cross-sections for  $^{238}\text{U}$ ,  $^{241}\text{Am}$  and  $^{243}\text{Am}$ .

in the fission cross-sections.

The main contributors to the capture cross-sections are  $^{238}\text{U}$  in the MOX fuel, and  $^{241}\text{Am}$  and  $^{243}\text{Am}$  in the actinide-fuel. The explanation for the relative changes in capture cross-sections arises from slight shifts in the neutron energy spectra following the change of coolant. LBE moderates fast neutrons through inelastic scattering, to a higher extent than helium do, and consequently, gives a softer spectrum. Figure 6.4 shows how the microscopic capture cross-sections vary for the three nuclides of interest. It should be noted that the gradients of the cross-sections are quite steep at neutron energies above 1 MeV.

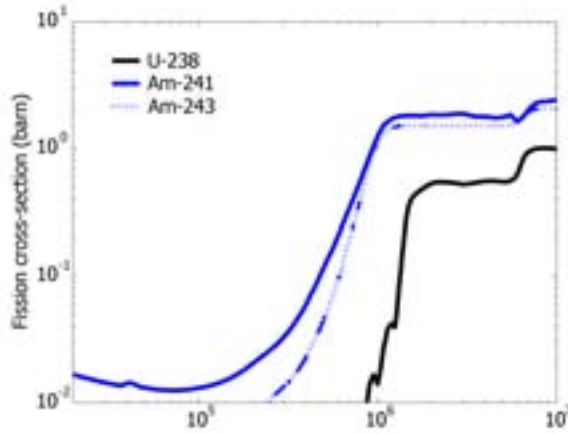


Figure 6.5: Fission cross-sections for  $^{238}\text{U}$ ,  $^{241}\text{Am}$  and  $^{243}\text{Am}$ .

Changing the fuel, for the same coolant also gives an effect on  $\psi^*$ . When replacing the MOX fuel with actinide fuel,  $^{238}\text{U}$  is replaced by, mainly, americium. The effect is that the relative differences in cross-sections between fission and source neutrons increase significantly for both fission and capture. These changes both act towards a lower  $\psi^*$  for the actinide fuel, just as observed (Table 6.9). It is not quite clear which changes in the neutron spectra that cause the changes in the capture cross-sections. However it is clear that the difference in capture cross-sections for the fission and for the source neutron spectra is larger when americium is dominating the fuel.

The explanation for the changes in the fission cross-sections also arises from the substitution of  $^{238}\text{U}$  for  $^{241}\text{Am}$  and  $^{243}\text{Am}$ . Figure 6.5 shows how the microscopic fission cross-sections for these three nuclides vary with energy. All three nuclides have a steep increase in fission cross-section. This occurs at around 1 MeV in  $^{238}\text{U}$  and somewhat lower in energy for the americium nuclides. This explains the change in relative fission cross-section between fission and source neutrons. The change in microscopic cross-section is simply very different for different nuclides even though the shift in energy may be rather similar.

It also seems reasonable that the neutron yield,  $\nu$ , from the average fission reaction would have an impact on  $\psi^*$ . In case there is a large difference in fission yield between source and fission neutron induced fission reactions, this would have a large effect. It turns out however that the differences in  $\nu$  for source and fission neutron induced fission varies in the range of one to three percent. That variation in itself is not sufficient to explain the variations in  $\psi^*$  observed.

**Conclusions**

Utilising americium rich fuels in a sub-critical core reduces the proton source efficiency,  $\psi^*$ , by 10% compared to utilising MOX fuel. In a helium-cooled sub-critical core  $\psi^*$  is 10% higher than in a LBE-cooled core. Both of these effects arise from the strong energy dependence of cross-sections for even-N nuclides in the 1 MeV region. Small variations in spectrum yield large changes in cross-sections.

## Chapter 7

### Concluding remarks

Even though it at first might seem hard to combine efficiency and safety of a helium-cooled transmutation core, a closer look shows that it is possible. The core presented in the first paper, shows an excellent transmutation performance, consumption and production of curium is in balance already in the first recycle, when the core is loaded with spent MOX fuel. In metal cooled systems, this would be expected at first after several recycles, when the recycled actinide vector is approaching its equilibrium.

In the second paper an entirely different approach is suggested. The transmutation performance is somewhat sacrificed to improve the safety performance of the core. As a consequence of this, a higher power-per-fuel-mass is possible leading to faster transmutation. The relative burn-up figures for each nuclide for this design might at first glance give the impression of a disappointment, especially for the curium nuclides. However, when comparing the figures to those of other designs as in Table 6.5 it is clear that even this helium-cooled core, that shows a somewhat softer neutron spectrum, outperforms other designs when it comes to transmutation efficiency, showing significantly higher fission to absorption cross-section ratios. Further, the high burn-up, 15% in 600 days, is beneficial since it yields a short fuel cycle and thus a short time needed to complete the task of transmuting the long lived actinides.

In conclusion, it is possible to transmute actinides in the hard neutron spectrum of a helium-cooled core. It might even show to be the better option, since the transmutation efficiency is good and the source efficiency for helium-cooled cores is better than for lead-bismuth-cooled cores.

Much work remain before the first transmutation core will start incinerating the growing stock-piles of actinides. However if nuclear is to remain an important source of energy it will eventually be a necessity.

# Bibliography

- [1] T. Ginsburg. *Die friedliche Anwendung von nuklearen Explosionen*. Verlag Karl Thiemig KG, 1965. In german.
- [2] A.E. Waltar and A.B. Reynolds. *Fast Breeder Reactors*. Pergamon Press, 1981.
- [3] *Uranium 2003: Resources, Production and Demand*. OECD/NEA, 2004.
- [4] J. S. Walker. *Three Mile Island - A Nuclear Crisis in Historical Perspective*. University of California Press, 2004.
- [5] *Age Dependent Doses to Members of the Public from Intake of Radionuclides: Part 5 - Compilation of Ingestion and Inhalation Dose Coefficients*. ICRP Publication 76, 1995.
- [6] The JEFF-3.0 nuclear data library. Technical Report JEFF Report 19, NEA Data Bank, 2005.
- [7] NEA Data Bank. Janis 2.1, <http://www.igcar.ernet.in/>, 2004.
- [8] Fast reactors and accelerator driven systems knowledge base. Technical Report IAEA-TECDOC-866, IAEA, 1996.
- [9] *Accelerator-driven Systems (ADS) and Fast Reactors (FR) in Advanced Nuclear Fuel Cycles - A Comparative Study*. OECD/NEA, 2002.
- [10] M. Fjaestad. Drömmen om blyreaktorn - teknik och utopi i Sveriges kärnkraftshistoria. *Dædalus 2003 - Tekniska museets årsbok*, (71st annual issue).
- [11] J. F. Sauvage. *Phènix - 30 years of history: the heart of a reactor*. CEA, 2004.
- [12] L. Rahmani et al. SPX significant events and whether it would have happened on EFR. In *Unusual occurrences during LMFR operation*, number IAEA-TECDOC-1180. IAEA, 2000.
- [13] R. Carle. Detailed design studies demonstrate major improvements in economics. *Nuclear Engineering International*, page 18, 1988.

- [14] A.A. Rineiskii et al. Commercialization of fast reactors. In *International Conference on Fast Reactors and Related Fuel Cycles, FR'91, October 28 - November 1, 1991, Kyoto, Japan*, pages 18.7–1, 1991.
- [15] K. Isozaki et al. Upgrade of cooling system heat removal capacity of the experimental fast reactor JOYO. *Nuclear Technology*, 150:56, 2005.
- [16] O.M. Saraev. Operating experience with Beloyarsk fast reactor BN600 NPP. In *Unusual occurrences in LMFBR operation*, IAEA-TECDOC-1180, page 101. IAEA, 2000.
- [17] B. Raj. The core of stage two. *Nuclear Engineering International*, september, 2005.
- [18] <http://www.igcar.ernet.in/>, October 2005.
- [19] A. Languille et al. CAPRA core studies - the oxide reference option. In *International Conference on Evaluation of Emerging Nuclear Fuel Cycle Systems, GLOBAL'95*, page 874. ANS, 1995.
- [20] H. Sztark et al. Core optimization of the European fast reactor EFR. In *International Conference on Fast Reactors and Related Fuel Cycles, FR'91*, 1991.
- [21] D.C. Wade and R.H. Hill. The design rationale of the IFR. *Progress in Nuclear Energy*, 31:13, 1997.
- [22] A Technology Roadmap for Generation IV Nuclear Energy Systems, 2002.
- [23] G. Melese-d'Hospital. Review of gas cooled reactor thermal hydraulics. In *Proceedings of the ANS/ASME/NRC International Topical Meeting on Nuclear Reactor Thermal-Hydraulics*, page 2147. ANS, 1980.
- [24] P. Fortescue and J.B. Dee. Gas-cooled fast breeder reactor studies. *Transactions of the American Nuclear Society*, 14:273, 1971.
- [25] J.B. Dee and G.B. Melese-d'Hospital. Part 1 - the 300 MW(e) GCFR demonstration plant. *Mechanical Engineering*, 94:18, 1972.
- [26] J.B. Dee and G.B. Melese-d'Hospital. Part 2 - performance studies of large GCFR plants. *Mechanical Engineering*, 94:28, 1972.
- [27] M. Konomura et al. A promising gas-cooled fast reactor concept and its R&D plan. In *International Conference on Future Nuclear Systems, GLOBAL'03*, page 57. ANS, 2003.
- [28] C.P. Gratton et al. A gas-cooled fast reactor using coated particle fuel. *Journal of the British Nuclear Energy Society*, 7:233, 1968.

- [29] G. Melese-d'Hospital. Performance of gas-cooled fast reactors with artificially roughened fuel elements. *Nuclear Science and Engineering*, 33:271, 1968.
- [30] M. Steinberg et al. Neutron burning of long-lived fission products for waste disposal. Technical Report BNL-8558, Brookhaven National Laboratory, 1964.
- [31] M.V. Gregory and M. Steinberg. A nuclear transmutation system for disposal of long-lived fission product waste in an expanding nuclear power economy. Technical Report BNL-11915, Brookhaven National Laboratory, 1967.
- [32] H. C. Claiborne. High-level radioactive waste disposal by transmutation. *Transactions of the American Nuclear Society*, 15:91, 1972.
- [33] D.G. Foster et al. Review of PNL study on transmutation processing of high level waste. Technical Report LA-UR-74-74, Los Alamos National Laboratory, 1974.
- [34] A.G. Croff et al. Actinide partitioning-transmutation program final report. Technical Report ORNL-5566, Oak Ridge National Laboratory, 1980.
- [35] Evaluation of actinide partitioning and transmutation. Technical Report 214, IAEA, 1982.
- [36] T. Takizuka et al. A study in incineration target system. In *Fifth OECD/NEA Information Exchange Meeting on Actinide and Fission Product Partitioning and Transmutation*, page 70. OECD/NEA, 1989.
- [37] H. Takahashi et al. A fast breeder and incinerator assisted by a proton accelerator. In *Specialist meeting on accelerator driven transmutation technology for radwaste*, page 552. LA-12205-C, Los Alamos National Laboratory, 1991.
- [38] J. Wallenius et al. Application of burnable absorbers in an accelerator driven system. *Nuclear Science and Engineering*, 137:96, 2001.
- [39] T. Mukaiyama et al. Partitioning and transmutation program "OMEGA" at JAERI. In *International Conference on Evaluation of Emerging Nuclear Fuel Cycle Systems, GLOBAL'95*, page 110. ANS, 1995.
- [40] H. Takano and T. Ikegami. Activities on of R&D partitioning and transmutation in Japan. In *Proceedings of the 7th Information Exchange Meeting, Jeju, Republic of Korea 14-16 October 2002*, page 29, 2002.
- [41] F. Carminati et al. An Energy Amplifier for cleaner and inexhaustible nuclear energy production driven by a particle beam accelerator. Technical Report CERN/AT/93-47(ET), 1993.
- [42] A Roadmap for Developing Accelerator Transmutation of Waste (ATW) Technology: A Report to Congress, 1999.

- [43] The European Technical Working Group on ADS. A european roadmap for developing Accelerator Driven Systems (ADS) for nuclear waste incineration. Technical Report ISBN 88-8286-008-6, ENEA, 2001.
- [44] B. Carlucci and P. Anzieu. Proposal for a gas cooled ADS demonstrator. In *Third International Conference on Accelerator-Driven Transmutation Technologies and Applications, ADTTA'99*. Praha, 1999.
- [45] J.J. Laidler et al. Development of pyroprocessing technology. *Progress in Nuclear Energy*, 31:131, 1991.
- [46] *World Energy Outlook: 2000*. OECD/IEA, 2000.
- [47] *Uranium 2001: Resources, Production and Demand*. OECD/NEA, 2002.
- [48] H. Murata and T. Mukaiyama. Fission reactor studies in view of reactor waste programs. *Atomkernenergie-Kerntechnik*, 45:23, 1984.
- [49] M. Salvatores. Advanced options for transmutation strategies. In *Proceedings of the Fifth International Information Exchange Meeting on Actinide and Fission Product Partitioning and Transmutation*. OECD/NEA, Mol, 1998.
- [50] D. Westlén. A cost benefit analysis of an accelerator driven transmutation system, 2001.
- [51] G.I. Bell and S. Glasstone. *Nuclear Reactor Theory*. van Norstrand Reinhold Company, 1970.
- [52] J. Wallenius and M. Eriksson. Neutronic design of minor actinide burning accelerator driven systems. *Nuclear Technology*, 152, 2005. In press.
- [53] J. Wallenius and M. Eriksson. Neutronics of minor actinide burning accelerator driven systems with ceramic fuel. *Nuclear Technology*, 152, 2005. In press.
- [54] H. Bailly et al. *The nuclear fuel of pressurized water reactors and fast reactors - Design and behaviour*. Lavoisier Publishing Inc., 1999.
- [55] T. Ogawa. Dedicated fuels for transmutation - nitrides and alloys. In *Lecture notes: Frederic Joliot/Otto Hahn Summer School'2002, Cadarache, France*. CEA/FZK.
- [56] Working materials of the technical working group on fast reactors, proceedings of the technical committee meeting on sodium removal and disposal from LMFBRs in normal operation in the framework of decommissioning, Aix-en-Provence, France. Technical Report IWGFR-98, IAEA, November 1997.
- [57] A.V. Zrodnikov et al. Use of russian technology of ship reactors with lead-bismuth coolant in nuclear power. In *Proceedings Heavy Liquid Metal Coolants in Nuclear Technology, Vol. 1, Obninsk, Russia*, 1998.



- [58] L.A. Lys et al. Gas turbine power conversion systems for helium cooled breeder reactors. Technical report, Eidg. Institut für Reaktorforschung, Würenlingen, Schweiz, 1970.
- [59] J. Cetnar et al. MCB - a continuous energy Monte Carlo Burnup code. In *Fifth international information exchange meeting*, page 523. OECD/NEA, Mol, 1998.
- [60] J.F. Briesmeister. *MCNP - A general Monte Carlo N-Particle transport code, version 4C*. LA-13709-M, Los Alamos National Laboratory, 2000.
- [61] J. S. Hendricks et al. *MCNPX, version 2.5.e*. Los Alamos National Laboratory, 2004.
- [62] P. Fortescue et al. A developmental gas-cooled fast breeder reactor plant. In *Proceedings Nuclex 69*, October 1969.
- [63] J. Wallenius. Neutronic aspects of inert matrix fuels for application in ADS. *Journal of Nuclear Materials*, 320:142, 2003.
- [64] J. Wallenius et al. Influence of  $^{15}\text{N}$  enrichment on neutronics, costs and  $^{14}\text{C}$  production in nitride fuel cycle scenarios. *Journal of Nuclear Materials*. Manuscript.
- [65] R. J. Puigh and M. L. Hamilton. In-reactor creep rupture behavior of the D19 and 316 alloys. In *Influence of Radiation on Material Properties: 13th International Symposium (Part II), Philadelphia*. American Society for Testing and Materials, 1987.
- [66] J.L Séran et al. Behaviour under neutron irradiation of the 15-15 Ti and Em10 steels used as standard materials of the Phénix fuel subassembly. In *Effects of Radiation on Materials, Proceedings 15th Int. Symp. Nashville*. ASTM, 1990.
- [67] J. T. Murgatroy et al. Technical specification of the core configuration for the gas-cooled XADS - deliverable 11 PDS-XADS. Technical Report DOC02-171 (C6862/TR/09 Rev 0), NNC, 2002.
- [68] C.W. Hunter et al. Mechanical properties of unirradiated fast reactor cladding during simulated overpower transients. *Nuclear Technology*, 27(3):376, 1975.
- [69] G. Melese-d'Hospital. Natural circulation cooling potential of  $\text{CO}_2$  and He for GCFR's. In *Proceedings of the ANS/ASME/NRC International Topical Meeting on Nuclear Reactor Thermal-Hydraulics*, page 2222. ANS, 1980.
- [70] T. Ogawa et al. Fuel elements and fuel cycle concepts of actinide burner reactors. Technical Report JAERI-M 89-123, JAERI, 1989.

- [71] M. Naganuma et al. Design study on core and fuel properties of helium gas cooled fast reactors (coated particle type fuel reactor / pin type fuel reactor) - results in JFY2001. Technical Report TN9400 2002-074, JNC, 2002. In japanese.
- [72] Core design summary report for the LBE-cooled XADS. Technical Report XADS 41 TNIX 064 Rev. 0, Ansaldo Nucleare, 2004.
- [73] PDS-XADS work package 4.2 deliverable 65: Core design summary. Technical Report C6862/TR/0028, NNC LTD, 2004.

# Acknowledgements

Even though my work the last few years have been a lot about thinking, calculating and writing, which were all tasks I had to carry out alone, I have had support from a large number of people. Some of them helped me with specific research problems or answered my endless number of questions thereby teaching me reactor physics, thermal hydraulics and the fine details in university bureaucracy. Others have contributed implicitly by taking part in discussions on research. Yet others have created the social environment necessary to cope with crashed calculations and malfunctioning coffee machines.

My supervisor Janne Wallenius and my colleagues Jerzy Cetnar, Kamil Tuček, Marcus Eriksson and Per Seltborg have shown endless patience answering my questions. I thank them for all their help. Waclaw Gudowski has given me great opportunities to work in my field of interest and to take part in interesting projects especially on the European level, which I am thankful for. Karin Lagerggren, Torbjörn Bäck, Mikael Jolkkonen and Karin Andgren deserve special thanks for the many enjoying lunch discussions. Christina Lagerstedt, Patrick Isaksson, Calle Persson, André Grisell, Alexandra Åhlander and Jitka Žáková have also been very important to me both by contributing to the atmosphere of the department, but also because they have been teaching me by asking me questions that forced me to learn. I also send my warm thanks to the rest of the nuclear and reactor physics group with whom I have had the great pleasure to share a working environment.

I wish to thank Per, Calle and Malin Beskow for proof reading the manuscript. Junji Hirohashi from the department of laser physics have translated two reports from Japanese to English which was of great value to me. I am grateful for his help.

Last, I want to thank my wonderful family and my supportive friends for being my, sometimes badly needed, link to the outside world.

Two-band modeling of  $\alpha$ -prime phase formation in Fe-CrPär Olsson,<sup>1</sup> Janne Wallenius,<sup>1,2</sup> Christophe Domain,<sup>3</sup> Kai Nordlund,<sup>4</sup> and Lorenzo Malerba<sup>5</sup><sup>1</sup>Department of Neutron Research, Uppsala University, Uppsala, Sweden<sup>2</sup>Department of Nuclear and Reactor Physics, Royal Institute of Technology, Stockholm, Sweden<sup>3</sup>Department of Materials and Mechanics of Components, EDF R&D, Moret sur Loing, France<sup>4</sup>Accelerator Laboratory, University of Helsinki, Helsinki, Finland<sup>5</sup>Reactor Materials Research Unit, SCK-CEN, Mol, Belgium

(Received 8 August 2005; revised manuscript received 25 October 2005)

We have developed a two-band model of Fe-Cr, fitted to properties of the ferromagnetic alloy. Fitting many-body functionals to the calculated mixing enthalpy of the alloy and the mixed interstitial binding energy in iron, our potential reproduces changes in sign of the formation energy as a function of Cr concentration. When applied in kinetic Monte Carlo simulations, the potential correctly predicts decomposition of initially random Fe-Cr alloys into the  $\alpha$ -prime phase as function of Cr concentration.

DOI: XXXX

PACS number(s): 61.66.Dk, 61.80.Hg, 61.82.Bg

## I. INTRODUCTION

The embedded atom method and second-moment tight-binding approximation many-body potentials have successfully been used to describe a number of physical properties of pure elements, including formation energies and mobilities of point defects.<sup>1-3</sup> When applied to alloys, Foiles and co-workers found that by fitting the ratio of  $s$ - and  $d$ -electron density, one could reproduce mixing energies that change sign as a function of alloy concentration, as is the case for Ni-Pd.<sup>4</sup> When including terms corresponding to  $d$ -electron density only, a strictly positive or negative heat of mixing results.<sup>5-7</sup> Hence, it appears that the small contribution of the  $s$ -band to the cohesive energy is essential for modeling of certain alloys. In a physically consistent picture, one should, however, consider that electronic structure calculations set limits to the variation of  $s$ -electron density. For  $3d$  transition metals, one finds that the integrated density of  $s$ -states remains approximately constant at a value of about 1.5, while the  $d$ -band density increases with increasing average valence number. Therefore, it is rather the strength of  $s$ -band interaction that should be fitted, than the density *per se*.

In the original derivation of the second-moment tight-binding approximation to the many-body interaction, the repulsive force due to kinetic energy of  $s$ -band electrons was neglected.<sup>8,9</sup> Although the contribution to the total cohesive energy of the  $s$ -electrons is small, the opposite is true for pressure and especially elasticity.<sup>10</sup>

A better formulation of the embedded atom method is therefore needed, especially in the case of application to the Fe-Cr system, the basic component of ferritic-martensitic stainless steel. Fe-Cr forms a perfect ferromagnetic alloy for Cr concentrations up to 10% at  $T=750$  K, but decomposes into two isomorphous phases, iron-rich  $\alpha$  and chromium-rich  $\alpha$ -prime, for Cr concentrations ranging from 10 to 90 at %.<sup>11-14</sup> The size of the chromium-rich precipitates is on the nanometer scale, and the kinetics of the phase separation is faster under irradiation than under thermal aging.<sup>15</sup>

In this paper we construct a two-band ( $s$  and  $d$ ) second-moment model that correctly describes the heat of mixing in Fe-Cr. The predictive capability of our potential is under-

lined by simulation of thermal aging, showing explicitly how the  $\alpha$ -prime phase forms, either by spinodal decomposition or by nucleation and growth.

## II. TWO-BAND MODEL OF TRANSITION METAL ALLOYS

A two-band model for Cs and other pure elements was recently suggested by Ackland.<sup>16</sup> Here, we apply the two-band approach in the Fe-Cr system. Extending Ackland's second-moment expression for the total energy of binary alloys with contributions from  $s$ -band electrons, we write for the energy of atom  $i$  (Refs. 5 and 17):

$$E_i = \frac{1}{2} \sum_j V(r_{ij}) + F_d(\rho_d) + F_s(\rho_s), \quad (1)$$

where  $V(r_{ij})$  is the pairwise (electrostatic) interaction between core electrons of the atoms at site  $i$  and  $j$ , and  $\rho_b = \sum \phi_b(r_{ij})$  represents the density of  $s$ - and  $d$ -band electrons yielding a many-body energy described by the functional  $F_b(\rho_b)$ . Note that the embedding functions for Fe and Cr are identical.

In line with Ackland, we write the band functional as

$$F_b(\rho_b) = A_1^b \sqrt{\rho_b} + A_2^b \rho_b^2 + A_3^b \rho_b^4, \quad (2)$$

where the coefficients  $A_i$  parametrize the relative strength of cohesive and repulsive forces.

In order to highlight the importance of the  $s$ -band contribution to the mixing enthalpy of the alloy, we present the following instructive example. Consider the case of a potential where the  $d$ -band yields a positive mixing enthalpy with a parabolic shape. For simplicity, assume equal density functions  $\phi^{AB}(r)$  of first nearest-neighbor range and no contribution from the kinetic energy. The  $d$ -band mixing enthalpy as a function of solute concentration  $C_B$  may then be written in arbitrary units (a.u.) as

$$H_d^{\text{mix}} = 1 - \sqrt{C_B^2 + C_B(1 - C_B) + (1 - C_B)^2}, \quad (3)$$

which has a maximum of 0.125 a.u. at  $C_B=50\%$ . Assuming that the impact of the  $s$ -band that we would like to catch is a

TABLE I. Spline coefficients and cutoffs for the Cr pair potential, electron-density function and band functional here used. Cutoffs are given in units of nearest-neighbor distance in Cr (2.4924 Å). The unit for the spline coefficients is electron volts per cubic angstroms.

| $i$   | 1        | 2                        | 3                        | 4          |
|-------|----------|--------------------------|--------------------------|------------|
| $r_i$ | 0.976    | 1.150                    | 1.216                    | 1.650      |
| $a_i$ | -165.0   | -78.49908                | -78.15495                | +1.8679553 |
| $r_k$ | 0.963    | 1.284                    | 1.685                    |            |
| $b_k$ | -11.0828 | +0.013905                | -0.447541                |            |
| $A_i$ | -0.56479 | $-8.8959 \times 10^{-4}$ | $+9.0265 \times 10^{-8}$ |            |

perturbation in the mixing enthalpy, we may set  $\phi_s^{AA} = \phi_s^{BB} = 0$ . Adding a cohesive energy of the  $s$ -band equal to

$$H_s^{\text{mix}} = -\sqrt{0.01C_B(1-C_B)}, \quad (4)$$

one finds minima in the formation energy at 1.0% concentration of solute atoms, having a magnitude of  $-0.005$  a.u., comparing to the maximum at equal concentrations of 0.85 a.u. The relative magnitude of the extrema is in good agreement with actual calculations of the formation energy in transition metal alloys.<sup>18</sup> Hence, an increase in electron density of merely 1% due to  $s$ -band mixed-pair interaction should be sufficient to allow the present model to reproduce the concentration dependence of the formation energy calculated *ab initio*.

### III. POTENTIALS FOR Fe AND Cr

The pair interaction and the many-body functionals for Fe were taken from the recent work of Ackland and Mendelev.<sup>17</sup> This potential provides values for self-interstitial formation energies in reasonable agreement with *ab initio* calculations and has therefore been applied to simulations of defect evolution. To the special features of this potential belong a cohesive energy of 4.03 eV and a density function normalized to the total electron number of iron, which is 26. Consequently, the Cr potential previously developed by us,<sup>7,19</sup> may not be directly coupled with the Ackland-Mendelev potential for Fe. We have chosen to refit our Cr potential to yield a cohesive energy of 3.84 eV in order to retain the difference in cohesive energy between Fe and Cr. The density function for Cr has the same shape as the one used for Fe by Ackland and Mendelev, but is normalized to a total electron density of 24 at equilibrium. The following parametric form of the pair interaction is assumed:

$$V(r) = \sum_i a_i (r - r_i)^3 H(r_i - r). \quad (5)$$

Here,  $r_i$  are cutoffs of the cubic splines used to represent the potential,  $H$  is the Heaviside step function, and  $a_i$  are spline coefficients. Similarly, the density function of chromium is represented by

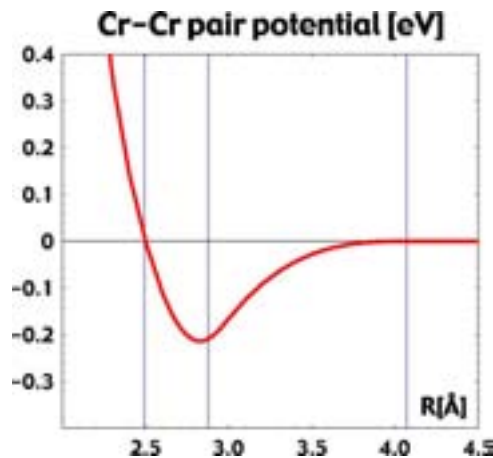


FIG. 1. (Color online) Pair interaction  $V(r)$  for pure Cr. The vertical lines represent positions of first, second, and third nearest neighbors.

$$\phi_d^{\text{CrCr}}(r) = \sum_k b_k (r - r_k)^3 H(r_k - r). \quad (6)$$

The coefficients of the pair potential and the many-body functional (2) were fitted to the experimental lattice parameter at 0 K, the elastic constants of paramagnetic chromium extrapolated to 0 K and the relaxed formation energies for vacancies and self-interstitials calculated with VASP using the PAW algorithm.<sup>20-22</sup>

In Table I, the coefficients and cutoffs for Cr used in the present paper are given. Note that although the coefficient of the squared electron density in the band functional is negative, as is the case for the Fe potential by Ackland and Mendelev, our band functional has a second derivative that is positive everywhere.

In Figs. 1 and 2, the resulting pair potential and band functional are displayed. The properties of chromium calculated with the potential are compared to experimental and/or *ab initio* data in Table II. We include values for nonrelaxed ( $E_{\text{vac}}^{\text{nr}}$ ) as well as relaxed ( $E_{\text{vac}}^{\text{rel}}$ ) vacancy formation energies to highlight the fact that the relaxation energy observed in the *ab initio* calculation is well reproduced by our potential.

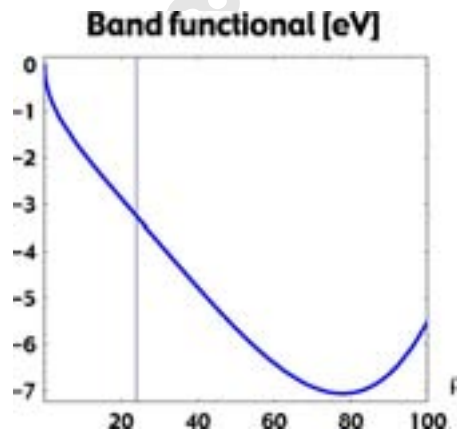


FIG. 2. (Color online)  $D$ -band functional  $F_d(\rho)$  for pure Cr. The vertical line represents the equilibrium density.

TABLE II. Properties of Cr calculated with the present potential. Comparison is made to experimental data for paramagnetic Cr extrapolated to 0 K and VASP calculations for paramagnetic Cr in the PAW formalism.<sup>22</sup>

|  | This work | Experiment           | VASP-PAW |
|--|-----------|----------------------|----------|
| $a_0$ (Å)                              | 2.878     | 2.878 <sup>a</sup>   | 2.834    |
| $B$ (GPa)                              | 208       | 208 <sup>b</sup>     |          |
| $C'$ (GPa)                             | 152       | 152 <sup>b</sup>     |          |
| $C_{44}$ (GPa)                         | 105       | 105 <sup>b</sup>     |          |
| $E_{\text{coh}}$ (eV)                  | 3.84      | 4.10                 |          |
| $E_{\text{vac}}^{\text{nr}}$ (eV)      | 2.88      |                      | 2.89     |
| $E_{\text{vac}}^{\text{rel}}$ (eV)     | 2.56      | 2.0±0.2 <sup>c</sup> | 2.59     |
| $E_{\text{vac}}^{\text{mig}}$ (eV)     | 0.99      | 0.95 <sup>d</sup>    |          |
| $E_{\text{fcc}} - E_{\text{bcc}}$ (eV) | 0.03      |                      |          |
| $E_{\langle 110 \rangle}^f$ (eV)       | 5.60      |                      | 5.66     |
| $E_{\langle 111 \rangle}^f$ (eV)       | 5.62      |                      | 5.68     |
| $E_{\langle 100 \rangle}^f$ (eV)       | 6.83      |                      | 6.78     |

<sup>a</sup>Reference 23.

<sup>b</sup>Reference 24.

<sup>c</sup>Reference 25.

<sup>d</sup>Reference 26.

#### IV. ALLOY POTENTIAL

In an alloy, one may expect that the electron density is dependent on the local environment. For the mixed-pair density we choose the square of a  $4s$ -type Slater function

$$\phi_s^{\text{FeCr}}(r) = (N_s r^3 e^{-\zeta_s r})^2, \quad (7)$$

where  $\zeta_s = 1.323$  is an average  $\zeta$  from single  $\zeta$  approximations of the  $4s$  Hartree-Fock Fe and Cr orbitals,<sup>27</sup> providing a natural cutoff at 5.3 Å.  $N_s = 5.0$  is chosen to yield an  $s$ -electron density at first nearest-neighbor distance equal to 2% of the corresponding  $d$ -electron density.

Our alloy potential should predict changes in the sign of the mixing enthalpy. *Ab initio* calculations made with the exact muffin-tin orbital method (EMTO)<sup>18,28</sup> indicate that this property is due to a minimum in the density of states at the Fermi level for a chromium concentration of 10%. Furthermore, there is a small increase in the relative  $s$ -band density of the alloy as compared to that of a linear interpolation between the pure elements. We may, hence, contain the entire concentration dependence of this deviation in the mixed-pair density function  $\phi_s^{\text{FeCr}}$ , setting  $\phi_s^{\text{FeFe}}$  and  $\phi_s^{\text{CrCr}}$  equal to zero.

First, we fit the mixed-pair potential to the lattice parameter of Fe-10Cr and a positive heat of mixing for equimolar composition.

Then, the coefficients of the  $s$ -band functional are fitted to the negative substitution energy of a single Cr atom in bcc Fe and the crossing point from negative to positive mixing enthalpy, while constraining the second derivative of the  $s$ -band functional to be everywhere positive. For small concentrations, the term dependent on the square root will have a larger weight than terms quadratic and quartic in mixed density. The opposite is true for intermediate compositions.

TABLE III. Spline coefficients, cutoffs, and band coefficients for the Fe-Cr potentials are presented here. Cutoffs are given in units of 2.861 Å for Fe-Cr. The unit for the spline coefficients is electron volts per cubic angstrom.

| $i$            | 1      | 2     | 3     | 4     |
|----------------|--------|-------|-------|-------|
| $r_i$          | 0.970  | 1.15  | 1.40  | 2.14  |
| $a_i$ (VASP)   | -47.3  | -8.10 | -7.82 | +0.15 |
| $a_i$ (EMTO)   | -67.0  | -5.60 | -8.40 | +0.14 |
| $A_i^s$ (VASP) | -0.503 | -0.60 | +0.50 |       |
| $A_i^s$ (EMTO) | -0.800 | -1.00 | +0.80 |       |

Two sets of data were used for fitting of the substitution and mixing energies. One set<sup>29</sup> corresponds to data obtained with EMTO using the coherent potential approximation (CPA).<sup>30,31</sup> With this method, it is possible to perform calculations for arbitrary Cr concentrations, as the unit cell contains just one effective atom. The other set<sup>22</sup> is calculated with VASP in the PAW formalism, at a number of discrete Cr concentrations given by inserting an integer number of Cr atoms in a unit cell of different size.

Finally, the mixed-pair potential was fitted to the binding energy of the  $\langle 110 \rangle$  mixed dumbbell in bulk iron, which was calculated using VASP.

The molecular dynamics code DYMOKA<sup>32</sup> was revised to enable two-band functionals, and was extensively used during the fitting procedure. Table III displays coefficients fitted to the two sets of mixing enthalpy data. The mixing enthalpy was calculated as a function of Cr concentration in boxes with 16 000 randomly distributed atoms and is shown in Fig. 3. The interatomic potentials reproduce the *unrelaxed* mixing energy previously calculated with EMTO up to about 50% Cr concentration,<sup>18</sup> as well as the relaxed mixing energy obtained with VASP-PAW.

For higher concentrations, existing discrete Fourier transform (DFT) methods do not provide the negative substitution energy of Fe in Cr that may be expected from the existence

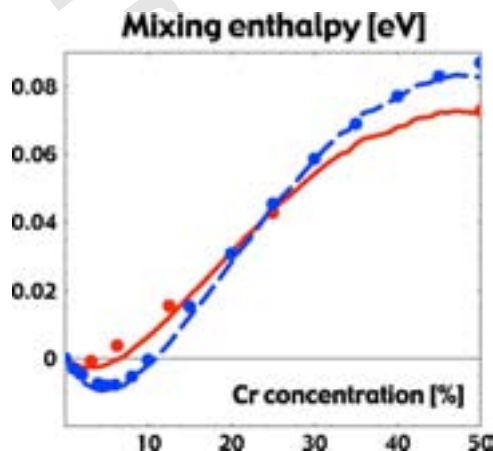


FIG. 3. (Color online) Mixing energy in random Fe-Cr alloys. Red circles: VASP mixing energy.<sup>29</sup> Blue circles: EMTO mixing energy.<sup>29</sup> Red solid line: relaxed MD mixing energy obtained with the potential fitted to VASP data. Dashed blue line: unrelaxed MD mixing energy obtained with the potential fitted to EMTO data.

TABLE IV. Substitutional and interstitial energies of Cr atom(s) in an iron lattice. Potential A is fitted to the mixing enthalpy calculated with VASP, potential B to the mixing enthalpy calculated with EMTO. Comparison is made with 128 and 129 atom VASP-PAW calculations.<sup>22</sup> Energies are given in electron volts.

|   | Pot A | Pot B | VASP <sup>22</sup> |
|---|-------|-------|--------------------|
| $E_{\text{sub}}^{\text{Cr}}$  | -0.02 | -0.27 | -0.02              |
| $E_{(110)}^{\text{Fe-Cr}} - E_{(110)}^{\text{Fe-Fe}} - E_{\text{sub}}^{\text{Cr}}$  | -0.12 | -0.13 | -0.12              |
| $E_{(111)}^{\text{Fe-Cr}} - E_{(111)}^{\text{Fe-Fe}} - E_{\text{sub}}^{\text{Cr}}$  | -0.32 | -0.38 | -0.42              |
| $E_{(110)}^{\text{Cr-Cr}} - E_{(110)}^{\text{Fe-Fe}} - 2E_{\text{sub}}^{\text{Cr}}$ | +0.32 | +0.46 | +0.30              |
| $E_{(111)}^{\text{Cr-Cr}} - E_{(111)}^{\text{Fe-Fe}} - 2E_{\text{sub}}^{\text{Cr}}$ | +0.04 | +0.24 | -0.34              |

of  $\alpha$ -prime precipitates. This is most likely due to the alloy being spin-density wave antiferromagnetic for Fe concentrations up to 16% at 0 K,<sup>33</sup> a configuration that has not yet been successfully modeled within density-functional theory.<sup>34</sup> At room temperature, a Fe concentration of just 2% is sufficient to make the alloy paramagnetic. In order to be consistent with experiment, we have not made any effort to adjust the negative substitution energy of Fe in Cr resulting from our fitting procedure.

Table IV displays substitutional and interstitial properties of Cr in a Fe crystal obtained using the potentials fitted to the mixing enthalpy calculated with VASP (potential A) and EMTO (potential B). VASP *ab initio* data are provided as a reference. In the VASP calculation, PAW pseudopotentials with 300 eV cutoff energies were used within the general gradient approximation. The supercell size was 128 lattice sites, the number of  $k$  points was 27, and atoms of different configurations were relaxed at constant volume. It was found that the most stable interstitial configuration was the mixed  $\langle 110 \rangle$  dumbbell with a binding energy of 0.12 eV relative to the pure iron dumbbell.<sup>22</sup> Note that the mixed-pair potential was fitted to the binding energy of the mixed  $\langle 110 \rangle$  dumbbell, but not to the other configurations. We observe that the potential fitted to a smaller substitution energy (potential A) yields interstitial binding energies in better agreement with *ab initio* data. Potential B, which was fitted to EMTO mixing enthalpy, performs less well for Cr-Cr dumbbell binding energies.

## V. SIMULATION OF THERMAL AGING

Using atomic kinetic Monte Carlo (AKMC) techniques, the time evolution of vacancy-driven thermal aging can be simulated in the alloy.

The AKMC simulation was performed with the LAKIMOCA code, based on the residence time algorithm.<sup>35</sup> A vacancy is introduced into the simulation box, and the kinetic Monte Carlo step consists of choosing one of the eight possible first-nearest vacancy jumps for a configuration according to their jump frequency  $\Gamma_k$  defined by

$$\Gamma_k^X = \nu e^{-\frac{E_{\text{mig}}^X + \Delta E/2}{kT}}, \quad (8)$$

where  $X$  is the the atom that jumps to the vacancy site and  $\nu$  is the attempt frequency. The migration energies  $E_{\text{mig}}$  given

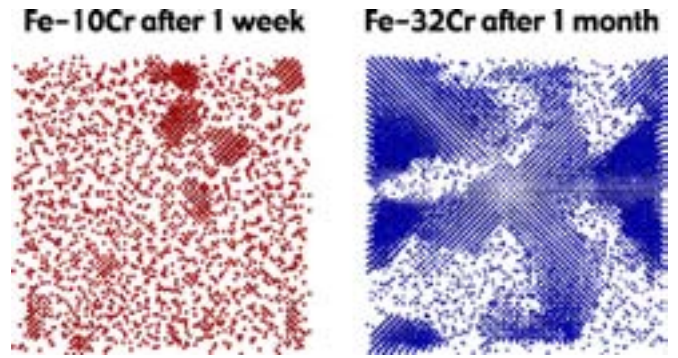


FIG. 4. (Color online) Cr distribution in initially random Fe-10Cr and Fe-32Cr aged at 740 K. The sharp precipitate boundaries found in Fe-10Cr are typical for nucleation processes, while the interconnected precipitates in Fe-32Cr result from spinodal decomposition. The potential fitted to VASP mixing enthalpy (potential A) was used in the simulation.

by the presently used potentials are 0.65 eV for Fe and 0.52 eV for a single Cr atom in iron.  $\Delta E$  is the energy difference of the system due to the vacancy jump, calculated using the potentials on a rigid lattice (without relaxation). The average time step associated to the kinetic Monte Carlo step in a BCC lattice is

$$dt = \frac{1}{\sum_{k=1,8} \Gamma_k}. \quad (9)$$

As the vacancy concentration in the simulation box is much larger than under experimental conditions, the simulated time has to be rescaled in order to obtain the aging time. The scaling factor is the ratio between the vacancy concentration in the simulation box and the thermal equilibrium concentration  $C_{\text{vac}}^{\text{eq}}(T) = e^{-G_f/kT}$ , where  $G_f$  is Gibbs energy for the formation of a vacancy.

In our previous works, the alloy potential did not provide any change in sign of the formation energy, and hence, the decomposition at Cr concentrations above 10% was driven to complete segregation of the elements.<sup>7</sup> With the present potentials, however, we would expect that the segregation should remain incomplete. Hence, we performed AKMC calculations in  $40 \times 40 \times 40$  lattice unit boxes for initially random distributions of Cr atoms in Fe-6Cr, Fe-8Cr, Fe-10Cr, and Fe-32Cr at  $T=740$  K. In the case of Fe-32Cr, experimental information about the time dependence of the Cr distribution at this temperature exists.<sup>12</sup>

In the simulations with an initial Cr concentration of 6%, the alloy remained random up to a simulated time of one week. For 8% initial chromium content, the alloy remained random up to one week of simulated time using potential B (having a negative mixing enthalpy at this concentration). Applying potential A, having a positive mixing enthalpy at this concentration, weak clustering tendencies were observed.

In Fig. 4, the spatial Cr distributions in initially random Fe-10Cr and Fe-32Cr are exemplified in  $40 \times 40 \times 10$  slices of the original box after  $2 \times 10^9$  and  $10^{10}$  vacancy jumps,

corresponding to one week and one month of simulated aging, respectively. Potential A was used for the simulation displayed, but no qualitative difference is observed when switching to potential B in this range of concentration. One may compare these results to the experimental solubility limit at  $T=670$  K, being 8.3%.<sup>15</sup>

Note that precipitate boundaries in Fe-10Cr are well defined, even for clusters located close to each other. Such geometries are typical for precipitate formation by nucleation, expected to occur where Gibbs' energy of formation has a positive curvature. Indeed, we observe that precipitates forming in Fe-10Cr are found at locations where the initial Cr concentration was slightly higher than the average due to random fluctuations. Furthermore, the size of the precipitates increase with time. In Fe-32Cr, the diffuse boundaries and interconnected precipitates result from spinodal decomposition, corresponding to a negative curvature of Gibbs' energy.

Local Cr concentrations were calculated by taking the mean concentration in boxes with, on average, 45 atoms. The boxes were constructed analogously to the experimental method<sup>12</sup> and were sampled along the  $\langle 110 \rangle$  direction. Figure 5 shows concentration profiles in Fe-10Cr and Fe-32Cr. Because of the method of sampling, the Cr concentration in the precipitates varies between 50 and 90%, consistent with the observation by Brenner *et al.*<sup>12</sup> For Fe-32Cr, we may compare the average size and distance of the precipitates in Fig. 4 to experimental data taken at 740 K, being 2 and 6 nm after 670 h of aging.<sup>12</sup> The cluster sizes and distances observed in our simulation are compatible with these data. To make a definite conclusion, a larger number of AKMC simulations would have to be done in order to provide statistical evidence.

## VI. CONCLUSIONS

We conclude that the two-band second-moment model of Fe-Cr here developed is able to reproduce thermodynamic properties of the alloy over the whole range of Cr concentration, including solubility limits and formation of the  $\alpha$ -prime phase under thermal aging. For this purpose, it was found sufficient to fit the mixed  $s$ -electron density functional to the mixing enthalpy. Our method enables one to model transition metal alloys with finite miscibility gaps in a quantitative manner. It will be instrumental in further studies of microstructure evolution in ferritic steels under thermal aging and irradiation conditions.

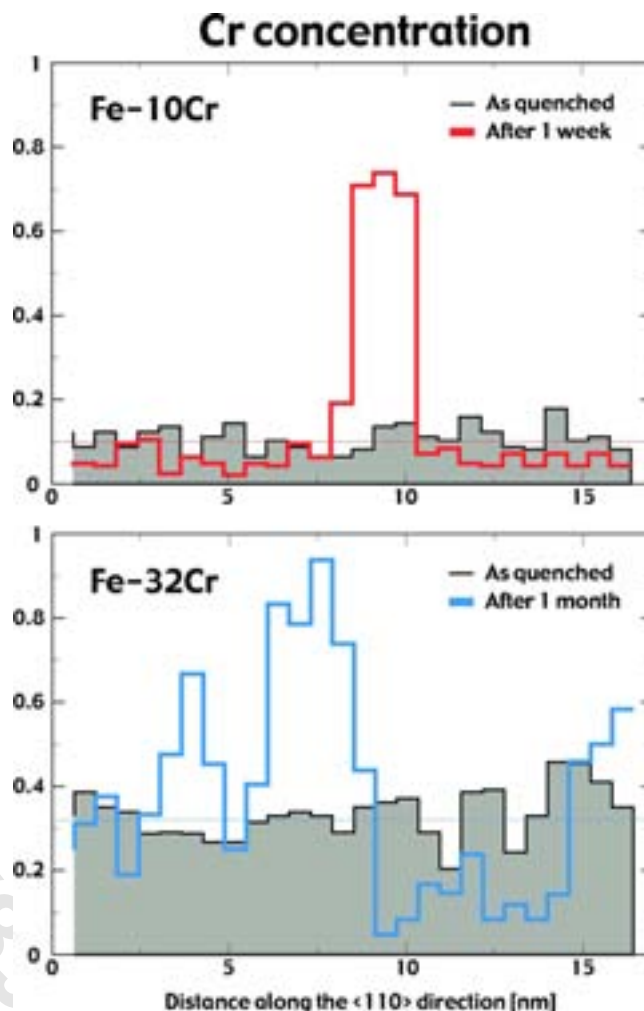


FIG. 5. (Color online) Cr concentration profile along the  $\langle 110 \rangle$  direction in initially random Fe-10Cr and Fe-32Cr aged at 740 K during one week and one month, respectively. The potential fitted to VASP mixing enthalpy (potential A) was used in the simulation.

## ACKNOWLEDGMENTS

The authors wish to thank Graeme Ackland, Vassilis Pontikis, and Igor Abrikosov for enlightening discussions. This work was funded by Svensk Kärnbränslehantering AB, the European Commission, and Vetenskapsrådet.

<sup>1</sup>M. S. Daw and M. I. Baskes, Phys. Rev. B **29**, 6443 (1984).

<sup>2</sup>M. Finnis and J. Sinclair, Philos. Mag. A **50**, 45 (1984).

<sup>3</sup>A. Voter, in *Intermetallic Compounds, Principles*, edited by J. H. Westbrook and R. L. Fleischer (Wiley, New York 1995), vol. 1.

<sup>4</sup>S. M. Foiles, M. I. Baskes, and M. S. Daw, Phys. Rev. B **33**, 7983 (1986).

<sup>5</sup>G. J. Ackland and V. Vitek, Phys. Rev. B **41**, 10324 (1990).

<sup>6</sup>E. M. Lopasso, M. Caro, A. Caro, and P. Turchi, Phys. Rev. B **68**, 214205 (2003).

<sup>7</sup>J. Wallenius, P. Olsson, C. Lagerstedt, N. Sandberg, R. Chakarova, and V. Pontikis, Phys. Rev. B **69**, 094103 (2004).

<sup>8</sup>F. Cyrot-Lackmann, J. Phys. Chem. Solids **29**, 1235 (1968).

<sup>9</sup>A. E. Carlsson and N. W. Ashcroft, Phys. Rev. B **27**, 2101 (1983).

<sup>10</sup>D. Pettifor, J. Phys. F: Met. Phys. **8**, 219 (1978).

<sup>11</sup>R. Fischer, E. Dulis, and K. Carroll, Trans. AIME **197**, 690 (1953).

<sup>12</sup>S. Brenner, M. Miller, and W. Soffa, Scr. Metall. **16**, 831 (1982).



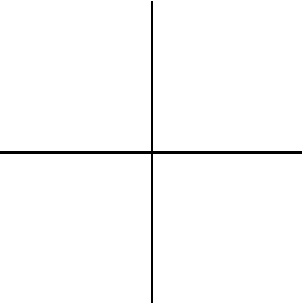
- <sup>13</sup>J. Hyde, A. Cerezo, M. Miller, and G. Smith, *Appl. Surf. Sci.* **76/77**, 233 (1994).
- <sup>14</sup>J. Hyde, M. Miller, A. Cerezo, and G. Smith, *Appl. Surf. Sci.* **87/88**, 311 (1995).
- <sup>15</sup>M. Mathon, Y. Carlan, G. Geoffrey, X. Averty, A. Alamo, and C. de Novion, *J. Nucl. Mater.* **312**, 236 (2003).
- <sup>16</sup>G. J. Ackland and S. K. Reed, *Phys. Rev. B* **67**, 174108 (2003).
- <sup>17</sup>G. Ackland, M. Mendeleev, D. Srolovitz, S. Han, and A. Barashev, *J. Phys.: Condens. Matter* **16**, S2629 (2004).
- <sup>18</sup>P. Olsson, I. Abrikosov, L. Vitos, and J. Wallenius, *J. Nucl. Mater.* **321**, 84 (2003).
- <sup>19</sup>J. Wallenius, P. Olsson, and C. Lagerstedt, *Nucl. Instrum. Methods Phys. Res. B* **228**, 122 (2005).
- <sup>20</sup>G. Kresse and D. Joubert, *Phys. Rev. B* **59**, 1758 (1999).
- <sup>21</sup>P. E. Blöchl, *Phys. Rev. B* **50**, 17953 (1994).
- <sup>22</sup>C. Domain, P. Olsson, and J. Wallenius (unpublished).
- <sup>23</sup>W. Pearson, *A Handbook of Lattice Spacings and Structures of Metals and Alloys* (Pergamon Press, New York, 1958).
- <sup>24</sup>K. Katahara, M. Nimalendran, M. Manghnani, and E. Fischer, *J. Phys. F: Met. Phys.* **9**, 2167 (1979).
- <sup>25</sup>G. Loper, L. Smedskjaer, M. Chason, and R. Siegel, in *Positron Annihilation*, edited by P. Jain, R. Singru, and K. Gopinathan (World Scientific, Singapore, 1985), p. 461.
- <sup>26</sup>H. Schultz, *Mater. Sci. Eng., A* **141**, 149 (1991).
- <sup>27</sup>E. Clementi and C. Roetti, *At. Data Nucl. Data Tables*, **14**(3)-(4), ■ (1974).
- <sup>28</sup>O. K. Andersen and T. Saha-Dasgupta, *Phys. Rev. B* **62**, R16219 (2000).
- <sup>29</sup>P. Olsson, I. Abrikosov, and J. Wallenius (unpublished).
- <sup>30</sup>B. Györfy, *Phys. Rev. B* **5**, 2382 (1972).
- <sup>31</sup>A. Kissavos, S. Simak, P. Olsson, L. Vitos, and I. Abrikosov, *Comput. Mater. Sci.* (to be published).
- <sup>32</sup>C. Becquart, K. Decker, C. Domain, J. Ruste, Y. Souffez, J. Turbatte, and J. V. Duysen, *Radiat. Eff. Defects Solids* **142**, 9 (1997).
- <sup>33</sup>S. Burke, R. Cywinski, J. Davis, and B. Rainford, *J. Phys. F: Met. Phys.* **13**, 451 (1983).
- <sup>34</sup>R. Hafner, D. Spisak, R. Lorenz, and J. Hafner, *J. Phys.: Condens. Matter* **13**, L239 (2001).
- <sup>35</sup>W. Young and E. Elcock, *Proc. Phys. Soc. London* **89**, 75 (1966).



# Simulation of Radiation Damage in Fe and FeCr

CHRISTINA LAGERSTEDT

Licentiate Thesis  
Stockholm, Sweden 2005



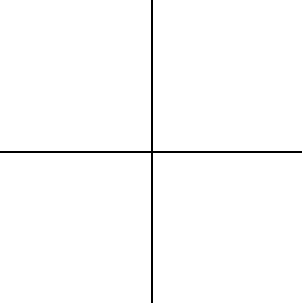
TRITA FYS 2005-61  
ISSN 0280-316X  
ISRN KTH/FYS/--05:61--SE  
ISBN 91-7178-198-6

KTH School of Science and Engineering  
SE-106 91 Stockholm  
SWEDEN

Akademisk avhandling som med tillstånd av Kungliga Tekniska högskolan fram-  
lägges till offentlig granskning för avläggande av Filosofie licentiatexamen i fysik  
fredagen den 25 november klockan 10.00 i FR4, AlbaNova Universitetscentrum,  
Roslagstullsbacken 21, Stockholm.

© Christina Lagerstedt, October 2005

Tryck: Universitetsservice US AB



## Abstract

Steel is an important structural material in nuclear reactors used for example in pressure vessels and fast reactor cladding. In reactor environments it has been observed that ferritic steels are more resistant to swelling than the austenitic steels typically used. Much effort has been put into developing basic models of FeCr alloys which can serve as model alloys for describing ferritic steels. As a result, a number of interatomic potentials for Fe and FeCr alloys exist today.

For the work in this thesis, basic material properties coming from experiments or *ab initio* calculations were used to fit interatomic potentials for Fe, Cr and FeCr implementing both the embedded atom method and the Finnis-Sinclair formalisms. The potentials were then validated by molecular dynamic calculations of material properties such as defect formation energies, migration energies and thermal expansion. Further studies of potential performance were carried out in simulations of radiation damage cascades and thermal aging.

The influence of the interatomic potential on the primary defect state in materials under irradiation was analyzed in a study comparing results obtained using four different potentials. The objective of the study was to find correlations between potential properties and the primary damage state produced in simulations of displacement cascades. The defect evolution and clustering during different cascade stages were also investigated to try to gain a better understanding of these processes.

# List of Papers

- I. J. Wallenius, P. Olsson, C. Lagerstedt, N. Sandberg, R. Chakarova and V. Pontikis  
*Modeling of chromium precipitation in Fe-Cr alloys*  
Physical Review B **69**, 094103 (2004)
- II. J. Wallenius, P. Olsson and C. Lagerstedt  
*Relation between thermal expansion and interstitial formation energy in Fe and Cr*  
Nuclear Instruments and Methods in Physics Research B 228 (2005) 122-125
- III. D. Terentyev, C. Lagerstedt, P. Olsson, K. Nordlund, J. Wallenius, C. S. Becquart and L. Malerba  
*Effect of the interatomic potential on the features of displacement cascades in  $\alpha$ -Fe: a molecular dynamics study*  
Submitted to Journal of Nuclear Materials, under review
- IV. C. Lagerstedt, d. Terentyev, P. Olsson, J. Wallenius and L. Malerba  
*Cluster formation mechanisms during relaxation and post-relaxation cascade stages in  $\alpha$ -Fe: a molecular dynamics study*  
To be submitted

## Author's contribution:

I performed calculations of material properties such as the thermal expansion in paper I and defect formation energies in paper II. For paper I, I also simulated and analyzed the displacement cascades presented there. For papers III and IV, I performed and analyzed a large number of the cascade simulations and wrote an appreciable part of both articles.

# Contents

|          |   |           |
|----------|---|-----------|
| <b>1</b> | <b>Introduction</b>                                   | <b>1</b>  |
| <b>2</b> | <b>Radiation Damage in Metals</b>                     | <b>4</b>  |
| 2.1      | Mechanisms . . . . .                                  | 4         |
| 2.2      | Primary Damage: Vacancies and Interstitials . . . . . | 5         |
| 2.3      | Primary Damage Evolution . . . . .                    | 9         |
| <b>3</b> | <b>Multiscale Modelling</b>                           | <b>14</b> |
| 3.1      | <i>Ab Initio</i> . . . . .                            | 14        |
| 3.2      | Interatomic Potentials . . . . .                      | 16        |
| 3.3      | Molecular Dynamics . . . . .                          | 20        |
| 3.4      | The Monte Carlo Method . . . . .                      | 22        |
| <b>4</b> | <b>Applications</b>                                   | <b>24</b> |
| 4.1      | Potential Construction . . . . .                      | 24        |
| 4.2      | Verification of Potentials . . . . .                  | 27        |
| 4.3      | Cascades Using Molecular Dynamics . . . . .           | 31        |
| <b>5</b> | <b>Summary and Outlook</b>                            | <b>33</b> |
|          | <b>Bibliography</b>                                   | <b>35</b> |

# Chapter 1

## Introduction

About 16% of the world's supply of electricity today comes from nuclear power [1]. As the world's energy demand rises, this percentage is expected to increase. The production of electricity in nuclear power plants has the advantage that there is no release of greenhouse gases such as carbon dioxide. We are however left with the problem of how to handle the radioactive waste produced. The favored way of fuel disposal is to place it in deep geological repositories built to contain the radioactivity released by the waste. The geological repositories are associated with some concerns. The radioactivity of the spent fuel needs to be contained for times of the order of  $10^5$  years before the radioactivity is on a level where it is deemed safe. The repositories must be constructed to contain the radioactivity for this time, a not so trivial technical problem.

One of the alternatives to direct disposal of the nuclear waste in geological repositories is transmutation, a method now under development. The concept of transmutation has existed since the 1970s [2] [3]. The idea is simple in the sense that it uses the same concept as traditional nuclear reactors; the splitting of atoms. The long lived radioactive isotopes such as Np, Pu, Am and Cm are transformed into more short lived isotopes by changing the nuclear structure. The storage times of the waste can be reduced by as much as a factor of 100 in this way, a more feasible timescale seen in the light of existing technologies.

The concept of transmutation requires some reactor features that are different from the conventional light water reactors (LWRs) that are most widely used today for electricity production. Especially of importance for this thesis is the need for neutrons of higher energy to be able to split the atoms in the fuel. More energetic neutrons means more damage to structures

surrounding the core. This can for example cause swelling and embrittlement of the steels used for structures in the reactor. Steels not designed to be radiation resistant can swell, something that seriously impairs the safety of a reactor. To ensure the safe operation of this type of future reactors and maintain the aging reactors in use today, it is important to find radiation resistant materials and to make sure that the limitations of the materials are known.

The response of a material to irradiation is not easy to predict. It depends on the dose that the material receives but also on the rate at which the material is exposed to the radiation. The damage usually does not depend linearly on the dose rate but instead shows a threshold behavior dependent on the total dose. Once the threshold dose is passed, the mechanical properties of the steel start to degrade rapidly. For steels not designed to be radiation resistant, the swelling can be as much as 1% per displacement per atom (dpa) while for ferritic steels a typical value is 0.2% per dpa. In LWRs, the dose rate is approximately 2 dpa per year and swelling in the structural materials are just starting to be seen after some 40 years of running. In fast reactors, so called because of the high energy or fast neutrons used to fission nuclei, the dose is a lot higher,  $\sim 40$  dpa per year, and the threshold for permanent damage is reached much sooner.

Experiments focused on the study of material behavior under irradiation is both a lengthy and expensive business. It is also difficult to study the microscopic evolution of the damage to the material at the atomic level with a high degree of precision. Instead, computer simulations are employed to model materials at the atomic levels that cannot be probed experimentally.

This thesis focuses on the modelling of metals and model alloys used in reactor environment. The modelling starts with *ab initio* calculations of basic material properties used for fitting interatomic potentials. The potentials are used in molecular dynamics simulations of the primary damage caused by neutron irradiation. The further evolution of the damage is studied with Monte Carlo schemes. This scheme of calculations and simulations are collectively known as multiscale modelling and covers time scales from femtoseconds to years and length scales from Ångströms to meters (see figure 1.1). Chapter 2 describes the damage caused by neutron irradiation on microscopic and macroscopic level and chapter 3 summarizes the theory behind the methods of multiscale modelling. In chapter 4, the work performed within the scope of this thesis is presented in the light of the theories discussed in the previous chapters. Finally, the thesis is summarized and an outlook for the future work is given.

---



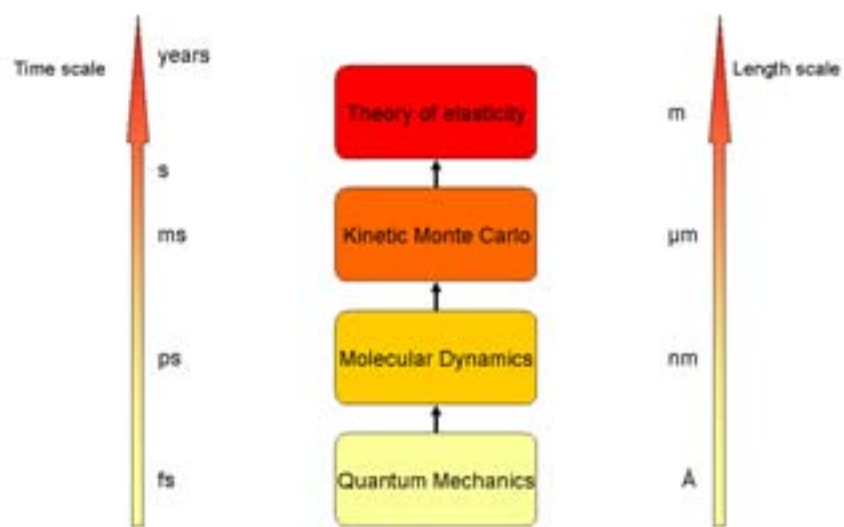


Figure 1.1: The length and time scales involved in the different stages of multiscale modelling.

## Chapter 2

# Radiation Damage in Metals

Like human defects, those of crystals come in a seemingly endless variety, many dreary and depressing, and a few fascinating.

**N. Ashcroft, N. Mermin**

The materials in a nuclear reactor exist in a harsh environment where they are continually bombarded by energetic neutrons. The atoms of the metal used to construct reactor parts such as the pressure vessel or the fuel cladding are arranged in crystal structures. The structures are made up of unit cells repeated in a periodic fashion. When the metal is subjected to neutron irradiation, the atoms in the crystal structure can be displaced, knocking atoms out of their places, leaving damage in the form of vacant lattice positions and atoms in interstitial positions and inducing nuclear reactions resulting in impurities. These defects and impurities change the microscopic structure of the metal and thereby macroscopic material properties and behavior. The following sections will describe the reactions that take place in metals under neutron irradiation, the primary damage that the radiation causes and radiation effects arising due to the primary damage.

### 2.1 Mechanisms

Neutrons incident on a material can interact with the atoms in the lattice by elastic or inelastic collisions depending on the neutron energy. At low neutron energies of less than 1 MeV, elastic collisions dominate. In an elastic collision, the total kinetic energy of the system is conserved. It may however be redistributed between the neutron and the atom taking part in the collision and the neutron can transfer energy to the atom causing it to recoil. In this energy range,  $(n, \gamma)$  reactions can also occur. Here the

neutron is absorbed by the nucleus. The nucleus de-excites by emitting a  $\gamma$ -photon causing the nucleus to recoil.

If the energy transfer to the nucleus is above a certain threshold value, the atom may be knocked out of its place and can go on to collide with other atoms in the crystal creating a collision sequence where the atom hit by the neutron is named the primary knock-on atom (PKA). The size of the threshold energy depends on the material but for bcc Fe it is in the range of tens of eV depending on the direction in which the atom is displaced.

At higher energies above 1 MeV, non-elastic processes such as  $(n, n')$ ,  $(n, \alpha)$  and  $(n, p)$  reactions dominate. Both the emitted particle and the recoiling nucleus can cause displacement of other atoms in the crystal. Nuclei in the crystal can also be fissioned by neutrons. The ionized fragments can then collide with surrounding atoms again displacing atoms.

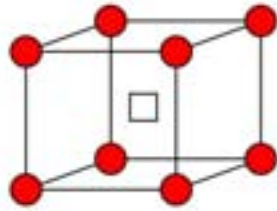
## 2.2 Primary Damage: Vacancies and Interstitials

The elastic and inelastic collisions between neutrons and atoms leads to displacements of nuclei as described in the section 2.1 where some or all of the neutron energy can be transferred to the PKA. The fate of the neutron then depends on how much energy it has left after the collision and where it is in the reactor. In the pressure vessel, it can continue to collide with atoms until its energy is dissipated or it can be absorbed either in the fuel or in the structural materials of the reactor.

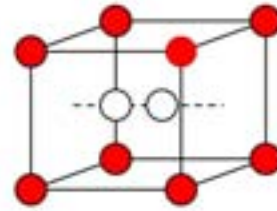
If the energy transferred from the neutron to the PKA is above some threshold energy called the displacement energy,  $E_d$ , the PKA atom will be knocked out of its position in the crystal structure initiating a displacement cascade as shown in figure 2.2(a). The displacement cascade results in a number of vacant lattice positions, vacancies, an equal number of atoms located in interstitial positions in the crystal, interstitials, and a number of replaced atoms. Examples of the defect configurations are shown in figure 2.1. A vacancy and an interstitial together make up what is called a Frenkel pair.

The vacancies and interstitials produced in displacement cascades constitute the primary damage state caused by neutron radiation. The amount of damage of course depends on the number of displaced atoms. Kinchin and Pease proposed a simple relationship between the damage energy and the number of displaced atoms [4]. According to their model, the number of displaced atoms is given by

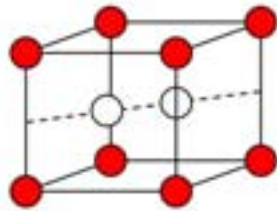
---



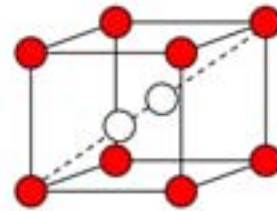
(a) Vacancy



(b) 100 dumbbell



(c) 110 dumbbell



(d) 111 dumbbell

Figure 2.1: Different types of defects that can arise in a bcc structure due to neutron irradiation. (a) shows a vacancy which is an empty lattice space where an atom has been knocked out of its position. Here the vacancy is represented by the square. (b), (c), and (d) show examples of different kinds of interstitial configurations.

---

$$N_d = \begin{cases} 0 & 0 < E < E_d \\ 1 & E_d < E < 2E_d \\ \frac{E}{2E_d} & 2E_d < E < E_1 \\ \frac{E_1}{2E_d} & E_1 < E < \infty \end{cases} \quad (2.1)$$

where  $E$  is the kinetic energy of the PKA. Below  $E_1$ , the PKA atom loses energy by hard-core elastic scattering while above this energy, energy loss comes from electron excitation only. This estimation makes a number of assumptions and several developments of the model exists. The most widely used formula in the field of radiation damage is the NRT estimate, an updated version of equation 2.1 by Norgett *et al.* [5]

$$N_d = \frac{\kappa(E - \hat{Q})}{2E_d} = \frac{\kappa\hat{E}}{2E_d}; \quad \hat{E} > \frac{2E_d}{\kappa} \quad (2.2)$$

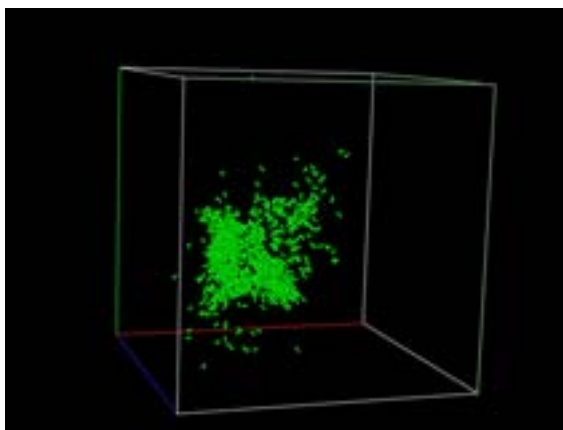
where  $\kappa$  is the displacement efficiency taken to be 0.8 at all temperatures,  $\hat{Q}$  is the energy lost by electron excitation and  $\hat{E}$  is the damage energy, i.e. the energy available for atomic displacement. The size of the displacement threshold energy depends on the material studied. For bcc Fe which is the focus of this thesis, a standard threshold energy of 40 eV is assumed [5].

The cascade region where most of the interstitials and vacancies are produced represents a highly disordered state. At high cascade energy, local melting may be considered to occur. Interstitials and vacancies that are close enough to each other to interact will recombine directly during the cascade and the deposited heat will dissipate during the first picoseconds of the cascade. Recombination will be the fate of most of the point defects produced during the cascade.

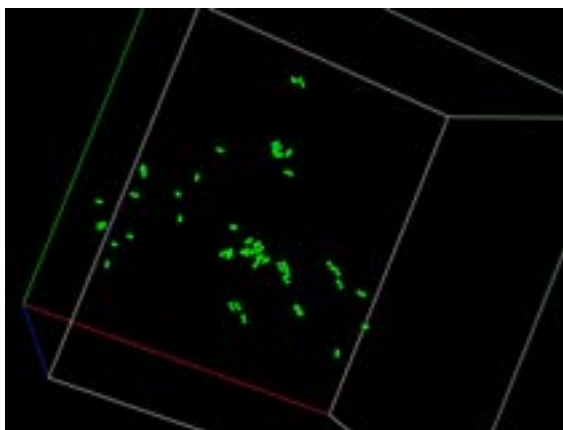
The interstitials that remain after the cascade are those that end up far enough from vacancies to escape annihilation. These interstitials are created in collision sequences where atoms are substituted in a chain of replacements through the crystal transporting them away from the initially vacant lattice space. In this way vacancies are seen to be concentrated at the center of the cascade region while interstitials are located in a halo surrounding the central area of the cascade. The point defects that escape annihilation make up what is called the primary damage in the crystal, an example of which can be seen in figure 2.2(b). The evolution of the primary damage is what determines the changes of micro- and macroscopic properties of the material.

The other reactions that take place in the crystal during neutron irradiations such as  $(n, \alpha)$ ,  $(n, p)$  or  $(n, 2n)$  result in a number of foreign atoms in

---



(a) Peak stage of the cascade.



(b) Final damage state of the cascade.

Figure 2.2: In this figure, different stages of a displacement cascade are exemplified. In (a) the cascade is seen at the peak stage defined as the time when the maximum number of defects are produced in the system. Most of these defects will recombine and disappear. Those that are left make up the primary damage state seen in (b).

---

the material which also affect material properties and influence the behavior of the vacancies and interstitials during the evolution of the material.

## 2.3 Primary Damage Evolution

After the recombination stage of the cascade, the resulting point defects will determine the evolution of the material. At low temperatures, the defects are immobile and will not be able to migrate in the metal. At temperatures above the migration energy of the defects, interstitials and vacancies will start to move in the crystal. Should a vacancy and an interstitial encounter each other they will annihilate. If instead they encounter another defect of the same kind they will form clusters. They can also be absorbed at preexisting sinks such as grain boundaries, dislocations or surfaces. The interstitial clusters will collapse into dislocation loops as they reach a certain size. Vacancy clusters can also collapse into vacancy loops. However, they are more stable and can also form voids in the crystal [6].

The clustering of point defects can be described by standard rate theory [7]. Here, the concentration of clusters are given by the discrete master equations

$$\frac{dC_j}{dt} = \sum_k w(k; j)C_k - \sum_k w(j; k)C_j + G_j - L_j \quad (2.3)$$

where  $C_j$  is the concentration of clusters of type  $j$ ,  $w(k; j)$  is the rate per unit concentration of cluster type  $k$  of transitions to a cluster of type  $j$ ,  $G_j$  is the rate of direct formation of clusters of type  $j$  and  $L_j$  is the loss rate of clusters of type  $j$  by absorption at sinks, destruction in cascades, etc. These equations can in principle be solved but this is feasible in a reasonable time for only a small number of equations. Instead, simplifications and approximations are introduced giving us the Fokker-Planck equation.

$$\begin{aligned} \frac{\partial C_j(t)}{\partial t} = & - \frac{\partial}{\partial j} \{C_j(t)[w(j; j+1) - w(j; j-1)]\} \\ & + \frac{1}{2} \frac{\partial^2}{\partial j^2} \{C_j(t)[w(j; j-1) + w(j; j+1)]\} \end{aligned} \quad (2.4)$$

The standard rate theory used to derive the Fokker-Planck equation assumes point defect generation to be homogeneous in space and time which is not always true. Point defects are produced in cascades and defect clusters are also seen to be generated directly during cascades so the number of freely

---

migrating vacancies and interstitials are not equal to each other. A large fraction of interstitials end up in mobile clusters while vacancies tend to end up in immobile configurations and thus there is a production bias in favor of interstitial mobility [8].

### 2.3.1 Swelling

The interstitials are more mobile than the vacancies and tend to move towards dislocations, grain boundaries or surfaces where they annihilate. The vacancies on the other hand remain in the bulk and gather in growing voids causing the material to swell. The swelling shows a threshold behavior depending on both the total dose and the exposure time. Although the swelling rate actually decreases with increasing dose rate, the total dose in a fast neutron spectrum is higher than in a thermal spectrum and the threshold for swelling is reached in a much shorter time.

From the Fokker-Planck equation (equation 2.4), an expression for the growth rate of a vacancy cluster can be derived [7]

$$\frac{dr_c}{dt} = \frac{\Omega}{r_c} (Z_i^d Z_v^c - Z_v^d Z_i^c) F \quad (2.5)$$

where  $r_c$  is the cluster radius,  $\Omega$  the atomic volume,  $Z$  are the capture efficiencies of cavities and dislocations and  $F$  is a function of total dislocation and cavity sink strengths, of dose rate and of point defect recombination. The term  $(Z_i^d Z_v^c - Z_v^d Z_i^c)$  is called the bias and has to be greater than zero for the cluster to grow.

The presence of helium in the material increases the swelling mainly due to internal pressurization of voids. The void growth rate depends on the thermal emission of vacancies from clusters. Once the cavity has attained a critical radius it will continue to grow. A larger internal pressure in the cavity makes it easier for the cavity to attain a critical radius and continue to grow. The swelling rate can be as large as 1–2% per dpa in a fast neutron spectrum depending on the temperature and dose rate [9] as can be seen in figure 2.3.

The dose dependency of the swelling rate can be divided into three stages. At low doses the material swelling is small. After a threshold dose is attained, the swelling rate increases and then levels out again at higher doses. Temperature also influences the swelling rate of a material under irradiation [7]. At low temperatures, the swelling will be small since vacancies are immobile and cannot move together to form clusters. At high temperatures, the thermal emission of vacancies from clusters will be high enough

---



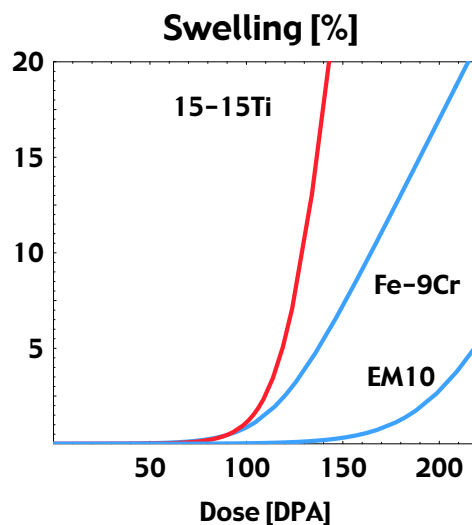


Figure 2.3: Swelling is shown as a function of the dose received by the material. At low doses the swelling is small while after the threshold dose is reached the swelling rate accelerates. The curves show the swelling behavior of different alloys. The 15-15Ti alloy is an austenitic steel with fcc structure with a swelling rate of 1% per dpa in the accelerated swelling phase. Bcc materials such as FeCr and the EM10 steel (Fe-9Cr-1Mo) have a lower swelling rate of 0.2% per dpa in the accelerated swelling phase. By adding Mo to the Fe-9Cr model alloy increases the threshold dose for accelerated swelling dramatically.

to compete with the influx of vacancies due to irradiation. This leaves the intermediate temperature regime where the largest swelling rates are seen. Here the thermal emission of vacancies from cavities is small and recombination is large while the flow of vacancies to voids is large. The definitions of low, high or intermediate temperature depends on the material but generally maximum swelling rates are seen at temperatures of 30 – 50% of the melting temperature,  $T_{melt}$ . No swelling is seen at temperatures above 60% of the melting temperature [10].

### 2.3.2 Hardening and Embrittlement

The mechanical properties of the material can be greatly affected by irradiation. Initially ductile materials can become hard and brittle and for

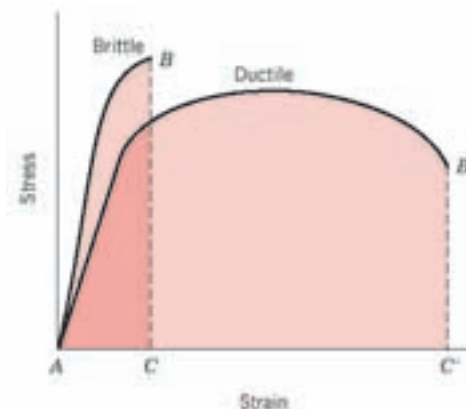


Figure 2.4: The figure shows stress-strain curves for ductile and brittle materials. The ductile material will deform plastically until it breaks while the brittle material shows almost no deformation before breaking [11].

materials with a ductile-to-brittle transition, the temperature at which this transition takes place can shift due to irradiation. These effects have complex dependencies on dose rates, material microstructure and temperature. Embrittlement is a safety issue as ductile deformation tends to occur over a longer time giving a slower fracture with a larger chance of discovery (see figure 2.4).

At temperatures below the ductile-to brittle transition temperature, (DBTT), the yield stress of a material is larger than the fracture stress. In this region the fracture will be brittle which means that the material will break with very little plastic deformation. The yield stress is more temperature dependent than the fracture stress. As the temperature is increased, the yield stress will become smaller than the fracture stress and the fracture mode of the material will become ductile and undergo plastic deformation before fracturing.

For dislocations to move in a material, they need a certain energy to overcome barriers and obstacles. By raising the temperature in the material, the dislocations are given more energy enabling them to pass obstacles in their way. However, irradiating a material introduces more obstacles and

---

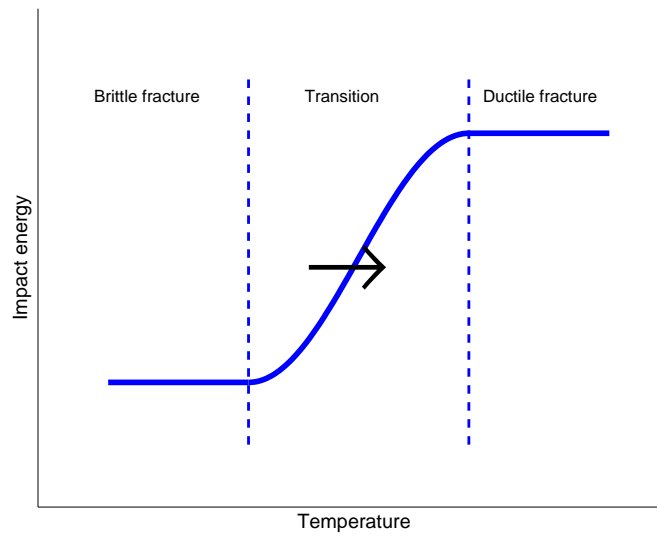


Figure 2.5: A general picture of the ductile to brittle transition in bcc metals such as ferritic steels. At low temperatures the material experiences brittle fracture and at high temperatures plastic fracture. In the transition region, both kinds of fracture are seen. When the material is irradiated, the transition region is shifted towards higher temperatures as shown by the arrow.

thus the dislocations need more energy to overcome the barriers. Thus the temperature at which the material turns from brittle to ductile is raised i.e. the DBTT is shifted towards higher temperatures as seen in figure 2.5.

## Chapter 3

# Multiscale Modelling

We all like to congregate at boundary conditions.

**Douglas Adams**

The most exact way of calculating material properties is to solve the Schrödinger equation directly. For complex systems such as metals however, the calculations soon become impossibly complicated and approximative methods have to be used instead. All approximative methods need some basis for comparison and development. With *ab initio* calculations, fundamental material properties can be provided as the basis for constructing and refining such methods.

The modelling of recoil cascades in metals requires the use of interatomic potentials which approximate the interaction between the atoms. The potentials are constructed by fitting to a combination of empirical and *ab initio* data. The potentials are then used in molecular dynamics and Monte Carlo simulations to study what happens in the material when it is irradiated by neutrons.

### 3.1 *Ab Initio*

To calculate basic properties of intermetallic compounds such as total energies, bulk and elastic moduli, relative stability of structures, etc *ab initio* methods are used. In quantum mechanics we are faced with the problem of finding a many-body wave function that solves the Schrödinger equation

$$\left[ -\frac{\hbar^2}{2m} \nabla^2 + V(\mathbf{r}) \right] \Psi(\mathbf{r}) = E\Psi(\mathbf{r}). \quad (3.1)$$

The problem is addressed in methods such as the Hartree-Fock theory but for large systems the calculations are too time consuming to be practically viable. Instead we rely on density functional theory (DFT) to overcome the problem of solving the many-body system.

DFT is a quantum mechanical approach that maps the many-body electron problem onto a single-body problem by the use of the electron density  $n(\mathbf{r})$  as a key variable from which other observables can be calculated.

DFT was first developed by Thomas and Fermi in the 1920's. Their theory was rather inaccurate due to the fact that it neglected electron correlation. The theoretical basis of DFT was developed by Hohenberg and Kohn [12] who published a theorem proving that a one-to-one mapping exists between the ground state electron density and the ground state electron wave function of a many-body system and that the ground state density minimizes the energy of the system.

The minimization of the energy can be done using a method developed by Kohn and Sham [13]. The nuclei in a solid are seen as fixed (the Born-Oppenheimer approximation) and generate a static potential in which the electrons move. Electronic interactions are represented by an effective potential

$$v_{eff}(\mathbf{r}) = v(\mathbf{r}) + v_H(\mathbf{r}) + v_{xc}(\mathbf{r}) \quad (3.2)$$

where  $v(\mathbf{r})$  is the external potential coming from the nuclei in the solid and any other external potential applied to the solid as a whole,  $v_H(\mathbf{r})$  is the Hartree potential

$$v_H[n](\mathbf{r}) = q^2 \int d^3r' \frac{n(\mathbf{r}')}{|\mathbf{r} - \mathbf{r}'|} \quad (3.3)$$

and the last term  $v_{xc}(\mathbf{r})$  is the exchange correlation potential. The electronic density is written

$$n(\mathbf{r}) = \sum_{i=1}^N |\Psi_i(\mathbf{r})|^2 \quad (3.4)$$

Equations 3.2 - 3.4 are known as the Kohn-Sham equations and can in principle be solved explicitly. However the function for the exchange correlation potential is not known. Several approximations of this function exist. One of the most common is the local density approximation, LDA. Here, the energy functional depends only on the electronic density at the point of evaluation. The local spin-density approximation, LSDA, is a generalization

---

of the LDA that includes electronic spin. In the general gradient approximation GGA, the exchange correlation functional is expressed in terms of the density and the density gradient at each point.

## 3.2 Interatomic Potentials

In the previous section, methods of calculating basic properties of a material using quantum mechanical methods was discussed. This of course gives the most exact results but at the expense of long computing times. For systems with more than 500 atoms or systems with large strain field distortions, quantum mechanical calculations are not feasible with today's computer capacity necessitating a simplified description of the system. Using approximate methods based on density functional theory, systems with a number of atoms of the order of 1000000 are possible to model.

The common factor for all atomistic methods of approximation is the description of how the particles interact in a material. This can be done by constructing interatomic potentials. Lennard-Jones introduced one of the first pair potentials in 1924 which gave a good description of the atomic interactions in noble gases. For the more complex systems of metals however, it is inadequate. In the 1980s, several methods of many-body potential construction were introduced for example by Daw and Baskes [14] [15] and Finnis and Sinclair [16]. The formalisms of relevance to this thesis are reviewed in the following sections.

### 3.2.1 The Embedded-Atom Method

The embedded-atom method, EAM, is a semi-empirical method used to describe metals and alloys [17]. The roots of EAM come from density functional theory (DFT) where each atom in a solid is seen as embedded into a host consisting of all the other atoms in the system and the energy of an individual atom can be expressed as a functional of the electronic density [12].

This functional, whose form is unknown, is a universal function independent of the host system. Making the approximation that the energy depends only on the local electronic density at the site of the atom, the total energy can be written

$$E_{tot} = \sum_i F_i(\rho_i) \tag{3.5}$$


---

where  $F_i$  is the embedding energy function of an atom in the solid,  $\rho_i = \sum_{j \neq i} \rho(r_{ij})$  is the electronic density at atom  $i$  and  $r_{ij}$  is the interatomic distance. However, this approximation does not give a correct description of the solid as it neglects contributions to the energy from gradients in the electronic density and repulsion between the cores of the atoms. Instead the energy is expressed as

$$E_{tot} = \sum_i E_i = \sum_i \left[ \frac{1}{2} \sum_{j \neq i} V(r_{ij}) + F(\rho_i) \right] \quad (3.6)$$

$V_{ij}(r_{ij})$  is a short-range potential that gives the contribution to the energy coming from the repulsion between the cores of the atoms. The pair potential is a function of the distance and the energy coming from this term varies with the radial distance between atoms. The method can be extended to an alloy system by writing the energy as

$$E_i = \frac{1}{2} \sum_{j \neq i} V_{t_i t_j}(r_{ij}) + F_{t_i}(\bar{\rho}_i) \quad (3.7)$$

where  $t_i$  represents atom  $i$  of type  $t$  and

$$\bar{\rho}_i = \sum_{j \neq i} \rho_{t_j}(r_{ij}) \quad (3.8)$$

Having found an expression for the energy of a solid, we are still left with the problem of finding  $V$  and  $F$ . In theory, this can be done from first principles but in practice it turns out to be difficult. Instead the functions can be found empirically from known properties of the solid or alloy. The function parameters for the pair potential can be fitted from solid properties such as lattice constant, cohesive energy or bulk modulus for example. For an example see section 4.1 where the fitting is described in more detail.

Finally, we are left with the function for the embedding energy. This energy can be found using the universal expression for the energy as a function of lattice parameter (equation of state) given by the Rose equation [18]. The equation scales the cohesive energy of the solid to a universal function as follows

$$\begin{aligned} E_{Rose}(\bar{a}) &= -E_{coh}(1 + \bar{a}) \exp(-\bar{a}) \\ \bar{a} &= \alpha \left( \frac{r_{1nn}}{r_{eq}} - 1 \right) \\ \alpha &= \sqrt{9B\Omega/E_{coh}} \end{aligned} \quad (3.9)$$

where  $E_{coh}$  is the cohesive energy,  $B$  is the bulk modulus,  $\Omega$  the atomic volume,  $r_{1nn}$  is the distance to the first nearest neighbor and  $r_{1nn}^{eq}$  the same distance at equilibrium. Having already chosen and fitted expressions for the pair energy, the embedding energy can be found from

$$F(r) = E_{Rose}(r) - V(r) \quad (3.10)$$

The embedding energy is then inverted to a function of density instead of  $r$  using the expression for the electronic density in the solid. An electron density function for the system is adopted depending on the solid or alloy that is to be described.

For alloys, the pure elements are fitted to their separate properties. A cross-wise pair potential is then fitted from the contributions to the energy coming from the interaction between atoms of different types. No cross-wise embedding energy needs to be calculated. The energy contribution coming from the embedding function is density dependent. The density in turn is a superposition of the separate densities of the atoms surrounding the sites and can be taken directly from the separate density functions for the pure elements.

The physical interpretation of the embedding energy term can be related to the concept of traditional chemical bonding. As more bonds are created, the total bonding energy will increase. However, the contribution from each successive bond will be smaller and smaller and the average bonding energy will decrease. Therefore, to have a physically consistent description of a material, the curvature of the embedding energy should be positive giving  $\frac{d^2 F}{d\rho^2} > 0$ .

The Cauchy pressure is seen to be directly proportional to the second derivative of the embedding energy. For some transition metals, the Cauchy pressure is negative and this would then imply that the bonding in the material is not correctly described arising from problems with directional bonding.

The modified embedded-atom method, MEAM, is a method developed as an extension of the EAM to include directional bonding [19] [20]. Angular terms are added to the electron density as a correction to the spherically symmetric electron density used in EAM. The embedding function is chosen as a simple function of the electron density including angular terms. The pair potential is then found using the Rose equation in the same manner as for the embedding function in EAM. The procedure for alloys will be different from EAM; this time cross-wise terms are also needed for the embedding function since the electron density now has angular terms.

---



### 3.2.2 The Second Moment Approximation

The second moment approximation bears a close resemblance to EAM but is based on tight binding theory, thus providing a correlation to the band structure of the electron energies in a solid [21]. The bonding energy is taken to be dependent on the density of states (DOS) of the electrons which in turn is approximated by  $\sqrt{\mu_{2i}}$ , the square root of the second moment of the DOS on atom  $i$ . The expression for the energy of an atom will in this formalism be

$$E_i = \frac{1}{2} \sum_{j \neq i} V(r_{ij}) - A \left( \sum_{j \neq i} h_{ij}^2(r_{ij}) \right)^{1/2} \quad (3.11)$$

Assuming

$$\rho(r) \equiv h_{ij}^2(r) \quad (3.12)$$

and

$$F(\bar{\rho}) \equiv -A(\bar{\rho})^{1/2} \quad (3.13)$$

the expression is seen to be in the same form as the EAM energy expression although with a modified embedding function. This way of expressing the energy has been developed by for example Finnis and Sinclair [16].

The negative square root dependence naturally gives a positive second derivative of the embedding function and is thus consistent with the interpretation of the bonding strength as discussed for the EAM in section 3.2.1.

### 3.2.3 Two-Band Models

It is well known that the  $d$  electrons are responsible for the cohesive energy of transition metals. Pettifor showed however that the  $s$  electrons give a large contribution to the pressure as well as the bulk modulus [22]. The pressure is a balance of the repulsive forces of the  $s$  electrons and the attractive forces of the  $d$  electrons while the bulk modulus is dominated by contributions from the  $s$  electrons. In the original second moment approximation, the  $s$  band contribution was neglected. The cohesive energy is therefore well reproduced but for the transition metals, the contribution from the  $s$  electrons could be very important for other material properties.

The two-band models can be included into the EAM model by extending the embedding part of the energy expression [23] [24]. The total energy is then written

$$E_i = \frac{1}{2} \sum_j V(r_{ij}) + F_d(\rho_d) + F_s(\rho_s) \quad (3.14)$$

where the density is given by

$$\rho_b = \sum \Phi_b(r_{ij}). \quad (3.15)$$

The embedding energy is given by

$$F_b(\rho_b) = A_1^b \sqrt{\rho_b} + A_2^b \rho_b^2 + A_3^b \rho_b^4 \quad (3.16)$$

The last two terms are added to reproduce the repulsive force of the  $d$  electrons at small distances where the electron density is high. In this way, the two-band models retain the simplicity of EAM and FS while giving a more correct physical description of the materials being modelled.

### 3.3 Molecular Dynamics

Molecular dynamics (MD) is based on Newton's classical equations of motion [25]. The forces between atoms in a system of  $N$  particles are described by

$$\mathbf{f}_i = m_i \ddot{\mathbf{r}}_i = -\nabla_{\mathbf{r}_i} V \quad (3.17)$$

where  $\mathbf{f}_i$  is the force on atom  $i$  in the system,  $m_i$  is the mass of atom  $i$ ,  $\ddot{\mathbf{r}}_i$  is the acceleration of atom  $i$  and  $V$  is the potential defined for the atoms in the system describing their interactions. From this it can be seen that the foundation of MD rests on a potential that describes atomic interactions as correctly as possible since all dynamic properties of the solid is calculated using it.

The motivation for using classical equations of motion can be seen by looking at the de Broglie wavelength of an atom. The de Broglie wavelength is given by

$$\lambda = \frac{h}{\sqrt{2mE_k}} \quad (3.18)$$

where  $h$  is Planck's constant,  $m$  is the mass and  $E_k$  the kinetic energy. Calculating the wavelength of an Fe atom at 100 K, this will give  $\lambda \sim 0.1$  Ångströms. As the lattice constant of bcc Fe is of the order of Ångströms, the transition from quantum to Newtonian mechanics is valid. At lower temperatures or for atoms of smaller mass, the de Broglie wavelength will

---

be of the order of Ångströms, and Newtonian mechanics will no longer be applicable.

To solve the equations of motions for the system, the finite differences method developed by Alder and Wainwright [26] can be employed. At the start of the simulation at time  $t_0$ , each atom is assigned a position and a random velocity at the temperature  $T$  specified for the system. Knowing these, the positions, velocities and accelerations of the atoms at time  $t_0 + \delta t$  are obtained. From the positions and velocities of the atoms, the forces and hence the accelerations of the atoms in their new positions can be calculated. These can be compared to the predicted values and corrected to give the correct atom trajectories. This procedure is then iterated for as many time steps as wanted and any variables that are of interest can be calculated after each time step in what is called a predictor-corrector scheme. Different variants of predictor-corrector algorithm exists, such as for example those by Gear [27] and Verlet [28]. The limiting factor in these calculations are of course time. For efficient computing, the time step  $\delta t$  should be as large as possible while for the precision of the calculations,  $\delta t$  should be small enough to minimize errors in the atom trajectories.

When running MD simulations, normally the system is chosen to be contained within a box although other configurations such as spherical systems exist. To simulate a bulk environment, periodic boundary conditions (PBC) are normally used. The simulation box is set up with the desired number of atoms which are given initial positions and velocities. The simulations can be run with different ensembles. The microcanonical constant or NVE ensemble or the canonical or constant NVT ensemble are often used. In the microcanonical ensemble, the number of atoms  $N$ , the volume  $V$  and the energy  $E$  of the system are constant parameters while in the canonical ensemble, the temperature  $T$  is kept constant instead of the energy. The ensemble chosen depends of course on the purpose of the simulation. When the simulation starts and the atoms close to the outer boundaries of the box begin to move, they may end up in a position outside the simulation box. With PBC, an atom that exits the box at one surface will enter the system again at the opposite surface of the box. This reduces the number of images needed to be saved during the simulation and also conserves the number density in the simulation box. The influence of PBC on thermodynamic properties and structures have been shown to be small enough to be neglected [25]. When performing cascade simulations (see section 4.3) the box has to be large enough to contain the cascade without any self-interaction at boundary crossing.

When calculating the forces on an atom, the interaction between this

---

atom and all other atoms should in principle be calculated. To reduce the simulation time, a potential cutoff is usually employed. The interactions with atoms further away than a certain distance are usually set to zero. As the largest contributions to the force on the atom usually comes from the closest atom this gives only a small error as long as the cutoff radius is large enough to include all atoms that are within the interaction range of the potential.

### 3.4 The Monte Carlo Method

The Monte Carlo (MC) method was developed at the end of the 2nd world war at Los Alamos as a way of studying diffusion in fissionable materials [29]. The name Monte Carlo originates in the fact that random numbers are so extensively used. The method is based on stochastic methods and generates a trajectory in phase space for each atom based on sampling from a chosen statistical ensemble.

A system is regarded as composed of a number of particles or objects of different kinds. A number of processes or events are defined. The particles or objects in the system are each associated with one or more of the processes meaning they can take part in this kind of activity. The rate at which a certain process occurs for an object in the system is then defined as

$$r_i = \nu_i e^{-\Delta E_i/kT} \quad (3.19)$$

where  $\nu_i$  is a prefactor associated with process  $i$ ,  $\Delta E_i$  is the activation energy for process  $i$ ,  $k$  is the Boltzmann constant and  $T$  is the temperature. If  $n_i$  particles or objects are associated with a certain process, then the rate at which this particular process takes place will be

$$R_i = n_i r_i \quad (3.20)$$

and the total rate of the system can be written

$$R = \sum_i n_i r_i \quad (3.21)$$

The probability of a certain process or event taking place is then given by

$$p_i = \frac{R_i}{R} \quad (3.22)$$

For each MC step, a process or event that will take place is chosen according to its probability and the particle that will take part in the process or event is

---

selected randomly from the number of particles associated with this process  $n_i$ .

In the above version of the Monte Carlo method, time is not included in the simulation. To introduce time, the kinetic Monte Carlo scheme was constructed. In the residence time algorithm by Young and Elcock [30], diffusion in the system is due to vacancy jumps, the rate of which are described by equation 3.19. The time associated with the process is then given by the inverse of the rate;

$$\Delta\tau = \frac{1}{\sum n_i R_i} \quad (3.23)$$

Different versions of the kinetic MC scheme exist such as atomistic kinetic Monte Carlo (AKMC) and object kinetic Monte Carlo OKMC depending on the purpose of the simulations [31]. AKMC is run on a rigid lattice and retains an atomistic level of description of the system. It always includes a calculation of the total energy of the system making it detailed but making simulations of larger systems time consuming. OKMC is so called since it treats what is termed as objects instead of atoms. Objects can be point defects, point defect clusters, solute atoms or any other system feature that the simulant wants to include in the system. This way of simulating makes longer time scales feasible. However, only interactions between objects defined and included in the system can be simulated. Any new processes cannot be found using this method. It is often used in conjunction with MD where the primary damage state of the system is found and used as input in the OKMC simulations.

---

## Chapter 4

# Applications

The work performed within the scope of this thesis has been concerned with modelling the FeCr system which serves as a model alloy for studying more complex systems such as those of steel. Ferritic steels, which are steels with a body-centred cubic (bcc) structure, are a common material used in reactor environments and knowledge of its behavior under irradiation is crucial for the upkeep of existing reactors and for the development of new reactor types. This section will describe applications of some of the theories and models previously described to the FeCr system.

### 4.1 Potential Construction

As has been mentioned, the success in modelling a material rests on the description of the atomic interactions in the system. In this work, potentials have been constructed within the EAM and FS formalisms. When looking at the binary alloy FeCr, the expression for the total energy (see equation 3.7) will be

$$\begin{aligned} E_{tot} = & \sum_{i_{Fe}} F_{Fe}(\rho_i) + \sum_{i_{Cr}} F_{Cr}(\rho_i) \\ & + \frac{1}{2} \sum_{i_{Fe}, j_{Fe}} \Phi_{Fe}(r_{ij}) + \frac{1}{2} \sum_{i_{Fe}, j_{Cr}} \Phi_{FeCr}(r_{ij}) \\ & + \frac{1}{2} \sum_{i_{Cr}, j_{Cr}} \Phi_{Cr}(r_{ij}) + \frac{1}{2} \sum_{i_{Cr}, j_{Fe}} \Phi_{FeCr}(r_{ij}). \end{aligned} \quad (4.1)$$

From this can be seen that we need to fit pair potentials for the pure elements Fe and Cr and a mixed potential for FeCr while for the embedding energy,

functions are needed for the pure elements only.

#### 4.1.1 Pair Potentials and Embedding Functions for Fe and Cr

The potentials fitted for Fe, Cr and FeCr are presented in papers I and II and examples are shown in figure 4.3. Those in paper I use the EAM formalism while those in paper II use the FS formalism. In each case, the pair potentials were chosen as spline functions of the form

$$V(r) = \sum_{i=1}^n a_i (r - r_i)^3 H(r_i - r) \quad (4.2)$$

where  $H$  is the Heaviside step function and  $r_i$  are the knot points of the spline. The pair potential fitting parameters  $a_i$  and the spline knot points  $r_i$  were fitted to material properties from experiments or *ab initio* calculations such as cohesive energy, lattice parameter and elastic moduli. The cohesive energy is given by the total energy of the system at equilibrium, the lattice constant can be found using the condition that the first derivative of the total energy should be zero at equilibrium and the elastic constants are given by the second derivatives of the total energy. The fitting is performed using the MERLIN code package developed for multiparametric optimization [32]. Once the pair potentials are fitted for the pure elements, the embedding functions can be found using the Rose expression (see section 3.2.1).

In the case of Cr, the applicability of the EAM method is not evident. At low temperatures, Cr is antiferromagnetic and has a negative Cauchy pressure. However, above the Néel temperature of 311 K, Cr turns paramagnetic and the Cauchy pressure becomes positive [33]. Here, the elastic constants are seen to depend linearly on the temperature as shown in figure 4.1. Extrapolating the values of the elastic constants of the paramagnetic material to 0 K, these can be used to fit the potential for the pure element. The potential will be valid for paramagnetic Cr only but in the case of materials used in reactor environments, operation temperatures are well above the Néel temperature.

To correctly reproduce atomic interactions at small distances, the potentials are stiffened at short range. For the Fe potential in paper I, this is done after fixing the embedding function which means that the pressure-volume relation given by the Rose equation is violated. For high densities resulting from anisotropic compression as in the vicinity of interstitials however, the material is not expected to be in equilibrium and this relation and

---

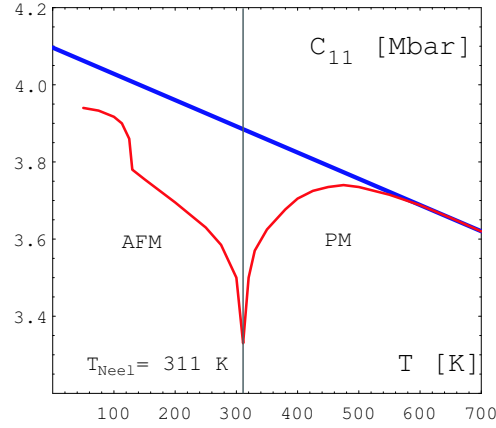


Figure 4.1: The figure shows the elastic constant  $C_{11}$  for Cr as a function of temperature. Notice the sharp cusp at the Néel temperature where Cr changes from the antiferromagnetic to the paramagnetic phase. Above 450 K, the curve is linear. The function above this temperature is extrapolated to 0 K and the value used as a fitting parameter for paramagnetic Cr.

the stiffening, though arbitrary, is motivated by being able to fit experimental values for phase stability, correct interstitial stability and thermal expansion. The potential for pure Cr in paper I is stiffened by fitting to the thermal expansion of the material. In paper II, the FS approach was adopted to be able to fit the embedding functions in a consistent way.

#### 4.1.2 Pair potentials for FeCr

Having found expressions for both the pair and the embedding energy of the pure elements, an expression for the energy of the interaction between two atoms of different types can be found using equation 4.1. The potential can then be further adjusted to reproduce relevant material properties.

For the FeCr system, *ab initio* calculations show that the mixing enthalpy seen in figure 4.2 is negative at low concentrations of Cr [34]. Different methods for reproducing the change in mixing enthalpy can be envisioned. For example, concentration dependent potentials can be fitted giving different mixing enthalpies as was done in paper I. Here, two potentials were provided, one fitted to the negative mixing enthalpy of the alloy with 5% Cr and one fitted to the positive mixing enthalpy at 20% Cr. This method makes it possible to reproduce the mixing enthalpy and to model the  $\alpha'$  precipitation



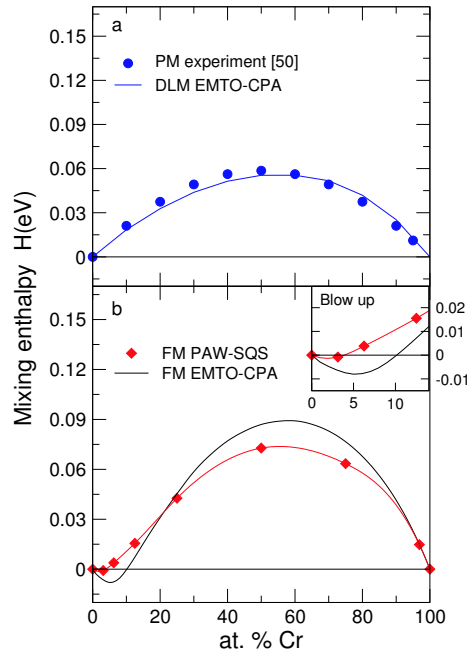
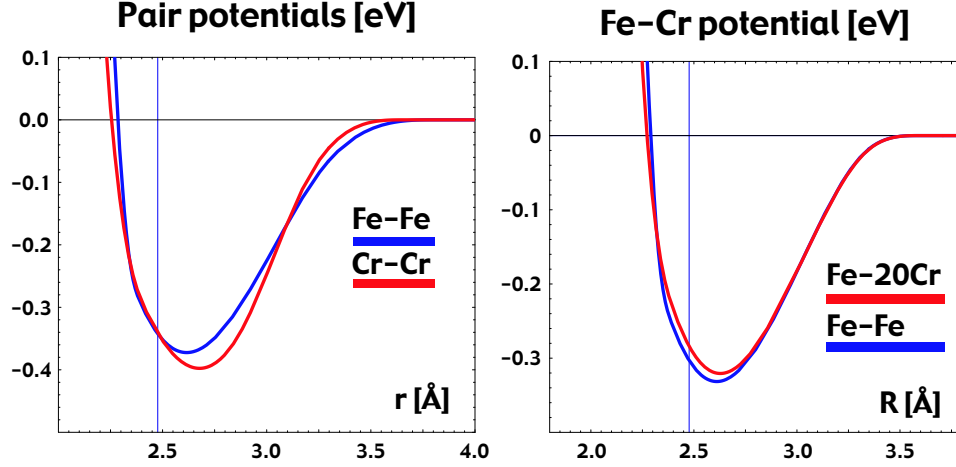


Figure 4.2: the mixing enthalpy of FeCr as a function of Cr content. The paramagnetic phase is shown in the graph at the top. The mixing enthalpy is seen to be positive at all Cr concentrations. For the ferromagnetic phase of the alloy shown in the graph at the bottom, it can be seen that for small Cr concentrations, the mixing enthalpy becomes negative. In this region, no formation of the  $\alpha'$  phase should be seen.

occurring at higher Cr concentrations, but working with a set of potentials is of course more cumbersome than having one potential that can describe the full range of concentrations of the alloy. A different approach is to employ the two-band model under development [24] which can reproduce the mixing enthalpy for all concentrations where the mixing enthalpy can be reproduced at all concentrations by one potential.

## 4.2 Verification of Potentials

Having constructed pair potentials and embedding functions for the FeCr system, they are tested by using them to calculate relevant material and defect properties to see that experimental and *ab initio* values are reproduced.



(a) Pair potentials for Fe and Cr.

(b) Mixed pair potential for FeCr.

Figure 4.3: Examples of pair potentials produced using EAM. These potentials can be found in paper I.

Below, examples of the calculation of several material and defect properties of relevance are given. To perform the calculations, molecular dynamics can be used. The work presented in papers I-IV includes a number of such calculations for different potentials. All of the MD calculations were performed using the DYMOKA code [35] except in the case of thermal expansion where the XMD code [36] gave a faster convergence.

#### 4.2.1 Calculations of Material and Defect Properties

##### Formation Energy

The formation energy of a defect of the kind  $X$  in the crystal can be calculated as

$$E_f^X = NE_{coh}^{relaxed}(X) - NE_{coh}^{relaxed}(ref) \quad (4.3)$$

The first term gives the cohesive energy of the relaxed system including  $X$  while the second term gives the relaxed energy of the reference system, i.e. without  $X$  and  $N$  is the number of atoms in the system.  $X$  can be defects such as vacancies or interstitials. A box representing the crystal is set up

with atoms at positions corresponding to the crystal structure, in our case bcc. This gives the energy of the reference structure without  $X$  included. The object  $X$  is then inserted into the simulation box, the structure is relaxed and the difference between the energies of the crystal with and without the defect can be calculated. When performing calculations for an alloy, the energies should be normalized to the number of atoms of each type.

### Binding Energy

The binding energy between two objects  $X$  and  $Y$  is given by

$$E_b^{XY} = NE_{coh}^{relaxed}(X\ Y\ \text{separated}) - NE_{coh}^{relaxed}(X\ Y\ \text{together}) \quad (4.4)$$

The first term gives the energy of the system when the two objects  $X$  and  $Y$ , though included in the system are positioned far enough from each other so that they cannot interact. The calculation procedure is the same as for the formation energies except that  $X$  and  $Y$  are included in the reference system.

### Substitution Energy

When working with an alloy, the energy of the system changes as the atomic configuration changes, for example when an atom of type A is replaced or substituted by an atom of type B. The substitution energy is given by

$$E_{sub} = NE_{coh}^{relaxed}(AB) - NE_{coh}^{relaxed}(ref) \quad (4.5)$$

where  $E_{coh}^{relaxed}(AB)$  is the energy of the system where an atom of type A has been replaced by an atom of type B.

### Migration Energy

How defects move in the solid is important since it governs the evolution of the primary damage state. It also has an impact on how defect clusters are formed. Clustering is, as we have seen, responsible for macroscopic effects such as swelling and embrittlement of the material. The migration energy between two sites in the crystal lattice can be calculated as

$$E_m^X = E_{coh}^{relaxed}(\text{saddle point}) - E_{coh}^{relaxed}(\text{initial position}) \quad (4.6)$$


---

where the saddle point is defined as the place along the minimum energy path between the two positions where the migrating object is in its maximum energy state. This can be compared to the experiments by calculating the activation energy measured in diffusivity studies which is given by

$$E_A^X = E_f^V + E_m^X \quad (4.7)$$

### Thermal Expansion

The thermal expansion of a material is characterized by the thermal expansion coefficient  $\alpha$  which is a measure of how the lattice constant changes as a function of temperature.  $\alpha$  is given by

$$\alpha = \frac{1}{a(T)} \cdot \frac{da(T)}{dT} \quad (4.8)$$

where  $T$  is the temperature  $a(T)$  is the lattice constant as a function of temperature.

#### 4.2.2 Potential Performance

The potentials presented in papers I and II generally reproduce fitted properties well. They are also able to reproduce the thermal expansion better than most potentials found in literature such as those of Simonelli *et al.* [37] and Mendeleev *et al.* [38]. The thermal expansion given by the thermal expansion coefficient  $\alpha$ , is related to the third derivative of the total energy. Thus  $\alpha$  can be seen as a measure of the anharmonicity of the potential. The stiffening performed at short distances for the potentials in paper I corresponds to making the potential more anharmonic giving a larger thermal expansion. From the potentials in paper II it was seen that changing the potentials at long range gives the same result but in this case motivated by the more physical approach of applying the FS formalism in fitting the potentials. As a result of the potential being stiff at short range, the activation energy for vacancy self-diffusion of the potentials in paper I is higher than those of other potentials found in the literature although they agree very well with those reported by Seeger *et al.* [39]. The correct interstitial configuration is predicted although the absolute value of the formation energies are higher than those of potentials found in the literature.

The mixing enthalpies of the two mixed potentials in paper I is well reproduced. Simulations of thermal aging show that precipitation of Cr clusters takes place when using the potential fitted to the positive mixing

---

enthalpy while no precipitation is seen for the potential fitted to the negative mixing enthalpy. The time and temperature scale of precipitation is seen to agree with what is found in experimental studies of hardening. The mixed pair potentials of paper I predicts the mixed  $\langle 110 \rangle$  FeCr dumbbell to be the most stable defect followed by the  $\langle 111 \rangle$  Cr-Cr dumbbell and the  $\langle 110 \rangle$  Fe-Fe dumbbell. Thus, Cr should tend to end up in defect structures during displacement cascades.

### 4.3 Cascades Using Molecular Dynamics

For further studies of the primary damage in material under neutron irradiation, simulations of displacement cascades have been performed using MD for the potentials presented in paper I. Papers III and IV concern cascade simulations done using four different potentials found in the literature with the aim of comparing the defect evolution of the different potentials and to try to correlate it to the properties of the potential

For all simulations, the simulation box was set up with the atoms in a bcc configuration where the Cr atoms were initially randomly distributed when working with the alloy. The NVE ensemble was used and periodic boundary conditions without temperature control after equilibration were applied as discussed in section 3.3.

#### 4.3.1 Cascades in FeCr

Analysis of the displacement cascades performed in FeCr alloys using the potentials of paper I show a general trend of a lower number of produced defects compared to displacement cascades performed in pure Fe. This is a result of the high interstitial formation energies of these potentials. It is also seen that the Cr tends to end up in defect configurations as expected since the mixed Fe-Cr dumbbell is predicted to be more stable than the pure Fe dumbbell (see section 4.2.2).

#### 4.3.2 Cascades in Fe

By studying the behavior of defects in cascade simulations using different potentials, correlations between potential properties and the defect evolution can be studied as has been done in papers III and IV. Four different potentials found in [40], [41], [42] and [43] were chosen. With these potentials, a set of displacement cascades were produced using a standardized simulation procedure so that the results could be compared.

---

The analysis of the cascades include calculations of magnitudes such as the final number of defects, cascade density and volume, the number of sub-cascades and clustered fractions for both vacancies and interstitials. Contrary to expectation it was found that the number of Frenkel pairs produced in a cascade does not correlate with the threshold energy of the potential. Instead a correlation between the stiffness of the potential and the number of defects created in cascades is seen. A high interstitial formation energy usually means that the potential is stiff giving diluted cascades with small average cluster sizes for both vacancies and interstitials. The number of final defects produced by the different potentials were found to be approximately the same independent of the potential properties. Thus the final number of defects is largely independent of how the cascade behaves at peak time. The clustering of the defects were seen to be quite different between the potentials, but a straightforward correlation between defect properties and clustering features is difficult to find.

---

## Chapter 5

# Summary and Outlook

Before I came here I was confused about this subject. Having listened to your lecture I am still confused. But on a higher level.

**Enrico Fermi**

This thesis concerns the field of multiscale modelling, starting from the level of *ab initio*, via MD and to Monte Carlo. A modelling scheme is discussed for the FeCr system, which is a basis point for the modelling of commercial steels. The FeCr system is described by constructing many-body interatomic potentials based on *ab initio* and experimental data governing the interaction between atoms in the material. The performance of the potential is then studied using molecular dynamics simulations.

We see that it is possible to construct potentials that reproduce many important material properties. However, we also find that it is not always straightforward to find the correlation between the potential description of microscopic features and the resulting macroscopic details of the material under irradiation. The development of new two-band potentials that include the separate contributions of the *s* and *d* valence electrons in Fe for example, are expected to give better physical validity of the potential and thus a better control over the relationship between the potential and its performance in simulations.

We are still far from describing a material that resembles the commercial steels in use today. One step in the direction of real life is to include C into the matrix as it is a basic constituent of steel influencing many material properties. Further efforts will go into producing potentials for the ternary system FeCrC which is close enough to reality to be able to give predictions of use in constructing the nuclear reactors of the future.

# Acknowledgements

I would like to thank my supervisor Jan Wallenius and all the rest of the people in the Reactor physics group at KTH for their support and friendship. A big thank you also goes to my colleagues and collaborators within the FeCr community who have aided and guided during the years.

The funding for this project comes from Svenskt Kärntekniskt Centrum.



# Bibliography

- [1] <http://www.iaea.org>, 2005.
- [2] H. C. Claiborne. High-level radioactive waste disposal by transmutation. *Transactions of the American Nuclear Society*, 15:91, 1972.
- [3] D.G. Foster et al. Review of PNL study on transmutation processing of high level waste. Technical Report LA-UR-74-74, Los Alamos National Laboratory, 1974.
- [4] G. H. Kinchin and R. S. Pease. The Displacement of Atoms in Solids by Radiation. *Reports on Progress in Physics*, 18:1-51, 1955.
- [5] M. J. Norgett, M. T. Robinson, and I. M. Torrens. A proposed method of calculating displacement dose rates. *Nuclear Engineering and Design*, 33:50-54, 1975.
- [6] J. Gittus. *Irradiation effects in crystalline solids*. Applied Science Publishers, Ltd., 1978.
- [7] L. K. Mansur. Theory and experimental background on dimensional changes in irradiated alloys. *Journal of Nuclear Materials*, 216:97-123, 1994.
- [8] C. H. Woo and B. N. Singh. Production bias due to clustering of point defects in irradiation-induced cascades. *Philosophical Magazine A*, 65(4):889-912, 1992.
- [9] C. H. Woo, B. N. Singh, and F. A. Garner. Production bias: a proposed modification of the driving force for void swelling under cascade damage conditions. *Journal of Nuclear Materials*, 191-194:1224-1228, 1992.
- [10] V. Levy and C. Lemaignan. *The Nuclear Fuel of Pressurized Water Reactors and Fast Reactors*. Lavoisier Publishing Inc., 1999.

- 
- [11] <http://www.people.virginia.edu/~lz2n/mse209/Chapter8.pdf>, 2005.
- [12] P. Hohenberg and W. Kohn. Inhomogeneous Electron Gas. *Physical Review*, 136:B864–B871, 1964.
- [13] W. Kohn. Self-Consistent Equations Including Exchange and Correlation Effects. *Physical Review*, 140:A1133–A1138, 1965.
- [14] M. S. Daw and M. I. Baskes. Semiempirical, Quantum Mechanical Calculation of Hydrogen Embrittlement in Metals. *Physical Review Letters*, 50:1285–1288, 1983.
- [15] M. S. Daw and M. I. Baskes. Embedded-atom method: Derivation and application to impurities, surfaces, and other defects in metals. *Physical Review B*, 29:6443–6453, 1984.
- [16] M. W. Finnis and J. E. Sinclair. A simple empirical N-body potential for transition metals. *Philosophical Magazine A*, 50(1):45–55, 1984.
- [17] A. F. Voter. *Intermetallic Compounds Principles and Practice*, volume 1. John Wiley and Sons Ltd., 1995.
- [18] J. H. Rose, J. R. Smith, and J. Ferrante. Universal features of bonding in metals. *Physical Review B*, 28:1835, 1983.
- [19] M. I. Baskes, J. S. Nelson, and A. F. Wright. Semiempirical modified embedded-atom potentials for silicon and germanium. *Physical Review B*, 40:6085–6100, 1989.
- [20] M. I. Baskes. Modified embedded-atom potentials for cubic materials and impurities. *Physical Review B*, 46:2727–2742, 1992.
- [21] F. Cyrot-Lackmann. Sur le calcul de la cohésion et de la tension superficielle des métaux de transition par une méthode de liaisons fortes. *Journal of Physics and Chemistry of Solids*, 29:1235–1243, 1968.
- [22] D. G. Pettifor. Theory of energy bands and related properties of 4d transition metals: III. s and d contributions to the equation of state. *Journal of Physics F: Metal Physics*, 8(2):219, 1978.
- [23] G. J. Ackland and S. K. Reed. Two-band second moment model and an interatomic potential for caesium. *Physical Review B*, 67:174108, 2003.
-

- 
- [24] P. Olsson, J. Wallenius, C. Domain, K. Nordlund, and L. Malerba. Two-band modelling of  $\alpha$ -prime formation in Fe-Cr. Submitted to Physical Review B, 2005.
- [25] M.P. Allen and D. J. Tildesley. *Computer Simulations of Liquids*. Oxford University Press, 1987.
- [26] J. Alder and T. E. Wainwright. Studies in Molecular Dynamics. I. General Method. *Journal of Chemical Physics*, 31(2):459, 1959.
- [27] C. W. Gear. *Numerical initial value problems in ordinary differential equations*. Prentice-Hall, Englewood, NJ, 1971.
- [28] L. Verlet. Computer "Experiments" on Classical Fluids. I. Thermodynamical Properties of Lennard-Jones Molecules. *Physical Review*, 159:98, 1967.
- [29] N. Metropolis and S. Ulam. The Monte Carlo Method. *Journal of the American Statistical Association*, 44(247):335, 1949.
- [30] W. M. Young and E. W. Elcock. Monte Carlo studies of vacancy migration in binary ordered alloys: I. *Proc. Phys. Soc.*, 89:735, 1966.
- [31] C. Domain, C. S. Becquart, and L. Malerba. Simulation of radiation damage in Fe alloys: an object kinetic Monte Carlo approach. *Journal of Nuclear Materials*, 335:121–145, 2004.
- [32] G. Evangelakis, J. Rizos, I. E. Lagaris, and I. N. Demetropoulos. *MERLIN, a portable system for multidimensional minimization*. University of Ioannina, 1986.
- [33] K. W. Katahara, N. Nimalendran, M. H. Manghnani, and E. S. Fisher. Elastic moduli of paramagnetic chromium and Ti-V-Cr alloys. *Journal of Physics F: Metal Physics*, 9(11):2167–2176, 1979.
- [34] P. Olsson, I. A. Abrikosov, L. Vitos, and J. Wallenius. Ab initio formation energies of Fe-Cr alloys. *Journal of Nuclear Materials*, 321:84–90, 2003.
- [35] C. S. Becquart, K. M. Decker, C. Domain, J. Ruste, Y. Souffez, J. C. Turbatte, and J. C. van Duysen. Massively parallel molecular dynamics simulations with EAM potentials. *Radiation Effects and Defects in Solids*, 142:9–21, 1997.
-

- 
- [36] J. Rifkin. XMD. Center for Materials Simulations, University of Connecticut, 1999.
- [37] G. Simonelli, R. Pasianot, and E. J. Savino. Embedded-atom-method interatomic potentials for bcc-iron. *Mat. Res. Soc. Symp*, 291:567, 1993.
- [38] M. I. Mendeleev et al. *Physical Magazine A*, 83:3977, 2003.
- [39] A. Seeger. Lattice Vacancies in High-Purity  $\alpha$ -Iron. *Physica Status Solidi A*, 167:289, 1998.
- [40] G. J. Ackland, D. J. Bacon, A. F. Calder, and T. Harry. *Philosophical Magazine A*, 75:713–132, 1997.
- [41] P. Olsson, L. Malerba, and A. Almazouzi. A first step towards a multi-scale modelling of Fe-Cr alloys. Technical report, SCK-CEN BLG-950 Report, 2003.
- [42] G. J. Ackland, M. I. Mendeleev, D. J. Srlolovitz, S. Han, and A. V. Barashev. *J. Phys.: Condens. Matter*, 16:1, 2004.
- [43] J. Wallenius, I. A. Abrikosov, R. Chakarova, C. Lagerstedt, L. Malerba, P. Olsson, V. Pontikis, N. Sandberg, and D. Terentyev. Development of an EAM potential for simulation of radiation damage in Fe-Cr alloys. *Journal of Nuclear Materials*, 329-333:1175–1179, 2004.
-

**Modeling of chromium precipitation in Fe-Cr alloys**J. Wallenius,<sup>1,2</sup> P. Olsson,<sup>2</sup> C. Lagerstedt,<sup>1</sup> N. Sandberg,<sup>1</sup> R. Chakarova,<sup>1</sup> and V. Pontikis<sup>3</sup><sup>1</sup>*Department of Nuclear and Reactor Physics, Royal Institute of Technology, Stockholm, Sweden*<sup>2</sup>*Department of Neutron Research, Uppsala University, Uppsala, Sweden*<sup>3</sup>*CNRS-CECM, Paris, France*

(Received 4 November 2003; published 5 March 2004)

We have implemented a set of Embedded Atom Method (EAM) potentials for simulation of Fe-Cr alloys. The functions for the pure elements were fitted to the respective elastic constants, vacancy formation energy, and thermal expansion coefficients. For Cr, properties of the paramagnetic state were applied, providing a positive Cauchy pressure and hence applicability of the EAM. By relaxing the requirement of reproducing the pressure–volume relation at short interaction distances, stability of the  $\langle 110 \rangle$  self-interstitial could be obtained. Our Fe-potential gives  $E_{\langle 110 \rangle}^f - E_{\langle 111 \rangle}^f = -0.23$  eV. Mixed Fe-Cr pair potentials were fitted to the calculated mixing enthalpy of ferromagnetic Fe-Cr, which is negative for Cr concentrations below 6%. Simulation of thermal aging in Fe-Cr alloys using a potential fitted to the mixing enthalpy of Fe-20Cr exhibited pronounced Cr-precipitation for temperatures below 900 K, in agreement with the phase diagram. No such ordering was observed at any temperature using a potential fitted to the mixing enthalpy of Fe-5Cr. Applied to recoil cascade simulations the new potentials predict a smaller number of surviving defects than potentials found in the literature. We obtain a cascade efficiency of 0.135 NRT for damage energies inbetween 10 and 20 keV. An enhanced probability for Cr atoms to end up in defect structures is observed.

DOI: 10.1103/PhysRevB.69.094103

PACS number(s): 61.66.Dk, 61.80.Hg, 61.82.Bg

**I. INTRODUCTION**

An improved understanding of the radiation effects in ferritic steels is of importance for development of new reactors and maintenance of already operating systems. Neutron and proton irradiation cause hardening, embrittlement, and dimensional instability of the construction components. The material response is complicated with a strong dependence on the particular composition. Experiments on irradiation of Fe-Cr alloys at doses below 15 DPA, where impact of He generation is possible to neglect, show that adding 2%–6% of Cr leads to a decrease in swelling as compared to pure Fe.<sup>1,2</sup> There is a general trend towards a minimum in ductile to brittle transition temperatures at about nine percent Cr content. Formation of the Cr rich  $\alpha'$  phase above Cr concentrations of 10% is a major cause of hardening, indicating that chromium plays a main role in the qualitative understanding of Fe-Cr properties in- and out of pile.<sup>3–7</sup>

The Molecular Dynamics (MD) method is widely used as a basic theoretical tool, providing physical insight into kinetic processes and interactions leading to the formation of defect clusters, dislocation loops, etc. The validity of the conclusions is directly related to the validity of the interaction potential adopted. A binary alloy potential is usually constructed on the basis of the potentials of the elements constituting the alloy.<sup>8,9</sup> Thus the quality of the potential is determined by the extent to which the pure element, and the alloy properties, are reproduced.

Two different types of many-body potentials have been used in MD studies of bcc-iron reported in the literature, namely Finnis-Sinclair potentials, relying on a second moment approximation to the tight binding theory,<sup>10–12</sup> and Embedded Atom Method (EAM) potentials,<sup>13–18</sup> having their roots in Density Functional Theory.

Fe-Cr alloy potentials have also been constructed using

the Finnis-Sinclair approach<sup>19</sup> as well as the EAM.<sup>20</sup> These are fitted to measurements of mixing enthalpy and to the lattice parameter of the alloy. The experimental values of the heat of mixing used in those works are however valid only for the paramagnetic state of the material (above the Curie temperature). Further, properties of antiferromagnetic (AFM) Cr were used in fitting of the Cr potential used by these authors, in spite of the negative Cauchy pressure of the AFM state.

The objective of the present work is to construct a set of Fe-Cr potentials that can reproduce essential properties of the alloy, such as the mixing enthalpy of the ferromagnetic (FM) state. The potentials should be applicable to simulations of the primary defect formation induced by high energy recoils, as well as to modeling of the subsequent defect evolution. It has to be noted that experimental data describing basic Fe-Cr alloy characteristics of use to the potential fitting, are not always available. In our case, there are experimental data for the bulk modulus of Fe-Cr alloys with different Cr contents. However, no measurements are reported for the mixing enthalpy of ferromagnetic Fe-Cr. Therefore, our modeling approach integrates *ab initio* calculations of Fe-Cr alloy properties, design of an EAM potential fitted to these data, and usage of the potential in MD cascade simulations.

In what follows, we will describe our approach to obtain physically consistent EAM-potentials for ferromagnetic iron, paramagnetic (PM) chromium, and ferromagnetic alloys of these elements. The applicability of our potentials is corroborated by kinetic Monte Carlo simulation of thermal ageing of alloys with varying concentrations of chromium. We then account for results from recoil cascade calculations, pointing out significant differences in defect production in the alloy, as compared to pure iron. Finally we discuss the impact of our results on the general understanding of Fe-Cr properties in- and out of pile.

## II. CONSTRUCTION OF THE EAM POTENTIAL

Within the EAM formalism, the total energy of the system of  $n$  atoms is written as a sum over atomic energies,<sup>13</sup>

$$E_{\text{tot}} = \sum_{i=1}^n E_i = \sum_{i=1}^n \left[ \frac{1}{2} \sum_{j=1}^n \Phi(r_{ij}) + F(\rho_i) \right], \quad (1)$$

where  $\Phi(r_{ij})$  is the pairwise (electrostatic) interaction between atoms  $i$  and  $j$ ; the function  $\rho_i = \sum_{j \neq i} \rho(r_{ij})$  represents the electron density of the host system with atom  $i$  removed and  $r_{ij}$  is the scalar distance between atoms  $i$  and  $j$ .  $F(\rho_i)$  is the many body term, i.e., the quantum mechanical energy required to embed atom  $i$  into a homogeneous electron gas of density  $\rho_i$ . Because the electron density depends only on scalar distances to neighboring atoms, the many body term here has no angular dependence. The curvature of  $F$  may be interpreted in terms of the traditional chemical bonding concept, where a new bond increases the total bonding energy but decreases the average energy per bond. In this context,  $\rho_i$  becomes a measure of the total bond order and  $\rho(r)$  is a bond sensor. The weakening of successive bonds corresponds to a positive curvature of  $F$ ,

$$\frac{\partial^2 F}{\partial \rho^2} > 0. \quad (2)$$

The complete EAM energy expression in the case of binary Fe-Cr alloys involves definitions for the pair potentials  $\Phi_{\text{Fe}}(r), \Phi_{\text{Cr}}(r)$  of pure Fe and Cr, the mixed pair potential  $\Phi_{\text{FeCr}}(r)$ , the electronic density functions  $\rho_{\text{Fe}}(r), \rho_{\text{Cr}}(r)$  and the embedding functions  $F_{\text{Fe}}(\rho)$  and  $F_{\text{Cr}}(\rho)$ ,

$$\begin{aligned} E_{\text{tot}} = & \sum_{i_{\text{Fe}}} F_{\text{Fe}}(\rho_i) + \sum_{i_{\text{Cr}}} F_{\text{Cr}}(\rho_i) + \frac{1}{2} \sum_{i_{\text{Fe}}, j_{\text{Fe}}} \Phi_{\text{Fe}}(r_{ij}) \\ & + \frac{1}{2} \sum_{i_{\text{Fe}}, j_{\text{Cr}}} \Phi_{\text{FeCr}}(r_{ij}) + \frac{1}{2} \sum_{i_{\text{Cr}}, j_{\text{Cr}}} \Phi_{\text{Cr}}(r_{ij}) \\ & + \frac{1}{2} \sum_{i_{\text{Cr}}, j_{\text{Fe}}} \Phi_{\text{FeCr}}(r_{ij}). \end{aligned} \quad (3)$$

It is seen from Eq. (3) that the potentials of the pure elements potentials are part of the alloy potential.

The following parametric form of the pair interaction terms is assumed:<sup>12,15</sup>

$$\Phi(r) = \sum_{i=1}^5 a_i (r - r_i)^3 H(r_i - r). \quad (4)$$

Here,  $r_i$  are knot points of the cubic splines used to represent the potential,  $H$  is the Heaviside step function, and  $a_i$  are spline coefficients. The atom electron density is approximated by the Thomas-Fermi screening function suggested in Ref. 15.

The Fe and Cr embedding functions are calculated by fitting the cohesive energy to the Rose expression, which gives the equation of state of a perfect crystal as a function of the reduced lattice parameter  $\bar{a}$ ,<sup>21</sup>

$$E_{\text{Rose}}(\bar{a}) = -E_{\text{coh}}(1 + \bar{a})e^{-\bar{a}} \quad (5)$$

with

$$\bar{a} = \sqrt{\frac{9\Omega B}{E_{\text{coh}}}} \left( \frac{R_1}{R_{1e}} - 1 \right), \quad (6)$$

where  $R_{1e}$  is the equilibrium value of the distance to the nearest neighbor.  $\Omega$  is the atomic volume and  $B$  denotes the bulk modulus. Note that the alloy bulk modulus is not involved in expression (6), but only the bulk modulus of the pure elements. Since the range of the interactions needs to be finite, a cut-off is introduced in the electron density, with a corresponding modification of the Rose expression for large lattice parameters.<sup>9,22</sup>

### A. Potentials for Fe and Cr

The fitting procedure has been performed in several steps. Three of the spline coefficients for ferromagnetic iron, corresponding to knot points larger than  $R_{1e}$ , were obtained by fitting to the lattice parameter, cohesive energy, vacancy formation energy, and elastic constants as measured at 0 K. A modified version of the MERLIN code package was written for this step of the procedure. The package is based on elastic theory of deformation, including multiparametric optimization with options for different algorithms.<sup>23,24</sup> The conditions of equilibrium are expressed as a requirement of no stresses in a perfect crystal. Stresses are evaluated by expanding the energy to the first order with respect to an infinitesimal homogeneous strain applied to the system. The second order elastic constants are evaluated by expanding the energy of the system to the second order with respect to an infinitesimal homogeneous stress. For example,

$$C_{44} = \frac{\partial^2 E_{\text{tot}}}{\partial \gamma^2} \quad (7)$$

with  $\gamma$  being the angle of distortion by shear deformation imposed on the crystal when keeping the volume constant. In the case of compression in one direction and expansion in the other, the amplitude of deformation for a constant volume is denoted by  $\epsilon$ , and the corresponding elastic constant is

$$C' = \frac{1}{2}(C_{11} - C_{12}) = \frac{1}{4} \frac{\partial^2 E_{\text{tot}}}{\partial \epsilon^2}. \quad (8)$$

The bulk modulus is obtained by simulating isotropic compression,

$$B = \frac{1}{9} \frac{\partial^2 E_{\text{tot}}}{\partial \epsilon^2}. \quad (9)$$

The embedding function of iron was then calculated using these three spline coefficients for the pair potential. After thus fixing the embedding function, the fourth spline coefficient was determined by fitting to the lattice parameter of iron at room temperature. The position of the corresponding knot point was adjusted to mimic the temperature depen-

TABLE I. Knot points and spline coefficients for the pair potentials of Fe and Cr obtained in the present work. The knot points are given in units of nearest neighbor distance.

| $i$ | Fe ( $a_0=0.2860$ nm) |           | Cr ( $a_0=0.2875$ nm) |           |
|-----|-----------------------|-----------|-----------------------|-----------|
|     | $r_i$                 | $a_i$     | $r_i$                 | $a_i$     |
| 1   | 0.945                 | 2633      | 0.945                 | 310       |
| 2   | 0.967                 | -2500     | 0.972                 | -603      |
| 3   | 1.030                 | 10.75857  | 1.150                 | 50.28020  |
| 4   | 1.320                 | -24.28842 | 1.280                 | -61.24700 |
| 5   | 1.540                 | 7.078864  | 1.470                 | 14.66964  |

dence of the thermal expansion coefficient in the temperature range 0–600 K. The molecular dynamics code XMD was used for this purpose, in which the condition of constant pressure is imposed by the *pressure clamp* command.<sup>25</sup> The final spline coefficient was set to ensure a smooth transition of the pair potential into the universal screened Coulomb function of Biersack *et al.*<sup>11,12,26</sup>

A similar procedure was implemented to obtain the potential for pure chromium. Previous attempts to fit a central many-body potential to the elastic constants of antiferromagnetic chromium have failed, as may be expected from the negative value of the Cauchy pressure at 0 K,

$$\frac{1}{2}(C_{12} - C_{44}) \approx -13 \text{ GPa}. \quad (10)$$

We note however, that at temperatures relevant for reactor operation ( $T > 450$  K), chromium is paramagnetic, featuring a positive Cauchy pressure.<sup>27</sup> Further, it is sufficient to add a few percent of iron or vanadium to obtain an alloy that is paramagnetic at room temperature.<sup>28,29</sup> We therefore fit our Cr potential to the elastic constants of paramagnetic chromium, linearly extrapolated down to 0 K. Stiffening of the pair potential is made by fitting to thermal expansion coefficients measured for paramagnetic Cr–5V, being equal to the expansion coefficient of pure Cr when  $T > 600$  K.<sup>29</sup> Considering that the Cr precipitates observed in real Fe–Cr alloys contain about 15% iron, we believe that our potential for paramagnetic Cr should be valid for describing Cr–Cr interactions in the present context.

In Table I we list the resulting spline coefficients and knot points for Fe and Cr. In Fig. 1 the pair-potentials are plotted as function of  $r$ . Note the slightly larger depth of the potential for paramagnetic Cr, reflecting the larger vacancy formation energy predicted for Cr.

We note that by stiffening the pair potentials inside the equilibrium nearest neighbor distance, *after having fixed* the embedding function, we violate the pressure–volume relation given by the Rose expression (5). The reason for doing so, is that we otherwise were unable to simultaneously fit experimental values for  $E_{\text{bcc}} - E_{\text{fcc}}$ ,  $E_{\langle 110 \rangle}^f - E_{\langle 111 \rangle}^f$  and the thermal expansion coefficient. Our potentials are hence not applicable to simulation of isotropic compression under high pressure. However, the presence of high electron densities in recoil cascades as well as in defect configurations are of local

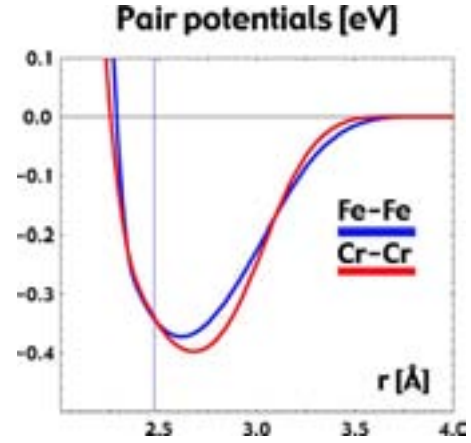


FIG. 1. (Color online) Pair potentials for ferromagnetic Fe (blue line) and paramagnetic Cr (red line) obtained in the present work.

character, which may be difficult to characterize through an equation of state like the Rose expression.

### B. Mixed Fe–Cr pair potentials

The potentials obtained for the pure elements have been further used in Eq. (3) to calculate the parameters  $a_i$  for the mixed Fe–Cr pair potential, fitting them to the mixing enthalpy of the ferromagnetic alloy. Table II displays the formation energy of ferromagnetic Fe–Cr calculated with the EMTO method.<sup>31</sup>

Previous attempts to construct mixed pair potentials for Fe–Cr (Refs. 18,20) relied on fitting to the formation energy of the paramagnetic state of the alloy, which is strictly positive. A single pair-potential for the Fe–Cr interaction would however not be able to reproduce the change in sign of the formation energy of the relevant magnetic state. Therefore, a set of potentials have to be created, providing the correct total energy of the random ferromagnetic alloy. In the present paper, we have performed the fitting for Cr-concentrations of 5% and 20%. The lower concentration should yield a potential with small but negative mixing enthalpy, thus ensuring phase stability at all temperatures. The larger concentration was selected to study a region where the predicted mixing enthalpy is positive, and Cr precipitation (formation of the  $\alpha'$  phase) is observed in real materials.<sup>3,5</sup>

TABLE II. Formation energies  $\Delta H_f$  of random ferromagnetic Fe–Cr alloys, calculated with the Exact Muffin Tin Orbital *Ab Initio* method (Ref. 31).

| Cr-fraction | $\Delta H_f$ (meV) |
|-------------|--------------------|
| 0.02        | -1.8               |
| 0.04        | -1.3               |
| 0.06        | +0.6               |
| 0.08        | +5.1               |
| 0.10        | +10.4              |
| 0.15        | +27.9              |
| 0.20        | +45.3              |

TABLE III. Knot points and spline coefficients for the mixed Fe-Cr pair potentials obtained in the present work. The knot points are given in units of nearest neighbor distance.

| $i$ | Fe-5Cr ( $a_0=0.2861$ nm) |         | Fe-20Cr ( $a_0=0.2863$ nm) |         |
|-----|---------------------------|---------|----------------------------|---------|
|     | $r_i$                     | $a_i$   | $r_i$                      | $a_i$   |
| 1   | 0.945                     | 2239    | 0.945                      | 2624    |
| 2   | 0.967                     | -2199   | 0.967                      | -2476   |
| 3   | 1.030                     | 0.000   | 1.030                      | 10.000  |
| 4   | 1.400                     | -12.737 | 1.320                      | -24.500 |
| 5   | 1.650                     | 4.210   | 1.53                       | 7.620   |

The parameters obtained for the Fe-Cr mixed pair potentials are given in Table III. The sharp dip in the measured bulk modulus at Cr concentrations about 5% (Ref. 30) lead us to assume a longer range for the corresponding pair potential. Due to the lack of thermal expansion data for the alloy, stiffening of the potentials at short distances was made in a rather arbitrary fashion, simply requiring a smooth transition to the universal Coulomb screening function at  $r \approx 1.7$  Å.

### III. VERIFICATION OF THE POTENTIALS

The quality of the potential has been inspected by calculations of elastic constants, structural stability, and formation energies of various defect configurations. The results are shown in Tables IV, V and VII. Comparing with experimental data and values obtained by other authors, one may note the following: The potential here presented reproduces more closely the experimental elastic characteristics and structural stability of pure iron than the EAM-potentials published by Simonelli *et al.*. Our relaxed vacancy formation energy (2.04 eV) was fitted to the resistivity measurements by De Schep *et al.*,<sup>34</sup> indicating a significantly higher value for  $E_{\text{vac}}^f$  than earlier measurements in less pure materials.<sup>40</sup> The potential *predicts* an activation energy for self-diffusion equal to 2.91 eV, in very good agreement with data obtained at temperatures sufficiently low for the influence of paramagnetism to be safely neglected.<sup>35,36</sup>

Our fit to thermal expansion data was made using a single spline coefficient, and can thus not be expected to reproduce measured data over the whole temperature range. One may note however that potentials not fitted to thermal expansion underestimates the expansion by a factor of 2 or more.

In comparison with the Finnis-Sinclair potential developed by Ackland and co-workers, our potential yields a stability of the  $\langle 110 \rangle$  interstitial with respect to the  $\langle 111 \rangle$  configuration that is in better agreement with measured data. The predicted absolute formation energy of the Fe self-interstitial is higher than what results from using any other potential found in literature. We note that the experimental values are derived from measurements of stored energy release per resistivity recovery ( $dQ/d\rho$ ) in samples irradiated at low temperature.<sup>38-41</sup> The enthalpy for formation of a Frenkel pair is obtained by multiplying  $dQ/d\rho$  with an assumed resistivity  $\rho_F$  for a single Frenkel pair. Estimates of  $\rho_F$  vary from 0.20 to 0.30  $\text{m}\Omega \times \text{cm}$ .<sup>42,43</sup> Selecting the higher value,

TABLE IV. Properties of pure iron obtained with the potential for ferromagnetic Fe here presented. Elastic constants are given in units of GPa, energies in eV, and thermal expansion coefficients in units of  $10^{-6}$ . Comparison is made with experimental data and values calculated using the potentials of Simonelli (Ref. 15) and Ackland (Ref. 12).

| Fe property   | This work | Expt.                        | Sim A | Sim B  | Ackland |
|---|-----------|------------------------------|-------|--------|---------|
| $B$   | 172       | 173 <sup>a</sup>             | 146   | 146    | 178     |
| $C'$  | 56.7      | 52.5 <sup>a</sup>            | 48.0  | 48.0   | 49.0    |
| $C_{44}$  | 135       | 122 <sup>a</sup>             | 115   | 115    | 116     |
| $E_{\text{coh}}$  | 4.28      | 4.28                         | 4.28  | 4.28   | 4.316   |
| $E_{\text{bcc}} - E_{\text{fcc}}$                       | -0.047    | -0.050 <sup>b</sup>          | -0.03 | -0.007 | -0.054  |
| $E_{\text{vac}}^f$                                      | 2.04      | $2.0 \pm 0.2$ <sup>c</sup>   | 1.63  | 1.56   | 1.70    |
| $E_{\text{vac}}^{\text{SD}}$                            | 2.91      | $2.91 \pm 0.04$ <sup>d</sup> | 2.32  | 2.29   | 2.48    |
| $E_{\langle 110 \rangle}^f$                             | 7.72      | $3-12$ <sup>e</sup>          | 3.66  | 4.11   | 4.87    |
| $E_{\langle 110 \rangle}^f - E_{\langle 111 \rangle}^f$ | -0.23     | -0.30 <sup>f</sup>           | +0.12 | -0.19  | -0.13   |
| $\alpha$ ( $T=300$ K)                                   | 12.8      | 11.7 <sup>g</sup>            | 5.8   | 3.4    | 7.4     |
| $\alpha$ ( $T=600$ K)                                   | 14.2      | 15.8 <sup>g</sup>            | 7.9   | 4.9    | 7.2     |

<sup>a</sup>Reference 32.

<sup>b</sup>Reference 33.

<sup>c</sup>Reference 34.

<sup>d</sup>References 35, 36.

<sup>e</sup>References 37, 38.

<sup>f</sup>Reference 38.

<sup>g</sup>Reference 39.

TABLE V. Properties of paramagnetic Cr calculated with the potential here presented. Comparison is made with experimental data for Cr in AFM and PM states, as well as values calculated using the potential of Farkas (Ref. 20). PM elastic constants were obtained by extrapolation to 0 K of high temperature data (Ref. 27). The paramagnetic thermal expansion coefficient at  $T=300$  K refers to measurements on Cr-5V (Ref. 29).

| Cr property   | This work | Expt. (AFM)      | Expt. (PM)                 | Farkas |
|---|-----------|------------------|----------------------------|--------|
| $B$   | 207       | 195 <sup>a</sup> | 207 <sup>a</sup>           | 148    |
| $C'$  | 153       | 153 <sup>a</sup> | 155 <sup>a</sup>           | 42.5   |
| $C_{44}$  | 105       | 104 <sup>a</sup> | 105 <sup>a</sup>           | ...    |
| $E_{\text{coh}}$  | 4.10      | 4.10             | 4.10                       | 4.10   |
| $E_{\text{bcc}} - E_{\text{fcc}}$                       | -0.025    | ...              | ...                        | -0.053 |
| $E_{\text{vac}}^f$                                      | 2.14      | ...              | $2.0 \pm 0.2$ <sup>b</sup> | 1.12   |
| $E_{\text{vac}}^{\text{SD}}$                            | 2.93      | ...              | 2.95 <sup>c</sup>          | 2.30   |
| $E_{\langle 110 \rangle}^f$                             | 5.16      | ...              | ...                        | 3.03   |
| $E_{\langle 110 \rangle}^f - E_{\langle 111 \rangle}^f$ | -0.62     | ...              | ...                        | 0.19   |
| $\alpha$ ( $T=300$ K)                                   | 7.5       | 4.4 <sup>d</sup> | 7.9 <sup>d</sup>           | 5.2    |
| $\alpha$ ( $T=600$ K)                                   | 9.8       | ...              | 9.6 <sup>d</sup>           | 9.5    |

<sup>a</sup>Reference 27.

<sup>b</sup>Reference 44.

<sup>c</sup>Reference 45.

<sup>d</sup>Reference 29.



TABLE VI. Comparison of Fe-Cr mixing enthalpy obtained with the potentials here presented, the Exact Muffin Tin Orbital calculation of Olsson *et al.* (Ref. 31), and values calculated using the potential of Farkas *et al.* (Ref. 20).

| Property                  | Data      | Fe-5Cr | Fe-20Cr |
|---------------------------|-----------|--------|---------|
| $H_{\text{FeCr}}^f$ (meV) | This work | -0.04  | +45     |
|                           | EMTO      | -0.05  | +45     |
|                           | Farkas    | +24    | +86     |

Wollenberger arrives at a formation energy  $E_F^f = 6.6$  eV for a Frenkel pair in electron irradiated  $\alpha$ -Fe, and  $E_F^f = 13.6$  eV for a neutron irradiated sample.<sup>41</sup> Subtracting a vacancy formation energy of 2.0 eV would then give  $E_{\langle 110 \rangle}^f = 4.6$  eV in the former case, and 11.6 eV in the latter. The uncertainty of these values is obviously large, since just by assuming  $\rho_F = 0.20$  m $\Omega \times$ cm, one could obtain  $E_{\langle 110 \rangle}^f = 7.7$  eV for the neutron irradiated sample. Note that results from the electron irradiation not necessarily are more accurate, since experimental boundary conditions are more difficult to control in stages  $I_A$  to  $I_C$  (absent in neutron irradiation) than in stage  $I_D$ .

The SIA formation energy in iron have recently been calculated with the *ab initio* package VASP as  $E_{\langle 110 \rangle}^f \approx 3.4$  eV.<sup>46</sup> This result is compatible with data from electron irradiations. However, since the calculation did not take into account possible effects of noncollinear magnetism, the discrepancy with data from neutron irradiated samples remains an open question. As will be seen later, the magnitude of the interstitial formation energy has a significant impact on defect recombination in recoil cascades, and we will argue that a high value is consistent with defect distributions actually observed.

Concerning the properties of chromium predicted by the potential here presented, we emphasize that the fit was made to elastic constants of *paramagnetic* chromium, extrapolated to 0 K. Hence we are able to retain a positive Cauchy pressure at all temperatures. The relaxed vacancy formation energy is compatible with experimental data, in contrast to the prediction of the potential by Farkas *et al.*,<sup>20</sup> for which an apparently incorrectly quoted value of  $E_{\text{vac}}^f$  has been used in the fit. We further note that the activation energy for vacancy diffusion predicted by the potential is in excellent agreement with measured data.<sup>45</sup>

As seen in Table VI, the alloy potentials well reproduce the mixing enthalpies of Fe-5Cr and Fe-20Cr calculated with the EMTO method. The heat of mixing obtained with Farkas' potential should be considered to represent the paramagnetic state of the alloy, and is hence not applicable for MD or KMC simulations below the Curie temperature.

Table VII displays formation and binding energies of a single mixed  $\langle 110 \rangle$  Fe-Cr dumbbell in an iron matrix. We find that the mixed  $\langle 110 \rangle$  Fe-Cr dumbbell is more stable than the  $\langle 110 \rangle$  Fe-Fe dumbbell in the case of local Cr concentrations less than 20%. The Cr-Cr dumbbell is even more stable, with a binding energy exceeding 0.3 eV. Hence one may expect that Cr will tend to accumulate in defect struc-

TABLE VII. Formation and binding energies of a single mixed  $\langle 110 \rangle$  Fe-Cr dumbbell in an iron matrix with lattice parameter  $a_0 = 2.860$  Å. Predictions of the alloy potentials are compared to VASP *ab initio* data (Ref. 47) and values calculated with Farkas' potential (Ref. 20).  $-E_{\langle 110 \rangle}^b = E_{\langle 110 \rangle}^{\text{Cr}} - E_{\langle 110 \rangle}^{\text{Fe}} - E_{\text{Cr}}^s$  is calculated relative to the energy of an Fe-Fe dumbbell, subtracting the substitution energy  $E_{\text{Cr}}^s$  of a single Cr atom.

| Property | $E_{\langle 110 \rangle}^f$ | $E_{\text{Cr}}^s$ | $E_{\langle 110 \rangle}^b$ | $E_{\langle 110 \rangle}^f - E_{\langle 111 \rangle}^f$ |
|----------|-----------------------------|-------------------|-----------------------------|---|
| Fe-5Cr   | 7.63                        | +0.18             | +0.27                       | -0.03   |
| Fe-20Cr  | 8.19                        | +0.46             | -0.01                       | -0.20   |
| VASP     | 3.06                        | -0.35             | -0.00                       | +0.36   |
| Farkas   | 4.31                        | +0.70             | +0.05                       | +0.07   |

tures created in collision cascades.

The sparse experimental data for the elastic constants of the alloy are unfortunately not fully consistent.<sup>30,48</sup> Below the solubility limit of Cr though, there is a clear tendency for a decrease in bulk modulus, which is supported by *ab initio* calculations. The range of the Fe-5Cr potential was therefore enlarged, in order to obtain a smaller bulk modulus. This procedure must however be considered as arbitrary, and better experimental data for the alloy, including thermal expansion, is of necessity to enable construction of fully consistent mixed pair potentials.

Due to the nonmonotonous behavior of the bulk modulus and the formation energy, a potential for a given Cr concentration can in general not be used for predicting alloy properties at a different concentration. Proper simulation of non-equilibrium behavior of the alloy would require use of different potentials for different local concentrations of chromium.

#### IV. APPLICATION OF THE Fe-Cr POTENTIAL IN SIMULATION OF THERMAL AGEING

It is well known that precipitation of Cr occurs under thermal aging at  $T < 900$  K in FeCr alloys with Cr content ranging from 10% to 90%.<sup>3,5</sup> The formation of the so-called  $\alpha'$  phase is responsible for hardening of the binary alloy.<sup>49,50</sup> The magnitude of the miscibility gap for low Cr concentrations could be theoretically explained only recently, when *ab initio* calculations showed that the mixing enthalpy of Fe-Cr is negative for the *ferromagnetic* state of the random alloy, if the Cr concentration is below 6%.<sup>31</sup> Above this limit, the formation energy is positive, providing a driving force for phase separation. In order to obtain the temperature dependence of the solubility, one needs to perform molecular dynamics, or rather kinetic Monte Carlo (KMC) simulations. We have performed such simulations of thermal aging at a range of temperatures, using several different techniques implemented in the DYMOKA code, developed by Electricite de France (EDF) and University of Lille.<sup>51</sup>

The out-of-pile process of segregation is assumed to be driven purely by vacancy assisted migration. According to classical diffusion theory, the frequency for a lattice atom to exchange lattice position with a neighboring vacancy is

$$\Gamma(T) = \nu C_{\text{vac}}(T) e^{-(E_m/k_B T)}, \quad (11)$$

where  $\nu$  is the attempt frequency of the jump and  $C_{\text{vac}}$  is the equilibrium concentration of vacancies. The vacancy concentration as function of temperature is given by

$$C_{\text{vac}}(T) = e^{-(G_f/k_B T)}. \quad (12)$$

Here,  $G_f = E_{\text{vac}}^f - TS_{\text{vac}}^f$  is the Gibbs energy of vacancy formation. The entropy of formation may be calculated from the following formula:<sup>52</sup>

$$S_{\text{vac}}^f = k_B \left( \sum_n^{3(N-1)} \ln \omega_n^{\text{vac}} - \frac{(N-1)}{N} \sum_n^{3N} \ln \omega_n^{\text{bulk}} \right), \quad (13)$$

where  $\omega_n$  are eigen frequencies of the force-constant matrices with an without a vacancy in the system, respectively. MD simulations using our potential for ferromagnetic iron gives  $S_{\text{vac}}^f = 1.78 k_B$  for a relaxed system of  $N = 432$  atoms.

Similarly, the attempt frequency  $\nu$  may be calculated from<sup>53</sup>

$$\nu = \frac{k_B}{2\pi} \frac{\prod_{n=1}^{3N} \omega_n^{\text{vac}}}{\prod_{n=1}^{3N-1} \omega_n^{\text{TST}}}, \quad (14)$$

where  $\omega^{\text{TST}}$  are the eigenfrequencies evaluated at the transition state of the vacancy jump. For the present potential we obtain  $\nu = 9.15 \times 10^{13} \text{ s}^{-1}$  which gives us a prefactor for self-diffusion in ferromagnetic iron:  $D_0 = 2.13 \times 10^{-5} \text{ m}^2/\text{s}$ . This value, valid in the harmonic approximation, is very close to the one observed in experiments.<sup>36</sup>

In general, the probability of all possible vacancy jumps in an alloy (8 first nearest neighbors in a bcc structure) should be computed for every Monte Carlo step, selecting one of them to be performed, weighted with that probability. Time is then introduced as the inverse of the system averaged jump frequencies. In our case, the vacancy assisted migration energy for Fe and Cr atoms are close to each other; 0.87 eV and 0.84 eV, respectively. We hence make a concentration weighted average for our system and calculate an average time step as

$$\Delta \tau = \frac{1}{8\Gamma(T)}. \quad (15)$$

We performed simulations of vacancy migration assuming a single vacancy in a box with 16 000 atoms. It was checked that the rate of energy loss in the Fe-20Cr alloy did not change significantly when increasing the box size.

In order to arrive at a fully segregated final state, we used a Metropolis Monte Carlo algorithm, together with the vacancy KMC. The metropolis algorithm exchanges all atoms of differing type if it is energetically favorable. If an exchange increases the energy it is accepted with a weight  $\exp(-E/kT)$ , where  $E$  is the potential energy of the system. The Metropolis MC method is much faster, but provides no explicit time scale. However, it was found that a time step

## Total energy per atom [eV]

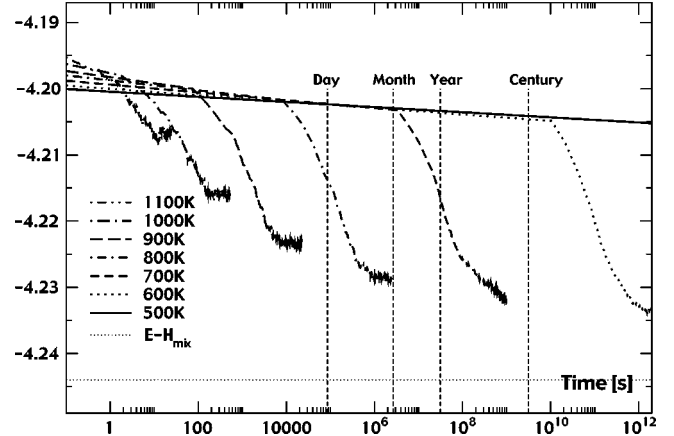


FIG. 2. Total energy of an initially random Fe-20Cr alloy, as a function of time and temperature.

could be assigned to each Metropolis MC step by fitting energy losses to the explicit vacancy KMC simulation.

In Fig. 2, the total energy of an initially random Fe-20Cr alloy is plotted as function of time and temperature. Since the mixing enthalpy of the random alloy is positive, a loss in energy is a sign of segregation. For infinite segregation, the energy loss would equal the formation energy  $\Delta H_{\text{Fe-20Cr}}^f = 45 \text{ meV}$ . In a finite box, however, there will always remain a surface to bulk factor. The surface atoms of a Cr cluster will all have Fe neighbors and thus a higher energy. In our most segregated case ( $T = 500 \text{ K}$ ) we arrive at 84% of the mixing enthalpy. This may be understood from the fact that a single Cr cluster of spherical shape in our simulation box has a surface to bulk ratio of Cr atoms equal to about 30%. On the cluster surface, half of the neighbors to Cr atoms are Fe atoms, and hence the surface energy of final Cr cluster provides the missing 16%.

We note that for 700 K, the time needed to obtain a significant energy loss is of the order of months, which is consistent with the experimental time threshold for observation of hardening in Fe-45Cr alloys aged at 673 K.<sup>50</sup> For 800 K segregation occurs in a matter of days, while for 900 K, the energy loss saturates within a few hours, before complete phase separation has taken place. At 1000 K, less than half the energy loss is achieved, which corresponds to a limited ordering of the system, without actual phase separation.

The process of segregation is illustrated in Fig. 3, where the distribution of Cr atoms is shown before and after ageing during 30 years at 700 K. This simulation was done with an initial Cr content equal to 12%, using the Fe-20Cr potential.

The final Cr-precipitate appearing during the simulation is free of Fe atoms, due to the fact that our potential incorrectly predicts a positive mixing enthalpy even for Cr concentrations in the vicinity of 90%.

In order to quantify the temperature dependence of the phase separation, we define the degree of segregation  $\xi$  as

$$\xi = \frac{1}{\xi_{\text{max}}} \frac{N_{\text{Cr}}^{\text{Emb}}}{N_{\text{Cr}}^{\text{Tot}}}. \quad (16)$$

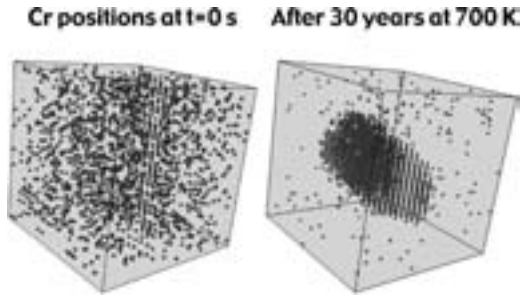


FIG. 3. Distribution of Cr atoms in a box with 16 000 atoms, before and after thermal aging at 700 K. A crystal clear segregation is observed, with formation of a single cluster.

Here,  $N_{\text{Cr}}^{\text{Tot}}$  is the number of Cr atoms in the system,  $N_{\text{Cr}}^{\text{Emb}}$  is the number of Cr atoms that only have Cr first nearest neighbors, and  $\xi_{\text{max}}$  is the theoretical maximum number of Cr atoms that may have Cr first nearest neighbors, accounting for the surface layer of a spherical cluster.

The degree of segregation produced by the Fe-20Cr potential after the energy loss has reached its asymptotic value is shown in Fig. 4. If an arbitrary limit of  $\xi > 0.5$  is set to distinguish the  $\alpha'$  phase from  $\alpha$ , we find that this corresponds to  $T < 900$  K. Considering that the range of temperature where the phase transition takes place is uncertain, quoted as  $750 \pm 125$  K in Ref. 7, our results may be considered to be in reasonable agreement with the phase diagram.

Performing the same type of simulations using the potential fitted to the mixing enthalpy of Fe-5Cr, no significant energy loss is found at any temperature, which means that the alloy remains random. We may thus conclude that our potentials reproduce the out-of pile state of ferromagnetic Fe-Cr as function of temperature and time at Cr concentrations of 0%, 5%, and 20%.

It is important to note that in reality, the driving force for the decomposition would be lost when the local concentration of Cr becomes too high or too low. Hence, in order to obtain the physically observed final states with an iron content in the  $\alpha'$  precipitates ranging from 10% to 20%, we would have to switch potentials during the simulation ac-

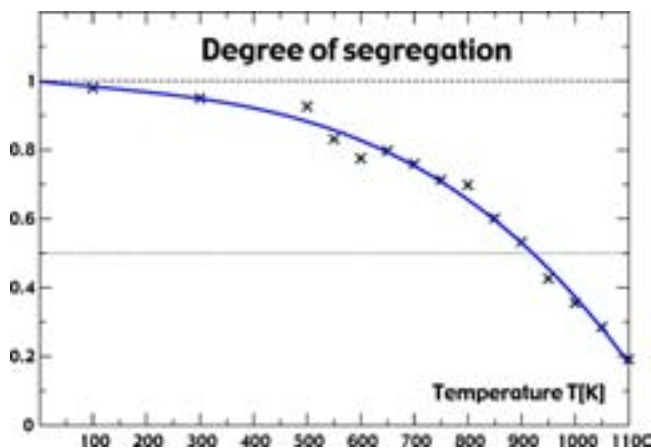


FIG. 4. (Color online) Degree of segregation  $\xi$  as a function of temperature. The line is a cubic fit to asymptotic averages obtained with the Metropolis Monte Carlo procedure.

TABLE VIII. Average number of surviving Frenkel pairs as function of recoil damage energy. The quoted uncertainty corresponds to one standard deviation.

| $E_{\text{dam}}$ | 5 keV         | 10 keV         | 20 keV         |
|------------------|---------------|----------------|----------------|
| Fe               | $7.4 \pm 0.7$ | $13.4 \pm 0.9$ | $27.0 \pm 1.0$ |
| Fe-5Cr           | $8.9 \pm 0.7$ | $14.0 \pm 0.8$ | $28.7 \pm 1.6$ |
| Fe-20Cr          | $8.5 \pm 0.6$ | $13.6 \pm 0.7$ | $27.0 \pm 1.3$ |

cording to the local density of Cr, a feature not yet implemented in the codes we have used. Therefore the size of the clusters we observe at infinite times cannot be expected to agree with the measured size distribution, being of the order of 2–4 nm.<sup>50</sup>

## V. APPLICATION OF THE Fe-Cr POTENTIAL IN CASCADE SIMULATIONS

The potentials here presented were applied in molecular dynamics simulations of collision cascades initiated by recoils having energies up to 20 keV. Periodic boundary conditions were used, and the sizes of the MD boxes were adjusted to make sure that the cascade did not interact with its periodic image. For 10 keV cascades, it was found that 128 000 atoms ( $40 \times 40 \times 40$  lattice units) was sufficient for recoils in the  $\langle 135 \rangle$  direction, while 250 000 atoms had to be used when launching in the  $\langle 111 \rangle$  direction. The initial atom velocities were sampled from a Maxwellian distribution for a particular temperature, set to  $T = 100$  K in the present study. The block is equilibrated for about a picosecond before launching an energetic recoil in the central region. The time step was varied from 0.02 fs (when the recoil is generated) up to 0.5 fs at the end of the simulation period (10 ps). The first thing to be noted is that the new potentials predict a much smaller number of surviving defects than potentials found in the literature.<sup>11,54</sup> This is a direct result of the higher interstitial formation energy, leading to larger probability for recombination of Frenkel pairs during cooling down of the cascade. Table VIII shows the average number of surviving defects in Fe and Fe-20Cr, for a set of representative recoil energies in the  $\langle 135 \rangle$  direction.

As seen the difference between the alloy and pure iron is statistically insignificant. For recoil energies between 10 and 20 keV, we arrive at a cascade efficiency of  $0.135 \pm 0.005$  NRT, which may be compared to a value of 0.3 NRT in pure Fe obtained at  $T = 100$  K with a Finnis-Sinclair potential yielding an SIA formation energy of 4.9 eV.<sup>54</sup>

The main impact of introducing chromium is found in the relative population of the elements in the defects produced by the cascade. In Fe-5Cr, where the Fe-Cr dumbbell is more stable than the pure Fe-Fe dumbbell, the fraction of chromium atoms in the surviving interstitial defects is as large as 19%, fairly independent of recoil energy. The mixed dumbbells are less mobile than pure Fe interstitials, and will thus act as obstacles for migration of Fe interstitial clusters. In Fe-20Cr, where the mixed Fe-Cr and pure Fe-Fe dumbbells have about the same energy, chromium atoms constitute roughly 30% of the interstitial atoms.

## VI. CONCLUSIONS

The set of EAM potentials for Fe-Cr alloys implemented in the present work yield activation energies for vacancy migration in the pure elements that are in very good agreement with experimental data. The predicted SIA formation energies arising from fitting to thermal expansion coefficients are higher than values obtained by other authors using both EAM and *ab initio* methods. While electron irradiation data seems to support lower numbers, the stored energy release measured in neutron irradiated samples is compatible with our results. Our potentials further correctly predict the  $\langle 110 \rangle$  interstitial to be the stable form in both the pure elements as well as in the alloy.

Applied to simulation of thermal aging, there is no sign of precipitation taking place when using the potential fitted to the negative formation energy previously calculated for ferromagnetic Fe-5Cr. KMC simulations using the potential fitted to the mixing enthalpy of Fe-20Cr yield formation of Cr clusters on a time and temperature scale that is in good agreement with measurements of hardening in high Cr binary alloys.

We predict that the  $\langle 110 \rangle$  Fe-Cr and Cr-Cr dumbbells are

more stable than the corresponding defect in pure iron. Consequently, Cr will tend to end up in defect structures forming during cooling down of recoil cascades, and we register that 19% of the interstitial atoms in Fe-5Cr are chromium atoms.

The total number of defects surviving after recoil cascades is smaller than predicted by Fe potentials from the literature. This fact is directly related to the higher SIA formation energy. For damage energies between 10 and 20 keV, we obtain a cascade efficiency of  $0.135 \pm 0.005$  NRT at  $T = 100$  K, which in part may explain the long standing mystery of the small number of freely migrating defects observed in experiments.<sup>55</sup>

## ACKNOWLEDGMENTS

The authors would like to thank I. Abrikosov, A. Almazouzi, L. Malerba, B. Singh, D. Bacon, and Y. Osetski for inspiring discussions. This work was supported in part by the Svensk Kärnbränslehantering AB (J.W.), EU 5th FP project SPIRE (J.W., R.C., and V.P.), STINT, EURATOM, and the Swedish Council (P.O.), and Svenskt Kärntekniskt Centrum (C.L.).

- 
- <sup>1</sup>E. Little and D. Stow, *J. Nucl. Mater.* **87**, 25 (1979).  
<sup>2</sup>F. Garner, M. Toloczko, and B. Sencer, *J. Nucl. Mater.* **276**, 123 (2000).  
<sup>3</sup>R. Fischer, E. Dulis, and K. Carroll, *Trans. AIME* **197**, 690 (1953).  
<sup>4</sup>E. Little and L. Stoter, in *Effect of Radiation on Materials, ASTM STP* (1982), Vol. 782, p. 207.  
<sup>5</sup>H. Kuwano, *Trans. JIM* **26**, 473 (1985).  
<sup>6</sup>M. Miller, J. Hyde, A. Cerezo, and G. Smith, *Appl. Surf. Sci.* **87/88**, 323 (1995).  
<sup>7</sup>M. Mathon, Y. Carlan, G. Geoffrey, X. Averty, A. Alamo, and C. de Novion, *J. Nucl. Mater.* **312**, 236 (2003).  
<sup>8</sup>R. Johnson, *Phys. Rev. B* **39**, 12554 (1985).  
<sup>9</sup>A. Voter, in *Intermetallic Compounds, Principles*, edited by J.H. Westbrook and R.L. Fleischer (Wiley, New York, 1995), Vol. 1.  
<sup>10</sup>M. Finnis and J. Sinclair, *Philos. Mag. A* **50**, 45 (1984).  
<sup>11</sup>A. Calder and D. Bacon, *J. Nucl. Mater.* **207**, 25 (1993).  
<sup>12</sup>G. Ackland, D. Bacon, A. Calder, and T. Harry, *Philos. Mag. A* **75**, 713 (1997).  
<sup>13</sup>M. Daw and M. Baskes, *Phys. Rev. B* **29**, 6443 (1984).  
<sup>14</sup>R. Pasianot, D. Farkas, and E. Savino, *Phys. Rev. B* **43**, 6952 (1991); **47**, 4149(E) (1993).  
<sup>15</sup>G. Simonelli, R. Pasianot, and E. Savino, *Mater. Res. Soc. Symp. Proc.* **291**, 567 (1993).  
<sup>16</sup>G. Simonelli, R. Pasianot, and E. Savino, *Phys. Rev. B* **50**, 727 (1994).  
<sup>17</sup>G. Simonelli, R. Pasianot, and E. Savino, *Phys. Status Solidi* **217**, 747 (2000).  
<sup>18</sup>O. Yifang, Z. Bangwei, L. Shuzhi, and J. Zhanpeng, *Z. Phys. B: Condens. Matter* **101**, 161 (1996).  
<sup>19</sup>T. Konishi, K. Ohsawa, H. Abe, and E. Kuramoto, *Comput. Mater. Sci.* **14**, 108 (1999).  
<sup>20</sup>D. Farkas, C. Schon, M. de Lima, and H. Goldstein, *Acta Mater.* **44**, 409 (1996).  
<sup>21</sup>J. Rose, J. Smith, and J. Ferrante, *Phys. Rev. B* **28**, 1835 (1983).  
<sup>22</sup>J. Adams and S. Foiles, *Phys. Rev. B* **41**, 3316 (1990).  
<sup>23</sup>P. Legrand, Ph.D. thesis, University of Paris, 1993.  
<sup>24</sup>G. Evangelakis, J. Rizos, I. Lagaris, and I. Demetropoulos, *MERLIN*, a portable system for multidimensional minimization, University of Ioannina, 1986.  
<sup>25</sup>J. Rifkin, XMD, Center for Materials Simulation, University of Connecticut, 1999.  
<sup>26</sup>J. Biersack and J. Sieglar, *J. Nucl. Inst. Methods* **141**, 93 (1982).  
<sup>27</sup>K. Katahara, M. Nimalendran, M. Manghnani, and E. Fischer, *J. Phys. F: Met. Phys.* **9**, 2167 (1979).  
<sup>28</sup>S. Burke, R. Cywinski, J. Davis, and B. Rainford, *J. Phys. F: Met. Phys.* **13**, 451 (1983).  
<sup>29</sup>G. White, R. Roberts, and E. Fawcett, *J. Phys. F: Met. Phys.* **16**, 449 (1986).  
<sup>30</sup>G. Speich, A. Schwobele, and W. Leslie, *Metall. Trans.* **3**, 2031 (1972).  
<sup>31</sup>P. Olsson, I. Abrikosov, L. Vitos, and J. Wallenius, *J. Nucl. Mater.* **321**, 84 (2003).  
<sup>32</sup>J. Rayne and B. Chandrasekar, *Phys. Rev.* **122**, 1714 (1961).  
<sup>33</sup>W. Bendick and W. Pepperhof, *Acta Metall.* **30**, 679 (1982).  
<sup>34</sup>L.D. Schepper, D. Segers, L. Dorikens-Vanpraet, M. Dorikens, G. Knuyt, L. Stals, and P. Moser, *Phys. Rev. B* **27**, 5257 (1983).  
<sup>35</sup>M. Lübbhusen and H. Mehrer, *Acta Metall. Mater.* **38**, 283 (1990).  
<sup>36</sup>A. Seeger, *Phys. Status Solidi A* **167**, 289 (1998).  
<sup>37</sup>P. Moser, *Mem. Sci. Rev. Metall.* **63**, 431 (1966).  
<sup>38</sup>H. Bilger, V. Hivert, J. Verdone, J. Leveque, and J. Soulie, in *International Conference on Vacancies and Interstitials in Metals* (Kernforschungsanlage Jülich, Germany, 1968), p. 751.

- <sup>39</sup>F. Nix and D. MacNair, *Phys. Rev.* **60**, 597 (1941).
- <sup>40</sup>H. Schaefer, K. Maier, M. Weller, D. Herlach, A. Seeger, and J. Diehl, *Scr. Metall.* **11**, 803 (1977).
- <sup>41</sup>H. Wollenberger, in *Physical Metallurgy*, edited by R. Cahn and P. Haasen (North-Holland, Amsterdam, 1996), Vol. 2.
- <sup>42</sup>P. Vajda, *Rev. Mod. Phys.* **49**, 481 (1977).
- <sup>43</sup>P. Erhart, *Mater. Res. Soc. Symp. Proc.* **41**, 13 (1985).
- <sup>44</sup>G. Loper, L. Smedskjaer, M. Chason, and R. Siegel, in *Positron Annihilation*, edited by P. Jain, R. Singru, and K. Gopinathan (World Scientific, Singapore, 1985), p. 461.
- <sup>45</sup>H. Schultz, *Mater. Sci. Eng., A* **141**, 149 (1991).
- <sup>46</sup>C. Domain and C. Becquart, *Phys. Rev. B* **65**, 024103 (2002).
- <sup>47</sup>C. Domain (private communication, 2002), quoted in Olsson *et al.*, SCK-CEN-BLG-950.
- <sup>48</sup>H. Maxumoto and M. Kikuchi, *Trans. JIM* **12**, 90 (1975).
- <sup>49</sup>S. Brenner, M. Miller, and W. Soffa, *Scr. Metall.* **16**, 831 (1982).
- <sup>50</sup>J. Hyde, M. Miller, A. Cerezo, and G. Smith, *Appl. Surf. Sci.* **87/88**, 311 (1995).
- <sup>51</sup>C. Domain and C. Becquart, *DYMOKA User's Guide*, 6th ed. (2002).
- <sup>52</sup>G. Grimvall, *Thermodynamic Properties of Materials* (Elsevier, New York, 1999).
- <sup>53</sup>G. Vineyard, *J. Phys. Chem. Solids* **3**, 121 (1957).
- <sup>54</sup>R. Stoller, G. Odette, and B. Wirth, *J. Nucl. Mater.* **251**, 49 (1997).
- <sup>55</sup>L. Rehn, *J. Nucl. Mater.* **174**, 144 (1990).



# Relation between thermal expansion and interstitial formation energy in pure Fe and Cr

Janne Wallenius<sup>a,b,\*</sup>, Pär Olsson<sup>b</sup>, Christina Lagerstedt<sup>a</sup>

<sup>a</sup> Department of Nuclear and Reactor Physics, KTH, AlbaNova University Centre, Stockholm 10691, Sweden

<sup>b</sup> Department of Neutron Research, Uppsala University, Uppsala, Sweden

## Abstract

By fitting a potential of modified Finnis–Sinclair type to the thermal expansion of ferromagnetic Fe and paramagnetic Cr, stability of the  $\langle 110 \rangle$  self-interstitial atom is obtained. The resulting potentials are relatively hard, yielding high SIA formation energies. Less hard potentials give lower interstitial formation energy, but predict too small thermal expansion. We also show that the formation energy of the  $\langle 111 \rangle$  SIA depends on distances in-between the 2nd and 3rd neighbour. By raising the value of the pair potential in this region, the energy difference with respect to the  $\langle 110 \rangle$  configuration calculated with VASP in the PAW approximation can be reproduced.

© 2004 Elsevier B.V. All rights reserved.

**Keywords:** Finnis–Sinclair potential; Iron; Chromium; Thermal expansion

## 1. Introduction

Conventional wisdom has it that the properties of Cr cannot be fitted by a many-body potential including only central interactions [1]. The present authors have however shown that paramagnetic Cr, having a positive Cauchy pressure, may be described by a classical EAM potential [2]. In our previous work, the many-body term was fixed in

an arbitrary fashion. Here, we introduce a modified Finnis–Sinclair term to obtain the many body interaction for Fe and Cr in a consistent manner. We further refit our potentials to exactly reproduce elastic constants measured at 0 K and recent ab initio data for vacancy formation energies. As these properties only determine the value and shape of the potential in the vicinity of perfect lattice distances, we use thermal expansion data to fit our potentials inside the first nearest neighbour distance. In what follows, we will account for details of the fitting procedure, comparing the performance of the resulting iron potential with those of other authors. We clarify the difference

\* Corresponding author. Tel.: +46 8 5537 8193; fax: +46 8 5537 8465.

E-mail address: [janne@neutron.kth.se](mailto:janne@neutron.kth.se) (J. Wallenius).

between EAM and FS type of potentials and discuss the impact of the shape of the potential in-between 2nd and 3rd neighbours on the relative stability of self-interstitial configurations.

## 2. Modified Finnis–Sinclair potentials for Fe and Cr

In previous work [2], we found that by fitting an EAM potential to thermal expansion data of iron, we could obtain stability of the  $\langle 110 \rangle$  SIA if the shape of the many-body function given by the Rose expression was fixed *before* stiffening the pair interaction inside the nearest neighbour distance. This approach obviously is somewhat arbitrary. In order to arrive at a physically consistent procedure, we instead choose to cast our potentials in the effective pair form [1], using a modified Finnis–Sinclair expression for the many-body term [3]. In the effective pair approach, it is assumed that the derivative of the many-body term is set to zero for the free electron density of the perfect crystal. As a result,  $C'$ ,  $C_{44}$ ,  $a_0$  and the unrelaxed vacancy formation energy are given exclusively by the pair potential, while the bulk modulus and the cohesive energy are fitted by the many-body term, i.e. the contribution to the total energy from the valence electron density. Consequently we need only the sum of two splines to fit the pair potential exactly to the selected properties, if we adopt the spline cut-offs as fitting parameters.

The following parametric form of the pair interaction terms is assumed:

$$\Phi(r) = \sum_{i=1}^n a_i (r - r_i)^3 H(r_i - r). \quad (1)$$

Here,  $r_i$  are cut-offs of the cubic splines used to represent the potential,  $H$  is the Heaviside step function and  $a_i$  are spline coefficients. Three parameters are required to fit the bulk modulus and cohesive energy with the many-body term, as the condition of zero derivative at equilibrium is imposed. We hence write the modified Finnis–Sinclair expression as

$$F(\rho) = A_0 \sqrt{\rho} + A_1 \rho + A_2 \rho^2, \quad (2)$$

where the term proportional to the square of the free electron density  $\rho$  corresponds to the electron kinetic energy neglected in the original derivation of the second moment tight binding approximation [4]. The term linear in electron density may be transferred to the pair interaction, if desired. We emphasize that the valence electron density in the Finnis–Sinclair formalism includes electrons generated by the atom at the position where the density is calculated. In the EAM model these electrons are neglected, which lead to inconsistencies in the case of alloys. Hence we should adopt electron density functions that are finite at the origin, here we assume a Fermi–Dirac function

$$\phi(r) = \frac{N}{1 + \text{Exp}[(r - R)/a]}, \quad (3)$$

where the norm  $N$  is set for the equilibrium electron density to reproduce the number of  $d$ -band electrons calculated with the ab initio method described in [5], being 6.56 for Fe and 4.61 for Cr.

Having fitted six properties of ferromagnetic iron at 0 K exactly, it was found that adding a single spline was sufficient to reproduce measured thermal expansion coefficients up to  $T = 500$  K, where effects of magnetic transitions start to play a role. A similar procedure was undertaken for Cr, with elastic constants of paramagnetic Cr at 0 K obtained by extrapolation from high temperature data [6], adopting thermal expansion coefficients of Cr–5V [7]. In the case of Cr, it was found that four splines in the representation of the pair interaction were required to achieve a good fit. Table 1 shows the resulting potential parameters for ferromagnetic Fe and paramagnetic Cr.

In Table 2 properties calculated with the above parametrised iron potential are compared with experiment, VASP calculations and the Fe-potential of Mendelev [3]. Note that the PAW approximation used by us when running VASP gives higher SIA formation energies than ultra-soft pseudo potentials [8] or the procedure used in SIESTA [9]. Our potential reproduces better the measured activation energy for vacancy self-diffusion than any other potential in the literature. It over-estimates the SIA formation energy measured in electron irradiation [10], but provides correct

Table 1

Spline coefficients ( $a_i$ ), cut-offs ( $r_i$ ), FS-coefficients ( $A_i$ ) and electron density parameters of the here fitted potentials

|    | $a_1$     | $a_2$      | $a_3$      | $a_4$ | $r_1$ | $r_2$ | $r_3$ | $r_4$ |
|----|-----------|------------|------------|-------|-------|-------|-------|-------|
| Fe | +4.276043 | -17.642833 | -1280      | -     | 1.610 | 1.328 | 0.969 | -     |
| Cr | +4.023728 | -71.420562 | +71.364433 | -450  | 1.610 | 1.223 | 1.151 | 0.967 |
|    | $A_0$     | $A_1$      | $A_2$      | $N$   | $R$   | $a$   |       |       |
| Fe | -1.387616 | +0.216403  | +0.004223  | 0.800 | 2.650 | 0.20  |       |       |
| Cr | -1.471893 | +0.345254  | +0.000360  | 0.431 | 2.878 | 0.25  |       |       |

The cut-offs are given in units of 1st neighbour distance.

Table 2

Properties of  $\alpha$ -Fe calculated with the Finnis–Sinclair potential given in Table 1

|  | This work     | Experiment             | VASP-PAW | Mendelev |
|--|---------------|------------------------|----------|----------|
| $a_0$ (Å)                              | 2.860         | 2.860                  | 2.83     | 2.855    |
| $B$ (GPa)                              | 173           | 173 [11]               | -        | 178      |
| $C'$ (GPa)                             | 52.5          | 52.5 [11]              | -        | 49.2     |
| $C_{44}$ (GPa)                         | 122           | 122 [11]               | -        | 116      |
| $E_{\text{coh}}$ (eV)                  | 4.28          | 4.28                   | -        | 4.01     |
| $E_{\text{vac}}^f$ (eV)                | 2.15          | $2.0 \pm 0.2$ [12]     | 2.12     | 1.73     |
| $E_{\text{vac}}^{\text{SD}}$ (eV)      | 2.95          | $3.0 \pm 0.1$ [13]     | -        | 2.38     |
| $E_{\text{fcc}} - E_{\text{bcc}}$ (eV) | 0.07 (0.09)   | 0.05 [14]              | 0.09     | 0.12     |
| $E_{(110)}^f$ (eV)                     | 6.53          | $3.0\text{--}5.4$ [10] | 4.01     | 3.45     |
| $E_{(110)}^f - E_{(111)}^f$ (eV)       | -0.04 (-0.67) | -                      | -0.67    | -0.50    |

Comparison is made with experiment, VASP ab initio calculations made by us in the PAW approximation, and Mendelev's FS-potential. Values given in parentheses are obtained after modifying the potential in-between 2nd and 3rd neighbour distances, as described in the text.

configuration stability, using just three splines. Mendelev's FS-potential, using 15 splines for the pair interaction, reproduces better  $E_{(110)}^f - E_{(111)}^f$  but yields too low vacancy activation energy.

Thermal expansion coefficients as function of temperature are displayed in Fig. 1. The potential of Mendelev et al. yields too small expansion coefficients. This is typical for potentials predicting "low" SIA formation energies, being relatively soft inside the nearest neighbour distance.

In order to further analyse the dependence of the interstitial formation energy on the shape of the potential, the relaxed distances to neighbouring atoms were calculated. It was found that the  $\langle 111 \rangle$  configuration had a larger number of neighbours in-between 3.2 and 3.5 Å, a region where the fitted properties provide very little information. Hence, by increasing the value of the pair potential in this region, the formation energy of the  $\langle 111 \rangle$  SIA as well as the *fcc* crystal energy is raised, while

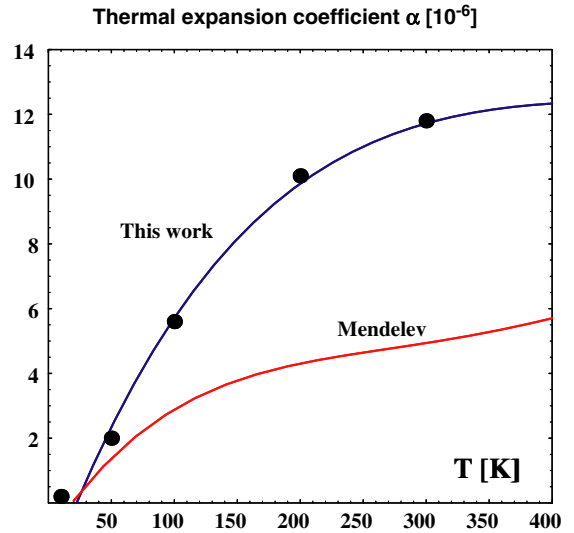


Fig. 1. Thermal expansion coefficient for  $\alpha$ -iron as function of temperature. Filled circles denote experimental data [15], lower solid line values obtained with the potential of Mendelev and co-workers.



leaving other properties untouched. Multiplying the effective pair interaction with  $1 - 0.79 \times \text{Exp}[-(r - 3.52)/0.006]$ , the difference in energy between the  $\langle 111 \rangle$  and  $\langle 110 \rangle$  configurations is raised to 0.67 eV, identical to the value calculated with VASP. The modification changes the potential by a factor less than  $10^{-5}$  at distances below 3.0 Å. The *fcc* energy is raised by 0.02 eV to a value in agreement with VASP calculations. A similar effect on the relative stability of the SIA:s is obtained by imposing a short range cut-off [16,17], though in the present case the magnitude of the SIA energy difference is considerably larger, thanks to stiffening at distances inside the nearest neighbour.

### 3. Conclusions

A systematical procedure for fitting a potential of modified Finnis–Sinclair type to elastic constants and thermal expansion of ferromagnetic Fe and para-magnetic Cr has been presented. The potentials obtained yield values for vacancy activation energy in good agreement with experiment, but overestimate absolute magnitude of interstitial formation energies. Stability of the  $\langle 110 \rangle$  SIA in Fe is obtained without any additional effort. By further modifying the pair interaction at distances in-between 2nd and 3rd neighbour, the energy difference between  $\langle 111 \rangle$  and  $\langle 110 \rangle$  configurations calculated with VASP in the PAW approximation (0.67 eV) is reproduced.

### Acknowledgements

The authors would like to thank G. Ackland, V. Pontikis, L. Malerba, D. Terentyev, R. Chakarova and I. Abrikosov for fruitful discussions and advice. This work was funded by the European Commission, SKB and SKC.

### References

- [1] R.A. Johnson, D.J. Oh, *J. Mater. Res.* 4 (1989) 1195.
- [2] J. Wallenius et al., *Phys. Rev. B* 69 (2004) 094103.
- [3] M.I. Mendeleev et al., *Philos. Mag. A* 83 (2003) 3977.
- [4] A.E. Carlsson, N.W. Ashcroft, *Phys. Rev. B* 27 (1983) 2101.
- [5] P. Olsson et al., *J. Nucl. Mater.* 321 (2003) 84.
- [6] J. Wallenius et al., *J. Nucl. Mater.* 329 (2004) 1175.
- [7] G.K. White, R.B. Roberts, E. Fawcett, *J. Phys. F* 16 (1986) 449.
- [8] C. Domain, C.S. Becquart, *Phys. Rev. B* 65 (2002) 024103.
- [9] C.C. Fu, F. Willaime, P. Ordejon, *Phys. Rev. Lett.* 92 (2004) 175503.
- [10] H. Bilger et al., *Int. Conf. on Vacancies and Interstitials in Metals*, Kernforschungsanlage Jülich, September 1968, p. 751.
- [11] J.A. Rayne, B.S. Chandrasekar, *Phys. Rev.* 122 (1961) 1714.
- [12] L. De Schepper et al., *Phys. Rev. B* 27 (1983) 5257.
- [13] M. Lübbehusen, H. Mehrer, *Acta Metall. Mater.* 38 (1990) 283.
- [14] W. Bendick, W. Pepperhof, *Acta Metall.* 30 (1982) 679.
- [15] F.C. Nix, D. MacNair, *Phys. Rev.* 60 (1941) 597.
- [16] G. Simonelli, R. Pasianot, E.J. Savino, *Mater. Res. Soc. Symp.* 291 (1993) 567.
- [17] G. Ackland et al., *Philos. Mag. A* 75 (1997) 713.

*Paper submitted for the Proceedings of the  
Symposium on Microstructural Processes in Irradiated Materials  
San Francisco, CA, 13-17 February 2005  
(Annual TMS meeting)  
To be published as special issue of the Journal of Nuclear Materials*

## **Effect of the interatomic potential on the features of displacement cascades in $\alpha$ -Fe: a molecular dynamics study**

D. Terentyev<sup>1,2</sup>, C. Lagerstedt<sup>3</sup>, P. Olsson<sup>4</sup>, K. Nordlund<sup>5</sup>, J. Wallenius<sup>3</sup>, C.S. Becquart<sup>6</sup>  
and L. Malerba<sup>1,\*</sup>

<sup>1</sup>*SCK•CEN, the Belgian Nuclear Research Centre, Boeretang 200, B-2400 Mol, Belgium*

<sup>2</sup>*Physique des Solides Irradiés et des Nanostructure CP234s, Université Libre de Bruxelles, Bd. du Triomphe, B-1050 Brussels, Belgium*

<sup>3</sup>*Dept. of Nuclear and Reactor Physics, Royal Institute of Technology  
Roslagstullsbacken 21, SE-106 91 Stockholm, Sweden*

<sup>4</sup>*Dept. of Neutron Research, Ångström Laboratory, Uppsala University  
Box 525, SE-751 20 Uppsala, Sweden*

<sup>5</sup>*Accelerator Laboratory, University of Helsinki, POB 43 (Pietari Kalmin katu 2) FIN-00014, Finland*

<sup>6</sup>*Laboratoire de Métallurgie Physique et Génie des Matériaux, UMR-8517, Université de Lille I, F-59655 Villeneuve d'Ascq Cedex, France*

### **Abstract**

The primary state of damage obtained in molecular dynamics (MD) simulations of displacement cascades in  $\alpha$ -Fe, particularly the fraction of point-defects in clusters, depends on the interatomic potential used to describe the atomic interactions. The differences may influence the microstructural evolution predicted in damage accumulation models which use results from MD cascade simulations as input. In this work, a number of displacement cascades of energy ranging from 5 to 40 keV have been simulated using the same procedure with four different interatomic potentials for  $\alpha$ -Fe, each of them providing, among other things, varying descriptions of self-interstitial atoms (SIA) in this metal. The behaviour of the cascades at their different phases and the final surviving defect population have been studied and compared applying the same cascade analysis criteria for all potentials. The outcome is discussed trying to identify the characteristics of the potential that have the largest influence on the predicted primary state of damage.

**Keywords:** Molecular Dynamics, Displacement Cascades, Interatomic Potentials,  $\alpha$ -Iron

**PACS codes:** 31.15.Qg; 61.72.Cc; 34.20.Cf; 61.82.Bg

---

\* Corresponding author, Phone #: +32-14-333090, Fax #: +32-14-321216, e-mail: lmalerba@sckcen.be

## 1. Introduction

Displacement cascades are the fundamental process of radiation damage production under neutron and ion irradiation. Their study by means of numerical simulation based on the use of an interatomic potential dates back to the 1960s [1-3]. In these pioneering works, the choice of the potential and the dependence of the results on it were priority issues [1]. On the contrary, over the last fifteen years, in spite of a real boom of displacement cascade simulations using many-body potentials [4-17], relatively little attention has been paid to this problem [15,16]. Nonetheless, different potentials do appear to produce cascades with different features, as demonstrated in a review of existing results for  $\alpha$ -Fe, proposed in these proceedings as companion paper to the present work [17]. Therefore, the question of determining which characteristics of the interatomic potential are mostly responsible for the result of the simulation arises as an important one. This paper strives to address this question, by comparing the characteristics of cascades simulated by molecular dynamics (MD) using four recent potentials for  $\alpha$ -Fe, each providing different descriptions of point-defects and featuring different threshold displacement energies (TDE) and stiffness. The comparison is significant because a sufficient number of cascades per case was simulated with the different potentials following exactly the same procedure and analysed using the same criteria. Therefore, differences in the results can only be ascribed to the inherent features of the potential used.

## 2. Simulation technique

### 2.1 Interatomic potentials

Four potentials for  $\alpha$ -Fe were used for the MD simulations here reported, namely: (i) the short-range (cutoff between 2<sup>nd</sup> and 3<sup>rd</sup> nearest neighbour distance) Finnis-Sinclair-type potential proposed by Ackland et al. [18], henceforth denoted as ABC; (ii) the long-range (cutoff between 3<sup>rd</sup> and 4<sup>th</sup> nearest neighbour distance) embedded-atom method (EAM) potential fitted by Chakarova et al. [19], henceforth denoted as CWP; (iii) the long-range EAM potential recently developed by Ackland et al. [20], denoted as AMS; and (iv) a

version of the long-range EAM potential recently developed by Wallenius et al. [21], denoted as WOL. These potentials were selected for being relatively recent and for providing significantly different descriptions of, in particular, self-interstitial atoms (SIA). While CWP incorrectly predicts the  $\langle 111 \rangle$  crowdion to be the most stable configuration, ABC, AMS and WOL feature the correct stability of the  $\langle 110 \rangle$  dumbbell. However, the energy difference between these two configurations is very small according to ABC and increasingly larger according to WOL and AMS (see Table 1, where the main properties of the four potentials are summarised). AMS belongs to a family of potentials for  $\alpha$ -Fe which has been shown to reproduce fairly closely the behaviour of the SIA as described by *ab initio* calculations [41]. WOL, on the other hand, predicts formation energies that are too large for all SIA configurations. These different descriptions of the SIA are expected to influence the mobility of SIA and SIA clusters predicted by each of these potentials [42,43]. In particular, the mobility of the SIA will be lower according to AMS, because rotation to and glide along the  $\langle 111 \rangle$  direction are not favoured compared to other potentials [43]. The selected potentials also exhibit partially different TDE and different range ( $R$ ) and stiffness ( $S$ ). The latter parameters are defined, respectively, as the interatomic distance where the interaction energy equals 30 eV and the gradient of the potential at the same distance. These magnitudes have been introduced in ref. [44] to describe the behaviour of the potential in the intermediate interval of interatomic distances, where the transition between near-equilibrium atomic oscillations and high energy regime occurs. In this interval, the many-body potentials used for MD simulations of cascades are typically joined to a high energy pair potential, more appropriate to describe collisions at close distances (stiffening of the potential, see e.g. [5,8,15]). The most frequently used high energy pair potential is the so-called ZBL universal potential [45]. The function used to smoothly join the equilibrium potential to the ZBL is *arbitrarily* chosen and the only criterion generally used to test it is that the TDE should be reasonable [5,8,15]. As an illustration of this point, in Fig. 1 the curves for the Fe-Fe pair interaction corresponding to the four potentials used in this work are presented. It can be seen that, although eventually, for high enough energies, all curves join the ZBL, the way the connection is made can greatly differ in the intermediate energy and distance region, thereby leading to possible differences in the cascade outcome. In particular, the parameters  $R$  and  $S$  have been shown, in a binary collision approximation

(BCA) study [44], to correlate with the number of replacement collision sequences (RCS) of the cascade. In addition, the stiffness at higher energies ( $\sim 200$  eV), here denoted as  $U$ , has been seen to influence the cascade density [44]. This BCA study suggests therefore that the features of the function chosen to stiffen the potential may have an important role on the outcome of the cascade. This suggestion is considered and tested here in the case of MD cascade simulations.

## 2.2 Cascade simulation

All simulations were performed using the MD code Dymoka [15] and following standard practice [4-16]. A block of atoms was initially equilibrated for 1 ps at 100 K. After equilibration, temperature was not controlled any more (microcanonical statistical ensemble with periodic boundary conditions) as this parameter has been shown to have negligible effect on the cascade simulation results [12,46]. However, the average temperature of the box at the end of the simulation was recorded and was seen never to rise by more than 100-200 K, compared to the initial temperature. The cascade was initiated by imparting the desired kinetic energy to a primary knock-on atom (PKA, or recoil), here referred to as *cascade energy*. Note that this energy will entirely go into defect creation and atomic oscillations, since electronic excitation is not an effect included in the simulation. Therefore, the energy of the corresponding *real* PKA is higher (see e.g. ref. [12]). The PKA was chosen to be at the centre of the cubic box and to move along  $\langle 135 \rangle$  directions in order to avoid channelling [11,12]. The cascade energies ranged between 5 and 40 keV and at least 10 cascades per potential and energy were produced. This is on the order of the number of cascade simulations per case typically produced in past, high-energy MD cascade investigations in  $\alpha$ -Fe [4-15,46] and is therefore considered to be enough to have statistics comparable with previously published studies. The cascade evolution was visually monitored in each case during the collisional and post-collisional stages, to make sure that there was no self-interaction when boundary crossing occurred [12]. The size of the box was increased for increasing cascade energies, as summarized in Table 2, and the box-size/cascade-energy/ ratio was kept comparable with, or larger than, the same ratio in ref. [12]. It was decided that the same box-size was to be used for simulations of the same

cascade energy for all four potentials, independently of the cascade volume provided by the potential. This decision made it impossible to simulate 40 keV cascades with WOL, because of the particularly large volume of cascades according to this potential (see below) and the subsequently unavoidable self-interaction.

In order to ensure that the finite difference method used in the MD code to integrate the equations of motion does not produce uncontrolled errors, the time-step,  $\Delta t$ , was adapted to the cascade phase as summarised in Table 3. During the ballistic phase, when some atoms possess very high kinetic energy and undergo long displacements in very short times,  $\Delta t$  was set to  $\sim 10^{-17}$  s (within this time, even the displacement of an Fe atom with 40 keV of kinetic energy is still on the order of  $10^{-3}$  nm, which is sufficiently short to guarantee the stability of the algorithm). During the post-collisional phase, in order to speed up the simulation without affecting the precision,  $\Delta t$  was extended to  $\sim 10^{-16}$  s. After the recombination phase of the cascade, the near-equilibrium evolution was followed for  $\sim 23$  ps using, for the last 10 ps, the typical time step of MD simulations ( $\Delta t \sim 10^{-15}$  s), until the block of atoms was fully thermalised. The temperature reached in the box at this point was recorded and used to determine the temperature increase induced by the introduction of the PKA.

### 2.3 Cascade analysis

Point-defects were identified and counted in two ways: (1) using the Wigner-Seitz (WS) cell method, and (2) using "displacement" (also called "equivalent spheres") analysis. The former method requires WS cells to be defined around each perfect lattice position: an empty cell means a vacancy, while two (or more) atoms in the same cell mean an interstitial configuration. The second method corresponds to using spheres instead of WS cells: the distance between the perfect lattice position and the displaced atom is measured and appropriate cut-off radii are used to decide whether a displacement has occurred and to identify the defect type [5,8]. This method was mainly used for comparison purposes, to make sure that the criterion used to identify point-defects did not significantly influence the result of the analyses. Either way, the evolution in time of the number of defects can be monitored so as to identify (i) the peak stage, in terms of time since cascade initiation, in

correspondence with the maximum number of defects, (ii) the recombination, or relaxation, phase and (iii) the number of surviving Frenkel pairs (FP). The defect analysis also allowed the defect positions to be recorded, thereby enabling the cascade evolution to be visualised with the aid of appropriate tools. Through visualisation, a rough estimate of the number of subcascades produced at high enough energy could be given as well.

As an indication of the duration of the recombination phase, which is roughly coincident with the thermal spike, the characteristic relaxation time,  $\tau_r$ , was also determined. Following Calder and Bacon [5], this parameter was estimated using an exponential decay approximation from peak time ( $t_{peak}$ ) for the number of FP ( $v_{FP}$ ) as a function of time:  $\{v_{FP} - v_{FP}^{end}\}(t - t_{peak}) = A \exp[-(t - t_{peak})/\tau_r]$ , where  $v_{FP}^{end}$  is the number of FP that survived recombination at the final, steady state of the cascade.

The cascade volume and density at peak stage were evaluated using so-called *component analysis*, described in detail elsewhere [47,48]. According to this procedure, the volume of the cascade is associated with an ellipsoid, whose axes (*components*) are defined based on the variance of the spatial point-defect distribution. The major axis has the direction maximising the variance, the second one maximises the variance of the distribution projected onto a plane perpendicular to the first one, and the third one has the direction minimising this variance. These directions are parallel to the directions of the eigenvectors of the covariance matrix of the point-defect distributions and the associated eigenvalues are the variances of the distribution projected onto the directions of the eigenvectors. Thus, the problem is reduced to the diagonalisation of a 3×3 symmetrical, real and positive matrix, which is a straightforward operation. This method is of course not completely justified when subcascade formation becomes important. Still, it provides a reference for comparison purposes, if used systematically for all cascades.

The number of defects in clusters (and the number of clusters) produced during the evolution of the cascade were determined using an automated procedure: point-defects located at a mutual distance below a certain cutoff were searched for and associated with the same cluster. However, the situation at the end of the cascade was further analysed by visual inspection. Different criteria (i.e. different cutoff distances) for the automated procedure were used: vacancy clusters were defined using both 2<sup>nd</sup> and 4<sup>th</sup> nearest neighbour (nn) criteria [12] and SIA clusters using both 1<sup>st</sup> [8,15] and 3<sup>rd</sup> nn [49] criteria. The visual

inspection was used in addition because it has been observed that automated procedures tend to provide somewhat smaller fractions of SIA in clusters [50].

### **3. Results**

#### **3.1 Peak stage and recombination phase**

The main features characterising the cascade peak stage are the maximum number of defects, the time elapsed from the initiation of the cascade when this number is reached (peak time), the cascade volume (according to the component analysis) and the cascade density (i.e. the number of defects per unit volume, given by the ratio between the maximum number of defects and the cascade volume, as provided by the component analysis), all of them as functions of cascade energy. Another feature that can be roughly estimated by visually inspecting the shape of the cascade at peak time is the number of subcascades.

The number of defects and the cascade density at peak time are shown in Fig. 2 for all four potentials used in this work. Clearly, WOL provides significantly less defects at peak time than any other potential and the cascade density is the smallest as a consequence of a large average cascade volume (figure not shown). At the other extreme, AMS produces the largest number of defects at peak time (a factor 2 to 5 compared to WOL) and exhibits the highest cascade density. The other two potentials lie in-between, with the ABC density closer to AMS and the CWP density closer to WOL. Fig. 3 shows the relaxation time as a function of cascade energy for the four potentials and it appears that the potential ranking according to this parameter is roughly the same as for the peak number of defects and cascade density. This fact will be discussed below.

Fig. 4 shows the average number of subcascades produced versus cascade energy, obtained by visual inspection. With WOL, the cascades appeared too dilute for subcascades to be identified, so no curve is given. These curves must be taken as indicative only, due to the arbitrariness of the criterion used to define a subcascade (visual appearance) and to the fact that the number of simulated cascades is too small to consider the sample statistically representative and to be fully quantitative in this particular case. The impression is,



however, that only above 20 keV can the average number of subcascades be larger than one, i.e. cascade splitting actually occurs only above this threshold, in agreement with what was reported by Stoller [12]. Finally, CWP seems to exhibit a stronger tendency to result in cascade splitting than the other potentials.

## 3.2 Primary state of damage

### 3.2.1 Defect production efficiency

Fig. 5 presents the defect production efficiency,  $\eta = v_{FP}^{end} / v_{NRT}$ , versus cascade energy, for all four potentials considered in this work. Here,  $v_{NRT} = 0.8E_D / 2E_d$  is the standard number of NRT displacements [51], where  $E_D$  is the damage energy, coincident with the cascade energy in the MD simulation (i.e. the kinetic energy imparted to the recoil in the simulation), and  $E_d$  is an average TDE which, following common practice [7,12,15,39,40,52], has been taken to equal 40 eV. Potentials providing different TDE (Table 1), as well as different numbers of defects and densities at peak time (Fig. 2), produce roughly the same number of defects at the end of the simulation. The only partial exception is WOL, which stands out for a slightly higher  $\eta$  (note that at peak time this potential produced the *fewest* defects). However, all potentials agree in providing efficiencies in the  $0.3 \pm 0.1$  range, in line with results obtained with other potentials available from the literature and in agreement with existing experimental assessments (see ref. [17] for a discussion on this point). AMS seems to exhibit a minimum efficiency at 10 and 20 keV, the latter minimum being in agreement with the behaviour observed by Stoller and attributed to onset of cascade splitting [12]. However, CWP displays a minimum at 5 keV which is not ascribable to sub-cascade formation above this energy (Fig. 4) and ABC presents an  $\eta$  steadily decreasing with increasing cascade energy, so most likely these minima and maxima should be attributed to statistic oscillations. The main observation is that no significant difference is found in the amount of surviving FP going from one potential to another at the same cascade energy.

### 3.2.2 Defect clustered fractions

The fraction of point-defects found in clusters and the cluster size distribution are fundamental information provided by displacement cascade studies to be used as input in damage accumulation models [53]. In Fig. 6, the point-defect clustered fraction,  $f_t^{cl}$  ( $t = V$  or SIA), is given as a function of cascade energy for the four potentials:  $f_{SIA}^{cl}$  was determined by visual inspection, while  $f_V^{cl}$  is the result of an automated analysis using a 2<sup>nd</sup> nn criterion. These magnitudes are known to be affected by large oscillations and a completely smooth, monotonous behaviour versus cascade energy is hardly ever obtained [12,15]. However, trends can be identified.

In broad agreement with observations made in previous works [7,9,12-14], the SIA clustered fraction tends to increase with increasing cascade energy until saturation well into the subcascade regime. This increase is particularly steep according to CWP and much less according to the other potentials. This fact may have some relationship with the tendency of CWP to form more subcascades (Fig. 4) since subcascade overlap seems to favour the formation of larger clusters [50]. AMS tends to produce smaller fractions of SIA in clusters than the others.

The vacancy clustered fraction, with the exception of a few outlying points, remains fairly constant for all potentials at all cascade energies. Its value is around 0.2-0.3 for three of the four potentials, but AMS stands out for a particularly high value ( $f_V^{cl} \sim 0.4-0.5$ ). This value broadly equals the fraction of SIA in clusters produced by the same potential, which therefore predicts the same amount of vacancies and SIA in cluster.

## 4. Discussion

### 4.1 Number of surviving defects

It is perhaps surprising that potentials which: (i) give different descriptions of point-defects, (ii) predict different TDE and (iii) provide largely different numbers of defects and cascade densities at peak time, end up producing essentially the same number of surviving FP. There must be features of the potentials that induce opposite effects, which compensate each other.

As explained in what follows, Figs. 2 and 3 suggest that the mutually offsetting results may be higher cascade density (and number of defects) at peak time, followed by longer relaxation (recombination) times.

As anticipated in the introduction, work on comparison of potentials performed in the BCA has shown that the cascade density may correlate with the stiffness  $U$  of the repulsive potential at energies around 200 eV: stiffer potentials in that region produce denser cascades [44]. At the same time, the stiffness  $S$  and the range  $R$  at 30 eV correlate with the production of RCS: stiffer and shorter-ranged potentials (i.e. characterised by a high  $S/R$  ratio) favour the process of energy transfer during the binary collision, thereby favouring the production of more, and longer, RCS [44]. In our study, WOL exhibits the largest  $S/R$  ratio ( $\sim 183$ ) and one of the lowest  $U$  and the cascades produced with this potential have the lowest density and a slightly higher number of surviving defects. In addition, at peak time WOL cascades appear very dilute, suggesting that indeed a significant part of the FP were the consequence of RCS (Figure 7). This is in contrast with the "cascade regime", observed and described by Calder and Bacon for cascades above 1 keV [5], characterised by shock-induced collective effects whereby whole regions of the crystal are displaced along close-packed directions. This regime seems to be easily reached with the other three potentials and in the case of AMS, which presents the smallest  $S/R$  ratio ( $\sim 50$ ) and the highest  $U$ , very dense and compact cascades are produced (Figure 7). In line with these observations, it has been observed in Ref. [17] that the potential there denoted as HA-VD [8] has  $S/R \sim 267$ , i.e. the highest of all, and that indeed this potential produces very dilute cascades, with an abnormally high number of surviving FP, as reported also in ref. [15]. Thus, it appears that the correlations observed in the BCA study of ref. [44] between potential stiffness and cascade density or number of RCS hold also in MD simulations. Too high a stiffness and too short a range in the  $\sim 30$  eV energy region, accompanied by a low stiffness at  $\sim 200$  eV, hinders the attainment of a full cascade regime. On the contrary, the attainment of the cascade regime is favoured when the potential is soft and long-ranged in the  $\sim 30$  eV energy region and stiff in the  $\sim 200$  eV energy region.

A full cascade regime involves a high energy density at peak time and the production of a state close to a melt [5]: how close will depend on the actual defect density at peak time and also on the melting point predicted by the potential. The cascade density is therefore an

index of the attainment of the cascade regime. In addition, in a dense and partially melted cascade region, the thermal spike will last longer and lead to more recombinations than in a dilute and still solid cascade region, where defects have been produced mostly by RCS. Consistently, Figs. 2 and 3 show that a higher density correlates not only with a higher number of peak time defects but also, roughly, with a longer relaxation time, i.e. with longer thermal spikes and more defect recombination. In the four potentials considered in this work, a lower  $S/R$  ratio roughly correlates with a higher  $U$  (see Table 1) Thus, a simplified picture based on the  $S/R$  ratio only can be adopted and both the density of the cascade and the relaxation time can be said to scale with the reverse of this ratio. The level of the curves in Figs. 2 and 3 can be hence roughly anticipated from the  $S/R$  value (CWP:  $S/R \sim 101$ ; ABC:  $S/R \sim 73$ ). Low- $S/R$  potentials, such as AMS, induce a full cascade regime and produce at peak time a much higher number of atomic displacements through collective motion (without RCS). However, in this case recombination will also be more important. The two phenomena (a large number of defects at peak time and a long relaxation time), although having the same origin (low  $S/R$ ), will therefore offset each other, eventually leading to a similar number of surviving FP as for potentials with higher  $S/R$ . The latter will in turn exhibit a smaller peak defect number, but also a shorter recombination time and therefore a number of surviving defects similar to that of low- $S/R$  potentials.

Nonetheless, high- $S/R$  potentials, such as WOL, can still produce a higher number of surviving defects, because relaxation is not, or only marginally, assisted by thermal effects and the larger dilution of damage reduces the probability of spontaneous recombination between SIA and vacancies. This effect is only mildly visible in WOL but reaches an extreme manifestation in the case of the HA-VD potential [8,15] discussed in ref. [17].

Thus, potential range and stiffness ( $R$ ,  $S$  and also  $U$ ) appear to offer a means to rationalise some of the cascade features that vary from one potential to another. On the contrary, however surprising it may seem, no explicit correlation is found between the number of defects, both at peak time and in the final defect state, and the TDE values. The potential with the largest average TDE (CWP) *does not* produce the smallest number of defects, during any of the phases of the cascade.

## 4.2 Clustered fraction

While the stiffness of the potential is of use to explain the differences concerning defect production, it is not as useful when it comes to rationalise differences in defect clustered fractions. In this case, the potential exhibiting the most peculiar behaviour is AMS, for which it is easy to see (Fig. 6) that the difference  $f_{SIA}^{cl} - f_V^{cl}$  is very close to zero in most cases. The other potentials display more uniform behaviour, although the steep increase of  $f_{SIA}^{cl}$  with CWP stands out as a peculiarity, too. In order to try to understand the reasons for the differences between AMS and the other potentials, the evolution of the clustered fraction for 23 ps after peak time has been monitored using automated procedures for both vacancies (2<sup>nd</sup> nn criterion) and SIA (3<sup>rd</sup> nn criterion). An example is given in Fig. 8 for cascades at 15 keV (the results for CWP are not presented because they are almost coincident with those of ABC). The reader should be warned that, strictly speaking, clusters cannot be defined at peak time based on a lattice site occupation criterion. In this case, the "clustered fraction" as we define it is in fact simply an index of how many of the displaced atoms appear to be at a mutual distance comparable to the distance between defects in a cluster. The physical interpretation of the "clustered fraction" versus time will therefore keep changing, as will be clear in the discussion below.

According to Bacon et al [9], two mechanisms of SIA cluster in-cascade formation can be devised. Partly they form at the end of the thermal spike, as a consequence of collective atomic motion in conditions of highly enhanced defect diffusion, due to high local temperature; partly by later local defect re-organization, driven by strain-field interaction among neighbouring and mobile SIA and SIA clusters. The upper graph in Fig. 8 reveals that both mechanisms may occur, but their respective weight is different depending on the potential. According to both AMS and ABC, the "clustered fraction" at peak time is close to unity. Since, as mentioned, speaking of clusters is inappropriate at peak time, this is a way of saying that collective atomic displacements are taking place, whereby the displaced atoms remain all very close to each other (high density) and are therefore recognised "as if" they were forming clusters. However, during relaxation this "clustered fraction" drops by about 50%. WOL, on the other hand, produces only a relatively small SIA "clustered fraction" at peak time, a sign that little or no collective displacement of atoms occurs, in

agreement with the above discussion on the dilution of damage, and the subsequent drop is limited to about 10%. That is, with WOL even at peak time the computed "clustered fraction" is mostly due to actual clusters. After relaxation, when the plotted clustered fraction becomes indeed the result of defect clustering, WOL and ABC exhibit similar behaviour: SIAs rearrange themselves into an increasing fraction of defects in cluster, via (perhaps thermally enhanced) diffusion. On the contrary, the fraction of SIA in clusters remains unchanged according to AMS. This is probably the effect of the different SIA mobility predicted by the two classes of potentials. According to AMS, glide of the SIA along the  $\langle 111 \rangle$  close-packed direction is unlikely, because of the large difference between the stable  $\langle 110 \rangle$  configuration and the  $\langle 111 \rangle$  crowdion configuration (see Table 1), which prevents rotation from one to the other. Migration is therefore fully three-dimensional and relatively slow, with an effective energy of  $\sim 0.3$  eV [41,43]. On the contrary, according to the other two potentials glide is possible and the effective SIA migration energy is much lower (a few tens of meV) with a consequently higher mobility [42,43]. Thus, SIA re-organisation via diffusion is possible on the scale of ps with all potentials, except with AMS.

Concerning vacancies, because of their much slower diffusivity compared to SIA, very similarly described by all potentials (Table 1), clustering is a priori only expected to occur during the ballistic phase and the thermal spike (unless collapse, so unusual in  $\alpha$ -Fe, occurs [49]). The lower graph of Fig. 8 shows, however, that this is not always the case. The peak and relaxation time behaviour is, with the three potentials, similar to the SIA case. But later, three different evolutions are possible. According to WOL, the vacancy clustered fraction experiences a mild decrease, most likely because of further, diffusion-driven recombination with rapidly migrating SIA. According to ABC the clustered fraction remains essentially unchanged. But according to AMS a clear increase is seen to occur. This is difficult to explain, because vacancy diffusion should be negligible on a ps scale. Different factors may combine to produce this post-relaxation vacancy clustering. The density of the cascade may be so high that a very small number of vacancy jumps may be sufficient to drive further clustering. Alternatively (or in addition), the temperature in the cascade region during this phase may for AMS be closer to the melting point predicted by the potential, thereby allowing enhanced vacancy diffusion and clustering compared to the other potentials. In fcc

metals, for example, it has been shown that the melting point affects the ion beam mixing and how vacancies are pushed towards the centre of the cascade to cluster [54]. In particular, the fact that following relaxation AMS exhibits a larger  $f_v^{cl}$  compared to the other potentials may be related to partial cascade collapse during the thermal spike and may correlate with either a lower melting point predicted by the potential or a higher cascade core temperature, due to the high density, or both. However, the effect of the melting point becomes negligible when the density of defects is not especially high. Indeed, the melting point of CWP has been calculated to be between 1800 and 1850 K [55], while the melting point of ABC is around 2200 K [56], but no difference in vacancy clustering has been observed. Further studies are therefore in course to clarify the origin of this behaviour of AMS [57]. Still, it is clear that the clustered fractions predicted by a certain potential are determined by a complicated combination of interacting factors, related partly to the point-defect mobility according to the potential, partly to the description that the potential gives of the cascade regime (i.e. to the influence of its stiffness in the repulsive region) and partly to other properties, such as the melting point.

## 5. Conclusions

The main goal of the present paper, driven by the review done in ref. [17], was to produce a set of cascade results for different potentials, adopting standard simulation procedures and rigorously identical analysis techniques, in order to find out whether different potentials provide different results and which, among the potential features, are primarily responsible for the differences. It can be concluded that:

- The number of Frenkel pairs produced in a cascade during the whole displacement process *does not* correlate with the threshold displacement energies predicted by the potential (provided that these are reasonable).
- A correlation is found instead with the stiffness and range of the potential in the region of tens and hundreds of eV interaction, as suggested by BCA studies [44], i.e. in the region of transition between equilibrium and repulsive potential, which is largely arbitrary [5,8,15]. With potentials too stiff and short-ranged in the 30 eV energy region, but with a lower stiffness around 200 eV, replacement collision sequences become the

main mechanism of damage production and a full cascade regime is never reached, even at high cascade energies. The dilute damage produced at peak time in these cases exhibits fewer defects and on average a larger distance between SIA and their vacancies (low density), partially preventing SIA-vacancy recombination during relaxation. On the other hand, a full cascade regime, characterised by collective atomic displacements, massive defect production at peak time, higher damage density and a pronounced thermal spike, is typical of potentials which are soft and long-ranged at low energy ( $\sim 30$  eV) and stiff at higher energy ( $\sim 200$  eV). The length of the thermal spike in this case may however also be influenced by the melting point predicted by the potential.

- In spite of largely different cascade processes, all potentials predict roughly the same final amount of surviving Frenkel pairs (with the only exception of specially pathological cases, as discussed in ref. [17]). This is likely to be the result of mutually offsetting effects of the stiffness. A larger stiffness ( $U$ ) causes a higher defect density at peak time, but also induces, as a consequence, a longer relaxation time with more recombinations, so that the final number of surviving defects is largely independent of the cascade features at peak time.
- Vacancy and SIA in-cascade clustering are potential dependent. Differences are the result of a complicated interplay between different features of the potential, from the description of the mobility of point-defects, to the density of the cascade at peak time (related to the stiffness) and the extent of the thermal spike, as well as the possibility of cascade collapse, which may also depend on the melting point predicted by the potential.

The most worrying conclusion is that the result of cascade simulations using a given potential may be greatly influenced by the partially arbitrary choices made when stiffening the potential in the region of tens to hundreds of eV [5,8,15], i.e. in the region of the transition between the equilibrium part of the potential and the high-energy ZBL pair potential typically used for very short interatomic distances [45]. The fit to the TDE in that region appears to be of little use as a guide for the stiffening [17]. For example, would cascades simulated with the AMS potential, probably the best one available right now for radiation damage in  $\alpha$ -Fe, still predict the same large amount of vacancies in clusters, if the connection in the transition region was significantly stiffer at tens of eV and softer at hundreds of eV? For the moment, there is no answer to this question.



## Acknowledgements

This work required a fairly large amount of CPU time to be performed: four PC clusters, at SCK•CEN, KTH, U. Uppsala and ULB (thanks to M. Hou for allowing its use) were simultaneously exploited for the task. This work, supported by the European Commission under the contract of Association between Euratom and the Belgian, Swedish and Finnish States, was carried out within the framework of the European Fusion Development Agreement (EFDA), task TTMS-007.

## References

- [1] J.B. Gibson, A.N. Goland, M. Milgram and G.H. Vineyard, *Phys. Rev.* 120(4) (1960) 1229.
- [2] C. Erginsoy, G.H. Vineyard and A. Englert, *Phys. Rev.* 133-2A (1964) A595.
- [3] C. Erginsoy, G.H. Vineyard and A. Shimizu, *Phys. Rev.* 139-1A (1965) A118.
- [4] C.A. English, A.J.E. Foreman, W.J. Phythian, D.J. Bacon and M.L. Jenkins, *Mater. Res. Forum* 97-99 (1992) 1.
- [5] A.F. Calder and D.J. Bacon, *J. Nucl. Mater.* 207 (1993) 25.
- [6] D.J. Bacon and T. Díaz de la Rubia, *J. Nucl. Mater.* 216 (1994) 275.
- [7] D.J. Bacon, A. F. Calder, F. Gao, V. G. Kapinos and S. J. Wooding, *Nucl. Instr. & Meth. B*102 (1995) 37.
- [8] R. Vascon and N. V. Doan, *Rad. Eff. & Def. in Solids* 141 (1997) 375; N.V. Doan and R. Vascon, *Annales Phys. C3*, suppl. nr. 3, 20 (1995) 57.
- [9] D.J. Bacon, A. F. Calder, F. Gao, *J. Nucl. Mater.* 251 (1997) 1.
- [10] R.S. Averback and T. Díaz de la Rubia, *Sol. State Phys.* 51 (1998) 281.
- [11] N. Soneda and T. Díaz de la Rubia, *Phil. Mag. A* 78(5) (1998) 995.
- [12] R. E. Stoller, *J. Nucl. Mater.* 276 (2000) 22; R.E. Stoller, G.R. Odette and B.D. Wirth, *J. Nucl. Mater.* 251 (1997) 49-60.
- [13] D.J. Bacon, F. Gao and Yu. Osetsky, *J. Nucl. Mater.* 276 (2000) 1.
- [14] D.J. Bacon, Yu.N. Osetsky, R.E. Stoller and R.E. Voskoboinikov, *J. Nucl. Mater.* 323 (2003) 152.
- [15] C. S. Becquart, C. Domain, A. Legris and J-C. van Duysen, *J. Nucl. Mater.* 280 (2000) 73.
- [16] Yu.N. Osetsky and D.J. Bacon, *Nucl. Instr. & Meth. B* 180 (2001) 85.
- [17] L. Malerba, "Molecular dynamics simulation of displacement cascades in  $\alpha$ -Fe: a critical review", these proceedings.
- [18] G.J. Ackland, D.J. Bacon, A.F. Calder and T. Harry, *Phil. Mag. A*75 (1997) 713.
- [19] R. Chakarova, V. Pontikis and J. Wallenius, "Development of Fe(bcc)-Cr many body potential and cohesion model", Delivery report WP6, SPIRE project, EC contract no. FIKW-CT-2000-00058 (June 2002), available at

- [www.neutron.kth.se/publications/library/DR-6.pdf](http://www.neutron.kth.se/publications/library/DR-6.pdf); P. Olsson, L. Malerba and A. Almazouzi, SCK•CEN Report, BLG-950 (June 2003).
- [20] G.J. Ackland, M.I. Mendeleev, D.J. Srolovitz, S. Han and A.V. Barashev, *J. Phys.: Condens. Matter* 16 (2004) 1.
  - [21] J. Wallenius, P. Olsson and C. Lagerstedt, *Nucl. Instr. & Meth. B* 228 (2005) 122.
  - [22] K. Nordlund, J. Wallenius and L. Malerba "Calculation of threshold energies in  $\alpha$ -Fe", submitted to *Nucl. Instr. & Meth. in Phys. Res. B*.
  - [23] G. Simmons and H. Wang, "Single crystal elastic constants and calculated aggregate properties: A handbook", MIT Press, Cambridge (1971).
  - [24] C. Domain and C.S. Becquart, *Phys. Rev. B* 65 (2001) 024103; C.-C. Fu, F. Willaime and P. Ordejón, *Phys. Rev. Lett.* 92(17) (2004) 175503.
  - [25] C. Kittel, "Introduction to Solid State Physics", 6th edition, John Wiley and Sons, Inc. (1987).
  - [26] W. Bendick and W. Pepperhof, *Acta Metall.* 30 (1982) 679.
  - [27] E.G. Moroni, G. Kresse, J. Hafner, J. Furthmüller, *Phys. Rev. B* 56 (1997) 15629.
  - [28] L. De Schepper et al, *Phys. Rev. B* 27(9) (1983) 5257.
  - [29] K. Maier, H. Metz, D. Herlach and H.-E. Schaefer, *J. Nucl. Mater.* 69&70 (1978) 589.
  - [30] H.-E. Schaefer et al, *Scripta Metall.* 11 (1977) 803; H. Matter, J. Winter and W. Triftshäuser, *Appl. Phys.* 20 (1979) 135.
  - [31] K. Fürderer et al. *Mater. Sci. Forum* 15-18 (1987) 125; A. Seeger, *Phys. Stat. Sol. (a)* 167 (1998) 289.
  - [32] L.J. Cuddy, *Acta Metall.* 16 (1968) 23.
  - [33] T. Tabata et al., *Scripta Metall.* 14 (1983) 1317.
  - [34] C.H. Woo and W. Frank, *Rad. Eff.* 77 (1983) 49; F. Philipp, *Mater. Sci. Forum* 15-18 (1987) 187.
  - [35] F.S. Buffington, K. Hirano and M. Cohen, *Acta Metall.* 9 (1961) 434.
  - [36] V.M. Amonenko, A.M. Blinkin, I.G. Ivantsov, *Phys. Met. Metall.* 17(1) (1964) 54.
  - [37] H. Wollenberger, in: R. Cahn and P. Haasen (Eds.), *Physical Metallurgy*, vol. 2, North-Holland (1996).
  - [38] F. Maury, M. Biget, P. Vajda, A. Lucasson and P. Lucasson, *Phys. Rev. B* 14 (1976) 5303.
  - [39] *Annual Book of ASTM Standard E693-94*, vol. 12.02 (1994).
  - [40] C.H.M. Broeders and A.Yu. Konobeyev, *J. Nucl. Mater.* 328 (2004) 197.
  - [41] F. Willaime, C-C. Fu, M.C. Marinica and J. Dalla Torre, *Nucl. Instr. & Meth. B* 228 (2005) 92.
  - [42] Yu.N. Osetsky et al, *J. Nucl. Mater.* 276 (2000) 65.
  - [43] D. Terentyev and L. Malerba on SIA mobility with different potentials, in preparation.
  - [44] C.S. Becquart, A. Souidi and M. Hou, *Phys. Rev. B* 66 (2002) 134104.
  - [45] J.F. Ziegler, J.P. Biersack and U. Littmark, *The Stopping and Range of Ions in Matter* (Pergamon, New York, 1985).
  - [46] F. Gao, D. J. Bacon, P. E. J. Flewitt and T. A. Lewis, *J. Nucl. Mater.* 249 (1997) 77.
  - [47] M. Hou, *Phys. Rev. B* 31(7) (1985) 4178.
  - [48] A. Souidi, M. Hou, C.S. Becquart and C. Domain, *J. Nucl. Mater.* 295 (2001) 179.
  - [49] N. Soneda, S. Ishino and T. Díaz de la Rubia, *Phil. Mag. Lett.* 81(9) 2001) 649.
  - [50] D.A. Terentyev, L. Malerba and M. Hou, *Nucl. Instr. & Meth. B* 228 (2005) 156.
  - [51] M. J. Norgett, M. T. Robinson and I. M. Torrens, *Nucl. Eng. & Design* 33 (1975) 50.

- [52] W.J. Phytian, A.J.E. Foreman, R.E. Stoller, D.J. Bacon and A.F. Calder, *J. Nucl. Mater.* 223 (1995) 245.
- [53] S.J. Zinkle and B.N. Singh *J. Nucl. Mater.* 199 (1993) 173.
- [54] K. Nordlund, L. Wei, Y. Zhong and R.S. Averback, *Phys. Rev. B (Rapid Comm.)* 57 (1998) 13965; K. Nordlund and R.S. Averback, *Phys. Rev. B* 59 (1999) 20.
- [55] D.A. Terentyev, L. Malerba, P. Olsson and M. Hou, in: *Proceedings of the 7<sup>th</sup> International Workshop on Nondestructive Testing and Computer Simulations in Science and Engineering*, A. I. Melker Editor, SPIE Proceedings, vol. 5400 (2004, The Society of Photo-Optical Instrumentation Engineers), ISBN 0-8194-5323-4.
- [56] E.M. Lopasso, M. Caro, A. Caro and P. E. A. Turchi, *Phys. Rev. B* 68 (2003) 214205.
- [57] C. Lagerstedt, D. Terentyev, P. Olsson, J. Wallenius and L. Malerba, in preparation.

## Tables

**Table 1** – Summary of the main properties of the four interatomic potentials used in this work for cascade simulations. Legend:  $a_0$  (lattice parameter);  $E_{coh}$  (cohesive energy);  $\Delta E_{fcc-bcc}$  (energy difference between the two phases);  $E_V^f$  and  $E_V^m$  (vacancy formation and migration energy);  $Q^{SD}$  (self-diffusion activation energy);  $E_{\langle 110 \rangle}^f$  and  $E_{\langle 111 \rangle}^f$  (SIA configuration formation energy);  $\Delta E_{\langle 111 \rangle \langle 110 \rangle}$  (relative stability of SIA configurations);  $db$  (dumbbell); TDE along the three main directions and in average, including median value, see ref. [22];  $S$  and  $U$  (stiffness) and  $R$  (range), see text.

| <b>Equilibrium properties</b>                        | <b>ABC</b>            | <b>CWP</b>       | <b>AMS</b>               | <b>WOL</b>       | <b>Exp.</b>  | <b>Ab initio</b>             |
|--|-----------------------|------------------|--------------------------|------------------|--|------------------------------|
| $a_0$ [Å] (0 K)                                      | 2.867                 | 2.866            | 2.855                    | 2.860            | 2.86 <sup>a</sup>  | 2.85-2.86 <sup>b</sup>       |
| $E_{coh}$ [eV]                                       | -4.316                | -4.28            | -4.013                   | -4.28            | -4.28 <sup>c</sup>   |                              |
| $\Delta E_{fcc-bcc}$ [meV]                           | 54                    | 50               | 121                      | 47               | 50 <sup>d</sup>  | 35 <sup>e</sup>              |
| <b>Point-defect energies [eV]</b>                    | <b>ABC</b>            | <b>CWP</b>       | <b>AMS</b>               | <b>WOL</b>       | <b>Exp.</b>  | <b>Ab initio<sup>b</sup></b> |
| $E_V^f$  | 1.70                  | 1.54             | 1.71                     | 2.08             | 2.0±0.2 <sup>f</sup> , 1.5 <sup>g</sup> ,<br>1.6±0.10 <sup>h</sup> ,<br>~1.6-1.75 <sup>i</sup> | 1.93-2.09                    |
| $E_V^m$  | 0.78                  | 0.73             | 0.63                     | 0.81             | 0.55 <sup>j</sup> ,<br>0.57±0.14 <sup>k</sup> , (1.3) <sup>l,w</sup>                           | 0.59-0.67                    |
| $Q^{SD} = E_V^f + E_V^m$                             | 2.48                  | 2.27             | 2.34                     | 2.89             | 2.48 <sup>m</sup> -3.13 <sup>n,*</sup>   | 2.52-2.76                    |
| $E_{\langle 110 \rangle}^f$                          | 4.87                  | 4.15             | 3.59                     | 6.45             | Stable config is<br>$\langle 110 \rangle$ db; $E^f=4.7-5^o$                                    | 3.64                         |
| $E_{\langle 111 \rangle}^f$                          | 5.00                  | 4.02             | 4.03                     | 6.87             |  | 4.34                         |
| $\Delta E_{\langle 111 \rangle \langle 110 \rangle}$ | 0.13                  | -0.13            | 0.44                     | 0.42             |  | 0.70                         |
| <b>TDE [eV]</b>                                      | <b>ABC</b>            | <b>CWP</b>       | <b>AMS</b>               | <b>WOL</b>       | <b>Exp.</b>  |                              |
| $\langle 100 \rangle$                                | 18                    | 20               | 18                       | 22               | 17 <sup>p</sup>  |                              |
| $\langle 110 \rangle$                                | 32                    | 48               | 34                       | 28               | >30 <sup>p</sup>   |                              |
| $\langle 111 \rangle$                                | 36                    | 30               | 34                       | 32               | 20 <sup>p</sup>  |                              |
| Mean (Median)  | 45.8±0.4<br>(42)      | 54.5±0.5<br>(54) | 40±0.3<br>(36)           | 41.8±0.3<br>(38) | (40) <sup>q</sup><br>(recomm. value)   |                              |
| <b>Stiffness</b>                                     | <b>ABC</b>            | <b>CWP</b>       | <b>AMS</b>               | <b>WOL</b>       |  |                              |
| R [Å]  | 1.30                  | 1.23             | 1.29                     | 1.11             |  |                              |
| S [eV/Å]   | -95                   | -124             | -65                      | -203             |  |                              |
| U [eV/Å]   | -3448                 | -2511            | -5123                    | -2886            |  |                              |
| <sup>a</sup> Ref [23]                                | <sup>g</sup> Ref [29] |                  | <sup>m</sup> Ref [35]    |                  |  |                              |
| <sup>b</sup> Ref [24]                                | <sup>h</sup> Ref [30] |                  | <sup>n</sup> Ref [36]    |                  |  |                              |
| <sup>c</sup> Ref [25]                                | <sup>i</sup> Ref [31] |                  | <sup>o</sup> Ref [37]    |                  |  |                              |
| <sup>d</sup> Ref [26]                                | <sup>j</sup> Ref [32] |                  | <sup>p</sup> Ref [38]    |                  |  |                              |
| <sup>e</sup> Ref [27]                                | <sup>k</sup> Ref [33] |                  | <sup>q</sup> Ref [39,40] |                  |  |                              |
| <sup>f</sup> Ref [28]                                | <sup>l</sup> Ref [34] |                  |                          |                  |  |                              |

<sup>w</sup> The value 1.3 seems to be the result of not high enough purity of Fe [33]

\* About 15 experimental measurements reported, giving values within this range, see e.g. website: [http://diffusion.nims.go.jp/index\\_eng.html](http://diffusion.nims.go.jp/index_eng.html)

**Table 2** – Summary of recoil energies, simulation box size and number of simulated cascades in this work.

| PKA energy<br>[keV] | Box size<br>[number of atoms] | Number of cascades<br>(per potential) |
|---------------------|-------------------------------|---------------------------------------|
| 5                   | 250000 ( $50a_0$ )            | 10                                    |
| 10                  | 250000 ( $50a_0$ )            | 10                                    |
| 15                  | 432000 ( $60a_0$ )            | 10                                    |
| 20                  | 432000 ( $60a_0$ )            | 10                                    |
| 30                  | 778034 ( $73a_0$ )            | 10                                    |
| 40                  | 778034 ( $73a_0$ )            | 10*                                   |

\* In the case of WOL no 40 keV cascades could be simulated (see text)

**Table 3** – Time-step scheme used for cascade simulations in this work.

| Cascade phase               | Duration       | Adopted time-step |
|-----------------------------|----------------|-------------------|
| Ballistic                   | 0 – 0.5 ps     | 0.01 fs           |
| Post-collisional            | 0.5 – 3.0 ps   | 0.05 fs           |
| Recombination               | 3.0 – 13.0 ps  | 0.1 fs            |
| Short-term defect evolution | 13.0 – 23.0 ps | 0.5 fs            |

## Figure captions

**Figure 1** – Fe-Fe pair interaction curves in the energy and distance intermediate region for the four potentials used in this work.

**Figure 2** – Number of defects (above) and cascade density (below) at peak time versus cascade energy according to the four potentials used in this work. Lines are guides for the eyes. Note that the error bars in the number of defects are "smaller than the symbol".

**Figure 3** – Relaxation time versus cascade energy according to the four potentials used in this work. Lines are linear interpolations used as guides for the eyes.

**Figure 4** – Estimated average number of subcascades (in addition to the single cascade always produced) versus cascade energy according to the four potentials used in this work, after visual inspection. Lines are guides for the eyes. The estimation is necessarily only a very rough one.

**Figure 5** – Defect production efficiency compared to NRT displacements (see text) according to the four potentials used in this work.

**Figure 6** – Fraction of SIA (above) and vacancies (below) in cluster according to the four potentials used in this work. The SIA clustered fraction was determined by visual inspection, while for the vacancies an automated procedure with 2<sup>nd</sup> nn distance criterion was applied.

**Figure 7** – Appearance at peak time of a typical 20 keV cascade simulated with WOL (above) and with AMS (below). The two potentials predict opposite cascade behaviour and the former is the softest, while the latter is the stiffest (at ~200 eV).

**Figure 8** – Evolution in time of the fraction of SIA (above) and vacancies (below) in cluster in 15 keV cascades, according to potentials AMS, ABC and WOL (CWP provides results extremely similar to ABC and the relevant curves are therefore not shown). SIA and V clusters are defined, respectively, using a 3<sup>rd</sup> nn and a 2<sup>nd</sup> nn criterion.

Figure 1

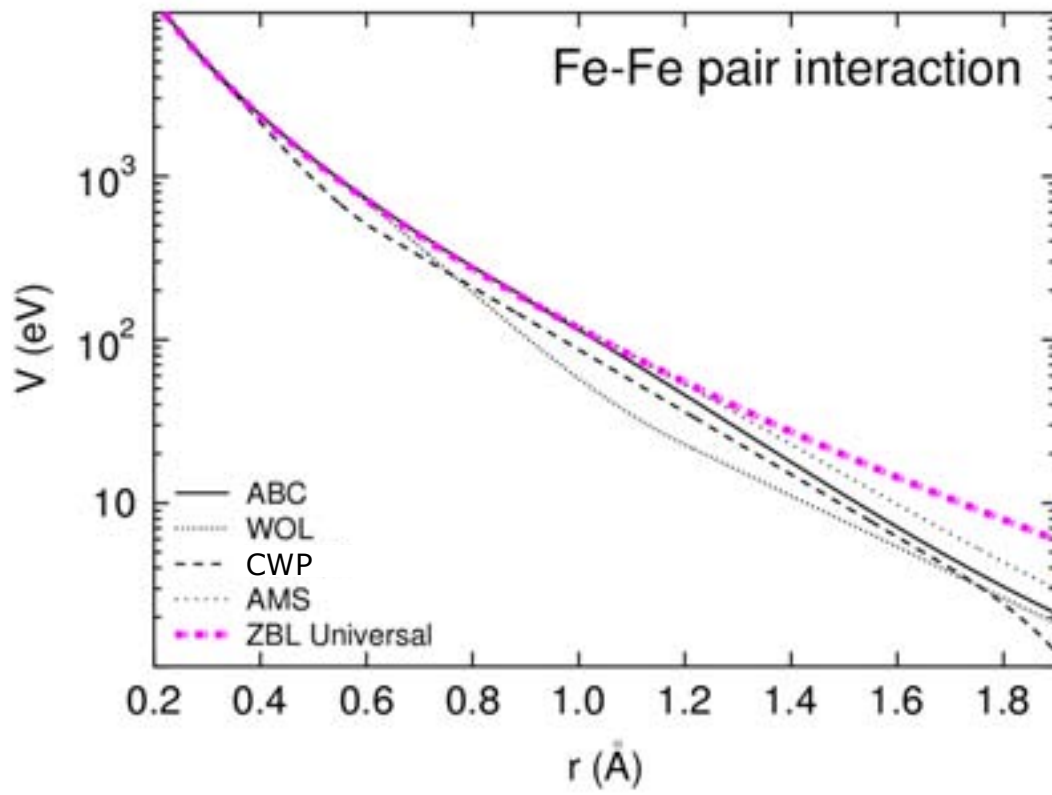




Figure 2

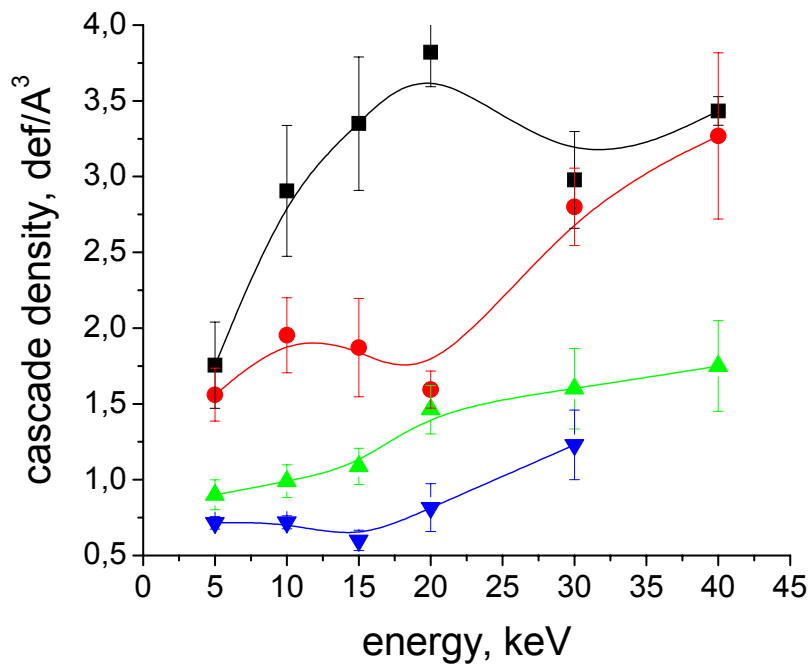
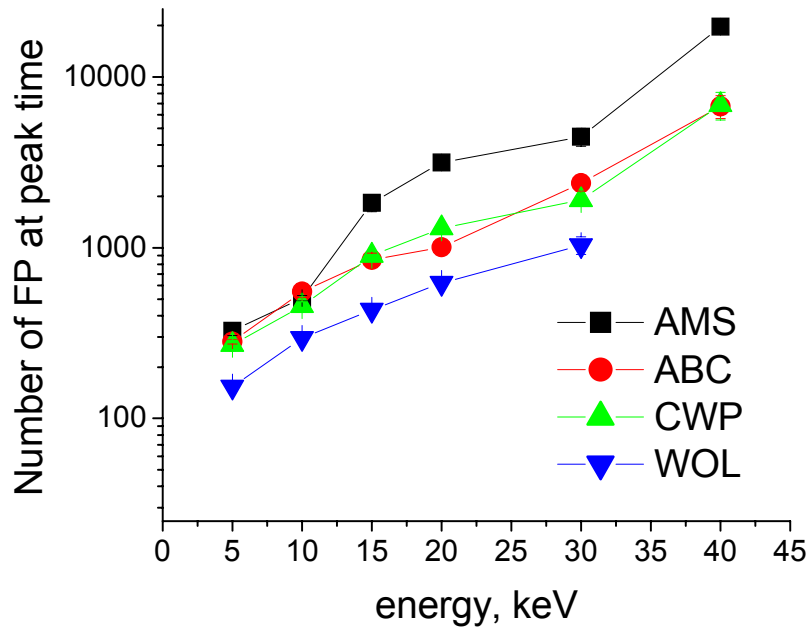


Figure 3

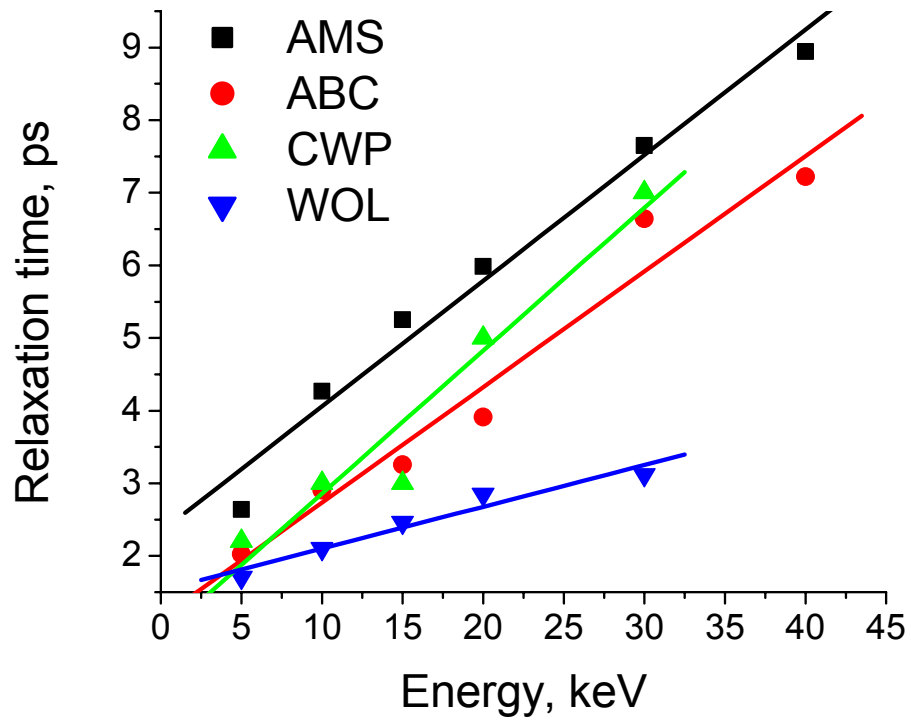


Figure 4

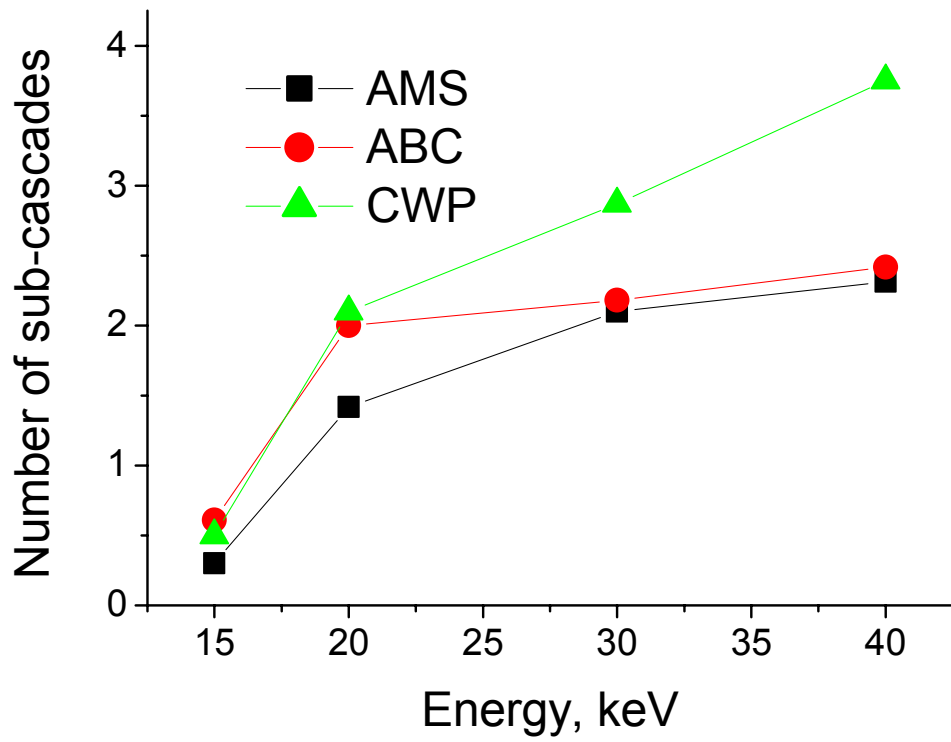


Figure 5

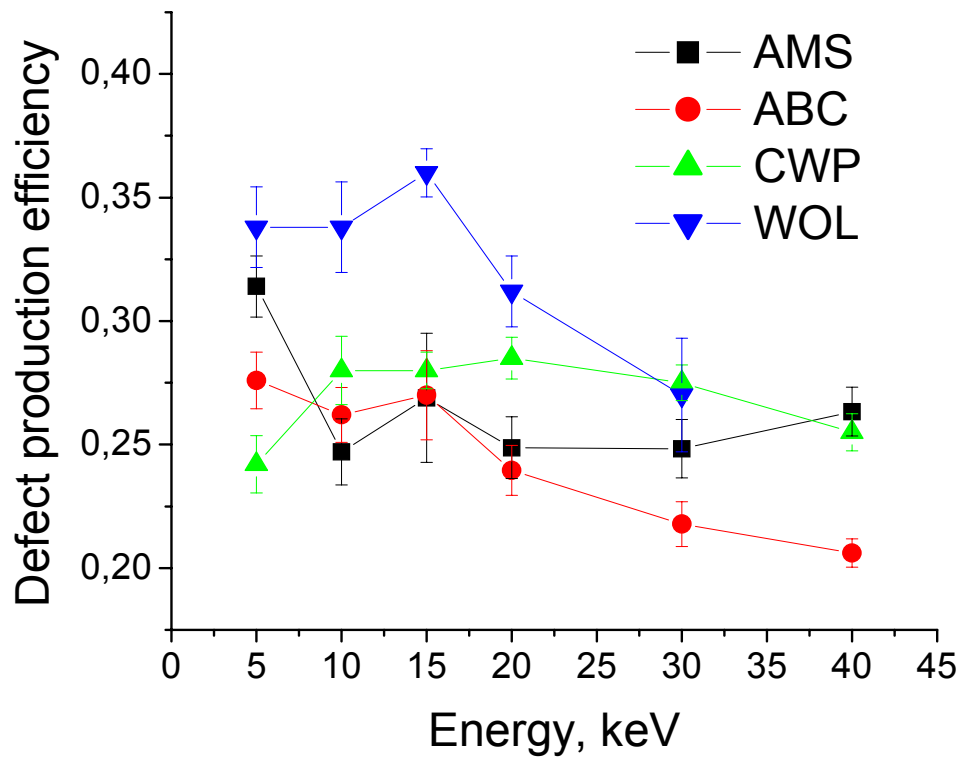
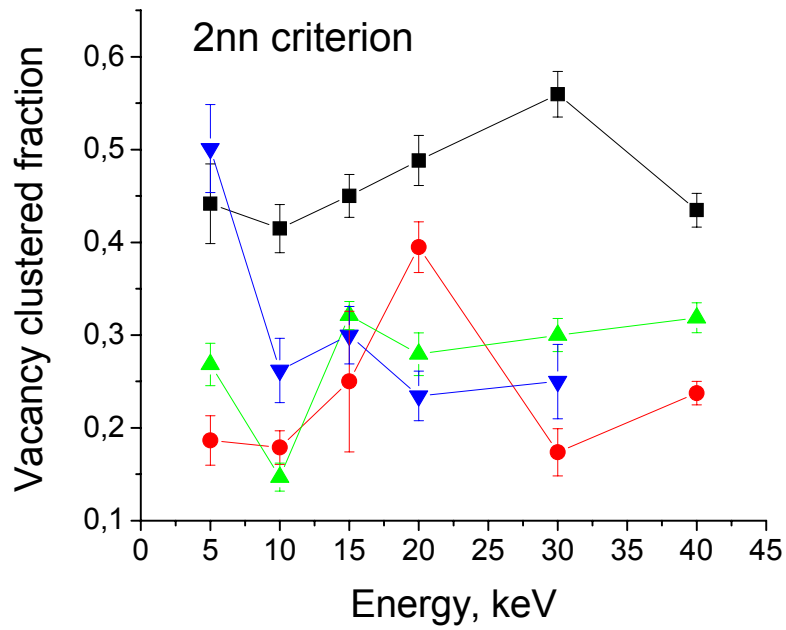
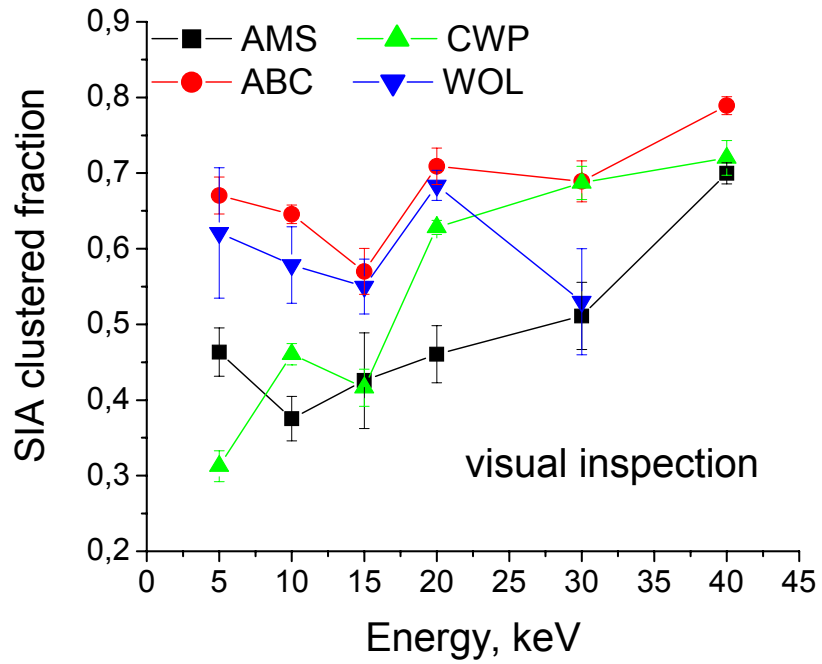


Figure 6



**Figure 7**

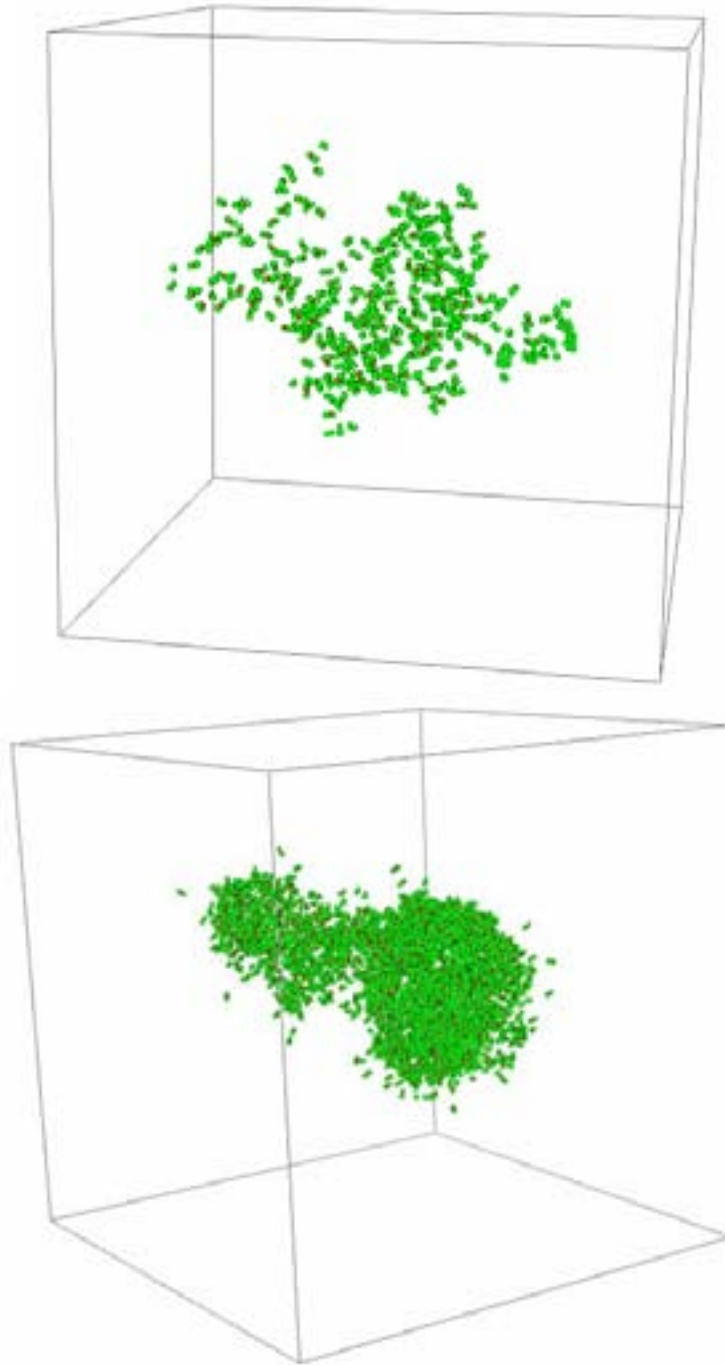
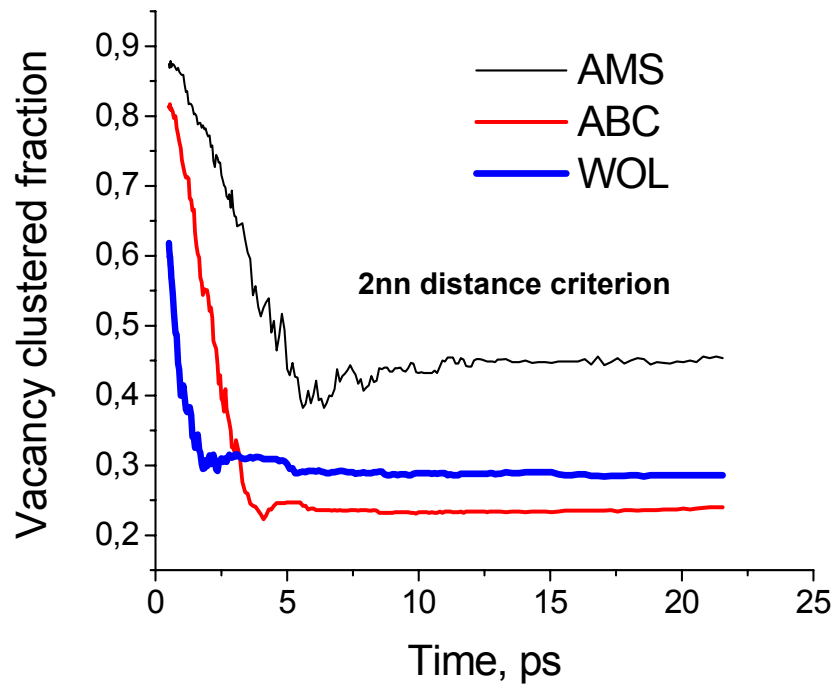
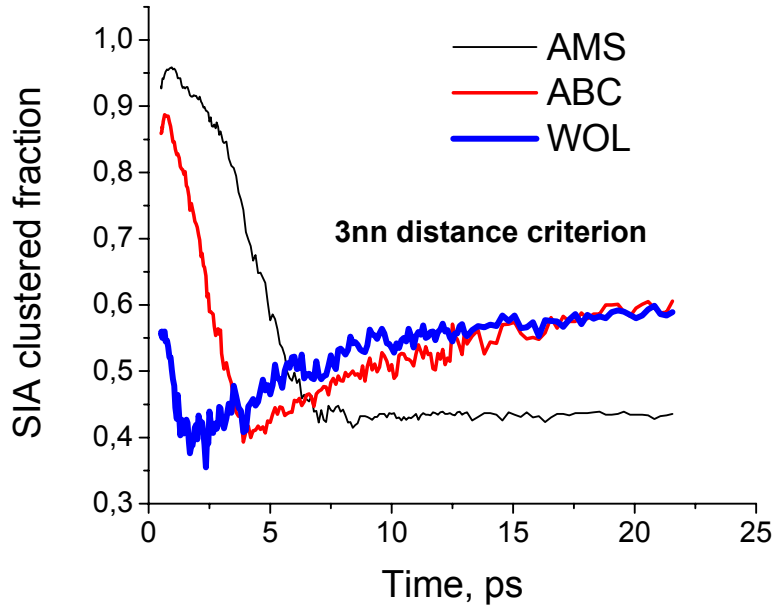


Figure 8



# Cluster formation mechanisms during relaxation and post-relaxation cascade stages in $\alpha$ -Fe: a molecular dynamics study

C. Lagerstedt<sup>1</sup>, D. Terentyev<sup>2</sup>, P. Olsson<sup>3</sup>, J. Wallenius<sup>1,3</sup> and L. Malerba<sup>2,\*</sup>

<sup>1</sup>Royal Institute of Technology, AlbaNova University Center, Dept. of Nuclear and Reactor Physics, SE-106 91 Stockholm, Sweden

<sup>2</sup>SCK•CEN, the Belgian Nuclear Research Centre – Boeretang 200, B-2400 Mol, Belgium

<sup>3</sup>Dept. of Neutron Research, Ångström Laboratory, Uppsala University  
Box 525, SE-751 20 Uppsala, Sweden

## Abstract

This work presents an analysis of cascade configurations aimed at gaining a better understanding of the processes taking place in the primary damage region. Previously, a comparative study of molecular dynamic simulations of displacement cascades up to 40 keV in bcc Fe using four different interatomic potentials was performed. Here the work is continued with the main purpose of finding mechanisms responsible for self interstitial atom (SIA) and vacancy clustering. Studying the clustered fraction and the mechanisms whereby clusters form during the different stages of the cascade is indeed vital to correctly assess the impact of cascade phenomena on radiation damage production and evolution. In the present work the following processes have been considered: formation of clusters during the relaxation stage and further clustering caused by high-temperature enhanced defect diffusion and spontaneous gathering of self interstitial atoms (SIA) driven by strain-field interactions. It is found that the mechanisms of defect diffusion and clustering are potential-dependent and that the stiffness of the potential in the intermediate energy and distance region, also related to the formation energy of the SIA, determines the processes taking place during the various stages of the cascade, as well as the final defect configuration. The defect clustered fractions and the recombination efficiencies are also influenced by which stable SIA configuration the potential reproduces.

*Keywords and PACS codes:* Molecular dynamics (M0200 31.15.Qg), Displacement cascades (R0100 61.72.Cc), Point-defect clusters (61.72.Ji), Mechanism of cluster formation.



\* Corresponding author, phone #: +32 14 33 30 96, fax #: +32 14 32 12 16, e-mail: [lorenzo.malerba@sckcen.be](mailto:lorenzo.malerba@sckcen.be)

## 1. Introduction

The production of self interstitial atom (SIA) clusters in cascades is nowadays an accepted fact [refs to MD cascade simulations in Fe and Cu where clusters are seen + R. Rauch, J. Peisl, A. Schmalzbauer and G. Wallner, J. Nucl. Mater. 168 (1989) 101 for exp observation by Huang diffusion scattering of SIA cluster formation in cascades in Cu]. However, the detailed mechanisms of formation of such defects directly within the cascade are not well known and even less is known concerning the influence of the potential used in the simulation on the role of these mechanisms. Nonetheless, detailed information about defect clustering is an important input parameter for the prediction of the long term evolution of radiation damage [S.J. Zinkle and B.N. Singh, J. Nucl. Mater. 199 (1993) 173]. This information can at the present moment be obtained only by applying MD tools. This is why much work devoted to the study of primary damage in  $\alpha$ -iron has been presented and published in recent years using a wide spectrum of potentials [8,9,10,11+12(i.e. my review)].

In a previous work we have compared cascades simulated with four different interatomic potentials and found that the number of surviving Frenkel pairs is approximately the same irrespective of the potential used. However, the potentials give a wide spread in the final fraction of SIAs and vacancies in clusters, as well as in the cluster size distribution [14, *that should become 13*]. A correlation between sub-cascade formation and final clustering was also found [13, *that should become 14*], for which possible reasons have been discussed but no detailed analysis has yet been done. In addition, the considered potentials give different descriptions of the near-equilibrium state such as defect diffusion properties, predicting in particular various mechanisms and energy barriers for self interstitial atom (SIA) migration. For instance, the difference in the SIA migration energy is as large as a factor of six between the recently published Ackland-Mendelev potential ( $E_m = 0.3$  eV) [15+ref Ackland] and the Ackland-Bacon potential ( $E_m = 0.058$  eV) [16]. The dimensionality of SIA motion depends on the potential as well and can vary from full 3D motion to rather pronounced 1D motion [17]. Such discrepancies will influence the motion of

SIA and small SIA clusters during the post-collisional stage which lasts a few tens of picoseconds and thus the cascade recombination stage and relevant clustering mechanisms will be affected as well. However, the relative importance of these and other potential features needs to be quantitatively assessed. [12].

A correlation between the stiffness and the range of a potential and the predicted cascade morphology and relaxation behavior was found in our previous work [14], in agreement with BCA studies [C.S. Becquart, A. Souidi and M. Hou, Phys. Rev. B 66 (2002) 134104.]. The range and stiffness describes the potential behavior at interatomic distances where the transition between the near-equilibrium and the high energy regimes occurs. The potential is stiffened by joining the many-body potential with a high energy potential such as the ZBL universal potential [Ref. ZBL]. The function joining the two parts is often chosen arbitrarily as long as the threshold displacement energy of the potential is seen to be reasonable. More specifically, potentials exhibiting long range R (distance where the interaction energy is  $\sim 30$  eV), low stiffness S in correspondence with R and high stiffness U at somewhat higher energy ( $\sim 200$  eV) form relatively dense cascade cores and provide a subsequent long relaxation stage. In contrast, potentials with a high stiffness S and a short range R at  $\sim 30$  eV, and low stiffness at  $\sim 200$  eV, produce a smaller number of defects at peak time, primarily via replacement collision sequences (RCS) and undergo a shorter relaxation stage. Since generally a low S/R ratio correlates with high U and vice versa, only the former parameter can be looked at and, for simplicity and compactness, potentials with low S/R ratio and large U, producing high cascade densities and long recombination stages, will be called "soft", while potentials characterized by large S/R ratio and low U, producing low cascade densities, will be said to be "hard".

When the cascade energy is high enough for sub-cascades to form, the influence of the stiffness of the potential appears again, although in a less clear. A "soft" potential will generally tend to produce a number of cascade cores, with a certain probability of overlapping. Moving from a "softer" to a "harder" potential, the sub-cascade cores start to become spread out allowing less overlapping between the cores.

In the present paper we try to give a more detailed and quantitative description of the contribution to defect clustering from the different features of the cascades at peak

time and the different mechanisms of defect diffusion and to discuss physical aspects associated with them.

## 2. Simulation method

### 2.1 Potentials

Four different potentials for  $\alpha$ -Fe were used for the MD simulations in this work:

- (i) the Finnis-Sinclair-type (FS) potential proposed by Ackland et al. [16], which will henceforth be denoted as ABC;
- (ii) the embedded-atom method (EAM) potential fitted by Chakarova et al. [18], which we shall call CWP;
- (iii) the EAM potential recently developed by Ackland et al. [19], which we will denote as AMS;
- (iv) a version of the EAM potential recently developed as part of an Fe-Cr potential by Wallenius et al. [20], that we will label WOL.

Table 1 summarises the defect properties of the four potentials used in. Some of these properties will be shown to have an influence on the SIA and vacancy clustering processes.

Table 1. Summary of the main properties of the four potentials used in this work.

| Point-defect energies [eV]                           | ABC   | CWP   | AMS  | WOL   | Exp.  | Ab initio <sup>a</sup> |
|--|-------|-------|------|-------|---|------------------------|
| $E_V^f$  | 1.70  | 1.54  | 1.71 | 2.08  | $2.0 \pm 0.2^b, 1.5^c,$<br>$1.6 \pm 0.10^d,$<br>$\sim 1.6-1.75^e$ | 1.93-2.17              |
| $E_V^m$  | 0.78  | 0.73  | 0.63 | 0.81  | $0.55^f,$<br>$0.57 \pm 0.14^g; (1.3)^{h,\pm}$                     | 0.59-0.67              |
| $Q^{SD} = E_V^f + E_V^m$                             | 2.48  | 2.27  | 2.34 | 2.89  | $2.48^i-3.13^{j,*}$   | 2.52-2.76              |
| $E_{\langle 110 \rangle}^f$                          | 4.87  | 4.15  | 3.59 | 6.45  | Stable config is<br>$\langle 110 \rangle$ db; $E^f=4.7-5^k$       | 3.64                   |
| $E_{\langle 111 \rangle}^f$                          | 5.00  | 4.02  | 4.03 | 6.87  |   | 4.34                   |
| $\Delta E_{\langle 111 \rangle-\langle 110 \rangle}$ | 0.13  | -0.13 | 0.44 | 0.42  |   | 0.70                   |
| $E_{SIA}^m$  | 0.058 | 0.056 | 0.31 | 0.061 | $0.25-0.34$   | 0.34                   |
| $E_{DL-VAC}^{bind} (1^{st} nn)$                      | 0.14  | 0.19  | 0.14 | 0.20  | N.A.  | 0.14                   |
| $E_{DL-VAC}^{bind} (2^{nd} nn)$                      | 0.20  | 0.21  | 0.24 | 0.27  | N.A.  | 0.28                   |
| <b>Stiffness</b>                                     |       |       |      |       |   |                        |

|                       |                       |                       |       |       |
|-----------------------|-----------------------|-----------------------|-------|-------|
| R [Å]                 | 1.30                  | 1.23                  | 1.29  | 1.11  |
| S [eV/Å]              | -95                   | -124                  | -65   | -203  |
| U [eV/Å]              | -3448                 | -2511                 | -5123 | -2886 |
| <sup>a</sup> Ref [21] | <sup>c</sup> Ref [25] | <sup>i</sup> Ref [29] |       |       |
| <sup>b</sup> Ref [22] | <sup>f</sup> Ref [26] | <sup>j</sup> Ref [30] |       |       |
| <sup>c</sup> Ref [23] | <sup>g</sup> Ref [27] | <sup>k</sup> Ref [31] |       |       |
| <sup>d</sup> Ref [24] | <sup>h</sup> Ref [28] | <sup>l</sup> Ref [32] |       |       |

<sup>±</sup> The value 1.3 seems to be the result of not high enough purity of Fe [27]

\* About 15 experimental measurements reported, giving values within this range, see e.g. website:  
[http://diffusion.nims.go.jp/index\\_eng.html](http://diffusion.nims.go.jp/index_eng.html)

## 2.2 Calculation details

The details of the MD aspects of the simulations are described in our previous article [14] and only a brief description will be given here. The classical MD code DYMOKA [32] was used in the NVE ensemble at a temperature of 100 K with periodic boundary conditions. The number of successfully simulated cascades for each potential was at least 10 per cascade energy and the total simulation time was 23 ps. After equilibrating of the system for 1 ps, the cascade was initiated by giving kinetic energy or cascade energy to a primary knock-on atom (PKA) chosen to be situated at the center of the cubic simulation box. To avoid channeling, the PKA was chosen to move in the  $\langle 135 \rangle$  direction. Overall, the simulation technique was standard and the results can therefore be safely compared with results available from the literature.

The defect space distributions were estimated using the Wigner Seitz cell criterion: an empty cell means a vacancy while two (or more) atoms in the same cell mean an interstitial configuration. The number and size of clusters were determined using a 2<sup>nd</sup> nearest neighbor (nn) distance criterion for vacancies and visual inspection for SIAs. In the case of vacancies, a distance criterion is enough since vacancy mobility is very limited within the simulation time frame at the simulation temperature. The high mobility of SIAs, especially in the case of the CWP potential, which incorrectly predicts the fast-gliding  $\langle 111 \rangle$  crowdion to be the most stable interstitial configuration instead of the  $\langle 110 \rangle$  dumbbell, requires more care. SIA clusters move in the  $\langle 111 \rangle$  direction by gliding, but the collective motion of a cluster is realized through independent jumps of the crowdions forming the cluster [33,34]. From time to time, a single SIA can jump as far apart from the others as 4<sup>th</sup> or even 5<sup>th</sup> nn distance, the binding energy of the SIA cluster being strong enough to prevent it from breaking up

[35]. The use of a large distance criterion like 5<sup>th</sup> nn for example would not solve the problem since it could lead to the inclusion of SIAs not actually belonging to it in the same cluster. Visual inspection over successive snapshots is hence the only way of correctly assigning all SIAs to the right cluster, provided that the clusters are not too large. Nonetheless, distance criteria have been widely used in previous work concerning Fe [8,9,10,11], so an analysis of the SIA clustered fraction as a function of time using a 3<sup>rd</sup> nn numeric distance criterion was done to be able to compare with the published results of others.

As an indication of the duration of the different phases, or stages, of the cascade, characteristic times were introduced. Three cascade stages were defined. The ballistic, or collisional, stage starts when the PKA is introduced and ends at peak time,  $\tau_p$ , which is defined as the time when the maximum number of defects (atomic displacements) is observed. The duration of the relaxation, or recombination, stage, roughly coincident with the so-called thermal spike, is measured by the relaxation time,  $\tau_r$ , which is defined following Calder and Bacon [Calder93+our previous paper]. The thermal spike is characterized by a rapid, local increase of temperature, during which a state close to a melt can be produced, followed by fast quench, thereby inducing atom mixing, enhanced defect diffusion and recombination. The relaxation stage is over when the number of defects is seen to be stable. Finally, the post-relaxation, or post-cascade, stage starts at  $\tau_p + \tau_r$  and lasts for the rest of the simulation time. During this phase the system reaches full thermalization and the defect population should reach a steady state known as the primary state of damage, although it will be shown that some diffusion processes are already active, so that the definition of the end of the post-cascade stage, which can also be denoted as "diffusional" stage remains arbitrary. In our case, we monitored the third cascade stage for approximately 15 ps. At the temperature at which the cascades were performed, this corresponds to about tens of SIA jumps at the most, depending on the potential used.

In order to understand how clusters evolve during the different stages of a cascade, the clustered fractions and the average cluster sizes were monitored as functions of time for the four considered potentials at all simulated cascade energies starting from  $\tau_{peak}$  to end of the simulation at 100 fs intervals using distance criteria for both

vacancies ( $2^{\text{nd}}$  nn) and interstitials ( $3^{\text{rd}}$  nn). Of course, at peak time and during most of the relaxation phase it is not appropriate to speak of clusters. Still, the "clustered fraction" will give an idea of the level of aggregation and depletion of displaced atoms during the cascade process, thereby giving an insight into the mechanisms playing a role in the final formation of clusters. Once the post-cascade stage is reached, additional magnitudes have been estimated such as the separate contribution to SIA and vacancy clustering occurring during the relaxation and post-cascade stages and the number of recombined defects within the post-cascade stage as a functions of cascade energy.

### ***3. Results and discussion***

In this section, results concerning SIA and vacancy clustering for the relaxation and post-cascade stages will be presented and discussed. We assume that clustering is the effect of defect accumulation during both of those stages. The final clustered fractions produced during the post-relaxation stage studied using different clustering criteria are presented in the section 3.1. In section 3.2, clustering as a function of time is analyzed and the influence of the thermal motion of defects (primarily SIAs and SIA clusters) and its contribution to the final clustered fractions is discussed.

#### ***3.1 Final clustered distributions***

##### ***3.1.1 Interstitials***

In figure [Y] the final SIA clustered fraction determined by visual inspection is shown as a function of cascade energy for all four potentials considered in this work. The general tendency is that the fraction increases with cascade energy except in the case of the WOL potential which exhibits a decrease. The absolute values clearly differ between individual potentials, but the correlation between potential properties and clustering is not straightforward. The ABC potential is soft and predicts correctly the  $\langle 110 \rangle$  dumbbell to be the lowest energy interstitial configuration and exhibits a high clustered fraction. However the AMS potential is also soft and predicts the correct SIA configurations, but predicts a low clustered fraction. The average size of SIA clusters also increases with rising cascade energy as can be seen in figure [Z]. Again, the WOL potential has the most aberrant behavior showing a much smaller rise than the other potentials.

SIA clusters have been counted both using distance criteria implemented in automated procedures and by visual inspection [ref to my review]. It is hence useful to study the difference in the results obtained using these two techniques. Figure [X] shows a comparison between the clustered fractions calculated using visual inspection and 3<sup>rd</sup> nn distance criterion for all studied potentials. In all cases, the fraction determined using the distance criterion is smaller than the fraction attained using visual inspection. The largest discrepancy is found for the CWP potential. This result should be taken into account when comparing the results of other authors who have used different approaches. Of course, using visual inspection introduces human error into the analysis. However, we find that visual inspection will not give larger errors than an automated analysis using distance criteria, unless the clusters are very large, so that it becomes easy to miscount the number of defects that they contain.

### ***3.1.2 Vacancies***

The vacancy clustered fractions determined using a 2<sup>nd</sup> nn distance criterion, are given in figure [YY] and show the same tendencies as the SIA clustered fractions of increasing with cascade energy, although the increase is less pronounced than in the previous case. The exception is once again WOL which exhibits a sharp decrease. The CWP and ABC potentials produce similar results while the clustered fraction of the AMS potential is higher. The average vacancy cluster size shown in figure [ZZ] rises with energy as expected. Here the ABC and the WOL potentials show similar behavior while the cluster size for the AMS potential is much larger.

The vacancy clustered fraction may be expected to correlate with the binding energies between vacancies (see table 1). However we see that this is not the case. The WOL potential has the highest vacancy binding energies at both 1<sup>st</sup> and 2<sup>nd</sup> nn distances but does not feature the largest vacancy clustered fraction, the most likely reason being the low density of the cascade core. With this potential, vacancies were formed mostly via RCS ending up quite far away from each other. Also, it is not possible to find a correlation between vacancy clustering and vacancy migration energy, since the values predicted by the different potentials are similar and, at any rate, with those values, vacancy migration is not expected to occur at the simulated temperature within the time frame of MD. Nonetheless, the discussion on the vacancy clustered fraction with AMS shows that vacancy migration may be playing a role there.

The conventional reason to use a 2<sup>nd</sup> nn distance criterion for vacancy cluster detection is that the di-vacancies are seen to be bound up to this order of distance, the 2<sup>nd</sup> nn distance binding energy being higher than the binding energy at 1<sup>st</sup> nn distance. In a work by Stoller [11], it was shown that the vacancy pair distributions have peaks at 2<sup>nd</sup> and 4<sup>th</sup> nn distances and for this reason he proposed a 4<sup>th</sup> nn distance criterion to detect clusters. Stoller argues that the 4<sup>th</sup> nn vacancies will eventually merge into compact clusters on longer time scales. The evolution of vacancy clustering can then be predicted by studying vacancies at this distance. All of the potentials used in this work give a good prediction of the vacancy binding energies when compared with ab initio calculations. The WOL potential has the highest 2<sup>nd</sup> nn binding energy and the ABC potential has the lowest. In order to characterize the vacancy distribution after the relaxation stage, the same calculations as those by Stoller were performed. Figure XX displays the spatial correlation of all vacancies at 15 keV for all four applied potentials. Peaks at 2<sup>nd</sup> and 4<sup>th</sup> nn distance can be seen in all cases, with the highest peak corresponding to the WOL potential which gives the largest binding energy between vacancies at 2<sup>nd</sup> nn distance.

### ***3.1.3 Production bias***

Due to the higher mobility of SIAs, their clustered fraction is expected to be larger than that of vacancies. The production bias, defined as the difference between the SIA clustered fraction and the vacancy clustered fraction, is shown in figure [YYY]. Again there is a clear difference between the potentials. The AMS potential shows a very small and for some energies negative production bias.

## ***3.2 Clustered fractions as a function of time***

### ***3.2.1 Vacancy clustered fraction***

The formation of small vacancy clusters in cascades with cascade energies of no more than 10 keV was found to be a stochastic process and no vacancy motion was observed during simulation. The formation of large vacancy clusters with more than six vacancies, takes place in high energy cascades with cascade energies of at least 20 keV. The clusters are due to the presence of an initial collision spike where they are formed. In the case of cascades where no splitting occurs, a locally heated area surrounding a large vacancy cluster forms. The heated area is enriched in vacancies



and depleted in SIAs. Isolated vacancies located inside the heated area can move towards each other or towards large vacancy clusters if they exist.

The evolution of the vacancy clustered fractions as functions of time were found to be qualitatively similar for all of the potentials, although a peculiar behavior was observed with the AMS potential during the post-relaxation phase [14], as will be discussed in more detail later. The vacancy clustered fraction as a function of time for the full range of cascade energies with this potential is presented in figure 1. Three typical features of the clustered fraction evolution should be emphasized. First, we note the presence of a minimum for each curve. Minima are indicated by circles in the figure for the lowest and highest energies. Second, there is a saturation plateau, shown by thick lines for the lowest and highest energies that can be clearly seen for all cascade energies. Third, there is a hump-like peak, shown by a rectangle, which can be observed for cascades of relatively high energies. As the cascade energy increases, the energy minima are shifted towards later times, the absolute value of the saturation level increases and as does the height of the hump increases although its position in time does not change. These features are broadly observed for the other potentials as well, but the minima are much less pronounced than for AMS. In addition, no hump-like peak is ever observed with WOL. The reason for these differences will be further discussed later. The positions of the minima were found to coincide roughly with the end of the relaxation stage. This means that there is no additional accumulation of vacancies during the relaxation stage, but only a decrease in the clustered fraction as the cavities formed during the ballistic stage shrink through recombinations.

The values of the observed minima are correlated with the stiffness of the potential and the cascade energy: the "softer" the potential and the higher the cascade energy, the shallower the minima. This can be interpreted to mean that non-dense or split cascades do not result in as high a clustering fraction as dense ones. It would also be consistent with the previously reported fact that vacancy clusters form at the center of cascade cores during the ballistic stage [3, Bacon93]. Another fact that indirectly supports the idea of larger vacancy clustered fractions in the case of soft potentials, which provide denser cascades, is the observed formation of a big planar vacancy cluster oriented along the  $\langle 100 \rangle$  direction in one of the cascades produced using the AMS potential at 40 keV. Note that in that cascade, a pronounced collision spike with no sub-cascade splitting was detected [36]. The situation is quite similar to the one

reported by Soneda in [37]. Dense cascades and cascades with no splitting would thus correspond to larger vacancy cores with some probability to collapse, while the possibility of this scenario is suppressed by cascade splitting.

The clustered fraction curves undergo oscillations in the saturation region. This can be explained by further recombination processes driven by mobile SIAs, which can lead to an increase (if single vacancies recombine) or a decrease (if clustered vacancies recombine) of the clustered fraction and only in very rare cases to no change at all. The amount of recombinations will depend on the spatial distribution of the defects, which is mainly defined during the ballistic stage. On the other hand, the description of defect mobility (i.e. the diffusion properties) defined by the potential will also play a role in the recombination process.

Figure 1 shows that with AMS, there is also a significant contribution to vacancy clustering during the post-relaxation stage, since the clustered fraction increases. This contribution can be evidenced by taking the difference between the final value of the clustered fraction and the value at the minimum (end of the relaxation stage). This contribution of the post-cascade stage to the clustered fraction is shown in figure 2 for all potentials. The contribution of 0.15 corresponds to 30% of the final vacancy clustering fraction at a cascade energy of 40 keV for the AMS potential. It can be seen that only the AMS potential predicts a substantial increase in the vacancy clustering during the post-cascade stage. Through visualization we observed that, except with the AMS potential, single vacancies were almost always immobile which is reasonable with an initial simulation temperature of 100 K. For the AMS potential, single vacancies were seen to migrate close to large vacancy clusters. This is surprising and can only be explained by considering that the cascade causes local heating in the area at the center of the cascade core which enhances vacancy diffusion. AMS is the softest potential among the considered ones [14] and thus the cascade core is particularly dense. The temperature reached in the core is expected to be higher and the thermal spike to linger longer than for the other potentials. As discussed already, the conditions are thus favorable for large vacancy clusters to form and, apparently, also for single vacancies around them to diffuse rapidly towards them due to the higher temperature, possibly combined with the attraction exerted on single vacancies by cavities.

Figure 3 shows the number of recombined atoms during the post-relaxation stage versus cascade energy. For two of the potentials (WOL and CWP), the tendency can be defined as linear as expected, since the probability of recombination can be considered proportional to the amount of defects. The smallest number of recombined atoms was found for the CWP potential and this can be ascribed to the character of SIA motion with this potential. As reported in previous studies [17 *but also others: Osetsky etc*], if the potential predicts the  $\langle 111 \rangle$  crowdion to be the most stable configuration, the motion of SIAs occurs exclusively by one-dimensional glide in the close packed direction with only occasional changes of direction which are very rare at low temperature. It is also known that the probability that one-dimensionally moving defects will encounter uniformly distributed spherical sinks (vacancies in this case) is orders of magnitudes lower than for three-dimensionally migrating defects [ref to Trinkaus, e.g. H. Trinkaus, BN Singh and S.I. Golubov, J. Nucl. Mater. 283-287 (2000) 89]. Thus, it is no surprise that CWP provides the lowest recombination rate during the post-cascade stage of the cascade.

The presence of a hump was observed only for high cascade energies where the formation of sub-cascades was also seen. Thus we assume that the presence of a hump can be correlated with sub-cascade formation processes. In the case of the WOL potential, no splitting of the cascades was ever seen, and no humps in the clustered fractions were observed at any energy which is another confirmation of our assumptions. The hump appears during the relaxation stage, which means that it is not due to the overlapping of sub-cascade cores. Probably the formation of sub-cascades somehow affects the motion of SIAs after the peak stage hindering recombination processes. The appearance of the humps could also be connected with the fact that above a certain energy when cascade splitting occurs, the SIAs in the clouds surrounding the cascade cores will interfere with each other and their motion will be hindered. The second maximum would be the result this interference of the clouds as less SIAs are available for recombinations with vacancies which then have a larger clustering probability. This could be checked by seeing if the humps grow at even larger cascade energies.

The estimation of the number of single vacancies which have recombined shows that for the AMS potential, about 80% of the annihilation events were reactions between single vacancies and SIA clusters. The other potentials give a 50/50 ratio in average,

meaning that the probability for single vacancy to recombine with a single SIA or with an SIA cluster was roughly the same. Since SIA clusters are more mobile than single SIAs, this behavior could explain the deviating trend of the vacancy clustering for the AMS potential during the post-cascade stage.

### ***3.2.2 SIA clustered fraction***

The SIA clustered fractions for the four studied potentials at 15 keV cascade energy are shown in figure 4. Minima and saturation levels are seen for SIAs as well as for vacancies. However, evidence of a hump was not seen at any cascade energy with any of the potentials. The dependence of the minima and the saturation levels on the cascade energy is the same as for the vacancy as for the SIA clustered fractions, i.e. as the energy rises, the minima shift towards later times and become shallower and the level of the saturation plateaus increase. The difference between the minimum and the saturation level is very small for the AMS potential, but it does exist. Analysis shows that the positions in time of the minima for the SIA clustered fractions are very close to the value of the relaxation time,  $\tau_r$ , just as they were for the vacancy clustered fractions.

The evolution of the clustered fraction differs significantly between the potentials. Looking at the absolute value of the "clustered fraction" during the relaxation stage, one can draw conclusions about the density of the produced cascades. As already reported in our previous paper [14], the very low clustered fraction for the WOL potential during the relaxation stage reflects the fact that the cascades were less dense compared with the cascades produced with the other potentials. The AMS potential on the other hand provides the densest cascades with the longest relaxation time.

Figure 5 gives a quantitative description of the contribution to the final SIA clustering as a function of cascade energy for all used potentials. The general tendency of a rising clustered fraction during the post-cascade stage is clear, although there are differences between potentials and variations even with the same potential. An increase in the SIA clustered fraction during the post-cascade, diffusional phase is indeed to be expected since SIAs, particularly in the  $\langle 111 \rangle$  crowdion configuration, are highly mobile and can perform up to tens of jumps within  $\sim 10$  ps. Only the WOL potential provides a contribution that is stable and increases linearly with cascade energy contributing approximately 40% to the final value. The ABC and the CWP

potentials predict between 30% and 50% contribution to the final clustered fraction during the post-cascade stage. The slightly smaller contribution with the CWP potential can be explained by the different dynamics of SIA motion, as already mentioned. With the CWP potential SIAs can aggregate only if they moving along parallel and neighboring  $\langle 111 \rangle$  lines, since change of  $\langle 111 \rangle$  direction is extremely unlikely at 100 K [38]. During the post-cascade stage, the clustered fraction of the CWP potential exhibits large oscillations. This possibly comes from problem with correct SIA description with the CWP potential and a discussion has already been given in section 2.2.

The values for the AMS potential look rather complicated and no definitive conclusion can be drawn. A significant contribution is present only for the lowest and highest energies and otherwise the contribution is negligible. Visual inspection and specific studies [ref to paper to be published] show that the mobility of SIAs with the AMS potential is much lower than with the other potentials, especially for isolated SIAs. Thus, a low contribution to SIA clustering during the post-cascade stage should be expected. However, the overlapping of cascades could give rise to a spontaneous accumulation of SIAs at the periphery of the cascade core, and hence, overlapping should lead not only to an increase in the SIA clustered fraction but also to an increase in the vacancy clustered fraction. With the formation of sub-cascades, the motion of SIAs at the periphery of the cascade core should be suppressed due to the spontaneous gathering of SIAs, which means that small mobile SIA clusters are located between the sub-cascade cores. Such distributions of defects would make recombinations between SIAs and vacancy clusters difficult.

Although the formation of sub-cascades for the AMS potential starts at 20 keV, a clear separation of sub-cascade cores starts only at 40 keV. This could therefore confirm the relationship between cascade overlapping and the increased contribution of the post-cascade stage to the SIA clustered fraction observed in figure 5, since the increase of such a contribution appears at cascade energies of about 30-40 keV. However, the number of cases where overlapping is seen, is too small to draw definitive conclusions from and the reason for the larger contribution at 5 keV remains unclear. One possible explanation could be that since the volume of the cascade is the smallest for the AMS potential [14] and since at 5 keV it has a relatively small density compared to the density at higher energies, the formation of a

"classical" sphere-like periphery was not always reached during the ballistic stage. It would then be possible to have further aggregation into clusters during the post-cascade phase.

### ***3.2.3 Remarks on the mechanisms of cluster formation***

For the AMS [*or CWP?*], ABC and WOL potentials, SIA clustering at low cascade energy is largely due to the spontaneous gathering of SIAs during the post cascade stage. A visualization of SIAs after the relaxation stage shows that for the ABC and WOL potentials some SIAs can move very short distances, so that clustering is more probable at short ranges (about 1 or 2 Burgers vector distance). Rotation of SIAs from  $\langle 110 \rangle$  dumbbells to  $\langle 111 \rangle$  crowdions was observed. Further, the crowdions did a few fast jumps towards other SIAs during post-cascade stage. For the AMS potential, all SIAs were frozen after the end of relaxation stage [*so what has just been said does not hold for AMS?*].

For higher cascade energies, sub-cascade formation begins. The probability of SIA clustering increases when sub-cascade splitting and overlapping occurs. This should give a tendency of increasing SIA clustering with higher cascade energy. For the WOL potential, the fact that no sub-cascade splitting was observed and that the formation of non-dense cascades was seen should reflect on the final SIA and vacancy clustered fractions.

With the CWP potential, only crowdions and not dumbbells are formed after the PKA introduction. In principle, the clustered fraction should depend on two processes correlated with the 1D fast motion of crowdions. First of all, such motion could lead to additional recombination between crowdions and vacancy clusters. The probability for a crowdion to recombine with a single vacancy is very low. The process would lead to an increasing SIA clustered fraction and a decreasing vacancy clustered fraction. On the other hand, while a crowdion is moving it can also couple with other collinear crowdions and form a cluster. The mobility of small  $\langle 111 \rangle$  clusters is still rather high, but the probability for non-collinear SIAs to join the cluster is very small due to the very high rotation energy of crowdion. Hence the small cluster could also effectively interact with isolated vacancies and vacancy clusters located inside the cluster glide prism. This should result in decreasing SIA and vacancy clustered fractions.

To summarize, we expect to see the formation of large SIA and vacancy clusters with the AMS and ABC potentials and small clusters with the WOL and CWP potentials. The SIA clustered fraction should be smallest for the AMS potential while the vacancy clustered fraction should be smallest for the CWP potential.

#### ***4. Conclusion and final remarks***

The objective of the present work was to perform a set of identical calculations using different potentials in order to investigate the mechanisms of in-cascade cluster formation and to try to correlate the efficiency of those mechanisms with certain features of the potential. Based on the results presented, a set of conclusions about defect clustering in cascades can be drawn:

- The ballistic phase of the cascade has the most important role in the formation of clusters and the evolution of the cascade during this phase is largely determined by the stiffness and range of the potential in the region of intermediate energies and, where the transition from equilibrium to ZBL potential occurs.
- The relaxation phase does not lead either to the formation of new clusters, or to the growth of existing ones; rather, the clustered fraction can only decrease during this phase.
- The clustered fraction can either continue to grow or remain constant during the post-cascade, post-relaxation stage of the cascade.
- The details of the process of vacancy and SIA clustering seem to be strongly dependent on the potential used and the diffusion properties of defects predicted by the potential certainly play a large role. In some cases, such as with the AMS potential, the increase of vacancy clustering due to migration can be significant.

As a result of both the work presented here and in previous papers [refs], a number of correlations between defect descriptions given by the potential and cascade results can be proposed. For example:

1. A high SIA formation energy is likely to be the result of a stiff potential, which leads to a larger distortion field around the defect and, simultaneously, favors the production of defects via RCS. In these conditions, cascades tend to be diluted, i.e. characterized by larger volumes and fewer defects at peak time. Hence, the average

size of the clusters of both vacancies and SIAs will be small and the fraction of defects in clusters will decrease with cascade energy, because defects will have increasingly less probability of meeting each other. This in turn leads to softer interactions and thus less energy losses and a longer recombination stage. It also results in larger cascade sizes which alters the recombination time and the final defect stage.

2. If the  $\langle 111 \rangle$  crowdion is predicted as the stable SIA configuration, diffusion can take place only via crowdion glide mechanism. Since the crowdion has a very low probability to change its orientation at low temperature in order to form a cluster, it becomes less likely that SIA clusters grow during the diffusional, post-cascade stage, giving a smaller SIA clustered fraction, unless other mechanisms, such as subcascade overlapping, contribute to the clustering. The stability of the crowdion rather than the dumbbell will also reduce the recombination efficiency during the post-relaxation stage and, if the cascade happens to be particularly diluted, this could lead to a larger final number of surviving defects.

3. Even when a reasonable SIA formation energy and stability is predicted by the potential, differences may still arise in the defect clustered fraction both from different stiffening and from different defect diffusion properties predicted by the potential. A "soft" potential, in the sense specified in the introduction, will produce dense cascades and this will generally impact on larger vacancy clusters and therefore give larger vacancy clustered fractions. In addition, with a potential that favors the dumbbell migration mechanism, rather than crowdion glide, the growth of clusters during the diffusional, post-cascade stage will be largely suppressed (unless other mechanisms, such as subcascade overlapping, intervene).

The third case corresponds to that of the most recently published iron potential [19], which is at the present moment accepted to give the best description of defect properties in  $\alpha$ -Fe [ref Fu&Willaime] when compared to ab initio indications such as melting point, phonon density spectra, etc.. The results concerning defect clustered fractions in cascades are with this potential quite different from the results obtained with most previous potentials. Not only final numbers differ but also the clustering mechanisms are not the same. We believe that the two parameters primarily responsible for those differences are the stiffness and the description of SIA



properties. But while in the latter case it is possible to state that this potential represents an improvement with respect to previous ones, the stiffening applied for the transition between equilibrium and ZBL remains arbitrary. Further investigation would therefore be required to establish up to what extent this particular aspect can change the results obtained in MD cascade simulations.

In the case of the WOL potential, the "hardest" one, no sub-cascade formation is observed up to 30 keV cascade energy and a single spread core is invariably produced.

### **Acknowledgements**

This work required a fairly large amount of CPU time to be performed. Four PC clusters at SCK-CEN, KTH, University of Uppsala and ULB (thanks to M. Hou for allowing its use) were simultaneously exploited for the task. The work was sponsored in part by Svenskt Kärntekniskt Centrum (C.L.)

### **References**

- [1] B. L. Eyre, A. F. Bartlett, *Philos. Mag.* **12**, 261 (1965).
- [2] N. Yoshida, M. Kiritani, F. Eiichi Fujita, *J. Phys. Soc. Jpn*, Vol.39, No.1, 1975 pp.170-179.
- [3] M. L. Jenkins, C.A. English, B. L. Eyre, *Phil. Mag. A*, vol. 38 (1978) 97.
- [4] I. M. Robertson, M.A. Kirk, W. E. King, *Scripta Metallurgica* vol. 18 (1984) p. 317.
- [5] L.C. Nicol, M. Jenkins, M.A. Kirk, *Material Res. Soc. Symp.*, vol. 650 (2001) R1.3.1-R.1.3.6.
- [6] [Osetsky] Y. Osetsky, A. Serra, V. Priego, *JNM*, **276** (2000) 202-212.
- [7] [Wirth] J. Marian, B. Wirth, J. Perlado, *Phys. Rev. Lett.* **88** (2002) 255507.
- [8] [Domain] C. Domain, C. Becquart, *Phys. Rev. B* **65** (2001) 024103.
- [9] [Bacon] D. J. Bacon, A. Calder, F. Gao, *JNM* **251** (1997) 1.
- [10] [Soneda] N. Soneda, T. de la Rubia, *Phil. Mag. A* **78** (1998) 995.
- [11] [Stoller] R. Stoller, *JNM* **276** (2000) 22.

- [12] [Cascade-Review] Malerba, TMS paper, accepted for publication in JNM
- [13] [In-cascade clustering] D. Terentyev, L. Malerba, M. Hou, NIM B **228** (2005) 156-162.
- [14] [TMS-cascades] D. Terentyev, C. Lagerstedt, P. Olsson, K. Nordlund, J. Wallenius, C.S. Becquart, L. Malerba, accepted for publication in JNM
- [15] [Mendeleev original] M.I. Mendeleev, S. Han, D.J. Srolovitz, G.J. Ackland, D.Y. Sun, M. Asta, Phil. Mag. **83** (2003) 3977-3994.
- [16] [Original ACB] [Ackland97] G.J. Ackland, D.J. Bacon, A.F. Calder, T.Harry, Phil. Mag. A **75** (1997) 713-732.
- [17] [see work with OP and TMS paper SIA dif] D. Terentyev, L. Malerba, JNM **329-333** (2004) 1161-1165.
- [18] [Chakarova02] R. Chakarova, V. Pontikis, J. Wallenius, "Development of Fe(bcc)-Cr many body potential and cohesion model", Delivery report WP6, SPIRE project, EC contract no. FIKW-CT-2000-00058 (June 2002), available at [www.neutron.kth.se/publications](http://www.neutron.kth.se/publications); P. Olsson, L. Malerba and A. Almazouzi, SCK•CEN Report, BLG-950 (June 2003).
- [19] [Ackland04] [Mendeleev] G.J. Ackland, M.I. Mendeleev, D.J. Srolovitz, S. Han, A.V. Barashev, J. Phys.: Condens. Matter **16** (2004) 1.
- [20] [Wallenius04] J. Wallenius, I.A. Abrikosov, R. Chakarova, C. Lagerstedt, L. Malerba, P. Olsson, V. Pontikis, N. Sandberg, D. Terentyev, JNM **329-333** (2004) 1175-1179.

Table 1. – References??

- [21] C. Domain, C. S. Becquart, Phys. Rev. B **65** (2001) 024103; C.-C. Fu, F. Willaime, P. Ordejón, Phys. Rev. Lett. **92**(17) (2004) 175503.
- [22] L. De Schepper, D. Segers, L. Dorikens-Vanpraet, M. Dorikens, G. Knuyt, L. M. Stals, P. Moser, Phys. Rev. B **27**(9) (1983) 5257.
- [23] K. Maier, H. Metz, D. Herlach, H.-E. Schaefer, J. Nucl. Mater. **69&70** (1978) 589.

- [24] H.-E. Schaefer, K. Maier, M. Weller, D. Herlach, A. Seeger, J. Diehl, *Scripta Metall.* 11 (1977) 803; H. Matter, J. Winter, W. Triftshäuser, *Appl. Phys.* 20 (1979) 135.
- [25] K. Fürderer et al. *Mater. Sci. Forum* 15-18 (1987) 125; A. Seeger, *Phys. Stat. Sol. (a)* 167 (1998) 289.
- [26] L. J. Cuddy, *Acta Metall.* 16 (1968) 23.
- [27] T. Tabata, H. Fujita, H. Ishii, K. Igaki, M. Isshiki, *Scripta Metall.* 15 (1981) 1317.
- [28] C. H. Woo, W. Frank, *Rad. Eff.* 77 (1983) 49; F. Philipp, *Mater. Sci. Forum* 15-18 (1987) 187.
- [29] F. S. Buffington, K. Hirano, M. Cohen, *Acta Metall.* 9 (1961) 434.
- [30] V. M. Amonenko, A. M. Blinkin, I. G. Ivantsov, *Phys. Met. Metall.* 17(1) (1964) 54.
- [31] H. Wollenberger, in: R. Cahn and P. Haasen (Eds.), *Physical Metallurgy*, vol. 2, North-Holland (1996).
- [32] [DYMOKA] C. S. Becquart, C. Domain, A. Legris, J-C. van Duysen, *J. Nucl. Mater.* 280 (2000) 73.

[COSIRES]

- [33] [Barashev] Independent crowdion model, I will for it
- [34] [Wirth] B.D. Wirth, G.R. Odette, D. Maroudas, G.E. Lucas, *JNM* **276** (2000) 33-40.
- [35] [Osetsky] Y. N. Osetsky, D. J. Bacon, A. Serra, B. N. Singh, S. I. Golubov, *Phil. Mag.* **83**, (2003) 61-91.

[Bacon93]

- [36] [NTDSC'05] D. Terentyev, L. Malerba and M. Hou, article accepted to be published in proceedings of SPIE, all
- [37] N. Soneda, S. Ishino, T. Diaz de la Rubia, *Phil. Mag. Lett.* **81** (2001) 649-659.
- [38] [single SIA diffusion work] article in preparation

[COSIRES]

Figures:

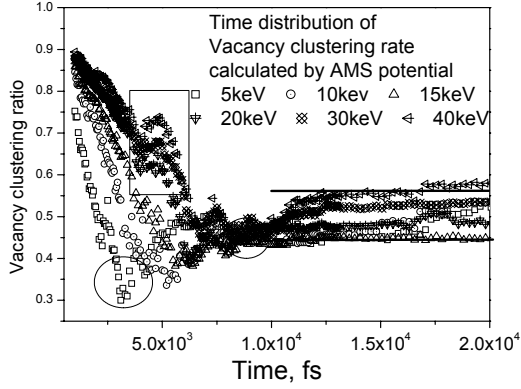


Figure 1. Vacancy clustered fraction as a function of time for the AMS potential.

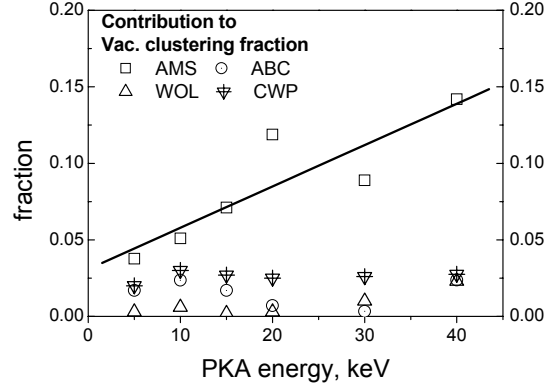


Figure 2. The contribution to vacancy clustered fraction due to post-cascade stage.

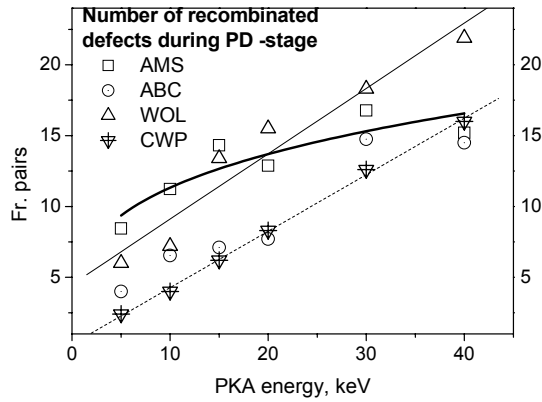


Figure 3. The number of recombined atoms during post-cascade stage.

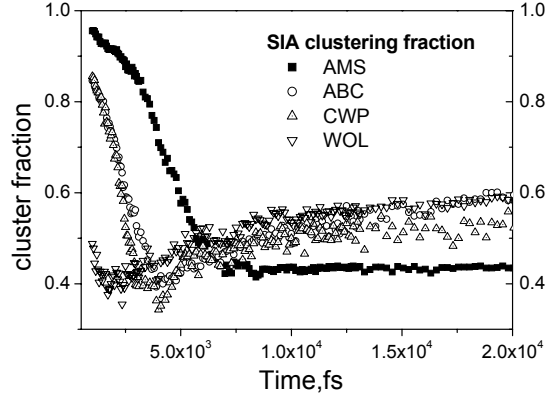


Figure 4. The SIA clustered fraction as a function of time.

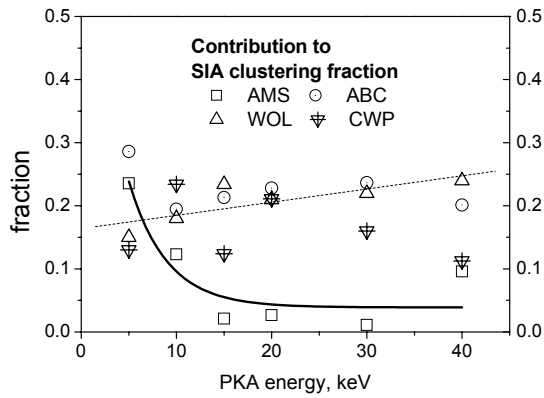


Figure 5. The contribution to the SIA clustered fraction during the post-cascade stage.

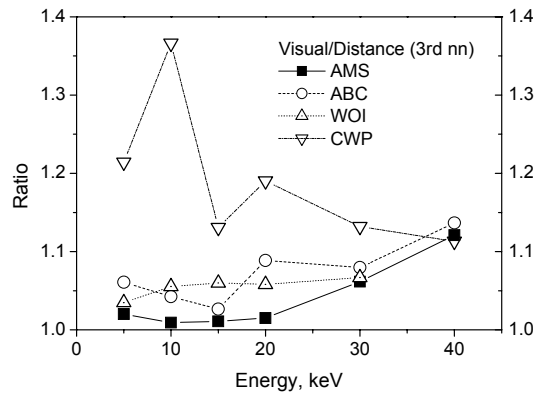


Figure X. The ratio between the clustered fractions of SIAs obtained using visual inspection and a 3<sup>rd</sup> nn distance criterion.

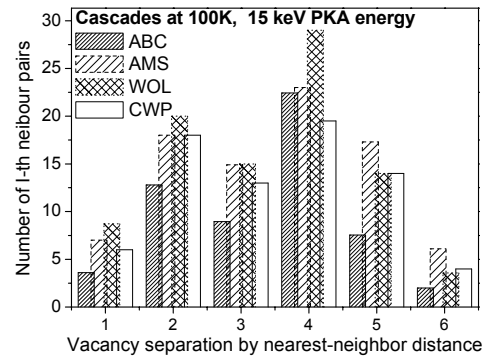


Figure XX. The number of vacancy pairs at a distance of  $i^{\text{th}}$  nn distance.

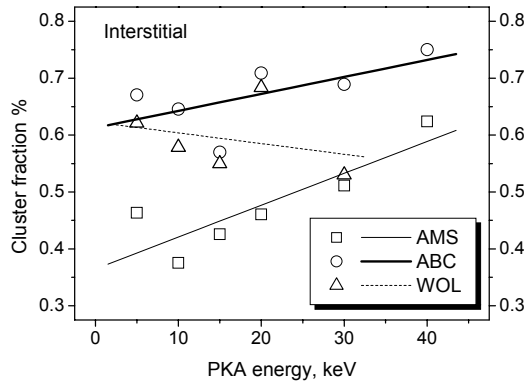


Figure Y. SIA clustered fraction of the final defect configurations as a function of energy. Parameters for the fitted curves can be found in table Y.

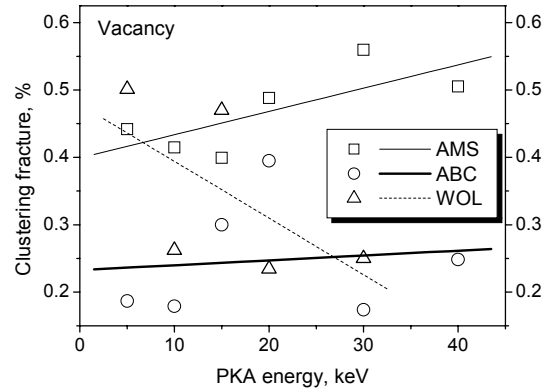


Figure YY. Vacancy clustered fraction of the final defect configuration as a function of energy. Parameters for the fitted curves can be found in table YY.

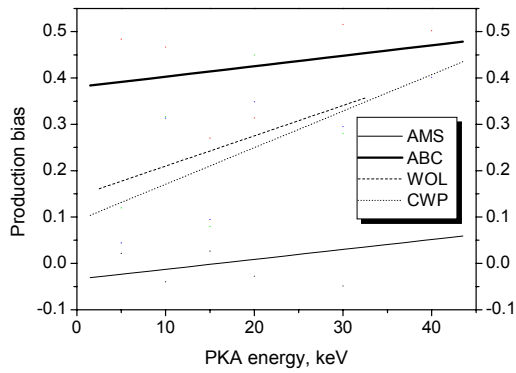


Figure YYY. Production bias between SIAs and vacancies.

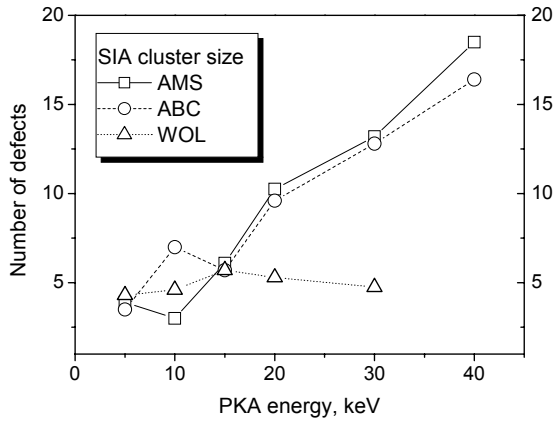


Fig. Z Average SIA cluster size.

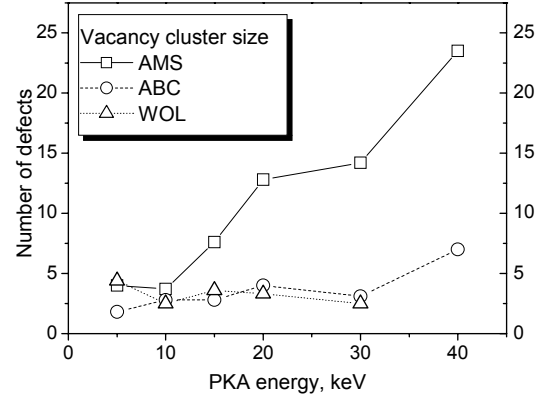


Fig.ZZ Average vacancy cluster size.

Table Y. Gives fitting parameters for SIA clustered fractions. The fit uses a power law form according to  $y = A \cdot E^B$

| Potential | A      | B       | $\chi^2$ |
|-----------|--------|---------|----------|
| AMS       | 0.2732 | 0.2108  | 7.64     |
| ABC       | 0.5589 | 0.0660  | 5.40     |
| CWP       | 0.1586 | 0.4250  | 5.79     |
| WOL       | 0.6301 | -0.0312 | 3.51     |

Table YY. Gives fitting parameters for vacancy clustered fractions. The fit uses a power law form  $y = A \cdot E^B$

| Potential | A      | B       | $\chi^2$ |
|-----------|--------|---------|----------|
| AMS       | 0.4240 | 0.0179  | 0.59     |
| ABC       | 0.1783 | 0.0981  | 4.40     |
| CWP       | 0.1791 | 0.1286  | 5.81     |
| WOL       | 0.7829 | -0.3337 | 2.39     |



**KTH Engineering Sciences**

# **Analysis of Fuel Cycle Scenarios for Transmutation of Nuclear Waste**

Alexandra Ålander

Master of Science Thesis  
Department of Nuclear and Reactor Physics  
Royal Institute of Technology

Stockholm 2005



## Abstract

This study is a first step in investigating, from a Swedish perspective, the option of using transmutation of spent nuclear fuel to ease the radiotoxic burden on a final nuclear waste repository. The investigation is a rough estimation, where focus was put on analysing the subsequent reduction of LWR-accumulated plutonium and americium, by deploying accelerator-driven systems (ADS). Several scenarios are examined with the Swedish light water reactor (LWR) park, consisting of 10 light water reactors and a once-through fuel cycle, as the reference scenario. The simulations addresses one long-term scenario and one phase-out scenario where plutonium and americium are incinerated using ADS in order to decrease the accumulated LWR-generated transuranics (TRU). A complementary simulation of the equilibrium scenario is analyzed with the modification of having LWR MOX-recycling prior to the TRU burning in ADS. The objective of the long-term scenario is to assess the ratio of LWRs over the number of ADS needed to consume the TRU in a quasi-equilibrium cycle, in a LWR-park operating with a constant energy production. The phase-out scenario aim to assess the number of ADS needed to significantly reduce the LWR-accumulated plutonium and americium content of the Swedish spent fuel, following a phase-out of all reactors after 40 years of operation.

The simulation of equilibrium scenarios shows that four ADS, of 800 MWt each, are sufficient to burn an amount of plutonium and americium, corresponding to the build-up of those isotopes in a system of 10 LWRs, with an installed capacity of approximately 10 GW. Furthermore it shows that the plutonium inventory could be more reduced by MOX-recycling in LWRs prior to the ADS operations, but on account of slightly higher americium production.

The short-term phase-out simulation shows that incineration of TRU in three to four ADS, with a lifetime of 50 years, appears suitable in a LWR-park with an installed capacity of 10 GWe, where 10 reactors are operated for a time period of 40 years.

The Nuclear Fuel Cycle Simulation (NFCSim) code is the simulation tool used in all calculations [1].

## **Acknowledgements**

I wish to thank Waclaw Gudowski for opening the door to a whole new world, in which I intend to stay, and giving me the opportunity to participate in a number of exciting projects through which I deepened my knowledge of both physics and cultural experiences. I also wish to thank the department of Nuclear and Reactor Physics which was a part of that world. Especially Calle and Malin with whom I travelled a lot, Daniel, Per and Mikael for valuable comments during text editing, Janne for advice and general support, Torbjörn for giving a hand whenever a computer crisis arose, Jan for fruitful cooperation and everybody contributing to the friendly and stimulating environment at the department.

Furthermore I am grateful to my mother and grandmother for always providing me with good advices, my dear friends for supporting me and being patience during times of hard work, Bromma Ridklubb for being my second family and Äppelvikens Ridskola my second home.

Finally I would like to acknowledge the Swedish Centre for Nuclear Technology (SKC) for financial support and Tomas Lefvert for professional counsel.

## Abbreviations

|         |                                      |
|---------|--------------------------------------|
| ADS     | Accelerator-driven systems           |
| BOL     | Beginning of life                    |
| BWR     | Boiling water reactor                |
| EOL     | End of life                          |
| eV      | Electron volt                        |
| FR      | Fast reactor                         |
| GWd/tHM | Gigawatt days per ton of heavy metal |
| GWt     | Gigawatt thermal power               |
| GWe     | Gigawatt electric power              |
| LINAC   | Linear accelerator                   |
| LWR     | Light water reactor                  |
| MA      | Minor actinides                      |
| MWd/tHM | Megawattdays per ton of heavy metal  |
| MWt     | Megawatt thermal power               |
| MWe     | Megawatt electric power              |
| MOX     | Mixed oxide fuel                     |
| PWR     | Pressurized water reactor            |
| TRU     | Transuranic elements                 |
| tHM     | Tons of heavy metal                  |
| UOX     | Uranium oxide fuel                   |

|       |   |    |
|-------|---|----|
| 1     | Introduction.....   | 1  |
| 2     | Generating nuclear power.....                               | 4  |
| 2.1   | The reactor core.....                                       | 4  |
| 2.2   | Moderator.....  | 4  |
| 2.3   | Coolant.....  | 5  |
| 2.4   | Thermal reactors.....                                       | 6  |
| 2.4.1 | Pressurized water reactors.....                             | 6  |
| 2.4.2 | Boiling water reactors.....                                 | 7  |
| 3     | The Nuclear Fuel Cycle.....                                 | 9  |
| 3.1   | Uranium.....  | 9  |
| 3.2   | Mining and milling.....                                     | 9  |
| 3.3   | Conversion.....   | 10 |
| 3.4   | Enrichment.....   | 10 |
| 3.5   | Fuel fabrication and components.....                        | 10 |
| 3.5.1 | Burnup.....   | 11 |
| 3.5.2 | Uranium oxide (UOX).....                                    | 12 |
| 3.5.3 | Fuel cladding.....  | 12 |
| 3.5.4 | Burnable poisons.....                                       | 12 |
| 3.6   | Reprocessing.....   | 13 |
| 3.7   | Spent nuclear fuel.....                                     | 13 |
| 3.7.1 | Transuranium elements.....                                  | 14 |
| 3.7.2 | Fission products.....                                       | 15 |
| 3.8   | Nuclear waste.....  | 17 |
| 3.8.1 | Different categories of waste.....                          | 17 |
| 3.8.2 | Radioactivity of nuclear waste.....                         | 17 |
| 3.9   | Spent fuel storage and disposal.....                        | 18 |
| 4     | Swedish Spent Fuel Storage and Disposal.....                | 20 |
| 4.1   | CLAB – Central interim storage facility for spent fuel..... | 20 |
| 4.2   | SFR – Repository for radioactive operational waste.....     | 20 |
| 4.3   | SKB – Swedish nuclear fuel and waste management.....        | 21 |
| 4.4   | The Swedish Geological Repository Model.....                | 21 |
| 4.4.1 | Äspö Hard Rock Laboratory.....                              | 22 |
| 4.4.2 | The canister.....   | 22 |
| 4.4.3 | The canister laboratory.....                                | 23 |
| 4.4.4 | The encapsulation plant.....                                | 23 |
| 5     | The Simulation Tool.....                                    | 25 |
| 5.1   | NFCSim classes.....   | 25 |
| 5.2   | The Material list.....                                      | 26 |
| 5.3   | Criticality calculations.....                               | 26 |
| 6     | Nuclear Fuel Cycles studied in the Red-Impact Project.....  | 28 |
| 6.1   | European transmutation project Red-Impact.....              | 28 |
| 6.2   | Fuel cycle scenarios within the Red-Impact.....             | 28 |
| 7     | Advanced Nuclear Fuel Cycles selected for this study.....   | 30 |
| 7.1   | Assumptions.....  | 30 |
| 7.2   | The Swedish reactor fleet.....                              | 31 |
| 8     | Characterization of the ADS Conceptual Design.....          | 32 |

|      |   |    |
|------|---|----|
| 9    | ADS and MOX Transmutation Strategy - Equilibrium Scenarios..... | 34 |
| 9.1  | Scenario I – LWR reference scenario .....                       | 34 |
| 9.2  | Scenario II - LWR + ADS .....                                   | 34 |
| 9.3  | Scenario III - LWR + MOX + ADS .....                            | 34 |
| 10   | Results - Equilibrium Scenarios.....                            | 35 |
| 10.1 | Scenario I – LWR reference scenario .....                       | 35 |
| 10.2 | Scenario II - LWR + ADS .....                                   | 36 |
| 10.3 | Scenario III - LWR + MOX + ADS .....                            | 36 |
| 10.4 | Discussion of results - Equilibrium Scenarios .....             | 37 |
| 11   | ADS Transmutation Strategy – Phase-Out Scenarios.....           | 39 |
| 11.1 | Scenario IV – LWR reference scenario .....                      | 39 |
| 11.2 | Scenario V - LWR + 3 ADS .....                                  | 39 |
| 11.3 | Scenario VI - LWR + 4 ADS.....                                  | 39 |
| 12   | Results - Phase-Out Scenarios .....                             | 40 |
| 12.1 | Scenario IV – LWR reference scenario .....                      | 40 |
| 12.2 | Scenario V - LWR + 3 ADS .....                                  | 41 |
| 12.3 | Scenario VI - LWR + 4 ADS.....                                  | 41 |
| 12.4 | Discussion of results - Phase-out Scenarios.....                | 42 |
| 13   | Conclusions.....  | 43 |
|      | References.....   | 45 |
|      | Appendix A - Nuclear Fission .....                              | 47 |
|      | A.1 The fission process.....                                    | 47 |
|      | A.2 Neutron-induced fission.....                                | 48 |
|      | A.3 Fissile and fertile nuclides.....                           | 48 |
|      | A.4 Fission neutrons .....                                      | 49 |
|      | A.5 Fission energy .....  | 49 |
|      | A.6 Thermal neutrons .....                                      | 49 |
|      | A.7 Cross sections.....   | 50 |
|      | A.8 The fission chain reaction .....                            | 52 |
|      | Appendix B - Transmutation of Nuclear Waste .....               | 54 |
|      | B.1 Transmutation.....  | 54 |
|      | B.2 Transmutation reactors.....                                 | 55 |
|      | B.3 Subcritical accelerator-driven systems.....                 | 56 |
|      | B.3.2 Spallation target.....                                    | 58 |
|      | B.3.3 Coolant .....   | 58 |
|      | Appendix C - The Swedish Referendum .....                       | 59 |

# 1 Introduction

Sweden is the world biggest consumer of nuclear power per capita. About 50% of the total electricity production (around 145 TWh per year) in Sweden is produced by nuclear power and with 9 million inhabitants it makes 8 MWh of nuclear energy produced per inhabitant and year. Since 1972 when the first nuclear reactor was connected to the grid there has been discussions on whether Sweden should continue the use of nuclear power or not. However according to latest decisions made by the government, the Swedish nuclear power is to be phased out and replaced by renewable energy sources. How this will be done is not yet clear. In 1999 Barsebäck-1 was shut down and after years of discussions between the government and the industry, concerning the shut down of Barsebäck-2, the discussion was terminated without reaching any consensus. Instead the government decided in December 2004 that the reactor should be shut down in May 2005. So far the energy compensation for Barsebäck 1 and 2 is compensated with energy from burning coal in Poland, Denmark and Germany and also with imported nuclear power from Finland and Russia. On the other hand power up-grades are conducted at the other Swedish reactors and when finalized in a couple of years this will fully compensate for the power supply lost by shutting down the two units at Barsebäck.

All present sources of energy has to deal with the consequences of having impacts on the environment, which in the case of firing coal, oil and gas, is the release of greenhouse gases. Nuclear power has the advantage of not releasing any pollution to the atmosphere and thus not contributing to climate heating and is in this sense a clean energy source. The biggest concern connected to nuclear power is that of managing the spent fuel which will need survey for thousands of years after discharge. Of most concern regarding the disposal of the nuclear waste are the actinides which constitute a major part of the radiotoxic burden. The actinides are, unlike the fission products, fissionable and may undergo fission by absorbing neutrons. Research of advanced nuclear reactors has proven the subcritical accelerator-driven systems (ADS) to be efficient in transmuting the actinides present in the spent fuel (Appendix B - Transmutation of Nuclear Waste). Transmutation in ADS is thus a way to reduce the long term radiotoxicity of the nuclear waste. According to recent studies it could achieve a hundredfold reduction of the actinide radiotoxic inventory compared to the once-through cycle [2]. The elements considered for transmutation of nuclear waste are plutonium, americium, curium and neptunium.

Some selected aspects of the nuclear fuel cycles leading to optimization of the management of light water reactor (LWR) spent fuel is a key goal of this work.

Important technological assumptions must be done while studying advance fuel cycles, which are in reality far away from the existing industrial practice today. In particular:

- the development of new techniques to partition and reprocess spent fuel isotopes with minimal process losses not exceeding 0.1% and acceptable doses to workers and the public
- the successful design of innovative reactors in particular accelerator-driven systems and dedicated reactors with a fast neutron spectra
- the development of new fuel materials containing a large fraction of transuranics with acceptable safety performance while achieving high burnup
- the development of economical reprocessing and fabrication of those advanced technologies
- public and political acceptance for deployment of the advanced reprocessing facilities and new reactors/subcritical systems

The successful transmutation goal requires availability of suitable reactors/subcritical systems leading to a net reduction, or at least stabilization, of the total actinide inventory and reduction of the radiotoxic inventory of the final waste. In this respect reactors and subcritical systems operated in the fast neutron spectrum are preferred for the purpose of incineration of transuranics (TRU), as fast neutronics guarantees a sufficient surplus of neutrons for transmutation and superior fission to capture ratios of many higher actinides [2]. Furthermore is the recycling of plutonium as Mixed Oxide Fuel (MOX) in LWRs proposed in order to extract more energy from the LWR-fuel cycle and stabilize the plutonium stockpile of the final spent fuel. Mono-recycling (single pass) of plutonium in conventional LWRs is today an industrial practice (French PWR 900 series) leading to a reduction of the net amount of plutonium produced every year by LWRs. However, multi-recycling of plutonium in ordinary LWRs, requires further studies as it leads to the degradation of the safety characteristics of LWR-MOX cores [3].

This thesis presents a study of advanced nuclear fuel cycles aimed to optimize the nuclear waste management for the Swedish nuclear reactor fleet, i.e. a medium size nuclear power system based currently on a simple once-through strategy. The reference scenario is the Swedish LWR-park which aims at characterizing the final spent nuclear fuel inventory of the Swedish LWR fleet when it is retired. The accumulated spent LWR-fuel is then used to feed a park of accelerator-driven systems, with the goal to reduce the radiotoxic inventory through incineration of plutonium and americium. Subsequently the benefits of deploying the ADS are examined.

Two types of scenarios are analyzed; one long-term equilibrium scenario and one phase-out scenario. The objective of the equilibrium scenario is to assess the ratio of LWRs over number of ADS needed to consume the LWR-generated TRU. In the equilibrium scenario the Swedish reactor park operates at a constant nuclear electricity production, with an optimal number of ADS integrated into the park, in order to stabilize the plutonium and americium production/destruction. The simulation covers the time period from the start-up of the first reactor Oskarshamn-1 in 1972 until 2100. A modification of the equilibrium scenario is also performed, with the introduction of LWR MOX-recycling prior to actinide burning in ADS.

The short-term phase-out scenario addresses a country adopting a phase-out of existing reactors. The approach is to find an optimal number of ADS to reduce the radiotoxic burden of the final waste, through the recycling of the spent LWR generated americium and plutonium. The future need for electricity supply is of no concern but instead focus was put on reducing the burden of radiotoxic spent fuel for the Swedish spent fuel repository. As to the referendum in 1980 (Appendix C - The Swedish Referendum) the nuclear power in Sweden is to be phased out and the phase-out simulations were carried out under these assumptions and thus decommissioning the reactors after 40 years of operation.

Chapter 2 starts with an introduction to nuclear power (reactors and components) and continues in Chapter 3 with the different steps of the nuclear fuel cycle. Chapter 4 is a description of the Swedish spent nuclear fuel disposal model. Chapter 5 describes the methods of calculation, followed by a presentation of the studied scenarios in chapter 6 and 7. Chapter 8 presents the conceptual design of the ADS used as a model in the simulations. Chapter 9, 10, and 11 contains the simulation details followed by the results in chapter 12 and finally the conclusion is found in chapter 13. General descriptions of the basic physics of nuclear fission is found in Appendix A - Nuclear Fission, an introduction to transmutation and accelerator-driven systems in Appendix B - Transmutation of Nuclear Waste, as well as a short summary of the Swedish referendum in 1980 in Appendix C - The Swedish Referendum.

The study made part of the European Project Red-Impact (Impact of Partitioning and Transmutation and Waste Reduction Technologies on the Final Nuclear Waste Disposal).



## 2 Generating nuclear power

Fission is the main process generating energy in nuclear reactors (Appendix A). When nucleus fission (which in a reactor might be uranium or plutonium nuclei) it splits in two smaller fragment, called fission products. Most of the energy released during fission is carried away by the fission products as kinetic energy. The kinetic energy is transformed to heat when the fission products collide with a coolant material (5) inside the reactor core. The coolant (which in the case of light water reactors is water) passes through the fuel elements in the reactor vessel and removes the heat produced in the fuel. The coolant turns water into steam which drives a turbine. The turbine, connected to an electricity producing generator, turns the mechanical energy into electricity and with the efficiency of around 32% a typical large reactor with a thermal output of 3200 MWt is generating an electricity of 1000 MWe. There are today around 442 commercial nuclear power plants operating in 31 countries [4] of which 214 are pressurized water reactors (PWR) and 89 are boiling water reactors (BWR) [5]. Together they have an installed capacity of almost 400 GWe and they supply around 17% of the world's electricity [6].

### 2.1 The reactor core

The reactor core is the part of the nuclear power plant where the fission chain-reaction occurs and heat is generated. It is an assembly of fuel elements, control rods, coolant and moderator, contained in a reactor vessel. The control rods serve the purpose of controlling the power and while moving them in or out of the core, the neutrons available for the chain reaction are varied and the rate of fission controlled. The control rods are made of a neutron absorbing material and two commonly used control rod materials in LWRs are cadmium and boron. The coolant (2.3) serves the purpose of keeping the core from getting too hot by transferring the heat generated in the core. It is also the media which transfers the heat to the turbines that generate the energy. The moderator (2.2) is the material used in thermal reactors to slow down the neutrons to preferable energies (0.025 eV), to enhance the chances of a  $^{235}\text{U}$  to capture a neutron and fission. Common moderator materials in today's reactors are light water and graphite.

### 2.2 Moderator

The fission cross-section for  $^{235}\text{U}$ , which is the isotope causing fission LWRs, is much higher with thermal neutrons than with fast neutrons (**Figure 15**). As prompt fission neutrons have energies around 1-2 MeV the reactors fuelled with  $^{235}\text{U}$  need to slow down the prompt neutrons to thermal energies. This is achieved by

combining the fuel with a material, called the moderator. Neutrons slow down by colliding with the moderator atoms where in every collision they lose some energy. If the neutrons do not leak out, they will continue to scatter until they reach thermal energies and are absorbed in the core, preferably in the fuel. A moderator should have a high scattering cross-section, low mass number and low capture cross-section, since the neutrons must be scattered and not absorbed by the moderator. For thermal reactors there are different choices of moderator material. Most suitable moderator materials are water, heavy water and graphite and they all have advantages and disadvantages. Water is cheap with a good scattering cross section however its capture cross section is rather high. Heavy water has very low capture cross section and good slowing down properties, but it is very expensive to separate heavy water from ordinary water. Graphite is not very expensive and has a low capture cross section, but together with water as coolant the safety aspects are not fulfilled. If the temperature rises in the water the density of the water will decrease and the void in the water (bubbles) increase. Less neutrons will be captured in the water and more neutrons will be available to cause fission in the fuel. As the graphite is still continuing to slow down the neutrons, the fission rate will increase and result in a dangerous positive temperature feedback contribution. The graphite and water moderated reactor (Russian RBMK reactors) is said to have a positive total temperature feedback at 20% of full power and the physical properties in the case of large temperature increase will increase the reactivity. LWRs on the other hand, where water serves as both moderator and coolant, have a negative temperature feedback on the reactivity. When the neutron capture characteristics of the coolant are reduced, in case of a temperature rise, it will also affect the moderator characteristics. The density decrease and the void increase, which in the case of graphite moderated reactors only results in decreased neutron capture, will in the case of a LWR have the effect of also reducing the moderating effect. Subsequently fewer neutrons will be slow-downed and fewer neutrons will be able to cause fission in the fuel. If the fission rate decreases, it will eventually make the temperature go down, stabilizing the reactor operation.

### **2.3 Coolant**

For a nuclear reactor the main function of the coolant is not only to transfer heat to the turbines but also to cool the core and surrounding materials. Because radioactive decay causes continued heat production, even after the reactor is shut down, it is necessary to maintain cooling to avoid a core melt down.

The coolant depends on type of reactor and can be water or heavy water, a gas like helium or carbon dioxide (British MAGNOX and AGR), or a liquid metal such as sodium or liquid lead alloys (fast reactors). For thermal reactors the most common used coolants are light water and carbon dioxide. In light water- and heavy water reactors the coolants serve as moderator as well. Important characteristics of

coolants are low neutron capture cross section to avoid loss of neutrons through absorption in the coolant, high specific heat conductivity and heat transfer coefficient and good stability against chemical interaction with other components of the reactor.

## 2.4 Thermal reactors

Nuclear reactors are often classified by the energy of the neutrons that cause most of the fissions. In a thermal reactor almost all fissions are caused by thermal neutrons. The fission neutrons are slowed down to thermal energies through collisions with the moderator, until they reach energy equilibrium with the moderator material. The neutrons will then have energies around 0.025 eV (in a fast reactor on the other hand, it is the fast fission neutrons that cause fission and the moderator material is avoided as the neutrons should not be slowed down) (**Figure 14**). All power producing nuclear reactors present in the world today are thermal reactors, a majority of which are LWRs - boiling water reactors (BWRs) and pressurized water reactors (PWRs).

### 2.4.1 Pressurized water reactors

The pressurized water reactor (PWR) is the most widely used type of power reactor in the world – 214 PWRs are operating worldwide [4]. It belongs to the category light water reactor and uses water both as a coolant and moderator. A typical PWR core contains 190 to 240 fuel assemblies of  $17 \times 17$  arrays of fuel pins, with a total of 90 000 to 125 000 kg of  $\text{UO}_2$ . The core is around 3.5 m in diameter and 4 m high. The PWR employs two water loops. The primary water pumped through the core is held at a high pressure (typically 15.5 MPa) preventing the water from boiling. It enters the vessel with a temperature of about  $290^\circ \text{C}$  and exits at about  $325^\circ \text{C}$ . It then causes the water in a secondary water loop to generate steam, which in turn pass through a turbine. The use of a two-loop system, ensures that no radioactivity pass through the turbine [7]. **Figure 1**. Pressurized water reactor. 1-control rod drive, 2-control rod, 3-inlet from reactor coolant pump, 4-outlet to steam generator, 5-reactor vessel, 6-fuel assembly, 7-thermal shielding, 8-lower core plate (courtesy of Kärnkraftsäkerhet och Utbildning AB). An example of a PWR is shown in **Figure 1**.

## PRESSURIZED WATER REACTOR

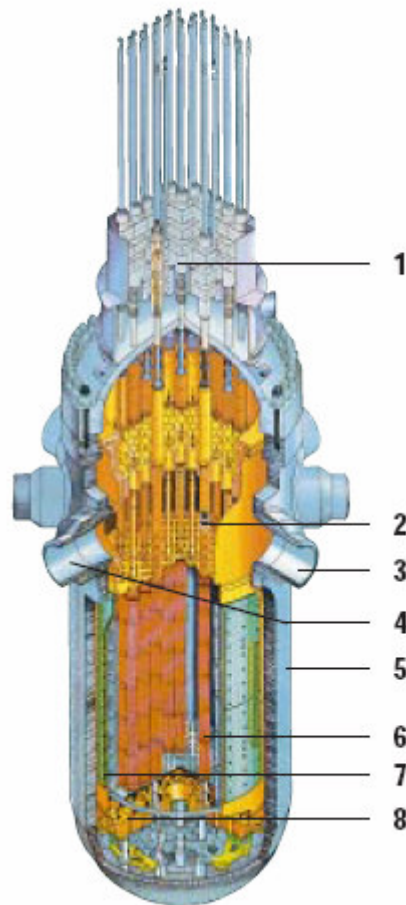


**Figure 1.** Pressurized water reactor. 1-control rod drive, 2-control rod, 3-inlet from reactor coolant pump, 4-outlet to steam generator, 5-reactor vessel, 6-fuel assembly, 7-thermal shielding, 8-lower core plate (courtesy of Kärnkraftsäkerhet och Utbildning AB).

### 2.4.2 Boiling water reactors

Like the PWR the boiling water reactor (BWR) belongs to the category light water reactor and uses water both as a coolant and moderator. After the PWR it is the most common type of reactor and 89 BWRs are operating in the world today [4]. Typically 750 fuel assemblies of 8x8 to 10x10 arrays of fuel pins, containing 140 000 to 160 000 kg of  $\text{UO}_2$ , constitute the boiling water reactor core. The uranium enrichment varies from 2 to 4%  $^{235}\text{U}$ . In a BWR the water is allowed to boil while passing through the core. The water enters the vessel at the top, at a pressure of about 7.2 MPa, flows down the vessel wall and then upward through the core. The water then exits the core as steam at about 290 °C. The steam passes directly to the turbine, getting condensed after leaving the turbine and is pumped back into the reactor. The fact that BWRs have only one loop avoids the need for

steam-generators and other equipment connected to it [7]. An example of a BWR is shown in **Figure 2**.

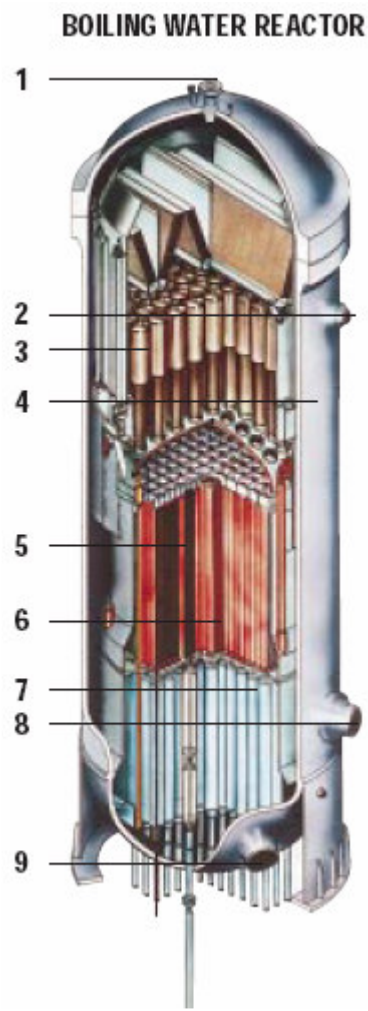


**Figure 2.** Boiling water reactor. 1-inlet for head cooling spray, 2-steam outlet, 3-moisture separator, 4-reactor vessel, 5-control rod, 6-fuel assembly, 7-control rod guide tube, 8-outlet to main circulation pump, 9-inlet from main circulation pump (courtesy of Kärnkraftsäkerhet och Utbildning AB).

### 3 The Nuclear Fuel Cycle

The nuclear fuel cycle (NFC) describes the different steps of the nuclear fuels' path from the mining of uranium, through conversion, enrichment and fuel fabrication – which make up the front-end of the fuel cycle, to irradiation of the fuel in the reactors, reprocessing, cooling, storage and finally the disposal – which make up the back-end. The fuel cycle is thus all the steps required to supply a nuclear reactor with fuel and take care/make use of the spent fuel. The most common nuclear fuel today is Uranium Oxide (UOX) and Mixed Oxide Fuel (MOX). Other nuclear fuels considered for industrial use are metallic fuel and nitride fuel.

#### 3.1 Uranium

Uranium is a metal that occurs naturally in the earth's crust, with an abundance of around 2 g/ton. In, for example, Australia, USA and Kazakhstan, the concentration of uranium in the ground is sufficient to extract for use as nuclear fuel (0.03% to more than 0.5%). Natural uranium consists of different uranium isotopes, where the fissile isotope  $^{235}\text{U}$  has an abundance of 0.72% and the rest is mainly  $^{238}\text{U}$ . The fissile isotope  $^{235}\text{U}$  is driving the process by which energy is produced in most nuclear reactors. A self sustained fission chain reaction is not possible if the fraction of  $^{235}\text{U}$  in the fuel is too small and consequently the reactor will not operate. The fraction of the isotope  $^{235}\text{U}$  must thus be increased and before the fuel manufacturing takes place the uranium is enriched in  $^{235}\text{U}$  at an enrichment plant (3.4). To be able to perform the enrichment the uranium must be in the form of a gas and that is done at a conversion plant (3.3).

#### 3.2 Mining and milling

The first step of the nuclear fuel cycle involves the mining of the uranium. The mining is usually done by either surface (open cut), in situ (solution mining) or underground mining techniques, depending on the depth at which the ore body is found. After the mining of the uranium ore it is sent to a mill, often located close to the mine. At the mill a uranium oxide concentrate is produced ( $\text{U}_3\text{O}_8$ ), even known as yellowcake. The remainders of the uranium ore, called tailings, are produced in very large volumes. The tailings contain low concentrations of naturally occurring radioactive materials, such as  $^{232}\text{Th}$  and  $^{226}\text{Ra}$ , which decays to the radioactive gas  $^{222}\text{Rn}$  [8]. The total radioactivity of the tailings is however less than in the original ore [6].

### 3.3 Conversion

At the conversion facility the yellowcake is first refined to uranium dioxide ( $\text{UO}_2$ ), which can be used as fuel in the type of reactors not requiring enriched uranium (Canadian CANDU and British MAGNOX reactors use natural uranium as fuel). The uranium allocated for fuel in LWRs needs enrichment. To perform the enrichment the uranium must be in a gaseous form and is therefore converted into uranium hexafluoride ( $\text{UF}_6$ ) - a solid at room temperature and a gas at slightly higher temperature. The conversion is carried out at conversion plants in Europe, Russia or North America.

### 3.4 Enrichment

The enrichment is done by separating the uranium isotopes  $^{235}\text{U}$  and  $^{238}\text{U}$ . This is done when the uranium is in the form of the gaseous uranium hexafluoride by subsequently removing the  $^{238}\text{U}$  isotope. Two enrichment processes are in commercial use, gaseous diffusion and gas centrifuge, and they both use the mass difference between  $^{235}\text{U}$  and  $^{238}\text{U}$  to separate the isotopes. Enrichment accounts for almost half of the cost of nuclear fuel and about 5% of the total cost of the electricity generated [6]. Commercial enrichment plants are in operation in France, Germany, Netherlands, UK, USA and Russia. Smaller plants are in operation elsewhere. The first enrichment plants were built in the USA and used the gaseous diffusion process, but more modern plants in Europe and Russia use the centrifuge process. The centrifuge process has the advantage of using much less power per unit of enrichment and can be built in smaller, more economic units. As the enrichment technology could be used by clandestine weapon programs to enrich weapon-grade uranium for non-peaceful use, the enrichment facilities are one of the most crucial steps of the fuel cycle and subject to proliferation concerns.

### 3.5 Fuel fabrication and components

After the enrichment the uranium is chemically converted back to uranium dioxide and processed into fine powder. The powder is sintered<sup>1</sup> into pellets with a diameter of 7-10 mm, depending on reactor type. The pellets are loaded into fuel rods, made of metal or ceramic rods with a sheet of a cladding material, and backfilled with helium gas [9]. Additional volumes at the top and bottom ends of the rods allow space for fission gas production. The rods are collected in fuel assemblies and loaded into the reactor core.

---

<sup>1</sup>The sintering process increases the density of the pellet by partial fusion of the powder grains under high temperature (1650°C) but without exceeding the melting point.

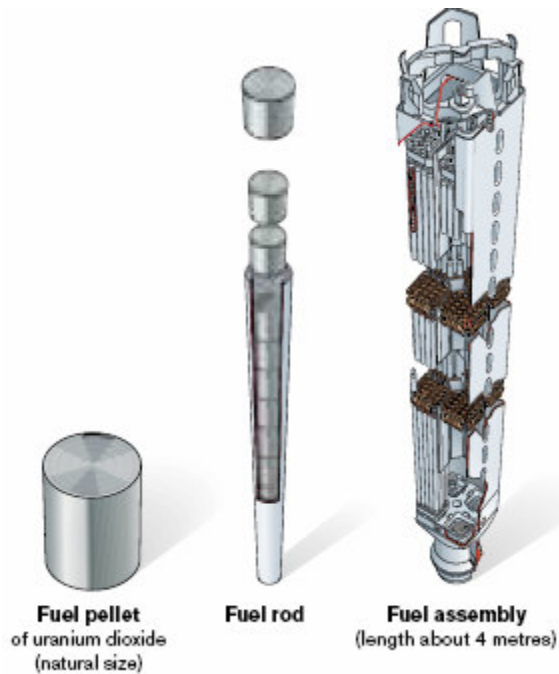


**Fig. 3** Fuel element (courtesy of SKB).

During years of irradiation in the core the composition of the fuel will change with time and power outage. Fissile material is consumed and fission products produced. The fuel assemblies have to be moved around during its time in the core, to get an optimal core configuration. Fresh fuel with a high enrichment are often located at the boundary of the core and moved further against the centre as it gets more burned up and after about three years in the core, the fuel elements will be replaced by fresh fuel [7]. To function properly the reactor core environment the fuel and cladding material must be designed to withstand high temperatures and irradiation, which expose the fuel to chemical, physical and isotopic changes. The most important constrains imposed on the fuel are not to reach the melting point and not to release any fission products to the coolant and thereby to the environment. The materials therefore constitute an important role in the reactor design and pose a limiting condition on the operation.

### 3.5.1 Burnup

Burnup is a measure of the power outage of the fuel. It is defined as the thermal effect, produced during a certain operating time and per unit mass of uranium. Depending on the time spent in the core, the fuel reaches different burnups. Today a typical maximum burnup in LWRs is around 40 GWd/tHM. For economical reasons there is an urge to increase the burnup and thus the power outage, as long as it poses no safety risk.



### 3.5.2 Uranium oxide (UOX)

The uranium oxide is the fuel currently in use in LWR (a part may be replaced by MOX fuel, see chapter 3.6). It is a ceramic fuel, which is a solid and brittle inorganic material. The UOX is chemically stable, has a high melting point (2865°C) and the fission products are retained within the UO<sub>2</sub> crystal even at a high burnup. UOX has a low thermal neutron capture cross section, which together with all what was said above, and the fact that the fabrication cost is low make the UOX attractive as fuel material. One drawback of having a ceramic fuel is its relatively poor thermal conductivity which is inferior to that of uranium metal (used in British Magnox reactors). But the uranium metal causes environmental and security-related problems as they corrode more easily in contact with water and decays into uranium hybrid.

### 3.5.3 Fuel cladding

The fuel cladding surrounds the fuel and serves many purposes. It must provide the heat in the fuel to be transferred to the coolant, but prevent corrosion of the fuel by the coolant. Although bombarded with neutrons the cladding must also be able to retain the fission products. Finally not to affect too seriously the neutron economics of the core, the cladding material must have a small thermal neutron absorption cross section. The cladding material used in LWRs is called zircaloy which is a composite based on zirconium with a few percent of the elements tin, iron, chromium and nickel. Zirconium is a relative abundant element in the earth's crust, with a melting temperature of 1845°C.

### 3.5.4 Burnable poisons

Burnable poisons are neutron absorbing materials, which are necessary in the fuel to accomplish a more efficient reactivity control and a better fuel utilization. The reactor core must have a sufficient excess of reactivity in order to increase the power and to compensate for fuel depletion, fission products with a high neutron absorption cross section and temperature effects that introduce negative reactivity. But once the desired power is reached the net reactivity must be zero for constant operation. The reactivity control may be achieved by the use of control rods, but burnable poisons allow for better fuel utilization as they reduce the excess reactivity which otherwise would exceed the predetermined safety limit. The burnable poisons reduce the excess reactivity by absorbing neutrons from the core and as the excess reactivity of the fuel is the highest at the beginning of the cycle, so is the amount of burnable poisons. By the end of the cycle the amount of burnable poisons is of course reduced due to the neutron capture. The fuel is by then considerable depleted and the excess reactivity less and thus is the need for control rods or other reactivity control reduced. Chemical compounds of boron (B<sub>4</sub>C) and gadolinium (Gd<sub>2</sub>O<sub>3</sub>) are two materials used as burnable poisons.

### 3.6 Reprocessing

The plutonium content in the spent fuel from a normal operation of a light water reactor is usually around 1.1% [2]. Some countries recover that plutonium to recycle as new fuel. To recover the plutonium the spent fuel must first be reprocessed. During the reprocessing process the uranium and plutonium are separated from the waste products and fuel assembly cladding, by chopping up the fuel rods and dissolving them in acid. The recovered uranium can be returned to the conversion plant for conversion to uranium hexafluoride and subsequent re-enrichment and the plutonium, as an oxide ( $\text{PuO}_2$ ), is mixed with uranium (natural or depleted) oxide and recycled as new fuel. The mixture is called mixed oxide fuel (MOX) and it can replace some of the UOX fuel elements in the core.

For use of MOX in LWRs, the proportion of plutonium is usually 3-10% [10]. MOX fuel, consisting of about 7% plutonium, is equivalent to UOX fuel enriched to about 4.5%  $^{235}\text{U}$ , assuming that the plutonium has about 60-65% of  $^{239}\text{Pu}$ . If weapons plutonium is used, which consists of more than 90%  $^{239}\text{Pu}$ , only about 5% plutonium is needed in the mix, due to the higher fission probability of  $^{239}\text{Pu}$  compared to the other plutonium isotopes  $^{240}\text{Pu}$ ,  $^{241}\text{Pu}$  and  $^{242}\text{Pu}$ .

Four plants in the European Union currently produce commercial quantities of MOX fuel; two at the reprocessing facility La Hague in France, one in Dessel, Belgium, and a fourth plant is operating at Sellafield in the UK [3].

### 3.7 Spent nuclear fuel

During the years of irradiation in the core the composition of the fuel will change with time due to fission and neutron capture. After about 12-24 months irradiation in the core, the fraction of fissile material in the fuel is too low and a part of the fuel in the core has to be exchanged for fresh fuel. After a normal operation in a LWR the discharged (UOX) fuel consists of about 95% uranium (mostly  $^{238}\text{U}$ ) and the rest of radiotoxic nuclides; fission products ~ 4% and transuranics ~ 1%. Some of the main elements present in spent UOX are found in **Table 1**.

**Table 1.** Main elements present in spent fuel [3]

The periodic table is color-coded and annotated as follows:

- heavy nuclei:** Elements 89-103 (actinides).
- activation products:** Elements 24-30, 42-48, 56-66, 74-80, 82-90, 92-103.
- fission products:** Elements 37-54, 87-91, 93-103.
- fission and activation products:** Elements 40, 41, 50, 51, 52, 53.
- long-lived radionuclides:** Elements 1, 2, 3, 4, 11, 12, 13, 14, 15, 16, 17, 18, 19, 20, 21, 22, 23, 25, 26, 27, 28, 29, 30, 31, 32, 33, 34, 35, 36, 37, 38, 39, 40, 41, 42, 43, 44, 45, 46, 47, 48, 49, 50, 51, 52, 53, 54, 55, 56, 57, 58, 59, 60, 61, 62, 63, 64, 65, 66, 67, 68, 69, 70, 71, 72, 73, 74, 75, 76, 77, 78, 79, 80, 81, 82, 83, 84, 85, 86, 87, 88, 89, 90, 91, 92, 93, 94, 95, 96, 97, 98, 99, 100, 101, 102, 103.

### 3.7.1 Transuranium elements

Transuranium elements or transuranics (TRU) are the elements which have an atomic number higher than that of uranium i.e. plutonium, americium, neptunium, curium etc. all the way to lawrencium (**Table 1**). Practically none of the transuranics occur naturally and must be synthesized by nuclear reactions. One example is when actinide<sup>2</sup> nuclei capture neutrons during reactor operation. Instead of undergoing fission the nuclei are transmuted through  $\beta$ -decay into heavier isotopes – transuranics. One such reaction is when the uranium isotope  $^{238}\text{U}$  captures a neutron and forms  $^{239}\text{Pu}$  through two successive  $\beta$ -decays of  $^{239}\text{U}$  and  $^{239}\text{Np}$ . The half-lives of  $^{239}\text{U}$  and  $^{239}\text{Np}$  are 24 minutes and 2.3 days respectively and the reaction may be written:



The transuranic composition in the nuclear fuel is an equilibrium composition where neutron captures, decay and fission of TRU equilibrates after a few years in the reactor core. Even though the yield of transuranics in the spent fuel is not big, the intense radioactivity of most of the transuranics necessitates the use of very strict shielding. Half-life and amount of most important actinides from LWR-UOX discharges are shown in **Table 2**.

<sup>2</sup> Radioactive metallic element with atomic number 89-103 and similar chemical properties []

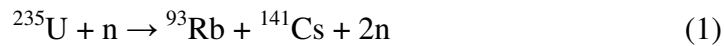
**Table 2.** Half-life and relative mass of uranium and main transuranium elements in discharged LWR-UOX fuel (41.2 GWd/tHM and 3.7% initial enrichment) after four years of cooling [26].

| <b>Nuclide</b>    | <b>Half-life<br/>[years]</b> | <b>Relative Mass</b> |
|-------------------|------------------------------|----------------------|
| <b>Uranium</b>    |                              |                      |
| <sup>235</sup> U  | $7.04 \cdot 10^8$            | 0.8%                 |
| <sup>236</sup> U  | $2.34 \cdot 10^7$            | 0.6%                 |
| <sup>238</sup> U  | $4.47 \cdot 10^9$            | 98.6%                |
| <b>Neptunium</b>  |                              |                      |
| <sup>237</sup> Np | $2.14 \cdot 10^6$            | 100                  |
| <b>Plutonium</b>  |                              |                      |
| <sup>238</sup> Pu | 87.7                         | 2.5%                 |
| <sup>239</sup> Pu | 24100                        | 54.2%                |
| <sup>240</sup> Pu | 6563                         | 23.8%                |
| <sup>241</sup> Pu | 14.4                         | 12.6%                |
| <sup>242</sup> Pu | $3.73 \cdot 10^5$            | 6.8%                 |
| <b>Americium</b>  |                              |                      |
| <sup>241</sup> Am | 432                          | 63.8%                |
| <sup>243</sup> Am | 7370                         | 036.0%               |
| <b>Curium</b>     |                              |                      |
| <sup>243</sup> Cm | 29.1                         | 1.0%                 |
| <sup>244</sup> Cm | 18.1                         | 92.2%                |
| <sup>245</sup> Cm | 8500                         | 5.7%                 |
| <sup>246</sup> Cm | 4730                         | 1.1%                 |

Of particular importance to the spent fuel radiotoxicity are the minor actinides (MA), i.e. neptunium, americium and curium. They contribute to less than 0.1% of the spent fuel, but are still of major concern as they belong to the long-lived products, whose removal would decrease the long-term radioactivity in the waste.

### 3.7.2 Fission products

When a nucleus in a reactor core undergoes fission, it splits into two smaller nuclei (fission products), one bigger than the other. Normally the fission products induced by thermal neutrons will have mass numbers of around 90 and 140 each, where instead higher energy neutron induced fission yields more equally fragments (**Fig. 4**). A typical fission reaction induced by thermal neutrons is [12]



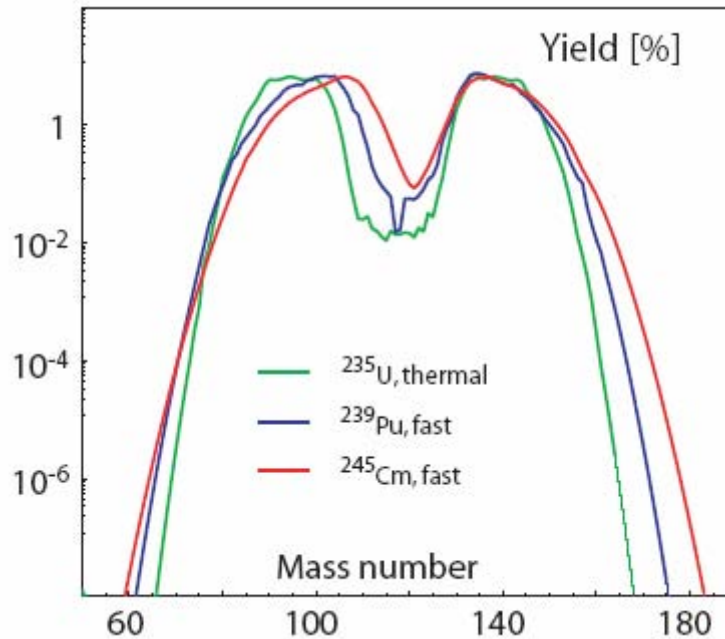


**Fig. 4.** Fission product yield as function of mass number [13].

Due to the many fission products, the irradiated fuel will contain up to more than 200 different isotopes of almost 40 different elements. The fission products are often far above the isotopic stability region and very radioactive as they decay toward stable isobars, emitting  $\beta$ -particles (electrons) and gamma radiation. Many of the fission products decay quickly, from seconds to minutes, and others have long half-lives, up to  $10^6$  years. The fission products from spent fuel which are of most concern are xenon, krypton, iodine, caesium and strontium. They are all volatile or gaseous elements, difficult to store and hazardous to people and may cause damage to human health if digested or inhaled. The main fission products in discharged UOX fuel are found in **Table 3**.

**Table 3.** Main fission products in discharged UOX fuel (41.2 GWd/tHM and 3.7% initial enrichment) after 4 years of cooling [26]

| <b>Fission Product</b> | <b>Half-life [years]</b> | <b>Relative Mass</b> |
|------------------------|--------------------------|----------------------|
| $^{93}\text{Zr}$       | $1.53 \cdot 10^6$        | 30.6%                |
| $^{99}\text{Tc}$       | $2.11 \cdot 10^5$        | 35.2%                |
| $^{107}\text{Pd}$      | $6.50 \cdot 10^6$        | 9.5%                 |
| $^{126}\text{Sn}$      | $\sim 1 \cdot 10^5$      | 1.1%                 |
| $^{129}\text{I}$       | $1.57 \cdot 10^6$        | 7.4%                 |
| $^{135}\text{Cs}$      | $2.30 \cdot 10^6$        | 16.2%                |

## 3.8 Nuclear waste

When removed from the reactor the spent fuel is very radioactive. It emits both radiation and heat and must be kept from getting out into the open through water and/or air diffusion. The uranium still present in the spent fuel does not require a very long storage, but the transuranics and fission products do. There are two options of handling the spent fuel. Either it is considered as waste (as in Sweden and the United States today) where the only option is long-term storage and final disposal, or it is considered as spent fuel which can be reprocessed and reused. That later option is what for example is done in France, where the plutonium has for a long time being separated from the spent fuel and reused as MOX fuel (3.6). But there is also the more advanced option of reprocessing and that is having a fuel cycle where the minor actinides are recycled using dedicated burners such as fast reactors and ADS. These advanced nuclear fuel scenarios could enable to decrease the radiotoxic content as well as the amount of spent fuel that needs to be disposed of and features an even more optimistic view on what is waste and what is not (6.2).

### 3.8.1 Different categories of waste

Waste is classified differently in each country. In Sweden there is no legal definition of radioactive waste, but for general purposes may be classified as low-level waste (LLW), intermediate-level waste (ILW) and high-level waste (HLW) and in summary described as “any material which contains or is contaminated by radionuclides and for which no use is foreseen” [14]. The LLW and ILW contribute to the majority of the waste and are produced during reactor operation or when a nuclear power plant is decommissioned, but also hospitals, industry and research facilities in Sweden produce LLW and ILW. These types of waste are generally called operational and decommissioning waste. The operational waste consists of things as used filters, replaced components, contaminated tools and used protective clothing. The decommissioning waste includes scrap metal and building materials. The total activity for LLW and ILW in the disposal facility must be less than 100 GBq, with a specific activity of individual waste packages less than 300 KBq/kg for radionuclides with half-lives greater than 5 years. The HLW consists of the spent nuclear fuel and is therefore highly radioactive. The HLW needs to be cooled and stored for a long time, whereas the LLW and ILW need not be cooled but nevertheless has to be stored for about 500 years.

### 3.8.2 Radioactivity of nuclear waste

Radioactive nuclear waste is essentially characterized by the type of elements it contains and by the activity level per unit of volume or mass. The activity is expressed in becquerels (Bq), which is the number of spontaneous disintegrations per second. Every radioactive element (also called radionuclide) is unstable and decays through the emission of radiation. Each of them is characterized by a

corresponding radioactive decay half-life (indicating the time it takes to reduce its activity level by a factor of 2), a radiation emission type (alpha, beta, gamma or neutrons) and the energy transmitted by this radiation. Due to the instability of the radionuclides the characteristics of the waste evolve with time and the radioactive nuclei give birth not only to other stable nuclei, but also to other radioactive nuclei (daughters) that will in turn disintegrate. The nuclear waste therefore stays highly radioactive for a long time and has to be isolated for as long as hundreds of thousands of years, until it reaches the same level of radioactivity as has the natural uranium ore (Fig. 5).

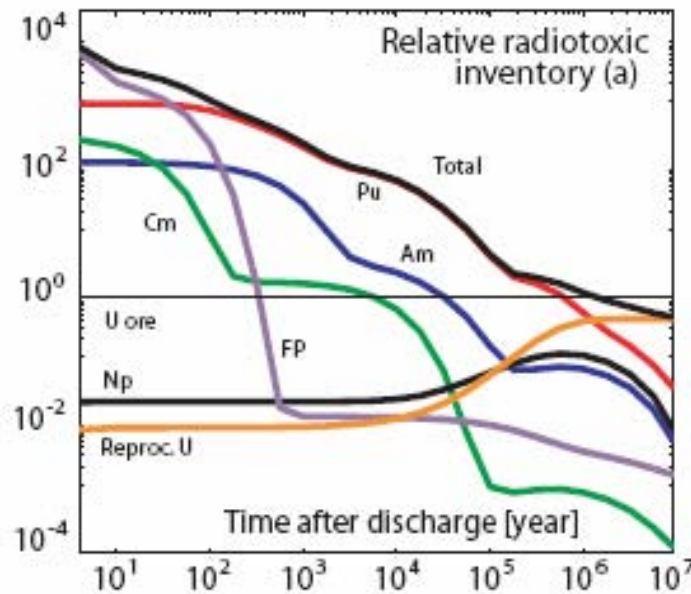


**Fig. 5.** Radiotoxic inventory of spent UOX (41.2 GWd/tHM with an initial uranium enrichment of 3.7 %) [26].

In a time perspective of 100 years the isotopes  $^{238}\text{Pu}$  and  $^{241}\text{Am}$  and the fission products  $^{90}\text{Sr}$  and  $^{137}\text{Cs}$  dominate the radiotoxicity of the spent nuclear fuel. In the long time perspective the radiotoxicity is determined by the transuranium elements, such as  $^{239}\text{Pu}$  (up to 100 000 years),  $^{242}\text{Pu}$ ,  $^{237}\text{Np}$  and the long-lived fission products  $^{129}\text{I}$ ,  $^{135}\text{Cs}$  and  $^{99}\text{Tc}$ . Fission products like iodine, caesium and technetium are very mobile compared to the transuranics, but after they have declined it is the long-lived transuranics that constitute the biggest problem concerning the final deep repository [7].

### 3.9 Spent fuel storage and disposal

When taken out from the reactor core, the spent fuel is cooled in pools at a first stage at the reactor sites, where it is kept for several months to years. The water

shields the radiation and absorbs the heat. Depending on particular regulations in different countries, the spent fuel is then either reprocessed or transferred to central storage facilities, where it will be prepared for permanent disposal.

A number of countries perform investigations on options for permanent nuclear waste disposal and the most favoured option seems to be a placement into deep geological repositories. Finland is the only country in the world to have chosen a site where to start the construction of a final spent fuel repository. An underground test facility is under construction at Olkiluoto NPP with the name ONKALO. ONKALO will give detailed information about the bedrock of the disposal site and enable technologies to be tested under actual conditions. But it will not only serve research purposes, it has been designed to serve as access route to the final repository. ONKALO will take 6-7 years to complete and once it is completed the work on the encapsulation plant and repository will start around 2010. The repository is supposed to be ready to commence spent fuel disposal by the year 2020 [15].



## **4 Swedish Spent Fuel Storage and Disposal**

The fuel cycle employed today in Sweden, and in many other countries, is the once-through fuel cycle based on standard LWRs. According to the Swedish law spent nuclear fuel is to be stored in a deep geological repository without reprocessing. Every year about one fifth of each Swedish reactor core is being exchanged for fresh fuel [16]. This makes in all an amount of 200 tons of spent fuel, or high level waste (HLW), being removed per year. Up to now the accumulated amount of spent fuel in Sweden is about 4500 tons and the total estimated amount for the entire Swedish Nuclear Program is around 10 000 tons, according to the work done in this report<sup>3</sup>.

### **4.1 CLAB – Central interim storage facility for spent fuel**

When taken out of the reactor core, the spent fuel is at first cooled in water basins at the reactor sites for a couple of years before being transported by boat to CLAB (the Central Interim Storage Facility for Spent Fuel). At CLAB it is temporary stored in pools and kept for at least 40 years before it will be encapsulated in canisters and put into a final deep repository. CLAB is situated in the bedrock near Oskarshamn and has been under operation since 1985. It has a total capacity of storing 5000<sup>4</sup> tons of spent fuel and can receive around 300 tons per year [16].

### **4.2 SFR – Repository for radioactive operational waste**

The spent fuel is not the only waste that has to be disposed of. As mentioned before, there is also radioactive material from operating the power plants and from medical care, research and industry, which is classified as low- and intermediate-level waste (3.8.1). This material is not as radioactive as the spent nuclear fuel but still it has to be sheltered. SFR (Repository for Radioactive Operational Waste), an underground repository in Forsmark, is taking care of the final disposal of low- and intermediate-level waste. SFR has a capacity of storing 63 000m<sup>3</sup> of waste if the total activity of the disposed radioactive nuclides not exceeds 10<sup>16</sup> Bq, according to regulations made by the Swedish Radiation Protection Authority (SSI) [19]. Every year the repository receives 500-600 m<sup>3</sup> of waste and since the start in 1988 it has received about 30 000 m<sup>3</sup> [21].

---

<sup>3</sup> According to the Swedish National Council for Nuclear Waste, the total amount of spent nuclear fuel will be around 9000 tons [28].

<sup>4</sup> A 3000 ton additional pool is under construction next to the existing pool

### **4.3 SKB – Swedish nuclear fuel and waste management**

Swedish Nuclear Fuel and Waste Management (SKB) is responsible of managing and disposing of the spent nuclear fuel and radioactive waste from the Swedish nuclear power plants. SKB was formed by the four power companies in the early 1970s, at the time when nuclear power production started in Sweden. SKB governs both SFR and CLAB but they also conduct the planning and investigations for the final deep repository. SKB will have to find a location for and then build a deep repository for the spent nuclear fuel – a repository that requires no monitoring by future generations.

### **4.4 The Swedish Geological Repository Model**

Overview studies and feasibility studies enabled to decide on three locations in which SKB wanted to carry out site investigations. One of the three declined and there are now site investigations performed in Forsmark and Oskarshamn. These investigations will provide sufficient information about the rock to decide whether the site is suitable or not. The site investigations started in 2002 and are expected to be finished by 2007. Applications will be submitted to the Environmental Court and the Government the following year and SKB expect to obtain permits to start building the deep repository on one of the investigated sites in 2010. Presumably it will be possible to deposit the first canister with spent nuclear fuel in the deep repository around 2017.

The deep repository incorporates a series of safety features and will be built according to the multiple barrier principle (KBS-3 method). The fuel will be kept in a copper canister with the function to isolate the fuel from the environment. As long as the canister is intact, no radionuclides should be able to escape. The canister will be surrounded by a layer of bentonite clay which prevents corrosion and protects the canister against small movements in the rock. The clay will also act as a filter if water comes into contact with the canister. In that case the clay will swell and prevent the nuclides from escape. The bedrock itself retards the transport of the radionuclides, but its primary purpose is to protect the canister from mechanical damage and to offer a stable chemical environment. Another safety restriction of the Swedish repository is to have the possible to easily retrieve the spent fuel if necessary.

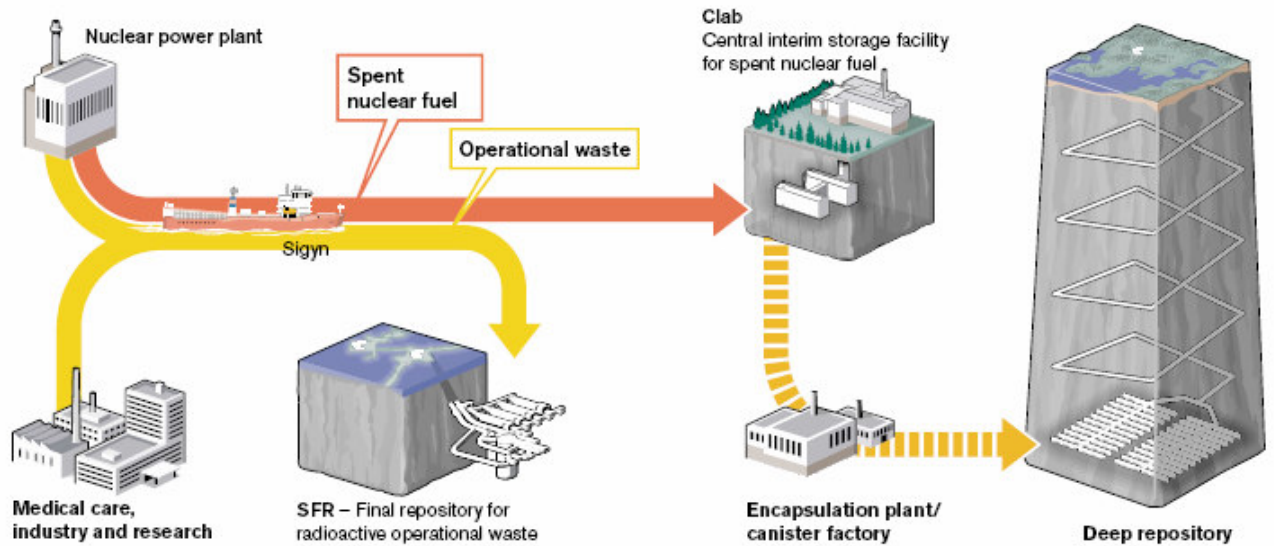


**Fig. 6.** Swedish nuclear waste management (courtesy of SKB)

#### 4.4.1 Äspö Hard Rock Laboratory

A prototype repository has been constructed, at a depth of 450 meters in the bedrock at the Äspö Hard Rock Laboratory (HRL), outside of Oskarshamn. Ongoing experiments with six full scale canisters are performed under realistic conditions to get knowledge about the processes that occurs in a deep repository [20].

#### 4.4.2 The canister

The canister, in which the spent fuel will be enclosed, is made of copper on the outside and iron on the inside. It is five meters long and has a diameter of just over one meter. It weighs between 25 and 27 tons when filled with fuel.

There are mainly two types of fuel assemblies to be encapsulated; PWR assemblies from pressurized water reactors (Ringhals NPP units 2, 3 and 4) and BWR assemblies from boiling water reactors (other Swedish reactors). The type of fuel assemblies to be encapsulated does not affect the appearance or dimensions of the copper shell, but it does affect the design of the insert. An insert intended for BWR assemblies holds twelve fuel assemblies, while one for PWR assemblies holds four [21].

The canister must protect the radiotoxic nuclides from getting to the groundwater for an extremely long period of time (~100 000 year). If for some reason the repository is not performing satisfactorily the canisters must be retrievable, therefore experiments on how to retrieve the canisters are performed at Äspö HRL.



**Fig. 7.** Copper Canister [18]

The operating phase of the deep repository begins with an initial phase where between 200 and 400 canisters are deposited during a period of about five years. When regular operation starts the deposition rate will increase to about 200 canisters per year. Regular operation is estimated to last about 30 years. A total of about 4,500 canisters will be deposited during initial and regular operation.

#### 4.4.3 The canister laboratory

Two alternative welding techniques for the copper canisters have been developed at the canister laboratory in Oskarshamn. One technique used is electron beam welding where the parts are fused together by an electron beam. Another technique is friction stir welding which entails a fusing of heated, soft material by a rotating tool. Both methods are already in use today in the manufacture of industrial products. In 2005 the friction stir welding method was chosen as the option to which further efforts should be focused.

#### 4.4.4 The encapsulation plant

An encapsulation plant will be built adjacent to CLAB. Having the encapsulation plant next to CLAB enables the plant to benefit from the long experience of

handling spent fuel at CLAB. It also allow for several of the existing systems and parts of CLAB to be utilized by both facilities. At the encapsulation plant the copper canisters will be filled with spent fuel and welded before transported to the repository. The plant will have a capacity to fill and seal one canister with fuel every day. According to regulations should the encapsulation plant be able to start operating in 2017 and operate for at least 60 years.

## 5 The Simulation Tool

The fuel cycle simulations in this thesis were done using the Nuclear Fuel Cycle Simulation code - NFCSim, developed at Los Alamos National Laboratory. NFCSim tracks the size and composition of the nuclear material which evolves with time. It contains a detailed description with time-dependent accounting of location and accessibility of nuclear reactors, enrichment plants, reprocessing facilities, fuel fabrication plants and storage facilities. The code models life-cycle material balances for an arbitrary number of reactors and includes a cost database. The modelling capabilities include LWR oriented fuel cycles with the option of actinide recycling in fast reactors and ADS. NFCSim groups fuel batches by fuel type and burnup calculations are carried out for each batch. The burnup and reactivity calculations are performed through invoke of the burnup code ORIGEN2.2 [24]. All the necessary one-group cross-section libraries were prepared using the 3D continuous energy Monte Carlo burnup code Monteburns [25].

With NFCSim it is possible to assess the transient effects (reactor start-up and shutdown) of a nuclear growth scenario, where the size and composition of the reactor fleet evolve with time. It is thus possible to analyze the impact of a certain fuel cycle scenario on spent fuel repositories concerning mass heat and radiotoxicity and to analyze its sustainability and economics.

### 5.1 NFCSim classes

NFCSim is written in Java, where every simulated element of the fuel cycle is represented as an object. Every object may receive nuclear material to which it performs some operation before it sends the material to the next object in the nuclear fuel cycle. Objects with similar properties and/or functions are grouped into classes. The classes contain fields with the class properties and methods that modify fields or return the result of a calculation. Reactors with common properties (same power, enrichment, tons of initial heavy metal etc) permit the formation of a class where each object represents a unique copy of its class. One class contains a simulation clock which makes the reactors run from the previous date to the current date on the simulation clock. Running the reactor objects might be the same as starting up, shutting down, restarting, ordering fuel, discharging fuel or decommissioning the reactor. Another class simulates the movement of charges. This method cycles through a time-loop and on each pass through the loop it interrogates every NFC object in search of events that should occur on that current pass. When the class detects an object with a date equal to the date on the simulation clock, it runs a method to get the current properties of the fuel charge.

Secondly it performs an operation on that material and sends the material to the next object in the fuel cycle. The mass and composition of a fuel batch, loaded into a reactor during a scheduled power outage, is then changed appropriately as it moves through each process of the nuclear fuel cycle.

## 5.2 The Material list

The material list outlines what elements and/or isotopes are followed throughout the NFC and can be as simple as  $M = \{U, Pu, MA, FP\}$  or  $M = \{^{233}U, ^{234}U, ^{235}U, ^{236}U, ^{238}U, ^{238}Pu, ^{239}Pu\dots\}$ . Fission products are treated in a more aggregated sense; those of importance to waste disposal ( $^{99}Tc, ^{129}I, ^{90}Sr\dots$ ) are tracked explicitly. Others are lumped into broader categories, e.g. lanthanides.

Arrays of efficiencies are used when simulating material balances. For example when separating the spent TRU fuel (where everything is recycled except the fission products) with the material list  $M = \{U, Pu, MA, FP\}$  and efficiencies:  $e_1 = \{0, 0, 0, 0\}$ ,  $e_2 = \{0.998, 0.998, 0.998, 0\}$  and  $e_3 = \{0, 0, 0, 0.998\}$ , the recycled TRU sent to the TRU fuel fabricator is  $e_2 \cdot M$ . The fission products sent to repository<sup>5</sup> are  $(M - e_2 \cdot M) \cdot e_3$ , and the high level waste (HLW) sent to the spent nuclear fuel (SNF) repository is  $(M - e_2 \cdot M) - (M - e_2 \cdot M) \cdot e_3$ .

## 5.3 Criticality calculations

To constrain average core reactivity equal to zero by the time a fuel batch is discharged, initial fuel composition must meet the burnup or residence time specified by NFCSim. Neutron production and destruction rates are calculated for each individual fuel batch and specific reactor, for one initial kilogram of all actinide isotopes present in the charged fuel. The reactivity and burnup calculations are performed through invoke of ORIGEN. In a core with N fuel batches, the core-wide reactivity  $\rho$  is calculated from a modified point reactivity model,

$$\rho = 1 - \frac{\sum_{i=1}^N D_i}{P_{NL} \sum_{i=1}^N P_i}$$

where  $P_{NL}$  is a non-leakage probability,  $D_i$  [neutrons/s] is the neutron destruction rate and  $P_i$  [neutrons/s] is the neutron production rate for the  $i^{\text{th}}$  batch.

The neutron production rate,  $P_i$ , is calculated using a batch production coefficient  $p(F)$  [ $\text{cm}^2/\text{kg}$ ] (i.e. the production rate normalized to the flux).

---

<sup>5</sup> NFCSim adopts a specific fission product repository

If a batch initially consists of  $Z$  distinct actinide isotopes and  $f_z$  is the initial mass fractions of the  $z^{\text{th}}$  batch (where  $z = 1 \dots Z$ ), the production coefficient may be written as

$$p(F) = \sum_{z=1}^Z f_z p_z(F)$$

where  $p_z(F)$  is the production coefficient of the  $z^{\text{th}}$  actinide at fluence  $F$  [neutrons/kb].

If the mass of the  $i^{\text{th}}$  batch is  $M_i$  [kg], the neutron production rate  $P_i$  [neutrons/s] in the batch is

$$P_i = M_i \phi_i p_i(F)$$

where the flux averaged over the entire fuel batch is approximated by the time rate of change of fluence,  $dF/dt$ ,

$$\phi_i \approx \frac{\Delta F}{\Delta t} = \frac{F(B(t_i + \Delta t)) - F(B(t_i))}{\Delta t}$$

and the burnup  $B$  [MWd/kg] is calculated analogously to the batch production coefficient.

Furthermore, if the initial heavy metal inventory of the core is  $M$  and the mass of the non-fuel components of the core (moderator, structural materials etc.) is  $M_{\text{nf}}$ , the neutron destruction rate  $D_i$  [neutrons/s] for the  $i^{\text{th}}$  batch is computed through

$$D_i = M_i \left( \frac{M_{\text{nf}}}{M} \frac{\xi \sum_{a,\text{nf}}}{\rho_{\text{nf}}} + d_i(F) \right) \phi_i$$

where the batch destruction coefficient,  $d$  [ $\text{cm}^2/\text{kg}$ ], is calculated analogously to the batch production coefficient,  $\xi$  is a disadvantage factor,  $\sum_{a,\text{nf}}$  is the spatially-averaged macroscopic absorption cross-section of the non-fuel components and  $\rho_{\text{nf}}$  is the mass density of the non-fuel components [1].

With the core-average reactivity available, the initial composition of a reload fuel batch is iteratively derived to satisfy the criterion of  $\rho = 0$  at discharge.



## **6 Nuclear Fuel Cycles studied in the Red-Impact Project**

This work was done in the framework of the European project Red-Impact.

### **6.1 European transmutation project Red-Impact**

*Impact of Partitioning, Transmutation and Waste Reduction Technologies on the Final Nuclear Waste Disposal* (Red-Impact) is a 3-year European project within the Sixth Framework Programme. The objective of the project is to evaluate the impact of Partitioning and Transmutation (P&T) and waste reduction technologies on the final waste disposal and to assess economical, environmental and societal benefits and costs of P&T.

The work of the project is subdivided into six work packages (WPs):

WP1: Waste management and transmutation strategies will be reviewed and a number of representative scenarios will be selected for in-depth impact studies.

WP2: Feasibility of the industrial deployment of selected scenarios will be made and their impact on waste management will be studied.

WP3: Assessment of waste streams, waste features, leach resistance, heat generation, reprocessing capability etc will be studied for selected fuel cycles.

WP4: Assessment will be made of the benefits and costs of P&T in advanced fuel cycles for waste management and geological disposal.

WP5: Economic, environmental and societal assessment of fuel cycle strategies will be performed.

WP6: Synthesis and dissemination of results of the above studies will be made to stakeholders.

The work performed in this thesis is submitted within WP3.

### **6.2 Fuel cycle scenarios within the Red-Impact**

The selection of the representative scenarios was based on an overview of previous studies of P&T strategies performed in previous EU framework programs, the NEA/OECD and IAEA international organizations [26] and independently by the partners. Five different scenarios and one reference scenario will be investigated. Those 6 scenarios are grouped into two categories called “near term industrial scenarios (A)” and “advanced scenarios (B)”:

A1 Reference scenario:

A scenario based on LWRs with direct disposal of the spent fuel where the reactors are operated for 40 years and the average burnup is 50 GWd/tHM. This scenario is the reference case for the comparison with other fuel cycle strategies.

A2 Near term industrial scenario:

A scenario with single recycling of standard MOX in pressurized water reactors. In this scenario the spent fuel is partitioned and some of its elements are reloaded into the reactors. Plutonium will be partially or completely recycled.

A3 Near term industrial scenario:

A scenario with multi-recycling of plutonium in Sodium Fast Reactor (FR).

B1 Long term Generation IV<sup>6</sup> scenario with FR:

This scenario employs infinite recycling of plutonium and minor actinides in fast reactors.

B2 Long term double strata without FR:

A simplified double strata scenario, without FR. UOX and MOX are irradiated in PWRs and plutonium and minor actinides are burnt in accelerator driven systems. The MA from the original uranium and the reprocessed fuel is transmuted in fast neutron spectrum ADS, where the fuel is continuously recycled after pyrochemical reprocessing

B3 Long term double strata with FR:

A double strata scenario with FR and ADS, where UOX and MOX are irradiated in PWRs and additional plutonium burning in FRs prior to minor actinide burning in ADS.

---

<sup>6</sup> “Generation IV” is the name for next generation nuclear energy systems with the objectives to provide sustainable energy systems that meets clean air objectives, minimizes nuclear waste, excels in safety and reliability and has a level of financial risk comparable to other energy projects [27] Generation IV designs will tend to have closed fuel cycles and burn the long-lived actinides so that fission products are the only high-level waste. Many will be fast neutron reactors.

## 7 Advanced Nuclear Fuel Cycles selected for this study

The Swedish reactor fleet operates with a mix of BWRs and PWRs and has a predestined fuel cycle back-end, where the spent fuel is to be stored without any reprocessing. This study is an investigation of one equilibrium scenario and one phase-out scenario with advanced fuel cycles and the Swedish once-through fuel cycle as the reference scenario. In the equilibrium scenarios the Swedish LWR-park was operated with a constant electricity production. An optimal number of ADS were introduced into the LWR-park, in order to keep the plutonium and americium production/destruction at a constant level. The objective was to assess the ratio of LWRs over the number of ADS needed to consume the LWR-generated plutonium and americium in a quasi-equilibrium cycle. A modification of the equilibrium scenarios was also performed with the introduction of LWR MOX-recycling, prior to the actinide burning in ADS. The phase-out scenarios focused at optimizing a strategy to reduce the radiotoxic burden of the Swedish spent fuel inventory, through the recycling of plutonium and americium in ADS. This scenario focused on a reasonably economically “as soon as possible” reduction of the Swedish TRU content, without paying attention to any nuclear electricity demand constraints, but showing a potential of the advanced fuel cycle to clean the back-end of the fuel cycle.

### 7.1 Assumptions

Data for all existing Swedish facilities (such as start-up and shutdown dates, power, core inventory, uranium enrichment etc.) was compiled through information provided by the power plants and literature. Some of these data are only temporal and changes over time, as in the case of the power output. For simplicity they are assumed to be constant, as it is unlikely that the impact of these changes would be very significant.

Recovery efficiencies for separated uranium and transuranics are assumed to be 99.99% and 99.8% throughout all simulations. Maximum TRU fraction in the fuel is set to 80% and the americium to plutonium ratio in the fuel to 20%. In NFCSim  $k_{\text{eff}}$  is constrained not to go above 0.97 at BOL. Furthermore, all data used by NFCSim concerning mines, conversion, fabrication and enrichment plants, are based on current US infrastructure. We also assume that no ADS facility would be industrially available before 2035 and that their lifetime would not exceed 50 years.

## 7.2 The Swedish reactor fleet

The Swedish reactor fleet consists of 12 nuclear reactors at a power of around 10 GW in all, but due to the shutdown of Barsebäck-1 in 1999 and Barsebäck-2 in 2005, only 10 of the reactors are in operation today. Nine of the Swedish reactors are BWRs and three of them are PWRs (**Table 4**). The reactors were constructed and taken into operation between the years 1972 and 1985, with an expected life time of 25 years. According to today's knowledge their expected life time is prolonged to 40 years, which also is adopted in the simulations done in this work.

**Table 4.** Swedish Reactor Data

| Reactor name | Reactor type | Thermal power [MWt] | Electric power [MWe] | Grid connection [year] | Uranium enrichment [%] | Burn-up [MWd/kg] | Initial core inventory [tons] |
|--------------|--------------|---------------------|----------------------|------------------------|------------------------|------------------|-------------------------------|
| Barsebäck-1  | BWR          | 1800                | 595                  | 1975                   | 3.25                   | 40               | 80                            |
| Barsebäck-2  | BWR          | 1800                | 595                  | 1977                   | 2.97                   | 40               | 80                            |
| Forsmark-1   | BWR          | 2929                | 970                  | 1980                   | 3.25                   | 40               | 121                           |
| Forsmark-2   | BWR          | 2929                | 970                  | 1981                   | 3.20                   | 41               | 121                           |
| Forsmark-3   | BWR          | 3300                | 1150                 | 1985                   | 3.30                   | 43               | 126                           |
| Oskarshamn-1 | BWR          | 1375                | 445                  | 1972                   | 2.80                   | 40               | 82                            |
| Oskarshamn-2 | BWR          | 1800                | 602                  | 1975                   | 3.00                   | 40               | 82                            |
| Oskarshamn-3 | BWR          | 3300                | 1160                 | 1985                   | 3.10                   | 40               | 127                           |
| Ringhals-1   | BWR          | 2500                | 830                  | 1976                   | 3.21                   | 43               | 125                           |
| Ringhals-2   | PWR          | 2652                | 870                  | 1975                   | 3.92                   | 44               | 80.5                          |
| Ringhals-3   | PWR          | 2775                | 920                  | 1981                   | 3.94                   | 43               | 82.1                          |
| Ringhals-4   | PWR          | 2775                | 915                  | 1983                   | 3.92                   | 44               | 82.1                          |

## 8 Characterization of the ADS Conceptual Design

The ADS conceptual design used as model in the simulations is a lead-bismuth cooled ADS. It employs a fertile-free fuel, in the form of a solid solution of a TRU-nitride, contained in an inert matrix. The thermal power is 800MWt and the burnup 200 MWd/kg, with a net plutonium consumption of 188 kg/efpy<sup>7</sup> and a net MA consumption of 21 kg/efpy.

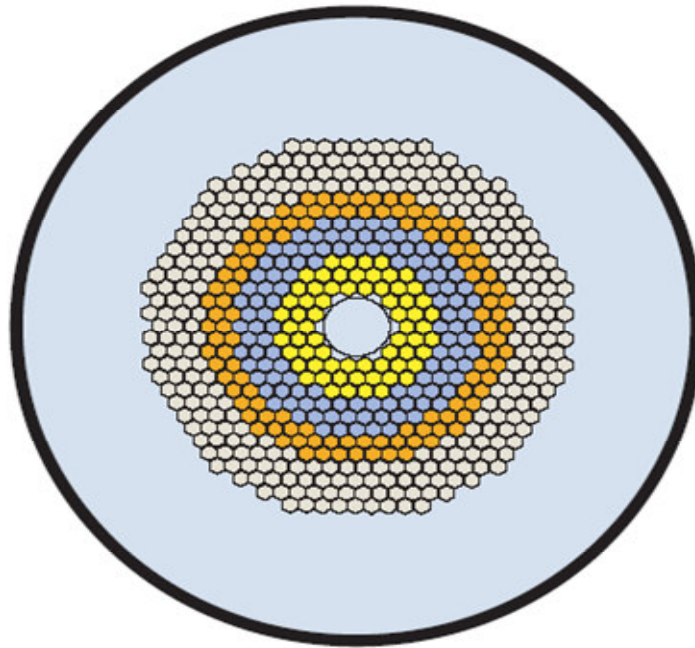


**Figure 8.** Cross-section of the conceptual Pb/Bi-cooled ADS core design with 282 sub-assemblies, three enrichment zones and a steel-reflector [13].

The TRU-nitride fuel is thought to be homogeneously mixed with the absorbing material hafnium-nitride (HfN). Hafnium has a very high melting temperature and good thermal conductivity. Furthermore the HfN-based fuel provides a good combination of neutronics, burnup and thermal characteristics. It provides an acceptable coolant void reactivity and decreases the reactivity swing, which mitigates the power peaking. Hafnium is also a good absorber of neutrons in the thermal and resonance energy regions, which hardens the neutron spectrum and thus minimizes the production of actinides in the fuel cycle (a fraction of two higher fission probability of <sup>241</sup>Am and <sup>243</sup>Am than typical systems employing inert matrix fuel [13]). Lead-bismuth eutectic is proposed as coolant. It combines low melting and high boiling temperatures with good voiding characteristics. Pb-Bi also features low chemical activity with surrounding materials.

---

<sup>7</sup> effective full power year

The core has 282 sub-assemblies, divided into three different zones of fuel enrichment, surrounded by a steel-reflector (see **Table 5** for TRU volume fractions and **Figure 8** for the cross-section of the conceptual core design).

**Table 5.** TRU volume fractions in fuel [13]

| <b>Sub-assembly row/zones</b>    | <b>1-3</b> | <b>4-6</b> | <b>7-8</b> | <b>9-12</b> |
|----------------------------------|------------|------------|------------|-------------|
| <b>Actinide fraction (vol %)</b> | 32         | 37         | 45         | -           |

## **9 ADS and MOX Transmutation Strategy - Equilibrium Scenarios**

The objective of the equilibrium simulations was to assess the ratio of LWRs over the number of ADS needed to consume the LWR-generated TRU in order to stabilize the plutonium and americium inventory. The Swedish LWR-park were operated with a constant electricity production and a number of ADS were then introduced into the LWR-park to stabilize the plutonium and americium production/destruction. (Scenario II). The simulation covered the time period from the start-up of the first reactor Oskarshamn-1 in 1972 until 2100. A modification of this scenario was also performed, with LWR MOX-recycling prior to the plutonium and americium burning in ADS (Scenario III).

### **9.1 Scenario I – LWR reference scenario**

The first simulation was the reference scenario consisting of the Swedish LWR-park, with an open once-through fuel cycle and no reprocessing of the spent fuel. The power (varying from 1800 to 3300 MWt depending on reactor) and burn-up (approximately 40 MWd/kg) were kept constant through the entire simulation (**Table 4**). The simulation covered the time period from 1972 until 2100.

### **9.2 Scenario II - LWR + ADS**

Investigations showed that four ADS introduced into the Swedish LWR-park was enough to consume the LWR-generated actinides and keep them at an approximately constant level. Minimum cooling time for the separated plutonium and americium was three years. The simulation covered the time period from 1972 and ended in 2100, with the ADS operating from year 2030 until 2100.

### **9.3 Scenario III - LWR + MOX + ADS**

This scenario was similar to scenario II with the modification of introducing MOX-recycling in two of the LWRs, prior to the americium and plutonium burning in ADS. The two full-core MOX LWRs was operated from 2000 until 2100, with a burn-up of 50 MWd/kg.

## 10 Results - Equilibrium Scenarios

### 10.1 Scenario I – LWR reference scenario

With a phase-in of the first Swedish reactor in 1972 the LWR reference scenario ended up with a total inventory of 25 000 tons spent UOX by the end of 2100 (**Table 6**). The spent fuel was considered as waste and stored without further treatment. After discharged of the all LWRs the total amount of stored spent fuel contained 281 tons of plutonium (**Figure 9**) and 29 tons of americium (**Figure 10**). The equilibrium production of plutonium when the LWRs were operated at a constant energy production was about 86 g/MWtyr, when normalized to the total amount of produced energy. The americium production was about 9 g/MWtyr.

**Table 6.** Inventory of spent fuel in equilibrium scenarios

| Scenario     | Spent UOX inventory [tons] | Reprocessed spent UOX [tons] | Pu mass inventory [tons] | Pu mass decrease* [tons] | Am mass inventory [tons] | Am mass decrease* [tons] |
|--------------|----------------------------|------------------------------|--------------------------|--------------------------|--------------------------|--------------------------|
| Scenario I   | 25 000                     | -                            | 281                      | -                        | 29                       | -                        |
| Scenario II  | 6000                       | 19000 (76%)                  | 118                      | 163 (58%)                | 6                        | 23 (79%)                 |
| Scenario III | 3000                       | 22 000 (88%)                 | 86                       | 195 (69%)                | 9                        | 20 (69%)                 |

\* compared to Scenario I (LWR reference scenario)

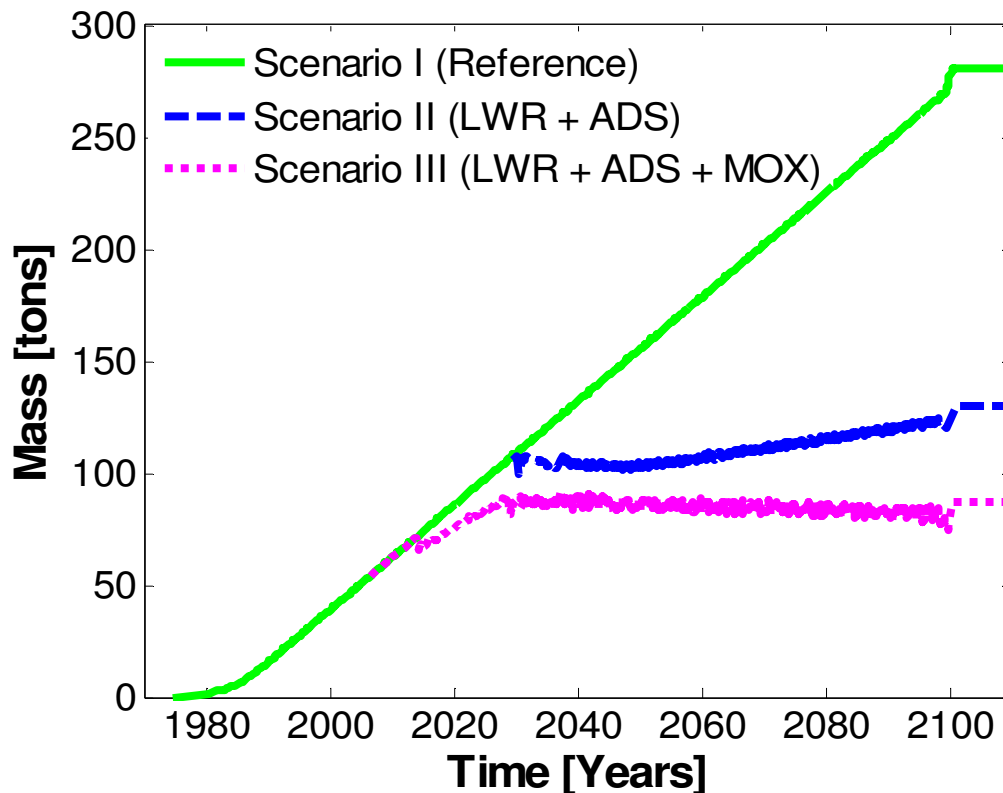


**Figure 9.** Plutonium out of core inventory in the equilibrium scenarios.



## 10.2 Scenario II - LWR + ADS

Stabilization of the LWR generated actinides, by incineration of plutonium and americium in four ADS, resulted in a total reduction of plutonium by 58% (163 tons) and americium by 79% (23 tons). The remainder of the plutonium inventory was 118 tons by the end of the simulation (compared 281 tons in the once-through reference scenario) and the americium inventory 6 tons (compared to 29 tons) (**Figure 10**). The main objective was to show that the actinide production could be stabilised and even decreased by introducing fast spectrum burners like ADS into a LWR-park (**Figure 9**). Even more, if one looks at the graph showing the amount of plutonium normalized to the total electricity production (**Figure 11**), one can easily see how the amount is decreasing with the amount of energy produced, compared to the reference scenario where it is constant.

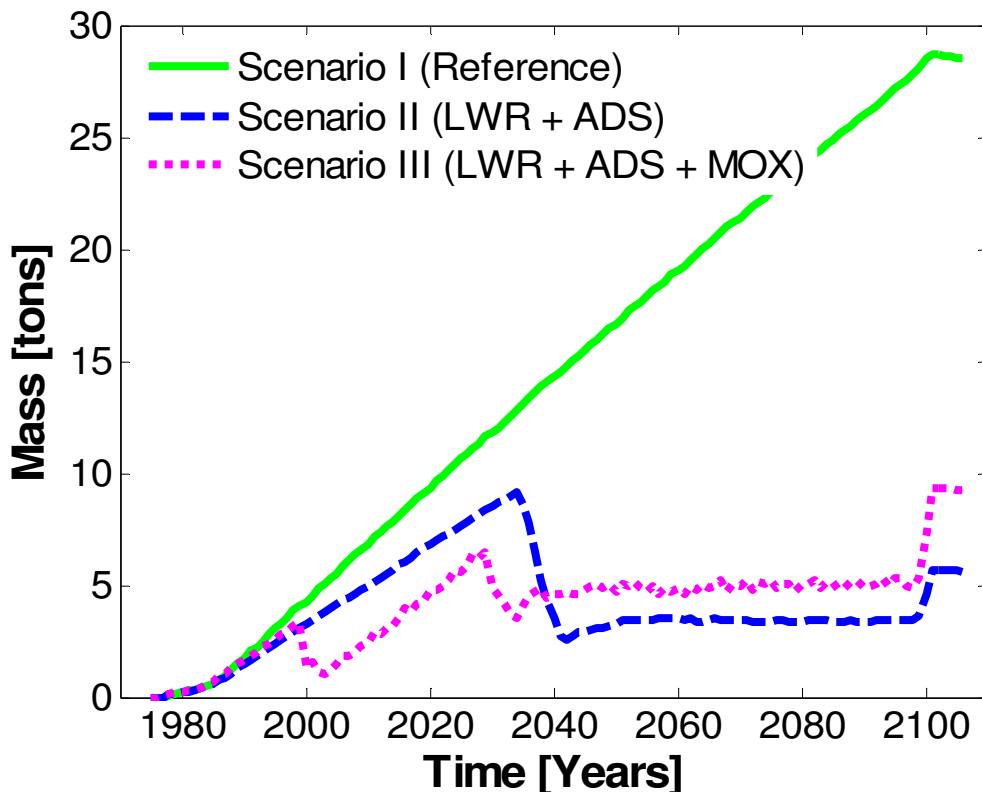


**Figure 10.** Americium out of core inventory in the equilibrium scenarios.

## 10.3 Scenario III - LWR + MOX + ADS

This scenario, based on Scenario II, with the addition of plutonium burning in two MOX-LWRs (operated between 2000-2100), reduced the amount of plutonium by 69% (195 tons) and americium by 69% (20 tons) (**Table 6**). In this scenario the plutonium inventory was slightly decreasing during the operation (**Figure 9**). By

the shut-down of the ADS, the plutonium inventory was 86 tons (compared to 281 tons in the reference scenario) and the americium inventory 9 tons (compared to 29 tons) (**Figure 10**). The fact that a smaller fraction of americium decreased in this scenario, compared to Scenario II, is due to the americium production which was built up from plutonium transmutation in the MOX fuel (32 tons more plutonium was burnt in scenario III). Again, if looking at the graph showing the amount of plutonium normalized to the total electricity production (**Figure 11**), one can see how the amount of plutonium is decreasing with the amount of energy produced, as in scenario II. Note that the plot is not constant from the beginning but increasing significantly until it reaches the constant level. This is due to the fact that NFCSim is not accounting for the plutonium inside the reactor cores, but ‘sees’ only the plutonium in the spent fuel storage, cooling etc.

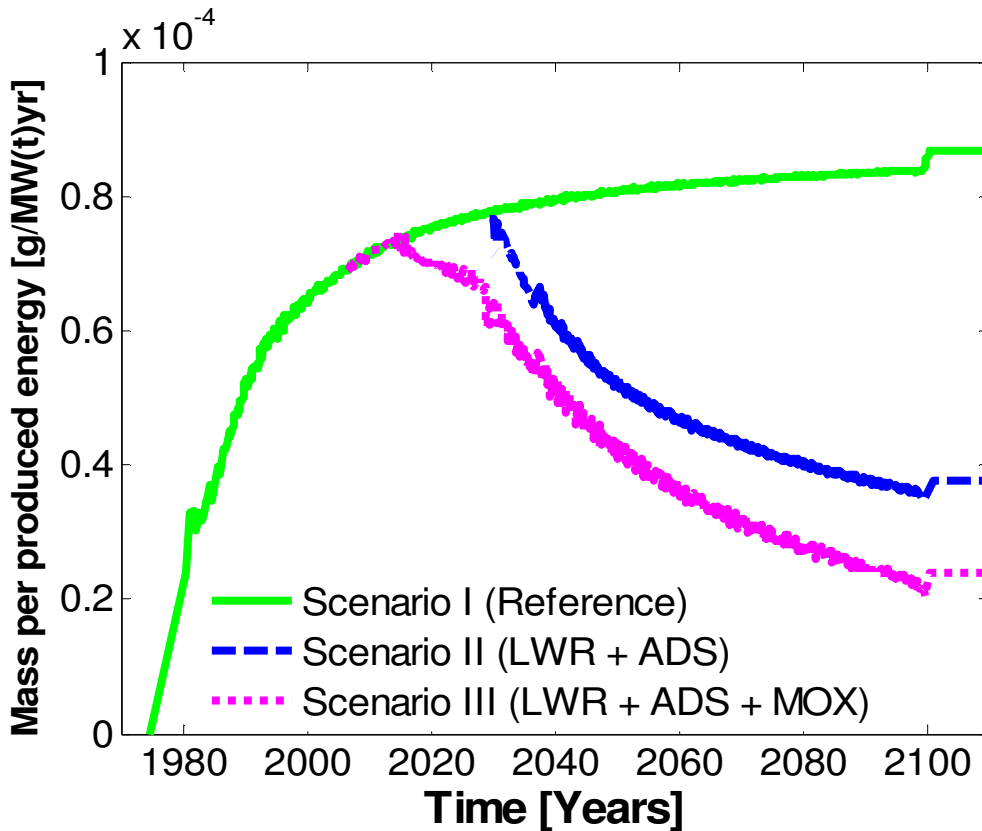


**Figure 11.** Plutonium mass per total produced energy. The figure shows how the plutonium mass per total produced energy is decreasing in scenarios II and III.

#### 10.4 Discussion of results - Equilibrium Scenarios

Investigations showed that four ADS were enough in order to stabilize the plutonium and americium generated from LWR-operations in a long-term scenario. The fraction of plutonium and americium in the spent fuel was significantly reduced when ADS were integrated into the LWR-park. MOX

recycling in Scenario III resulted in a slightly increase of americium compared to Scenario II, where only ADS were deployed. The simulations of these long-term scenarios indicate the enormous difference made by operating ADS for incineration of spent LWR fuel. Even though this study only deals with mass differences the impact on the final disposal from a radiotoxic point of view is obvious.

## **11 ADS Transmutation Strategy – Phase-Out Scenarios**

The goal with the phase-out scenarios was to optimize a strategy to reduce the radiotoxic burden through the recycling of plutonium and americium in an optimal number of ADS. The future need for electricity supply was of no concern but instead focus was put on reducing the burden of radiotoxic spent fuel for the Swedish spent fuel repository. As to the referendum in 1980 (Appendix C - The Swedish Referendum) the nuclear power in Sweden is to be phased out and the phase-out simulations were carried out under these assumptions and thus decommissioning the reactors after 40 years of operation. The first LWR, Oskarshamn-1, was taken into operation in 1972 and the two last LWRs to be phased-out, Oskarshamn-3 and Forsmark-3, were shut down in 2025. Three respectively four ADS were introduced into the park of LWRs in 2035 and were operated for a period of 50 years (Scenario V and Scenario VI). Subsequently the improvements over the results without ADS were examined.

### **11.1 Scenario IV – LWR reference scenario**

The objective of Scenario IV was to estimate the amount and isotopic composition of the spent nuclear fuel, discharged from the Swedish reactor park, to be fed into the ADS in Scenario V and VI. The simulation commenced with the start up of Oskarshamn-1 in 1972 and ended with the shut-down of Forsmark-3 and Oskarshamn-3 in 2025. All reactor data are found in Table 4.

### **11.2 Scenario V - LWR + 3 ADS**

Scenario V consisted of three ADS, where the conceptual design of the ADS was that of the ADS described in chapter 8. The plutonium and americium from the spent UOX fuel, discharged from the LWRs in Scenario IV (the reference scenario), was separated and cooled for three years before used as fuel in the ADS. By the year 2035 the ADS were put into operation for a time period of 50 years.

### **11.3 Scenario VI - LWR + 4 ADS**

Scenario VI was similar to Scenario V, with the addition of one more ADS. All ADS were supposed to operate for a time period of 50 years, and all were put into operating at the beginning of 2035.

## 12 Results - Phase-Out Scenarios

### 12.1 Scenario IV – LWR reference scenario

The simulation of the phase-out reference scenario resulted in an accumulated inventory of 9000 tons of spent UOX discharged from the Swedish LWRs by 2025 (Table 7). At that point the spent fuel contained a total of 107 tons of plutonium and 7.2 tons of americium (Figure 12), which served as stockpile to Scenarios V and VI where it was used as fuel in the fast spectrum ADS.

**Table 7.** Inventory of spent fuel in phase-out scenarios

| Scenario     | Spent UOX inventory [tons] | Reprocessed spent UOX [tons] | Pu mass inventory [tons] | Pu mass decrease* [tons] | Am mass inventory [tons] | Am mass decrease* [tons] |
|--------------|----------------------------|------------------------------|--------------------------|--------------------------|--------------------------|--------------------------|
| Scenario I   | 9900                       | -                            | 107                      | -                        | 7.2                      | -                        |
| Scenario II  | 600                        | 9300 (94%)                   | 29                       | 78 (73%)                 | 2.6                      | 4.6 (64%)                |
| Scenario III | 10                         | 9890 (99.9%)                 | 37                       | 70 (65%)                 | 3.7                      | 3.5 (49%)                |

\* compared to Scenario IV (LWR reference scenario)

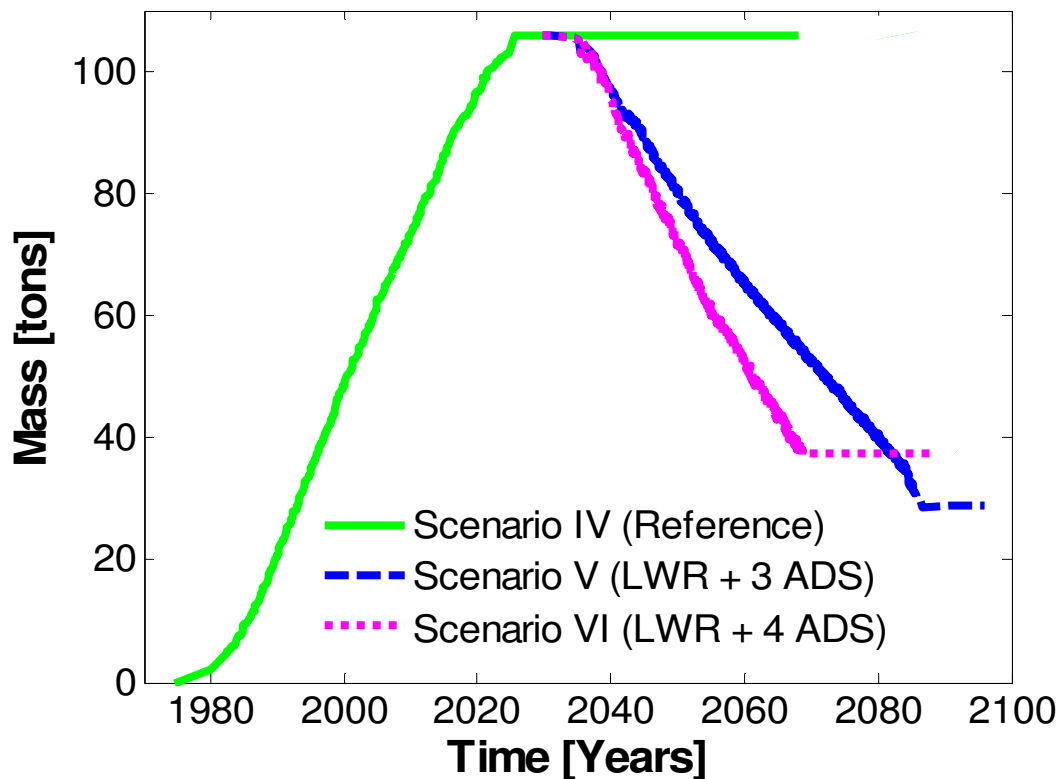


**Figure 12.** Plutonium out of core inventory in the phase-out scenarios.

## 12.2 Scenario V - LWR + 3 ADS

Burning the plutonium and americium recovered from the Swedish spent fuel, by operating three ADS during 50 years, contributed to reduce the inventory of plutonium by 73% (78 tons) and americium by 64% (4.6 tons) (**Table 7**). After shut-down of the ADS, the amount of plutonium in the system was 29 tons (27 tons in the interim storage and 2 tons of HLW<sup>8</sup>) compared to the 107 tons in the reference scenario. The amount of stored americium was by then 2.6 tons, compared to 7.2 tons (**Figure 13**).

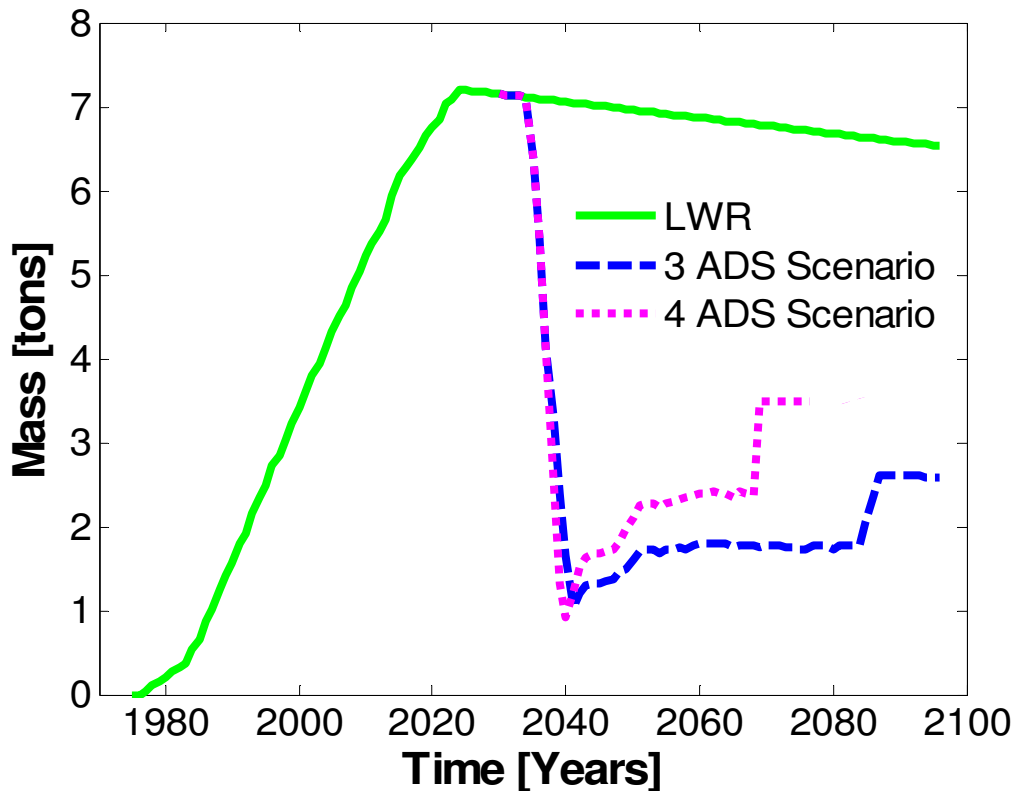


**Figure 13.** Americium out of core inventory for phase-out scenarios.

## 12.3 Scenario VI - LWR + 4 ADS

When feeding four ADS with the plutonium and americium from the Swedish spent fuel storage, NFCSim ended the simulation in 2070 after 35 years of running the ADS (**Figure 12**) due to an insufficient amount of plutonium in the interim storage. NFCSim does not account for the plutonium in the rest of the system and finds only what is stored in the interim storage waiting to be fed into the cores. At

<sup>8</sup> High level waste (HLW) is what is lost during the reprocessing. For TRU it was assumed to be 0.2%.

the time of shut-down only 7 tons of plutonium remained in the storage but in the rest of the system<sup>9</sup> as much as 37 tons of plutonium was still present. One way should of course be to continue the operation of one or two of the ADS with the plutonium taken out from the other ADS in order to burn the remaining plutonium and americium. This option was not further investigated in detail in this thesis, but is discussed in chapter 12.4 (Discussion of Results).

Anyway the reduction of plutonium during the 35 years of operation was 65% (70 tons) compared to the reference scenario. The americium inventory was reduced by 49% (3.5 tons) and ended at 3.7 tons (**Figure 13** and **Table 7**).

## 12.4 Discussion of results - Phase-out Scenarios

According to the Swedish Nuclear Fuel and Waste Management Company (SKB), the total amount of spent fuel after 40 years of operating the Swedish reactors, amounts to 9300 tons [28]. The NFCSim simulation of the Swedish LWR-park, with 40 years of lifetime (Scenario IV), gave a total amount of 9900 tons of spent fuel. Furthermore, the amount of plutonium and minor actinides present in the fuel, according to the NFCSim simulations, also seems reasonable. Their fraction in LWR-discharged fuel normally is about ~1% plutonium and ~0.05% americium which for plutonium was the same in the NFCSim output, whereas in the case of americium the fraction was 0.07%. The NFCSim-simulations of the reference scenario was thus not significantly different from the SKB expectations.

The optimal solution in a Swedish phase-out scenario seems to be a scenario where three to four ADS would burn the majority of the spent fuel inventory and one or two ADS would terminate the core inventory of the first ones. This could optimise the transmutation strategy and finish as much as possible of the remaining plutonium and americium still available in the system. A rough estimation, when looking at Scenario V, where 78 tons of plutonium and 4.6 tons of americium were burnt during a time period of 50 years in three ADS, one could expect each ADS to consume around 500 kg of plutonium and 30 kg of americium annually. A reactor park consisting of the Swedish LWR-park together with four ADS seems suitable. The last ADS would operate after shutdown of the first three ADS to terminate as much as possible of their cores.

---

<sup>9</sup> ADS cores, fuel fabrication, cooling storage, transportation, interim storage and high level waste.

## 13 Conclusions

This study is a first step in investigating, from a Swedish perspective, the option of using transmutation of spent nuclear fuel (UOX) to ease the radiotoxic burden on a final nuclear waste repository. The investigation is a rough estimation, where focus was put on analysing the subsequent decrease of LWR-accumulated plutonium and americium through the use of ADS. The reference scenario was the Swedish LWR-park and two types of scenarios were simulated; one long-term equilibrium scenario and one phase-out scenario. The equilibrium scenario aimed to assess the ratio of ADS over LWRs, needed to stabilize the inventory of LWR-produced plutonium and americium, in a reactor-park based on LWRs and ADS. The phase-out scenario aimed to assess the number of ADS needed to significantly reduce the LWR-accumulated plutonium and americium content of the Swedish spent fuel, following a phase-out of all reactors after 40 years of operation.

The simulation of the equilibrium scenarios showed that four ADS, of 800 MWt each, were sufficient to burn an amount of plutonium and americium, corresponding to the build-up of those isotopes in a system of 10 LWRs, with an installed capacity of approximately 10 GWe. Furthermore it was showed that the plutonium inventory could be more reduced by MOX-recycling in LWR prior to the ADS operations, but on account of slightly higher americium production.

The simulation of phasing-out the Swedish LWR-park, after 40 years of operating the reactors, ended up with a total amount of 9900 tons of spent fuel. Incorporating ADS in the phase-out scenario showed that 3-4 ADS appeared suitable in order to reduce the spent nuclear fuel inventory. In the scenario deploying three ADS all three ADS were operating through the predicted life-time of 50 year, with the result of decreasing the plutonium and americium inventory with 70% and 60% respectively. While in the scenario deploying four ADS, the simulation was terminated after only 35 years. The early shutdown by NFCSim in this scenario was caused by the fact that NFCSim only accounts for the amount of spent fuel stored in the spent fuel inventory and not the amount that is loaded into the reactor cores. In this case the plutonium inventory was not sufficient to continue feeding the four ADS cores, although more plutonium remained in the system which was thereby left un-recycled. In a virtual scenario the operation would of course continue and the optimal solution, in a Swedish phase-out scenario, could be to have three or four ADS running at a first round. One ADS would take off where the first three ADS finished, in order to finish as much as possible of the remaining plutonium and americium contained in the cores of the first ones.

From an economically point of view it is open to discussion if it would be worth the price to construct a park of ADS, with the purpose of closing a fuel cycle of a



LWR-park which is doomed to be phased-out. Although the amount of long-lived radiotoxic elements will be significantly less in a scenario pursuing transmutation, a certain amount of long-lived elements will always remain, due to losses in reprocessing and fuel fabrication. If instead, Sweden (or a country with similar energy policy), wishes to sustain/develop the use of nuclear power, the construction of ADS for transmutation of nuclear waste in a long-term perspective (compared to a phase-out scenario), is more justified economically. And even more important, considering the continued use of nuclear power, the most valuable argument pro-transmutation, in the perspective of long-lived radioactive elements, would not be purely of economically character but that of the morally and ethnically aspect. Pursuing transmutation would obliterate most of the 100 000 years heritage of radiotoxicity and should be considered a necessity to clear the back-end of the fuel cycle, in order not to shove the radiotoxic burden to future generations.

As discussed above; even though transmutation is adopted as a strategy to decrease the burden of nuclear waste, the need to manage high level waste will always exist, as losses occur during the reprocessing and fuel fabrication. And even though the waste management of irradiated ADS fuel will not need as long supervision as spent UOX fuel it will demand other disposal techniques. Further investigation of transmutation strategies, concerning Swedish nuclear waste management, would need to investigate not only this but should also include a cost analysis and a much more detailed analysis of the radiotoxic inventory, isotopic composition and doses to public and workers. However, these investigations are beyond the scope of this study.

## References

1. C. G. Bathke and E. A. Schneider, *NFCSim User's Manual*, Los Alamos National Laboratory Report LA-UR-04-8369 (2004).
2. OECD Nuclear Energy Agency, *Accelerator-driven Systems and Fast Reactor in Advanced Nuclear Fuel Cycles*, Paris (France), (2002).
3. P. Leconte, *Radioactive waste management research: today's results bringing tomorrow's solutions*, Clefs CEA no. 46 (2002).
4. [www.iaea.org](http://www.iaea.org)
5. ELECNUC, *Les Centrales Nucléaires dans le Monde*, CEA (2003).
6. [www.world-nuclear.org](http://www.world-nuclear.org)
7. B. Pershagen. *Lättvattenreaktorers säkerhet*. Energiforskningsnämndens Efn-rapport nr 20.
8. *The Nuclear Waste Primer*. The League of Women Voters Education Fund. New York (1993).
9. R. G. Cochran and N. Tsoulfanidis, *The Nuclear Fuel Cycle: Analysis and Management*, American Nuclear Society, Illinois (1999).
10. Uranium Information Centre website; [uic.com](http://uic.com)
11. N. Kaltsoyannis, P. Scott, *The f elements*, Oxford University Press, New York (1999).
12. K.S Krane, *Introductory Nuclear Physics*, Wiley, New York (1998).
13. K. Tucek. *Neutronic and Burnup Studies of Accelerator-driven Systems dedicated to Nuclear Waste Transmutation*, Doctoral Thesis, Stockholm (Sweden) 2004.
14. *Radioactive waste categories – current position (98) in the EU Member States and in the Baltic and central European countries*, EUR 18324 EN, European Commission (1998).
15. POSIVA Report 2003-03, *ONKALO Underground characterization and research programme (UCRP)*, Olkiluoto, Finland (2003).
16. *Anläggningar, CLAB – Central Interim Storage Facility for Spent Fuel*. Information booklet by the Swedish Nuclear Fuel and Waste Management Co (2001).
17. SKI website, [www.ski.se](http://www.ski.se)
18. FUD-PROGRAM 2001 - Program för forskning, utveckling och demonstration av metoder för hantering och slutförvaring av kärnavfall. SKB report (2001).
19. *Uppdaterade driftsvillkor för SFR 1*, Decision Dnr 6222/3744/03 by Swedish Radiation Protection Authority, (2003).
20. *Experiments at the Äspö Hard Rock Laboratory*. Information booklet by the Swedish Nuclear Fuel and Waste Management Co (2004).
21. SKB website, [www.skb.se](http://www.skb.se)

22. Working Party on the Physics of Plutonium Fuels and Innovative Fuel Cycles (WPPR), [www.nea.fr/html/science/wppr/index.html](http://www.nea.fr/html/science/wppr/index.html), eighth meeting, 4-5 February 1999, Issy-les-Moulineaux, (France).
23. Cogema website; [www.cogema.com](http://www.cogema.com)
24. G. Croff. *A Users Manual for the ORIGEN2 Computer Code*, Oak Ridge National Laboratory Report ORNL/TM-7175 (1980).
25. D. I. Poston, H. R. Trellue, *User's Manual, Version 2.0 for Monteburns, Version 1.0*, LA-UR-99-4999 (1999).
26. OECD Nuclear Energy Agency, *Actinide and Fission Product Partitioning and Transmutation; Status and Assessment Report*, Paris (France), (1999).
27. U.S DOE Nuclear Energy Research Advisory Committee and the Generation IV International Forum, *A Technology Roadmap for Generation IV Nuclear Energy Systems*, GIF-002-00, December 2002.
28. *Kunskapsläget på kärnavfallsområdet 2004*. Rapport av Statens råd för kärnavfallsfrågor – KASAM, SOU 2004:67.
29. Reactor Physics Course, KTH, 2004.
30. W.M. Stacey, *Nuclear Reactor Physics*, Wiley, New York (2001).
31. R.L Loftness, *Nuclear Power Plants*, D. Van Nostrand Company (1964).
32. S. Pillon and J. Wallenius. Oxide and nitride TRU-fuels: lessons drawn from the CONFIRM and FUTURE projects of the 5<sup>th</sup> European framework programme, Nimes (France) 2004.
33. S. Stambach et al., *The 0.9 MW Proton Beam at PSI and Studies on a 10 MW Cyclotron*, Proc. Second Int. Conf. on Accelerator Driven Transmutation Technologies and Applications, Kalmar (Sweden), (June 3-7 1996).
34. Review of the Spallation Neutron Source (SNS), DOE/ER-0705 (June 1997).
35. S. O. Schriber, *Developments of Linacs for ADTT in the USA*, Proc. Second Int. Conf. on Accelerator Driven Transmutation Technologies and Applications, Kalmar (Sweden), (June 3-7 1996).
36. ESS Instrumentation Group: Reports SAC Workshop, (May 2001).
37. H. Nifenecker, O. Medplan, S. David, *Accelerator Driven Subcritical Reactors*, Institute of Physics Publishing, London (2003).
38. *Kärnkraftsopinionen oktober 2004*. Temundersökning på uppdrag av Kärnkraftsäkerhet och utbildning AB (KSU), T-110883.

## Appendix A - Nuclear Fission

Fission is the main process generating energy in nuclear reactors. Fission is the splitting of a nucleus into two smaller fragments (fission products), gamma radiation, beta particles, neutrinos and a couple of neutrons. When fission occurs there is also a big amount of energy released. Most of the released energy is carried away by the fission products as kinetic energy which in a nuclear reactor may be transformed to heat and electricity. A chain reaction of fissions can occur very rapidly and without control, as in an explosive, or slowly and under control, as in a nuclear reactor.

### A.1 The fission process

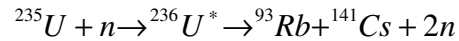
In some heavy elements, most of them with mass number above 250 (californium and above), fission may occur spontaneously as a naturally decay process. It happens when the strong nuclear force, which keeps the nucleons (protons and neutrons) in the nucleus together, is overcome by the repulsive Coulomb force. The nuclear force is short ranged ( $\sim 10^{-15}\text{m}$ ) and proportional to the number of nucleons. The repulsive Coulomb force on the other hand is proportional to the number of protons squared,  $Z^2$ . The more the protons contained in the nucleus, the stronger is the Coulomb repulsion and the more unstable is the nucleus against decay or fission.

When the nucleus fission it will split into two smaller fragments – fission products - and release energy. The two fission products will each get higher binding energy than the original nucleus. The binding energy is the mass difference – or so called mass defect - between a nucleus mass and the mass of its constituents (neutrons and protons) as free particles. A nucleus with a high binding energy per nucleon is more stable against decay or fission. For light elements the binding energy per nucleon increases rapidly from a value of 1.1 MeV for  $^2\text{H}$  until a maximum is reached at about 8.8 MeV for isotopes of mass number around 60. Thereafter the binding energy per nucleon decreases slowly to a value of 7.6 for  $^{238}\text{U}$ . The higher up on the binding energy curve the more stable is the nucleus. And any reaction which goes in the direction of increased binding energy, in other words, a reaction whose products have greater binding energy than the original nuclei, is an energy-releasing reaction. Lighter elements can thus gain binding energy by merging two elements into one bigger in what is called fusion. Heavier elements gain binding energy the opposite way by splitting into smaller elements through fission.

While undergoing fission the nucleus releases 1-5 neutrons, depending on the type of nucleus. The neutrons released in one fission event may continue to cause fission in another nucleus which in turn may cause yet another nucleus to fission and so on. In that way a fission reaction chain may be sustained. In an operating

nuclear power reactor under normal conditions the fission reaction chain is kept in such a way that the same amount of neutrons are produced as are consumed through fission, leakage or absorption in other materials.

A typical fission takes place in less than  $10^{-17}$ s from that the neutron is entering the nucleus [12]. One example of a fission reaction is shown below.

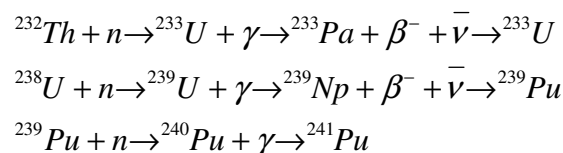


## A.2 Neutron-induced fission

Heavy nuclei which do not have a high probability of spontaneous fission may undergo fission if there is an extra amount of energy added to it by an incident particle - neutron or photon. If an incident neutron is absorbed by a heavy nucleus, a compound nucleus is formed and put in an excited state. The binding energy per nucleon in the compound nucleus will be less than that of the original nucleus and the compound nucleus will therefore be less stable. The extra energy brought to the compound nucleus by the neutron may help to overcome the fission barrier and if the excitation energy is higher than a certain critical energy the nucleus will be undergoing fission. All nuclides with more than 90 protons will undergo fission with high probability when a neutron with kinetic energy in excess of about 1 MeV is absorbed.

## A.3 Fissile and fertile nuclides

Some nuclei will undergo fission with the absorption of neutrons of any energy level or even with neutrons of zero kinetic energy. They are referred to as fissile nuclides. The most common fissile nuclide used in commercial power reactors is the uranium isotope  ${}^{235}\text{U}$  and  ${}^{235}\text{U}$  has a high probability of undergoing fission with thermal neutrons (**Figure 15**). Thermal neutrons are neutrons moving in equilibrium with the thermal motion of the surrounding materials with a kinetic energy around 0.0025eV.  ${}^{235}\text{U}$  is the only naturally occurring element fissile by thermal neutrons. However, there are three other isotopes of interest as nuclear reactor fuel, produced when the fertile elements  ${}^{232}\text{Th}$  and  ${}^{238}\text{U}$  are converted in a process called breeding. The fertile elements will transform into the fissile elements  ${}^{233}\text{U}$ ,  ${}^{239}\text{Pu}$  and  ${}^{241}\text{Pu}$  through neutron capture, followed by  $\beta$ -decay as following equation shows [12].



## **A.4 Fission neutrons**

The majority of neutrons emitted in the fission process are released at the instant of fission within  $10^{-16}$ s. These neutrons are known as prompt neutrons and they constitute 99% of the fission neutrons. The average number of emitted prompt neutrons,  $\nu$ , is around 2-4 neutrons per fission. It is dependent on the incident neutron energy and the type of fission nuclei. The prompt neutrons have an average energy of around 1-2 MeV per neutron. Due to their fast energies they are also referred to as fast neutrons (Fast neutrons are defined as neutrons having energies between 0.1 MeV and above). Some of the neutron rich fission products decay by neutron emission, thus constituting an additional source of neutrons. These emitted neutrons are the delayed neutrons. They depend on the half-life of the fission products and are released some seconds after the fission event. The delayed neutrons constitute only a small fraction of the fission neutrons compared to the prompt ones. Nevertheless, due to their lifetime, they have an important impact on the neutron flux and the reactor control.

## **A.5 Fission energy**

A nucleus undergoing fission will release around 200 MeV of energy of which 160 MeV will be carried away as kinetic energy by the fission products. The smaller fission fragment will carry away a slightly bigger amount of energy than the bigger fission fragment. The prompt neutrons will carry an average energy of 2 MeV per neutron and the remaining energy will be carried by prompt gammas (around 8 MeV), gamma decay (around 7 MeV) and beta decay (around 19 MeV of which 12 MeV is carried away by neutrinos). The energy released will soon be transformed into heat due to scattering (collisions) of the particles with surrounding media, such as coolant, cladding and structural material. Except for the energy taken away by the neutrinos which are not interacting with the reactor components and therefore not contributing to neither the heating of the reactor fuel nor to the energy recovered [12].

## **A.6 Thermal neutrons**

When fast neutrons slow down, they will eventually come into thermal equilibrium with the motion of the nuclei in the medium in which they are moving. In such a thermal equilibrium, the neutrons are as likely to gain energy through scattering with a fast moving nucleus, as they are to lose energy through scattering with a slowly moving nucleus. Those neutrons are referred to as thermal neutrons. At room temperature, the average speed of a thermal neutron is about 2200 m/s, corresponding to an average kinetic energy of 0.025 eV. This energy is almost nothing compared to the energy released in fission (~200 MeV) induced by such slow moving neutrons. However are the thermal neutrons causing most of the

fission in LWRs and other reactors operating in the thermal spectrum. That is why a moderator is needed in those types of reactors in order to slow down the neutrons to preferable energies where they are most likely to cause fission.

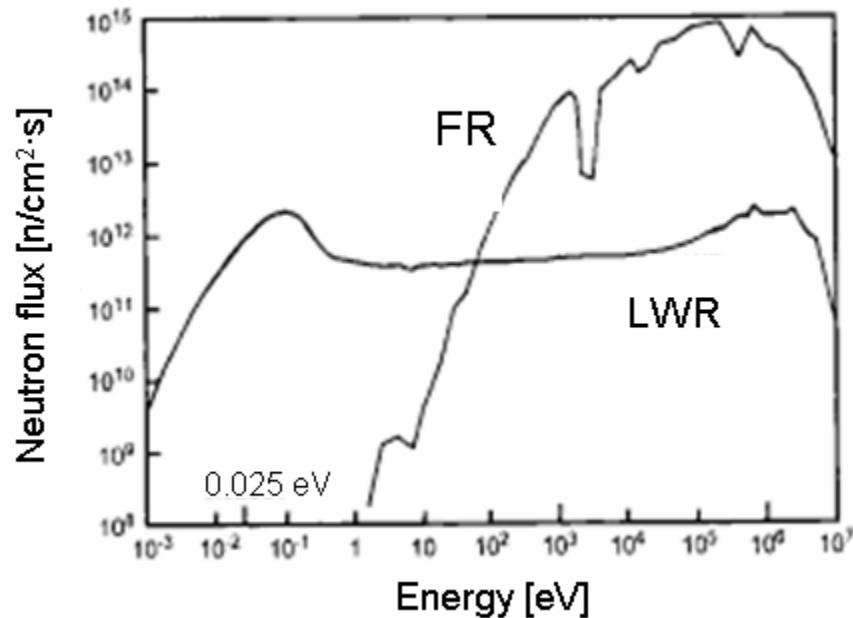


**Figure 14.** Representative thermal (LWR) and fast reactor (FR) neutron energy distributions [30].

### A.7 Cross sections

The probability of an isotope to interact with another particle is defined as the cross section, measured in barns [ $10^{-24}$  cm<sup>2</sup>]. The fission cross section for a nucleus, as a function of neutron energy, estimates the probability on how likely that nucleus will undergo fission. The uranium isotope <sup>235</sup>U, for example, is most likely to fission with thermal neutrons of energies less than 1 eV, where the cross section is around 580 barns. In the MeV neutron energy region the <sup>235</sup>U cross section is only 1 barn (**Figure 15**) and the isotope is thus less likely to fission by neutrons of energies that high.

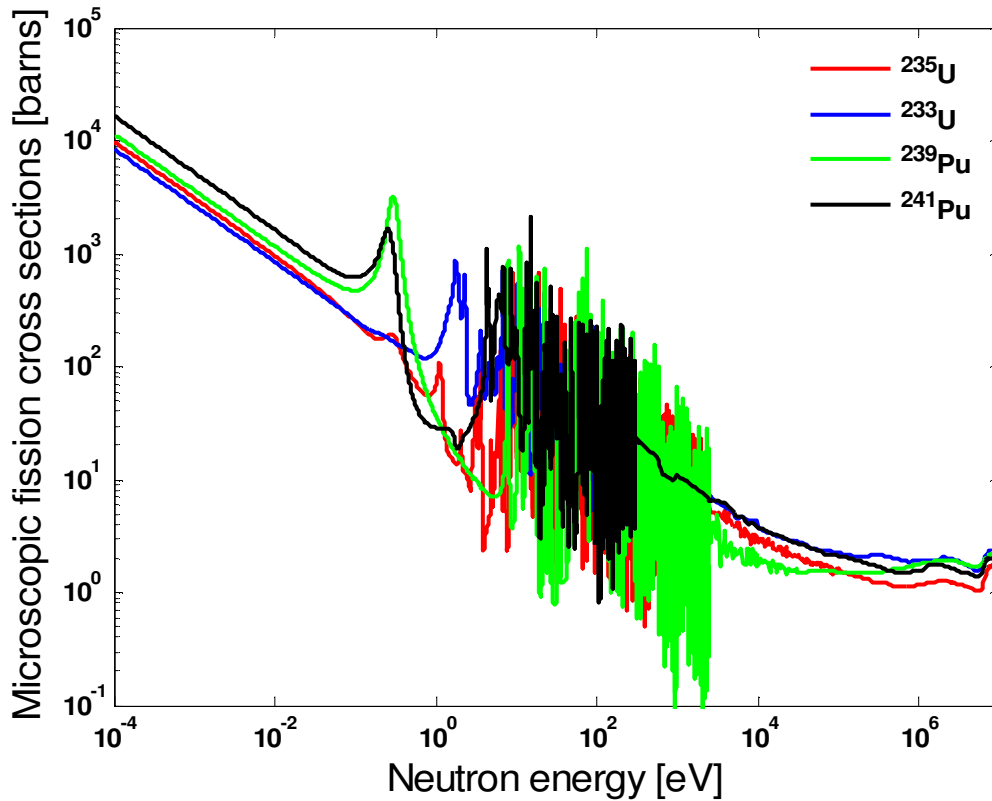


**Figure 15.** Cross sections of neutron induced fission in the fissile nuclei  $^{233}\text{U}$ ,  $^{235}\text{U}$ ,  $^{239}\text{Pu}$ , and  $^{241}\text{Pu}$  (JEFF-3.0).

The capture cross section for a certain isotope describes the probability of that isotope to capture a neutron, but without undergoing fission. The uranium isotope  $^{238}\text{U}$  has a low probability to undergo fission with neutrons of energies lower than 1MeV. But instead it has a very high capture cross section for certain distinct energies in that same spectrum, so called resonances (**Figure 16**). The neutron capture in  $^{238}\text{U}$  nuclei will thus influence the fission probability and the reactivity of a reactor. Some neutrons will always be lost in the resonances while they are slowing down to thermal energies and if the temperature in the fuel is increasing the absorption in the resonances will also increase. This phenomenon is called the Doppler effect and occurs when the fission rate is increasing. More fission means more fission heating and when the temperature is rising in the fuel it will cause the resonance peaks to broaden. At the same time as the peaks are broadened the neutron capture is increased, leading to a reduction of the reactivity.



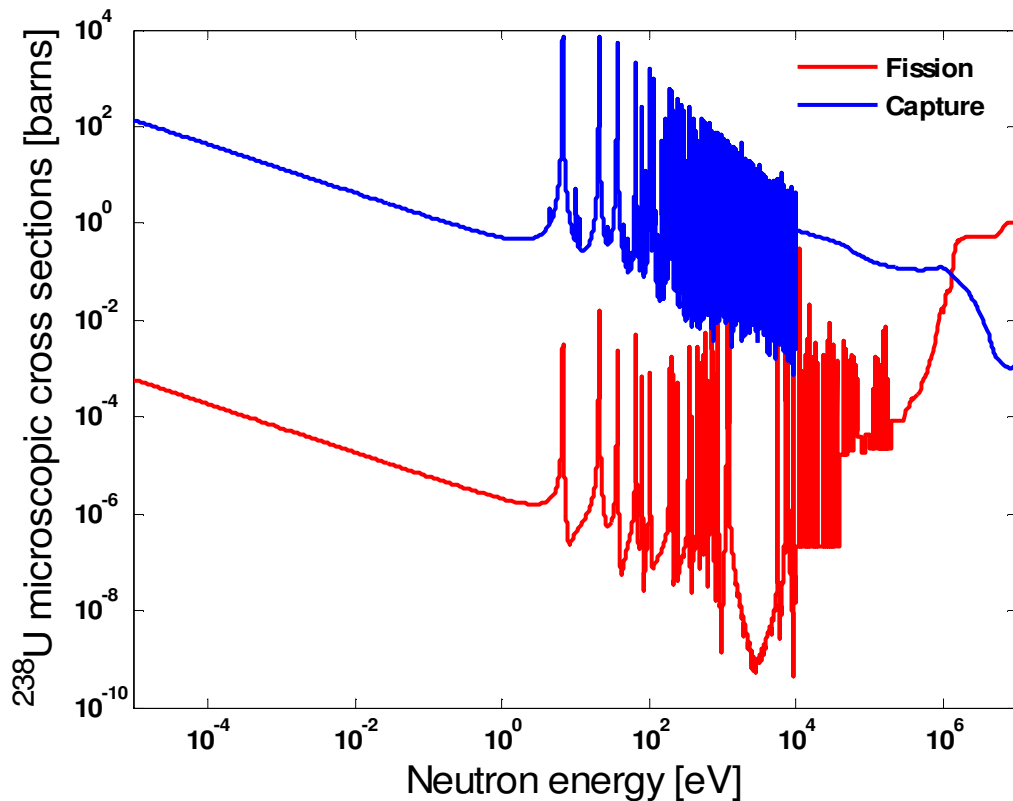


**Figure 16.** Microscopic neutron induced fission and capture cross sections of  $^{238}\text{U}$ .

### A.8 The fission chain reaction

The reactor kinetics is described by the ability to multiply neutrons. When a neutron is born in the reactor, it might slow down through scattering with surrounding material and then get absorbed in the fuel, causing fission. But, it might as well leak out of the core or getting absorbed by other material such as cladding or structural materials. A condition for a stable self-going chain reaction is that for one fission event, releasing 2.5 neutrons on average for  $^{235}\text{U}$ , one neutron will cause another nucleus to fission, from which there is a second neutron born which in turn is causing a second fission and so on. In such a state the neutron density and fission rate remain constant in the reactor. The multiplication factor,  $k_{\text{eff}}$ , is defined as the ratio of the number of neutrons in present generation to the number of neutrons in the preceding generation. If in one generation there are  $N$  neutrons, there will be  $Nk_{\text{eff}}$  neutrons in the second one,  $Nk_{\text{eff}}^2$  neutrons in the third one etc. When the multiplication factor is exactly one, the condition for a stable, self-sustained chain reaction is fulfilled and the reactor is critical. If the multiplication factor is less than one the reactor is said to be subcritical and the chain reaction will eventually die out. If the multiplication factor exceeds one, the chain reaction will diverge and cause a fission rate increase, which might lead to

uncontrolled power in less than seconds. In a simplified model of an infinite thermal reactor fuelled with uranium, where there is no leakage, the multiplication of neutrons is described by the infinite multiplication factor

$$k_{\infty} = \varepsilon \cdot p \cdot f \cdot \eta$$

where

$\varepsilon$  = the fast fission factor

$p$  = the resonance escape probability

$f$  = the thermal utilization factor

$\eta$  = number of neutrons produced by thermal fission in  $^{235}\text{U}$

The fast fission factor is the additional number of neutrons from fission in  $^{238}\text{U}$ , induced by fast neutrons (**Figure 16**). The resonance escape probability is the fraction of fast neutrons which escapes capture in  $^{238}\text{U}$  resonances while slowing down to thermal neutrons. The thermal utilization factor is the fraction of thermal neutrons absorbed in the fuel to the thermal neutrons absorbed in moderator, coolant and structural material.

But the infinite multiplication factor is a simplified version because if we want to calculate the multiplication of neutrons in a finite reactor we must take into account that neutrons will leak out of the reactor. We then need to consider the effective multiplication factor defined as

$$k_{eff} = \varepsilon \cdot p \cdot f \cdot \eta \cdot P_{NL_F} \cdot P_{NL_{TH}} = k_{\infty} \cdot P_{NL_F} \cdot P_{NL_{TH}}$$

where

$P_{NL_F}$  = the fast non-leakage probability

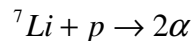
$P_{NL_{TH}}$  = the thermal non-leakage probability

The fast non-leakage probability is the fraction of fast neutrons that will not leak out during slow down. The thermal non-leakage probability is the fraction of thermal neutrons that will not leak out.

## Appendix B - Transmutation of Nuclear Waste

### B.1 Transmutation

Transmutation – the transformation of one isotope into another isotope or element by changing its chemical properties was first demonstrated by Rutherford in 1919. He transmuted  $^{14}\text{N}$  into  $^{17}\text{O}$  by  $\alpha$ -particles from naturally radioactive isotopes. A nucleus may be transformed by absorption of a particle, such as  $\alpha$ -particles, protons or neutrons, possibly followed by fission. But since the Coulomb barrier surrounding heavy nuclei are too great to permit the entry of particles from naturally radioactive isotopes, the transmutation of heavier elements needs higher energy particles to penetrate the nucleus. The development of particle accelerators opened new possibilities for transmutation experiments and in 1939 the first accelerator-driven transmutation was demonstrated by Cockroft and Walton. They let energetic protons collide with a lithium-target in the reaction



However the most favourable nuclear process used for transmutation of radiotoxic isotopes is neutron absorption. Neutrons are not repelled by nuclei and interaction cross-sections for many transmutation reactions are sufficiently large. Nuclear reactors, existing and also advanced reactor systems, can be used for neutron transmutation as they constitute an extensive source of neutrons.

Transmutation, in the context of nuclear waste, is a process which reduces the long term radiotoxicity. Of most concern regarding the disposal of the nuclear waste are the actinides and they are, unlike the fission products, fissionable. They may undergo fission, directly or by absorbing neutrons, followed by beta decay, until a fissile nuclide is formed. Most of them will not fission under a certain threshold energy, but above that threshold their fission cross-section is relatively high (Figure 17).

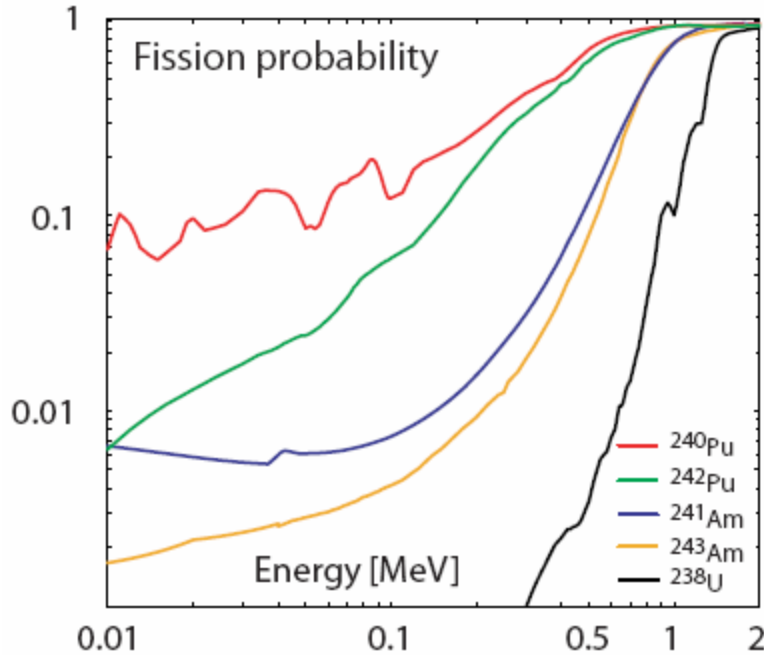


Figure 17. Fission probability  $\sigma_f/\sigma_a$  as a function of neutron energy [13].

The TRU considered for transmutation of nuclear waste are plutonium, americium, curium and neptunium. Transmutation of minor actinides and plutonium in fast-spectrum systems (FR and/or ADS) could achieve a hundredfold reduction in actinide radiotoxic inventory compared to the once-through cycle [2]. Fission products, especially  $^{90}\text{Sr}$  and  $^{137}\text{Cs}$  which dominate the radiotoxicity of the spent fuel during the first hundreds of years following discharge, may not be effectively transmuted by neutron absorption. Theoretically they might be transmuted to shorter lived or stable nuclides through neutron capture but due to their low neutron capture cross-section they need to be irradiated a rather long time. The transmutation rate will be small in relation to the natural decay of these nuclides. The short half-life of these fission products thus makes it more reasonable to retain them in storage facilities [2].

## B.2 Transmutation reactors

One of the purposes of a dedicated transmutation reactor is to incinerate (burn) the transuranics in an efficient and safe way with the goal to promote fission rather than neutron capture. The reasons for this is to convert the initial nucleus into relatively short-lived fission products, to limit the negative impact on neutron balance, and to limit the chain production of minor actinides that are more toxic than the initial nucleus. Moreover the reactors own production of TRU should be minimized (by minimizing the amount of fertile material in the fuel) and the burnup maximized.

In a fast neutron spectrum the neutron-transuranics interaction is dominated by fission, this is why preference is given to reactors with fast neutron spectra. For long-lived fission products, which cannot fission but only be transmuted by neutron capture into more stable isotopes, intense neutron fluxes are preferred and neutrons with energies in thermal and epithermal spectrum. Possible transmutation reactors with high neutron flux and a fast neutron spectrum are the subcritical accelerator-based systems and the fast reactors.

### **B.3 Subcritical accelerator-driven systems**

Accelerator-driven systems (ADS) have been proposed as one way to transmute/incinerate the radiotoxic isotopes confined in the spent nuclear fuel. They are working in a subcritical mode meaning they do not have a self-sustained fission chain reaction and the multiplication factor is thus less than one ( $k_{\text{eff}} < 1$ ). The ADS consists of a subcritical core and a proton accelerator. Because the fission process in a subcritical reactor is not self-sustained, it needs an external contribution of neutrons. The extra neutrons are supplied from the accelerated proton beam with energies around 1 GeV, where the protons are collided with a heavy metal target inside the ADS core. The heavy target nucleus, while collided with the protons, will fragment and release neutrons and charged particles in a so called spallation process. Around 20-30 neutrons per spallation will be released, which is much more than the neutrons released in a normal fission. Most of the charged particles are slowed down and stopped inside the target as an effect of the Coulomb interaction, while the neutrons penetrate the target and surrounding subcritical core. Some of the spallation neutrons will be captured in the fuel and cause further fission and thus support a fission chain controlled by the proton beam.

In a fast spectrum critical reactor, where the multiplication factor equals one ( $k_{\text{eff}} = 1$ ), the fission of transuranics is difficult to control and the safety margins are much smaller than in a thermal critical reactor or a subcritical system. The thermal reactors benefit of the Doppler-effect which has a negative temperature feed-back. If the temperature in the fuel increases so will the resonance capture of  $U^{238}$ , which results in less fission and thus a reactivity reduction. The benefit of the subcritical system to balance the fission chain reaction is due to the proton accelerator. The proton accelerator, which sustains the fission chain in the core, can be switched off if needed to prevent an uncontrolled neutron explosion. The safety margins are therefore bigger in the ADS than in a fast spectrum reactor operating in a critical mode.

The power production in the ADS is conducted in the same way as conventional reactors where the conversion of heat from the core into electricity is done through steam generators, turbines and generators. The electricity generated by the ADS is

more than sufficient to operate the accelerator and it is thus able to supply its own need of electricity.

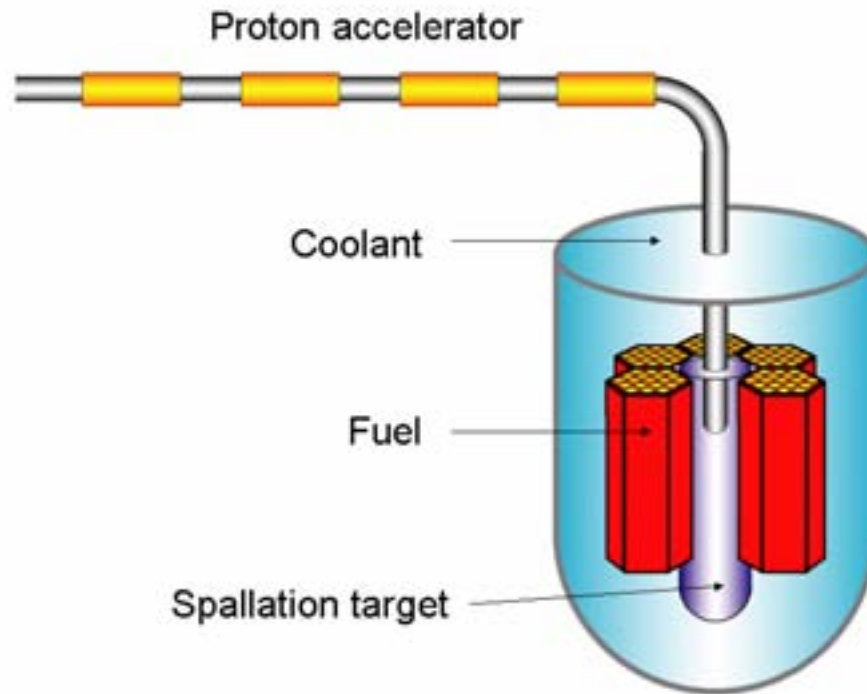


**Figure 18. Schematic design of an ADS.**

### B.3.1 Accelerator

Linacs and cyclotrons are two types of accelerators considered for the operation of the ADS. The linear accelerator (linac) may in principle accelerate a proton current two orders of magnitude higher than the cyclotron. A proton energy of about 1 GeV together with an accelerator current of 20-30 mA is required to operate a large scale industrial ADS (~1000 MWt), but no such accelerators have been built yet. Examples of existing high-power research accelerators are the cyclotron at the Paul Scherrer Institute (PSI), running at 1.4 mA and 590 MeV [33] and the proton linac at the Los Alamos Neutron Science Centre (LANSCE) running up to 1.5 mA and a maximum power of 0.8 GeV [33]. Although they do not meet the demands imposed by a full scale ADS. Several large scale accelerators are currently planned or under construction, one example is the 1.4 mA and 1 GeV linac Spallation Neutron Source (SNS) under construction in Oak Ridge (US) [34] and another is the European Spallation Source (ESS), a 1.33 GeV pulsed linac [36] planned to be built somewhere in Europe. Beam powers delivered by present accelerators are one order of magnitude lower than that needed to operate a future ADS and although the physics of accelerators are well

understood it is important to examine and validate the feasibility and new concepts of high-intensity accelerators [37].

### B.3.2 Spallation target

Solid or liquid metals are the two main candidates considered as spallation targets. Liquid metal target seems to be the realistic choice for a large scale ADS as it better handles the extremely high power densities created during operation. A liquid metal target has a better heat removal capability and a significant reduction of radiation damage to the target. Lead and lead-bismuth eutectic (LBE) have come to be among the favourite candidates where LBE has the advantage of having a lower melting point compared to pure lead. The main disadvantage of LBE is the production of  $^{210}\text{Po}$ , formed by neutron irradiation of bismuth.  $^{210}\text{Po}$  has a half-life of 138 days and emits alpha particles during the decay.

The key technological problem for the target design is a design of a target window which can withstand radiation damages of proton beam, backscattered neutrons and thermal stresses caused by accelerator trips.

### B.3.3 Coolant

Different conceptual designs have been proposed for the coolant in the last few years. The very common feature for most of them is the choice of a fast neutron spectrum in order to transmute efficiently minor actinides. As a consequence a liquid lead or lead-bismuth eutectic (LBE) as a coolant became a primary choice of many groups [32]. LBE was the choice made by former USSR as coolant for their most modern nuclear submarines. If LBE should be chosen as core coolant and target, compatibility between the target loop and the primary core coolant loop would be achieved.

Sodium is also an efficient coolant with good thermal properties. It has been used in operating fast reactors (EBR2, Phenix and Superphenix) and is thus the best known liquid metal coolant for fast reactor systems. A major drawback of having sodium as coolant is its high probability to interact with air and water with the consequent risk of a hydrogen explosion. Main advantages of liquid metals are the possibility of operating close to atmospheric pressure and their good thermal properties. But the opacity of the metals makes inspections and repairing difficult.

## **Appendix C - The Swedish Referendum**

In a referendum about the Swedish nuclear power in 1980 the Swedish people could choose between three lines, proposed by the governing parties. The three lines were basically:

**Line 1** "continue to construct the six already planned nuclear power plants but phase out the nuclear power with respect to energy maintenance in the await of renewable energy sources"

**Line 2** "same as line 1 with the addition of having an intense development of renewable energy sources, where coal and oil consuming energy is avoided"

**Line 3** "a phase out within ten years and no further expansion"

Line 2 got most of the votes (39.1%) and together with line 1 it got almost 60% of the total number of votes. The Parliament decided afterwards to fulfil the power plants already under construction but to have no further expansion and a phase out of nuclear power until the year 2010, presumed the welfare and employment was not threatened. However, according to contemporary public opinion, a clear majority of Swedish people is for a continued use of nuclear power. In an investigation, commissioned by the Nuclear Safety and Training Centre (KSU) in October 2004, 35% of the people want to continue the use of existing reactors until they need to be shut down on safety reasons [38]. It needs to be said that when the Swedish reactors were built their expected lifetime was 25 years, a number which has been prolonged to 40 years. According to this the Swedish reactors could operate for more than 20 years to come without hazarding the safety aspects. 47% voted for a development of nuclear power production but only 15% of the people supported the governmental phase-out program. For 76% of the interviewed people the most important environmental issue was to decrease the release of greenhouse gases.





# From Once-through Nuclear Fuel Cycle to Accelerator-Driven Transmutation

Alexandra Åhlander, Jan Dufek, Waclaw Gudowski

*Kungliga Tekniska Hogskolan, AlbaNova University Centre, 106 91 Stockholm, Sweden*

**Elsevier use only:** Received date here; revised date here; accepted date here

---

## Abstract

In this study, simulation of different nuclear fuel cycle scenarios, are performed. The reference scenario corresponds to a middle size nuclear power country, with 10 light water reactors (LWRs) and a once-through fuel cycle. The study addresses long-term, equilibrium fuel cycle scenarios, with and without plutonium recycling (MOX) in LWRs and transuranium burning in accelerator driven system (ADS). But also short-term, phase-out scenarios, with transuranics (TRU) burning in ADS, are performed. The equilibrium simulation showed that four ADS units, of 800 MWt, are sufficient to burn an amount of plutonium and americium corresponding to the build-up of those isotopes. The phase-out simulation of a country adopting an 'as soon as possible' approach, to reduce the spent nuclear fuel inventory, showed that a complementary burning of TRU in three ADS units appeared to be more suitable than a reactor park employing four ADSs. The fuel cycle simulations have been performed using the Nuclear Fuel Cycle Simulation (NFCSim) code [1] and MonteBurns codes [2].

Keywords: Accelerator Driven Systems; ADS; Fuel Cycle; MonteBurns; MOX; NFCSim; ORIGEN2  
PACS: 28.50.Dr; 28.50.Qd; 28.41; 28.52

---

## 1. Introduction

Transmutation of nuclear spent fuel and waste reduction technologies may reduce the burden associated with the disposal of radiotoxic nuclear waste [3]. This paper is an attempt to investigate some transmutation strategy options in nuclear radioactive waste management from a national perspective.

A fuel cycle describes all the steps required to supply a nuclear reactor with fuel and take care/make use of the spent fuel. The fuel cycle commences with the uranium mining and continues through conversion, enrichment and fuel fabrication – which make up the front-end of the fuel cycle, to irradiation of the fuel in the reactors, reprocessing, cooling,

storage and finally the disposal – which make up the back-end [4].

The work done in this paper is an investigation of different advanced fuel cycle scenarios applied to the existing Swedish light water reactor park. It concentrates on analyzing the mass changes of plutonium and americium for the different chosen scenarios.

The Swedish reactor fleet consists of 12 nuclear reactors at a power of around 10 GW in all. Due to the shutdown of Barsebäck-1 in 1999 and Barsebäck-2 in 2005, only 10 of the reactors are in operation today. Nine of the Swedish reactors are BWRs and three of them are PWRs (see Table 1). The reactors were constructed and taken into operation between the years 1972 and 1985, with an expected life-time of 25 years. According to today's knowledge their expected life time is prolonged to 40 years.

Sweden pursues a once-through fuel cycle with a direct disposal of the spent nuclear fuel. Instead of separation and recycling of the spent fuel it will be encapsulated in copper canisters and kept in a deep geological repository. Unlike for example France, Sweden does not vitrify the components of the spent fuel before storage. Sweden adopts a strategy where it should be possible to easily retrieve the spent fuel if necessary. This approach puts Sweden in an optimal starting point when it comes to recover the minor actinides and plutonium, which is a big issue when considering recycling of transuranics (TRU).

In the first simulation, the Swedish LWR park was operated at a constant nuclear electricity production, during a hundred-year period. Plutonium and minor actinides production/destruction were kept at a constant level through the introduction of an optimal number of ADSs into the existing reactor park. This was done in order to assess the ratio of LWRs over a number of “actinide burners” needed to consume LWR-generated TRU in a quasi-equilibrium cycle. The simulation covers the time period from the start-up of the first reactor Oskarshamn-1 in 1972 until 2100.

A modification of the near-equilibrium state was also done with the introduction of LWR MOX-recycling prior to the actinide burning in ADSs.

The second scenario looked at optimizing the phase-out of all the LWRs. The goal was to adopt an ‘as soon as possible’ strategy, with a reduction of the

radiotoxic burden through the recycling of plutonium and americium in ADSs. The future need for electricity supply was of no concern in this case, the important matter was only to try to reduce the burden of radiotoxic spent fuel for the Swedish spent fuel repository.

Four scenarios were investigated and compared to their respectively reference scenarios:

#### **Equilibrium Reference Scenario – LWR**

The reference scenario was the open “once-through” fuel cycle of the existing Swedish LWR park. The reactors were operated at a burn-up of approximately 40 MWd/kg, during a period of hundred years and with direct disposal of the spent fuel.

#### **Equilibrium Scenario #1 - LWR + ADS**

Four ADSs were integrated into the Swedish LWR park to incinerate plutonium and americium. The ADSs were all started in 2030 and shut down in 2100.

#### **Equilibrium Scenario #2 - LWR + MOX + ADS**

This scenario was similar to scenario #2, with the exception of having plutonium-MOX recycling in two LWRs prior to the burning of plutonium and americium in ADS (Fig. 1). The MOX-LWRs was started in 2000 and operated as all the other reactors until 2100.

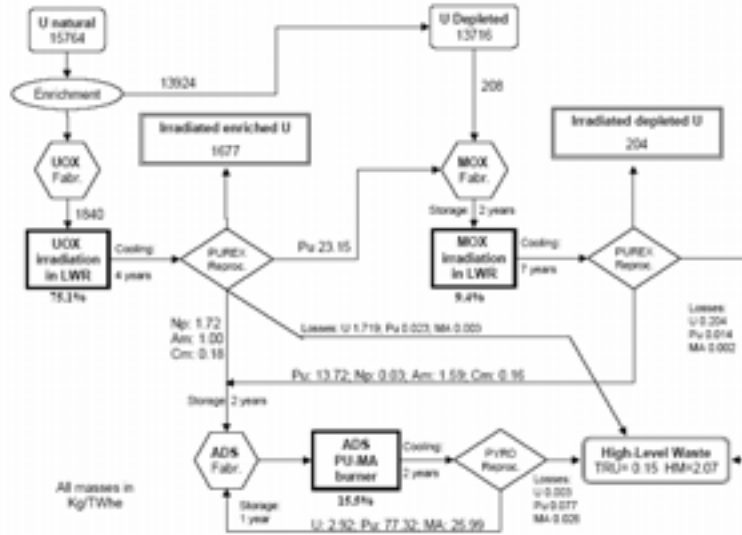


Fig. 1 Scenario #3 – LWR + MOX + ADS [5]

**Phase-out Reference Scenario**

The phase-out reference scenario was a ‘realistic’ transient scenario with the objective to estimate the amount of spent fuel discharged from the existing Swedish reactor park. The LWRs were operated during a lifetime of 40 years.

**Phase-out Scenario #3 – LWR + 3 ADS**

This scenario looked at decreasing the amount of plutonium and americium in the spent fuel

inventory with an ‘as soon as possible’ approach. The plutonium and americium were incinerated in three ADSs integrated to the Swedish LWR park. Each ADS was operated during a time period of 50 years and they all were started at the beginning of year 2035.

**Phase-out Scenario #4 – LWR + 4 ADS**

This scenario was similar to Scenario #3, with the addition of one more ADS.

Table 1. Swedish reactor data [6], [7], [8]

| Reactor Name | Reactor type | Power (MWt) | Power (MWe) | Grid Connection (year) | Shut Down (year) | Burn-up (MWd/kg) | Initial Heavy Metal Inventory [kg] | Uranium Enrichment [%] |
|--------------|--------------|-------------|-------------|------------------------|------------------|------------------|------------------------------------|------------------------|
| Barsebäck-1  | BWR          | 1800        | 595         | 1975                   | 1999             | 40               | 80000                              | 3.25                   |
| Barsebäck-2  | BWR          | 1800        | 595         | 1977                   | 2005             | 40               | 80000                              | 2.97                   |
| Forsmark-1   | BWR          | 2929        | 970         | 1980                   | 2020             | 40               | 121000                             | 3.25                   |
| Forsmark-2   | BWR          | 2929        | 970         | 1981                   | 2021             | 41               | 121000                             | 3.20                   |
| Forsmark-3   | BWR          | 3300        | 1150        | 1985                   | 2025             | 43               | 126000                             | 3.30                   |
| Oskarshamn-1 | BWR          | 1375        | 445         | 1972                   | 2012             | 40               | 82000                              | 2.80                   |
| Oskarshamn-2 | BWR          | 1800        | 602         | 1975                   | 2015             | 40               | 82000                              | 3.00                   |
| Oskarshamn-3 | BWR          | 3300        | 1160        | 1985                   | 2025             | 40               | 127000                             | 3.10                   |
| Ringhals-1   | BWR          | 2500        | 830         | 1976                   | 2016             | 43               | 125000                             | 3.21                   |
| Ringhals-2   | PWR          | 2652        | 870         | 1975                   | 2015             | 44               | 80500                              | 3.92                   |
| Ringhals-3   | PWR          | 2775        | 920         | 1981                   | 2021             | 43               | 82100                              | 3.94                   |
| Ringhals-4   | PWR          | 2775        | 915         | 1983                   | 2023             | 44               | 82100                              | 3.92                   |

## 2. Calculation Model

The fuel cycle simulations were done using the Nuclear Fuel Cycle Simulation code (NFCSim), developed at Los Alamos National Laboratory. It tracks the size and composition of the nuclear material which evolves with time. NFCSim contains a detailed description with time-dependent accounting of location and accessibility of nuclear reactors, enrichment plants, reprocessing facilities, fuel fabrication plants and storage facilities. The code models life-cycle material balances for an arbitrary number of reactors and includes a cost database. The modeling capabilities include LWR oriented fuel cycles with the option of actinide recycling in a suite of fast reactors and ADS. NFCSim groups fuel batches by fuel type and burn-up calculations are carried out for each batch. The burn-up and reactivity calculations are done by ORIGEN2.2 [9]. All the necessary one-group cross-section libraries, for specific burn-up calculations, have been prepared using the 3D continuous energy Monte Carlo burn-up code MonteBurns.

## 3. Assumptions

Recovery efficiencies for separated uranium and transuranics were assumed to be 99.99% and 99.8% throughout all simulations. Maximum TRU fraction in the fuel was 80% and the americium to plutonium ratio in the fuel 10%. The effective multiplication factor,  $k_{\text{eff}}$ , in the ADS core was constrained not to go above 0.97 at BOL<sup>1</sup> and not below 0.92 at EOL<sup>2</sup>. Furthermore, all data used by NFCSim concerning mines, conversion, fabrication and enrichment plants, were based on current US infrastructure.

The reactor park in this study involved the following reactor components:

### Light Water Reactors with UOX fuel

The UOX fuel was irradiated to a burn-up of approximately 40 MWd/kgHM, in BWRs and PWRs. The thermal power of the different reactors

<sup>1</sup> Beginning of life (BOL)

<sup>2</sup> End of life (EOL)

varied from 1800 to 3300 [MWt] depending on reactor (see Table 1).

#### **Light Water Reactors with MOX fuel**

The MOX fuel was irradiated to a burn-up of 50 MWd/kgHM, beginning in year 2000.

#### **Accelerator driven system (ADS)**

The conceptual ADS design was a lead/bismuth cooled core with an initial heavy metal inventory of 2140 kg. The thermal power was 800MW and the burn-up 200 MWd/kg [10].

## **4. Results**

### **Equilibrium Reference scenario – LWR**

With a phase-in of the first Swedish reactor in 1972 and the other reactors following in a suite, this once-through scenario ends up with a total inventory of 25 000 tons spent UOX, after a continued operation during more than 100 years. 281 tons of the spent UOX was plutonium and 29 tons was americium. The equilibrium production of plutonium in this scenario was about 86 g/MW(t)yr, when normalized to total produced energy. The americium production was about 9 g/MW(t)yr.

### **Equilibrium Scenario #1 - LWR + ADS**

With a constant operation of LWRs and start-up of 4 ADS by the year 2030 (all reactors and ADS were shut down in 2100), the plutonium inventory slightly increased during the ‘equilibrium phase’, whereas the americium inventory decreased. The additional fast spectrum burners contributed to reduce the Swedish spent fuel inventory of plutonium and americium by 58% (163 tons) and 79% (23 tons) respectively. The remainder of the plutonium inventory was 118 tons by the year of shutdown (compared 281 tons in the once-through reference scenario) and the americium inventory 6 tons (compared to 29 tons).

### **Equilibrium Scenario #2 - LWR + MOX + ADS**

This scenario, which was based on Scenario #1 with the addition of plutonium burning in two MOX-LWRs (started in 2001 and run until 2100), reduced the amount of plutonium by 69% (195 tons) and

americium by 66% (19 tons). In this case the plutonium inventory was slightly decreasing during the operation, whereas americium inventory was constant at a level of 10 tons. By the shut-down of the ADSs, the plutonium inventory was 86 tons (compared 281 tons in the once-through reference scenario) and the americium inventory 10 tons (compared to 29 tons). The fact that a smaller fraction of americium decreased in this scenario, compared to scenario #1 (13 tons less), was due to the americium production built up from plutonium transmutation in the MOX fuel (32 tons more plutonium was burnt in scenario #2).

Fig. 2 shows the plutonium inventory in the ‘equilibrium scenarios’. One can see that while the plutonium inventory has a slightly increasing tendency in scenario #1 (LWR+ADS) from 2045, scenario #2 (LWR+MOX+ADS) has a slightly decreasing tendency from 2030.

Fig. 3 shows the plutonium inventory per produced total thermal energy. Although the plutonium inventory in scenario #1 grows a little from 2045 (LWR+ADS), it falls rapidly in the same time period when normalized to the total energy production.

Fig. 4 compares the americium inventory in the equilibrium scenarios. Most efficient, from americium transmutation point of view, is scenario #1 (LWR+ADS), which was able to decrease the americium inventory by almost 80% during its lifetime. Scenario #2 (LWR+MOX+ADS) kept the americium inventory at steady-state of 10 tons.

Fig. 5 describes the americium inventory per produced total thermal energy. Equilibrium production of americium in the reference scenario is about 9 g/MW(t)yr whereas americium inventory per produced energy falls rapidly in both scenario #1 and #2.

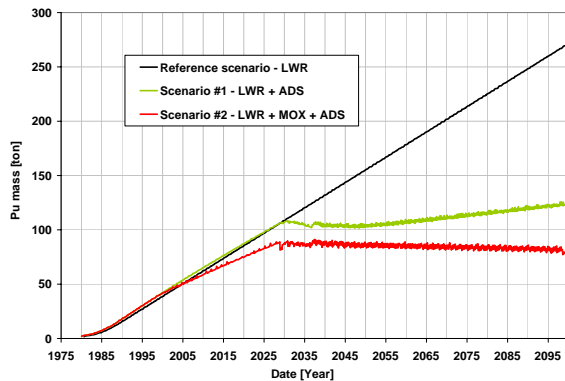


Fig. 2. Plutonium inventory in equilibrium scenarios [ton]

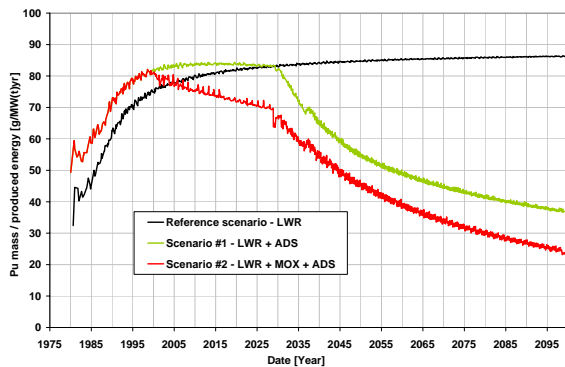


Fig. 3. Plutonium inventory per produced thermal energy in equilibrium scenarios [g/MW(t)yr]

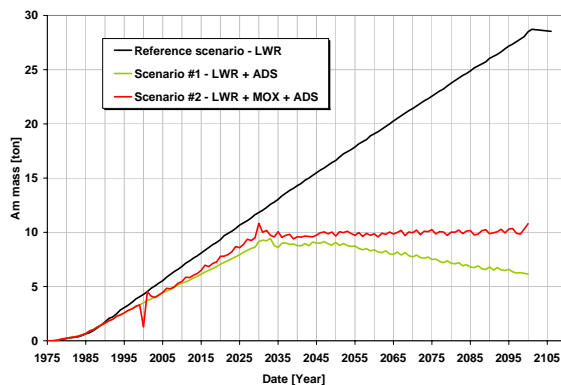


Fig. 4. Americium inventory in equilibrium scenarios [ton]

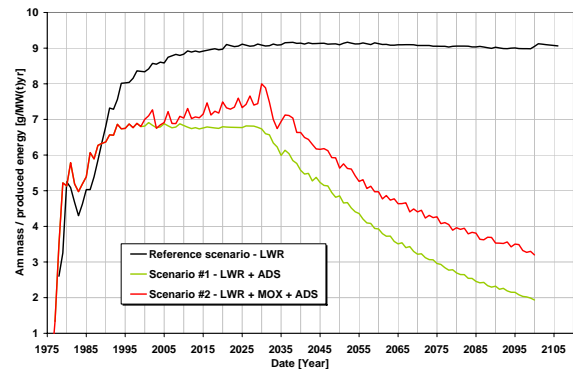


Fig. 5. Americium inventory per produced thermal energy in equilibrium scenarios [g/MW(t)yr]

### Phase-out Reference Scenario

The simulation of the phase-out reference scenario, resulted in an accumulated inventory of 10 000 tons of spent UOX, discharged from the Swedish LWRs by 2025. The spent fuel then contained a total of 107 tons of plutonium and 7 tons of americium, which served as stockpile to scenarios #3 and #4, where it was used as fuel in the ADSs.

### Phase-out Scenario #3 – LWR + 3 ADS

Burning the plutonium and americium, recovered from the Swedish spent fuel, by operating 3 ADS during 50 years, contributed to reduce the inventory of plutonium by 72% (78 tons) and americium by 63% (4.4 tons). After shut-down of the ADSs in 2089, the amount of plutonium in the system was 29 tons (27 tons in the interim storage and 2 tons of HLW<sup>3</sup>). The amount of stored and separated americium was by then 2.6 tons.

### Phase-out Scenario #4 – LWR + 4 ADS

When feeding 4 ADS units with the plutonium and americium from the Swedish spent fuel storage, the ADSs had to be shut down in 2070, after 35 years of operation. This development was due to not having a sufficient amount of plutonium in the interim storage to feed the ADSs (only 7 tons remained at the time of shut-down). The total amount of

<sup>3</sup> High level waste (HLW) is what is lost during the reprocessing. For TRU it was assumed to be 0.2%.

plutonium in the system<sup>4</sup> though, was as much as 37 tons at that moment, which is a reduction of 65% (70 tons). The americium inventory was reduced by 66% (4.6 tons) and ended at 2.4 tons. The fraction of burned plutonium was thus less than in the scenario employing only three ADS, but the fraction of americium did not differ significantly.

Fig. 6 compares the plutonium inventory in the phase-out scenarios. Fig. 7 describes these scenarios plutonium inventory per total produced thermal energy.

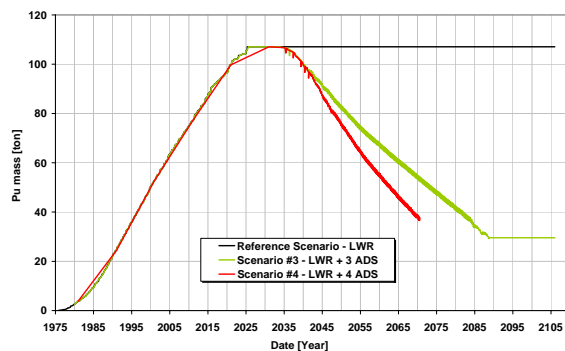


Fig. 6. Plutonium inventory in the phase-out scenarios [ton]

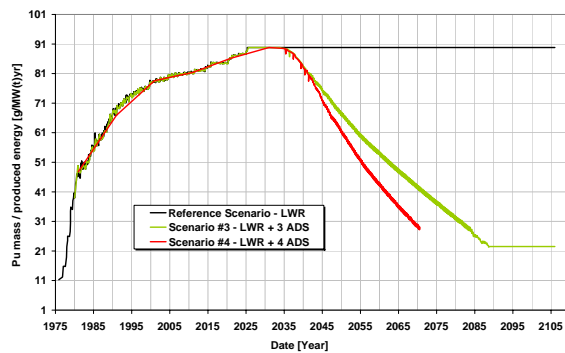


Fig. 7. Plutonium inventory per produced thermal energy in the phase-out scenarios [g/MW(t)yr]

<sup>4</sup> ADS cores, fuel fabrication, cooling storage, transportation, interim storage and high level waste.

## 5. Conclusions

The simulation of long-term equilibrium scenarios showed that in a system of approximately 10 LWRs, four ADS units of 800 MWt are sufficient to burn an amount of plutonium and americium, corresponding to the build-up of those isotopes.

The plutonium inventory can be more reduced by MOX recycling, but on account of much higher americium production.

The phase-out scenario, employing four ADSs, succeeded in burning 65% of the total inventory of plutonium in 35 years. Whereas, the scenario employing three ADS burnt 75% of the plutonium inventory during their lifetime of 50 years. The difference between the two scenarios in amount of reduced americium was not significant; the fraction was about 66% in both cases.

If Sweden wishes to adopt a phase-out of nuclear power, with the approach of ‘as soon as possible’ reducing the spent nuclear fuel inventory, scenario #3, employing three ADS units, appears to be more suitable than scenario #4, employing four ADS units. As the amount of the plutonium inventory is not sufficient to feed four ADS units during the expected lifetime of 50 years, an amount of 37 tons will remain un-recycled in the system. When in the case of three ADS units they may all three of them operate through their predicted life-time, with the result of burning more plutonium.

## Acknowledgments

This work was done in the framework of the European project Red-Impact: *Impact of Partitioning and Transmutation and Waste Reduction Technologies on the Final Nuclear Waste Disposal* - EC Contract No. FI6W-CT-2004-002408. Part of this work was also sponsored by the Swedish Nuclear Fuel and Waste Management Company, SKB.

## References

- [1] C. G. Bathke and E. A. Schneider, *NFCsim User's Manual*, Los Alamos National Laboratory Report LA-UR-04-8369, (2004).
- [2] D. I. POSTON, H. R. TRELLE, *User's Manual, Version 2.0 for Monteburns*, Version 1.0, LA-UR-99-4999 (1999).
- [3] M. Salvatores et al., *Long-Lived Radioactive Waste Transmutation and the role of Accelerator Driven (hybrid) Systems*, Nuclear Instruments and Methods in Physics Research, Cadarache (1997).
- [4] R. G. Cochran and N. Tsoulfanidis, *The Nuclear Fuel Cycle: Analysis and Management*, 2<sup>nd</sup> ed., Illinois (1999).
- [5] OECD Nuclear Energy Agency, *Accelerator-driven Systems and Fast Reactor in Advanced Nuclear Fuel Cycles*, Paris (France), (2002).
- [6] Ringhals webpage; [www.ringhals.se](http://www.ringhals.se)
- [7] Forsmark webpage; [www.forsmark.com](http://www.forsmark.com)
- [8] Oskarshamn webpage; [www.okg.se](http://www.okg.se)
- [9] G. CROFF. *A Users Manual for the ORIGEN2 Computer Code*, Oak Ridge National Laboratory Report ORNL/TM-7175 (1980).
- [10] K. Tuček. *Neutronic and Burnup Studies of Accelerator-driven Systems dedicated to Nuclear Waste Transmutation*, Doctoral Thesis, Stockholm (Sweden), 2004.





# The Subcritical Assembly in DUBNA (SAD) – Part I: Coupling all Major Components of an Accelerator Driven System (ADS)

V.N.Shvetsov<sup>a</sup>, C. Broeders<sup>b</sup>, I.S. Golovnin<sup>c</sup>, E.Gonzalez<sup>d</sup>, W. Gudowski<sup>e</sup>, F. Mellier<sup>f</sup>, B.I. Ryabov<sup>g</sup>, A. Stanculescu<sup>h</sup>, I.T. Tretyakov<sup>i</sup>, M.T. Vorontsov<sup>j</sup>\*

<sup>a</sup> Joint Institute for Nuclear Research, 141980 Dubna, Russia

<sup>b</sup> Forschungszentrum Karlsruhe, 76021 Karlsruhe, Germany

<sup>c</sup> VNIINM, 123060, Moscow, Russia

<sup>d</sup> CIEMAT, 2804 Madrid, Spain

<sup>e</sup> Kungliga Tekniska Högskolan, 106 91 Stockholm, Sweden

<sup>f</sup> CEA Cadarache, 13108 St. Paul les Durance, France

<sup>g</sup> Industrial Association "Mayak", 456780 Ozersk, Russia

<sup>h</sup> IAEA, 1400 Vienna, Austria

<sup>i</sup> NIKIET, 101000 Moscow, Russia

<sup>j</sup> GSPI, 107078 Moscow, Russia

**Elsevier use only:** Received date here; revised date here; accepted date here

---

## Abstract

A demonstration facility for Accelerator Driven Systems has been proposed to be constructed at the Joint Institute of Nuclear Research in Dubna. The Subcritical Assembly in Dubna (SAD) project proposes to couple an existing proton accelerator of 660 MeV and 1  $\mu$ A current with a specially designed U-Pu MOX subcritical core. Project objectives, technical description and current status of the project are presented in this paper.

---

**Keywords:** Accelerator Driven System; subcritical reactors; Subcritical Assembly in Dubna; SAD; Transmutation  
**PACS:** 28.50.Dr; 28.50.Qd; 28.41; 28.52

---

\* Corresponding author. Tel.: +46 8 55378200; fax: +46 8 5537 84 65 ; e-mail: wacek@neutron.kth.se.

## 1. Introduction

The construction of sizeable accelerator driven systems (ADS) being able to transmute kilograms of transuranic elements should be preceded by a smaller experimental facility being able to proof problem free operation of a subcritical core coupled through a spallation target with a proton accelerator [1]. The most important issues to be addressed are:

- Ensuring operational safety of subcritical systems implying:
  - Reliable control of the ADS power;
  - Reliable monitoring of the subcriticality  $k_{\text{eff}}$ ;
- Measurement of the contribution of the high-energy part ( $E > 10$  MeV) of the neutron spectrum, being particularly important for the design of radiation protection.
- Engineering of the coupling of an accelerator with a sub-critical reactor system;

Experimental ADS with thermal power in a range of 20-30 kW, as proposed in the SAD project, can properly address these problems and can demonstrate in practice feasibility of the accelerator-subcritical core coupling.

Joint Institute of Nuclear Research in Dubna is a unique centre with broad competence both in accelerators and in subcritical systems, with experimental and theoretical research activities in this field conducted since the middle of the 50-s under the scientific label “*electronuclear*” research [2][3]. Neutron yields and spectra in lead and uranium targets have been measured, as well as neutron cross-sections for a number of isotopes, important for the estimation of the efficiency of various modes of transmutation [4][5][6]. For the analysis of the *electronuclear* systems properties, mathematical models with appropriate databases and software have been developed [7].

## 2. Basic parameters of SAD

One of the important arguments to start the SAD project in Dubna was existence of the proton accelerator “Phasotron” [8] with its predetermined characteristics. Subcritical core being designed for SAD facility has been based on the regular Russian MOX fuel elements of the BN-600 reactor type [8]. The proton beam with current of maximum value 3.2  $\mu\text{A}$  impinging on a spallation target determines together with  $k_{\text{eff}}$  of a subcritical core, thermal power of the SAD installation.

The basic data of the SAD are listed in the following tables:

TABLE I: SAD INSTALLATION BASIC DATA

| Parameter   | Value                             |
|---|-----------------------------------|
| Thermal power                                     | up to 30 kW                       |
| Proton energy                                     | 660 MeV                           |
| Beam power  | up to 1 kW                        |
| Proton beam / target orientation                  | Vertical                          |
| Fuel elements orientation                         | Vertical                          |
| Criticality coefficient                           | $k_{\text{eff}} \approx 0.95$     |
| Fuel - see table below for details on composition | MOX, $\text{UO}_2 + \text{PuO}_2$ |
| Cladding tubes max. temperature                   | 400°C                             |
| Spallation target                                 | Replaceable: Pb, W                |
| Reflector   | Pb                                |
| Coolant   | Air                               |

TABLE II: BASIC FEATURES OF THE SAD CORE FUEL

| Parameter   | Value                          |
|---|--------------------------------|
| Fuel composition  | $(\text{UO}_2 + \text{PuO}_2)$ |
| Plutonium dioxide content in the fuel, %(mass)  | up to 30*                      |
| $^{239}\text{Pu}$ content in Pu %(mass), not less than (accuracy not worse than $10^{-4}$ for basic isotopes) | 95                             |
| Fuel density, $\text{g}/\text{cm}^3$  | $10.4 \pm 0.2$                 |
| Fuel pellet diameter, mm  | 5.95*                          |

### 3. Subcritical assembly

The sub-critical blanket of SAD (Figure 1) is placed within a biological shielding, which is made of heavy concrete and placed in radial and top directions from the core (AC). Pipes are foreseen in the shielding blocks to provide the allocation of the cooling loops for the target, the core, the experimental channels (vertical and horizontal), the power control channels, the proton guide etc. The upper part of the biological shielding will provide access to the blanket and to the experimental channels during fuel loading/reloading operations and to experiments with detectors and samples. The SAD core consists of 141 fuel assemblies; each assembly by itself combines 18 fuel pins, separated by wire spacers, and welded onto the cladding tube in helical manner. The fuel assembly does not have sidewalls, but only lower and top frames where the FE are fixed. A central supporting rod made of stainless steel achieves the integrity. The low specific energy release in the system allows the usage of air-cooling, both for the target and for the core.

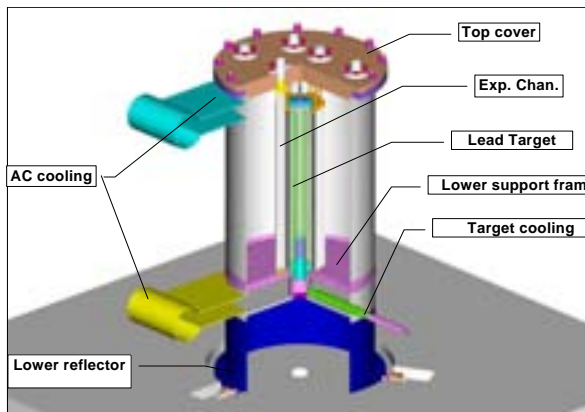


Figure 1 SAD core general view, fuel assemblies and lead reflector not shown.

The lead target assembly consists of a set of hexagonal lead prisms with air-cooling of the central 7 prisms (Figure 3). Other materials than lead and other dimensions will be used for the target in the course of the SAD experimental program.

The active core is surrounded by a lead reflector of 60 cm thickness in radial direction and of 20 cm in axial direction at the top and at the bottom. The lead

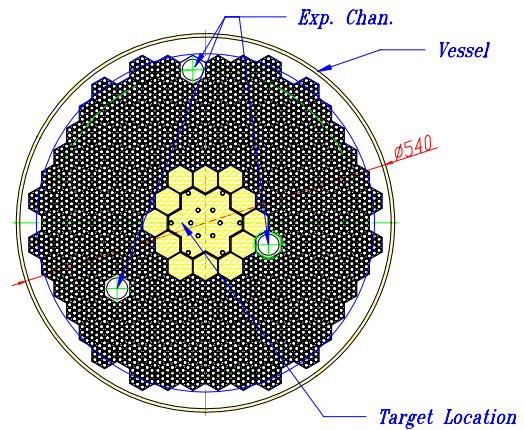


Figure 2: Horizontal cross-section of the SAD core.: 141 fuel assemblies x 18 fuel elements, 395 kg of  $\text{UO}_2$  -  $\text{PuO}_2$  MOX fuel. 29.5 weight % of  $\text{PuO}_2$

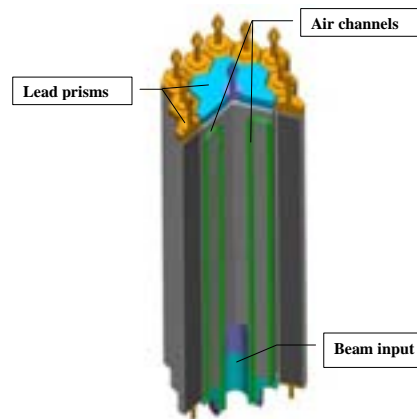


Figure 3: Lead spallation target design

density is  $11.15 \text{ g/cm}^3$ . A  $\text{B}_4\text{C}$  layer of 3 cm thickness to reduce the number of low energy neutrons in the concrete and shorten neutron lifetime in core is located between the lead reflector and the concrete shielding in radial direction.

The SAD facility will be equipped with experimental channels (EC) and actuators, which will allow to place detectors and isotopic samples in different parts of the installation and to extract them after irradiation. Three vertical EC are located in the

central part of subcritical assembly, substituting three fuel assemblies. One channel – in the vicinity of spallation target (EC1), next one in the middle of the core (EC 2) and the third one on the periphery of the core close to the Pb reflector (EC 3). Inner diameter of the channels 1-3 is equal to 33 mm. Another three vertical EC with inner diameter 60 mm are situated in Pb reflector.

The last vertical EC has diameter 45 mm and is placed in the top lead reflector on the beam axis.

Two horizontal EC with diameter 100 mm are located in the lower and side lead reflectors.

On the basis of the data, listed above, preliminary neutron spectra in experimental channels were calculated with MCNP [10] and MCNPX [11]. The results for neutron spectra calculations for 3 vertical channels in the fuel part of the core (1-3) and for 3 vertical channels in the side reflector (4-6) are shown in Figure 4.

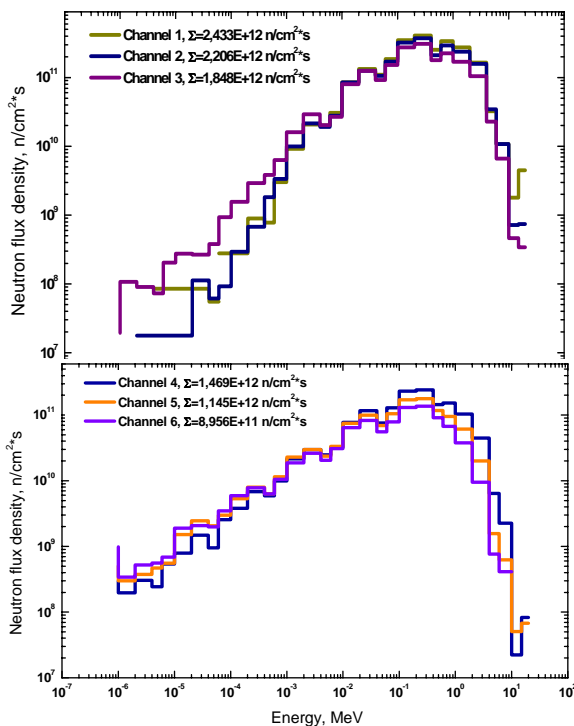


Figure 4: Neutron spectra in the centers of vertical experimental channels 1-6.

#### 4. Accelerator and beam transport line

The PHASOTRON accelerator has 10 beam channels, used in various experiments. The normal beam losses at transition through the longest beam lines do not exceed 5%.

The beam transfer from horizontal into a vertical

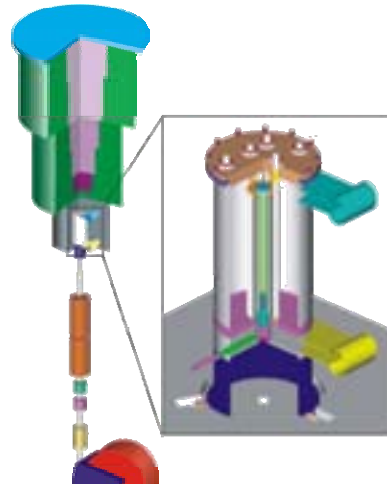


Figure 5: A scheme of vertical injection of the proton beam into SAD-core

plane, entering from the bottom of the core, will be realised using two strong bending magnets which have to be designed and constructed – see Fig. 5

The total number of magnetic elements in the beam line is about 40 including diagnostic elements and correction magnets. Beam current and spatial distribution will be monitored at different places along beam line using inductive sensors, ionization chambers and profilers. Beam current will be measured with high precision giving possibility for precise experimental monitoring of the core power to beam current ratio.

#### 5. Status of the SAD project

The technical design of the SAD facility has been completed, the safety analysis report is under preparation, the technology of fuel pellet fabrication has been adopted and the experimental batch of fuel pellets has been manufactured.

## 6. Conclusion

The SAD project is in principle ready for licensing and realization. If no unexpected troubles appear the first proton can be shot on the spallation target in 4 years from now.

Research program and supporting experiments which are being conducted are described in a separate paper [12].

## Acknowledgments

The SAD project is supported by the International Science and Technology Centre (project #2267) and is conducted in a close collaboration with the European partners: Kungliga Tekniska Högskolan, Stockholm, CEA - Cadarache, FZK – Karlsruhe and CIEMAT – Madrid.

## References

- [1] Waclaw Gudowski, "Accelerator-driven Transmutation Projects. The Importance of Nuclear Physics Research for Waste Transmutation", Nuclear Physics A654 (1999) 436.
- [2] Dzhelepov V.P, Satarov V.I and Golovin B.M. "Total cross sections for neutrons at 590 MeV interaction with nucleus of some elements", ZhETP 29 N3 (1955) 369
- [3] Vasilkov V.G., Goldansky V.I, Dzhelepov V.P. and Dmitrievsky V.P, "Electronuclear method of neutron generation and fissile materials production", Atomic Energy 29 N3 (1970) 151.
- [4] Chultem D. a.o, "Measurement of the Neutron Component in a Shower Generated in a Lead Target by Relativistic Nuclear Beam", Nucl. Instr. Meth. Phys. Res. A381 N2,3 (1996) 488
- [5] Bamblevski V.P. a.o, "The Investigation of the Radiation Field around the Thick Lead Target Irradiated by the 650 MeV Protons. Part 1. The Neutron Spectra Measurement around the Target", Dubna, 2000. JINR E1-2000-307
- [6] Bamblevski V.P. a.o, "The Investigation of the Radiation Field around the Thick Lead Target Irradiated by the 650 MeV Protons. Part 2. The Measurements of the Angular and Spatial Distributions of the Hadron's Yield from the Target", Dubna, 2000, JINR E1-2000-308
- [7] Barashenkov V. S., Zheregi F. G. and Musul'manbekov Zh. Zh., "The Cascade Mechanism of Inelastic Interactions of High-Energy Nuclei", Yad. Fiz. 39 (1984) 1133, [Sov. J. Nucl. Phys. 39, 715–716 (1984)]
- [8] Vorozhtsov S.B., Shakun N.G., "Orbit Parameters in the Central Region of the JINR Phasotron. Microbunch Acceleration." (In Russian) Dubna JINR, JINR-P9-83-658, Sep 1983, 8pp.
- [9] Moses D.L. a.o., "Plutonium disposition in the BN-600 fast-neutron reactor at the Beloyarsk nuclear power plant", Nucl. Instr. Meth. Phys. Res. A414 (1998) 28-35
- [10] J.F. Briesmeister (Ed.). "MCNP - A General Monte Carlo N-Particle Transport Code". Report LA-12625-M, Los-Alamos National Laboratory, New Mexico, USA.
- [11] L. S. WATERS, "MCNPXTM User's Manual – Version 2.1.5," Los Alamos National Laboratory, November 14, (1999). See also <http://mcnpx.lanl.gov>
- [12] W. Gudowski et al, The Subcritical Assembly in Dubna (SAD) – Part II: Research Program for ADS-Demo Experiment, AccApp-05, Venice, August 28 – September 3, 2005



# The Subcritical Assembly in Dubna (SAD) – Part II: Research Program for ADS-Demo Experiment.

Waclaw Gudowski <sup>a1</sup>, Valery Shvetsov <sup>b</sup>, Aleksander Polanski <sup>b</sup>, Cornelis Broeders <sup>c</sup>

<sup>a</sup> *Kungliga Tekniska Högskolan, 106 91 Stockholm, Sweden*

<sup>b</sup> *Joint Institute for Nuclear Research, 141980 Dubna, Russia*

<sup>c</sup> *Forschungszentrum Karlsruhe, 76021 Karlsruhe, Germany*

**Elsevier use only:** Received date here; revised date here; accepted date here

---

## Abstract

Subcritical Assembly in Dubna (SAD), a project funded by the International Science and Technology Centre, driven in collaboration with many European partners, may become the first Accelerator Driven Subcritical experiment coupling an existing proton accelerator of 660 MeV with a compact MQX-fuelled subcritical core. The main objective of the SAD experiment is to study physics of ADS ranging from a very deep subcriticality up to  $k_{eff}$  of 0.98. All experiences with subcriticality monitoring from previous subcritical experiments like MUSE, Yalina and IBR-30 booster mode will be verified in order to select the most reliable subcriticality monitoring technique. Particular attention will be given to validation of the core power/beam current relation. Moreover some studies have been done to assess possibility of power upgrade for SAD.

*Keywords:* Accelerator Driven System; subcritical reactors; Subcritical Assembly in Dubna; SAD; Transmutation

*PACS:* 28.50.Dr; 28.50.Qd; 28.41; 28.52

---

## 1. Introduction

The Subcritical Assembly in Dubna (SAD) may become the first Accelerator Driven System (ADS) coupling an existing 660 MeV proton accelerator at the Joint Institute for Nuclear Research (JINR) in Dubna with a specially designed compact MOX-fuelled subcritical core.

SAD is today in an advanced design stage, in parallel with manufacturing of the first fuel pellets

and conducting many supporting experiments. The design of the SAD is based on the core with a nominal power up to 30 kW, multiplication coefficient  $k_{eff}=0.95$  and accelerator beam power of 1 kW. Details of SAD design are presented in a separate paper [1].

---

<sup>1</sup> Corresponding Author: Waclaw Gudowski, tel. +46 8 5537 82 00, email: wacek@neutron.kth.se

## 2. Key parameters of SAD and supporting experiments

A lot of simulations using MCNPX [2] and LAHET [3] codes have been performed in order to choose optimal parameters for SAD [4],[5],[6]. Different combinations of the target, fuel and reflector materials have been considered. In particular thermal power the subcritical core driven with 1 kW proton beam has been studied in as a function of  $k_{eff}$ , as presented on Fig 1, [7].

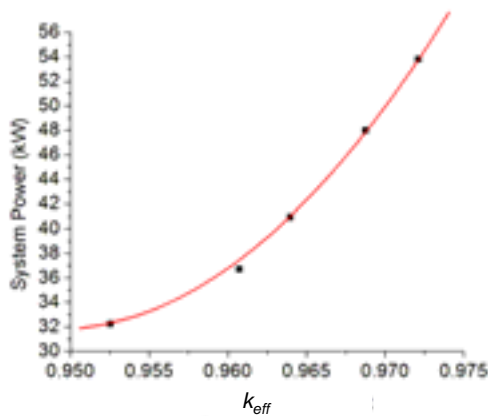


Fig.1. SAD power as function of  $k_{eff}$  for 1 kW proton beam power.

We can find from Fig. 1 that at an average power gain – defined as a ratio of the power generated in the core to the proton beam power - is  $G=30$  for  $k_{eff}=0.952$  and  $G=50$  for  $k_{eff}=0.972$ .

Fig. 2 shows the neutron flux in experimental channel per 1 kW proton beam as a function of  $k_{eff}$ .

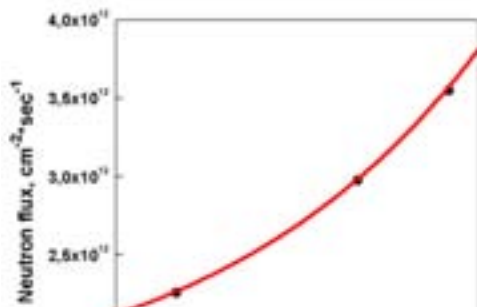


Fig.2. Dependence of the neutron flux in the experimental channel on  $k_{eff}$ .

Maximum neutron flux in the experimental channel near the target reaches  $2.26 \cdot 10^{12} \text{ cm}^{-2} \text{ s}^{-1}$ , for  $k_{eff} = 0.952$  and  $3.55 \cdot 10^{12} \text{ cm}^{-2} \text{ s}^{-1}$  for  $k_{eff} = 0.972$ .

### 2.1. Heat generation and neutron flux in the target and experimental channels for different target materials and different position of the target in the subcritical assembly.

Particular attention in SAD research program will be given to validation of the core power/beam current relationship as the main tool of monitoring subcriticality of this facility.

Beam current and shape will be monitored at different locations along beam line using inductive sensors, ionization chambers and profilometers. Beam profile will be measured with high precision. Al activation detectors, matrix of thermoluminescent detectors and profilometer will be used based on the existing experiences from accelerator operation.

The shape of the measured average proton beam profile is presented on Fig.3, [8].

Power level of SAD will be monitored in two dedicated channels with 3 neutron sensors (high sensitivity fission chamber, low sensitivity fission chamber; boron current chamber). Additional neutron detectors may also be installed in SAD experimental channels. SAD has been designed from the very beginning to be a high precision validation test-bed for ADS simulation codes. Each fuel element - a weapon grade Pu-MOX, will have its own certificate with a precise fuel isotopic content. Constructional materials also will be certified. It will give a unique possibility for precise modeling of this subcritical assembly and code benchmarking/validation activities.

To measure spatial and energy characteristics of the neutron field inside the subcritical assembly the target and the core will be instrumented with threshold activation detectors (foils). To investigate high energy part of the neutron spectrum absolute reaction rates will be determined for foils of  $^{12}\text{C}$ ,  $^{27}\text{Al}$ ,  $^{59}\text{Co}$ ,  $^{63}\text{Cu}$ ,  $^{115}\text{In}$ ,  $^{197}\text{Au}$ ,  $^{209}\text{Bi}$ .

A multicomponent alloy  $^{55}\text{Mn} + ^{63}\text{Cu} + ^{197}\text{Au} + ^{176}\text{Lu}$  will be also used for measurements (n, $\gamma$ ) reaction rates in thermal and resonance energy region (up to 1 MeV).

The following spectral indices will be measured using  $^{235}\text{U}$ ,  $^{239}\text{Pu}$ , and  $^{238}\text{U}$ :

- $^{235}\text{U}(n,f)/^{238}\text{U}(n,\gamma)$ ;
- $^{239}\text{Pu}(n,f)/^{235}\text{U}(n,f)$ ;
- $^{238}\text{U}(n,f)/^{235}\text{U}(n,f)$ .

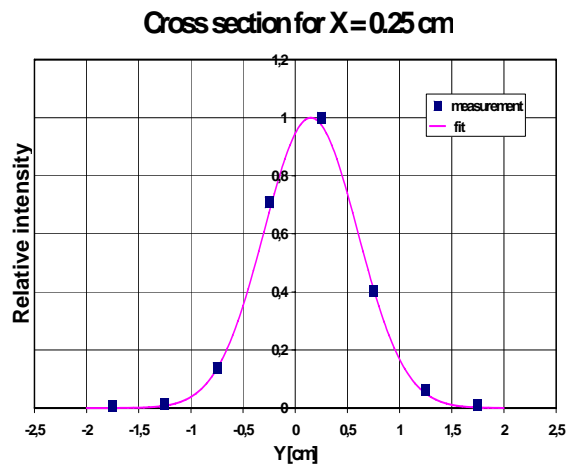
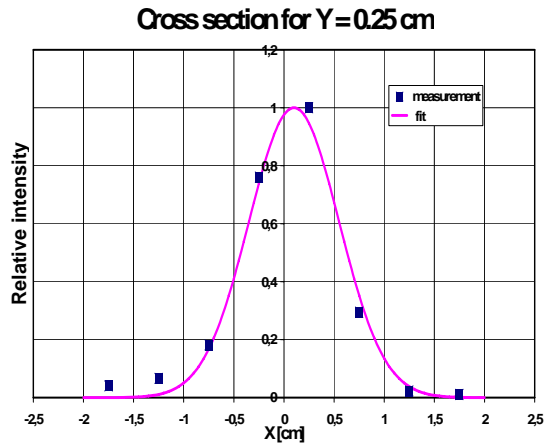


Fig. 3 Average proton beam profile.

It is also planned to instrument the spallation target with devices registering spallation product yields in combined proton/neutron field. In particular a helium loop passing through the target at different distances from the beam entrance point will be designed and created. Recoiled spallation products will penetrate the helium loop and will pass with a stream of He to the gamma-spectroscopy setup analyzing isotope composition and absolute values of

activities of spallation products. Extremely small passage time (1–5 seconds) permits to measure short-lived products with a good accuracy.

2.2. Radioactivity induced in the spallation target.

SAD will have a replaceable spallation target, Pb and W options are foreseen with different sizes, changeable proton spot-point and different beam Fission rates actinides will be measured at SAD for different isotopes. For fission products (FP) detection the dielectric (glass) track detectors (SSNTD) will be used taking advantage of their insensitivity to types of radiation. In each measurement one array containing studied isotope and track detector will be placed in designated locations inside the core together with similar array consisting of track detector and monitoring isotope ( $^{235}\text{U}$  or  $^{239}\text{Pu}$ ).

shapes.

In order to prepare accurate experimental technique for SAD, preliminary measurements have been performed using activation detectors of  $^{12}\text{C}$ ,  $^{27}\text{Al}$ ,  $^{59}\text{Co}$ ,  $^{63}\text{Cu}$ ,  $^{115}\text{In}$ ,  $^{197}\text{Au}$ ,  $^{209}\text{Bi}$  with Pb and W targets.

Activation measurements compared with simulation results for distribution of hadrons along the Pb-spallation target are presented in Fig. 4, [9].

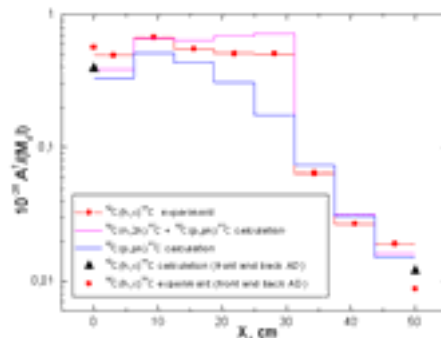


Fig. 4 Distribution of specific radioactivity of the C detectors located on a surface of a Pb target

For quantitative evaluation some nuclides were selected to study their axial distributions inside the Pb target. The results for  $^{210}\text{Po}$  are presented in the Fig. 5.



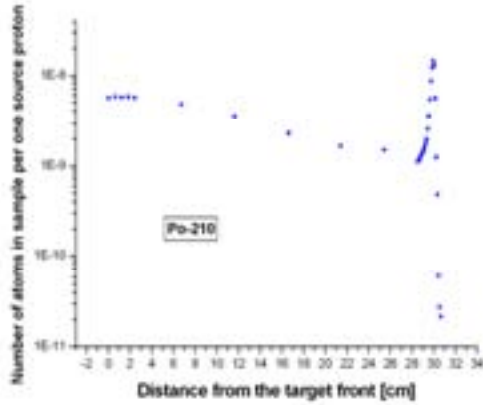


Fig. 5 Distributions of the  $^{210}\text{Po}$  activity in  $^{209}\text{Bi}$  samples along the Pb target irradiated with 660 MeV protons.

### 2.3. Kinetics of SAD

One of the most important tasks for studies of subcritical systems is measurement and monitoring of reactivity in particular in deep subcriticality.

Special experiments are foreseen on the existing Fast Neutron Pile (BFS in Obninsk) in SAD-like configuration with a small pulsed neutron generator (PNG -  $10^8$  n/s, 1  $\mu\text{s}$  pulse width, 20 Hz repetition rate). Experiments will be performed starting from reference critical configuration down to a deep subcriticality. Based on these experiments an experimental technique will be developed accumulating all experiences from MUSE, YALINA subcritical experiments and JINR experiments with IBR-30 booster. The experimental technique developed during experiments on BFS will be transferred directly to the SAD facility and applied during the physical start-up.

### 3. Radiation protection and shielding aspects of high energy neutrons and protons

Spallation neutron source driven by 660 MeV proton beam generates neutrons with energy up to impinging proton energy and therefore requires special attention to be paid to shielding aspects. Those high energy neutrons emerging from the spallation target create new challenges for radiation shielding.

There are some options considered for radiation shielding experiments.

1) Activation methods using the simple reactions, such as  $^{209}\text{Bi}(n, xn)^{209-x}\text{Bi}$ ,  $^{27}\text{Al}(n, \alpha)^{24}\text{Na}$  and spallation products on  $^{197}\text{Au}$  target.

2) For measurements of neutron spectrum and attenuation of high energy neutrons, activation detectors are foreseen in slots in the concrete shield at different locations

3) For measurement of high energy neutron spectrum behind the shield proton recoil method is considered..

4) ..as well Bonner spheres can be used.

An example of measurements of neutron spectra around the Pb target with Bonner spheres method is presented in Fig 6, [10].

The details of this experiment do not fit into the frame of this publication but it can be concluded that differences between various high-energy transport models used in LAHET and MCNPX codes seem to be very small for this type of experiments and much more refined measurements and better statistics in simulations are needed to make any conclusions concerning the performance of the specific models. This is in principle a good message for those who

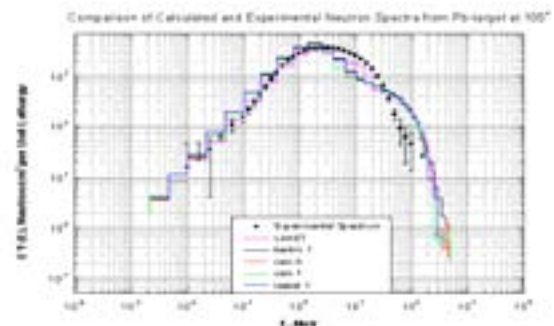


Fig. 6 Comparison of experimental results of the neutron spectra measurements at the specified angle with computer simulations of LAHET and MCNPX using different options for high-energy interactions

simulate accelerator - driven systems i.e. - neutron yields and their spectra in high-energy region are not very sensitive on different models used for high-energy transport simulations.

#### 4. Conclusions

SAD facility if aggressively pursued may be operational in 4 years opening new experimental possibilities for the international ADS community. Moreover, the experimental program of SAD is well adjusted to the objectives of the European Project "Eurotrans" and may significantly contribute to this project.

A lot of supporting experiments have already been conducted and produced valuable data.

#### Acknowledgments

The SAD project is supported by the International Science and Technology Centre (project #2267) and is conducted in a close collaboration with the European partners: Kungliga Tekniska Högskolan, Stockholm, CEA - Cadarache, FZK – Karlsruhe and CIEMAT – Madrid.

#### References

[1] V. Shvetsov et al., The Subcritical Assembly in DUBNA (SAD) – Part I: Coupling all Major Components of an Accelerator Driven System (ADS), AccApp-05, Venice, August 28 – September 3, 2005

[2] Waters, L. S., "MCNPXTM User's Manual – Version 2.1.5," Los Alamos National Laboratory, November 14, (1999)

[3] R.E. Prael, H. Lichtenstein. "User Guide to LCS: The LAHET Code System". Report LA-UR- 89-3014, Los-Alamos National Laboratory, New-Mexico, USA .

[4] P. Seltborg et al, The investigation of the Radiation Field of the Experimental Subcritical Assembly in Dubna, International Conference on Radiation Shielding ICRS-10, May 9-14 2004, Funchal, Madeira Island, Portugal (2004).

[5] A. Polanski, Monte Carlo Modeling of Electronuclear Processes in Experimental Accelerator Driven Systems, Acta Phys. Polonica, Vol. B11, No.1, p. 95,2000.

[6] V.S. Barashenkov, I.V. Puzynin A.Polanski, Mathematical Experiments with Electronuclear Systems, Journal of Computational Methods in Science and Engineering, vol2, no1-2,2002, pp5-11 ISSN 1472-7978.

[7] A. Polanski, C. Broeders, W. Gudowski, S. Petrochenkov, Possible extension of experimental program. Increase of system power to maximum 100 kW. Materials of the Workshops on ISTC Project No 2267 and SAD/YALINA Steering Committee, 24-25 January 2005, Dubna, JINR CD-ROM.

[8] W. Pohorecki, Horwacik T., Janczyszyn J., Taczanowski S., Bamblevski V.P., Gustov S.A., Mirokhin I.V., Molokanov A.G., Polanski A., Spatial Distributions of Residuals Production Inside a Spallation Target, Proceedings of the Conference ICRS-10 - RPS 2004. Madeira Island (Portugal) from 9-14 May 2004, J. Radiation Protection in press.

[9] Bamblevski V.P., Krylov A.R., Polanski A., Timoshenko G.N., Shvetsov V.N., The Investigation of the Radiation Field Around the Thick Lead Target Irradiated by the 650 MeV Protons. Part 2. The Measurement of the Angular and Spatial Distributions of the Hadron's Yield from the Target, Preprint JINR E1-2000-308, Dubna, 2000.

[10] V.P. Bamblevski, Gudowski W., Krylov A.R., Polanski A., Timoshenko G.N., Shvetsov V.N., The Investigation of the Radiation Field Around the Thick Lead Target Irradiated by the 650 MeV Protons. Part 1, JINR Report E1- 2000 - 307, Dubna ,2000.



ASSEMBLÉE  
NATIONALE

RÉPUBLIQUE FRANÇAISE  
LIBERTÉ-ÉGALITÉ-FRATERNITÉ

OFFICE PARLEMENTAIRE  
D'ÉVALUATION DES CHOIX  
SCIENTIFIQUES ET  
TECHNOLOGIQUES

Paris, 6 December 2004

Dear Professor Gudowski,

Our report on the 'progress and prospects of research on the management of radioactive wastes' for the Parliamentary Office for Science and Technology Assessment (Office parlementaire d'évaluation des choix scientifiques et technologiques), is nearly completed.

As you know, it was the National Assembly Bureau which, at the initiative of the chairmen of the four political groups, vested the Office with the conduct of a study on this subject of major importance both for the future of the French nuclear power industry and for opinion.

Parliament played a decisive role in drafting and passing the Act of 30 December 1991 on research on the management of radioactive wastes.

We feel its role will also be decisive in 2006, the date laid down by the 1991 Act to examine a report on the progress of research and discuss a new Bill setting forth new stages.

In accordance with the methods of the Office, at end January 2005 we will organise public hearings in Paris to which we would like to give a high profile and which will meet the expectation of wide swaths of society. **Three full days of public hearings open to the press will therefore be held in Paris, at the very beginning of the coming year.**

We are writing to invite you to participate in the Thursday 20 January 2005 hearings to present in English the situation in your country and to participate in our discussions which will be interpreted simultaneously in English and French and placed online in real time on the Internet and recorded as a DVD.

We are convinced that with your help these public hearings will usefully contribute to the prior dialogue which is essential in defining consensual and lasting solutions for the back end of the nuclear cycle.

Yours faithfully,



Christian BATAILLE  
Deputy, Nord



Claude BIRRAUX  
Deputy, Haute Savoie

**Professor Waclaw GUDOWSKI**  
**KTH**  
**Alba Nova University Centre**  
**SE-106 91 STOCKHOLM**  
**SUEDE**

*Please contact the Opecst secretariat – Mr Gaillochet 33 1 01 40 63 97 85 [pgaillochet@assemblee-nationale.fr](mailto:pgaillochet@assemblee-nationale.fr)  
– for further information*

*Préparation du rapport sur  
l'état d'avancement et les perspectives des  
recherches  
relatives à la gestion des déchets radioactifs*

**AUDITIONS PUBLIQUES OUVERTES À LA PRESSE**

*organisées par*



*Christian BATAILLE,  
Député du Nord,  
Rapporteur*



*Claude BIRRAUX,  
Député de la Haute-Savoie,  
Rapporteur*

**Jeudi 20 janvier 2005 : 9h - 18h**

**La séparation et la transmutation  
- Axe 1 de la loi du 30 décembre 1991 -  
Liste des participants**

*Mise à jour du mardi 11 janvier 2005*

*Assemblée nationale - Salle Lamartine - 101 rue de l'Université Paris 7<sup>ème</sup>*



**Jeudi 20 janvier 2005 – 9h-18h**  
**La séparation et la transmutation**  
**- Axe 1 de la loi du 30 décembre 1991 -**

*LISTE DES PARTICIPANTS -*

*Mise à jour du mardi 11 janvier 2005*

**1. Orateurs dont la présence est confirmée**

***BELGIQUE***

M. Paul GOVAERTS

Directeur général du SCK-CEN

M. H. Aït ABDERRAHIM

Chef du projet MYRRHA

***ETATS-UNIS***

Dr Herman GRUNDER

Directeur du Laboratoire national d'Argonne

Dr H. PASAMEHMETOGLU

Laboratoire national d'Idaho - Advanced Fuel Cycle Initiative (AFCI)/Generation IV National Technical Director for Fuels

***ITALIE***

Professeur Carlo RUBBIA

Prix Nobel de physique

***SUEDE***

Professeur Waclaw GUIDOWSKI

KTH – Institut Royal Polytechnique de Stockholm

***FRANCE***

**MINISTÈRE DÉLÉGUÉ À LA RECHERCHE**

M. François d'AUBERT

Ministre délégué à la recherche

**AREVA**

Mme Anne LAUVERGEON

Présidente du Directoire

M. Philippe GARDERET

Directeur de la recherche et de l'innovation

**CEA**

M. Alain BUGAT

Administrateur général

M. Bernard BIGOT

Haut Commissaire à l'énergie atomique

M. Philippe PRADEL

Directeur de l'énergie nucléaire

M. Bernard BOULLIS

Chef du Département radiochimie et procédés

Mme Sylvie PILLON

Chef du Département transmutation

M. Jean-Pierre VIGOUROUX

Chargé des relations avec le Parlement

**COMMISSION NATIONALE D'ÉVALUATION**

M. Bernard TISSOT

Président

**CNRS**

M. Michel SPIRO

Directeur de l'IN2P3

M. Sydney GALÈS

Directeur adjoint scientifique de l'IN2P3

M. Christian LEBRUN

Responsable du programme GEDEPEON

M. Hubert DOUBRE

Responsable du programme PACE (Programme sur l'aval du cycle électronucléaire)

M. Sylvain DAVID

Systèmes innovants réacteurs

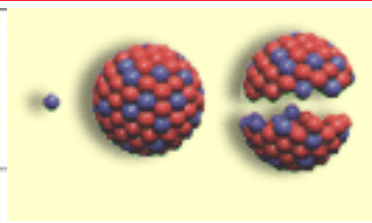
**DGEMP**

Mme Sophie GALEY-LERUSTE

Directrice des ressources énergétiques et minérales

Mme Florence FOUQUET

Chargée de la sous-direction de l'industrie nucléaire



**Jeudi 20 janvier 2005 – 9h-18h**  
**La séparation et la transmutation**  
**- Axe 1 de la loi du 30 décembre 1991 -**

**DGSNR**

M. André-Claude LACOSTE

Directeur général de la sûreté nucléaire et de la radioprotection

**EDF**

M. Bernard DUPRAZ

Directeur général adjoint – production, ingénierie

M. Daniel LEROY

Directeur du combustible

M. Bertrand LE THIEC

Chargé des relations avec le Parlement

**IRSN**

M. Jacques REPUSSARD

Directeur général

Mme Michèle VIALA

Directrice du programme « gestion des déchets »

**DIRECTION DE LA TECHNOLOGIE - MINISTÈRE DÉLÉGUÉ A LA RECHERCHE**

M. Bernard FROIS

Directeur du département énergie, transport, environnement, ressources naturelles

**2. Participants dont la présence est confirmée****PARLEMENT**

M. Henri REVOL

Sénateur de la Côte d'Or, Président de l'Office parlementaire d'évaluation des choix scientifiques et technologiques (OPECST)

M. Roland COURTEAU

Sénateur de l'Aude

M. François-Michel GONNOT

Député de l'Oise

M. Bruno SIDO

Sénateur de la Haute-Marne, Membre de l'OPECST, Président du Conseil général de la Haute-Marne

**AEN-OCDE**

M. Claudio PESCATORE, Chef-adjoint, division de gestion des déchets radioactifs

**ANDRA**

M. Paul RIGNY, Conseiller scientifique

**ASSEMBLEE NATIONALE**

M. Eric HEITZ, Chargé de mission Présidence AN

**ASSOCIATIONS DE PROTECTION DE L'ENVIRONNEMENT**

Mme Monique SENÉ, GSIEN

**CEA**

Mme BALBAUD-CELERIER, DDIN

Mme Fanny BAZILE, Directrice prospective et communication, Saclay

Mme BOHAR, Assistante du Directeur de l'énergie nucléaire

M. Jean CAZALET, Directeur adjoint développement et innovation nucléaires

M. Giin ERMONT, Inspecteur nucléaire



**Jeudi 20 janvier 2005 – 9h-18h**  
**La séparation et la transmutation**  
**- Axe 1 de la loi du 30 décembre 1991 -**

Mme Lydie LEYVAL, Auditrice  
 M. Thierry LIEVEN, Saclay  
 M. Jean-Claude PETIT, Directeur de programme  
 Mme Annie RIVOALLAN, Chargée de mission énergie nucléaire  
 M. MARTIN-DEDIER, Directeur du CEA/Valrho  
 M. Dominique WARIN, Chef de projet  
 M. Alain REGENT, Chef du cabinet du Haut Commissaire  
 Mme Michèle TALLEC, DDIN

**CITE DES SCIENCES ET DE L'INDUSTRIE**

Mme Marie-Pierre HERMANN, Chef du département veille technologique  
 Mme Brigitte PAGES, Chargée de mission

**CNRS**

M. Jean-Claude LE SCORNET, IN2P3

**COLLECTIVITES LOCALES**

M. Eric CHAGNEAU, Directeur du GIP Meuse  
 M. Jean MASSON, Directeur du GIP Haute Marne

**COMMISSION NATIONALE D'EVALUATION (CNE)**

M. Robert GUILLAUMONT, Membre de la Commission nationale d'évaluation  
 M. Jacques LAFUMA, Membre de la Commission nationale d'évaluation  
 M. Jean-Claude LEFEVRE, Membre de la Commission nationale d'évaluation  
 M. Jean-Claude SCHAPIRA, Membre de la Commission nationale d'évaluation  
 M. Rémi PORTAL, Secrétaire scientifique de la CNE

**DGEMP, Sous-direction de l'industrie nucléaire**

M. Arnaud LOCUFIER  
 M. Philippe PIERRARD

M. Cyrille VINCENT

**ECRIN**

M. Christian NGÔ, Délégué général

**EXPERTS INDEPENDANTS**

M. Pierre BACHER, Ancien directeur technique d'EDF

**INSTITUT DE PHYSIQUE NUCLEAIRE**

M. Alex MUELLER

**MISSION DE COORDINATION IMPLANTATION LABORATOIRES SOUTERRAINS**

M. Bernard FÉRY, Coordonnateur

**SYNDICATS**

Mme Michèle LE PELLEC, Fédération CFTC

M. Edouard CAHEN, Secrétaire fédéral FO

**3. Représentants de la presse et des médias dont la présence est confirmée**

Mme Anne de BECCO, La Correspondance nucléaire  
 M. Bruno BUCHE, France 3, Magazine « *C'est pas sorcier* »  
 Mme Julie CHAUVEAU, Les Echos  
 M. Guy CLAVEL, AFP  
 M. Xavier COEYTAUX, Wise Paris  
 M. Patrice COLLEN, AFP  
 Mme Nicole FOUCHÉ, Revue générale nucléaire  
 M. François GERVAIS, Lettre « *Horizons politiques* »  
 Maël KNOLL, Biofutur  
 M. Valéry LARAMEE, Enerpresse  
 M. Bernard LE SOLLEU, OUEST FRANCE  
 Mme Ann McLACHLAN, Nucleonics Week  
 M. Yves MARIIGNAC, Wise Paris  
 Mme Guitta PESSIS-PASTERNAK, journaliste scientifique  
 M. Adrien WILLOT, Industries

*Mise à jour du mardi 11 janvier 2005*



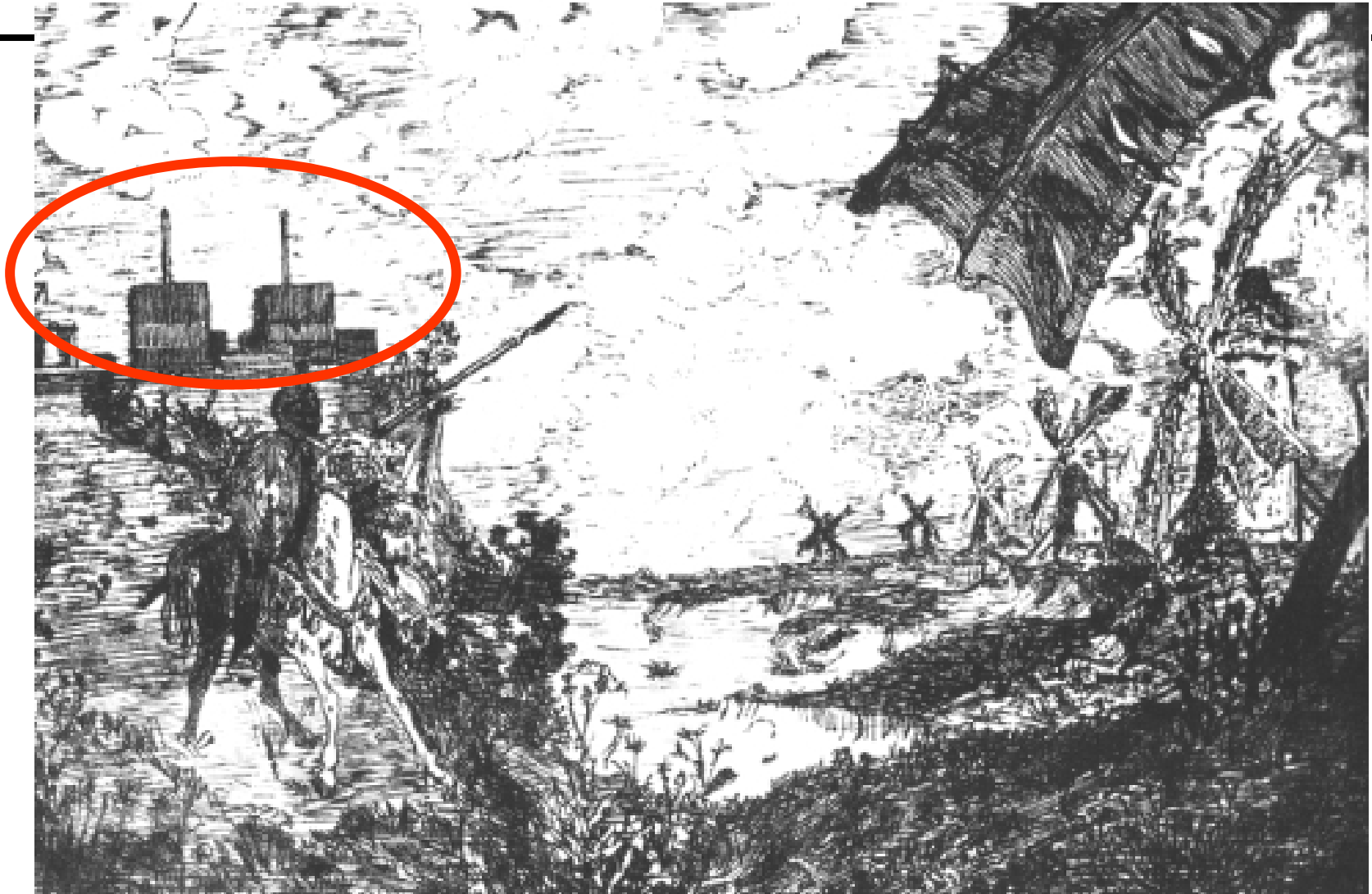
# Optimizing the Nuclear Fuel Cycle by means of Partitioning/Conditioning and/or Transmutation

*Prof. Waclaw Gudowski  
Dept. of Nuclear and Reactor Physics  
Royal Institute of Technology  
Stockholm*





I am neither Don Kichot fighting against  
wind mills..



..nor dr Strangelove being non-critically fascinated with nuclear...



....nor I am a Nobel Prize Winner  
...yet...

However, I have done transmutation  
related research since 1991 and  
conducted a lot of large research projects  
in this field



# Some pre-declarations for this talk..



# Pre-declarations

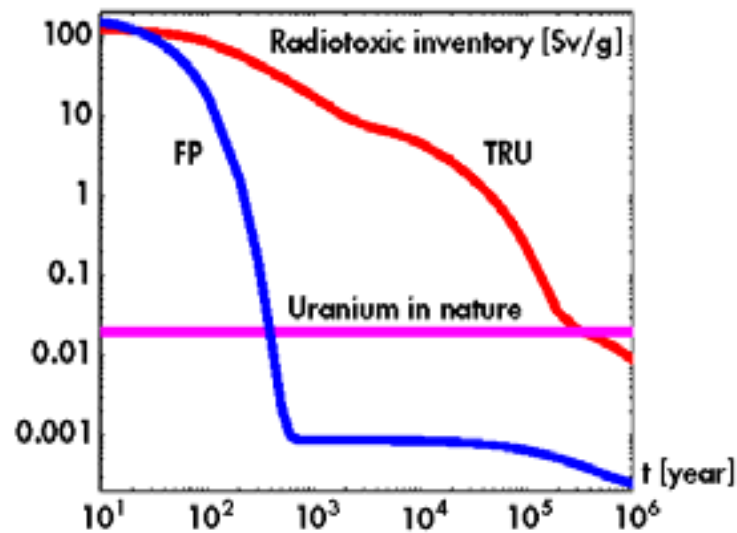
---

**We need TRANSMUTATION and/or BREEDING not because we do not like Geological Repositories but BECAUSE IT IS THE ONLY WAY TO MAKE NUCLEAR ENERGY REALLY SUSTAINABLE and consequently to make it more acceptable**



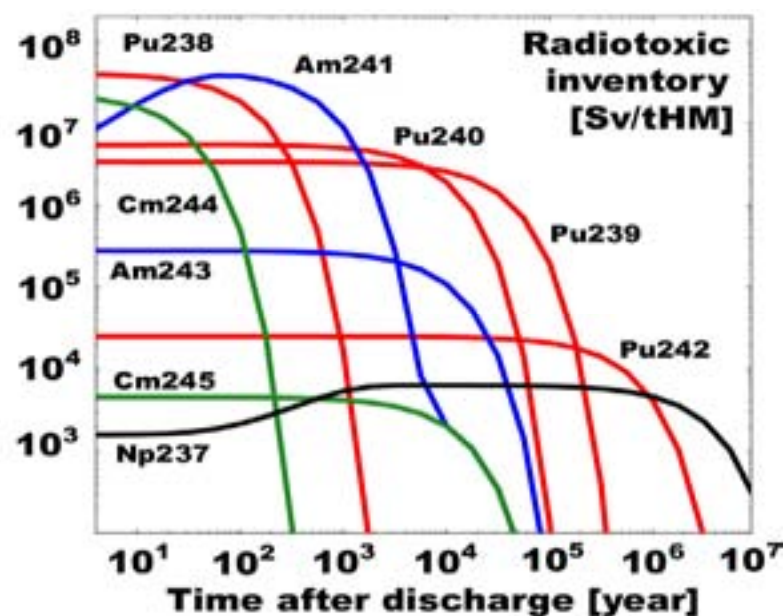
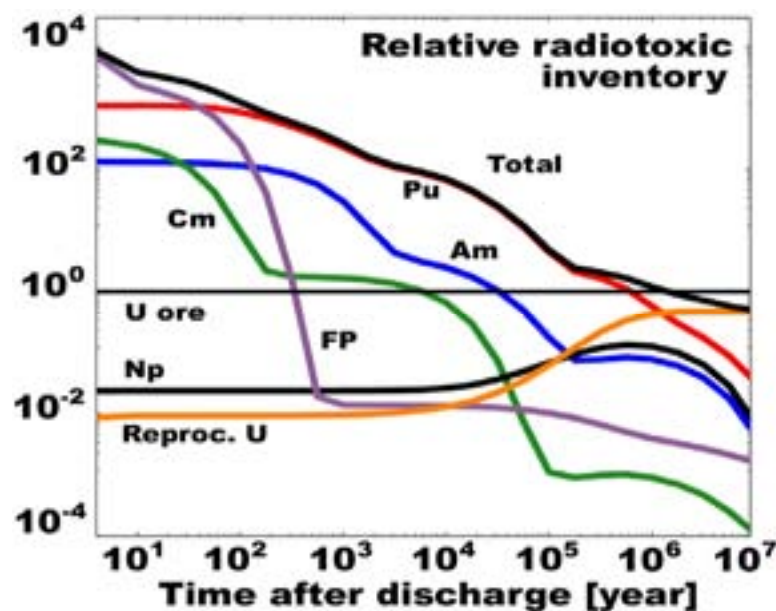
# Pre-declarations

- Concerns related to Geological Repositories are today much more of **SOCIO-POLITICAL** and **ETHICAL** character than **TECHNICAL ONE**.



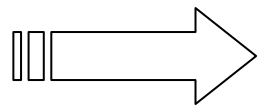
# Objectives of P&T

Objective is a maximum reduction of radiotoxic inventory of spent fuel (repository source term), if a factor of **100** is to be achieved **Pu**, **Am** and **Cm** have to be transmuted



# Partitioning and Transmutation

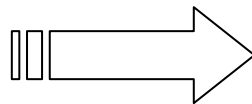
**GOAL:** maximum net consumption of TRU (and possibly FP)



limited content or no U-238 → no *breeding*

fast reactor spectrum → high *fission-to-absorption ratios*

**Problems to solve:** deterioration of neutronic and kinetic parameters, i.e. deterioration of safety



- moderator void and temperature coefficient
- fuel temperature coefficient (Doppler constant  $K_D$ )
- (effective) delayed neutron fraction ( $\beta$ ,  $\beta_{\text{eff}}$ )
- neutron lifetimes ( $\tau$ )





We can today do or we know how to do efficiently  
Partitioning (Separation) on the level of required  
**0.1% efficiency**

**CAN WE EQUALLY WELL  
TRANSMUTATION?**

**The answer is: “NO”, but we know there are no  
OBVIOUS SHOW STOPPERS!**



# Fuel cycle analysis ...

---

- ... is a pretty complicated endeavor. A lot of studies have been done, a lot of projects have been devoted to this research:
  - **Most recent** – European Project RED-IMPACT – Impact of Transmutation and Reduction/Conditioning of Nuclear Waste on Final Waste Repository. Final report will be delivered in March 2007!
  - A very good Status Report was recently published by the Swedish SKB, “Partitioning and Transmutation. Current developments – 2004”, Report TR-04-15, <http://www.skb.se>



**BUT.....**  
**First estimations are easy...**



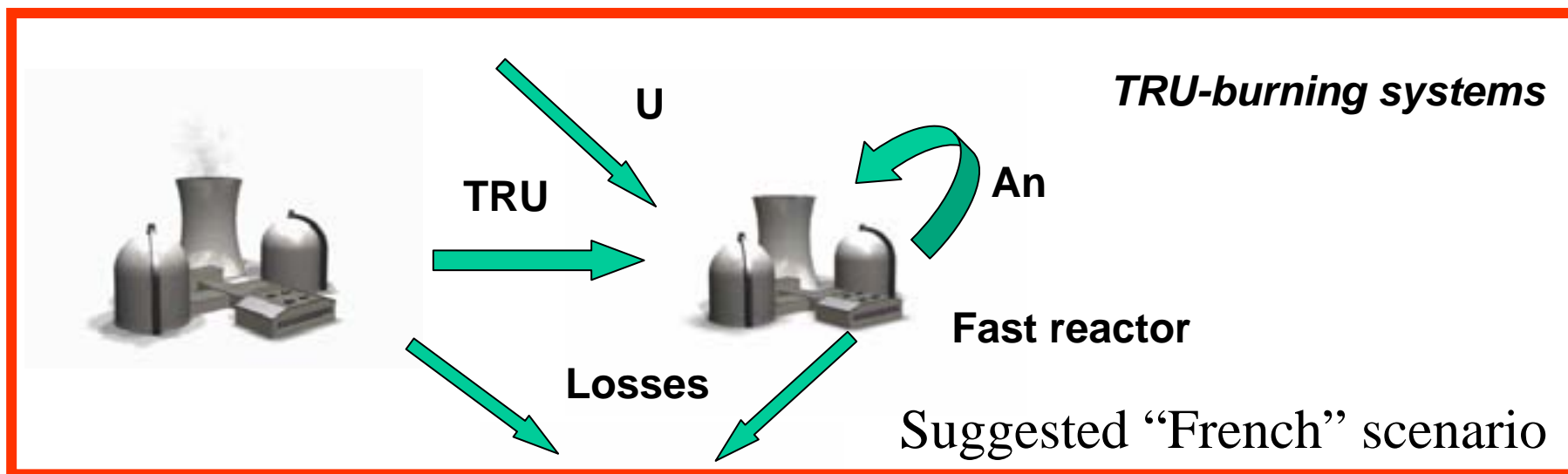
# Fuel cycle analysis for LAYMEN:

---

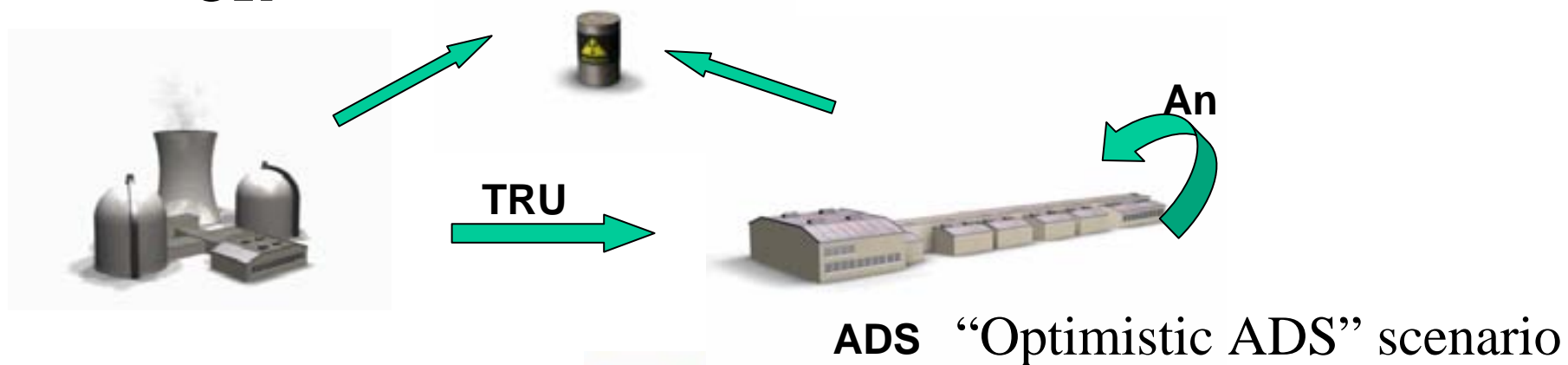
- Transmutation/reactor system burns 100kg/year of Heavy Metals in 300 MWth of power
- Feasible burnup of the fuel is **5%** of HM for “regular” systems and up to **20%** in very advanced systems (impossible in critical reactors), it means that we need an inventory 5 to 20 times larger than an annual consumption, i.e. 500 to 2000 kg for 300 MWth of power.
- Having inventory of 1000 of tons ( $10^6$  kg) of HM we shall need MANY, MANY, MANY reactor/ADS\*years to get rid of this inventory.
- “In equilibrium” we need about 1 ADS per 4-5 LWRs or 1 per ~20 Fast Reactors to burn produced HM wastes
- **BUT AT THE SAME TIME WE PRODUCE AND DELIVER ENERGY. NUCLEAR WASTE DOES NOT NEED TO BE VIEWED ONLY AS A LIABILITY.**



# Options for Advanced Nuclear Fuel Cycles

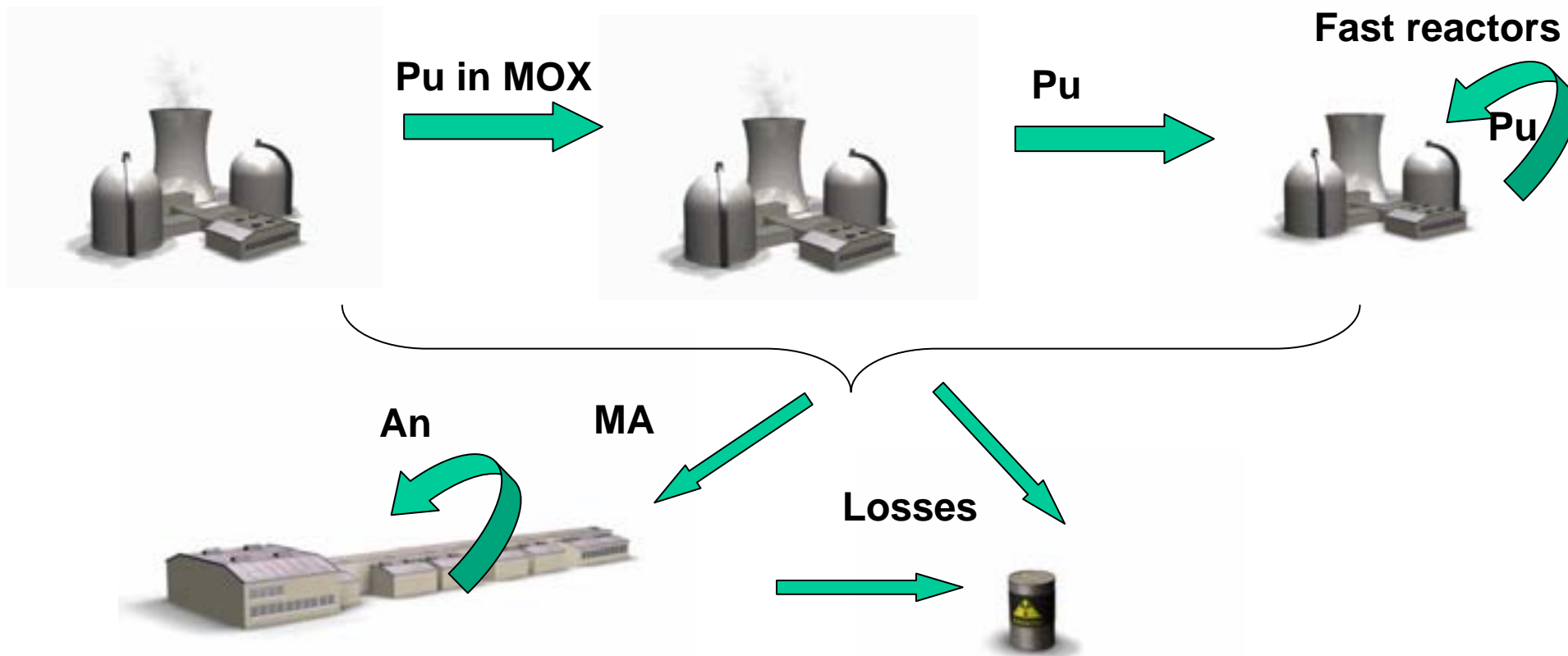


**OR**



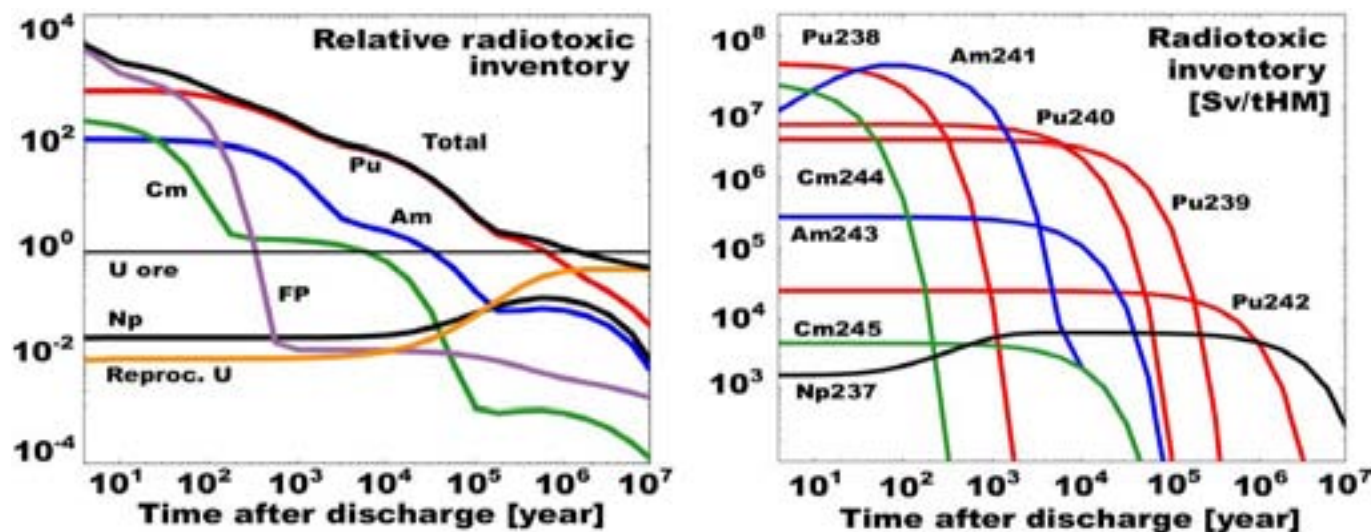
# A vision of the Most Advanced Fuel Cycle

## "Triple" Strata



# A vision of the Advanced Fuel Cycle:

It is not SUFFICIENT to recirculate and re-use (incinerate, burn, transmute – you name it) only Pu! One has to get rid of at least Americium and if feasible Curium and Np



Pu can be pretty efficiently (but slowly)  
burnt in critical reactors (FAST) but  
Am, Cm and Np NOT!

Ergo:

We need subcritical systems because of  
SAFETY and EFFICIENCY





# Positive conclusions of recent Fuel Cycle Analysis

---

*While P&T will **not eliminate** the need for appropriate geological disposal of high-level waste, different transmutation strategies could significantly reduce, i.e. a **hundred-fold**, the long-term radiotoxicity of the waste and thus improve the environmental friendliness of the nuclear energy option. P&T can significantly contribute to a sustainable nuclear energy system.*



# Positive conclusions of recent Fuel Cycle Analysis

---

- *Very effective fuel cycle strategies, including both fast spectrum transmutation systems (FR and/or ADS) and multiple recycling with very low losses (0.1%), are required to achieve **100-fold reduction of radiotoxicity**.*
- *The **pyrochemical reprocessing** techniques are essential for fuel cycles employing ADS and FRs where very high MA-content fuels are used.*
- *In strategies where Pu and MA are managed separately, **ADS can provide additional flexibility** by enabling Pu-consumption in conventional reactors and minimising the fraction of dedicated fast reactors in the nuclear system*



# Positive conclusions of recent Fuel Cycle Analysis

---

- Conditioning of the waste can have a significant impact on the final repository
  - Separate management of Cs and Sr can have a large impact on capacity of the geological repository
- We should not forget **NUCLEAR REACTOR** concepts minimising significantly **NUCLER WASTE**
  - E.g. dedicated Gas Cooled Graphite Reactors with amazing Pu-consumption potential and good safety features
  - Molten Salt Reactors
  - and last but not least – Thorium fuel cycle



# Answering some myths and arguments against transmutation

---

- Transmutation systems are **VERY EXPENSIVE** and required long development
- Answers:
  - Studies show that the cost of electricity will increase by 10 - 20% (the highest estimate 50%) compared to “once through” LWRs
  - The costs will be spread over long time and the major part should be looked upon as investments for energy production
  - Today’s LWRs were designed in 50s,60s (with a technological philosophy of those times), work and will work efficiently until 2030-2040. This is a very long term, efficient investment. After all this situation is valid for any power generation technology!
  - A cost of one ADS is not higher than the cost of **one week** of the “oil war” in Iraq (private and web estimates). **No more comments here!**



# Answering some myths and arguments against transmutation

---

Transmutation systems are **TECHNICALLY VERY COMPLICATED** and required long development

Answers:

- It is a long-term strategy for recycling and recovering energy from materials that otherwise are seen as very troublesome wastes.
- A successful development of **TRANSMUTATION SYSTEMS** decreases the requirements on the engineered barriers in the deep repository and also decrease the volumes needed for disposal of wastes. Compare those two time scales
- Having the same approach we should immediately abandon all work on **FUSION** systems. **No more comments here!**



I am leaving **conclusions** to the Honorable Audience and I hope my talk was not perceived even by the biggest opponents to nuclear as the H. Bosch painting..

